

Wind Energy Handbook

**Tony Burton • Nick Jenkins • Ervin Bossanyi
David Sharpe • Michael Graham**

THIRD EDITION

WILEY

Wind Energy Handbook

Wind Energy Handbook

Third Edition

Tony Burton

Wind Energy Consultant, London, UK

Nick Jenkins

Cardiff University, UK

Ervin Bossanyi

DNV GL, Bristol, UK

David Sharpe

Wind Energy Consultant, Essex, UK

Michael Graham

Imperial College, London, UK

WILEY

This third edition first published 2021
© 2021 John Wiley & Sons Ltd.

Edition History

John Wiley & Sons Ltd. (1e 2001; 2e 2011)

All rights reserved. No part of this publication may be reproduced, stored in a retrieval system, or transmitted, in any form or by any means, electronic, mechanical, photocopying, recording or otherwise, except as permitted by law. Advice on how to obtain permission to reuse material from this title is available at <http://www.wiley.com/go/permissions>.

The right of Tony Burton, Nick Jenkins, Ervin Bossanyi, David Sharpe and Michael Graham to be identified as the authors of this work has been asserted in accordance with law.

Registered Offices

John Wiley & Sons, Inc., 111 River Street, Hoboken, NJ 07030, USA

John Wiley & Sons Ltd, The Atrium, Southern Gate, Chichester, West Sussex, PO19 8SQ, UK

Editorial Office

The Atrium, Southern Gate, Chichester, West Sussex, PO19 8SQ, UK

For details of our global editorial offices, customer services, and more information about Wiley products visit us at www.wiley.com.

Wiley also publishes its books in a variety of electronic formats and by print-on-demand. Some content that appears in standard print versions of this book may not be available in other formats.

Limit of Liability/Disclaimer of Warranty

While the publisher and authors have used their best efforts in preparing this work, they make no representations or warranties with respect to the accuracy or completeness of the contents of this work and specifically disclaim all warranties, including without limitation any implied warranties of merchantability or fitness for a particular purpose. No warranty may be created or extended by sales representatives, written sales materials or promotional statements for this work. The fact that an organization, website, or product is referred to in this work as a citation and/or potential source of further information does not mean that the publisher and authors endorse the information or services the organization, website, or product may provide or recommendations it may make. This work is sold with the understanding that the publisher is not engaged in rendering professional services. The advice and strategies contained herein may not be suitable for your situation. You should consult with a specialist where appropriate. Further, readers should be aware that websites listed in this work may have changed or disappeared between when this work was written and when it is read. Neither the publisher nor authors shall be liable for any loss of profit or any other commercial damages, including but not limited to special, incidental, consequential, or other damages.

Library of Congress Cataloging-in-Publication Data

Names: Burton, Tony, 1947- author. | Jenkins, Nick, 1954- author. | Bossanyi, Ervin, author. | Sharpe, David, author. | Graham, Michael, author.

Title: Wind energy handbook / Tony Burton, Nick Jenkins, Ervin Bossanyi, David Sharpe, Michael Graham.

Description: Third edition. | Hoboken, NJ : Wiley, 2021. | Includes bibliographical references and index.

Identifiers: LCCN 2020036473 (print) | LCCN 2020036474 (ebook) | ISBN 9781119451099 (cloth) | ISBN 9781119451150 (adobe pdf) | ISBN 9781119451167 (epub)

Subjects: LCSH: Wind power--Handbooks, manuals, etc.

Classification: LCC TJ820 .B869 2021 (print) | LCC TJ820 (ebook) | DDC 621.31/2136--dc23

LC record available at <https://lccn.loc.gov/2020036473>

LC ebook record available at <https://lccn.loc.gov/2020036474>

Cover Design: Wiley

Cover Image: Designed by Dr. Georgios Deskos

Set in 10/12pt TimesNewRoman by SPi Global, Chennai, India

Contents

About the Authors	xxi
Preface to Second Edition	xxiii
Preface to Third Edition	xxv
Acknowledgements for the First Edition	xxix
Acknowledgements for the Second Edition	xxxi
Acknowledgements for the Third Edition	xxxiii
List of Symbols	xxxv
Figures C1 and C2 – coordinate systems	xlv
1 Introduction	1
1.1 Historical development of wind energy	1
1.2 Modern wind turbines	6
1.3 Scope of the book	8
References	9
Websites	10
Further reading	10
2 The wind resource	11
2.1 The nature of the wind	11
2.2 Geographical variation in the wind resource	13
2.3 Long-term wind speed variations	14
2.4 Annual and seasonal variations	14
2.5 Synoptic and diurnal variations	16
2.6 Turbulence	16
2.6.1 The nature of turbulence	16
2.6.2 The boundary layer	18
2.6.3 Turbulence intensity	20
2.6.4 Turbulence spectra	22
2.6.5 Length scales and other parameters	24

2.6.6	Asymptotic limits	26
2.6.7	Cross-spectra and coherence functions	27
2.6.8	The Mann model of turbulence	29
2.7	Gust wind speeds	30
2.8	Extreme wind speeds	31
2.8.1	Extreme winds in standards	33
2.9	Wind speed prediction and forecasting	35
2.9.1	Statistical methods	35
2.9.2	Meteorological methods	36
2.9.3	Current methods	36
2.10	Turbulence in complex terrain	37
	References	37
3	Aerodynamics of horizontal axis wind turbines	39
3.1	Introduction	40
3.2	The actuator disc concept	41
3.2.1	Simple momentum theory	42
3.2.2	Power coefficient	43
3.2.3	The Betz limit	43
3.2.4	The thrust coefficient	44
3.3	Rotor disc theory	45
3.3.1	Wake rotation	45
3.3.2	Angular momentum theory	46
3.3.3	Maximum power	49
3.4	Vortex cylinder model of the actuator disc	49
3.4.1	Introduction	49
3.4.2	Vortex cylinder theory	51
3.4.3	Relationship between bound circulation and the induced velocity	51
3.4.4	Root vortex	52
3.4.5	Torque and power	53
3.4.6	Axial flow field	54
3.4.7	Tangential flow field	54
3.4.8	Axial thrust	56
3.4.9	Radial flow and the general flow field	57
3.4.10	Further development of the actuator model	58
3.4.11	Conclusions	59
3.5	Rotor blade theory (blade-element/momentum theory)	59
3.5.1	Introduction	59
3.5.2	Blade element theory	59
3.5.3	The BEM theory	61
3.5.4	Determination of rotor torque and power	63
3.6	Actuator line theory, including radial variation	65
3.7	Breakdown of the momentum theory	66
3.7.1	Free-stream/wake mixing	66
3.7.2	Modification of rotor thrust caused by wake breakdown	66
3.7.3	Empirical determination of thrust coefficient	67

3.8	Blade geometry	68
3.8.1	Introduction	68
3.8.2	Optimal design for variable-speed operation	68
3.8.3	A simple blade design	72
3.8.4	Effects of drag on optimal blade design	74
3.8.5	Optimal blade design for constant-speed operation	77
3.9	The effects of a discrete number of blades	77
3.9.1	Introduction	77
3.9.2	Tip-losses	77
3.9.3	Prandtl's approximation for the tip-loss factor	82
3.9.4	Blade root losses	85
3.9.5	Effect of tip-loss on optimum blade design and power	86
3.9.6	Incorporation of tip-loss for non-optimal operation	90
3.9.7	Radial effects and an alternative explanation for tip-loss	91
3.10	Stall delay	92
3.11	Calculated results for an actual turbine	95
3.12	The performance curves	98
3.12.1	Introduction	98
3.12.2	The $C_P - \lambda$ performance curve	99
3.12.3	The effect of solidity on performance	100
3.12.4	The $C_Q - \lambda$ curve	101
3.12.5	The $C_T - \lambda$ curve	101
3.13	Constant rotational speed operation	102
3.13.1	Introduction	102
3.13.2	The $K_P - 1/\lambda$ curve	102
3.13.3	Stall regulation	103
3.13.4	Effect of rotational speed change	104
3.13.5	Effect of blade pitch angle change	104
3.14	Pitch regulation	106
3.14.1	Introduction	106
3.14.2	Pitching to stall	106
3.14.3	Pitching to feather	106
3.15	Comparison of measured with theoretical performance	107
3.16	Estimation of energy capture	109
3.17	Wind turbine aerofoil design	113
3.17.1	Introduction	113
3.17.2	The NREL aerofoils	115
3.17.3	The Risø aerofoils	116
3.17.4	The Delft aerofoils	120
3.17.5	General principles for outboard and inboard blade sections	120
3.18	Add-ons (including blade modifications independent of the main structure)	121
3.18.1	Devices to control separation and stalling	122
3.18.2	Devices to increase $C_{L\max}$ and lift/drag ratio	123
3.18.3	Circulation control (jet flaps)	124

3.19	Aerodynamic noise	126
3.19.1	Noise sources	126
3.19.2	Inflow turbulence-induced blade noise	127
3.19.3	Self-induced blade noise	127
3.19.4	Interaction between turbulent boundary layers on the blade and the trailing edge	128
3.19.5	Other blade noise sources	128
3.19.6	Summary	129
	References	130
	Websites	132
	Further reading	132
	Appendix A.3 Lift and drag of aerofoils	133
A3.1	Drag	134
A3.2	The boundary layer	135
A3.3	Boundary layer separation	136
A3.4	Laminar and turbulent boundary layers and transition	138
A3.5	Definition of lift and its relationship to circulation	141
A3.6	The stalled aerofoil	145
A3.7	The lift coefficient	145
A3.8	Aerofoil drag characteristics	147
A3.8.1	Symmetric aerofoils	147
A3.8.2	Cambered aerofoils	149
4	Further aerodynamic topics for wind turbines	153
4.1	Introduction	153
4.2	The aerodynamics of turbines in steady yaw	153
4.2.1	Momentum theory for a turbine rotor in steady yaw	154
4.2.2	Glauert's momentum theory for the yawed rotor	156
4.2.3	Vortex cylinder model of the yawed actuator disc	160
4.2.4	Flow expansion	163
4.2.5	Related theories	169
4.2.6	Wake rotation for a turbine rotor in steady yaw	170
4.2.7	The blade element theory for a turbine rotor in steady yaw	171
4.2.8	The blade-element-momentum theory for a rotor in steady yaw	172
4.2.9	Calculated values of induced velocity	175
4.2.10	Blade forces for a rotor in steady yaw	177
4.2.11	Yawing and tilting moments in steady yaw	177
4.3	Circular wing theory applied to a rotor in yaw	180
4.3.1	Introduction	180
4.3.2	The general pressure distribution theory of Kinner	181
4.3.3	The axisymmetric loading distributions	182
4.3.4	The anti-symmetric loading distribution	184
4.3.5	The Pitt and Peters model	187
4.3.6	The general acceleration potential method	188
4.3.7	Comparison of methods	188

4.4	Unsteady flow	189
4.4.1	Introduction	189
4.4.2	The acceleration potential method to analyse unsteady flow	190
4.4.3	Unsteady yawing and tilting moments	191
4.5	Unsteady aerofoil aerodynamics	194
4.5.1	Introduction	194
4.5.2	Aerodynamic forces caused by aerofoil acceleration	195
4.5.3	The effect of the shed vortex wake on an aerofoil in unsteady flow	196
4.6	Dynamic stall	201
4.6.1	Introduction	201
4.6.2	Dynamic stall models	201
4.7	Computational fluid dynamics	207
4.7.1	Introduction	207
4.7.2	Inviscid computational methods	208
4.7.3	RANS and URANS CFD methods	211
4.7.4	LES and DES methods	213
4.7.5	Numerical techniques for CFD	214
4.7.6	Discrete methods of approximating the terms in the Navier–Stokes equations over the flow field	218
4.7.7	Grid construction	219
4.7.8	Full flow field simulation including ABL and wind turbines	220
	References	222
	Further reading	225
5	Design loads for HAWTs	227
5.1	National and international standards	227
5.1.1	Historical development	227
5.1.2	IEC 61400-1	228
5.2	Basis for design loads	228
5.2.1	Sources of loading	228
5.2.2	Ultimate loads	229
5.2.3	Fatigue loads	229
5.2.4	Partial safety factors	229
5.2.5	Functions of the control and safety systems	231
5.3	Turbulence and wakes	231
5.4	Extreme loads	233
5.4.1	Operational load cases	233
5.4.2	Non-operational load cases	237
5.4.3	Blade/tower clearance	238
5.4.4	Constrained stochastic simulation of wind gusts	238
5.5	Fatigue loading	240
5.5.1	Synthesis of fatigue load spectrum	240
5.6	Stationary blade loading	240
5.6.1	Lift and drag coefficients	240
5.6.2	Critical configuration for different machine types	241
5.6.3	Dynamic response	241

5.7	Blade loads during operation	248
5.7.1	Deterministic and stochastic load components	248
5.7.2	Deterministic aerodynamic loads	249
5.7.3	Gravity loads	258
5.7.4	Deterministic inertia loads	259
5.7.5	Stochastic aerodynamic loads: analysis in the frequency domain	260
5.7.6	Stochastic aerodynamic loads: analysis in the time domain	270
5.7.7	Extreme loads	274
5.8	Blade dynamic response	277
5.8.1	Modal analysis	277
5.8.2	Mode shapes and frequencies	280
5.8.3	Centrifugal stiffening	281
5.8.4	Aerodynamic and structural damping	283
5.8.5	Response to deterministic loads: step-by-step dynamic analysis	284
5.8.6	Response to stochastic loads	289
5.8.7	Response to simulated loads	292
5.8.8	Teeter motion	292
5.8.9	Tower coupling	297
5.8.10	Aeroelastic stability	302
5.9	Blade fatigue stresses	302
5.9.1	Methodology for blade fatigue design	302
5.9.2	Combination of deterministic and stochastic components	305
5.9.3	Fatigue prediction in the frequency domain	305
5.9.4	Wind simulation	307
5.9.5	Fatigue cycle counting	308
5.10	Hub and low-speed shaft loading	309
5.10.1	Introduction	309
5.10.2	Deterministic aerodynamic loads	310
5.10.3	Stochastic aerodynamic loads	311
5.10.4	Gravity loading	312
5.11	Nacelle loading	312
5.11.1	Loadings from rotor	312
5.11.2	Nacelle wind loads	315
5.12	Tower loading	315
5.12.1	Extreme loads	315
5.12.2	Dynamic response to extreme loads	316
5.12.3	Operational loads due to steady wind (deterministic component)	318
5.12.4	Operational loads due to turbulence (stochastic component)	319
5.12.5	Dynamic response to operational loads	322
5.12.6	Fatigue loads and stresses	323
5.13	Wind turbine dynamic analysis codes	325
5.14	Extrapolation of extreme loads from simulations	331
5.14.1	Derivation of empirical cumulative distribution function of global extremes	331

5.14.2	Fitting an extreme value distribution to the empirical distribution	332
5.14.3	Comparison of extreme value distributions	337
5.14.4	Combination of probability distributions	338
5.14.5	Extrapolation	339
5.14.6	Fitting probability distribution after aggregation	339
5.14.7	Local extremes method	340
5.14.8	Convergence requirements	341
	References	342
Appendix A.5	Dynamic response of stationary blade in turbulent wind	345
A5.1	Introduction	345
A5.2	Frequency response function	345
	A5.2.1 Equation of motion	345
	A5.2.2 Frequency response function	346
A5.3	Resonant displacement response ignoring wind variations along the blade	347
	A5.3.1 Linearisation of wind loading	347
	A5.3.2 First mode displacement response	347
	A5.3.3 Background and resonant response	348
A5.4	Effect of across wind turbulence distribution on resonant displacement response	349
	A5.4.1 Formula for normalised co-spectrum	351
A5.5	Resonant root bending moment	352
A5.6	Root bending moment background response	354
A5.7	Peak response	355
A5.8	Bending moments at intermediate blade positions	358
	A5.8.1 Background response	358
	A5.8.2 Resonant response	358
	References	359
6	Conceptual design of horizontal axis wind turbines	361
6.1	Introduction	361
6.2	Rotor diameter	361
	6.2.1 Cost modelling	362
	6.2.2 Simplified cost model for machine size optimisation: an illustration	362
	6.2.3 The NREL cost model	365
	6.2.4 The INNWIND.EU cost model	367
	6.2.5 Machine size growth	367
	6.2.6 Gravity limitations	369
	6.2.7 Variable diameter rotors	369
6.3	Machine rating	370
	6.3.1 Simplified cost model for optimising machine rating in relation to diameter	370
	6.3.2 Relationship between optimum rated wind speed and annual mean	373
	6.3.3 Specific power of production machines	373

6.4	Rotational speed	375
6.4.1	Ideal relationship between rotational speed and solidity	375
6.4.2	Influence of rotational speed on blade weight	376
6.4.3	High-speed rotors	376
6.4.4	Low induction rotors	377
6.4.5	Noise constraint on rotational speed	378
6.4.6	Visual considerations	379
6.5	Number of blades	379
6.5.1	Overview	379
6.5.2	Ideal relationship between number of blades, rotational speed, and solidity	379
6.5.3	Effect of number of blades on optimum C_P in the presence of tip-loss and drag	380
6.5.4	Some performance and cost comparisons	381
6.5.5	Effect of number of blades on loads	385
6.5.6	Noise constraint on rotational speed	386
6.5.7	Visual appearance	387
6.5.8	Single bladed turbines	387
6.6	Teetering	388
6.6.1	Load relief benefits	388
6.6.2	Limitation of large excursions	389
6.6.3	Pitch-teeter coupling	390
6.6.4	Teeter stability on stall-regulated machines	391
6.7	Power control	391
6.7.1	Passive stall control	391
6.7.2	Active pitch control	391
6.7.3	Passive pitch control	396
6.7.4	Active stall control	397
6.7.5	Yaw control	397
6.8	Braking systems	398
6.8.1	Independent braking systems: requirements of standards	398
6.8.2	Aerodynamic brake options	399
6.8.3	Mechanical brake options	400
6.8.4	Parking versus idling	400
6.9	Fixed-speed, two-speed, variable-slip, and variable-speed operation	400
6.9.1	Fixed-speed operation	401
6.9.2	Two-speed operation	401
6.9.3	Variable-slip operation (see also Section 8.3.8)	403
6.9.4	Variable-speed operation	403
6.9.5	Generator system architectures	406
6.9.6	Low-speed direct drive generators	406
6.9.7	Hybrid gearboxes, medium-speed generators	410
6.9.8	Evolution of generator systems	410
6.10	Other drive trains and generators	411
6.10.1	Directly connected, fixed-speed generators	411
6.10.2	Innovations to allow the use of directly connected generators	414

6.10.3	Generator and drive train innovations	415
6.11	Drive train mounting arrangement options	419
6.11.1	Low-speed shaft mounting	419
6.11.2	High-speed shaft and generator mounting	421
6.12	Drive train compliance	425
6.13	Rotor position with respect to tower	426
6.13.1	Upwind configuration	426
6.13.2	Downwind configuration	426
6.14	Tower stiffness	427
6.14.1	Stochastic thrust loading at blade passing frequency	427
6.14.2	Tower top moment fluctuations due to blade pitch errors	428
6.14.3	Tower top moment fluctuations due to rotor mass imbalance	429
6.14.4	Tower stiffness categories	430
6.15	Multiple rotor structures	430
6.15.1	Space frame support structure	430
6.15.2	Tubular cantilever arm support structure	432
6.15.3	Vestas four-rotor array	432
6.15.4	Cost comparison based on fundamental scaling rules	433
6.15.5	Cost comparison based on NREL scaling indices	433
6.15.6	Discussion	434
6.16	Augmented flow	435
6.17	Personnel safety and access issues	435
	References	437
7	Component design	441
7.1	Blades	441
7.1.1	Introduction	441
7.1.2	Aerodynamic design	442
7.1.3	Practical modifications to optimum aerodynamic design	443
7.1.4	Structural design criteria	444
7.1.5	Form of blade structure	444
7.1.6	Blade materials and properties	447
7.1.7	Static properties of glass/polyester and glass/epoxy composites	451
7.1.8	Fatigue properties of glass/polyester and glass/epoxy composites	457
7.1.9	Carbon fibre composites	468
7.1.10	Properties of wood laminates	471
7.1.11	Material safety factors	473
7.1.12	Manufacture of composite blades	473
7.1.13	Blade loading overview	478
7.1.14	Simplified fatigue design example	486
7.1.15	Blade resonance	495
7.1.16	Design against buckling	500
7.1.17	Blade root fixings	506
7.1.18	Blade testing	508
7.1.19	Leading edge erosion	509
7.1.20	Bend-twist coupling	511

7.2	Pitch bearings	519
7.3	Rotor hub	521
7.4	Gearbox	524
7.4.1	Introduction	524
7.4.2	Variable loads during operation	525
7.4.3	Drive train dynamics	527
7.4.4	Braking loads	527
7.4.5	Effect of variable loading on fatigue design of gear teeth	528
7.4.6	Effect of variable loading on fatigue design of bearings and shafts	531
7.4.7	Gear arrangements	532
7.4.8	Gearbox noise	534
7.4.9	Integrated gearboxes	536
7.4.10	Lubrication and cooling	536
7.4.11	Gearbox efficiency	537
7.5	Generator	537
7.5.1	Fixed-speed induction generators	537
7.5.2	Variable-slip induction generators	540
7.5.3	Variable-speed operation	541
7.5.4	Variable-speed operation using a DFIG	542
7.5.5	Variable-speed operation using a full power converter	546
7.6	Mechanical brake	548
7.6.1	Brake duty	548
7.6.2	Factors governing brake design	548
7.6.3	Calculation of brake disc temperature rise	550
7.6.4	High-speed shaft brake design	552
7.6.5	Two-level braking	554
7.6.6	Low-speed shaft brake design	554
7.7	Nacelle bedplate	555
7.8	Yaw drive	555
7.9	Tower	558
7.9.1	Introduction	558
7.9.2	Constraints on first mode natural frequency	558
7.9.3	Steel tubular towers	559
7.9.4	Steel lattice towers	569
7.9.5	Hybrid towers	570
7.10	Foundations	570
7.10.1	Slab foundations	570
7.10.2	Multi-pile foundations	572
7.10.3	Concrete monopile foundations	572
7.10.4	Foundations for steel lattice towers	573
7.10.5	Foundation rotational stiffness	574
	References	574
8	The controller	579
8.1	Functions of the wind turbine controller	580
8.1.1	Supervisory control	580

8.1.2	Closed-loop control	581
8.1.3	The safety system	581
8.2	Closed-loop control: issues and objectives	583
8.2.1	Pitch control	583
8.2.2	Stall control	584
8.2.3	Generator torque control	585
8.2.4	Yaw control	585
8.2.5	Influence of the controller on loads	586
8.2.6	Defining controller objectives	587
8.2.7	PI and PID controllers	588
8.3	Closed-loop control: general techniques	589
8.3.1	Control of fixed-speed, pitch-regulated turbines	589
8.3.2	Control of variable-speed, pitch-regulated turbines	590
8.3.3	Pitch control for variable-speed turbines	593
8.3.4	Switching between torque and pitch control	593
8.3.5	Control of tower vibration	595
8.3.6	Control of drive train torsional vibration	598
8.3.7	Variable-speed stall regulation	599
8.3.8	Control of variable-slip turbines	601
8.3.9	Individual pitch control	602
8.3.10	Multivariable control – decoupling the wind turbine control loops	603
8.3.11	Two axis decoupling for individual pitch control	605
8.3.12	Load reduction with individual pitch control	607
8.3.13	Individual pitch control implementation	609
8.3.14	Further extensions to individual pitch control	611
8.3.15	Commercial use of individual pitch control	611
8.3.16	Estimation of rotor average wind speed	612
8.3.17	LiDAR-assisted control	613
8.3.18	LiDAR signal processing	616
8.4	Closed-loop control: analytical design methods	617
8.4.1	Classical design methods	617
8.4.2	Gain scheduling for pitch controllers	622
8.4.3	Adding more terms to the controller	622
8.4.4	Other extensions to classical controllers	623
8.4.5	Optimal feedback methods	625
8.4.6	Pros and cons of model based control methods	628
8.4.7	Other methods	629
8.5	Pitch actuators	629
8.6	Control system implementation	631
8.6.1	Discretisation	631
8.6.2	Integrator desaturation	632
	References	633
9	Wake effects and wind farm control	637
9.1	Introduction	637
9.2	Wake characteristics	638

9.2.1	Modelling wake effects	639
9.2.2	Wake turbulence in the IEC standard	639
9.2.3	CFD models	640
9.2.4	Simplified or ‘engineering’ wake models	640
9.2.5	Wind farm models	651
9.3	Active wake control methods	652
9.3.1	Wake control options	653
9.3.2	Control objectives	654
9.3.3	Control design methods for active wake control	656
9.3.4	Field testing for active wake control	658
9.4	Wind farm control and the grid system	658
9.4.1	Curtailment and delta control	659
9.4.2	Fast frequency response	661
	References	661
10	Onshore wind turbine installations and wind farms	665
10.1	Project development	666
10.1.1	Initial site selection	667
10.1.2	Project feasibility assessment	670
10.1.3	Measure–correlate–predict	670
10.1.4	Micrositing	672
10.1.5	Site investigations	672
10.1.6	Public consultation	673
10.1.7	Preparation of the planning application and environmental statement	674
10.1.8	Planning requirements in the UK	676
10.1.9	Procurement of wind farms	676
10.1.10	Financing of wind farms	676
10.2	Landscape and visual impact assessment	678
10.2.1	Landscape character assessment	679
10.2.2	Turbine and wind farm design for minimum visual impact	681
10.2.3	Assessment of visual impact	683
10.2.4	Shadow flicker	685
10.3	Noise	687
10.3.1	Terminology and basic concepts	688
10.3.2	Wind turbine noise	692
10.3.3	Measurement of wind turbine noise	693
10.3.4	Prediction and assessment of wind farm noise	695
10.3.5	Low frequency noise	697
10.4	Electromagnetic interference	698
10.4.1	Impact of wind turbines on communication systems	700
10.4.2	Impact of wind turbines on aviation radar	703
10.5	Ecological assessment	706
10.5.1	Impact on birds	707
10.5.2	Impact on bats	710
	References	712
	Software	715

11 Wind energy and the electric power system	717
11.1 Introduction	717
11.1.1 The electric power system	718
11.1.2 Electrical distribution networks	719
11.1.3 Electrical transmission systems	721
11.2 Wind turbine electrical systems	721
11.2.1 Wind turbine transformers	722
11.2.2 Protection of wind turbine electrical systems	723
11.2.3 Lightning protection of wind turbines	725
11.3 Wind farm electrical systems	730
11.3.1 Power collection system	730
11.3.2 Earthing (grounding) of wind farms	732
11.4 Connection of wind farms to distribution networks	735
11.4.1 Power system studies	737
11.4.2 Electrical protection of a wind farm	738
11.4.3 Islanding and anti-islanding protection	741
11.4.4 Utility protection of a wind farm	742
11.5 Grid codes and the connection of large wind farms to transmission networks	742
11.5.1 Continuous operation capability	744
11.5.2 Reactive power capability	744
11.5.3 Frequency response	747
11.5.4 Fault ride through	748
11.5.5 Fast fault current injection	748
11.5.6 Synthetic inertia	749
11.6 Wind energy and the generation system	750
11.6.1 Development (planning) of a generation system including wind energy	751
11.6.2 Operation of a generation system including wind energy	753
11.6.3 Wind power forecasting	754
11.7 Power quality	756
11.7.1 Voltage flicker perception	760
11.7.2 Measurement and assessment of power quality characteristics of grid connected wind turbines	762
11.7.3 Harmonics	763
References	764
Appendix A.11 Simple calculations for the connection of wind turbines	766
A11.1 The per-unit system	766
A11.2 Power flows, slow voltage variations, and network losses	767
12 Offshore wind turbines and wind farms	771
12.1 Offshore wind farms	771
12.2 The offshore wind resource	776
12.2.1 Winds offshore	776
12.2.2 Site wind speed assessment	776
12.2.3 Wakes in offshore wind farms	777

12.3	Design loads	781
12.3.1	International standards	781
12.3.2	Wind conditions	782
12.3.3	Marine conditions	784
12.3.4	Wave spectra	784
12.3.5	Ultimate loads: operational load cases and accompanying wave climates	785
12.3.6	Ultimate loads: non-operational load cases and accompanying wave climates	792
12.3.7	Fatigue loads	795
12.3.8	Wave theories	797
12.3.9	Wave loading on support structure	805
12.3.10	Constrained waves	818
12.3.11	Analysis of support structure loads	820
12.4	Machine size optimisation	822
12.5	Reliability of offshore wind turbines	824
12.5.1	Machine architecture	824
12.5.2	Redundancy	825
12.5.3	Component quality	826
12.5.4	Protection against corrosion	826
12.5.5	Condition monitoring	826
12.6	Fixed support structures – overview	828
12.7	Fixed support structures	829
12.7.1	Monopiles – introduction	829
12.7.2	Monopiles – geotechnical design	830
12.7.3	Monopiles – steel design	840
12.7.4	Monopiles – fatigue analysis in the frequency domain	845
12.7.5	Gravity bases	860
12.7.6	Jacket structures	866
12.7.7	Tripod structures	875
12.7.8	Tripile structures	877
12.7.9	S-N curves for fatigue design	877
12.8	Floating support structures	883
12.8.1	Introduction	883
12.8.2	Floater concepts	884
12.8.3	Design standards	887
12.8.4	Design considerations	887
12.8.5	Spar buoy design space	892
12.8.6	Semi-submersible design space	893
12.8.7	Station keeping	898
12.8.8	Spar buoy case study – Hywind Scotland	901
12.8.9	Three column semi-submersible case study – WindFloat Atlantic	904
12.8.10	Ring shaped floating platform – Floatgen, France	906

12.9	Environmental assessment of offshore wind farms	908
12.9.1	Environmental impact assessment	908
12.9.2	Contents of the environmental statement of an offshore wind farm	909
12.9.3	Environmental monitoring of wind farms in operation	911
12.10	Offshore power collection and transmission systems	913
12.10.1	Offshore wind farm transmission systems	914
12.10.2	Submarine AC cable systems	916
12.10.3	HVdc transmission	920
	References	922
	Appendix A.12 Costs of electricity	931
A12.1	Levelised cost of electricity	931
A12.2	Strike price and contract for difference	931
	Index	933

About the Authors

Tony Burton: After an early career in long-span bridge design and construction, Tony Burton joined the Wind Energy Group (WEG) in 1982 to coordinate Phase IIB of the Offshore Wind Energy Assessment for the UK Department of Energy. This was a collaborative project involving British Aerospace, GEC, and the CEBG, which had the task of producing an outline design and costing of a 100 m diameter wind turbine in a large offshore array. Following this, he worked on the design development for the UK prototype 3 MW turbine, before moving to Orkney to supervise its construction and commissioning. In 1992, he moved to Wales to be site engineer for the construction and operation of one of the first UK wind farms at Cemmaes, which consisted of 24 300 kW WWEG turbines. He worked as a consultant in wind turbine foundation design from 1995 until 2012, when he joined GL Garrad Hassan to work on the design of offshore support structures until retirement in 2017.

Nick Jenkins completed a PhD in wind-diesel systems at Imperial College London and is now Professor of Renewable Energy at Cardiff University. His career has included 14 years of industrial experience, of which 5 years were in developing countries. His final position in industry was as a projects director for Wind Energy Group, a developer and manufacturer of wind turbines. While at the university, he has developed teaching and research activities in electrical power engineering and renewable energy. He is a Distinguished Member of CIGRE and a Fellow of the IET, IEEE, Royal Academy of Engineering, and the Learned Society of Wales. From 2009–2011 he was the Shimizu Visiting Professor to the Atmosphere and Energy Program at Stanford University.

Ervin Bossanyi: After graduating in theoretical physics and completing a PhD in energy economics at Cambridge University, Ervin Bossanyi has been working in wind energy since 1978. He was a Research Fellow at Reading University and then Rutherford Appleton Laboratory before moving into industry in 1986, where he worked on advanced control methods for the Wind Energy Group. Since 1994, he has been with international consultants Garrad Hassan, now DNV GL, where he is senior principal researcher in renewables. He received the 2014 Scientific Award of the European Academy of Wind Energy for outstanding contributions to the development of wind energy and has had an honorary visiting professorship at Bristol University since 2016.

David Sharpe has worked in the aircraft industry for the British Aircraft Corporation as a structural engineer. From 1969 to 1995, he was a Senior Lecturer in aeronautical engineering at Kingston Polytechnic and at Queen Mary College, University of London. Between 1996 and 2003, he was at Loughborough University as a Senior Research Fellow at the Centre for Renewable Energy Systems Technology. David is a member of the Royal Aeronautical Society and was a member of the British Wind Energy Association at its inception. He has been active in wind turbine aerodynamics research since 1976. Currently, he is a Visiting Professor in the Future Wind and Marine Technology Innovation Centre at the University of Strathclyde, Glasgow.

Michael Graham graduated in mathematics followed by part 2 of the engineering degree from Cambridge University. He has a PhD in aeronautics from Imperial College London, where he has been Professor of Unsteady Aerodynamics since 1990 and was Head of the Department of Aeronautics from 1999 to 2003. He has worked in wind energy research since 1990, coordinating the EU Joule II project ROTOW and as a partner in a number of other EU and EPSRC research programmes dealing with aerodynamics of wind turbine rotors and latterly their wakes. He is a Fellow of the Royal Academy of Engineering, the RAeS, and RINA.

Preface to Second Edition

The second edition of the *Wind Energy Handbook* seeks to reflect the evolution of design rules and the principal innovations in the technology that have taken place in the 10 years since the first edition was published. A major new direction in wind energy development in this period has been the expansion offshore and so the opportunity has been taken to add a new chapter on offshore wind turbines and wind farms.

The offshore chapter begins with a survey of the present state of offshore wind farm development, before consideration of resource assessment and array losses. Then wave loading on support structures is examined in depth, including a summary of the combinations of wind and wave loading specified in the load cases of the IEC standard and descriptions of applicable wave theories. Linear (Airy) wave theory and Dean stream function theory are explained, together with their translation into wave loadings by means of Morison's equation. Diffraction and breaking wave theories are also covered.

Consideration of wave loading leads to a survey of the different types of support structure deployed to date. Monopile, gravity bases, jacket structures, tripods, and tripiles are described in turn. In view of their popularity, monopiles are accorded the most space and, after an outline of the key design considerations, monopile fatigue analysis in the frequency domain is explained.

Another major cost element offshore is the undersea cable system needed to transmit power to land. This subject is considered in depth in the section on the power collection and transmission cable network. Machine reliability is also of much greater importance offshore, so developments in turbine condition monitoring and other means of increasing reliability are discussed. The chapter is completed by sections covering the assessment of environmental impacts, maintenance and access, and optimum machine size.

The existing chapters in the first edition have all been revised and brought up to date, with the addition of new material in some areas. The main changes are as follows:

Chapter 1: Introduction This chapter has been brought up to date and expanded.

Chapter 2: The wind resource Descriptions of the high frequency asymptotic behaviour of turbulence spectra and the Mann turbulence model have been added.

Chapters 3 and 4: Aerodynamics of horizontal axis wind turbines The contents of Chapters 3 and 4 of the first edition have been rearranged so that the fundamentals are covered in Chapter 3 and more advanced subjects are explored in Chapter 4. Some material on field testing and performance measurement has been omitted to

make space for a survey of wind turbine aerofoils and new sections on dynamic stall and computational fluid dynamics.

Chapter 5: Design loads for horizontal axis wind turbines The description of IEC load cases has been brought up to date and a new section on the extrapolation of extreme loads from simulations added. The size of the ‘example’ wind turbine has been doubled to 80 m, in order to be more representative of the current generation of turbines.

Chapter 6: Conceptual design of horizontal axis wind turbines The initial sections on choice of machine size, rating, and number of blades have been substantially revised, making use of the NREL cost model. Variable speed operation is considered in greater depth. The section on tower stiffness has been expanded to compare tower excitation at rotational frequency and blade passing frequency.

Chapter 7: Component design New rules for designing towers against buckling are described and a section on foundation rotational stiffness has been added.

Chapter 8: The controller Individual blade pitch control is examined in greater depth.

Chapter 9: Wind turbine installations and wind farms A survey of recent research on the impact of turbines on birds has been added.

Chapter 10: Electrical systems New sections covering (a) Grid Code requirements for the connection of large wind farms to transmission networks and (b) the impact of wind farms on generation systems have been added.

Preface to Third Edition

The 10 years since the preparation of the second edition of the *Wind Energy Handbook* have seen further innovation in many areas of turbine design, and these form the basis for the changes in this new edition. Refinements to blade design, together with improved and better-understood material properties, have enabled the trend to larger machines to continue. Upwind, three bladed, pitch-regulated, variable-speed machines are still firmly established as the norm, despite the scope for the deployment of two bladed downwind machines offshore. However, the one-time monopoly of high-speed gearboxes continues to be eroded, thanks to the rise of direct drive turbines and the increased use of medium-speed gearboxes with permanent magnet generators. The design of fixed offshore support structures continues to evolve, but the most exciting development has been the successful deployment of floating wind turbines.

The third edition retains most of the material of the previous edition, as the fundamental theory underpinning wind turbine design has not changed, but many chapters have been expanded to cover recent developments. In view of the significant effects of wakes on wind farm energy yield and turbine loadings, the opportunity has been taken to add a completely new chapter (Chapter 9) entitled ‘Wake Effects and Wind Farm Control’. This includes a detailed treatment of engineering models of the wake and their implications for wind farm control, which is emerging as a way to both increase wind farm energy production and reduce turbine fatigue loading by mitigating wake interaction effects. There is also a section on wind farm control and the grid system, recognising the increasing importance of using wind farms to provide ancillary services to the grid.

The main changes to the existing chapters are as follows:

Chapter 1: Introduction This chapter has been brought up to date to reflect the continuing increase in the size of wind turbines and wind farms.

Chapter 2: The Wind Resource Updated to include edition 4 of the IEC standard. An illustrative example of the Gumbel method for extreme winds has been added. The description of turbulence in wakes and wind farms has been replaced by a more comprehensive treatment in the new Chapter 9.

Chapters 3 and 4: Aerodynamics of Horizontal Axis Wind Turbines, and Further Aerodynamic Topics for Wind Turbines Chapters 3 and 4 continue the split, as in the second edition, between fundamentals in Chapter 3 and more advanced topics in

Chapter 4. In Chapter 3, minor changes have been made to Section 3.8 dealing with the tip-loss factor, and additions have been inserted on flat-back aerofoils and low noise designs in Sections 3.17 and 3.19 with new sections on ‘add-on’ devices to control separation, lift, and drag (3.18) and on aerodynamic noise and blade design (3.19). The appendix to chapter 3 has been shortened by abbreviating the section on drag. In Chapter 4, Section 4.3, the mathematical analysis of the Kinner circular wing, has been abbreviated, retaining the final results, the Section 4.6 on dynamic stall has been extended and a new Section 4.7 on applications of computational fluid dynamics to rotor aerodynamics and wakes has been added.

Chapter 5: Design Loads for HAWTs The changes are mainly minor. The description of IEC load cases has been updated as necessary. A structurally more efficient blade cross-section has been adopted for the trial blade design, while retaining the existing plan-form. New figures have been added showing effect of yaw and wind shear on blade root bending moments for a pitch-regulated turbine.

Chapter 6: Conceptual Design of Horizontal Axis Wind Turbines New sections have been added covering high-speed rotors, low induction rotors, multiple rotor structures, and the effect of the number of blades on C_p . Also the initial sections on choice of machine size and rating have been amended to reflect the growth in turbine size. The section on generators has been expanded to include innovative approaches to drive trains and power conversion.

Chapter 7: Component Design The section on blade design has undergone major revision and expansion, including a more detailed treatment of the static and fatigue properties of laminates. A simplified example of the fatigue design of a blade with spar caps is presented to illustrate the steps involved. The manufacturing process is described in more detail and new sub-sections on blade testing, leading edge erosion, and bend-twist coupling have been added.

Chapter 8: The Controller New sections have been added to cover wind speed estimation and LiDAR-assisted control.

Chapter 9: Wake Effects and Wind Farm Control – see above.

Chapter 10: Onshore Wind Turbine Installations and Wind Farms (previously Chapter 9) This chapter has been revised and updated to take account of important developments in understanding and managing the environmental impact of wind energy developments. Since the second edition, there has been a considerable increase in the literature on environmental impact and in the sophistication of software tools for the effective, sustainable development of wind farms.

Chapter 11: Wind Energy and the Electric Power System (previously Chapter 10) Wind energy is an increasingly important source of electricity generation, and practice for connecting turbines and wind farms to the network and integrating their operation is developing rapidly. The chapter has been revised and updated to address these important developments, including evolving Grid Code requirements and the increasing integration of wind energy into power system operation.

Chapter 12: Offshore Wind Turbines and Wind Farms (previously Chapter 11) The introductory section has been updated to chart recent growth of installed capacity and trends in levelised cost of energy, while the Contract for Difference support mechanism is explained in a new appendix. The section on the offshore wind resource has been extended to include recent research on wake losses, their spatial extent downwind, and the wind farm blockage effect.

Floating offshore wind turbines offer the opportunity to dramatically increase the exploitable resource, and the technology is now moving beyond the prototype stage, with several pilot wind farms already in operation. A new section on floating offshore wind turbine structures has therefore been added, encompassing different configurations, governing design criteria and design methods. Three case studies are also included.

The section on monopile design has been extended to include the new approach to geotechnical design made possible by the PISA research project. The description of different types of fixed support structure has been updated to reflect current developments and a new section added covering fatigue design curves.

Publicly funded monitoring programmes have enabled much to be learned about the environmental impacts of offshore wind farms, and some of these findings are reported in a new section on environmental monitoring. Finally, the section on power collection and transmission has been updated to describe the use of modular multi-level convertors for HVdc transmission.

Acknowledgements for the First Edition

A large number of individuals have assisted the authors in a variety of ways in the preparation of this work. In particular, however, we would like to thank David Infield for providing some of the content of Chapter 4, David Quarton for scrutinising and commenting on Chapter 5, Mark Hancock, Martin Ansell, and Colin Anderson for supplying information and guidance on blade material properties reported in Chapter 7, and Ray Hicks for insights into gear design. Thanks are also due to Roger Haines and Steve Gilkes for illuminating discussions on yaw drive design and braking philosophy, respectively, and to James Shawler for assistance and discussions about Chapter 3.

We have made extensive use of ETSU and Risø publications and record our thanks to these organisations for making documents available to us free of charge and sanctioning the reproduction of some of the material therein.

While acknowledging the help we have received from the organisations and individuals referred to above, the responsibility for the work is ours alone, so corrections and/or constructive criticisms would be welcome.

Extracts from British Standards reproduced with the permission of the British Standards Institution under licence number 2001/SK0281. Complete Standards are available from BSI Customer Services (Tel +44 (0) 20 8996 9001).

Acknowledgements for the Second Edition

The second edition benefited greatly from the continuing help and support provided by many who had assisted in the first edition. However, the authors are also grateful to the many individuals not involved in the first edition who provided advice and expertise for the second, especially in relation to the new offshore chapter. In particular the authors wish to acknowledge the contribution of Rose King to the discussion of offshore electric systems, based on her PhD thesis, and of Tim Camp to the discussion of offshore support structure loading. Thanks are also due to Bieshoy Awad for the drawings of electrical generator systems, Rebecca Barthelmie and Wolfgang Schlez for advice on offshore wake effects, Joe Phillips for his contribution to the offshore wind resource, Sven Eric Thor for provision of insights and illustrations from the Lillgrund wind farm, Marc Seidel for information on jacket structures, Jan Wienke for discussion of breaking wave loads, and Ben Hendricks for his input on turbine costs in relation to size.

In addition, several individuals took on the onerous task of scrutinising sections of the draft text. The authors are particularly grateful to Tim Camp for examining the sections on design loading, on- and offshore, Colin Morgan for providing useful comments on the sections dealing with support structures, and Graeme McCann for vetting sections on the extrapolation of extreme loads from simulations and monopile fatigue analysis in the frequency domain. Nevertheless, responsibility for any errors remains with the authors. (In this connection, thanks are due to those who have pointed out errors in the first edition.)

Tony Burton would also like to record his thanks to Martin Kuhn and Wim Bierbooms for providing copies of their PhD theses – entitled, respectively, ‘Dynamics and Design Optimisation of Offshore Wind Energy Conversion Systems’ and ‘Constrained Stochastic Simulation of Wind Gusts for Wind Turbine Design’ – both of which proved invaluable in the preparation of this work.

Acknowledgements for the Third Edition

The authors would like to acknowledge the assistance provided by the many colleagues and individuals in the wider wind energy community who have shared their knowledge and expertise. Of these, a number have been particularly generous with their time and warrant special mention here.

The revised and expanded section on blade design necessitated the gathering of much new material. In this context, Tony Burton would like to thank Mark Hancock for sharing his insights into the practicalities of blade design, Daniel Samborsky for shedding light on the lessons from laminate fatigue testing, and Tomas Vronsky for hosting an informative visit to the Vestas blade testing facility on the Isle of Wight.

The new section on monopile geotechnical design focuses on the more sophisticated design methods made possible by the PISA joint industry research project. Tony Burton would like to thank two lead participants in the project, Byron Byrne and Guy Houlsby of Oxford University, for hosting a tutorial on the project findings, and their research student, Toby Balaam, for his part in arranging it.

Tony Burton would also like to record his gratitude to those who have taken on the chore of reviewing parts of the text. Amongst these are Mark Hancock, Daniel Samborsky, and Samuel Scott, who have reviewed different parts of the blade design section; Byron Byrne, who checked the section on monopile geotechnical design; and James Nicholls and Kevin Drake, who critiqued the floating support structures section. However, responsibility for any errors in these sections remains with the author.

Nick Jenkins would like to express his thanks to Alan Harris of ReSoft for his advice and the use of images from the Windfarm design tool. He would also like to acknowledge and thank Prof. Janaka Ekanayake of Peradeniya University for his contributions to and scrutiny of Chapter 11.

A workspace free from interruptions and distractions is vital for any author. Tony Burton would like to thank former colleague Richard Stonor for providing a quiet and congenial place of work in his home, until evacuation was mandated by Covid-19 guidelines in March 2020.

We have made extensive use of publications by NREL, Sandia Laboratories, Montana State University, DNV GL, and Danish Technical University and record our thanks to these organisations for making documents available to us free of charge and sanctioning the reproduction of some of the material therein. Thanks are also due to Georgios Deskos (Imperial College London and now at National Renewable Energy Laboratory, CO. USA) for the cover design taken from his numerical simulation of flow through a wind farm.

List of Symbols

Note: This list is not exhaustive and omits many symbols that are unique to particular chapters

a	axial flow induction factor; a_b at blade
\bar{a}	azimuthally averaged
a	flange projection beyond bolt centre
a'	tangential flow induction factor; a'_b at blade
\bar{a}'	azimuthally averaged
a'_t	tangential flow induction factor at the blade tip
a_0	two-dimensional lift curve slope, $(dC_l/d\alpha)$
a_1	constant defining magnitude of structural damping
A, A_D	rotor swept area
A_∞, A_w	upstream and downstream streamtube cross-sectional areas
A_c	Charnock's constant
b	face width of gear teeth; eccentricity of bolt to tower wall in bolted flange joint; wake width
b_r	unbiased estimator of β_r
B	number of blades
c	blade chord; Weibull scale parameter; dispersion of distribution; flat plate half width; half of cylinder immersed width
c^*	half of cylinder immersed width at time t^*
\hat{c}	damping coefficient per unit length
c_i	generalised damping coefficient with respect to the i th mode
C	decay constant; wave celerity, L/T; constrained wave crest elevation
$C(v), C(k)$	Theodorsen's function, where v or k is the reduced frequency: $C(v) = F(v) + iG(v)$
C_d	sectional drag coefficient
C_D	drag coefficient in Morison's equation
C_{DS}	steady flow drag coefficient in Morison's equation
C_f	sectional force coefficient (i.e. C_d or C_l as appropriate)
C_l, C_L	sectional lift coefficient
C_M	inertia coefficient in Morison's equation; moment coefficient (Section 4.6)

C_n^m	coefficient of a Kinner pressure distribution
C_N	normal force coefficient (Section 4.6)
C_p	pressure coefficient
C_P	power coefficient or coefficient of performance
C_Q	torque coefficient
C_T	thrust coefficient; total cost of wind turbine
C_{TB}	total cost of baseline wind turbine
C_x	coefficient of sectional blade element force normal to the rotor plane
C_y	coefficient of sectional blade element force parallel to the rotor plane
$C(\Delta r, n)$	coherence – i.e. normalised cross-spectrum – for wind speed fluctuations at points separated by distance s measured in the across wind direction
$C_{jk}(n)$	coherence – i.e. normalised cross-spectrum – for longitudinal wind speed fluctuations at points j and k
d	streamwise distance between vortex sheets in a wake; water depth;
d_{PL}	floating support structure draft
d_1	pitch diameter of pinion gear
D	pitch diameter of planet gear
D	drag force; tower diameter; rotor diameter; flexural rigidity of plate; constrained wave trough elevation
E	energy capture, i.e. energy generated by turbine over defined time period; modulus of elasticity
E_1	longitudinal elastic modulus of uniaxial composite ply
E_2	transverse elastic modulus of uniaxial composite ply
$E\{\}$	time averaged value of expression within brackets
$E(H_s \bar{U})$	expected value of significant wave height conditional on a hub-height mean wind speed \bar{U}
f	tip-loss factor; Coriolis parameter; wave frequency; source intensity
$f()$	probability density function
$f_1(t)$	support structure first mode hub displacement
$f_j(t)$	blade tip displacement in j th mode
$f_{in}(t)$	blade tip displacement in i th mode at the end of the n th timestep
$f_J(t)$	blade j first mode tip displacement
f_p	wave frequency corresponding to peak spectral density
$\hat{f}_T(t)$	hub displacement for tower first mode
F	force; force per unit length
F_x	load in x (downwind) direction
F_Y	load in y direction
F_t	force between gear teeth at right angles to the line joining the gear centres
$F(\mu)$	flow expansion function determining the radial distribution of the radial component of induced velocity normal to the wake axis
$F()$	cumulative probability distribution function
$F(x U_k)$	cumulative probability distribution function for variable x conditional on $U = U_k$
g	acceleration due to gravity; vortex sheet strength; peak factor, defined as the number of standard deviations of a variable to be added to the mean

g_0	to obtain the extreme value in a particular exposure period, for zero up-crossing frequency, v
G	peak factor as above, but for zero up-crossing frequency n_0
G_{12}	geostrophic wind speed; shear modulus; gearbox ratio
$G(f)$	shear modulus of composite ply
$G(t)$	transfer function divided by dynamic magnification ratio
h	t second gust factor
h	height of atmospheric boundary layer; duration of timestep; thickness of thin-walled panel; maximum height of single gear tooth contact above critical root section; height of centre of buoyancy above centre of gravity for a spar buoy
$h(\psi)$	root vortex influence function
H	hub height; wave height; hub height above mean sea level
H_1	1 year extreme wave height
H_{50}	50 year extreme wave height
H_{jk}	elements of transformational matrix, \mathbf{H} , used in wind simulation
$H_i(n)$	complex frequency response function for the i th mode
$H(f)$	frequency-dependent transfer function
H_s	significant wave height
H_{s1}	1 year extreme significant wave height based on 3 hour reference period
H_{s50}	50 year extreme significant wave height based on 3 hour reference period
H_B	breaking wave height
I	turbulence intensity; second moment of area; moment of inertia; electrical current (shown in bold when complex)
I_0	ambient turbulence intensity
I_+	added turbulence intensity
I_{++}	added turbulence intensity above hub height
I_b	blade inertia about root
I_r	inertia of rotor about horizontal axis in its plane
I_{ref}	reference turbulence intensity, defined as expected value of hub-height turbulence intensity at reference mean wind speed of 15 m/s
I_u	longitudinal turbulence intensity
I_v	lateral turbulence intensity
I_w	vertical turbulence intensity
I_{wake}	total wake turbulence intensity
i, j	$\sqrt{-1}$
k	shape parameter for Weibull function; shape parameter for GEV distribution; integer; reduced frequency, $(\omega c/2W)$; wave number, $2\pi/L$; surface roughness; turbulence energy (Section 4.7.3)
k_i	generalised stiffness with respect to the i th mode, defined as $m_i \omega_i^2$
K	constant on right hand side of Bernoulli equation
K_C	Keulegan–Carpenter number
K_P	power coefficient based on tip speed
K_{SMB}	size reduction factor accounting for the lack of correlation of wind fluctuations over structural element or elements

$K_{Sx}(n_1)$	size reduction factor accounting for the lack of correlation of wind fluctuations at resonant frequency over structural element or elements
$K_v()$	modified Bessel function of the second kind and order v
$K(\chi)$	function determining the induced velocity normal to the plane of a yawed rotor
L	length scale for turbulence (subscripts and superscripts according to context); lift force; wave length
xL_u	integral length scale for the along-wind turbulence component, u , measured in the longitudinal direction, x
m	mass per unit length; integer; depth below seabed of effective monopole fixity; inverse slope of log-log plot of $S-N$ curve
m_a	added mass per unit span of blade
m_i	generalised mass with respect to the i th mode
m_{T1}	generalised mass of tower, nacelle, and rotor with respect to tower first mode
$\frac{M}{M}$	moment; integer; tower top mass; mass of floating structure
M_0	mean bending moment
$M_1(t)$	peak quasi-static mudline moment
M_T	fluctuating cantilever root bending moment due to excitation of first mode
M_X	teeter moment
M_Y	blade in-plane moment (i.e. moment causing bending in plane of rotation); tower side-to-side moment
M_Z	blade out-of-plane moment (i.e. moment causing bending out-of-plane of rotation); tower fore-aft moment
M_{YS}	blade torsional moment; tower torsional moment
M_{ZS}	low-speed shaft moment about rotating axis perpendicular to axis of blade 1
M_{YN}	low-speed shaft moment about rotating axis parallel to axis of blade 1
M_{ZN}	moment exerted by low-speed shaft on nacelle about (horizontal) y axis
n	moment exerted by low-speed shaft on nacelle about (vertical) z axis
n	frequency (Hz); number of fatigue loading cycles; integer; distance measured normal to a surface
n_0	zero up-crossing frequency of quasi-static response
n_1	frequency (Hz) of first mode of vibration
N	number of timesteps per revolution; integer; design fatigue life in number of cycles for a given constant stress range
$N(r)$	centrifugal force
$N(S)$	number of fatigue cycles to failure at stress level S
p	static pressure
$p()$	probability density function
P	aerodynamic power; electrical real (active) power
$P_n^m()$	associated Legendre polynomial of the first kind
$q(r, t)$	fluctuating aerodynamic lift per unit length
Q	rotor torque; electrical reactive power
\dot{Q}_a	aerodynamic torque
\dot{Q}	rate of heat flow

\bar{Q}	mean aerodynamic lift per unit length
Q_D	dynamic factor defined as ratio of extreme moment to gust quasi-static moment
Q_g	load torque at generator
Q_L	loss torque
$Q_n^m()$	associated Legendre polynomial of the second kind
$Q_1(t)$	generalised load, defined in relation to a cantilever blade by Eq. (A5.13)
r	radius of blade element or point on blade; correlation coefficient between power and wind speed; radius of tubular tower; radius of monopile
r'	radius of point on blade
r_1, r_2	radii of points on blade or blades
R	blade tip radius; ratio of minimum to maximum stress in fatigue load cycle; electrical resistance
Re	Reynolds number
$R_u(n)$	normalised power spectral density, $n.S_u(n)/\sigma_u^2$, of longitudinal wind speed fluctuations, u , at a fixed point
s	distance inboard from the blade tip; distance along the blade chord from the leading edge; separation between two points; Laplace operator; slip of induction machine; spacing of columns of a semi-submersible
s_1	separation between two points measured in the along-wind direction
S	wing area; autogyro disc area; fatigue stress range; surface area
$S()$	(apparent) electrical power (bold indicates a complex quantity)
$S()$	uncertainty or error band
$S_{jk}(n)$	cross-spectrum of longitudinal wind speed fluctuations, u , at points j and k (single-sided)
$S_M(n)$	single-sided power spectrum of bending moment
$S_{Q1}(n)$	single-sided power spectrum of generalised load
$S_u(n)$	single-sided power spectrum of longitudinal wind speed fluctuations, u , at a fixed point
$S_u^o(n)$	single-sided power spectrum of longitudinal wind speed fluctuations, u , as seen by a point on a rotating blade (also known as <i>rotationally sampled spectrum</i>)
$S_u^o(r_1, r_2, n)$	cross-spectrum of longitudinal wind speed fluctuations, u , as seen by points at radii r_1 and r_2 on a rotating blade or rotor (single-sided)
$S_v(n)$	single-sided power spectrum of lateral wind speed fluctuations, v , at a fixed point
$S_w(n)$	single-sided power spectrum of vertical wind speed fluctuations, w , at a fixed point
$S_{\eta\eta}(n)$	single-sided power spectrum of sea surface elevation
t	time; gear tooth thickness at critical root section; tower wall thickness; monopole wall thickness; thickness of aerofoil section (maximum)
T	rotor thrust; duration of discrete gust; wind speed averaging period; wave period for regular waves; time step
T_c	mean period between wave crests
T_p	peak wave period, $1/f_p$

T_z	mean zero crossing wave period
u	fluctuating component of wind speed in the x direction; induced velocity in upstream direction (as in Figure 4.5); perturbation velocity in x direction (downstream, as in Figure 4.11); in-plane plate deflection in x direction; gear ratio; water particle velocity in x direction
u^*	friction velocity in boundary layer
U_∞	free-stream velocity
U_0	free-stream velocity
$U, U(t)$	instantaneous wind speed in the along-wind direction
\bar{U}	mean component of wind speed in the along-wind direction – typically taken over a period of 10 min or 1 h
U_{ave}	annual average wind speed at hub height
U_D	streamwise velocity at the rotor disc
U_i	turbine lower cut-in wind speed
U_W	streamwise velocity in the far wake
U_{e1}	extreme 3 s gust wind speed with 1 year return period
U_{e50}	extreme 3 s gust wind speed with 50 year return period
U_0	turbine upper cut-out wind speed
U_r	turbine rated wind speed, defined as the wind speed at which the turbine's rated power is reached
U_{ref}	reference wind speed defined as 10 min mean wind speed at hub height with 50 year return period
U_1	strain energy of plate flexure
U_2	in-plane strain energy
v	fluctuating component of wind speed in the y direction; induced velocity in y direction; in-plane plate deflection in y direction
V	airspeed of an autogyro; streamwise velocity at rotor disc, $U_\infty(1 - \alpha)$ (Section 7.1.15); voltage (shown in bold when complex)
VAr	reactive power volt-amperes-reactive
$V(t)$	instantaneous lateral wind speed
VA	apparent power electrical volt-amperes
V_f	fibre volume fraction in composite material
w	fluctuating component of wind speed in the z direction; induced velocity in z direction; out-of-plane plate deflection; weighting factor; water particle velocity in z direction
$w(r)$	blade shell skin thickness (Section 6.4.2)
W	wind velocity relative to a point on rotating blade; electrical power loss
x	downwind coordinate – fixed and rotating axis systems; horizontal co-ordinate in the direction of wave propagation; downwind displacement
$x(t)$	stochastic component of a variable
x_n	length of near wake region
x_0	mode of distribution
\bar{x}_1	first mode component of steady tip displacement
X	electrical inductive reactance
X_n	coefficient of n th term in Dean's stream function

y	lateral coordinate with respect to vertical axis (starboard positive) – fixed axis system
y	lateral coordinate with respect to blade axis – rotating axis system
y	lateral displacement; reduced variate of distribution; height above seabed
z	vertical coordinate (upwards positive) – fixed axis system; height above ground datum; height above water level; delay operator
z	radial coordinate along blade axis – rotating axis system
z_0	ground roughness length
z_1	number of teeth on pinion gear
$z(t)$	periodic component of a variable
Z	section modulus; externally applied load on flanged joint
Z	electrical impedance (bold indicates a complex quantity)

Greek

α	angle of attack – i.e. angle between air flow incident on the blade and the blade chord line; wind-shear power law exponent; exponent of reduced variate in three parameter Weibull distribution; exponent of JONSWAP spectrum peak shape parameter; direction change of geostrophic wind relative to surface
α_x	meridional elastic imperfection reduction factor
β	inclination of local blade chord to rotor plane (i.e. blade twist plus pitch angle, if any); pitch angle (Sections 8.3.5 & 8.3.16) radius of environmental contour
β_r	probability weighted moment raised to power r
γ	yaw angle; Euler's constant ($= 0.5772$); JONSWAP spectrum peak shape parameter
γ_L	load factor
γ_{mf}	partial safety factor for material fatigue strength
γ_{mu}	partial safety factor for material ultimate strength
Γ	blade circulation; vortex strength
$\Gamma()$	gamma function
δ	logarithmic decrement of combined aerodynamic and structural damping; width of tower shadow deficit region; depth of surface irregularity; width of jet slot; wake velocity deficit
δ_3	angle between axis of teeter hinge and the line perpendicular to both the rotor axis and the low-speed shaft axis
δ_a	logarithmic decrement of aerodynamic damping
δ_s	logarithmic decrement of structural damping
Δ	$1 - \nu_{12}\nu_{21}$; discrete jump (e.g. $(0^- - 0^+)$)
ε	proportion of axial stress to total stress; eddy viscosity
ε	turbulence dissipation
$\varepsilon_1, \varepsilon_2, \varepsilon_3$	proportion of time in which a variable takes the maximum, mean, or minimum values in a three-level square wave
ζ	teeter angle

η	ellipsoidal coordinate; shaft tilt; one eighth of Lock number (defined in Section 5.8.8); skewness parameter; water surface elevation
η_b	crest elevation above still water level for a breaking wave
θ	blade pitch angle; wind speed direction change; random phase angle; azimuthal direction; cylindrical panel coordinate; brake disc temperature
κ	von Karman's constant
$\kappa(t - t_0)$	auto-correlation function
$\kappa_L(s)$	cross-correlation function between velocity components at points in space a distance s apart, in the direction parallel to the line joining them
$\kappa_T(s)$	cross-correlation function between velocity components at points in space a distance s apart, in the direction perpendicular to the line joining them
$\kappa_u(r, \tau)$	auto-correlation function for along-wind velocity component at radius r on stationary rotor
$\kappa_u^o(r, \tau)$	auto-correlation function for along-wind velocity component as seen by a point at radius r on a rotating rotor
$\kappa_u(r_1, r_2, \tau)$	cross-correlation function between along-wind velocity components at radii r_1 and r_2 (not necessarily on same blade), for stationary rotor
$\kappa_u^o(r_1, r_2, \tau)$	cross-correlation function between along-wind velocity components as seen by points (not necessarily on same blade) at radii r_1 and r_2 on a rotating rotor
λ	tip speed ratio; latitude; ratio of longitudinal to transverse buckle half wavelengths; relative shell slenderness; curling factor of breaking wave
λ_r	tangential speed of blade element at radius r divided by wind speed: local speed ratio
$\lambda(d)$	ratio measuring influence of loading near cantilever root on first mode resonance (Section 12.7.4)
$\lambda^*(d)$	approximate value of $\lambda(d)$
Λ	yaw rate
μ	non-dimensional radial position, r/R ; viscosity; coefficient of friction
$\mu_i(r)$	mode shape of i th blade mode
$\mu_1(y)$	mode shape of first mode of offshore support structure
$\mu_i(z)$	mode shape of i th tower mode
$\mu_T(z)$	tower first mode shape
$\mu_{Tj}(r)$	normalised rigid body deflection of blade j resulting from excitation of tower first mode
μ_z	mean value of variable z
ν	ellipsoidal coordinate; mean zero up-crossing frequency; rank in series of data points; kinematic viscosity; Poisson's ratio
ν_{12}, ν_{21}	Poisson's ratios for uniaxial composite ply
ξ	damping ratio
ρ	air density; water density
$\rho_u^o(r_1, r_2, \tau)$	normalised cross-correlation function between along-wind velocity components as seen by points (not necessarily on same blade) at radii r_1 and r_2 on a rotating rotor (i.e. $\kappa_u^o(r_1, r_2, \tau)/\sigma_u^2$)
σ	blade solidity; standard deviation; stress

$\bar{\sigma}$	mean stress
σ_{cr}	elastic critical buckling stress
σ_M	standard deviation of bending moment
σ_{M1}	standard deviation of first mode resonant bending moment, at blade root for blade resonance, and at tower base for tower resonance
σ_{MB}	standard deviation of quasi-static bending moment (or bending moment background response)
σ_{Mh}	standard deviation of hub dishing moment
σ_{MT}	standard deviation of teeter moment for rigidly mounted, two bladed rotor
$\sigma_{\bar{M}}$	standard deviation of mean of blade root bending moments for two bladed rotor
σ_{Q1}	standard deviation of generalised load with respect to first mode rotor solidity at a given radius, r , i.e. $Bc/(2\pi r)$
σ_r	standard deviation of fluctuating component of wind in along-wind direction
σ_v	standard deviation of wind speed in across-wind direction
σ_w	standard deviation of wind speed in vertical direction
σ_{x1}	standard deviation of first mode resonant displacement, referred to blade tip for blade resonance and to nacelle for tower resonance
τ	time interval; non-dimensional time; shear stress
v	Poisson's ratio
ϕ	flow angle of resultant velocity W to rotor plane; velocity potential; blade azimuth (Section 8.3.11)
$\Phi()$	standard normal distribution function
$\Phi(x, y, z, t)$	velocity potential due to unit source
Φ	Wagner (impulsive heave motion) function (Sections 4.5.3 and 4.6.2)
χ	wake skew angle: angle between the axis of the wake of a yawed rotor and the axis of rotation of rotor; buckling strength reduction factor; fibre inclination to blade panel axis
χ_{M1}	weighted mass ratio defined in Section 5.8.6
ψ	blade azimuth; angle subtended by cylindrical plate panel; stream function parameter with respect to fixed reference frame; wake amplification factor
$\bar{\psi}$	stream function parameter with respect to frame of reference moving at same speed as wave crests and troughs
$\psi_{uu}(r, r', n)$	real part of normalised cross-spectrum
Ψ	Kussner (indicial gust) function
ω	angular frequency (rad/s)
ω_d	demanded generator rotational speed
ω_i	natural frequency of i th mode (rad/s)
ω_g	generator rotational speed
ω_r	induction machine rotor rotational speed
ω_s	induction machine stator field rotational speed
Ω	rotational speed of rotor; Earth's rotational speed

Subscripts

a	aerodynamic
B	baseline
c	compressive
d	disc; drag; design
e	motion due to elastic deformation
$e1$	extreme value with return period of 1 year
$e50$	extreme value with return period of 50 years
ext	extreme
f	fibre
i	mode i
j	mode j
J	blade J
k	characteristic
l	lift
m	matrix
M	moment
max	maximum value of variable
min	minimum value of variable
n	value at end of n th timestep
Q	generalised load
R	value at tip radius, R
s	structural
t	tensile
T	thrust
u	downwind; ultimate
v	lateral
w	vertical
w	wake
x	deflection in along-wind direction

Superscripts

o	rotationally sampled (applied to wind speed spectra)
-----	--

Figures C1 and C2 – coordinate systems

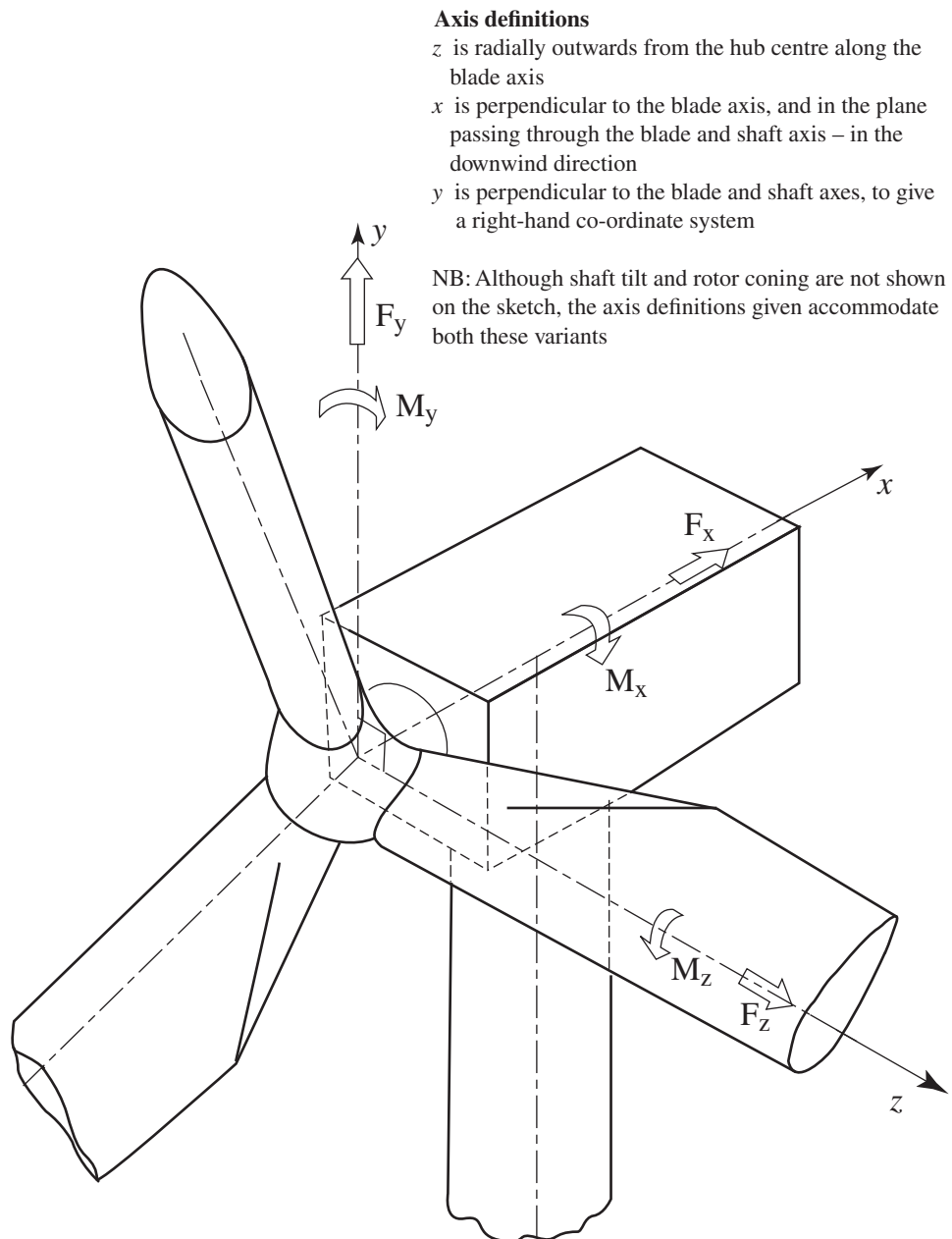


Figure C1 Coordinate system for blade loads, positions, and deflections (rotates with blade).

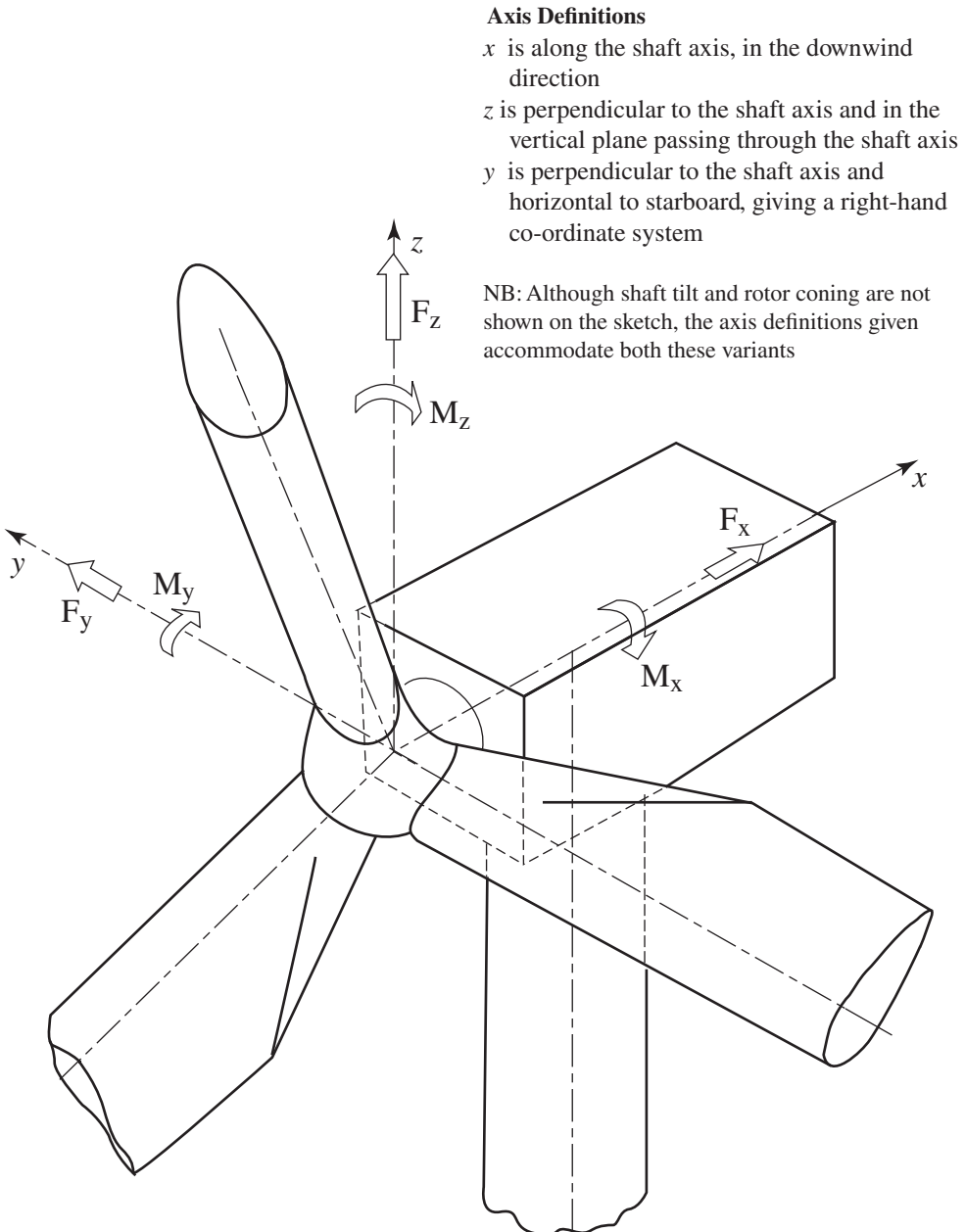


Figure C2 Fixed coordinate system for hub loads and deflections, and positions with respect to hub.

1

Introduction

1.1 Historical development of wind energy

Windmills have been used for at least 3000 years, mainly for grinding grain or pumping water, while the wind has been the essential source of power in sailing ships for even longer. From medieval times, horizontal axis windmills were an integral part of the rural economy throughout Europe and only fell into disuse with the advent of cheap fossil-fuelled stationary engines and then the spread of rural electrification (Musgrove 2010).

The use of windmills (or wind turbines) to generate electricity can be traced back to the late nineteenth century with the 12 kW direct current windmill generator constructed by Charles Brush in the USA and the research undertaken by Poul la Cour in Denmark. However, for much of the twentieth century, there was little interest in using wind energy, other than for battery charging for remote dwellings; these low power systems were quickly removed once more reliable and higher power electricity supplies from the public electricity network became available. One notable development was the 1250 kW Smith-Putnam wind turbine constructed in the USA in 1941. This remarkable machine had a steel rotor 53 m in diameter, full-span pitch control, and flapping blades to reduce loads. Although a blade spar failed catastrophically in 1945, it remained the largest wind turbine constructed for some 40 years (Putnam 1948).

Golding (1955) and Spera (1994) provide a fascinating history of early wind turbine development. They record the 100 kW 30 m diameter Balaclava wind turbine in the USSR in 1931 and developments in the UK during the 1950s, including the John Brown Engineering, 15 m diameter turbine erected on a high wind speed site on Orkney and the Andrea Enfield 100 kW 24 m diameter pneumatic design. In this novel turbine, hollow blades, open at the tip, were used to draw air up through the tower, where an air turbine drove the generator. In Denmark, the 200 kW 24 m diameter Gedser machine was built in 1956 and operated for 11 years to provide an important foundation of knowledge for the later development of early commercial turbines. Electricité de France tested a 1.1 MW 35 m diameter turbine in 1963, while in Germany, Professor Ulrich Hutter constructed a

2 INTRODUCTION

number of innovative, lightweight turbines in the 1950s and 1960s. In spite of these technical advances and the enthusiasm of Golding at the Electrical Research Association in the UK, among others, there was little sustained interest in wind generation until the price of oil rose dramatically in 1973.

The sudden increase in the price of oil stimulated a number of substantial, government-funded programmes of research, development, and demonstration. In the USA, this led to the construction of a series of prototype turbines starting with the 38 m diameter 200 kW Mod-0 in 1975 and culminating in the 97.5 m diameter 3.2 MW Mod-5 in 1987. Similar programmes were pursued in Germany with the Growian, 100 m diameter 3 MW turbine built in 1982 and in the UK with the LS-1 60 m diameter 3 MW turbine in 1988, both of which had two blades (Hau 2010). There was considerable uncertainty as to which architecture might prove most cost-effective, and several innovative concepts were investigated at full scale. In Canada, a 4 MW vertical axis Darrieus wind turbine was constructed, and this concept was also investigated in the 34 m diameter Sandia vertical axis test facility in the USA. In the UK, an alternative, vertical axis design using straight blades in an ‘H’ type rotor was proposed by Dr Peter Musgrove and a 500 kW prototype constructed. In 1981, the innovative Schachle-Bendix horizontal axis 3 MW wind turbine was built and tested in the USA (Spera 1994). This used hydraulic transmission, and, as an alternative to a bearing at the top of the tower and yaw drive, the entire structure was orientated into the wind. Several prototypes used a single blade and counterweight, including the 600 kW MBB Monopteros in 1985 (Hau 2010).

Much important scientific and engineering information was gained from these government-funded research programmes, and the prototypes generally worked as designed. However, the problems of operating very large wind turbines, unmanned and in difficult wind climates, were often underestimated, and the reliability of the prototypes was not good. At the same time as the multi-megawatt prototypes were being constructed, private companies, often with considerable state support, were constructing much smaller and simpler turbines for commercial sale. In particular, the financial support mechanisms in California in the mid-1980s resulted in the installation of a very large number of quite small (around 100 kW) wind turbines of various designs. Many of these designs also suffered from various problems, but, being smaller, they were easier to repair and modify.

The so-called ‘Danish wind turbine’ concept emerged of a three blade, upwind, stall regulated rotor and a fixed speed, induction generator. This design was installed widely in Denmark and Germany, supported by Feed-in Tariffs that paid a fixed premium rate for electricity generated by wind energy. The deceptively simple architecture of the Danish wind turbine proved to be remarkably successful and was implemented on turbines as large as 60 m in diameter and at power ratings of up to 1.5 MW. However, at larger rotor diameters and generator ratings, the architecture ceases to be effective because, with larger rotors, aerodynamic stall is increasingly difficult to predict, and the larger induction generators were no longer able to provide enough damping and torsional compliance in the drive train. Also, the requirements of the electrical Transmission System Operators for connecting wind farms to the network become very difficult to meet with a simple fixed speed induction generator. Hence, as the size of commercially available turbines approached or exceeded that of the large prototypes of the 1980s, the concepts investigated then of variable-speed operation and full-span control of the blade pitch as well as advanced materials and modern control systems were increasingly

adopted. The evolution of modern wind turbines is described in Serrano-González and Lacal-Arántegui (2016).

In 1991, the first offshore wind farm, consisting of 11 450 kW wind turbines, was constructed at Vindeby, 3 km off the coast of Denmark. Throughout the 1990s, small numbers of offshore wind turbines were placed close to shore, while in 2002, the Horns Rev, 160 MW wind farm, was constructed some 20 km off the western coast of Denmark. At the time of writing (2020), there was around 29 GW of offshore wind energy capacity in operation (Global Wind Energy Council 2020), concentrated mainly off the coasts of northern Europe and eastern China. There are a number of offshore wind farms of capacity greater than 500 MW, and even larger installations are under construction or planned. The wind turbines installed in the early offshore wind farms were marinised conventional designs that had been proved onshore. More recently, very large wind turbines designed specially for transport directly by sea from the factory to the offshore site have been installed. Further, the possibility of higher blade tip speeds because of more relaxed noise constraints and a reduced emphasis on the visual appearance of wind farms far from land continue to lead to interest in the development of very large, lower solidity rotors (Jamieson 2018).

The stimulus for the development of wind energy in 1973 was the increase in the price of oil and concern over limited fossil fuel resources. From around 1990, the main driver for the use of wind turbines to generate electrical power has been the very low CO₂ emissions, over the entire life cycle of manufacture, installation, operation, and de-commissioning, and the potential of wind energy to help mitigate climate change. In 2007, the European Union established a policy that 20% of all energy should be from renewable sources by 2020. Because of the difficulty of using renewable energy for transport and heat, this implies that in some countries 30–40% of electrical energy should come from renewables, with wind energy playing a major part. Energy policy continues to develop rapidly, with the European Union extending its target for the share of energy to come from renewables by 2030 to 32% and many countries now adopting a commitment to reduce or eliminate greenhouse gas emissions before 2050.

Figure 1.1 shows the remarkable growth in the installed capacity of wind power worldwide over 15 years to 2019. The typical annual rate of increase of capacity was more

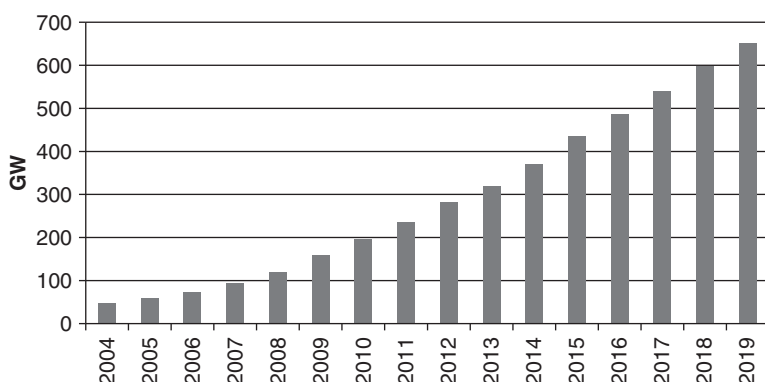


Figure 1.1 Wind power capacity worldwide (World Wind Energy Association 2020).

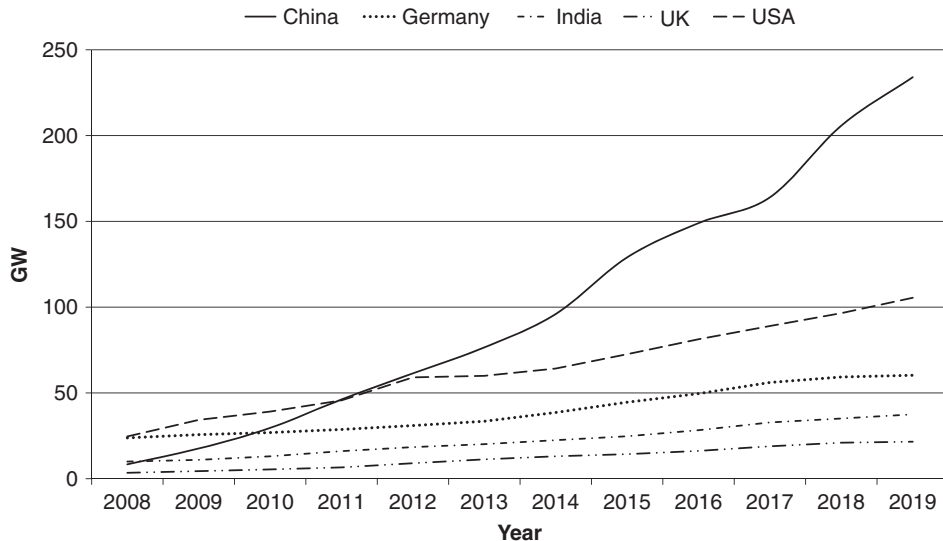


Figure 1.2 Wind power capacity by country (US Energy Information Administration 2019; REN21 2020).

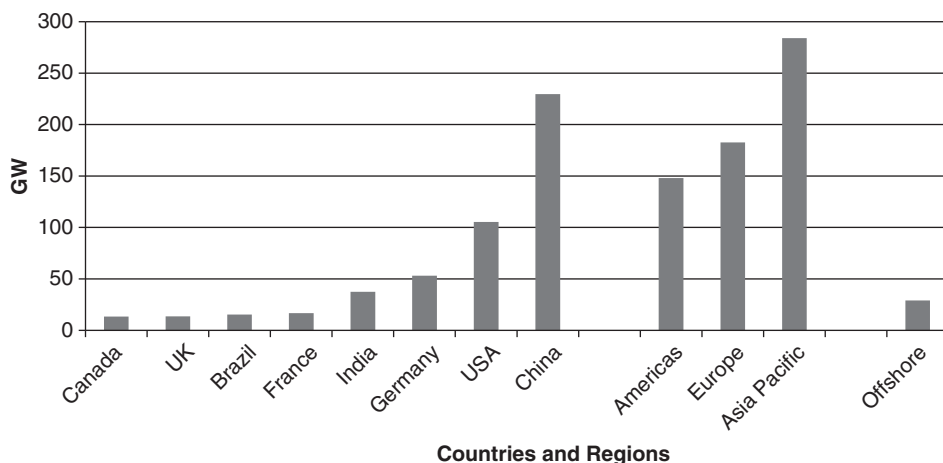


Figure 1.3 Installed onshore wind power capacity in countries with more than 10 GW, regions, and total offshore (Global Wind Energy Council 2020).

than 10%. Figure 1.2 shows the growth of wind energy capacity by country, dominated by China and the USA. Figure 1.3 summarises current capacity (2019) by country and region of the world.

The development of wind energy in some places has been more rapid than in others, and this cannot be explained simply by differences in the wind speeds. Important factors include the financial support mechanisms for wind generated electricity, access to the



Figure 1.4 Onshore wind turbines in flat terrain. Source: Stockr/Shutterstock.com.

electrical network, the permitting process by which the local civil authorities give permission for the construction of wind farms, and the perception of the general population, particularly with respect to visual impact. The development of offshore sites, although at considerably increased cost, is in response to these concerns over the environmental impact of onshore wind farms.

Figure 1.4 shows modern wind turbines in flat open terrain, and Figure 1.5 shows an offshore wind farm.

When it was a new electricity generation technology, wind energy required financial support for some years to encourage its development and stimulate investment from private companies. Such support was provided in many countries in recognition of the contribution that wind generation makes to mitigating climate change and the security of national energy supplies. Feed-in Tariffs continue to be offered in a number of countries. These are fixed prices paid for each kWh generated from renewable sources with different rates for wind energy, photovoltaic solar energy, and other renewable energy technologies. This support mechanism has the benefit of giving certainty of the revenue stream from a successful project and is credited by its supporters for the very rapid development of wind energy, and other renewables, in these countries.

Large wind farms are now often supported through competitive auctions that establish a price that a project developer can expect for the electrical energy. This acts to reduce uncertainty and hence project financing costs. The cost of generating electricity from wind power continues to fall and is now below the retail price of electricity in most countries and lower than the cost of generation from alternative sources of energy under



Figure 1.5 Offshore wind farm. Source: fokke baarssen/Shutterstock.com.

favourable conductions of high site wind speed and low wind farm constriction costs. These cost reductions mean the need for national subsidies is rapidly reducing.

1.2 Modern wind turbines

The power output from a wind turbine is given by the well-known expression:

$$P = \frac{1}{2} C_p \rho A U^3$$

ρ is the density of air (1.25 kg/m^3)

C_p is the power coefficient

A is the rotor swept area

U is the free wind speed

The density of air is rather low, 800 times less than water, which powers hydro turbines, and this leads inevitably to the large size of a wind turbine. Depending on the design wind speed that is chosen, a 3.5 MW wind turbine may have a rotor that is 100 m in diameter. The power coefficient describes that fraction of the power in the wind that may be converted by the turbine into mechanical work. It has a maximum value of $16/27$ or 0.593, and rather lower peak values are achieved in practice (see Chapter 3). Incremental improvements in the power coefficient are continually being sought by detailed design changes of the rotor, and by operating at variable speed it is possible to maintain the maximum power coefficient over a range of wind speeds. However, these measures will give

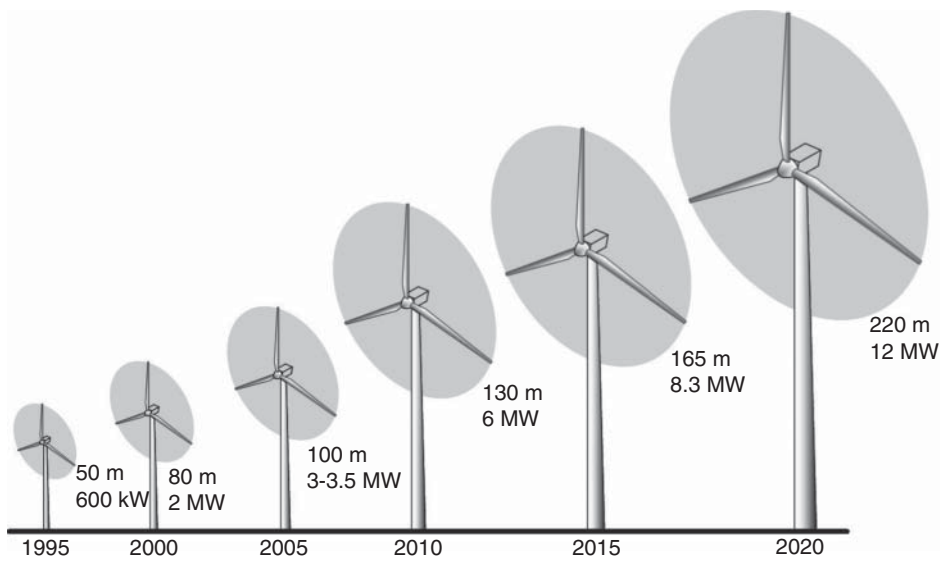


Figure 1.6 Largest commercially available wind turbines.

only a modest increase in the power output. Major increases in the output power can only be achieved by increasing the swept area of the rotor or by locating the wind turbines in higher wind speeds.

Hence, over the last 25 years there has been a continuous increase in the rotor diameter of commercially available wind turbines from around 40 m to several manufacturers offering turbines of more than 170 m (Figure 1.6). A tripling of the rotor diameter leads to a nine times increase in power output. The influence of the wind speed is even more pronounced, with a doubling of wind speed leading to an eightfold increase in power. Thus, there have been considerable efforts to ensure that wind farms are developed in areas of the highest wind speeds and the turbines optimally located within wind farms. In certain countries, with modest wind speeds, very high towers are being used to take advantage of the increase of wind speed with height.

In the past a number of studies were undertaken to determine the optimum size of a wind turbine by balancing the complete costs of manufacture, installation, and operation of various sizes of wind turbines against the revenue generated (Molly et al. 1993). However, these early estimates would now appear to be too low, and more recent studies indicate that the lowest cost of energy is obtained with rotors approaching 150 m diameter, although smaller turbines may be preferred on some sites for reasons of environmental impact and difficulty of transporting very large components to the site. Even larger turbines give the lowest cost of energy offshore, where the foundation and cabling costs of individual turbine are high and the very large blades can be transported by ship directly from the factory to the site.

All modern electricity generating wind turbines use the lift force derived from the blades to drive the rotor. A high rotational speed of the rotor is desirable to reduce the gearbox ratio required, and this leads to a low solidity rotor (the ratio of blade area to rotor swept area). The low solidity rotor acts as an effective energy concentrator, and as

a result the energy generated over a wind turbine's life is much greater than that used for its manufacture and installation. An energy balance analysis of a 3 MW wind turbine showed that the expected average time to generate a similar quantity of energy to that used for its manufacture, operation, transport, dismantling, and disposal was six to seven months (European Wind Energy Association 2009). A similar time was calculated for offshore wind turbines. Offshore the higher mean wind speeds, and hence greater energy output, compensate for the higher wind farm costs and energy expended in construction and operation.

Until around the year 2000, the installed wind turbine generating capacity was so low that its output was viewed by electricity Transmission System Operators simply as negative load that supplied energy but played no part in the operation of the power system and maintaining its stability. Since then, with the greatly increased capacity of wind generation, turbines are required to contribute to the operation of the power system. The requirements for their performance are defined through the Grid Codes, issued by the Transmission System Operators (Roberts 2018). Compliance is mandatory and must be demonstrated before connection to the network is allowed. Compliance with the Grid Code requirements is difficult to achieve with simple fixed speed induction generators using the Danish concept, and these regulations have been a major driver for the use of variable-speed generators.

1.3 Scope of the book

The use of wind energy to generate electricity is now well accepted, with a large industry manufacturing and installing up to 50 GW of new capacity each year. Although there are exciting new developments, particularly in very large offshore turbines, and many challenges remain, there is a considerable body of established knowledge concerning the science and technology of wind turbines. This book records some of this knowledge and presents it in a form suitable for use by students (at final year undergraduate or post-graduate level) and by those involved in the design, manufacture, or operation of wind turbines. The overwhelming majority of wind turbines presently in use are horizontal axis connected to a large electricity network. These turbines are the subject of this book.

Chapter 2 discusses the wind resource. Particular reference is made to wind turbulence due to its importance in wind turbine design. Chapter 3 sets out the basis of the aerodynamics of horizontal axis wind turbines, while Chapter 4 discusses more specialised aspects of wind turbine aerodynamics. Any wind turbine design starts with establishing the design loads, and these are discussed in Chapter 5. Chapter 6 sets out the various design options for horizontal axis wind turbines, with approaches to the design of some of the important components examined in Chapter 7. The functions of the wind turbine controller and some of the possible techniques used to design and implement the controllers are discussed in Chapter 8. Wake effects and wind farm control are discussed in Chapter 9. This is a new chapter in this edition. In Chapter 10, wind farms and the development of wind energy projects are reviewed, with particular emphasis on

environmental impact. Chapter 11 considers how wind turbines are connected to electrical networks and their characteristics as an increasingly important source of generation. Very large wind farms with multi-megawatt turbines are now being constructed many kilometres offshore, and a considerably expanded Chapter 12 deals with the important topic of offshore wind energy.

The book attempts to record well-established knowledge that is relevant to wind turbines that are currently commercially significant. Thus, it does not discuss a number of interesting research topics or areas where wind turbine technology is still evolving. Although they were investigated in considerable detail in the 1980s, large vertical axis wind turbines have not proved to be commercially competitive and are not currently manufactured in significant numbers. Hence, the particular issues of vertical axis turbines are not dealt with in this text.

There are presently around one billion people in the world without access to reliable mains electricity, and, in conjunction with other generators (e.g. batteries, diesel engines, and solar photovoltaic units), wind turbines may in the future be an effective means of providing some of them with power. However, autonomous power systems (sometimes known as *autonomous microgrids*) are extremely difficult to operate reliably, particularly in remote areas of the world and with limited budgets. A small autonomous microgrid has all the technical challenges of a large national electricity system but, due to the low inertia of the generators, requires a very fast, sophisticated control system to maintain stable operation as well as a store of energy. Over the last 40 years there have been a number of attempts to operate autonomous wind-diesel systems on islands or for other remote communities throughout the world, but with only limited success. This class of installation has its own particular characteristics, and, given the limited size of the market at present, this specialist area is not dealt with in this book.

References

- European Wind Energy Association (2009). *Wind Energy – The Facts*. London: Earthscan.
- Golding, E.W. (1955). *The Generation of Electricity from Wind Power*. London: E. & F.N. Spon (reprinted R.I. Harris, London 1976).
- Hau, E. (2010). *Wind Turbines: Fundamentals, Technologies, Application, Economics*, 2e. Heidelberg: Springer.
- Jamieson, P. (2018). *Innovation in Wind Turbine Design*, 2e. Chichester: Wiley.
- Molly, J.P., Keuper, A., and Veltrup, M. (1993). Statistical WEC design and cost trends. Proceedings of the European Wind Energy Conference, Travemunde (8–12 March 1993), pp. 57–59.
- Musgrove, P. (2010). *Wind Power*. Cambridge: Cambridge University Press.
- Putnam, G.C. (1948). *Power from the Wind*. New York: Van Nostrand Reinhold.
- Roberts C. (2018) Review of international grid codes, Lawrence Berkeley National Laboratory file:///Users/scenj/Downloads/eScholarship%20UC%20item%205sv540qx.pdf (accessed 7 December 2019).
- Serrano-González, J. and Lacal-Arántegui, R. (2016). Technological evolution of onshore wind turbines – a market-based analysis. *Wind Energy* 19: 2171–2187.
- Spera, D.A. (1994). *Wind Turbine Technology: Fundamental Concepts of Wind Turbine Engineering*. New York: ASME Press.

Websites

- Global Wind Energy Council (2020). Global wind report 2019. <https://gwec.net/global-wind-report-2019/> (accessed 30 July 2020).
- REN21 (2020). 2020 Global status report. <https://www.ren21.net/gsr-2020/> (accessed 31 July 2020).
- US Energy Information Administration, (2019). International data. <https://www.eia.gov/beta/international/data> (accessed 26 May 2019).
- World Wind Energy Association (2020). Statistics. <https://wwindea.org/blog/category/statistics/> (accessed 30 July 2020).

Further Reading

- Anderson, C. (2020). *Wind Turbines: Theory and Practice*. Cambridge University Press.
- Boyle, G. (ed.) (2017). *Renewable Energy and the Grid*. London: Earthscan.
- Eggleston, D.M. and Stoddard, F.S. (1987). *Wind Turbine Engineering Design*. New York: Van Nostrand Reinhold.
- Freris, L.L. (ed.) (1990). *Wind Energy Conversion Systems*. New York: Prentice-Hall.
- Harrison, R., Hau, E., and Snel, H. (2000). *Large Wind Turbines, Design and Economics*. Chichester: Wiley.
- Manwell, J.W., McGown, J.G., and Rogers, A.L. (2009). *Wind Energy Explained: Theory, Design and Application*, 2e. Oxford: Wiley Blackwell.
- Orkney Sustainable Energy (1955). Costa Head experimental wind turbine. www.orkneywind.co.uk/costa.html (accessed 3 January 2020).
- Twidell, J.W. and Weir, A.D. (2015). *Renewable Energy Resources*, 3e. Abingdon: Routledge.
- Twidell, J.W. and Gaudiosi, G. (eds.) (2009). *Offshore Wind Power*. Brentford: Multi-science Publishing Co.

2

The wind resource

2.1 The nature of the wind

The energy available in the wind varies as the cube of the wind speed, so an understanding of the characteristics of the wind resource is critical to all aspects of wind energy exploitation, from the identification of suitable sites and predictions of the economic viability of wind farm projects through to the design of wind turbines themselves, along with understanding their effect on electricity distribution networks and consumers.

From the point of view of wind energy, the most striking characteristic of the wind resource is its variability. The wind is highly variable, both geographically and temporally. Furthermore, this variability persists over a very wide range of scales, both in space and time. The importance of this is amplified by the cubic relationship to available energy.

On a large scale, spatial variability describes the fact that there are many different climatic regions in the world, some much windier than others. These regions are largely dictated by the latitude, which affects the amount of insolation. Within any one climatic region, there is a great deal of variation on a smaller scale, largely dictated by physical geography – the proportion of land and sea, the size of land masses, and the presence of mountains or plains, for example. The type of vegetation may also have a significant influence through its effects on the absorption or reflection of solar radiation, affecting surface temperatures, and on humidity.

More locally, the topography has a major effect on the wind climate. More wind is experienced on the tops of hills and mountains than in the lee of high ground or in sheltered valleys, for instance. More locally still, wind velocities are significantly reduced by obstacles such as trees or buildings.

At a given location, temporal variability on a large scale means that the amount of wind may vary from one year to the next, with even longer-scale variations on a scale of decades or more. These long-term variations are not well understood and may make it difficult to make accurate predictions of the economic viability of particular wind farm projects, for instance.

On timescales shorter than a year, seasonal variations are much more predictable, although there are large variations on shorter timescales still, which although reasonably well understood are often not very predictable more than a few days ahead. Depending on location, there may also be considerable variations with the time of day (diurnal variations), which again are usually fairly predictable. On these timescales, the predictability of the wind is important for integrating large amounts of wind power into the electricity network, to allow the other generating plant supplying the network to be organised appropriately.

On still shorter timescales of minutes down to seconds or less, wind speed variations known as *turbulence* can have a very significant impact on the design and performance of the individual wind turbines as well as on the quality of power delivered to the network and its effect on consumers.

Van der Hoven (1957) constructed a wind speed spectrum from long- and short-term records at Brookhaven, New York, showing clear peaks corresponding to the synoptic, diurnal, and turbulent effects just referred to (Figure 2.1). This spectrum shows a distinct ‘spectral gap’ between the diurnal and turbulent peaks, showing that the synoptic and diurnal variations can be treated as quite distinct from the higher frequency fluctuations of turbulence, with very little energy in the spectrum in the region between 2 hours and 10 minutes. As indicated in the next section, however, the nature of the wind regime in different geographical locations can vary widely, so the Van der Hoven spectrum cannot be assumed to be universally applicable, and the spectral gap may not always be so distinct. Nevertheless, the concept of a spectral gap at frequencies below 10 minutes is very often used, often implicitly, when making assumptions about the wind regime; for example, when defining turbulence intensity.

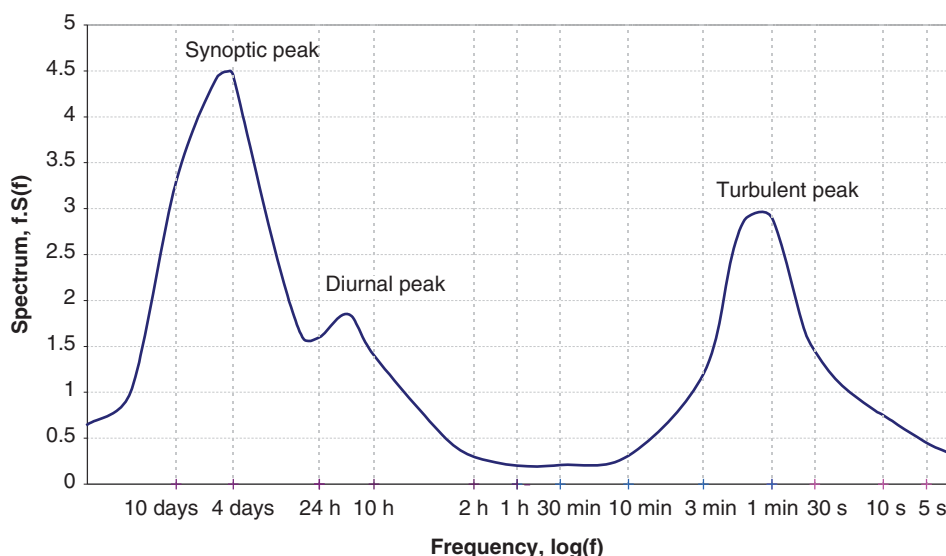


Figure 2.1 Wind spectrum from Brookhaven based on work by Van der Hoven (1957)

2.2 Geographical variation in the wind resource

Ultimately the winds are driven almost entirely by the sun's energy, causing differential surface heating. The heating is most intense on land masses closer to the equator, and obviously the greatest heating occurs in the daytime, which means that the region of greatest heating moves around the earth's surface as it spins on its axis. Warm air rises and circulates in the atmosphere to sink back to the surface in cooler areas. The resulting large-scale motion of the air is strongly influenced by Coriolis forces due to the earth's rotation. The result is a large-scale global circulation pattern. Certain identifiable features of this such as the trade winds and the 'roaring forties' are well known.

The non-uniformity of the earth's surface, with its pattern of land masses and oceans, ensures that this global circulation pattern is disturbed by smaller-scale variations on continental scales. These variations interact in a highly complex and non-linear fashion to produce a somewhat chaotic result, which is at the root of the day-to-day unpredictability of the weather in particular locations. Clearly though, underlying tendencies remain that lead to clear climatic differences between regions. These differences are tempered by more local topographical and thermal effects.

Hills and mountains result in local regions of increased wind speed. This is partly a result of altitude – the boundary layer flow over the earth's surface means that wind speed generally increases with height above the ground, and hill tops and mountain peaks may 'project' into the higher wind speed layers. It is also partly a result of the acceleration of the wind flow over and around hills and mountains and funnelling through passes or along valleys aligned with the flow. Equally, topography may produce areas of reduced wind speed, such as sheltered valleys or areas in the lee of a mountain ridge or where the flow patterns result in stagnation points.

Thermal effects may also result in considerable local variations. Coastal regions are often windy because of differential heating between land and sea. While the sea is warmer than the land, a local circulation develops in which surface air flows from the land to the sea, with warm air rising over the sea and cool air sinking over the land. When the land is warmer, the pattern reverses. The land will heat up and cool down more rapidly than the sea surface, and so this pattern of land and sea breezes tends to reverse over a 24-hour cycle. These effects were important in the early development of wind power in California, where an ocean current brings cold water to the coast, not far from desert areas that heat up strongly by day. An intervening mountain range funnels the resulting air flow through its passes, generating locally very strong and reliable winds (which are well correlated with peaks in the local electricity demand caused by air conditioning loads).

Thermal effects may also be caused by differences in altitude. Thus, cold air from high mountains can sink down to the plains below, causing quite strong and highly stratified 'downslope' winds.

The brief general descriptions of wind speed variations in Sections 2.1–2.5 are illustrative, and more detailed information can be found in standard meteorological texts. Section 10.1.3, in Chapter 10, describes how the wind regimes at candidate sites can be assessed, while wind forecasting is covered in Section 2.9 and Section 11.6.3.

Section 2.6 presents a more detailed description of the high frequency wind fluctuations known as *turbulence*, which are crucial to the design and operation of wind turbines and have a major influence on wind turbine loads. Extreme winds are also important for the survival of wind turbines, and these are described in Section 2.8.

2.3 Long-term wind speed variations

There is evidence that the wind speed at any particular location may be subject to very slow long-term variations. Although the availability of accurate historical records is a limitation, careful analysis by, for example, Palutikof et al. (1991) has demonstrated clear trends. Clearly these may be linked to long-term temperature variations for which there is ample historical evidence. There is also much debate at present about the likely effects of global warming, caused by human activity, on climate, and this will undoubtedly affect wind climates in the coming decades.

Apart from these long-term trends, there may be considerable changes in windiness at a given location from one year to the next. These changes have many causes. They may be coupled to global climate phenomena such as *el niño*, changes in atmospheric particulates resulting from volcanic eruptions, and sunspot activity, to name a few.

These changes add significantly to the uncertainty in predicting the energy output of a wind farm at a particular location during its projected lifetime.

2.4 Annual and seasonal variations

While year-to-year variation in annual mean wind speeds remains hard to predict, wind speed variations during the year can be well characterised in terms of a probability distribution. The Weibull distribution has been found to give a good representation of the variation in hourly mean wind speed over a year at many typical sites. This distribution takes the form

$$F(U) = \exp\left(-\left(\frac{U}{c}\right)^k\right) \quad (2.1)$$

where $F(U)$ is the fraction of time for which the hourly mean wind speed exceeds U . It is characterised by two parameters, a ‘scale parameter’ c and a ‘shape parameter’ k , which describes the variability about the mean. The parameter c is related to the annual mean wind speed \bar{U} by the relationship

$$\bar{U} = c \Gamma(1 + 1/k) \quad (2.2)$$

where Γ is the complete gamma function. This can be derived by consideration of the probability density function

$$f(U) = -\frac{dF(U)}{dU} = k \frac{U^{k-1}}{c^k} \exp\left(-\left(\frac{U}{c}\right)^k\right) \quad (2.3)$$

because the mean wind speed is given by

$$\bar{U} = \int_0^\infty U f(U) dU \quad (2.4)$$

A special case of the Weibull distribution is the Rayleigh distribution, with $k = 2$, which is actually a fairly typical value for many locations. In this case, the factor $\Gamma(1 + 1/k)$ has the value $\sqrt{\pi}/2 = 0.8862$. A higher value of k , such as 2.5 or 3, indicates a site where the variation of hourly mean wind speed about the annual mean is small, as is sometimes

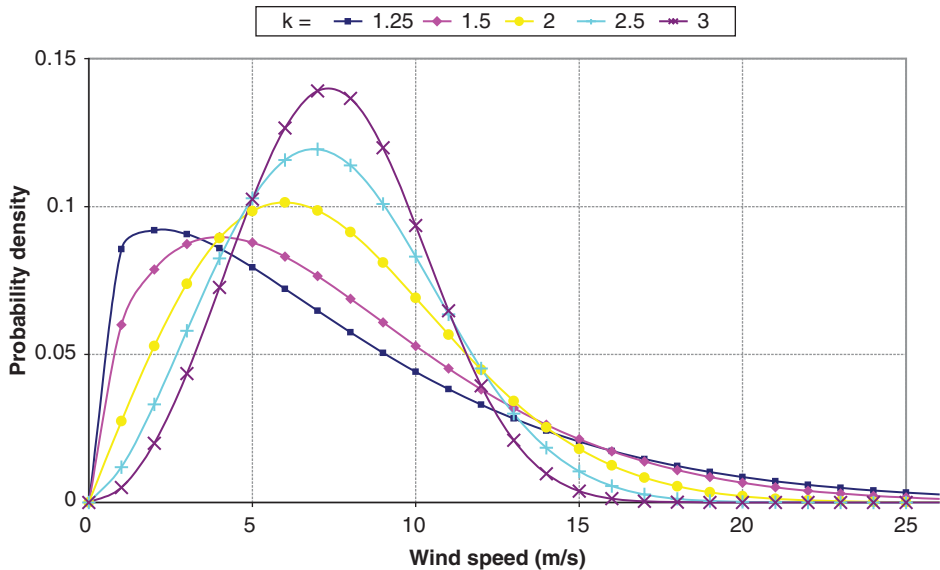


Figure 2.2 Example Weibull distributions

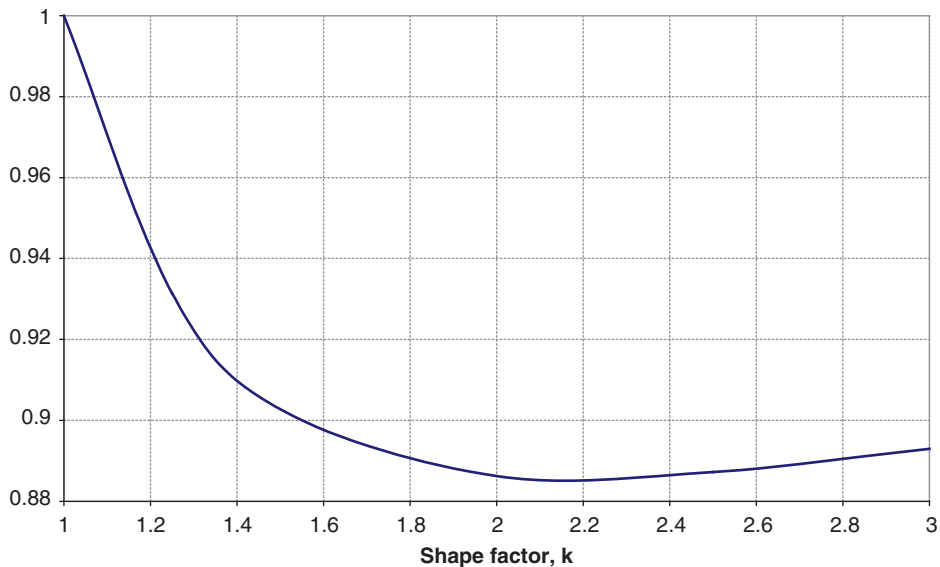


Figure 2.3 The factor $\Gamma(1 + 1/k)$

the case in the trade wind belts, for instance. A lower value of k , such as 1.5 or 1.2, indicates greater variability about the mean. A few examples are shown in Figure 2.2. The value of $\Gamma(1 + 1/k)$ varies little, between about 1.0 and 0.885: see Figure 2.3.

The Weibull distribution of hourly mean wind speeds over the year is clearly the result of a considerable degree of random variation. However, there may also be a strong

underlying seasonal component to these variations, driven by the changes in insolation during the year as a result of the tilt of the earth's axis of rotation. Thus, in temperate latitudes the winter months tend to be significantly windier than the summer months. There may also be a tendency for strong winds or gales to develop around the time of the spring and autumn equinoxes. Tropical regions also experience seasonal phenomena, such as monsoons and tropical storms, that affect the wind climate. Indeed, the extreme winds associated with tropical storms may significantly influence the design of wind turbines intended to survive in these locations.

Although a Weibull distribution gives a good representation of the wind regime at many sites, this is not always the case. For example, some sites showing distinctly different wind climates in summer and winter can be represented quite well by a double-peaked 'bi-Weibull' distribution, with different scale factors and shape factors in the two seasons, i.e.

$$F(U) = F_1 \exp\left(-\left(\frac{U}{c_1}\right)^{k_1}\right) + (1 - F_1) \exp\left(-\left(\frac{U}{c_2}\right)^{k_2}\right) \quad (2.5)$$

Certain parts of California are good examples of this.

2.5 Synoptic and diurnal variations

On shorter timescales than the seasonal changes described in Section 2.4, wind speed variations are somewhat more random and less predictable. Nevertheless, these variations contain definite patterns. The frequency content of these variations typically peaks at around four days or so. These are the 'synoptic' variations, which are associated with large-scale weather patterns, such as areas of high and low pressure and associated weather fronts as they move across the earth's surface. Coriolis forces induce a circular motion of the air as it tries to move from high- to low-pressure regions. These coherent large-scale atmospheric circulation patterns may typically take a few days to pass over a given point, although they may occasionally 'stick' in one place for longer before finally moving on or dissipating.

Following the frequency spectrum to still higher frequencies, many locations will show a distinct diurnal peak, at a frequency of 24 hours. This is usually driven by local thermal effects. Intense heating in the daytime may cause large convection cells in the atmosphere, which die down at night. This process is described in more detail in Section 2.6 because it also contributes significantly to turbulence, on timescales representative of the size of the convection cells. Land and sea breezes, caused by differential heating and cooling between land and sea, also contribute significantly to the diurnal peak. The daily direction reversal of these winds would be seen as a 12-hour peak in the spectrum of wind speed magnitude.

2.6 Turbulence

2.6.1 The nature of turbulence

Turbulence refers to fluctuations in wind speed on a relatively fast timescale, typically less than about 10 minutes. In other words, it corresponds to the highest frequency spectral

peak in Figure 2.1. It is useful to think of the wind as consisting of a mean wind speed determined by the seasonal, synoptic, and diurnal effects described previously, which varies on a timescale of one to several hours, with turbulent fluctuations superimposed. These turbulent fluctuations then have a zero mean when averaged over about 10 minutes. This description is a useful one as long as the ‘spectral gap’ as illustrated in Figure 2.1 is reasonably distinct.

Turbulence is generated mainly from two causes: ‘friction’ with the earth’s surface, which can be thought of as extending as far as flow disturbances caused by such topographical features as hills and mountains, and thermal effects, which can cause air masses to move vertically as a result of variations of temperature and hence in the density of the air. Often these two effects are interconnected, such as when a mass of air flows over a mountain range and is forced up into cooler regions where it is no longer in thermal equilibrium with its surroundings.

Turbulence is clearly a complex process and one that cannot be represented simply in terms of deterministic equations. Clearly it does obey certain physical laws, such as those describing the conservation of mass, momentum, and energy. However, to describe turbulence using these laws it is necessary to take account of temperature, pressure, density, and humidity as well as the motion of the air itself in three dimensions. It is then possible to formulate a set of differential equations describing the process, and in principle the progress of the turbulence can be predicted by integrating these equations forward in time starting from certain initial conditions and subject to certain boundary conditions. In practice of course, the process can be described as ‘chaotic’ in that small differences in initial conditions or boundary conditions may result in large differences in the predictions after a relatively short time. For this reason it is generally more useful to develop descriptions of turbulence in terms of its statistical properties.

There are many statistical descriptors of turbulence that may be useful, depending on the application. These range from simple turbulence intensities and gust factors to detailed descriptions of the way in which the three components of turbulence vary in space and time as a function of frequency.

The turbulence intensity is a measure of the overall level of turbulence. It is defined as

$$I = \frac{\sigma}{\bar{U}} \quad (2.6)$$

where σ is the standard deviation of wind speed variations about the mean wind speed \bar{U} , usually defined over 10 minutes or an hour. Turbulent wind speed variations can be considered to be roughly Gaussian, meaning that the speed variations are normally distributed, with standard deviation σ , about the mean wind speed \bar{U} . However, the tails of the distribution may be significantly non-Gaussian, so this approximation is not reliable for estimating, say, the probability of a large gust within a certain period.

The turbulence intensity clearly depends on the roughness of the ground surface and the height above the surface. However, it also depends on topographical features, such as hills or mountains, especially when they lie upwind, as well as more local features, such as trees or buildings. It also depends on the thermal behaviour of the atmosphere: for example, if the air near to the ground warms up on a sunny day, it may become buoyant enough to rise up through the atmosphere, causing a pattern of convection cells that are experienced as large-scale turbulent eddies.

Clearly as the height above ground increases, the effects of all these processes that are driven by interactions at the earth’s surface become weaker. Above a certain height, the air flow can be considered largely free of surface influences. Here it can be considered to be

driven by large-scale synoptic pressure differences and the rotation of the earth. This air flow is known as the *geostrophic wind*. At lower altitudes, the effect of the earth's surface can be felt. This part of the atmosphere is known as the *boundary layer*. The properties of the boundary layer are important in understanding the turbulence experienced by wind turbines.

2.6.2 The boundary layer

The principal effects governing the properties of the boundary layer are the strength of the geostrophic wind, the surface roughness, Coriolis effects due to the earth's rotation, and thermal effects.

The influence of thermal effects can be classified into three categories: stable, unstable, and neutral stratification. Unstable stratification occurs when there is a lot of surface heating, causing warm air near the surface to rise. As it rises, it expands due to reduced pressure and therefore cools adiabatically. If the cooling is not sufficient to bring the air into thermal equilibrium with the surrounding air, then it will continue to rise, giving rise to large convection cells. The result is a thick boundary layer with large-scale turbulent eddies. There is a lot of vertical mixing and transfer of momentum, resulting in a relatively small change of mean wind speed with height.

If the adiabatic cooling effect causes the rising air to become colder than its surroundings, its vertical motion will be suppressed. This is known as *stable stratification*. It often occurs on cold nights when the ground surface is cold. In this situation, turbulence is dominated by friction with the ground, and wind shear (the increase of mean wind speed with height) can be large.

In the neutral atmosphere, adiabatic cooling of the air as it rises is such that it remains in thermal equilibrium with its surroundings. This is often the case in strong winds, when turbulence caused by ground roughness causes sufficient mixing of the boundary layer. For wind energy applications, neutral stability is usually the most important situation to consider, particularly when considering the turbulent wind loads on a turbine, because these are largest in strong winds. Nevertheless, unstable conditions can be important because they can result in sudden gusts from a low level, and stable conditions can give rise to significant asymmetric loadings due to high wind shear. There can also be large veer (change in wind direction with height) in this situation.

In the following sections, a series of relationships are presented that describe the properties of the atmospheric boundary layer, such as turbulence intensities, spectra, length scales, and coherence functions. These relationships are partly based on theoretical considerations and partly on empirical fits to a wide range of observations from many researchers taken in various conditions and in various locations.

In the neutral atmosphere, the boundary layer properties depend mainly on the surface roughness and the Coriolis effect. The surface roughness is characterised by the roughness length z_o . Typical values of z_o are shown in Table 2.1.

The Coriolis parameter f is defined as

$$f = 2\Omega \sin(|\lambda|) \quad (2.7)$$

Table 2.1 Typical surface roughness lengths.

Type of terrain	Roughness length z_0 (m)
Cities, forests	0.7
Suburbs, wooded countryside	0.3
Villages, countryside with trees and hedges	0.1
Open farmland, few trees and buildings	0.03
Flat grassy plains	0.01
Flat desert, rough sea	0.001

where Ω is the angular velocity of the earth's rotation, and λ is the latitude. In temperate latitudes, the height of the boundary layer is given by

$$h = u^*/(6f) \quad (2.8)$$

but it is clear from the division that this and the subsequent derivations cannot be valid at the equator, where $f = 0$, so a pragmatic recommendation is to use a latitude of 22.5° for all tropical regions. Here u^* is known as the *friction velocity*, given by

$$u^*/\overline{U}(z) = \kappa/[\ln(z/z_0) + \Psi] \quad (2.9)$$

where κ is the von Karman constant (approximately 0.4), z is the height above ground, and z_0 is the surface roughness length. Ψ is a function that depends on stability: it is negative for unstable conditions, giving rise to low wind shear, and positive for stable conditions, giving high wind shear. For neutral conditions, ESDU (1985) gives $\Psi = 34.5fz/u^*$, which is small compared to $\ln(z/z_0)$ for situations of interest here. If Ψ is ignored, the wind shear is then given by a logarithmic wind profile:

$$\overline{U}(z) \propto \ln(z/z_0) \quad (2.10)$$

A power law approximation,

$$\overline{U}(z) \propto z^\alpha \quad (2.11)$$

is often used, where the exponent α is typically about 0.14 onshore and lower offshore but varies with the type of terrain. However, the value of α should also depend on the height interval over which the expression is applied, making this approximation less useful than the logarithmic profile.

The wind turbine design standards typically specify that a given exponent should be used; the International Electrotechnical Commission (IEC) and Germanischer Lloyd (GL) standards, for example, specify an exponent of $\alpha = 0.20$ for normal wind conditions onshore and $\alpha = 0.14$ for normal wind conditions offshore. Both standards specify an exponent of $\alpha = 0.11$ for extreme wind conditions (onshore and offshore). For conservatism, edition 4 of the IEC standard (IEC 61400-1 2019) allows a higher exponent (0.3) to be used for turbines of 'medium' size (swept area from 200 to 1000 m²).

If there is a change in the surface roughness, the wind shear profile changes gradually downwind of the transition point, from the original to the new profile. Essentially, a new boundary layer starts, and the height of the boundary between the new and old boundary layers increases from zero at the transition point until the new boundary layer is fully established. The calculation of wind shear in the transition zone is covered by, for example, Cook (1985).

By combining Eqs. (2.8) and (2.9), we obtain the wind speed at the top of the boundary layer as

$$\bar{U}(h) = \frac{u^*}{\kappa} \left(\ln \left(\frac{u^*}{fz_0} \right) - \ln 6 + 5.75 \right) \quad (2.12)$$

This is similar to the so-called ‘geostrophic wind speed’, G , which is the notional wind speed driving the boundary layer as calculated from the pressure field. The geostrophic wind speed is given by

$$G = \frac{u^*}{\kappa} \sqrt{\left[\ln \left(\frac{u^*}{fz_0} \right) - A \right]^2 + B^2} \quad (2.13)$$

where, for neutral conditions, $A = \ln 6$ and $B = 4.5$. This relationship is often referred to as the geostrophic drag law.

The effect of surface roughness is not only to cause the wind speed to decrease closer to the ground. There is also a change in direction between the ‘free’ pressure-driven geostrophic wind and the wind close to the ground. Although the geostrophic wind is driven by the pressure gradients in the atmosphere, Coriolis forces act to force the wind to flow at right angles to the pressure gradient, causing a characteristic circulating pattern. Thus in the northern hemisphere, wind flowing from high pressure in the south to low pressure in the north will be forced eastwards by Coriolis effects, in effect to conserve angular momentum on the rotating earth. The result is that the wind circulates anti-clockwise around low-pressure areas and clockwise around high-pressure areas, or the other way round in the southern hemisphere. Close to the ground, these flow directions are modified due to the effect of surface friction. The total direction change, α , from the geostrophic to the surface wind is given by

$$\sin \alpha = \frac{-B}{\sqrt{\left[\ln \left(\frac{u^*}{fz_0} \right) \right]^2 + B^2}} \quad (2.14)$$

2.6.3 Turbulence intensity

The turbulence intensity in the neutral atmosphere clearly depends on the surface roughness. For the longitudinal component, the standard deviation σ_u is approximately constant with height, so the turbulence intensity decreases with height. More precisely, the relationship $\sigma_u \approx 2.5u^*$ may be used to calculate the standard deviation, with the friction velocity u^* calculated as in the previous section. More recent work (ESDU 1985) suggests a variation given by

$$\sigma_u = \frac{7.5\eta(0.538 + 0.09 \ln(z/z_0))^p u^*}{1 + 0.156 \ln(u^*/f.z_0)} \quad (2.15)$$

where

$$\eta = 1 - 6fz/u^* \quad (2.16)$$

$$p = \eta^{16} \quad (2.17)$$

This approximates to $\sigma_u = 2.5u^*$ close to the ground, but gives larger values at greater heights. The longitudinal turbulence intensity is then

$$I_u = \sigma_u / \bar{U} \quad (2.18)$$

The lateral (v) and vertical (w) turbulence intensities are given (ESDU 1985) by

$$I_v = \frac{\sigma_v}{\bar{U}} = I_u \left(1 - 0.22 \cos^4 \left(\frac{\pi z}{2h} \right) \right) \quad (2.19)$$

$$I_w = \frac{\sigma_w}{\bar{U}} = I_u \left(1 - 0.45 \cos^4 \left(\frac{\pi z}{2h} \right) \right) \quad (2.20)$$

Note that specific values of turbulence intensity for use in design calculations are prescribed in some of the standards used for wind turbine design calculations, and these may not always correspond with the above expressions. For example, the now superseded Danish standard (DS 472 1992) specified

$$I_u = 1.0 / \ln(z/z_0) \quad (2.21)$$

with $I_v = 0.8 I_u$ and $I_w = 0.5 I_u$.

The IEC edition 2 standard (IEC 61400-1 1999) gives

$$I_u = I_{15}(a + 15/\bar{U})/(a + 1) \quad (2.22)$$

where $I_{15} = 0.18$ for ‘higher turbulence sites’ and 0.16 for ‘lower turbulence sites’, with corresponding values of a of 2 and 3, respectively. For the lateral and vertical components, a choice is allowed: either $I_v = 0.8 I_u$ and $I_w = 0.5 I_u$, or an isotropic model with $I_u = I_v = I_w$.

Editions 3 (IEC 61400-1 2005) and 4 (IEC 61400-1 2019) of the IEC standard specify

$$I_u = I_{\text{ref}}(0.75 + 5.6/\bar{U}) \quad (2.23)$$

where $I_{\text{ref}} = 0.16, 0.14$, or 0.12 depending on the wind class. For lateral and vertical components, I_v must be at least $0.7I_u$, and I_w at least $0.5I_u$. Standard deviations are assumed constant with height, so the turbulence intensity will change with height as the mean wind speed changes due to wind shear.

The earlier GL rules (GL 1993) simply specified 20% turbulence intensity, but the later edition (GL 2003) follows IEC edition 2.

Figure 2.4 shows example longitudinal turbulence intensities for the GL, IEC, and Danish standards. The low value for the Danish standard is for 90 m height with roughness length 0.01 m; the high value is for 30 m height with roughness length 0.3 m. The high values for IEC editions 2, 3, and 4 are the same, but the low value is significantly lower in editions 3 and 4 than in edition 2.

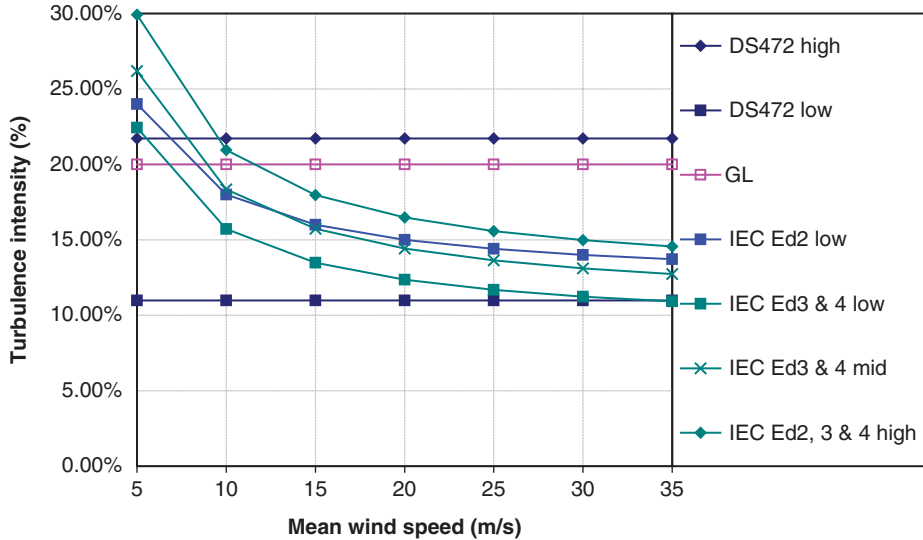


Figure 2.4 Turbulence intensities according to various standards

2.6.4 Turbulence spectra

The spectrum of turbulence describes the frequency content of wind speed variations. According to the Kolmogorov law, the spectrum must approach an asymptotic limit proportional to $n^{-5/3}$ at high frequency (here n denotes the frequency, in Hz). This relationship is based on the decay of turbulent eddies to higher and higher frequencies as turbulent energy is dissipated as heat.

Two alternative expressions for the spectrum of the longitudinal component of turbulence are commonly used, both tending to this asymptotic limit. These are the Kaimal and the von Karman spectra, which take the following forms:

Kaimal:

$$\frac{nS_u(n)}{\sigma_u^2} = \frac{4nL_{1u}/\bar{U}}{(1 + 6nL_{1u}/\bar{U})^{5/3}} \quad (2.24)$$

von Karman:

$$\frac{nS_u(n)}{\sigma_u^2} = \frac{4nL_{2u}/\bar{U}}{(1 + 70.8(nL_{2u}/\bar{U})^2)^{5/6}} \quad (2.25)$$

where $S_u(n)$ is the autospectral density function for the longitudinal component and L_{1u} and L_{2u} are length scales. For these two forms to have the same high frequency asymptotic limit, these length scales must be related by the ratio $(36/70.8)^{-5/4}$, i.e. $L_{1u} = 2.329 L_{2u}$. The appropriate length scales to use are discussed in the next section.

According to Petersen et al. (1998), the von Karman spectrum gives a good description for turbulence in wind tunnels, although the Kaimal spectrum may give a better fit to empirical observations of atmospheric turbulence. Nevertheless, the von Karman spectrum is often used for consistency with analytical expressions for the correlations. The length scale L_{2u} is identified as the integral length scale of the longitudinal component in the longitudinal direction, denoted $\int_0^\infty \kappa(r_x) dr_x$ where $\kappa(r_x)$ is the

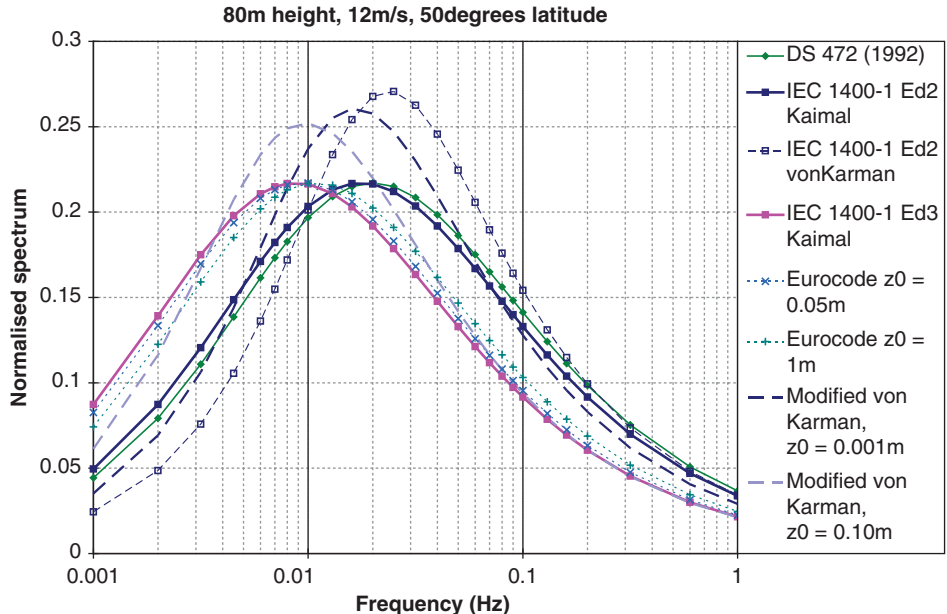


Figure 2.5 Comparison of spectra at 12 m/s

cross-correlation function between the turbulence component u at two points separated longitudinally by a distance r_x and measured simultaneously (similar definitions apply to the integral length scales of the longitudinal component of turbulence in the lateral and vertical directions, $y L_u$ and $z L_u$, which are used in the definitions of cross-spectra below, and also to the integral length scales of the lateral and vertical components in the three directions). It is important to recognise that the power spectra and accompanying length scales are theoretical constructs, and attempts to fit them to real atmospheric data result in semi-empirical models in which the length scales may not be fully consistent with theory.

The Kaimal spectrum has a lower, broader peak than the von Karman spectrum: see Figures 2.5 and 2.6. More recent work suggests that the von Karman spectrum gives a good representation of atmospheric turbulence above about 150 m but has some deficiencies at lower altitudes. Several modifications have been suggested (Harris 1990), and a modified von Karman spectrum of the following form is recommended (ESDU 1985):

$$\frac{nS_u(n)}{\sigma_u^2} = \beta_1 \frac{2.987nL_{3u}/\bar{U}}{(1 + (2\pi nL_{3u}/\bar{U})^2)^{5/6}} + \beta_2 \frac{1.294nL_{3u}/\bar{U}}{(1 + (\pi nL_{3u}/\bar{U})^2)^{5/6}} F_1 \quad (2.26)$$

All three of these spectra have corresponding expressions for the lateral and vertical components of turbulence. The Kaimal spectra have the same form as for the longitudinal component but with different length scales, L_{Iv} and L_{Iw} , respectively. The von Karman spectrum for the i component ($i = v$ or w) is

$$\frac{nS_i(n)}{\sigma_i^2} = \frac{4(nL_{2i}/\bar{U})(1 + 755.2(nL_{2i}/\bar{U})^2)}{(1 + 283.2(nL_{2i}/\bar{U})^2)^{11/6}} \quad (2.27)$$

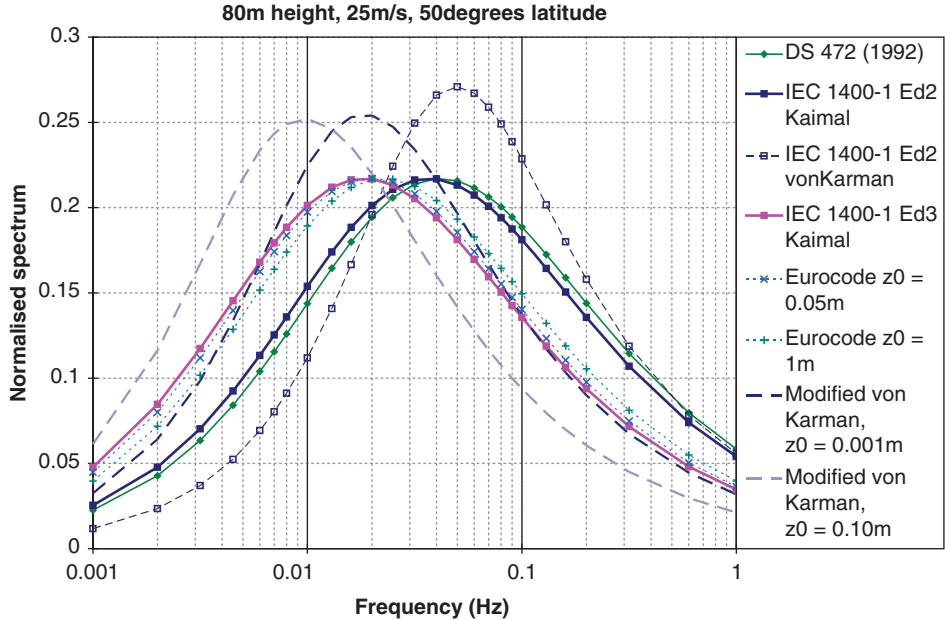


Figure 2.6 Comparison of spectra at 25 m/s

where $L_{2v} = {}^xL_v$ and $L_{2w} = {}^xL_w$. For the modified von Karman spectrum of Eq. (2.26), it is

$$\frac{nS_i(n)}{\sigma_i^2} = \beta_1 \frac{2.987(nL_{3i}/\bar{U}) \left(1 + \frac{8}{3}(4\pi nL_{3i}/\bar{U})^2\right)}{(1 + (4\pi nL_{3i}/\bar{U})^2)^{11/6}} + \beta_2 \frac{1.294nL_{3i}/\bar{U}}{(1 + (2\pi nL_{3i}/\bar{U})^2)^{5/6}} F_{2i} \quad (2.28)$$

2.6.5 Length scales and other parameters

To use the spectra defined above, it is necessary to define the appropriate length scales. Additional parameters β_1 , β_2 , F_1 , and F_2 are also required for the modified von Karman model.

The length scales are dependent on the surface roughness z_0 as well as on the height above ground (z): proximity to the ground constrains the size of turbulent eddies and thus reduces the length scales. If there are many small obstacles on the ground of typical height z' , the height above ground should be corrected for the effect of these by assuming that the effective ground surface is at a height $z' - 2.5z_0$ (ESDU 1975). Far enough above the ground, i.e. for z greater than some height z_i , the turbulence is no longer constrained by the proximity of the surface and becomes isotropic. According to ESDU (1975), $z_i = 1000z_0^{0.18}$, and above this height ${}^xL_u = 280$ m, and ${}^yL_u = {}^zL_u = {}^xL_v = {}^zL_v = 140$ m. Even for very small roughness lengths z_0 , the isotropic region is well above the height of

a wind turbine, and the following corrections for $z < z_i$ should be applied:

$$\begin{aligned} {}^x L_u &= 280(z/z_i)^{0.35} \\ {}^y L_u &= 140(z/z_i)^{0.38} \\ {}^z L_u &= 140(z/z_i)^{0.45} \\ {}^x L_v &= 140(z/z_i)^{0.48} \\ {}^z L_v &= 140(z/z_i)^{0.55} \end{aligned} \quad (2.29)$$

together with ${}^x L_w = {}^y L_w = 0.35z$ (for $z < 400$ m). Expressions for ${}^y L_v$ and ${}^z L_w$ are not given. The length scales ${}^x L_u$, ${}^x L_v$, and ${}^x L_w$ can be used directly in the von Karman spectra. For the Kaimal spectra we already have $L_{1u} = 2.329 {}^x L_u$, and to achieve the same high frequency asymptotes for the other components we also have $L_{1v} = 3.2054 {}^x L_v$, $L_{1w} = 3.2054 {}^x L_w$.

Later work based on measurements for a greater range of heights (Harris 1990; ESDU 1985) takes into account an increase in length scales with the thickness of the boundary layer, h , which also implies a variation of length scales with mean wind speed. This yields more complicated expressions for the nine length scales in terms of z/h , σ_u/u^* , and the Richardson number $u^*/(fz_0)$.

Note that some of the standards used for wind turbine loading calculations prescribe that certain turbulence spectra and/or length scales are to be used. These are often simplified compared to the expressions given above. Thus the Danish standard (DS 472 1992) specifies a Kaimal spectrum with

$$\begin{aligned} L_{1u} &= 150 \text{ m, or } 5z \text{ for } z < 30 \text{ m} \\ L_{1v} &= 0.3 L_{1u} \\ L_{1w} &= 0.1 L_{1u} \end{aligned} \quad (2.30)$$

while the IEC edition 2 standard (IEC 61400-1 1999) gives a choice between a Kaimal model with

$$\begin{aligned} \Lambda_1 &= 21 \text{ m, or } 0.7z \text{ for } z < 30 \text{ m} \\ L_{1u} &= 8.1\Lambda_1 = 170.1 \text{ m, or } 5.67z \text{ for } z < 30 \text{ m} \\ L_{1v} &= 2.7\Lambda_1 = 0.3333 L_{1u} \\ L_{1w} &= 0.66\Lambda_1 = 0.08148 L_{1u} \end{aligned} \quad (2.31)$$

and an isotropic von Karman model with

$$\begin{aligned} {}^x L_u &= 73.5 \text{ m, or } 2.45z \text{ for } z < 30 \text{ m} \\ {}^x L_v &= {}^x L_w = 0.5 {}^x L_u \end{aligned} \quad (2.32)$$

Editions 3 (IEC 61400-1 2005) and 4 (IEC 61400-1 2019) of the IEC standard give a choice of between a slightly different Kaimal model and the Mann model. The Kaimal

model has the same form [Eq. (2.24)] but with

$$\begin{aligned}\Lambda_1 &= 42 \text{ m, or } 0.7z \text{ for } z < 60 \text{ m} \\ L_{1u} &= 8.1\Lambda_1 = 340.2 \text{ m, or } 5.67z \text{ for } z < 60 \text{ m} \\ L_{1v} &= 2.7\Lambda_1 = 0.3333 L_{1u} \\ L_{1w} &= 0.66\Lambda_1 = 0.08148 L_{1u}\end{aligned}\tag{2.33}$$

The Mann model has a rather different form and is described in Section 2.6.8.

The Eurocode (EN 1991-1-4:2005) standard for wind loading specifies a longitudinal spectrum of Kaimal form with $L_{1u} = 1.7L_i$, where

$$L_i = 300(z/200)^\alpha\tag{2.34}$$

for $z < 200$ m, with $\alpha = 0.67 + 0.05 \ln(z_0)$. This standard is used for buildings but not usually for wind turbines.

With so many variables, it is difficult to present a concise comparison of the different spectra, so a few examples are presented in Figures 2.5 and 2.6. These are plots of the normalised longitudinal spectrum $nS_u(n)/\sigma_u^2$ against frequency, which means that the area under the curve is representative of the fraction of total variance in any given frequency range. A typical hub height of 80 m has been used, with 50° latitude assumed for the modified von Karman model.

Figure 2.5 shows spectra for a typical rated wind speed of 12 m/s. The IEC edition 2 Kaimal spectrum is clearly very similar to DS 472, while the IEC editions 3 and 4 spectrum has clearly moved to lower frequencies, being now more consistent with Eurocode (in fact identical for 80 m height and $z_0 = 0.01$ m). Note the characteristic difference between the Kaimal and von Karman spectra, the latter being rather more sharply peaked. The modified von Karman spectrum is intermediate in shape; with a very small roughness length the peak is at a similar frequency to the IEC edition 2 spectra, but with higher roughness length it comes closer to edition 3.

Figure 2.6 shows a similar figure for a typical cut-out wind speed of 25 m/s. All peaks have moved to higher frequency as expected, but the modified von Karman now matches IEC editions 3 and 4 better with the very small roughness length.

2.6.6 Asymptotic limits

Other spectra may also be used, but to comply with the IEC standard the high frequency asymptotic behaviour must tend to the following relationship:

$$\frac{S_u(n)}{\sigma_u^2} \xrightarrow{n=\infty} 0.05 \left(\frac{\Lambda_1}{\bar{U}} \right)^{-2/3} n^{-5/3}\tag{2.35}$$

with Λ_1 defined as above: it is a function only of height above ground but differs between edition 2 and edition 3 for heights above 30 m. Expressing this as

$$\frac{S_u(n)}{\sigma_u^2} \xrightarrow{n=\infty} A \bar{U}^{-2/3} n^{-5/3}\tag{2.36}$$

the asymptotic parameter A can then be compared for different spectra, as in Figure 2.7. This shows how the DS 472 asymptote is similar to IEC edition 2 (both Kaimal and von

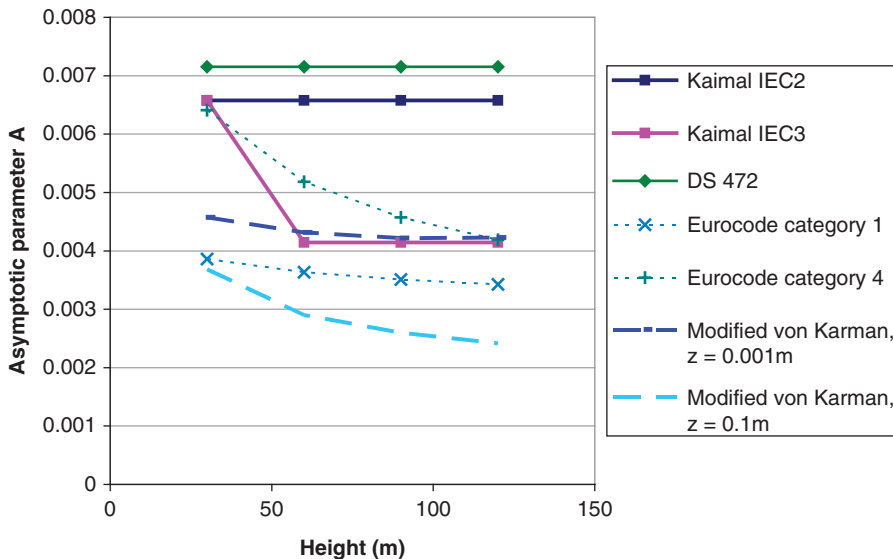


Figure 2.7 Some asymptotic limits

Karman spectra in that standard have the same asymptote), but the asymptote becomes much lower for IEC editions 3 and 4 above 30 m height and is now more comparable with Eurocode. The ESDU modified von Karman spectrum is more difficult to characterise because the asymptote now varies also with wind speed, surface roughness, and geographical latitude. Figure 2.7 shows the results for 20 m/s wind speed and 50° latitude for two different roughness lengths. The asymptote can be made to match the IEC editions 3 and 4 specification, but only by choosing a very small roughness length – even smaller to match edition 2. However, if such a low roughness length is selected, the turbulence intensity implied by the ESDU model will be much smaller than that required by the standards. It is common practice when using the ESDU model to adjust the surface roughness at each wind speed until the turbulence intensity matches the standard, although this clearly makes little physical sense. Obviously it is not possible to adjust the roughness to match both the required asymptote and the required turbulence intensity at the same time. Compared to the physical model, therefore, the standards are probably conservative, which is surely to be expected. It can also be argued that the physical model is valid for flat terrain, while many wind farms are built in complex terrain where the turbulence intensities will indeed be higher, and the length scales shorter.

Note also that the IEC edition 3 and 4 standards further specify that $S_v(n) = S_w(n) = \frac{4}{3}S_u(n)$ in the high frequency limit.

2.6.7 Cross-spectra and coherence functions

The turbulence spectra presented in the preceding sections describe the temporal variation of each component of turbulence at any given point. However, as the wind turbine blade sweeps out its trajectory, the wind speed variations it experiences are not well represented by these single-point spectra. The spatial variation of turbulence in the lateral

and vertical directions is clearly important, because this spatial variation is ‘sampled’ by the moving blade and thus contributes to the temporal variations experienced by it.

To model these effects, the spectral description of turbulence must be extended to include information about the cross-correlations between turbulent fluctuations at points separated laterally and vertically. Clearly these correlations decrease as the distance separating two points increases. The correlations are also smaller for high frequency than for low frequency variations. They can therefore be described by ‘coherence’ functions, which describe the correlation as a function of frequency and separation. The coherence $C(\Delta r, n)$ is defined by

$$C(\Delta r, n) = \frac{|S_{12}(n)|}{\sqrt{S_{11}(n)S_{22}(n)}} \quad (2.37)$$

where n is frequency, $S_{12}(n)$ is the cross-spectrum of variations at the two points separated by Δr , and $S_{11}(n)$ and $S_{22}(n)$ are the spectra of variations at each of the points (usually these can be taken as equal).

Starting from von Karman spectral equations, and assuming Taylor’s frozen turbulence hypothesis, an analytical expression for the coherence of wind speed fluctuations can be derived. Accordingly for the longitudinal component at points separated by a distance Δr perpendicular to the wind direction, the coherence $C_u(\Delta r, n)$ is:

$$C_u(\Delta r, n) = 0.994 \left(A_{5/6}(\eta_u) - \frac{1}{2} \eta_u^{5/3} A_{1/6}(\eta_u) \right) \quad (2.38)$$

Here $A_j(x) = x^j K_j(x)$ where K is a fractional order modified Bessel function, and

$$\eta_u = \Delta r \sqrt{\left(\frac{0.747}{L_u} \right)^2 + \left(c \frac{2\pi n}{U} \right)^2} \quad (2.39)$$

with $c = 1$. L_u is a local length scale that can be defined as

$$L_u(\Delta r, n) = 2f_u(n) \sqrt{\frac{(^y L_u \Delta y)^2 + (^z L_u \Delta z)^2}{\Delta y^2 + \Delta z^2}} \quad (2.40)$$

where Δy and Δz are the lateral and vertical components of the separation Δr , and $^y L_u$ and $^z L_u$ are the lateral and vertical length scales for the longitudinal component of turbulence. Normally $f_u(n) = 1$, but ESDU (1975) suggests a modification at low frequencies where the wind becomes more anisotropic, with $f_u(n) = \text{MIN}(1.0, 0.04n^{-2/3})$.

The (1999) edition 2 standard allows only an isotropic turbulence model to be used if the von Karman spectrum is used, in which $^x L_u = 2 ^y L_u = 2 ^z L_u$, and then $L_u = ^x L_u$, and $f_u(n) = 1$.

The modified von Karman model described in Eq. (2.26) also uses $f_u(n) = 1$, but the factor c in Eq. (2.39) is modified instead (ESDU 1985).

For the lateral and vertical components, the corresponding equations are as follows. The analytical derivation for the coherence, based as before on the von Karman spectrum and Taylor’s hypothesis, is

$$C_i(\Delta r, n) = \frac{0.597}{2.869\gamma_i^2 - 1} [4.781\gamma_i^2 A_{5/6}(\eta_i) - A_{11/6}(\eta_i)] \quad (2.41)$$

for $i = u$ or v , where η_i is calculated as in Eq. (2.39) but with L_u replaced by L_v or L_w , respectively, and with $c = 1$. Also

$$\gamma_i = \frac{\eta_i L_i(\Delta r, n)}{\Delta r} \quad (2.42)$$

and L_v and L_w are given by expressions analogous to Eq. (2.40).

The expressions for spatial coherence in Eqs. (2.38) and (2.41) are derived theoretically from the von Karman spectrum, although there are empirical factors in some of the expressions for length scales, for example. If a Kaimal rather than a von Karman spectrum is used as the starting point, there are no such relatively straightforward analytical expressions for the coherence functions. In this case a simpler, and purely empirical, exponential model of coherence is often used. The (1999) edition 2 standard, for example, gives the following expression for the coherence of the longitudinal component of turbulence:

$$C_u(\Delta r, n) = \exp\left(-H\Delta r \sqrt{\left(\frac{0.12}{L_c}\right)^2 + \left(\frac{n}{U}\right)^2}\right) \quad (2.43)$$

where $H = 8.8$ and $L_c = L_u$. This can also be approximated by

$$C_u(\Delta r, n) \cong \exp(-1.4\eta_u) \quad (2.44)$$

with η_u as in Eq. (2.39).

The standard also states that this may also be used with the von Karman model, as an approximation to Eq. (2.38). The standard does not specify the coherence of the other two components to be used in conjunction with the Kaimal model, so the following expression is often used:

$$C_v(\Delta r, n) = C_w(\Delta r, n) = \exp\left(-H\Delta r \frac{n}{U}\right) \quad (2.45)$$

In the later editions, IEC (2005) and IEC (2019), a slightly modified form is specified, in which $H = 12$ and $L_c = L_{Iu}$.

The three turbulence components are usually assumed to be independent of one another. This is a reasonable assumption, although it ignores the effect of Reynolds stresses that result in a small correlation between the longitudinal and vertical components near to the ground, an effect that is captured by the Mann model described in Section 2.6.8.

Clearly there are significant discrepancies between the various recommended spectra and coherence functions. Also these wind models are applicable to flat sites, and there is only limited understanding of the way in which turbulence characteristics change over hills and in complex terrain. Given the important effect of turbulence characteristics on wind turbine loading and performance, this is clearly an area in which there is scope for further research.

2.6.8 The Mann model of turbulence

Alongside the Kaimal model, editions 3 and 4 of the IEC standard (IEC 2005, 2019) give the option to use a rather different form of turbulence model developed by

Mann (1994, 1998). The other models described above make use of a one-dimensional fast Fourier transform (FFT) to generate time histories from spectra, applied to each turbulence component independently. In contrast, the Mann model is based on a three-dimensional spectrum tensor representation of the turbulence, and one three-dimensional FFT is then used to generate all three components of turbulence simultaneously. The three-dimensional spectrum tensor is derived from rapid distortion theory, in which isotropic turbulence described by the von Karman spectrum is distorted by a uniform mean vertical velocity shear. This means that the three turbulence components are no longer independent, as energy is transferred between the longitudinal and vertical components by distortion of the eddies in the flow, resulting in a realistic representation of the correlation between the longitudinal and vertical components described by the Reynolds stress. The spectral density for any three-dimensional wavenumber vector is derived, and all three components of turbulence are then generated simultaneously by summing a set of such wavenumber vectors, each with the appropriate amplitude and a random phase.

This is in many ways a rather elegant approach, but in practice there are some computational limitations that can make it difficult to use. The summation requires a three-dimensional FFT to achieve reasonable computation time. The number of points in the longitudinal, lateral, and vertical directions must be a power of two for efficient FFT computation. In the longitudinal direction, the number of points is determined by the length of time history required and the maximum frequency of interest and is therefore typically at least 1024. The maximum wavelength used is the length of the turbulence history to be generated (i.e. the mean wind speed multiplied by duration of the required time series), and the minimum wavelength is twice the longitudinal spacing of points (which is the mean wind speed divided by the maximum frequency of interest). In the lateral and vertical directions, a much smaller number of points must be used, perhaps as low as 32, depending on available computer memory. The maximum wavelength must be significantly greater than the rotor diameter, because the solution is spatially periodic, with period equal to the maximum wavelength in each direction. The number of FFT points then determines the minimum wavelength in these directions. With a realistic number of points, the resulting turbulence spectra are deficient at the high frequency end (Veldkamp 2006). Mann (1998) suggests that this may be realistic, because it represents averaging of the turbulence over finite volumes of space, which is appropriate for practical engineering applications. However, a practical simulation tool will perform all necessary spatial averaging in any case, and so the high frequency variations are really lost. Mann (1998) does suggest a remedy for this, but in practice it is extremely intensive computationally.

2.7 Gust wind speeds

It is often useful to know the maximum gust speed that can be expected to occur in any given time interval. This is usually represented by a gust factor G , which is the ratio of the gust wind speed to the hourly mean wind speed. G is obviously a function of the turbulence intensity, and it also clearly depends on the duration of the gust – thus the gust factor for a one-second gust will be larger than for a three-second gust, because every three-second gust has within it a higher one-second gust.

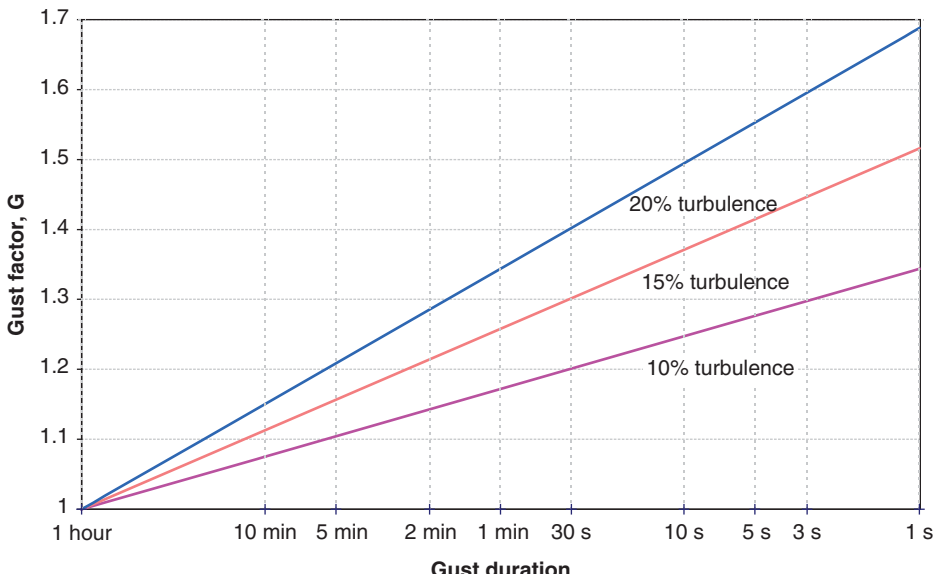


Figure 2.8 Gust factors calculated from Eq. (2.46)

While it is possible to derive expressions for gust factors starting from the turbulence spectrum (Greenway 1979; ESDU 1983), an empirical expression due to Weiringa (1973) is often used because it is much simpler and agrees well with theoretical results. Accordingly, the t -second gust factor is given by

$$G(t) = 1 + 0.42 I_u \ln \frac{3600}{t} \quad (2.46)$$

where I_u is the longitudinal turbulence intensity. Figure 2.8 shows the gust factors for several different turbulence intensities and gust durations calculated according to this expression.

2.8 Extreme wind speeds

In addition to the foregoing descriptions of the average statistical properties of the wind, it is clearly of interest to be able to estimate the long-term extreme wind speeds that might occur at a particular site.

A probability distribution of hourly mean wind speeds such as the Weibull distribution will yield estimates of the probability of exceedance of any particular level of hourly mean wind speed. However, when used to estimate the probability of extreme winds, an accurate knowledge of the high wind speed tail of the distribution is required, and this will not be very reliable because almost all of the data that was used to fit the parameters of the distribution will have been recorded at lower wind speeds. Extrapolating the distribution to higher wind speeds cannot be relied upon to give an accurate result.

Fisher and Tippett (1928) and Gumbel (1958) have developed a theory of extreme values that is useful in this context. If a measured variable (such as hourly mean wind speed \bar{U}) conforms to a particular cumulative probability distribution $F(\bar{U})$, that is, $F(\bar{U}) \rightarrow 1$ as \bar{U} increases, then the peak values of hourly mean wind speed in a given period (a year, for example) will have a cumulative probability distribution of F^N , where N is the number of independent peaks in the period. In the UK, for example, according to Cook (1982), there are about 100 independent wind speed peaks per year, corresponding to the passage of individual weather systems. Thus, if $F(\bar{U}) = 1 - \exp(-(\bar{U}/c)^k)$ as for a Weibull distribution, the wind speed peaks in 1 year will have a cumulative probability distribution given approximately by $[1 - \exp(-(\bar{U}/c)^k)]^{100}$. However, as indicated previously, this is unlikely to give accurate estimates for extreme hourly means, because the high-wind tail of the distribution cannot be considered to be reliably known. However, Fisher and Tippett (1928) demonstrated that for any cumulative probability distribution function that converges towards unity at least exponentially (as is usually the case for wind speed distributions, including the Weibull distribution), the cumulative probability distribution function for extreme values \hat{U} will always tend towards an asymptotic limit

$$F(\hat{U}) = \exp(-\exp(-a(\hat{U} - U'))) \quad (2.47)$$

as the observation period increases. U' is the most likely extreme value, or the *mode* of the distribution, while $1/a$ represents the width or spread of the distribution and is termed the *dispersion*.

This makes it possible to estimate the distribution of extreme values based on a fairly limited set of measured peak values, for example, a set of measurements of the highest hourly mean wind speeds \hat{U} recorded during each of N storms. The N measured extremes are ranked in ascending order, and an estimate of the cumulative probability distribution function is obtained as

$$\tilde{F}(\hat{U}) \cong \frac{m(\hat{U})}{N+1} \quad (2.48)$$

where $m(\hat{U})$ is the rank, or position in the sequence (starting with the lowest), of the observation \hat{U} . Then a plot of $G = -\ln(-\ln(F(\hat{U})))$ against \hat{U} is used to estimate the mode U' and dispersion $1/a$ by fitting a straight line to the data points. This is the method due to Gumbel.

An illustration of the Gumbel method is provided in Figure 2.9, using some sample extreme wind data for a particular 29-year period. The upper plot shows the sample of extreme values. The middle plot shows the estimated cumulative distribution obtained by ordering these values, with the dashed line showing the fitted distribution obtained using the Gumbel method. The lower plot shows how that fit is obtained, giving a mode $U' = 27.8$ m/s with a dispersion of 2.52 m/s from the inverse slope.

Lieblein (1974) has developed a numerical technique that gives a less biased estimate of U' and $1/a$ than a simple least squares fit to a Gumbel plot.

Having made an estimate of the cumulative probability distribution of extremes $F(\hat{U})$, the M -year extreme hourly mean wind speed can be estimated as the value of \hat{U} corresponding to the probability of exceedance $F = 1 - 1/M$.

According to Cook (1985), a better estimate of the probability of extreme winds is obtained by fitting a Gumbel distribution to extreme values of wind speed squared.

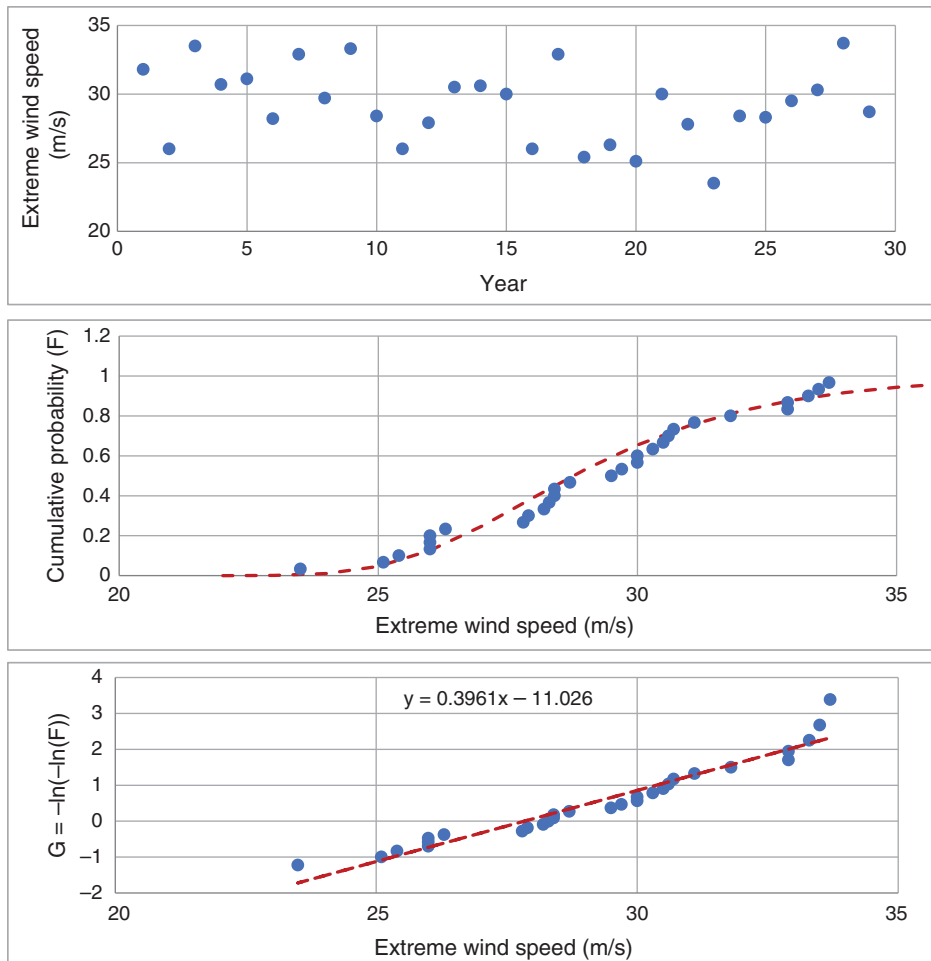


Figure 2.9 Illustration of the Gumbel method

This is because the cumulative probability distribution function of wind speed squared is closer to exponential than the distribution of wind speed itself, and it converges much more rapidly to the Gumbel distribution. Therefore, by using this method to predict extreme values of wind speed squared, more reliable estimates can be obtained from a given number of observations.

2.8.1 Extreme winds in standards

The design of wind turbines must allow them to withstand extremes of wind speed as well as responding well to the more ‘typical’ conditions described earlier. Therefore the various standards also specify the extremes of wind speed that must be designed for. This includes extreme mean wind speeds as well as various types of severe gust.

Extreme conditions may be experienced with the machine operating, parked or idling with or without various types of fault or grid loss, or during a particular operation such as a shut-down event. The extreme wind conditions may be characterised by a ‘return time’: for example, a 50-year gust is one that is so severe that it can be expected to occur on average only once every 50 years. It would be reasonable to expect a turbine to survive such a gust, provided there was no fault on the turbine.

It is always possible that the turbine happens to be shut down on account of a fault when a gust occurs. If the fault impairs the turbine’s ability to cope with a gust, for example, if the yaw system has failed and the turbine is parked at the wrong angle to the wind, then the turbine may have to withstand even greater loads. However, the probability of the most extreme gusts occurring at the same time as a turbine fault is very small, and so it is usual to specify that a turbine with a fault need only be designed to withstand, for example, the annual extreme gust and not the 50-year extreme gust.

For this to be valid, it is important that the faults in question are not correlated with extreme wind conditions. Grid loss is not considered to be a fault with the turbine and is actually quite likely to be correlated with extreme wind conditions.

Clearly the extreme wind speeds and gusts (both in terms of magnitude and shape) may be quite site-specific. They may differ considerably between flat coastal sites and rugged hill tops, for example.

The IEC standard, for example, specifies a ‘reference wind speed’ V_{ref} that is five times the annual mean wind speed. The 50-year extreme wind speed is then given by 1.4 times V_{ref} at hub height and varying with height using a power law exponent of 0.11. The annual extreme wind speed is taken as 75% of the 50-year value in the 1999 edition 2 standard, or 80% in the 2004 edition 3 standard.

The IEC edition 2 standard goes on to define a number of transient events that the turbine must be designed to withstand. These include:

- *Extreme operating gust (EOG)*: A decrease in speed, followed by a steep rise, a steep drop, and a rise back to the original value. The gust amplitude and duration vary with the return period.
- *Extreme direction change (EDC)*: This is a sustained change in wind direction, following a cosine-shaped curve. The amplitude and duration of the change once again depend on the return period.
- *Extreme coherent gust (ECG)*: This is a sustained change in wind speed, again following a cosine-shaped curve with the amplitude and duration depending on the return period.
- *Extreme coherent gust with direction change (ECD)*: Simultaneous speed and direction transients similar to EDC and ECG.
- *Extreme wind shear (EWS)*: A transient variation in the horizontal and vertical wind gradient across the rotor. The gradient first increases and then falls back to the initial level, following a cosine-shaped curve.

These transient events are deterministic gusts intended to represent the extreme turbulent variations that would be expected to occur at the specified return period. They are not intended to occur *in addition* to the normal turbulence described previously. Such

deterministic coherent gusts, however, have little basis in terms of actual measured or theoretical wind characteristics. Therefore in the later editions of the standard, some of the extreme loads are estimated instead by carrying out a large number of simulations and applying statistical extrapolation methods to the peak loads from each simulation. Appropriate probability distributions are fitted to the simulated peaks, and the 50-year extreme load is estimated from the tail of the distribution – see Section 5.14.

2.9 Wind speed prediction and forecasting

Because of the variable nature of the wind resource, the ability to forecast wind speed some time ahead is often valuable. Such forecasts fall broadly into two categories: predicting short-term turbulent variations over a timescale of seconds to minutes ahead, which may be useful for assisting with the operational control of wind turbines or wind farms, and longer-term forecasts over periods of a few hours or days, which may be useful for planning the deployment of other power stations on the network.

Short-term forecasts necessarily rely on statistical techniques for extrapolating the recent past, whereas the longer-term forecasts can make use of meteorological methods. A combination of meteorological and statistical forecasts can give very useful predictions of wind farm power output.

2.9.1 Statistical methods

The simplest statistical prediction is known as a *persistence forecast*: the prediction is set equal to the last available measurement. In other words, the last measured value is assumed to persist into the future without any change:

$$\hat{y}_k = y_{k-1} \quad (2.49)$$

where y_{k-1} is the measured value at step $k-1$ and \hat{y}_k is the prediction for the next step.

A more sophisticated prediction might be some linear combination of the last n measured values, that is,

$$\hat{y}_k = \sum_{i=1}^n a_i y_{k-i} \quad (2.50)$$

This is known as an n^{th} order autoregressive model, or $AR(n)$. We can now define the prediction error at step k by

$$e_k = \hat{y}_k - y_k \quad (2.51)$$

and then use the recent prediction errors to improve the prediction:

$$\hat{y}_k = \sum_{i=1}^n a_i y_{k-i} + \sum_{j=1}^m b_j e_{k-j} \quad (2.52)$$

This is known as an n^{th} order autoregressive, m^{th} order moving average model, or $ARMA(n,m)$. This can be further extended to an ARMAX model, where the X stands for an ‘exogenous’ variable: another measured variable that is included in the prediction because it influences y .

The model parameters a_i, b_j can be estimated in various ways. A useful technique is the method of recursive least squares, or RLS (Ljung and Söderström 1983). Estimates of the model parameters are updated on each timestep in such a way as to minimise the expected value of the sum of squares of the prediction errors. By including a so-called ‘forgetting factor’, the influence of older observations can be progressively reduced, leading to an adaptive estimation of the parameters, which will gradually change to accommodate variations in the statistical properties of the variable y .

Bossanyi (1985) investigated the use of ARMA models for wind speed predictions from a few seconds to a few minutes ahead, obtaining reductions in root mean square (rms) prediction errors of up to 20% when compared to a persistence forecast. The best results were obtained when predicting 10 minutes ahead from 1-minute data.

Kariniotakis et al. (1997) compare ARMA methods against a selection of more recent techniques such as neural network, fuzzy logic, and wavelet-based methods. The fuzzy logic method is tentatively selected as giving the best predictions over periods of 10 minutes to 2 hours, with improvements of 10–18% compared to persistence.

Nielsen and Madsen (1999) use an ARX model with RLS to predict wind farm power output based on previous values of power output, and measured wind speed as an exogenous variable, supplemented by a function describing the diurnal variations of wind speed and by meteorological forecasts of wind speed and direction. Predictions up to 48 hours ahead are considered, and the inclusion of meteorological forecasts is shown to improve the predictions significantly, especially for the longer period forecasts.

2.9.2 Meteorological methods

As indicated in the previous section, much better predictions can be made by using meteorological forecasts than by using purely statistical methods, when predictions over timescales of a few hours or days are considered. Very sophisticated meteorological forecasts are available from highly detailed simulation models of the atmosphere, fed by many recorded observations of pressure, temperature, wind speed, etc. over wide areas of land and sea.

Landberg (1997, 1999) describes the use of such models to predict wind farm output, by extrapolating the large-scale wind predictions produced by these models down to the specific wind farm site. The geostrophic drag law and the logarithmic wind shear profile (Section 2.6.2) are used to extrapolate the wind forecasts down to ground level. Modifications to the flow resulting from the topography, the physical geography, and surface roughness conditions in the area surrounding the wind farm are then modelled by the WA^sP program (Mortensen et al. 1993). A turbine wake interaction model, PARK (Sanderhoff 1993), then takes account of wind direction in relation to the actual turbine positions to calculate wake losses, and, finally, a statistical model (as described in the previous section) combines the meteorological forecasts with recent measurements on the wind farm to give predictions of the energy output that are good enough to be useful in planning the deployment of other power stations on the network.

2.9.3 Current methods

In recent years, wind power forecasting has become very important economically. Wind plant operators have to predict their output as accurately as possible, from a quarter or half an hour ahead to 24 or 48 hours, depending on the marketing arrangements for the

power produced. There may be financial penalties for under- or overproducing. As well as the actual forecast, an estimate of the reliability of each forecast helps the operator to decide how much power to promise in forthcoming periods. Consequently, increasingly sophisticated methods are now being used, with combinations of meteorological forecasts, often from more than one source, together with statistical methods including machine learning and ensemble averaging to weight the results of different methods and estimate the forecasting uncertainties. Forecasting has become a major topic in its own right, and is covered in more detail in Section 11.6.3.

2.10 Turbulence in complex terrain

Predicting the turbulence intensity and spectrum at a given point within an area of complex terrain is not straightforward. Hilly terrain upwind of the site in question will lead to generally higher turbulence levels, and some authors have suggested that this can be calculated from a ‘regional roughness length’ that takes the topography into account as well as the surface roughness (Tieleman 1992). On the other hand, distortion of the flow by the local terrain may reduce the turbulence intensity. At heights above ground that are of importance for wind turbines, rapid distortion theory applies, which means that the variance of the turbulent fluctuations will not change much as the flow passes over terrain features such as hills. Therefore if there is acceleration of the flow as it passes over a hill, the turbulence intensity will decrease, and the length scale will increase, resulting in a shift of the turbulence spectrum towards lower frequencies, without any change of shape (Schlez 2000). This effect is therefore easily estimated once a model such as WASP has been used to calculate the speed-up factor at a particular point. However, the effect is also accompanied by a shift of turbulent energy from the longitudinal to the lateral and vertical components of turbulence, causing the turbulence on hill tops to be more isotropic (Petersen et al. 1998).

References

- Bossanyi, E.A., (1985). Short-term stochastic wind prediction and possible control applications. Proceedings of the Delphi Workshop on Wind Energy Applications (May 1985).
- Cook, N.J. (1982). Towards a better estimation of extreme wind speeds. *J. Wind Eng. Ind. Aerodyn.* 9: 295–323.
- Cook, N.J. (1985). *The Designer's Guide to Wind Loading of Building Structures, Part 1*. Oxford: Butterworth-Heinemann.
- DS 472 (1992): *Code of practice for loads and safety of wind turbine constructions*. Copenhagen: Danish Standards Foundation.
- ESDU (1975). Characteristics of atmospheric turbulence near the ground. Part III: Variations in space and time for strong winds (neutral atmosphere). *ESDU 75001, Engineering Sciences Data Unit*.
- ESDU (1983). Strong winds in the atmospheric boundary layer. Part 2: Discrete gust speeds. *ESDU 83045, Engineering Sciences Data Unit*.
- ESDU (1985). Characteristics of atmospheric turbulence near the ground. Part II: Single point data for strong winds (neutral atmosphere). *ESDU 85020, Engineering Sciences Data Unit* (amended 1993).
- EN-1991-1-4:2005 (2005). *Eurocode 1: Actions on structures – Part 1-4: General actions – Wind actions*. Brussels: European Committee for Standardization.

- Fisher, R.A. and Tippett, L.H.C. (1928). Limiting forms of the frequency distribution of the largest or smallest member of a sample. *Proc. Cambridge Philosophical Society* 24: 180–190.
- Germanischer Lloyd (GL) (1993). *Rules and regulations IV – Non-marine technology, Part 1 – Wind Energy* (supplemented 1994, 1998).
- Germanischer Lloyd (GL) (2003). *Rules and guidelines IV – Industrial services, I – Guideline for the certification of wind turbines*, edition 2003 with supplement 2004.
- Greenway, M.E. (1979). An analytical approach to wind velocity gust factors. *J. Wind Eng. Ind. Aerodyn.* 5: 61–91.
- Gumbel, E.J. (1958). *Statistics of Extremes*. New York: Columbia University Press.
- Harris, R.I. (1990). Some further thoughts on the spectrum of gustiness in strong winds. *J. Wind Eng. Ind. Aerodyn.* 33: 461–477.
- IEC 61400-1 (1999). *Wind turbine generator systems – Part 1: Safety requirements* (2nd edition), International Standard 61400-1 edition 2.
- IEC 61400-1 (2005). *Wind turbines – Part 1: Design requirements* (3rd edition). Geneva, Switzerland: International Electrotechnical Commission.
- IEC 61400-1 (2019). *Wind turbines – Part 1: Design requirements* (4th edition). Geneva, Switzerland: International Electrotechnical Commission.
- Kariniotakis, G., Nogaret, E., and Stavrakakis, G. (1997). Advanced short-term forecasting of wind power production. Proceedings of the European Wind Energy Conference, Dublin 1997, pp. 751–754.
- Landberg, L. (1997). Predicting the power output from wind farms. Proceedings of the European Wind Energy Conference, Dublin 1997, pp. 747–750.
- Landberg, L. (1999). Operational results from a physical power prediction model. Proceedings of the European Wind Energy Conference, Nice 1999, pp. 1086–1089.
- Lieblein, J. (1974). Efficient methods of extreme-value methodology. *NBSIR 74-602*, National Bureau of Standards, Washington, DC, USA.
- Ljung, L. and Söderström, T. (1983). *Theory and Practice of Recursive Identification*. MIT Press.
- Mann, J. (1994). The spatial structure of neutral atmospheric surface-layer turbulence. *J. Fluid Mech.* 273: 141–168.
- Mann, J. (1998). Wind field simulation. *Probab. Eng. Mech.* 13 (4): 269–282.
- Mortensen, N.G., Landberg, L., Troen, I. and Petersen, E.L. (1993). Wind Atlas Analysis and Application Program (WA^sP), user's guide. Risø-I-666-(EN)(v.2).
- Nielsen, T.S. and Madsen, H. (1999). Experiences with statistical methods for wind power prediction. Proceedings of the European Wind Energy Conference, Nice 1999, pp. 1066–1069.
- Palutikof, J.P., Guo, X., and Halliday, J.A. (1991). The reconstruction of long wind speed records in the UK. Proceedings of the 13th British Wind Energy Association Conference, Swansea, April 1991.
- Petersen, E.L., Mortensen, N.G., Landberg, L. et al. (1998). Wind power meteorology. Part I: climate and turbulence. *Wind Energy* 1 (1): 2–22.
- Sanderhoff, P. (1993). PARK – User's guide. Risø-I-668(EN).
- Schlez, W. (2000). Voltage fluctuations caused by groups of wind turbines. PhD thesis. Loughborough University.
- Tieleman, H.W. (1992). Wind characteristics in the surface layer over heterogeneous terrain. *J. Wind Eng. Ind. Aerodyn.* 41–44: 329–340.
- Van der Hoven, I. (1957). Power spectrum of horizontal wind speed in the frequency range from 0.0007 to 900 cycles per hour. *J. Meteorol.* 14: 160–164.
- Veldkamp, H.F. (2006). Chances in wind energy: A probabilistic approach to wind turbine fatigue design. PhD dissertation. Delft University of Technology.
- Weiringa, J. (1973). Gust factors over open water and built-up country. *Boundary Layer Meteorol.* 3: 424–441.

3

Aerodynamics of horizontal axis wind turbines

Author's note on aerodynamics

To study the aerodynamics of wind turbines, some knowledge of fluid dynamics in general is necessary and, in particular, aircraft aerodynamics. Excellent text books on aerodynamics are readily available, a reference list and a further reading list are given at the end of this chapter, and any abbreviated account of the subject that could have been included in these pages would not have done it justice; recourse to text books would have been necessary anyway. Some direction on which aerodynamics topics are necessary for the study of wind turbines would, however, be useful to the reader, and a brief introduction is given in Appendix A3.

For Sections 3.2 and 3.3, a knowledge of Bernoulli's theorem for steady, incompressible flow is required together with the concept of continuity.

For Section 3.4, which may be omitted at first reading, an understanding of vortices and the flow field induced by vortices is desirable. The Biot–Savart law, which will be familiar to those with a knowledge of electric and magnetic fields, is used to determine velocities induced by vortices. The Kutta–Joukowski theorem for determining the force on a bound vortex should also be studied.

For Sections 3.5 to 3.8, a knowledge of the lift and drag of aerofoils is essential, including stalled flow.

3.1 Introduction

A wind turbine is a device for extracting kinetic energy from the wind. By removing some of its kinetic energy, the wind must slow down, but only that mass of air that passes through the rotor disc is directly affected. Assuming that the affected mass of air remains separate from the air that does not pass through the rotor disc and does not mix with it, a boundary surface can be drawn containing the affected air mass, and this boundary can be extended upstream as well as downstream, forming a long streamtube of circular cross-section. No air flows across the boundary, and so the mass flow rate of the air flowing along the streamtube will be the same for all streamwise positions along the streamtube. Outside the streamtube, air that passes close to the rotor is not retarded in the same way but is subject to both retardation and acceleration associated with the divergence of the streamlines around the rotor. Because the air within the streamtube slows down, but is effectively incompressible at these speeds, the cross-sectional area of the streamtube must expand to accommodate the slower moving air; see Figure 3.1.

Although kinetic energy is extracted from the air flow, a sudden step change in velocity is neither possible nor desirable because of the enormous accelerations and forces this would require. Pressure energy *can* be extracted in a step-like manner, however, and all wind turbines, whatever their design, operate in this way.

The presence of the turbine causes the approaching air, upstream, gradually to slow down such that when the air arrives at the rotor disc its velocity is already lower than the free-stream wind speed. The streamtube expands as a result of the slowing down and, because no work has yet been done on, or by, the air, its static pressure rises to absorb the decrease in kinetic energy.

As the air passes through the rotor disc, by design, there is a drop in static pressure such that, on leaving, the air is below the atmospheric pressure level. The air then proceeds downstream with reduced speed and static pressure: this region of the flow is

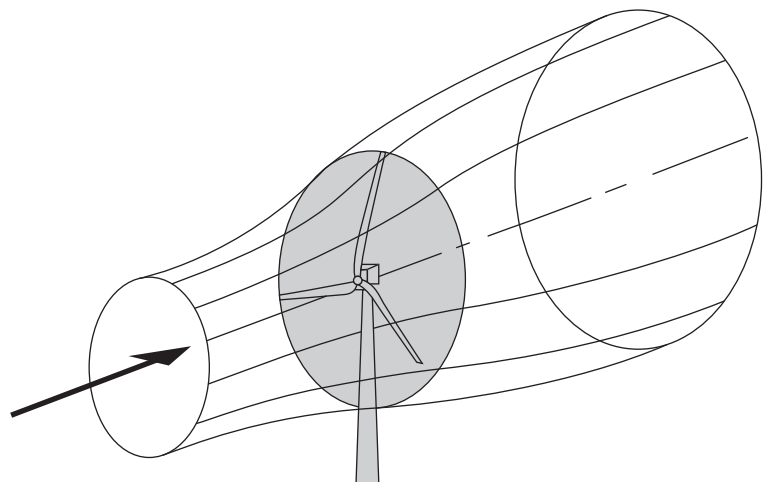


Figure 3.1 The energy extracting streamtube of a wind turbine.

called the *wake*. Eventually, far downstream, the static pressure in the wake must return to the atmospheric level for equilibrium to be achieved. The rise in static pressure is at the expense of the kinetic energy and so causes an additional slowing down of the wind. Thus, between the far upstream and far wake conditions, no difference in static pressure exists, but there is a reduction in kinetic energy.

3.2 The actuator disc concept

The mechanism described above accounts for the extraction of kinetic energy but in no way explains what happens to that energy: it may well be put to useful work, but some may be spilled back into the wind as turbulence and eventually be dissipated as heat.

Nevertheless, we can begin an analysis of the aerodynamic behaviour of wind turbines without any specific turbine design just by considering the energy extraction process. The general device that carries out this task is called an *actuator disc*; see Figure 3.2.

Upstream of the disc, the streamtube has a cross-sectional area smaller than that of the disc and an area larger than the disc downstream. The expansion of the streamtube is because the mass flow rate must be the same everywhere. The mass of air that passes through a given cross-section of the streamtube in a unit length of time is $\rho A U$, where ρ is the air density, A is the cross-sectional area, and U is the flow velocity. The mass flow rate must be the same everywhere along the streamtube, and so

$$\rho A_\infty U_\infty = \rho A_D U_D = \rho A_W U_W \quad (3.1)$$

The symbol ∞ refers to conditions far upstream, D refers to conditions at the disc, and W refers to conditions in the far wake.

It is usual to consider that the actuator disc induces a velocity variation that must be superimposed on the free-stream velocity. The streamwise component of this induced flow at the disc is given by $-a U_\infty$, where a is called the *axial flow induction factor*, or the

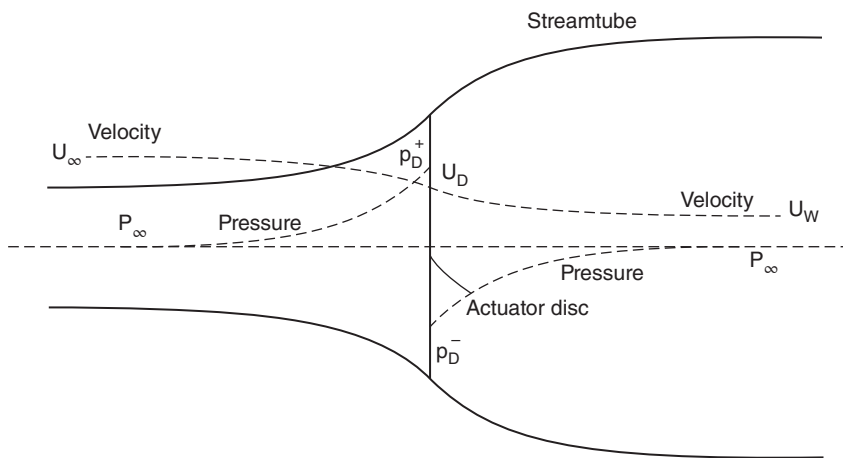


Figure 3.2 An energy extracting actuator disc and streamtube.

inflow factor. At the disc, therefore, the net streamwise velocity is

$$U_D = U_\infty(1 - a) \quad (3.2)$$

3.2.1 Simple momentum theory

The air that passes through the disc undergoes an overall change in velocity, $U_\infty - U_W$, and a rate of change of momentum equal to the overall change of velocity times the mass flow rate:

$$\text{Rate of change of momentum} = (U_\infty - U_W)\rho A_D U_D \quad (3.3)$$

The force causing this change in momentum comes entirely from the pressure difference across the actuator disc and the axial component of the pressure acting on the curved surface of the streamtube. This latter pressure is usually assumed to be ambient and therefore to give zero contribution, without further explanation. In fact this pressure is different from ambient due to the axial variation of velocity along the streamtube, but the integral of its axial component from far upstream to far downstream can be shown to be exactly equal to zero, the streamwise contribution upstream of the actuator disc exactly balancing the downstream contribution that opposes the stream (Jamieson 2018).

Therefore,

$$(p_D^+ - p_D^-)A_D = (U_\infty - U_W)\rho A_D U_\infty(1 - a) \quad (3.4)$$

To obtain the pressure difference ($p_D^+ - p_D^-$), Bernoulli's equation is applied separately to the upstream and downstream sections of the streamtube: separate equations are necessary because the total energy is different upstream and downstream. Bernoulli's equation states that, under steady conditions, the total energy in the flow, comprising kinetic energy, static pressure energy, and gravitational potential energy, remains constant provided no work is done on or by the fluid. Thus, for a unit volume of air,

$$\frac{1}{2}\rho U^2 + p + \rho gh = \text{const} \quad (3.5a)$$

Upstream, therefore, we have

$$\frac{1}{2}\rho_\infty U_\infty^2 + p_\infty + \rho_\infty gh_\infty = \frac{1}{2}\rho_D U_D^2 + p_D^+ + \rho_D g h_D \quad (3.5b)$$

Assuming the flow speed to be at low Mach number M (typically $M < 0.3$ is sufficient), it may be treated as incompressible ($\rho_\infty = \rho_D$) and to be independent of buoyancy effects ($\rho g h_\infty = \rho g h_D$) then,

$$\frac{1}{2}\rho U_\infty^2 + p_\infty = \frac{1}{2}\rho U_D^2 + p_D^+ \quad (3.5c)$$

Similarly, downstream,

$$\frac{1}{2}\rho U_W^2 + p_\infty = \frac{1}{2}\rho U_D^2 + p_D^- \quad (3.5d)$$

Subtracting these equations, we obtain

$$(p_D^+ - p_D^-) = \frac{1}{2}\rho(U_\infty^2 - U_W^2) \quad (3.6)$$

Equation (3.4) then gives

$$\frac{1}{2}\rho(U_{\infty}^2 - U_W^2)A_D = (U_{\infty} - U_W)\rho A_D U_{\infty}(1 - a) \quad (3.7)$$

and so,

$$U_W = (1 - 2a)U_{\infty} \quad (3.8)$$

That is, half the axial speed loss in the streamtube takes place upstream of the actuator disc and half downstream.

3.2.2 Power coefficient

The force on the air becomes, from Eq. (3.4),

$$T = (p_D^+ - p_D^-)A_D = 2\rho A_D U_{\infty}^2 a(1 - a) \quad (3.9)$$

As this force is concentrated at the actuator disc, the rate of work done by the force is TU_D and hence the power extraction from the air is given by

$$Power = TU_D = 2\rho A_D U_{\infty}^3 a(1 - a)^2 \quad (3.10)$$

A *power coefficient* is then defined as

$$C_P = \frac{Power}{\frac{1}{2}\rho U_{\infty}^3 A_D} \quad (3.11)$$

where the denominator represents the power available in the air, in the absence of the actuator disc. Therefore,

$$C_P = 4a(1 - a)^2 \quad (3.12)$$

3.2.3 The Betz limit

(This limit is also referred to as the *Lanchester–Betz limit* or the *Betz–Joukowski limit*).¹

The maximum value of C_P occurs when

$$\frac{dC_P}{da} = 4(1 - a)(1 - 3a) = 0$$

that gives a value of $a = \frac{1}{3}$

Hence,

$$C_{P\max} = \frac{16}{27} = 0.593 \quad (3.13)$$

The maximum achievable value of the power coefficient is known as the *Betz limit* after Albert Betz (1919), the German aerodynamicist. Frederic Lanchester (1915), a British aeronautical pioneer, worked earlier on a similar analysis and is sometimes given prior

¹ There is not complete agreement on the appropriate name for this limit because Lanchester (1915), Betz (1919, 1920), and Joukowski (1920) all published relevant papers. *Betz limit* is the most commonly used name. See also comment in Chapter 1.

credit, and Joukowski (1920) also contributed an analysis. To date, no unducted wind turbine has been designed that is capable of exceeding the Betz limit. The limit is caused not by any deficiency in design because, as yet in our discussion, we have no design. However, because the streamtube has to expand *upstream* of the actuator disc, the cross-section of the tube where the air is at the full, free-stream velocity is smaller than the area of the disc.

The *efficiency of the rotor* might more properly be defined as

$$\frac{\text{Power extracted}}{\text{Power available}} = \frac{\text{Power extracted}}{\frac{16}{27} \cdot \left\{ \frac{1}{2} \rho U_{\infty}^3 A_D \right\}} \quad (3.14)$$

but note that C_P is not the same as this efficiency.

3.2.4 The thrust coefficient

The force on the actuator disc caused by the pressure drop, given by Eq. (3.9), can also be non-dimensionalised to give a *coefficient of thrust* C_T

$$C_T = \frac{\text{Thrust}}{\frac{1}{2} \rho U_{\infty}^2 A_D} \quad (3.15)$$

$$C_T = 4a(1 - a) \quad (3.16)$$

A problem arises for values of $a \geq \frac{1}{2}$ because the wake velocity, given by $(1 - 2a)U_{\infty}$, becomes zero, or even negative: in these conditions the momentum theory, as described, no longer applies, and an empirical modification has to be made (Section 3.7).

The variation of power coefficient and thrust coefficient with a is shown in Figure 3.3. The solid lines indicate where the theory is representative and the dashed lines where it is not.

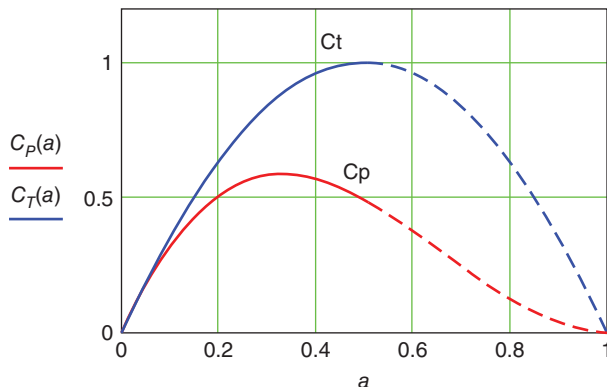


Figure 3.3 Variation of C_P and C_T with axial induction factor a .

3.3 Rotor disc theory

The manner in which the extracted energy is converted into usable energy depends upon the particular turbine design. The most common type of wind energy converter, the horizontal axis wind turbine or HAWT, employs a rotor with a number of blades rotating with an angular velocity Ω about an axis normal to the rotor plane and parallel to the wind direction. The blades sweep out a disc and by virtue of their aerodynamic design develop a pressure difference across the disc, which, as discussed in the previous section, is responsible for the loss of axial momentum in the wake. Associated with the loss of axial momentum is a loss of energy that can be collected by, say, an electrical generator attached to the rotor shaft. As well as a thrust, the rotor experiences a torque in the direction of rotation that will oppose the torque that the generator exerts. The work done by the aerodynamic torque on the generator is converted into electrical energy. The required aerodynamic design of the rotor blades to provide a torque as well as a thrust is discussed in Section 3.5.

3.3.1 Wake rotation

The exertion of a torque on the rotor disc by the air passing through it requires an equal and opposite torque to be imposed upon the air. The consequence of the reaction torque is to cause the air to rotate in a direction opposite to that of the rotor; the air gains angular momentum, and so in the wake of the rotor disc the air particles have a velocity component in a direction that is tangential to the rotation as well as an axial component; see Figure 3.4.

The acquisition of the tangential component of velocity by the air means an increase in its kinetic energy that is compensated for by a fall in the static pressure of the air in the wake in addition to that which is described in the previous section.

The flow entering the actuator disc has no rotational motion at all. The flow exiting the disc does have rotation, and that rotation remains constant as the fluid progresses down the wake. The transfer of rotational motion to the air takes place entirely across the thickness of the disc (see Figure 3.5). The change in tangential velocity is expressed in terms of a tangential flow induction factor a' . Upstream of the disc the tangential velocity is zero. Immediately downstream of the disc the tangential velocity is $2r\Omega a'$. In

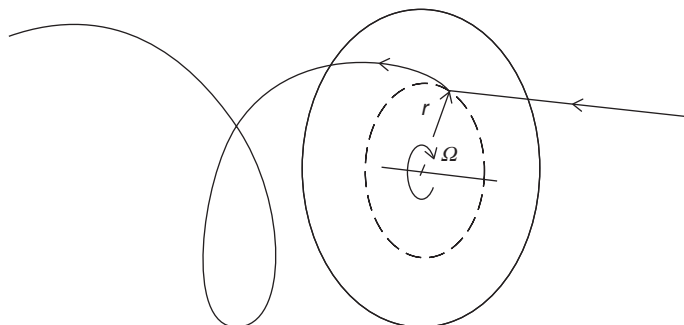


Figure 3.4 The trajectory of an air particle passing through the rotor disc.

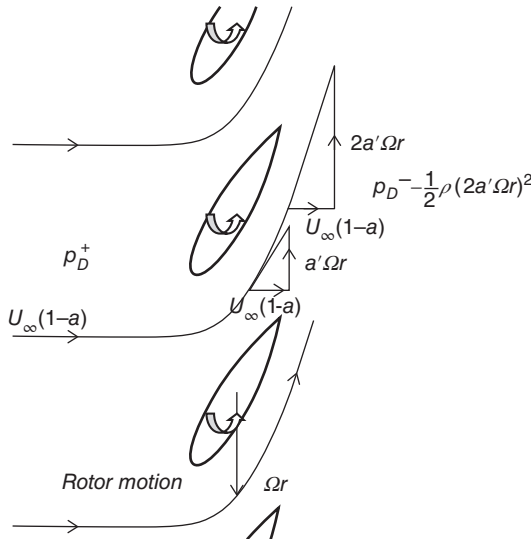


Figure 3.5 Tangential velocity grows across the disc thickness.

the plane of the disc the tangential velocity is $r\Omega a'$ (see also Figure 3.10 and the associated discussion). Because it is produced in reaction to the torque, the tangential velocity is opposed to the motion of the rotor.

An abrupt acquisition of tangential velocity cannot occur in practice and must be gradual. Figure 3.5 shows, for example, a sector of a rotor with multiple blades. The flow accelerates in the tangential direction through the ‘actuator disc’ as it is turned between the blades by the lift forces generated by their angle of attack to the incident flow.

3.3.2 Angular momentum theory

The tangential velocity will not be the same for all radial positions, and it may well also be that the axial induced velocity is not the same. To allow for variation of both induced velocity components, consider only an annular ring of the rotor disc that is of radius r and of radial width δr .

The increment of rotor torque acting on the annular ring will be responsible for imparting the tangential velocity component to the air, whereas the axial force acting on the ring will be responsible for the reduction in axial velocity. The whole disc comprises a multiplicity of annular rings, and each ring is assumed to act independently in imparting momentum only to the air that actually passes through the ring.

The torque on the ring will be equal to the rate of change of angular momentum of the air passing through the ring.

$$\begin{aligned} \text{Thus, torque} &= \text{rate of change of angular momentum} \\ &= \text{mass flow rate through disc} \times \text{change of tangential velocity} \times \text{radius} \end{aligned}$$

$$\delta Q = \rho \delta A_D U_\infty (1 - a) 2 \Omega a' r^2 \quad (3.17)$$

where δA_D is taken as being the area of an annular ring.

The driving torque on the rotor shaft is also δQ , and so the increment of rotor shaft power output is

$$\delta P = \delta Q \Omega$$

The total power extracted from the wind by slowing it down is therefore determined by the rate of change of axial momentum given by Eq. (3.10) in Section 3.2.2:

$$\delta P = 2\rho\delta A_D U_\infty^3 a(1-a)^2$$

Hence

$$2\rho\delta A_D U_\infty^3 a(1-a)^2 = \rho\delta A_D U_\infty(1-a)2\Omega^2 a' r^2$$

and

$$U_\infty^2 a(1-a) = \Omega^2 r^2 a'$$

Ωr is the tangential velocity of the spinning annular ring, and so $\lambda_r = \frac{r\Omega}{U_\infty}$ is called the *local speed ratio*. At the edge of the disc $r = R$ and $\lambda = \frac{R\Omega}{U_\infty}$ is known as the *tip speed ratio*.

Thus

$$a(1-a) = \lambda_r^2 a' \quad (3.18)$$

The area of the ring is $\delta A_D = 2\pi r \delta r$, therefore the incremental shaft power is, from Eq. (3.17),

$$\delta P = \delta Q \Omega = \left(\frac{1}{2} \rho U_\infty^3 2\pi r \delta r \right) 4a'(1-a)\lambda_r^2$$

The first term in brackets represents the power flux through the annulus in the absence of any rotor action; the term outside these brackets, therefore, is the efficiency of the blade element in capturing that power.

Blade element efficiency is

$$\eta_r = 4a'(1-a)\lambda_r^2 \quad (3.19)$$

in terms of power coefficient

$$\begin{aligned} \frac{dC_P}{dr} &= \frac{4\pi\rho U_\infty^3 (1-a)a'\lambda_r^2 r}{\frac{1}{2}\rho U_\infty^3 \pi R^2} = \frac{8(1-a)a'\lambda_r^2 r}{R^2} \\ \frac{dC_P}{d\mu} &= 8(1-a)a'\lambda^2 \mu^3 \end{aligned} \quad (3.20)$$

where $\mu = \frac{r}{R}$.

Knowing how a and a' vary radially [Eq. (3.20)] can be integrated to determine the overall power coefficient for the disc for a given tip speed ratio λ .

It was argued by Glauert (1935b) that the rotation in the wake required energy that is taken from the flow and is unavailable for extraction, but this can be shown not to be the case. The residual rotation in the far wake is supplied by the rotation component $a'\Omega$ induced at the rotor. The lift forces on the blades forming the rotor disc are normal to the resultant velocity relative to the blades, and so no work is done on or by the fluid.

Therefore, Bernoulli's theorem can be applied to the flow across the disc, relative to the disc spinning at angular velocity Ω , to give for an annulus of radius r

$$\begin{aligned} & \frac{1}{2}\rho U_\infty^2(1-a)^2 + \frac{1}{2}\rho\Omega^2r^2 + \frac{1}{2}\rho w^2 + p_D^+ \\ &= \frac{1}{2}\rho U_\infty^2(1-a)^2 + \frac{1}{2}\rho\Omega^2(1+2a')^2r^2 + \frac{1}{2}\rho w^2 + p_D^- \end{aligned}$$

where w is the radial component of velocity, which is assumed continuous across the disc.

Consequently,

$$\Delta p_D = 2\rho\Omega^2(1+a')a'r^2$$

The pressure drop across the disc clearly has two components. The first component

$$\Delta p_{D1} = 2\rho\Omega^2a'r^2 \quad (3.21)$$

is shown to be, from Eq. (3.18), the same as that given by Eq. (3.9) in the simple momentum theory in which rotation plays no part. The second component is

$$\Delta p_{D2} = 2\rho\Omega^2a'^2r^2 \quad (3.22)$$

Δp_{D2} can be shown to provide a radial, static pressure gradient

$$\frac{dp}{dr} = \rho(2\Omega a')^2 r$$

in the rotating wake that balances the centrifugal force on the rotating fluid, because [see Eq. (3.33) $a'(r) = a'(R)R^2/r^2$. This pressure causes a small discontinuity in the pressure at the wake boundary equal to $2\rho(a'(R)\Omega R)^2$, which in reality, along with the other discontinuities there, is smeared out.]

The kinetic energy per unit volume of the rotating fluid in the wake is also equal to the drop in static pressure of Eq. (3.22), and so the two are in balance and there is no loss of available kinetic energy.

However, the pressure drop of Eq. (3.22) balancing the centrifugal force on the rotating fluid does cause an additional thrust on the rotor disc. In principle, the low-pressure region close to the axis caused by the centrifugal forces in the wake can increase the local power coefficient. This is because it sucks in additional fluid from the far upstream region that accelerates through the rotor plane. This effect would cause a slight reduction in the diverging of the inflow streamlines. However, the degree to which this effect might allow a useful increase in power to be achieved is still the subject of discussion; see, e.g. the analyses given by Sorensen and van Kuik (2011), Sharpe (2004), and Jamieson (2011). The ideal model with constant blade circulation right in to the axis is not consistent due to the effect on the blade angle of attack by the arbitrarily large rotation velocities induced there, and in reality, the circulation must drop off smoothly to zero at the axis, and the root vortex must be a vortex with a finite diameter. This is discussed later in Section 3.4, where the vortex model of the wake is analysed. Numerical simulations of optimum actuator discs by Madsen et al. (2007) have not found the optimum power coefficient ever to exceed the Betz limit. But the relevance of the issue is that it may be possible to extract more power than predicted by the Betz limit in cases of turbines running at very low tip speed ratios, even recognising that the rotor vortex has a finite sized core or is shed as a helix at a radius greater than zero, and taking account of the small amount of residual rotational energy lost in the far wake.

3.3.3 Maximum power

The values of a and a' that will provide the maximum possible efficiency can be determined by differentiating Eq. (3.19) by either factor and putting the result equal to zero. Hence

$$\frac{da}{da'} = \frac{1-a}{a'} \quad (3.23)$$

From Eq. (3.18)

$$\frac{da}{da'} = \frac{\lambda_r^2}{1-2a}$$

giving

$$a' \lambda_r^2 = (1-a)(1-2a) \quad (3.24)$$

The combination of Eqs. (3.18) and (3.21) gives the required values of a and a' that maximise the incremental power coefficient:

$$a = \frac{1}{3} \text{ and } a' = \frac{a(1-a)}{\lambda_r^2} \quad (3.25)$$

The axial flow induction for maximum power extraction is the same as for the non-rotating wake case, that is, $a = \frac{1}{3}$, and is therefore uniform over the entire disc. However, a' varies with radial position.

From Eq. (3.20) the power coefficient for the whole rotor is

$$C_P = 8 \int_0^1 (1-a)a' \lambda^2 \mu^3 d\mu$$

Substituting for the expression for a' in Eq. (3.25) gives maximum power as

$$C_P = 8 \int_0^1 (1-a) \frac{a(1-a)}{\lambda^2 \mu^2} \lambda^2 \mu^3 d\mu = 4a(1-a)^2 = \frac{16}{27} \quad (3.26)$$

which is precisely the same as for the non-rotating wake case.

3.4 Vortex cylinder model of the actuator disc

3.4.1 Introduction

The momentum theory of Section 3.1 uses the concept of the actuator disc across which a pressure drop develops, constituting the energy extracted by the rotor. In the rotor disc theory of Section 3.3, the actuator disc is depicted as being swept out by a multiplicity of aerofoil blades, each represented by a radial vortex of constant strength $\Delta\Gamma$ that denotes the bound circulation around each blade section (the totality of spanwise vorticity in the blade surface sheets). Each of these vortex lines is usually considered to lie along the quarter-chord line of the blade but cannot terminate in the flow field at the tip. Therefore, each vortex is shed at the tip of the blade and convects downstream with the local flow velocity, forming a wake vortex in the form of a helix with strength $\Delta\Gamma$. If the number, B , of blades is assumed to be very large but the solidity of the total is finite and small, then

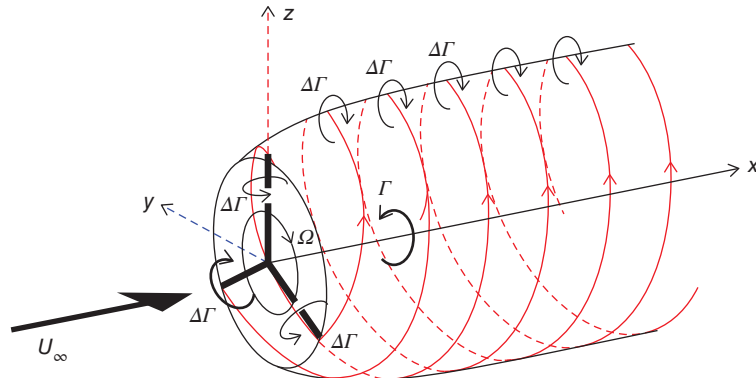


Figure 3.6 Helical vortex wake shed by rotor with three blades each with uniform circulation $\Delta\Gamma$.

the accumulation of helical tip vortices will form the surface of a tube. As the number of blades approaches infinity, the tube surface will become a continuous tubular vortex sheet; see Figure 3.6.

From the root of each blade, assuming it reaches to the axis of rotation, a line vortex of strength $\Delta\Gamma$ will extend downstream along the axis of rotation, contributing to the total root vortex of strength $\Gamma (=B\Delta\Gamma)$. The streamtube will expand in radius as the flow of the wake inside the tube slows down. Because the axial convection of the tip vortices is therefore slowing from the rotor to the far wake, their spacing decreases and hence the vorticity density on the tube sheet representing the tip vortices increases. The vorticity is confined to the surface of this tube, the root vortex, and to the bound vortex sheet swept by the multiplicity of blades to form the rotor disc; elsewhere in the wake and everywhere else in the entire flow field the flow is irrotational.

The nature of the tube's expansion cannot be determined by means of the momentum theory but is known from numerical simulations to be usually fairly small. Therefore, as an approximation, the tube is considered to remain cylindrical, as shown in Figure 3.7.

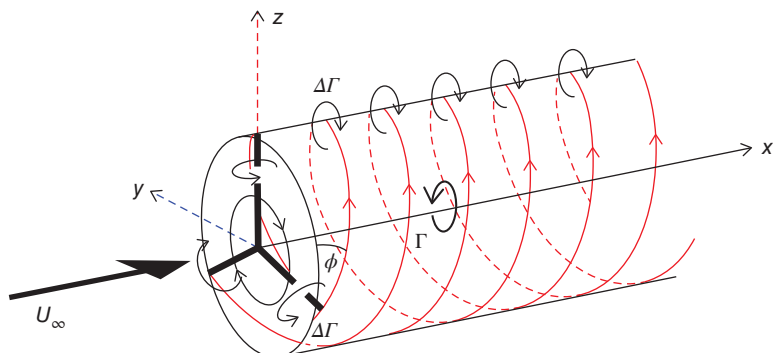


Figure 3.7 Simplified helical vortex wake ignoring wake expansion.

The Biot–Savart law is used to determine the induced velocity at any point in the vicinity of the actuator disc. The cylindrical vortex model allows the whole flow field to be determined and is accurate within the limitations of the non-expanding cylindrical wake.

3.4.2 Vortex cylinder theory

In the limit of an infinite number of blades and ignoring expansion the tip vortices form a cylinder with surface vorticity that follows a helical path with a helix angle ϕ_t , which is the same as the flow angle at the outer edge of the disc. The strength of the vorticity is $g = \frac{\Delta\Gamma}{\Delta n}$, where Δn is the distance along the tube surface in a direction normal to $\Delta\Gamma$ between two successive tip vortices. g has components g_θ in the azimuthal direction and g_x in the axial direction. Due to g_θ the axial (parallel to the axis of rotor rotation) induced velocity u_d at the rotor plane is *uniform* over the rotor disc and can be determined by means of the Biot–Savart law as

$$u_d = -\frac{g_\theta}{2} = -aU_\infty \quad (3.27)$$

In the far wake the axial induced velocity u_w is also uniform within the cylindrical wake and is

$$u_w = -g_\theta = -2aU_\infty \quad (3.28)$$

The ratio of the two induced velocities corresponds to that of the simple momentum theory and justifies the assumption of a cylindrical vortex sheet.

3.4.3 Relationship between bound circulation and the induced velocity

The total circulation on all of the multiplicity of blades is Γ , which is shed at a uniform rate into the wake in one revolution. So, from Figure 3.8 in which the cylinder has been slit longitudinally and opened out flat, we must have for the strength of the axial vorticity that

$$g_x = \Gamma/2\pi R \quad (3.29)$$

since irrespective of the vortex convection velocities the whole circulation Γ is distributed over the peripheral length $2\pi R$.

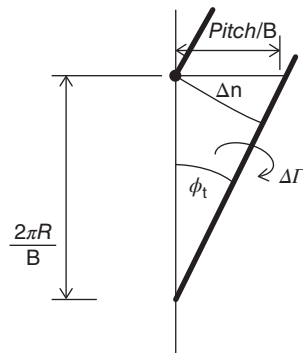


Figure 3.8 The geometry of the vorticity in the cylinder surface.

To evaluate the strength of the azimuthal vorticity, we require the axial spacing over which it is distributed, i.e. the axial spacing of any tip vortex between one vortex and the next. Vortices and sheets of vorticity must be convected at the velocity of the local flow field if they are to be force-free. This velocity can be evaluated as the velocity of the whole flow field at the vortex or vorticity element location less its own local (singular) contribution. In the case of a continuous sheet, it is the average of the velocities on the two sides of the sheet. For axial convection in the ‘far’ wake the two axial velocities are:

$$U_{\infty}(1 - 2a) \text{ (inside) and } U_{\infty} \text{ (outside)}$$

so that the axial convection velocity is $U_{\infty}(1 - a)$. However, the vortex wake also rotates relative to stationary axes at a rate similarly calculated as halfway between the rotation rate of the fluid just inside the downstream wake = $2a'\Omega R$ and just outside = 0. Therefore, the helical wake vortices (or vortex tube in the limit) rotate at $a'\Omega R$. The result is that the pitch of the helical vortex wake (see Figure 3.8) is

$$X_p = 2\pi U_{\infty}(1 - a)/\Omega(1 + a') \quad (3.30)$$

Using this value we obtain

$$g_{\theta} = \lambda\Gamma(1 + a')/2\pi R(1 - a) \quad (3.31)$$

where $\lambda = \Omega R/U_{\infty}$ the tip speed ratio and the rotation period = $2\pi/\Omega$.

So, the total circulation is related to the induced velocity factors

$$\Gamma = \frac{4\pi U_{\infty}^2 a(1 - a)}{\Omega(1 + a')} \quad (3.32)$$

It is similarly necessary to include the rotation induction factor to calculate the angle of slant φ_t of the vortices:

Thus $\tan \varphi_t = (1 - a)/(1 + a')\lambda$

3.4.4 Root vortex

Just as a vortex is shed from each blade tip, a vortex is also shed from each blade root. If it is assumed that the blades extend to the axis of rotation, obviously not a practical option, then the root vortices will each be a line vortex running axially downstream from the centre of the disc. The direction of rotation of all of the root vortices will be the same, forming a core, or root, vortex of total strength Γ . The root vortex is primarily responsible for inducing the tangential velocity in the wake flow and in particular the tangential velocity on the rotor disc.

On the rotor disc surface the tangential velocity induced by the root vortex, given by the Biot–Savart law, is

$$\frac{\Gamma}{4\pi r} = a'\Omega r$$

so

$$a' = \frac{\Gamma}{4\pi r^2 \Omega} \quad (3.33)$$

This relationship can also be derived from the momentum theory – the rate of change of angular momentum of the air that passes through an annulus of the disc of radius r and radial width δr is equal to the torque increment imposed upon the annulus:

$$\delta Q = \rho U_\infty (1 - a) 2\pi r 2a' r^2 \Omega \delta r \quad (3.34)$$

The torque per unit span acting on all the blades is given by the Kutta–Joukowski theorem. The lift per unit radial width L is

$$L = \rho (W \times \Gamma)$$

where $(W \times \Gamma)$ is a vector product, and W is the relative velocity of the air flow past the blade:

$$\delta Q = \rho W \times \Gamma r \sin \phi_t \delta r = \rho \Gamma r U_\infty (1 - a) \delta r \quad (3.35)$$

Equating the two expressions for δQ gives

$$a' = \frac{\Gamma}{4\pi r^2 \Omega}$$

If a' in Eq. (3.32) is now treated as being negligible with respect to 1 (which it is in normal circumstances) then:

$$a' = \frac{U_\infty^2 a (1 - a)}{(\Omega r)^2} = \frac{a(1 - a)}{\lambda_r^2}$$

At the outer edge of the disc the tangential induced velocity is

$$a'_t = \frac{a(1 - a)}{\lambda^2} \quad (3.36)$$

Equation (3.36) is exactly the same as Eq. (3.23) of Section 3.3.3.

If a' is retained in Eq. (3.32), there is a small inconsistency here between vortex theory and the one-dimensional actuator disc theory, which ignores rotation effects.

3.4.5 Torque and power

The torque on an annulus of radius r and radial width δr (ignoring a' as actuator disc theory ignores rotation) is

$$\frac{dQ}{dr} \delta r = \rho W T r \sin \phi_t \delta r = \frac{\rho 4\pi r U_\infty^3 a (1 - a)^2}{\Omega} \delta r \quad (3.37)$$

The radial distribution of power is

$$\frac{dP}{dr} = \Omega \frac{dQ}{dr} = \frac{1}{2} \rho U_\infty^3 2\pi r 4a(1 - a)^2 \quad (3.38)$$

and, therefore, the total power is

$$P = \frac{1}{2} \rho U_\infty^3 \pi R^2 4a(1 - a)^2 \quad (3.39)$$

Power coefficient:

$$C_P = 4a(1 - a)^2 = 4a'_t(1 - a)\lambda^2 \quad (3.40)$$

Again, a result that is identical to that predicted by the simple momentum theory.

What is particularly interesting is that the residual rotational flow in the wake makes no apparent reduction in the efficiency of the power extraction.

3.4.6 Axial flow field

The induced velocity in the windwise (axial) direction can be determined both upstream of the disc and downstream in the developing wake, as well as on the disc itself. This velocity is induced by the azimuthal component of vorticity in the cylindrical wake sheet at radius R (which generates an axisymmetric axial back-flow within the wake) as shown for a radial section in Figure 3.9. Both radial and axial distances are divided by the disc radius, with the axial distance being measured downstream from the disc and the radial distance being measured from the rotational axis. The velocity is divided by the wind speed.

The axial velocity within the wake in this model falls discontinuously across the wake boundary from the external value and is radially uniform at the disc and in the far wake, just as the momentum theory predicts. There is a small acceleration of the flow around the disc immediately outside of the wake. The induced velocity at the wake cylinder surface itself and hence its convection velocity is $-\frac{1}{2}a$ at the disc and $-a$ in the far wake.

3.4.7 Tangential flow field

The tangential induced velocity is induced by three contributions: that due to the root line vortex along the axis (which generates a rising swirl from zero upstream to a constant value in the far wake), that due to the axial component of vorticity $g \sin \phi_t$ in the cylindrical sheet at radius R , and that due to the bound vorticity, everywhere in the radial direction on the disc. The bound vorticity causes rotation in opposite senses upstream and downstream of the disc with a step change across the disc. The upstream rotation,

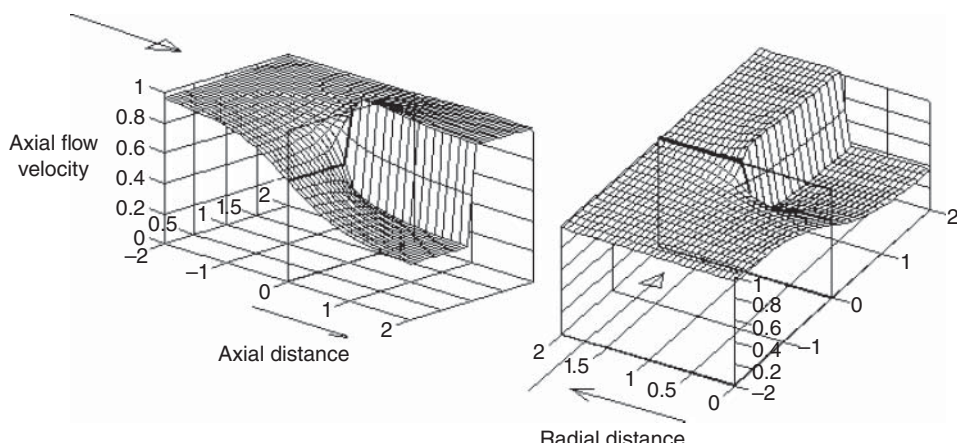


Figure 3.9 The radial and axial variation of axial velocity in the vicinity of an actuator disc, $a = \frac{1}{3}$.

which is in the same sense as the rotor rotation, is nullified by the root vortex, which induces rotation in the opposite sense to that of the rotor. The downstream rotation is in the same sense for both the root vortex and the bound vorticity, the streamwise variations of the two summing to give a uniform velocity in the streamwise sense. The vorticity located on the surface of the wake cylinder makes a small contribution.

Note that the bound vorticity (being the circulation on the rotor blades in response to the incident and induced flow) induces zero rotation *at* the disc and decays axially up and downstream. The discontinuity in tangential velocity at the disc is because the idealised changes are assumed to take place through a disc of zero thickness. In reality the azimuthal velocity rises rapidly but continuously as the flow passes through the rotor blades, which sweep through a disc and influence region of finite thickness as shown in Figure 3.5.

At the disc itself, because the bound vorticity induces no rotation and the wake cylinder induces no rotation within the wake cylinder either, it is only the root vortex that does induce rotation, and that value is half the total induced generally in the wake. Hence the root vortex induced rotation that is only half the rotational velocity is used to determine the flow angle at the disc. At a radial distance equal to half the disc radius, as an example, the axial variation of the three contributions is shown in Figure 3.10.

The rotational flow is confined to the wake, that is, inside the cylinder, and tends asymptotically to $2a'\Omega$ well downstream of the rotor. There is no rotational flow anywhere outside the wake, neither upstream of the disc nor at radial distances outside the wake cylinder. Because of this there is no first order transverse effect of the proximity of a ground plane on the downstream convection of the vortex wake of a wind turbine as there is on the trailing vortices of a fixed wing aircraft. The rotational flow within the wake cylinder decreases radially from the axis to the wake boundary but is not zero at the outer edge of the wake, therefore there is an abrupt fall of rotational velocity across this cylindrical wake surface vortex sheet.

And because of this profile of rotation the cylindrical vortex sheet itself, therefore, rotates with the mean of the inside and outside angular velocities, $a'_t\Omega$, and so the

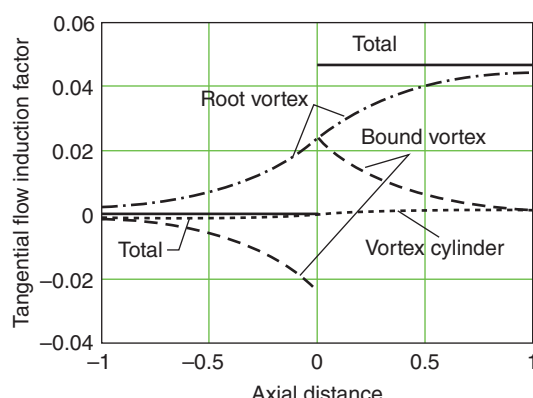


Figure 3.10 The axial variation of tangential velocity in the vicinity of an actuator disc at 50% radius, $a = \frac{1}{3}$, $\lambda = 6$.

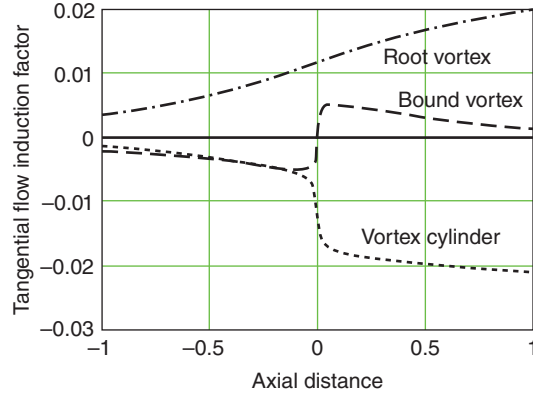


Figure 3.11 The axial variation of tangential velocity in the vicinity of an actuator disc at 101% radius, $a = \frac{1}{3}$, $\lambda = 6$.

rotation of the flow relative to the disc is $(1 + a')\Omega$. The helix angle ϕ_t takes this additional rotation into account, as determined from Eq. (3.30).

The contributions of the three vorticity sources to the rotational flow at a radius of 101% of the disc radius are shown in Figure 3.11: the total rotational flow is zero at all axial positions, but the individual components are not zero.

3.4.8 Axial thrust

The axial thrust T on the disc can be determined using the Kutta–Joukowski theorem:

$$\frac{dT}{dr} = \rho \Gamma V$$

where V is the tangential velocity component at the disc. If $V = r\Omega(1 + a')$, then, using Eq. (3.32) ignoring any additional inflow at the disc caused by the centrifugal pressure reduction due to wake swirl discussed at the end of Section 3.3.2:

$$\frac{dT}{dr} = \rho 4\pi r U_\infty^2 a(1 - a) \quad (3.41)$$

Integration of Eq. (3.41) over the entire disc gives the thrust coefficient as

$$C_T = 4a(1 - a) \quad (3.42)$$

That is, the same as for the simple momentum theory and so in balance with the rate of change of axial momentum. Note that if the induced tangential velocity $a'r\Omega$ is included in V as it is in blade-element/moment (BEM) theory and the blade circulation is constant from the axis to the tip, there is a singularity in the axial force on the blade section at the axis as there is also at the outer tip. This points to the failure of a simple constant strength bound vortex model at the blade ends as discussed in the section on tip-loss corrections.

3.4.9 Radial flow and the general flow field

Although the vortex cylinder model has been simplified by not allowing the cylinder to expand, the vortex theory nevertheless predicts flow expansion. A radial velocity is predicted by this theory as in Figure 3.12, which shows a longitudinal section of the flow field through the rotor disc. The theory is in fact a ‘small disturbance theory’ in which the singularities in the flow field (the vortex sheets in the present case) are placed on the surfaces they would lie on in the limit of vanishingly small disturbance by the rotor.

The radial velocity field that is predicted is largest on any given streamline at the actuator disc rising from zero at the axis to a weak logarithmic infinite value at the edge of the disc, which is the path of the blade tips. The infinite radial velocity at the edge is associated with non-zero disc loading right up to the edge. This is not realistic, being a consequence of assuming the rotor to consist of an infinite number of blades whose effect is ‘smeared’ uniformly over the disc, but being a weak singularity does not significantly affect the rest of the flow field. In applying the more detailed BEM theory the tip region is corrected by a tip correction factor to recognise that in reality the blade loading must fall to zero at the blade tips.

An alternative method of deriving the velocity field of the actuator disc has been given more recently by Conway (1998). This method takes the approach of building up the flow field from a sum of Bessel functions that are fundamental solutions of a cylindrical potential flow. The method has advantages if it is required to calculate the velocity at general points throughout the flow field both within the bounding streamtube that forms the boundary of the wake and outside it. For the streamwise velocity U_1 in the simple uniform actuator disc flow:

$$U_1(r, x) = 1 - a_1 \int_0^{\infty} e^{xx'} J_1(x') J_0(rx') dx' \quad x < 0$$

$$U_1(r, x) = 1 - a_1 \int_0^{\infty} (2 - e^{-xx'}) J_1(x') J_0(rx') dx' \quad x \geq 0$$

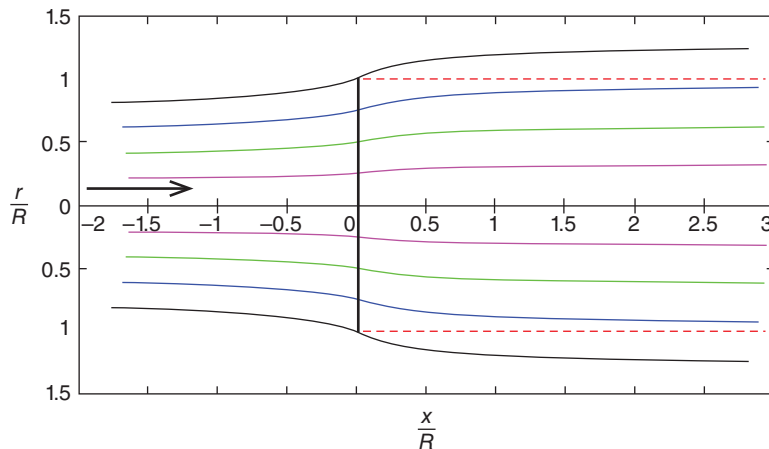


Figure 3.12 Flow field through an actuator disc for $a = 1/3$.

where r and x here are radial and streamwise coordinates non-dimensionalised by the tip radius, a_1 is the wake induction factor, and J_0 and J_1 are Bessel functions of the first kind.

This flow field may also be computed by solving the axisymmetric flow equations numerically either as inviscid Euler equations or as the full Navier–Stokes equations to compute the effects of viscous (or turbulent) mixing in the wake of the rotor (see section on computational fluid dynamics [CFD] in Chapter 4). Both stream function – vorticity and primitive variable (velocity – pressure) formulations have been used to do this; see, e.g. Mikkelsen (2003), Soerensen et al. (1998), Madsen et al. (2010).

The limiting condition of the cylindrical wake model of the flow through an actuator disc occurs as the loading on the actuator disc is increased so that the wake induction factor a approaches a value of 0.5. At this value the streamwise velocity in the wake $U_w (= (1 - 2a)U_\infty)$ falls to zero, and the wake is therefore predicted to expand indefinitely to an infinite cross-section. Beyond this value the wake flow is predicted to be negative, and the theory must break down. The wakes of rotors and also of porous discs normal to a flow that similarly correspond to actuator discs all reach a state when the pressure in the wake region immediately downstream of the body has fallen sufficiently that steady streamline flow can no longer continue stably in the near wake region. Castro (1971) has studied the wake of a porous disc in detail, showing how a reverse flow bubble forms downstream in the wake and moves upstream towards the actuator disc as the loading increases further. This regime is known as the *turbulent wake state* for a turbine rotor and will be discussed further in the following Section 3.5 on BEM theory.

3.4.10 Further development of the actuator model

The one-dimensional actuator disc model and associated vortex cylinder representation of the flow field is the simplest model of a HAWT that can provide useful results. This model may be developed in several ways to be more representative of the details of the flow.

Radial variation across the actuator disc may be considered as in BEM theory, Section 3.5 below.

Also, recognition may be given to the fact that the turbine has a finite number of blades, usually a small number such as two or three, each of which may be treated individually as a momentum sink actuator. In the simplest version taking average values, the forces on each blade are assumed to be radially constant. The lift and drag forces calculated from the flow angles at the blades with the relevant aerofoil section characteristics (as in Section 3.5.2) are converted into rotating axial and tangential momentum sinks projected onto a larger field grid computation. This is the basis of the simplest actuator line model (see Section 3.6).

With the development of large wind farms, particularly offshore, it has become important to simulate the flow through the whole wind farm to calculate the effect of multiple wakes interacting with each other and with the incident atmospheric boundary layer (ABL) and impinging on downstream rotors. Wake interactions have a very significant effect on power generated by turbines downstream of others (see, e.g. Argyle et al. 2018) and on the buffeting of downstream rotors. The usual method of carrying out these computations is to embed actuator models of the turbines within much larger numerical grid representations of the flow through and surrounding the whole wind farm. This outer large-scale flow is solved numerically on the grid by conventional, and

now well-established, CFD Reynolds averaged Navier–Stokes (RANS) or higher fidelity but much more computationally expensive large eddy simulation (LES) computer codes. The actuator model embedded in the grid to represent the action of each turbine may be at the simplest level of an actuator disc model, in which the thrust force on the rotor disc is inserted as a momentum sink, i.e. a step change in momentum in the streamwise direction across grid cells that are intersected by the rotor disc. However, it is usually found desirable to go to a higher level of representation including swirl and embed an actuator line model for each turbine blade in the grid. The rotating actuator lines are now the momentum sinks of both axial and azimuthal forces including the radial variations, which are projected at each timestep onto the adjacent grid points (see, for example, Soerensen and Shen 2002).

3.4.11 Conclusions

Despite the exclusion of wake expansion, the vortex theory produces results in agreement with the momentum theory and enlightens understanding of the flow through an energy extracting actuator disc. However, the infinite radial velocity predicted at the outer edge of the disc is further evidence that the actuator disc is physically unrealisable.

3.5 Rotor blade theory (blade-element/momentum theory)

3.5.1 Introduction

The aerodynamic lift (and drag) forces on the spanwise elements of radius r and length δr of the several blades of a wind turbine rotor are responsible for the rate of change of axial and angular momentum of all of the air that passes through the annulus swept by the blade elements. In addition, the force on the blade elements caused by the drop in pressure associated with the rotational velocity in the wake must also be provided by the aerodynamic lift and drag. As there is no rotation of the flow approaching the rotor, the reduced pressure on the downwind side of the rotor caused by wake rotation appears as a step pressure drop just as is that which causes the change in axial momentum. Because the wake is still rotating in the far wake, the pressure reduction associated with the rotation is still present and so does not contribute to the axial momentum change.

3.5.2 Blade element theory

It is assumed that the forces on a blade element can be calculated by means of two-dimensional (2-D) aerofoil characteristics using an angle of attack determined from the incident resultant velocity in the cross-sectional plane of the element. Applying the independence principle (see Appendix 3.1), the velocity component in the spanwise direction is ignored. Three-dimensional (3-D) effects are also ignored.

The velocity components at a radial position on the blade expressed in terms of the wind speed, the flow factors, and the rotational speed of the rotor together with the blade pitch angle will determine the angle of attack. Having information about how the aerofoil characteristic coefficients C_l and C_d vary with the angle of attack, the forces on the blades for given values of a and a' can be determined.

Consider a turbine with B blades of tip radius R each with chord c and set pitch angle β measured between the aerofoil chord-line and the plane of the disc. (Note that in referencing the pitch to the blade chord line the zero incidence lift coefficient must be included). Both the chord length, section profile (thickness and camber), and the pitch angle may vary along the blade span. Let the blades be rotating at angular velocity Ω and let the wind speed be U_∞ . The tangential velocity experienced by the blade element shown in Figure 3.13 is $(1 + a')r\Omega$. The actuator disc is infinitesimally thin; the change in tangential velocity is abrupt, but it is only the component induced by the root vortex that contributes. This varies smoothly across the region of the actuator disc (Figure 3.10). The bound velocity induced by the vorticity on the disc does not contribute.

Figure 3.14 shows all the velocities and forces relative to the blade chord line at radius r .

From Figure 3.14, the resultant relative velocity at the blade is

$$W = \sqrt{U_\infty^2(1 - a)^2 + r^2\Omega^2(1 + a')^2} \quad (3.43)$$

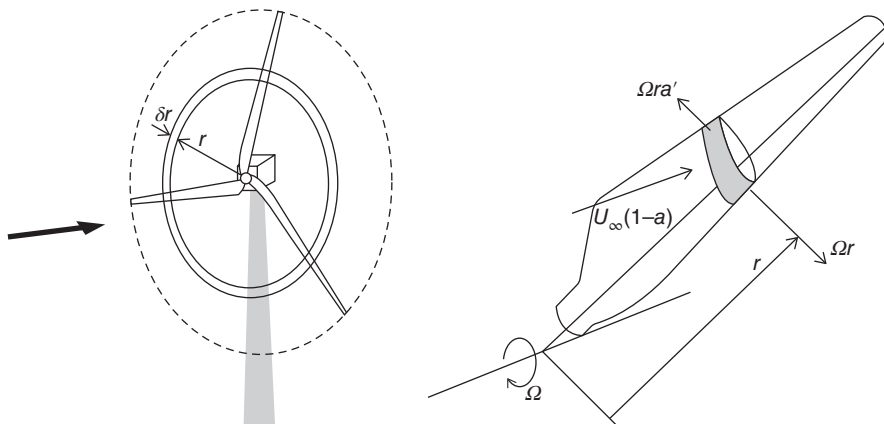


Figure 3.13 A blade element sweeps out an annular ring.

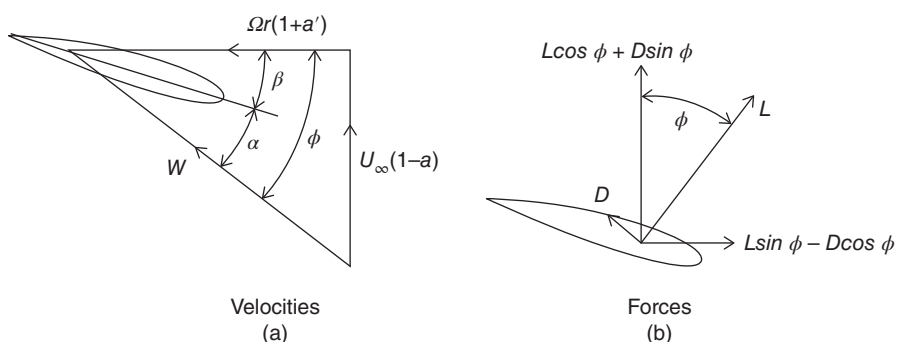


Figure 3.14 Blade element velocities and forces: (a) velocities, and (b) forces.

that acts at an angle ϕ to the plane of rotation such that

$$\sin \phi = \frac{U_\infty(1-a)}{W} \text{ and } \cos \phi = \frac{r\Omega(1+a')}{W} \quad (3.44)$$

The angle of attack α is then given by

$$\alpha = \phi - \beta \quad (3.45)$$

The basic assumption of the blade element theory is that the aerodynamic lift and drag forces acting upon an element are the same as those acting on an isolated, identical element at the same angle of attack in 2-D flow.

The lift force on a spanwise length δr of each blade, normal to the direction of W , is therefore

$$\delta L = \frac{1}{2}\rho W^2 c C_l \delta r$$

and the drag force parallel to W is

$$\delta D = \frac{1}{2}\rho W^2 c C_d \delta r$$

The axial thrust on an annular ring of the actuator disc is

$$\delta T = \delta L \cos \phi + \delta D \sin \phi = \frac{1}{2}\rho W^2 B c (C_l \cos \phi + C_d \sin \phi) \delta r \quad (3.46)$$

The torque on an annular ring is

$$\delta Q = (\delta L \sin \phi - \delta D \cos \phi) r = \frac{1}{2}\rho W^2 B c r (C_l \sin \phi - C_d \cos \phi) \delta r \quad (3.47)$$

where B is the number of blades.

3.5.3 The BEM theory

The basic assumption of the BEM theory is that the force of a blade element is solely responsible for the change of axial momentum of the air that passes through the annulus swept by the element. It is therefore to be assumed that there is no radial interaction between the flows through contiguous annuli: a condition that is, strictly, only true if pressure gradients acting axially on the curved streamlines can be neglected if the axial flow induction factor does not vary radially. In practice, the axial flow induction factor is seldom uniform, but experimental examination of flow through propeller discs by Lock (1924) shows that the assumption of radial independence is acceptable.

Equating the axial thrust on all blade elements, given by Eq. (3.46), with the rate of change of axial momentum of the air that passes through the annulus swept out by the elements, given by Eq. (3.9), with $A_D = 2\pi r \delta r$

$$\delta T = \frac{1}{2}\rho W^2 B c (C_l \cos \phi + C_d \sin \phi) \delta r = 2\pi r \delta r \rho U_\infty (1-a) 2a U_\infty \quad (3.48)$$

It should be noted here that the right hand side of Eq. (3.48) ignores the effect of the swirl velocity ($2a'\Omega r$) on the axial momentum balance through generating a centrifugal pressure gradient in the far wake from the axis to the wake boundary. The resulting pressure

reduction that generates an additional pressure drop across the disc was termed Δp_{d2} when considered previously in Eq. (3.22).

Equating the torque on the elements, given by Eq. (3.47), with the rate of change of angular momentum of the air passing through the swept annulus, given by Eq. (3.34),

$$\delta Q = \frac{1}{2} \rho W^2 B c r (C_L \sin \phi - C_D \cos \phi) \delta r = 2\pi r \delta r \rho U_\infty (1-a) 2a' r^2 \Omega \quad (3.49)$$

If drag is eliminated from the above two equations, to make a comparison with the results of the vortex theory of Section 3.4, the flow angle ϕ can be determined:

$$\tan \phi = \frac{a' r \Omega}{a U_\infty} = \frac{a'}{a} \frac{r}{R} \lambda$$

However, from the velocity triangle at a blade element given by Eq. (3.44), the flow angle is also

$$\tan \phi = \frac{1-a}{\lambda_r (1+a')}$$

Equating the two above expressions for $\tan \phi$

$$\begin{aligned} \frac{a'}{a} \frac{r}{R} \lambda &= \frac{1-a}{\lambda_r (1+a')} \\ a(1-a) &= \lambda_r^2 a' (1+a') \end{aligned} \quad (3.50a)$$

At the outer edge of the rotor $\mu = 1$ and $a' = a'_t$, so

$$a(1-a) = \lambda^2 a'_t (1+a'_t) \quad (3.50b)$$

Equation (3.2) is consistent with the earlier Eqs. (3.32) and (3.33).

With drag included the thrust Eq. (3.48) can be reduced to

$$\frac{W^2}{U_\infty^2} B \frac{c}{R} (C_l \cos \phi + C_d \sin \phi) = 8\pi a(1-a)\mu \quad (3.51)$$

where the parameter $\mu = \frac{r}{R}$.

If the pressure drop term Δp_{d2} is not ignored, the right hand side of Eq. (3.51) becomes $8\pi\mu\{a(1-a) + (a'\lambda\mu)^2\}$. The additional term $(a'\lambda\mu)^2$ is small and usually negligible except very close to the rotor axis or at low tip speed ratios.

The torque Eq. (3.49) simplifies to

$$\frac{W^2}{U_\infty^2} B \frac{c}{R} (C_l \sin \phi - C_d \cos \phi) = 8\pi \lambda \mu^2 a' (1-a) \quad (3.52)$$

It is convenient to put

$$C_l \cos \phi + C_d \sin \phi = C_x \quad (3.53a)$$

and

$$C_l \sin \phi - C_d \cos \phi = C_y \quad (3.53b)$$

Solving Eqs. (3.51) and (3.52) to obtain values for the flow induction factors a and a' using 2-D aerofoil characteristics requires an iterative process for which the following

equations, derived from (3.51), (3.52), and (3.53a and b), are convenient. The right hand sides are evaluated using existing values of the flow induction factors, yielding simple equations for the next iteration of the flow induction factors:

$$\frac{a}{1-a} = \frac{\sigma_r}{4\sin^2\phi} C_x \quad (3.54a)$$

$$\frac{a'}{1+a'} = \frac{\sigma_r C_y}{4\sin\phi\cos\phi} \quad (3.55)$$

If the additional pressure-drop term Δp_{d2} at the rotor due to wake rotation is included in the analysis, following from Eq. (3.48), Eq. (3.54a) becomes

$$\frac{a}{1-a} = \frac{\sigma_r}{4\sin^2\phi} \left(C_x - \frac{\sigma_r}{4} \frac{C_y^2}{\sin^2\phi} \right) \quad (3.54b)$$

Blade solidity σ is defined as total blade area divided by the rotor disc area and is a primary parameter in determining rotor performance. Chord solidity σ_r is defined as the total blade chord length at a given radius divided by the circumferential length around the annulus at that radius:

$$\sigma_r = \frac{B}{2\pi r} \frac{c}{R} = \frac{B}{2\pi\mu} \frac{c}{R} \quad (3.56)$$

It is argued by Wilson et al. (1974) that the drag coefficient should not be included in Eqs. (3.54a or b) and (3.55) because the velocity deficit caused by drag is confined to the narrow wake that flows from the trailing edge of the aerofoil. Furthermore, Wilson and Lissaman reason, the drag based velocity deficit is only a feature of the wake and does not contribute to the velocity deficit upstream of the rotor disc. The basis of the argument for excluding drag in the determination of the flow induction factors is that, for attached flow, drag is caused only by skin friction and does not affect the pressure drop across the rotor. Clearly, in stalled flow the drag is overwhelmingly caused by pressure. In attached flow – see, e.g. Young and Squire (1938) – the modification to the inviscid pressure distribution around an aerofoil caused by the boundary layer has a small effect both on lift and drag. The ratio of pressure drag to total drag at zero angle of attack is approximately the same as the thickness to chord ratio of the aerofoil and increases as the angle of attack increases.

One last point about the BEM theory: the theory neglects the axial components of the pressure forces at curved boundaries between streamtubes. It is more accurate if the blades have uniform circulation, i.e. if a is uniform. For non-uniform circulation there is increased radial interaction and exchange of momentum as a result of normal pressure and viscous shear forces between flows through adjacent elemental annular streamtubes. However, in practice, it appears that the error involved is small for tip speed ratios greater than three.

3.5.4 Determination of rotor torque and power

The calculation of torque and power developed by a rotor requires a knowledge of the flow induction factors, which are obtained by solving Eqs. (3.54a or b) and (3.55). The solution is usually carried out iteratively because the 2-D aerofoil characteristics are non-linear functions of the angle of attack.

To determine the complete performance characteristic of a rotor, that is, the manner in which the power coefficient varies over a wide range of tip speed ratio, requires the iterative solution.

The iterative procedure is to assume a and a' to be zero initially, determining ϕ , C_l , and C_d on that basis, and then to calculate new values of the flow factors using Eqs. (3.54a or b) and (3.55). The iteration is repeated until convergence is achieved.

From Eq. (3.49), the torque developed by the blade elements of spanwise length δr is

$$\delta Q = 4\pi\rho U_\infty \Omega r a' (1 - a) r^2 \delta r$$

If drag, or part of the drag, has been excluded from the determination of the flow induction factors, then its effect must be introduced when the torque is calculated [see Eq. (3.49)]:

$$\delta Q = 4\pi\rho U_\infty \Omega r a' (1 - a) r^2 \delta r - \frac{1}{2} \rho W^2 B c C_d \cos \phi r \delta r$$

The complete rotor, therefore, develops a total torque Q :

$$Q = \frac{1}{2} \rho U_\infty^2 \pi R^3 \lambda \int_0^R \mu^2 \left(8a'(1-a)\mu - \frac{W}{U_\infty} \frac{B \frac{c}{R}}{\pi} C_d (1+a') \right) d\mu \quad (3.57)$$

The power developed by the rotor is $P = Q\Omega$

The power coefficient is, therefore, $C_P = \frac{P}{\frac{1}{2} \rho U_\infty^3 \pi R^2}$

Solving the blade element – momentum Eqs. (3.54a or b) and (3.55) for a given, suitable blade geometrical and aerodynamic design yields a series of values for the power and torque coefficients that are functions of the tip speed ratio. A typical performance curve for a modern, high-speed wind turbine is shown in Figure 3.15.

The maximum power coefficient occurs at a tip speed ratio for which the axial flow induction factor a , which in general varies with radius, approximates most closely to the Betz limit value of $\frac{1}{3}$. At lower tip speed ratios the axial flow induction factor can be much

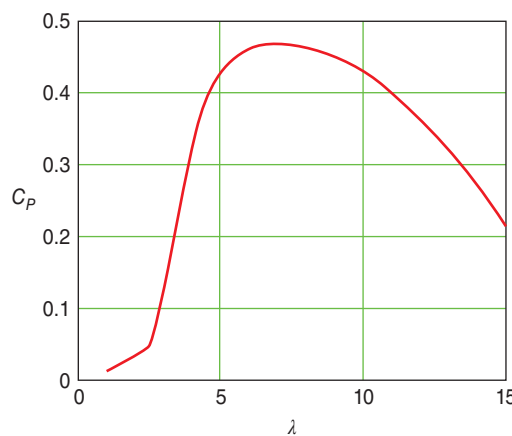


Figure 3.15 Power coefficient – tip speed ratio performance curve.

less than $\frac{1}{3}$ and aerofoil angles of attack are high, leading to stalled conditions. For most wind turbines stalling is more likely to occur at the blade root because, from practical constraints, the pitch angle β due to built-in twist of a blade is not large enough in that region. At low tip speed ratios blade stalling is the cause of a significant loss of power, as demonstrated in Figure 3.15. At high tip speed ratios a is high, angles of attack are low, and drag begins to predominate. At both high and low tip speed ratios, therefore, drag is high and the general level of a is non-optimum so the power coefficient is low. Clearly, it would be best if a turbine can be operated at all wind speeds at a tip speed ratio close to that which gives the maximum power coefficient.

3.6 Actuator line theory, including radial variation

Actuator line theory combines the 2-D blade sectional characteristics used in BEM theory with, usually, a CFD grid calculation of the whole flow field external to the rotor blades including the wake. It is particularly useful for calculating the aerodynamic loads and flow field quantities where wind turbine rotors operate within a larger complex flow field such as a wind farm or a non-simple ABL topography.

In this method, the outer flow is computed on a finite volume or element grid by some method of numerical simulation (usually viscous and turbulent) of the unsteady flow equations, such as unsteady Reynolds averaged Navier–Stokes (URANS) or LES (see discussion in Chapter 4). A number of open-source or commercial codes are available to do this with varying degrees of fidelity and cost. Because the computations are carried out over a sequence of timesteps and are spatially 3-D, this always requires significant computing resource. The discretisation scale should be appropriate to resolve the major structures of the ABL and its turbulence and the rotor (diameters) and the turbulent structures in their wakes. But it does not resolve the flows on the length scales of the blade chords and their boundary layers and hence is orders of magnitude faster than a complete simulation of all scales in the flow field.

Instead of resolving the sectional blade flows, these are replaced, as in BEM theory, by aerofoil characteristics from look-up tables (or possibly a fast panel method such as XFOIL; Drela 1989). The rotor blades are tracked through the outer flow grid and the velocity field, which has been computed on that grid, is interpolated onto the designated rotor blade sections. The resulting sectional blade forces obtained by interpolating from the blade characteristic look-up tables are projected back onto the outer grid as a series of momentum sinks for the components of force in the three coordinate directions. These sinks then form part of the grid flow field calculation at the next timestep. This coupling between the inner and outer flow calculations may be either loose going from timestep to timestep as indicated or may be a strong coupling in which the flow is converged within each timestep by iteration or by solving the whole in a single very large matrix. Transfer of force and large-scale velocities between the inner and outer flow fields is well established, but methods of determining the effective turbulence input from the smaller-scale structures in the rotor blade flows as sources for the larger-scale outer flow are not, and further work is required here. Good references for this method are Mikkelsen (2003) and Troldborg et al. (2006).

3.7 Breakdown of the momentum theory

3.7.1 Free-stream/wake mixing

For heavily loaded turbines, when a is high, the momentum theory predicts a reversal of the flow in the wake. Such a situation cannot actually apply uniformly throughout the far wake as predicted. What happens is that the wake becomes unstable with local flow reversal and breakdown into turbulence. This increases the mixing process, which entrains air from outside the wake, re-energising the slow moving air that has passed through the rotor.

A rotor operating at increasingly high tip speed ratios presents a decreasingly permeable disc to the flow. Eventually, when λ is high enough for the axial flow factor to be equal to one, the flow field of the disc would appear to have reached a condition like that of a normal solid disc, including the flow in the wake.

As this condition is approached, the flow through a rotor has many of the features of flow through a porous disc of low and decreasing permeability and hence a large increasing resistance to through-flow. The air that does pass through the rotor emerges into a low-pressure region and is moving slowly. There is insufficient kinetic energy to provide the rise in static pressure necessary to achieve the ambient atmospheric pressure that exists outside the wake and must exist in the wake far downstream. The air can only achieve this ambient pressure by gaining energy from mixing with the flow that has bypassed the rotor disc and is outside the wake. Castro (1971) has studied in detail the wake of a porous plate as the plate is made increasingly impermeable to flow. At a certain level of resistance, a counter-rotating vortex pair (in planar 2-D flow) or a ring vortex (in axisymmetric flow) forms downstream in the wake as a result of the instability of the wake shear. This vortex structure generates a growing region of reversed flow near the plane of symmetry or axis of the wake. As the resistance is increased further, the vortex structure and region of reversed flow moves upstream until it reaches the downstream face of the plate. Depending on the Reynolds number, but increasingly so for a high Reynolds number, the vortex structure develops further instability and the wake becomes turbulent, greatly increasing mixing with the external flow and recovery of kinetic energy. The wake of a rotor has some significant differences from that of a porous disc: in particular that the latter does not have the strong helical vortex structure present in the wake of a rotor. Nevertheless, the behaviour of the rotor wake as its resistance is increased is qualitatively very similar, although the point at which the ordered axial flow through a rotor reverses and breaks down into turbulence is not exactly the same as for a porous disc.

3.7.2 Modification of rotor thrust caused by wake breakdown

When flow reversal and breakdown into turbulence in the wake of a porous plate occurs, typically starting when the resistance coefficient K ($= \Delta p / (\frac{1}{2} \rho U^2)$) exceeds 4, experimental measurements show that the axial force on the body departs from the well-known theory of Taylor (1944) for ordered flow through a porous plate. Similarly, experimental measurements of the thrust force coefficient for a rotor – for example, reported by Glauert (1926) and plotted in Figure 3.16 – show a departure from the actuator disc momentum theory $C_T = 4a(1-a)$. In both cases the measured forces are larger than the predictions

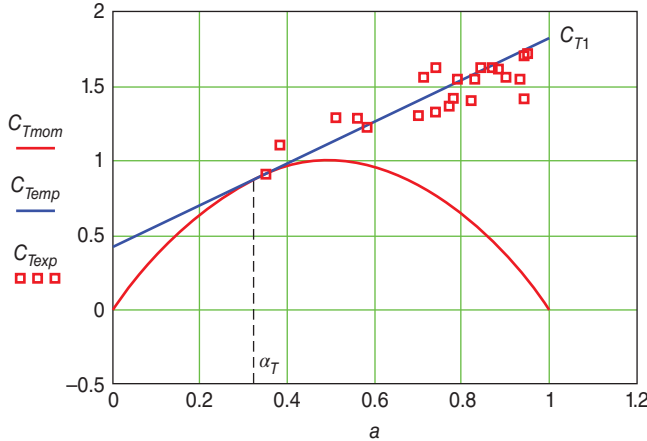


Figure 3.16 Comparison of theoretical and measured values of C_T .

of theory, and in both cases the point of break-away is near the maximum predicted by the momentum theory.

The thrust (or drag) coefficient for a simple, flat circular plate is given by Hoerner (1965) as 1.17 but, as demonstrated in Figure 3.16, the thrust on the rotor reaches a higher value. A major difference between the wake of the circular plate and of the rotor is that the latter contains a strong rotating component even after flow reversal in the wake has started.

It would follow from the above arguments that for high values of the axial induction factor a large part of the pressure drop across the disc is not simply associated with blade circulation, just as it is absent in the case of the circular plate. Circulation would cause a pressure drop similar to that given by the momentum theory determined by the very low axial velocity of the flow that actually permeates the disc.

3.7.3 Empirical determination of thrust coefficient

A suitable straight line through the experimental points would appear to be possible, although Glauert proposed a parabolic curve, and provides an empirical solution to the problem of the thrust on a heavily loaded turbine (a rotor operating at a high value of the axial flow induction factor).

Most authors assume that the entire thrust on the rotor disc is associated with axial momentum change. Therefore, for the empirical line to be useful it must be assumed that it applies not only to the whole rotor but also to each separate streamtube. Let C_{T1} be the empirical value of C_T when $a = 1$. Then, as the straight line must be a tangent to the momentum theory parabola at the transition point, the equation for the line is

$$C_T = C_{T1} - 4(\sqrt{C_{T1}} - 1)(1 - a) \quad (3.58)$$

and the value of a at the transition point is

$$a_T = 1 - \frac{1}{2}\sqrt{C_{T1}}$$

By inspection, C_{T1} must lie between 1.6 and 2: $C_{T1} = 1.816$ would appear to be the best fit to the experimental data of Figure 3.16, whereas Wilson et al. (1974) favour the lower value of $C_{T1} = 1.6$. Glauert fits a parabolic curve to the data [replacing a in the mass flow expression by $4a(1-a)/(0.6 + 0.61a + 0.79a^2)$ when $a > 1/3$] giving much higher values of C_{T1} at high values of a but he was considering the case of an *airscrew* in the windmill brake state where the angles of attack are negative. De Vaal et al. (2014) suggest a be replaced by $0.25a(5 - 3a)$, similarly giving a somewhat lower windmill brake state result.

The flow field through the turbine under heavily loaded conditions cannot be modelled easily, and the results of this empirical analysis must be regarded as being only approximate at best. They are, nevertheless, better than those predicted by the momentum theory. For most practical designs the value of the axial flow induction factor rarely exceeds 0.6 and for a well-designed rotor will be in the vicinity of 0.33 for much of its operational range.

For values of a greater than a_T , it is common to replace the momentum theory thrust in Eq. (3.9) with Eq. (3.58), in which case Eq. (3.1) is replaced by

$$(1-a)^2 \frac{\sigma_r}{\sin^2 \phi} C_x + 4(\sqrt{C_{T1}} - 1)(1-a) - C_{T1} = 0 \quad (3.59)$$

However, as the additional pressure drop is caused by breakdown of the streamline wake, this course of action is questionable, and it may be more appropriate to retain Eq. (3.54).

3.8 Blade geometry

3.8.1 Introduction

The purpose of most wind turbines is to extract as much energy from the wind as possible, and each component of the turbine has to be optimised for that goal. Optimal blade design is influenced by the mode of operation of the turbine, that is, fixed rotational speed or variable rotational speed and, ideally, the wind distribution at the intended site. In practice engineering compromises are made, but it is still necessary to know what would be the best design.

Optimising a blade design means maximising the power output, and so a suitable solution to BEM Eqs. (3.54 or (3.59) and (3.55)) is necessary.

3.8.2 Optimal design for variable-speed operation

A turbine operating at variable speed can maintain the constant tip speed ratio required for the maximum power coefficient to be developed regardless of wind speed. To develop the maximum possible power coefficient requires a suitable blade geometry, the conditions for which will now be derived.

For a chosen tip speed ratio λ the torque developed at each blade station is given by Eq. (3.49) and is maximised if

$$\frac{d}{da'} a'(1-a) = 0$$

giving

$$\frac{da}{da'} = \frac{1-a}{a'} \quad (3.60)$$

From Eqs. (3.51) and (3.52) a relationship between the flow induction factors can be obtained. Dividing Eq. (3.52) by the modified Eq. (3.51), modified to include the additional loss of axial momentum from the pressure drop term Δp_{d2} in the far wake due to the centrifugal swirl generated radial pressure gradient, leads to:

$$\frac{C_l/C_d \tan\phi - 1}{C_l/C_d + \tan\phi} = \frac{\lambda\mu a'(1-a)}{a(1-a) + (a'\lambda\mu)^2} \quad (3.61)$$

The flow angle ϕ is given by

$$\tan\phi = \frac{1-a}{\lambda\mu(1+a')} \quad (3.62)$$

Substituting Eq. (3.62) into Eq. (3.61) gives

$$\frac{C_l/C_d \frac{1-a}{\lambda\mu(1+a')} - 1}{C_l/C_d + \frac{1-a}{\lambda\mu(1+a')}} = \frac{\lambda\mu a'(1-a)}{a(1-a) + (a'\lambda\mu)^2}$$

Simplifying:

$$\begin{aligned} & [(1-a)C_L - \lambda\mu(1+a')C_D].[a(1-a) + (a'\lambda\mu)^2] \\ &= [\lambda\mu(1+a')C_L + (1-a)C_D]\lambda\mu a'(1-a) \end{aligned} \quad (3.63)$$

At this stage the process is made easier to follow if drag is ignored; Eq. (3.63) then reduces to

$$a(1-a) - \lambda^2\mu^2 a' = 0 \quad (3.64)$$

Differentiating Eq. (3.64) with respect to a' gives

$$(1-2a)\frac{da}{da'} - \lambda^2\mu^2 = 0 \quad (3.65)$$

and substituting Eq. (3.60) into (3.65)

$$(1-2a)(1-a) - \lambda^2\mu^2 a' = 0 \quad (3.66)$$

Equations (3.64, 3.66), together, give the flow induction factors for optimised operation:

$$a = \frac{1}{3} \text{ and } a' = \frac{a(1-a)}{\lambda^2\mu^2} \quad (3.67)$$

These are consistent at the rotor tip (where $\mu = 1$) with Eq. (3.2) provided a' is sufficiently small compared with unity for terms in a'^2 to be neglected. This is normally true at the rotor tip, and these results agree exactly with the momentum theory prediction, because no losses such as aerodynamic drag have been included, and the number of blades is assumed to be large. This last assumption means that every fluid particle that passes through the rotor disc interacts strongly with a blade, resulting in the axial velocity being more uniform over the area of the disc. If the same analysis is followed excluding the swirl pressure drop term, then $a = 1/3 - a$ small term $\sim 2/(9\lambda\mu)^2$, which is negligible except very close to the axis (blade root) or when the rotor tip speed ratio is very low.

To achieve the optimum conditions, the blade design has to be specific and can be determined from either of the fundamental Eqs. (3.48) and (3.49). Choosing Eq. (3.49),

because it is the simpler, ignoring the drag, and assuming $a' \ll 1$, the torque developed in optimised operation is

$$\delta Q = 4\pi\rho U_\infty \Omega r a' (1-a) r^2 \delta r = 4\pi\rho \frac{U_\infty^3}{\Omega} a (1-a)^2 r \delta r$$

The component of the lift per unit span in the tangential direction is therefore

$$L \sin \phi = 4\pi\rho \frac{U_\infty^3}{\Omega} a (1-a)^2$$

By the Kutta–Joukowski theorem the lift per unit span is

$$L = \rho W \Gamma$$

where Γ is the sum of the individual blade circulations and W is the component of incident velocity mutually perpendicular to both Γ and L .

It is important to note that where the incident velocity varies spatially, as here, W takes the value that would exist at the effective position of the bound vortex representing the local blade circulation excluding its own induced velocity.

Consequently,

$$\rho W \Gamma \sin \phi = \rho \Gamma U_\infty (1-a) = 4\pi\rho \frac{U_\infty^3}{\Omega} a (1-a)^2 \quad (3.68)$$

so

$$\Gamma = 4\pi \frac{U_\infty^2}{\Omega} a (1-a) \quad (3.69)$$

If, therefore, a is to take everywhere the optimum value (1/3), the circulation must be uniform along the blade span, and this is a condition for optimised operation.

To determine the blade geometry, that is, how should the chord size vary along the blade and what pitch angle β distribution is necessary, neglecting the effect of drag, we must return to Eq. (3.52) with C_D set to zero:

$$\frac{W^2}{U_\infty^2} B \frac{c}{R} C_l \sin \phi = 8\pi \lambda \mu^2 a' (1-a)$$

substituting for $\sin \phi$ gives

$$\frac{W}{U_\infty} B \frac{c}{R} C_l (1-a) = 8\pi \lambda \mu^2 a' (1-a) \quad (3.70)$$

The value of the lift coefficient C_l in the above equation is an input, and it is commonly included as above on the left side of Eq. (3.70) with a ‘chord solidity’ parameter representing blade geometry. The lift coefficient can be chosen as that value that corresponds to the maximum lift/drag ratio $\frac{C_l}{C_d}$, as this will minimise drag losses: even though drag has been ignored in the determination of the optimum flow induction factors and blade geometry, it cannot be ignored in the calculation of torque and power. Blade geometry

also depends upon the tip speed ratio λ , which is also an input. From Eq. (3.70) the blade geometry parameter can be expressed as

$$\frac{B}{2\pi} \frac{c}{R} = \frac{4\lambda\mu^2 a'}{\frac{w}{U_\infty} C_l}$$

Hence

$$\sigma_r \lambda \mu C_l = \frac{B}{2\pi} \frac{c}{R} \lambda C_l = \frac{4\lambda^2 \mu^2 a'}{\sqrt{(1-a)^2 + (\lambda\mu(1+a'))^2}} \quad (3.71)$$

Introducing the optimum conditions of Eq. (3.67),

$$\sigma_r \lambda \mu C_l = \frac{Bc}{2\pi R} \lambda C_l = \frac{\frac{8}{9}}{\sqrt{\left[1 - \frac{1}{3}\right]^2 + \lambda^2 \mu^2 \left[1 + \frac{2}{9\lambda^2 \mu^2}\right]^2}} \quad (3.72)$$

The parameter $\lambda\mu$ is the *local speed ratio* λ_r and is equal to the tip speed ratio where $\mu = 1$.

If, for a given design, C_l is held constant, then Figure 3.17 shows the blade plan-form for increasing tip speed ratio. A high design tip speed ratio would require a long, slender blade (high aspect ratio) whilst a low design tip speed ratio would need a short, fat blade. The design tip speed ratio is that at which optimum performance is achieved. Operating a rotor at other than the design tip speed ratio gives a less than optimum performance even in ideal drag-free conditions.

In off-optimum operation, the axial inflow factor is not uniformly equal to 1/3; in fact, it is not uniform at all.

The local inflow angle ϕ at each blade station also varies along the blade span, as shown in Eq. (3.73) and Figure 3.18:

$$\phi = \tan^{-1} \left\{ \frac{1-a}{\lambda\mu(1+a')} \right\} \quad (3.73)$$

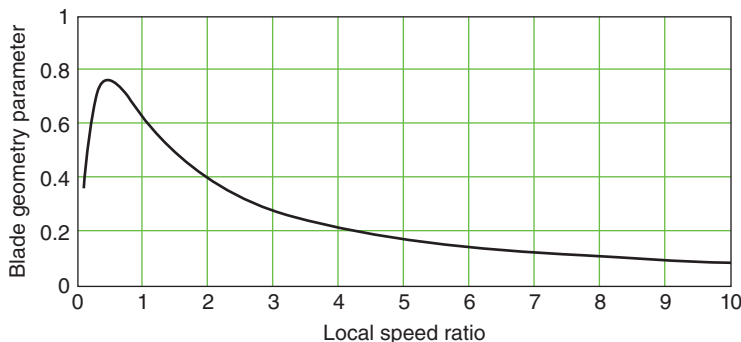


Figure 3.17 Variation of blade geometry parameter with local speed ratio.

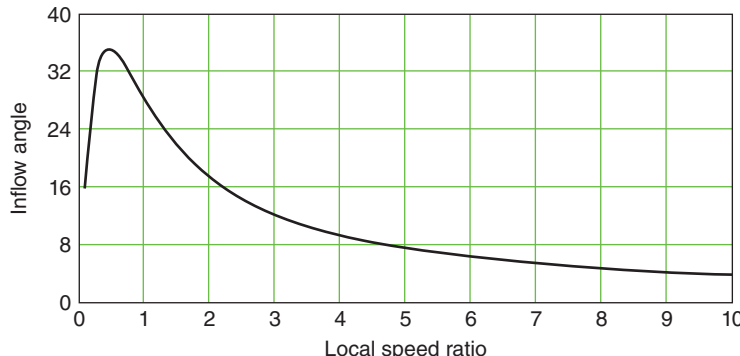


Figure 3.18 Variation of inflow angle with local speed ratio.

which, for optimum operation, is

$$\phi = \tan^{-1} \left\{ \frac{1 - \frac{1}{3}}{\lambda \mu \left(1 + \frac{2}{9\lambda^2 \mu^2} \right)} \right\} \quad (3.74)$$

Close to the blade root the inflow angle is large, which could cause the blade to stall in that region. If the lift coefficient is to be held constant such that drag is minimised everywhere, then the angle of attack α also needs to be uniform at the appropriate value. For a prescribed angle of attack variation, the design pitch angle $\beta = \phi - \alpha$ of the blade must vary accordingly.

As an example, suppose that the blade aerofoil is National Advisory Committee for Aeronautics (NACA) 4412, popular for hand-built wind turbines because the bottom (high-pressure) side of the profile is almost flat, which facilitates manufacture. At a Reynolds number of about $5 \cdot 10^5$, the maximum lift/drag ratio occurs at a lift coefficient of about 0.7 and an angle of attack of about 3° . Assuming that both C_l and α are to be held constant along each blade and there are to be three blades operating at a tip speed ratio of 6, then the blade design in pitch (twist) and plan-form variation are shown in Figures 3.19a and b, respectively. This blade solidity becomes very large at the root but can be accommodated to around $r/R = 0.1$ depending on the location of the blade axis.

3.8.3 A simple blade design

The blade design of Figure 3.19 is efficient but complex to build and therefore costly. Suppose the plan-form was prescribed to have a uniform taper such that the outer part of the blade corresponds closely to Figure 3.19b. The straight line given by Eq. (3.75) and shown as the solid line in Figure 3.20 has been derived to minimise the departure from the true curve [Eq. (3.72)] in the outer region $0.7 < r/R < 0.9$. This linear taper not only simplifies the plan-form but removes a lot of material close to the root.

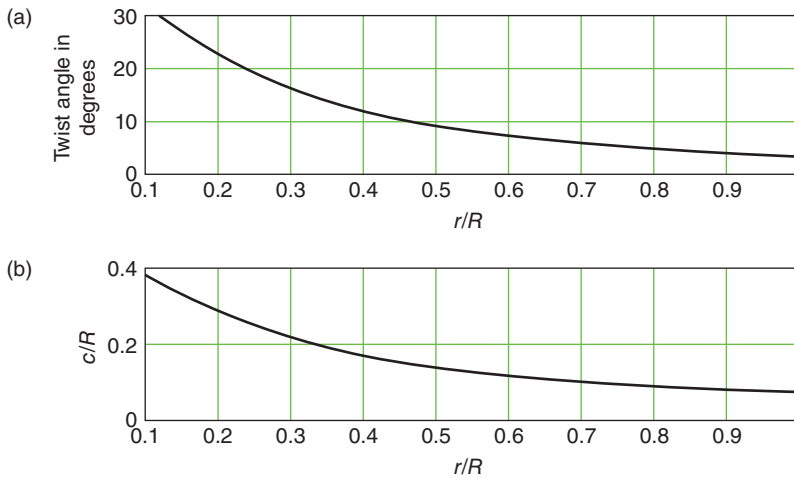


Figure 3.19 Optimum blade design for three blades and $\lambda = 6$: (a) blade twist distribution, and (b) blade plan-form.

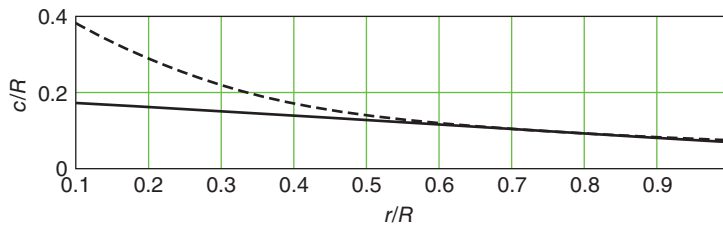


Figure 3.20 Uniform taper blade design for optimal operation.

The expression for this chord distribution approximation to the optimum plan-form (Figure 3.20) is

$$c_{lin} = \frac{8}{9 \cdot 0.8\lambda} \left(2 - \frac{\lambda\mu}{0.8\lambda} \right) \frac{2\pi R}{C_l \lambda B} \quad (3.75)$$

The 0.8 in Eq. (3.75) refers to the 80% point, approximating in this case the solid line between target points 0.7 and 0.9 by the tangent at 0.8, which is very close to it.

Equation (3.75) can then be combined with Eq. (3.72) to give the modified spanwise variation of C_l for optimal operation of the uniformly tapered blade (Figure 3.21):

$$C_l = \frac{8}{9} \frac{1}{\frac{B c_{lin} \lambda}{2\pi R} \sqrt{\left(1 - \frac{1}{3}\right)^2 + \lambda^2 \mu^2 \left(1 + \frac{2}{9\lambda^2 \mu^2}\right)^2}}$$

Close to the blade root the lift coefficient approaches the stalled condition and drag is high, but the penalty is small because the adverse torque is small in that region.

Assuming that stall does not occur, for the aerofoil in question, which has a 4% camber (this approximates to a zero lift angle of attack of -4°), the lift coefficient is given

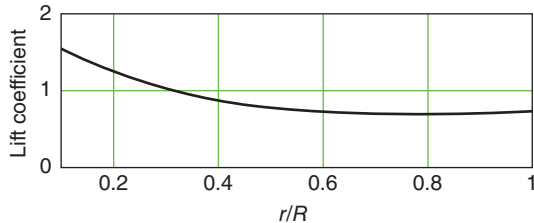


Figure 3.21 Spanwise distribution of the lift coefficient required for the linear taper blade.

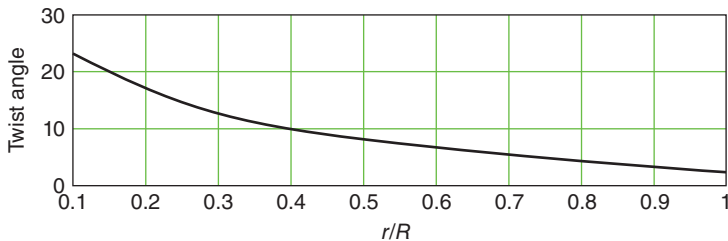


Figure 3.22 Spanwise distribution of the twist in degrees required for the linear taper blade.

approximately by

$$C_l = 0.1(\alpha + 4^\circ)$$

where α is in degrees and 0.1 is a good approximation to the gradient of the C_l vs α° for most aerofoils, so $\alpha = \frac{C_l}{0.1} - 4^\circ$.

The blade twist distribution can now be determined from Eqs. (3.74) and (3.45) and is shown in Figure 3.22.

The twist angle close to the root is still high but lower than for the constant C_l blade.

3.8.4 Effects of drag on optimal blade design

If, despite the views of Wilson et al. (1974) – see Section 3.5.3, the effects of drag are included in the determination of the flow induction factors, we must return to Eq. (3.48) and follow the same procedure as described for the drag-free case.

In the current context, the effects of drag are dependent upon the magnitude of the lift/drag ratio, which, in turn, depends on the aerofoil profile but largely on Reynolds number and on the surface roughness of the blade. A high value of lift/drag ratio would be about 150, whereas a low value would be about 40.

Unfortunately, with the inclusion of drag, the algebra of the analysis is complex. Polynomial equations have to be solved for both a and a' . The details of the analysis are left for the reader to discover.

In the presence of drag, the axial flow induction factor for optimal operation is not uniform over the disc because it is in the hypothetical drag-free situation. However, the

departure of the axial flow distribution from uniformity is not great, even when the lift/drag ratio is low, provided the flow around a blade remains attached.

The radial variation of the axial and tangential flow induction factors is shown in Figure 3.23 for zero drag and for a lift/drag ratio of 40. The tangential flow induction factor is lower in the presence of drag than without because the blade drags the fluid around in the direction of rotation, opposing the general rotational reaction to the shaft torque.

From the torque/angular momentum Eq. (3.52), the blade geometry parameter becomes

$$\frac{Bc\lambda}{2\pi R} C_l = \frac{4\lambda^2 \mu^2 a'(1-a)}{\frac{W}{U_\infty} \left[(1-a) - \frac{C_d}{C_l} \lambda \mu (1+a') \right]} \quad (3.76)$$

Figure 3.24 compares the blade geometry parameter distributions for zero drag and a lift/drag ratio of 40, and, as is evident, drag has very little effect on blade optimal design.

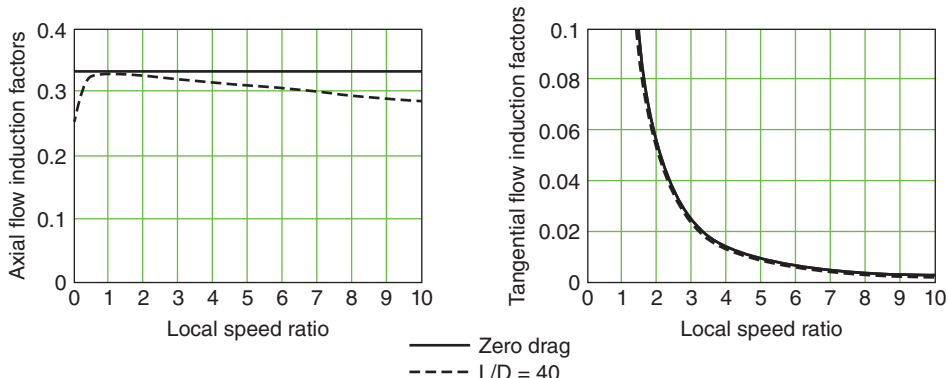


Figure 3.23 Radial variation of the flow induction factors with and without drag.

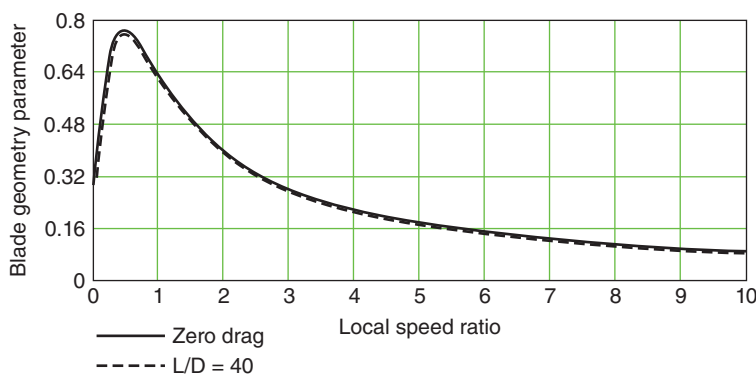


Figure 3.24 Spanwise variation of the blade geometry parameter with and without drag.

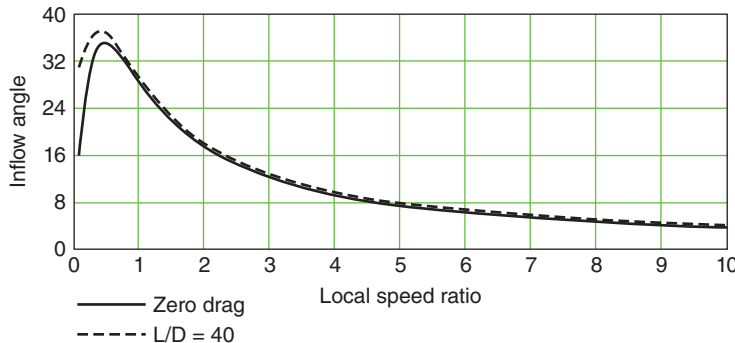


Figure 3.25 Variation of inflow angle with local speed ratio with and without drag.

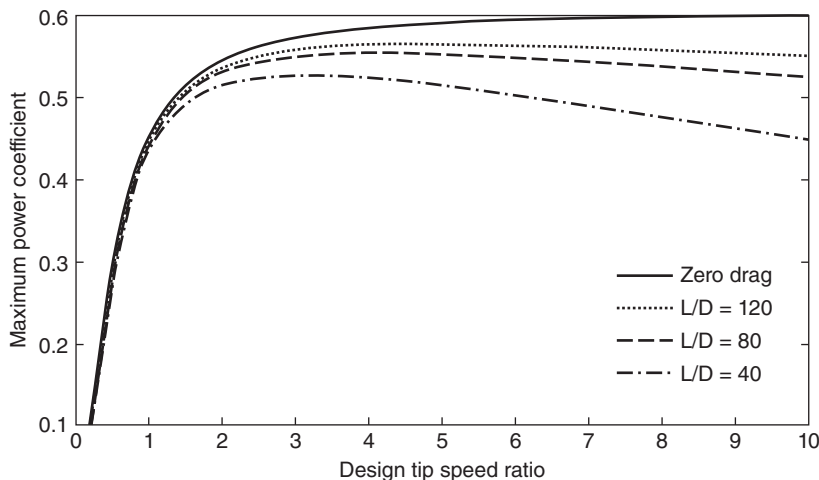


Figure 3.26 The variation of maximum C_P with design λ for various lift/drag ratios.

A similar result is apparent for the inflow angle distribution (Figure 3.25), in which drag is also seen to have little influence.

As far as blade design for optimal operation is concerned, drag can be ignored, greatly simplifying the process.

The results of Eq. (3.57) show that the maximum power coefficients for a range of design tip speed ratios and several lift/drag ratios are as shown in Figure 3.26. The flow induction factors have been determined without drag using Eqs. (3.54a) and (3.55), but the torque has been calculated using Eq. (3.57), which includes drag. The losses caused by drag are significant and increase with increasing design tip speed ratio. As will be shown later, when tip-losses are also taken into account, the losses at low tip speed ratios are even greater.

3.8.5 Optimal blade design for constant-speed operation

If the rotational speed of a turbine is maintained at a constant level, then the tip speed ratio is continuously changing, and a blade optimised for a fixed tip speed ratio would not be appropriate. Closed-form solutions have been derived for optimum wind turbines; see Peters and Modarres (2013) and Jamieson (2018).

No simple technique is available for the optimal design of a blade operating at constant rotational speed. Non-linear (numerical) optimisation techniques may be used to solve the problem of maximising energy capture at a given site incorporating the data on its specific wind speed distribution. Alternatively, a design tip speed ratio can be chosen corresponding to the wind speed at the specified site that contains the most energy, or, more practically, the pitch angle for the whole blade can be adjusted to maximise energy capture.

3.9 The effects of a discrete number of blades

3.9.1 Introduction

The analysis described in all prior sections assumes that the rotor has an infinite number of blades of infinitesimal chord so that every fluid particle passing through the rotor disc passes close to a blade through a region of strong interaction, i.e. that the loss of momentum in any annulus is uniform with respect to azimuth angle θ . With a finite (usually small, two or three) number of blades, some fluid particles will interact more strongly with the blades and some less strongly. The immediate loss of (kinetic) momentum by a particle will depend on the distance between its streamline and the blade as the particle passes through the rotor disc. These differences are subsequently reduced but not eliminated by the action of pressure forces between the adjacent curved streamlines and eventually by mixing. The axial induced velocity will therefore vary around the disc, the average value determining the overall axial momentum of the flow. What is also relevant is the incident velocity (relative angle and speed) that each blade section senses, i.e. to which it responds, as it rotates. When as here the incident flow is not uniform, a blade section senses a weighted average of the flow induced in the region occupied by the section in the absence of its own self-generated flow field. This is usually evaluated as the velocity at the quarter chord of the section (cf. lifting line theory). For a rotor for which the product $\sigma\lambda$ of solidity and tip speed ratio is not too small, as is usual, it is found that the combination of incident wind, average axial induced velocity, and blade rotation speed gives a very good approximation to this incident velocity except close to the tip and root ends of the blade, where the sectional approximation breaks down.

3.9.2 Tip-losses

Where the axial flow induction factor a becomes large at the blade position, then, by Eqs. (3.44), the inflow angle ϕ will reduce, and for a given pitch angle the angle of attack α and hence the lift force will become small. At the tip the lift force must decrease to zero because the blade surface pressures must be continuous around the tip. The component of the lift force in the tangential direction in the tip region will therefore be small and

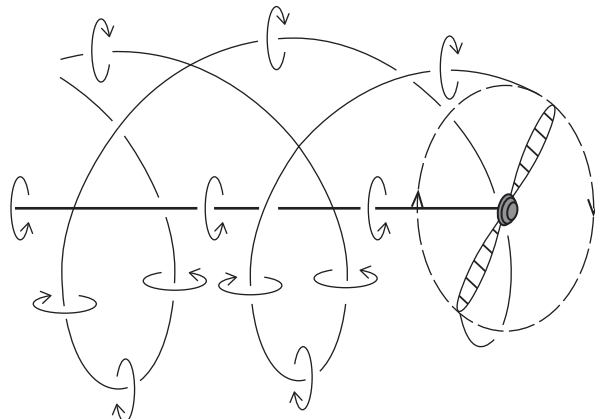


Figure 3.27 Helical trailing tip vortices of a horizontal axis turbine wake.

so will be its contribution to the torque. A reduced torque means reduced power, and this reduction is known as *tip-loss* because the effect occurs at the outermost parts of the blades. A similar effect occurs for the same reason at the blade root but being at small radius has much less effect on torque and power.

To account for tip-losses, the manner in which the axial flow induction factor varies azimuthally needs to be known, but, unfortunately, this requirement is beyond the abilities of the BEM theory.

Just as a vortex trails from the tip of an aircraft wing so does a vortex trail from the tip of a wind turbine blade. Because the blade tip follows a circular path, it leaves a trailing vortex as a helical structure that convects downstream with the wake velocity. For example, on a two blade rotor, unlike an aircraft wing, the bound circulations on the two blades shown in Figure 3.27 are opposite in sign and so combine in the idealised case of the blade root being at the rotational axis to shed a straight line vortex along the axis with strength equal to the blade circulation times the number of blades. If as is usual in practice the blade root is somewhat outboard of the axis, the two blade root vortices form independent helices similar to the blade tips but of small radius, close together, and the combined straight line axis vortex is not a bad approximation of their effect.

For a single vortex to be shed from the blade at its tip, only the circulation strength along the blade span must be uniform right out to the tip with an abrupt drop to zero at the tip. As has been shown, such a uniform circulation provides optimum power coefficient. However, the uniform circulation requirement assumes that the axial flow induction factor is uniform across the disc. With an infinite number of blades, the tip vortices form a continuous cylindrical sheet of vorticity directed at a constant angle around the surface. Such a sheet is consistent with a uniform value of the axial induction factor over the disc. But, as has been argued above, with a finite number of blades rather than a uniform disc, the flow factor is not uniform. Sustaining uniform circulation until very close to the two ends (tip and root) of a blade results in a very large gradient of the blade circulation at the tips, which in turn induces large radial variations in the induced velocity factors a and a' in those regions, with both tending to infinity in the limit of constant circulation up to the tip and root.

As in Figure 3.27, close to a blade tip a single concentrated tip vortex would on its own cause very high values of the flow factor a with an infinite value at the tip such that, locally, the net flow past the blade is in the upstream direction. This effect is similar to what occurs for the simple ‘horseshoe vortex’ model for a fixed wing aircraft showing that this model is not applicable at a blade or wing tip where a more detailed induced flow analysis is required. The azimuthal average of the axial induction a is uniform radially. Higher values of a tend to be induced close to the blades towards root and tip, becoming higher the closer to the tips. Therefore, low values relative to the average must occur in the regions between the blades. The azimuthal variation of a for a number of radial positions is shown in Figure 3.28 for a three blade rotor operating at a tip speed ratio of 6. The calculation for Figure 3.28 assumes a discrete vortex for each blade with a constant pitch and constant radius helix and is calculated from the effect of the shed wake vortices only.

At a particular radial position the ratio of the azimuthal average of a (which from here on will be written as \bar{a}) to the value $a_b(r)$ at the blade quarter chord is shown in Figure 3.29, being unity for most of the blade span, and only near the tip does it begin to fall to zero. This ratio is called the *tip-loss factor*.

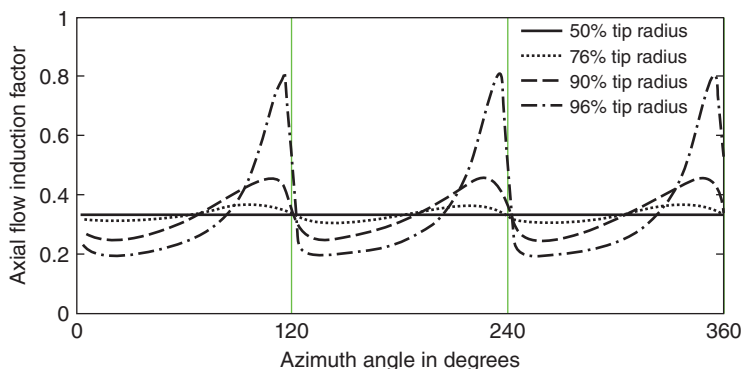


Figure 3.28 Azimuthal variation of a for various radial positions for a three blade rotor with uniform blade circulation operating at a tip speed ratio of 6. The blades are at 120°, 240°, and 360°.

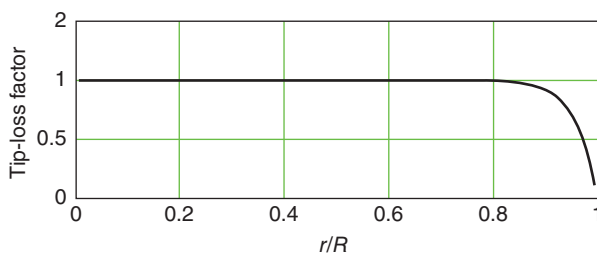


Figure 3.29 Spanwise variation of the tip-loss factor for a blade with uniform circulation.

From Eq. (3.20) and in the absence of tip-loss and drag the contribution of each blade element to the overall power coefficient is

$$\delta C_P = 8\lambda^2 \mu^3 a'(1-a)\delta\mu \quad (3.77)$$

Substituting for a' from Eq. (3.25) gives

$$\delta C_P = 8\mu a(1-a)^2 \delta\mu \quad (3.78)$$

From the Kutta–Joukowski theorem, the circulation Γ on the blade, which is uniform, provides a torque per unit span of

$$\frac{dQ}{dr} = \rho |W \times \Gamma| \sin \phi_r r$$

where the angle ϕ_r is determined by the flow velocity local to the blade.

If the strength of the total circulation for all three blades is still given by Eq. (3.69), in the presence of tip-loss, the increment of power coefficient from a blade element is

$$\delta C_P = 8\mu a(1-a)(1-a_b)\delta\mu \quad (3.79)$$

in agreement with Eq. (3.78), except that the factor $a(1-a)$, which relates Γ to the angular momentum loss in the wake, must be expressed as $\bar{a}(1-\bar{a})$ in terms of the azimuthally averaged axial flow induction factor \bar{a} , which = 1/3 for optimum operation. However, the final induction term $(1-a_b)$ relates to the flow angle at the blade and must therefore be in terms of a_b , the axial induction factor at the blade, with $a_b = \bar{a}/f$, and therefore $a_b \approx \bar{a}$ except near the tips. The notation \bar{a}, a_b, \bar{a}' , and a'_b defined as here will be used in this section where required to distinguish them.

The high value of the axial flow induction factor a_b at the tip, due to the proximity of the tip vortex, acts to reduce the angle of attack in the tip region and hence the circulation so that the circulation strength $\Gamma(r)$ cannot be constant right out to the tip but must fall smoothly through the tip region to zero at the tip. Thus, the loading falls smoothly to zero at the tip, as it must for the same reason as on a fixed wing, and this is a manifestation of the effect of tip-loss on loading. The result of the continuous fall-off of circulation towards the tip means that the vortex shedding from the tip region that is equal to the radial gradient of the bound circulation is not shed as a single concentrated helical line vortex but as a distributed ribbon of vorticity that then follows a helical path. The effect of the distributed vortex shedding from the tip region is to remove the infinite induction velocity at the tip, and, through the closed loop between shed vorticity, induction velocity and circulation, converge to a finite induction velocity together with a smooth reduction in loading to zero at the tip. The effect on the loading is incorporated into the BEM method, which treats all sections as independent ‘2-D’ flows, by multiplying a suitably calculated tip-loss factor $f(r)$ by the axial and rotational induction factors a_b and a'_b that have been calculated by the uncorrected BEM method. Because the blade circulation must similarly fall to zero at the root of the blade, a similar ‘tip-loss’ factor is applied there in the same way.

It is important to note that tip-loss factors should only be applied in methods that assume disc-type actuators (i.e. azimuthally uniform), such as the BEM method, and

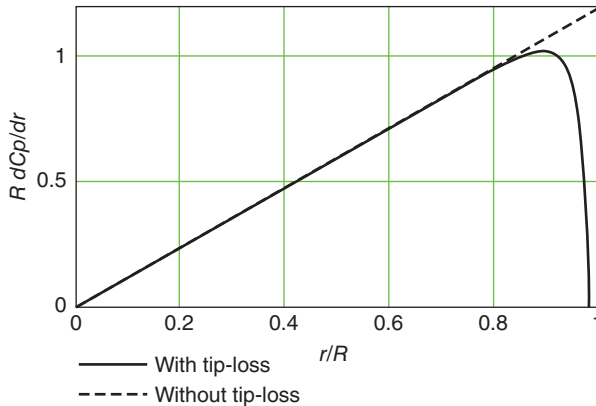


Figure 3.30 Spanwise variation of power extraction in the presence of tip-loss for a blade with uniform circulation on a three blade turbine operating at a tip speed ratio of 6.

not, for example, to the line actuator method because methods such as this that compute individual blades and the velocities induced at them already incorporate the tip effect.

The results from Eq. (3.79) with and without this tip-loss factor are plotted in Figure 3.30 and clearly show the effect of tip-loss on power. Equation (3.78)) has assumed that $\bar{a} = 1/3$ uniformly over the whole disc, but applying the tip-loss factor means recognising that \bar{a} cannot be uniform radially. The tip-loss results from the tip vortices, which generate the induction factor a (effectively the induced drag). It is important to note that there is no additional effective drag associated with tip-loss.

If the circulation varies along the blade span, vorticity is shed into the wake in a continuous fashion from the trailing edge of all sections where the spanwise (radial) gradient of circulation is non-zero.

Therefore, each blade sheds a helicoidal sheet of vorticity, as shown in Figure 3.31, rather than a single helical vortex, as shown in Figure 3.27. The helicoidal sheets convect with the wake velocity and so there can be no flow across the sheets, which can therefore be regarded as impermeable. The intensity of the vortex sheets is equal to the rate of change of bound circulation along the blade span and so usually increases rapidly towards the blade tips. There is flow around the blade tips because of the pressure difference between the blade surfaces, which means that on the upwind surface of the blades the flow moves towards the tips and on the downwind surface the flow moves towards the root. The flows from either surface leaving the trailing edge of a blade will not be parallel to one another and will form a surface of discontinuity of velocity in a radial sense within the wake; the axial velocity components will be equal. The surface of discontinuity is called a *vortex sheet*. A similar phenomenon occurs with aircraft wings, and a textbook of aircraft aerodynamics will explain it in greater detail.

The azimuthally averaged value of \bar{a} can be expressed as $a_b(r)f(r)$, where $f(r)$ is known as the *tip-loss factor*, has a value of unity inboard, and falls to zero at the edge of the rotor disc.

In the application of the BEM theory, it is argued that the rate of change of axial momentum is determined by the azimuthally averaged value of the axial flow induction

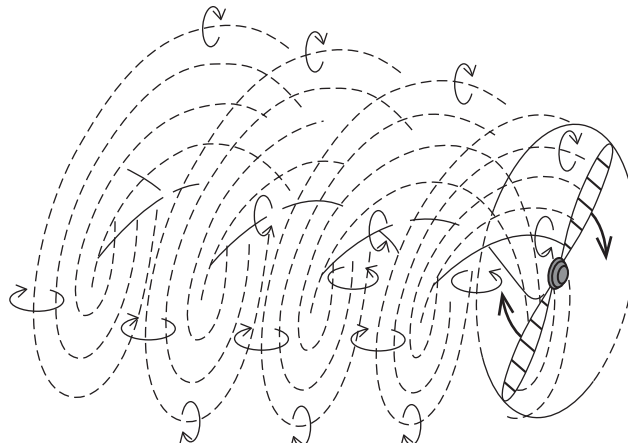


Figure 3.31 A (discretised) helicoidal vortex sheet wake for a two bladed rotor whose blades have radially varying circulation.

factor, whereas the blade forces are determined by the value of the flow factor that the blade element ‘senses’. This needs careful interpretation, as discussed in Section 3.9.2.

The mass flow rate through an annulus = $\rho U_\infty (1 - \bar{a}(r)).2\pi r \delta r$.

The azimuthally averaged overall change of axial velocity = $2\bar{a}(r).U_\infty$.

The rate of change of axial momentum = $4\pi\rho U_\infty^2 (1 - \bar{a}(r)).\bar{a}(r)\delta r$.

The blade element forces are $\frac{1}{2}\rho W^2 B c C_l$ and $\frac{1}{2}\rho W^2 B c C_d$, where W and C_l are determined using $a_b(r)$.

The torque caused by the rotation of the wake is also calculated using an azimuthally averaged value of the tangential flow induction factor $2\bar{a}'(r)$ with tip-loss similarly applied for the value at a blade because both induction velocities are induced by the same distribution of shed vorticity.

3.9.3 Prandtl's approximation for the tip-loss factor

The function for the tip-loss factor $f(r)$ is shown in Figure 3.29 for a blade with uniform circulation operating at a tip speed ratio of 6 and is not readily obtained by analytical means for any desired tip speed ratio. Sidney Goldstein (1929) did analyse the tip-loss problem for application to propellers and achieved a solution in terms of Bessel functions, but neither that nor the vortex method with the Biot–Savart solution used above is suitable for inclusion in the BEM theory. Fortunately, in 1919, Ludwig Prandtl, reported by Betz (1919), had already developed an ingenious approximate solution that does yield a relatively simple analytical formula for the tip-loss function.

Prandtl's approximation was inspired by considering that the vortex sheets could be replaced by material sheets, which, provided they move with the velocity dictated by the wake, would have no effect upon the wake flow. The theory applies only to the developed wake. To simplify his analysis Prandtl replaced the helicoidal sheets with a succession of discs, moving with the uniform, central wake velocity $U_\infty(1 - a)$ and separated by the same distance as the normal distance between the vortex sheets. Conceptually, the discs,

travelling axially with velocity $U_\infty(1 - \bar{a})$, would encounter the unattenuated free-stream velocity U_∞ at their outer edges. The fast flowing free-stream air would tend to weave in and out between successive discs. The wider apart successive discs the deeper, radially, the free-stream air would penetrate. Taking any line parallel to the rotor axis at a radius r , somewhat smaller than the wake radius R_w (\sim rotor radius R), the average axial velocity along that line would be greater than $U_\infty(1 - \bar{a})$ and less than U_∞ . Let the average velocity be $U_\infty(1 - af(r))$, where $f(r)$ is the tip-loss function, has a value less than unity and falls to zero at the wake boundary. At a distance from the wake edge the free stream fails to penetrate, and there is little or no difference between the wake-induced velocity and the velocity of the discs, i.e. $f(r) = 1$.

A particle path, as shown in Figure 3.32, may be interpreted as an *average* particle passing through the rotor disc at a given radius in the actual situation: the azimuthal variations of particle axial velocities at various radii are shown in Figure 3.28, and a ‘Prandtl particle’ would have a velocity equal to the azimuthal average of each. Figure 3.32 depicts the wake model.

The mathematical detail of Prandtl’s analysis is given in Glauert (1935a), and because it is based on a somewhat strangely simplified model of the wake will not be repeated here. It has, however, remained the most commonly used tip-loss correction because it is reasonably accurate and, unlike Goldstein’s theory, the result can be expressed in closed solution form. The Prandtl tip-loss factor is given by

$$f(r) = \frac{2}{\pi} \cos^{-1} \left\{ e^{-\pi \left(\frac{R_w - r}{d} \right)} \right\} \quad (3.80)$$

$R_w - r$ is a distance measured from the wake edge. Distance d between the discs should be that of the distance travelled by the flow between successive vortex sheets. Glauert (1935a), takes d as being the normal distance between successive helicoidal vortex sheets.

The helix angle of the vortex sheets ϕ_s is the flow angle assumed to be the same as ϕ_t , the helix angle at the blade tip, and so with B sheets intertwining from B blades and assuming that the discs move with the mean axial velocity in the wake, $U_\infty(1 - \bar{a})$:

$$d = \frac{2\pi R_w}{B} \sin \phi_s = \frac{2\pi R_w}{B} \frac{U_\infty(1 - \bar{a})}{W_s} \quad (3.81)$$

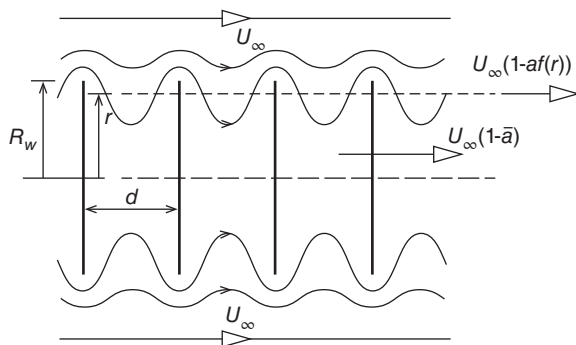


Figure 3.32 Prandtl’s wake-disc model to account for tip-losses.

Prandtl's model has no wake rotation, but whether the discs are considered to spin is irrelevant to the flow field, as it is inviscid, thus α' is zero and W_s is the resultant velocity (not including the radial velocity) at the edge of a disc. Glauert (1935a) argues that $\frac{R_w}{W_s} \approx \frac{r}{W}$, which is more convenient to use,

$$W = \sqrt{[U_\infty(1 - \bar{a})]^2 + (r\Omega)^2}$$

so

$$\pi \left(\frac{R-r}{d} \right) = \frac{B}{2} \left(\frac{R_w - r}{r} \right) \sqrt{1 + \frac{(r\Omega)^2}{[U_\infty(1 - \bar{a})]^2}}$$

and

$$f(\mu) = \frac{2}{\pi} \cos^{-1} \left\{ \exp \left[-\frac{B(1-\mu)}{2\mu} \sqrt{1 + \left(\frac{\lambda\mu}{1-\bar{a}} \right)^2} \right] \right\} \quad (3.82)$$

Although the physical basis of this model is not correct, it does quite effectively represent a convenient approximation to the attenuation towards the tips of the real velocities induced by the helicoidal vortex sheets.

The Prandtl tip-loss factor for a three blade rotor operating at a tip speed ratio of 6 is compared with the tip-loss factor of the helical vortex wake in Figure 3.33.

It should also be pointed out that the vortex theory of Figure 3.28 also predicts that the tip-loss factor should be applied to the tangential flow induction factor.

It is now useful to know what the variation of circulation along the blade is. For the previous analysis, which disregarded tip-losses, the blade circulation was uniform [Eq. (3.69)].

Following the same procedure from which Eq. (3.68) was developed:

$$\rho WT \sin\phi = \rho \Gamma U_\infty (1 - a_b(r)) = 4\pi \rho \frac{U_\infty^3}{\Omega} \bar{a}(r) (1 - \bar{a}(r)) (1 - a_b(r))$$

Recall that $a_b(r)$ is the flow factor local to the blade at radius r and $\bar{a}(r)$ is the average value of the flow factor at radius r .

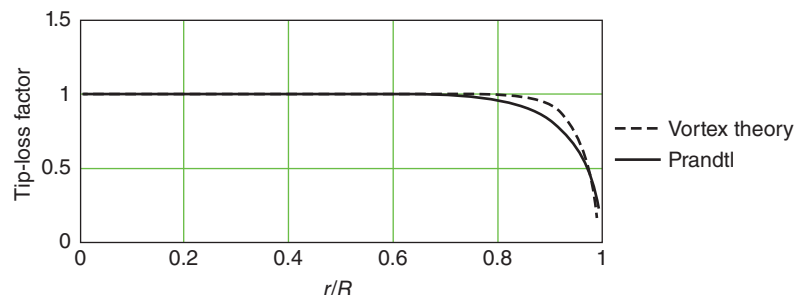


Figure 3.33 Comparison of Prandtl tip-loss factor with that predicted by a vortex theory for a three blade turbine optimised for a tip speed ratio of 6.

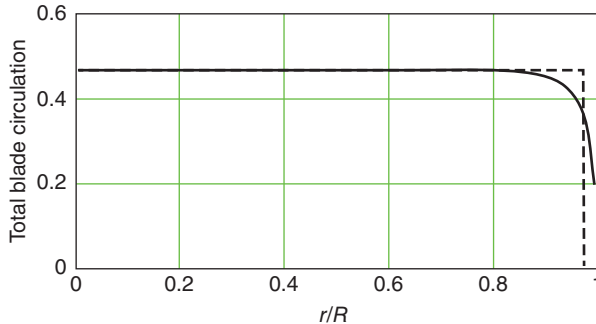


Figure 3.34 Spanwise variation of blade circulation for a three blade turbine optimised for a tip speed ratio of 6.

Therefore,

$$\frac{\Gamma(r)}{U_\infty R} = \frac{4\pi}{\lambda(1 - a_b(r))} \bar{a}(r)(1 - \bar{a}(r))(1 - a_b(r)) \quad (3.83)$$

$\Gamma(r)$ is the total circulation for all blades and is shown in Figure 3.34, and, as can be seen, it is almost uniform except near to the tip. The dashed vertical line shows the effective blade length (radius) $R_{ef} = 0.975$ if the circulation is assumed to be uniform at the level that pertains at the blade sections away from the tip.

The Prandtl tip-loss factor that is widely used in industry codes appears to offer an acceptable, simple solution to a complex problem; not only does it account for the effects of discrete blades, it also allows the induction factors to fall to zero at the edge of the rotor disc.

A more recently derived tip-loss factor that has been calibrated against experimental data and appears to give improved performance was given by Shen et al. (2005). The spanwise distribution of axial and tangential forces is multiplied by the factor

$$F_1(r) = \frac{2}{\pi} \cos^{-1} \left\{ \exp \left(-g_1 \frac{B(R-r)}{2rs \sin(\phi(r))} \right) \right\} \text{ where } g_1 = 0.1 + \exp \left\{ -c_1(B\lambda - c_2) \right\} \text{ with } c_1 = 0.125 \text{ and } c_2 = 21.0.$$

This formulation is similar to Glauert's (1935a) original simplification of the Prandtl tip-loss correction but introduces a variable factor g_1 rather than unity. Wimshurst and Willden (2018) suggest that a better fit is given in the above by using different constants for the axial force correction ($c_1 \sim 0.122$ and $c_2 \sim 21.5$) and for the tangential force correction to be similarly defined but with ($c_1 \sim 0.1$ and $c_2 \sim 13.0$).

3.9.4 Blade root losses

At the root of a blade the circulation must fall to zero as it does at the blade tip, and so it can be presumed that a similar process occurs. The blade root will be at some distance from the rotor axis, and the air flow through the disc inside the blade root radius will be at the free-stream velocity. Actually, the vortex theory of Section 3.4 can be extended to show that the flow through the root disc is somewhat higher than the free-stream velocity. It is usual, therefore, to apply the Prandtl tip-loss function at the blade root as well as at the tip (see Figure 3.35).

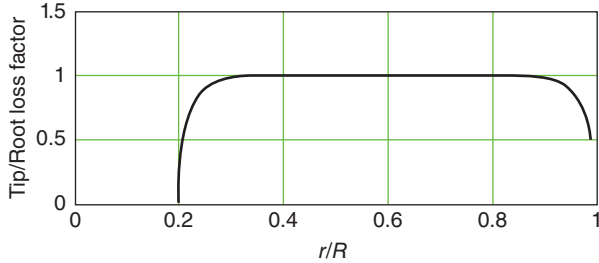


Figure 3.35 Spanwise variation of combined tip/root loss factor for a three blade turbine optimised for a tip speed ratio of 6 and with a blade root at 20% span.

If μ_R is the normalised root radius, then the root loss factor can be determined by modifying the tip-loss factor of Eq. (3.82):

$$f_R(\mu) = \frac{2}{\pi} \cos^{-1} \left\{ e^{-\frac{B(\mu-\mu_R)}{2\mu}} \sqrt{1 + \frac{(\lambda\mu)^2}{(1-\bar{a})^2}} \right\} \quad (3.84)$$

If Eq. (3.82) is now termed $f_T(r)$ the complete tip/root loss factor is

$$f(\mu) = f_T(\mu)f_R(\mu) \quad (3.85)$$

3.9.5 Effect of tip-loss on optimum blade design and power

With no tip-loss the optimum axial flow induction factor is uniformly 1/3 over the whole swept rotor. The presence of tip-loss changes the optimum value of the average value of a , which reduces to zero at the edge of the wake but local to the blade tends to increase in the tip region.

For the analysis involving induction factors from here on in this chapter, only the azimuthal averages and the local values at the blade are required so it is convenient to use $a(r)$ and $a'(r)$ to mean *azimuthal averages* at radius r with $a_b = \frac{a(r)}{f(r)}$ and $a'_b = \frac{a'(r)}{f(r)}$ for the local values at the blade, thus avoiding the need for the overbar and subscript b notation in the algebraic expressions. The inflow angle ϕ at the blade is from Eq. (3.62):

$$\tan \phi = \frac{1}{\lambda\mu} \left(\frac{1 - \frac{a}{f}}{1 + \frac{a'}{f}} \right) \quad (3.86)$$

but Eq. (3.61) derives $\tan \phi$ from the ratio of the non-dimensional rate of change of angular momentum to the non-dimensional rate of change of axial momentum, which is not changed because it deals with the average flow through the disc and so uses average values. If drag is ignored for the present, Eq. (3.62) becomes

$$\tan \phi = \frac{\lambda\mu a'(1-a)}{a(1-a) + (a'\lambda\mu)^2} \quad (3.87)$$

Hence

$$\frac{(1-a)\lambda\mu a'}{a(1-a)+(a'\lambda\mu)^2} = \frac{\left(1-\frac{a}{f}\right)}{\lambda\mu\left(1+\frac{a'}{f}\right)}$$

which becomes

$$\lambda^2\mu^2\frac{(f-1)}{f}a'^2 - \lambda^2\mu^2(1-a)a' + a(1-a)\left(1-\frac{a}{f}\right) = 0 \quad (3.88)$$

A great simplification can be made to Eq. (3.88) by ignoring the first term because, clearly, it disappears for much of the blade, where $f = 1$, and for the tip region the value of a'^2 is very small. For tip speed ratios greater than 3, neglecting the first term makes negligible difference to the result:

$$\lambda^2\mu^2a' = a\left(1-\frac{a}{f}\right) \quad (3.89)$$

As before, Eq. (3.60) still applies, $\frac{da}{da'} = \frac{1-a}{a'}$

$$\text{From Eq. (3.89), } \frac{da'}{da} = \frac{1}{\lambda^2\mu^2}\left(1-2\frac{a}{f}\right)$$

Consequently,

$$(1-a)\left(1-2\frac{a}{f}\right) = \lambda^2\mu^2a'$$

which, combined with Eq. (3.89), gives

$$a^2 - \frac{2}{3}(f+1)a + \frac{1}{3}f = 0$$

so

$$a = \frac{1}{3} + \frac{1}{3}f - \frac{1}{3}\sqrt{1-f+f^2} \quad (3.90)$$

The radial variation of the average value of a , as given by Eq. (3.90), and the value local to the blade $\frac{a}{f}$ is shown in Figure 3.36. An exact solution would also have the local induced velocity falling to zero at the blade tip.

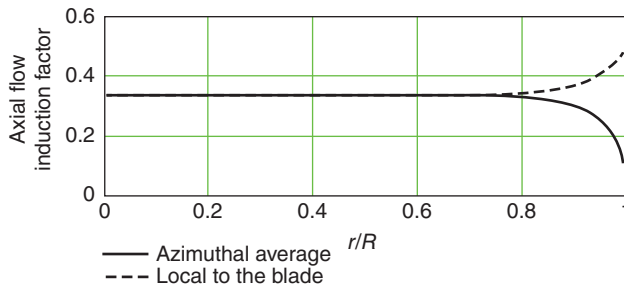


Figure 3.36 Axial flow factor variation with radius for a three blade turbine optimised for a tip speed ratio of 6.

Clearly, the required blade design for optimal operation would be a little different to that which corresponds to the Prandtl tip-loss factor because $a_b = \frac{a}{f}$; the local flow factor does not fall to zero at the blade tip. The use of the Prandtl tip-loss factor leads to an approximation, but that was recognised from the outset.

The blade design, which gives optimum power output, can now be determined by adapting Eqs. (3.70) and (3.71), noting that the left hand side of Eq. (3.70) refers to a local inflow angle at the blade, hence the factor becomes $(1 - a/f)$:

$$\mu\sigma_r\lambda C_l = \frac{4\lambda^2\mu^2 a'}{\sqrt{\left(1 - \frac{a}{f}\right)^2 + \left[\lambda\mu\left(1 + \frac{a'}{f}\right)\right]^2}} \left(\frac{1-a}{1-\frac{a}{f}}\right)$$

Introducing Eq. (3.89) gives

$$\mu\sigma_r\lambda C_l = \frac{4a(1-a)/\mu}{\sqrt{\left(1 - \frac{a}{f}\right)^2 + \left[\lambda\mu\left(1 + \frac{a(1-\frac{a}{f})}{\lambda^2\mu^2 f}\right)\right]^2}} \quad (3.91)$$

The blade geometry parameter given by Eq. (3.91) is shown in Figure 3.37 compared with the design that excludes tip-loss. As shown, only in the tip region is there any difference between the two designs.

Similarly, the inflow angle distribution, shown in Figure 3.38, can be determined by suitably modifying Eq. (3.73):

$$\tan \phi = \frac{1 - \frac{a}{f}}{\lambda\mu\left(1 + \frac{a(1-\frac{a}{f})}{\lambda^2\mu^2 f}\right)} \quad (3.92)$$

Again, the effects of tip-loss are confined to the blade tip.

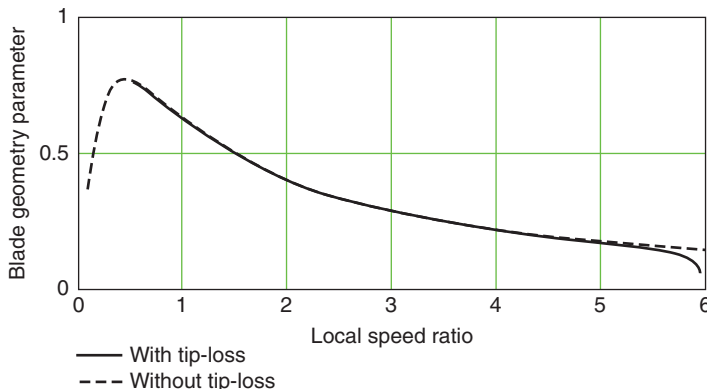


Figure 3.37 Variation of blade geometry parameter with local speed ratio, with and without tip-loss for a three blade rotor with a design tip speed ratio of 6.

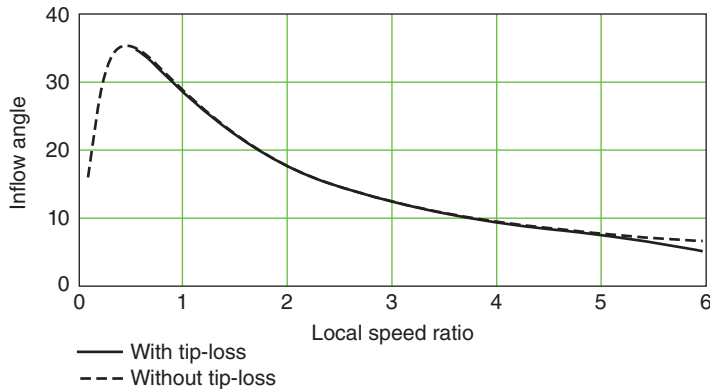


Figure 3.38 Variation of inflow angle with local speed ratio, with and without tip-loss for a three blade rotor with a design tip speed ratio of 6.

The power coefficient for an optimised rotor, operating at the design tip speed ratio, without drag and tip-losses is equal to the Lanchester–Betz limit 0.593, but with tip-loss there is obviously a reduced optimum power coefficient. Equation (3.20) determines the power coefficient; see Figure 3.39:

$$C_P = \frac{P}{\frac{1}{2} \rho U_\infty^3 \pi R^2} = 8\lambda^2 \int_0^1 \{a'(1-a)/(1+a'/f)\} \mu^3 d\mu \quad (3.93)$$

for which a' and a are obtained from Eqs. (3.89) and (3.90). This differs from the result given by Eq. (3.20) by the term a'/f in the denominator, which is very small except close to the root at low tip speed ratio.

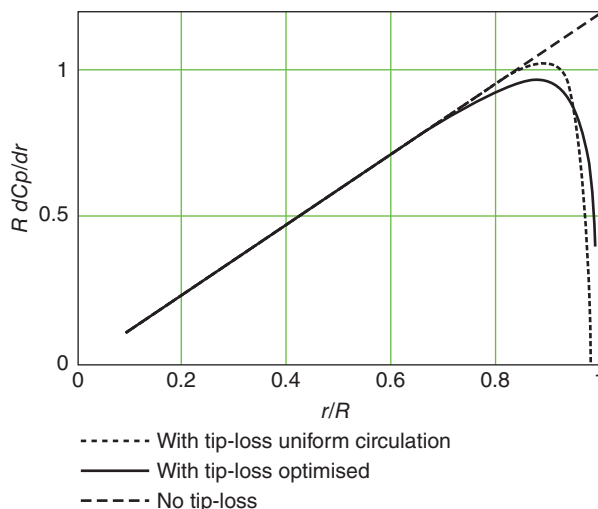


Figure 3.39 Spanwise variation of power extraction in the presence of tip-loss for three blades with uniform circulation and of optimised design for a tip speed ratio of 6.

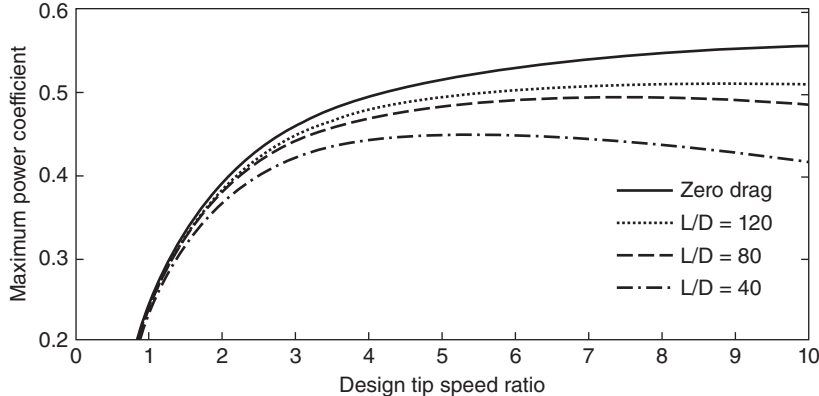


Figure 3.40 The variation of maximum C_P with design λ for various lift/drag ratios and including tip-losses for a three bladed rotor.

The maximum power coefficient that can be achieved in the presence of both drag and tip-loss is significantly less than the Betz limit at all tip speed ratios. As is shown in Figure 3.40, drag reduces the power coefficient at high tip speed ratios, but the effect of tip-loss is most significant at low tip speed ratios because the pitch of the helicoidal vortex sheets is larger.

An alternative formulation for incorporating tip-loss effect is to assume that tip-loss effect may be applied to correct the blade section forces directly ensuring that they fall to zero at the blade root and tip. Thus the tip-loss only appears as a factor f multiplying the right hand sides of Eqs. (3.48) and (3.49), which predict δT and δQ in terms of the momentum losses in the wake; see, for example, Wilson et al. (1974) and Jamieson (2018). This formulation if used simplifies the foregoing analysis of power coefficient because f only appears as a factor multiplying the expression for C_P .

But in the following analysis, we will continue to follow the method of applying the tip-loss factor derived in Section 3.9.2.

3.9.6 Incorporation of tip-loss for non-optimal operation

The BEM Eqs. (3.54a) and (3.55) are used to determine the flow induction factors for non-optimal operation. With tip-loss included the BEM equations have to be modified. The necessary modification depends upon whether the azimuthally averaged values of the flow factors are to be the determined or the maximum (local to a blade element) values. If the former alternative is chosen, then, in the momentum terms, the averaged flow factors a and a' remain unmodified, but in the blade element terms, the flow factors must appear as the average values divided by the tip-loss factor. Choosing to determine the maximum values of the flow factors, i.e. a_b and a'_b , means that they are not modified in the blade element terms but are multiplied by the tip-loss factor in the momentum terms. The former choice allows the simpler modification of Eqs. (3.54a) and (3.55):

$$\frac{a}{1 - a/f} = \frac{\sigma_r}{4\sin^2\phi} C_x \frac{1 - a/f}{1 - a} \quad (3.54c)$$

$$\frac{a'}{1+a'/f} = \frac{\sigma_r}{4\sin\phi\cos\phi} C_y \frac{1-a/f}{1-a} \quad (3.55a)$$

where the flow factor values determined are the averaged values a and a' .

There remains the problem of the breakdown of the momentum theory when wake mixing occurs. The helicoidal vortex structure may not exist, and so Prandtl's approximation is less physically appropriate. Nevertheless, due to the finite length of the blades and radius of the vortex wake, the application of a tip-loss factor is necessary. Prandtl's approximation is the only practical method available and so is commonly used. In view of the manner in which the experimental results of Figure 3.16 were gathered, it is the average value of a that should determine at which stage the momentum theory breaks down.

3.9.7 Radial effects and an alternative explanation for tip-loss

The flow approaching the rotor is expanding because it is slowing down and so is not axial, that is, it is not parallel to the rotation axis or the undisturbed flow direction. Consequently, there is a radial flow velocity component at the upwind side of the rotor that arises because there is a radial pressure gradient with lower pressure in the tip region than in the inner region. The change of radial momentum at a point on the rotor disc is approximately balanced by the equal and opposite radial momentum at the diametrically opposite point. The magnitude of the radial velocity increases with radius, and so its effects will be greatest at the tip region. The kinetic energy associated with the radial flow does not directly affect the energy capture because it does not influence the aerodynamic force on the blade.

At the blade tip the blade chord length becomes zero (usually but not always in a gradual fashion) and so must also the axial force exerted on the air flow beyond the blade tip that bypasses the rotor. The idealised actuator disc theory predicts a logarithmically singular radial velocity at the tip. This is not possible, and the pressure difference across the disc must fall continuously radially over a small tip region to zero at the tip.

Both a and ψ , which is the angle of the resultant flow to the axial direction at the rotor plane, will vary radially and will change according to how the circulation on the disc varies radially. Disc circulation, or the bound vorticity on the disc, must also rise and fall from blade root to blade tip, as shown in Figure 3.41.

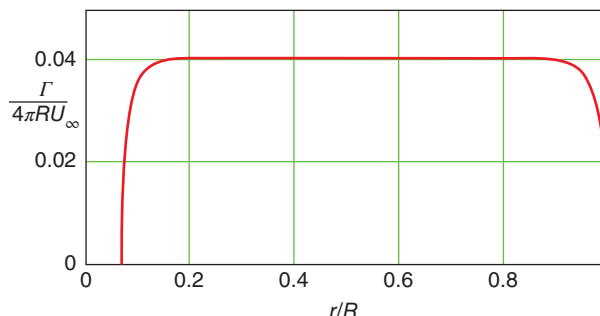


Figure 3.41 The variation of circulation along the length of a blade.

Using just the momentum theory, it is not possible to determine the manner of the variation of a and ψ , but it is clear that the integration with respect to radius r of Eq. (3.93) with (3.89) would result in a value for the optimised power coefficient that would be less than the Betz limit.

Throughout the BEM analysis, it is assumed implicitly that the swirl component generated in the wake of the rotor is sufficiently small that its influence on the pressure field may be ignored and specifically that the pressure far downstream in the wake where the momentum balance is calculated is uniform and ambient. However, as discussed earlier at the end of Section 3.3.2, under lower tip speed ratio conditions, typically within streamtubes that pass close to the blade roots so that the local speed ratio $\lambda = \Omega r/U_\infty < 2$, this is increasingly untrue. However, there is not as yet any fully agreed analysis for this effect except that it may offer the possibility of achieving local power coefficients in excess of the Betz limit. In practical terms the possible increase in total rotor power is unlikely to be very significant.

3.10 Stall delay

A phenomenon first noticed on propellers by Himmelskamp (1945) is that of lift coefficients being attained at the inboard section of a rotating blade that are significantly in excess of the maximum value possible in 2-D static tests. In other words, the angle of attack at which stall occurs is greater for a rotating blade than for the same blade tested statically. The power output of a rotor is measurably increased by the stall delay phenomenon and, if included, improves the comparison of theoretical prediction with measured output. It is noticed that the effect is greater near the blade root and decreases with radius.

The reason for stall delay has been much discussed, but as yet there is no fully agreed explanation. Partly this may be because stall regulation of fixed-pitch rotors has been largely phased out for modern turbines that use pitch control. Stall occurs on an aerofoil section when the adverse pressure gradient on the surface following the suction peak is sufficiently strong to reduce the momentum in the lower layers of the boundary layer to zero faster than viscous or turbulent diffusion can re-energise them. At this point flow reversal occurs, and the boundary layer separates from the surface, causing the aerofoil to stall, decreasing or even changing the sign of the lift curve slope and rapidly increasing the drag. However, on a turbine blade, particularly near the blade root, there is a strong outward radial component to the flow, and the pressure gradient following the streamlines in the boundary layer is less adverse than the section and local incidence would suggest. This may explain at least part of the phenomenon.

Aerodynamic analyses (Wood 1991; Snel et al. 1993) of rotating blades using computational fluid dynamic techniques, which include the effects of viscosity, also do show a decreased adverse pressure gradient. It is agreed that the parameter that influences stall delay predominantly is the local blade solidity $c(r)/r$.

The evidence that does exist shows that for attached flow conditions, below what would otherwise be the static (non-rotating) stall angle of attack, there is little difference between 2-D flow conditions and rotating conditions. Due to the rotation, the air that is moving slowly with respect to the blade close to its surface in the boundary layer

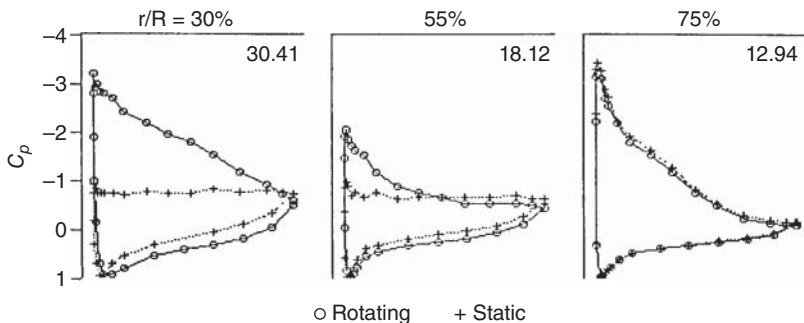


Figure 3.42 Pressure measurements on the surface of a wind turbine blade while rotating and while static by Ronsten (1991).

is subject to strong centrifugal forces. The centrifugal force manifests as a radial pressure gradient, causing a component of velocity radially outwards. Prior to stalling taking place, this effect tends to reduce the adverse pressure gradient along the surface streamlines and hence the growth of boundary layer displacement thickness, thus decreasing the tendency to separate. When stall does occur, the region of slow moving air becomes much thicker throughout a growing separated region, and comparatively large volumes of air flow radially outwards, changing the flow patterns, reducing spanwise pressure gradients in the separated flow regions and hence changing the chordwise surface pressure distributions significantly.

Blade surface pressures have been measured by Ronsten (1991) on a blade while static and while rotating. Figure 3.42 shows the comparison of surface pressure coefficients for similar angles of attack in the static and rotating conditions (tip speed ratio of 4.32) for three spanwise locations. At the 30% span location, the estimated angle of attack at 30.41° is well above the static stall level, which is demonstrated by the static pressure coefficient distribution. The rotating pressure coefficient distribution at 30% span shows a high leading edge suction pressure peak with a uniform pressure recovery slope over the rear section of the upper surface of the chord. The gradual slope of the pressure recovery indicates a reduced adverse pressure gradient with the effect on the boundary layer that it is less likely to separate. The level of the leading edge suction peak, however, is much less than it would be if, in the non-rotating situation, it were possible for flow still to be attached at 30.41° .

The situation at the 55% spanwise location is similar to that at 30%; the static pressures indicate that the section has stalled, but the rotating pressures show a leading edge suction peak that is small but significant. At the 75% span location there is almost no difference between static and rotating blade pressure coefficient distributions at an angle of attack of 12.94° , which is below the static stall level: the leading edge suction pressure peak is little higher than that at 30% span, much higher than that at 55%, but the pressure recovery slope is much steeper. The measured pressure distributions are very different from those corresponding to stall, suggesting that the flow may still be attached at the 30% and 55% span locations on the rotating blade. However, the suction pressure peaks are much too low for the corresponding fully attached flow at these angles of attack, so stall appears to be greatly delayed, and the low adverse pressure gradient shown by the reduced slope of the pressure recovery may be a reason for the delay. At 30% span the

ratio $\frac{c}{r} = 0.374$, $\frac{c}{r} = 0.161$ at 55% span, and at the 75% location $\frac{c}{r} = 0.093$. The increased lift also occurs in the post-stall region and is attributed to the radial flow in the separated flow regions.

Snel et al. (1993) have proposed a simple, empirical modification to the usually available 2-D, static aerofoil lift coefficient data that fits the measured lift coefficients by Ronsten (1991) and the computed results given by 3-D RANS CFD.

If the linear part of the static, 2-D, $C_l - \alpha$ curve is extended beyond the stall, then let ΔC_l be the difference between the two curves. Then the correction to the 2-D curve to account for the rotational, 3-D, effects is $3\left(\frac{c}{r}\right)^2 \Delta C_l$:

$$C_{l,3D} = C_{l,2D} + 3\left(\frac{c}{r}\right)^2 \Delta C_l \quad (3.94)$$

Table 3.1 compares the measured static ($C_{l,2D}$) and rotating ($C_{l,3D}$) lift coefficients with the calculated values for the rotating values using Snel's correction of Eq. (3.94). The correction is quite good and is very simple to apply. An example of the correction is given by Snel in (1993) and is shown in Figure 3.43.

Table 3.1 Summary of Ronsten's measurements of lift coefficient and lift coefficients corrected to rotating conditions using Eq. (3.94).

$r/R*100$	30%	55%	75%
c/r	0.374	0.161	0.093
Angle of attack α	30.41°	18.12°	12.94°
C_l static (measured)	0.8	0.74	1.3
C_l rotating (measured)	1.83	0.93	1.3
C_l rotating (Snel)	1.87	0.84	1.3

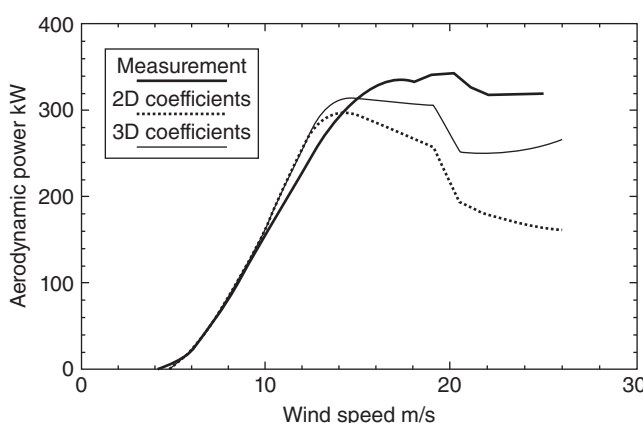


Figure 3.43 A comparison of measured and Snel's predicted power curves for a NORD-TANK 300 kW turbine.

3.11 Calculated results for an actual turbine

The blade design of a turbine operating at constant uniform rotational speed and fixed pitch is given in Table 3.2, and the aerofoil characteristics are shown in Figure 3.44.

The complete $C_P - \lambda$ curve for the design is given in Figure 3.15.

Using the above data the results shown in Figure 3.45 are obtained.

The blade is designed for optimum performance at a tip speed ratio of about 6 and, ideally, the angle of attack, uniform along the span at the level for which the lift/drag ratio is a maximum, is about 7° for the aerofoil concerned. At the lowest tip speed ratio shown in Figure 3.45, the entire blade is stalled, and for a rotational speed of 60 rpm, the corresponding wind speed will be 26 m/s, which is the cut-out speed. For the highest tip speed ratio shown, the corresponding wind speed will be 4.5 m/s, the cut-in speed. Maximum power is developed at a tip speed ratio of 4.0 in a wind speed of 13 m/s and, clearly, much of the blade is stalled.

The axial flow induction factor is not uniform along the span at any tip speed ratio, indicating that the blade design is an engineering compromise, but at the tip speed ratio of 6.0 there is a range where the value is a little higher than 1/3. The flow factors shown in Figure 3.46 are those local to the blade, and so the average value of axial flow factor will be close to 1/3 at a tip speed ratio of 6.

Generally, the axial flow factor increases with tip speed ratio while the tangential flow factor decreases with tip speed ratio. The angular velocity of the wake increases sharply

Table 3.2 Blade design of a 17 m diameter rotor.

Radius r mm	$\mu = \frac{r}{R}$	Chord c mm	Pitch β deg	Thickness/chord ratio of blade %
1700	0.20	1085	15.0	24.6
2125	0.25	1045	12.1	22.5
2150	0.30	1005	9.5	20.7
2975	0.35	965	7.6	19.5
3400	0.40	925	6.1	18.7
3825	0.45	885	4.9	18.1
4250	0.50	845	3.9	17.6
4675	0.55	805	3.1	17.1
5100	0.60	765	2.4	16.6
5525	0.65	725	1.9	16.1
5950	0.70	685	1.5	15.6
6375	0.75	645	1.2	15.1
6800	0.80	605	0.9	14.6
6375	0.85	565	0.6	14.1
7225	0.90	525	0.4	13.6
8075	0.95	485	0.2	13.1
8500	1.00	445	0.0	12.6

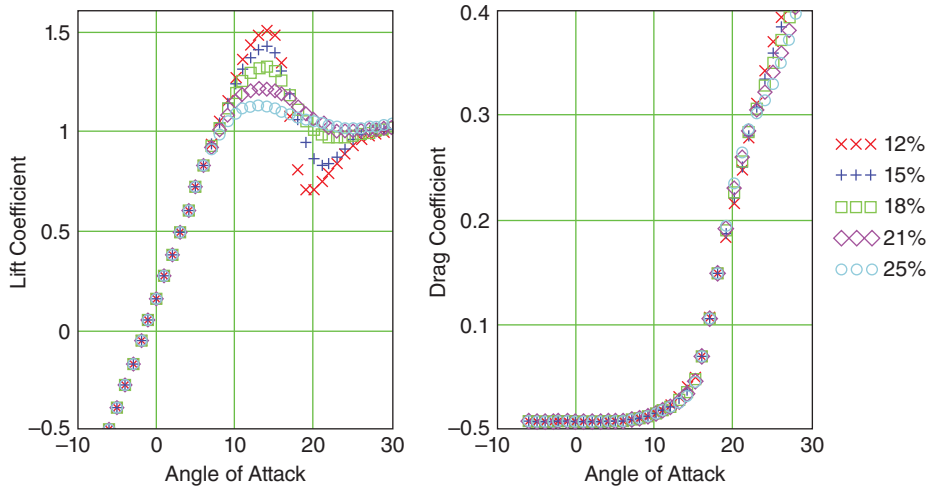


Figure 3.44 The aerodynamic characteristics of the NACA632XX aerofoil series. (XX corresponding to the percentage thickness ratio of each section indicated.)

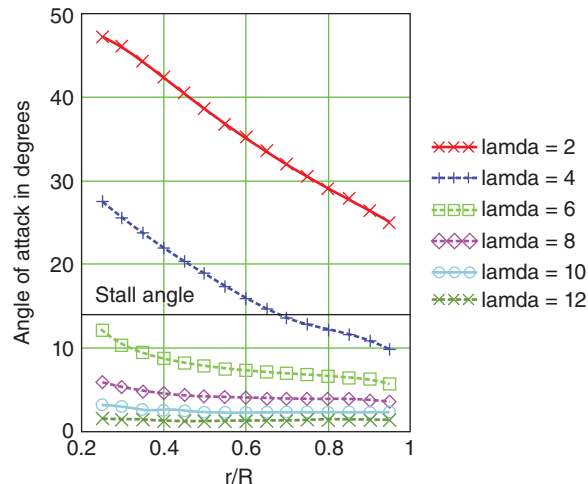


Figure 3.45 Angle of attack distribution for a range of tip speed ratios.

with decreasing radius because it is mainly determined by the root vortex, the angular velocity about a straight line vortex being inversely proportional to distance.

The importance of the outboard section of the blade is clearly demonstrated in Figure 3.47. The dramatic effect of stall is shown in the difference in torque distribution between the tip speed ratio of 4 and the tip speed ratio of 2. Note, also, the flat distribution of torque at the high tip speed ratio of 12; this is caused by the effect of

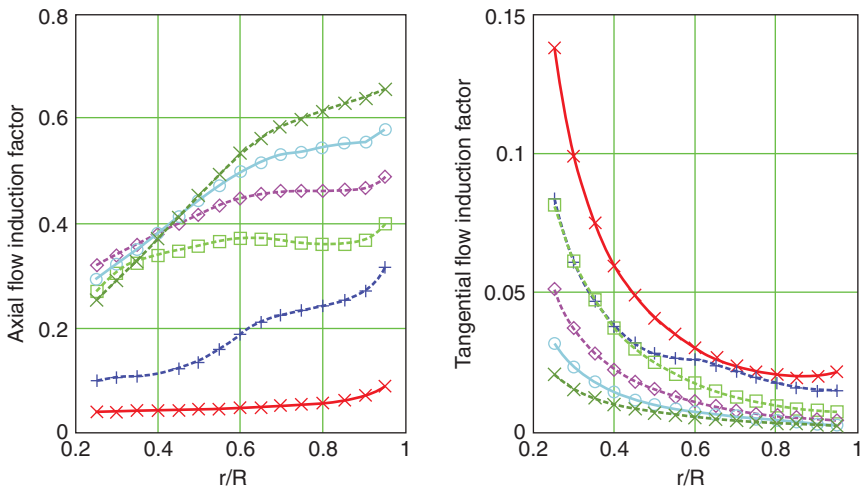


Figure 3.46 Distribution of the flow induction factors for a range of tip speed ratios (lines and symbols as for Figure 3.45).

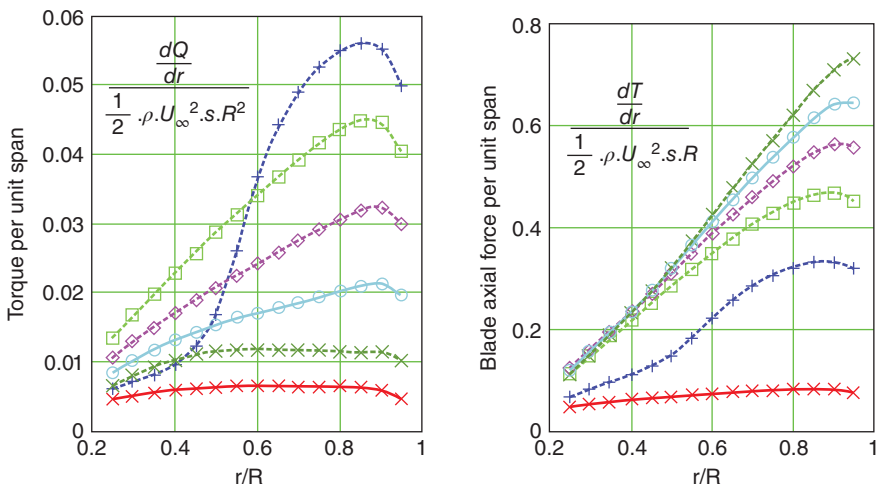


Figure 3.47 Distribution of blade loads for a range of tip speed ratios (lines and symbols as for Figure 3.45).

drag, which reduces torque as the square of the local speed ratio and with the low angle of attack at $\lambda = 12$ drag causes a significant loss of power.

Although the blade thrust *coefficient* increases with tip speed ratio as shown in Figure 3.48, it must be remembered that the actual thrust force increases with wind speed, as is demonstrated in Figure 3.49.

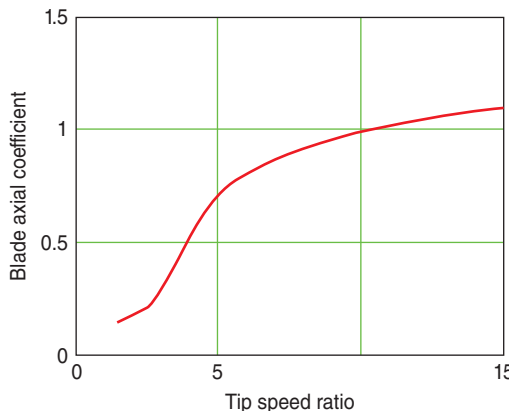


Figure 3.48 Variation of thrust coefficient with tip speed ratio.

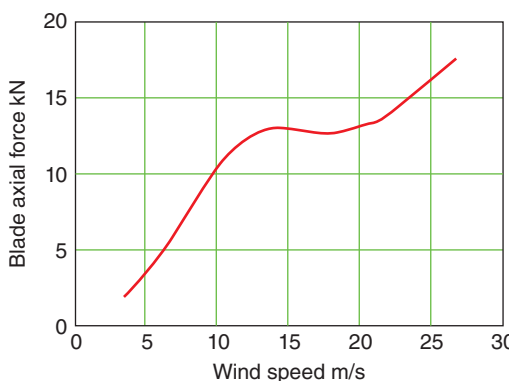


Figure 3.49 Variation of the actual force with wind speed.

3.12 The performance curves

3.12.1 Introduction

The performance of a wind turbine can be characterised by the manner in which the three main indicators, power, torque, and thrust, vary with wind speed. The power determines the amount of energy captured by the rotor, and the torque developed determines the size of the gearbox and must be matched by whatever generator is being driven by the rotor. The rotor thrust has great influence on the structural design of the tower. It is usually convenient to express the performance by means of non-dimensional, characteristic performance curves from which the actual performance can be determined regardless of how the turbine is operated, e.g. at constant rotational speed or some regime of variable rotor speed. Assuming that the aerodynamic performance of the rotor blades does not deteriorate, the non-dimensional aerodynamic performance of the rotor will depend upon the tip speed ratio and, if appropriate, the pitch setting of the blades. It is usual, therefore, to display the power, torque, and thrust coefficients as functions of tip speed ratio.

3.12.2 The $C_P - \lambda$ performance curve

The theory described earlier in this chapter gives the wind turbine designer a means of examining how the power developed by a turbine is governed by the various design parameters. The usual method of presenting power performance is the non-dimensional $C_P - \lambda$ curve, and the performance curve under fixed-pitch conditions for a typical three bladed turbine of the type used for large-scale generation of electrical power is shown in Figure 3.50.

The first point to notice is that the maximum value of C_P is only 0.47, achieved at a tip speed ratio of 7, which is much less than the Betz limit for that tip speed ratio. The discrepancy is caused, in this case, by drag and tip-losses, but the stall also reduces the C_P at low values of the tip speed ratio.

Even with no losses included in the analysis, the Betz limit is not reached because the blade design is not perfect; see Figure 3.51.

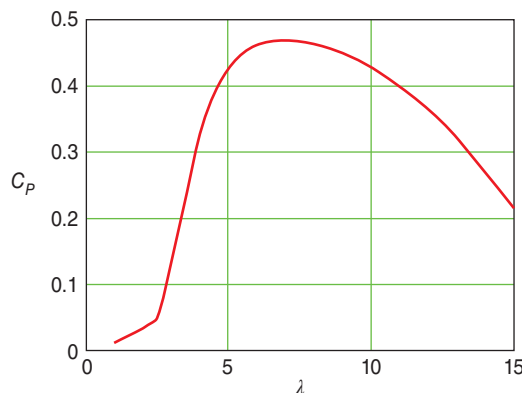


Figure 3.50 $C_P - \lambda$ performance curve for a modern three blade turbine.

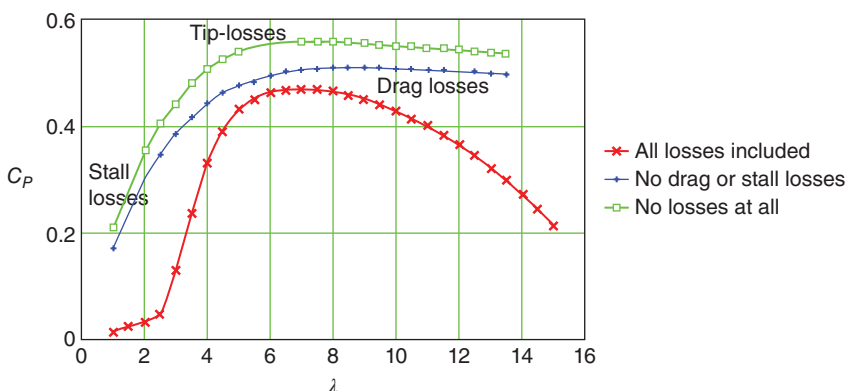


Figure 3.51 $C_P - \lambda$ performance curve for a modern three blade turbine showing losses.

3.12.3 The effect of solidity on performance

At this stage, the other principal parameter to consider is the solidity, defined as total blade area divided by the swept area. For the three blade machine, above, the solidity is 0.0345, but this can be altered readily by varying the number of blades, as shown in Figure 3.52.

The solidity could also have been changed by changing the blade chord.

The main effects to observe of changing solidity are:

1. Low solidity produces a broad, flat curve, which means that the C_P will change very little over a wide tip speed ratio range, but the maximum C_P is low because the drag losses are high (drag losses are roughly proportional to the cube of the tip speed ratio).
2. High solidity produces a narrow performance curve with a sharp peak, making the turbine very sensitive to tip speed ratio changes and, if the solidity is too high, has a relatively low maximum C_P . The reduction in $C_{P\max}$ is caused by stall losses.
3. An optimum solidity appears to be achieved with three blades, but two blades might be an acceptable alternative because although the maximum C_P is a little lower, the spread of the peak is wider, and that might result in a larger energy capture.

It might be argued that a good solution would be to have a large number of blades of small individual solidity, but this greatly increases production costs and results in blades that are structurally weak and very flexible.

There are applications that require turbines of relatively high solidity; one is the directly driven water pump, and the other is the very small turbine used for battery charging. In both cases it is the high starting torque (high torque at very low tip speed ratios)

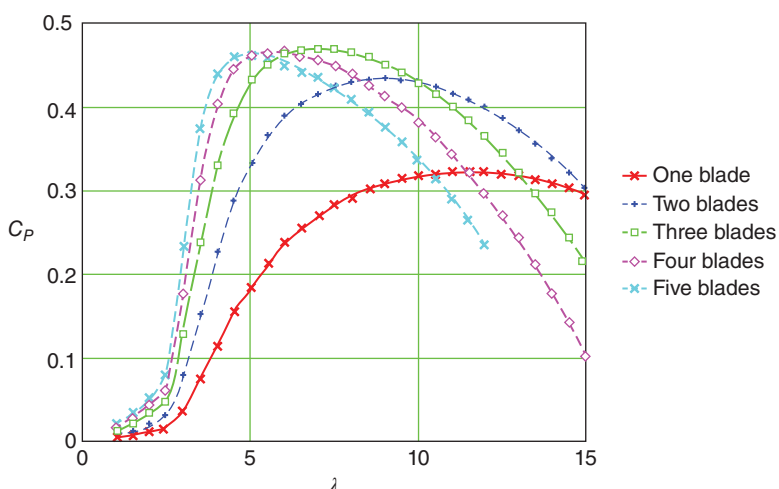


Figure 3.52 Effect of changing solidity.

that is of importance, and this also allows small amounts of power to be developed at very low wind speeds, ideal for trickle charging batteries.

3.12.4 The $C_Q - \lambda$ curve

The torque coefficient is derived from the power coefficient simply by dividing by the tip speed ratio, and so it does not give any additional information about the turbine's performance. The principal use of the $C_Q - \lambda$ curve is for torque assessment purposes when the rotor is connected to a gearbox and generator.

Figure 3.53 shows how the torque developed by a turbine rises with increasing solidity. For modern high-speed turbines designed for electricity generation, as low a torque as possible is desirable to reduce gearbox costs. However, the multi-bladed, high solidity turbine, developed in the nineteenth century for water pumping, rotates slowly and has a very high starting torque coefficient necessary for overcoming the torque required to start a positive displacement pump.

The peak of the torque curve is at the stall onset and occurs at a lower tip speed ratio than the peak of the power curve.

3.12.5 The $C_T - \lambda$ curve

The thrust force on the rotor is directly applied to the tower on which the rotor is supported and so considerably influences the structural design of the tower.

Generally, the thrust on the rotor increases with increasing solidity, as shown in Figure 3.54. These results are computed using Eq. (3.48) without the additional contribution from the rotational wake pressure term Δp_{d2} [see Eq. (3.22) and the discussion following Eq. (3.48)]. Including this term increases the value of C_T by the order of 1% when $\lambda = 8$ (specifically 1.39% for $\lambda = 8$, $a = 1/3$ and blade root at $r/R = 0.135$).

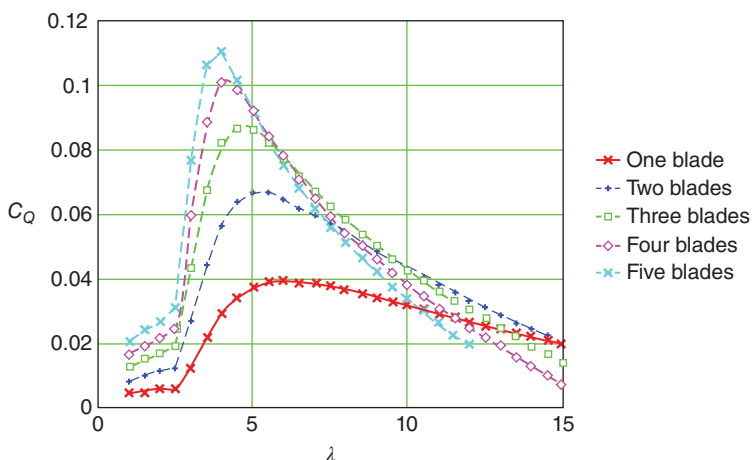


Figure 3.53 The effect of solidity on torque.

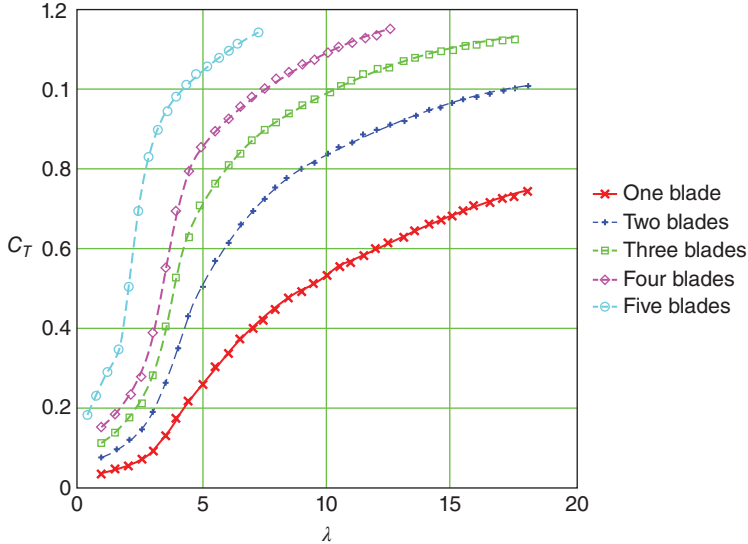


Figure 3.54 The effect of solidity on thrust.

3.13 Constant rotational speed operation

3.13.1 Introduction

The majority of wind turbines currently installed generate electricity. Whether or not these turbines are grid connected, they need to produce an electricity supply that is of constant frequency else many common appliances will not function properly. Consequently, a mode favoured in the early years of wind turbine development has been operation at constant rotational speed. Connected to the grid a constant-speed turbine is automatically controlled, whereas a stand-alone machine needs to have speed control and a means of dumping excess power.

3.13.2 The $K_p - I/\lambda$ curve

An alternative performance curve can be produced for a turbine controlled at constant speed. The $C_p - \lambda$ curve shows, non-dimensionally, how the power would vary with rotational speed if the wind speed was held constant. The $K_p - I/\lambda$ curve describes, again non-dimensionally, how the power would change with wind speed when constant rotational speed is enforced. K_p is defined as

$$K_p = \frac{\text{Power}}{\left(\frac{1}{2}\right) \rho (\Omega R)^3 A_d} = \frac{C_p}{\lambda^3} \quad (3.95)$$

The $C_p - \lambda$ and $K_p - I/\lambda$ curves for a typical fixed-pitch wind turbine are shown in Figure 3.55. The $K_p - I/\lambda$ curve, as stated above, has the same form as the power–wind speed characteristic of the turbine. The efficiency of the turbine (given by the $C_p - \lambda$

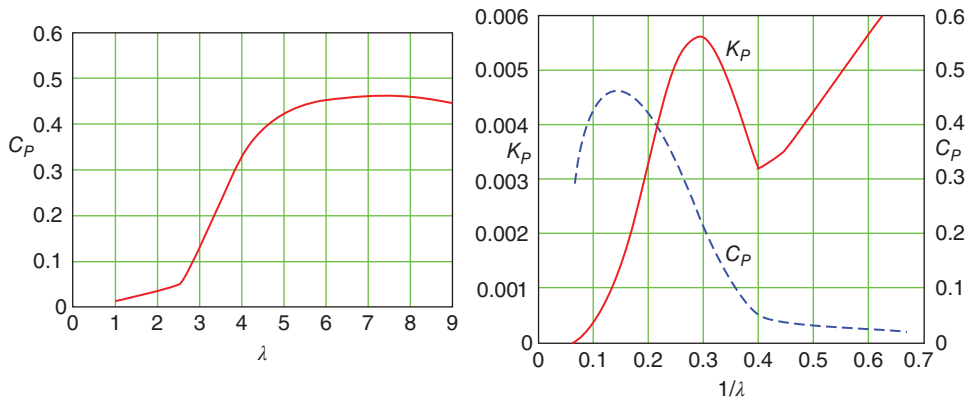


Figure 3.55 Non-dimensional performance curves for constant-speed operation.

curve) varies greatly with wind speed, a disadvantage of constant-speed operation, but it should be designed such that the maximum efficiencies are achieved at wind speeds where there is the most energy available.

3.13.3 Stall regulation

An important feature of this $K_P - 1/\lambda$ curve is that the power, initially, falls off once stall has occurred and then gradually increases with wind speed. This feature provides an element of passive power output regulation, ensuring that the generator is not overloaded as the wind speed increases. Ideally, the power should rise with wind speed to the maximum value and then remain constant regardless of the increase in wind speed: this is called *perfect stall regulation*. However, stall-regulated turbines do not exhibit the ideal, passive stall behaviour.

Stall regulation provides the simplest means of controlling the maximum power generated by a turbine to suit the sizes of the installed generator and gearbox. The principal advantage of stall control is simplicity, but there are significant disadvantages. The power vs wind speed curve is fixed by the aerodynamic characteristics of the blades, in particular the stalling behaviour. The post-stall power output of a turbine varies very unsteadily and in a manner that, so far, defies prediction (see Figure 3.62, for example). The stalled blade also exhibits low vibration damping because the flow about the blade is unattached to the low-pressure surface, and blade vibration velocity has little effect on the aerodynamic forces. The low damping can give rise to large vibration displacement amplitudes, which will inevitably be accompanied by large bending moments and stresses, causing fatigue damage. When parked in high, turbulent winds, the fixed-pitch, stationary blade may well be subject to large aerodynamic loads that cannot be alleviated by adjusting (feathering) the blade pitch angle. Consequently, the blades of a fixed-pitch, stall-regulated turbine must be very strong, involving an appropriate cost penalty.

3.13.4 Effect of rotational speed change

The power output of a turbine running at constant speed is strongly governed by the chosen, operational rotational speed. If a low rotation speed is used, the power reaches a maximum at a low wind speed, and consequently it is very low. To extract energy at wind speeds higher than the stall peak, the turbine must operate in a stalled condition and so is very inefficient. Conversely, a turbine operating efficiently at a high speed will extract a great deal of power at high wind speeds, but at moderate wind speeds it will be operating inefficiently because of the high drag losses. Figure 3.56 demonstrates the sensitivity to rotation speed of the power output – a 33% increase in rpm from 45 to 60 results in a 150% increase in peak power, reflecting the increased wind speed at which peak power occurs at 60 rpm.

At low wind speeds, however, there is a marked fall in power with increasing rotational speed, as shown in Figure 3.57. In fact, the higher power available at low wind speeds if a lower rotational speed is adopted has led to two speed turbines being built. Operating at one fixed speed that maximises energy capture at wind speeds at or above the average level will result in a rather high cut-in wind speed, the lowest wind speed at which generation is possible. Employing a lower rotational speed at low wind speeds reduces the cut-in wind speed and increases energy capture. The increased energy capture is, of course, offset by the cost of the extra machinery.

3.13.5 Effect of blade pitch angle change

Another parameter that affects the power output is the pitch setting angle of the blades β_s . Blade designs almost always involve twist, but the blade can be set at the root with an overall pitch angle. The effects of a few degrees of pitch are shown in Figure 3.58.

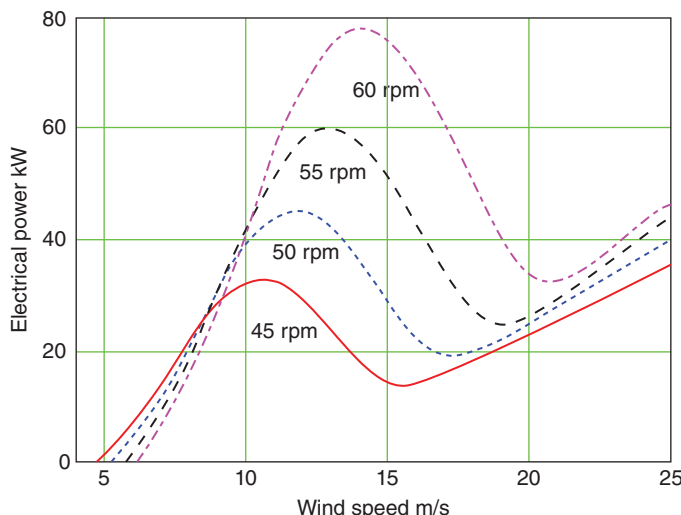


Figure 3.56 Effect on extracted power of rotational speed.

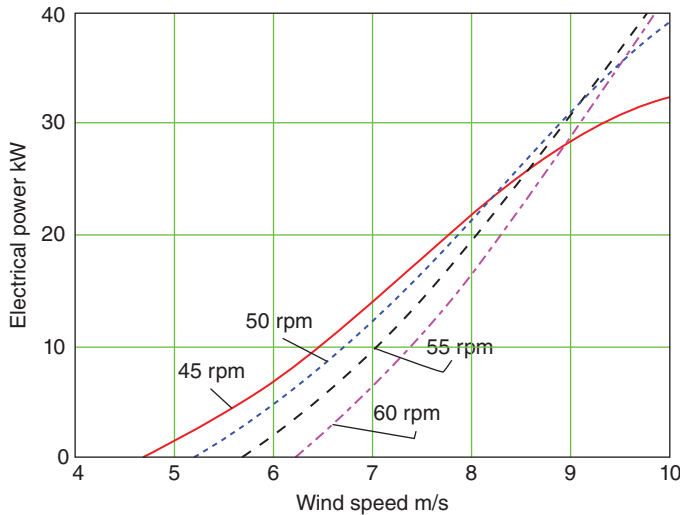


Figure 3.57 Effect on extracted power of rotational speed at low wind speeds.

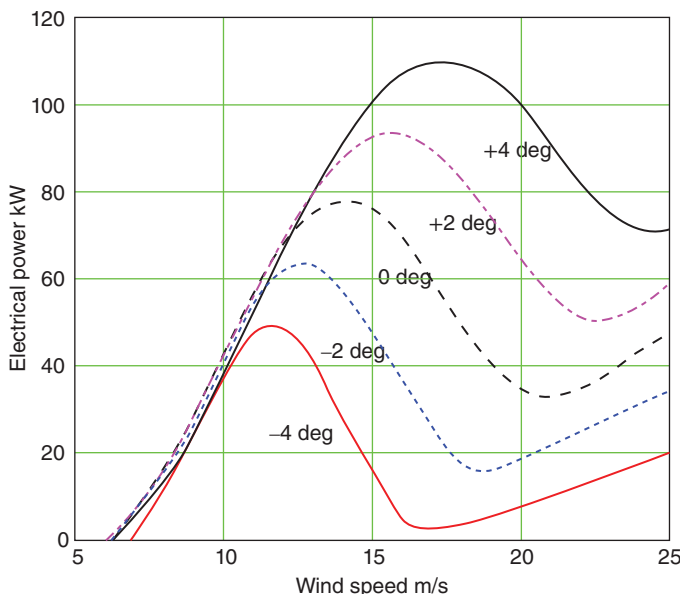


Figure 3.58 Effect on extracted power of blade pitch set angle.

Small changes in pitch setting angle can have a dramatic effect on the power output. Positive pitch angle settings increase the design pitch angle and so decrease the angle of attack. Conversely, negative pitch angle settings increase the angle of attack and may cause stalling to occur, as shown in Figure 3.58. A turbine rotor designed to operate optimally at a given set of wind conditions can be suited to other conditions by appropriate adjustments of blade pitch angle and rotational speed.

3.14 Pitch regulation

3.14.1 Introduction

Many of the shortcomings of fixed-pitch/pассиве stall regulation can be overcome by providing active pitch angle control. Figure 3.58 shows the sensitivity of power output to pitch angle changes.

The most important application of pitch control is for power regulation, but pitch control has other advantages. By adopting a large positive pitch angle, a large starting torque can be generated as a rotor begins to turn. A 90° pitch angle is usually used when the rotor is stationary because this will minimise forces on the blades such that they will not sustain damage in high winds. At 90° of positive pitch the blade is said to be ‘feathered’. The blades need not be as strong, therefore, as for a stall-regulated turbine, which reduces blade costs. Only a small change of pitch angle is needed to provide an assisted start-up.

The principal disadvantages of pitch control are lower reliability and cost, but the latter is offset by lower blade costs.

Power regulation can be achieved either by pitching to promote stalling or pitching to feather, which reduces the lift force on the blades by reducing the angle of attack.

3.14.2 Pitching to stall

Figure 3.58 shows the power curves for a turbine rated at 60 kW, which is achieved at 12 m/s. At wind speeds below the rated level, the blade pitch angle is kept at zero degrees. As rated power is reached, only a small negative pitch angle, initially of about 2°, is necessary to promote stalling and so to limit the power to the rated level. As the wind speed increases, small adjustments in both the positive and negative directions are all that are needed to maintain constant power.

The small size of the pitch angle adjustments make pitching to stall very attractive to designers, but the blades have the same damping and fatigue problems as fixed-pitch turbines.

3.14.3 Pitching to feather

By increasing the pitch angle as rated power is reached, the angle of attack can be reduced. A reduced angle of attack will reduce the lift force and the torque. The flow around the blade remains attached. Figure 3.59 is for the same turbine as Figure 3.58, but only the zero degree power curve is relevant below the rated level. Above the rated level, fragments of power curves for higher-pitch angles are shown as they cross the rated power line: the crossing points give the necessary pitch angles to maintain rated power at the corresponding wind speeds. As can be seen in Figure 3.59, the required pitch angles increase progressively with wind speed and are generally much larger than is needed for the pitching to stall method. In gusty conditions, large pitch excursions are needed to maintain constant power, and the inertia of the blades will limit the speed of the control system’s response.

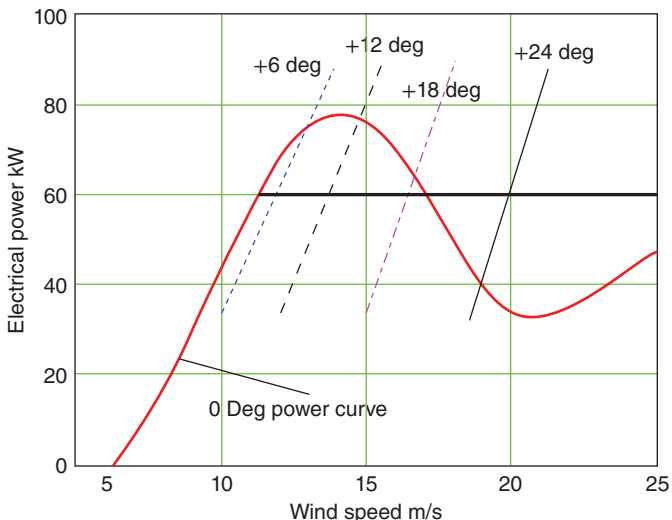


Figure 3.59 Pitching to feather power regulation requires large changes of pitch angle.

Because the blades remain unstalled if large gusts occur at wind speeds above the rated level, large changes of angle of attack will take place with associated large changes in lift. Gust loads on the blades can therefore be more severe than for stalled blades.

The advantages of the pitching to feather method are that the flow around the blade remains attached, and so well understood, and provides good, positive damping. Feathered blade parking and assisted starting are also available.

Pitching to feather has been the preferred pitch control option mainly because the blade loads can be predicted with more confidence than for stalled blades.

3.15 Comparison of measured with theoretical performance

The turbine considered in this section is stall regulated and is run at constant rotational speed. More detail about this method of operation will be discussed in the next section, but the main feature is that there is, theoretically, a unique power output for a given wind speed.

When the turbine was under test, the chosen rotational speed was 44 rpm. Energy output and wind speed were measured over one-minute time intervals and the average power and wind speed determined. The test was continued until a sufficient range of wind speeds had been covered. The one-minute average results were then sorted in ‘bins’ 0.5 m/s of wind speed wide, and a fairly smooth power vs wind speed curve was obtained, as shown in Figure 3.60.

The turbine has a diameter of 17 m and would be expected to produce rather more power than shown above if operated at a higher rotational speed.

From the data in Figure 3.60, the $C_P - \lambda$ curve can be derived. The tip speed of the blades is $(44\pi)/30 \text{ rad/s} \times 8.5 \text{ m} = 39.2 \text{ m/s}$, the swept area is $8.5^2 \cdot \pi = 227 \text{ m}^2$, and the air density was measured (from air pressure and temperature readings) at 1.19 kg/m^3 .

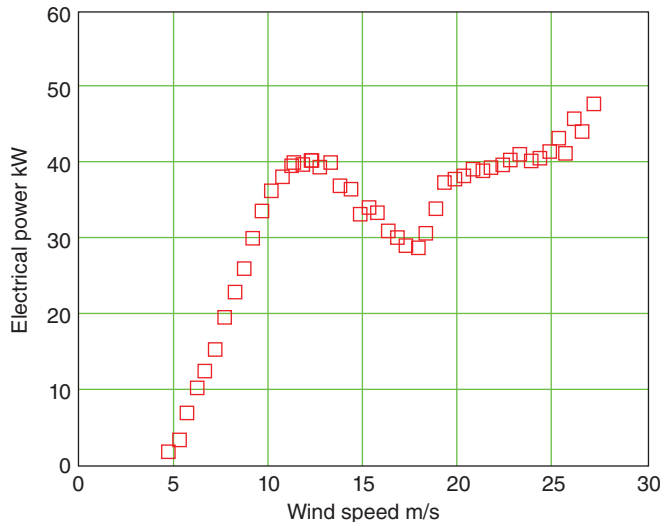


Figure 3.60 Power vs wind speed curve from the binned measurements of a three blade stall-regulated turbine.

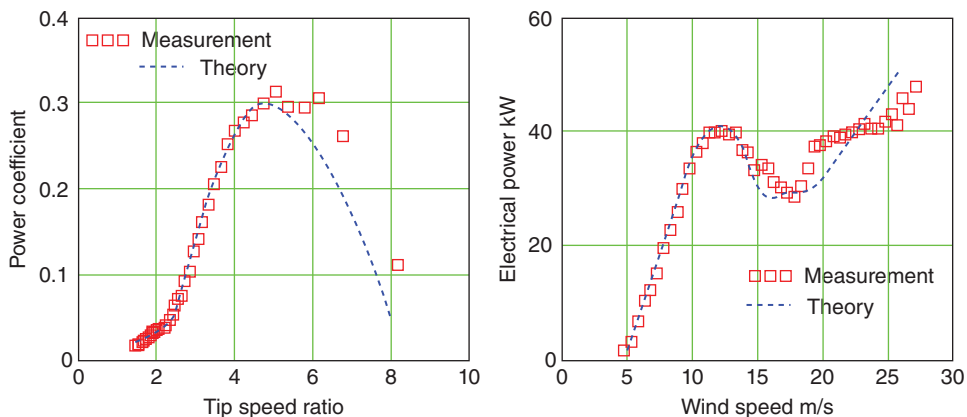


Figure 3.61 Comparison of measured and theoretical performance curves.

Therefore,

$$\lambda = \frac{39.2}{windspeed} \quad \text{and} \quad C_P = \frac{\text{Power } \lambda^3}{\frac{1}{2} \cdot 1.19 \cdot 39.2^3 \cdot 227} \quad (3.96)$$

The mechanical and electrical losses were estimated at 5.62 kW, and this value was used to adjust the theoretical values of C_P . The resulting comparison of measured and theoretical results is shown in Figure 3.61.

This comparison looks reasonable and shows that the theory is reliable, but the quality of the theoretical predictions really relies upon the quality of the aerofoil data. The blade and aerofoil design are the same as given in Section 3.11.

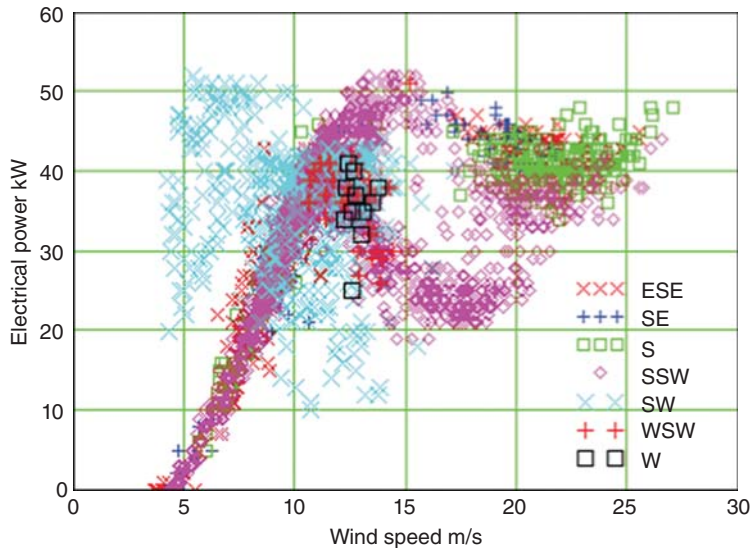


Figure 3.62 Measured raw results of a three blade wind turbine.

One last point should be made before classifying the theory as complete: it would be as well to look at the raw, one-minute average data before it was reduced down by a binning process; this is shown in Figure 3.62. In the post-stall region, there seems to be a much more complex process taking place than the simple theory predicts, and this could be caused by unsteady aerodynamic effects or a bistable separation condition.

3.16 Estimation of energy capture

The quantity of energy that can be captured by a wind turbine depends upon the power vs wind speed characteristic of the turbine and the wind speed distribution at the turbine site.

Wind speed distribution is discussed in Section 2.4. The distribution at a given site is described by a probability density function, Eq. (2.3), with parameters specified for the site.

A performance curve is shown in Figure 3.63 for a turbine designed with an optimum tip speed ratio of 7. As an example, assume that this turbine is stall regulated and operates at a fixed rotational speed at a site where the average wind speed is 6 m/s and the Weibull shape factor $k = 1.8$, then, from Eq. (2.2), the scale factor $c = 6.75 \text{ m/s}$.

Figure 3.64 shows the $K_P - 1/\lambda$ curve for the turbine: from inspection of that curve the tip speed ratio at which stall (maximum power) occurs is 3.7, and the corresponding C_P is 0.22.

The required maximum electrical power of the machine is 500 kW, the transmission loss is 10 kW, the mean generator efficiency is 90%, and the availability of the turbine (amount of time for which it is available to operate when maintenance and repair time is taken into account) is 98%.

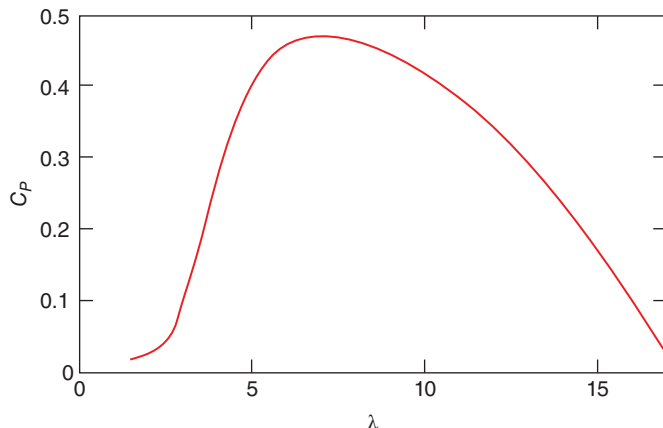


Figure 3.63 C_p - λ curve for a design tip speed ratio of 7 at 7 m/s.

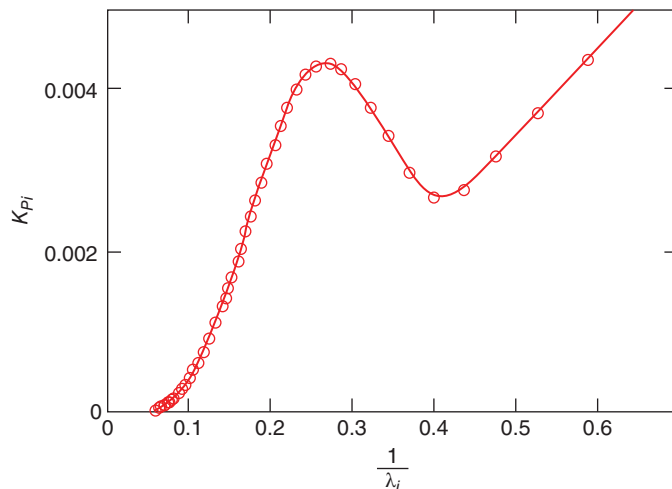


Figure 3.64 K_p - $1/\lambda$ curve for a fixed-speed, stall-regulated turbine.

The maximum rotor shaft power (aerodynamic power) is then

$$P_s = (500 + 10)/0.9 = 567 \text{ kW} \quad (3.97)$$

The wind speed at which maximum power is developed (where $dC_p/d\lambda = 3C_p/\lambda$ for fixed speed) is 13 m/s, therefore the rotor swept area must be, assuming an air density of 1.225 kg/m^3 ,

$$567\,000 / (1/2 \times 1.225 \times 13^3 \times 0.22) = 1.92 \times 10^3 \text{ m}^2$$

The rotor radius is therefore 24.6 m.

The tip speed of the rotor will be $3.7 \times 13 \text{ m/s} = 48.1 \text{ m/s}$, and so the rotational speed will be

$$48.1/24.6 \text{ rad/s} = 1.96 \text{ rad/s}, \text{ which is } 1.96 \times 60/2\pi \text{ rev/min} = 18.7 \text{ rev/min.}$$

The power vs wind speed curve for the turbine can then be obtained from Figure 3.64.

Power (electrical)

$$= (K_P \times 1/2 \times 1.225 \text{ kg/m}^3 \times (48.1 \text{ m/s})^3 \times 1.92 \times 10^3 \text{ m}^2 - 10 \times 1000 \text{ W}) \times 0.9 \quad (3.98)$$

since wind speed = $48.1 \text{ m/s} / \lambda$, and these are shown in Figure 3.65.

To determine the energy capture of the turbine over a time period T , the product of the power characteristic $P(u)$ with the probability $f(u)$ is integrated with respect to time over T . This can be converted to an integral with respect to wind speed u over the wind speed range, since $f(u)$ is the proportion of time T spent at wind speed u , and therefore:

$$f(u) \cdot \delta u = \frac{\delta T}{T} \quad (3.99)$$

with

$$\int_0^\infty f(u) \cdot du = 1 \quad (3.100)$$

$P(u)f(u)$ can be plotted against u as in Figure 3.66 and then integrated over the operational wind speed range of the turbine to give the total energy capture.

The operational speed range will be between the cut-in speed and the cut-out speed. The cut-in speed is determined by the transmission losses: at what wind speed does the turbine begin to generate power? The cut-in speed is usually chosen to be somewhat higher than the zero power speed, in the present case, say 4 m/s.

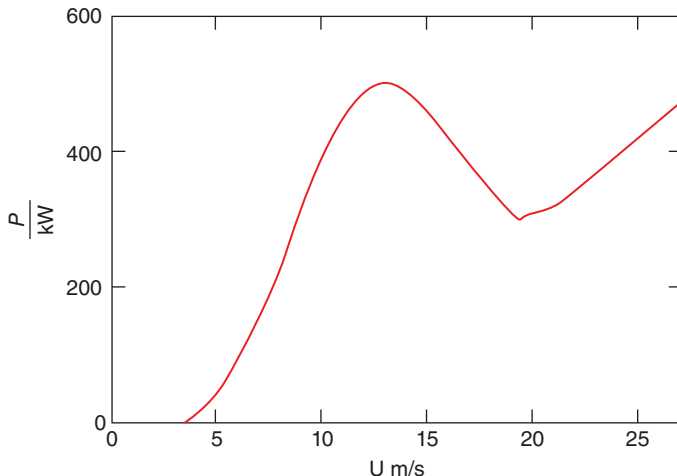


Figure 3.65 Power vs wind speed.

The cut-out speed is chosen to protect the turbine from high loads, usually about 25 m/s.

The total energy captured (E) by the turbine in a time period T is

$$T \int_{U_{ci}}^{\frac{U_{co}}{U}} P(u)f(u)du = E \quad (3.101)$$

which is the area under the curve of Figure 3.66 times the time T . Unfortunately, the integral does not have a closed mathematical form in general, and so a numerical integration is required, such as the trapezoidal rule or, for better accuracy, Simpson's rule.

For a time period of one year, the energy capture can be calculated numerically as indicated in Figure 3.67 to be

$$E = 4.5413 \cdot 10^8 \text{ kWh} \quad (3.102)$$

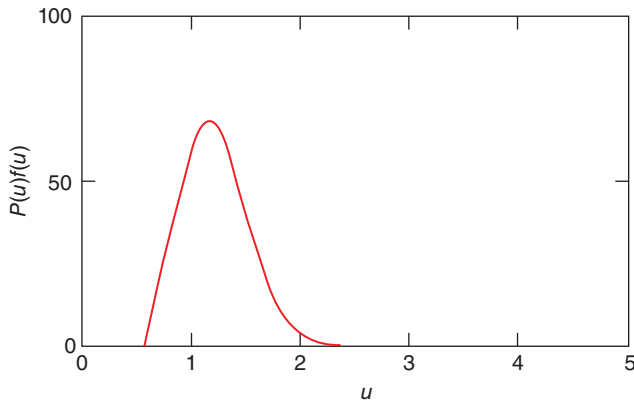


Figure 3.66 Energy capture curve.

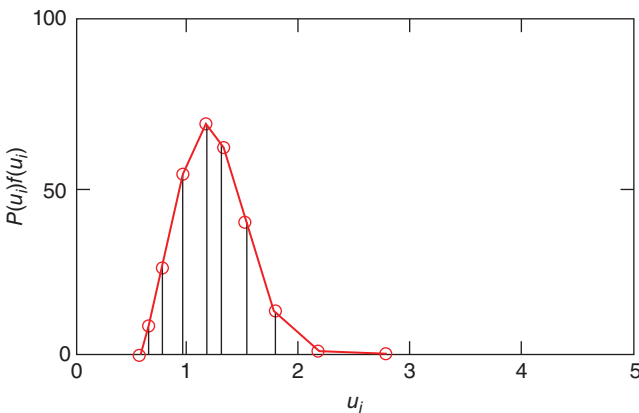


Figure 3.67 Energy capture curve for numerical integration.

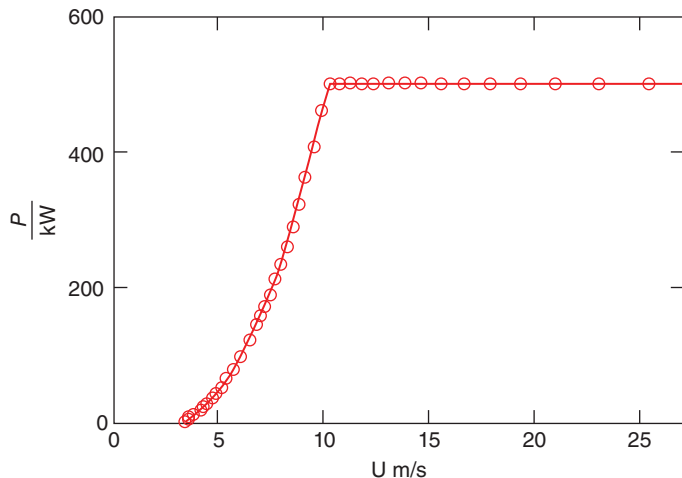


Figure 3.68 Power vs wind speed for variable-speed turbine.

The upper limit of integration $u_{co} = 4.17$ in this case is well above the highest value of u shown in Figure 3.67 for which there is any significant energy.

A turbine that has pitch control would be able to capture more energy but at the expense of providing the control system and the concomitant reduction in reliability. A turbine operating at variable speed (constant tip speed ratio) until maximum power is reached and thence at constant speed and pitch control would capture the maximum possible amount of energy in a given time. The power curve for such a machine is shown in Figure 3.68.

The annual energy capture would be $E = 4.8138 \cdot 10^8$ kWh which is a 6% increase in energy capture compared with the fixed-speed, stall-regulated machine. Variable-speed operation has a number of other advantages that are discussed in Section 6.9.4; it is increasingly being implemented.

3.17 Wind turbine aerofoil design

3.17.1 Introduction

For many years the wind turbine industry relied on aeronautical experience for the aerodynamic design of turbine blades, but it became clear that aerofoil sections that were optimum for aircraft wings were not necessarily optimum for wind turbine blades.

A major problem for modern wind turbines in the early years of development was sensitivity to insect deposition on the leading edge regions of the blades. There were reports of turbines in the 1970s having to be regularly hosed with water to clear accumulated debris on the blades to restore power levels that had fallen dramatically. An aerofoil that was tolerant to leading edge roughness was required.

Most early turbines of rated power greater than about 50 kW operated at constant rotational speed and relied upon passive stall for power control. With many aircraft aerofoil sections, the stall produced a sudden sharp loss of power output that was not recovered until the wind speed increased. The stalling resulted in significant losses of energy capture. Thus another requirement for a wind turbine aerofoil was a gentle stall.

Aerofoil stall occurs when the boundary layer on the low-pressure surface starts to separate at some point before the trailing edge is reached, as shown in Figure A3.12. This process, which is due to sufficiently long and strong regions of rising surface pressure following the ‘suction peak’, is discussed in more detail in A3.3. The process is strongly dependent on the state of the boundary layer (whether laminar or turbulent) and hence the location of transition from laminar to turbulent boundary layer flow and what happens immediately after transition. Transition itself is generated by the presence of flow disturbances in the form of small-scale turbulence in the incident flow, acoustic noise impinging the blade, roughness elements on the surface, the presence of velocity inflexions ($\frac{\partial^2 U}{\partial y^2} = 0$) – see Figures A3.2 and A3.3 – or profiles near to this state in the boundary layer, and by the thickness of the boundary layer. Usually the incident turbulence in the atmosphere is too large scale to affect transition other than by unsteady ‘sloshing’ effects but it is possible that wake turbulence from other turbines could be significant. There are undoubtedly some acoustic disturbances, but the most significant disturbance for a wind turbine blade is the presence of dirt, insects, and other solid particles accreting on blades, particularly near the leading edge. Velocity profiles tending towards inflexion as described above, which result from regions of adverse pressure gradient, are more sensitive to instability. [Classical inviscid hydrodynamic stability theory – see, for example, Lin (1955), shows that an inflected velocity profile is immediately unstable to disturbances unless the Reynolds number is very low.] If the blade is fairly thick and rounded near the leading edge and the Reynolds number is sufficiently high, transition occurs soon after attachment at the leading edge, and the resulting turbulent boundary layer remains attached to fairly high angles of attack because the adverse pressure gradients are only moderately strong, and separation first occurs at the trailing edge where the boundary layer is thickest. As the angle of attack is increased further, the separation point moves steadily forward. The result is a reasonably high $C_{L_{max}}$ with a more gradual rounded maximum of the C_L -alpha curve, giving a gradual stall known as *trailing edge stall*. For somewhat thinner aerofoil sections and/or lower Reynolds numbers, the adverse pressure gradient developing with increased angle of attack on the suction surface causes the laminar boundary layer to separate before transition. Once separated, the resulting free shear layer is highly unstable (because of the inflexion in the profile) and immediately transitions to turbulence followed by rapid reattachment, forming a small separation bubble downstream of which the turbulent boundary layer remains attached up to the trailing edge. Two possibilities then can follow as the angle of attack is further increased: (i) the separation bubble grows steadily in length until reattachment just passes the trailing edge, the bubble bursts, and the aerofoil stalls, or (ii) the bubble remains short, reducing further in length, and suddenly bursts. Possibility (i) is known as *thin aerofoil stall* and occurs for rather thin sections at fairly low Reynolds numbers. The stall is gradual but not usually relevant to wind turbine blades. Possibility (ii) is known as *leading edge stall*, giving a very abrupt fall in lift at the stall, is usually very disadvantageous, and can occur on smaller size wind turbine blades. Mixed stalls can also occur involving two or three of

the above types in a mixed sequence. Gault (1957) has given a very useful correlation to predict stall type by analysing the behaviour of a large number of (clean) NACA sections in low turbulence wind-tunnel tests. But it is clear from the above that the occurrence of dirt or insects on many of these sections can drastically change the stall type. Hence it has been of considerable importance to develop aerofoil sections that are less sensitive to dirt accretion. A further complication of stalling is that since the presence of a large separation region on the aerofoil section changes its suction surface pressure distribution, when the angle of attack of a stalled aerofoil is reduced systematically, reattachment and unstalling do not usually occur at the same angle of attack as separation and stalling did when the angle of attack was being increased. Thus the stall–unstall cycle results in a hysteresis loop with the early post-stall region exhibiting two possible levels of lift depending on the direction of change in angle of attack.

Because of data availability, a popular range of aerofoil sections for wind turbine blades was, but less so now, the NACA six-digit series, an example of which is discussed in Section 3.9. Although more tolerant to leading edge roughness, the NACA six-digit series is no better overall than the NACA four-digit series described in Appendix A3. The main reason for the popularity of the NACA aerofoils is because high quality experimental data is available from tests that were carried out in the 1930s in the pressurised wind tunnel built by NACA (superseded by NASA in 1959). The NACA technical reports are available free on the NASA website, and much of the force data is given in *Theory of Wing Sections* by Abbott and von Doenhoff (1959).

3.17.2 The NREL aerofoils

The development of special-purpose aerofoils for HAWTs began in 1984 jointly between the National Renewable Energy Laboratory (NREL), formerly the Solar Energy Research Institute (SERI), and Airfoils, Incorporated (Tangler and Somers 1995). Since that time, nine aerofoil families (see Table 3.3) have been designed for various size rotors. The principal requirement, depending to some extent on Reynolds number and hence rotor size, is that they have a maximum lift coefficient that is maintained in the presence of leading edge surface roughness.

The primary design tool was based on the work of Eppler (1990, 1993), who developed a method of determining the nature of the 2-D viscous flow around an aerofoil of any profile. The Eppler method includes flow separation in the initial stages of stall and has proved to be very successful.

In addition, several different aerofoil families have been designed for stall-regulated, variable-pitch, and variable-rpm wind turbines.

For stall-regulated rotors, improved post-stall power control is achieved through the design of aerofoils for the outer sections of a blade that limit the maximum lift coefficient. The same aerofoils have a relatively high thickness to chord ratio to accommodate overspeed control devices.

For variable-pitch and variable-speed rotors, outer section aerofoils have a high maximum lift coefficient, allowing low blade solidity.

Generally, aerofoil cross-sections with a high thickness to chord ratio give structural designs of high stiffness and strength without causing a large weight penalty, and aerofoils of low thickness result in less drag.

Table 3.3 Summary of the NREL aerofoils and their applications.

Diameter	Type	Aerofoil thickness	Primary	Tip	Root
3–10 m	Variable speed	Thick	---	S822	S823
	Variable pitch				
10–20 m	Variable speed	Thin	S802	S802	S804
	Variable pitch			S803	
10–20 m	Stall regulated	Thin	S805 S805A	S806 S806A	S807 S808
10–20 m	Stall regulated	Thick	S819	S820	S821
20–30 m	Stall regulated	Thick	S809 S812	S810 S813	S811 S814, S815
20–40 m	Variable speed	—	S825	S826	S814
	Variable pitch				S815
30–50 m	Stall regulated	Thick	S816	S817	S818
40–50 m	Stall regulated	Thick	S827	S828	S818
40–50 m	Variable speed	Thick	S830	S831	S818
	Variable Pitch			S832	

Annual energy capture improvements that are claimed for the NREL airfoil families are of the order of 23–35% for stall-regulated turbines, 8–20% for variable-pitch turbines, and 8–10% for variable-rpm turbines. The improvement for stall-regulated turbines has been verified in field tests.

The aerofoil shape coordinates for some of the NREL aerofoils are available on the website of the National Wind Technology Center (NWTC) at Golden, Colorado. Measured aerofoil data for some aerofoils is also available. A licence must be purchased for information about those aerofoils that are restricted.

Some of the NREL large blade aerofoil profiles are illustrated in Figure 3.69.

3.17.3 The Risø aerofoils

The Risø National Laboratory in Denmark have also developed families of aerofoil designs for wind turbines with similar objectives to the NREL series (Fugslang and Bak 2004). Although the aerodynamic design techniques of the two laboratories were different, there is, perhaps not surprisingly, a significant similarity about the actual designs.

The design tools for the Risø aerofoils were the X-FOIL code developed by Drela (1989), a development of the work of Eppler (1990, 1993), and the Ellipsys-2D CFD code developed at the Technical University of Denmark by Sørensen (1995).

Three families of aerofoils have been developed at Risø – Risø-A, Risø-P, and Risø-B. The Risø-A family was designed in the 1990s and was intended for stall-controlled turbines; however, sensitivity to surface roughness was found to be higher than expected in field tests. The Risø-A family of aerofoil profiles is illustrated in Figure 3.70 and listed in Table 3.4.

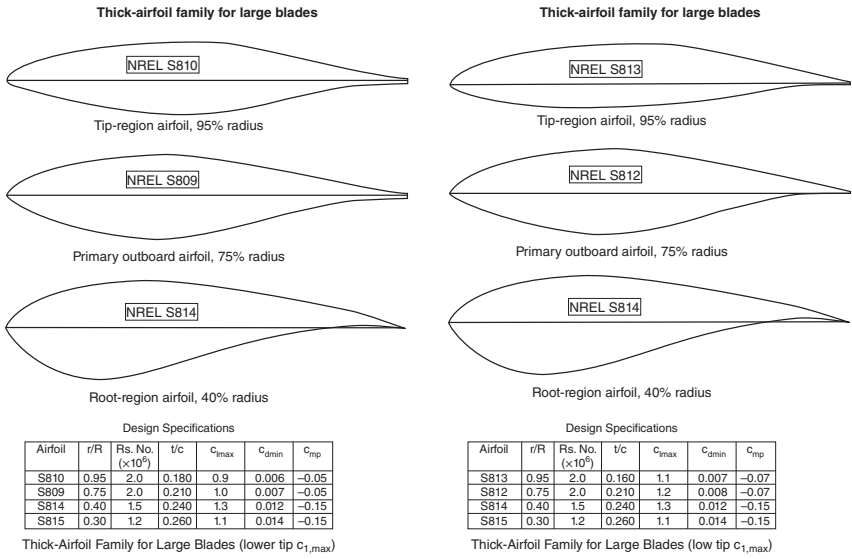


Figure 3.69 NREL aerofoil profiles for large blades.

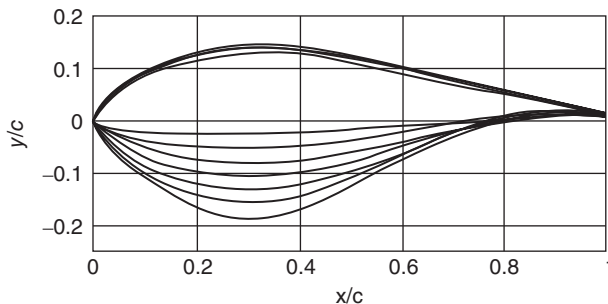


Figure 3.70 The Risø-A series of aerofoil profiles.

Table 3.4 The principal characteristics of the Risø-A series.

Aerofoil	Max t/c %	x/c at max t/c	y/c at TE	$Re \times 10^{-6}$	α_0	c_l max	Design α	Design c_l	Max c_l/c_d
Risø-A1-15	15	0.325	0.0025	3.00	-4.0	1.50	6.0	1.13	168
Risø-A1-18	18	0.336	0.0025	3.00	-3.6	1.53	6.0	1.15	167
Risø-A1-21	21	0.298	0.005	3.00	-3.3	1.45	7.0	1.15	161
Risø-A1-24	24	0.302	0.01	2.75	-3.4	1.48	7.0	1.19	157
Risø-A1-27	27	0.303	0.01	2.75	-3.2	1.44	7.0	1.15	N/A
Risø-A1-30	30	0.300	0.01	2.50	-2.7	1.35	7.0	1.05	N/A
Risø-A1-33	30	0.304	0.01	2.50	-1.6	1.20	7.0	0.93	N/A

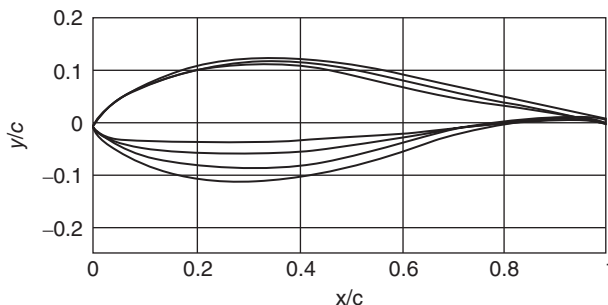


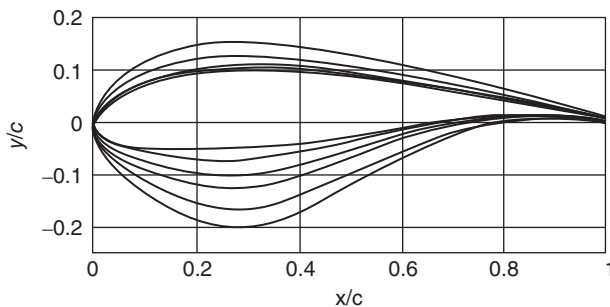
Figure 3.71 The Risø-P series of aerofoil profiles.

The Risø-P family of just four aerofoils, shown in Figure 3.71 and Table 3.5, was designed to replace the corresponding profiles in the Risø-A series for use on variable-pitch and variable-speed rotors.

The Risø-B family was designed as six separate aerofoils with an extended range of thickness to chord ratio from 15% to 36%. The aerofoils, generally, have high maximum

Table 3.5 The principal characteristics of the Risø-P series.

Aerofoil	Max t/c %	x/c at max t/c	y/c at TE	Re $\times 10^{-6}$	α_0	c_l max	Design α	Design c_l	Max c_l/c_d
Risø-P-15	15	0.328	0.0025	3.00	-3.5	1.49	6.0	1.12	173
Risø-P-18	18	0.328	0.0025	3.00	-3.7	1.50	6.0	1.15	170
Risø-P-21	21	0.323	0.005	3.00	-3.5	1.48	6.0	1.14	159
Risø-P-24	24	0.320	0.01	2.75	-3.7	1.48	6.0	1.17	156

**Figure 3.72** The Risø-B series of aerofoil profiles.**Table 3.6** The principal characteristics of the Risø-B series.

Aerofoil	Max t/c %	x/c at max t/c	y/c at TE	Re $\times 10^{-6}$	α_0	c_l max	Design α	Design c_l	Max c_l/c_d
Risø-B1-15	15	0.278	0.006	6.00	-4.1	1.92	6.0	1.21	157
Risø-B1-18	18	0.279	0.004	6.00	-4.0	1.87	6.0	1.19	166
Risø-B1-21	21	0.278	0.005	6.00	-3.6	1.83	6.0	1.16	139
Risø-B1-24	24	0.270	0.007	6.00	-3.1	1.76	6.0	1.15	120
Risø-B1-30	30	0.270	0.01	6.00	-2.1	1.61	5.0	0.90	N/A
Risø-B1-36	36	0.270	0.012	6.00	-1.3	1.15	5.0	0.90	N/A

lift coefficients for use on multi-megawatt size rotors with low solidity, flexible blades having variable-speed pitch control. This family of aerofoil profiles is shown in Figure 3.72 and Table 3.6.

In the tables above, the ‘design c_l ’ is the value of the lift coefficient that corresponds to the maximum lift to drag ratio and the ‘design α ’ the corresponding angle of attack. An optimised variable-speed turbine should be designed so that the blade sections operate at this angle of attack. It is a design feature of the Risø aerofoils that the design c_l is high so that a blade will be most efficient at low solidity.

3.17.4 The Delft aerofoils

The Delft University of Technology in the Netherlands has also developed a number of aerofoils for wind turbine rotors (Timmer and van Rooij 2003). As with the NREL and Risø aerofoils, the principal feature driving the designs was surface roughness insensitivity, but more emphasis was placed upon seeking designs for thick aerofoils to gain a structural advantage. The Delft University series of aerofoil profiles are illustrated in Figure 3.73 and listed in Table 3.7.

The design tool for the Delft aerofoils was the RFOIL code, a modification made at Delft of the XFOIL code to include the effects of stall delay.

The two thickest of these aerofoils have not been tested in a wind tunnel, and the characteristics have been determined by calculation.

3.17.5 General principles for outboard and inboard blade sections

The aerofoil sections of the outboard half of the blade are responsible for extracting the major part of the wind energy. These sections should therefore be efficient with a high lift/drag ratio, hence reasonably thin, consistent with adequate structural strength. Thickness ratios around 18% are usual with relatively high $C_{L\max}$ so that the operating C_L where the best C_L/C_D ratio occurs is significantly below $C_{L\max}$. This allows efficient operation while keeping sufficiently clear of the stall to avoid its adverse effects when wind gusts momentarily push up the angle of attack too quickly for pitch regulation to respond sufficiently.

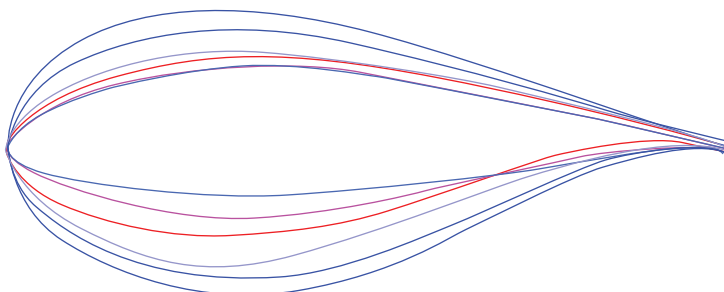


Figure 3.73 The Delft University series of aerofoil profiles.

Table 3.7 The principal characteristics of the Delft University series.

Aerofoil	Max t/c %	x/c at max t/c	y/c at TE	$Re \times \alpha_0 \times 10^{-6}$	c_l max	Design α	Design c_l	Max c_l/c_d
DU 96-W-180	18	0.3	0.0018	3.00–2.7	1.26	6.59	1.07	145
DU 00-W-212	21.2	0.3	0.0023	3.00–2.7	1.29	6.5	1.06	132
DU 91-W2-250	25	0.3	0.0054	3.00–3.2	1.37	6.68	1.24	137
DU 97-W-300	30	0.3	0.0048	3.00–2.2	1.56	9.3	1.39	98
DU 00-W-350	35	0.3	0.01	3.00–2.0	1.39	7.0	1.13	81
DU 00-W-401	40.1	0.3	0.01	3.00–3.0	1.04	5.0	0.82	54

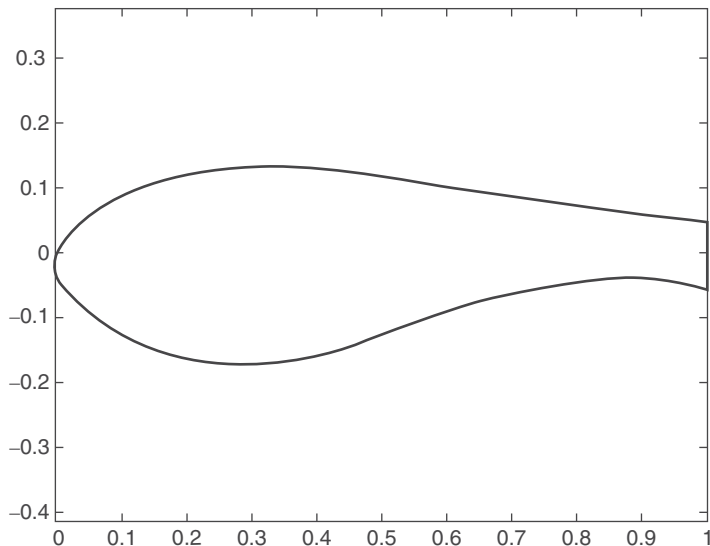


Figure 3.74 Flat-back aerofoil derived from DU-97-W-300.

The inboard sections of a wind turbine blade are much more strongly dictated by structural bending strength requirements. Hence increasingly thick sections are used as the radius reduces to the root. Blade sections at the root end may be up to 40% thick. Inboard of the root end of the aerodynamic sections of the blade, the blade often merges continuously into a circular or other bluff section joining the blade to the hub. To accommodate these very thick sections and at the same time retain a high $C_{L\max}$ for power purposes, blades are often fitted with vortex generators (VGs) (see later) near the location of early separation, and so-called ‘flat-back’ sections with blunt trailing edges have been designed. An example is the aerofoil shown in Figure 3.74, which is derived by thickening the rear half of the more conventional DU-97-W-300. A computational analysis of the aerodynamics and aeroacoustics of this aerofoil has been given by Lynch and Smith (2009).

3.18 Add-ons (including blade modifications independent of the main structure)

There are a number of small devices that can be added (and sometimes are) to existing wind turbine blades post-design without compromising the blade structural performance. These devices have often been derived from aircraft usage and are usually incorporated either to improve performance that has turned out to be below the designed level or, more often, to provide additional performance beyond the intended where circumstances dictate. An example of the latter is the desirability of increasing the design lift coefficient for a turbine blade that is to be operated in significantly reduced air density due to the altitude of the wind turbine site.

3.18.1 Devices to control separation and stalling

Vortex generators (VGs) are small triangular, rectangular, or similar pieces of flat, rigid sheet that act as very small half-wings of low aspect ratio set perpendicular to the blade surface at a large angle of incidence ($\sim 30^\circ$) to the local flow direction, as shown in Figure 3.75. Such plates generate strong leading edge (triangular delta VGs) or tip (rectangular VGs) vortices. The vortices stream over the main blade surface, stirring up the flow in the boundary layer, re-energising the lower (inner) layers by bringing flow down from the upper (outer) layers and hence inhibiting separation. It is found that a line of small devices of this type of height about equal to the boundary layer thickness δ are very effective in inhibiting separation on the blade when placed a moderate distance upstream of the expected line of separation. VGs are easily added to the blade by fixing them via a lug at the base and are usually set to have an alternating positive and negative angle of incidence so that the rotation direction of the vortices alternates. They may be set moderately close together as in the example in the figure or farther apart up to the order of 10δ to still retain continuous effectiveness over the downstream region. In this way $C_{L\max}$ can be increased. The main drawback of such devices is that being fixed passive devices they operate continuously even when not required, and because they continue to generate vortices, they increase slightly the pre-stall drag of the blade.

Micro VGs are much smaller versions of ordinary VGs, being of order $\delta/10$ in height and spaced somewhat more closely. Micro VGs operate in the inner region of the boundary layer, where for a turbulent boundary layer much the strongest part of the velocity gradient normal to the blade surface exists. They can be nearly as effective as standard VGs in suppressing separation and have the advantage of generating a smaller increase in drag.

Surface air jets are inclined jets sited in a similar location as VGs would be sited but rather closer together. The jets are often fed by higher-pressure air from near



Figure 3.75 VGs on a blade suction surface. (Flow is from right to left.)

the stagnation region of the blade section or sometimes from inboard regions taking advantage of the centrifugal pressure difference between inboard locations and those farther outboard. The jets act to re-energise the lower boundary layer through their own momentum and thus prevent stalling. They have the advantage that they can be turned off when not required. Their main disadvantage is the additional complexity, ‘plumbing’, and therefore cost required to provide each jet and the vulnerability of the jet slots.

Massless or synthetic jets are a variation of surface air jets that operate by an oscillating piston within a cavity that forces a pulsatile jet out through a small hole in the blade surface. No net mean mass flow occurs, hence their name, equal mass flows occurring into and out of the orifice. During the intake phase the flow is a sink flow that produces relatively little disturbance, whereas the outflow phase is a jet that forms a vortex ring so that the oscillatory operation of the device generates a sequence of vortex rings that can re-energise the boundary layer. No separate intake or piping is required, but each device (orifice) must be separately actuated. They are not as yet used on wind turbine blades but may be an option for the future because they have been found effective in controlling separation in other situations. They appear to be reasonably unaffected by dirt due to the exhaust phase in each cycle.

3.18.2 Devices to increase $C_{L\max}$ and lift/drag ratio

Deployable conventional flaps (see Figure 3.76a) are trailing edge flaps (TE flaps), leading edge flaps being very unusual, and are similar to conventional aircraft control surfaces such as ailerons, hinged at the rear of the blade section and operated by a mechanical actuator. They increase or decrease section lift by increasing or decreasing the effective camber of the blade section. They have been proposed for wind turbine blades but are rarely ever used because of the additional mechanical complexity, weight near the blade tips where they would be most useful, cost, and maintenance issues. Their main advantage is that they can be sited where changes in lift are most useful, typically outboard regions. As turbine blade lengths increase and the blades become ever more flexible, this localisation offers the possibility of distributed control with advantages over pitch control at the blade root, and it is possible that more use will be made of them in future. This is particularly relevant for active control to mitigate the effect of turbulence and gusts because small flaps can be actuated very rapidly and act locally.

Morphing blade sections (Figure 3.76b) are a recent development that is really a variation of the conventional trailing edge flap. The actuator is within the rear section of the blade, which is fabricated from a flexible composite. The result when actuated is to generate a flap effect but with a more smoothly curved camber and with all mechanical parts protected by being internal and hence presumed to be less vulnerable to dirt and corrosion. The continuous curvature of the camber can be tailored for maximum aerodynamic efficiency. The technology is considered to be a promising method of providing distributed control with some mechanical benefits over conventional TE flaps.

Fixed (Gurney) flaps (Figure 3.76c, named after Dan Gurney, who invented this flap for down-force wings used in motor racing) are small fixed flaps in the form of a length of thin, right-angle bar section fixed to the trailing edge of a blade on the pressure side. A Gurney flap is thus like a small trailing edge flap deployed at 90° in the direction to increase lift. Such flaps usually have a flap chord (i.e. ‘height’ from the blade) equal to only 1% or 2% of the blade section chord. With that small length but large deployment angle,

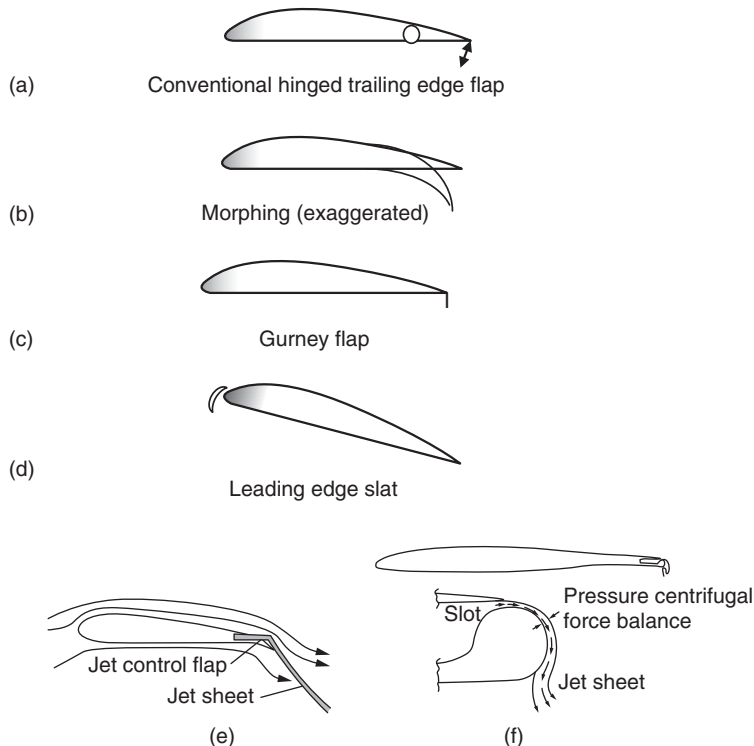


Figure 3.76 Flaps and similar acting devices: (a) conventional trailing edge flap, (b) morphing rear blade section, (c) Gurney flap, (d) leading edge slat, (e) jet flap, and (f) circulation control.

a useful increase in lift coefficient (0.1 to 0.25) can be obtained at the expense of a small increase in drag coefficient. The result with a well-designed flap is that the lift coefficient can be increased while the lift/drag ratio remains constant or may even increase slightly. See, for example, Giguere et al. (1997).

Slats (Figure 3.76d), as deployed at the leading edges of aircraft wings to prevent separation during high angle of attack operation (during take-off and landing), have also been tried on wind turbine blades for the same reason.

3.18.3 Circulation control (jet flaps)

The circulation and hence the lift around an aerofoil section can be controlled very rapidly by the action of a jet applied at the trailing edge. The jet may be directed over the suction surface of the blade at the trailing edge. This may simply have a suitably oriented exhaust nozzle (Figure 3.76e) or may use the Coanda effect running over a short length of curved surface (Figure 3.76f [lower]) to generate a jet sheet deflected so as to increase the effective camber of the section and hence the lift. It acts in a manner very similar to a conventional structural flap, hence is known as a *jet flap*, and is as shown in Figure 3.76e. Alternatively, jets may be emitted from slots either side of a

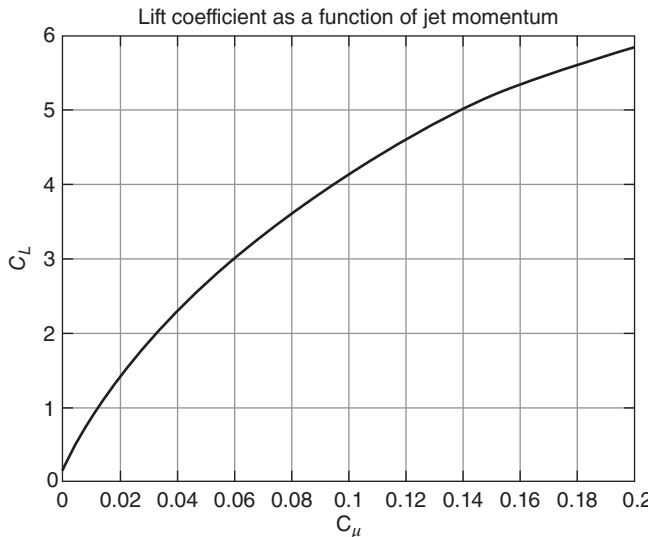


Figure 3.77 Lift coefficient vs jet momentum coefficient for jet circulation control.

rounded trailing edge to produce a highly deflected jet in either direction to control the circulation and hence the lift on the blade section, as shown in Figure 3.76f (upper). Figure 3.77 shows a plot of lift coefficient vs jet momentum coefficient for a device of this type where the jet momentum coefficient $C_\mu = 2(U_j/U_\infty)^2 \cdot t/c$, U_j is the jet velocity and t it should be noted is the *thickness of the jet exit slot* (not to be confused here with the maximum thickness of the aerofoil section). Very high values of lift coefficient are possible if sufficient jet momentum is applied with a large deflection angle because the jet momentum removes the separation limit of a conventional flap.

These devices mimic the effect of a conventional (solid) flap but have the advantage that large rates of change of lift can be achieved very quickly by sudden changes in the jet pressure and hence momentum. The effectiveness of both in controlling circulation is due to the Coanda effect, whereby an exiting ‘wall-jet’ sticks to a highly curved surface. In the jet flap case, the effectively ‘active’ length and curvature of the jet sheet depends on the jet momentum. In the rounded trailing edge case, the jet sticks to the highly rounded surface to a greater or lesser extent according to the jet momentum, thus exhausting from the aerofoil trailing edge at a greater or lesser angle. The resulting free jet in both cases simulates a deployed structural flap but without the need to overcome significant inertia in rapid activation. Such devices deployed along the outboard trailing edge of the blade give two advantages. They allow high lift coefficients to be obtained (not limited in the same way by separation as a solid flap) so that the blade chord may be substantially reduced to achieve the same power production. This reduces the weight of the blade and also blade loads when the parked blade is impacted by high wind gusts at large angles to the blade. Second, very rapid control is possible. However, the system has obvious disadvantages of complexity, maintenance, and cost (although less prone to problems of dirt ingress, as it is an overpressure device), the aerofoil section with the jet turned off generates higher drag than a typical ‘sharp’ trailing edge section, and there is a power

requirement to provide the jet momentum. Johnson et al. (2008) give an extensive review of many of the above types of devices for blade load control.

3.19 Aerodynamic noise

3.19.1 Noise sources

Since deployment of wind turbines became widespread onshore from the 1990s onwards, growing public resistance to the siting of turbines in areas close to dwellings has become a major planning issue. The two most important points of objection are normally visibility and noise. Efforts to minimise the first of these focus on detailed siting and surface appearance of the turbine, noting that there is generally a conflict between siting to reduce visibility and siting to maximise wind energy capture. The issue of noise, however, is closely related to turbine operation because the two main sources of wind turbine noise are the machinery and the blade aerodynamics. Radiated noise from wind turbine machinery (generator, gearbox, etc.) has been greatly reduced in modern wind turbine designs over the last two or three decades. Considerable attention has been paid with successful results to reducing the intensity of mechanical noise by identifying and suppressing sources of noise within the machinery and providing noise insulation. As a result, mechanical noise is now regarded as much less important than aerodynamic noise for large modern wind turbines.

This section deals with aerodynamic noise generated by the blades and methods of reducing it in the form of modifications to blade geometry and section profile. A fuller description of wind turbine noise and its measurement, prediction and assessment of environmental impact is given in Section 10.3.

Aerodynamic noise arises mainly from two sources: (i) self-noise, which is generated by the air flow over the blades interacting locally with the blades, an effect that would occur even if the incident wind flow were to be smooth, and (ii) noise induced by the turbulence in the inflow (mainly atmospheric turbulence but also on occasion wake turbulence from upstream turbines, interacting with blades and inducing fluctuating blade loading). Aero-acoustic noise may be either broadband or tonal. The latter is less common but more irritating if significant. There are also a number of other specific noise sources. One important example is the cyclic interaction between the blades and the tower. Although the blade passing frequency is below the audible range, the frequency content from the quasi-impulsive interaction as a blade passes through the quite narrow influence field of the tower can in some circumstances contribute audible sound at a significant level (in addition to the unsteady loading). The effect can be made small to negligible for an upwind rotor because the aerodynamic interaction between blade and tower reduces as the square of the separation distance between the blade and the tower axis. The interaction is usually therefore minimal unless the blade passes very close to the tower. The main effect can be effectively removed by providing adequate clearance (> 1 tower diameter) through nacelle overhang and rotor tilt. It then only becomes appreciable in high wind operation when blades tend to bend towards the tower, reducing the clearance, but in this case blade noise is less of an issue because of background wind noise. Blade–tower interaction noise can be significant for downwind rotors with solid towers of non-negligible diameter. This type of design is very uncommon, and hence

this noise source has not been studied greatly. When it does occur, it can be difficult to remedy because the noise originates from the interaction of the blades passing through the tower wake, and such wakes only diffuse gradually over large distances. For the general aero-acoustic sources present on wind turbine rotors, a very good review is given by Wagner et al. (1996).

Those noise sources that arise from unsteady incident flows inducing fluctuating forces on the turbine blades scale as the sixth power of the local inflow wind speed relative to the aerofoil section, and the noise is generally low frequency. Self-noise that is broadband through the auditory range and usually dominates is found to depend on the relative wind speed over the blade at between the fifth and sixth power but closer to the former. Because the tip speed ratio is normally high, this relative flow speed is effectively the local blade speed, and the noise sources are therefore mainly significant over the outer 25% of the blade and when the rotor is operating. Because of the high power dependence of the radiated sound intensity, therefore, on rotor tip speed, the ‘simplest’ way to reduce aerodynamic noise radiation from a wind turbine is to run the rotor at a lower tip speed ratio. This has always been known and is a major reason why turbines with fewer than three blades are not favoured for onshore designs, since optimum tip speed ratio increases as rotor solidity decreases. But as there are efficiency constraints also on lowering tip speed ratio, a major effort continues aimed at reducing the aerodynamic blade noise sources themselves.

3.19.2 Inflow turbulence-induced blade noise

Inflow turbulence interacts with the blades and generates noise due to the unsteady blade forces that arise as a result. This noise source is generally found to be a less strong source than the blade’s self-induced noise, although this is not always so. The only obvious method of alleviating the inflow noise is through a control system to mitigate the unsteady loading of individual blades due to the turbulence. Distributed control capable of operation at frequencies high enough to affect the audible noise spectrum is not yet a feature of wind turbines. Inflow noise intensity is mainly only at a level to be of concern in high, gusty winds where, because there is so much wind noise from other sources in the environment, the additional turbine noise is less significant. There is a long history and a great deal of theory developed for the prediction of rotor blade noise due to turbulent inflow because of its importance in noise radiation from aircraft turbojet engines and rotorcraft. The method originated by Amiet (1975) based on prediction of unsteady blade loading taking into account compressibility was originally developed for aero-engines. It has been further developed and is still current as a prediction method for wind turbine rotors but involves fairly extensive computational effort. Moriarty et al. (2005) have produced a simpler model based on parameterised results for standard blade geometries.

3.19.3 Self-induced blade noise

Self-induced aerodynamic noise arises from a number of causes: (i) interaction of the blade turbulent boundary layers with the trailing edge, (ii) noise due to locally separated flow, (iii) noise due to the vortex wake, usually due to and from a blunt trailing edge but at low Reynolds numbers can alternatively be laminar wake instability, and (iv) noise due to the blade-tip vortex.

3.19.4 Interaction between turbulent boundary layers on the blade and the trailing edge

Interaction of turbulent eddies in the blade boundary layer with the trailing edge [i.e. (i) in the previous section] is usually regarded as the most important noise source, and efforts are continuing to design blades to minimise it. Modelling techniques have been developed to predict the aero-acoustic radiation from this source; see Brooks et al. (1989) and Zhu et al. (2005). Two main methods of reducing the intensity have been considered:

1. Blade profile design to reduce the thickness of the suction surface boundary layer (which, being the thicker of the two, therefore has the larger turbulent eddy scales as well as the greater source layer thickness) at the trailing edge. Some progress has been achieved in reducing this boundary layer's thickness by reducing the strength of the suction pressure on the suction surface while compensating to maintain overall lift and particularly lift/drag ratio by increasing the positive pressure downstream of stagnation on the pressure surface. This method, perhaps because of the constraints involved, has yielded moderate noise reductions of up to about 2 dB. Families of low noise aerofoils have been designed, such as the DTU-LNxxx series shown in Figure 3.78a–c; see also Wang et al. (2015).
2. Making the trailing edge serrated (see Figure 3.79) or by adding flexible ‘brushes’ to it. This concept is based on Howe’s (1991) analysis of the reduction in radiation efficiency of a trailing edge as a result of making it serrated in plan. Although Howe’s theory doesn’t give a very good prediction of the actual sound power reduction that is achieved, nonetheless the technique has been shown to give useful noise reductions of more than 3 db. Serrations of this type appear to be possible without significantly affecting the section lift or drag. They may be part of the outer blade design or have been sometimes in the form of an add-on to existing blades. A good description is given in Zhu et al. (2016).

3.19.5 Other blade noise sources

The remaining three sources of aerodynamic blade self-noise are usually less significant than i) above involving interaction between the turbulent boundary layers and a sharp trailing edge:

- ii) Noise due to locally separated flow is more usual from the inner blade where intensities are limited by low relative velocities. Significant separation is unusual on the outer blade under low to moderate wind conditions for which blade noise may be a concern.
- iii) Noise due vortex shedding from the trailing edge of the blade can be of concern. It should be considered only if the outer blade aerofoil section has a particularly blunt trailing edge. If it occurs, it can be more irritating than purely broadband noise because of the strong tonal content.
- iv) Tip vortex noise does not seem to be particularly well understood but can be minimised by a well-designed tip with appropriate rounding.

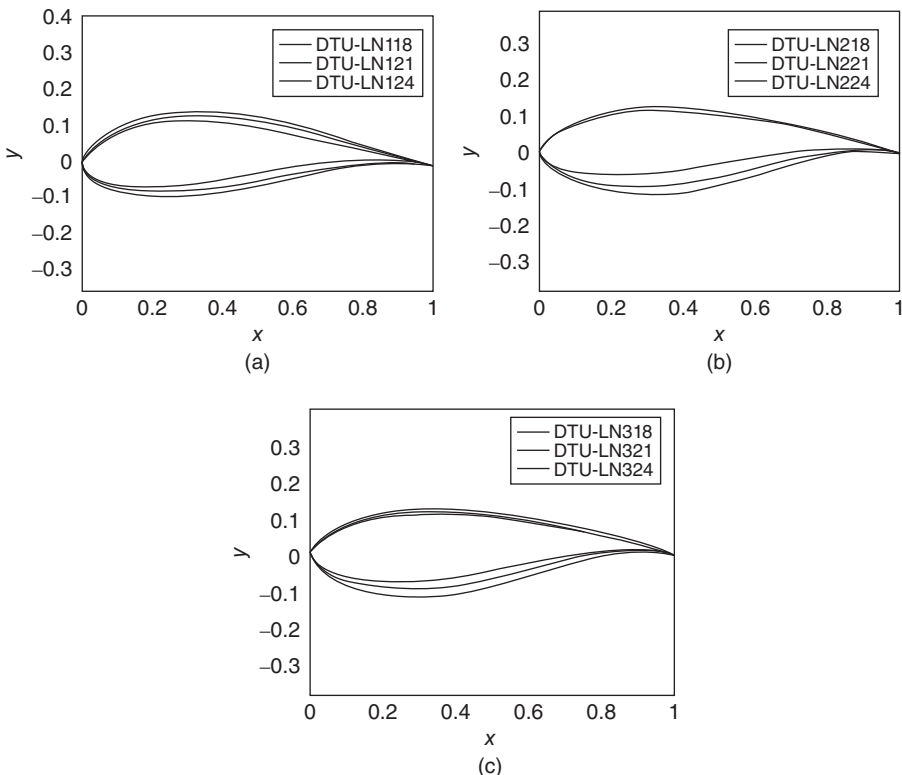


Figure 3.78 Low noise aerofoil family: (a) DTU-LN1xx, (b) DTU-LN2xx, and (c) DTU-LN3xx. Source: From Zhu, Shen, and Soerensen (2016).

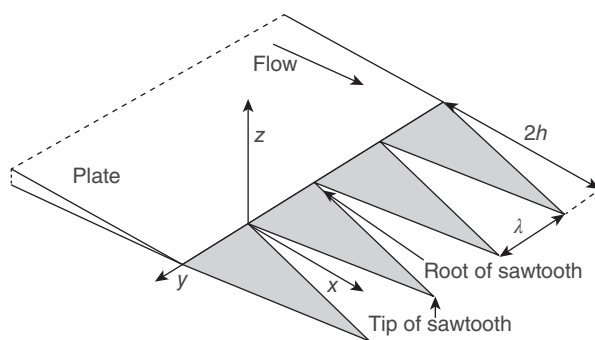


Figure 3.79 Diagram of serrated trailing edge for reduction of TE noise.

3.19.6 Summary

The effect of noise on adjacent populations is the reason for concern about noise. Mainly in the case of wind turbines this concerns human populations. However, underwater

propagation of sound from offshore wind turbines may need to be kept in mind with respect to marine animals but is very unlikely to be as significant as it is for tidal stream turbines. Noise effect on adjacent populations is normally defined by a geographical noise footprint based on contours of perceived noise (PNdB). In drawing these up account has to be taken of the different efficiencies of propagation of noise at different frequencies, in particular that low frequency noise travels much farther than high frequencies, and of the non-uniform sensitivity of the ear over the audible frequency range. Because of the major issues surrounding aircraft noise and the siting of runways, there is a great deal of research published on this.

This Section 3.19 on aerodynamic noise has only attempted to summarise the main issues and research into the subject where it concerns noise arising from wind turbine rotor blades. In practice this is the most important source of noise from a wind turbine, and because noise has become one of the major planning constraints for siting wind turbines, it is likely that the industry will continue considerable effort into the development of methods to suppress it. An excellent reference on the theories describing aerodynamic noise and the sources, radiation, and propagation of sound is the book by Richards and Mead, *Noise and Acoustic Fatigue in Aeronautics* (1968).

References

- Abbott, I.H. and von Doenhoff, A.E. (1959). *Theory of Wing Sections*. USA: Dover Books.
- Amiet, R. (1975). *Acoustic radiation from an aerofoil in a turbulent stream*. *J. Sound Vib.* 41: 407–420.
- Argyle, P., Watson, S., Montavon, C. et al. (2018). *Modelling turbulence intensity within a large offshore wind-farm*. *Wind Energy Res.* <https://doi.org/10.1002/we.2257>.
- Betz, A. (1919). *Schraubenpropeller mit geringstem Energieverlust*. Delft: Gottinger Nachrichten.
- Betz, A. (1920). Das Maximum der theoretisch möglichen Ausnutzung des Windes durch Windmotoren. *Zeitschrift für das gesamte Turbinenwesen* 26: 307–309.
- Brooks, T.F., Pope, D.S., and Marcolini, M.A. (1989). Airfoil self-noise and prediction. *NASA Ref. Pub. 1218*.
- Castro, I.P. (1971). *Wake characteristics of two-dimensional perforated plates normal to an airstream*. *J. Fluid Mech.* 46: 599–609.
- Conway, J.T. (1998). *Exact actuator disc solutions for non-uniform heavy loading and slipstream contraction*. *J. Fluid Mech.* 365: 235–267.
- De Vaal, J.B., Hansen, M.O.L., and Moan, T. (2014). *Effect of wind turbine surge motion on rotor thrust and induced velocity*. *Wind Energy* 17: 105–121. <https://doi.org/10.1002/we.1562>.
- Drela, M. (1989). *X-Foil: an analysis and design system for low Reynolds number Airfoils*. In: *Low Reynolds Number Aerodynamics*, vol. 54 (ed. T.J. Mueller), 1–12. Springer-Verlag Lec. Notes in Eng.
- Eppler, R. (1990). *Airfoil Design and Data*. Berlin: Springer-Verlag.
- Eppler, R. (1993). Airfoil Program System user's guide.
- Fuglsang, P. and Bak, C. (2004). *Development of the Risø wind turbine airfoils*. *Wind Energy* 7: 145–162.
- Gault, D.E. (1957). A correlation of low speed airfoil section stalling characteristics with Reynolds number and airfoil geometry. *NACA Tech. Note 3963*.
- Giguere, P., Dumas, G., and Lemay, J. (1997). *Gurney flap scaling for optimum lift-to-drag ratio*. *AIAA J.* 35: 1888–1890.
- Glauert, H. (1926). The analysis of experimental results in the windmill brake and vortex ring states of an airscrew. *ARC R&M No. 1026*.

- Glauert, H. (1935a). *Airplane propellers*. In: *Aerodynamic Theory*, vol. 4, Division L (ed. W.F. Durand), 169–360. Berlin: Julius Springer.
- Glauert, H. (1935b). *Windmills and fans*. In: *Aerodynamic Theory*, vol. 4, Division L (ed. W.F. Durand), 169–360. Berlin: Julius Springer.
- Goldstein, S. (1929). *On the vortex theory of screw propeller*. *Proc. R. Soc. Lond.* 123: 440.
- Himmelskamp, H. (1945). Profile investigations on a rotating airscrew. Doctoral thesis, Gottingen.
- Hoerner, S.F. (1965). *Pressure drag on rotating bodies*. In: *Fluid-Dynamic Drag*, 3–13. Midland Park, NJ, USA: Hoerner.
- Howe, M.S. (1991). *Noise produced by a saw-tooth trailing edge*. *J. Acoust. Soc. Am.* 90: 482–487.
- Jamieson, P. (2011). *Innovation in Wind Turbine Design*. UK: Wiley.
- Jamieson, P. (2018). *Innovation in Wind Turbine Design*, 2e. UK: Wiley.
- Johnson, S.J., van Dam, C.P., and Berg, D.E. (2008). Active load control techniques for wind turbines. *Sandia Rept.*, SAND2008-4809.
- Joukowski, J.N. (1920). Windmills of the NEJ type. *Transactions of the Central Institute for Aero-Hydrodynamics of Moscow*: 405–430.
- Katz, J. and Plotkin, A. (1991). *Low Speed Aerodynamics: From Wing Theory to Panel Methods*. New York, USA, McGraw-Hill.
- Lanchester, F.W. (1915). *A contribution to the theory of propulsion and the screw propeller*. *Trans. Inst. Naval Architects* 57: 98.
- Lin, C.C. (1955). *The Theory of Hydrodynamic Stability*. UK: Cambridge University Press.
- Lock, C.N.H. (1924). Experiments to verify the independence of the elements of an airscrew blade. *ARCR R&M No. 953*.
- Lynch, C.E. and Smith, M. (2009). A computational study of the aerodynamics and aeroacoustics of a flat-back airfoil using hybrid RANS-LES. ResearchGate, <https://www.researchgate.net/publication/253982002>.
- Madsen, H.A., Mikkelsen, R.F., Oye, S. et al. (2007). *A detailed investigation of the blade element momentum (BEM) model based on analytical and numerical results and proposal for modifications of the BEM model*. *Jnl. Physics Conf. Series* 75: 012016.
- Madsen, H.A., Bak, C., Doessing, M. et al. (2010). *Validation and modification of the blade element momentum theory based on comparisons with actuator disc simulations*. *Wind Energy* 13: 373–389.
- Mikkelsen R.F. (2003). Actuator disc methods applied to wind turbines. PhD thesis, Tech. University of Denmark, Lyngby.
- Moriarty, P.J., Guidati, G., and Migliore, P. (2005). Prediction of turbulent inflow and trailing edge noise for wind turbines. *AIAA paper 2005-2881*.
- Peters, D.A. and Modarres, R. (2013, 2014). A compact closed-form solution for the optimum, ideal wind turbine. *Wind Energy* 17 (4): 589–603. Published online in 2013, <https://doi.org/doi.org/10.1002/we.1592>.
- Richards, E.J. and Meade, D.J. (1968). *Noise and Acoustic Fatigue in Aeronautics*. UK: Wiley.
- Ronsten, G. (1991). Static pressure measurements in a rotating and a non-rotating 2.35 m wind turbine blade. Comparison with 2D calculations. Proceedings of the EWEC '91 Conference, Amsterdam.
- Sharpe, D.J. (2004). *Aerodynamic momentum theory applied to an energy extracting actuator disc*. *Wind Energy* 7: 177–188.
- Shen, W.Z., Mikkelsen, R.F., and Soerensen, J.N. (2005). *Tip-loss corrections for wind turbine computations*. *Wind Energy* 8: 457–475.
- Snel, H., Houwink, R., Bousschers Piers, W.J., van Bussel, G.J.W. and Bruining, A. (1993). Sectional prediction of 3-D effects for stalled flow on rotating blades and comparison with measurements. Proceedings of the EWEC '93 Conference, Lübeck-Travemünde, Germany.
- Soerensen, J.N. and Shen, W.Z. (2002). *Numerical modelling of wind turbine wakes*. *J. Fluids Eng.* 124: 393–399.

- Soerensen, J.N. and van Kuik, G.A.M. (2011). *General momentum theory for wind turbines at low tip speed ratios*. *Wind Energy* 14: 821–839.
- Soerensen, J.N., Shen, W.Z., and Munduate, X. (1998). *Analysis of wake states by a full-field actuator-disc model*. *Wind Energy* 88: 73–88.
- Sørensen, N.N. (1995). General purpose flow solver applied to flow over hills. *Risø-R-827(EN)*.
- Tangler, J. L., and Somers, D. M. (1995). NREL airfoil families for HAWTs. *AWEA '95*, Washington, DC, USA.
- Taylor, G.I. (1944). The air resistance of flat plates of very porous material. *Aero. Res. Council (UK), Rept. & Memo. No. 2236*.
- Timmer, W.A. and van Rooij, R.P.J.O.M. (2003). *Summary of the Delft University wind turbine dedicated airfoils*. *J. Solar Energy Eng.* 125: 488–496.
- Troldborg, N., Soerensen, J.N., and Mikkelsen, R.F. (2006). Actuator line computations of wakes of wind turbines in wind-farms. IEA. Annual Rept. Annex XI Proc. Joint Action on Aerodynamics of Wind Turbines.
- Wagner, S., Bareiss, R., and Guidati, G. (1996). *Wind Turbine Noise*. New York: Springer Verlag.
- Wang, Q., Chen, J.T., Cheng, J.T. et al. (2015). *Wind turbine airfoil design method with low noise and experimental analysis*. *J. Beijing Univ. Aero. Astro.* 41: 23–28. Also as DTU-Orbit: <https://doi.org/10.13700/j.bh.1001-5965.2014.0072>.
- White, F.M. (1991). *Viscous Fluid Flow*. New York: McGraw-Hill.
- Wilson, R.E., Lissaman, P.B.S., and Walker S.N. (1974). Applied aerodynamics of wind power-machines. *Oregon State University, NTIS: PB-238-595*.
- Wimshurst, A. and Willden, R. (2018). *Computational observations of the tip-loss mechanisms experienced by horizontal axis rotors*. *Wind Energy* 21: 792.
- Wood, D.H. (1991). *A three-dimensional analysis of stall-delay on a horizontal-axis wind turbine*. *J. Wind Eng. Ind. Aerodyn.* 37: 1–14.
- Young, A.D. and Squire, H.B. (1938). The calculation of the profile drag of aerofoils. *Aero. Res. Council (UK), Rept. & Memo. No. 1838*.
- Zhu, W.T., Heilskov, N., Shen, W.Z., and Soerensen, J.N. (2005). *Modeling of aerodynamically generated noise from wind turbines*. *J. Solar Energy Eng.* 127: 517–528.
- Zhu, W.T., Shen, W.Z., and Soerensen, J.N. (2016). *Low noise airfoil and wind turbine design*. In: *Wind Turbine Design, Control and Applications*, Ch.3. (ed. A.G. Aissaoui), 55. Intech Open <https://doi.org/10.5772/63335>.

Websites

- <http://www.nrel.gov/wind>
<http://www.nrel.gov/wind/publications.html>
https://wind.nrel.gov/airfoils/Shapes/S809_Shape.html.
<http://www.windpower.org/en>
<http://www.lr.tudelft.nl/live/pagina.jsp?id=9e2f503f-3b65-44bc-aba4-a30033400ea7&lang=en>

Further Reading

- Anderson, J.D. (1991). *Fundamentals of Aerodynamics*, 2e. Singapore: McGraw-Hill.
- Ashill, P.R., Fulker, J.L., and Hackett, K.C. (2005). *A review of recent developments in flow control*. *Aeronaut. J.* 109: 205–232.
- Barnard, R.H. and Philpott, D.R. (1989). *Aircraft Flight: A Description of the Physical Principles of Aircraft Flight*. Singapore: Longman.

- Duncan, W.J., Thom, A.S., and Young, A.D. (1970). *Mechanics of Fluids*, 2e. London: Edward Arnold.
- Eggleston, D.M. and Stoddard, F.S. (1987). *Wind Turbine Engineering Design*. New York: Van Nostrand Reinhold Co.
- Fung, Y.C. (1969). *An Introduction to the Theory of Aeroelasticity*. New York: Dover.
- Hansen, M.O.L. (2000). *Aerodynamics of Wind Turbines*. London: James & James.
- Johnson, W. (1980). *Helicopter Theory*. New York: Dover.
- Manwell, J.F., McGowan, J.G., and Rogers, A.L. (2002). *Wind Energy Explained*. Chichester: Wiley.
- Prandtl, L. and Tietjens, O.G. (1957). *Applied Hydro- and Aeromechanics*. New York: Dover.
- Stepniewski, W.Z. and Keys, C.N. (1984). *Rotary-Wing Aerodynamics*. New York: Dover.

Appendix A3 Lift and drag of aerofoils

The lift and drag of a body immersed in an oncoming flow are defined as the components of force on the body in the directions normal and parallel, respectively, to the incident flow direction.

Dimensional analysis shows that in low-speed, steady flow (that is, flow at low Mach number, so that the relative speed of the flow is much less than the speed of sound), the lift L and drag D may be expressed in the form of non-dimensional parameters, the lift and drag coefficients:

$$C_L = \frac{L}{\frac{1}{2}\rho U^2 A} \text{ and } C_D = \frac{D}{\frac{1}{2}\rho U^2 A}$$

which are both functions of the Reynolds number,

$$Re = \frac{U l}{\nu}$$

of the flow.

Here ρ is the density and ν the kinematic viscosity of the fluid, in this case air, U is the flow speed, l is a characteristic length scale (often the mean chord c), and A is an appropriate area of the body. In the case of aerofoils, wings, or turbine blades, A is usually taken to be the plan-form area s.c, where s is the span of the whole body or of a section of the body on which the force is evaluated. Most '*lifting surfaces*' that are designed to provide lift with minimum accompanying drag, such as the wings of subsonic aircraft and the blades of high tip speed ratio HAWTs, are of high aspect ratio with relatively gradual changes of section (chord c , thickness, camber, and twist) with respect to the spanwise direction. For these bodies the aspect ratio is defined as the span of the blade or wings divided by the mean chord. For aircraft the span is defined as the distance between the two wing tips of the wing pair, but in the case of a wind turbine, the span is the distance from the axis of rotation to the tip of a single blade. Because of the gradual variation of properties along a wing or blade, it is very convenient and in practice sufficiently accurate usually to analyse whole wing or blade forces in terms of the sum of sectional forces and sectional force coefficients. This is taken up in Section A3.8.

This form of non-dimensionalisation is used because it is found that for similar configurations over most regimes involving air (or water), flows of typical speeds and length scales of most practical flows, force coefficients expressed in this way vary relatively slowly

with respect to the other main non-dimensional parameter of the flow, the Reynolds number. Expressing flow-induced forces in term of these coefficients is particularly convenient when testing flows at model scale or comparing forces induced on similar shaped bodies in different fluids or flow speeds. Typical Reynolds numbers relevant to flow around wind turbine blades are of order 10^6 to 10^7 (order 10^5 for small rotors of diameter ~ 1 m). In this context the term ‘low Reynolds number’ is often used to describe flows where the Reynolds number is less than about 10^5 . This regime can occur in wind-tunnel testing of small model turbines. Strictly in fluid dynamics, the term ‘low Reynolds number’ refers to the Stokes flow regime for which the Reynolds number is of order 1 and the flow approximately satisfies the Stokes Equations. It is not relevant here. It should be noted that the factor $\frac{1}{2}$ was not originally in the denominator in the definition of these coefficients but was introduced later in further development of the subjects of fluid dynamics during the twentieth century because of its occurrence in related terms in Bernoulli’s equation for pressure. It is now established in use for all force, pressure, and power coefficient definitions but is not completely universal, being, for example, omitted in US definitions of rotor power and thrust coefficients for helicopters.

A3.1 Drag

Flow-induced forces on a body in a viscous fluid arise from:

1. A tangential stress exerted on the surface, the skin friction, which is caused directly by the viscosity in the fluid coupled with the fact that there cannot be any relative motion of a viscous fluid with respect to the body at its surface, the no-slip condition.
2. A normal stress exerted at the surface, the pressure.

Both types of stress contribute to the drag.

It is convenient to consider the drag exerted on 2-D bodies across a uniform flow, because many general practical bodies are of a configuration that has one long cross-flow dimension such that the flow varies only gradually in that ‘long’ direction. In such cases, 2-D flow is a good local approximation to the flow about any section of the body normal to the long axis. These configurations may be termed *quasi-2-D*. Wind turbine blades and towers are examples of such bodies.

All fluids (with a very few special exceptions, such as liquid helium) have some viscosity, although in the case of two of the most common fluids, air and water, it is relatively small. In the absence of any viscous effect, the flow slips relative to the body at its surface, can be described by a potential function, and is called *potential flow*. The drag in this case on a 2-D body in fully subsonic, steady inviscid flow is exactly zero because no wake is generated.

The action of viscosity is to diffuse vorticity and hence momentum in a way analogous to the diffusion of heat, out from the body surface where the flow is retarded by the no-slip condition, which now applies at the surface. If the fluid has small kinematic viscosity and a comparatively large length scale and velocity so that the Reynolds number is high, the viscous diffusion effects spread outwards at a very much slower speed than the main

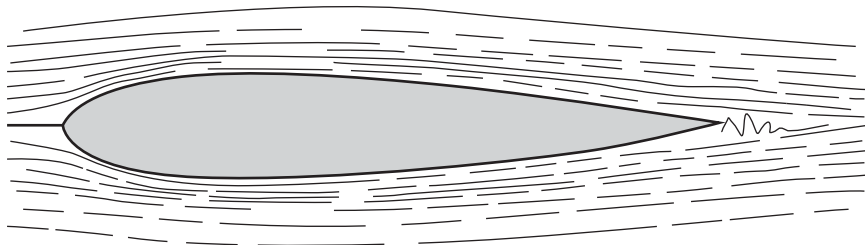


Figure A3.1 Flow past a streamlined body.

velocity convection speed along the body surface and as a result remain confined to a thin layer adjacent to the body surface, the boundary layer.

Generally, bodies are subdivided into two categories: streamlined and bluff. The main characteristics of streamlined bodies (see, e.g. Figure A3.1) are that the boundary layers remain thin over the whole body surface to the rearmost part of the body, where they recombine and stream off in a thin wake and the drag coefficient is comparatively small. Bodies such as wings and rotor blades whose sections are aerofoils are examples. Bodies on which not all of the boundary layers remain attached in this way up to a trailing edge but rather detach at earlier points creating a thick wake are termed *bluff bodies*. The flows around such bodies, for example, circular cylinders and fully stalled aerofoils (see Figure A3.12), result in a comparatively high drag coefficient. More general 3-D bodies may also belong to another category, that of slender bodies (slender in the flow direction), which are not relevant here.

Many practical bodies such as wind turbines or aircraft involve a complex assembly of components that individually belong to the preceding categories. Forces on such bodies are usually calculated by breaking the body down into quasi-2-D elements, and interactions between elements are dealt with, when significant, by interference coefficients. In some cases where it is appropriate to consider sectional flow, such as for the blades of a wind turbine, the flow is not exactly in the plane of the section and may contain a non-zero ‘lengthwise’ or transverse component. It is usual and can be demonstrated that if boundary layer effects are neglected, the pressures and forces on any body section normal to the long axis result from only those flow components that are in the plane of the section and are insensitive to the velocity component parallel to the long axis. This is known as the *independence principle* and holds quite accurately for real attached viscous flows up to angles of yaw between the flow and the long axis from normal flow (0° of yaw) to about 45° of yaw. This covers the usual range for such elements as wind turbine blades. For larger yaw angles than this the independence principle is increasingly in error, and as the yaw angle approaches 90° the flow becomes more like that of a slender body.

A3.2 The boundary layer

The velocity of the flow adjacent to the surface of any solid body, and in particular wind turbine blades and aerofoils, reduces to zero relative to the body at its surface (the no-slip condition) due to viscous stresses in the fluid. At usual flow Reynolds numbers [$O(10^5)$] to

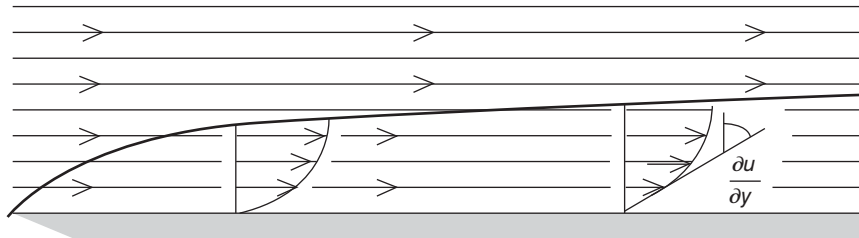


Figure A3.2 Boundary layer showing the velocity profile.

$O(10^8)$] occurring in practice, diffusion is much slower than streamwise convection. As a result nearly all of the change in velocity takes place in very thin regions next the body surface called *boundary layers*, which therefore exhibit a strongly sheared velocity profile; see Figure A3.2. These boundary layers grow in thickness from the attachment point and are shed eventually into the wake of the body. They convect downstream as *free shear layers*, forming a wake where viscous stresses are similarly significant. Outside the boundary layers and wake the flow behaves almost as if inviscid. The integrated streamwise component of the skin friction on the body surface due to the viscous stresses gives rise to an important component of the drag on the body, the *skin friction drag*. The other component is the *pressure drag* (the integrated streamwise component of the normal forces on the body surface). This component is small because the front half streamwise component of the pressures on the body nearly balances the downstream half; the thinner the boundary layer, the nearer they are in balance. The pressure drag is usually similar in size to the skin friction drag for streamlined bodies, such as aerofoils, but becomes much larger if boundary layer separation occurs. The combined skin friction and pressure drag for an aerofoil section in 2-D flow is known as the *profile drag*. The profile drag coefficient of an aerofoil is quite small for these Reynolds numbers while the flow remains attached, depending weakly on the Reynolds number and the angle of attack.

A3.3 Boundary layer separation

The flow over any body, such as a wing, blade, or aerofoil, that generates lift (conventionally regarded as positive ‘upwards’) does so due to the body geometry causing the streamlines of the flow to curve around it (mainly concave downwards) so that downward momentum is added to the vertical component of the momentum in the flow as it exits the influence of the body. The resulting surface pressure distribution can be understood qualitatively by considering the *normal* pressure gradient required to balance the flow curvature. Therefore, the pressure must fall from ambient far away from the aerofoil to a lower value on its upper surface and rise from ambient towards the lower surface. Bernoulli’s equation for energy [e.g. Eq. (3.5a)] shows that decreasing pressure (energy) in a flow must be balanced by increasing kinetic energy, hence increasing velocity, and vice versa. To conserve mass flow rate, higher flow speeds imply streamlines becoming closer together. The general difference in surface flow speed between the upper and lower surfaces of the aerofoil means that any closed circuit integral of flow speed around the body

(termed the *circulation*) is non-zero. Circulation proportional to the lift is as shown by the Kutta–Joukowski theorem, Eq. (A3.1). A more detailed discussion of circulation is given in Section A3.6. The ‘tighter’ the streamline curvature, as round the nose of an aerofoil section at high angle of attack, the greater the fall in surface pressure resulting in a strong suction peak in this region.

The flow approaching a body such as a blade section has one incident streamline that ‘attaches’ at the front stagnation point where the flow speed falls to zero. The flow speed along the streamline’s either side falls to its lowest value close to the body, and pressure there is highest, before the streamline bifurcates, passing either side of the body. Following such a streamline just outside the boundary layer, the flow then rapidly speeds up as it passes over the body surface, to higher values than in the approach flow. Part of this speed-up is due to the effect of the thickness of the body constricting the streamlines and hence increasing flow speed. Part in the case of a body generating lift is due to the fall in pressure associated with the lift or circulation described above. The increase in flow speed on the ‘upper’ or ‘suction’ surface when the body is an aerofoil section at a significant angle of attack to the ambient flow is much greater than on the ‘lower’ or ‘pressure’ surface. Following the suction and velocity peak, the flow on the upper surface must slow down again to reach near-ambient pressure conditions before streaming off into the wake. As the flow slows the pressure rises, and this ‘adverse’ *streamwise* pressure gradient acting on the much reduced momentum in the flow layers very close to the surface within the boundary layers further reduces their momentum, eventually to zero and if strong enough to a reverse flow, although the external flow may not yet have even slowed to ambient; see Figure A3.3. The process is opposed by viscous mixing with higher momentum from the external flow. But if the adverse pressure gradient is strong enough, reversed flow occurs in the boundary layer. This is known as *separation* and the boundary layer *separates* from the surface at that point. The separated region becomes much thicker and dramatically alters the pressure distribution around the body. This strongly affects both the lift force, even causing it to fall abruptly, and the near balance of the front and rear streamwise components of the integrated pressures, causing the pressure drag to increase rapidly to much larger values. The phenomenon is known as the *stall* condition for the aerofoil. A boundary layer that does not separate from the surface before it reaches the downstream end of the surface (the trailing edge on an aerofoil) is termed

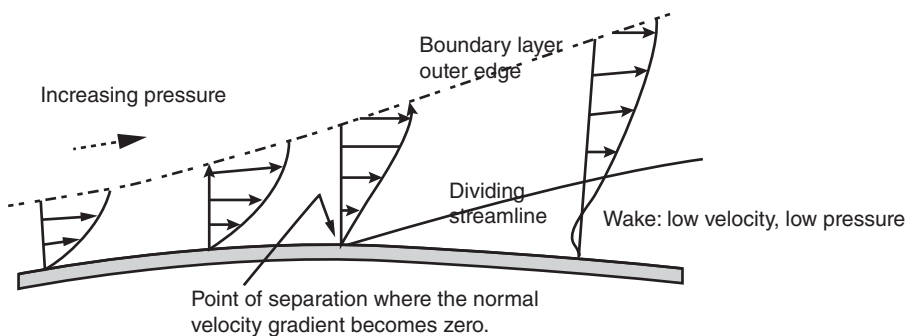


Figure A3.3 Separation of a boundary layer.

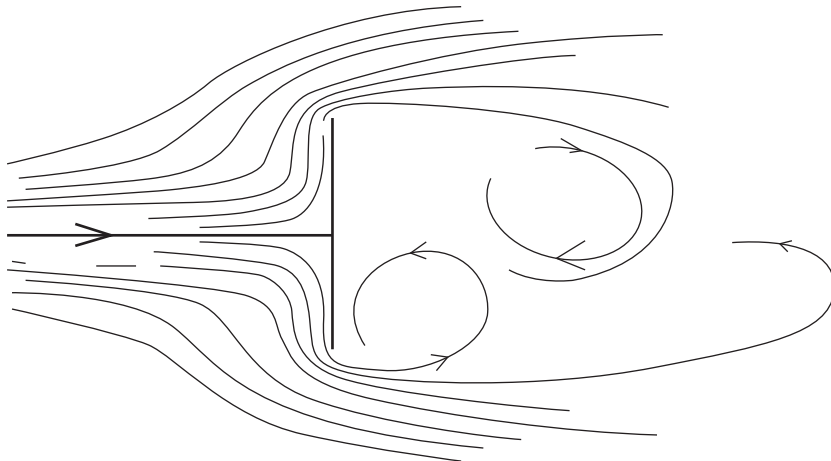


Figure A3.4 Separated flow past a flat plate.

unseparated. It finally sheds (or separates) from this downstream edge by virtue of the sudden change of surface slope. Flow around any sharp edge is not sustainable, because this would generate a very high velocity at the edge followed by an extreme adverse pressure gradient as the flow slows down again. In the case of streamlined (i.e. unseparated) flow over an aerofoil, both surface boundary layers remain unseparated until they meet at the trailing edge, from which they convect together downstream in a thin wake, and the pressure drag remains very small.

On some bluff (i.e. non-streamlined) bodies, the boundary layers separate from different downstream edges and do not meet up, such as is shown in Figure A3.4 for a flat plate normal to the flow. In these cases, as for the cases of boundary layer separation from continuous surfaces, a thick wake results, which often contains large eddying motions, and the pressure drag is high. A sharp edge on a body will *always* cause separation. For the flat plate broad-side onto the flow, Figure A3.4, the boundary layer separates at the sharp edges and C_D is almost independent of Re but *is* dependent upon the plate's aspect ratio.

A3.4 Laminar and turbulent boundary layers and transition

Unless the incident flow contains high intensity, small length scale turbulence, the flow just downstream of the attachment point forms *laminar boundary layers*. Eventually, unless the Reynolds number is rather low, due to boundary layer growth in thickness with downstream distance and the effects of adverse pressure gradient on the velocity profile, laminar boundary layers become unstable, and the instabilities grow into turbulence. This is the *transition point* and downstream of it the boundary layer becomes a *turbulent boundary layer*; see Figure A3.5. The transition point on an aerofoil has a strong influence on the drag of the aerofoil and on the angle of attack at which stall starts to develop. Its location depends strongly on (i) the Reynolds number and boundary layer

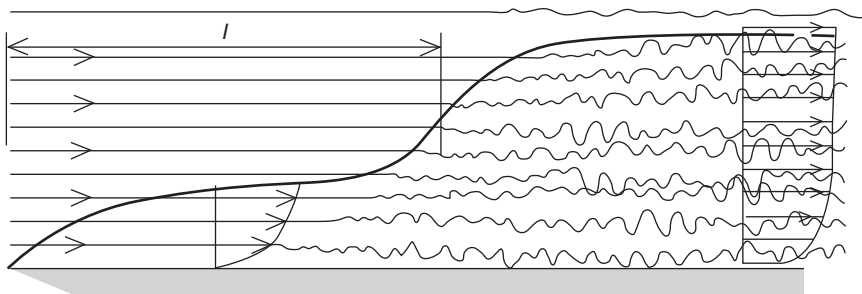


Figure A3.5 Laminar and turbulent boundary layers.

thickness, (ii) the surface pressure distribution, particularly the strength of adverse pressure gradient, (iii) the roughness of the surface, and (iv) the turbulence in the external stream. Points (i) and (ii) being large lead to instability growth, (iii) and (iv) to finite sized disturbances that seed the growth of turbulence. An additional very potent factor (v) in promoting transition is the occurrence of very small regions of separation known as *separation bubbles*. Because a shear layer profile with a point of inflection is in practice immediately unstable, both separation bubbles and laminar boundary layers in the regions of strong adverse pressure gradient just after a very low-pressure peak can be regarded for practical purposes as giving rise immediately to transition unless they have completely separated first. Unfortunately, because of the very small scales involved, direct simulation of transition even on a simple aerofoil profile requires very large computing capacity and in practice simple semi-empirical methods such as the e^n method (where $n \sim 9$, White 1991) are used to predict its occurrence. After transition the boundary layer becomes turbulent and, because of the greatly enhanced mixing that occurs, generates a fuller profile with much higher shear but only within a thin region adjacent to the body surface. The effects of this are to increase the skin friction considerably (therefore the skin friction drag increases and the boundary layer thickens more rapidly) but also to oppose more strongly the effects of adverse pressure gradient in causing separation. Turbulent boundary layers are much more resistant to separation. The outer limit of a boundary layer beyond which viscous shear is negligible is not a precise interface but usually taken as the surface at which the mean velocity has reached 99.5% of the ‘external’ flow velocity. This is a difficult state to define precisely if the external pressure field is varying, as is, for example, the case with the ABL. Also, in the case of a turbulent boundary layer the instantaneous interface is highly corrugated in space and time due to the turbulent eddies.

The coefficient of drag, therefore, in these cases can vary with Reynolds number in a complex fashion. Figure A3.6 shows the classic result for a circular cylinder. At moderate to low Reynolds numbers (small diameters and/or low speeds), the boundary layers remain laminar, and separation takes place just ahead of 90° from the front attachment point. As the Reynolds number increases to a critical value, transition to turbulence that is taking place in the wake moves upstream to the separation point, and the turbulent separated layer immediately reattaches, forming a small separation bubble. Downstream of this is a turbulent boundary layer that does not separate until much further round the cylinder, forming a narrow wake, and the drag coefficient falls abruptly. With further

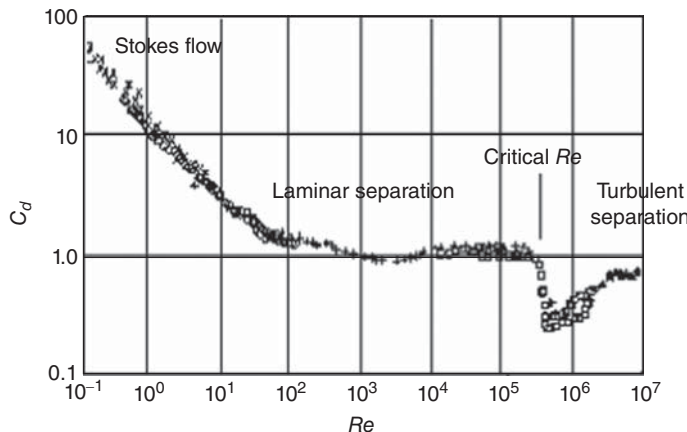


Figure A3.6 Variation of C_d with Re for a long cylinder.

increase of Reynolds number, turbulent separation continues, and the drag coefficient slowly increases again. This effect of Reynolds number on separation and forces is usually less complex on many other types of body, but particularly when separation bubbles are formed; as can happen in many aerofoil stall regimes, the behaviour of the force characteristics with Reynolds number can be complex and abrupt.

Transition to turbulence is highly sensitive to levels of small length-scale turbulence or high frequency acoustic noise in the incident flow (by-pass transition) and to elements or distributed roughness of the body surface. It can be artificially triggered by deliberately roughening the surface or distributing a band of roughness elements or by fixing a ‘trip wire’ to the surface. Insect deposition on the leading edges of wind turbine blades may similarly trigger transition.

Streamlined bodies such as aerofoils taper gently in the aft region so that the adverse pressure gradient is fairly small and separation is delayed until very close to the trailing edge. This produces a very much narrower wake and a very low drag because significant pressure drag is avoided.

On an aerofoil at higher angles of attack, stall onset may be delayed by earlier transition in the suction surface boundary layer. The phenomenon may also include the occurrence of separation bubbles where a laminar separation is followed immediately by transition in the separated shear layer and then turbulent mixing causing reattachment and formation of a ‘bubble’ on the surface. Because of these effects, the onset of turbulence in the boundary layer and particularly the occurrence of separation bubbles controls the angle of attack at which an aerofoil stalls and the type of stall that occurs. Because turbulence in the free stream and surface roughness both tend to promote transition, they can both affect the lift and drag of bodies. In the case of turbulence, the length scale must be small to affect the boundary layer transition. For an aerofoil the effects are particularly influential around the stall region, and on many aerofoils that operate in regions of dirty air close to the ground, it is advisable to periodically clean accumulated dirt or insects from the leading edge regions. More modern designs seek profiles that are relatively insensitive to surface roughness around the leading edge. As on all bodies

on which separated flow occurs, early transition when it delays or suppresses separation reduces the pressure drag.

A useful categorisation of aerofoil stall types is given by Gault (1957).

A3.5 Definition of lift and its relationship to circulation

The lift on a body immersed in a flow is defined as the force on the body in a direction normal to the incident flow direction.

In subsonic steady flow, a body only generates lift if the flow incorporates a circulatory component about the body. The body section is then said to have *circulation*. This type of flow may be illustrated by that which occurs about a spinning circular cylinder in a uniform incident flow field of velocity U . In the resulting flow field, as shown in Figure A3.7, the velocity above the cylinder is increased and the static pressure reduced. Conversely, the velocity beneath is slowed and the static pressure increased. An upwards force on the cylinder results with a strong component normal to the free stream, the lift force.

The phenomenon of lift generated by a spinning cylinder is known as the *Magnus effect* after its original discoverer and explains, for example, why spinning balls veer in flight.

The circulatory component of this flow is shown in Figure A3.8 and has the same distribution of velocity outside the boundary layer as a line vortex.

The lift force due to circulation is given by the Kutta–Joukowski theorem, called after the two pioneering aerodynamicists who, independently, realised that this was the key to the understanding of the phenomenon of lift generated in subsonic flow on all bodies, including the spinning cylinder:

$$L = \rho(\Gamma \times U) \quad (\text{A3.1})$$

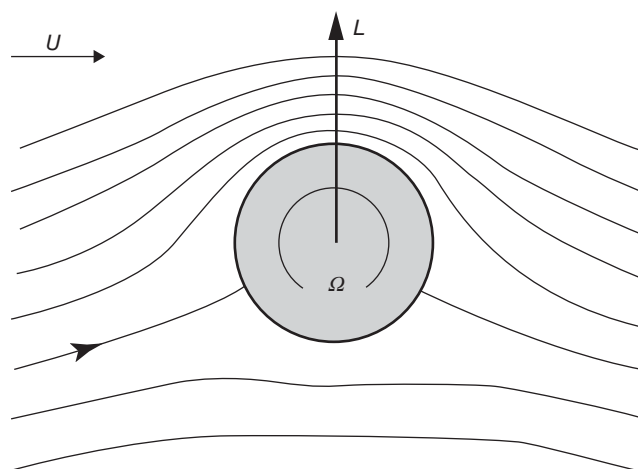


Figure A3.7 Flow past a rotating cylinder.

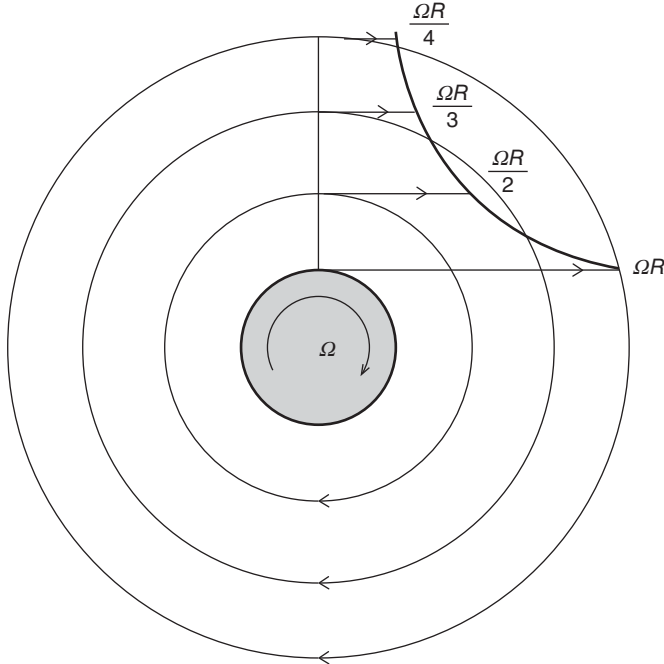


Figure A3.8 Circulatory flow round a rotating cylinder.

Here Γ is the circulation, or vortex strength, defined as the integral

$$\Gamma = \oint v ds \quad (\text{A3.2})$$

around any path enclosing the body, and v is the velocity tangential to the path s .

Two-dimensional inviscid potential flow about a general 2-D body section is non-unique and is only fixed by defining where the flow separates. A non-rotating body can have a circulatory flow about any section, the circulation being controlled by where on the section the boundary layers separate. On an aerofoil section, pre-stall, the sharp trailing edge is the only edge at which the flow separates. Such a flow about an aerofoil as shown in Figure A3.9 can be composed of (i) a non-circulatory flow induced by the approaching free stream, and (ii) a purely circulatory flow that is equivalent to a distribution of vorticity around the section. In general, neither of these flows separate from the trailing edge, i.e. appropriately, but by adding a suitable amount of the latter, thus fixing the circulation, to the former (iii) a composite flow is obtained that does separate from the trailing edge. The condition enforcing separation of the inviscid flow from the trailing edge is known as the *Kutta-Joukowski condition*. At large distances radially from the axis of a (quasi-) 2-D body, the flow field is a combination of the uniform incident flow with a vortex flow if the body has lift (and a line-source flow if it has significant viscous drag.) The v -component of the free stream U in Eq. (A3.2) (and similarly the source flow component if present) integrates around the closed circuit to zero. The v -component due to a line vortex, taken, for example, on a circular path

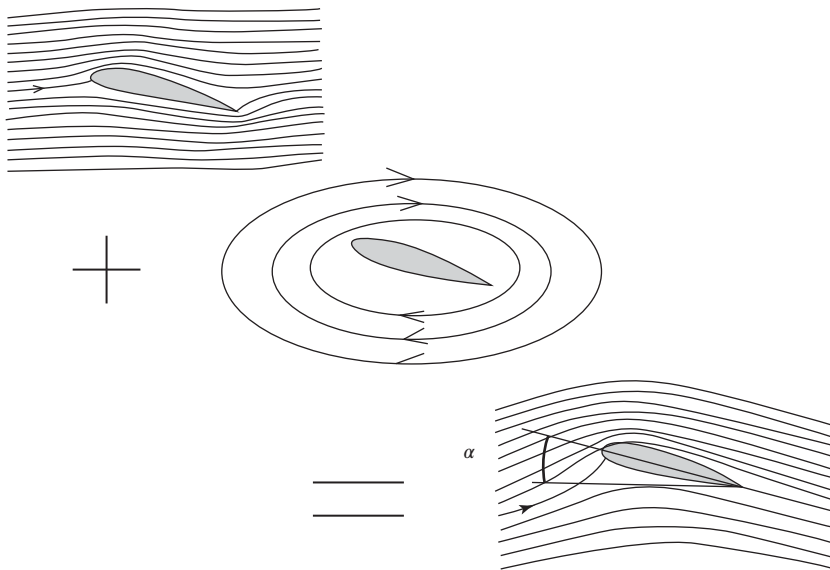


Figure A3.9 Flow past an aerofoil at a small angle of attack: (a) inviscid flow, (b) circulatory flow, and (c) real flow.

concentric with the vortex, is $v = k/r$, where k is a constant. This integrates around the circuit in Eq. (A3.2) to the circulation:

$$\Gamma = 2\pi k$$

(easily seen for circular circuits defined by constant r , but true for all circuits enclosing the vortex). Hence the section lift/unit span is

$$L = 2\pi \rho U k$$

In the case of streamlined lifting bodies such as aerofoils, the circulation Γ that is fixed by the Kutta–Joukowski condition at the trailing edge can be shown to increase with angle of attack α in proportion to $\sin \alpha$. Although the velocities and pressures above and below the aerofoil at the trailing edge must be the same, the particles that meet there are not the same ones that parted company at the leading edge. The particle that travelled over the aerofoil upper surface, even though a longer distance, normally reaches the trailing edge before the one travelling over the shorter lower surface because its speed-up by the circulation is proportionately greater.

In the corresponding case of a real viscous flow, the boundary layers separate at the trailing edge as discussed earlier, very closely approximating this condition. Thus, pre-stall lift on an aerofoil section in real flow is quite accurately predicted by inviscid potential flow analysis. However, inviscid flow analysis does not predict the drag, the inviscid (profile) drag being identically zero because in this case the section of itself generates no wake.

The pressure variation (minus the ambient static pressure of the undisturbed flow) around an aerofoil is shown in Figure A3.10. The upper surface is subject to suction

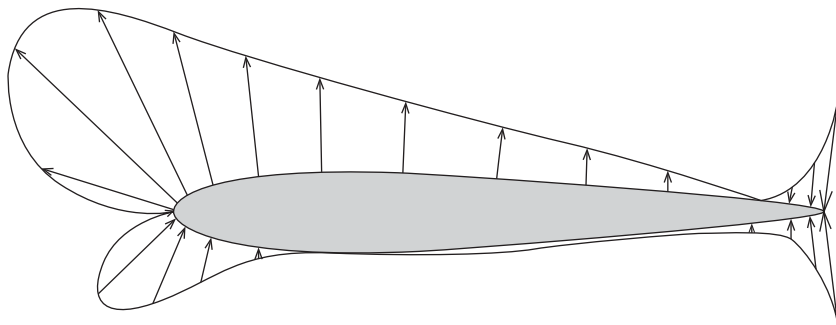


Figure A3.10 The pressure distribution around the NACA0012 aerofoil at $\alpha = 5^\circ$ (shown schematically around the aerofoil).

(with the ambient pressure subtracted) and is responsible for most of the lift force. The pressure distribution is calculated without the presence of the boundary layer because the normal pressure difference across the boundary layer is small enough to be neglected. Higher order, more accurate solutions for the pressures and forces may be obtained by taking account of the effect of the slowed velocity in the boundary layer displacing the streamlines of the quasi-inviscid flow outwards by a small amount like a small thickness addition to the profile.

Figure A3.11 shows the same distribution with the pressure coefficient ($C_p = \frac{p-p_\infty}{\frac{1}{2}\rho U^2}$) plotted against the chordwise coordinate of the aerofoil profile: the full line shows the pressure distribution if the effects of the boundary layer are ignored, and the dashed line shows the actual distribution.

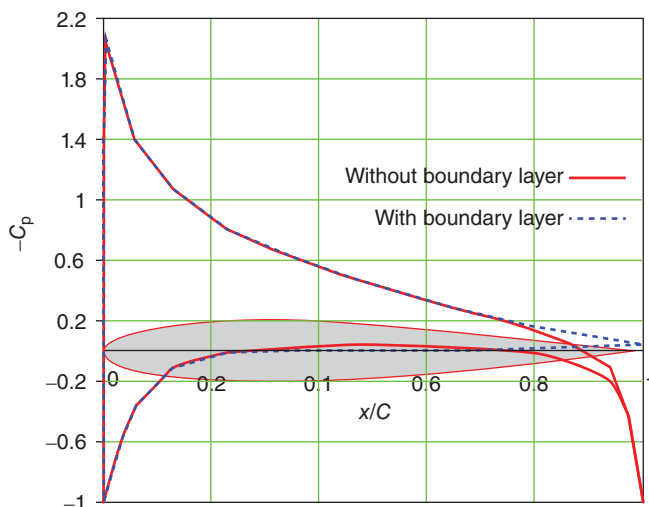


Figure A3.11 The pressure distribution around the NACA0012 aerofoil at $\alpha=5^\circ$ (pressure coefficient C_p vs x/c).

The effect of the boundary layer is to modify the pressure distribution at the rear of the aerofoil such that lower pressure occurs there than if there is no boundary layer. There is no stagnation pressure at the trailing edge, where the pressure tends to be much closer to ambient. The boundary-layer-modified pressure distribution gives rise to pressure drag that is added to the skin friction drag, also caused by the boundary layer.

A3.6 The stalled aerofoil

If the angle of attack exceeds a certain critical value (typically 10° to 16° , depending on the Re), separation of the boundary layer on the ‘suction’ (or upper) surface takes place. A wake forms above the aerofoil starting from this separation (Figure A3.12), and the circulation and hence the lift are reduced and the drag increased. The flow past the aerofoil has then stalled. A flat plate at an angle of attack will also behave like an aerofoil and develop circulation and lift but will stall at a very low angle of attack because of the sharp leading edge. Cambering (or curving) the plate will increase the angle of attack for stall onset, but a much greater improvement can be obtained by giving thickness to the aerofoil together with a suitably rounded leading edge.

A3.7 The lift coefficient

The lift coefficient is defined as

$$C_l = \frac{Lift}{\frac{1}{2}\rho U^2 A} \quad (\text{A3.3})$$

U is the flow speed and A is the plan area of the body. For a long body, such as an aircraft wing or a wind turbine blade, the lift per unit span is used in the definition, the plan area now being taken as the chord length (multiplied by unit span):

$$C_l = \frac{\text{Lift}/\text{unitspan}}{\frac{1}{2}\rho U^2 c} = \frac{\rho(\Gamma \times U)}{\frac{1}{2}\rho U^2 c} \quad (\text{A3.4})$$

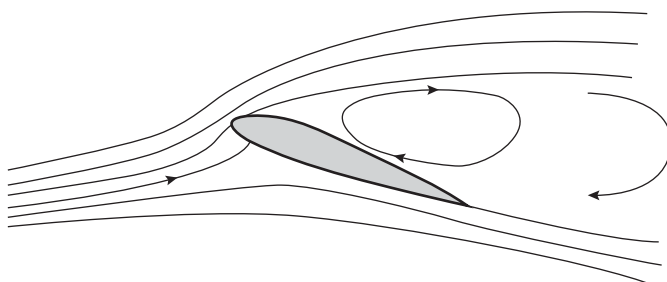


Figure A3.12 Stalled flow around an aerofoil.

In practice it is convenient to write for pre-stall conditions:

$$C_l = a_0 \sin \alpha + C_{l0} \quad (\text{A3.5})$$

where a_0 , called the *lift-curve slope* $\frac{dC_l}{d\alpha}$, is about 6.0 ($\sim 0.1/\text{deg.}$).

Note that a_0 should not be confused with the flow induction factor.

Thin aerofoil potential flow theory shows that for a flat plate or very thin aerofoil, the Kutta–Joukowsky condition is satisfied by

$$\Gamma = \pi U c \sin(\alpha - \alpha_0)$$

where α_0 is the angle of attack for zero lift and proportional to the camber, being negative for positive camber (convex upwards).

Therefore

$$C_l = a_0 \sin(\alpha - \alpha_0)$$

with $a_0 = 2\pi$.

Generally, thickness increases a_0 and viscous effects (the boundary layer) decrease it.

Lift, therefore, depends on two parameters, the angle of attack α and the flow speed U . The same lift force can be generated by different combinations of α and U .

The variation of C_l with the angle of attack α is shown in Figure A3.13 for a typical *symmetrical* aerofoil (NACA0012). Notice that the simple relationship of Eq. (A3.5) is only valid for the pre-stall region, where the flow is attached. Because the angle of attack is small ($< 16^\circ$) the equation is often simplified to

$$C_l = a_0 \alpha + C_{l0} \quad (\text{A3.6})$$

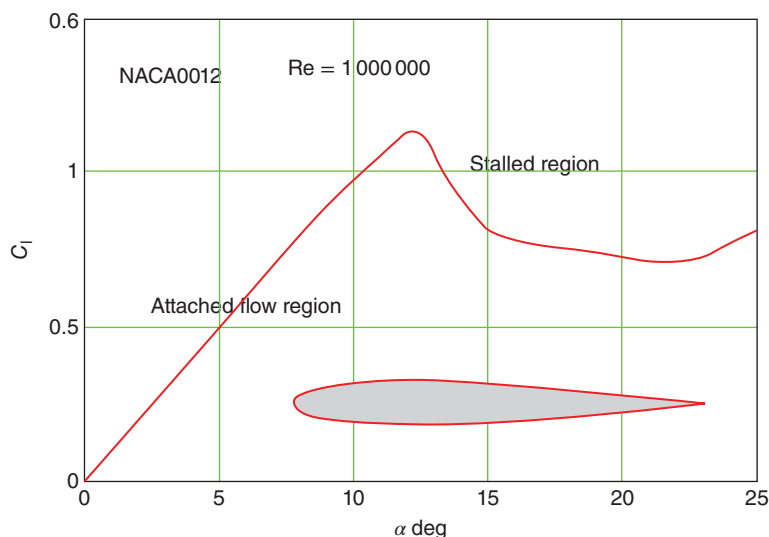


Figure A3.13 $C_l - \alpha$ curve for a symmetrical aerofoil.

The potential velocity and pressure field around aerofoil sections may be calculated using transformation theory (classically) or more usually now by the boundary integral panel method. Many commercial CFD codes also include an option to compute the potential flow calculation by field methods (finite difference, volume or element). The resulting potential flow solution may then be made more realistic, taking into account the effects of the laminar and/or turbulent boundary layers by using the potential flow results for the surface pressure or velocity to drive *boundary layer calculations* of displacement thickness that in turn modify the potential flow as well as providing estimates of drag. Direct methods are used for this while the flow remains unseparated but inverse methods must be used as separation develops. These methods are very efficient computationally and give good results up to angles of attack at which a shallow separation has started the aerofoil stall. Once a large separation has developed (full stall), they become less accurate, and CFD methods (discussed in Chapter 4) must be used. The well-known code XFOIL (Drela 1989) is a widely used example of this type of method. These techniques are discussed in more detail in Katz and Plotkin (1991).

A3.8 Aerofoil drag characteristics

The definition of the drag coefficient for a streamlined body, such as an aircraft wing or a wind turbine blade, because of the relevance of surface friction drag is based not on the frontal area but on the plan area. The flow past a body that has a large span normal to the flow direction is locally quasi-2-D, and in such cases the drag coefficient can be based upon the drag force per unit span using the streamwise chord length for the definition:

$$C_d = \frac{\text{Drag}/\text{unitspan}}{\frac{1}{2}\rho U^2 c} \quad (\text{A3.7})$$

The drag coefficient of an aerofoil varies with angle of attack. For a well-designed aerofoil at moderate to high Reynolds number [$O(10^6)$ – $O(10^7)$], the value of C_d is $O(0.01)$ in the minimum drag range of angle of attack (called the *drag bucket*).

The following sections show some results for two classical NACA four-digit aerofoils that, although not now used except exceptionally for wind turbines, do demonstrate the typical force behaviour of aerofoil sections.

A3.8.1 Symmetric aerofoils

Figure A3.11 shows that on the upper surface pressure is rising as the flow moves from the suction peak towards the trailing edge. This is an adverse pressure gradient that slows the air down. It also thickens the boundary layer more rapidly, causing more velocity momentum to be lost. If the flow *above* (i.e. just off) the surface within the boundary layer is slowed to a standstill, the surface streamlines separate from the surface, stall occurs, and the pressure drag rises sharply. The strength of the adverse pressure gradient increases with angle of attack, and therefore the drag will also rise with angle of attack. Figure A3.14 shows the variation of C_d with α for the symmetrical NACA0012 aerofoil.

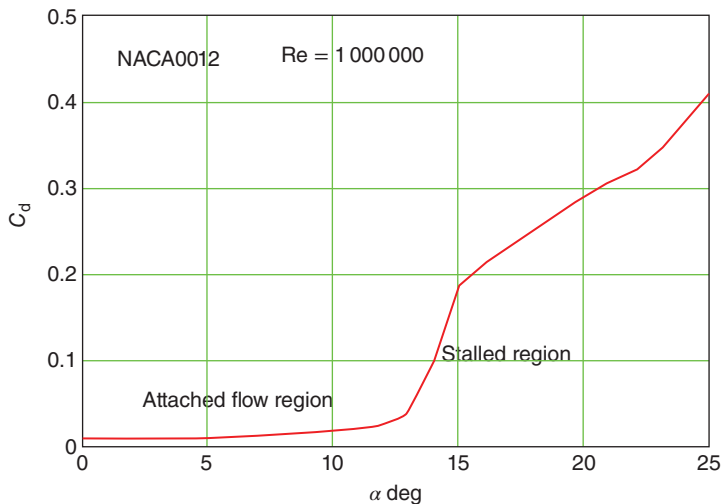


Figure A3.14 Variation of C_d with α for the NACA0012 aerofoil.

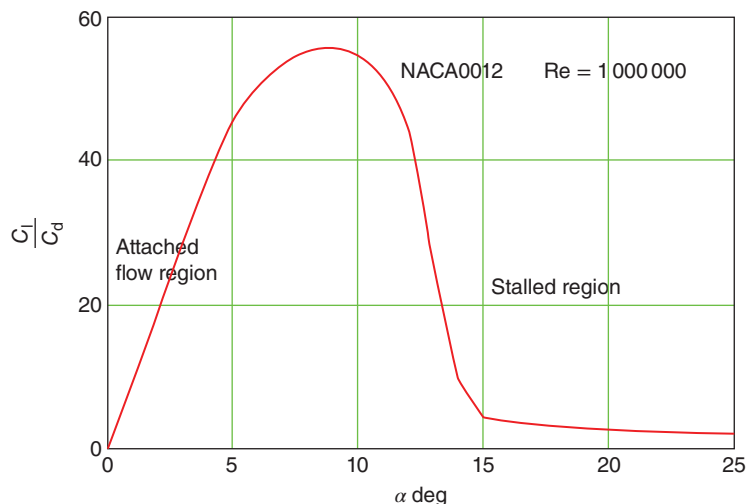


Figure A3.15 Lift/drag ratio variation for the NACA0012 aerofoil.

The efficiency of a wind turbine rotor blade is significantly affected by the lift/drag ratio of its aerofoil section(s) (as shown in Figure A3.15), and it is desirable that a turbine blade operates at the maximum ratio point.

The nature of the flow pattern around an aerofoil is determined by the Reynolds number, and this affects the values of the lift and drag coefficients. The general level of the drag coefficient increases with decreasing Reynolds number. The effect on the lift coefficient is largely concerned with the angle of attack at which stall occurs. Below a

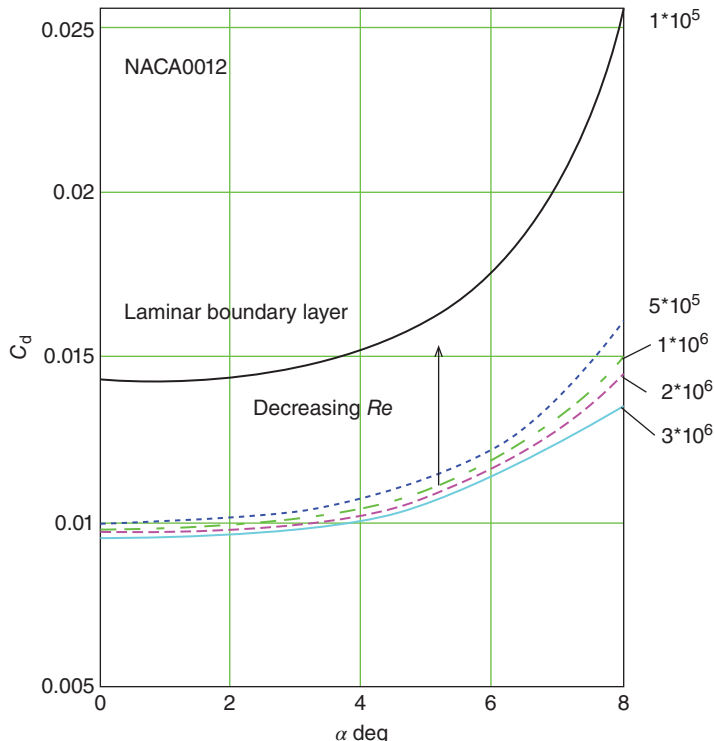


Figure A3.16 Variation of the drag coefficient with Reynolds number at low angles of attack.

critical Reynolds number of about 200 000, the boundary layer remains laminar, usually leading to early stall or partial separation (long bubbles) at low angles of attack.. As the Reynolds number rises, so does the stall angle and, because the lift coefficient increases linearly with angle of attack below the stall, the maximum value of the lift coefficient also rises.

Characteristics for the NACA0012 aerofoil are shown in Figures A3.16 and A3.17.

A3.8.2 Cambered aerofoils

Cambered aerofoils, such as the NACA4412 shown in Figure A3.18, like cambered plates have curved mean lines, and this allows them to produce lift at zero angle of attack.

Generally, cambered aerofoils have their minimum drag range (drag bucket) at angles of attack well above zero. Thus, they are able to attain higher maximum lift/drag ratios than symmetrical aerofoils for positive angles of attack and useful lift coefficients, and this is the reason for their use.

The classification of the NACA four-digit range of aerofoils, which were commonly used on earlier wind turbines, is very simple and is illustrated in Figure A3.19: from left to right, the first digit represents the amount of camber as a percentage of the chord length,

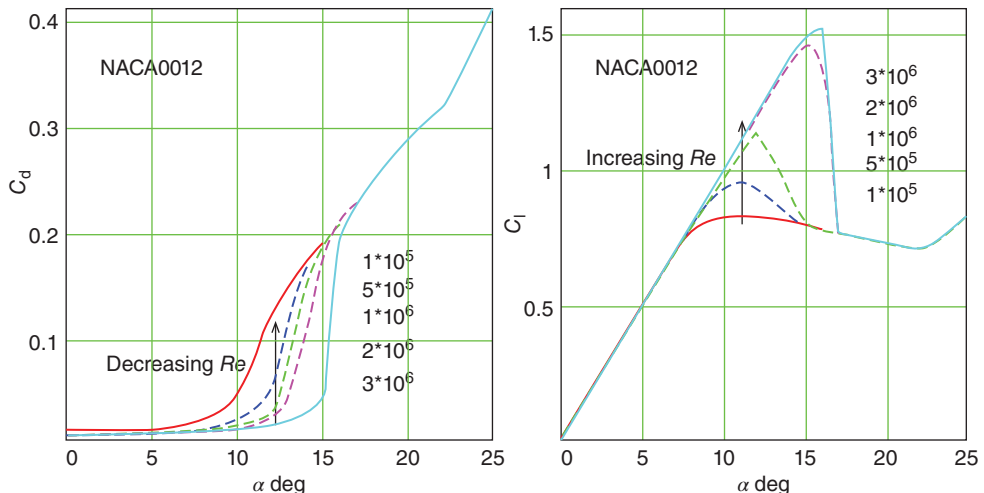


Figure A3.17 Variation of the drag and lift coefficients with Reynolds number in the stall region.

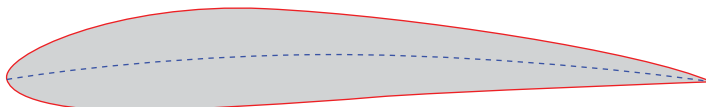


Figure A3.18 The profile of the NACA4412 aerofoil.

the second digit represents the percentage chord position, in units of 10%, at which the maximum camber occurs, and the last two digits are the maximum thickness to chord ratio, as a percentage of the chord length, which, in this family of aerofoils, is at the 30% chord position. The cambered mean line, called the *camber line*, comprises two parabolic arcs that join smoothly at the point of maximum camber. For details of the extensive range of five- and six-digit NACA aerofoils the reader should refer to *Theory of Wing Sections* by Abbott and von Doenhoff (1959).

The angle of attack α is measured from the chord line, which is now defined as the straight line joining the ends of the camber line.

Note that the lift at zero angle of attack is no longer zero; zero lift occurs at a small negative angle of attack. With most cambered aerofoils, the zero lift angle in degrees is approximately equal to $-A^\circ$, where A is the percentage camber.

The behaviour of the NACA4412 aerofoil is shown in Figure A3.20 for angles of attack below and just above the stall. Positive lift occurs at zero angle of attack. Zero lift occurs at a small negative angle of attack of approximately -4° .

The centre of pressure (i.e. the point at which the lift acts), which is at the quarter-chord position on symmetrical aerofoils, lies aft of the quarter-chord position on cambered aerofoils and moves towards the leading edge with increasing angle of attack until the stall. After the stall the centre of pressure on all aerofoils moves

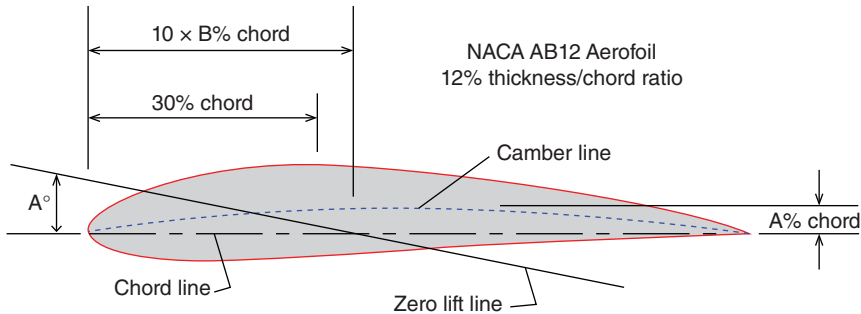


Figure A3.19 Classification of the NACAXXXX aerofoil range.

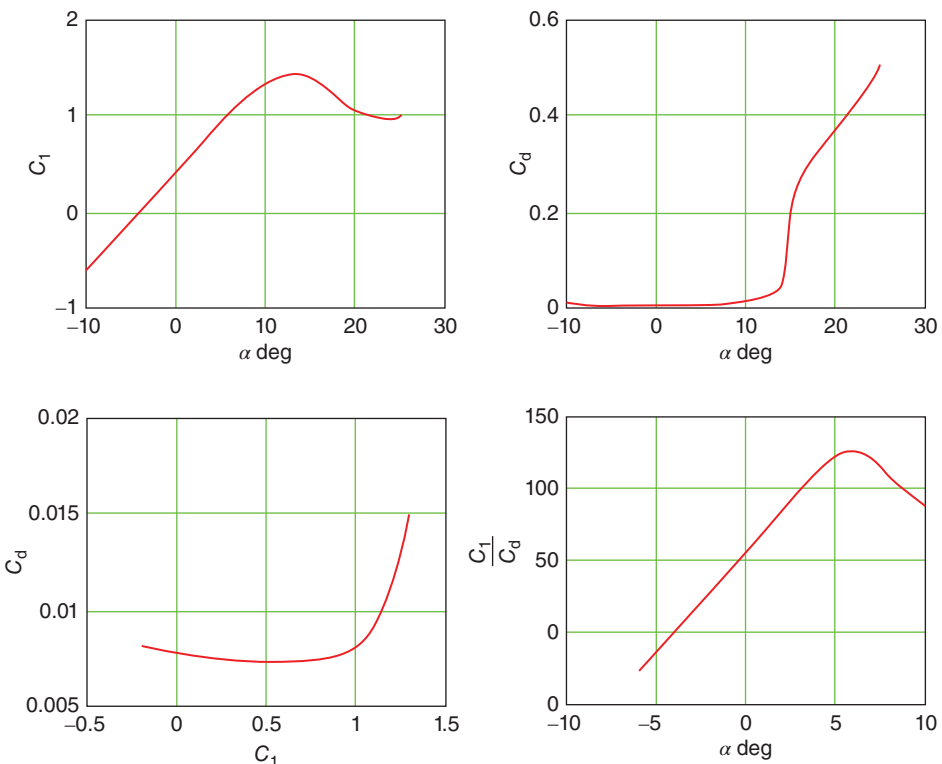


Figure A3.20 The characteristics of the NACA4412 aerofoil for $Re = 1.5 \cdot 10^6$.

rearward towards the midchord. However, if forces are evaluated with reference to a fixed chordwise position, then the resultant force through this point is accompanied by a pitching moment about this point (nose-up positive, by convention). The reference point is usually the quarter-chord point ($c/4$ back from the leading edge), but sometimes it is the midchord and sometimes the torsion axis of the section. If a pitching moment

coefficient is defined as

$$C_m = \frac{\text{Pitching}/\text{unitspan}}{\frac{1}{2}\rho U^2 c^2} \quad (\text{A3.8})$$

then there will be a position, called the *aerodynamic centre*, for which $\frac{dC_m}{dC_l} = 0$. Theoretically, the aerodynamic centre lies at the quarter-chord position and is close to this point for most practical aerofoils.

The value of C_m depends upon the degree of camber, but for the NACA4412 the value is -0.1 . Note that pitching moments are always negative in practice (nose down) despite the sign convention.

Above the stall the pre-stall position of the aerodynamic centre usually continues to be used, although no longer satisfying the above definition.

4

Further aerodynamic topics for wind turbines

4.1 Introduction

Chapter 3 deals with the aerodynamic behaviour of wind turbines in steady wind conditions and with the rotor aligned with the wind direction but, of course, in reality wind turbine rotors operate imperfectly aligned with the wind direction, usually having nose-up tilt for tower clearance and some yaw because the rotor does not follow the wind direction instantaneously as it veers. Chapter 4 deals with rotor–wind misalignment and also with unsteady aerodynamics of the rotor resulting from this misalignment and from other effects that cause rapid changes in the flow conditions. Included in this is the phenomenon of dynamic stall of the blades. The final section of Chapter 4 introduces computational fluid dynamics (CFD) as a predictive tool for wind turbine aerodynamics.

4.2 The aerodynamics of turbines in steady yaw

The rotor axis of a wind turbine rotor is usually not aligned with the wind, as shown in Figure 4.1, because the wind is continuously changing direction. To follow the veering of the wind without imposing excessive accelerations, the yaw control system has a relatively long time constant so that the rotor direction typically lags the wind direction by a few degrees. The yawed rotor is less efficient than the non-yawed rotor and is subject to increased unsteady loading, so it is vital to assess the effects of yaw for purposes of energy production and loads estimation.

In the yawed condition, even in a steady wind, the angle of attack on each blade is continuously changing as it rotates, and so the loads on the rotor blades are fluctuating, causing fatigue damage.

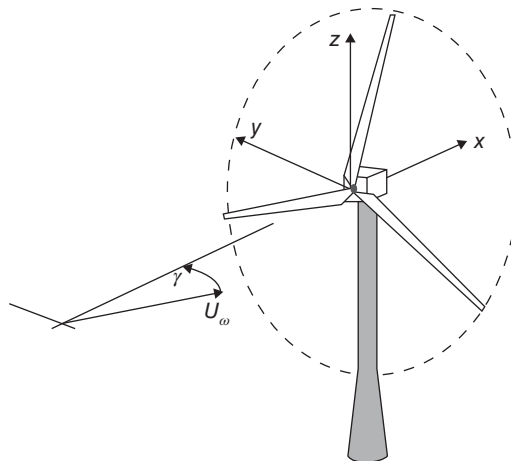


Figure 4.1 A wind turbine yawed to the wind direction.

The changes in angle of attack mean that the blade forces cause not only a thrust in the axial direction but also moments about the yaw (z) axis and the tilt axis.

Even if the rotor is operating with a uniform induced velocity over the rotor disc when aligned with a steady wind, once the rotor is mis-aligned the induced velocity varies both azimuthally and radially, which makes its determination much more difficult.

4.2.1 Momentum theory for a turbine rotor in steady yaw

The application of the momentum theory to an actuator disc representing a yawed rotor is somewhat problematical. The momentum theory is only capable of determining an average induced velocity for the whole rotor disc because it is based on a momentum balance between the rotor and the far wake, which can only be satisfied in an average sense, but in the yawed case the blade circulation is also continuously changing with azimuth position. If it is assumed that the force on the rotor disc, which is a pressure force and so normal to the disc, is responsible for the rate of change of momentum of the flow, then the average induced velocity must also be in a direction at right angles to the disc plane, i.e. in the *axial* direction. The wake is therefore deflected to one side because a component of the induced velocity is at right angles to the wind direction. As in the non-yawed case, ignoring effects of wake expansion, the average induced velocity at the disc is half that in the wake.

Let the rotor axis be held at an angle of yaw γ to the steady wind direction (Figure 4.2). Then, assuming that the rate of change of momentum in the axial direction is equal to the mass flow rate through the rotor disc times the change in velocity normal to the plane of the rotor,

$$T = \rho A_D U_\infty (\cos \gamma - a) 2a U_\infty \quad (4.1)$$

Therefore, the thrust coefficient is

$$C_T = 4a(\cos \gamma - a) \quad (4.2)$$

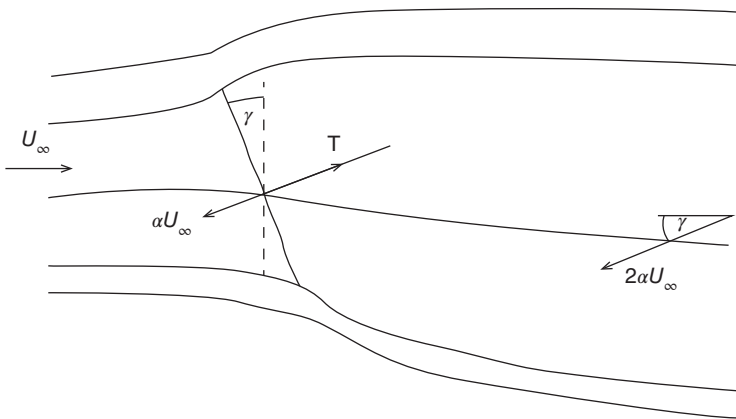


Figure 4.2 Deflected wake of a yawed turbine and induced velocities.

and the power developed is $T U_\infty (\cos \gamma - a)$:

$$C_P = 4a(\cos \gamma - a)^2 \quad (4.3)$$

To find the maximum value of C_P , differentiate Eq. (4.3) with respect to a and set equal to zero, whence

$$a = \frac{\cos \gamma}{3} \text{ and } C_{P\max} = \frac{16}{27} \cos^3 \gamma \quad (4.4)$$

This $\cos^3 \gamma$ rule is commonly adopted for power assessment in yawed flow. Figure 4.3 shows decrease in power as the yaw angle increases.

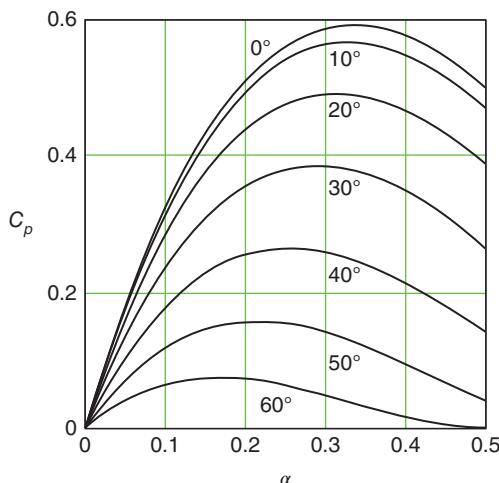


Figure 4.3 Power coefficient variation with yaw angle and axial flow factor.

A question remains: is it legitimate to apply the momentum theory in the above manner to the yawed rotor? Transverse pressure gradients that cause the wake to skew sideways may well also contribute to the net force on the flow in the axial direction, influencing the axial induced velocity. The above analysis might be satisfactory for determining the average axial induced velocity, but there is even less justification to apply the momentum theory to each blade element position than there is in the non-yawed case. If a theory is going to be of any use in design it must be capable of determining the induced velocity at each blade element position to a satisfactory accuracy. The satisfactory calculation of blade forces is as important as the estimation of power.

4.2.2 Glauert's momentum theory for the yawed rotor

Glauert (1926) was primarily interested in the autogyro, which is an aircraft with a freely windmilling rotor to provide lift and a conventional propeller to provide forward thrust. The lifting rotor has a rotational axis that inclines backwards from the vertical, and by virtue of the forward speed of the aircraft, air flows through the rotor disc, causing it to rotate and to provide an upward thrust. Thus, the autogyro rotor is just like a wind turbine rotor in yaw, when in forward flight. At high forward speeds, the yaw angle is large, but in a power-off vertical descent, the yaw angle is zero.

Glauert maintained that at high forward speed the rotor disc, which is operating at a high tip speed ratio, is like a wing of circular plan-form at a small angle of attack (large yaw angle), and so the thrust on the disc is the lift on the circular wing. Simple lifting line wing theory (see Prandtl and Tietjens 1957) gives the result that the down-wash at the wing (equivalent to the induced velocity at a rotor), caused by the trailing vortex system, is uniform over the wing span (transverse diameter of the disc) for an untwisted wing with an elliptical plan-form, and this would include the circular plan-form of the autogyro rotor.

The theory gives the uniform (average) induced velocity as

$$u = \frac{2L}{\pi(2R)^2 \rho V} \quad (4.5)$$

where L is the lift and V is the forward speed of the aircraft.

The lift acts in a direction normal to the effective incident velocity W (see Figure 4.4) and so is not vertical but inclined backwards, the inclination being due to the inclination of the relative velocity W downwards by the wake-induced velocity u . The vertical component of the lift supports the weight of the aircraft, and the horizontal component generates induced drag. In horizontal flight the vertical component of the lift does no work, but the induced drag does do work.

The vector triangles of Figure 4.4 show that

$$D/L = u/W \quad (4.6)$$

The induced velocity u_w in the far wake of the aircraft caused by the trailing vortices is greater than that at the rotor. A certain mass flow rate of air, ρVS , passing through the rotor system, where S is an area yet to be determined that is normal to the incident velocity V , undergoing a downward change in velocity of u_w in the far wake, may be

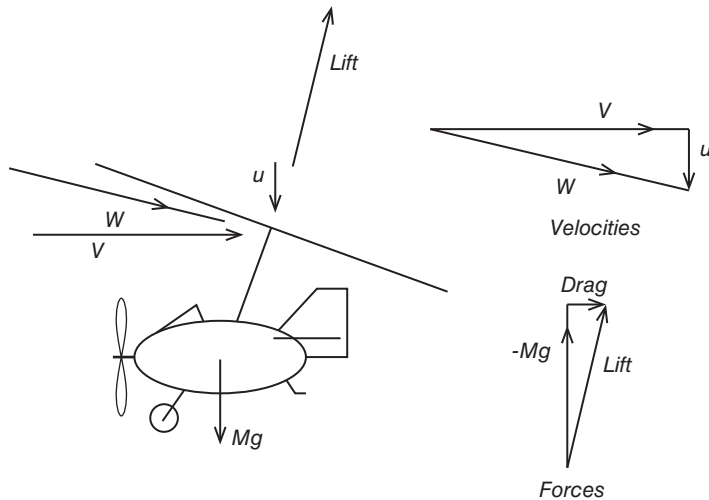


Figure 4.4 Velocities and lift and induced drag forces on an autogyro in fast forward flight.

considered as representative of the varying downflow induced on the whole airstream affected by the rotor. Noting that the lift vector L in Figure 4.4 is normal to the *deflected* velocity W and therefore inclined from the vertical by an angle $\cos^{-1}(V/W)$, equating the vertical force by the momentum theory to the rate of change of downward momentum, therefore,

$$(V/W)L = \rho VS u_w \quad (4.7)$$

Using this representation, the rate of work done by the drag DV must be equal to the rate at which kinetic energy is created in the wake $\frac{1}{2}\rho u_w^2 VS$, because the ambient static pressure in the wake of the aircraft is the same as the pressure ahead of the aircraft:

$$DV = \frac{1}{2}\rho u_w^2 VS \quad (4.8)$$

Combining Eqs. (4.6)–(4.8) gives

$$D = \frac{L^2}{2\rho V^2 S} \quad (4.9)$$

and shows that

$$u_w = 2u \quad (4.10)$$

Equation (4.10) is the same relationship as occurs for non-yawed rotors. Combining Eq. (4.5), the lifting line theory's assessment of the induced velocity at the rotor, with Eq. (4.6) gives

$$D = \frac{2L^2}{\rho V^2 \pi (2R)^2} \quad (4.11)$$

Comparing Eqs. (4.9) and (4.11) leads to an estimate of the effective area S :

$$S = \pi R^2 \quad (4.12)$$

where S has the same area as the rotor disc but is normal to the flight direction.

Note that the above analysis has been simplified by assuming that the angle of attack is small. This model is very much simplified, not only assuming a small angle of attack but also ignoring other small effects such as that the trailing vortices from the rotor are influenced by their own induced velocity and so trail downwards behind the rotor. The drag is termed *induced drag* as it comes about by the backward tilting of the lift force caused by the induced velocity and has nothing to do with viscosity; it is entirely a pressure drag. Because u is small, the angle between V and W is small, and Eq. (4.5) can therefore be modified to replace V by W , the resultant velocity at the disc, and the area S will be in a plane normal to W . Also, W has a direction that lies close to the plane of the rotor, and so the lift force L will be almost the same as the thrust force T , which is normal to the plane of the rotor. By the same argument, the induced velocity is almost normal to the plane of the rotor, and therefore from Eq. (4.5):

$$u = \frac{2T}{\pi \rho W(2R)^2} \quad (4.13)$$

It can be assumed that a wind turbine rotor at high angles of yaw behaves just like the autogyro rotor.

At zero yaw the thrust force on the wind turbine rotor disc, given by the momentum theory, is

$$T = \pi R^2 \frac{1}{2} \rho 4 u (U_\infty - u) \quad (4.14)$$

where wind speed U_∞ now replaces aircraft speed V , so the induced velocity is

$$u = \frac{2T}{\pi \rho (U_\infty - u)(2R)^2} \quad (4.15)$$

The area S now coincides with the rotor disc area.

Putting $W = U_\infty - u$ to represent the resultant velocity of the flow at the disc in Eq. (4.15) gives exactly the same equation as (4.13), which is for a large angle of yaw. On the basis of this argument, Glauert assumed that Eq. (4.13), which is the simple momentum theory, could be applied at all angles of yaw, taking the effective area S through which the mass flow rate is determined, always lying in a plane normal to the resultant velocity as $S = \pi R^2$. This definition of the area S is a crucially different assumption to that of the theory of Section 4.2.1 (which will now be referred to as the axial momentum theory) and allows for part of the thrust force to be attributable to an overall lift on the rotor disc.

Thus

$$T = \rho \pi R^2 2uW \quad (4.16)$$

where

$$W = \sqrt{U_\infty^2 \sin^2 \gamma + (U_\infty \cos \gamma - u)^2} \quad (4.17)$$

Thrust is equal to the mass flow rate times the change in velocity in the direction of the thrust. Both T and u are assumed to be normal to the plane of the disc.

The thrust coefficient is then

$$C_T = 4a\sqrt{1 - a(2 \cos \gamma - a)} \quad (4.18)$$

The power developed is a scalar quantity and can be evaluated from the scalar product of the thrust force vector and the resultant velocity vector W at the disc. Hence, the power coefficient is

$$C_P = 4a(\cos \gamma - a)\sqrt{1 - a(2 \cos \gamma - a)} \quad (4.19)$$

Equation (4.19) gives a slightly larger value of C_P than Eq. (4.3). However, the formulation ignores the components of force and velocity in the plane of the disc, which are in opposite directions and hence imply that the true power is slightly less. It does include a contribution from the lift on the rotor disc acting as on a circular wing that does not extract power from the wind being normal to the modified wind direction W at the disc. Consequently, the axial momentum theory, Eq. (4.3), is more likely to estimate the power extraction correctly, whereas Eq. (4.18) is more likely to estimate the thrust correctly.

The induced velocity through the rotor disc is not uniform, due to the varying streamwise distance between front and back, and this was predicted by Glauert's autogyro theory. The flow through the yawed rotor is depicted in Figure 4.5, and a simplification of the contributions to the velocity normal to the plane of the rotor along the rotor diameter parallel to the flight direction is shown. The mean induced velocity through the rotor, as determined by Eq. (4.13), is shown as u_0 , the normal component of the forward velocity of the aircraft is $U_\infty \cos \gamma$, also uniform over the disc, but, to account for the flow pattern shown, there needs to be a non-uniform component that decreases the normal induced velocity at the leading edge of the rotor disc and increases it at the rear. From symmetry, the induced velocity along the disc diameter normal to the flight direction (normal to the plane of the diagram) is uniform. The simplest form of the non-uniform component of induced velocity would be

$$u_1(r, \psi) = u_1 \frac{r}{R} \sin \psi \quad (4.20)$$

where ψ is the blade azimuth angle measured in the direction of rotation, 0° being when the blade is normal to the flight direction (or when the wind turbine blade is vertically upwards), and u_1 is the amplitude of the non-uniform component, which is dependent on the yaw angle. There would, of course need to be induced velocities parallel to the plane of the rotor disc, but these are of secondary importance; the normal induced velocity has a much greater influence on the blade angle of attack than the in-plane component and therefore a much greater influence on blade element forces.

The value of u_1 in Eq. (4.20) cannot be determined from momentum theory, but Glauert suggested that it would be of the same order of magnitude as u_0 . The total induced velocity, normal to the rotor plane, may then be written as

$$u = u_0 \left(1 + K \frac{r}{R} \sin \psi \right) \quad (4.21)$$

The value of K must depend upon the yaw angle.

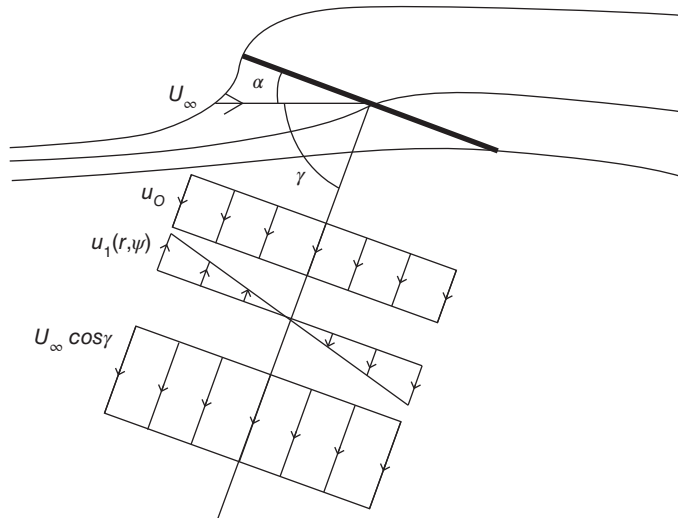


Figure 4.5 Velocities normal to the yawed rotor.

4.2.3 Vortex cylinder model of the yawed actuator disc

The vortex theory for the non-yawed rotor given in Section 3.4 is demonstrated to be equivalent to the momentum theory in its main results but, in addition, was shown to give much more detail about the flow field. As the momentum theories of Sections 4.2.1 and 4.2.2 yield very limited results, using the vortex approach for the yawed rotor may also prove to be useful, giving more flow structure detail than the momentum theory and, perhaps, a means of alloying it with the blade element theory.

The wake of a yawed rotor is skewed to one side because the thrust T on the disc is normal to the disc plane and so has a component normal to the flow direction. The force on the flow therefore is in the opposite sense to T , causing the flow to decelerate upwind and also deflect (i.e. accelerate) sideways. The centre line of the wake will be at an angle χ to the axis of rotation (axis normal to the disc plane), known as the *wake skew angle*. The skew angle will be greater than the yaw angle. The same basic theory as in Section 3.4 can be carried out for an actuator disc with a wake skewed to the rotor axis by an angle χ . There is an important proviso, however, that to be consistent with the simple model in which all of the vorticity shed into the wake is in a sheet on its outer boundary and in a line along its axis, the bound circulation on the rotor disc must be assumed to be radially and azimuthally uniform. As will be demonstrated, the angle of attack of the blades is changing cyclically, and so it would be impossible for the uniform circulation condition ever to be valid. What must be assumed is that the variation of circulation around a mean value has but a small effect on the induced velocity, and the wake is therefore dominated by the vorticity shed from the blade tips by the mean value of circulation (see Figure 4.6).

The expansion of the wake again imposes a difficulty for analysis and so, as before, it will be ignored (Figure 4.7).

The analysis of the yawed rotor was first carried out for purposes of understanding a helicopter rotor in forward flight by Coleman et al. (1945), but it can readily be applied to

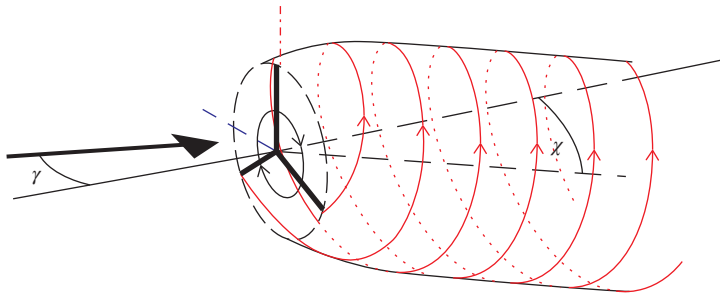


Figure 4.6 The deflected vortex wake of a yawed rotor showing the shed vortices of three blades.

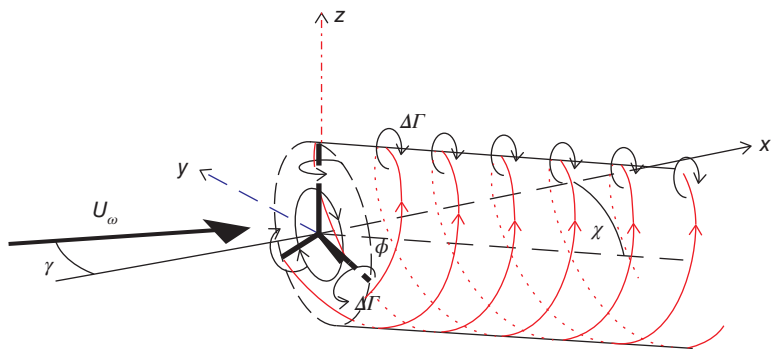


Figure 4.7 A yawed rotor wake without wake expansion.

a wind turbine rotor by reversing the signs of the circulation and the induced velocities. An infinite number of blades is assumed as in the analysis of Section 3.4. The vorticity g_ψ in the ψ direction where ψ is the azimuthal angle remains parallel to the yawed disc, and assuming it to be uniform (not varying with the azimuth angle), using the Biot–Savart law, induces an *average* velocity at the disc of $aU_\infty \sec \frac{\chi}{2}$ in a direction that bisects the skew angle, as shown in Figure 4.8. The average axial induced velocity, normal to the rotor plane, is aU_∞ , as in the non-yawed case. In the fully developed wake, the induced velocity is twice that at the rotor disc.

Because the average induced velocity at the disc is not in the rotor's axial direction, as is assumed for the momentum theory of Sections 4.2.1 and 4.2.2, the force T on the disc, which must be in the axial direction, cannot be solely responsible for the overall rate of change of momentum of the flow; there is a change of momentum in a direction normal to the rotor axis.

The velocity components normal and in-plane at the rotor disc define the skew angle:

$$\tan \chi = \frac{2 \tan \frac{\chi}{2}}{1 - \tan^2 \frac{\chi}{2}} = \frac{U_\infty (\sin \gamma - a \cdot \tan \frac{\chi}{2})}{U_\infty (\cos \gamma - a)} \quad (4.22)$$

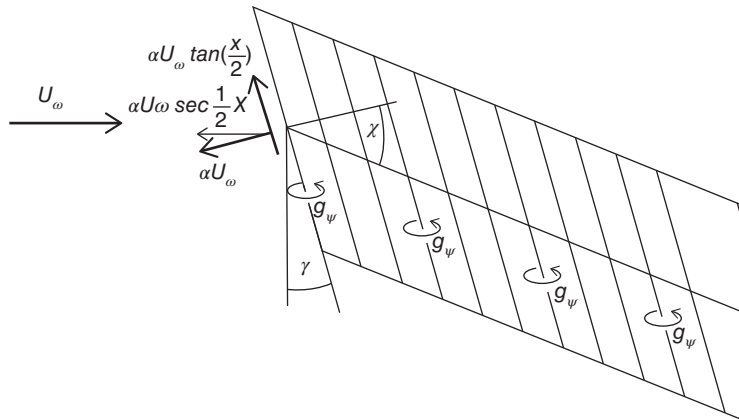


Figure 4.8 Plan view of yawed actuator disc and the skewed vortex cylinder wake.

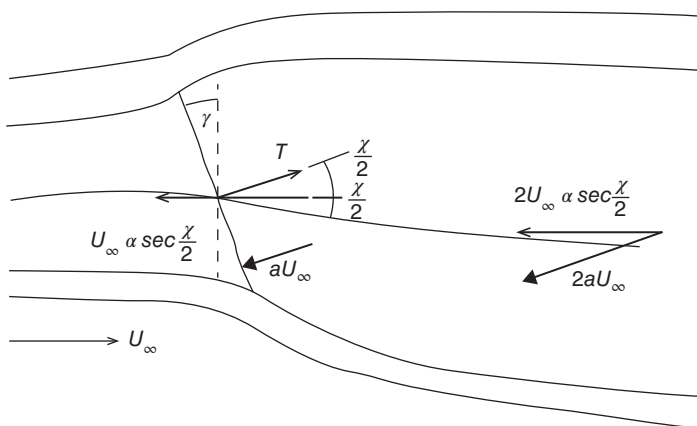


Figure 4.9 Average induced velocities caused by a yawed actuator disc.

From which it can be shown that a close, approximate relationship between χ , γ , and a is

$$\chi = (0.6a + 1)\gamma \quad (4.23)$$

Using the velocities shown in Figure 4.9, a fresh analysis can be made of the flow. The average force on the disc can be determined by applying Bernoulli's equation to both the upwind and downwind regions of the flow, subscript D denoting conditions at the disc:

Upwind

$$p_\infty + \frac{1}{2}\rho U_\infty^2 = p_D^+ + \frac{1}{2}\rho U_D^2$$

Downwind

$$p_D^- + \frac{1}{2}\rho U_D^2 = p_\infty + \frac{1}{2}\rho U_\infty^2 \left[(\cos \gamma - 2a)^2 + \left(\sin \gamma - 2a \tan \frac{\chi}{2} \right)^2 \right]$$

where U_D is the resultant velocity at the disc.

Subtracting the two equations to obtain the pressure drop across the disc,

$$p_D^+ - p_D^- = \frac{1}{2} \rho U_\infty^2 4a \left(\cos \gamma + \tan \frac{\chi}{2} \sin \gamma - a \sec^2 \frac{\chi}{2} \right)$$

The coefficient of thrust on the disc is, therefore,

$$C_T = 4a \left(\cos \gamma + \tan \frac{\chi}{2} \sin \gamma - a \sec^2 \frac{\chi}{2} \right) \quad (4.24)$$

and the power coefficient is

$$C_P = 4a(\cos \gamma - a) \left(\cos \gamma + \tan \frac{\chi}{2} \sin \gamma - a \sec^2 \frac{\chi}{2} \right) \quad (4.25)$$

In a similar manner to the Glauert theory, it is not clear how much of the thrust in Eq. (4.24) is capable of extracting energy from the flow, and so the expression for power in Eq. (4.25) will probably be an overestimate. A comparison of the maximum C_P values derived from the three theories, as a function of the yaw angle, is shown in Figure 4.10.

4.2.4 Flow expansion

The averaged induced velocity component parallel to the axis of the disc has value aU_∞ , as shown in Figure 4.9. The horizontal component of the induced velocity in the plane of the disc is also uniform over the area of the disc with a value $aU_\infty \tan \frac{\chi}{2}$.

In addition to the velocities induced by the cylindrical wake model of Figure 4.9, the expansion of the flow gives rise to velocities in the y and z directions (i.e. directions in a plane normal to the wake axis and therefore at the skew angle χ to the rotor plane; see Figure 4.11). When resolved into the rotor plane, a component of the flow expansion velocities will give rise to a non-uniform normal induced velocity of the type

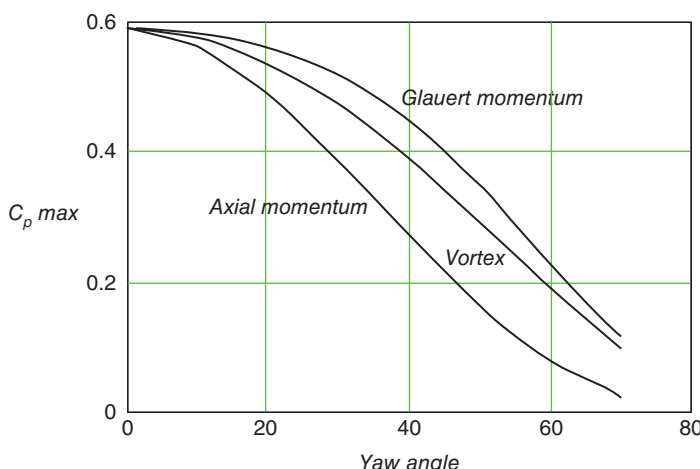


Figure 4.10 Maximum power coefficient variation with yaw angle, comparison of momentum, and vortex theories.

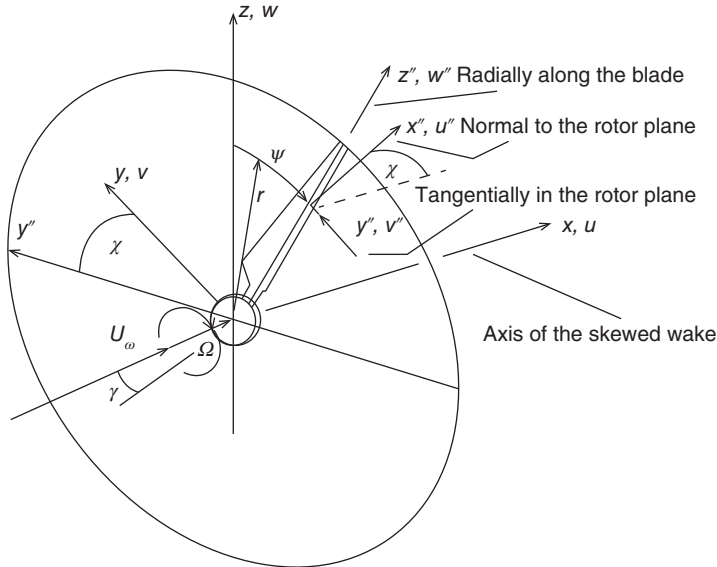


Figure 4.11 Axis system for a yawed rotor.

predicted by Glauert in Eq. (4.21). It should be noted that while wake-induced velocity u is conventionally positive when directed as usual upstream, the convention for perturbation velocities u , v , w as in the following analysis is to follow the sign convention of the incident velocity field, and in particular axial perturbation velocities u , u'' , etc. are positive in the downstream direction.

At a point on the disc at radius r and azimuth angle ψ , defined in Figure 4.11, the induced flow expansion velocities are non-simple functions of r and ψ . Across the horizontal diameter, where $\psi = \pm 90^\circ$, Coleman et al. obtained an analytical solution for the flow expansion velocity in the y direction that involves complete elliptic integrals: the solution is not very practicable because numerical evaluation requires calculating the difference between two large numbers. Simplification of the analytical solution leads to the following expression for the horizontal flow expansion velocity that removes the evaluation difficulty but is not in closed form:

$$v(\chi, \psi, \mu) = \frac{-2aU_\infty\mu \sin \psi}{\pi} \int_0^{\frac{\pi}{2}} \frac{\sin^2 2\epsilon}{\sqrt{(1+\mu)^2 - 4\mu \sin^2 \epsilon}} \frac{1}{(\mu + \cos 2\epsilon)^2 \cos^2 \chi + \sin^2 2\epsilon} d\epsilon \quad (4.26)$$

where $\mu = \frac{r}{R}$, ϵ is the integration variable for the definite (elliptic) integral that arises, and aU_∞ is the average induced velocity as previously defined. An important feature of Eq. (4.26) is that the flow expansion velocity is proportional to the average axial flow induction factor and varies sinusoidally with azimuth angle ψ . Furthermore, if Eq. (4.26) is divided by $\sec^2 \frac{\chi}{2}$, the result is almost independent of the skew angle χ . Let $\frac{v(\chi, \psi, \mu)}{aU_\infty \sec^2 \frac{\chi}{2} \sin \psi}$

be defined as the flow expansion function $F(\mu)$, which is shown in Figure 4.12, clearly demonstrating how little $F(\mu)$ changes over a range of skew angles from 0° to 60° .

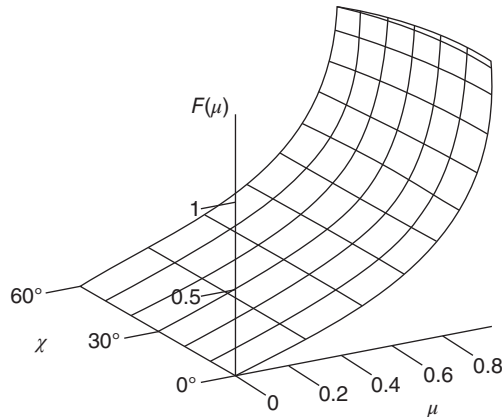


Figure 4.12 Flow expansion function variation with radial position and skew angle.

At all skew angles, the value of the flow expansion function is infinite at the edge of the rotor disc, indicating a singularity in the flow that, of course, does not occur in practice but is a result of assuming uniform blade circulation. Circulation must fall to zero at the disc edge in a smooth fashion.

No analytical expressions for the flow expansion velocity components for values of ψ other than $\pm 90^\circ$ were developed by Coleman et al., but numerical evaluations of the flow expansion velocities can be made using the Biot–Savart law.

The radial variation of the vertical flow expansion velocity across the vertical diameter of the rotor disc is much the same as $F(\mu)$ for skew angles between $\pm 45^\circ$, but outside of this range the vertical velocity increases more sharply than the horizontal velocity at the disc edge. As will be shown, the vertical expansion velocity is of less importance than the horizontal velocity in determining the aerodynamic behaviour of the yawed rotor.

The variation of the horizontal and vertical flow expansion velocities along radial lines on the rotor disc surface at varying azimuth angles (a radius sweeping out the disc surface as it rotates about the yawed rotor axis) shows that some further simplifications can be made for small skew angles.

Figure 4.13 shows the variation of the flow expansion velocities across the rotor disc for a skew angle of 30° . It should be emphasised that the velocity components lie in planes that are normal to the skewed axis of the wake. Inspection of the variations leads to simple approximations for the two velocity components:

$$v(\chi, \psi, \mu) = -aU_\infty F(\mu) \sec^2 \frac{\chi}{2} \sin \psi \quad (4.27)$$

$$w(\chi, \psi, \mu) = aU_\infty F(\mu) \sec^2 \frac{\chi}{2} \cos \psi \quad (4.28)$$

where

$$F(\mu) = \frac{2\mu}{\pi} \int_0^{\frac{\pi}{2}} \frac{\sin^2 2\epsilon}{\sqrt{(1+\mu)^2 - 4\mu \sin^2 \epsilon}} \frac{\cos^2 \chi/2}{(\mu + \cos 2\epsilon)^2 \cos^2 \chi + \sin^2 2\epsilon} d\epsilon \quad (4.29)$$

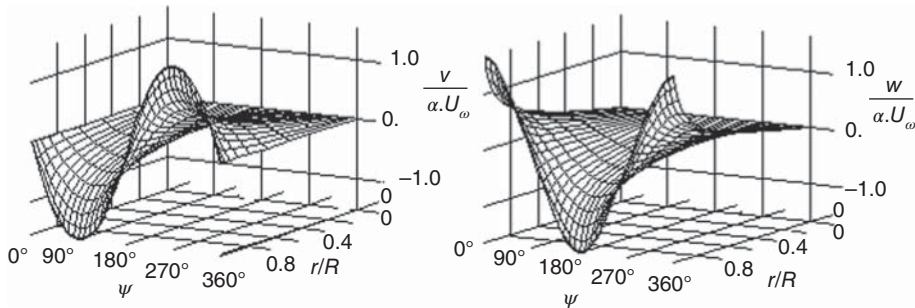


Figure 4.13 Azimuthal and radial variation of horizontal (v) and vertical (w) velocities in the rotor plane for a skew angle of 30° .

The drawback of Eqs. (4.27) and (4.28) is the singularity in the flow expansion function (4.29) at the outer edge of the disc. If the actuator disc is replaced with a rotor that has a small number of blades, then the flow expansion function changes very significantly. Conducting a calculation using the Biot–Savart law for a non-yawed, single bladed rotor represented by a lifting line vortex of radially uniform strength, the flow expansion function can be determined numerically. It is found that the flow expansion velocity along the radial lifting line is a function of the helix (flow) angle of the discrete line vortex shed from the tip of the lifting line (blade). The vortex wake is assumed to be rigid in that the helix angle and the wake diameter are fixed everywhere at the values that pertain at the rotor. The solutions for a single blade rotor can be used to determine the flow fields for multi-blade rotors by a simple process of superposition. The resulting flow expansion functions $F(\mu)_N$ for N blades are depicted in Figure 4.14 for one, two, and three blade rotors.

The radial variations in Figure 4.14 have been extended beyond the rotor radius to show the continuity that exists for the discrete blade situation as compared with the singularity that occurs for the actuator disc. There are two striking features of the flow expansion functions of Figure 4.14: the function is heavily modified by the value of the

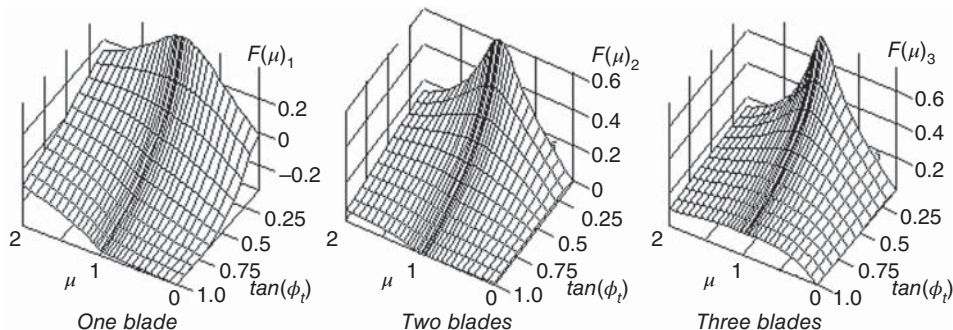


Figure 4.14 Flow expansion functions for one, two and three blade rotors by lifting line theory.

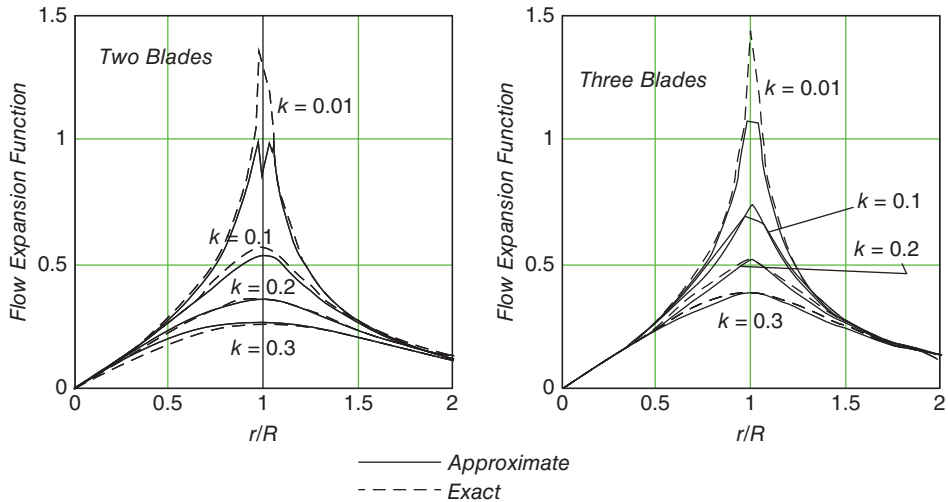


Figure 4.15 Approximate flow expansion functions for two and three blade rotors ($k = \tan \phi_t$).

helix angle ϕ_t , at which the tip vortex is shed from the blade tips, and the negative values (flow contraction) that can occur for the single blade rotor.

An analytical expression that approximates the form of the diagrams shown in Figure 4.14 for two and three bladed rotors is (see Figure 4.15):

$$F_a(\mu, \phi_t, N) = \frac{F(\mu)}{\sqrt{1 + 50 \frac{\tan^2 \phi_t}{N^2} \left(\frac{1}{\tan \phi_t} + 8 \right) F(\mu)^2 [\mu(2 - \mu)F(\mu)]^{0.05 \cot \phi_t}}} \quad (4.30)$$

where $\tan \phi_t = \frac{1-a}{\lambda(1+a)}$ is the tangent of the flow angle.

When transformed as components of velocity with respect to axes rotating about the rotor axis (x'' , y'' , and z'' axes as shown in Figure 4.11), the flow expansion velocities of Eqs. (4.27) and (4.28) are resolved into the components that are normal and tangential to the blade element (see Figure 4.11).

The normal component is

$$u'' = -aU_\infty \left(1 + 2\sin \psi \tan \frac{\chi}{2} F(\mu) \right) \quad (4.31)$$

and the tangential component is

$$v'' = aU_\infty \cos \psi \tan \frac{\chi}{2} \left(1 + 2\sin \psi \tan \frac{\chi}{2} F(\mu) \right) \quad (4.32)$$

to which must be added the components of the wind velocity U_∞ : the normal component,

$$U'' = U_\infty \cos \gamma \quad (4.33)$$

and the tangential component,

$$V'' = -U_\infty \cos \psi \sin \gamma \quad (4.34)$$

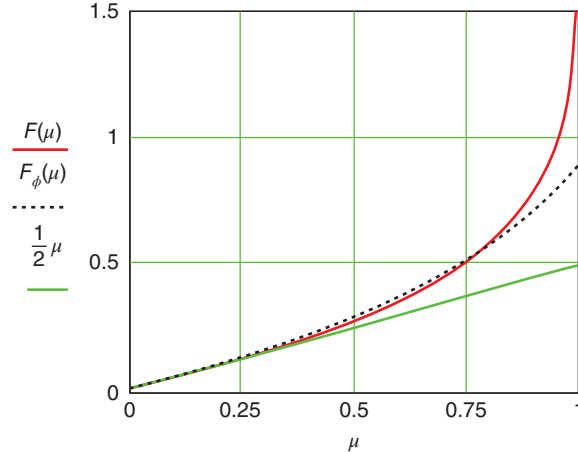


Figure 4.16 Øye's curve fit to Coleman's flow expansion function.

Different implementations use slightly different replacements for the factor $2F(\mu)$ in the above equations depending on how $F(\mu)$ is approximated [see, for example, Figure 4.16 and also Eq. (4.79)].

There is a radial (spanwise) velocity component, but this will not influence the angle of attack so can be ignored.

Clearly, from Eq. (4.31), the Coleman theory determines the function $K_C(\chi)$, see Eq. (4.21), as being

$$K_C(\chi) = 2 \tan \frac{\chi}{2} \quad (4.35)$$

taking $F(\mu) \approx \mu = r/R$ [but see also Eq. (4.36) and Figure 4.16, where another approximation, $F(\mu) \approx 0.5\mu$, which is convenient but less accurate in the outer region, is assumed].

In addition, there is the tangential velocity Ωr due to blade rotation and also the induced wake rotation, but the latter will be ignored initially.

The velocities of Eqs. (4.31)–(4.34) will produce a lower angle of attack when the azimuth angle ψ is positive – see Figure 4.17 – than when it is negative, and so the angle of attack will vary cyclically. When ψ is positive, the incident normal velocity u'' lies closer to the radial axis of the blade than when ψ is negative. The difference in angle of attack can be attributed to flow expansion, as depicted in Figure 4.17.

The variation of the angle of attack makes the flow about a blade aerofoil unsteady, and so the lift will have a response of the kind discussed in Section 4.4. The blade circulation will therefore vary during the course of a revolution, which means that the vortex model is incomplete because it is derived from the assumption that the circulation is constant.

There is clearly additional spanwise vorticity in the wake being shed from the blades' trailing edges as well as azimuthally varying strength in the helical vorticity. Both influence the induced velocity and are not accounted for in the theory. The additional induced velocity would be cyclic so would probably not affect the average induced

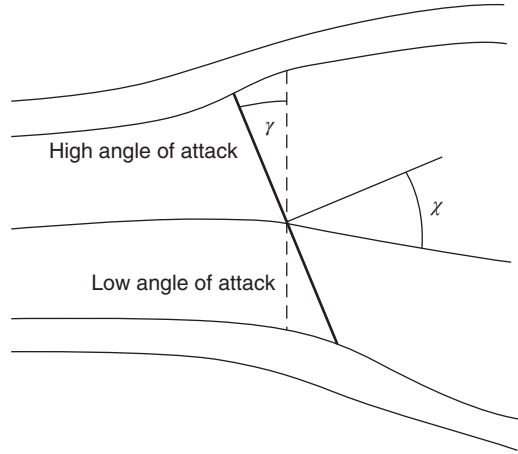


Figure 4.17 Flow expansion causes a differential angle of attack.

velocity normal to the rotor disc but would affect the amplitude and phasing of the angle of attack.

Further numerical analysis of the Coleman vortex theory reveals that at skew angles greater than $\pm 45^\circ$, higher harmonics than just the one per revolution term in Eq. (4.21) become significant in the flow expansion induced velocities. Only odd harmonics are present, reflecting the anti-symmetry about the yaw axis.

4.2.5 Related theories

A number of refinements to the Glauert and Coleman theories have been proposed by other researchers, mostly addressing helicopter aerodynamics, but some have been directed specifically at wind turbines. In particular, Øye (1992) undertook the same analysis as Coleman and proposed a simple curve fit to Eq. (4.29):

$$F_O(\mu) = \frac{1}{2}(\mu + 0.4\mu^3 + 0.4\mu^5) \quad (4.36)$$

Øye has clearly avoided the very large values that Eq. (4.29) produces close to the outer edge of the disc, and Eq. (4.35) is in general accordance with the flow expansion functions shown in Figure 4.14 for typical tip speed ratios.

Meijer Drees (1949) has extended the Coleman et al. vortex model to include a cosinusoidal time variation of blade circulation. The main result is a modification to the function $K_C(\chi)$, but Meijer-Drees retained Glauert's assumption of linear variation of normal induced velocity with radius:

$$u'' = -aU_\infty \left[1 + \frac{4}{3}\mu \left(1 - 1.8 \left(\frac{\sin \gamma}{\lambda} \right)^2 \right) \sin \psi \tan \frac{\chi}{2} \right] \quad (4.37)$$

(see Snel and Schepers 1995).

4.2.6 Wake rotation for a turbine rotor in steady yaw

Wake rotation is, of course, present in the wake flow but under yawed conditions cannot be related only to the torque. The vortex theory must include the root vortex, which will be convected and always lie along the wake axis. The rotation in the wake under yawed conditions will therefore be about the skewed wake axis, which is not the same as the axis of rotation of the rotor. The wake rotation velocity will lie in a plane normal to the skewed wake axis.

To determine the wake rotation velocity, the rate of change of angular momentum about the skewed wake axis will be equated to the moment about the axis produced by blade forces.

If the wake rotation velocity is described, as before, in terms of the angular velocity of the rotor, then

$$\nu''' = \Omega r''' a' h(\psi) \quad (4.38)$$

where the triple prime denotes an axis system rotating about the wake axis, and $h(\psi)$ is a function that determines the intensity of the root vortex's influence. In the non-yawed case, the root vortex induces a velocity at the rotor that is half of what it induces in the far wake at the same radial distance, and the same would apply to a disc normal to the skewed axis with a centre located at the same position as the actual rotor disc. The distance upstream or downstream of a point on the actual rotor disc from a plane through the centre of the disc normal to the wake axis determines the value of the root vortex influence function $h(\psi)$. The value of $h(\psi)$ will be equal to 1.0 at points on the vertical diameter and vary sinusoidally about this value around the azimuth with amplitude up to 1.0 for very large yaw angles.

From the Biot–Savart law, the velocity induced by a semi-infinite line vortex of strength Γ lying along the x axis from zero to infinity at a point with cylindrical coordinates (x''', ψ''', r''') is

$$\vec{V}''' = \frac{\Gamma}{4\pi r'''} \begin{bmatrix} 0 \\ 1 + \frac{x'''}{\sqrt{x''''^2 + r''''^2}} \\ 0 \end{bmatrix} = \begin{bmatrix} 0 \\ v''' \\ 0 \end{bmatrix} \quad (4.39)$$

The induced velocity when $x''' = \infty$ is twice that when $x''' = 0$ and is zero when $x''' = -\infty$.

For a point on the rotor disc $(0, \psi, r)$ the corresponding coordinates (x''', ψ''', r''') in normal disc axes are

$$x''' = -y'' \sin \chi = r \sin \psi \sin \chi, r''' = r \sqrt{\cos^2 \psi + \cos^2 \chi \sin^2 \psi}$$

and

$$\cos \psi''' = \frac{r}{r'''} \cos \psi, \sin \psi''' = \frac{r}{r'''} \sin \psi \cos \chi \quad (4.40)$$

Hence substituting

$$4\pi r''''^2 \Omega a'$$

for the circulation [as in Eq. (3.33)], the induced velocity at the same point is

$$v''' = \Omega r''' a' \left[1 + \frac{x'''}{\sqrt{x'''^2 + r'''^2}} \right] \quad (4.41)$$

So, transforming the velocity of (4.39) to the rotating axes in the plane of the rotor disc:

$$\vec{V} = \begin{bmatrix} 1 & 0 & 0 \\ 0 & \cos \psi & \sin \psi \\ 0 & -\sin \psi & \cos \psi \end{bmatrix} \begin{bmatrix} \cos \chi & \sin \chi & 0 \\ -\sin \chi & \cos \chi & 0 \\ 0 & 0 & 1 \end{bmatrix} \begin{bmatrix} 1 & 0 & 0 \\ 0 & \cos \psi''' & -\sin \psi''' \\ 0 & \sin \psi''' & \cos \psi''' \end{bmatrix} \begin{bmatrix} 0 \\ v''' \\ 0 \end{bmatrix} \quad (4.42)$$

Substituting (4.40) and (4.41) into (4.42) gives

$$\vec{V}'' = \begin{bmatrix} \cos \psi \sin \chi \\ \cos \psi \\ 0 \end{bmatrix} \Omega r a' (1 + \sin \psi \sin \chi) \quad (4.43)$$

Thus, the wake rotation produces two velocity components, one in the rotor plane and one normal to the rotor plane; there is no radial component.

4.2.7 The blade element theory for a turbine rotor in steady yaw

There is doubt about the applicability of the blade element theory in the case of a yawed turbine because the flow, local to a blade element, is unsteady and because the theory representing the vortex half of the equation, which replaces the momentum theory, is incomplete in this respect. However, it is not clear how large or significant the unsteady forces are. In a steady yawed condition, the flow velocities in a fixed earth frame at a fixed point on the rotor disc do not change with time, if an infinity of blades is assumed, and so there is no effect to consider. However, the change of angle of attack with time at a point on the blade does mean that the two-dimensional (2-D) lift force should really be modified by an unsteady lift function similar to that determined by Theodorsen (1935) for the rectilinear wake of a sinusoidally pitching aerofoil.

Neglecting the effects of shed vorticity, the net velocities in the plane of a local blade element are shown in Figure 4.18. The radial (spanwise) velocity component is not shown in Figure 4.18, but it is neglected because it is not considered to have any influence on the angle of attack and therefore on the lift force.

The flow angle ϕ is then determined by the components of velocity shown in Figure 4.18:

$$\begin{aligned} \tan \phi &= V_x / V_y \\ V_x &= U_\infty (\cos \gamma - a(1 + F(\mu)K(\chi)) \sin \psi) + \Omega r a' \cos \psi \sin \chi (1 + \sin \psi \sin \chi) \\ V_y &= \Omega r (1 + a' \cos \chi (1 + \sin \psi \sin \chi)) \\ &\quad + U_\infty \cos \psi \left(a \cdot \tan \frac{\chi}{2} (1 + F(\mu)K(\chi)) \sin \psi - \sin \gamma \right) \end{aligned} \quad (4.44)$$

where $\mu = \frac{r}{R}$ is measured radially from the axis of rotor rotation.

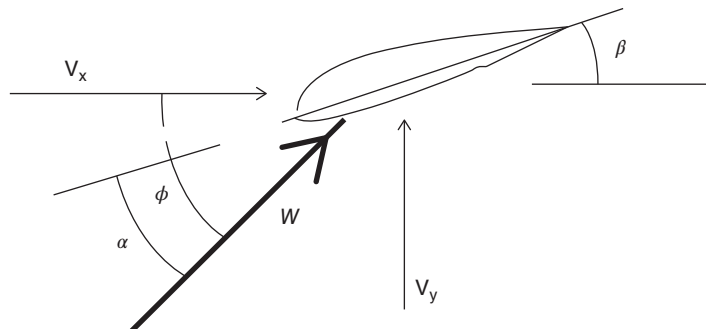


Figure 4.18 The velocity components in the plane of a blade cross-section.

The angle of attack α is found from

$$\alpha = \phi - \beta \quad (4.45)$$

Lift and drag coefficients taken from 2-D experimental data, just as for the non-yawed case, are determined from the angle of attack calculation for each blade element (each combination of μ and ψ).

4.2.8 The blade-element-momentum theory for a rotor in steady yaw

The forces on a blade element can be determined via Eqs. (4.44) and (4.45) for given values of the flow induction factors.

The thrust force will be calculated using Eq. (3.46) in Section 3.5.2, which is for a complete annular ring of radius r and radial thickness δr :

$$\delta L \cos\phi + \delta D \sin\phi = \frac{1}{2} \rho W^2 B c (C_l \cos\phi + C_d \sin\phi) \delta r$$

For an elemental area of the annular ring swept out as the rotor turns through an angle $\delta\psi$, the proportion of the force is

$$\delta F_b = \frac{1}{2} \rho W^2 B c (C_l \cos\phi + C_d \sin\phi) \delta r \frac{\delta\psi}{2\pi}$$

Then putting $C_x = C_l \cos\phi + C_d \sin\phi$ and $\sigma_r = B c / (2\pi r)$:

$$\delta F_b = \frac{1}{2} \rho W^2 \sigma_r C_x r \delta r \delta\psi \quad (4.46)$$

Using mean values of C_l and C_d here assumes quasi-steady behaviour and neglects unsteady effects due to the ever-changing blade circulation with azimuth angle, which will depend upon the level of the reduced frequency of the circulation fluctuation.

Unsteady effects become significant if the reduced frequency, $k = \pi f c / W$, is greater than about 0.05. Here f is the frequency (Hz) of the unsteady flow, which in this case is the rotation frequency, and W is the time-mean relative velocity at a blade section. This value can be easily exceeded as the blades rotate through the wind shear.

If it is chosen to ignore drag, or uses only that part of the drag attributable to pressure, then Eq. (4.46) should be modified accordingly.

The rate of change of momentum will use either Eq. (4.18), Glauert's theory, or Eq. (4.24), the vortex cylinder theory; in both equations, the flow induction factor a should be replaced by af to account for Prandtl tip-loss.

For Glauert's theory,

$$\delta F_m = \frac{1}{2} \rho U_\infty^2 4af \sqrt{1 - af(2 \cos \gamma - af)} r \delta \psi \delta r \quad (4.47)$$

Or, for the vortex theory,

$$\delta F_m = \frac{1}{2} \rho U_\infty^2 4af \left(\cos \gamma + \tan \frac{\chi}{2} \sin \gamma - af \sec^2 \frac{\chi}{2} \right) r \delta \psi \delta r \quad (4.48)$$

The algebraic complexity of estimating the wake rotation velocities is great, and even then fluctuation of bound circulation is ignored. The drop in pressure caused by wake rotation, however, is shown to be small in the non-yawed case, except where the speed ratio is small, and so it is assumed that it can safely be ignored in the yawed case.

The moment of the blade element force about the wake axis is

$$\delta M_b = \frac{1}{2} \rho W^2 B c (C_y \cos \chi - C_x \cos \psi \sin \chi) r \delta r \frac{\delta \psi}{2\pi} \quad (4.49)$$

where

$$C_y = C_l \sin \phi - C_d \cos \phi$$

therefore,

$$\delta M_b = \frac{1}{2} \rho W^2 \sigma_r (C_y \cos \chi - C_x \cos \psi \sin \chi) r^2 \delta r \delta \psi \quad (4.50)$$

The rate of change of angular momentum is the mass flow rate through an elemental area of the disc times the tangential velocity times radius.

$$\delta M_m = \rho U_\infty (\cos \gamma - af) r \delta \psi \delta r 2a' f \Omega r'''^2 \quad (4.51)$$

where

$$r'''^2 = r^2 (\cos^2 \psi + \cos^2 \chi \sin^2 \psi)$$

therefore,

$$\delta M_m = \frac{1}{2} \rho U_\infty^2 \lambda \mu 4a' f (\cos \gamma - af) (\cos^2 \psi + \cos^2 \chi \sin^2 \psi) r^2 \delta r \delta \psi \quad (4.52)$$

The momentum theory, as developed, applies only to the whole rotor disc where the flow induction factor a is the average value for the disc. However, it may be argued that it is better to apply the momentum equations to an annular ring, as in the non-yawed case, to determine a distribution of the flow induction factors varying with radius, reflecting radial variation of circulation. Certainly, for the angular momentum case the tangential flow factor a' will vary little with azimuth position because it is generated by the root vortex and although, in fact, the axial flow factor a does vary with azimuth angle, it is consistent to use an annular average for this factor as well.

To find an average for an annular ring, the elemental values of force and moment must be integrated around the ring.

For the axial momentum case, taking the vortex method as an example,

$$\int_0^{2\pi} \frac{1}{2} \rho U_\infty^2 4af \left(\cos \gamma + \tan \frac{\chi}{2} \sin \gamma - af \sec^2 \frac{\chi}{2} \right) \delta\psi r \delta r = \sigma_r \int_0^{2\pi} \frac{1}{2} \rho W^2 C_x \delta\psi r \delta r \quad (4.53)$$

Therefore,

$$8\pi af \left(\cos \gamma + \tan \frac{\chi}{2} \sin \gamma - af \sec^2 \frac{\chi}{2} \right) = \sigma_r \int_0^{2\pi} \frac{W^2}{U_\infty^2} C_x d\psi \quad (4.54)$$

The resultant velocity W and the normal force coefficient C_x are functions of ψ .

(Note that care is required solving Eq. (4.54) because iteration can result in complex roots for a .)

And for the angular momentum case

$$\begin{aligned} & \int_0^{2\pi} \frac{1}{2} \rho U_\infty^2 \lambda \mu 4a' f (\cos \gamma - af) (\cos^2 \psi + \cos^2 \chi \sin^2 \psi) r^2 d\psi \delta r \\ &= \int_0^{2\pi} \frac{1}{2} \rho W^2 (C_y \cos \chi - C_x \sin \chi \cos \psi) r^2 d\psi \delta r \end{aligned} \quad (4.55)$$

which reduces to

$$4a'f(\cos \gamma - af)\lambda\mu\pi(1 + \cos^2 \chi) = \sigma_r \int_0^{2\pi} \frac{W^2}{U_\infty^2} (C_y \cos \chi - C_x \sin \chi \cos \psi) d\psi \quad (4.56)$$

The non-dimensionalised resultant velocity relative to a blade element is given by

$$\begin{aligned} \frac{W^2}{U_\infty^2} &= [\cos \gamma - a + \lambda\mu a' \sin \chi \cos \psi (1 + \sin \chi \sin \psi)]^2 \\ &+ \left[\lambda\mu (1 + a' \cos \chi (1 + \sin \chi \sin \psi)) + \cos \psi \left(a \tan \frac{\chi}{2} - \sin \gamma \right) \right]^2 \end{aligned} \quad (4.57)$$

Note that the flow expansion terms, those terms that involve $F(\mu)K(\chi)$ in Figure 4.18, have been excluded from the velocity components in Eq. (4.57) because flow expansion is not represented in this wake model, and so there is no associated momentum change. The blade force, which arises from the flow expansion velocity, is balanced in the wake by pressure forces acting on the sides of the streamtubes, which have a streamwise component because the streamtubes are expanding.

Equations (4.51) and (4.56) can be solved by iteration, the integrals being determined numerically. Initial values are chosen for a and a' , usually zero. For a given blade geometry, at each blade element position μ and at each blade azimuth position ψ , the flow angle ϕ is calculated from Eq. (4.44), which has been suitably modified to remove the flow expansion velocity, in accordance with Eq. (4.57). Then, knowing the blade pitch angle β at the blade element, the local angle of attack can be found. Lift and drag coefficients are obtained from tabulated aerofoil data. Once an annular ring (constant μ) has been completed, the integrals are calculated. The new value of axial flow factor a is determined from Eq. (4.54), and then the tangential flow factor a' is found from Eq. (4.56).

Iteration proceeds for the same annular ring until a satisfactory convergence is achieved before moving to the next annular ring (value of μ). As written, Eq. (4.54) is quadratic in a on the left hand side. The solution can lead to complex and therefore unrealistic roots. A more stable solution procedure can be set up by removing the quadratic term in a to the right hand side (either by dividing by the factor a or by subtracting it) and iterating the solution of the resulting linear equation. It should also be noted that much of the above algebra is often carried out more compactly by using matrix notation for the mappings.

Although the theory supports only the determination of azimuthally averaged values of the axial flow induced velocity, once the averaged tangential flow induction factors have been calculated, the elemental form of the momentum [Eq. (4.48)] and the blade element forces [Eq. (4.46)] can be employed to yield values of a that vary with azimuth.

For the determination of blade forces, the flow expansion velocities must be included. The total velocity components, normal and tangential to a blade element, are then as shown in Figure 4.18, and the resultant velocity is

$$\begin{aligned} \frac{W^2}{U_\infty^2} = & [\cos \gamma - a(1 + F(\mu)K(\chi) \sin \psi) + \lambda\mu a' \sin \chi \cos \psi(1 + \sin \chi \sin \psi)]^2 \\ & + \left[\lambda\mu(1 + a' \cos \chi(1 + \sin \chi \sin \psi)) \right. \\ & \left. + \cos \psi \left(a \cdot \tan \frac{\chi}{2}(1 + F(\mu)K(\chi) \sin \psi) - \sin \gamma \right) \right]^2 \end{aligned} \quad (4.58)$$

4.2.9 Calculated values of induced velocity

The measurement of the induced velocities of a wind turbine rotor in yaw has been undertaken at Delft University of Technology (Snel and Schepers 1995). The tests were carried out using a small wind tunnel model so that a steady yaw could be maintained in a steady wind with no tower shadow and no wind shear. The rotor had two blades of 1.2 m diameter that were twisted but had a uniform chord length of 80 mm. The blade root was at a radius of 180 mm, and the blade twist was 9° at the root varying linearly with radius to 4° at 540 mm radius and remaining at 4° from there to the tip. The blade aerofoil profile was NACA0012. The rotor speed was kept constant at 720 rev/min and the wind speed was held constant at 6.0 m/s. Tests were carried out at 10°, 20°, and 30° of yaw angle.

Calculated induced velocities using the vortex momentum equation for the Delft turbine are shown in Figure 4.19: these are the average values for each annulus obtained using Eqs. (4.54) and (4.56).

The component velocities at each blade element, as defined in Figure 4.18, are shown in Figure 4.20. Because of the rotational speed of the blades, the tangential velocity is much greater than the normal velocity, but it is the latter that most influences the variation in angle of attack at the important, outboard sections of the blades, shown in Figure 4.21.

At the inboard sections of the blades, it is the variation in tangential velocity that mostly influences the angle of attack variation, and this is largely as a result of the changing geometry with azimuth angle rather than the effect of induced velocity.

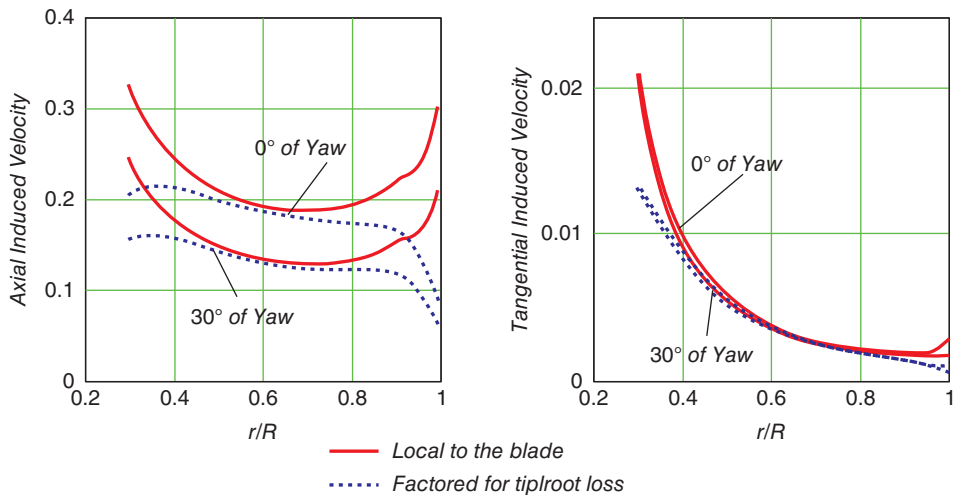


Figure 4.19 Azimuthally averaged induced velocity factors for the Delft turbine.

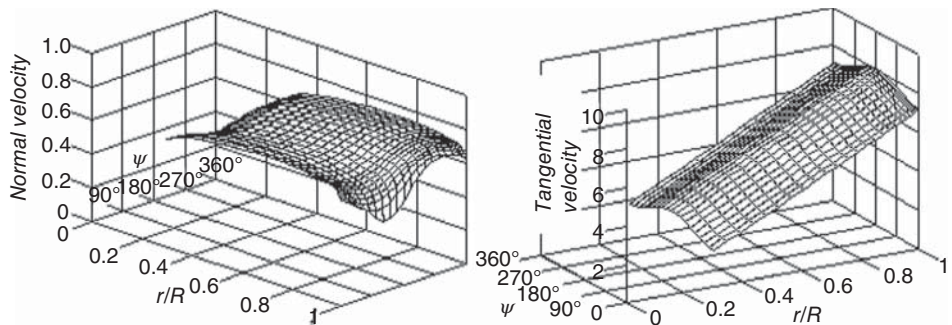


Figure 4.20 Component velocities, normalised with wind speed, at 30° of yaw.

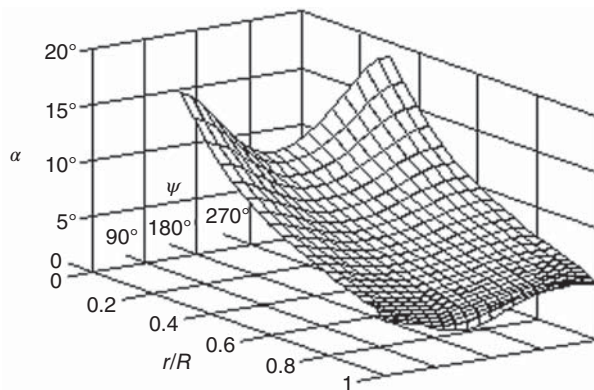


Figure 4.21 Angle of attack variation at 30° of yaw.

4.2.10 Blade forces for a rotor in steady yaw

Once the flow induction factors have been determined, blade forces can then be calculated. Although the flow expansion velocity is excluded from the determination of the flow induction factors, on the grounds that the consequent blade forces do not cause any change in the momentum of the flow, it must be included when the blade forces are calculated. The flow expansion velocity should be dependent on an overall average value of the axial flow induction factor, but it is more convenient to use the annular average value as determined by Eqs. (4.54) and (4.56).

The flow angle and the angle of attack need to be determined anew at each blade element position μ and at each blade azimuth position ψ because the flow expansion velocity must now be included, so Eq. (4.44) is used in its unmodified form. Drag must also be included in the determination of forces even if it was not in the calculation of the induced velocities.

The blade force per unit span normal to the plane of rotation is

$$\frac{dF_x}{dr} = \frac{1}{2} \rho W^2 c C_x \quad (4.59)$$

which will vary with the azimuth position of the blade. The total force normal to the rotor plane can be obtained by integrating Eq. (4.59) along the blade length for each of the blades, taking account of their azimuthal separation, and summing the results. The total normal force will also vary with rotor azimuth.

Similarly, the tangential blade force per unit span is

$$\frac{dF_y}{dr} = \frac{1}{2} \rho W^2 c C_y \quad (4.60)$$

and the blade torque contribution about the axis of rotation is

$$\frac{dQ}{dr} = \frac{1}{2} \rho W^2 c r C_y \quad (4.61)$$

The total torque is found by integrating along each blade and summing over all the blades, just as for the normal force. Again, the torque on the rotor will vary with azimuth position, so to find the average torque will require a further integration with respect to azimuth.

4.2.11 Yawing and tilting moments in steady yaw

The asymmetry of the flow through a yawed rotor, caused by the flow expansion, means that a blade sweeping upwind has a higher angle of attack than when it is sweeping downwind, as shown in Figure 4.17. The blade lift upwind will therefore be greater than the lift downwind, and a similar differential applies to the forces normal to the rotor plane. It can be seen, therefore, that there is a net moment about the yaw (vertical axis) in a direction that will tend to restore the rotor axis to a position aligned with the wind direction. The yawing moment is obtained from the normal force of Eq. (4.59):

$$\frac{dM_z}{dr} = \frac{1}{2} \rho W^2 c r C_x \sin \psi \quad (4.62)$$

which will also vary with the azimuth position of the blade. The total single-blade yawing moment at each azimuth position is obtained by integrating Eq. (4.62) along the length of the blade. Summing the moments for all blades, suitably separated in phase, will result in the yawing moment on the rotor.

A similar calculation can be made for the tilting moment, the moment about the horizontal diametral axis (y axis) of the rotor:

$$\frac{dM_y}{dr} = \frac{1}{2}\rho W^2 cr C_x \cos \psi \quad (4.63)$$

The existence of yawing and tilting moments predicted by the blade element theory is inconsistent with the momentum and the vortex cylindrical wake theories because they assume steady conditions in the wake. In principle, the momentum and vortex theories predict velocities from which it is only possible to deduce an azimuthally uniform pressure distribution.

Measured results of rotor yaw moment for the Delft turbine are shown in Figure 4.22, and the corresponding calculated yawing moments are shown in Figure 4.23.

The measured yawing moments were derived from strain gauge readings of the flapwise bending strain at a radial position close to the root of the blade at 129 mm radius. Flapwise (or flatwise) bending causes displacements normal to the rotor plane. The calculated yawing moments are determined at the same radial position on the blade and are, therefore, not quite equal to the true yawing moments about the actual yaw axis.

The comparison between the measured and calculated yaw moments is quite good, taking into account the limitations of the theory. At 30° of yaw, the calculated values underestimate the measurements significantly, whereas at the two lower angles the correspondence is much closer.

It should be noted that the mean yawing moment is not zero and that the sign of the moment, being negative, means that it endeavours to restore the rotor axis to alignment with the wind direction.

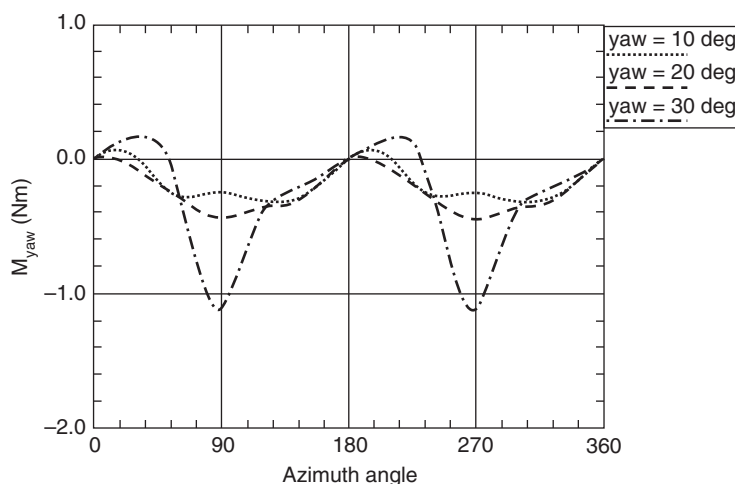


Figure 4.22 Measured yaw moments on the Delft turbine.

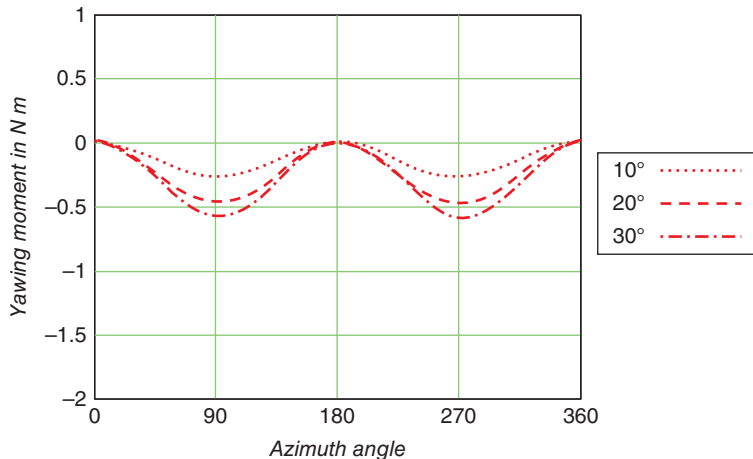


Figure 4.23 Calculated yaw moments on the Delft turbine.

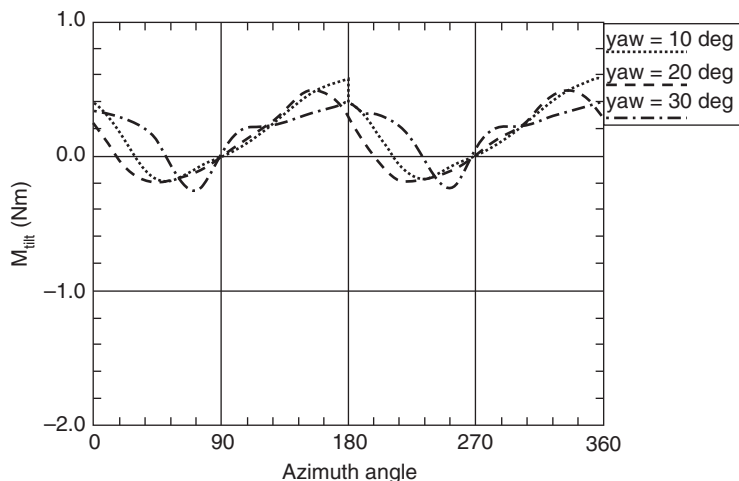


Figure 4.24 Measured tilt moments on the Delft turbine.

The yawing moment comparison is a test of the usefulness of the theory developed in this section, and it would seem that for general engineering purposes it passes the test.

The measured tilting moments (Figure 4.24) appear to be of about the same amplitude for all three yaw angles, whereas the calculated moments (Figure 4.25) increase with yaw angle.

For 30° of yaw, the magnitudes of the measured and calculated tilting moments are comparable. The measured mean tilting moment is quite definitely non-zero and positive, but the calculated mean moment is much smaller although still positive. A positive tilt rotation would displace the upper part of the rotor disc in the downwind direction. In theory, the small mean tilting moment is caused by the wake rotation velocities.

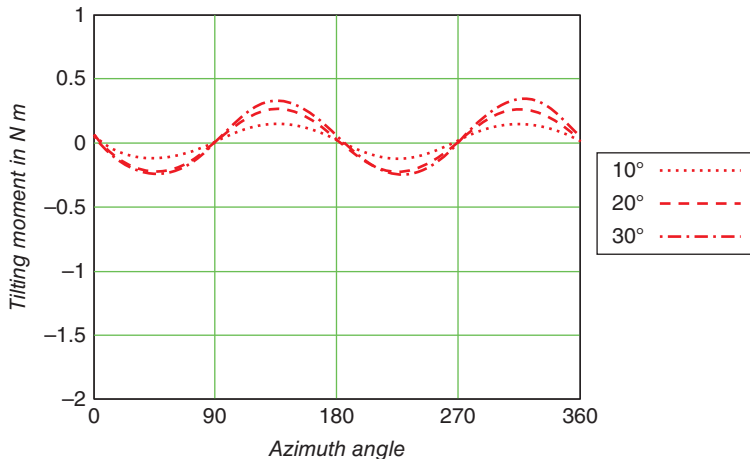


Figure 4.25 Calculated tilt moments on the Delft turbine.

Results obtained from CFD provide a much more accurate prediction of the aerodynamics of a wind turbine in yaw. However, the heavy computational resource (time and memory) requirements usually associated with CFD solutions precludes their routine use in favour of the simple theory outlined in these pages.

4.3 Circular wing theory applied to a rotor in yaw

4.3.1 Introduction

An aerodynamic model that is applied to the performance of helicopters in forward flight, which is to represent the rotor as a circular wing at low angle of attack, can also be applied to wind turbine rotors that are lightly loaded. This method of analysis represents the flow field in terms of a series of solutions of Laplace's equation for potential in ellipsoidal coordinates (which are the 'natural' coordinates for this geometry). It gives a mathematically correct solution, provided potential theory applies (high Reynolds number flow) and the perturbation of the incident flow is small, and it is able to give more details of the flow field and load distribution than Glauert's semi-empirical method. The method solves for the perturbation pressures, equivalent to acceleration potential, allowing more general distributions of pressure drop across the actuator disc than the uniform pressure distribution of the momentum theory. The model has been expounded by Kinner (1937), inspired by Prandtl, who has developed expressions for the pressure field in the vicinity of an actuator disc, treating it as a circular wing. As for the non-yawed actuator disc, the circular wing model strictly assumes an infinity of very slender blades while retaining finite and small solidity.

Kinner's theory is for inviscid flow and derived from the Euler equations. The perturbation velocities u , v , and w due to the rotor in the x , y , and z directions are assumed to be much smaller than the free-stream velocity U_∞ (which is a constant). Substituting into

the Euler equations and linearising leads to x , y , and z direction momentum equations:

$$\rho U_\infty \frac{\partial u}{\partial x} = -\frac{\partial p}{\partial x} \quad (4.64a)$$

$$\rho U_\infty \frac{\partial v}{\partial x} = -\frac{\partial p}{\partial y} \quad (4.64b)$$

$$\rho U_\infty \frac{\partial w}{\partial x} = -\frac{\partial p}{\partial z} \quad (4.64c)$$

Combining these with the incompressible mass flow continuity equation leads to Laplace's equation:

$$\frac{\partial^2 p}{\partial x^2} + \frac{\partial^2 p}{\partial y^2} + \frac{\partial^2 p}{\partial z^2} = 0 \quad (4.65)$$

Given the boundary conditions at the actuator disc, Eq. (4.65) can be solved for the pressure field and, in particular, the pressure distribution at the disc. The pressure is continuous everywhere except across the disc surfaces, where there is the usual pressure discontinuity, or pressure drop, in the wind turbine case.

In Coleman's analysis, the pressure drop distribution across the disc is uniform (it is only as a result of combining the theory with the blade element theory that a non-uniform pressure distribution can be achieved) but falls to zero, abruptly, at the disc edge. Kinner assumes that the pressure drop is zero at the disc edge and changes in a continuous manner as radius decreases.

The linearised Euler Eqs. (4.64a)–(4.64c) allow the perturbation pressure to be regarded as an (acceleration) potential field from which the velocity field can be obtained by integration. Commencing upstream where the known free-stream conditions apply, the velocity components can be determined by progressive integration towards the disc.

The pressure discontinuity across the rotor disc is as shown in Figure 3.2. As in the case of the unyawed actuator disc, half the pressure difference across the disc is accounted for by the rise in pressure just upstream and the other half by an equal rise in pressure just downstream, back to ambient in the far wake. The pressure gradient, however, normal to the rotor disc, is continuous across the disc.

4.3.2 The general pressure distribution theory of Kinner

Kinner's (1937) solution is mathematically complex, derived in terms of Legendre polynomials P_n^m , Q_n^m in an ellipsoidal coordinate system (v, η, ψ) , where ψ is azimuth angle, transformed from the Cartesian coordinates (x'', y', z) , which are centred in the rotor plane; see Figure 4.11:

$$\frac{x''}{R} = v\eta, \frac{y'}{R} = \sqrt{1-v^2}\sqrt{1+\eta^2} \sin \psi \text{ and } \frac{z}{R} = \sqrt{1-v^2}\sqrt{1+\eta^2} \cos \psi \quad (4.66)$$

On the surface of the rotor disc $\eta = 0$ and $\frac{r}{R} = \mu = \sqrt{1-v^2}$ or, conversely, $v = \sqrt{1-\mu^2}$.

The complete solution for the pressure field $p(v, \eta, \psi)$ surrounding the rotor disc takes the form of a double series: $\sum \sum P_n^m(v) Q_n^m(i\eta) \{\sin(m\psi), \cos(m\psi)\}$ in Legendre polynomials of the first and second kind $P_n^m(v)$ and $Q_n^m(i\eta)$ multiplying terms in $\cos(m\psi)$ and

$\sin(m\psi)$. This solution is anti-symmetric with respect to η , taking alternate signs across the rotor disc $\eta = +/-0$. The resulting discontinuity that gives rise to the pressure drop across the disc may be written in the form

$$\Delta p(v, \psi) = \sum_{m=0}^M \sum_{n=m}^N P_n^m(v) Q_n^m(0) (C_n^m \cos m\psi + D_n^m \sin m\psi) \quad (4.67)$$

where the strictly infinite series are truncated at suitably large positive integer values M and N , only those terms for which $m+n$ is odd provide a pressure discontinuity and hence non-zero loading on the disc, and C_n^m and D_n^m are arbitrary constants that can be related to the forces on the disc.

4.3.3 The axisymmetric loading distributions

For the wind turbine rotor disc, the simplest situation is for $m = 0$, which means that the pressure distribution is axisymmetric. The permitted values of n must then be odd. A pressure drop (loading) distribution obtained from a combination of the first two of these solutions satisfying the conditions of zero loading at the axis (assumed blade root) and blade tip is

$$\Delta p_{1-2}(\mu) = \frac{15}{4} C_T \mu^2 \sqrt{1 - \mu^2} \quad (4.68)$$

which is shown in Figure 4.26. The loading distribution Δp_{1-2} given in Eq. (4.68) is formed from the first two solutions Δp_1 minus Δp_2 so that Δp_{1-2} satisfies the necessary condition at the axis that $\Delta p(\mu=0) = 0$. Δp_1 , Δp_2 , and Δp_{1-2} are shown in Figure 4.26. Note that these loading distributions are normalised by the free-stream dynamic pressure, $0.5\rho U_\infty^2$.

As most modern wind turbines are designed to achieve as uniform a pressure distribution as practicable, to maximise efficiency, the solution requires modification. A uniform disc loading distribution can be formed by summing many terms in the solution series

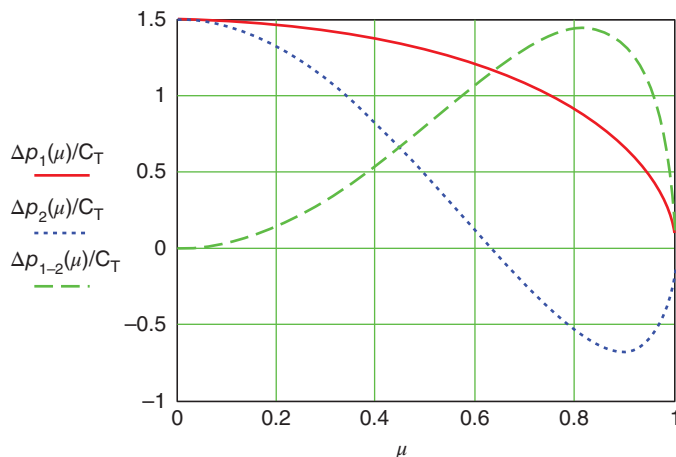


Figure 4.26 Radial loading distributions of the first two solutions and their combination to satisfy the requirements at the rotor axis.

but, because the pressure discontinuity must still go to zero at the disc edge, a very large number are in practice required to represent the infinite gradient there. Tip-loss effects that require a more gradual approach to zero loading at both blade tip and root mitigate this, and for most of the blade span the pressure should be uniform. It should be pointed out that the *blade loading* for uniform disc loading does increase linearly with radius.

The induced velocity field caused by the axisymmetric loading distribution has to be obtained from the pressure field by integrating Eqs. (4.64a)–(4.64c) commencing far upstream where free-stream conditions are assumed to apply. The upstream conditions also depend upon the angle of yaw of the disc. The integration continues until a point on the disc is reached where the induced velocity is to be determined.

The particular induced velocity component that is most important for determining the angle of attack on a blade element is normal to the rotor disc, i.e. the axial induced velocity. Mangler and Squire (1950) calculated the axial induced velocity distribution as a function of yaw angle by expressing the velocity as a Fourier series of the azimuth angle ψ :

$$\frac{u}{U_\infty} = C_T \left(\frac{A_0(\mu, \gamma)}{2} + \sum_{k=1}^{\infty} A_k(\mu, \gamma) \sin k\psi \right) \quad (4.69)$$

For the loading distribution of Eq. (4.68), the Fourier coefficients in Eq. (4.69) are

$$A_0(\mu, \gamma) = -\frac{15}{8} \mu^2 \sqrt{1 - \mu^2} \quad (4.70)$$

$$A_1(\mu, \gamma) = -\frac{15\pi}{256} \mu(9\mu^2 - 4) \tan \frac{\gamma}{2} \quad (4.71)$$

$$A_3(\mu, \gamma) = -\frac{45\pi}{256} \mu^3 \tan^3 \frac{\gamma}{2} \quad (4.72)$$

Higher order odd terms are zero while even terms have the general form

$$A_k = -(-1)^{\frac{k-2}{2}} \frac{3}{4} \left[\frac{k+\nu}{k^2-1} \left(\frac{9\nu^2+k^2-6}{k^2-9} \right) + \frac{3\nu}{k^2-9} \right] \left(\frac{1-\nu}{1+\nu} \right)^{\frac{k}{2}} \tan^{\frac{k}{2}} \frac{\gamma}{2} \quad (4.73)$$

where $\nu^2 = 1 - \mu^2$, and k is an even integer greater than zero.

The average value of the axial induced velocity is independent of yaw angle and is given by

$$a_0 = \frac{u_0}{U_\infty} = \frac{1}{4} C_T \quad (4.74)$$

where u_0 is the average axial induced velocity.

Thus, the *average* value of the axial flow induced velocity is related to the thrust coefficient by

$$C_T = 4a_0 \quad (4.75)$$

compared with the momentum theory, in which $C_T = 4a_0(1 - a_0)$, or compared with any of the expressions developed for yawed conditions, Eqs. (4.2), (4.18), and (4.24).

This circular wing theory is linearized with respect to the induced velocities, and hence Eq. (4.75) is only valid if the induced velocity is small compared with the flow velocity so that a_0 and C_T are small and terms in a_0^2 and higher powers are ignored.

For non-zero yaw, the once per revolution term in Eq. (4.69) will cause an angle of attack variation and, hence, a lift variation that will cause a yawing moment on the disc.

However, an axisymmetric pressure distribution, such as (4.68), cannot cause a yawing moment. The situation is much the same as for the vortex theory of Coleman et al. (1945).

Pitt and Peters (1981) use or, rather, impose Glauert's assumption [Eq. (4.21)] for the variation of the axial induced flow factor:

$$a = a_0 + a_s \mu \sin \psi \quad (4.76)$$

The value of a_s is obtained by equating the first moment about the yaw axis of Eq. (4.76) with the first moment of (4.69) using the Mangler and Squire velocity distributions of Eqs. (4.70)–(4.73):

$$\begin{aligned} & \int_0^{2\pi} \int_0^1 \mu \sin \psi (a_0 + a_s \mu \sin \psi) \mu d\mu d\psi \\ &= - \int_0^{2\pi} \int_0^1 C_T \mu \sin \psi \left(\frac{A_0(\mu, \gamma)}{2} + \sum_{k=1}^{\infty} A_k(\mu, \gamma) \sin k\psi \right) \mu d\mu d\psi \end{aligned} \quad (4.77)$$

All terms, apart from that containing A_1 , vanish on integration, giving

$$a_s = \frac{15\pi}{128} C_T \tan \frac{\gamma}{2} \quad (4.78)$$

Hence, using Eq. (4.75), the axial induced velocity becomes

$$a = a_0 \left(1 + \frac{15\pi}{32} \mu \tan \frac{\gamma}{2} \sin \psi \right) \quad (4.79)$$

which, apart from the use of the yaw angle instead of the wake skew angle, has the same form as Eqs. (4.21) and (4.31), and so there is some consistency in the various methods for dealing with yawed flow.

4.3.4 The anti-symmetric loading distribution

As determined in Section 4.2.11, there is a moment about the vertical diameter of a yawed wind turbine rotor disc, the restoring yaw moment. An axisymmetric pressure distribution, however, is not capable of producing a yaw moment, so more terms from the series solution of Eq. (4.67) need to be included.

The only terms in Eq. (4.67) that will yield a yawing moment are those for which $m = 1$ and for which $D_n^1 \neq 0$. Terms for which $m = 1$ and $C_n^1 \neq 0$ will cause a tilting moment. Recalling that $m + n$ must be odd to achieve a pressure discontinuity across the disc, the values of n that may be combined with $m = 1$ must be even.

Because of the nature of the Legendre polynomials, only one term in the series of Eq. (4.67) will produce a net thrust, and only one term will produce a yawing moment, which is a first moment. Similarly, only one term will produce a second moment, and so on.

The unique term in (4.67) that yields a yawing moment is that for which $m = 1, n = 2$, and $C_n^1 \neq 0$, therefore,

$$P_2^1(v) = 3v\sqrt{1-v^2} = 3\mu\sqrt{1-\mu^2} \quad (4.80)$$

and

$$Q_2^1(\eta) = 3i\eta\sqrt{1+\eta^2}\tan^{-1}\frac{1}{\eta} - 3i\sqrt{1+\eta^2} + \frac{i}{\sqrt{1+\eta^2}}, \quad (4.81)$$

so

$$Q_2^1(0) = -2i \quad (4.82)$$

A zero pressure gradient at the rotor axis is not appropriate in this case because the pressure distribution is anti-symmetric about the yaw axis, therefore,

$$\Delta p(\mu, \psi) = P_2^1(\mu)Q_2^1(0)D_2^1 \sin \psi = -6iD_2^1\mu\sqrt{1-\mu^2} \sin \psi \quad (4.83)$$

This loading distribution is shown in Figure 4.27.

The yawing moment coefficient is defined by

$$C_{mz} = \frac{M_z}{\frac{1}{2}\rho \cdot U_\infty^2 \pi \cdot R^3} \quad (4.84)$$

As before, if the loading in Eq. (4.83) is non-dimensionalised by the free-stream dynamic pressure $\frac{1}{2}\rho \cdot U_\infty^2$, then

$$\begin{aligned} C_{mz} &= \frac{1}{\pi} \int_0^{2\pi} \int_0^1 \mu \sin \psi \cdot \Delta p(\mu, \psi) \mu \cdot d\mu d\psi \\ &= -\frac{1}{\pi} 6iD_2^1 \int_0^1 \mu^3 \sqrt{1-\mu^2} d\mu \int_0^{2\pi} \sin^2 \psi d\psi \end{aligned} \quad (4.85)$$

which gives

$$iD_2^1 = -\frac{5}{4} \cdot C_{mz} \quad (4.86)$$

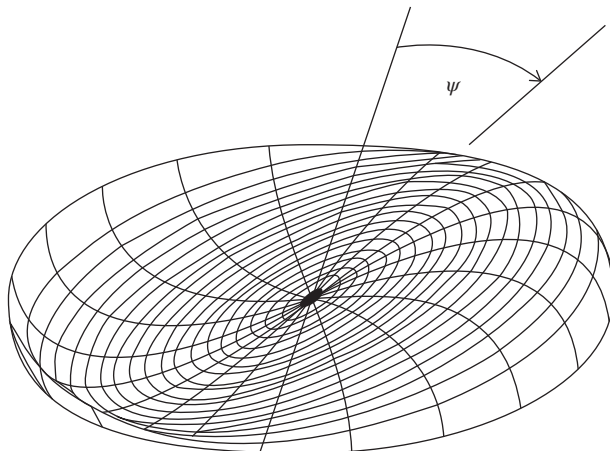


Figure 4.27 The form of the loading distribution that yields a yawing moment.

To establish a relationship between the yawing moment coefficient and the axial velocity induced by the pressure field corresponding to the loading distribution of Eq. (4.83), the velocity distribution has to be obtained by integrating Eqs. (4.64a)–(4.64c). Unfortunately, no analytical solution has been determined for the anti-symmetric case, as Mangler and Squire have done for the symmetric case. Numerical values of induced velocities need to be calculated from Eqs. (4.64a)–(4.64c) using the coefficients given by Eqs. (4.80) and (4.82).

Pitt and Peters (1981) have determined the axial velocity distribution for values of the yaw angle from 0° to 90° : the yaw angle determines the far upstream conditions where the integration commences. The velocity distribution found corresponds to that of Eq. (4.69) for the axisymmetric case. Pitt and Peters again impose the form of Eq. (4.76) and determine the average value of the axial induced velocity a_0 and the value of a_s , using the same method of Eq. (4.77): in both cases, of course, numerical integration is necessary.

The values of a_0 are not zero, as might have been expected from the anti-symmetric loading distribution, and have the same factor as in the result for a_s in Eq. (4.78) found for the axisymmetric loading distribution, but now multiplying the yaw moment coefficient. The variation of the two coefficients a_0 and a_s with yaw angle γ is determined numerically, but, using the Mangler and Squire analytical forms for guidance, analytical variations can be inferred. Pitt and Peters found that the linearised axial induced velocity distribution is

$$a_0 = -\frac{15}{128}\pi \tan \frac{\gamma}{2} C_{mz} \quad (4.87)$$

and

$$a_s = -\left(1 - \tan^2 \frac{\gamma}{2}\right) C_{mz} \quad (4.88)$$

Pitt and Peters also include a cosine term with induction coefficient a_c in the linearised axial induced flow factor representation of Eq. (4.76) that will only arise if $C_2^1 \neq 0$:

$$a = a_0 + a_s \mu \sin \psi + a_c \mu \cos \psi \quad (4.89)$$

in which case there is an additional contribution to the pressure drop given by

$$\Delta p(\mu, \psi) = P_2^1(\mu) Q_2^1(0) C_2^1 \cos \psi = -6iC_2^1 \mu \sqrt{1 - \mu^2} \cos \psi \quad (4.90)$$

The tilting moment coefficient is given by

$$\begin{aligned} C_{my} &= \frac{1}{\pi} \int_0^{2\pi} \int_0^1 \mu \cos \psi \Delta p(\mu, \psi) \mu d\mu d\psi \\ &= -\frac{1}{\pi} 6iC_2^1 \int_0^1 \mu^3 \sqrt{1 - \mu^2} d\mu \int_0^{2\pi} \cos^2 \psi d\psi \end{aligned} \quad (4.91)$$

Therefore,

$$iC_2^1 = -\frac{5}{4} C_{my} \quad (4.92)$$

The axial induced velocity distribution resulting from the pressure field corresponding to the loading distribution of Eq. (4.90) is calculated by numerical integration of Eqs. (4.64a)–(4.64c) and is then matched with the linear velocity distribution of Eq. (4.89) using again the same method for Eq. (4.77):

$$\begin{aligned} & \int_0^{2\pi} \int_0^1 \mu \cos \psi (a_0 + a_c \mu \cos \psi) 2\pi \mu d\mu d\psi \\ &= \int_0^{2\pi} \int_0^1 \mu \cos \psi C_T \left(\frac{1}{2} A_0(\mu, \gamma) + \sum_{k=1}^{\infty} A_k(\mu, \gamma) \cos k\psi \right) \mu d\mu d\psi \end{aligned} \quad (4.93)$$

the functions $A_n(\mu, \gamma)$ being then determined numerically.

Again, using the Mangler and Squire results as guidance, an expression for a_c is found:

$$a_c = -\sec^2 \frac{\gamma}{2} \cdot C_{my} \quad (4.94)$$

4.3.5 The Pitt and Peters model

Pitt and Peters (1981) have developed the linear theory that relates the axial induced flow factors to the thrust and moment coefficients given in Eqs. (4.75), (4.78), (4.87), (4.88), (4.89), and (4.94) expressed in matrix form:

$$\begin{bmatrix} a_0 \\ a_c \\ a_s \end{bmatrix} = \begin{bmatrix} \frac{1}{4} & 0 & -\frac{15}{128}\pi \tan \frac{\chi}{2} \\ 0 & -\sec^2 \frac{\chi}{2} & 0 \\ \frac{15}{128}\pi \tan \frac{\chi}{2} & 0 & -\left(1 - \tan^2 \frac{\chi}{2}\right) \end{bmatrix} \begin{bmatrix} C_T \\ C_{my} \\ C_{mz} \end{bmatrix} \quad (4.95)$$

$$(\mathbf{a}) = [L](\mathbf{C}) \quad (4.96)$$

The solution procedure is to assume initial values for the vector (\mathbf{a}) from which the values of the vector (\mathbf{C}) can be calculated from blade element theory. New values of (\mathbf{a}) are then found from Eq. (4.94), and an iteration proceeds.

For the wind turbine the value of a_0 may not be small compared with 1, and so the above procedure will converge on values of a_0 that are too small compared with what the momentum theory would deliver.

To produce more realistic results, that is, results in line with Glauert's momentum theory, the expression for C_T may be taken as

$$C_T = 4a \sqrt{1 - a(2 \cos \gamma - a)} = 4aA_G(a) \quad (4.97)$$

or, from the Coleman theory,

$$C_T = 4a \left(\cos \gamma + \tan \frac{\chi}{2} \sin \gamma - a \sec^2 \frac{\chi}{2} \right) = 4aA_C(a) \quad (4.98)$$

The matrix $[L]$ then becomes

$$[L] = \begin{bmatrix} \frac{1}{4A(a_0)} & 0 & -\frac{15}{128}\pi \tan \frac{\chi}{2} \\ 0 & -\sec^2 \frac{\chi}{2} & 0 \\ \frac{15}{128A(a_0)}\pi \tan \frac{\chi}{2} & 0 & -\left(1 - \tan^2 \frac{\chi}{2}\right) \end{bmatrix} \quad (4.99)$$

where $A(a_0)$ is chosen according to which momentum theory is to be used. Note that it is usual, as in the above, for the wake skew angle to be used in matrix $[L]$ instead of the yaw angle. This does give a sinusoidal yawing moment on a three bladed rotor because the lift force depends non-linearly on the sinusoidal axial induction factor.

The Pitt and Peters method does not include any determination of induced velocities in the plane of the rotor disc, and as a consequence it is not possible to account for wake rotation. From Eqs. (4.64a)–(4.64c) the tangential (azimuthal) velocity is proportional to $\partial p/\partial\psi$, and the form of the Kinner solution, therefore, does not give any contribution that has non-zero average over $0 < \psi < 2\pi$. The momentum theory of Section 3.3 can, but it predicts an infinite pressure at the axis of rotation because of wake rotation, as also does any model involving a finite strength shed vortex along the axis from the blade root. In practice, of course, the bound vorticity (circulation) must decrease to zero at a finite rate at the blade root (axis) as well as at the tip, and the singularity does not occur.

With or without wake rotation, a flow angle ϕ can be determined from which a torque can be found. The normal force due to the lift on an element of the rotor disc is equal to $\delta L \cos \phi$, and the tangential force is $\delta L \sin \phi$.

4.3.6 The general acceleration potential method

Peters with a number of associates has developed the theory further, and a reading of references Pitt and Peters (1981), Goankar and Peters (1988), and HaQuang and Peters (1988) is recommended.

The acceleration potential method has been developed specifically for wind turbines by van Bussell (1995), where a much more comprehensive account of the theory is given.

The coefficients for the terms in the Kinner pressure distribution can be determined from the incident normal velocity field at the rotor disc from a sufficient number of points over the disc, matching the forces with blade element theory.

4.3.7 Comparison of methods

A project to compare existing methods of predicting yaw behaviour, among other aspects of the aerodynamic behaviour of wind turbines, is reported in Snel and Schepers (1995). Figure 4.28 shows results obtained by various methods for predicting the yawing moment of the 2 MW, three blade turbine at Tjæreborg in Denmark at a yaw angle of 32° and a wind speed of 8.5 m/s.

Most of the theoretical predictions in Figure 4.28 have the correct or nearly correct phasing and approximately the correct mean yawing moment, but the amplitude of the predicted cyclic variation in the yawing moment varies considerably between methods,

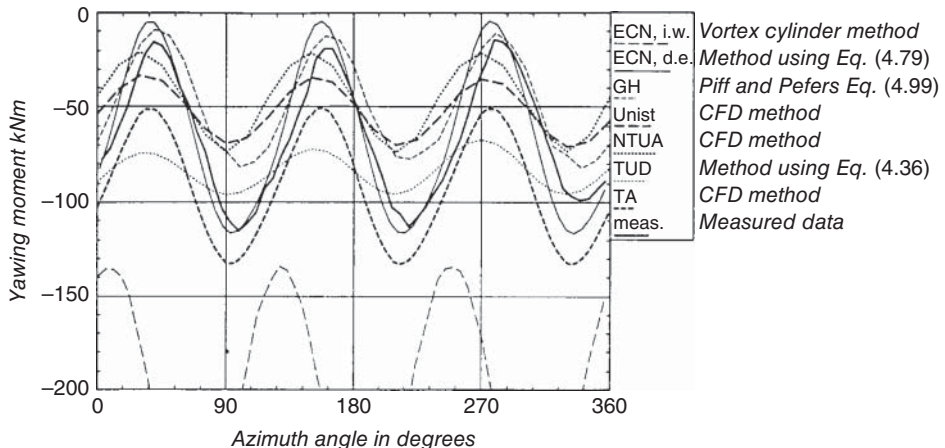


Figure 4.28 Yawing moment on the Tjæreborg turbine at 32° yaw and 8.5 m/s.

generally being under-predictions. In this comparison, the second method bears the closest comparison with the measured data.

4.4 Unsteady flow

4.4.1 Introduction

The momentum theories (actuator disc and blade-element/momentum) are fundamentally steady flow theories because of the requirement to consider the far downstream wake conditions in calculating force on the rotor. This approach ignores the time over which the wake takes to develop to a steady state after changes in conditions (e.g. the incident wind speed or the blade pitch angle) have occurred at some given time at the rotor. Natural winds are almost never steady in either strength or direction, and so it is seldom that the conditions for the momentum theory apply. It takes a finite time for the wind to travel from far upwind of a rotor to far downwind, and if in that time wind conditions change, the new equilibrium state if ever achieved lags the change.

In addition to changes in incident wind speed, many other phenomena give rise to time-dependent conditions at the rotor: cyclic changes in incident wind speed experienced by the blades as they rotate through the mean shear in the wind, due to yaw error of the rotor and due to blade interaction with the flow around the tower; sudden control operations such as changes in blade pitch or rotor speed; and multi-frequency blade vibrations due to the structural dynamics of the system.

Several approximate solutions offer themselves for the determination of the dynamic flow conditions at the rotor disc. It could be assumed that the induced velocity remains fixed at the level determined by the averaged wind speed over a specified period of time that may be quite short. The wake remains frozen while the unsteady component of the wind passes through the rotor disc unattenuated by the action of the rotor. The unsteady forces that would impose zero mean force on the rotor would be determined by the blade

element theory. Alternatively, the induced velocity through the rotor disc could be determined from the instantaneous wind velocity as if the flow field was steady and the wake adjusted instantaneously, equilibrium in the wake being maintained at all times. However, in reality the wake takes a finite time (typically a few rotor cycles) to equilibrate, and the resulting lag in wake effect at the rotor is known as *dynamic inflow*. It is responsible for considerable over- or under-shoots in blade loading when the blade pitch changes suddenly and to a lesser extent when the incident velocity changes.

The acceleration potential method is one method of analysing unsteady flows, which by making assumptions about the wake avoids explicit reference to it. It allows the flow conditions at the rotor disc to be determined from the upwind flow field, which is much simpler to determine than that of the wake.

In steady flow conditions, the velocity at a fixed point in the far upwind flow field is constant, but closer to the rotor acceleration of the flow experienced by a fluid particle takes place (e.g. $\sim u \frac{\partial u}{\partial x}$ in the x direction); there is no rate of change with time of the velocity at any fixed point in space (thus, for example, $\frac{\partial u}{\partial t} = 0$). In unsteady flow, conditions at a fixed point do change with time, and the total acceleration in the x direction is then $\frac{\partial u}{\partial t} + u \frac{\partial u}{\partial x}$. The additional acceleration causes an additional inertia effect in the flow, the reaction to which changes the force on the rotor disc. The additional force is often termed the *added mass force* because for a body accelerating in a steady fluid, the additional force appears as an additional apparent mass of fluid m_a attached to the body.

4.4.2 The acceleration potential method to analyse unsteady flow

By assuming that the velocities induced by the action of the rotor are small compared with the incident flow, the inviscid Euler equations describing the flow field may be linearized and taken with the condition for continuity of the flow,

$$\frac{\partial u}{\partial x} + \frac{\partial v}{\partial y} + \frac{\partial w}{\partial z} = 0 \quad (4.100)$$

to show that the perturbation pressure field due to the rotor satisfies Laplace's equation

$$\frac{\partial^2 p}{\partial x^2} + \frac{\partial^2 p}{\partial y^2} + \frac{\partial^2 p}{\partial z^2} = 0 \quad (4.101)$$

Because the perturbation pressure p satisfies

$$\frac{\nabla p}{\rho} = -\frac{\partial u}{\partial t} - U_\infty \nabla u \quad (4.102)$$

it is often called an *acceleration potential*.

By transforming the problem of unsteady flow past an actuator disc into ellipsoidal coordinates (ν, η, ψ) and as in Section 4.3.2 deriving a series solution in terms of Legendre polynomials, a result can be obtained from the Kinner pressure distributions, which combines all unsteady wake effects with the inertia as added mass.

The analysis gives the added mass for the actuator disc to be

$$m_a = \frac{128}{75} \rho R^3 \quad (4.103)$$

This may be compared with the value of $m_a = (8/3)\rho R^3$ for a solid disc given by, e.g. Tuckerman (1925). Although Pitt and Peters (1981) determine the value 128/75, in subsequent papers by Peters and other workers the value 8/3 is recommended and has come

to be generally accepted. The resulting time constant for the dynamic inflow decay rate associated (Leishman 2002) with an added mass of $(8/3)\rho R^3$ is approximately $0.086R/(\sigma U_\infty)$, where σ is the rotor solidity, which is typically about 1.5 rotor revolutions and approximately correct.

4.4.3 Unsteady yawing and tilting moments

For unsteady flow in yaw, the normal unsteady acceleration potential distribution on the disc is required to have the same form of linear variation as the velocity, given in Eq. (4.89) in terms of flow factors:

$$\frac{\partial a}{\partial \tau} = \frac{\partial a_0}{\partial \tau} + \frac{\partial a_s}{\partial \tau} \mu \sin \psi + \frac{\partial a_c}{\partial \tau} \mu \cos \psi \quad (4.104)$$

where rotor non-dimensional time $\tau = U_\infty t/R$.

The condition that causes a yawing moment arises from the anti-symmetric loading distribution of Section 4.3.4 and can be obtained from Eqs. (4.80)–(4.83). The pressure field surrounding the rotor disc corresponding to this loading distribution (see Section 4.3.2) is

$$p(v, \eta, \psi) = -\frac{3}{2} D_2^1 v \sqrt{1-v^2} \left(3i\eta \sqrt{1+\eta^2} \tan^{-1} \frac{1}{\eta} - 3i\sqrt{1+\eta^2} + \frac{i}{\sqrt{1+\eta^2}} \right) \sin \psi \quad (4.105)$$

which, on the disc, produces the loading shown in Figure 4.27. The coefficient D_2^1 is related to the yawing moment coefficient in Eq. (4.85); see Eq. (4.86):

$$iD_2^1 = -\frac{5}{4} C_{mz}$$

Therefore,

$$p(v, \eta, \psi) = \frac{15}{8} \pi \cdot C_{mz} v \sqrt{1-v^2} \left(3\eta \sqrt{1+\eta^2} \tan^{-1} \frac{1}{\eta} - 3\sqrt{1+\eta^2} + \frac{1}{\sqrt{1+\eta^2}} \right) \sin \psi \quad (4.106)$$

As before, the pressure $p(v, \eta, \psi)$ in Eq. (4.106) is non-dimensionalised by the free-stream dynamic pressure $\frac{1}{2}\rho \cdot U_\infty^2$.

Using the linearised relationship between perturbation velocity and pressure [Eq. (4.102)] and relating x'' to v and η to differentiate Eq. (4.106) with respect to x'' , we get at the rotor disc, where $\eta = 0$,

$$\frac{\partial u_s}{\partial t} = \frac{45}{32} \pi \frac{U_\infty^2}{R} C_{mzD} \mu \sin \psi \quad (4.107)$$

In terms of non-dimensional time and velocity

$$\frac{\partial a_s}{\partial \tau} = \frac{45}{32} \pi C_{mzD} \mu \sin \psi \quad (4.108)$$

Similarly, if there is a tilting moment then the corresponding acceleration is

$$\frac{\partial a_c}{\partial \tau} = \frac{45}{32} \pi C_{myD} \mu \cos \psi \quad (4.109)$$

The subscript D in the above equations denotes inertia force contributions due to flow acceleration $\partial U_\infty / \partial t$, which would be added mass in the case of C_T .

The radial variation is linear, and so no linearisation adjustment is necessary as there is in the case of the velocity distribution. Again, the acceleration potential is independent of yaw angle. The mean acceleration potential is zero, and so there is no coupling between the cases.

The relationship between acceleration potential flow factors and force coefficients is, therefore,

$$\begin{bmatrix} \frac{16}{3\pi} & 0 & 0 \\ 0 & \frac{32}{45\pi} & 0 \\ 0 & 0 & \frac{32}{45\pi} \end{bmatrix} \begin{bmatrix} \frac{\partial a_0}{\partial \tau} \\ \frac{\partial a_c}{\partial \tau} \\ \frac{\partial a_s}{\partial \tau} \end{bmatrix} = \begin{bmatrix} C_T \\ C_{my} \\ C_{mz} \end{bmatrix}_D \quad (4.110)$$

or

$$[M] \left\{ \frac{\partial a}{\partial \tau} \right\} = \{C\}_D \quad (4.111)$$

The complete equation of motion combines Eq. (4.111) and the steady yaw Eqs. (4.95) and (4.96). The combination is achieved by adding the corresponding force coefficients, and the combined equation must be inverted:

$$[M] \left\{ \frac{\partial a}{\partial \tau} \right\} + [L]^{-1} \{a\} = \{C\}_D + \{C\}_S \quad (4.112)$$

The right hand side of Eq. (4.112) can also be determined from blade element theory and will be a time-dependent function of the inflow factor. The blade forces will vary in a manner determined by the time-varying velocity of the oncoming wind and consequent dynamic structural deflections of the necessarily elastic rotor. Equation (4.112) applies to the whole rotor disc, and the blade element forces need to be integrated along the blade lengths.

Numerical solutions to Eq. (4.112) require a procedure for dealing with first order differential equations, and the increased accuracy of the fourth order Runge–Kutta method is recommended. Starting with a steady state solution, the progress in time of the induced velocity as an unsteady flow passes through the rotor can be tracked. Non-dimensionalisation with respect to mean wind speed is possible, but it is common to work directly in terms of induced velocity rather than flow factors.

Equation (4.112) really applies to the whole rotor, and the only spatial variation of the induced velocity and acceleration potential that is permitted is as defined in Eq. (4.89) and from (4.104). However, an alternative approach considering radial variation has been adopted by several workers, see, for example, Snel and Schepers (1995), where the induced velocities are determined for separate annular rings, as described in Section 4.2.7. The added mass term for an annular ring can be taken as a proportion of the whole added mass according to the appropriate acceleration potential distribution.

Figure 4.29 shows measured and calculated flapwise (out of the rotor plane) blade root bending moments for the Tjæreborg turbine caused by a pitch change from 0.070° to 3.716° with the reversed change 30 seconds later. The turbine was not in yaw, and the

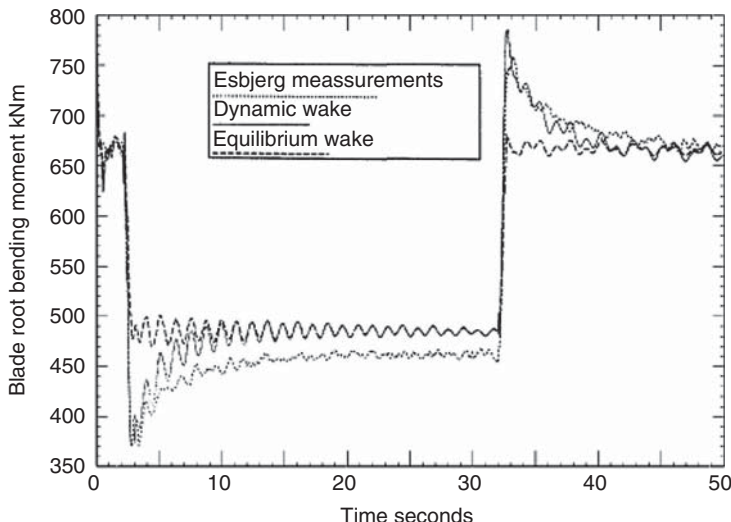


Figure 4.29 Measured and calculated blade root bending moment responses to blade pitch angle changes on the Tjæreborg turbine. Source: From Lindenburg (1996).

wind speed was 8.7 m/s. The calculated results were made according to the equilibrium wake method and with a differential equation method similar to that of Eq. (4.112).

The comparison with the measured results clearly shows that the dynamic analysis predicts the initial overshoot in bending moment, whereas the equilibrium wake method does not. Neither theory predicts very accurately the steady state bending moment achieved between the pitch changes. Figure 4.29 is taken from Lindenburg (1996), describing the PHATAS III aero-elastic code developed at ECN in the Netherlands. The Tjæreborg turbine is sited near Esbjerg in Denmark, details of which can be obtained from Snel and Schepers (1995).

The solution procedure requires the time-varying blade element force to determine the right hand side of Eq. (4.112), but calculating the lift and drag forces on a blade element in unsteady flow conditions is not a straightforward process. The lift force on a blade element is dependent upon the circulation, which is changing. The changing circulation causes spanwise (radial) vorticity to be shed into the blade wake. The velocity field that is induced by this modifies the angle of attack, which in turn determines the circulation. Therefore, in a continuously changing situation the lift is not in phase with the original angle of attack given by the incident flow and does not have a magnitude that can be determined using static, 2-D aerofoil lift versus angle of attack data.

The overshoot in blade forces after a sudden change in blade pitch angle is due to the lag in build-up of a new wake and hence of the changed asymptotic wake induction factor. This *dynamic inflow* resulting from a sudden pitch change is a strong effect. A similar but weaker effect (see, e.g. McNae 2014) occurs as a result of sudden changes in incident wind speed. Several simpler approximate methods have been developed to predict this effect without the need for extensive analysis and computation. An example is the method of Øye (1992), which solves a linked pair of first order differential equations for the induction factor development over time.

4.5 Unsteady aerofoil aerodynamics

4.5.1 Introduction

Section 4.5 focuses on unsteady effects on a blade section, which are the most important when the frequency is high, in which case the spanwise shed vorticity is dominant and the flow can be considered locally to be effectively 2-D. Three-dimensional (3-D) effects including changes to streamwise vorticity (e.g. the helical wake vortices) are smaller and usually not considered.

As already discussed, when a rotor blade section encounters changing flow conditions, inertial effects occur associated with the temporal accelerations in the flow field as well as effects of the changing vorticity shed into the wake due to the changes in circulation occurring on the blades. This shed vorticity is normal to the section and aligned with the spanwise direction. A complete solution for a rotor blade or blades needs to be done in three dimensions and time, which usually requires a very intensive level of computation, discussed later. However, the concept of blade element analysis incorporated into annular momentum balances for the steady component of the flow is possibly more appropriate for unsteady flow, and local unsteady aerofoil analysis may be applied at the section level.

When the oncoming flow relative to the aerofoil section is unsteady, the angle of attack is continuously changing, and so the lift also is changing with time. This may be dealt with quasi-steadily by assuming that the instantaneous angle of attack corresponds to the same lift coefficient as if that angle of attack were steady, determined by the instantaneous oncoming flow velocity and the velocity of the blade's motion. Thin aerofoil theory (see, e.g. Anderson 1991) shows that using a single point to determine the blade circulation from the effective angle of attack due to relative velocity normal to the blade (e.g. blade pitching or flapping) is optimum when at 3/4 of the chord length from the leading edge.

The velocities that determine the effective quasi-steady angle of attack for a rotor blade element are shown in Figure 4.30; the dot represents differentiation with respect to time t .

The flow velocity $W(t)$, which includes the rotational speed of the blade element, varies in magnitude and direction $\alpha_w(t)$ with the unsteady wind. $W(t)$ also includes the induced velocities caused by the rotor disc as might be determined by Eq. (4.112). The elastic deflection velocities (subscript e) caused by blade vibration also influence the

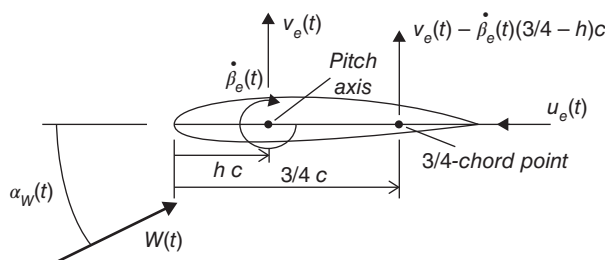


Figure 4.30 Unsteady flow and structural velocities adjacent to a rotor blade.

quasi-steady angle of attack, which is

$$\alpha(t) = \alpha_w(t) - \left(v_e(t) - \frac{\partial \beta_e}{\partial t} \left(\frac{3}{4} - h \right) c \right) \frac{1}{W(t)} \quad (4.113)$$

The structural velocity caused by chordwise (edgewise) deflections of the blade will also influence the angle of attack but by a very small amount. The non-dimensional parameter h defines the position of the pitching axis (flexural axis, shear centre position) of the blade element.

Assuming the structural deflection velocities to be small, the lift force is then

$$L_c(t) = L_{c0} + \frac{1}{2} \rho W(t)^2 c \frac{dC_l}{d\alpha} \sin \alpha(t) \quad (4.114)$$

The lift-curve slope $\frac{dC_l}{d\alpha}$ is assumed here to be the same as for the static case.

This quasi-steady approach is satisfactory provided the characteristic timescale of the changes $\tau > > c/W_{\text{rel}}$, where W_{rel} is the local incident flow velocity relative to the aerofoil section.

4.5.2 Aerodynamic forces caused by aerofoil acceleration

If an aerofoil is moving with changing velocity there are, in addition to the circulatory forces, the added mass forces on the aerofoil caused by the inertia of the surrounding air that is accelerated as the aerofoil accelerates. The added mass m_a per unit span of blade can be shown to be equivalent to the mass of a circular cylinder of air of diameter equal to the aerofoil chord, so $m_a = \frac{\pi c^2}{4} \rho$. There are two components to the added mass force; see Fung (1969):

- 1) A lift force with the centre of pressure at the mid-chord point with value equal to the added mass times the normal acceleration of the mid-chord point:

$$L_{m1}(t) = -\frac{1}{4} \pi c^2 \rho \left(\frac{\partial v_e}{\partial t} - c \left(\frac{1}{2} - h \right) \frac{\partial^2 \beta_e}{\partial t^2} \right) \quad (4.115)$$

- 2) A lift force with the centre of pressure at the 3/4-chord point, of the nature of a rotational inertia force, with value equal to the added mass times $W(t) \frac{\partial \beta_e}{\partial t}$:

$$L_{m2}(t) = -\frac{1}{4} \pi c^2 \rho W(t) \frac{\partial \beta_e}{\partial t} \quad (4.116)$$

There is also a nose-down pitching moment equal to an added moment of inertia $I_a = \frac{\pi}{128} c^4 \rho$ times the pitching acceleration $\frac{\partial^2 \beta_e}{\partial t^2}$:

$$M_m = \frac{\pi}{128} c^4 \rho \frac{\partial^2 \beta_e}{\partial t^2} \quad (4.117)$$

(Note that I_a is equivalent to the inertia of a cylinder of diameter $c/\sqrt{2}$ and only a quarter of the moment of inertia per unit length of the added mass cylinder of air of diameter c .)

Inertia forces arise similarly on a body in an incident flow that is varying in time, such as due to turbulent gusts in the wind. In this case, there is an additional (Archimedes type of buoyancy) force arising from the pressure gradients in the fluid associated with the incident flow accelerations acting on the volume of the body. These can be important when the fluid has an appreciable density, such as water, but are not usually so for air or where the section is thin, such as an aerofoil, and they are then normally ignored.

In addition to inertia forces, the spanwise vorticity shed into the wake as a result of changing circulation induces significant velocities that add to those in Figure 4.30.

4.5.3 The effect of the shed vortex wake on an aerofoil in unsteady flow

If the effective angle of attack of the flow relative to an aerofoil changes, the strength of the circulation also changes, but more slowly than steady flow theory would predict lagging the change in angle of attack. It is useful first to determine how the lift on an aerofoil actually develops with time after an impulsive change of angle of attack occurs, including the effect of the wake in the analysis. For example, if a sudden increase of α causes a build-up of circulation around the aerofoil, then due to Kelvin's theorem of conservation of circulation in the whole flow, this change must be matched by vorticity of equal and opposite circulation being shed into the wake.

The bound circulation on an aerofoil is the sum of the circulation of the vortex sheet distributed around the surface of the aerofoil (or along the chord in the thin aerofoil approximation). For simplicity, it is often represented by a concentrated vortex Γ at the aerodynamic centre (1/4-chord point). In steady flow conditions, the boundary condition that no flow penetrates the aerofoil surface anywhere can be replaced approximately by the simplified single-point condition discussed in Section 4.5.1 that the velocity induced by the vortex Γ , normal to the chord line, at the 3/4-chord point is exactly equal and opposite to the component of the flow velocity normal to the chord line. This approximation gives the correct result for cases of simple camber or flapping or pitching motion. Hence the 3/4-chord point is used generally as the control point for this simplified model of the flow, which assumes that the aerofoil can be represented by conditions applied at its chord line, the thin aerofoil representation.

In unsteady flow conditions, the presence of a shed vortex wake means that the velocity (often referred to as *downwash*) induced at the 3/4-chord point is caused jointly by the bound vortex and the wake vorticity; see Figure 4.31. But to continue satisfying the no penetrating flow boundary condition, the bound circulation vortex Γ must adjust so

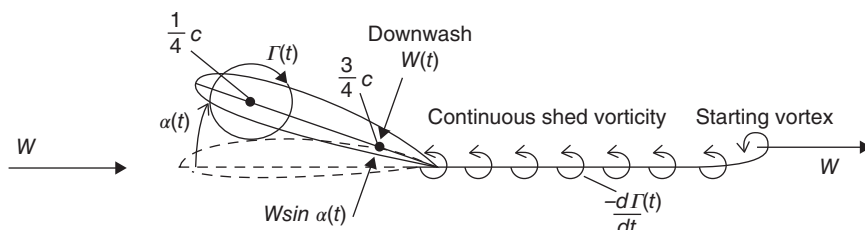


Figure 4.31 Wake development after an impulsive change of angle of attack.

that the downwash that it and the wake vortices induce is still equal and opposite to the upwash component of the incident flow velocity normal to the chord line.

After an impulsive change of angle of attack, there is a sudden change in this upwash component ($W \sin \alpha$), against which the aerofoil induces a downwash. These changes of the flow around the aerofoil cause both the growth of circulatory lift and added mass force on the aerofoil. The rapidly increasing circulation must be matched by equal and opposite strength vorticity being shed into the wake, which rolls up into a ‘starting vortex’ and convects downstream. In the linearised analysis the wake vorticity is approximated by a growing length of planar sheet aligned with the free-stream direction. The influence of the starting vortex on the downwash gets gradually weaker as the starting vortex moves away, and the bound vortex thus increases in strength with time to maintain the total downwash continuing to match the upwash. The increasing strength of the bound vortex means that, to conserve the overall angular momentum of the flow (an alternative statement of Kelvin’s theorem), continuous vorticity of the opposite sense must be shed into the wake, which in turn contributes to the downwash.

This process continues, setting up a decreasingly positive rate of change of bound circulation and accompanying shedding of vorticity into the wake as the steady condition appropriate to the new angle of attack is asymptotically approached. In reality, the shed vortex wake sheet, strongest at the starting vortex, tends to roll up about that vortex and deviate somewhat from a plane shape, as shown in Figure 4.31 (see also Graham 1983).

However, for thin aerofoil sections and small angles of attack, an analytical solution to the problem can be obtained following the thin aerofoil approximations. The bound vorticity is assumed distributed over the aerofoil chord line, and a plane wake is assumed to develop convecting at the free-stream speed. The solution first obtained by Wagner (1925) is complex and expressed in terms of Bessel functions, but several approximations exist for the Wagner indicial function (i.e. response to a step change), the most used being the one given by Jones (1945):

$$\frac{L_c(\tau)}{\frac{1}{2} \rho W^2 c \frac{dC_L}{da} \sin \alpha} = \Phi(\tau) = 1 - 0.165e^{-0.0455\tau} - 0.335e^{-0.30\tau} \quad (4.118)$$

where $\tau = 2Wt/c$ is the non-dimensional time for the aerofoil (as distinct from the non-dimensional time for the whole rotor in Section 4.4.3) based upon the half-chord length $\frac{c}{2}$ of the aerofoil. $\frac{dC_L}{da}$ is the slope of the static lift versus angle of attack characteristic of the aerofoil. This non-dimensional time τ can also be regarded as the number of half-chord lengths travelled downstream by the starting vortex after a time t has elapsed since the impulsive change of angle of attack. Equation (4.118) describes the indicial function shown in Figure 4.32.

Figure 4.32 shows the progression of the growth of the lift as time proceeds from the original impulsive change of angle of attack when the combination of circulatory and non-circulatory lift immediately takes half the final value. The steady state, full circulatory lift is achieved asymptotically.

In the situation where the angle of attack is continuously changing, which is the case, for example, for a vibrating wind turbine blade, the circulation never reaches an equilibrium state and the added mass lift never dies away. Thin aerofoil theory being a linear theory, the continuous variation in angle of attack may be built up from a sequence of

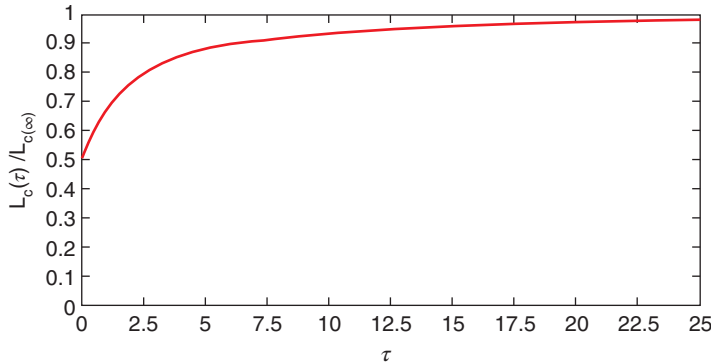


Figure 4.32 Lift development after an impulsive change of angle of attack.

impulsive steps, each of which generates a small increment in lift following the Wagner function.

Similarly, if the blade is subject to an impulsive change in the incident wind so that the blade section ‘cuts through’ the non-uniform wind profile, a lift response similar to the Wagner response to impulsive change in angle of attack takes place. This problem was first solved by Kussner (1936), and response to continuous changes in incident velocity may similarly be built up from a sequence of impulsive increments using the Kussner function.

However, an alternative to the impulsive response method for continuous changes (of body motion or incident velocity) is to calculate them as a sum of sinusoidal time variations (a Fourier decomposition). These may also be analysed from first principles by considering continuous response of the body to a sinusoidal input. The method follows the theories developed by Theodorsen (1935) and Sears (1941). In practice, this analysis based on response to sinusoidal inputs is the better where it is desired to evaluate spectral and stochastic responses, and the use of impulse responses is the better for evaluating response to arbitrary deterministic inputs such as deterministic gusts or control actions.

The impulsive response technique can be expressed by a convolution integral as follows.

Assume that the flow has been in progress for a long time, t_o , and let t be any time prior to t_o , the lift at time t is then given by

$$L_c(\tau) = L_c(0) + \frac{1}{2} \rho \frac{dC_l}{d\alpha} c \int_0^\tau W(\tau') \Phi(\tau - \tau') \frac{dw(\tau')}{d\tau'} d\tau' \quad (4.119)$$

where $\delta w = \frac{dw(\tau')}{d\tau'} \delta \tau'$ is the change in velocity normal to the aerofoil chord determined by the change in $W(\tau')$ and the changes in blade motion during the time interval.

Where varying velocity causes problems with non-dimensionalising time in the above equation, it can often be more convenient to use actual time in the numerical integration.

Theodorsen (1935) first solved Eq. (4.119) for the case of an aerofoil oscillating sinusoidally in pitch and heave (flapping motion) at fixed frequency ω and immersed in a steady oncoming wind U . Because the relationship for small amplitudes is linear, the

unsteady lift on the aerofoil is also sinusoidal but not in phase with the angle of attack variation, and the amplitude of the lift variation related to the amplitude of the angle of attack may be quite different from the static aerofoil characteristics, depending on the size of the reduced frequency parameter $k = \frac{\omega c}{2U}$, where $\omega t = k\tau$.

Theodorsen's solution shows that the circulatory lift on the aerofoil equals the quasi-steady lift of Eq. (4.116) multiplied by Theodorsen's function $C(k)$ that has both real and imaginary parts that determine the phase relationship between the lift and the effective angle of attack. This includes the added mass contribution to the lift, given by Eqs. (4.115) and (4.116):

$$\begin{aligned} C(k) &= \frac{1}{1 + A(k)} = \frac{1}{1 + \left(\frac{Y_0(k) + iJ_0(k)}{J_1(k) - iY_1(k)} \right)} \\ &= H_1^{(2)}(k) / \{H_1^{(2)}(k) + iH_0^{(2)}(k)\} \end{aligned} \quad (4.120)$$

where $J_n(k)$ and $Y_n(k)$ are Bessel functions of order n of the first and second kind. $H_n^{(2)}(k)$ is the Hankel function $J_n(k) - iY_n(k)$.

The Bessel functions are the solutions to a second order ordinary differential equation called *Bessel's equation*:

$$k^2 \frac{d^2 y}{dk^2} + k \frac{dy}{dk} + (k^2 - n^2) = 0 \quad (4.121)$$

Unlike the Legendre polynomials, the Bessel functions cannot be expressed in closed form but only as infinite series. However, they are readily available for use in computations in a number of sources (e.g. MATLAB).

Theodorsen's function is often divided into two functions, one describing the real part and the other the imaginary part:

$$C(k) = F(k) + iG(k) \quad (4.122)$$

From Jones's approximation to the Wagner function, Eq. (4.123), an approximation to Theodorsen's function is obtained:

$$C(k) = 1 - \frac{0.165}{1 - i\frac{0.0455}{k}} - \frac{0.355}{1 - i\frac{0.30}{k}} = F(k) + iG(k) \quad (4.123)$$

The exact and approximated parts of $C(k)$ are shown in Figure 4.33a and b.

The real part of $C(k)$ gives the lift that is in phase with the angle of attack defined in Eq. (4.122), and the imaginary part gives the lift that is 90° out of phase with the angle of attack (or velocity of motion) and in phase with its time derivative (or motion acceleration).

If instead of aerofoil motion the section moves through a sinusoidal change in velocity (for example, frequency component of inflow turbulence), the corresponding function is that given by Sears's (1941) analysis. In practice, because of the scale of atmospheric boundary layer (ABL) gusts to the blade chord lengths, this function, which takes account of spatial convection across the blade as well as temporal variation, is much less usually evaluated for wind turbine rotors, and the Theodorsen function is regarded as sufficiently accurate.

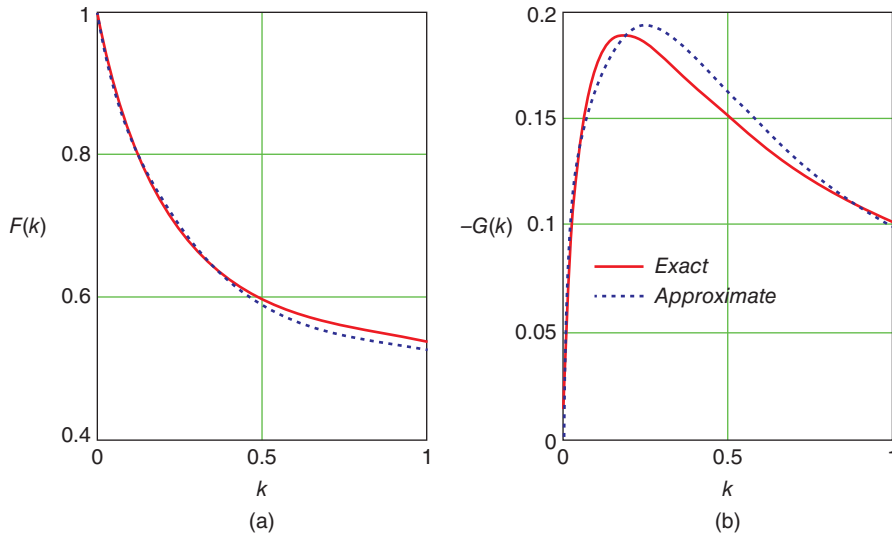


Figure 4.33 The (a) real and (b) imaginary parts of Theodorsen's function.

The limitation of the Theodorsen and Sears functions for rotor blade application is that they are derived on the basis that the shed vortex wake streams away from the blade in a straight line, whereas a rotor blade wake is helical and the blades are influenced by a stack of segments of wakes including those of other blades. Loewy (1957) developed an improved theory for a rotor blade that accounts for the repeated wake in a similar manner to Prandtl (see Section 3.9.3) but still limited by the assumption that the wakes are plane. As Theodorsen had done, Loewy used 2-D, thin aerofoil theory and produced a modification to Theodorsen's function. In Eq. (4.120), the Bessel function of the first kind $J_n(k)$ is multiplied by $(1 + W(k))$, where $W(k)$ is called the *Loewy wake-spacing function*:

$$W(k) = \frac{1}{e^{\left(2\frac{d}{c}k+i2\pi\right)} - 1} \quad (4.124)$$

d is the wake spacing defined in Eq. (3.81) and c is the chord of the aerofoil.

Miller (1964) arrived at a very similar result to Loewy by using a discrete vortex wake model.

Loewy's and Miller's theories apply only to the non-yawed rotor, but Peters, Boyd, and He (1989) have developed a more extensive theory based upon the method of acceleration potential. A sufficient number of Kinner pressure distributions are required to model both the radial and azimuthal pressure distribution on a helicopter rotor such that the pressure spikes of individual blades are represented. The theory obviates the use of blade element theory and includes automatically unsteady effects and tip-losses. Modelling of the blade geometry by this method does present some problems, however. Suzuki and Hansen (1999) have applied the theory of Peters, Boyd, and He to wind turbine rotors and make comparisons with the blade-element/moment theory. Van Bussel's (1995) theory is very similar to that of Peters, Boyd, and He but is specific for application to wind turbines.

4.6 Dynamic stall

4.6.1 Introduction

In higher wind speeds, because of unsteadiness in the ambient flow, or because of the changing angle of attack that occurs with a yawed rotor, the flow about a blade may go into and out of stall. In such circumstances the input to the stalling process is dynamic, and experience shows that it is significantly different to so-called ‘static stall’. Actually, the very process of stalling is always dynamic.

In the case of static, leading edge stall, an increase in angle of attack beyond the stall angle, initially gives rise to an adverse pressure gradient just behind the leading edge on the suction surface of the aerofoil sufficient to cause separation. The separation is not completed over this surface instantaneously. The separated flow forms a vortex that moves towards the trailing edge. While the vortex is still above the aerofoil, the flow on the suction surface upstream of the vortex is separated, but downstream the flow remains attached. Viscosity, instability, and turbulence cause the vortex to dissipate rapidly, and, although the low pressure in the vicinity of the vortex maintains lift on the aerofoil, when the vortex reaches the trailing edge and leaves the aerofoil the stall is complete and the circulation falls. The process is transient. The pressure distribution on the aerofoil changes dramatically because there is a rearward movement of the centre of pressure causing a rise in the nose-down pitching moment and a rise in pressure drag.

If the angle of attack is changing continuously as the static stall angle is reached, during the finite time for the separated vortex to progress towards the trailing edge, the angle of attack still increasing causes a further increase in lift and increase in the strength of the vortex. Lift can therefore rise to values well above the static stall level. Once the vortex has passed the trailing edge, the lift falls suddenly, even though the angle of attack may still be increasing. Once the flow is fully stalled, if the angle of attack now decreases, the lift remains low and fairly constant until re-attachment of the flow occurs. Re-attachment does not take place until the angle of attack is significantly lower than the static stall level. The whole cycle, shown in Figure 4.34, is known as *dynamic stall*.

Dynamic stall will occur on a wind turbine when the rotor is yawed and at a low tip speed ratio (high wind speed), when the rotor encounters a gust, and on emerging from tower shadow. The loads experienced by a blade during dynamic stall can be large and can cause significant fatigue damage.

4.6.2 Dynamic stall models

A number of dynamic stall models have been put forward and used over the years: the Boeing model (simplest and considers time lags only; Tarzanin 1972), Johnson (1969), Gormont (1973), Beddoes (1975), Gangwani (1982), and the ONERA, Petot (1989) are among the best known. Leishman and Beddoes (1989) developed later a model specifically for rotorcraft that improved on the original Beddoes (1975) theory. It is now the preferred method for wind turbines as well as helicopter rotors. A study of the dynamic stall behaviour of a National Renewable Energy Laboratory (NREL) wind turbine aerofoil is given by Gupta and Leishman (2006). A report from the Risø National Laboratory

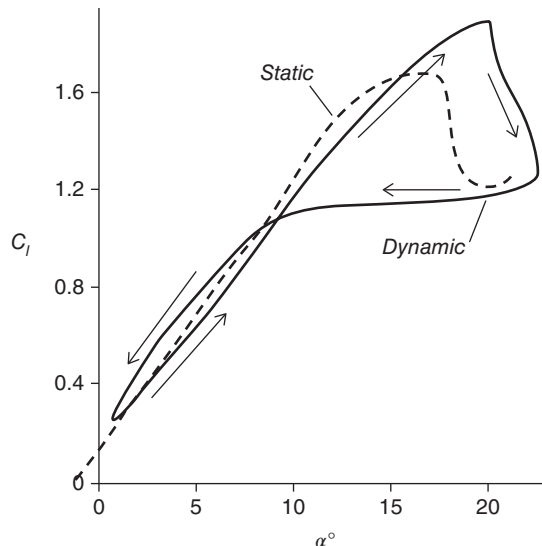


Figure 4.34 Typical dynamic stall behaviour.

in Denmark by Hansen, Gaunaa, and Madsen (2004) also discusses the application for wind turbines.

The Leishman–Beddoes model

The Leishman–Beddoes (1989) model will be described in some detail. It is built up from a number of components (analytical, unsteady attached flow theory, and separated flow theory).

Consider a blade section undergoing time-varying angle of attack ($\alpha(t)$, usually oscillatory, $= \alpha_0 e^{i\omega t}$) due to heave motion or interaction with a gust. The force coefficients C_N (normal force), C_M (moment), and C_{cT} (chordwise thrust) are considered to be functions of α and $d\alpha/dt$ only. These coefficients are made up of a non-circulatory (impulsive) part (I), a circulatory part that is subject to reduction due to separation (S), and a vortex force increment (V). Thus:

$$\begin{aligned} C_N &= C_I^N + C_S^N + C_V^N \\ C_M &= C_I^M + C_S^M + C_V^M \\ C_{cT} &= C_S^M \end{aligned} \quad (4.125)$$

Changes with time are modelled as a series of small steps, the impulsive part of the force being taken directly from the Wagner or Kussner attached flow theories for the appropriate impulsive motion (see Section 4.5.3). The circulatory force coefficients depend on the classical Kirschoff formulae (Thwaites 1987) for steady separated flow forces. These must be modified for the lags that occur in the development of the separation position and for the reduction in the lift curve slope due to attached flow unsteady effects.

The Kirchhoff formulae give values of the force coefficients C^S in terms of the separation position on the suction surface. Beddoes proposed formulae for this:

$$f(\alpha, \alpha_1) = x_s/c = 1.0 - 0.3 \exp\{(\alpha - \alpha_1)/0.05\} \text{ if } 0 \leq \alpha \leq \alpha_1$$

and

$$= 0.04 + 0.66 \exp\{(\alpha_1 - \alpha)/0.05\} \text{ if } \alpha > \alpha_1 \quad (4.126)$$

where α_1 is the static stall angle;

$$C_N^S = 0.5\pi\alpha\Phi(\tau)\{1 + \sqrt{f_1}\}^2 \quad (4.127)$$

$$C_M^S = 0.5\pi\alpha\Phi(\tau)[-0.135(1-f_0) + 0.04 \sin(\pi f_0^2)](1 + \sqrt{f_0})^2 \quad (4.128)$$

$$C_{cT}^S = 0.5\eta\sqrt{f_1.(C_N^S)^2/\pi} \quad (4.129)$$

where η is a reduction factor ~ 0.95 .

$\Phi(\tau)$ is the lift function from the relevant unsteady thin aerofoil theory (e.g. Wagner's theory, Section 4.5). τ is the dimensionless time, $2Wt/c$, which is non-dimensionalised by the mean incident velocity W at the blade section and the semi-chord $c/2$. All of the time constants in the following analysis are similarly non-dimensional. f is the value of the separation point ratio x_s/c , and f_0 , f_1 , and f_2 are dimensionless functions of time, described below, which modify the attached flow forces for the effects of separation.

During a rapid increase of incidence a delay occurs in the movement of the separation point that is strongly affected by the growth of the leading edge pressure peak. This can be characterised by a normal force coefficient C_N^* that satisfies the lag equation:

$$dC_N^*/d\tau = (C_N^S - C_N^*)/T_P \quad (4.130)$$

where the time constant T_P is taken to have a value of 1.7. An equivalent angle of incidence for computing the separation position is then written as $C_N^*/(dC_N^S/d\alpha) \approx 0.5C_N^*/\pi$.

The separation position f_1 itself satisfies a lag equation with time constant T_f :

$$df_1/d\tau = \{f(0.5C_N^*/\pi, \alpha_1) - f_1\}/T_f \quad (4.131)$$

However, the pitching moment is found to require a different dynamic separation point given by $f_0 = \max\{f_1, f_2\}$, where f_2 satisfies another lag equation with time constant T_{f0} :

$$df_2/d\tau = \{f(\alpha, \alpha_1) - f_2\}/(0.5T_{f0}) \quad (4.132)$$

Leishman and Beddoes state that the accurate prediction of the onset of leading edge separation is very important. This is assumed to occur when a critical leading edge (negative) pressure peak and hence adverse gradient are reached. These in turn are related to the normal force so that separation occurs when $C_N \geq C_{N1}$ (≈ 1.55 for a NACA0012 aerofoil at high Reynolds number). Vortex shedding is taken to occur at $\tau = \tau_1$ when C_N reaches the critical value C_{N1} . The vortex force increment is then evaluated by considering the growth and convection of the resulting shed vortex (see Figure 4.35) from the time τ_1 when it is shed to the time $\tau_1 + T_{vl}$ when it reaches the trailing edge. τ_v is the 'vortex time' variable, $= \tau - \tau_1$.

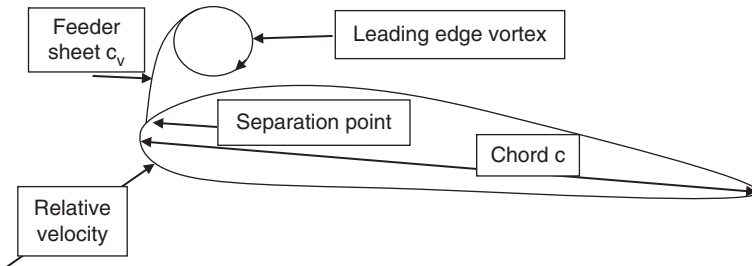


Figure 4.35 Growing leading edge vortex and idealised feeding sheet.

A lag equation with time constant T_v , where T_v and T_{vl} are given below, is used for C_N :

$$dC_N^v/d\tau = dc_v/d\tau - C_N^v/T_v \text{ if } dc_v/d\tau > 0 \text{ and } 0 < \tau < 2T_{vl} \quad (4.133)$$

$$dC_N^v/d\tau = -C_N^v/T_v \text{ otherwise;}$$

$$C_M^v = -0.25\{1 - \cos(\pi t/T_{vl})\}C_N^v \text{ if } t \leq 2T_{vl}, \text{ and } = 0 \text{ if } t > 2T_{vl} \quad (4.134)$$

c_v represents the contribution to the vortex force of the vortex sheet that feeds the growing vortex (considered to be the ‘inner spiral’) joining it to the shedding point at the leading edge, as shown in Figure 4.35:

$$c_v = 2\pi\alpha\Phi(\tau) - C_N^S = 2\pi\alpha\Phi(\tau)\{1 - 0.25(1 + \sqrt{f_1})^2\} \quad (4.135)$$

and its derivative is:

$$dc_v/d\tau = (\pi/2)\{-\Phi(\tau).(df_1/d\tau)(1 + 1/\sqrt{f_1}) + (d(\alpha\Phi(\tau))/d\tau)(4 - (1 + \sqrt{f_1})^2)\} \quad (4.136)$$

To model the different lags in movement of the separation point when incidence α is increasing or decreasing (values given here are for a NACA0012 aerofoil),

$$\alpha_1 = \alpha_{10} = 0.27 \text{ for } \alpha \text{ increasing and } \alpha_1 = \alpha_{10} - 0.037(1 - f_1)^{1/4} \text{ for } \alpha \text{ decreasing.}$$

The timescales T_f and T_v are given by the following relationships to the empirical (non-dimensional) times T_{f0} , T_{v0} , and T_{vl} , where suggested values for these are 3.0, 4.0, and 6.0, respectively (S114 aerofoil, Sheng et al. 2010):

For α increasing:	$T_f = T_{f0}$,	$T_v = T_{v0}$	$0 \leq \tau \leq T_{vl}$
	$T_f = \frac{1}{3}T_{f0}$,	$T_v = 0.25T_{v0}$	$T_{vl} < \tau \leq 2T_{vl}$
	$T_f = 4T_{f0}$,	$T_v = 0.90T_{v0}$	$2T_{vl} < \tau \leq 4T_{vl}$
For α decreasing:	$T_f = \frac{1}{2}T_{f0}$,	$T_v = 0.50T_{v0}$	$0 \leq \tau \leq T_{vl}$
	$T_f = \frac{1}{2}T_{f0}$,	$T_v = 0.50T_{v0}$	$T_{vl} < \tau \leq 2T_{vl}$
	$T_f = 4T_{f0}$,	$T_v = 0.90T_{v0}$	$2T_{vl} < \tau \leq 4T_{vl}$

After the flow reattaches and $C_N < C_{N1}$ again, $T_v = T_{v0}$.

Some methods include the effect of the feeding sheet during periods when the incidence is decreasing, but Bjorck et al. (1999), who has implemented the model for wind turbine dynamic stall, has stated that it should only apply when α and the vortex are increasing.

These three component parts of the dynamic stall forces are then substituted into Eq. (4.125) to give the total force coefficients C_N , C_M , and C_{cT} . The calculation procedure is in principle iterative because the calculation of the separation position [Eqs. (4.126) and (4.131)] and the onset of separation at the leading edge (τ_1) require computation of the components of C_N at that time. Because stall proceeds sequentially, it is generally possible to incorporate this into the timestepping solution procedure by computing the value of C_N at an interim step without further iteration.

The following summarises a calculation procedure for the normal force due to aerofoil heave motion.

A series of non-dimensional timesteps τ_0 , $\tau_1 = \tau_0 + \Delta\tau$, etc. are set up to cover the motion in question from τ_0 to τ_N .

Then for $\tau = \tau_1, \tau_2, \dots$

- 1) Evaluate and store the effective angle of attack $\alpha(\tau) = w(\tau)/U_\infty$ from the assumed known aerofoil heave motion $w(\tau)$.
- 2) Compute the normal force $L(\tau)$ by numerical integration of the convolution product in Eq. (4.119) of the Wagner function $\Phi(\tau)$ and $dw/d\tau$ at each timestep for the whole sequence of times from τ_0 to the current time τ . In this example, $W = U_\infty$ assumed constant. (For small angles of attack lift and normal force are assumed to be equal.)
- 3) Compute the impulsive (added mass) force coefficient $C_N^I(\tau) = (\pi dw/d\tau)/U_\infty$.
- 4) Tabulate T_f and T_v according to the range of τ in the table for both α increasing and decreasing, given values of non-dimensional time constants T_{f0} , T_{v0} , and T_{f1} .
- 5) Evaluate $f(\tau)$ given the values of α and α_1 and hence with time constants T_{f0} , T_f , and T_v numerically integrate Eqs. (4.130)–(4.132) for C_N^* , C_N^S , f_1 , and f_2 , using a predictor-corrector or other multi-step method in which intermediate values of the above variables are used in the integration over each timestep.
- 6) Compute $C_N(\tau) = C_N^I(\tau) + C_N^S(\tau)$, and when C_N reaches the critical value C_{N1} at which shedding of a growing vortex starts at the leading edge, set $\tau_1 = \tau$ and define $\tau_v = \tau - \tau_1$ for subsequent times.
- 7) Evaluate $C_N^V(\tau)$ by timestepping integration of Eq. (4.133) with Eq. (4.136), again using a multi-step method and the time constant T_v from the stored table according to the value of τ_v .
- 8) Compute $C_N(\tau) = C_N^I(\tau) + C_N^S(\tau) + C_N^V(\tau)$.

The above equations are for an aerofoil undergoing changes of incidence through heave motion. If pitching is involved there are some additional $d\alpha/dt$ terms, but the procedure is exactly the same. If the dynamic stalling is caused by a blade interacting with a gust or convecting flow disturbance, the Wagner function $\Phi(\tau)$ is replaced by the Kussner function $\Psi(\tau)$, but otherwise the process is the same. The timestepping procedure

using indicial functions is the more usual treatment rather than the alternative procedure of assuming sinusoidal motion throughout using the Theodorsen or Sears functions for the underlying attached flow, particularly because that requires an assumption of quasi-linearity. The empirical coefficients in the procedure are dependent on the aerofoil section and were originally derived as functions of the Mach number. They are given here for incompressible (i.e. low Mach number) flow and for a NACA0012 aerofoil. There are also a number of variants of the method.

Results computed with this model are compared in Figure 4.36 with test data and a CFD simulation of moderate dynamic stall for an aerofoil undergoing oscillatory incidence variation:

$$\alpha = \alpha_0 + \alpha' \sin(0.1\tau) \quad (4.137)$$

The expressions in Eqs. (4.127)–(4.129) assume that the idealised steady flow lift (or for moderately small angles the normal force) coefficient of $2\pi\alpha$ applies. To take account of the effects of Reynolds number and thickness on the force coefficient, 2π is often replaced by a_0 , the actual, experimentally, or numerically determined steady lift curve slope.

The ONERA model

In the ONERA model (Petot 1989), the lift and moment generated during the dynamic stall are calculated as a combination of a linear (unsteady) attached flow result and a non-linear increment resulting from the development of the stall. The model is based

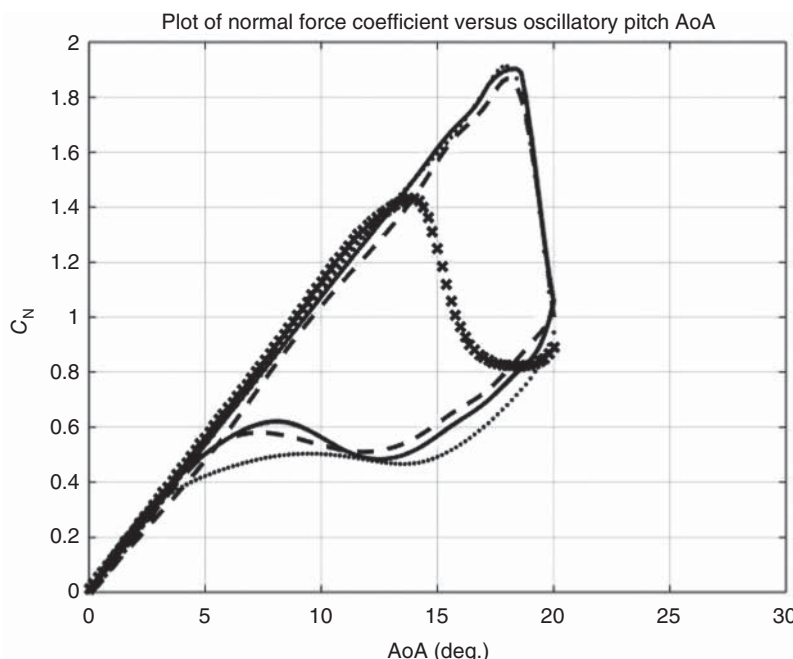


Figure 4.36 Normal force coefficients for a NACA0012 aerofoil in cyclic pitch through the stall regime. x, static data; ..., measured; - -, CFD; - Leishman–Beddoes model.

on a quite large number of empirical coefficients that have been obtained by parameter identification from experimental measurements on oscillating aerofoils.

The Gangwani model

The Gangwani model (Gangwani 1982) is based on a time-domain representation of the linear unsteady attached flow using an approximation to the Wagner function. The non-linear separated flow part is based on empirical equations incorporating time lags in the apparent angle of attack. These equations require a large number of coefficients that have mostly been obtained from experimental measurements on oscillating aerofoils.

The three dynamic stall models discussed have some similarities. However, the Leishman–Beddoes model (1989) has probably achieved the widest usage.

4.7 Computational fluid dynamics

4.7.1 Introduction

The methods for analysing the flow through a wind turbine in various conditions developed in Chapters 3 and 4 are all simplifications necessary to facilitate the calculations; to obtain accurate solutions to the flow conditions, a much more complex method is required. CFD is a very large and highly developed subject with extensive references available. Only a very limited overview is given here for low Mach number flow applications.

The analysis of the flow approaching a turbine rotor that is not stalled can be undertaken, with little loss of accuracy provided predictions of viscous drag effects are not important, by using the equations of inviscid flow known as the *Euler (momentum) equations*, developed in the eighteenth century. These are, for vector velocity \mathbf{U} :

$$\frac{\partial \mathbf{U}}{\partial t} + \mathbf{U} \cdot \nabla \mathbf{U} = -\frac{1}{\rho} \nabla p \quad (4.138)$$

The Euler equations, together with the continuity equation, can form the basis of a numerical procedure to obtain a solution to the flow conditions. However, during the course of the flow through the rotor and in the wake, the Euler equations may no longer be adequate because they cannot deal with boundary-layer flow close to a blade surface or with separated flow conditions and the wake. In the nineteenth century, the fully viscous flow equations of Navier and Stokes were developed and are used today to predict both laminar and turbulent flows. The additional terms in the Navier–Stokes momentum equations, shown below, introduce the effect of a constant kinematic viscosity ν^1 derived from Newton's theory of viscous flow:

$$\frac{\partial \mathbf{U}}{\partial t} + \mathbf{U} \cdot \nabla \mathbf{U} = -\frac{1}{\rho} \nabla p + \nu \nabla^2 \mathbf{U} \quad (4.139)$$

Equation (4.139) is known as the *velocity-pressure* or *primitive variable* formulation of the Navier–Stokes equations.

¹ Constant kinematic viscosity is appropriate for low-speed air flows typical of those through wind turbine rotors.

CFD is essentially a numerical solution of these equations. For the analysis of a wind turbine rotor, the flow volume influenced by it is divided into a 3-D mesh (or a 2-D mesh in the case of sectional analysis, such as of a blade). At the rotor surfaces the mesh needs to be very fine to model attached flow boundary layers, whereas in the wake a coarser mesh will suffice. Especial care needs to be taken in regions of high shear such as the wake boundary and close to the vicinity of shed vortices. The number of unknowns (degrees of freedom) to be solved in most 3-D problems is very large, and, because the solution process is iterative, the solution times are of long duration. The wind turbine rotor introduces a further complication because the rotor and other parts of the wind turbine together with the incident wind field are in relative rotation to each other. Much of the skill and effort required to carry out an analysis is invested in the mesh generation, including the need for moving boundaries. A principal advantage of the full CFD method for wind turbine blades is that no experimentally based aerofoil data is required because the method calculates the flow conditions surrounding a blade surface.

Because of computational cost, CFD methods are still used more for research but are also used by wind turbine designers for specific validations of analyses, which themselves are based on simpler, faster methods such as blade-element-momentum.

4.7.2 Inviscid computational methods

In the case of flow analysis of rotor blades, which in practice is one of the most important areas of wind turbine aerodynamics, some aspects of the flow field may be treated adequately by solutions of the inviscid (i.e. Euler) equations. This is particularly true for flows in which there is little or no separation over the blades, where pressure dominated forces need to be predicted and where values of viscous drag are either not required or are more conveniently obtained empirically. The advantage of restricting solutions to the Euler equations is that these equations can be solved much more quickly than the Navier–Stokes equations. Examples where computational efficiency is particularly important are the prediction of unsteady flows such as those associated with structural vibration, flutter and effects of incident gusts and turbulence, wake interactions and unsteady effects of yaw, incident shear, and sudden changes of blade pitch. In many of these flows, large numbers of frequency cases or long time histories must be computed to provide converged statistical quantities such as spectra, for example, and fast methods of solution for each case are necessary.

The Euler equations are widely used for solving general 2-D and 3-D compressible flows (i.e. where the Mach number of the flow is not very small), particularly due to the information that can be gained on flows with shock waves. These flows are not relevant to flow around wind turbine rotors for which the incident blade Mach number rarely exceeds 0.3. If the velocities are considerably smaller than the speed of sound, as is the case for wind turbines, and provided the frequencies that are important are not very high, the density ρ may be considered to be constant, and the flow is referred to as *incompressible*. Field methods (as distinct from body surface panel methods considered below) in which the whole of the relevant flow field is discretised on a grid have been used to compute inviscid rotor flows. There is often an option in commercial Navier–Stokes codes to run them as inviscid flow solvers of the Euler equations. Alternatively, the Euler and incompressible mass flow continuity equations may be converted to a streamfunction(ψ) – vorticity(ω) formulation and solved on a grid over the flow field for axisymmetric flows such as for an

actuator disc (see, for example, Soerensen et al. 1998) or for 2-D planar (sectional) flows. Such grid based methods of solving the Euler equations follow many numerical procedures similar to those described below for the Navier–Stokes equations, but because of the absence of the large gradients associated with viscous and turbulent stresses in the boundary layers, they are able to achieve comparable accuracy on much larger grid mesh cells. Hence, they require much shorter computation times to achieve comparable accuracy because of the fewer degrees of freedom in the solution.

In addition to the grid methods of solution involving meshing the whole flow field around the body, there exist a class of methods known as *boundary-integral* or *panel methods*, which may be used when the equations governing the velocity field can be made linear and reduce the dimension of the problem by one. Thus 3-D field problems become solutions to be computed over 2-D surfaces, and similarly 2-D sectional field solutions reduce to line integrals around the section perimeter. In the general case the surfaces of the body and any thin wakes are meshed (divided into discrete panels) that provide a sum of fundamental solutions. These are known as *singularity* solutions because of their property of being unit flow fields localised to a singular point where the solution takes an infinite value. This reduction of dimension of the problem allows faster solutions to be computed but depends on the inviscid equations for the velocity being expressible in linear form. In that case, a linear combination of the fundamental panel based singularity solutions makes up the whole flow, the coefficients being defined by the boundary conditions.

Flows can be treated as inviscid if all vorticity (which will be represented here by the vector symbol ω and is the cross-product derivative of the velocity field, $\nabla \times \mathbf{U}$) mainly originates on the body surfaces), remaining confined to thin sheets on these surfaces and within their wake, with effectively zero vorticity outside these sheets where the flow is termed *irrotational* flow.

This condition:

$$\boldsymbol{\omega} = \nabla \times \mathbf{U} = 0 \quad (4.140)$$

allows the velocity to be written as the gradient of a scalar velocity-potential ϕ :

$$\mathbf{U} = \nabla \phi \quad (4.141)$$

which combined with the equation for conservation of mass:

$$\nabla(\rho \mathbf{U}) = 0 \quad (4.142)$$

leads to a second order partial differential equation for the potential ϕ .

In that case, the equation for the potential ϕ becomes Laplace's equation:

$$\nabla^2 \phi = 0 \quad (4.143)$$

Because this equation is linear, panel methods that construct the solution from a sum of fundamental solutions of the equation may be used, requiring a linear sum with unknown coefficients to satisfy the boundary condition of zero flow through the body surfaces. Many panel methods have been developed, the earliest and one of the most widely used for closed body cases where wake effects are less important being the source panel method.

One of the panel methods most applicable to wind turbine rotor flows is the vortex method. In this method the panels that may be on the body surface (or on the mean single camber surface applying a further level of approximation for thin blade sections) are composed, most often, of a network or lattice of vortex lines lying along the edges of the panels. Where a thin wake is present the vortex panels are spread over the mean wake surface being freely convected with it. Because this convection process is non-linear due to the velocity field induced by the wake elements themselves contributing to their movement, it is frequently assumed that the wake-induced convection can be linearised, simplified by assuming that the wake travels with the undisturbed air flow. This vortex panel method, known as the *vortex lattice method (VLM)* (see Figure 4.37), is exactly equivalent to the constant dipole panel method, which consists of a uniform source density and a uniform sink density of equal and opposite strength spread uniformly over either surface of the panel sheet. There is an extension of the method for unsteady flow: the *unsteady vortex lattice method (UVLM)*. Boundary conditions have to be satisfied on the body surface or, in the case of the thin aerofoil approximations, on the mean or camber surface. The most usual boundary condition is that there is zero normal velocity relative to the body at its surface. However, in the case of a thick body with closed surface, an internal zero tangential velocity boundary condition evaluated on the inside of the surface may be used instead and can give superior accuracy.

The UVLM can be used very efficiently to give satisfactorily accurate predictions of steady or unsteady flow over aerofoils, wind turbine blades, and complete rotors provided there is no large-scale separation of the flow (stalling) leading to thick regions containing vorticity, and skin friction drag is dealt with separately. *Low Speed Aerodynamics* by Katz and Plotkin (1991) gives a very detailed discussion of the method.

At the lowest level of representation, the panels covering the aerofoil or rotor blade can be reduced to a single panel chordwise with a suitable number of divisions spanwise. In this case the strength of each chordwise panel is equal to the circulation about the blade at that section, the vortex line at the front of the panel is aligned with the quarter chord of the section, and the boundary condition is evaluated at the three-quarter chord (see earlier discussion in Section 4.5.1). The panel is completed by a vortex line downstream of the trailing edge of the blade section. This arrangement satisfies the Kutta–Joukowski trailing edge condition and provides at each timestep the vortex just shed into the wake from the blade trailing edge. Thereafter, in accordance with vorticity transport, the vortex is convected downstream with the local flow velocity evaluated at its position. This representation is the basis of actuator line theory (see Mikkelsen 2003).

Panel methods, because they are lower order of accuracy and omit viscous effects, are usually regarded as distinct from and often not categorised as CFD. If information is required regarding viscous effects such as evaluation of blade drag force, the inviscid panel pressure solution may be supplemented by boundary-layer calculations

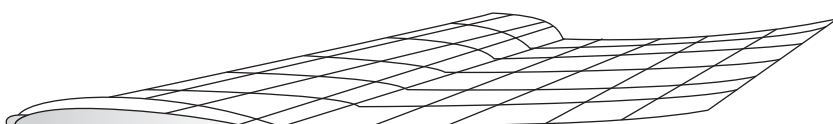


Figure 4.37 Sketch of vortex lattice panels on a blade surface and wake.

on the blade surfaces ‘driven’ by the inviscid pressure distribution. This is formally an inner-outer approximation procedure to provide a viscous-inviscid solution that not only enables a first order calculation of skin friction and drag to be computed but also provides through the boundary-layer displacement thickness (in effect an outward displacement of the body surface due to the retarded velocity in its growing boundary layer) a correction to the pressure distribution and lift force for viscous effects. The procedure is strictly only applicable where the viscous layers remain thin, and hence the boundary layers remain attached or have at most moderate separation, in which case the procedure involves an inverse calculation. Some widely used panel based methods use this procedure (see, e.g. XFOIL, Drela 1989).

4.7.3 RANS and URANS CFD methods

Numerical methods of solving the full viscous flow equations, the Navier–Stokes equations, are referred to as direct Navier–Stokes (DNS) methods to indicate that there is no modelling of turbulence involved. All scales down to the smallest are resolved on the grid and solved directly. This requires extremely large computing resources even for flows well below practical scales. Up to the present time, DNS solutions have only been obtained for unsteady, 3-D flows up to Reynolds numbers Re of the order of 10^4 and simple geometries.

Turbulence is normally present in flows at practical scales, and the size of the smallest eddies of the turbulence relative to the local flow length scale being of order ($Re^{-3/4}$) require meshes with the order of ($Re^{9/4}$) cells. Typically, at least four unknowns need to be resolved at each node point and at every timestep, presenting a presently infeasible size of problem.

Therefore, it is usual to model the turbulence in the Navier–Stokes equations for most practical flows. In addition, where turbulence is modelled, there is a need to consider the transition process from laminar (‘smooth’ turbulence-free flow) to turbulent flow and provide a method of predicting where it occurs.

The simplest level of modelling turbulence solves the time-averaged Navier–Stokes equations.

The vector velocity field is written as:

$$\mathbf{U}(t) = \overline{\mathbf{U}} + \mathbf{u}'$$

where $\overline{\mathbf{U}}$ is the time mean velocity, \mathbf{u}' is a turbulent fluctuation with $\overline{\mathbf{u}'} = 0$, and (overbar $\overline{}$) indicates a mean value. Inserting this into the Navier–Stokes equations [see Eq. (4.139)] and taking the time mean (indicated by an overbar throughout) gives:

$$\overline{\mathbf{U}}\nabla\overline{\mathbf{U}} + \overline{\mathbf{u}'\nabla\mathbf{u}'} = -\nabla\frac{\overline{p}}{\rho} + \nu\nabla^2\overline{\mathbf{U}} \quad (4.144)$$

These are the Reynolds averaged Navier–Stokes (RANS) equations. $\overline{\mathbf{u}'\nabla\mathbf{u}'}$ is the resulting Reynolds stress term, which is the effective stress due to the turbulence in the flow acting on the mean velocity field and typically much larger than the viscous stress term $\nu\nabla^2\overline{\mathbf{U}}$. As a result, the latter may often be treated as negligible when Reynolds stress is present in the RANS equations, except in certain regions such as the sub-layer of a turbulent boundary layer.

The simplest and earliest methods modelled the Reynolds stress with an eddy viscosity ν_e (see, e.g. Anderson 1991) analogous to the molecular viscosity but defined by the local flow conditions. Many turbulence models of this type were developed requiring minimal computation, the earliest and simplest being the Prandtl *mixing length* model.

By the 1960s, more advanced methods were developed that solved additional equations derived from the Navier–Stokes equations for convection of the turbulence energy $k = \frac{1}{2} u'_j u'_j$ or the Reynolds stresses $u'_j u'_k$. Here the subscript indices j and k may take any value 1–3 for the three directions, and a repeated index implies summation over all three. In these equations some terms can be evaluated exactly, but others (for example, turbulence diffusion and dissipation) must be modelled using empirical equations or formulae (such as the algebraic stress models; see, e.g. Speziale 1991). It has also been common practice to replace the inner region of turbulent boundary layers by the analytically derived ‘log law’ or wall layer to avoid having to use very small grid cells in this region adjacent to the body surface. This replacement, often an option, is quite accurate for attached turbulent boundary layers but not so in more general situations, such as beneath a separation region.

The best known of the turbulence modelling methods is the k - ε method, where ε is the turbulence dissipation. Many other variants are now widely used, the k - ω ($\omega = \varepsilon/k$) and shear stress transport (SST) methods being other versions with improved properties. The reader is advised to consult the many papers and books (see, e.g. Menter et al. 2003) that describe these methods. Many well-used RANS codes, particularly commercial codes, allow the turbulence model to be selected from a suite of models provided in the code. A reason for this is that not only do models vary in computational cost but, being models, they are found to be more or less appropriate for different flows and different regions of flow. The empirical coefficients and dependencies used in these methods have often been developed from experimental data measured in thin shear-layer turbulence (turbulent boundary layers, jets, and wakes) and can be found to be less successful in modelling regions of large-scale separation.

As mentioned above, prediction of the onset of turbulence (transition) is required because, of themselves, these methods being time-averaged cannot predict instability onset but can predict where the modelled turbulence becomes self-sustaining. Two methods of predicting transition and developing a turbulent flow are commonly used. The first is the ‘ e^n ’ method ($n \sim 9$; see, e.g. White 1991), which predicts the exponential growth of transition from infinitesimal disturbances in the flow. The second is the method of seeding the flow with low level turbulence at the inlet boundary. This latter is easily done, and turbulence grows in the flow from where turbulence production (equal to the product of the turbulence energy or stress terms with the mean flow gradients) begins to exceed the dissipation. This method should be regarded as a model of *bypass transition* in which a significant level of external flow turbulence of the right scale drives transition in the boundary layers. Bypass transition is common in turbomachinery but not for wind turbine rotor blades because the incoming turbulence length scales in the ABL are relatively very large.

At high angles of attack as stall is approached, the presence and type of separation bubbles that cause transition are frequently crucial in defining where and how separation takes place on aerofoil sections and in defining the type of blade stall that occurs. Empirical correlations such as provided by Gault (1957) provide useful information,

since, because of the very small size of separation bubbles, reliable resolution of the transition process within the separated shear layer of a bubble is extremely difficult.

More recently the RANS method has been expanded to unsteady flows. This is justifiable in the context of Reynolds averaging provided the characteristic timescale of the main flow field is much longer than the timescale of the turbulence so that the small timescale turbulence can be Reynolds averaged (\sim), while the time-dependent main flow field \tilde{U} is resolved to give the unsteady Reynolds averaged Navier–Stokes (URANS) equations:

$$\frac{\partial \tilde{U}}{\partial t} + \tilde{U} \nabla \tilde{U} + \widetilde{u' u'} = -\widetilde{\nabla p / \rho} + \nu \nabla^2 \tilde{U} \quad (4.145)$$

The URANS method is suitable for modelling, for example, the turbulent boundary layers on an aerofoil or wind turbine blade undergoing typical unsteady motions due to cyclic variations or structural dynamic response but less good for modelling large-scale time-dependent separations such as occur during dynamic stall. Experience with URANS indicates some improvements over steady RANS in representing large-scale separation regions but generally still poor accuracy in many cases.

4.7.4 LES and DES methods

The rapid development of computing capability and the disappointing predictions of RANS and URANS particularly for separated flows has led to the development of the large eddy simulation (LES) technique. This follows a turbulence averaging philosophy somewhat similar to URANS in that the flow is segregated into a part in which the fluctuations in the flow having larger spatial and timescales are resolved on the grid and a part containing the smaller eddy scales that are modelled. Strict applications of the method assume that the modelled scales are restricted to the isotropic eddies at the high frequency end of the turbulence spectra. This puts great constraints on the size of the grid to be able to resolve all eddy scales that are larger. Therefore, in practice this constraint is often relaxed somewhat. The small turbulent eddies are modelled by a sub-grid eddy viscosity. Theoretical work has developed and improved the methods of computing the sub-grid eddy viscosity to deal accurately with an increasing range of flows (Germano et al. 1991). The main constraint on the LES method is the computation costs because of the requirement for extremely small grid cells. A more economic version has been developed, termed *detached eddy simulation (DES)*, in which the LES method is confined to regions where the flow is separated. This limits the LES to a few separated and wake regions of the whole flow field in which the scale of turbulence is somewhat larger than in the attached boundary layers. URANS is used everywhere else in the flow (such as attached turbulent boundary layers, which would otherwise require extremely small grid sizes for LES but where URANS performs well). The combination method is rapidly becoming the dominant method of providing accurate flow simulations, including those involved in wind turbine and wind farm studies. However, these methods are still too expensive for routine industrial use and should be regarded as providing the basis for validation of the more approximate methods widely used in the industry. Secondly, they can now often provide a better insight into physical mechanisms occurring in those flows, which are difficult to get from physical experiments. Wind tunnel experiments being far from representative in Reynolds number and constrained by blockage and full-scale experiments being restricted by measurement and controllability issues are limited in this respect.

4.7.5 Numerical techniques for CFD

Having dealt with panel methods for inviscid flows in Section 4.7.2, this section focuses on field methods of solution in which the discretized equations are solved on a mesh of nodes or cells that entirely covers the flow domain of interest out to boundaries where disturbances from ambient conditions may be considered negligible or able to be specified simply.

Inviscid flow

The time-dependent Navier–Stokes equations for momentum and continuity for low speed, constant density flows in three dimensions require a discrete timestepped solution of four variables, three velocities, and pressure. The pressure can be eliminated by taking the curl ($\nabla \times \dots$) of the equations to give the vorticity transport equation:

$$\frac{\partial \boldsymbol{\omega}}{\partial t} + \mathbf{U} \nabla \boldsymbol{\omega} = \boldsymbol{\omega} \nabla \cdot \mathbf{U} + \nu \nabla^2 \boldsymbol{\omega} \quad (4.146)$$

where $\boldsymbol{\omega} = \nabla \times \mathbf{U}$ is the vorticity.

This equation shows that provided the flow through the blades of a rotor remains ‘attached’ or ‘unseparated’ until it separates from the trailing edge of the blades and diffusion remains small (true for high Reynolds numbers), the vorticity that is created by the no-slip condition on the blade surfaces remains within very thin layers on the blades and within thin sheets in the wake. Because to first order pressure forces are continuous across thin sheets of vorticity, this result is the basis of the applicability of the Euler equations to provide reasonably accurate predictions of the pressure fields and therefore the dominant forces on rotors. Farther downstream the vortex sheets rapidly become unstable, breaking down into large volumes of turbulent wake, but while these may affect other downstream wind turbines, they have little effect on the rotor generating the wake.

In 2-D flows the vorticity only has one non-zero component, which is in the direction normal to the flow plane and is therefore effectively a scalar. The two components of velocity may be expressed as the derivatives of a scalar streamfunction ψ :

$$\frac{\partial \psi}{\partial y} = -U, \quad \frac{\partial \psi}{\partial x} = V \quad (4.147)$$

Substituting this definition of ψ , which identically satisfies the (constant density) mass flow conservation Eq. (4.142), shows that ψ satisfies the Poisson equation:

$$\frac{\partial^2 \psi}{\partial x^2} + \frac{\partial^2 \psi}{\partial y^2} = -\omega \quad (4.148)$$

Similarly, substituting the definition of ψ into the vorticity transport equation leads to ψ - ω equations that are known as the *derived variables* formulation. For 2-D planar or axisymmetric flow, they only involve the two scalar variables ψ and ω and therefore have a significant computational advantage over the velocity-pressure formulation, which involves three. Because the ψ - ω formulation has intrinsically satisfied mass conservation, it avoids the difficulties with the pressure terms in *incompressible flow*, which cannot be calculated directly from mass conservation.

In 3-D flows the advantage of fewer variables is lost because the $\psi\text{-}\omega$ formulation requires the solution of six variables, three components of ψ (which is now a vector) and three of vorticity. This is two more in total than the primitive variable formulation [Eq. (4.139)]. The function ψ is defined by:

$$U = \nabla \times \psi \text{ with } \nabla \cdot \psi = 0 \quad (4.149)$$

It no longer has the properties of a streamfunction and is often referred to as a *vector potential*. In addition, the boundary conditions at a body surface become more difficult to apply. For all the above reasons, the $\psi\text{-}\omega$ formulation is rarely used in 3-D flows, and nearly all CFD methods are based on the velocity-pressure formulation. A variation of the above method expresses the velocity field as the curl of the function ψ together with the gradient of a potential φ , which is used to satisfy the boundary conditions. Another related method is the velocity-vorticity formulation, which dispenses with ψ and solves a Poisson equation for each velocity component. These methods may be used for both inviscid flow by omitting the viscous diffusion term $\nu \nabla^2 \omega$ and the no-slip boundary condition, or for viscous flow by retaining them. They are more usually used for inviscid rather than viscous flows and are described in more detail in references such as Aziz and Hellums (1967), Morino (1993), and Gatski et al. (1982).

Viscous flow (primitive variable methods)

In practice primitive variable methods are by far the most common method of numerically solving the Navier–Stokes equations for 3-D flows. A number of these methods are available mainly involving different ways of dealing with the difficulties associated with the pressure term. In the Navier–Stokes equations for compressible flow, information and errors propagate from the boundary conditions numerically through the solution grid over the flow domain. Pressure signals propagate up- and downstream at the speed of sound and vortical disturbances at the flow speed. If the flow is at low Mach number and therefore nearly incompressible, the speed of sound relative to the flow velocity tends to infinity and is therefore much greater than the vortical disturbance speed. These speeds, which are, respectively, the speeds at which pressure changes and vorticity changes travel through the flow, are now orders of magnitude different, and the equations become very ‘stiff’ and prone to solution instability and errors. A further complication is that because the pressure only occurs in the equations as a gradient driving the velocity field, collocation of all variables on grid nodes can lead to a ‘checkerboard’ instability. For steady flow problems, solution convergence is more efficiently carried out by iteration of the steady flow equations than by analysis over long time periods using the unsteady flow equations because techniques exist to speed up the convergence. However, most problems in wind energy requiring CFD methods to be used involve inherently unsteady flow, and convergence issues only relate to sub-step iteration needed within each timestep to deal with the pressure. The following is no more than a brief summary of techniques, and those interested can obtain much more detailed information from the many books on CFD (e.g. Ferziger and Peric 1997) and CFD code manuals. Many codes now offer a choice of methods because apart from the issue of how turbulence is simulated or modelled, all publicly available codes should be relied on to converge accurately given sufficient numerical resolution, but different approaches are often found to be more computationally efficient for different problems.

1. *Treatment as a compressible flow:* In compressible flow the local pressure is linked to the density, which is specified in turn by solving the compressible form of the mass conservation equation, and no special procedures are needed to deal with the pressure and mass conservation. However, wind turbine rotor flows, while being technically compressible flows, are at very low Mach number. They may be solved using the numerical methods for compressible flow, but because the flow is nearly incompressible, the ratio of the propagation speeds of pressure and vortical disturbances as discussed above is extremely large, requiring very small and inefficient timesteps for a stable solution. Some efficiency may be regained by timestepping the equations in a pseudo-time within each real-time step. This is a form of preconditioning of the solution matrix, which can be used for both steady and unsteady flows.
2. *Method of artificial compressibility:* A variation on the above procedure, originally due to Chorin (1967), is to set up an artificial relationship between pressure and mass flow divergence, keeping the density constant, typically

$$\frac{1}{\beta} \frac{\partial p}{\partial \tau} + \nabla \cdot \mathbf{U} = 0 \quad (4.150)$$

where the coefficient β is chosen to be of order (ρU^2) to make the equations less stiff, and τ is an artificial time.

For steady flow problems the equations are timestepped in pseudo-time τ to a steady solution, at which point the artificial time derivative of pressure in Eq. (4.150) becomes zero and the solution satisfies the true incompressibility mass conservation law. In unsteady flow the equation is timestepped in the pseudo-time τ within each real timestep to achieve convergence before proceeding to the next timestep. Using pseudo-time τ allows the artificial compressibility equations to be solved more quickly to the incompressible flow solution, and the equations are much less stiff. Jameson (see, e.g. Farmer et al. 1993) has developed applications of the method to unsteady flows.

The above two methods are sometimes described as ‘coupled methods’ but are much less commonly used for wind turbine rotor aerodynamics than the following ‘pressure correction’ methods, which retain the exact incompressible mass conservation equation and split the timestep using an estimated pressure field followed by a correction.

3. *Iterative pressure correction methods:* These methods retain the incompressible mass conservation equation exactly and follow an iterative procedure to continuously correct the pressure gradient term in the Navier–Stokes momentum equations within each timestep. Of these the SIMPLE (Semi-Implicit Method for Pressure Linked Equations) family of methods are very widely used and form the basis of many commercial and other CFD codes.

The pressure field p must be consistent with the velocity field being advanced over a timestep to a new value u that satisfies mass flow conservation. It is therefore written in the form

$$p = p^* + \alpha.p' \quad (4.151)$$

and the velocity field similarly

$$\mathbf{U} = \mathbf{U}^* + \mathbf{u}' \quad (4.152)$$

where p^* and \mathbf{U}^* are (initial) estimated values in the current timestep for the pressure and velocity fields, p' and \mathbf{u}' are the corrections required to satisfy a divergence-free flow, and α is a relaxation parameter ($0 < \alpha < 1$) to provide stability in the iteration.

The estimate \mathbf{U}^* of the velocity field is found from the momentum equations using the pressure p^* , estimated from its previous value. This is computed using a staggered grid to avoid the checkerboard instability mentioned earlier.

A simplified approximation of the momentum equations omitting the quadratic term gives a relationship between velocity correction \mathbf{u}' and pressure correction p' :

$$\frac{\partial \mathbf{u}'}{\partial t} = -\frac{1}{\rho} \nabla p' \quad (4.153)$$

Because the final velocity \mathbf{u} in the timestep after applying the correction \mathbf{u}' must satisfy the mass flow conservation Eq. (4.142), substituting Eq. (4.143) into Eq. (4.142) leads to a Poisson equation for the pressure correction:

$$\nabla^2 p' = \frac{\rho}{\Delta\tau} \nabla \cdot \mathbf{u}^* \quad (4.154)$$

In this equation $\Delta\tau$ is a sub-timestep for the iteration that takes place within the real timestep Δt .

The correction value p' is then substituted into (4.151) to update p^* and into (4.153) to update \mathbf{u}^* and the procedure iterated within the timestep until convergence is obtained.

Several versions of the SIMPLE method have been developed subsequently to offer greater speed and accuracy. Most codes supply information regarding these, but see also books on CFD (e.g. Ferziger and Peric 1997).

4. *Splitting methods:* These methods are sometimes known as *projection methods*. They split the timestep following a similar approach with first a predictor step to compute an intermediate velocity field. This velocity field has not been forced to satisfy incompressible mass flow conservation, and therefore the predictor step is followed by a corrector step in which the pressure field, computed from a Poisson equation whose source term is formed from the mass conservation error at the predictor stage, is used to correct the velocity field. The procedure sets up these two sub-steps in such a way that at least second order accuracy is maintained.

Thus, writing the NS momentum equations as:

$$\frac{\partial \mathbf{U}}{\partial t} = f(\mathbf{U}) - \frac{1}{\rho} \nabla p \quad \text{where } f(\mathbf{U}) = \nu \nabla^2 \mathbf{U} - \mathbf{U} \nabla \cdot \mathbf{U} \quad (4.155)$$

Predictor step:

$$\mathbf{U}^* - \mathbf{U}^{(n)} = \frac{\Delta t}{2} \{f(\mathbf{U}^*) + f(\mathbf{U}^{(n)})\} - \frac{\Delta t}{2\rho} \nabla p^{(n)} \quad (4.156)$$

Corrector step:

$$\mathbf{U}^{(n+1)} - \mathbf{U}^* = -\frac{\Delta t}{2\rho} \nabla p^{(n+1)} \quad (4.157)$$

where (n + 1) and (n) superscripts indicate time level.

Requiring the velocity $\mathbf{U}^{(n+1)}$ to satisfy incompressible mass flow conservation leads similarly to a Poisson equation for $p^{(n+1)}$:

$$\nabla^2 p^{(n+1)} = \frac{2\rho}{\Delta t} \nabla \mathbf{U}^* \quad (4.158)$$

After solving Eq. (4.158) for $p^{(n+1)}$, Eq. (4.157) is used to provide the velocity field $\mathbf{U}^{(n+1)}$ for the next timestep.

Again, many versions of this two-sub-step approach have been developed. They are probably used more widely in codes for research work than in codes for industrial design.

4.7.6 Discrete methods of approximating the terms in the Navier–Stokes equations over the flow field

There are three main alternative techniques available to convert the Navier–Stokes equations into discrete form so that they may be solved from a set of linear equations in the flow variables over the flow domain.

The finite difference method (FDM)

This method approximates the derivatives of the velocity and pressure variables as finite differences of selected orders of accuracy over a regular, usually Cartesian, or regular cylindrical grid. Such a grid may have graded cell sizes but normally cannot fit the complex surface of a practical body, such as an aerofoil, rotor blade, entire rotor, or entire wind turbine.

Two main techniques are available to deal with this problem:

- 1) The immersed boundary technique, which interpolates the body surface within the regular grid.
- 2) The use of grid transformation so that the grid fits the body surface locally but the Navier–Stokes equations must be transformed. This method can be quite algebraically complicated but is better able to achieve accuracy close to the body surface.

Finite volume method (FVM)

This method converts the flow equations into statements of conservation of volume flow and momentum fluxes through the boundaries of every cell in the grid. The cells are most commonly irregular hexahedra that can be constructed to fit general body surfaces and vary in size as required by flow gradient conditions. To retain accuracy cell size variation should be gradual and cell shapes should be designed to keep cell boundaries reasonably close to orthogonal. This method is probably the most favoured because it is fairly easy to set up and guarantees that the conservation quantities remain conserved exactly.

Finite element method (FEM)

This method forms integral expressions of the equations, evaluated by suitable interpolation of the variables over the elements that form the grid. The method is not as widely used in fluid mechanics as the FVM but does have the advantages that it is much more tolerant of very irregular or distorted cell shapes and error norms can be evaluated. As with FVM the grid of cells is constructed to fit the body surface(s).

Some of the most commonly used CFD codes, all FVM except Nektar, which is a Spectral Element (high order FEM) code, are Open Foam (open source code), Nektar (open source code), SIMPLE (commercial code), CFX (commercial code), and Star-CCM (commercial code).

4.7.7 Grid construction

In practice the most labour-intensive part of carrying out a CFD investigation of a flow about a complex body such as a rotor or wind turbine is the construction of a suitable grid. A number of well-established computer programs are available to do this, and CFD codes are often associated with particular grid generators (e.g. Gambit). Where the body is complex, grids may be constructed in separate blocks that are patched together with an appropriate level of interpolation at the interfaces. Where one part of a body rotates relative to another part, normally required for a full wind turbine rotor and tower simulation, sliding interfaces between blocks are used. Particular attention must be given to the order of interpolation of the variables across the interface to get the desired accuracy.

The most important part of a grid is usually the region next to the body surface where the flow gradients will be highest. Further from the surface a gradual increase in cell size is usual for reasons of computational efficiency, but care is needed in arranging this to preserve adequate smoothness. In finite volume (and where used finite difference) methods highly skewed grid cells far from orthogonal should be avoided as far as possible, but this constraint is less important for finite element methods. Usually grids are constructed to be *boundary conforming*, that is, every body boundary is identical with a surface in the grid and is a union of cell boundaries. However, recently *immersed boundary* techniques have become popular because of the greater ease of mesh construction. This is particularly the case for flows with moving boundaries for which conforming mesh approaches require continuous remeshing where immersed boundary methods do not. In this system the grid does not conform to the boundaries but cuts through them. The drawbacks and dangers are the need to preserve conservation quantities within the flow field in the cut cells and to provide adequate resolution efficiently in all regions of high gradients.

Body conforming grids may have some regularity in their construction using analytic (algebraic) methods and parameterized coordinate surfaces or have a random structure. Of the latter, there are three main construction techniques, point methods where individual nodes are placed satisfying, for example, the Delaunay criterion, which prevents very ‘thin’ mesh elements occurring with small interior angles in triangular (2-D) or tetrahedral (3-D) meshes; advancing front techniques, again subject to controlling criteria; or recursive decomposition from initially large blocks particularly useful for complex multi-component bodies. Additionally, for bodies involving relative motion, particularly rotation as in the case of a wind turbine, it is usual to have relative motion of mesh blocks that are patched together at the sliding interface where careful interpolation is required

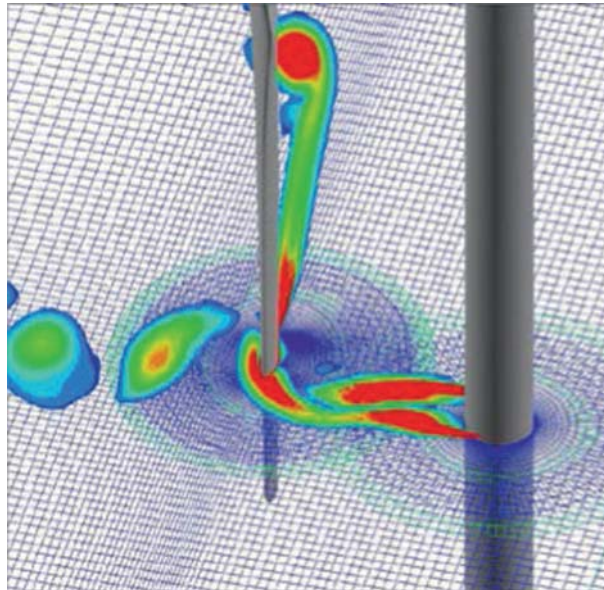


Figure 4.38 Vorticity downstream of a rotor–blade–tower interaction.

to preserve the order of accuracy. Once a grid is constructed, small changes of geometry or flow conditions are easily and simply accommodated so that extensive investigations only incur one heavy overhead of the initial grid construction.

Figure 4.38 shows part of a CFD (EllipSys3D) simulation of a rotor flow field with overlaid grid blocks to handle relative movement (Zahle et al. 2007).

4.7.8 Full flow field simulation including ABL and wind turbines

Incident flow field (ABL)

As in wind-tunnel testing, most CFD flow simulations model the inlet flow, which is incident on the body being studied as a uniform inlet flow. But increasingly, wind turbine flow studies are examining the effects on rotor forces of the turbulence and vertical shear present in the natural wind, i.e. the ABL. Effects of shear can be studied in isolation by providing a suitable profile of horizontal velocity on the inlet boundary with open or closed surface boundary conditions on all other boundaries of the computational domain. Standard profiles of velocity may be used to represent the ABL:

1. Power law profiles:

$$\frac{U}{U_{ref}} = \left(\frac{z}{z_{ref}} \right)^{\alpha} \quad (4.159)$$

where α is an exponent (typically 1/7 or 0.14) chosen to represent the ground plane condition. z is height above the local datum, and z_{ref} is the standard value of z at which the reference wind speed U_{ref} is measured,

2. Logarithmic profiles:

$$U/u_* = (1/K) \log(z/z_0) + B \quad (4.160)$$

where z_0 is the ground roughness length scale; $u_* = U_{\text{ref}} \sqrt{(C_f/2)}$; C_f is the ground friction coefficient; K , von Karman's constant = 0.41; and B , a function of atmospheric stability and of z_0 and z (weakly) if profiles above 200 m are to be represented accurately. Typically B has a value around 8.5. These profiles are shown compared with ABL measurements in Deaves and Harris (1978). See also the discussion in Section 2.6.2.

Such profiles are appropriate when simulating the cyclic response of a turbine due to the effects of vertical shear. However, it should be noted that a profile imposed at the upstream inlet plane in a computational simulation will tend to develop gradually with distance downstream of the inlet away from the original specification unless stresses and mean velocity profile are correctly balanced. To avoid any problems in such cases, the inlet boundary should not be too far upstream of the simulated rotor but just far enough to avoid its upstream influence.

When turbulence is to be included in the inflow, for example, to simulate buffet response, it is possible to represent the turbulence so that it conforms statistically (spectra etc.) with the turbulence occurring in the ABL and allow this turbulence to convect in a 'frozen' state with uniform velocity past the rotor or turbine. A widely used method of simulating such turbulence in the time domain uses appropriately filtered random noise, such as the generator developed by Veers (1988). Both turbulence in the time dimension only and turbulence varying over two spatial dimensions and time with correct cross-spectral properties are possible using the Veers 3-D wind simulation method (Veers 1988). Three-dimensional simulation is becoming increasingly important as rotors (~ 150 m+) increase in diameter to become of similar size to the transverse length scales in ABL turbulence. Then reduced correlation across the turbine disc becomes significant. This method of turbulence simulation is more appropriate for flows local to the rotor where the aim is to predict unsteady buffet forces on the blades.

For simulation of turbulence over longer flow distances, the better methods now combine both turbulence and shear and seek to establish a balanced boundary layer in which the feedback loop between mean velocity gradient and turbulence shear stress production is closed and in balance. This is done by repetitively computing the simulated ABL through the empty domain feeding the output at the downstream end back into the upstream inlet and continuing until statistical convergence shows that the mean and turbulent flows are 'balanced'. Such a simulated ABL may then be used for computations of rotor/turbine/ABL flow field simulations to be undertaken. These full time-domain solutions can only be realistically undertaken using LES methods and hence are very costly. This method of repeatedly computing the ABL until statistical convergence has also been used with RANS codes to provide a balanced ABL simulation, but because the approach in this case is limited to statistical means, it is not able to drive time-dependent buffet studies without further empiricism to provide time-domain sequences.

It should be noted that placing the rotor in a defined inflow field also has effects that distort this field, and simulations should ideally treat the whole flow field as a composite process.

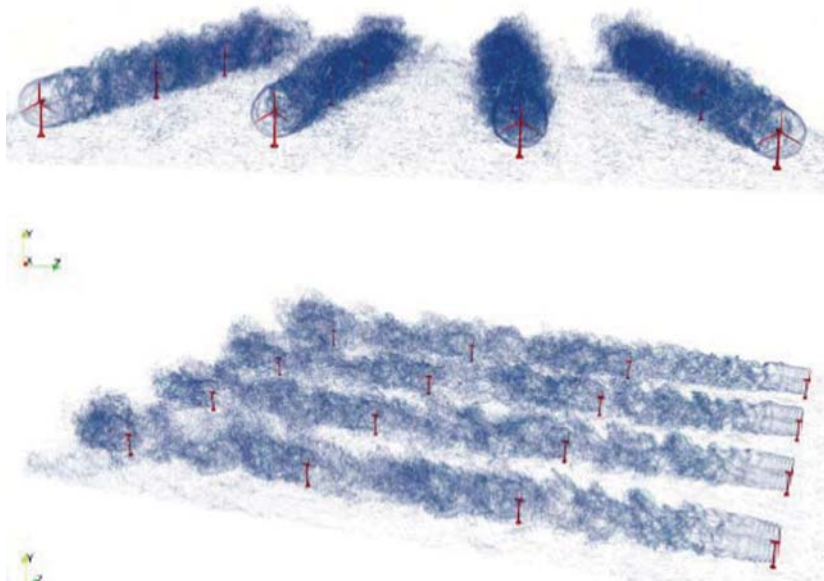


Figure 4.39 Volume rendering of computed turbulent wakes of a 4×4 array of wind turbine rotors (upper looking downwind, lower with flow right to left.).

Large-scale wind farm simulations

One of the main applications of CFD in wind energy in 2020 is the large-scale simulation of the flow of a turbulent ABL through arrays of wind turbine rotors representing a wind farm. The detailed siting of large numbers of turbines in a farm can have significant influence on the total energy that can be captured and on the level of adverse effects due to wake interactions. Such computations are very computer intensive, and therefore the rotors themselves are usually represented at the simple actuator disc or actuator line level, whereas LES is used for the turbulent wind farm flow field (Martinez-Tossas et al. 2018). Figure 4.39 (Deskos et al. 2019) shows an example of a flow field calculated in this way for a 4×4 array of turbines.

References

- Anderson, J.D. (1991). *Fundamentals of Aerodynamics*. New York: McGraw-Hill.
- Aziz, K. and Hellums, J.D. (1967). Numerical solutions of the three-dimensional equations of motion for laminar natural convection. *Phys. Fluids* 10: 314.
- Beddoes, T.S. (1975). A synthesis of unsteady aerodynamic effects including stall hysteresis. Proceedings of 1st European Rotorcraft Forum, Southampton.
- Bjorck, A., Mert, M. and Madsen, H.A. (1999). Optimal parameters for the FFA-Beddoes dynamic stall model. Proceedings of the EWEC, Nice, France, p. 125.
- Chorin, A.J. (1967). A numerical method for solving incompressible flow problems. *J. Comput. Phys.* 2: 12–26.

- Coleman, R.P., Feingold, A.M., and Stempin, C.W.(1945). Evaluation of the induced velocity field of an idealised helicopter rotor. *NACA ARR No. L5E10*.
- Deaves, D.M. and Harris, R.I. (1978). A mathematical model of the structure of strong winds. *Construction Industry Research and Information Association report No. 76*.
- Deskos, G., Laizet, S., and Piggott, M. (2019). Turbulence resolving simulations of wind turbine wakes. *Renewable Energy* 134: 989–1002.
- Drela, M. (1989). XFOIL: An analysis and design system for low Reynolds number airfoils. In: *Low Reynolds Number Aerodynamics*, 1–12. Springer.
- Farmer, J.J., Martinelli, L. and Jameson, A. (1993). A fast multi-grid method for solving incompressible hydrodynamic problems with free surfaces. AIAA 93-0767, 31st AIAA Aerospace Sciences Meeting, Reno, Nevada, USA.
- Ferziger, J.H. and Peric, M. (1997). *Computational Methods for Fluid Dynamics*. Springer.
- Fung, Y.C. (1969). *An Introduction to the Theory of Aeroelasticity*. New York: Dover.
- Gangwani, S.T. (1982). Prediction of dynamic stall and unsteady airloads for rotor blades. *J. Am. Helicopter Soc.* 27: 57–64.
- Gatski, T., Grosch, C., and Rose, M. (1982). A numerical study of the two-dimensional Navier–Stokes equations in vorticity-velocity variables. *J. Comput. Phys.* 48: 1–22.
- Gault, D.E. (1957). A correlation of low speed airfoil section stalling characteristics with Reynolds number and airfoil geometry. *NACA. Tech. Note 3963*.
- Germano, M., Piomelli, U., Moin, P., and Cabot, W.H. (1991). A dynamic sub-grid scale eddy viscosity model. *Phys. Fluids A* 3: 1760–1765.
- Glauert, H. (1926). A general theory of the autogyro. *ARCR R&M No. 1111*.
- Goankar, G.H. and Peters, D.A. (1988). Review of dynamic inflow modelling for rotorcraft flight dynamics. *Vertica* 2 (3): 213–242.
- Gormont, R.E. (1973). A mathematical model of unsteady aerodynamics and radial flow for application to helicopter rotors. *USAAMRDL technical report*.
- Graham, J.M.R. (1983). The lift on an aerofoil in starting flow. *J. Fluid Mech.* 133: 413–425.
- Gupta, S. and Leishman, J.G. (2006). Dynamic stall modelling of the S809 aerofoil and comparison with experiments. *Wind Energy* 9: 521–547.
- Hansen M. H., Gaunaa, M. and Madsen, H.A. (2004). A Beddoes-Leishman type dynamic stall model in state-space and indicial formulation. *Riso-R-1354(EN)*.
- HaQuang, N., Peters, D.A. (1988). Dynamic inflow for practical applications. Technical note. *J. Am. Helicopter Soc.*
- Johnson, W. (1969). The effect of dynamic stall on the response and airloading of helicopter rotor blades. *J. Am. Helicopter Soc.* 14: 68.
- Jones, W.P. (1945). Aerodynamic forces on wings in non-uniform motion. *ARC R&M 2117*.
- Katz, J. and Plotkin, A. (1991). *Low Speed Aerodynamics: From Wing Theory to Panel Methods*. New York: McGraw-Hill.
- Kinner, W. (1937). The principle of the potential theory applied to the circular wing (trans. M. Flint, R.T.P.). Translation No 2345. *Ing. Arch.* VIII: 47–80.
- Kussner, H.G. (1936). Zusammenfassender Bericht über den instationären Auftrieb von Flugeln. *Luftfahrtforschung* 13: 410–424.
- Leishman, J.G. (2002). Challenges in modelling the unsteady aerodynamics of wind turbines. AIAA-2002-0037, 21st ASME Wind Energy Symposium, Reno, Nevada, USA.
- Leishman, J.G. and Beddoes, T.S. (1989). A semi-empirical model for dynamic stall. *J. Am. Helicopter Soc.* 34 (3): 3–17.
- Lindenburg, C. (1996). Results of the PHATAS-III development. IEA 28th Meeting of Experts, Lyngby, Denmark.
- Loewy, R.G. (1957). A two-dimensional approach to the unsteady aerodynamics of rotary wings. *J. Aeronaut. Sci.* 24 (2): 81.

- McNae, D.M. (2014). Unsteady hydrodynamics of tidal stream turbines. PhD thesis, Imperial College London.
- Mangler, K.W., Squire, H.B. (1950). The induced velocity field of a rotor. *ARCR R&M No. 2642*.
- Martinez-Tossas, L.A., Churchfield, M.J., Yilmaz, A.E. et al. (2018). Comparison of four large eddy simulation research codes and effect of model coefficient and inflow turbulence in actuator-line based wind turbine modelling. *J. Renewable Sustainable Energy* 10: 033301.
- Meijer Drees, J. (1949). A theory of airflow through rotors and its application to some helicopter problems. *J. Helicopter Assoc. Great Britain* 3 (2): 79–104.
- Menter, F.R., Kuntz, M., and Langtry, R. (2003). Ten years of industrial experience with the SST turbulence model. *Turbulence Heat Mass Trans.* 4: 625–632.
- Mikkelsen, R.F. (2003). Actuator disc methods applied to wind turbines. PhD thesis, Tech. Uni. Dk., Lyngby.
- Miller, R.H. (1964). Rotor blade harmonic air loading. *AIAA J.* 2 (7): 1254.
- Morino, L. (1993). Boundary integral equations in aerodynamics. *Appl. Mech. Rev.* 46: 445–486.
- Øye, S. (1992). Induced velocities for rotors in yaw. Proceedings of the Sixth IEA Symposium on the Aerodynamics of Wind Turbines, ECN, Petten.
- Peters, D.A., Boyd, D.D., and He, C.J. (1989). Finite state induced flow model for rotors in hover and forward flight. *J. Am. Helicopter Soc.* 34 (4): 5–17.
- Petot, D. (1989). Modelisation de decrochage dynamique. *La Recherche aérospatiale* 5: 60.
- Pitt, D.M. and Peters, D.A. (1981). Theoretical prediction of dynamic inflow derivatives. *Vertica* 5: 21–34.
- Prandtl, L. and Tietjens, O.G. (1957). *Applied Hydro- and Aeromechanics*. New York: Dover.
- Sears, W.R. (1941). Some aspects of non-stationary airfoil theory and its practical applications. *J. Aerosp. Sci.* 8: 104–108.
- Sheng, W., Galbraith, R.A.M., and Coton, F.N. (2010). Applications of low speed dynamic stall model to the NREL airfoils. *J. Sol. Energy Eng.* 132 (1): 1–8.
- Snel, H. and Schepers, J.G. (1995). Joint investigation of dynamic inflow effects and implementation of an engineering method. *ECN Report: ECN-C-94-107*.
- Soerensen, J.N., Shen, W.Z., and Munduate, X. (1998). Analysis of wake states by a full field actuator disc model. *Wind Energy* 88: 73–88.
- Speziale, C.G. (1991). Analytical models for the development of Reynolds stress closures in turbulence. *Ann. Rev. Fluid Mech.* 23: 107.
- Suzuki, A and Hansen, A.C. (1999). Generalized dynamic wake model for Yawdyn. AIAA-99-0041, AIAA Wind Symposium, Reno, Nevada, USA.
- Tarzanin, F.J. (1972). Prediction of control loads due to blade stall. *J. Am. Helicopter Soc.* 1: 33.
- Theodorsen, T. (1935). General theory of aerodynamic instability and the mechanism of flutter. *NACA Report 496*.
- Thwaites, B. (1987). *Incompressible Aerodynamics*. New York, NY: Dover.
- Tuckerman, L.B. (1925). Inertia factors of ellipsoids for use in airship design. *NACA Report Number 210*.
- Van Bussel, G.J.W. (1995). The aerodynamics of horizontal axis wind turbine rotors explored with asymptotic expansion methods. Doctoral thesis, Delft University of Technology.
- Veers, P.S. (1988). Three-dimensional wind simulation. *Sandia Report SAND88-0152 UC-261*.
- Wagner, H. (1925). Über die Entstehung des dynamischen Auftriebes von Tragflügel. *Z. Angew. Math. Mech.* 5 (1): 17.
- White, F.M. (1991). *Viscous Fluid Flow*. New York: McGraw-Hill.
- Zahle, F., Soerensen, N.N., Johansen, J. and Graham, J.M.R. (2007). Wind turbine rotor-tower interaction using an incompressible overset grid method. AIAA-2007-0425, 42nd AIAA Aerospace Sciences meeting, Reston, Virginia, USA.

Further Reading

- Bertagnolio, F., Sørensen, N.N. and Johansen, J. (2006). Profile catalogue for airfoil sections based on 3D computations. *Riso-R-1581(EN)*.
- Himmelskamp, H. (1945). Profile investigations on a rotating airscrew. Doctoral thesis, Gottingen.
- Johnson, W. (1980). *Helicopter Theory*. New York: Dover.
- Leishman, G.J. (2000). *Principles of Helicopter Aerodynamics*, 390–392. Cambridge: Cambridge University Press.
- Sørensen, N.N. (2002). 3D background aerodynamics using CFD. *Riso-R-1376(EN)*.
- Stepniewski, W.Z. and Keys, C.N. (1984). *Rotary-Wing Aerodynamics*. New York: Dover.

5

Design loads for HAWTs

5.1 National and international standards

5.1.1 Historical development

The preparation of national and international standards containing rules for the design of wind turbines began in the eighties. The first publication was a set of regulations for certification drawn up by Germanischer Lloyd (GL) in 1986. These initial rules were subsequently considerably refined as the state of knowledge grew, leading to the publication by GL of the *Regulation for the Certification of Wind Energy Conversion Systems* in 1993. Revised editions – latterly entitled *Guideline for the Certification of Wind Turbines* – were published in 1999, 2003, and 2010. Meanwhile national standards were published in The Netherlands (NEN 6096) and Denmark (DS 472) in 1988 and 1992, respectively.

The International Electrotechnical Commission (IEC) began work on the first international standard in 1988, leading to the publication of IEC 1400-1, *Wind Turbine Generator Systems – Part 1: Safety Requirements* in 1994. Second, third, and fourth editions, each containing some significant changes and bearing the new number IEC 61400-1, appeared in 1999, 2005, and 2019, respectively. IEC-61400-1 has now superseded the national standards referred to previously.

Following the merger of DNV and GL in 2013 to form DNVGL, separate standards have been published for design loads (DNVGL-ST-0437 2016) and for the design of individual components (e.g. DNVGL-ST-0376 2015, *Rotor Blades for Wind Turbines*). The standard for design loads covers both onshore and offshore wind turbines.

The following sub-section describes the scope of the IEC 61400-1 requirements in outline.

Table 5.1 Wind speed parameters for wind turbine classes.

	Class I	Class II	Class III
Reference wind speed, U_{ref} (m/s)	50	42.5	37.5
Reference wind speed for cyclones, U_{refT} (m/s)	57	57	57
Annual average wind speed, U_{ave} (m/s)	10	8.5	7.5
50 year return gust speed, $1.4U_{ref}$ (m/s)	70	59.5	52.5
1 year return gust speed, $1.12U_{ref}$ (m/s)	56	47.6	42

5.1.2 IEC 61400-1

IEC 61400-1 *Wind Turbines – Part 1: Design Requirements* identifies three different classes of wind turbines to suit differing site wind conditions, with increasing class designation number corresponding to reducing average and extreme wind speeds. The wind speed parameters for each class are given in Table 5.1, where the reference wind speed is defined as the 10 minute mean wind speed at hub height with a 50 year return period. For some (but not all) areas subject to tropical cyclones, a higher reference wind speed, U_{refT} , of 57 m/s is specified.

Rigorous procedures are laid down for demonstrating that the wind conditions at a particular wind turbine site conform to those of the designated wind turbine class. To allow for sites where conditions do not conform to any of these classes, a fourth class (Class S) is provided, in which the basic wind speed parameters are to be specified by the manufacturer.

The standard identifies a total of 23 different load cases (18 ultimate, 5 fatigue), which, as a minimum, require consideration in the design of the turbine. Each load case is defined in terms of a different combination of wind conditions and machine state – for example, extreme wind shear (EWS) during power production. The standard does not extend to the prescription of particular methods of loading analysis.

Subsequent sections cover requirements for the control and protection systems, the various mechanical systems, the electrical system, installation, commissioning, operation, and maintenance. A final section details the requirements for turbines operating at temperatures below -20° C or where there is a risk of icing.

5.2 Basis for design loads

5.2.1 Sources of loading

The sources of loading to be taken into account may be categorised as follows:

- Aerodynamic loads.
- Gravitational loads.
- Inertia loads (including centrifugal and gyroscopic effects).
- Operational loads arising from actions of the control system (e.g. braking, yawing, blade pitch control, generator disconnection).

5.2.2 Ultimate loads

The load cases selected for ultimate load design must cover realistic combinations of a wide range of external wind conditions and machine states. It is common practice to distinguish between normal and extreme wind conditions on the one hand, and between normal machine states and fault states on the other. The load cases for design are then chosen from:

- Normal wind conditions in combination with normal machine states.
- Extreme wind conditions in combination with normal machine states.
- Machine fault states in combination with appropriate wind conditions.

Extreme wind conditions are generally defined in terms of the worst condition occurring with a 50 year return period. It is assumed that machine fault states arise infrequently and are uncorrelated with extreme wind conditions, so that the occurrence of a machine fault in combination with the 50 year return wind condition is an event with such a high return period that it need not be considered as a load case. However, IEC 61400-1 wisely stipulates that if there *is* some correlation between an extreme external condition and a fault state, then the combination should be considered as a design case.

5.2.3 Fatigue loads

A typical wind turbine is subjected to a severe fatigue loading regime. The rotor of a 2 MW machine will rotate some 10^8 times during a 20 year life, with each revolution causing a complete gravity stress reversal in the low-speed shaft and in each blade, together with a cycle of blade out-of-plane loading due to the combined effects of wind shear, yaw error, shaft tilt, tower shadow, and turbulence. It is therefore scarcely surprising that the design of many wind turbine components is often governed by fatigue rather than by ultimate load.

The design fatigue load spectrum should be representative of the loading cycles experienced during power production over the full operational wind speed range, with the numbers of cycles weighted in accordance with the proportion of time spent generating at each wind speed. For completeness, load cycles occurring at start-up and shut-down, and, if necessary, during shut-down, should also be included.

It is generally assumed that the extreme load cases occur so rarely that they will not have a significant effect on fatigue life.

5.2.4 Partial safety factors

Partial safety factors for loads

Limit state design requires characteristic loads to be multiplied by appropriate partial safety factors when calculating the design loads. Although traditionally, different partial safety factor values have been assigned to different kinds of load in static analyses, IEC 61400-1 edition 3 specifies a single partial safety factor for aerodynamic, operational, gravity, and inertia loads for each class of load case. This avoids the pitfalls inherent in any attempt to formulate equations of motions for a dynamic analysis in which different

Table 5.2 Partial safety factors for loads, IEC 61400-1 edition 4.

Unfavourable loads		Favourable loads
Class of design load case		
Normal	Abnormal	
1.35*	1.1	0.9

^a Exceptionally, the partial factor for design load case 1.1 (see Section 5.4.1) is set at 1.25, because, in this case, the loads are determined using statistical load extrapolation, and factors less than 1.35 apply for the fault design load cases 2.1 and 2.5.

terms have been distorted relative to one another by the application of different load factors.

Ultimate load cases are divided into three classes, normal, abnormal, and transport/erection, with a different partial safety factor for each, as set out in Table 5.2. Most load cases are assigned to the normal class, with the abnormal class reserved for the more unlikely fault conditions. The partial factor for fatigue loads is unity.

Partial safety factors for the consequences of failure

In addition to the partial safety factors for loads and materials intrinsic to limit state design, IEC 61400-1 also specifies the use of a partial safety factor for the consequences of failure, which varies according to the nature of the component under consideration. Three classes of component are identified, as follows:

- Component class 1 – used for ‘fail-safe’ structural components whose failure does not result in the failure of a major part of a wind turbine.
- Component class 2 – used for ‘non fail-safe’ structural components whose failure may lead to the failure of a major part of a wind turbine.
- Component class 3 – used for ‘non fail-safe’ mechanical components that link non-redundant actuators and brakes required for turbine protection to main structural components.

Recommended minimum values for the partial safety factor for the consequences of failure are given in Table 5.3.

Table 5.3 Partial safety factors for the consequences of failure, IEC 61400-1 edition 4.

Type of strength assessment	Ultimate strength	Fatigue strength
Component class 1	0.9	0.9
Component class 2	1.0	1.0
Component class 3	1.2	1.2

IEC 61400-1 requires the partial safety factor for the consequences of failure to be introduced at the stage of assessing component design strength, but as it could equally well have been applied in the derivation of the design load, it is instructive to introduce the concept here.

5.2.5 Functions of the control and safety systems

A primary function of the control system is to maintain the machine operating parameters within their normal limits. The purpose of the safety system (referred to as ‘protection system’ in IEC 61400-1 editions 1–3) is to ensure that, should a critical operating parameter exceed its normal limit as a result of a fault or failure in the wind turbine or the control system, the machine is maintained in a safe condition. Normally the critical operating parameters are:

- Turbine rotational speed.
- Power output.
- Vibration level.
- Twist of pendant cables running up into nacelle.

For each parameter it is necessary to set an activation level at which the safety system is triggered. This has to be set at a suitable margin above the normal operating limit to allow for overshooting by the control system but sufficiently far below the maximum safe value of the parameter to allow scope for the safety system to rein it in. The rotor speed at which the safety system is activated is a key input to the design load case involving rotor overspeed.

IEC 61400-1 edition 4 allows a separate safety system (termed *secondary layer protection*) to be dispensed with if it can be demonstrated that the actions of the control system are inherently safe.

5.3 Turbulence and wakes

Fluctuation of the wind speed about the short-term mean, or turbulence, naturally has a major impact on the design loadings, as it is the source of both the extreme gust loading and a large part of the blade fatigue loading. The latter is exacerbated by the gust slicing effect, in which a blade will slice through a localised gust repeatedly in the course of several revolutions.

The nature of free-stream turbulence and its mathematical description in statistical terms form the subject of section 2.6. IEC 61400-1 edition 4 addresses the variation in turbulence intensity from site to site arising from different terrain types by defining four turbulence categories, according to the expected value, I_{ref} , of the hub-height turbulence intensity at a reference mean wind speed, \bar{U} , of 15 m/s. These are categories A+, A, B, and C for I_{ref} values of 0.18, 0.16, 0.14, and 0.12, respectively.

Measurements have shown (see, for example, Risø paper R-1111 1999 by Larsen et al.) that there is significant variability in turbulence intensity at a particular site, even at a particular mean wind speed. Accordingly, IEC 61400-1 edition 4 specifies that the design

value is to be taken as the 90% quantile (i.e. the value with a 10% exceedance probability), defined as

$$I_u = \sigma_u / \bar{U} = I_{ref}(0.75 + 5.6 / \bar{U}) \quad (5.1)$$

where σ_u is the standard deviation of the turbulent wind speed fluctuations, \bar{U} is the hub-height mean wind speed, and I_{ref} is defined above. This relationship results in reducing turbulence intensity with increasing wind speed, as illustrated in Figure 5.1, and is termed the *normal turbulence model (NTM)*. Note that σ_u does not vary with height, so I_u reduces with increasing height, because of wind shear.

There is also a requirement to consider the *maximum* turbulence expected to occur, in load case 1.3 – see Section 5.4.1. This is defined by the extreme turbulence model (ETM), in which the turbulence intensity is given by

$$I_u = \sigma_u / \bar{U} = I_{ref}(0.036(U_{ave} + 6)(1 - 8 / \bar{U}) + 20 / \bar{U}) \quad (5.2)$$

This relationship is shown by the dashed line on Figure 5.1.

For any particular candidate wind farm site, ambient turbulence levels have to be determined from site wind speed measurements and used to derive an estimate of the augmented turbulence levels including wake effects at each turbine location – e.g. using the method suggested in IEC 61400-1 edition 4 annex E. An appropriate design turbulence category (A+, A, B, or C) may then be identified by showing that the 90% quantile of the estimated turbulence intensity including wake effects is less than the 90% quantile

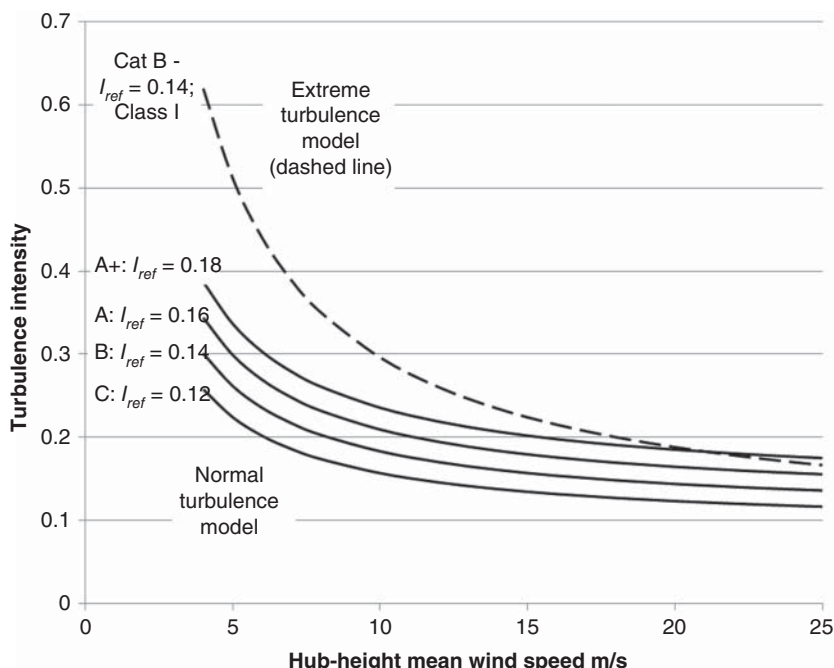


Figure 5.1 Variation of turbulence intensity with wind speed for the normal and extreme turbulence models.

value given by Eq. (5.1) for that category, for all wind speeds between the annual average wind speed, U_{ave} , and $2U_{ave}$.

Computer simulation of the turbulent wind field also requires the definition of the power spectra of the fluctuations of the three orthogonal velocity components and their spatial correlation, which comprise the turbulence model. Edition 2 of the standard details two spectra – those due to von Karman (1948) and Kaimal (1972) – and their corresponding coherence functions (see Sections 2.6.4 and 2.6.7). However, the von Karman spectrum is omitted from editions 3 and 4 and replaced by the Mann (1994) uniform shear turbulence model (see Section 2.6.8).

Some recent simulations of turbulent flow past wind turbines have instead modelled the whole flow field using large eddy simulation and this (computationally very expensive but higher fidelity approach) is starting to be given more consideration; see Section 4.7.8.

5.4 Extreme loads

5.4.1 Operational load cases

A variety of load cases have to be investigated in this category, so that the effects of extremes of gust loading, wind direction change, and wind shear – with or without faults – can be evaluated in turn. The IEC 61400-1 load cases can be divided into two distinct types, depending on whether the wind field is specified in deterministic or stochastic terms. In the deterministic load cases, simple mathematical expressions are used to define the wind speed variation over time, direction changes, and wind shears. In the stochastic load cases the statistical properties of the wind are defined and the cases have to be analysed using a minimum of six 10 minute time domain simulations of the wind field incident on the rotor.

The deterministic load cases have the merit of simplicity but are open to the criticism that they fail to model the behaviour of the real wind accurately. Accordingly, the number of load cases defined by deterministic discrete gusts or sudden direction changes has been reduced in IEC 61400-1 editions 3 and 4 compared with earlier editions, in favour of greater reliance on cases requiring simulation of the turbulent wind field. In the longer term it may be possible to eliminate more deterministic load cases in favour of stochastic ones, by constraining the turbulent wind simulations to model a particular gust profile – see Section 5.4.4.

IEC 61400-1 edition 3 requires account to be taken of the following in all operational load cases:

- Wind shear according to the power law $U(z) \propto z^{0.2}$, which is termed the *normal wind profile (NWP) model*.
- Tower shadow (described in Section 5.7.2).
- Inclination of the mean air flow of up to 8° with respect to the horizontal plane.
- Rotor aerodynamic imbalance (e.g. due to blade pitch and twist deviations) and rotor mass imbalance.
- Yaw tracking errors.

Air density is to be taken as 1.225 kg/m^3 .

The individual ultimate load cases defined in edition 4 of IEC 61400-1 are described below in turn. Note that, except where indicated otherwise, the full range of mean wind speeds between cut-in and cut-out are to be investigated in each case. (The annotated acronyms in capitals are those used by the code to identify the different wind conditions.)

Power production load cases – normal machine state

Load case 1.1: Operation in turbulent wind field defined by the normal turbulence model (NTM) – see Section 5.3. Wind speeds between cut-in wind speed, U_i , and cut-out wind speed, U_o , to be investigated. For this load case and others where a range of wind speeds are to be investigated, wind speed steps of 2 m/s are considered sufficient, except close to rated wind speed. (The rated wind speed is defined as the uniform, steady wind speed at which the turbine's rated power is reached.) Normal partial load factor (exceptionally 1.25).

A minimum of 15 10 minute simulations are required for each wind speed between 2 m/s below the rated wind speed, U_r , and the cut-out wind speed. The characteristic load – i.e. that having a 50 year recurrence period – in each element of the structure is to be determined by statistical extrapolation of the extreme value distribution – see Section 5.14. Alternatively, as a simplification, it is permitted to take the characteristic load as 1.2 times the 99% percentile of the 10 minute extremes determined for each wind speed or 1.35 times the 93.3% percentile.

[Load case 1.2 is a fatigue load case.]

Load case 1.3: Operation in turbulent wind field defined by the extreme turbulence model (ETM). Wind speeds between cut-in wind speed and cut-out wind speed, U_o , to be investigated. Normal partial load factor. As this load case is intended to capture the extreme loading arising from the *maximum* anticipated turbulence intensity, no extrapolation is required.

Load case 1.4: Extreme coherent gust with direction change (ECD). Hub-height wind speed equal to the rated wind speed, U_r , ± 2 m/s plus a 15 m/s rising gust, in conjunction with a simultaneous wind direction change of $720^\circ / U_r$ – i.e. 60° for a rated wind speed of 12 m/s, for example. The gust rise time and the period over which the direction change takes place are both specified as 10 seconds. Normal partial load factor.

Load case 1.5: Extreme wind shear (EWS). Additional vertical or horizontal transient wind shear superimposed on the normal wind profile (NWP) model. Normal partial load factor. The additional wind shears are specified as

$$\left(\frac{z - z_{hub}}{D} \right) \left(2.5 + 0.2\beta\sigma_u \left(\frac{D}{\Lambda_1} \right)^{0.25} \right) \left(1 - \cos \left(\frac{2\pi t}{T} \right) \right) \text{ m/s for } 0 < t < T, \text{ for vertical shear} \quad (5.3a)$$

$$\left(\frac{y}{D} \right) \left(2.5 + 0.2\beta\sigma_u \left(\frac{D}{\Lambda_1} \right)^{0.25} \right) \left(1 - \cos \left(\frac{2\pi t}{T} \right) \right) \text{ m/s for } 0 < t < T, \text{ for horizontal shear} \quad (5.3b)$$

where

z is the height above ground

y is the lateral coordinate with respect to the hub

D is the rotor diameter

$\beta = 6.4$

σ_u is as defined in Eq. (5.1)

Λ_1 is the longitudinal turbulence scale parameter of $0.7z_{\text{hub}}$, or 42 m, whichever is the lesser, and

T is the duration of the transient wind shear, set at 12 seconds

The two shears are to be applied independently as separate cases, not simultaneously. In the case of a 60 m hub height, 80 m diameter machine operating in a 25 m/s wind speed, the resulting maximum additional wind speed at the tip of a blade is 8.36 m/s, assuming category A turbulence.

Fault occurrence during power production

This group of load cases covers faults both internal and external to the machine, including grid loss. If the connection to the grid is lost, then the aerodynamic torque will no longer meet with any resistance from the generator – which therefore experiences ‘loss of load’ – and so the rotor will begin to accelerate until the braking systems are brought into action. Depending on the speed of braking response, grid loss may well result in critical rotor loadings. The fault cases are as follows:

Load case 2.1: Operation in turbulent wind field defined by the normal turbulence model (NTM), together with ‘normal’ control system fault or loss of the electrical network. A ‘normal’ control system fault is defined as one having a return period of 50 years or less. Normal partial load factor (except that, for a ‘normal’ control system fault return period between 10 and 50 years, the factor tapers down to 1.1).

Twelve 10 minute simulations are to be carried out, with the characteristic load defined as the mean of the six largest 10 minute extremes.

Load case 2.2: Operation in turbulent wind field defined by the NTM, together with abnormal control system fault or protection system fault. Faults jeopardising protection against overspeed, generator overload, blade pitch runaway, uncontrolled yawing, and excessive vibration are to be considered. These faults are considered to be rare events, so the abnormal partial load factor is applied. The characteristic load is to be calculated as for load case 2.1.

Load case 2.3: Extreme operating gust (EOG), superimposed on hub-height wind speed of $U_r \pm 2$ m/s or the cut-out wind speed, U_o , in conjunction with external or internal electrical system fault, including loss of electrical network. The wind speed variation is defined as

$$U(z, t) = \bar{U}(z) - \frac{1.221 \sigma_u}{1 + 0.1(D/\Lambda_1)} \sin(3\pi t/T)[1 - \cos(2\pi t/T)] \quad (5.4)$$

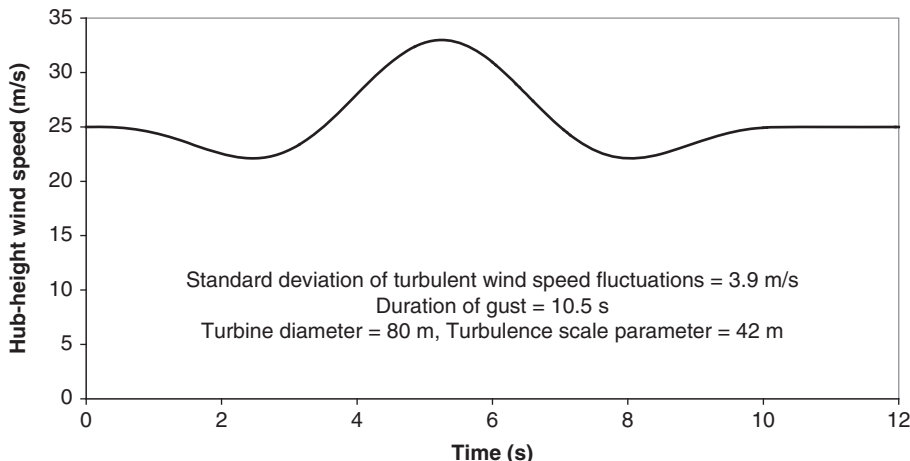


Figure 5.2 IEC 61400-1 extreme rising and falling gust with 50 year return period for steady wind speed of 25 m/s and category A turbulence.

where t is the time elapsed since the onset of the gust and T is the gust duration, specified at 10.5 seconds. Although termed an *EOG*, the gust magnitude is only about 70% of the 1 year return EOG defined in IEC 61400-1 edition 2, so the return period of the current EOG is likely to be only a few days. The gust profile, which incorporates a dip in the wind speed both before and after the main gust, is illustrated in Figure 5.2 for a hub-height wind speed of 25 m/s, Class A turbulence, a turbine diameter of 80 m, and a turbulence length scale of 42 m. The combination of the gust and the electrical system fault is considered to be a rare event, so the abnormal partial load factor is to be applied.

[Load case 2.4 is a fatigue load case.]

Load case 2.5: Operation in steady wind defined by NWP model together with a low voltage ride through (LVRT) event (see Section 11.5.4). The voltage drop and its duration are normally specified by the grid operator. LVRT is considered as normal, but a reduced partial load factor of 1.2 is specified.

Start-up load cases

[Load case 3.1 is a fatigue load case.]

Load case 3.2: Extreme operating gust (EOG) (as defined for load case 2.3, above) during start-up, superimposed on hub-height wind speed of U_i , $U_r \pm 2$ m/s or U_o . Normal partial load factor.

The magnitude of the gust has been chosen so that its recurrence period in conjunction with a start-up or shut-down is one in 50 years.

Load case 3.3: Extreme direction change (EDC) during start-up, for steady hub-height wind speed of U_i , $U_r \pm 2$ m/s or U_o . The direction change, θ_e , is defined as

$$\theta_e = \pm 4 \arctan \left(\frac{\sigma_u}{U_{hub}[1 + 0.1(D/\Lambda_1)]} \right) \quad (5.5a)$$

with the direction varying over time according to the relation:

$$\theta(t) = 0.5\theta_e \{1 - \cos(\pi t/T)\} \text{ for } 0 < t < T \quad (5.5b)$$

The direction change takes place over a period T of 6 seconds. Normal partial load factor.

For a hub-height wind speed of 12 m/s, Class A turbulence, a turbine diameter of 80 m, and a turbulence length scale of 42 m, the direction change is 37°, with a lower value applying at the cut-out wind speed because of the reduced turbulence intensity.

Shut-down load cases

[Load case 4.1 is a fatigue load case.]

Load case 4.2: Extreme operating gust (EOG) (as defined for load case 2.3, above) during shut-down, superimposed on hub-height wind speed of $U_r \pm 2$ m/s or U_o . Normal partial load factor.

Load case 5.1: Emergency shut-down during operation in turbulent wind field defined by the NTM, for steady hub-height wind speed of $U_r \pm 2$ m/s or U_o . Normal partial load factor. The characteristic load is to be calculated as for load case 2.1.

5.4.2 Non-operational load cases

Normal machine state

When non-operational, a turbine is either stationary, i.e. ‘parked’, or idling. In this condition it is exposed to the full range of wind speeds and is therefore required to survive the extreme wind conditions defined for the applicable wind class. IEC 61400-1 permits these wind conditions to be described in terms of either a steady wind speed corresponding to the 3 second gust with a 50 year return period or a turbulent wind with a 10 minute mean equal to the 50 year return value (the ‘reference wind speed’) and a fixed turbulence intensity of 0.11. The 50 year return gust value is defined as 1.4 times the 50 year return 10 minute mean. Both gust and 10 minute mean are specified at hub height and are to be used in conjunction with a reduced wind shear exponent of 0.11.

The magnitude of the 50 year return gust depends on the gust duration chosen, which in turn should be based on the size of the loaded area. For example, CP3: chapter V, part 2 of the UK *Code of Basic Data for the Design of Buildings: Wind Loading* states that a 3 second gust can envelope areas up to 20 m but advises that for larger areas up to 50 m across, a 5 second gust is appropriate. However, IEC 61400-1 and the GL rules (Germanischer Lloyd 2010) specify the use of gust durations of 3 seconds regardless of the turbine size.

Recognising that the turbulent wind speed fluctuations are likely to excite blade and tower natural frequencies, IEC 61400-1 requires turbine dynamic response to be accounted for, whether using the deterministic or turbulent extreme wind models.

It is worth noting that Eurocode 1, Part 1-4 (EN 1991-1-4:2005) bases extreme loads on the dynamic pressure resulting from the extreme 10 minute mean wind speed rather than a 3 second gust. The loads resulting from the extreme 10 minute mean wind speed are augmented by a factor that takes into account both wind gusting and the excitation of resonant oscillations thereby.

The IEC 61400-1 non-operational load cases in the absence of faults or grid loss cater for varying yaw misalignments and may be summarised as follows:

Load case 6.1: Extreme wind with 50 year return period (EWM_{50}). Yaw misalignment up to $\pm 15^\circ$ using the steady wind model, or up to $\pm 8^\circ$ using the turbulence model, provided resistance against yaw slippage can be guaranteed. Normal partial safety factor.

Load case 6.3: Extreme wind with one year return period (EWM_1) and extreme yaw misalignment of up to $\pm 30^\circ$ using the steady wind model, or up to $\pm 20^\circ$ using the turbulence model. The extreme wind speed with a return period of 1 year is to be taken as 80% of the 50 year return value. Normal partial safety factor.

Loss of grid connection can prevent the yaw system tracking any subsequent changes in wind direction, unless back-up is provided for the operation of the yaw system. Accordingly, IEC 61400-1 specifies loss of grid connection as a separate load case, which is summarised below. The use of the abnormal safety factor indicates that the combination of extreme wind and grid loss is considered rare.

Load case 6.2: EWM_{50} and loss of grid connection. Yaw misalignment due to wind direction change up to $\pm 180^\circ$ unless back-up power for yawing provided. Abnormal partial safety factor.

The consequences of yaw slippage should be investigated in all non-operational load cases, if this is a possibility.

[Load case 6.4 is a fatigue load case.]

Machine fault state

Examples of faults in this category are ones involving the failure of the yaw or pitch mechanisms. On the assumption that there is no correlation between such a failure and extreme winds, the design wind condition for this load case is normally taken as the extreme wind condition with a return period of 1 year. The load case in this category is summarised below.

Load case 7.1: EWM_1 and machine fault. Yaw misalignment up to $\pm 180^\circ$ in case of yaw system fault. Abnormal partial safety factor.

5.4.3 Blade/tower clearance

In addition to checking the acceptability of stresses arising from the above load cases, the designer is also required to check that none can result in a collision between the blade and the tower, even after multiplying the blade tip deflection by the appropriate partial load factor and the partial safety factor for elasticity of the blade material. For load case 1.1, the characteristic blade tip deflection is to be determined by extrapolation in the same manner as the characteristic load.

5.4.4 Constrained stochastic simulation of wind gusts

Although time-domain simulations of the turbulent wind field are able to accurately model the behaviour of the wind, very long simulations indeed are required if the extreme

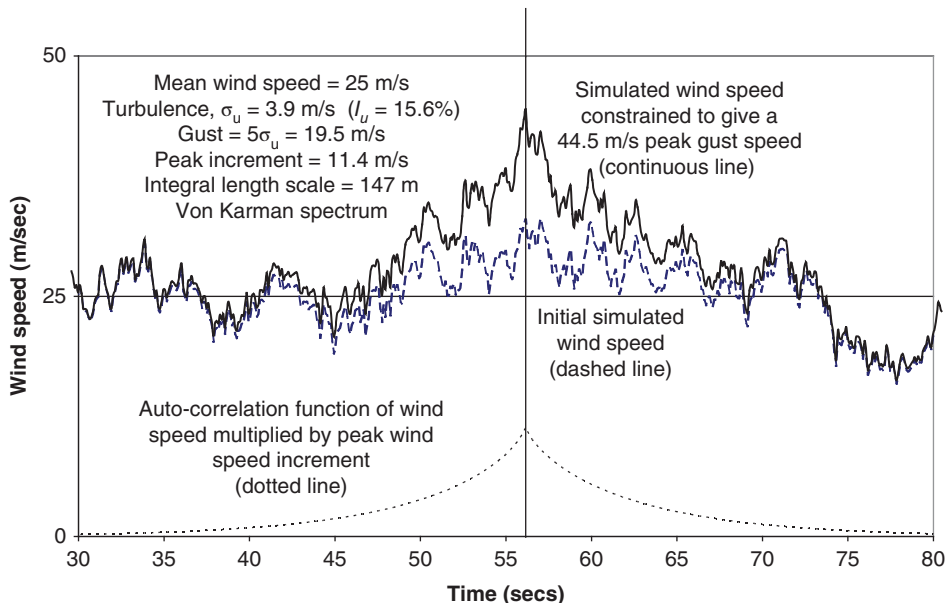


Figure 5.3 Simulated wind speed time series constrained to give a 44.5 m/s peak wind speed.

events required for design purposes are to be encountered by chance. Rather than select the desired extreme event from an extremely long wind speed time series, it is clearly desirable to ‘precipitate’ the desired event by constraining the time series in such a way that the statistical properties of the time series are unaffected.

A method of constraining gusts in wind simulations has been set out by Bierbooms (2005). In its simplest form, it consists in superposing a gust profile having the form of the wind speed auto-correlation function on a local maximum of the simulated wind time series. This is illustrated in Figure 5.3.

In this example, the gust magnitude of 19.5 m/s approximates to the 50 year return value for a Class 1A site, based on exposure to a 24–26 m/s wind speed for about 4 hours per annum. [The peak factor of 5 is calculated using Eq. (A5.42) in Appendix A5, taking $v = 0.25 \text{ Hz}$.] The wind speed auto-correlation function, derived from the power spectrum, is multiplied by the desired peak wind speed increment and added to the initial simulated wind speed time series, with the peak of the auto-correlation function centred on the selected maximum of the initial time series.

There is no need for the timing of the peak of the constrained gust to coincide with a maximum of the initial time series. In the general case, the time series of the constrained gust, $u_c(t)$, can be obtained from the initial time series, $u(t)$ as follows:

$$u_c(t) = u(t) + \kappa(t - t_0)(A - u(t_0)) - \frac{\dot{\kappa}(t - t_0)}{\dot{\kappa}(0)} \dot{u}(t_0) \quad (5.6)$$

where $k(t - t_0)$ is the wind speed auto-correlation function and A the desired peak wind speed at time $t = t_0$.

The method can also be extended to gusts constrained to rise by a prescribed amount within a certain time (Bierbooms 2005). Such gusts are important in relation to the design of pitch-controlled machines.

Although constrained stochastic stimulation appears to be a promising method of modelling extreme events, it is not, as yet, recognised by design standards.

5.5 Fatigue loading

5.5.1 Synthesis of fatigue load spectrum

The complete fatigue load spectrum for a particular wind turbine component has to be built up from separate load spectra derived for turbine operation at different wind speeds and from the load cycles experienced at start-up and normal shut-down and while the machine is parked or idling. Firstly, the cycle counts for each stress range for 1 hour's operation in a particular wind speed band are calculated and scaled up by the predicted number of hours of operation in that band over the machine lifetime. This prediction can be based on the Weibull distribution (Section 2.4), with the annual mean wind speed set according to the turbine class (see Section 5.1.2). Finally, the lifetime cycle counts obtained for operation in the different wind speed bands are combined and added to those calculated for start-ups, shut-downs, and periods of non-operation.

5.6 Stationary blade loading

5.6.1 Lift and drag coefficients

Maximum blade loadings are in the out-of-plane direction and occur when the wind direction is either approximately normal to the blade, giving maximum drag, or at an angle of between 12° and 16° to the plane of the blade when the angle of attack is such as to give maximum lift.

In the absence of data on drag coefficients for air flow normal to the blade, designers formerly utilised the drag coefficient for an infinitely long flat plate of 2.0, with an adjustment downwards based on the aspect ratio. Thus, on a typical blade with a mean chord equal to 1/15th of the radius, the length to width ratio would be taken as 30, because free flow cannot take place around the inboard end of the blade. Following EN 1991-1-4:2005, *Eurocode 1: Actions on Structures – Part 1-4: General Actions – Wind Actions*, this would give a drag coefficient of 1.64. However, field measurements have shown that such an approach is unduly conservative, with drag coefficients of 1.24 being reported for the LM 17.2 m blade (Rasmussen 1984) and 1.25 for the Howden HWP-300 blade (Jamieson and Hunter 1985). The 1992 edition of Danish Standard DS 472, *Loads and Safety of Wind Turbine Construction*, stipulated a minimum value of 1.3 for the drag coefficient.

The choice of lift coefficient value is more straightforward, because aerofoil data for low angles of attack is more generally available and is, in any case, required for assessing rotor performance. The maximum lift coefficient rarely exceeds 1.6, but values down to as low as 1.1 will obtain on the thicker, inboard portion of the blade. The minimum value

of lift coefficient of 1.5 specified in the 1992 edition of DS 472 for the calculation of blade out-of-plane loads is therefore probably conservative.

5.6.2 Critical configuration for different machine types

It was shown in the preceding section that the maximum lift coefficient is likely to exceed the maximum drag coefficient for a wind turbine blade, so consequently the maximum loading on a stationary blade will occur when the air flow is in a plane perpendicular to the blade axis and the angle of attack is such as to produce maximum lift. For a stall-regulated machine, this will be the case when the blade is vertical and the wind direction is 75°–80° to the nacelle axis. In the case of a pitch-regulated machine, with the blade chords oriented perpendicular to the plane of the rotor (i.e. at full feather) at shut-down, the blade only needs to be approximately vertical with a wind direction at 10°–20° to the nacelle axis to attract maximum load.

5.6.3 Dynamic response

Tip displacement

Wind fluctuations at frequencies close to the first flapwise mode blade natural frequency excite resonant blade oscillations and result in additional, inertial loadings over and above the quasi-static loads that would be experienced by a completely rigid blade. As the oscillations result from fluctuations of the wind speed about the mean value, the standard deviation of resonant tip displacement can be expressed in terms of the wind turbulence intensity and the normalised power spectral density at the resonant frequency, $R_u(n_1) = n_1 S_u(n_1)/\sigma_u^2$, as follows:

$$\frac{\sigma_{x1}}{\bar{x}_1} = 2 \frac{\sigma_u}{\bar{U}} \frac{\pi}{\sqrt{2\delta}} \sqrt{R_u(n_1)} \sqrt{K_{Sx}(n_1)} \quad (5.7)$$

Here \bar{x}_1 is the first mode component of the steady tip displacement, \bar{U} is the mean wind speed (usually averaged over 10 minutes), δ is the logarithmic decrement of damping, and $K_{Sx}(n_1)$ is a size reduction factor, which results from the lack of correlation of the wind along the blade at the relevant frequency. Note that the dynamic pressure, $\frac{1}{2}\rho U^2 = \frac{1}{2}\rho(\bar{U} + u)^2 = \frac{1}{2}\rho(\bar{U}^2 + 2\bar{U}u + u^2)$, is linearised to $\frac{1}{2}\rho\bar{U}(\bar{U} + 2u)$ to simplify the result. See Appendix A5.2-4 for the derivations of Eq. (5.7) and the expression for $K_{Sx}(n_1)$.

Damping

It is evident from Eq. (5.7) that a key determinant of resonant tip response is the level of damping present. Generally, the damping consists of two components, aerodynamic and structural. In the case of a vibrating blade flat on to the wind, the aerodynamic force per unit length is given by $\frac{1}{2}\rho(\bar{U} - \dot{x})^2 C_D c(r)$, where \dot{x} is the blade flatwise velocity, C_D the drag coefficient, and $c(r)$ the local blade chord. Hence the aerodynamic damping per unit length, $\hat{c}_a(r)$, is $\rho\bar{U}C_D c(r)$, and the first mode aerodynamic damping ratio,

$$\xi_{a1} = c_{a1}/2m_1\omega_1 = \int_0^R \hat{c}_a(r)\mu_1^2(r)dr/2m_1\omega_1$$

is given by

$$\xi_{a1} = \rho \overline{U} C_D \int_0^R \mu_1^2(r) c(r) dr / 2m_1 \omega_1$$

Here $\mu_1(r)$ is the first mode shape,

$$m_1 = \int_0^R m(r) \mu_1^2(r) dr$$

is the generalised mass, and ω_1 is the first mode natural frequency in radians per second. The logarithmic decrement is obtained by multiplying the damping ratio by 2π .

When the wind direction is angled to the blade so as to generate maximum lift, the blade will be approaching stall, with the result that the aerodynamic damping is effectively zero. In this situation, tip deflections are limited only by the blade structural damping. Structural damping is discussed in Section 5.8.4, and values for typical blade materials given.

Root bending moment

The standard deviation of tip displacement in combination with the blade mode shape yields an inertial loading distribution from which the standard deviation of the resulting bending moment at any position along the blade may be calculated. In particular, the standard deviation of the root bending moment may be expressed in terms of the mean root bending moment as follows:

$$\frac{\sigma_{M1}}{M} = 2 \frac{\sigma_u}{\overline{U}} \frac{\pi}{\sqrt{2\delta}} \sqrt{R_u(n_1)} \sqrt{K_{Sx}(n_1)} \cdot \lambda_{M1} = \frac{\sigma_{x1}}{\bar{x}_1} \cdot \lambda_{M1} \quad (5.8a)$$

where

$$\lambda_{M1} = \frac{\int_0^R m(r) \mu_1(r) r dr}{m_1 \cdot \int_0^R c(r) r dr} \cdot \int_0^R c(r) \mu_1(r) dr \quad (5.8b)$$

See Appendix A5.5 for the derivation of the expression for λ_{M1} .

The standard deviation of the quasi-static root bending moment fluctuation, or root bending moment *background* response, is expressed in terms of the mean root bending moment by

$$\frac{\sigma_{MB}}{M} = 2 \frac{\sigma_u}{\overline{U}} \sqrt{K_{SMB}} \quad (5.9)$$

where K_{SMB} is a size reduction factor to take account of lack of correlation of wind fluctuations along the blade. As shown in Appendix A5.6, K_{SMB} is usually only slightly less than unity because the blade length is small compared with the integral length scale of longitudinal turbulence measured in the across wind direction.

The variance of the total root bending moment fluctuations is equal to the sum of the resonant and background response variances – i.e.

$$\sigma_M^2 = \sigma_{M1}^2 + \sigma_{MB}^2$$

Hence

$$\frac{\sigma_M}{M} = 2 \frac{\sigma_u}{\overline{U}} \sqrt{K_{SMB} + \frac{\pi^2}{2\delta} R_u(n_1) K_{Sx}(n_1) \cdot \lambda_{M1}^2} \quad (5.10)$$

The design extreme root bending moment is typically calculated as that due to the 50 year return, 10 minute mean wind speed plus the number of standard deviations of the root bending moment fluctuations corresponding to the likely peak excursion in a 10 minute period. Thus

$$M_{\max} = \bar{M} + g \cdot \sigma_M \quad (5.11)$$

where g is known as the *peak factor* and depends on the number of cycles of root bending moment fluctuations in 10 minutes, according to the formula

$$g = \sqrt{2 \ln(600v)} + \frac{0.577}{\sqrt{2 \ln(600v)}} \quad (5.12)$$

Here, v is the mean zero-upcrossing frequency of the root bending moment fluctuations, which will be intermediate between that of the quasi-static wind loading and the blade natural frequency, n_1 – see Appendix A5.7. (Note that, as g varies relatively slowly with frequency, it is a reasonable approximation to set g at an upper limit of 3.9, which corresponds to a frequency of about 1.9 Hz.)

Substituting Eq. (5.10) into Eq. (5.11) yields

$$M_{\max} = \bar{M} \left[1 + g \frac{\sigma_M}{\bar{M}} \right] = \bar{M} \left[1 + g \left(2 \frac{\sigma_u}{U} \right) \sqrt{K_{SMB} + \frac{\pi^2}{2\delta} R_u(n_1) K_{Sx}(n_1) \lambda_{M1}^2} \right] \quad (5.13)$$

The expression in square brackets is similar to the numerator of the structural factor, $c_s c_d$, in EN 1991-1-4:2005:

$$c_s c_d = \frac{1 + 2k_p I_v(z_s) \sqrt{B^2 + R^2}}{1 + 7I_v(z_s)} \quad (5.14)$$

in which k_p is the peak factor, $I_v(z_s)$ is the turbulence intensity at height z_s and $R^2 = \frac{\pi^2}{2\delta} R_u(n_1) K_{Sx}(n_1)$.

It is often necessary to express the maximum moment in terms of the quasi-static moment due to the 50 year return gust speed, U_{e50} . To do this, we equate the latter quantity to the quasi-static component of Eq. (5.13), obtaining

$$C_f \cdot \frac{1}{2} \rho U_{e50}^2 \int_0^R c(r) r dr = \bar{M} \left(1 + g_0 \cdot 2 \frac{\sigma_u}{U} \sqrt{K_{SMB}} \right) \quad (5.15)$$

Here the peak factor, g , takes a lower value, g_0 , corresponding to the lower frequency of the quasi-static root bending moment fluctuations. Equation (5.15) can then be combined with Eq. (5.13) to yield

$$M_{\max} = C_f \cdot \frac{1}{2} \rho U_{e50}^2 \int_0^R c(r) r dr \cdot Q_D \quad (5.16)$$

where Q_D is a dynamic factor given by

$$Q_D = \frac{1 + g \left(2 \frac{\sigma_u}{U} \right) \sqrt{K_{SMB} + \frac{\pi^2}{2\delta} R_u(n_1) K_{Sx}(n_1) \lambda_{M1}^2}}{1 + g_0 \left(2 \frac{\sigma_u}{U} \right) \sqrt{K_{SMB}}} \quad (5.17)$$

The dynamic factor Q_D equates to the EN 1991-1-4 dynamic factor, c_d , if g_0 is 3.5 and the ratio λ_{M1} is unity. The EN 1991-1-4 structural factor, $c_s c_d$, given in Eq. (5.14) is the product of the dynamic factor, c_d , and the size factor, c_s , given by $c_s = \frac{1 + 7.I_v(z_s)\sqrt{B^2}}{1 + 7.I_v(z_s)}$.

There is considerable advantage in starting with the extreme gust speed and calculating the extreme root moment as the product of $C_f \cdot \frac{1}{2} \rho U_{e50}^2 \int_0^R c(r).r.dr$ and Q_D , because it eliminates most of the error associated with linearising the formula for dynamic pressure. For example, if the extreme gust is 1.4 times the extreme 10 minute mean wind speed, as postulated in IEC 61400-1 (which implies that the product $g_0 \frac{\sigma_u}{U}$ is 0.4), then the dynamic pressure due to the gust will be $1.4^2 = 1.96$ times that due to the 10 minute mean, rather than 1.8 times as given by the formula $1 + g_0 \left(2 \frac{\sigma_u}{U} \right)$.

Example 5.1 Evaluate the dynamic factor, Q_D , for the blade root bending moment for a 40 m long stationary blade under extreme loading.

Consider a trial 40 m long fibreglass blade design (designated blade SC40) utilising NACA 632XX aerofoil sections with the chord and thickness distributions shown in Figure 5.4a. The thickness distribution has a pronounced knee near mid-span to minimise the thickness to chord ratio in the outer half of the span.

The blade structure is assumed to consist of an aerodynamic shell strengthened by spar caps and linking shear webs, as illustrated in Figure 7.6. The spar cap thickness is required to be a maximum at the knee at 17 m radius and tapers down to zero between there and the root while varying as the blade chord in the outboard section. The thickness of the fibreglass skins of the foam sandwich panels forming the aerodynamic shell and their spacing vary as the chord except in the root region. [The blade structure chosen for the SC40 blade is intended to be more realistic (and structurally more efficient) than the blade structure of the T40 blade used for this example in the first and second editions. In the latter, there were no spar caps, and the thickness of the fibreglass skins was uniform along the blade. The SC40 blade has a mass of 7.7 t, compared with the T40 blade mass of 16.3 t.]

The resulting mass and stiffness distributions are as shown in Figure 5.4b, and modal analysis as described in Section 5.8.2 yields the first and second mode shapes shown in Figure 5.4c. The first mode shape for a blade of constant cross-section (i.e. a uniform cantilever) is also shown for comparison purposes, and it is evident that the high stiffness of the inboard portion of the tapered blade results in dramatically reduced deflections there as a proportion of tip deflection. For a fibreglass blade, typical values of the Young's modulus and material density would be 43 GPa and 1.9 t/m³, respectively, resulting in a first mode natural frequency of 0.88 Hz and a second mode natural frequency of 2.73 Hz.

Values of the other parameters assumed are:

Blade height, z	70 m
50 year return 10 minute mean wind speed, \bar{U} , at blade height	50 m/s
Eurocode 1 terrain category	I (Roughness length, $z_o = 0.01$ m)
Turbulence intensity, $I(z) = 1/\ln(z/z_0)$	0.113

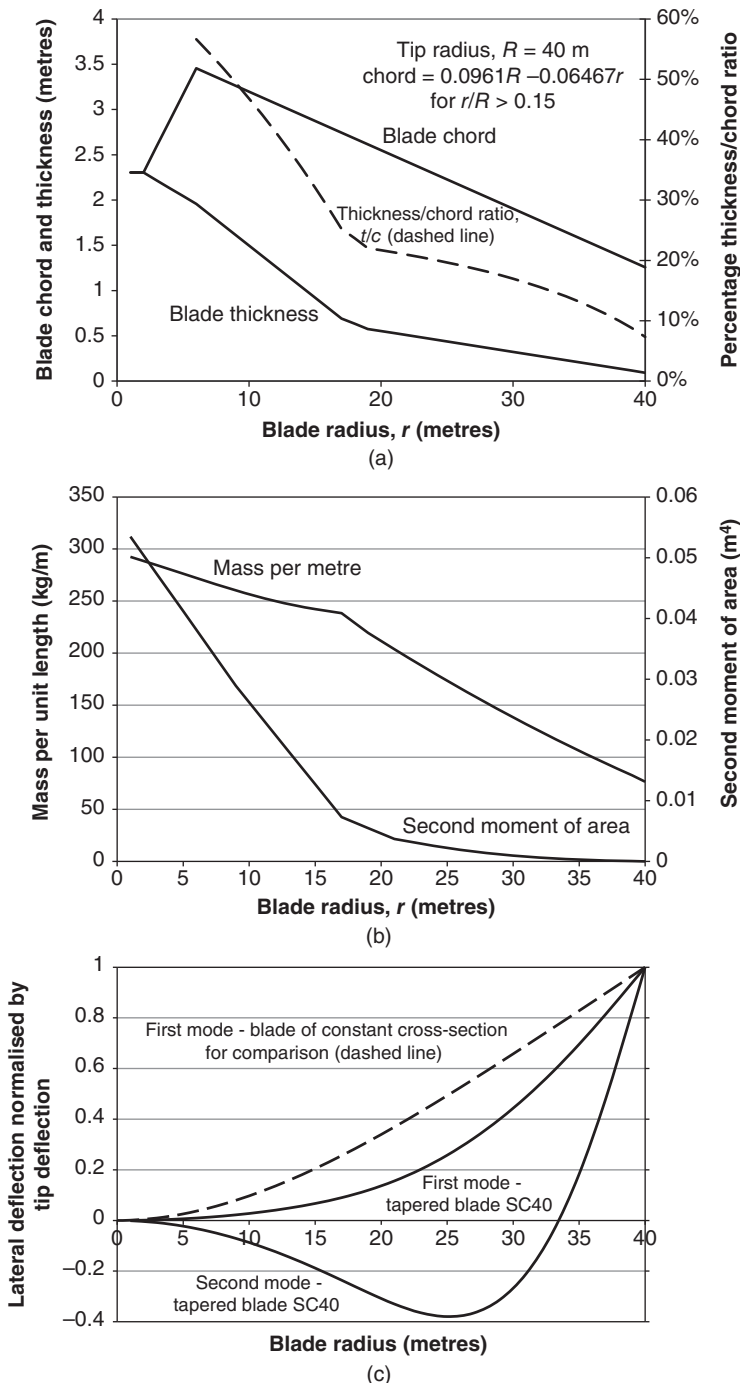


Figure 5.4 (a) Blade SC40 chord and thickness distributions. (b) Blade SC40 mass and stiffness distribution. (c) Blade SC40 first and second mode shapes.

The corresponding integral length scale for longitudinal turbulence is 189 m according to EN 1991-1-4:2005.

The values of the parameters in Eq. (5.7) governing the resonant tip response are determined as follows:

1. The aerodynamic damping is assumed to be zero, so the damping logarithmic decrement is taken as 0.05, corresponding to the structural damping value for fibreglass.
2. The non-dimensional power spectral density of longitudinal wind turbulence, $R_u(n) = n.S_u(n_1)/\sigma_u^2$, is calculated at the blade first mode natural frequency of 0.881 Hz according the Kaimal power spectrum defined in EN 1991-1-4 [Eq. (A5.8) in Appendix A5] as 0.0606.
3. A value of 10 is taken for the non-dimensional decay constant, C , in the exponential expression for the normalised co-spectrum used in the derivation of the size reduction factor, $K_{Sx}(n_1)$, in Eq. (A5.25).

The various stages in the derivation of the extreme root bending moment and the dynamic factor, Q_D , are set out below. The figures in square brackets are the corresponding values obtained using the method of annex C of EN 1991-1-4:2005, which are included for comparison.

Size reduction factor for resonant response, $K_{Sx}(n_1)$	0.372	Eq. (A5.25)	[0.308]
--	-------	-------------	---------

Ratio of standard deviation of resonant tip displacement
to the first mode component of steady tip
displacement,

$$\frac{\sigma_{y1}}{\bar{y}_1} = 2 \frac{\sigma_u}{U} \frac{\pi}{\sqrt{2\delta}} \sqrt{R_u(n_1)} \sqrt{K_{Sx}(n_1)}$$

$$= 2 \times 0.113 \times 9.935 \times \sqrt{0.0606} \cdot \sqrt{0.372}$$

$$= 2 \times 0.113 \times 9.935 \times 0.246 \times 0.610 = 2 \times 0.113 \times 1.490 \quad 0.337 \quad \text{Eq. (5.7)} \quad [\text{N/A}]$$

Root moment factor, λ_{M1}	0.683	Eq. (5.8b)	[N/A]
------------------------------------	-------	------------	-------

Ratio of standard deviation of resonant root moment to mean value, $\frac{\sigma_{M1}}{\bar{M}} = \frac{\sigma_{x1}}{\bar{x}_1} \cdot \lambda_{M1}$	0.230	Eq. (5.8a)	[0.306]
--	-------	------------	---------

Size reduction factor for quasi-static or background response, K_{SMB}	0.829	Eq. (A5.40)	[0.871]
---	-------	-------------	---------

Ratio of standard deviation of quasi-static root moment response to mean value, $\frac{\sigma_{MB}}{\bar{M}} = 2 \frac{\sigma_u}{U} \sqrt{K_{SMB}} = 2 \times 0.113 \times 0.910$	0.206	Eq. (5.9)	[0.197]
---	-------	-----------	---------

Ratio of standard deviation of total root moment response to mean value,			
$\frac{\sigma_M}{M} = \sqrt{\left(\frac{\sigma_{MB}}{M}\right)^2 + \left(\frac{\sigma_{M1}}{M}\right)^2} = \sqrt{0.206^2 + 0.230^2}$	0.308		[0.364]
Zero up-crossing frequency of quasi-static response, n_0	0.342 Hz	Eq. (A5.57)	[N/A]
Zero up-crossing frequency of total root moment response, ν	0.695 Hz	Eq. (A5.54)	[N/A]
Peak factor, g , based on ν	3.64	Eq. (5.12)	[3.66]
Ratio of extreme moment to mean value,			
$\frac{M_{\max}}{\bar{M}} = 1 + g \left(\frac{\sigma_M}{\bar{M}} \right) = 1 + 3.64(0.308)$	2.12	Eq. (5.13)	[2.33]
Peak factor, g_0 , based on n_0	3.44		[3.5]
Ratio of quasi-static component of extreme moment to mean value			
$= 1 + g_0 \frac{\sigma_{MB}}{M} = 1 + 3.44(0.206)$	1.708	Eq. (5.15)	[1.79]
Dynamic factor, $Q_D = 2.12/1.708$	1.243	Eq. (5.17)	[1.30]

It is apparent that the EN 1991-1-4 method yields a larger value of the extreme root bending moment. However, the EN 1991-1-4 ratio of extreme to mean bending moment is intended to apply at all points along the blade, so a conservative value at the root is inescapable, as is shown in the next section, which examines the variation of bending moment along the blade.

Spanwise variation of bending moment

The resonant and quasi-static components of bending moments at intermediate positions along the blade can be related to those at the root in a straightforward way.

As far as the quasi-static bending moment fluctuations are concerned, the variation along the blade follows closely the bending moment variation due to the steady loading, although slight changes in the size reduction factor have a small effect. The bending moment diagram for the resonant oscillations is, however, of a very different shape, because of the dominance of the inertia loading on the tip. An expression for the resonant bending moment variation along the blade is given in Appendix A5.8, and it is plotted out for the example above in Figure 5.5a, with the quasi-static bending moment variation alongside for comparison. It is seen that the resonant bending moment diagram is closer to linear than the quasi-static one, which approximates to a parabola.

A consequence of the much slower decay of the resonant bending moment out towards the tip is an increase in the ratio of the resonant bending moment standard deviation to the local steady moment with radius. This results in an increase in the dynamic magnification factor, Q_D , from 1.24 at the root to 1.85 near the tip for the example above. See Figure 5.5b.

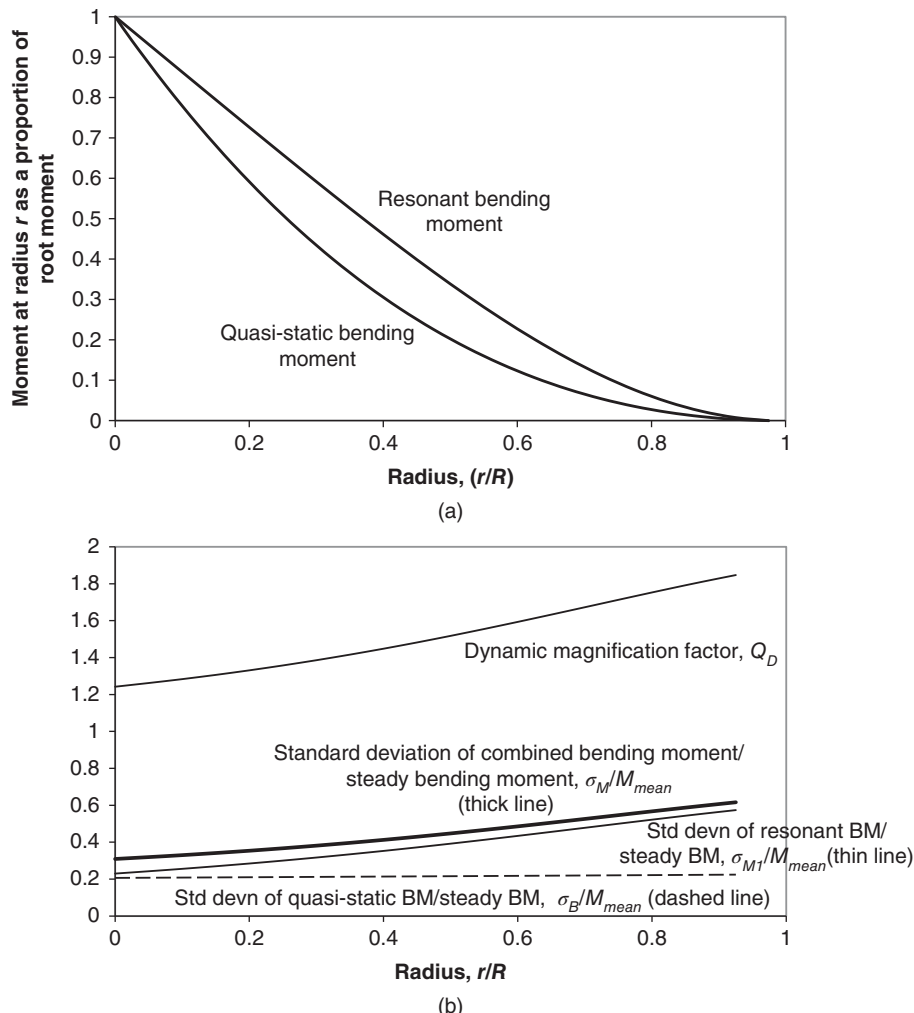


Figure 5.5 (a) Spanwise variation of resonant and quasi-static moments – blade SC40. (b) Spanwise variation of (i) bending moment standard deviations in terms of local steady bending moment, and (ii) dynamic magnification factor – for blade SC40.

5.7 Blade loads during operation

5.7.1 Deterministic and stochastic load components

It is normal to separate out the loads due to the steady wind on the rotating blade from those due to wind speed fluctuations and analyse them in different ways. The periodic loading on the blade due to the steady spatial variation of wind speed over the rotor swept area is termed the *deterministic load component*, because it is uniquely determined by a limited number of parameters – i.e. the hub-height wind speed, the rotational speed, the wind shear, etc. On the other hand, the random loading on the blade due to wind

speed fluctuations (i.e. turbulence) has to be described probabilistically and is therefore termed the *stochastic load component*.

In addition to wind loading, the rotating blade is also acted on by gravity and inertial loadings. The gravity loading depends simply on blade azimuth and mass distribution and is thus deterministic, but the inertial loadings will be affected by turbulence – as, for example, in the case of a teetering rotor, or a flexing blade – and so will contain stochastic as well as deterministic components.

5.7.2 Deterministic aerodynamic loads

Steady, uniform flow perpendicular to plane of rotor

The application of momentum theory to a blade element, which is described in Section 3.5.3, enables the aerodynamic forces on the blade to be calculated at different radii. Eqs. (3.54a) and (3.55) are solved iteratively for the flow induction factors, a and a' , at each radius, enabling the flow angle, ϕ , the angle of attack, α , and hence the lift and drag coefficients to be determined.

For loadings on the outboard portion of the blade, allowance for tip-loss must be made, so Eqs. (3.54a) and (3.55) are replaced by Eqs. (3.54c) and (3.55a) in Section 3.9.6. These equations can be arranged to give the following expressions for the forces per unit length on an element perpendicular to the plane of rotation and in the direction of blade motion, known as the *out-of-plane* and *in-plane forces*, respectively.

Out-of-plane force per unit length:

$$F_X = C_x \cdot \frac{1}{2} \rho W^2 \cdot c = \frac{4\pi r \rho}{B} U_\infty^2 (1 - af) af \quad (5.18)$$

In-plane force per unit length:

$$F_Y = C_y \cdot \frac{1}{2} \rho W^2 \cdot c = \frac{4\pi r^2 \rho}{B} \Omega U_\infty (1 - af) a' f \quad (5.19)$$

The parameters in the expressions are as defined in Chapter 3. f is the tip-loss factor, and B is the number of blades.

The variation of the in-plane and out-of-plane forces with radius is shown in Figure 5.6 for a typical machine operating in uniform, steady winds of 8 and 10 m/s. The 80 m stall-regulated turbine considered in this example is fitted with three SC40 blades as described in Example 5.1 and rotates at 15 rpm. The blade twist distribution (Figure 5.6) is linear with respect to the reciprocal of the radius in line with Eq. (3.74) and selected to produce the maximum energy yield for an annual mean wind speed of 7.5 m/s. It is evident that the out-of-plane load per unit length increases approximately linearly with radius, in spite of the reducing blade chord, until the effects of tip-loss are felt beyond about 80% of tip radius. The tip-loss effect is relatively greater for a 10 m/s wind speed compared with 8 m/s due to the greater spacing of the vortex sheets (Section 3.9.3). Note that the form of the variation would be the same for any combination of rotational speed, wind speed, and tip radius yielding the same tip speed ratio, because it is the tip speed ratio that determines the radial distribution of flow angle ϕ and of the induction factors a and a' .

Integration of these forces along the blade then yields in-plane and out-of-plane aerodynamic blade bending moments. The variation of these moments with radius is shown

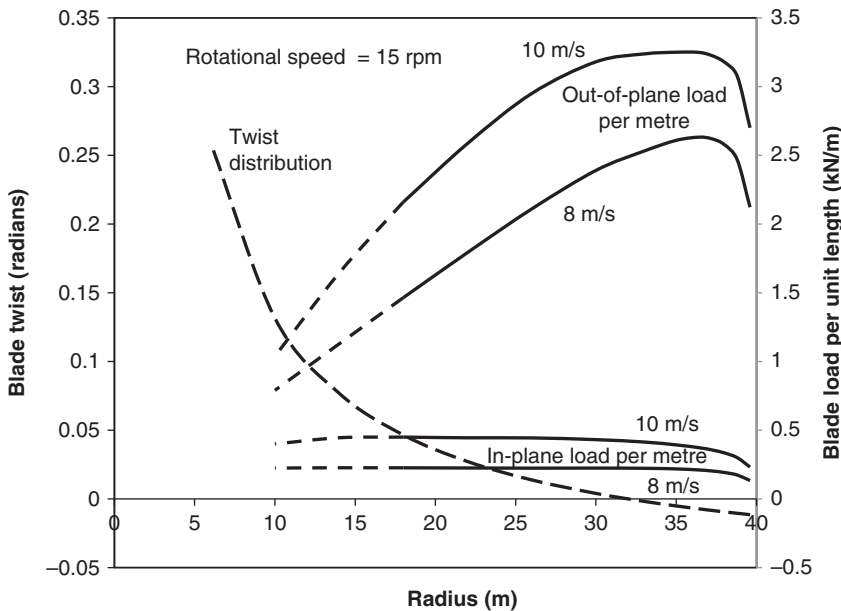


Figure 5.6 Distribution of blade in-plane and out-of-plane aerodynamic loads during operation of an example 80 m diameter machine in steady, uniform winds of 8 and 10 m/s.

in Figure 5.7 for the example above. The blade bending moments effectively decrease linearly with increasing radius over the inboard third of the blade because of the concentration of loading outboard.

The variation of the blade root out-of-plane bending moment with wind speed is illustrated in Figure 5.8 for the 80 m diameter example machine described above. As explained in Section 3.10, the phenomenon of stall delay results in significantly increased values of the lift coefficient at higher wind speeds on the inboard section of the rotating blade than predicted by static aerofoil data, such as that reproduced in Figure 3.43. Accordingly, Figure 5.8 and the other figures referred to in this section have been derived using realistic aerofoil data for a rotating LM 19.0 blade reported in Petersen et al. (1998), which is based on an empirical modification of static or two-dimensional (2-D) aerofoil data. The modified data is reproduced in Figure 5.9, and it displays significantly higher lift coefficients for the thicker, inboard blade sections at high angles of attack than for the thinner, outboard blade sections because of stall delay at the inboard sections.

Figure 5.8 shows the blade root out-of-plane bending moment increasing nearly linearly with wind speed at first and then levelling off, becoming almost constant for winds between 12 and 16 m/s, as the blade goes into stall. Thereafter the root moment increases again, but much more gently than before.

Also shown on Figure 5.8 is the variation of blade root out-of-plane bending moment with wind speed for the same machine with pitch regulation to limit the power output to 1700 kW. It is evident that the bending moment drops away rapidly at wind speeds above rated.

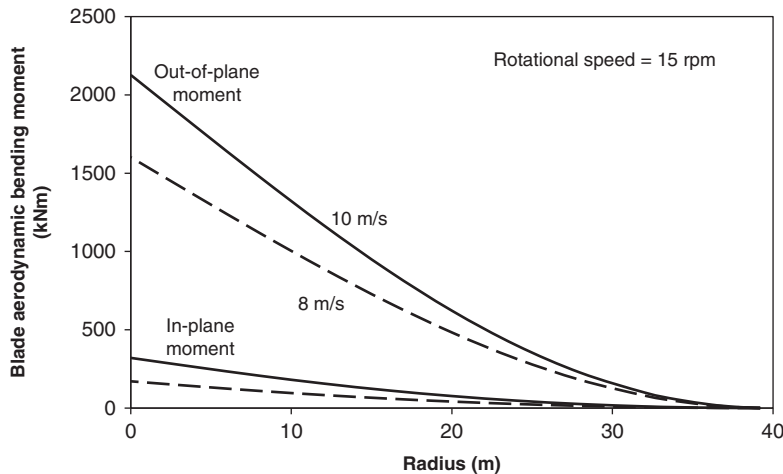


Figure 5.7 Distribution of blade in-plane and out-of-plane aerodynamic bending moments during operation of an example 80 m diameter machine in steady, uniform winds of 8 and 10 m/s.

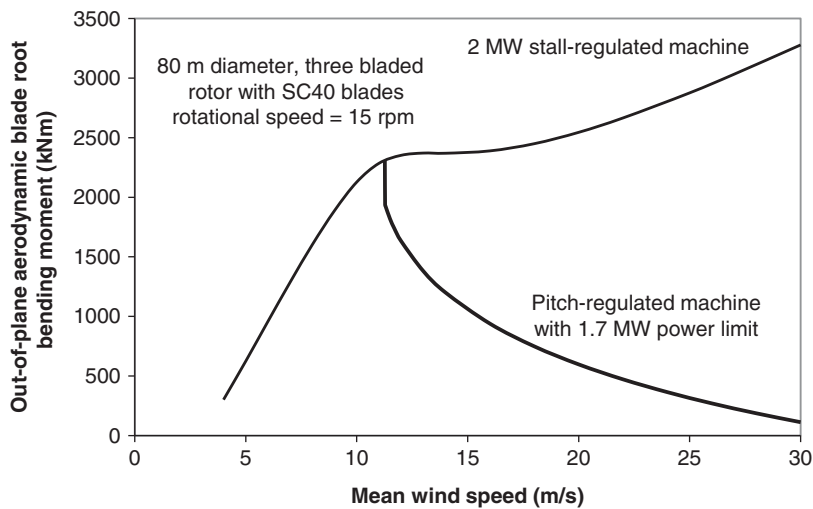


Figure 5.8 Blade out-of-plane root bending moment during operation in steady, uniform wind – variation with wind speed for similar stall-regulated and pitch-regulated machines.

Yawed flow

The application of blade-element/moment theory to steady yawed flow is described in Section 4.2.8. This methodology has been used to derive Figure 5.10a, which shows the variation of the blade root out-of-plane and in-plane moments with

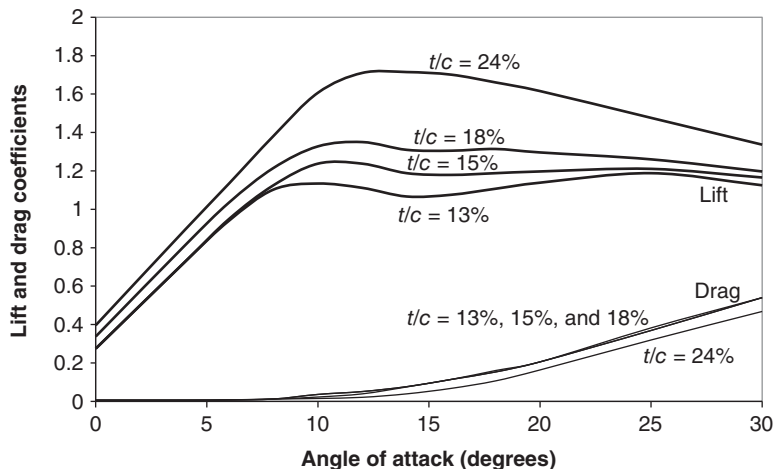


Figure 5.9 Aerofoil data for LM 19.0 blade for various thickness/chord ratios. Source: From Petersen et al. (1998).

azimuth for the 80 m diameter stall-regulated machine described above, operating at a steady yaw angle of +20°. Note that the blade azimuth is measured in the direction of blade rotation, from a zero value at top dead centre, and the yaw angle is defined as positive when the lateral component of air flow with respect to the rotor disc is in the same direction as the blade movement at zero azimuth. [Note that in this and subsequent figures, the blade root moments plotted are actually the values extrapolated to the shaft axis rather than those at the blade/hub interface.]

Figure 5.10a reveals a distinct difference between the behaviour at 10 m/s on the one hand and 15–20 m/s on the other. In the latter case, the bending moment variation is sinusoidal with a maximum value at 180° azimuth, indicating that the variation is dominated by the effect of the fluctuation of the air velocity relative to the blade, W . At 10 m/s, however, the maximum out-of-plane bending moment occurs at about 225° azimuth, suggesting that the non-uniform component of induced velocity, u_1 [Eq. (4.20)] is also significant. As wind speed increases, of course, the induction factor, a , becomes small, reducing the impact of u_1 .

For comparison, the variation in blade root bending moment with azimuth for an example 2 MW, 80 m diameter pitch-regulated, variable-speed machine operating at a steady 20° yaw is shown in Figure 5.10b – again for wind speeds of 10, 15, and 20 m/s. The turbine operates at a constant tip speed ratio of 8 up to a wind speed of 11 m/s, with the tip speed limited to 88 m/s thereafter, giving a maximum rotational speed of 21 rpm. The blade has the same plan-form and thickness profile as the SC40 blade, but the blade twist distribution is optimised to maximise power output when the tip speed ratio is 8 (while remaining linear with respect to the reciprocal of the radius). It is seen that both the maximum out-of-plane root bending moment and its range of variation with azimuth are somewhat reduced at the higher wind speeds compared with the stall-regulated machine. However, at 10 m/s, these quantities are increased significantly because of the increased rotational speed (19 rpm).

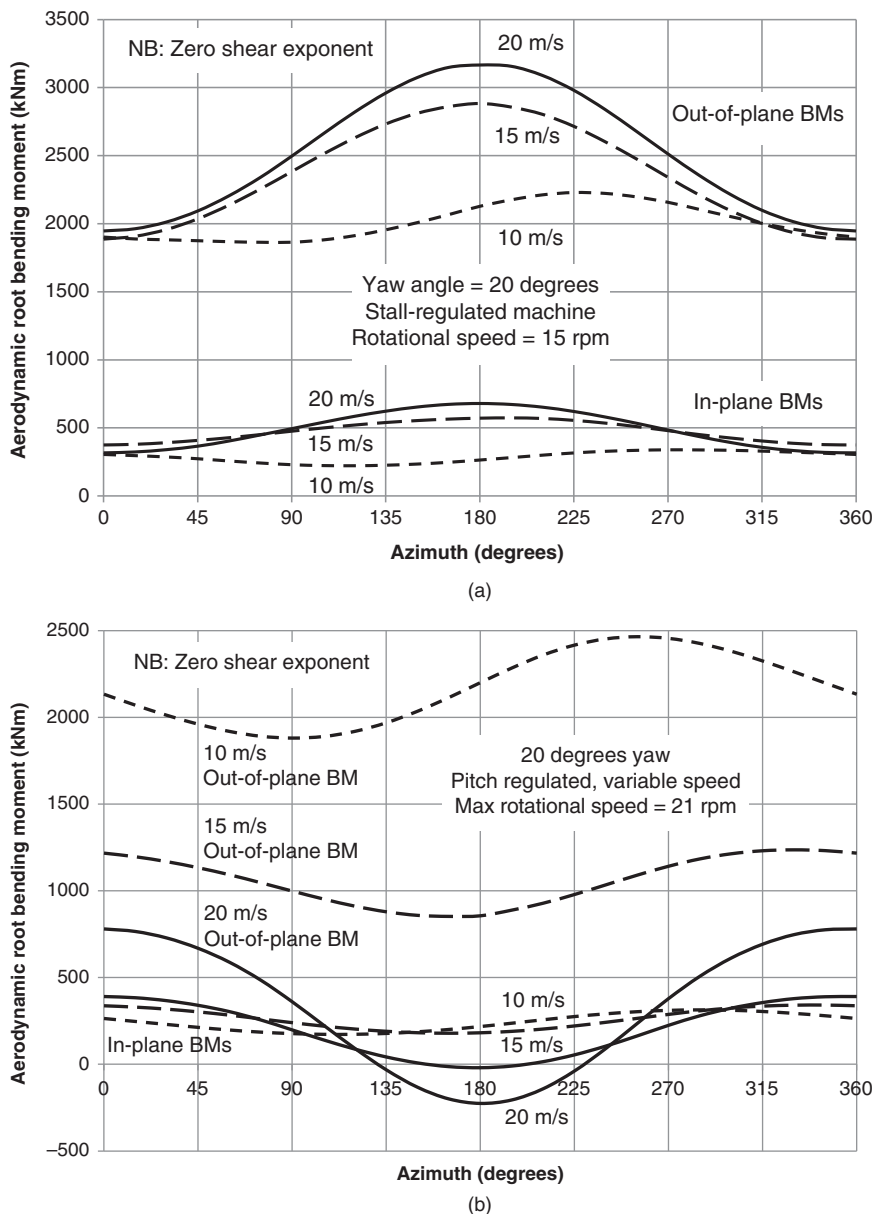


Figure 5.10 (a) Variation of blade root bending moment with azimuth, for an example 80 m diameter stall-regulated machine operating at 15 rpm at a steady 20° yaw. (b) Variation of blade root bending moment with azimuth, for an example 80 m diameter pitch-regulated, variable-speed machine operating at a steady 20° yaw with a tip speed ratio of 8 below 11 m/s and a maximum rotational speed of 2.2 rad/s (21 rpm).

Shaft tilt

Upwind machines – that is, wind turbines with the rotor positioned between the tower and the oncoming wind – normally have the rotor shaft tilted upwards by several degrees to increase the clearance between the rotor and the tower. Thus, as for the case of yaw misalignment, the flow is inclined to the rotor shaft axis but tilted upwards rather than sideways, so the treatment of shaft tilt mirrors that of yawed flow.

Wind shear

The increase of wind speed with height is known as *wind shear*. The theoretical logarithmic profile, $U(z) \propto \ln(z/z_0)$, is usually approximated by the power law, $U(z) \propto (z/z_{ref})^\alpha$, for wind turbine design purposes. The appropriate value of the exponent α increases with the surface roughness, z_0 , with a figure of 0.14 typically quoted for level countryside, although the speed-up of air flow close to the ground over rounded hills usually results in a lower value at hill tops. As already noted, IEC 61400-1 specifies a conservative value of 0.20.

In applying momentum theory to this case, the velocity component at right angles to the plane of rotation is expressed as $U_\infty \left(1 + \frac{r \cos \psi}{z_{hub}}\right)^\alpha (1 - a)$ and the momentum equations are solved for the induction factors at each azimuth and radius. The variation of blade root bending moments with azimuth due to wind shear is illustrated in Figure 5.11a for the example 80 m diameter stall-regulated machine, taking the exponent as 0.20 and the hub height as 60 m and considering hub-height wind speeds of 10, 15, and 20 m/s. In the 10 m/s case, the variation in out-of-plane moment due to wind shear is significant, but in the 15 m/s case there is negligible variation, as the blade is in stall.

Figure 5.11b shows the variation of blade root bending moments with azimuth due to wind shear for the example 2 MW, 80 m diameter pitch-regulated, variable-speed machine. It is seen that the out-of-plane moment range increases with increasing hub-height wind speed because of the increased range of wind speeds encountered over a blade revolution.

Tower shadow

Blocking of the air flow by the tower results in regions of reduced wind speed both upwind and downwind of the tower. This reduction is more severe for tubular towers than for lattice towers and, in the case of tubular towers, is larger on the downwind side because of flow separation. As a consequence, designers of downwind machines usually position the rotor plane well clear of the tower to minimise the interference effect.

The velocity deficits upwind of a tubular tower can be modelled using potential flow theory. The flow around a cylindrical tower is derived by superposing a doublet – that is, a source and sink at very close spacing – on a uniform flow, U_∞ , giving the stream function:

$$\psi = U_\infty y \left(1 - \frac{(D/2)^2}{x^2 + y^2}\right) \quad (5.20)$$

where D is the tower diameter, and x and y are the longitudinal and lateral coordinates with respect to the tower centre – see Figure 5.12. Differentiation of ψ with respect to y yields the following expression for the flow velocity in the x direction:

$$U = U_\infty \left(1 - \frac{(D/2)^2(x^2 - y^2)}{(x^2 + y^2)^2}\right) \quad (5.21)$$

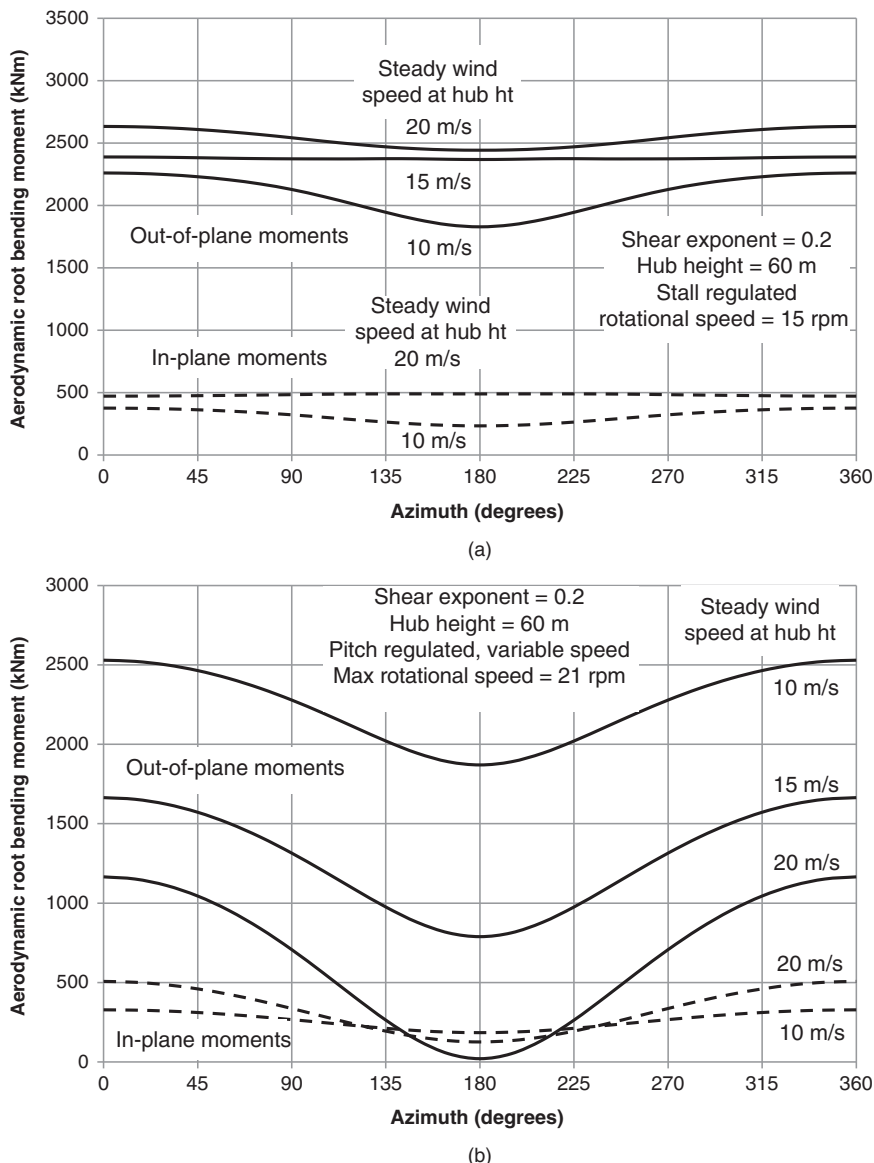


Figure 5.11 (a) Variation of blade root bending moments with azimuth due to wind shear, for the example 80 m diameter stall-regulated machine operating in steady hub-height winds of 10, 15, and 20 m/s with 0.2 shear exponent. (b) Variation of blade root bending moments with azimuth due to wind shear, for the example 80 m diameter pitch-regulated, variable-speed machine operating in steady hub-height winds of 10, 15, and 20 m/s with 0.2 shear exponent. The machine operates at a tip speed ratio of 8 in winds below 11 m/s and at a limiting rotational speed of 2.2 rad/s (21 rpm) in higher winds.

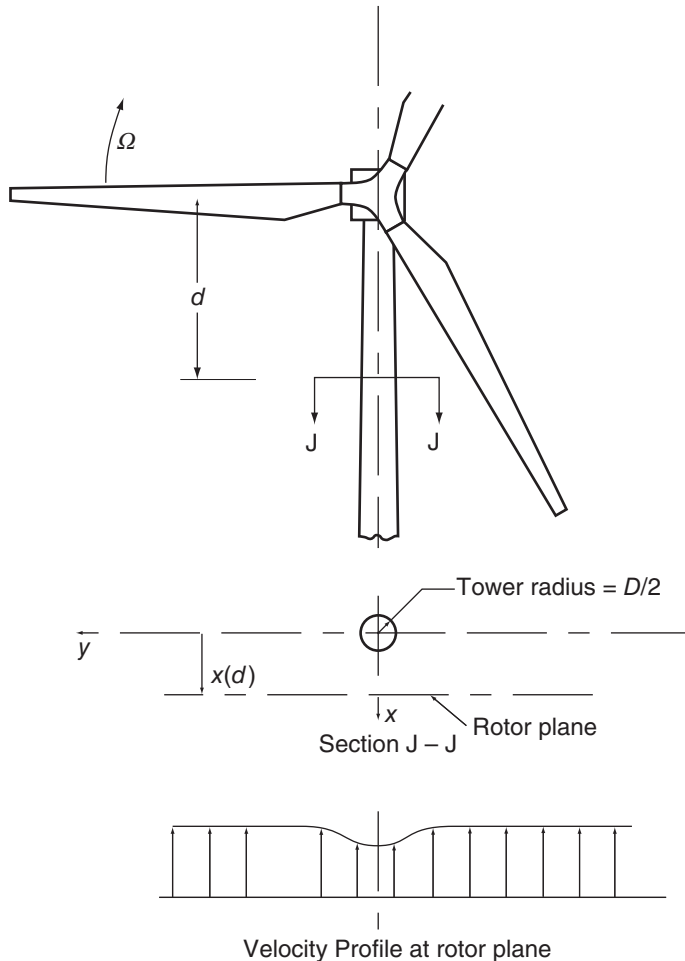


Figure 5.12 Tower shadow parameters.

The second term within the brackets, which is the velocity deficit as a proportion of the undisturbed wind speed, is plotted out against the lateral coordinate, y , divided by tower diameter, for a range of upwind distances, x , in Figure 5.13. The velocity deficit on the flow axis of symmetry is equal to $U_\infty(D/2x)^2$, and the total width of the deficit region is twice the upwind distance. Consequently, the velocity gradient encountered by a rotating blade decreases rapidly as the upwind distance, x , increases.

The effect of tower shadow on blade loading can be estimated by setting the local velocity component at right angles to the plane of rotation equal to $U(1-a)$ in place of $U_\infty(1-a)$ and applying blade element theory as usual. Results for blade root bending moments for the example 80 m diameter stall-regulated machine are given in Figure 5.14, assuming a tower diameter of 4 m and ignoring dynamic effects. The plots show the variation of in-plane and out-of-plane root moments with azimuth during operation in wind speeds of 10 and 20 m/s, for a blade-tower clearance equal to the tower radius – i.e. for

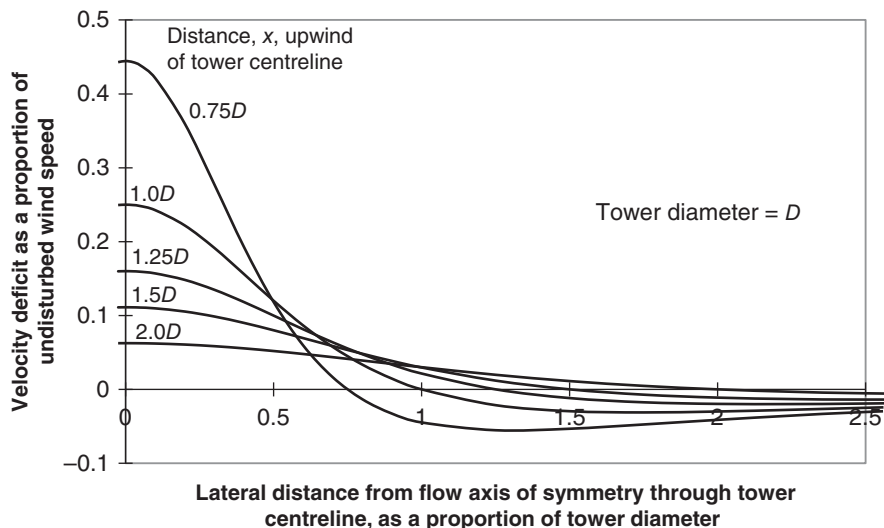


Figure 5.13 Profiles of velocity deficit due to tower shadow at different distances x upwind of tower centreline.

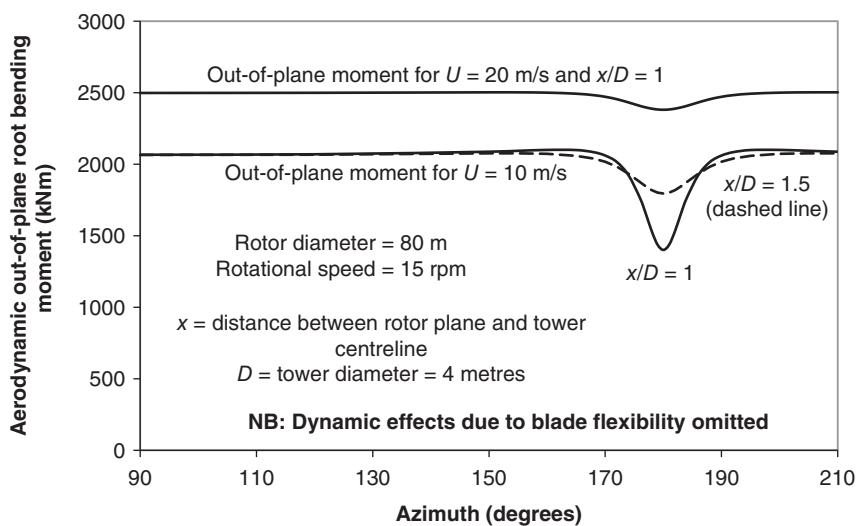


Figure 5.14 Variation of blade root out-of-plane bending moment with azimuth due to tower shadow, for typical 80 m diameter stall-regulated upwind machine operating in steady, uniform winds of 10 and 20 m/s.

$x/D = 1$. Note that the dip in out-of-plane bending moment is more severe at the lower wind speed. Also shown are 10 m/s plots for $x/D = 1.5$, which exhibit a much less severe disturbance.

In the case of downwind turbines, the flow separation and generation of eddies that take place are less amenable to analysis, so empirical methods are used to estimate the

mean velocity deficit. Commonly, the profile of the velocity deficit is assumed to be of cosine form, so that

$$U = U_\infty \left(1 - k \cos^2 \left(\frac{\pi y}{\delta} \right) \right) \quad (5.22)$$

where δ is the total width of the deficit region. The slight enhancement of velocities beyond the deficit region is usually ignored. See also Section 6.13.2.

The sharp dip in blade loading caused by tower shadow is more prone to excite blade oscillations than the smooth variations in load due to wind shear, shaft tilt, and yaw, and this aspect is considered in the ‘Blade Dynamic Response’ section.

Wake effects

Within a wind farm, it is common for one turbine to be operating wholly or partly in the wake of another. In the latter case, which is more severe, the downwind turbine is effectively subjected to horizontal wind shear, and the blade load fluctuations can be analysed accordingly. Wake effects are described in detail in Chapter 9.

5.7.3 Gravity loads

Gravity loading on the blade results in a sinusoidally varying edgewise bending moment that reaches a maximum when the blade is horizontal and that changes sign from one horizontal position to the other. It is thus a major source of fatigue loading. For the blade SC40 (see Example 5.1), the maximum gravity moment, $\int_0^R m(r)rdr$, is 1260 kNm, so the edgewise bending moment range due to gravity is 2520 KNm. This significantly exceeds the variations in edgewise moment due to yaw or wind shear, which are typically less than a tenth this value below rated and less than a sixth above. The spanwise distribution of gravity bending moment is shown in Figure 5.15 for blade SC40.

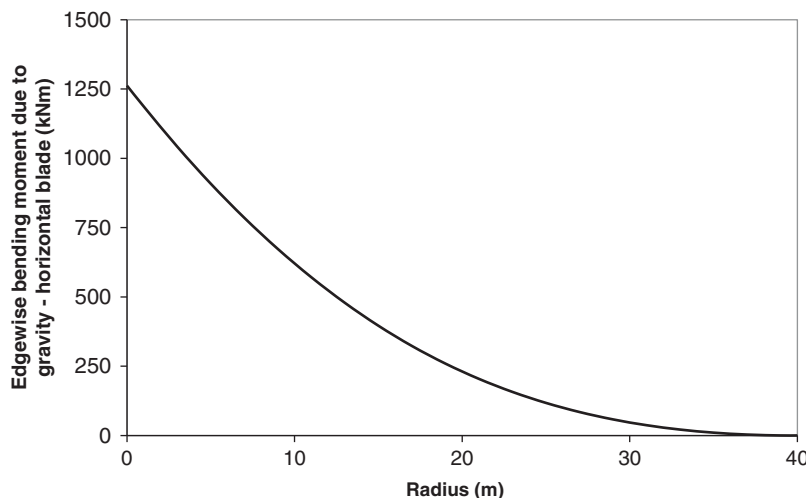


Figure 5.15 Blade SC40 gravity bending moment distribution.

5.7.4 Deterministic inertia loads

Centrifugal loads

For a rigid blade rotating with its axis perpendicular to the axis of rotation, the centrifugal forces generate a simple tensile load in the blade that at radius r^* is given by the expression $\Omega^2 \int_{r^*}^R m(r) r dr$. As a result, the fluctuating stresses in the blade arising from all loading sources always have a tensile bias during operation. For blade SC40 rotating at 15 rpm, the centrifugal force at the root amounts to 320 KN – approximately four times its weight.

Thrust loading causes flexible blades to deflect downwind, with the result that the centrifugal forces generate blade out-of-plane moments in opposition to those due to the thrust. This reduction of the moment due to thrust loading is known as *centrifugal relief*. The phenomenon is non-linear, so iterative techniques are required to arrive at a solution. Greater centrifugal relief can be obtained by coning the rotor so that the blades are inclined downwind in the first place. A balance can be struck so that the maximum forward out-of-plane moment due to centrifugal loads in very low wind is approximately equal to the maximum rearward out-of-plane moment due to the thrust loading in combination with centrifugal loads during operation in rated wind.

Gyroscopic loads

When an operating machine yaws, the blades experience gyroscopic loads perpendicular to the plane of rotation. Consider the point A on a rotor rotating clockwise at a speed of Ω rad/sec, as illustrated in Figure 5.16. The instantaneous horizontal velocity component of point A due to rotor rotation is Ωz , where z is the height of the point above the hub. If the machine is yawing clockwise in plan at a speed of Λ rad/sec, then it can be shown that point A accelerates at $2\Omega\Lambda z$ towards the wind, assuming the rotor is rigid. Integrating the resulting inertial force over the blade length gives the following expression for the blade out-of-plane bending moment about the shaft axis:

$$M_Y = \int_0^R 2\Omega\Lambda z r m(r) dr = 2\Omega\Lambda \cos \psi \int_0^R r^2 m(r) dr = 2\Omega\Lambda \cos \psi I_B \quad (5.23)$$

where I_B is the blade inertia about the shaft axis.

As an example, consider an 80 m diameter machine with SC40 blades yawing at one degree per second during operation at 15 rpm. The blade inertia about the shaft axis is 3000 Tm^2 , so the maximum value of M_Y is $2(\pi/2)(0.0175)3000 = 164 \text{ KNm}$. This is only about a 20th of the maximum out-of-plane moment due to aerodynamic loads.

Braking loads

Rotor deceleration due to mechanical braking introduces edgewise blade bending moments that are additive to the gravity moments on a descending blade.

Teeter loads

Blade out-of-plane root bending moments can be eliminated entirely by mounting each blade on a hinge so that it is free to rotate in the fore-aft direction. Although centrifugal forces are effective in controlling the cone angle of each blade at normal operating

speeds, the need for alternative restraints during start-up and shut-down means that such hinges are rarely used. However, in the case of two bladed machines, it is convenient to mount the whole rotor on a single shaft hinge allowing fore-aft rotation or ‘teetering’, and this arrangement is frequently adopted to reduce out-of-plane bending moment fluctuations at the blade root and to prevent the transmission of blade out-of-plane moments to the low-speed shaft. As teetering is essentially a dynamic phenomenon, consideration of teeter behaviour is deferred to Section 5.8.

5.7.5 Stochastic aerodynamic loads: analysis in the frequency domain

As noted in Section 5.7.1, the random loadings on the blade due to short-term wind speed fluctuations are known as *stochastic aerodynamic loads*. The wind speed fluctuations about the mean at a *fixed* point in space are characterised by a probability distribution – which, for most purposes, can be assumed to be normal – and by a power spectrum that describes how the energy of the fluctuations is distributed between different frequencies (see Sections 2.6.3 and 2.6.4).

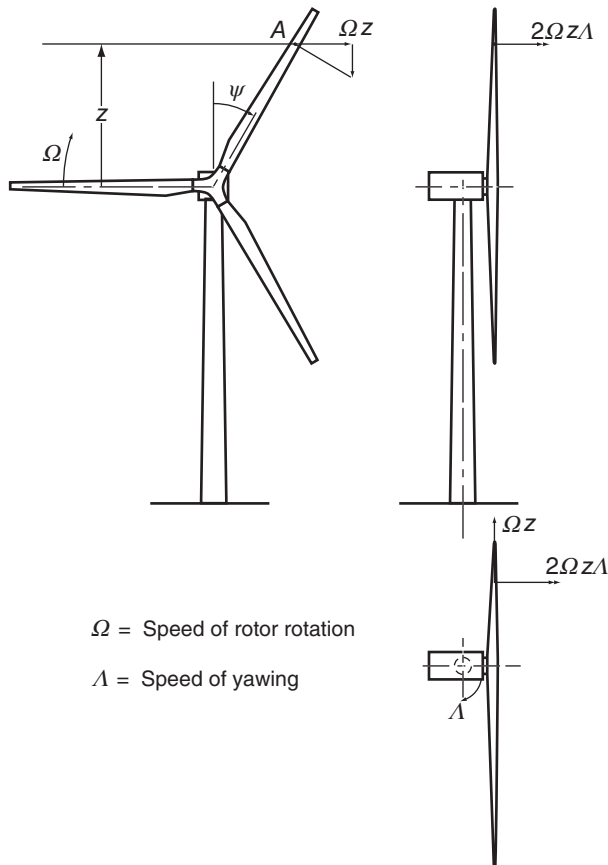


Figure 5.16 Gyroscopic acceleration of a point on a yawing blade.

The stochastic loads are most conveniently analysed in the frequency domain, but to facilitate this, it is usual to assume a linear relation between the fluctuation, u , of the wind speed incident on the aerofoil and the resultant loadings. This is a reasonable assumption for an unstalled blade at high tip speed ratio, as will be shown. The fluctuating aerodynamic lift per unit length, L , is $\frac{1}{2}\rho W^2 C_L c$, where W is the air velocity relative to the blade, C_L is the lift coefficient, and the drag term is ignored. See Figure 3.14. Because the flow angle, ϕ , is small at high tip speed ratio, λ , the relative air velocity, W , can be assumed to be changing much more slowly with the wind speed than C_L , so that dW/du can be ignored. As a result,

$$\frac{dL}{du} = \frac{1}{2}\rho W^2 c \frac{dC_L}{d\alpha} \frac{d\alpha}{du} \text{ where } \alpha, \text{ the angle of attack} = \phi - \beta \quad (5.24)$$

If the blades are not pitching, then the local blade twist, β , is constant, so that $d\alpha/du = d\phi/du$. To preserve linearity, it is necessary to assume that the rate of change of lift coefficient with angle of attack, $dC_L/d\alpha$ is constant, which is tenable only if the blade remains unstalled. Assuming for simplicity that the wake is frozen, i.e. that the induced velocity, $\bar{U}a$, remains constant, despite the wind speed fluctuations, u , we obtain

$$\tan \phi \cong (\bar{U}(1-a) + u)/\Omega r$$

so that, for ϕ small,

$$\begin{aligned} \frac{d\phi}{du} &\cong \frac{1}{\Omega r} \quad \text{and } W \cong \Omega r, \text{ leading to} \\ \Delta L = L - \bar{L} &= u \frac{dL}{du} = \frac{1}{2}\rho(\Omega r)^2 c \frac{dC_L}{d\alpha} \frac{u}{\Omega r} = \frac{1}{2}\rho \Omega r c \frac{dC_L}{d\alpha} u \end{aligned} \quad (5.25)$$

Hence

$$\sigma_L = \left(\frac{1}{2}\rho \Omega \frac{dC_L}{d\alpha} \right) r c \sigma_u$$

Theoretically the slope of the lift curve $\frac{dC_L}{d\alpha}$ is 2π , but in practice it is about 6.0 – see Appendix A3.7.

If the turbulence integral length scale is large compared to the blade radius, then the expression for the standard deviation of the blade root fore-aft bending moment – assuming a completely rigid blade – approximates to

$$\sigma_M = \int_0^R \sigma_L r dr = \frac{1}{2}\rho \Omega \frac{dC_L}{d\alpha} \sigma_u \int_0^R c(r) r^2 dr \quad (5.26)$$

where σ_u is the standard deviation of the wind speed incident on the rotor disc, which, by virtue of the ‘frozen wake’ assumption (see Section 4.4.1), equates to the standard deviation of the wind speed in the undisturbed flow. Note that the expression for σ_M in Eq. (5.26) should include the cosine of the flow angle, ϕ , but this is assumed to approximate to unity, as ϕ is small.

If, as will be the case in practice, the longitudinal wind fluctuations are not perfectly correlated along the length of the blade, then

$$\sigma_M^2 = \left(\frac{1}{2}\rho \Omega \frac{dC_L}{d\alpha} \right)^2 \int_0^R \int_0^R \kappa_u(r_1, r_2, 0) c(r_1) c(r_2) r_1^2 r_2^2 dr_1 dr_2 \quad (5.27)$$

where $\kappa_u(r_1, r_2, 0)$ is the cross-correlation function $\kappa_u(r_1, r_2, \tau)$ between the wind fluctuations at radii r_1 and r_2 with the time lag τ set equal to zero, i.e.

$$\kappa_u(r_1, r_2, 0) = \left[\frac{1}{T} \int_0^T u(r_1, t) u(r_2, t) dt \right] \quad (5.28)$$

In reality, of course, the blade will not be completely rigid, so the random wind loading will excite the natural modes of blade vibration. To quantify these excitations, it is first necessary to know the energy content of the incident wind fluctuations *as seen by each point on the rotating blade* at the blade natural frequencies – information that is provided by the ‘rotationally sampled spectrum’. This spectrum is significantly different from the fixed-point spectrum, because a rotating blade will often slice through an individual gust (defined as a volume of air travelling at above average speed) several times, as the gust dimensions are frequently large compared with the distance travelled by the air in one turbine revolution. This phenomenon, known as *gust slicing*, considerably enhances the frequency content at the rotational frequency, and, to a lesser extent, at its harmonics also.

The method for deriving the rotational spectrum is described below. The dynamic response of a flexible blade to random wind loading is explored in Section 5.8.

Rotationally sampled spectrum

The derivation of the power spectrum of the wind seen by a point on a rotating blade is based on the Fourier transform pairs:

$$S_u(n) = 4 \int_0^\infty \kappa_u(\tau) \cos 2\pi n\tau d\tau \quad (5.29)$$

$$\kappa_u(\tau) = \int_0^\infty S_u(n) \cos 2\pi n\tau dn \quad (5.30)$$

where $S_u(n)$ is the single-sided spectrum of wind speed fluctuations at a fixed point in terms of frequency in Hz. Firstly, the latter equation is used to obtain the auto-correlation function, $\kappa_u(\tau)$, for the along-wind turbulent fluctuations at a fixed point in space from the corresponding power spectrum. Secondly, $\kappa_u(\tau)$ is used to derive the related auto-correlation function, $\kappa_u^Q(r, \tau)$, for a point on the rotating blade at radius r . Finally this function is transformed using Eq. (5.29) to yield the rotationally sampled spectrum. The three steps are set out in more detail below. Note that three key simplifying assumptions are made – that the turbulence is homogeneous and isotropic, and that the flow is incompressible.

Step 1 – Derivation of the auto-correlation function at a fixed point: The von Karman spectrum is chosen as the input spectrum, because it is isotropic and homogeneous and analytic expressions exist for the correlations. The power spectrum of the along-wind wind speed fluctuations at a fixed point in space is given by Eq. (2.25):

$$\frac{S_u(n)}{\sigma_u^2} = \frac{4L/\bar{U}}{(1 + 70.8(nL/\bar{U})^2)^{\frac{5}{6}}} \quad (5.31)$$

where L is the integral length scale of the longitudinal component of turbulence in the longitudinal direction (i.e. L_{2u} or ${}^x L_u$, as defined in Section 2.6.4). It can

be shown that Eq. (5.30) yields the following expression for the corresponding auto-correlation function:

$$\kappa_u(\tau) = \frac{2\sigma_u^2}{\Gamma\left(\frac{1}{3}\right)} \left(\frac{\tau/2}{T'}\right)^{\frac{1}{3}} K_{1/3}\left(\frac{\tau}{T'}\right) \quad (5.32)$$

where T' is related to the integral length scale, L , by the formula

$$T' = \frac{\Gamma\left(\frac{1}{3}\right)}{\Gamma\left(\frac{5}{6}\right)} \frac{L}{\sqrt{\pi} U} \cong 1.34 \frac{L}{U} \quad (5.33)$$

$\Gamma()$ is the Gamma function and $K_{1/3}(x)$ is a modified Bessel function of the second kind and order $v = 1/3$. See eqs. (13.5) and (13.6) in Harris and Deaves (1980), with the cross-correlation function converted to an auto-correlation function by setting the spatial separation, λ , of the two points considered to zero. The general definition of $K_v(x)$ is as follows:

$$K_v(x) = \frac{\pi}{2 \sin \pi v} \sum_{m=0}^{\infty} \frac{(x/2)^{2m}}{m!} \left[\frac{(x/2)^{-v}}{\Gamma(m-v+1)} - \frac{(x/2)^v}{\Gamma(m+v+1)} \right] \quad (5.34)$$

[Note: Better approximations for $K_v(x)$ exist – see Abramowitz and Stegun (1958). Also, Bessel functions are available as built-in functions in computer programmes such as MATLAB.]

Step 2 – Derivation of the auto-correlation function at a point on the rotating blade: This derivation makes use of Taylor's 'frozen turbulence' hypothesis, by which the instantaneous wind speed at point C at time $t = \tau$ is assumed to be equal to that at a point B a distance $\bar{U}\tau$ upwind of C at time $t = 0$, \bar{U} being the mean wind speed. Thus, referring to Figure 5.17a, the auto-correlation function $\kappa_u^o(r, \tau)$ for the along-wind wind fluctuations seen by a point Q at radius r on the rotating blade is equal to the cross-correlation function $\kappa_u(\vec{s}, 0)$ between the simultaneous along-wind wind fluctuations at points A and B. Here A and C are the positions of point Q at the beginning and end of time interval τ , respectively, B is $\bar{U}\tau$ upwind of C, and \vec{s} is the vector BA. (Note that the superscript o denotes that the auto-correlation function relates to a point on a rotating blade rather than a fixed point. The same convention will be adopted in relation to power spectra.)

Batchelor (1953) has shown that, if the turbulence is assumed to be homogeneous and isotropic, the cross-correlation function, $\kappa_u(\vec{s}, 0)$, is given by

$$\kappa_u(\vec{s}, 0) = (\kappa_L(s) - \kappa_T(s)) \left(\frac{s_1}{s} \right)^2 + \kappa_T(s) \quad (5.35)$$

where $\kappa_L(s)$ is the cross-correlation function between velocity components at points A and B, s apart, in a direction parallel to AB (v_L^A and v_L^B in Figure 5.17a), and $\kappa_T(s)$ is the corresponding function for velocity components (v_T^A and v_T^B) in a direction perpendicular to AB. s_1 is the separation of points A and B measured in the

along-wind direction – i.e. $\bar{U}\tau$. The variation of the cross-correlation functions $\kappa_L(s)$ and $\kappa_T(s)$ with separation distance, s , is shown in Figure 5.17b, with the separation distance normalised by the integral length scale of the longitudinal component of turbulence in the longitudinal direction, L ($= {}^x L_u$). Note that the integral length scale of the longitudinal component of turbulence in the transverse directions is $0.5L$.

As the distance between points A and C on the rotor disc is $2r\sin(\Omega\tau/2)$, we have

$$s^2 = \bar{U}^2\tau^2 + 4r^2\sin^2(\Omega\tau/2) \quad (5.36)$$

Hence

$$\kappa_u(\vec{s}, 0) = \kappa_L(s) \left(\frac{\bar{U}\tau}{s} \right)^2 + \kappa_T(s) \left[1 - \left(\frac{\bar{U}\tau}{s} \right)^2 \right] = \kappa_L(s) \left(\frac{\bar{U}\tau}{s} \right)^2 + \kappa_T(s) \left(\frac{2r\sin(\Omega\tau/2)}{s} \right)^2 \quad (5.37)$$

For incompressible flow, it can also be shown (Batchelor 1953) that

$$\kappa_T(s) = \kappa_L(s) + \frac{s}{2} \frac{d\kappa_L(s)}{ds} \quad (5.38)$$

Substitution of Eq. (5.38) in Eq. (5.37) gives

$$\kappa_u(\vec{s}, 0) = \kappa_L(s) + \frac{s}{2} \frac{d\kappa_L(s)}{ds} \left(\frac{2r\sin(\Omega\tau/2)}{s} \right)^2 \quad (5.39)$$

When the vector \vec{s} is in the along-wind direction, $\kappa_L(s)$ translates to $\kappa_u(s_1)$, which, by Taylor's 'frozen turbulence' hypothesis, equates to the auto-correlation function at a fixed point, $\kappa_u(\tau)$ [Eq. (5.32)], with $\tau = s_1/\bar{U}$. Thus,

$$\kappa_L(s_1) = \frac{2\sigma_u^2}{\Gamma\left(\frac{1}{3}\right)} \left(\frac{s_1/2}{T'\bar{U}} \right)^{\frac{1}{3}} K_{1/3} \left(\frac{s_1}{T'\bar{U}} \right) \quad (5.40)$$

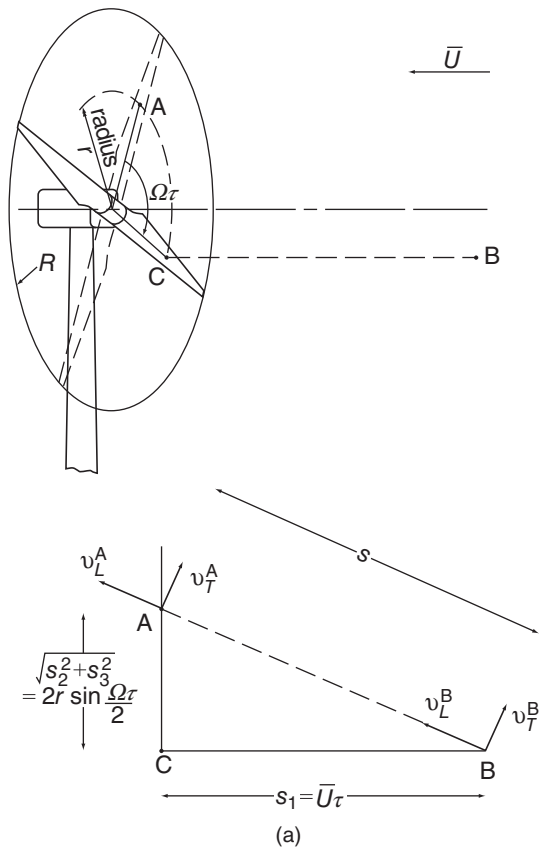
Because the turbulence is assumed to be isotropic, $\kappa_L(s)$ is independent of the direction of the vector \vec{s} , so we can write, with the aid of Eq. (5.33):

$$\kappa_L(s) = \frac{2\sigma_u^2}{\Gamma\left(\frac{1}{3}\right)} \left(\frac{s/2}{T'\bar{U}} \right)^{\frac{1}{3}} K_{1/3} \left(\frac{s}{T'\bar{U}} \right) = \frac{2\sigma_u^2}{\Gamma\left(\frac{1}{3}\right)} \left(\frac{s/2}{1.34L} \right)^{\frac{1}{3}} K_{1/3} \left(\frac{s}{1.34L} \right) \quad (5.41)$$

Noting that $\frac{d}{dx}[x^\nu K_\nu(x)] = -x^\nu K_{(1-\nu)}(x)$, the following expression for the auto-correlation function for the along-wind fluctuations at a point at radius r on the rotating blade is obtained by substituting Eq. (5.41) in Eq. (5.39):

$$\begin{aligned} \kappa_u^o(r, \tau) &= \kappa_u(\vec{s}, 0) = \frac{2\sigma_u^2}{\Gamma\left(\frac{1}{3}\right)} \left(\frac{s/2}{1.34L} \right)^{\frac{1}{3}} \\ &\times \left[K_{1/3} \left(\frac{s}{1.34L} \right) - \frac{s}{2(1.34L)} K_{2/3} \left(\frac{s}{1.34L} \right) \left(\frac{2r\sin(\Omega\tau/2)}{s} \right)^2 \right] \end{aligned} \quad (5.42)$$

where s is defined in terms of τ by Eq. (5.36) above.



(a)

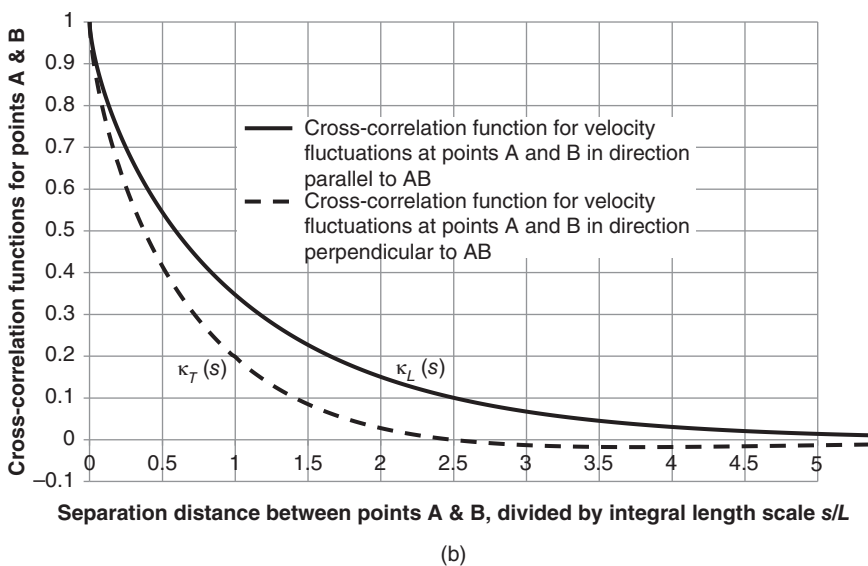


Figure 5.17 (a) Geometry for the derivation of the velocity auto-correlation function for a point on a rotating blade. (b) Cross-correlation functions for velocity fluctuations at points A and B – parallel and perpendicular to AB.

Step 3 – Derivation of the power spectrum seen by a point on the rotating blade: The rotationally sampled spectrum is obtained by taking the Fourier transform of $\kappa_u^o(r, \tau)$ from Eq. (5.42):

$$\begin{aligned} S_u^o(n) &= 4 \int_0^\infty \kappa_u^o(r, \tau) \cos 2\pi n \tau d\tau \\ &= 2 \int_{-\infty}^\infty \kappa_u^o(r, \tau) \cos 2\pi n \tau d\tau \text{ as } \kappa_u^o(r, \tau) = \kappa_u^o(r, -\tau) \end{aligned} \quad (5.43)$$

As no analytical solution has been found for the integral, a solution has to be obtained numerically using a discrete Fourier transform (DFT). First the limits of integration are reduced to $-T/2, +T/2$, as $\kappa_u^o(r, \tau)$ tends to zero for large τ . Then the limits of integration are altered to $0, T$ with $\kappa_u^o(r, \tau)$ set equal to $\kappa_u^o(r, T - \tau)$ for $\tau > T/2$, as $\kappa_u^o(r, \tau)$ is now assumed to be periodic with period T . Thus,

$$S_u^o(n) = 2 \int_0^T \kappa_u^{*o}(r, \tau) \cos 2\pi n \tau d\tau \quad (5.44)$$

where the asterisk denotes that $\kappa_u^o(r, \tau)$ is ‘reflected’ for $T > T/2$. The DFT then becomes

$$S_u^o(n_k) = 2T \left[\frac{1}{N} \sum_{p=0}^{N-1} \kappa_u^{*o}(r, pT) \cos(2\pi kp/N) \right] \quad (5.45)$$

Here, N is the number of points taken in the time series of $\kappa_u^{*o}(r, pT)$, and the power spectral density is calculated at the frequencies $n_k = k/T$ for $k = 0, 1, 2, \dots, N-1$. The expression in square brackets can be evaluated using a standard fast Fourier transform (FFT), provided N is chosen equal to a power of 2. Clearly N should be as large as possible if a wide range of frequencies is to be covered at high resolution. Just as $\kappa_u^{*o}(r, \tau)$ is symmetrical about $T/2$, the values of $S_u^o(n_k)$ obtained from the FFT are symmetrical about the mid-range frequency of $N/(2T)$, and the values above this frequency have no real meaning. Moreover, the values of power spectral density calculated by the DFT at frequencies approaching $N/(2T)$ will be in error as a result of aliasing, because these are falsely distorted by frequency components above $N/(2T)$ which contribute to the $\kappa_u^{*o}(r, pT)$ series. Assuming that the calculated spectral densities are valid up to a frequency of $N/(4T)$, then the selection of $T = 200$ seconds and $N = 4096$ would enable the FFT to give useful results up to a frequency of about 5 Hz at a frequency interval of 0.005 Hz.

Example 5.2 As an illustration, results have been derived for points on a 40 m radius SC40 blade rotating at 15 rpm in a mean wind speed of 8 m/s. Following the recommendations for the use of the von Karman isotropic turbulence model in IEC 61400-1 edition 2 (1999), the isotropic integral length scale, L , is taken as 3.5 times the IEC 61400-1 turbulence scale parameter, Λ_1 . However, Λ_1 is taken as 42 m, as recommended in edition 3 (2005) and edition 4 (2019) for a hub height exceeding 60 m, giving $L = 147$ m. (These values compare with $\Lambda_1 = 21$ m and $L = 73.5$ m recommended in edition 2.) Figure 5.18 shows how the normalised auto-correlation function, $\rho_u^o(r, \tau)$ ($= \kappa_u^o(r, \tau)/\sigma_u^2$), for the longitudinal wind fluctuations varies with the number of rotor revolutions at 40 m, 20 m, and 0 m radii. For $r = 20$ m, and even more so for $r = 40$ m, these curves display pronounced peaks after each full revolution, when the blade may be thought of as encountering the initial gust or lull once more.

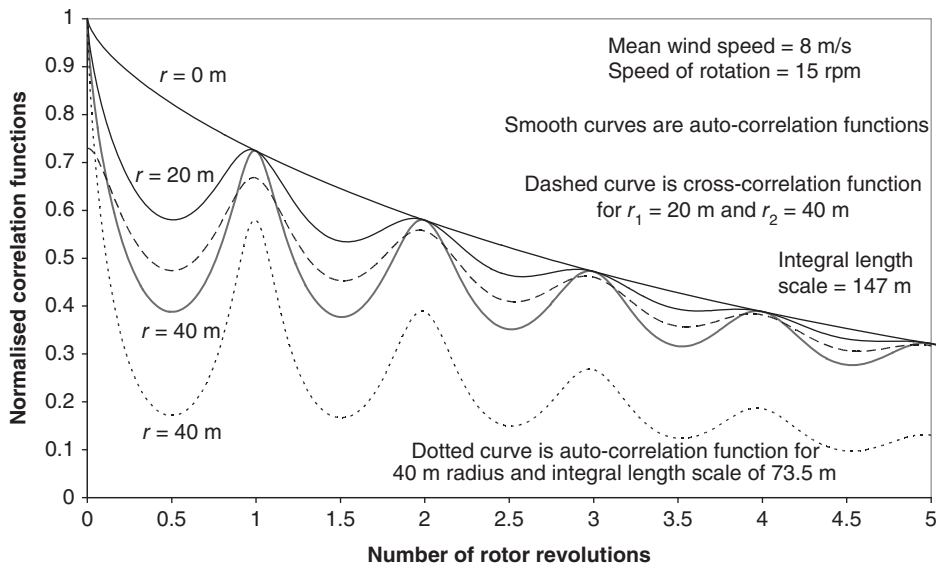


Figure 5.18 Normalised auto-correlation and cross-correlation functions for along-wind wind fluctuations as seen by points on a rotating blade at different radii.

Figure 5.19a shows the corresponding rotationally sampled power spectral density function, $R_u^o(r, n)$ ($= nS_u^o(r, n)/\sigma_u^2$), plotted out against frequency, n , using a logarithmic scale for the latter. It is clear that there is a substantial shift of the frequency content of the spectrum to the frequency of rotation and, to a lesser degree, to its harmonics, with the extent of the shift increasing with radius. Figure 5.19b is a repeat of Figure 5.19a, but with a logarithmic scale used on both axes.

It is instructive to consider how the various input parameters affect the shift of energy to the rotational frequency. As $\kappa_u^o(r, \tau) = \kappa_u(\vec{s}, 0)$ decreases monotonically with increasing s , Eq. (5.36) indicates that the depths of the troughs in this function – and hence the transfer of energy to the rotational frequency – increase roughly in proportion to the tip speed ratio, $\Omega r/U$, and will thus be most significant for fixed-speed two bladed machines (which generally rotate faster than three bladed ones) in low wind speeds.

Effect of reduced length scale

The effect of adopting a reduced isotropic integral length scale, L , of 73.5 m as opposed to 147 m on the auto-correlation function and the rotationally sampled power spectrum is illustrated for a radius of 40 m in Figures 5.18 and 5.20, respectively.

It is seen that, despite the more rapid attenuation of auto-correlation function, the reduction of length scale has negligible effect on the spectral peak at the rotational frequency.

Rotationally sampled cross-spectra

The expressions for the spectra of blade bending moments and shears are normally functions of entities known as *rotationally sampled cross-spectra* for pairs of points along the

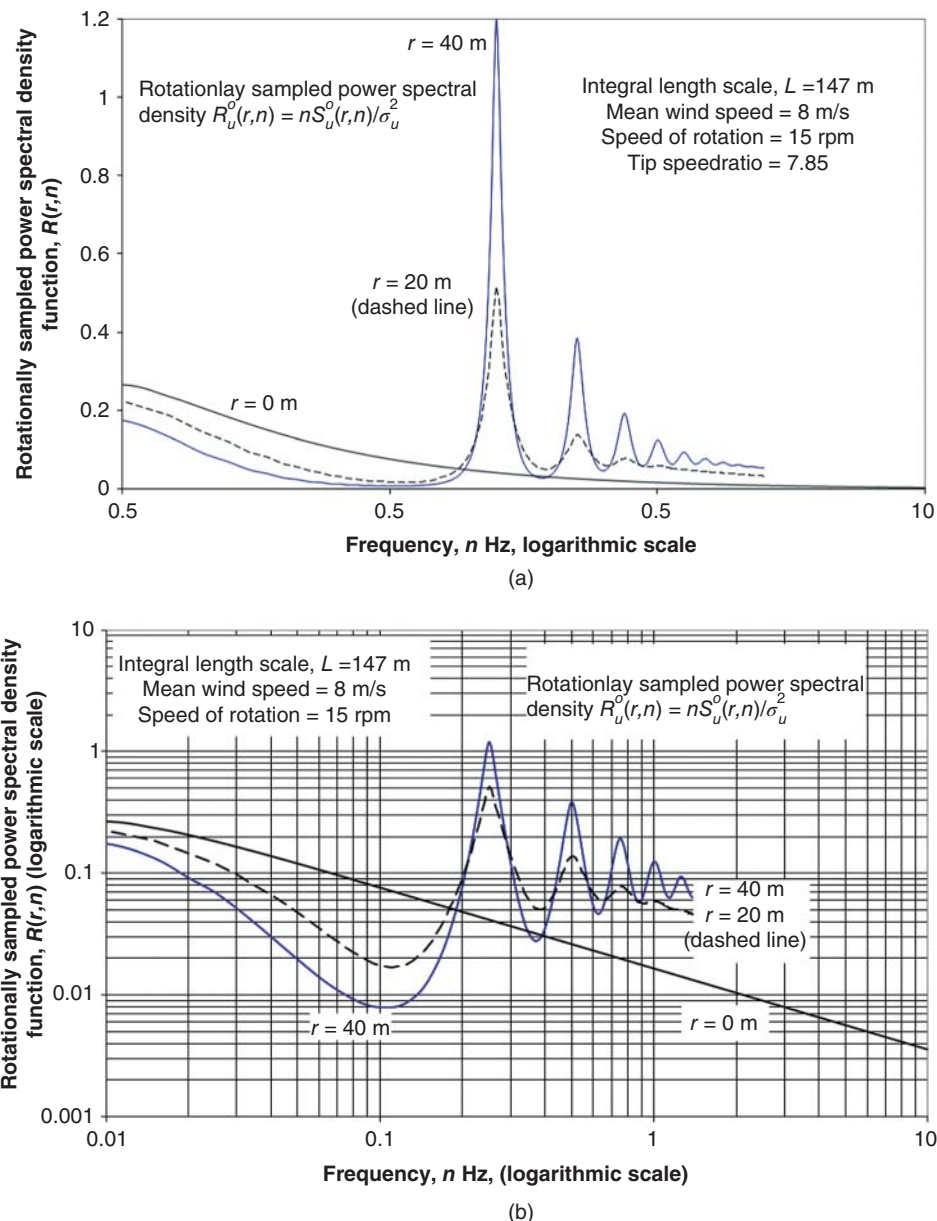


Figure 5.19 (a) Rotationally sampled power spectra of longitudinal wind speed fluctuations at different radii. (b) Rotationally sampled power spectra of longitudinal wind speed fluctuations at different radii: log-log plot.

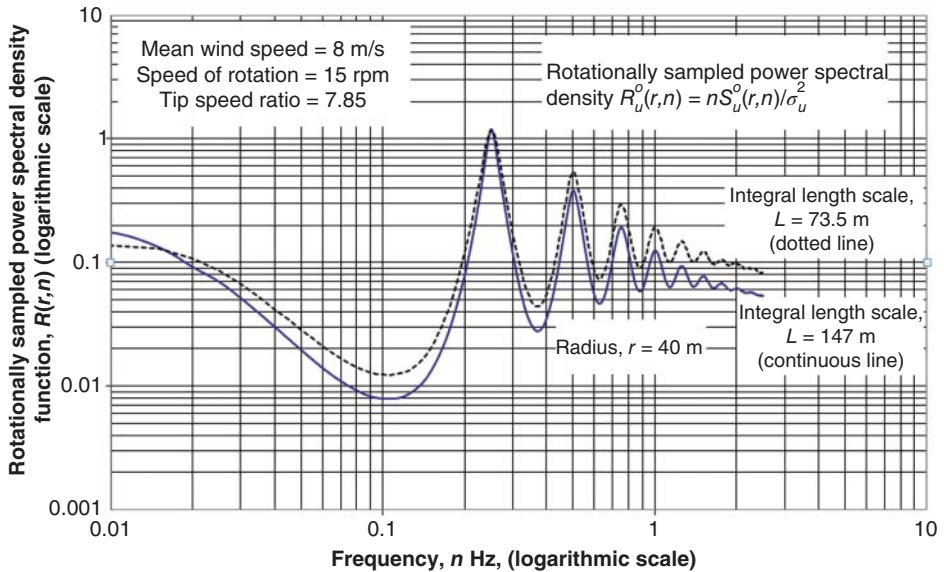


Figure 5.20 Comparison of rotationally sampled power spectra at 40 m radius for different integral length scales.

blade, which are analogous to the rotationally sampled ordinary spectra for single points described above. The cross-spectrum for a pair of points at radii r_1 and r_2 on a rotating blade is thus related to the corresponding cross-correlation function by the Fourier transform pair

$$S_u^o(r_1, r_2, n) = 4 \int_0^\infty \kappa_u^o(r_1, r_2, \tau) \cos 2\pi n \tau d\tau \quad (5.46a)$$

$$\kappa_u^o(r_1, r_2, \tau) = \int_0^\infty S_u^o(r_1, r_2, n) \cos 2\pi n \tau dn \quad (5.46b)$$

Setting $\tau = 0$ in Eq. (5.46b) gives

$$\kappa_u^o(r_1, r_2, 0) = \int_0^\infty S_u^o(r_1, r_2, n) dn \quad (5.47)$$

which, when substituted into the expression for the standard deviation of the blade root bending moment in Eq. (5.27), gives

$$\sigma_M^2 = \left(\frac{1}{2} \rho \Omega \frac{dC_L}{d\alpha} \right)^2 \int_0^R \int_0^R \left[\int_0^\infty S_u^o(r_1, r_2, n) dn \right] c(r_1) c(r_2) r_1^2 r_2^2 dr_1 dr_2 \quad (5.48)$$

From this, it can be deduced that the power spectrum of the blade root bending moment is

$$S_M(n) = \left(\frac{1}{2} \rho \Omega \frac{dC_L}{d\alpha} \right)^2 \int_0^R \int_0^R S_u^o(r_1, r_2, n) c(r_1) c(r_2) r_1^2 r_2^2 dr_1 dr_2 \quad (5.49)$$

The derivation of the rotationally sampled cross-spectrum, $S_u^o(r_1, r_2, n)$, exactly parallels the derivation of the rotationally sampled single-point spectrum given above, with the cross-correlation function $\kappa_u^o(r_1, r_2, \tau)$ between the longitudinal wind fluctuations at points at radii r_1 and r_2 on the rotating blade replacing the auto-correlation function in step 2. Here the expression for the separation distance, s , given in Eq. (5.36), is replaced by

$$s^2 = \bar{U}^2 \tau^2 + r_1^2 + r_2^2 - 2r_1 r_2 \cos \Omega \tau \quad (5.50)$$

The expression for the cross-correlation function thus becomes:

$$\begin{aligned} \kappa_u^o(r_1, r_2, \tau) &= \frac{2\sigma_u^2}{\Gamma\left(\frac{1}{3}\right)} \left(\frac{s/2}{1.34L} \right)^{\frac{1}{3}} \\ &\times \left[K_{1/3} \left(\frac{s}{1.34L} \right) - \frac{s}{2(1.34L)} K_{2/3} \left(\frac{s}{1.34L} \right) \left(\frac{r_1^2 + r_2^2 - 2r_1 r_2 \cos(\Omega\tau)}{s^2} \right) \right] \end{aligned} \quad (5.51)$$

with s defined by Eq. (5.50).

The form of the resulting normalised cross-correlation function, $\rho_u^o(r_1, r_2, \tau) = \kappa_u^o(r_1, r_2, \tau)/\sigma_u^2$, is illustrated in Figure 5.18 for the case considered in Example 5.2, taking $r_1 = 20$ m and $r_2 = 40$ m. In Figure 5.21, the rotationally sampled cross-spectrum for this case is compared with the rotationally sampled single-point spectra or ‘autospectra’ at these radii. It can be seen that the form of the cross-spectrum curve is similar to that of the autospectra, with a pronounced peak at the rotational frequency roughly midway between the peaks of the two autospectra. At higher frequencies, however, the cross-spectrum falls away much more rapidly.

The evaluation of the power spectrum of the blade root bending moment is, in practice, carried out using summations to approximate to the integrals in Eq. (5.49), as follows:

$$S_M(n) = \left(\frac{1}{2} \rho \Omega \frac{dC_L}{d\alpha} \right)^2 \sum_j \sum_k S_u^o(r_j, r_k, n) c(r_j) c(r_k) r_j^2 r_k^2 (\Delta r)^2 \quad (5.52)$$

Limitations of analysis in the frequency domain

As noted at the beginning of this section, analysis of stochastic aerodynamic loads in the frequency domain depends for its validity on a *linear* relationship between the incident wind speed and the blade loading. Thus the method becomes increasingly inaccurate for pitch-regulated machines as winds approach the cut-out value, and it breaks down completely for stall-regulated machines once the wind speed is high enough to cause stall. To avoid these limitations, it is necessary to carry out the analysis in the time domain.

5.7.6 Stochastic aerodynamic loads: analysis in the time domain

Wind simulation

The analysis of stochastic aerodynamic loads in the time domain requires, as input, a simulated wind field extending over the area of the rotor disc and over time. Typically,

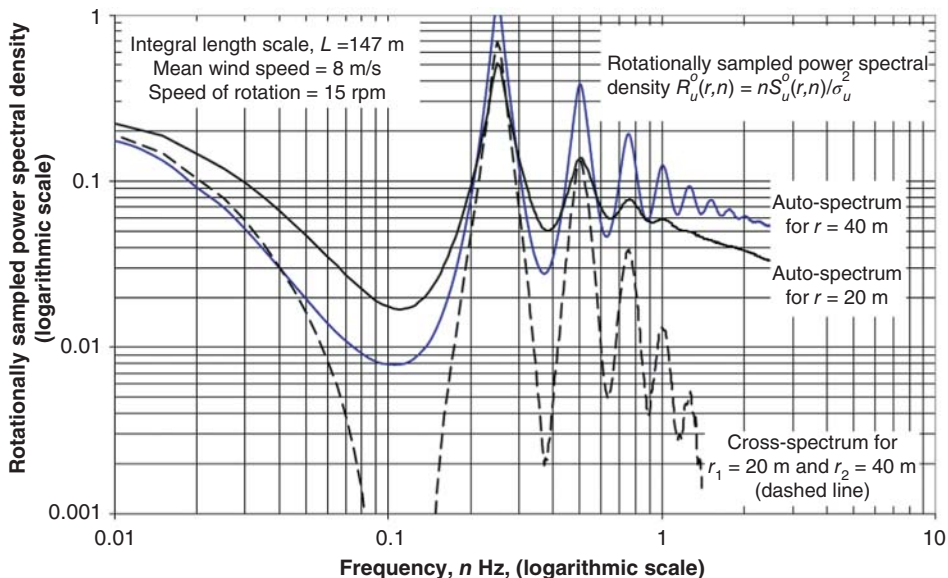


Figure 5.21 Rotationally sampled cross-spectrum of longitudinal wind speed fluctuations at 20 and 40 m radii compared with auto-spectra: log-log plot.

this is obtained by generating simultaneous time histories at points over the rotor disc, which have appropriate statistical properties both individually and in relation to each other. Thus, the power spectrum of each time history should conform to one of the standard power spectra (e.g. von Karman or Kaimal), and the normalised cross-spectrum (otherwise known as the *coherence function*) of the time histories at two different points should equate to the coherence function corresponding to the chosen power spectrum and the distance separating the points. For example, the coherence of the longitudinal component of turbulence corresponding to the Kaimal power spectrum for points j and k separated by a distance Δs_{jk} perpendicular to the wind direction is

$$C_{jk}(n) = C(\Delta s_{jk}, n) = \frac{S_{jk}(n)}{S_u(n)} = \exp\left(-H.\Delta s_{jk} \sqrt{\left(\frac{n}{U}\right)^2 + \left(\frac{0.12}{L}\right)^2}\right) \quad (5.53)$$

The constant H was specified as 8.8 in IEC 61400-1 edition 2 but increased to 12 in editions 3 and 4. The $(0.12/L)$ term is negligible except at frequencies below 0.01 Hz. (Note that coherence is sometimes termed *coherency*, and that some authors define coherence as the *square* of the normalised cross-spectrum.) See Section 2.6.7 for details of the coherence corresponding to the von Karman spectrum.

Three distinct approaches have been developed for generating simulation time histories as follows:

1. The transformational method, based on filtering Gaussian white noise signals.

2. The correlation method, in which the velocity of a small body of air at the end of a timestep is calculated as the sum of a velocity correlated with the velocity at the start of the timestep and a random, uncorrelated increment.
3. The harmonic series method, involving the summation of a series of cosine waves at different frequencies with amplitudes weighted in accordance with the power spectrum.

This last method is probably now the one in widest use, and it is described in more detail below. The description is based on that given in Veers (1988).

Wind simulation by the harmonic series method

The spectral properties of the wind speed fluctuations at N points can be described by a spectral matrix, \mathbf{S} , in which the diagonal terms are the *double-sided* single-point power spectral densities at each point, $S_{kk}(n)$, and the off-diagonal terms are the cross-spectral densities, $S_{jk}(n)$, also double-sided. This matrix is equated to the product of a triangular transformation matrix, \mathbf{H} , and its transpose, \mathbf{H}^T , as follows:

$$\begin{bmatrix} S_{11} & S_{21} & S_{31} & \dots \\ S_{21} & S_{22} & S_{32} & \dots \\ S_{31} & S_{32} & S_{33} & \dots \\ \dots & \dots & \dots & S_{NN} \end{bmatrix} = \begin{bmatrix} H_{11} & & & \\ H_{21} & H_{22} & & \\ H_{31} & H_{32} & H_{33} & \\ \dots & \dots & \dots & H_{NN} \end{bmatrix} \begin{bmatrix} H_{11} & H_{21} & H_{31} & \dots \\ H_{22} & H_{32} & \dots & \\ H_{33} & \dots & & \\ \dots & & & H_{NN} \end{bmatrix}$$

resulting in a set of $N(N+1)/2$ equations linking the elements of the \mathbf{S} matrix to the elements of the \mathbf{H} matrix as follows:

$$S_{11} = H_{11}^2 \quad S_{21} = H_{21} \cdot H_{11} \quad S_{22} = H_{21}^2 + H_{22}^2 \quad S_{31} = H_{31} \cdot H_{11}$$

$$S_{32} = H_{31} \cdot H_{21} + H_{32} \cdot H_{22} \quad S_{33} = H_{31}^2 + H_{32}^2 + H_{33}^2$$

$$S_{jk} = \sum_{l=1}^k H_{jl} \cdot H_{kl} \quad S_{kk} = \sum_{l=1}^k \sqrt{H_{kl}^2} \quad (5.54)$$

As with the elements of the \mathbf{S} matrix, the elements of the \mathbf{H} matrix are all double-sided functions of frequency n .

Noting that the expression for the power spectral density S_{kk} resembles that for the variance of the sum of group of k independent variables, it is apparent that the elements of the \mathbf{H} matrix can be considered as the weighting factors for the linear combination of N independent, unit magnitude, white noise inputs to yield N correlated outputs with the correct spectral matrix. Thus the elements in the j th row of \mathbf{H} are the weighting factors for the inputs contributing to the output at point j . The formula for the linear combination is

$$u_j(n) = \sum_{k=1}^j H_{jk}(n) \cdot \Delta n \cdot \exp(-i\theta_k(n)) \quad (5.55)$$

where $u_j(n)$ is the complex coefficient of the discretised frequency component at n Hz of the simulated wind speed at point j . The frequency bandwidth is Δn . $\theta_k(n)$ is the phase

angle associated with the n Hz frequency component at point k and is a random variable uniformly distributed over the interval $0\text{--}2\pi$.

The values of the weighting factors, H_{jk} , which are $N(N+1)/2$, in number are derived from Eq. (5.54), giving:

$$H_{11} = \sqrt{S_{11}} \quad H_{21} = S_{21}/H_{11} \quad H_{22} = \sqrt{S_{22} - H_{21}^2} \quad H_{31} = S_{31}/H_{11}, \text{etc.} \quad (5.56)$$

Hence

$$u_1(n) = \sqrt{S_{11}(n)} \cdot \Delta n \cdot \exp(-i\theta_1(n))$$

$$u_2(n) = \sqrt{S_{22}(n)} \cdot \Delta n [C_{21}(n) \cdot \exp(-i\theta_1(n)) + \sqrt{1 - C_{21}^2(n)} \cdot \exp(-i\theta_2(n))], \text{etc.} \quad (5.57)$$

where $C_{21}(n)$ is the coherence, defined as $C_{21}(n) = \frac{S_{21}(n)}{\sqrt{S_{11}(n)S_{22}(n)}}$.

Time series for the wind speed fluctuations are obtained by taking the inverse DFT of the coefficients $u_j(n)$ at each point j . Lateral and vertical wind speed fluctuations can also be simulated, if desired, using the same method. As an illustration, examples of time series derived by this method for two points 10 m apart are shown in Figure 5.22, based on the von Karman spectrum. The mean wind speed and integral length scale xL_u in this example are taken as 10 m/s and 73.5 m, respectively, giving an integral time scale, ${}^xL_u/\bar{U}$, of 7.35 seconds.

In his 1988 paper, Veers pointed out that the computation time required can be reduced by arranging for the simulated wind speed to be calculated at each point only at those times when a blade is passing – i.e. at a frequency of $\Omega B/2\pi$, where B is the number of blades. This is achieved by applying a phase shift to each frequency component at each point of $\psi_j \cdot n \cdot 2\pi/\Omega$, where ψ_j is the azimuth angle of point j .

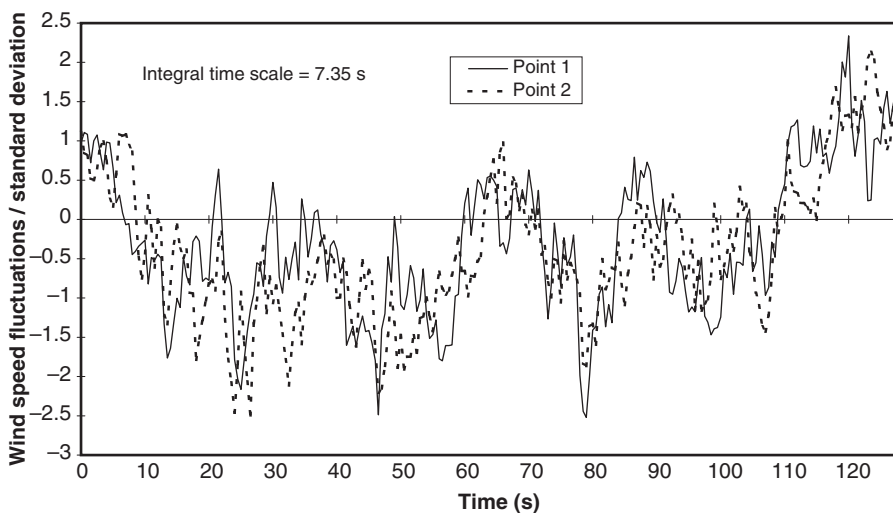


Figure 5.22 Simulated time series of wind speed fluctuations at two points 10 m apart for mean wind speed of 10 m/s.

Blade load time histories

Once the simulated wind speed time histories have been generated across the grid, the calculation of blade load histories at different radii can begin. If the wake is assumed to be ‘frozen’, then the axial induced velocity, $a\bar{U}$, and the tangential induced velocity, $a'\Omega r$, are taken as remaining constant over time, at each radius, at the values calculated for a steady wind speed of \bar{U} . The instantaneous value of the flow angle, ϕ , and, hence, the values of the lift and drag coefficients, may then be calculated directly from the instantaneous value of the wind speed fluctuation (including lateral and vertical components, if calculated) by means of the velocity diagram.

Alternatively, an equilibrium wake may be assumed. In this case, the induced velocities are taken to vary continuously so that the momentum equations are satisfied at each blade element at all times. Obviously, this requires that these equations are solved afresh at each timestep, which is computationally much more demanding.

Neither the equilibrium wake model nor the frozen wake model provides an accurate description of wake behaviour. A better model is provided by unsteady flow theory, which assumes that there is some delay before induced velocities react to changes in the incident wind field. See Section 4.4.

Note that, if desired, the spatial wind variations causing deterministic loading can be included in the simulated wind field, enabling the combined deterministic and stochastic loading on the blade to be calculated in a single operation.

5.7.7 Extreme loads

The derivation of extreme loads should properly take into account dynamic effects, which form the subject of the next section. However, in the interests of clarity, this section will be restricted to the consideration of extreme loads in the absence of dynamic effects.

As described in Section 5.4.1, it was customary for wind turbine design codes to specify extreme operating load cases in terms of deterministic gusts. The extreme blade loadings are then evaluated at intervals over the duration of the gust, using blade element and momentum theory as described in Section 5.7.2.

Although deterministic gusts have the advantage of clarity of definition, they are essentially arbitrary in nature. The alternative approach of employing a stochastic representation of the wind provides a much more realistic description of the wind itself, and it has been adopted to a greater extent in IEC 61400-1 editions 3 and 4. Although stochastic representation of the wind lends itself to analysis in the frequency domain, the solution is inevitably approximate because of the linearity assumptions [Eq. (5.24) et seq], so the standard specifies analysis in the time domain using simulations. Nevertheless, analysis in the frequency domain can provide useful insights in the absence of stall and is considered further in the paragraphs that follow.

Normally the loading under investigation, for example, the blade root bending moment, will contain both periodic and random components. Although it is straightforward to predict the extreme values of each component independently, the prediction of the extreme value of the combined signal is quite involved. Madsen et al. (1984) have proposed the following simple, approximate approach and have demonstrated that it is reasonably accurate.

The periodic component, $z(t)$, is considered as an equivalent three-level square wave, in which the variable takes the maximum, mean (μ_z), and minimum values of the original waveform, for proportions ε_1 , ε_2 , and ε_3 of the wave period, respectively. It is easy to show that

$$\varepsilon_1 = \frac{\sigma_z^2}{(z_{\max} - \mu_z)(z_{\max} - z_{\min})}, \quad \varepsilon_3 = \frac{\sigma_z^2}{(\mu_z - z_{\min})(z_{\max} - z_{\min})} \quad (5.58)$$

Extreme values of the combined signal are only assumed to occur during the proportion of the time, ε_1 , for which the square wave representation of the periodic component is at the maximum value, z_{\max} .

Davenport (1964) gives the following formula for the extreme value of a random variable over a time interval T :

$$\frac{x_{\max}}{\sigma_x} = \sqrt{2 \ln(vT)} + \frac{\gamma}{\sqrt{2 \ln(vT)}} \quad (5.59)$$

where v is the zero up-crossing frequency (i.e. the number of times per second the variable changes from negative to positive) given by Eq. (A5.46) and $\gamma = 0.5772$ (Euler's constant). Thus, the extreme value of the combined periodic and random components is taken to be

$$z_{\max} + x_{\max} = z_{\max} + \sigma_x \left(\sqrt{2 \ln(v\varepsilon_1 T)} + \frac{\gamma}{\sqrt{2 \ln(v\varepsilon_1 T)}} \right) = z_{\max} + g_1 \cdot \sigma_x \quad (5.60)$$

where g_1 is termed the *peak factor*.

The variation of x_{\max}/σ_x with exposure time, T , is shown in Table 5.4 for a zero up-crossing frequency of 1 Hz. The periodic component is assumed to be a simple sinusoid, giving $\varepsilon_1 = 0.25$.

The method for determining the extreme load described above has to be applied with caution when the wind fluctuations exceed the rated wind speed. In the case of a stall-regulated machine, the linearity assumption breaks down completely, invalidating the method. With pitch-regulated machines, however, the blade pitch will respond to wind fluctuations at frequencies below, say, half the rotor rotational frequency to limit power, causing a parallel reduction in blade loading. This will modify the spectrum of blade loading dramatically, effectively removing the frequency components below the pitch system cut-off frequency and consequently reducing the magnitude of σ_x to be substituted in Eq. (5.60).

To illustrate the method, the procedure for calculating the extreme flapwise blade root bending moment of a pitch-regulated machine operating at rated wind speed is described as follows:

Table 5.4 Extreme values of random component for different exposure times.

T	1 min	10 min	1 h	10 h	100 h	1000 h	1 yr
T (secs)	60	600	3600	36 000	360 000	3 600 000	31 536 000
$\varepsilon_1 T$ (secs)	15	150	900	9000	90 000	900 000	7 884 000
x_{\max}/σ_x	2.57	3.35	3.84	4.40	4.90	5.35	5.74

- Eq. (5.48) for the standard deviation of the random component of blade root bending moment is first modified to eliminate the contribution of frequencies below half the rotational speed to account for the blade pitching response, and then discretised to give

$$\sigma_M^2 = \left(\frac{1}{2} \rho \Omega \frac{dC_L}{d\alpha} \right)^2 \sum_{j=1}^m \sum_{k=1}^m \left[\int_{\Omega/2}^{\infty} S_u^o(r_j, r_k, n) dn \right] c(r_j)c(r_k) r_j^2 r_k^2 (\Delta r)^2 \quad (5.61)$$

Here the blade is assumed to be divided up into m sections of equal length $\Delta r = R/m$.

- After evaluation of the integrals of the $m(m+1)/2$ different curtailed rotational spectra, the standard deviation of the blade root bending moment is obtained from Eq. (5.61).
- The time, T , that the machine spends in a wind speed band centred on the rated wind speed is estimated using the Weibull curve and multiplied in turn by the factor ε_1 appropriate to the waveform of the periodic component of blade root bending moment and by the zero up-crossing frequency of the random root bending moment fluctuations, to give the effective number of peaks, $v\varepsilon_1 T$.
- The predicted extreme value of the total moment is calculated by substituting the standard deviation of the blade root bending moment, σ_M ($= \sigma_x$), the effective number of peaks, $v\varepsilon_1 T$, and the extreme value of the periodic moment into Eq. (5.60).

In the case of a machine with a rated wind speed of 13 m/s operating at a site with an annual mean of 7 m/s, the expected proportion of the time spent operating within a 2 m/s wide band centred on the rated wind speed is 5.6%. Taking the machine lifetime as 20 years, a zero up-crossing frequency equal to the rotational speed of 15 rpm (0.25 Hz) and $\varepsilon_1 = 0.25$, this results in a peak factor, g_1 , of 5.5. For the 80 m diameter machine considered in Section 5.7.2, a turbulence intensity of 20%, and a turbulence isotropic length scale of 147 m, the standard deviation of the random component of blade root bending moment given by Eq. (5.60) is 315 kNm, resulting in a peak value of about 1730 KNm. This compares with the extreme value of the periodic component, including wind shear, of about 1830 KNm. It should be emphasised that the peak value of the random component quoted is a theoretical one – i.e. it assumes the linearity assumptions are maintained even for the large wind speed fluctuation needed to generate this moment. In practice, a machine operating in a steady wind speed equal to rated is usually not all that far from stall, so the larger fluctuations may induce stall. In this example, the square root of the weighted mean of the integrals of all of the curtailed rotational spectra is about $0.5\sigma_u$, so the idealised uniform wind speed fluctuation equivalent to the extreme root moment is about $0.20 \times 13 \times 0.5 \times 5.5 = 7.2$ m/s.

The method outlined above has more validity at higher wind speeds, when the blades are pitched back and are operating further away from stall. However, it is important to note that the other linearity assumption used in deriving Eq. (5.26), namely, that ϕ is small, becomes increasingly in error.

It will be now be evident that the calculation of stochastic extreme loads is fraught with difficulties because non-linearities are likely to arise as the extremes are approached. In so far as lift forces ‘saturate’ due to stall, or even drop back, as wind speed increases, a

crude and simple approach to extreme out-of-plane operational loads is to calculate an upper bound based on the maximum lift coefficient for the local aerofoil section and the relative air velocity, W . The induction factors will be small and can be ignored.

The most sophisticated approach, however, is to analyse the loads generated by a simulated wind field. As computing costs normally restrict the length of simulated ‘campaigns’ to a few hundred seconds or less, statistical methods have to be used to extrapolate from the extreme values of loadings calculated during the campaign to the extreme values to be expected over the machine design life.

One method, which is discussed by Thomsen and Madsen (1997), is to use Eq. (5.60) with T set equal to the appropriate exposure period over the machine design life, and values of z_{\max} and σ_x abstracted from the simulation time history with the aid of azimuthal binning to separate the periodic and stochastic components. The danger of this approach with simulations of short duration is that the azimuthal binning process treats some load fluctuations due to the slicing of low frequency gusts as periodic rather than stochastic, so that the standard deviation of the stochastic component, σ_x , is underestimated.

Extrapolation techniques are considered further in Section 5.14.

5.8 Blade dynamic response

5.8.1 Modal analysis

Although dynamic loads on the blades will, in general, also excite the tower dynamics, tower head motion will initially be excluded from consideration to focus on the blade dynamic behaviour itself. The treatment is further limited to the response of blades in unstalled flow because of the inherent difficulty in predicting stalled behaviour.

The equation of motion for a blade element at radius r subject to a time-varying load $q(r,t)$ per unit length in the out-of-plane direction is

$$m(r)\ddot{x} + \hat{c}(r)\dot{x} + \frac{\partial^2}{\partial r^2} \left[EI(r) \frac{\partial^2 x}{\partial r^2} \right] = q(r, t) \quad (5.62)$$

where the terms on the left hand side are the loads on the element due to inertia, damping, and flexural stiffness, respectively. $I(r)$ is the second moment of area of the blade cross-section about the weak principal axis (which for this purpose is assumed to lie in the plane of rotation), and x is the out-of-plane displacement. The expressions $m(r)$ and $\hat{c}(r)$ denote mass per unit length and damping per unit length, respectively.

The dynamic response of a cantilever blade to the fluctuating aerodynamic loads upon it is most conveniently investigated by means of modal analysis, in which the excitations of the various different natural modes of vibration are computed separately and the results superposed, as follows:

$$x(t, r) = \sum_{j=1}^{\infty} f_j(t) \mu_j(r) \quad (5.63)$$

where $\mu_j(r)$ is the j th mode shape, arbitrarily assumed to have a value of unity at the tip, and $f_j(t)$ is the variation of j th mode tip displacement with time. Eq. (5.62) then becomes

$$\sum_{j=1}^{\infty} \left\{ m(r)\mu_j(r)\ddot{f}_j(t) + \hat{c}(r)\mu_j(r)\dot{f}_j(t) + \frac{d^2}{dr^2} \left[EI(r)\frac{d^2\mu_j(r)}{dr^2} \right] f_j(t) \right\} = q(r, t) \quad (5.64)$$

For low levels of damping, the beam natural frequencies are given by

$$m(r)\omega_j^2 \mu_j(r) = \frac{d^2}{dr^2} \left[EI(r)\frac{d^2\mu_j(r)}{dr^2} \right] \quad (5.65)$$

so Eq. (5.64) becomes

$$\sum_{j=1}^{\infty} \left\{ m(r)\mu_j(r)\ddot{f}_j(t) + \hat{c}(r)\mu_j(r)\dot{f}_j(t) + m(r)\omega_j^2 \mu_j(r)f_j(t) \right\} = q(r, t) \quad (5.66)$$

Multiplying both sides by $\mu_i(r)$ and integrating over the length of the blade, R , gives:

$$\begin{aligned} \sum_{j=1}^{\infty} & \left\{ \int_0^R m(r)\mu_i(r)\mu_j(r)\ddot{f}_j(t) dr + \int_0^R \hat{c}(r)\mu_i(r)\mu_j(r)\dot{f}_j(t) dr + \int_0^R m(r)\omega_j^2 \mu_i(r)\mu_j(r)f_j(t) dr \right\} \\ & = \int_0^R \mu_i(r)q(r, t) dr \end{aligned} \quad (5.67)$$

The undamped mode shapes are orthogonal as a result of Bettis's law (Clough and Penzien 1993), so they satisfy the orthogonality condition:

$$\int_0^R m(r)\mu_i(r)\mu_j(r) dr = 0 \quad \text{for } i \neq j \quad (5.68)$$

If we assume that the variation of the damping per unit length along the blade, $\hat{c}(r)$, is proportional to the variation in mass per unit length, $m(r)$, i.e. $\hat{c}(r) = a \cdot m(r)$, then

$$\int_0^R \hat{c}(r)\mu_i(r)\mu_j(r) dr = 0 \quad \text{for } i \neq j \quad (5.69)$$

As a result, all the cross-terms on the left hand side of Eq. (5.67) drop out, and it reduces to

$$m_i \ddot{f}_i(t) + c_i \dot{f}_i(t) + m_i \omega_i^2 f_i(t) = \int_0^R \mu_i(r)q(r, t) dr \quad (5.70)$$

where $m_i = \int_0^R m(r)\mu_i^2(r) dr$ and is known as the *generalised mass*, $c_i = \int_0^R \hat{c}(r)\mu_i^2(r) dr$, and $\int_0^R \mu_i(r)q(r, t) dr = Q_i(t)$ is termed the *generalised fluctuating load* with respect to the i th mode. Eq. (5.70) is the fundamental equation governing modal response to time-varying loading.

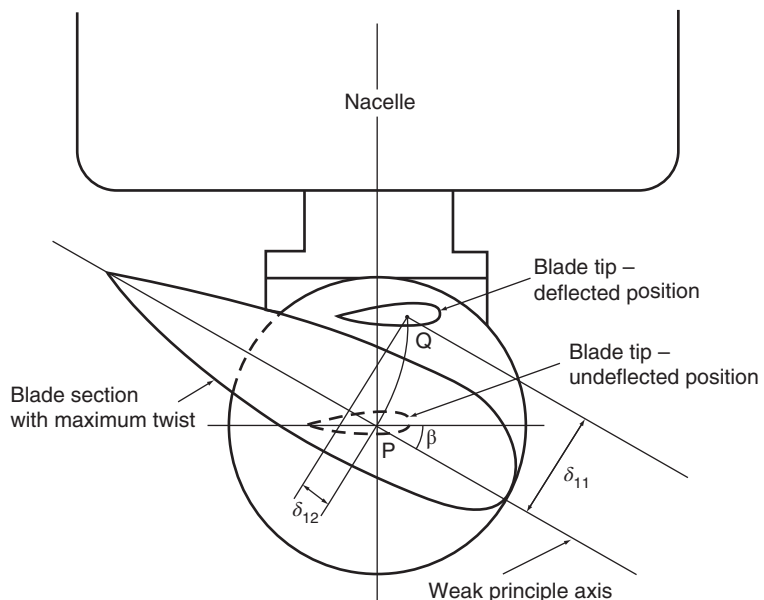


Figure 5.23 Deflection of tip due to flapwise bending of twisted blade (viewed along blade axis).

Blade flexural vibrations occur in both the flapwise and edgewise directions (i.e. about the weak and strong principal axes, respectively). Blades are typically twisted some 15° , so the weak principal axis does not, in general, lie in the plane of rotation as assumed above. Consequently, blade flexure about one principal axis inevitably results in some blade movement perpendicular to the other. This is illustrated in Figure 5.23, in which the maximum blade twist near the root has been exaggerated for clarity. Point P represents the undeflected position of the blade tip, point Q represents the deflected position as a result of flexure about the weak principal axis, and the line between them is built up of the contributions to the tip deflection made by flexure of each element along the blade, $M(R-r)\Delta r/EI$.

The interaction between flexure about the two principal axes can be explored with the help of some simplifying assumptions. If M varies as $(R-r)$ for the first mode and I varies as $(R-r)^2$, then each of the tip deflection contributions referred to above are equal, so that, for a linear twist distribution, the line PQ is the arc of a circle. If the twist varies between zero at the tip and a maximum value of β towards the root, then the tip deflection, δ_{12} , in the direction of the weak principal axis, at the blade section with maximum twist, is $\beta/2$ times the tip deflection, δ_{11} , perpendicular to this axis. Hence in the case of $\beta = 15^{\circ}$, the ratio δ_{12}/δ_{11} approximates to 0.13, with the result that blade first mode flapwise oscillations will result in some relatively small simultaneous edgewise inertia loadings. These will not excite significant edgewise oscillations, because the edgewise first mode natural frequency is typically about double the flapwise one.

It can be seen from the above that the effects of interaction between flapwise and edgewise oscillations are generally minor, so they will not be considered further.

Blades will also be subject to torsional vibrations. In the past, it has generally been possible to ignore these, both because the exciting loads were small and because the high torsional stiffness of a typical hollow blade placed the torsional natural frequencies well above the exciting frequencies. However, with the development of larger, more flexible blades, this is no longer always the case. Blade torsion, which can accompany flapwise bending due to offset of the cross-section centre of mass from the shear centre, for example, may significantly alter the angle of attack in the tip region.

Finally, in the case of a blade hinged at the root, the whole blade will experience oscillations involving rigid body rotation about the hinge. This phenomenon is considered in the ‘Teeter Motion’ section.

5.8.2 Mode shapes and frequencies

The mode shape and frequency of the first mode can be derived by an iterative technique called the *Stodola method* after its originator. Briefly, this consists of assuming a plausible mode shape, calculating the inertia loads associated with it for an arbitrary frequency of one radian per second, and then computing the beam deflected profile resulting from these inertia loads. This profile is then normalised, typically by dividing the deflections by the tip deflection, to obtain the input mode shape for the second iteration. The process is repeated until the mode shape converges. Then, in view of the fact that the inertia loads calculated for the input tip deflection combined with a frequency of 1 rad per second must be the same as those calculated for the output tip deflection combined with the actual frequency, the first mode natural frequency can be obtained from the following formula:

$$\omega_1 = \sqrt{\frac{\text{Tip deflection input to last iteration}}{\text{Tip deflection output from last iteration}}}$$

If the mode shapes are orthogonal, advantage can be taken of this property to simplify the derivation of the mode shapes and frequencies of the higher modes, provided this is carried out in ascending order. A trial mode shape is assumed as before, but before using it to calculate the inertia loadings, it is ‘purified’ so that it does not contain any lower mode content. For example, ‘purification’ of a second mode trial mode shape, $\mu_{2T}(r)$, of first mode content is achieved by subtracting

$$\mu_{2C}(r) = \mu_1(r) \frac{\int_0^R \mu_1(r) \mu_{2T}(r) m(r) dr}{\int_0^R \mu_1^2(r) m(r) dr} = \mu_1(r) \frac{\int_0^R \mu_1(r) \mu_{2T}(r) m(r) dr}{m_1} \quad (5.71)$$

from it. The modified second mode trial mode shape, $\mu_{2M}(r) = \mu_{2T}(r) - \mu_{2C}(r)$, then satisfies the orthogonality condition

$$\int_0^R \mu_1(r) \mu_{2M}(r) m(r) dr = 0$$

After ‘purification’ of the trial mode shape, the Stodola method can be applied exactly as before. Further ‘purification’ before succeeding iterations should not be necessary if the lower mode shapes used for the initial ‘purification’ are accurate enough. See Clough and Penzien (1993) for a rigorous treatment of the method.

The first mode frequency for out-of-plane oscillations of blade SC40 in the absence of centrifugal force is 0.881 Hz, compared with the corresponding frequency for in-plane

oscillations of 1.183 Hz. The relatively small difference between the frequencies stems from the dominant contributions of the spar caps to the respective stiffnesses. In the absence of spar caps, the blade would be much stiffer in edgewise bending than in flapwise bending, and the frequency ratio would approach 2.

5.8.3 Centrifugal stiffening

When a rotating blade deflects either in its plane of rotation or perpendicular to it, the centrifugal force on each blade element exerts a restoring force that has the effect of stiffening the blade and thereby increasing the natural frequency compared with the stationary value. The centrifugal forces act radially outwards perpendicular to the axis of rotation, so in the case of an out-of-plane blade deflection, they are parallel to the undeflected blade axis and act at greater lever arms to the inboard part of the blade than they do in the case of in-plane blade deflection. This is illustrated in Figure 5.24.

In order to take account of the effects of centrifugal loads, the equation of motion for a blade element loaded in the out-of-plane direction is modified by the addition of an additional term to become

$$m(r)\ddot{x} + \hat{c}(r)\dot{x} - \frac{\partial}{\partial r} \left[N(r) \frac{\partial x}{\partial r} \right] + \frac{\partial^2}{\partial r^2} \left[EI \frac{\partial^2 x}{\partial r^2} \right] = q(r, t) \quad (5.72)$$

where the centrifugal force at radius r , $N(r)$, is the summation of the forces acting on each blade element outboard of radius r , that is, $N(r) = \sum_{r=r}^{r=R} m(r)\Omega^2 r \cdot \Delta r$.

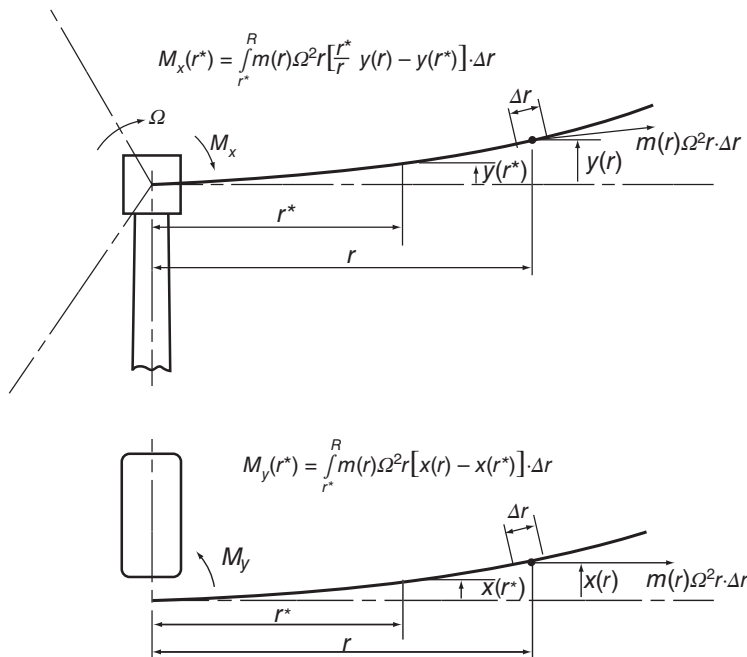


Figure 5.24 Restoring moments due to centrifugal force for in-plane and out-of-plane blade deflections.

The Stodola method for deriving blade mode shapes and frequencies described in the preceding section can be modified to take account of centrifugal effects. In the case of out-of-plane modes, the procedure is as follows:

1. Assume plausible trial mode shape $\mu(r)$.
2. ‘Purify’ trial mode shape of any lower mode content.
3. Assume trial value for frequency, ω_j^2 .
4. Calculate bending moment distribution due to lateral inertia forces according to

$$M_{Y.Lat}(r^*) = \int_{r^*}^R m(r) \omega_j^2 \mu(r) [r - r^*] dr \quad (5.73)$$

5. Calculate bending moment distribution due to centrifugal forces according to

$$M_{Y..CF}(r^*) = - \int_{r^*}^R m(r) \Omega^2 r [\mu(r) - \mu(r^*)] dr \quad (5.74)$$

6. Calculate combined bending moment distribution.
7. Calculate new deflected profile resulting from this bending moment distribution.
8. Calculate revised estimate of natural frequency from

$$\omega'_j = \omega_j \sqrt{\frac{\text{Trial tip deflection}}{\text{Tip deflection calculated for new deflected profile}}}$$

9. Repeat steps 2–8 with revised mode shape and frequency until calculated mode shape converges.

It is important to note that the lateral loads and deflections of a centrifugally loaded beam do not conform to Betti’s theorem, so, as a consequence, the mode shapes are *not* orthogonal. It is for this reason that the ‘purification’ stage has been included in each cycle of iteration. When convergence of the calculated mode shape has occurred, it will be found that it differs significantly from the ‘purified’ mode shape input into each iteration, indicating that a true solution has not been obtained. It is then necessary to use a trial and error approach to modify the magnitudes of the ‘purifying’ corrections applied until the output mode shape and input ‘purified’ mode shape match. A few further iterations will be required until the natural frequency settles down.

A quick estimate of the first mode frequency of a rotating blade can be derived using the Southwell formula for a uniform rotating beam reported by Putter and Manor (1978) as follows:

$$\omega_1 = \sqrt{\omega_{1,0}^2 + \phi_1 \Omega^2} \quad (5.75)$$

in which $\omega_{1,0}$ is the corresponding frequency for the non-rotating blade. The value of ϕ_1 depends on the blade mass and stiffness distribution, and Madsen et al. (1984) suggest the value 1.73 for wind turbine blade out-of-plane oscillations. In the case of blade SC40 rotating at 15 rpm, this yields a percentage increase in first mode frequency due to centrifugal stiffening of 6.7% compared to the correct value of 6.2%. Typically, centrifugal stiffening results in an increase of the first mode frequency for out-of-plane oscillations of between 5% and 10%. For higher modes, the magnitude of the centrifugal forces is less in proportion to the lateral inertia forces, so the percentage increase in frequency due to centrifugal stiffening becomes progressively less.

The procedure for deriving the blade first mode shape and frequency in the case of in-plane oscillations is the same as that described above for out-of-plane vibrations, except that the formula for the bending moment distribution due to the centrifugal forces has to be modified to

$$M_{X,CF}(r^*) = \int_{r^*}^R m(r) \Omega^2 r \left[\frac{r^*}{r} \mu(r) - \mu(r^*) \right] dr \quad (5.76)$$

where $\mu(r)$ is now the trial *in-plane* mode shape.

The smaller lever arms at which the centrifugal loads act in the case of in-plane oscillations (Figure 5.24) means that their effect on the in-plane natural frequency is much less than on the out-of-plane one. In the case of the SC40 blade, the increase in the first mode frequency for in-plane oscillations due to centrifugal force is only 0.8%.

5.8.4 Aerodynamic and structural damping

Blade motion is generally resisted by two forms of viscous damping, aerodynamic and structural, which are considered in turn.

An approximate expression for the aerodynamic damping per unit length in the flapwise direction can be derived by a method analogous to that used in Section 5.7.5 to derive the linear relation:

$$q = \frac{1}{2} \rho \Omega r c(r) \frac{dC_L}{d\alpha} u \quad [\text{see Eq.(5.25)}]$$

between blade load fluctuations per unit length, q , and fluctuations in the incident wind, u . The wind speed fluctuation, u , is simply replaced by the blade flapwise velocity, $-\dot{x}$, giving

$$\hat{c}_a(r) = \frac{q}{-\dot{x}} = \frac{1}{2} \rho \Omega r c(r) \frac{dC_L}{d\alpha} \quad (5.77)$$

The rate of change of lift coefficient with angle of attack, $\frac{dC_L}{d\alpha}$, is constant and equal to 2π before the blade goes into stall but can become negative post-stall, leading to the risk of instability – see Section 7.1.15.

It can be seen that the aerodynamic damping per unit length, $\hat{c}_a(r)$, varies spanwise as the product of radius and blade chord and is therefore not very close to being proportional to the mass per unit length, as is required to satisfy the orthogonality condition. This will result in some aerodynamic coupling of modes, which is not accounted for in normal modal analysis.

The aerodynamic damping ratio for the i th mode is defined as

$$\xi_{ai} = c_{ai}/2m_i\omega_i = \int_0^R \hat{c}_a(r) \mu_i^2(r) dr / 2m_i\omega_i \quad (5.78)$$

Substituting the expression for $\hat{c}_a(r)$ given in Eq. (5.77) leads to

$$\xi_{ai} = \frac{\frac{1}{2} \rho \Omega \frac{dC_L}{d\alpha} \int_0^R r c(r) \mu_i^2(r) dr}{2\omega_i \int_0^R m(r) \mu_i^2(r) dr} \quad (5.79)$$

In the case of fibreglass blade SC40 described in Example 5.1, this yields values of 0.26 and 0.065 for the first and second modes, respectively. These high values are a

consequence of the lightness of the blade in relation to its width in the vicinity of the tip, an area that dominates the integrals thanks to the mode shape weighting. The corresponding first mode logarithmic decrement ($=2\pi\xi_a$) is thus 1.6.

It is evident from Eq. (5.79) that the damping ratio is inversely proportional to blade mass if the natural frequency remains constant. As the adoption of more accurate blade design techniques allows reduced safety factors to be used (see Table 7.10), the trend towards lighter blades will continue, resulting in increased aerodynamic damping ratios.

Structural damping arises from the conversion of mechanical energy to thermal energy during oscillatory motion, as a result of frictional resistance within the flexing material. Denoting the strain energy at peak displacement for the n th cycle as S_n and the loss per cycle as ΔS_n , it can be shown that

$$\frac{\Delta S_n}{S_n} = \frac{2\Delta\sigma_n}{\sigma_n} \quad (5.80)$$

where σ_n is the peak stress for the n th cycle, $\Delta\sigma_n = \sigma_n - \sigma_{n+1}$ and $S_n = \oint \frac{\sigma_n^2}{2E} dr$, with the integral taken over the whole volume of the beam. Hence the logarithmic decrement of damping, defined as the natural logarithm of the ratio of successive peak displacements in the same direction – i.e. as $\ln(\sigma_n/\sigma_{n+1})$ for elastic behaviour – approximates to $\Delta\sigma_n/\sigma_n = 0.5(\Delta S_n/S_n)$.

Test results on fibreglass (see, for example, Gibson et al. 1982) indicate that the energy loss per cycle is unaffected by frequency. However, the percentage energy loss per cycle increases quite rapidly with stress range (Creed 1993), although it is usual to treat it as independent of stress range for analysis purposes.

Values for the structural damping logarithmic decrement, $\delta_s = 2\pi\xi_s$ at the fundamental natural (i.e. first mode) frequency were given in the 1992 edition of Danish Standard DS 472, *Loads and Safety of Wind Turbine Construction*, for several different materials, and these are reproduced in Table 5.5, together with corresponding values from EN 1991-1-4:2005. Equivalent values of the structural damping ratio are also shown. Note that the first mode structural damping ratio for a fibreglass blade is much smaller than the aerodynamic damping ratio for blade SC40 derived above.

Damping ratios for the first and second flapwise modes of the SC40 blade are presented in Table 5.6.

It is seen that the damping ratio for the second mode is less than a third of that for the first.

5.8.5 Response to deterministic loads: step-by-step dynamic analysis

As set out in Section 5.8.1, blade dynamic response to time-varying loading is best analysed in terms of the separate excitation of each blade mode of vibration, for which, under the assumptions of unstalled flow and mass-proportional aerodynamic damping, the governing equation is

$$m_i \ddot{f}_i(t) + c_i \dot{f}_i(t) + m_i \omega_i^2 f_i(t) = \int_0^R \mu_i(r) q(r, t) dr = Q_i(t) \quad [\text{see Eq.(5.70)}]$$

Table 5.5 Values of first mode structural damping logarithmic decrements for different materials.

Standard	DS 472 (1992)	EN 1991-1-4 (2005)	DS 472	EN 1991-1-4
Material	Logarithmic decrement, δ_s	Logarithmic decrement, δ_s	Structural damping ratio, ξ_s	Structural damping ratio, ξ_s
Concrete	0.05	0.03 (towers and chimneys)	0.008	0.005
Steel – welded	0.02	0.012 (chimney)	0.003	0.002
Steel – bolted	0.05	0.03 (high strength bolts) 0.05 (ordinary bolts)	0.008 0.008	0.005 0.008
Glass fibre reinforced plastic	0.05	0.04–0.08 (bridges)	0.008	0.006–0.012
Timber	0.05	0.06–0.12 (bridges)	0.008	0.01–0.02

Table 5.6 SC40 blade damping ratios for first two flapwise modes.

		First mode	Second mode
Natural frequency including centrifugal stiffening		0.94 Hz	2.83 Hz
Structural damping ratio		0.008	0.008
Blade SC40 weighing 7.7 t	Aerodynamic damping ratio	0.26	0.065
	Combined damping ratio	0.27	0.073

where $f_i(t)$ and $\mu_i(r)$ are the tip displacement and mode shape for the i th mode, respectively. Starting with the initial tip displacement, velocity, and acceleration arbitrarily set at zero, this equation can be used to derive values for these quantities at successive timesteps over a complete blade revolution by numerical integration. The procedure is then repeated for several more revolutions until the cyclic blade response to the periodic loading becomes sensibly invariant from one revolution to the next.

Linear acceleration method

The precise form of the equations linking the tip displacement, velocity, and acceleration at the end of a timestep to those at the beginning depends on how the acceleration is assumed to vary over the timestep. Newmark has classified alternative assumptions in terms of a parameter β , which measures the relative weightings placed on the initial and final accelerations in deriving the final displacement. The simplest assumption is that the acceleration takes a constant value equal to the average of the initial and final values ($\beta = 1/4$). Clough and Penzien (1993), however, recommend that the acceleration

is assumed to vary linearly between the initial and final values, as this will be a closer approximation to the actual variation. Step-by-step integration with this assumption is known as either the *linear acceleration method* or the *Newmark $\beta = 1/6$ method*.

Expressions for the tip displacement, velocity, and acceleration at the end of the first timestep – f_{i1} , \dot{f}_{i1} , and \ddot{f}_{i1} , respectively – are derived in terms of the initial values – f_{i0} , \dot{f}_{i0} , and \ddot{f}_{i0} – as follows. The acceleration at time t during the timestep of total duration h is

$$\ddot{f}_i(t) = \ddot{f}_{i0} + \left(\frac{\ddot{f}_{i1} - \ddot{f}_{i0}}{h} \right) t \quad (5.81)$$

This can be integrated to give the velocity at the end of the timestep as

$$\dot{f}_{i1} = \dot{f}_{i0} + \ddot{f}_{i0}h + (\ddot{f}_{i1} - \ddot{f}_{i0})h/2 \quad (5.82)$$

Equation (5.81) can be integrated twice to give an expression for the displacement at the end of the timestep, which, after rearrangement, yields the following expression for the corresponding acceleration:

$$\ddot{f}_{i1} = \frac{6}{h^2}(f_{i1} - f_{i0}) - \frac{6}{h}\dot{f}_{i0} - 2\ddot{f}_{i0} \quad (5.83)$$

Substituting Eq. (5.83) into Eq. (5.82) yields

$$\dot{f}_{i1} = \frac{3}{h}(f_{i1} - f_{i0}) - 2\dot{f}_{i0} - \ddot{f}_{i0}h/2 \quad (5.84)$$

Eq. (5.70) can be written as

$$m_i \ddot{f}_{in} + c_i \dot{f}_{in} + m_i \omega_i^2 f_{in} = \int_0^R \mu_i(r) q_n(r) dr = Q_{in} \quad (5.85)$$

where the suffix n refers to the state at the end of the n th timestep. Substituting Eqs. (5.83) and (5.84) into Eq. (5.85) with $n = 1$ and collecting terms yields the displacement at the end of the first timestep as follows:

$$f_{i1} = \frac{Q_{i1} + m_i \left(\frac{6}{h^2} f_{i0} + \frac{6}{h} \dot{f}_{i0} + 2\ddot{f}_{i0} \right) + c_i \left(\frac{3}{h} f_{i0} + 2\dot{f}_{i0} + \frac{h}{2} \ddot{f}_{i0} \right)}{m_i \omega_i^2 + \frac{3c_i}{h} + \frac{6m_i}{h^2}} \quad (5.86)$$

The velocity and acceleration at the end of the first timestep are then obtained by substituting f_{i1} in Eqs. (5.84) and (5.85), respectively.

The full procedure for obtaining the blade dynamic response to a periodic loading using the Newmark $\beta = 1/6$ method (which is just one of many available) may be summarised as follows:

1. Calculate the blade mode shapes, $\mu_i(r)$.
2. Select the number of timesteps, N , per complete revolution. Then the timestep, $h = 2\pi / N\Omega$.
3. Calculate the blade element loads, $q(r, \psi_n) = q_n(r)$, at blade azimuth positions corresponding to each timestep (i.e. at $2\pi/N$ intervals) using momentum theory. (Here, the suffix n denotes the number of the timestep.)

4. Calculate the generalised load with respect to each mode, $Q_{in} = \int_0^R \mu_i(r)q_n(r)dr$ for each timestep.
5. Assume initial values of blade tip displacement, velocity, and acceleration.
6. Calculate first mode blade tip displacement, velocity, and acceleration at end of first timestep, using Eqs. (5.86), (5.84), and (5.83), respectively (with $i = 1$).
7. Repeat stage 6 for each successive timestep over several revolutions until convergence achieved.
8. Calculate cyclic blade moment variation at radii of interest by multiplying the cyclic tip displacement variation by appropriate factors derived from the modal analysis.
9. Repeat stages 6–8 for higher modes.
10. Combine the responses from different modes to obtain the total response.

Figure 5.25 shows some results of the application of the above procedure to the derivation of the out-of-plane root bending moment response of a 40 m radius blade to tower shadow loading on a stall-regulated machine. The blade is similar to blade SC40 but has a reduced first mode damping ratio of 0.17. The case chosen is for a mean wind speed of 12 m/s, uniform across the rotor disc, and an x/D ratio of 1 (where x is the distance between the blade and the tower centreline, and D is the tower diameter), giving a maximum reduction in the blade root bending moment for a rigid blade of 600 KNm (see Figure 5.26). Centrifugal stiffening is included in the derivation of the mode shapes and frequencies. It is evident from Figure 5.25 that the tower shadow gives the blade a sharp ‘kick’ away from the tower, but the duration is too short in relation to the duration of the first mode half cycle for the blade to ‘feel’ the root bending moment reduction that would be experienced by a completely rigid blade. The blade oscillations have largely died away after a complete revolution because of aerodynamic damping.

The response of the blade out-of-plane root bending moment to tower shadow combined with wind shear is shown in Figure 5.26 for a hub-height wind speed of 12 m/s. Also plotted is the corresponding bending moment for a completely rigid blade.

The wind shear loading is approximately sinusoidal (see Figure 5.11), and, consequently, the response is also. However, it is worth noting that the amplitude of the dominating first mode response to wind shear is the result of two effects working against each other – in other words, the increase due to the dynamic magnification factor of about 9% is largely cancelled out by the reduction due to centrifugal stiffening.

Avoidance of resonance: the Campbell diagram

In the course of blade design, it is important to avoid the occurrence of a resonant condition, in which a blade natural frequency equates to the rotational frequency or a harmonic with a significant forcing load. This is often done with the aid of a Campbell diagram, in which the blade natural frequencies are plotted out against rotational frequency together with rays from the origin representing integer multiples of the rotational frequency. Then any intersections of the rays with a blade natural frequency over

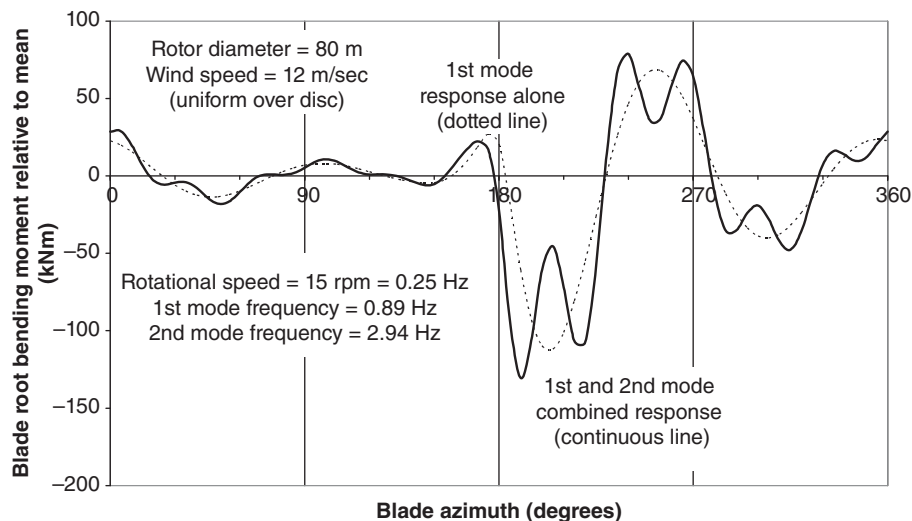


Figure 5.25 Blade out-of-plane root bending moment dynamic response to tower shadow.

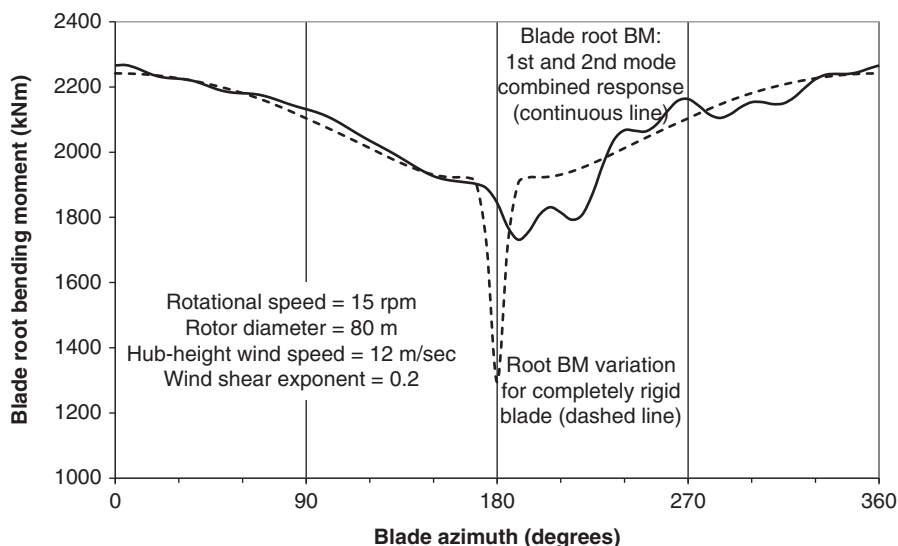


Figure 5.26 Blade out-of-plane root bending moment dynamic response to tower shadow and wind shear.

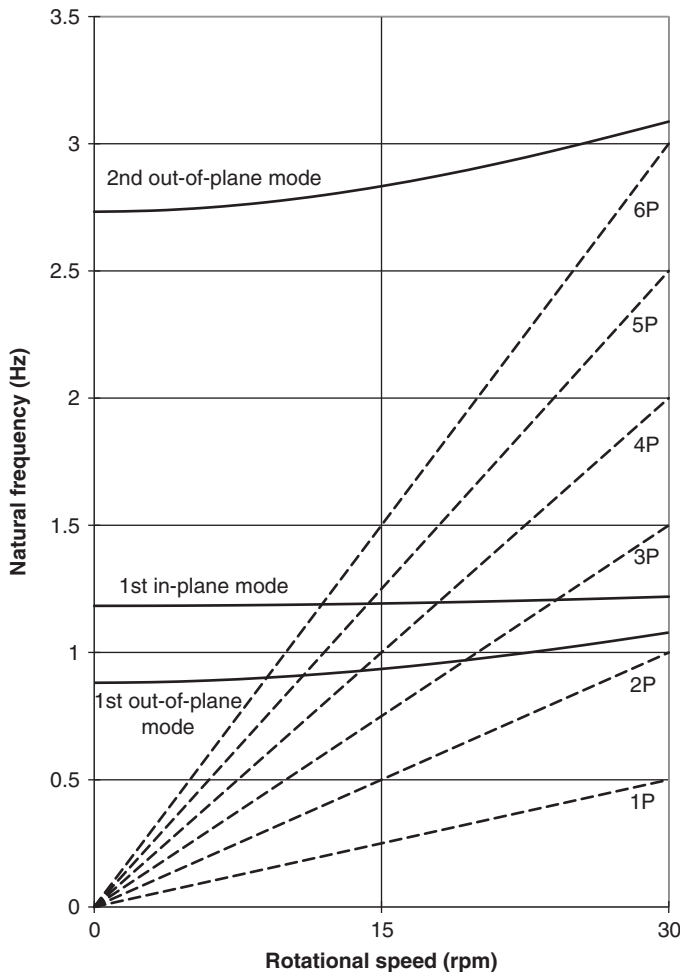


Figure 5.27 Campbell diagram for blade SC40.

the turbine rotational speed operating range represent possible resonances. An example of a Campbell diagram is shown in Figure 5.27.

Clearly blade periodic loading is dominated by the loading at rotational frequency from wind shear, yawed flow, and shaft tilt (Section 5.7.2), gravity (Section 5.7.3), and gust slicing (Section 5.7.5). However, the short-lived load relief resulting from tower shadow will be dominated by higher harmonics.

5.8.6 Response to stochastic loads

The analysis of stochastic loads in the frequency domain has already been described in Section 5.7.5 for a rigid blade, and this will now be extended to cover the dynamic response of the different vibration modes of a flexible blade using the governing equation,

Eq. (5.70). Note that the restriction to an unstalled blade operating at a relatively high tip speed ratio still applies.

Power spectrum of generalised blade loading

The generalised fluctuating load with respect to the i th mode is $Q_i = \int_0^R \mu_i(r) q(r) dr$, where

$$q(r) = \frac{1}{2} \rho \Omega \frac{dC_L}{d\alpha} u(r, t) c(r) r \quad [\text{see Eq.(5.25)}]$$

Hence

$$Q_i = \frac{1}{2} \rho \Omega \frac{dC_L}{d\alpha} \int_0^R \mu_i(r) u(r, t) c(r) r dr \quad (5.87)$$

An expression for the standard deviation of Q_i , σ_{Q_i} , can be derived by a method analogous to that given in Section A5.4 of Appendix A for a non-rotating blade, yielding

$$\sigma_{Q_i}^2 = \left(\frac{1}{2} \rho \Omega \frac{dC_L}{d\alpha} \right)^2 \int_0^R \int_0^R \left[\int_0^\infty S_u^o(r_1, r_2, n) dn \right] \mu_i(r_1) \mu_i(r_2) c(r_1) c(r_2) r_1 r_2 dr_1 dr_2 \quad (5.88)$$

Here $S_u^o(r_1, r_2, n)$ is the rotationally sampled cross-spectrum for a pair of points on the rotating blade at radii r_1 and r_2 . Eq. (5.88) is parallel to Eq. (A5.16) in Appendix A5 with r and r' replaced by r_1 and r_2 and $(\rho \bar{U} C_F)^2$ replaced by $\left(\frac{1}{2} \rho \Omega \frac{dC_L}{d\alpha} \right)^2$. From this it can be deduced that the power spectrum of the generalised load with respect to the i th mode is

$$S_{Q_i}(n) = \left(\frac{1}{2} \rho \Omega \frac{dC_L}{d\alpha} \right)^2 \int_0^R \int_0^R S_u^o(r_1, r_2, n) \mu_i(r_1) \mu_i(r_2) c(r_1) c(r_2) r_1 r_2 dr_1 dr_2 \quad (5.89)$$

In practice, this expression is evaluated using summations to approximate to the integrals.

Power spectrum of tip deflection

The expression for the amplitude of the i th mode blade tip response to excitation by a harmonically varying generalised load is given by Eq. (A5.4) in Appendix A5. Hence the power spectrum of the tip displacement is related to the power spectrum of the generalised load by

$$S_{xi}(n) = \frac{S_{Q_i}(n)}{k_i^2} \frac{1}{[(1 - n^2/n_i^2)^2 + 4\xi_i^2 n^2/n_i^2]} \quad (5.90)$$

This can be written $S_{xi}(n) = \frac{S_{Q_i}(n)}{k_i^2} [DMR]^2$, where DMR stands for the dynamic magnification ratio. n_i is the i th mode natural frequency in Hz.

Figure 5.28 shows the power spectrum of first mode tip deflection, $S_{x1}(n)$, for blade SC40 operating at 15 rpm in a mean wind of 8 m/s. The turbulence intensity has been arbitrarily set at 12.5%, so that $\sigma_u = 1$ m/s. Also shown is the first mode tip deflection spectrum ignoring dynamic magnification, $S_{Q1}(n)/k_1^2$, which, when multiplied by the square of the dynamic magnification ratio (also plotted), yields the $S_{x1}(n)$ curve. The standard deviation of first mode tip deflection, $\sigma_{x1} = \int_0^\infty S_{x1}(n) dn$, comes to 122 mm. This is only 5%

larger than the value without dynamic magnification, reflecting the large damping ratio and the large separation between the rotational and first out-of-plane vibration mode frequencies.

Power spectrum of blade root bending moment

If the amplitude of tip deflection due to excitation of the blade resonant frequency is defined as $x_R(n_1)$, the amplitude of the corresponding blade root bending moment, $M_Y(n_1)$ is given by

$$M_Y(n_1) = \omega_1^2 x_R(n_1) \int_0^R m(r) \mu_1(r) r dr \quad (5.91a)$$

Noting that $\omega_1^2 = k_1/m_1$, this becomes

$$\frac{M_Y(n_1)}{x_R(n_1)} = k_1 R \frac{\int_0^R m(r) \mu_1(r) (r/R) dr}{m_1} = k_1 R \chi_{M1} \quad (5.91b)$$

This relationship applies at all exciting frequencies, because the right hand side is essentially a function of mode shape. Hence the power spectrum of blade root bending moment due to excitation of the first mode is given by

$$S_{My1}(n) = (k_1 R \chi_{M1})^2 S_{x1}(n) = (R \chi_{M1})^2 S_{Q1}(n) \cdot \frac{1}{[(1 - n^2/n_1^2)^2 + 4\xi_1^2 n^2/n_1^2]} \quad (5.91c)$$

For blade SC40, the ratio χ_{M1} takes a value of 1.41.

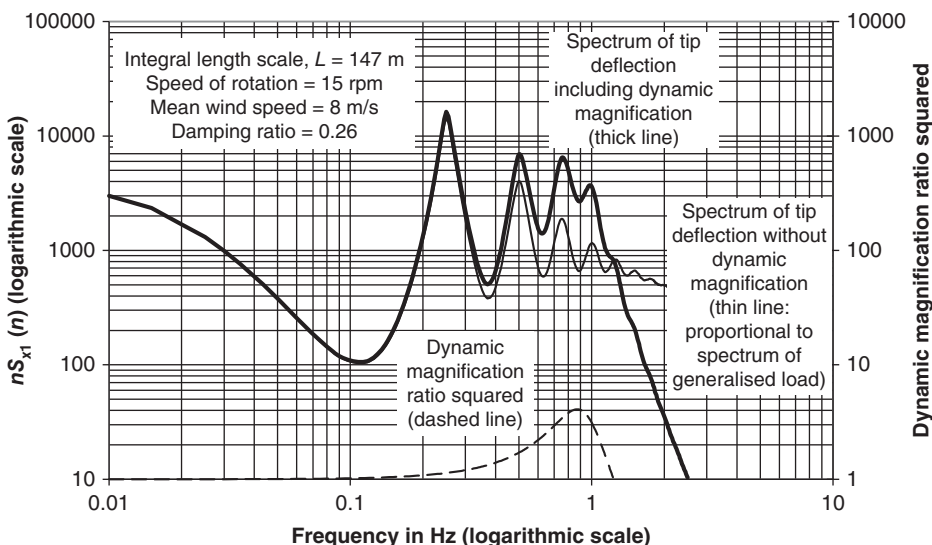


Figure 5.28 Power spectrum of blade SC40 first out-of-plane mode tip deflection.

5.8.7 Response to simulated loads

The blade dynamic response to time-varying loading derived from wind simulation (Section 5.7.6) can be obtained by a step-by-step dynamic analysis such as that described for use with deterministic loads in Section 5.8.5. The procedure is essentially the same, except that it is more important to select realistic values for the initial blade tip displacement, velocity, and acceleration, unless the results from the first few rotation cycles are to be discarded.

5.8.8 Teeter motion

When the rotor is rigidly mounted on the shaft, out-of-plane aerodynamic loads on the blades result in fluctuating bending moments in the low-speed shaft additional to those due to gravity. In the case of two bladed machines, the transfer of blade out-of-plane aerodynamic moments to the shaft can be eliminated and blade root bending moments reduced by mounting the rotor on a hinge with its axis perpendicular to both the low-speed shaft and the axis of the rotor. This allows the rotor to teeter to and fro in response to differential aerodynamic loads on each blade.

The restoring moment acting on a rotor rotating at a constant teeter angle is generated by the lateral components of the centrifugal force acting on each blade element (see Figure 5.29). For small teeter angles – up to, say 5 degrees – it may be approximated by

$$M_R = \int_0^R r.m(r)\Omega^2 r.\zeta .dr = I\Omega^2 \zeta \quad (5.92)$$

where ζ is the teeter angle, Ω is the rotational speed and I is the rotor moment of inertia about its centre. The equation of motion for small free teeter oscillations thus becomes $I\ddot{\zeta} + I\Omega^2 \zeta = 0$ (omitting the aerodynamic damping term for the moment), indicating that the natural frequency of the teeter motion with the teeter hinge perpendicular to the rotor axis is equal to the rotational frequency. Because both the deterministic and stochastic components of the exciting moment are dominated by this frequency, it is clear that the system operates at resonance, with aerodynamic damping alone controlling the magnitude of the teeter excursion. In the absence of stochastic wind loads, a teetering rotor can be thought of as rotating in a fixed plane at an angle ζ_0 to the plane perpendicular to the shaft axis (with ζ_0 equal to the maximum teeter angle), because the teetering frequency is equal to the rotational frequency.

The magnitude of teeter excursions would clearly be reduced if the teeter natural frequency were moved away from the rotational frequency. This can be done by rotating the teeter hinge axis relative to the rotor in the plane of rotation, as illustrated in Figure 5.29, so that teeter motion results in a change of blade pitch – positive in one blade and negative in the other – known as *Delta 3 coupling*. Consider the case of blade A slicing through a gust. The increased thrust on the blade will cause it to move in the downwind direction, by rotating about the teeter hinge. If the teeter angle, defined as the rotation of the blade in its own radial plane, is ζ , then the increase in blade A's pitch angle will be $\zeta \tan \delta_3$, where δ_3 is as defined in Figure 5.29. The increase in the pitch angle of blade A will reduce the angle of attack, α , and thereby reduce the thrust loading on it. The net result of this and a simultaneous increase in the thrust loading on blade B is to introduce an additional restoring moment which will further help to reduce the teeter motion.

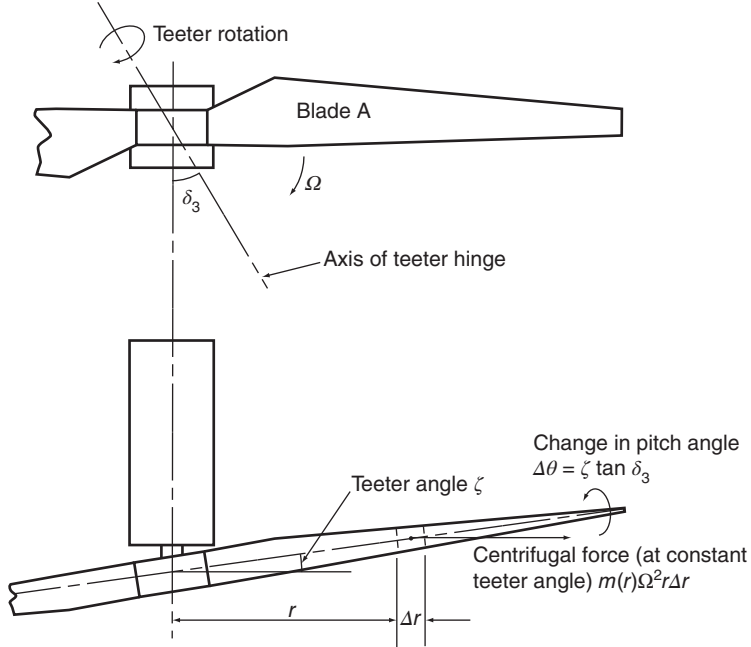


Figure 5.29 Teeter geometry.

The first stage for the exploration of teeter response to different loadings is the derivation of the complete equation of motion. It is assumed that the blades are unstalled and are operating at a relatively high tip speed, so that the linear relations adopted in the derivation of Eq. (5.25) in Section 5.7.5 can be retained. The various contributions to the change in the aerodynamic force on a blade element relative to the steady state situation are, therefore,

$$\frac{1}{2}\rho\Omega rc \frac{dC_L}{d\alpha} (u - \dot{\zeta}r) - \frac{1}{2}\rho(\Omega r)^2 c \frac{dC_L}{d\alpha} \cdot \Delta\theta \quad (5.93)$$

where the three terms result from the fluctuation of the incident wind, teeter motion, and Delta 3 coupling, respectively. Multiplication of these terms by radius, integration over the length of the blade, and addition of the centrifugal and inertia hub moment terms yields the following equation of motion for the teeter response:

$$\begin{aligned}
 & I\ddot{\zeta} + \frac{1}{2}\rho\Omega \frac{dC_L}{d\alpha} \left[2 \int_0^R r^3 c(r) dr \right] \dot{\zeta} + \frac{1}{2}\rho\Omega \frac{dC_L}{d\alpha} \left[2 \int_0^R r^3 c(r) dr \right] \Omega \tan \delta_3 \zeta + I\Omega^2 \zeta \\
 &= \frac{1}{2}\rho\Omega \frac{dC_L}{d\alpha} \int_{-R}^R u(r, t) c(r) \cdot r \cdot |r| dr
 \end{aligned} \quad (5.94)$$

assuming a frozen wake. By dividing through by the moment of inertia and writing

$$\eta = \frac{1}{2} \frac{\rho}{I} \frac{dC_L}{d\alpha} \left[2 \int_0^R r^3 c(r) dr \right] \quad (5.95)$$

this can be simplified to

$$\ddot{\zeta} + \eta \Omega \dot{\zeta} + (1 + \eta \tan \delta_3) \Omega^2 \zeta = \frac{1}{2} \rho \frac{\Omega}{I} \frac{dC_L}{d\alpha} \int_{-R}^R u(r, t) c(r) r |r| dr \quad (5.96)$$

η is a measure of the ratio of aerodynamic to inertial forces acting on the blade and is one eighth of the Lock number.

Delta 3 coupling thus raises the natural frequency, ω_n , of the teeter motion from Ω to $\Omega \sqrt{1 + \eta \tan \delta_3}$. In the case of an 80 m diameter rotor consisting of two SC40 blades, the rotor inertia about the hub centre comes to about 5980 Tm^2 , giving $\eta = 1.46$. When the rotor is mounted on a teeter hinge set at a δ_3 angle of 30° , $\tan \delta_3 = 0.577$, so the increase in natural frequency due to the δ_3 angle is 36%. The corresponding damping ratio, given by $\xi = \frac{\eta}{2\sqrt{1 + \eta \tan \delta_3}}$, is quite high at 0.54.

Teeter response to deterministic loads

The teeter response to deterministic loads can be found using the same step-by-step integration procedure set out in Section 5.8.5. However, as the loadings due to wind shear and yaw are both approximately sinusoidal, an estimate of the maximum teeter angle for these cases may be obtained by using the standard solution for forced oscillations. For a harmonically varying teeter moment, $M_T = M_{TO} \cos \Omega t$ due to wind shear, the teeter angle is given by

$$\zeta = \frac{M_{TO}}{I \omega_n^2} \frac{\cos(\Omega t - \vartheta)}{\sqrt{(1 - (\Omega/\omega_n)^2)^2 + (2\xi\Omega/\omega_n)^2}} \quad (5.97a)$$

where $\vartheta = \tan^{-1} \left(\frac{2\xi\Omega/\omega_n}{1 - (\Omega/\omega_n)^2} \right) = 90^\circ - \delta_3$ is the phase lag with respect to the excitation. This reduces to

$$\zeta = \frac{M_{TO}}{\Omega^2 \rho \frac{dC_L}{d\alpha} \int_0^R r^3 c(r) dr} \frac{\cos(\Omega t - \vartheta)}{\sqrt{1 + \tan^2 \delta_3}} \quad (5.97b)$$

which is independent of rotor inertia.

For the two bladed turbine described above, rotating at 15 rpm in a wind with a hub-height mean of 10 m/s and a shear exponent of 0.2, the teeter moment amplitude, M_o , is approximately 430 KNm (see Figure 5.11a, which gives the blade root bending moment variation with azimuth for a fixed hub machine, based on momentum theory). For the teetering rotor with two SC40 blades considered above, $\omega_n = 1.36\pi/2 \text{ rad/sec}$, the maximum teeter angle comes to 0.99° for $\delta_3 = 30^\circ$. This increases to 1.15° if the δ_3 angle is reduced to zero.

If the wind speed variation due to wind shear experienced by a vertical blade is assumed to be linear with height, i.e. $u = \bar{U}(kr/R)$, and the teeter moment is calculated from the expression on the right hand side of Eq. (5.94), which assumes a frozen wake instead of the equilibrium wake resulting from momentum theory, a very simple expression for the teeter angle results in the case of zero δ_3 angle. The teeter moment becomes

$$M_T = M_{TO} \cdot \cos \Omega t = \frac{1}{2} \rho \Omega \frac{dC_L}{d\alpha} \frac{\bar{U}k}{R} \int_{-R}^R c(r) r^3 dr \cdot \cos \Omega t \quad (5.98)$$

Substitution of Eq. (5.98) in Eq. (5.97a), with ω_n set equal to Ω for the case of a zero δ_3 angle results in the following expression for the teeter angle:

$$\zeta = \frac{\bar{U}k}{\Omega R} \cos(\Omega t - (\pi/2)) \quad (5.99)$$

Thus, the magnitude of the teeter excursion is simply equal to the velocity gradient divided by the rotational speed. For a hub height of 60 m, the equivalent uniform velocity gradient over the rotor disc for the case above is $0.152\bar{U}/R = 0.0381$ m/s per metre, giving a teeter excursion of 0.024 rad or 1.39° . This differs from the earlier value of 1.15° because of the frozen wake assumption.

Teeter response to stochastic loads

As usual, it is convenient to analyse the response to the stochastic loads in the frequency domain. The teeter moment providing excitation is given by the right hand side of Eq. (5.94). By following a similar method to that used for the generalised load in Section 5.8.6, the following expression for the power spectrum of the teeter moment can be derived:

$$S_{MT}(n) = \left(\frac{1}{2} \rho \Omega \frac{dC_L}{d\alpha} \right)^2 \int_{-R}^R \int_{-R}^R S_u^o(r_1, r_2, n) c(r_1) c(r_2) r_1 r_2 |r_1||r_2| dr_1 dr_2 \quad (5.100)$$

where $S_u^o(r_1, r_2, n)$ is the rotationally sampled cross-spectrum. In practice, $S_u^o(r_1, r_2, n)$ is evaluated for a few discrete radius values and the integrals replaced by summations.

The power spectrum of the teeter angle response is related to the teeter moment power spectrum by a formula analogous to Eq. (5.90), as follows:

$$S_\zeta(n) = \frac{S_{MT}(n)}{(I\omega_n^2)^2} \frac{1}{[(1 - (2\pi n/\omega_n)^2)^2 + (2\xi \cdot 2\pi n/\omega_n)^2]} \quad (5.101)$$

This can be written $S_\zeta(n) = \frac{S_{MT}(n)}{(I\omega_n^2)^2} [DMR]^2$ where DMR stands for the dynamic magnification ratio.

Figure 5.30 shows the teeter angle power spectrum, $S_\zeta(n)$, for a two bladed rotor with SC40 blades and zero δ_3 angle operating at 15 rpm in a mean wind of 8 m/s. The turbulence intensity is taken as 20.3%, for a Class B site, and the damping ratio, $\xi = \eta/2$, is 0.731, calculated from Eq. (5.95). Also shown in the figure is the teeter angle power spectrum ignoring dynamic magnification, $S_{MT}(n)/(I\omega_n^2)^2$, which, when multiplied by

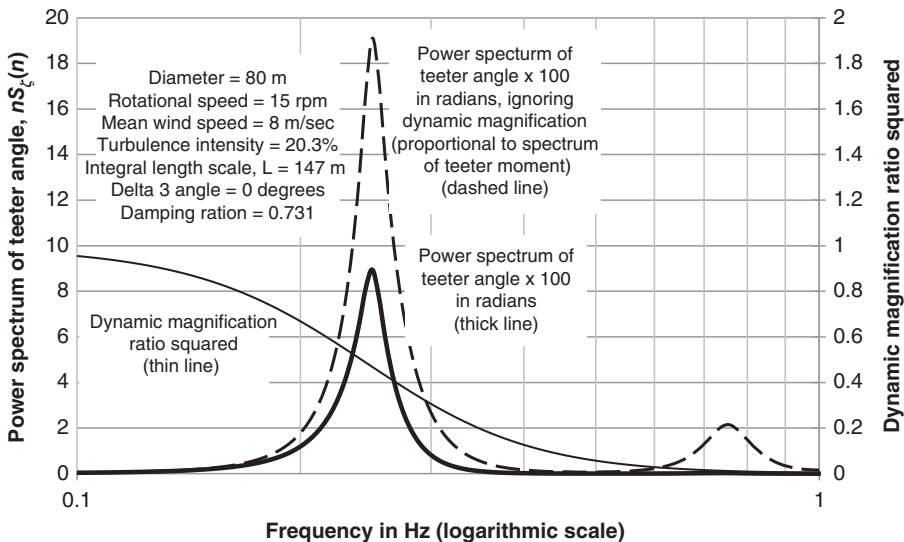


Figure 5.30 Teeter angle power spectrum for two bladed rotor with SC40 blades.

the square of the dynamic magnification ratio (also plotted), yields the $S_\xi(n)$ curve. Note that the high damping ratio means that the dynamic magnification ratio is less than unity across the whole frequency range. The resulting teeter angle standard deviation, obtained by taking the square root of the area under the power spectrum, is 0.77° .

Having calculated the teeter angle standard deviation, the extreme value over any desired exposure period can be predicted from Eq. (5.59). As is evident from Figure 5.30, the teeter angle power spectrum is all concentrated about the rotational frequency, Ω , so the zero up-crossing frequency, v , can be set equal to it. Thus, for a machine operating at 15 rpm, a 1 hour exposure period gives $vT = 900$ and $\zeta_{\max}/\sigma_\xi = 3.84$. The predicted maximum teeter angle due to stochastic loading over a 1 hour period for the case above is thus $3.84 \times 0.77^\circ = 3.0^\circ$. This reduces to 2.6° if a δ_3 angle of 30° is introduced.

As already mentioned, teetering relieves blade root bending moments as well as those in the low-speed shaft. The reduction of the stochastic component of root bending moment can be derived in terms of the standard deviations of blade root bending moment and hub teeter moment for a rigid hub two blade machine. Integration of Eq. (5.100) yields the following expression for the latter:

$$\sigma_{MT}^2 = \left(\frac{1}{2} \rho \Omega \frac{dC_L}{d\alpha} \right)^2 \int_{-R}^R \int_{-R}^R \kappa_u^o(r_1, r_2, 0) c(r_1) c(r_2) r_1 r_2 |r_1| |r_2| dr_1 dr_2 \quad (5.102a)$$

where, for convenience of notation, r_1 and r_2 take *negative* values on the second blade. $\kappa_u^o(r_1, r_2, 0)$ is the cross-correlation function between the longitudinal wind fluctuations between points at radii r_1 and r_2 on the rotating rotor and is given by the right hand side of Eq. (5.51), with $\Omega\tau$ set equal to zero when r_1 and r_2 define points on the same blade and replaced by π when r_1 and r_2 define points on different blades. Defining $\rho_u^o(r_1, r_2, 0)$ as the normalised cross-correlation function, $\kappa_u^o(r_1, r_2, 0)/\sigma_u^2$, Eq. (5.102a) can be rewritten

as

$$\sigma_{MT}^2 = \sigma_u^2 \left(\frac{1}{2} \rho \Omega \frac{dC_L}{d\alpha} \right)^2 \int_{-R}^R \int_{-R}^R \rho_u^o(r_1, r_2, 0) c(r_1) c(r_2) r_1 r_2 |r_1| |r_2| dr_1 dr_2 \quad (5.102b)$$

The corresponding expression for the standard deviation of the mean of the two blade root bending moments is

$$\sigma_M^2 = \frac{1}{4} \sigma_u^2 \left(\frac{1}{2} \rho \Omega \frac{dC_L}{d\alpha} \right)^2 \int_{-R}^R \int_{-R}^R \rho_u^o(r_1, r_2, 0) c(r_1) c(r_2) r_1^2 r_2^2 dr_1 dr_2 \quad (5.103)$$

By inspection of the integrals, it is easily shown that

$$\frac{1}{4} \sigma_{MT}^2 + \sigma_M^2 = \sigma_u^2 \left(\frac{1}{2} \rho \Omega \frac{dC_L}{d\alpha} \right)^2 \int_0^R \int_0^R \rho_u^o(r_1, r_2, 0) c(r_1) c(r_2) r_1^2 r_2^2 dr_1 dr_2 = \sigma_M^2 \quad (5.104)$$

where σ_M is the standard deviation of root bending moment for a rigidly mounted blade. Thus, if the rotor is allowed to teeter, the standard deviation of the blade root bending moment will drop from σ_M to σ_M where σ_M is given by the equation above. The extent of the reduction is driven primarily by the ratio of rotor diameter to the integral length scale of the wind turbulence. For a two bladed rotor with SC40 blades and an integral length scale of 147 m, the reduction is 11%.

5.8.9 Tower coupling

In the preceding sections, consideration of the dynamic behaviour of the blade has been based on the assumption that the nacelle is fixed in space – i.e. that the tower is rigid. In practice, of course, no tower is completely rigid, so fluctuating loads on the rotor will result in fore-aft flexure of the tower, which, in turn, will affect the blade dynamics. This section explores the effect the coupling of the blade and tower motion has on blade response.

The application of standard modal analysis techniques to the dynamic behaviour of the system comprising the tower and rotating rotor treated as a single entity is complicated by the system's continually changing geometry, which means that the mode shapes and frequencies of the structure taken as a whole would have to be re-evaluated at each succeeding rotor azimuth position.

An alternative approach is to base the analysis on the mode shapes and frequencies of the different elements of the structure considered separately, with the displacements arising from each set of modes superposed. Thus, the tower modes are calculated on the basis of a completely rigid rotor, and the blade modes are calculated as if the blades were cantilevered from a rigidly mounted shaft – i.e. in the same way as before. The blade modes are not orthogonal to the tower modes, so the equations of motion for the different modes are no longer independent of each other but contain coupled terms. Furthermore, the blade deflections arising from excitation of the tower modes vary with blade azimuth, so a step-by-step solution is required. The treatment that follows is limited to the fundamental blade and tower modes but could be extended to encompass higher modes.

The equation of motion of the blade is given by Eq. (5.62). The blade deflection for blade J may be written as

$$x(r, t) = \mu(r) f_J(t) + \mu_{TJ}(r) f_T(t) \quad (5.105)$$

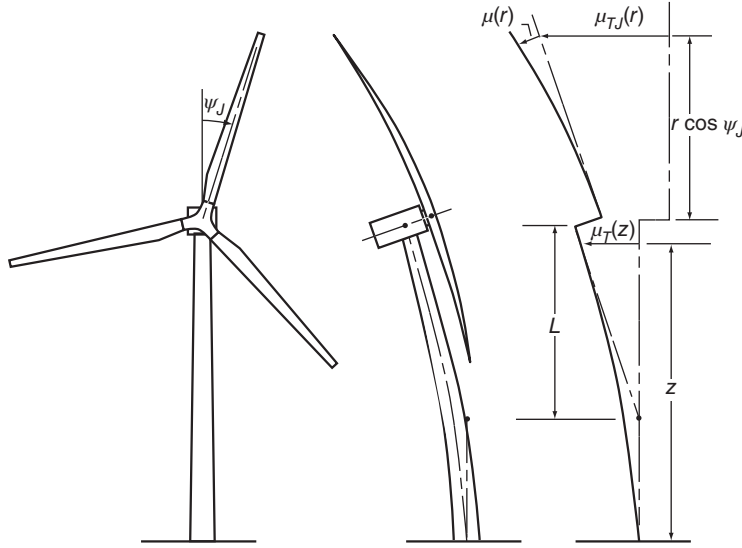


Figure 5.31 Fundamental mode shapes of blade and tower.

where $\mu(r)$ is the first blade mode shape for a rigid tower, and $\mu_{TJ}(r)$ is the normalised rigid body deflection of blade J resulting from excitation of the tower first mode. Assuming the normalisation is carried out with respect to hub deflection,

$$\mu_{TJ}(r) = 1 + \frac{r}{L} \cos \psi_J \quad (5.106)$$

where L is the depth below the hub of the intercept between the tangent to the top of the deflected tower and the undeflected tower axis, as illustrated in Figure 5.31.

Substitution of Eq. (5.105) into Eq. (5.62) yields, with the aid of Eq. (5.65),

$$\begin{aligned} m(r)\mu(r)\ddot{f}_J(t) + \hat{c}(r)\mu(r)\dot{f}_J(t) + m(r)\omega^2\mu(r)f_J(t) \\ = q(r, t) - m(r)\mu_{TJ}(r)\ddot{f}_T(t) - \hat{c}(r)\mu_{TJ}(r)\dot{f}_T(t) \end{aligned} \quad (5.107)$$

where the coupled terms have been transferred to the right hand side. Multiplying through by $\mu(r)$ and integrating over the length of the blade gives

$$\begin{aligned} m_1\ddot{f}_J(t) + c_1\dot{f}_J(t) + m_1\omega^2f_J(t) \\ = \int_0^R \mu(r)q(r, t)dr - \int_0^R m(r)\mu(r)\mu_{TJ}(r)dr\ddot{f}_T(t) - \int_0^R \hat{c}(r)\mu(r)\mu_{TJ}(r)dr\dot{f}_T(t) \end{aligned} \quad (5.108)$$

By analogy with Eq. (5.70), the equation of motion of the tower is

$$m_{T1}\ddot{f}_T(t) + c_{T1}\dot{f}_T(t) + m_{T1}\omega^2f_T(t) = \int_0^H \mu_T(z)q(z, t)dz \quad (5.109)$$

Here μ_T is the tower first mode shape, and m_{T1} is the generalised mass of the tower, nacelle, and rotor (including the contribution of rotor inertia), with respect to the first

mode, given by

$$m_{T1} = \int_0^H m_T(z) \mu_T^2(z) dz + m_N + m_R + I_R/L^2 \quad (5.110)$$

Here $m_T(z)$ is the mass per unit height of the tower, m_N and m_R are the nacelle and rotor masses, and I_R is the inertia of the rotor about the horizontal axis in its plane, which is constant over time for a three bladed rotor. For a two bladed, fixed hub rotor it varies with rotor azimuth, and for a teetering rotor it is omitted altogether.

The major component of the loading on the tower, $q(z,t)$, is the load fed in at hub height, H , from the blades. The inertia forces on the blades due to rigid body motion associated with the tower first mode have been accounted for by including rotor mass and inertia in m_{T1} , and the corresponding damping forces can be accounted for in the calculation of the damping coefficient, c_{T1} . However, the aerodynamic loads on the blades and the inertia and damping forces associated with blade flexure – all of which are transmitted to the tower top – have to be included in the right hand side of (5.109) as

$$\mu_T(H).F + \left(\frac{d\mu_T}{dz} \right)_H .M = F + M/L \quad (5.111)$$

where

$$F = \sum_B \int_0^R q_J(r, t) dr - \sum_B \int_0^R m_1(r) \mu(r) dr \ddot{f}_J(t) - \sum_B \int_0^R \hat{c}(r) \mu(r) dr \dot{f}_J(t) \quad (5.112)$$

and

$$\begin{aligned} M = & \sum_B \int_0^R r \cos \psi_J q_J(r, t) dr - \sum_B \int_0^R r \cos \psi_J m_1(r) \mu(r) dr \ddot{f}_J(t) \\ & - \sum_B \int_0^R r \cos \psi_J \hat{c}(r) \mu(r) dr \dot{f}_J(t) \end{aligned} \quad (5.113)$$

The suffix J refers to the J th blade, and B in the summations is the total number of blades.

Hence

$$\begin{aligned} F + M/L = & \sum_B \int_0^R \mu_{TJ} q_J(r, t) dr - \sum_B \int_0^R m_1(r) \mu(r) \mu_{TJ}(r) dr \ddot{f}_J(t) \\ & - \sum_B \int_0^R \hat{c}(r) \mu(r) \mu_{TJ}(r) dr \dot{f}_J(t) \end{aligned}$$

and Eq. (5.109) becomes

$$\begin{aligned} & m_{T1} \ddot{f}_T(t) + c_{T1} \dot{f}_T(t) + m_{T1} \omega_T^2 f_T(t) \\ & = \sum_B \int_0^R \mu_{TJ} q_J(r, t) dr - \sum_B \int_0^R m_1(r) \mu(r) \mu_{TJ}(r) dr \ddot{f}_J(t) - \sum_B \int_0^R \hat{c}(r) \mu(r) \mu_{TJ}(r) dr \dot{f}_J(t) \end{aligned} \quad (5.114)$$

omitting the term for loading on the tower itself.

Equations (5.108, 5.114) provide $(B + 1)$ simultaneous equations of motion with periodic coefficients μ_{TJ} corresponding to the $(B + 1)$ degrees of freedom assumed. The procedure for the step-by-step dynamic analysis that is based on these equations may be summarised as follows:

1. Substitute the displacements, velocities, and aerodynamic loads at the beginning of the first timestep into Eqs. (5.108) and (5.114), and solve for the initial accelerations.
2. Formulate the *incremental* equations of motion for the timestep, based on Eqs. (5.108) and (5.114), retaining the coupled terms on the right hand side – i.e. as pseudo forces.
3. Assume initially that the coupled terms are *constant* over the duration of the timestep, so that they disappear from the incremental equations of motion altogether, rendering them uncoupled.
4. Solve the uncoupled incremental equations of motion to obtain the increments of displacement and velocity over the timestep. Adopting the linear acceleration method (Section 5.8.5), the expressions for the displacement and velocity increments at the tip of blade J are as follows:

$$\Delta f_J = \frac{\Delta Q_J + m_1 \left(\frac{6}{h} \dot{f}_{J0} + 3\ddot{f}_{J0} \right) + c_1 \left(3\dot{f}_{J0} + \frac{h}{2} \ddot{f}_{J0} \right)}{m_1 \omega^2 + \frac{3c_1}{h} + \frac{6m_1}{h^2}} \quad (5.115)$$

$$\Delta \dot{f}_J = \frac{3}{h} \Delta f_J - 3\dot{f}_{J0} - \frac{h}{2} \ddot{f}_{J0} \quad (5.116)$$

The derivation of these expressions parallels that for the absolute values of displacement and velocity at the end of the timestep, given in Section 5.8.5. Similar expressions obtain for the displacement and velocity increments at the hub due to tower flexure.

5. Solve Eqs. (5.108) and (5.114) for the accelerations at the *end* of the timestep.
6. Solve the incremental equations of motion again – this time including the changes in the coupled terms on the right hand side over the timestep – to obtain revised increments of displacement and velocity over the timestep.
7. Repeat step 5 and step 6 until the increments of displacement and velocity converge.
8. Repeat steps 1–7 for the second and subsequent timesteps.

If the analysis is being carried out to obtain the response to deterministic loads, advantage may be taken of the fact that the behaviour of each blade mirrors that of its neighbours with an appropriate phase difference. This means that the number of equations of motion can be reduced to two and the analysis iterated over a number of revolutions until a steady state response is achieved. For example, in the case of a machine with three blades, A, B, and C, the values of blade B and blade C tip velocities and accelerations, which are required on the right hand side of Eq. (5.114), would be equated to the corresponding values for blade A occurring $T/3$ and $2T/3$ earlier (T being the period of blade rotation).

Figure 5.32 shows the results from the application of the above procedure to the derivation of blade tip and hub displacements in response to tower shadow loading, considering only the blade and tower fundamental modes. The three bladed machine is stall regulated, and the parameters chosen are, as far as the rotor is concerned, generally the same as for the rigid tower example in Section 5.8.5 illustrated in Figure 5.25. The tower natural frequency is 0.58 Hz, and the tower damping ratio (which is dominated by the aerodynamic damping of the blades) is taken as 0.022. The wind speed is a uniform 12 m/s.

It can be seen that the tower response is sinusoidal at blade passing frequency, which is the forcing frequency. The amplitude is only about 1/50th of the maximum blade tip displacement of about 60 mm, reflecting the large generalised mass associated with the tower mode relative to that associated with the blade mode. The tower shadow effect causes the blade to accelerate rapidly upwind as it passes the tower, with the maximum deflection occurring at an azimuth of about 205°. Also plotted on Figure 5.32 is the deflection that would occur if the nacelle were fixed, and it is seen from the comparison that one effect of tower flexibility is to slightly reduce the peak deflection. However, a more significant effect of the tower motion is the maintenance of the amplitude of the subsequent blade oscillations at a higher level prior to the next tower passing.

The modal analysis method outlined above forms the basis for a number of codes for wind turbine dynamic analysis, such as the Garrad Hassan *Bladed* code (DNVGL – Energy 2016, DNVGL 2020). Typically, these codes allow at least the first few blade modes, including flapwise, edgewise and torsional degrees of freedom, and several tower modes (fore-aft, side-to-side and torsional) to be represented together with drive train dynamics. See Section 5.13.

Rather than use modal analysis, the dynamic behaviour of coupled rotor/tower systems can also be investigated using finite elements. Standard finite element dynamics

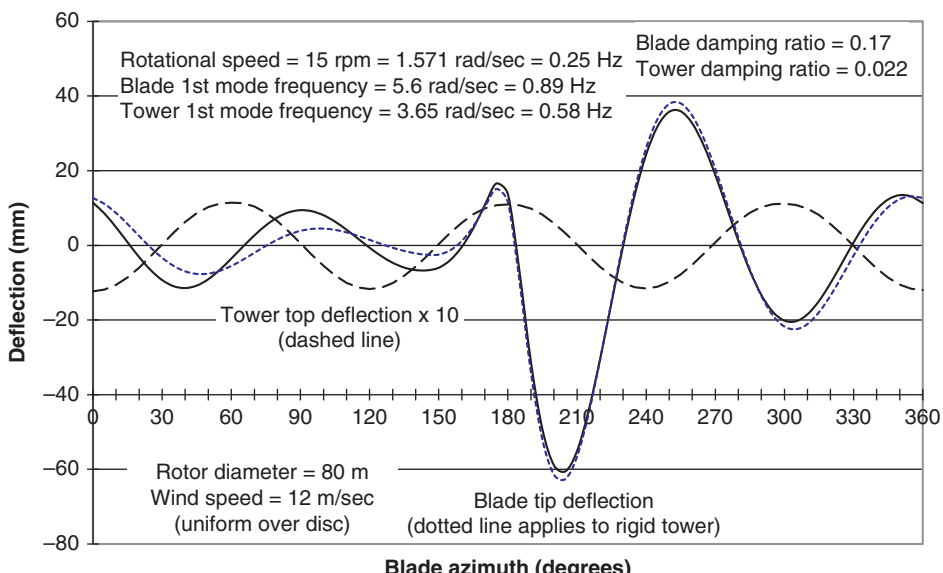


Figure 5.32 Tower top and blade tip deflections resulting from tower shadow, considering fundamental mode responses only.

packages are, however, inappropriate to the task, because they are only designed to model the displacements of structures with fixed geometry. Lobitz (1984) has pioneered the application of the finite element method to the dynamic analysis of wind turbines with two bladed, teetering rotors, and Garrad (1987) has extended it to three bladed, fixed hub machines. In both cases, equations of motion are developed in matrix form for the blade and tower displacement vectors and then amalgamated using a connecting matrix that is a function of blade azimuth and satisfies the compatibility and equilibrium requirements at the tower/rotor interface. Solution of the equations is carried out by a step-by-step procedure. The finite element method is more demanding of computing power, so the modal analysis method is generally preferred.

5.8.10 Aeroelastic stability

Aeroelastic instability can arise when the change in aerodynamic loads resulting from a blade displacement is such as to exacerbate the displacement rather than diminish it, as is normally the case. A theoretical example would be a teetering rotor operating in stalled flow, where the rate of change of lift coefficient with angle of attack is negative, so that the aerodynamic damping is negative likewise. In such circumstances, teeter excursions would be expected to grow until the limits of the negative damping band or of the teeter stops were reached. In practice, this phenomenon can be avoided if the blade is designed so that the blade root flapwise bending moment increases monotonically with wind speed over the full wind speed operational range (Armstrong and Hancock 1991).

A real instance of incipient aeroelastic instability was the development of an edge-wise blade resonance under stalled conditions on some larger three bladed machines. A negative rate of change of lift coefficient with angle of attack is believed to have been the prime cause – see Section 7.1.15.

Another potential instance of aeroelastic instability is classical flutter, encountered in the design of helicopter rotors, in which the blade structure is such that out-of-plane flexure in the downwind direction results in blade twisting, causing an increase in the angle of attack. During the development of some of the early large machines, the dangers of aeroelastic instability were considered to be a real concern, and much analysis work was directed to demonstrating that individual turbine designs would not be susceptible to it. However, partly no doubt because of the high torsional rigidity of the closed cell hollow structure adopted for most wind turbine blades, aeroelastic instability was not found to be critical in practice.

With the recent development of some very flexible blade designs for large machines, stability analyses are once again becoming important in the design process. Critical conditions include operation just below cut-out wind speed and standstill with extreme winds at yaw angles of 30 to 40 degrees.

5.9 Blade fatigue stresses

5.9.1 Methodology for blade fatigue design

The verification of the adequacy of a blade design in fatigue requires knowledge of the fatigue loading cycles expected over the lifetime of the machine at different radii, derivation of the resultant stress cycles, and calculation of the corresponding fatigue damage

number in relation to known fatigue properties of the material. The procedure is less or more complicated, depending upon whether blade loading in one or two planes is taken into account. If bending about only the weaker principal axis is taken into account, considering only aerodynamic lift forces, the steps involved are as follows:

1. Derive the individual fatigue load spectra for each mean wind speed and for each radius. This is a non-trivial task, because, unless wind simulation is used, the information on the periodic and stochastic load components is available in different forms, that is, as a time history and a power spectrum, respectively. Sections 5.9.2 and 5.9.3 consider methods of addressing this difficulty.
2. Synthesise the complete fatigue load spectrum at each radius from the separate load spectra for each mean wind speed, including start-ups and shut-downs (see Section 5.5.1).
3. Convert the fatigue load cycles (expressed as bending moments) to fatigue stresses by dividing by the appropriate section modulus. (The section modulus with respect to a particular principal axis is defined as second moment of area of the cross-section about that axis divided by the distance of the point under consideration from the axis).
4. Sum the fatigue damage numbers, n_i/N_i , according to Miner's rule, for each moment range 'bin' in the fatigue load spectrum, according to the appropriate S-N curve for the material. S-N curves for different blade materials are considered in Sections 7.1.8 and 7.1.9, together with the allowance necessary for mean stress.

Sections 5.9.2 and 5.9.3 are concerned with the first step of the preceding sequence. For a given mean wind speed, the periodic component of blade loading will be invariant over time, and the stochastic component will be stationary. As noted in Section 5.7.5, the stochastic component can be analysed either in the frequency domain (provided that a linear relationship between incident wind speed and blade loadings can be assumed) or in the time domain – i.e. by using wind simulation. Section 5.9.2 considers how the deterministic and stochastic components may be combined if the latter have been analysed in the frequency domain, and Section 5.9.3 looks in detail at the option of assessing fatigue damage completely in the frequency domain.

If the fatigue damage resulting from both in-plane and out-of-plane loading is to be computed, it is necessary to revise the ordering of the steps above to derive the periodic and stochastic components of the stress variation for each point under consideration and for each mean wind speed. For a chosen point, the procedure becomes:

- A1 For a given mean wind speed, calculate the time histories of the bending moments about the principal axes resulting from the periodic load components over one blade rotation. The derivation of aerodynamic moments from blade element loads is illustrated in Figure 5.33.
- A2 Convert these bending moment time histories to stress time histories by dividing by the appropriate section modulus, and adding them together.

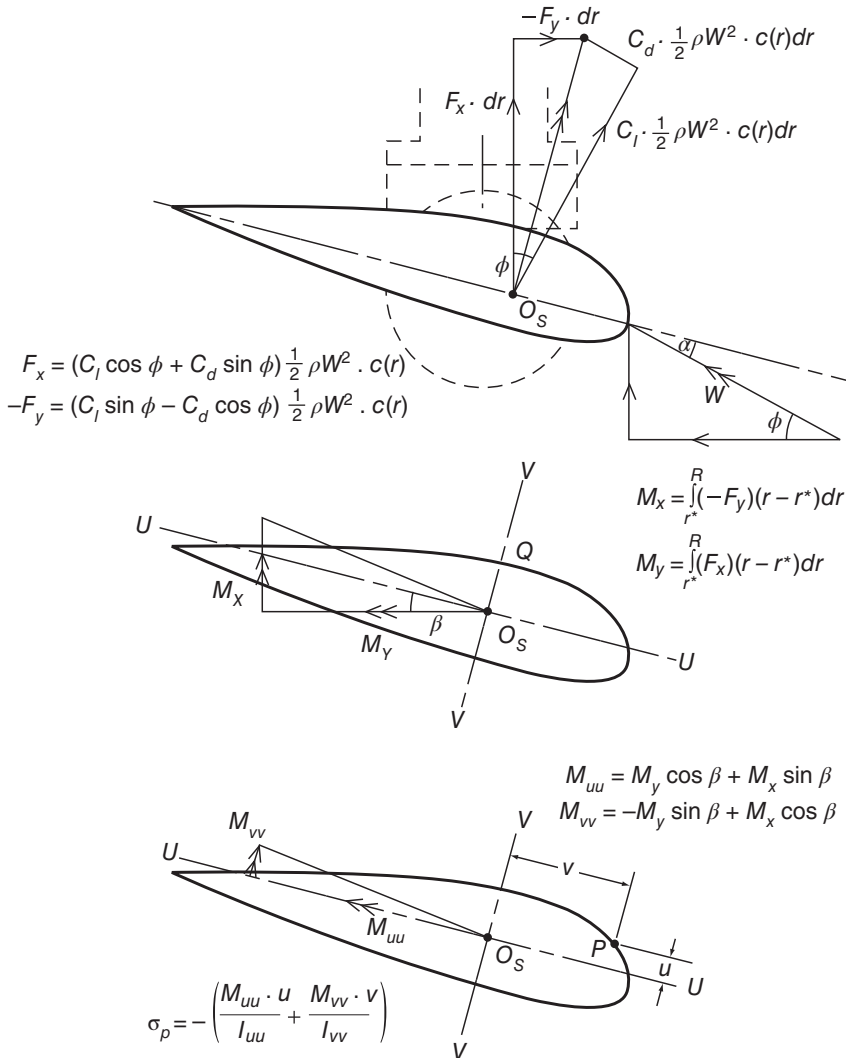


Figure 5.33 Derivation of blade bending stresses at radius r^* due to aerodynamic loads.

- For the same mean wind speed, convert the power spectrum of the stochastic bending moment component (which, because of the linearity assumption, arises from fluctuating lift only) to a power spectrum of stress at the chosen point.
- Calculate the fatigue damage resulting from the combined periodic and stochastic stress components, using the methods of Sections 5.9.2 and 5.9.3.
- Repeat the above steps for the other mean wind speeds.
- Add together the fatigue damages arising at each mean wind speed to obtain the total fatigue damage during normal running.

5.9.2 Combination of deterministic and stochastic components

Previous sections have shown how the deterministic (i.e. periodic) and stochastic components of blade bending moments can be characterised in terms of time histories and power spectra, respectively. Unfortunately, the spectral description of the stochastic loading is not in a suitable form to be combined with the time history of the periodic loading, but this difficulty can be resolved by one of two methods, as follows:

1. The power spectrum of the stochastic component can be transformed into a time history by inverse Fourier transform, which can then be added directly to the time history of the periodic component. Applications of this method have been reported by Garrad and Hassan (1986) and Warren et al. (1988). With the subsequent development of wind simulation techniques, this method is no longer commonly used because the use of transformations to generate time histories of *wind speed* rather than of wind loading avoids the need to assume that wind speed and wind loading are linearly related when deriving the power spectrum of the stochastic load component.
2. A probability density function (PDF) for the load cycle ranges can be derived empirically, based on the spectral properties of the power spectrum of the stochastic and periodic components of loading combined.

The second approach is considered in the next section.

5.9.3 Fatigue prediction in the frequency domain

The probability density function (PDF) of peaks of a narrow band, Gaussian process are given by the well-known Rayleigh distribution. As each peak is associated with a trough of similar magnitude, the PDF of cycle ranges is Rayleigh likewise.

Wind turbine blade loading cannot be considered as narrow band, despite the concentration of energy at the rotational frequency by ‘gust slicing’ (Section 5.7.5), and neither can it be considered as Gaussian because of the presence of periodic components. Dirlıkkı (1985) produced an empirical PDF of cycle ranges applicable to both wide and narrow band Gaussian processes, in terms of basic spectral properties determined from the power spectrum. This was done by considering 70 power spectra of various shapes, computing their rainflow cycle range distributions (see Section 5.9.5) and fitting a general expression for the cycle range PDF in terms of the first, second, and fourth spectral moments. Dirlıkkı’s expression for the cycle range PDF is

$$p(S) = \frac{\frac{D_1}{Q}e^{-Z/Q} + \frac{D_2Z}{R^2}e^{-(Z^2/2R^2)} + D_3Ze^{-(Z^2/2)}}{2\sqrt{m_o}} \quad (5.117)$$

where

$$Z = \frac{S}{2\sqrt{m_o}},$$

$$D_1 = \frac{2(x_m - \gamma^2)}{1 + \gamma^2}, \quad D_2 = \frac{(1 - \gamma - D_1 + D_1^2)}{1 - R}, \quad D_3 = 1 - D_1 - D_2$$

$$Q = \frac{1.25(\gamma - D_3 - D_2 R)}{D_1} \quad R = \frac{\gamma - x_m - D_1^2}{(1 - \gamma - D_1 + D_1^2)} \quad x_m = \frac{m_1}{m_0} \sqrt{\frac{m_2}{m_4}} \quad \gamma = \frac{m_2}{\sqrt{m_0 m_4}}$$

$$m_i = \int_0^\infty n^i S_\sigma(n) dn$$

$S_\sigma(n)$ is the power spectrum of stress and S is the cycle stress range.

Although the Dirlit cycle range PDF was not intended to apply to signals containing periodic components, several investigations (Hoskin et al. 1989; Morgan and Tindal 1990; Bishop et al. 1991) have been carried out to determine its validity for wind turbine fatigue damage calculations, using monitored data for flapwise bending from the MS1 wind turbine on Orkney. Cycle range PDFs were calculated from power spectra of monitored strains using the Dirlit formula and fatigue damage rates derived from these PDFs compared with damage rates derived directly from the monitored signal by rainflow cycle counting. The ratio of damage calculated by the Dirlit method to damage calculated by the rainflow method ranged from 0.84 to 1.46, from 1.01 to 2.48, and from 0.73 to 2.34 in the three investigations listed, using a S/N curve exponent of 5 in each case, as the blade structure was of steel. In view of the fact that the calculated damage rates vary as the fifth power of the stress ranges, these results indicate that the Dirlit method is capable of giving quite accurate results, despite the presence of the periodic components.

There are two main drawbacks to the application of the Dirlit formula to power spectra containing periodic components. Firstly, the presence of large spikes in the spectra due to the periodic components renders them very different from the smooth distributions Dirlit originally considered, and secondly information about the relative phases of the periodic components is lost when they are transformed to the frequency domain. Morgan

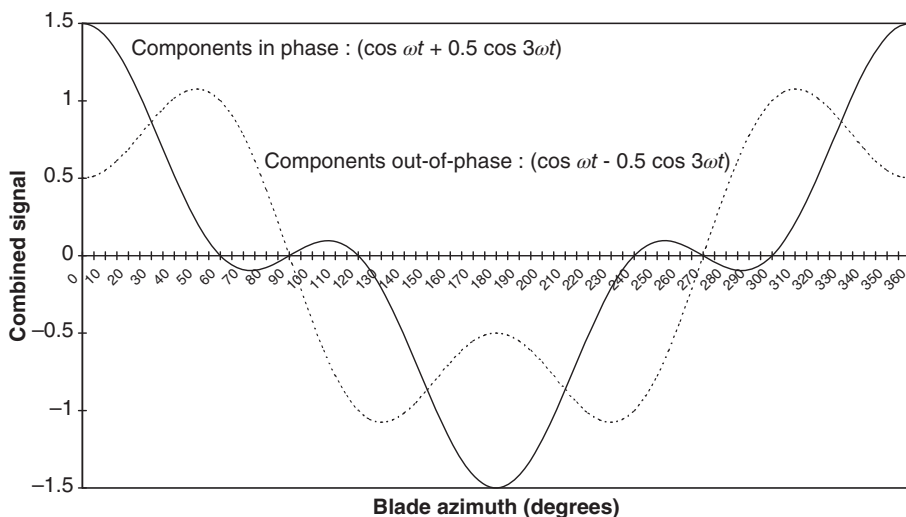


Figure 5.34 Effect of variation of phase angle between harmonics on combined signal.

and Tindal (1990) illustrate the effect of varying phase angles by a comparison of plots of $(\cos\omega t + 0.5\cos 3\omega t)$ and $(\cos\omega t - 0.5\cos 3\omega t)$, which is reproduced in Figure 5.34. For a material with a *S/N* curve exponent of 5, stresses conforming to the first time history would result in 5.25 times as much fatigue damage as stresses conforming to the second.

Bishop, Wang, and Lack (1995) developed a modified form of the Dirluk formula to include a single periodic component, using a neural network approach to determine the different parameters in the formula from computer simulations.

Madsen et al. (1984) adopted a different approach to the problem of determining fatigue damage resulting from combined stochastic and periodic loading, involving the derivation of a single equivalent sinusoidal loading that would produce the same fatigue damage as the actual loading. The method applies a reduction factor, g , which is dependent on bandwidth, to account for the reduced cycle ranges implicit in a wide band as opposed to a narrow band process, and utilises Rice's PDF for the peak value of a single sinusoid combined with a narrow band stochastic process, substituting half the maximum range of the periodic signal, including harmonics, for the amplitude of the sinusoid. A fuller summary is given in Hoskin et al. (1989). They concluded, along with Morgan and Tindal (1990), that the Madsen method yielded slightly less accurate fatigue damage values than the Dirluk method for the MS1 monitored data for flapwise bending referred to above.

Ragan and Manuel (2007) used about 2500 datasets of blade in-plane and out-of-plane bending moments from a 1.5 MW turbine in Colorado to compare fatigue damage equivalent loads calculated in the frequency domain by the Dirluk method with corresponding values calculated in the time domain. They concluded that the Dirluk method performed reasonably well for out-of-plane moments but very poorly for blade in-plane bending moments, which have a large periodic component.

5.9.4 Wind simulation

Wind simulation, which was introduced in Section 5.7.6, has two significant advantages over the methods described above for fatigue damage evaluation. Firstly, it can handle non-linear relationships between wind speed fluctuations and blade loadings in the calculation of stochastic loads, and secondly, it avoids the difficulty of deriving the fatigue stress ranges arising from combined periodic and stochastic load components. It is therefore currently the favoured method for detailed fatigue design. The procedure is essentially as follows:

1. Generate a three-dimensional (3-D) 'run of wind' for the chosen mean wind speed, with the desired shear profile and tower shadow correction.
2. Perform a step-by-step dynamic analysis on the turbine operating in this wind field, to obtain in-plane and out-of-plane bending moment time histories at different radii.
3. Convert these bending moment time histories to time histories of bending moments about the principal axes.

4. Compute stress time histories at chosen points on each cross-section.
5. Derive the number of cycles in each stress range ‘bin’ by rainflow cycle counting (see Section 5.9.5).
6. Scale up the cycle numbers in line with the predicted number of hours of operation at the chosen mean wind speed.
7. Calculate corresponding fatigue damage numbers based on the applicable $S-N$ curve.
8. Repeat above steps for different mean wind speeds, and total the resulting fatigue damages at each point.

A computationally simpler alternative is to generate a one-dimensional ‘run of wind’ (in which only the longitudinal component of turbulence is modelled) and run a number of simulations at different, fixed yaw angles.

The duration of wind simulations is limited by available computing power, with a time history length of 600 seconds being frequently chosen. A consequence of this is that a single simulation will not provide an accurate picture of the infrequent high stress range fatigue cycles, which can have a disproportionate effect on fatigue damage for materials with high m value, such as those used for blades. However, this inaccuracy can be reduced (and quantified) by running several simulations with different random number seeds at each wind speed – see Thomsen (1998).

5.9.5 Fatigue cycle counting

As noted in Section 5.9.4, the dynamic analysis of turbine behaviour in a simulated wind field yields time histories of loads or stresses that then need to be processed to abstract details of the fatigue cycles. There are two established methods of fatigue cycle counting: the reservoir method and the rainflow method, both of which yield the same result.

In the reservoir method, the load or stress history (with time axis horizontal) is imagined as the cross-section of a reservoir, which is successively drained from each low point, starting at the lowest and working up. Each draining operation then yields a load or stress cycle. See BS 5400 (British Standards Institution 1980) for a full description.

The rainflow method was first proposed by Matsuishi and Endo in 1968, and its title derives from the concept of water flowing down the ‘rooves’ formed when the time history is rotated so that the time axis is vertical. However, the following description not involving the rainflow analogy may be easier to understand.

The first step is to reduce the time history to a series of peaks and troughs, which are then termed *extremes*. Then, each group of four successive extremes is examined in turn to determine whether the values of the two intermediate extremes lie between the values of the initial and final extremes. If so, the two intermediate extremes are counted as defining a stress cycle, which is then included in the cycle count, and the two intermediate extremes are deleted from the time history. The process is continued until the complete series of extremes forming the time history has been processed in this way. Then the sequence remaining will consist simply of a diverging and a converging part from which the final group of stress ranges can be extracted. See ‘Fatigue Characteristics’ in the IEA series of Recommended Practices for Wind Turbine Testing and Evaluation

(International Energy Agency Wind Technology Collaboration Programme 1990) for a full description of the method and for details of algorithms that can be used for automating the process.

Although, in principle, the fatigue cycles obtained from, say, a 600 second time history could be listed individually, it is normal to reduce the volume of data by allocating individual cycles to a series of equal load or stress ranges known as *bins* – e.g. 0–2, 2–4, 4–6 N/mm², etc. The fatigue spectrum is then presented in terms of the number of cycles falling into each ‘bin’.

5.10 Hub and low-speed shaft loading

5.10.1 Introduction

The loadings on the hub consist of the aerodynamic, gravity, and inertia loadings on the blades and the equal and opposite (discounting hub self-weight) reaction from the shaft. For fixed hub machines, the loading on the shaft will include a significant moment arising from blade aerodynamic loads, but in the case of teetered two bladed rotors, this moment will be virtually eliminated. In either case, however, the cantilevered low-speed shaft will experience large fluctuating moments due to rotor weight as it rotates. Figure 5.35 shows a low-speed shaft and front bearing in a factory prior to assembly.

The shaft moments due to out-of-plane loads on the blades can be expressed as moments about a pair of rotating axes, one perpendicular to blade 1 and the other parallel

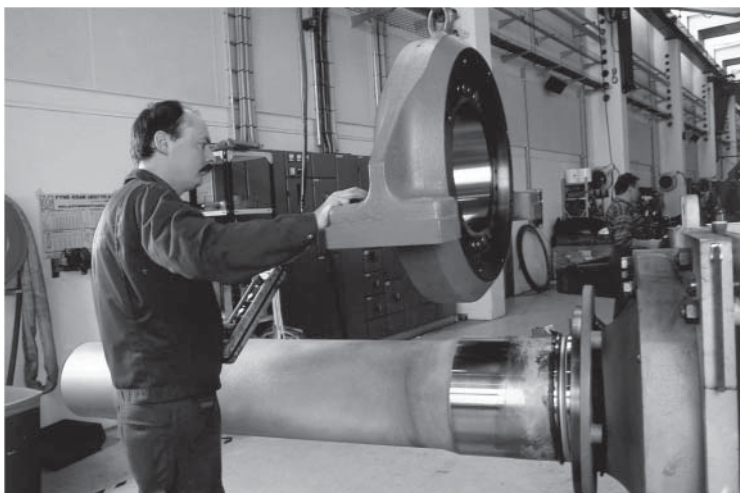


Figure 5.35 Low-speed shaft and front bearing before assembly. The hub mounting flange at the right hand end is bolted to a temporary support to allow the bearing to be threaded on the shaft. Source: Reproduced by permission of NEG Micon.

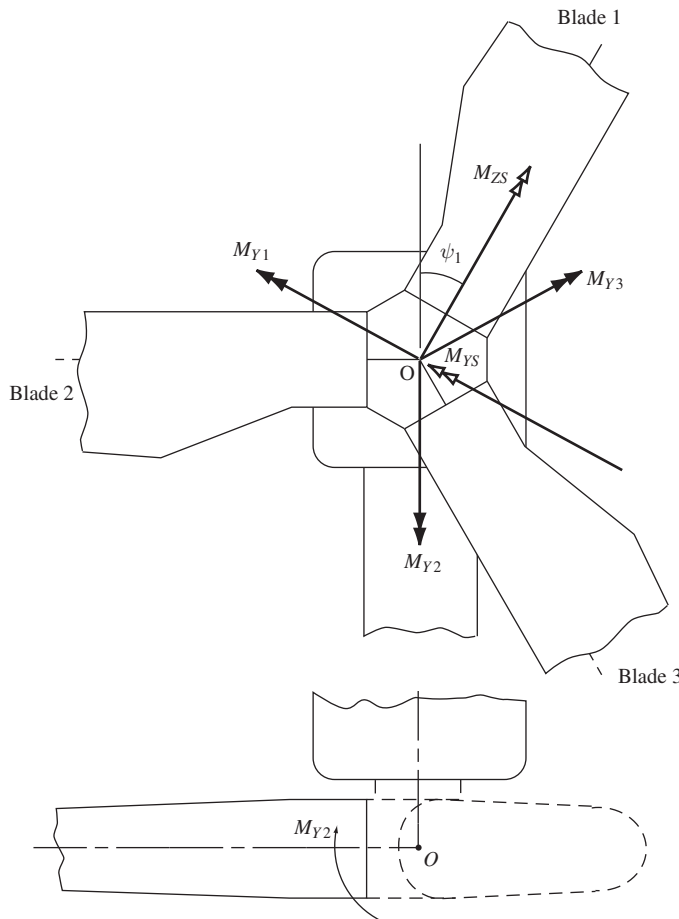


Figure 5.36 Shaft bending moments with rotating axis system referred to blade 1.

to it. In the case of a three bladed rotor, these moments are, respectively, as follows:

$$M_{YS} = \Delta M_{Y1} - \frac{1}{2}(\Delta M_{Y2} + \Delta M_{Y3}) \quad M_{ZS} = \frac{\sqrt{3}}{2}(\Delta M_{Y3} - \Delta M_{Y2}) \quad (5.118)$$

Here ΔM_{Y1} , ΔM_{Y2} , and ΔM_{Y3} are the fluctuations of the blade out-of-plane moments about the hub centre (M_{Y1} , M_{Y2} , and M_{Y3}) about the mean value. See Figure 5.36.

5.10.2 Deterministic aerodynamic loads

The deterministic aerodynamic loads on the rotor may be split up into a steady component, equal for each blade, and a periodic component, also equal for each blade, but with differing phase angles. The blade root out-of-plane bending moments due to the first component will be in equilibrium and will apply a ‘dishing’ moment to the hub that will result in tensile stresses in the front and compression stresses in the rear. These stresses will be uniaxial for a two bladed rotor and biaxial for a three bladed rotor.

The fluctuations in out-of-plane blade root bending moment due to wind shear, shaft tilt, and yaw misalignment will often be approximately sinusoidal, with a frequency equal

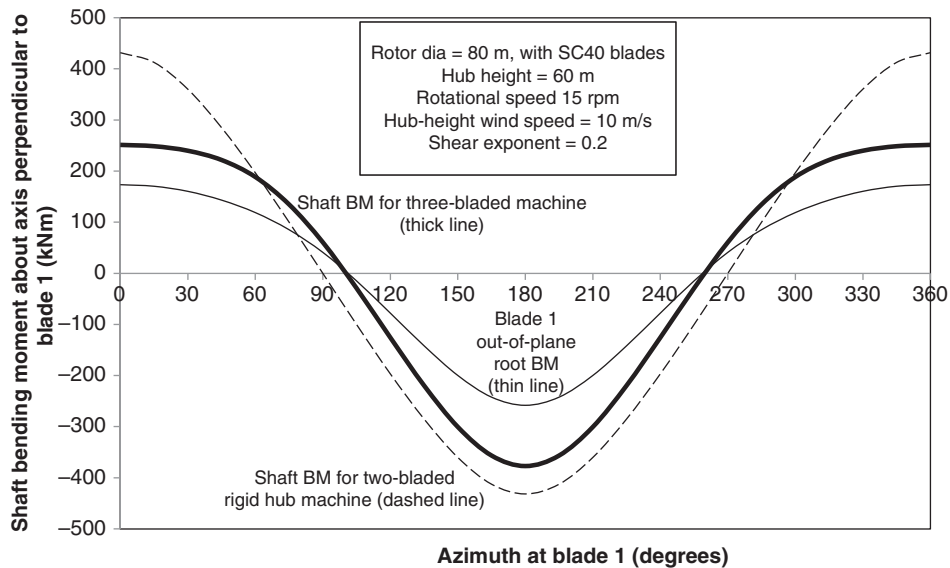


Figure 5.37 Shaft bending moment fluctuations due to wind shear.

to the rotational frequency. Using Eq. (5.118), it is easily shown that, for a sinusoidally varying blade root bending moment with range ΔM , the range of the resulting shaft bending moment is $1.5\Delta M$ for a three bladed machine and $2\Delta M$ for a rigid hub two bladed machine.

In the case of wind shear conforming to a power law, the loading on a horizontal blade is always greater than the average of the loadings on blades pointing vertically upwards and downwards, so the loading departs significantly from sinusoidal. The shaft bending moment fluctuations due to wind shear with a 0.2 exponent are compared in Figure 5.37 for two and three bladed 80 m diameter, 60 m hub height rigid hub machines operating at 15 rpm in a hub-height wind speed of 10 m/s. The ratio of moment ranges is still close to 2:1.5.

5.10.3 Stochastic aerodynamic loads

The out-of-plane blade root bending moments arising from stochastic loads on the rotor will result in both a fluctuating hub ‘dishing’ moment (see above) and fluctuating shaft bending moments. For a two bladed, rigid hub rotor, the shaft moment is equal to the difference between the two out-of-plane blade root bending moments, or teeter moment, the standard deviation of which is given by Eq. (5.102a). Similarly, the standard deviation of the mean of these two moments (i.e. the ‘dishing’ moment) is given by Eq. (5.103).

The derivation of the standard deviation of the shaft moment for a three bladed machine is at first sight more complicated, as the integration has to be carried out over three blades instead of two. However, if the shaft moment about an axis parallel to one of the blades, M_{ZS} (Figure 5.36), is chosen, the contribution of loading on that blade disappears, and the expression for the shaft moment standard deviation becomes

$$\sigma_{M_{ZS}}^2 = \left(\frac{1}{2} \rho \Omega \frac{dC_L}{d\alpha} \right)^2 \int_{-R}^R \int_{-R}^R \kappa_u^o(r_1, r_2, 0) c(r_1) c(r_2) \frac{\sqrt{3}}{2} r_1 \frac{\sqrt{3}}{2} r_2 |r_1| |r_2| dr_1 dr_2 \quad (5.119a)$$

where the limits of the integrations refer to the other two blades. $\kappa_u^o(r_1, r_2, 0)$ is given by Eq. (5.51), with $\Omega\tau$ set equal to zero when r_1 and r_2 are radii to points on the same blade, and replaced by $2\pi/3$ when r_1 and r_2 are radii to points on different blades. Note that, compared with the two bladed case, the cross-correlation function, $\kappa_u^o(r_1, r_2, 0)$, will be increased when r_1 and r_2 relate to *different* blades, because of the reduced separation between the two blade elements resulting from the 120° angle between the blades. Eq. (5.119a) can be rewritten in terms of the normalised cross-correlation function, $\rho_u^o(r_1, r_2, 0) = \kappa_u^o(r_1, r_2, 0)/\sigma_u^2$, as follows:

$$\sigma_{M_{zs}}^2 = \sigma_u^2 \left(\frac{1}{2} \rho \Omega \frac{dC_L}{d\alpha} \right)^2 \int_{-R}^R \int_{-R}^R \rho_u^o(r_1, r_2, 0) c(r_1) c(r_2) \frac{\sqrt{3}}{2} r_1 \frac{\sqrt{3}}{2} r_2 |r_1| |r_2| dr_1 dr_2 \quad (5.119b)$$

In the case of 80 m diameter turbines with SC40 blades operating in wind with a turbulence length scale of 147 m, the standard deviation of shaft moment due to stochastic loading for a three bladed machine is 82% of that for a two bladed, fixed hub machine rotating at the same speed. This ratio would rise to $\sqrt{3}/2$ if the effect on the cross-correlation function of the 120° blade spacing were ignored.

It is worth noting that, for a three bladed machine, the standard deviation of the shaft moment M_{ys} due to stochastic loading is the same as that of M_{zs} (see Figure 5.36 for definitions).

By analogy with the derivation of the shaft moment above, the standard deviation of the hub ‘dishing’ moment for a three bladed machine due to stochastic loading is given by

$$\sigma_{M_h}^2 = \frac{1}{4} \sigma_u^2 \left(\frac{1}{2} \rho \Omega \frac{dC_L}{d\alpha} \right)^2 \int_{-R}^R \int_{-R}^R \rho_u^o(r_1, r_2, 0) c(r_1) c(r_2) \frac{\sqrt{3}}{2} r_1^2 \frac{\sqrt{3}}{2} r_2^2 dr_1 dr_2 \quad (5.120)$$

where the integrations are carried out over two blades only, and the cross-correlation function is modified as before to account for the 120° angle between the blades.

It can be shown that

$$\frac{1}{4} \sigma_{M_{zs}}^2 + \sigma_{M_h}^2 = \frac{3}{4} \sigma_{My1}^2 \quad (5.121)$$

5.10.4 Gravity loading

An important component of shaft loading is the cyclic cantilever bending moment due to rotor weight, which usually has a dominant effect on shaft fatigue design. As an illustration, a rotor consisting of three SC40 blades weighing 7.7 t each, and a 25 t hub cantilevered 1.7 m beyond the shaft main bearing, will produce a shaft gravity moment range of about 1600 KNm. This compares with a shaft moment range due to wind shear of 630 KNm for a hub-height wind of 10 m/s and a shear exponent of 0.2, and a shaft moment standard deviation of 350 KNm due to turbulence, taking a turbulence intensity of 21% and the same hub-height mean wind speed. Note that the shaft moment due to wind shear relieves that due to gravity.

5.11 Nacelle loading

5.11.1 Loadings from rotor

The previous section considered the moments applied to the shaft by the rotor hub using an axis system rotating with the shaft. In addition to these moments, the shaft also

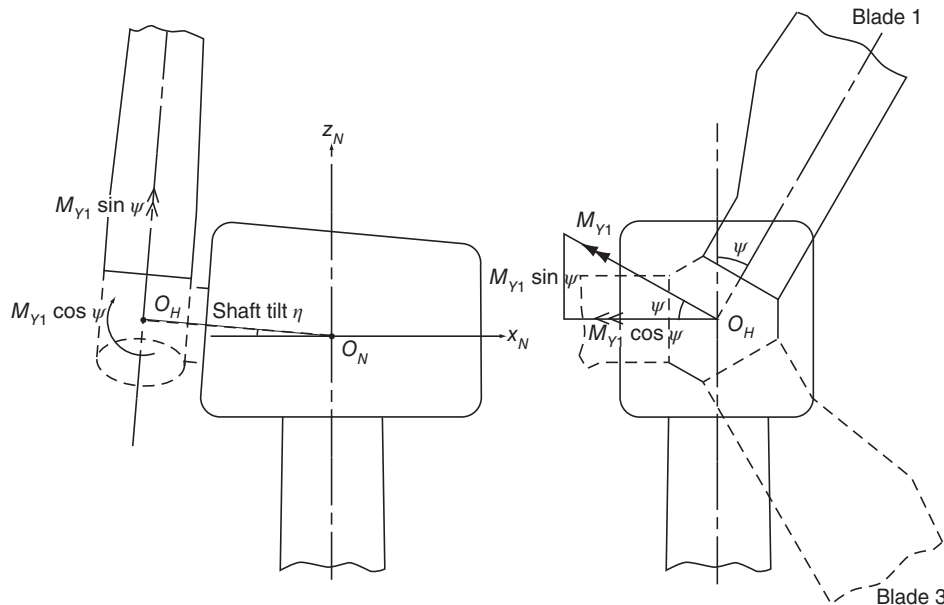


Figure 5.38 Components of blade 1 out-of-plane root bending moment about fixed set of axes.

experiences an axial load due to rotor thrust and radial forces arising from differential blade edgewise loadings and any out-of-balance centrifugal force.

To calculate loadings on the elements of the nacelle structure, it is first necessary to transform the shaft loads (or the constituent blade loads) defined in terms of the rotating axis system into nacelle loads expressed in terms of a fixed axis system. Here the conventional system in which the x axis is downwind, the y axis is horizontal to starboard, and the z axis is vertically upwards will be adopted. Thus the moments acting on the nacelle about the y and z axes as a result of the blade root out-of-plane bending moments are as follows for a three bladed machine with shaft tilt η :

$$M_{YN} = M_{Y1} \cos \psi + M_{Y2} \cos(\psi - 120^\circ) + M_{Y3} \cos(\psi - 240^\circ) \quad (5.122)$$

$$M_{ZN} = (M_{Y1} \sin \psi + M_{Y2} \sin(\psi - 120^\circ) + M_{Y3} \sin(\psi - 240^\circ)) \cos \eta \quad (5.123)$$

where ψ is the azimuth of blade 1. See Figure 5.38.

It is instructive to compare the moments acting on the nacelle due to deterministic loading for three bladed and two bladed machines. The fluctuations of out-of-plane root bending moment due to wind shear and yaw misalignment are approximately proportional to the cosine of blade azimuth for an unstalled blade. Substituting $M_{Y1} = M_0 \cos \psi$, $M_{Y2} = M_0 \cos(\psi - 2\pi/B)$, etc. into Eqs. (5.122) and (5.123) yields $M_{YN} = 1.5 M_0$ and $M_{ZN} = 0$ for a three bladed machine, whereas the corresponding results for a rigid hub two bladed machine are $M_{YN} = M_0 (1 + \cos 2\psi)$ and $M_{ZN} = M_0 \sin 2\psi \cos \eta$. Thus, the moments on the nacelle are constant for a three bladed machine but continually fluctuating with amplitude M_0 for a rigid hub two bladed machine. Parallel results are obtained for $M_{Y1} = M_0 \sin \psi$, which approximates to the out-of-plane root bending moment due to shaft tilt – again for an unstalled blade. The full comparison is given in Table 5.7.

Table 5.7 Comparison between nacelle moments due to deterministic loads for two and three bladed machines.

	Nacelle moments resulting from out-of-plane blade root bending moment fluctuations due to <i>wind shear and yaw misalignment</i> approximated by $M_{Y1} = M_0 \cos\psi$, $M_{Y2} = M_0 \cos(\psi - 2\pi/B)$, etc.		Nacelle moments resulting from out-of-plane blade root bending moment fluctuations due to <i>shaft tilt</i> approximated by $M_{Y1} = M_0 \sin\psi$, $M_{Y2} = M_0 \sin(\psi - 2\pi/B)$, etc.	
	Nacelle nodding moment, M_{YN}	Nacelle yaw moment, M_{ZN}	Nacelle nodding moment, M_{YN}	Nacelle yaw moment, M_{ZN}
Three bladed machine	$1.5 M_0$	Zero	Zero	$1.5 M_0 \cos\eta$
Two bladed, rigid hub machine	$M_0 (1 + \cos 2\psi)$	$M_0 \sin 2\psi \cos\eta$	$M_0 \sin 2\psi$	$M_0 (1 - \cos 2\psi) \cos\eta$

It is clear that the moments acting on the nacelle due to deterministic loading are much more benign for a three bladed rotor than for a two bladed rotor with rigid hub.

In the case of three bladed machines, the standard deviation of shaft bending moment due to stochastic rotor loading is independent of the rotating axis chosen (Section 5.10.3), so the standard deviation of the resulting moment on the nacelle will take the same value about both the nacelle y and z axes.

5.11.2 Nacelle wind loads

Except in the case of sideways wind loading, wind loads on the nacelle are not usually of great significance. They may be calculated according to the rules given in standard wind loading codes. For sideways wind loading, a drag factor of 1.2 will generally be found to be conservative.

5.12 Tower loading

5.12.1 Extreme loads

It is customary to base the calculation of extreme loads on a non-operational turbine on the 50 year return 3 second gust. Several loading configurations may need to be considered, and the critical load case for the tower base will generally differ from that for the tower top. In addition, it is necessary to investigate the extreme operational load cases, as these can sometimes govern instead if the tip speed is high in relation to the design gust speed.

In the case of non-operational, stall-regulated machines, the critical case for the tower base occurs when the wind is blowing from the front and inducing maximum drag loading on the blades. By contrast, sideways wind loading to produce maximum lift on a blade pointing vertically upwards or rear wind loading on the rotor with one blade shielded by the tower will produce the maximum tower top bending moment.

One of the benefits of pitch regulation of three bladed machines is that blade feathering at shut-down considerably reduces non-operational rotor loading. The critical configuration as far as tower base bending moment is concerned is sideways wind loading, with two of the blades inclined at 30° to the vertical. The horizontal component of the loading on these blades is $\cos^3 30^\circ$ of the loading on a vertical blade, so that the total rotor loading is only 43.3% ($= 100 \sqrt{3}/4$) of the maximum experienced by a stall-regulated machine.

The cases of sideways wind loading on a wind turbine referred to previously can only arise if the yaw drive is disabled by grid loss for sufficient time for a 90° wind direction change to take place, so IEC 61400-1 edition 3 treats this case (DLC 6.2) as an abnormal load case with a reduced load factor of 1.1 (in place of 1.35 for normal load cases). As a result of this, the load case causing extreme tower base overturning moment on pitch-regulated machines is not always clear cut. If the rotor is braked with one blade vertically upwards and the yaw angle is small (corresponding to IEC 61400-1 edition 3 DLC 6.1), the loading on the top blade could approach maximum lift. Loads on the other blades would be smaller, and their horizontal components would probably act in the opposite direction. The maximum loading on the top blade would be $(0.5\rho V^2)1.5A_B$, ignoring wind shear, where A_B is the blade area. On the other hand, DLC 6.2 gives a drag loading of $2\cos^3 30^\circ(0.5\rho V^2)1.3A_B = (0.5\rho V^2)1.69A_B$, again ignoring wind shear, which becomes $(0.5\rho V^2)1.86A_B$ after inclusion of the load factor. This is somewhat less than

the factored load on a vertical blade experiencing maximum lift of $2.025(0.5\rho V^2)A_B$. However, the drag loading on the blades in DLC 6.2 acts in the same direction as the drag load on the tower, whereas the lift load on the vertical blade in DLC 6.1 acts at right angles to the drag loading on the tower.

Information on the drag factors appropriate for cylindrical and lattice towers is to be found in EN 1991-1-4:2005, *Eurocode 1: Actions on Structures – Part 1-4: General Actions – Wind Actions*, and in national codes such as BS 8100 (British Standards Institution 1984) or DS 410 (1983). The drag factor for a cylindrical tower is typically 0.6–0.7. Rotor loading is generally the dominating component of tower base moment for stall-regulated machines, but with pitch-regulated machines, the contributions of tower loading and rotor loading are often of similar magnitude.

5.12.2 Dynamic response to extreme loads

Just as in the case of the single, stationary cantilevered blade considered in Section 5.6.3, the quasi-static bending moments in the tower calculated for the extreme gust speed will be augmented by inertial moments resulting from the excitation of resonant tower oscillations by turbulence. As before, it is convenient to express this augmentation in terms of a dynamic factor, Q_D , defined as the ratio of the peak moment over a 10 minute period, including resonant excitation of the tower, to the peak quasi-static moment over the same period. Thus

$$M_{Max} = \frac{1}{2}\rho U_{e50}^2 H \oint C_f \left(\frac{z}{H}\right)^{1+2\alpha} dA \cdot Q_D \quad (5.124)$$

where

U_{e50} is the 50 year return gust speed at hub height

z is height above ground

H is the hub height

C_f is the force factor (lift or drag) for the element under consideration

α is the shear exponent, taken as 0.11 in IEC 61400-1

and

$$Q_D = \frac{1 + g \left(2 \frac{\sigma_u}{U}\right) \sqrt{K_{SMB} + \frac{\pi^2}{2\delta} R_u(n_1) K_{Sx}(n_1) \lambda_{M1}^2}}{1 + g_0 \left(2 \frac{\sigma_u}{U}\right) \sqrt{K_{SMB}}} \quad [\text{see Eq.(5.17)}]$$

The integral sign \oint signifies that the integral is to be undertaken over each blade, the nacelle, and the tower. The derivation of Eq. (5.17) is explained in Section 5.6.3 and Appendix A5 in relation to a cantilevered blade.

The essentially similar procedure for a tower supporting a braked rotor and nacelle is as follows:

- Calculate the resonant size reduction factor, $K_{Sx}(n_1)$, which reflects the effect of the lack of correlation of the wind fluctuations at the tower natural frequency along the blades and tower. Adopting an exponential expression for the normalised co-spectrum as before, Eq. (A5.25) becomes

$$K_{Sx}(n_1) = \frac{\oint \oint \exp[-C s n_1 / \bar{U}] C_f^2 c(r)c(r')\mu_1(r)\mu_1(r')drdr'}{(\oint C_f c(r)\mu_1(r)dr)^2} \quad (5.125)$$

where

the integral sign \oint denotes integration over the blades and the tower

r and r' denote radius in the case of the blades and depth below the hub in the case of the tower

s denotes the separation between the elements dr and dr'

C_f is the relevant force coefficient

$c(r)$ denotes chord in the case of the blades and diameter in the case of the tower

$\mu_1(r)$ denotes the tower first mode shape

This expression can be considerably simplified by setting $\mu_1(r)$ to unity for the rotor and ignoring the tower loading contribution entirely. This is not unreasonable, as only loading near the top of the tower is of significance, and this does not add much to the spatial extent of the loaded area.

- Calculate the damping logarithmic decrement, δ , for the tower first mode. The aerodynamic component is given by

$$\delta_a = 2\pi\xi_a = 2\pi \frac{c_{a1}}{2m_{T1}\omega_1} = 2\pi \frac{\oint \hat{c}_a(r)\mu_1^2(r) dr}{2m_{T1}n_1} \quad (5.126)$$

where m_{T1} is the generalised mass of the tower, nacelle, and rotor (including the contribution of rotor inertia) with respect to the first mode given by Eq. (5.110), and n_1 is the tower natural frequency in Hz. For a stall-regulated machine facing the wind, the rotor contribution to aerodynamic damping is simply $\rho \bar{U} C_D A_R / 2m_{T1}n_1$, where A_R is the rotor area.

- Calculate the standard deviation of resonant nacelle displacement according to

$$\frac{\sigma_{x1}}{\bar{x}_1} = 2 \frac{\sigma_u}{\bar{U}} \frac{\pi}{\sqrt{2\delta}} \sqrt{R_u(n_1)} \sqrt{K_{Sx}(n_1)} \quad [\text{see Eq.(5.7)}].$$

- Calculate the ratio λ_{M1} , which relates the ratio of the standard deviation of resonant tower base moment to the mean value to the corresponding ratio for nacelle displacement as follows:

$$\frac{\sigma_{M1}}{\bar{M}} = \lambda_{M1} \frac{\sigma_{x1}}{\bar{x}_1} \quad [\text{see Eq.(5.8a)}]$$

If $\mu_1(r)$ is set to unity for the rotor, λ_{M1} is given by

$$\lambda_{M1} = \frac{\int_0^H m(z)\mu_1(z).z dz \left\{ C_D A_R + \int_0^H C_f \left[\frac{U(z)}{\bar{U}} \right]^2 d(z)\mu_1(z) dz \right\}}{m_{T1} H \left\{ C_D A_R + \int_0^H C_f \left[\frac{U(z)}{\bar{U}} \right]^2 d(z) \frac{z}{H} dz \right\}} \quad (5.127a)$$

where z is the height up the tower measured from the base, $d(z)$ is the tower diameter at height z and H is the hub height. If the loading on the tower is relatively small, this approximates to

$$\lambda_{M1} = \frac{\int_0^H m(z)\mu_1(z).z dz}{m_{T1}.H} \quad (5.127b)$$

which is close to unity because the tower head mass dominates the integral.

5. Calculate the size reduction factor for the root bending moment quasi-static or background response, K_{SMB} , which reflects the lack of correlation of the wind fluctuations along the blades and tower. K_{SMB} may be derived from a similar expression to that for the resonant size reduction factor given in Eq. (5.125) but with the exponential function modified to $\exp[-s/0.3L_u^x]$.
6. Calculate the peak factors for the combined (i.e. resonant plus quasi-static) and quasi-static responses in terms of the respective zero up-crossing frequencies. [In estimating the zero up-crossing frequency of the quasi-static response, the blade area should be replaced by the rotor area in Eq. (A5.57).]
7. Substitute the parameter values derived in steps 1–6 into Eq. (5.17) to obtain the dynamic factor, Q_D .

In the case of a rotor that is allowed to idle when shut down, turbine geometry is continually changing as the rotor rotates to and fro in response to wind gusts, so the calculation of resonant tower excitation, should it occur, becomes a complex undertaking.

5.12.3 Operational loads due to steady wind (deterministic component)

Tower fore and aft bending moments result from rotor thrust loading and rotor moments. The moments acting on the nacelle due to deterministic rotor loads have already been described in Section 5.11.1. Although the thrust loads on individual blades vary considerably with azimuth as a result of yaw misalignment, shaft tilt, or wind shear, the fluctuations on different blades balance each other, so that the total rotor thrust shows negligible azimuthal variation as a result of these effects. For example, on two bladed machines, a wind shear exponent of 0.2 results in a rotor thrust variation of about $\pm 1\%$.

Tower shadow loading results in a sinusoidal tower top displacement at blade passing frequency – see Figure 5.32.

Figure 5.39 illustrates the variation of rotor thrust with wind speed for stall- and pitch-regulated 80 m diameter three bladed machines.

5.12.4 Operational loads due to turbulence (stochastic component)

Analysis in the frequency domain

Except near the top of the tower, the dominant source of fore-aft stochastic tower bending moments is rotor thrust. The standard deviation of rotor thrust can be expressed in terms of the turbulence intensity and the cross-correlation function between wind fluctuations at different points on the rotor, following the method used for deriving the standard deviation of stochastic blade root bending moment in Section 5.7.5. As before, a linear relation between the wind fluctuations and the resultant load fluctuations is assumed, so that the perturbation of loading per unit length of blade, q , at radius r is given by

$$q = \frac{1}{2} \rho \Omega r c(r) \frac{dC_L}{d\alpha} u \quad [\text{see Eq.(5.25)}]$$

and the perturbation of rotor thrust by

$$\Delta T = \left(\frac{1}{2} \rho \Omega \frac{dC_L}{d\alpha} \right) \oint u c(r) r dr \quad (5.128)$$

where the integral sign \oint signifies that the integration is carried out over the whole rotor. Hence the following expression for the variance of the rotor thrust is obtained:

$$\sigma_T^2 = \left(\frac{1}{2} \rho \Omega \frac{dC_L}{d\alpha} \right)^2 \sigma_u^2 \oint \oint \rho_u^o(r_1, r_2, 0) c(r_1) c(r_2) r_1 r_2 dr_1 dr_2 \quad (5.129)$$

where $\rho_u^o(r_1, r_2, 0)$ is the normalised cross-correlation function, $\kappa_u^o(r_1, r_2, 0)/\sigma_u^2$ for points at radii r_1 and r_2 on the same or on different blades. $\kappa_u^o(r_1, r_2, 0)$ is given by Eq. (5.51), with $\Omega\tau$ replaced by the phase angle between the two blades on which are r_1 and r_2 .

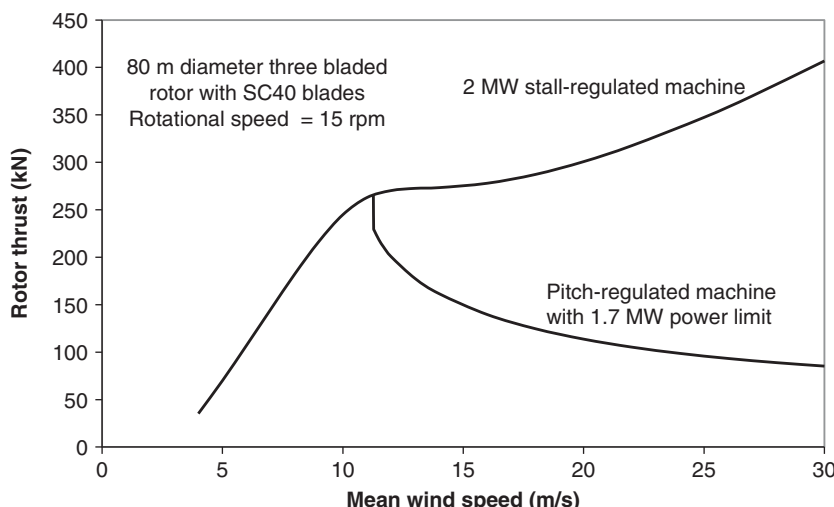


Figure 5.39 Rotor thrust during operation in steady, uniform wind: variation with wind speed for similar stall-regulated and pitch-regulated machines.

measured. For a three bladed, 80 m diameter rotor and an integral length scale of 147 m, the reduction in the standard deviation of the stochastic rotor thrust fluctuations is about 20% due to the lack of correlation of the wind speed variations over the rotor. If the machine is rotating at 15 rpm in an 8 m/s wind and the turbulence intensity is 20%, the rotor thrust standard deviation will be about 38 KN – i.e. 22% of the steady value.

The derivation of the expression for the power spectrum of rotor thrust parallels that for the power spectrum of blade root bending moment (Section 5.7.5), yielding

$$S_T(n) = \left(\frac{1}{2} \rho \Omega \frac{dC_L}{d\alpha} \right)^2 \oint \oint S_{uJ,K}^o(r_1, r_2, n) c(r_1) c(r_2) r_1 r_2 dr_1 dr_2 \quad (5.130)$$

where $S_{uJ,K}^o(r_1, r_2, n)$ is the rotationally sampled cross-spectrum for points at radii r_1 and r_2 on blades J and K, respectively. Note that on a machine with three blades, A, B, and C, $S_{uJ,K}^o(r_1, r_2, n)$ is complex when J and K are different, but $S_{uA,B}^o(r_1, r_2, n)$ and $S_{uA,C}^o(r_1, r_2, n)$ are complex conjugates, so the double integral in Eq. (5.130) is still real. An example power spectrum of rotor thrust for an 80 m diameter three bladed machine is shown in Figure 5.40. It can be seen that there is some concentration of energy at the blade passing frequency of 0.75 Hz due to gust slicing, but that the effect is not large. The concentration effect is significantly greater for two blade machines – see Figure 5.41. This shows the power spectrum of rotor thrust for a two bladed machine with the same blade plan-form but rotating 22.5% faster to give comparable performance.

In addition to thrust fluctuations, longitudinal turbulence will also cause rotor torque fluctuations and in-plane rotor loads due to differential loads on different blades, both of which will result in tower sideways bending moments. The expression for the in-plane component of aerodynamic lift per unit length, $-F_Y(r) = \frac{1}{2} \rho W^2 C_L c(r) \sin \phi$, can be differentiated with respect to the wind fluctuation as follows:

$$\begin{aligned} -\frac{dF_Y}{du} &= \frac{1}{2} \rho c(r) \frac{d}{du} [W^2 \sin \phi \cdot C_L] \\ &= \frac{1}{2} \rho c(r) \frac{d}{du} [W \{ U_\infty (1 - a) + u \} C_L] \cong \frac{1}{2} \rho c(r) W \left[C_L + \sin \phi \frac{dC_L}{d\alpha} \right] \end{aligned}$$

so, approximately,

$$-\frac{dF_Y}{du} = \left(\frac{1}{2} \rho \Omega \frac{dC_L}{d\alpha} \right) c(r) \cdot r \left[\frac{C_L}{dC_L/d\alpha} + \sin \phi \right] \quad (5.131a)$$

Thus the standard deviation of rotor torque is approximately given by

$$\sigma_Q = \left(\frac{1}{2} \rho \Omega \frac{dC_L}{d\alpha} \right) \sigma_u \left\{ \oint r^2 c(r) \left[\frac{C_L}{dC_L/d\alpha} + \sin \phi \right] dr \right\} \quad (5.131b)$$

[which parallels Eq.(5.26)] provided the relationship between blade loading and wind speed fluctuation remains linear and the turbulence length scale is large compared with rotor diameter. Eq. (5.131b) can be used to derive an expression for the variance of the rotor torque in the same way as for rotor thrust above. At the top of the tower the stochastic M_X (i.e. side-to-side) moment due to rotor torque fluctuations is typically of the same order of magnitude as the stochastic M_Y (i.e. fore-aft) moment due to differential out-of-plane loads on the rotor, but at the tower base the dominant effect of

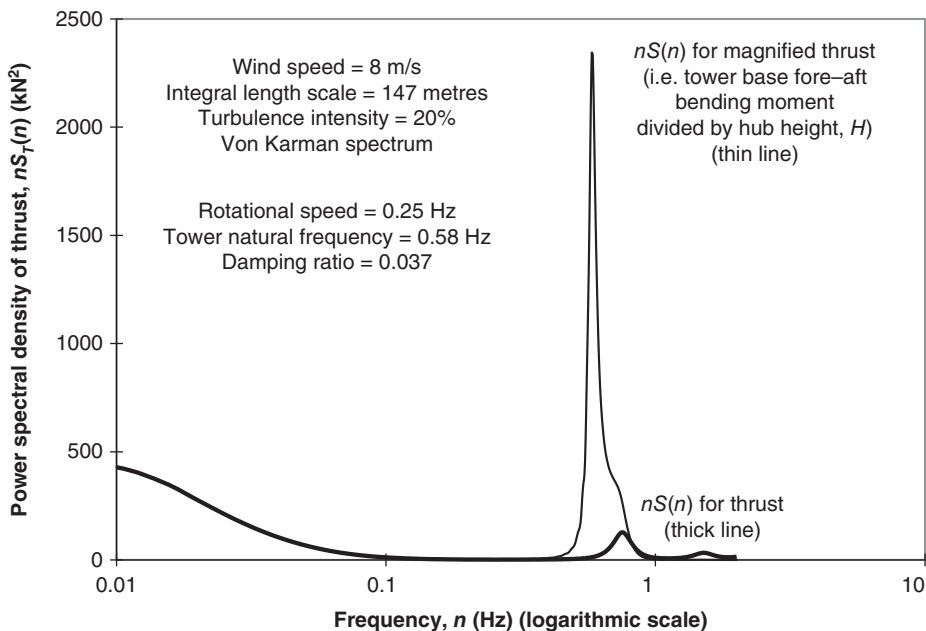


Figure 5.40 Power spectra of rotor thrust and resultant tower base fore-aft bending moment for three bladed, 80 m diameter turbine.

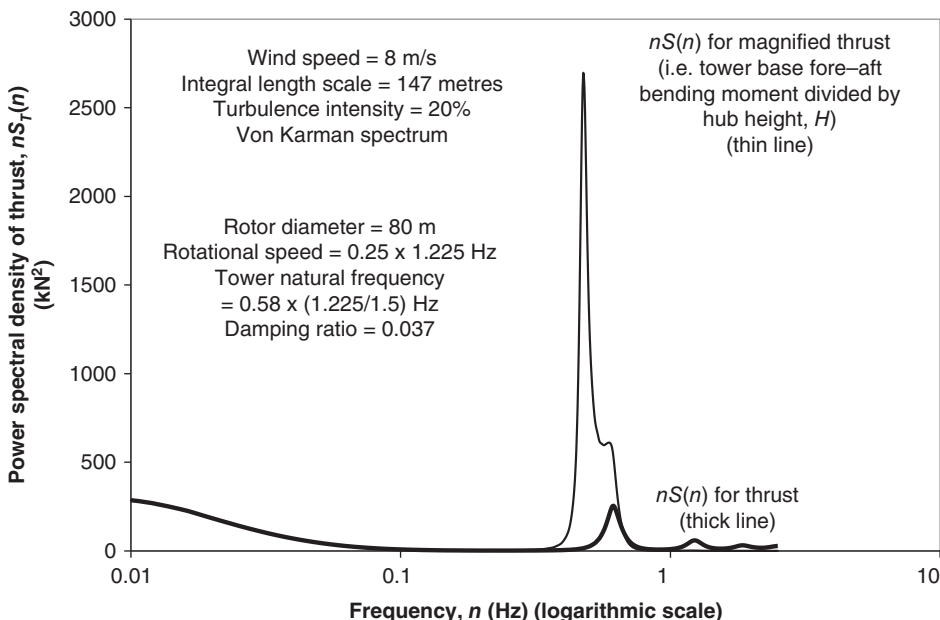


Figure 5.41 Power spectra of rotor thrust and resultant tower base fore-aft bending moment for two bladed, 80 m diameter turbine.

rotor thrust loading means that the stochastic side-to-side moments are usually significantly less than the stochastic fore-aft moments before the excitation of tower resonance is taken into account.

Analysis in the time domain

As noted in Section 5.7.5, there are situations, such as operation in stalled flow, when the linear relationship between blade loading and wind speed fluctuations required for analysis in the frequency domain does not apply. In these cases, recourse must be made to analysis in the time domain using wind simulation techniques such as described in Section 5.7.6.

5.12.5 Dynamic response to operational loads

The power spectrum of rotor thrust will usually contain some energy at the tower natural frequency, leading to dynamic magnification of deflections and hence of tower bending moments. The power spectrum of hub deflection, $S_{x1}(n)$, resulting from the excitation of the tower first fore-aft flexural mode, is related to the power spectrum of rotor thrust by

$$S_{x1}(n) = \frac{S_T(n)}{k_1^2} \frac{1}{[(1 - n^2/n_1^2)^2 + 4\xi_1^2 n^2/n_1^2]} \quad (5.132)$$

This relation is analogous to Eq. (5.90) and derived in the same way.

The amplitude of tower base fore-aft moment at resonance in the first mode, M_{Y1} , can be derived from the corresponding amplitude of hub deflection, x_{H1} , as follows

$$M_{Y1} = \omega_1^2 x_{H1} \int_0^H m(z) \mu(z) z dz = \omega_1^2 x_{H1} m_{T1} H \frac{\int_0^H m(z) \mu(z) z dz}{H \int_0^H m(z) \mu^2(z) dz} \quad (5.133)$$

The quotient on the right hand side is close to unity because of the dominance of the tower head mass, so, substituting k_1 for $\omega_1^2 m_{T1}$, the equation reduces to $M_{Y1} = x_{H1} k_1 H$, which applies at any exciting frequency. Hence the power spectrum for the tower base fore-aft bending moment due to rotor thrust loading is given by

$$S_{My1}(n) = S_T(n) H^2 \frac{1}{[(1 - n^2/n_1^2)^2 + 4\xi_1^2 n^2/n_1^2]} \quad (5.134)$$

The aerodynamic damping is almost entirely provided by the rotor, the damping ratio for the first tower mode being approximately

$$\xi_{a1} = B \frac{\frac{1}{2} \rho \Omega \int_0^R \frac{dC_l}{d\alpha} r c(r) dr}{2m_{T1}\omega_1} \quad (5.135)$$

where B is the number of blades (see Section 5.8.4). The overall damping ratio is obtained by adding this to the structural damping ratio for the tower (see Table 5.5) and is generally low compared to the blade first mode damping because of the large tower head mass. The effect of a low damping ratio is illustrated by the power spectrum of fore-aft tower bending moment shown in Figure 5.40, which has a very high peak at the tower natural frequency of 0.58 Hz, despite this frequency being somewhat removed from the blade passing frequency of 0.75 Hz. The damping ratio is calculated as 0.037, consisting of

0.035 due to aerodynamic damping (based on a tower head mass of 120 t) and 0.002 due to structural damping (for a welded steel tower).

In the example shown in Figure 5.40, the tower dynamic response increases the standard deviation of the tower base fore-aft bending moment by 9%. However, the effect of tower dynamic response results in a larger increase of 15% in the case of the two bladed machine featured in Figure 5.41, despite the reduction in tower natural frequency to maintain the same tower natural frequency to blade passing frequency ratio. The magnitude of the stochastic thrust loading at blade passing frequency in relation to the steady thrust is considered in Section 6.14.1.

It is important to note that the rotor provides negligible aerodynamic damping in the side-to-side direction, so that effectively the only damping present is the structural damping. This means that, even though the side-to-side loadings are small in relation to the fore-aft loads, the side-to-side tower moment fluctuations can sometimes approach the fore-aft ones in magnitude.

5.12.6 Fatigue loads and stresses

The tower moments at height z are related to the hub-height loads as follows, omitting the tower inertial loads:

$$\begin{aligned} M_Y(z, t) &= F_X(H, t).(H - z) + M_Y(H, t) & M_X(z, t) &= -F_Y(H, t).(H - z) + M_X(H, t) \\ M_Z(z, t) &= M_Z(H, t) \end{aligned} \quad (5.136)$$

For three bladed machines, the five hub-height fatigue loads are almost entirely stochastic, because the deterministic load component is either constant (for a given mean wind speed) or negligible, and it is instructive to consider how they relate to one another. Recognising that the centre of any gust lying off the rotor centre will be located at a random azimuth, then it is clear that the rotor out-of-plane loads – that is, the moment about the horizontal axis, $M_Y(H, t)$, the hub moment about the vertical axis, $M_Z(H, t)$, and the rotor thrust, $F_X(H, t)$ – will all be statistically independent of each other. The same will apply to the rotor in-plane loads – the rotor torque, $M_X(H, t)$, and the sideways load, $F_Y(H, t)$. However, as the out-of-plane and in-plane loads on a blade element are both assumed to be proportional to the local wind speed fluctuation, u , it follows that the rotor torque fluctuations will be in phase with the rotor thrust fluctuations, and the rotor sideways load fluctuations will be in phase with the fluctuations of the hub moment about the horizontal axis, $M_Y(H, t)$.

The preceding relationships have implications for the combination of fatigue loads. Clearly the power spectrum of the fore-aft tower moment at height z , $S_{M_X}(z, n)$, can be obtained by simply adding the power spectrum of the hub moment about the horizontal axis to $(H - z)^2$ times the power spectrum of the rotor thrust. Similarly, the power spectrum of the side-to-side tower moment at height z , $S_{M_Y}(z, n)$, can be obtained by adding the power spectrum of the rotor torque to $(H - z)^2$ times the power spectrum of the rotor sideways load.

Having obtained power spectra for the M_X , M_Y , and M_Z moments at height z , the corresponding fatigue load spectra can be derived with reasonable accuracy by means of the Dirlitk method described in Section 5.9.3. As the tower stress ranges will be enhanced by tower resonance, the input power spectra should incorporate dynamic magnification,

as outlined in Section 5.12.5. Ragan and Manuel (2007) compared fatigue loads calculated in the frequency and time domains (see Section 5.9.3) and concluded that the Dirlit method performed very well in estimating tower fatigue bending moments for the case investigated.

Fatigue stress ranges due to bending about the two axes can easily be calculated separately from the $M_X(z)$ and $M_Y(z)$ fatigue spectra, but the stress ranges due to the two fatigue spectra combined cannot be calculated precisely because of lack of information about phase relationships. However, as noted above, the $M_X(H)$ component of the $M_X(z)$ fluctuations is in phase with the $F_X(H)$ component of the $M_Y(z)$ fluctuations, and the $F_Y(H)$ component of the $M_X(z)$ fluctuations is in phase with the $M_Y(H)$ component of the $M_Y(z)$ fluctuations so the stress ranges due to the $M_X(z)$ and $M_Y(z)$ fatigue spectra combined can be conservatively calculated as if they were in phase too. Theoretically, this means pairing the largest $M_X(z)$ and $M_Y(z)$ loading cycles, the second largest, the third largest, and so on, right through the fatigue spectra, and calculating the stress range resulting from each pairing. In practice, of course, the $M_X(z)$ and $M_Y(z)$ load cycles are distributed between two sets of equal size ‘bins’, so they have to be reallocated to bins in a 2-D matrix of descending load ranges, as shown in the grossly simplified example given in Tables 5.8 and 5.9:

For a circular tower, the stress ranges would have to be computed at several points around the circumference to identify the location (with respect to the nacelle axis) where the fatigue damage was maximum.

A simpler but potentially cruder approach to the combination of the two fatigue spectra is to use the ‘damage equivalent load’ method. This involves the calculation of constant amplitude fatigue loadings, $M_{X,Del}$ and $M_{Y,Del}$, of, say 10^7 cycles each, that would, respectively, produce the same fatigue damages as the M_X and M_Y spectra, using the $S-N$ curve appropriate to the fatigue detail under consideration. If the M_X and M_Y fluctuations are treated as being in-phase as before, the combined ‘damage equivalent load’ moment is $\sqrt{M_{X,Del}^2 + M_{Y,Del}^2}$.

Table 5.8 Example M_X and M_Y fatigue spectra.

ΔM_Y (KNm)	No. of ΔM_Y cycles	ΔM_X (KNm)	No. of ΔM_X cycles
200–300	5	100–150	10
100–200	15	50–100	40
0–100	80	0–50	50

Table 5.9 Joint M_X and M_Y cycle distribution.

ΔM_X (KNm)	ΔM_Y (KNm)			Total no. of M_X cycles
	200–300	100–200	0–100	
100–150	5	5		10
50–100		10	30	40
0–50			50	50
Total no. of M_Y cycles	5	15	80	

5.13 Wind turbine dynamic analysis codes

A large modern turbine is a complex structure. Relatively sophisticated methods are required to predict the detailed performance and loading of a wind turbine. These methods should take into account:

- The aerodynamics of the rotating blade, including induced flows (i.e. the modification of the flow field caused by the turbine itself), 3-D flow effects, and dynamic stall effects when appropriate.
- Structural analysis of the blades, drive train, and tower, allowing their vibrational dynamics to be modelled.
- Aeroelastic feedback, i.e. the modification of the aerodynamic forces due to the vibrational velocities of the structure.
- Dynamic response of subsystems such as the generator, yaw system, and blade pitch control system.
- Control algorithms used during normal operation, start-up, and shut-down of the turbine.
- Temporal and spatial variations of the wind field impinging on the turbine, including the 3-D structure of the turbulence itself.

For offshore wind turbines, this should be extended to include:

- Hydrodynamic forces on the submerged structure.
- Hydroelastic feedback, i.e. the modification of the hydrodynamic forces due to the vibrational velocities of the structure.

Starting from a wind turbulence spectrum, it is possible to develop techniques in the frequency domain that account for many of these aspects, including rotational sampling of the turbulence by the blades, the response of the structure, and the control system. These techniques are set out in Sections 5.7.5, 5.8.6, 5.12.4, and elsewhere. However, although frequency-domain methods are elegant and computationally efficient, they can only be applied to linear time-invariant systems and therefore cannot deal with some important aspects of wind turbine behaviour, such as

- Stall aerodynamics and hysteresis.
- Non-linearities in sub-systems such as bearing friction and pitch rate limits.
- Non-linear aspects of control algorithms.
- Variable-speed operation.
- Start-up and shut-down.

As a result, time-domain methods almost exclusively are now used for wind turbine design calculations. The ready availability of computing power means that the greater computational efficiency of frequency-domain methods is no longer such an important consideration.

A number of codes are available commercially for the calculation of wind turbine performance and loads using time-domain simulations. These simulations use numerical techniques to integrate the equations of motion over time, by subdividing the time into short timesteps as described in Section 5.8.5. In this way, all the non-linearities and non-stationary aspects of the system, such as those listed above, can be dealt with to any desired level of accuracy. A useful early comparative survey of such codes was given by Molenaar and Dijkstra (1999).

As explained in Section 5.8.5, there are a number of different algorithms or solvers for integrating the equations of motion. Some use a fixed timestep h (which has to be short enough to account for all modal frequencies that are considered important), while others use a variable timestep that is continually adjusted during the simulation, keeping it as long as possible to maximise simulation speed while still keeping all the integrated states within a certain error tolerance.

The use of variable timestep methods also allows accurate modelling of discontinuities, because close to a discontinuity the timestep can be adjusted to find the exact moment when the characteristics of the system change. Discontinuities can occur for many reasons: for example, stick-slip friction (of pitch and yaw bearings, shaft brake, slipping clutch, etc.), grid loss, faults, controller or safety system actions, etc. Note that the equations of motion and structural resonant frequencies change at the moment when a friction element like a brake changes from slipping to sticking.

On the other hand, these codes can provide a valuable way to test turbine controllers, linking the real controller to the simulation model, which acts as a ‘virtual turbine’, and in this case a fixed timestep may be more appropriate, to allow regular communication with the controller running in real time and to ensure that the calculations for each timestep are completed within that real-time interval. Necessarily this may mean a loss of accuracy in predicting the effect of higher frequency modes and discontinuities. As an example, the *Bladed* code mentioned below normally uses a variable timestep but also provides a fixed step option for real-time applications such as controller testing.

Two principal approaches to the modelling of structural dynamics are embodied in time-domain simulation packages. Some use a full finite element representation of the structure, which is broken down into small elements. The equations of motion are solved for each element, with boundary conditions matched at the interfaces between elements. An example of such a code is Adams-WT (Hansen, 1998), which consists of a general purpose finite element code (Adams) interfaced to an aerodynamic module.

The other main approach is the modal analysis method as described in Section 5.8.1, in which simple finite element methods are used to predict just the first few modes of vibration of the main components, such as the rotor blades and the tower. These are typically modelled as beam elements, but it is important to include geometric stiffening effects so that, for example, the centrifugal stiffening of the blades is taken into account, i.e. the increase in apparent stiffness with rotational speed due to the effect of centrifugal force on the element mass. Additional degrees of freedom are added as required, for example, for the drive train rotation and torsion, pitch and yaw motion, etc. The equations of motion are then derived for the entire coupled system. Traditionally this can be done by constructing the Lagrangian for the system including all degrees of freedom. With full rotation of the yaw bearing on top of a flexible tower, and then full rotation of the rotor (also flexible) about the shaft axis, the coordinate transformations involved mean that the equations rapidly become very large, usually requiring some form of symbolic

processing to derive them in an automated way. More recently, methods based on the approach of multi-body dynamics (see, for example, Shabana 1998) have been used. This provides a generalised way to link together the separate equations of motion of each rigid or flexible component by means of defined linking elements, including rigid links, revolute hinges, sliding joints, etc. This is a very powerful technique that is readily extended to structures of arbitrary complexity. Using a technique originally proposed by Craig and Bampton (1968), the mode shapes of each modal component can be defined in a way that is independent of any other component to which it is attached.

One example of a widely used commercial code based on the component mode approach is *Bladed* (DNVGL 2020) developed by Garrad Hassan. Originally built using a Lagrangian approach, this code has recently been converted to use a multi-body approach. Beam-element models for the blades and tower are combined with elements representing other components of the transmission system, the yaw and pitch actuators, etc. The control system, which has a major influence on the performance as well as the loads, can be modelled in full detail. The code can also model the electrical generator and power converter, allowing detailed calculations of turbine response to network faults, generator short-circuit faults, etc. in a fully integrated way. Interfaces are provided to link in more detailed models of subcomponents, such as gearboxes. For most calculations this level of detail is not required, but where certain load cases are critical for the particular component, it may be useful to be able to run a more detailed model.

By using a limited number of modes, the modal approach results in rapid calculations, so that a complete set of design or certification load cases, typically amounting to several hundred load cases each consisting of a 10 minute simulation, can be run in a few hours on a standard desktop computer. A small number of modes is generally adequate for predicting the loads: the higher frequency modes generally have little effect. However, to model the deflections accurately it would be necessary to model more modes, because the modelled deflection is a linear combination of the mode shapes used, and a small number of mode shapes may not be sufficient to model the actual deflected shape. Rather than using more modes, the static improvement technique can be used (Barltrop and Adams 1991): effectively the calculated loading is used as if it were a static load, and it is combined with the stiffness matrix to recalculate the deflections.

The modal approach generally assumes that all deflections of the flexible bodies remain small. More complex non-linear beam-element models are being developed to help increase accuracy in case of larger deflections, such as may be found with very flexible blades. Alternatively, the non-linearity can be captured by modelling the blade as a number of shorter linear beam elements joined end to end.

For the aerodynamics, all of these codes generally use BEM theory as described in Chapter 3, as this is currently the only way to achieve rapid enough simulations for the standard sets of calculations that are normally needed. More advanced aerodynamic methods such as vortex wake and panel methods are starting to be used to examine specific cases where BEM is not sufficiently accurate. This might include highly yawed flow, tip vanes, ducted rotors, or the need to understand the aerodynamic interaction between the blades and the nacelle, for instance. Ultimately, computational fluid dynamics (CFD) methods based on direct solution of the Navier–Stokes equations could be used, and some general commercial CFD codes are now available, but these methods are still far too slow and cumbersome to be useful except perhaps to examine very special cases in detail.

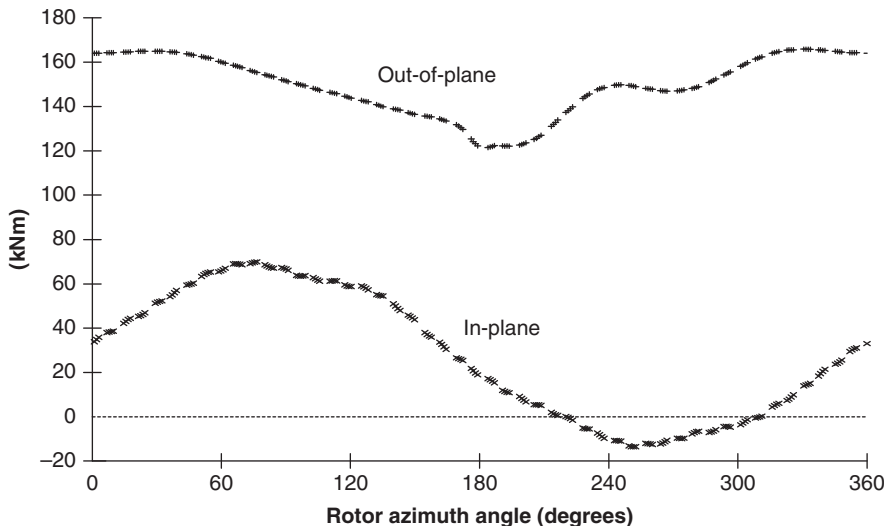


Figure 5.42 Blade root bending moment in steady wind.

It is important to be able to simulate 3-D turbulent wind fields because the dynamic wind speed variations across the rotor are of major importance in determining the loads. The Veers method (Veers 1988) as described in Section 5.7.6 is a convenient way to do this: a random number sequence is filtered using a representation of the spectrum and spatial coherence of the turbulence to generate a 3-D wind field that is consistent with the chosen spectral model. This method is used by the codes mentioned above. *Bladed* also incorporates a different technique due to Mann (1998), which generates a turbulence field by means of a 3-D inverse FFT of the 3-D wavenumber spectrum (see Chapter 2). For offshore turbines, *Bladed* uses a related method to generate stochastic wave time histories impacting on the submerged part of the structure, in addition to the loading from water currents. As with aerodynamics, hydrodynamic forces opposing the vibrational velocities of structural members provide some damping. When the turbine is running, rotor aerodynamic damping dominates over the hydrodynamic damping for reducing fore-aft vibrations, but hydrodynamic damping can help in other situations, including when jacket brace members are excited by a harmonic of rotor rotational frequency.

Jamieson et al. (2000) have demonstrated that if wind and wave loading are treated in isolation from each other, an overconservative design is likely to result.

The use of sophisticated calculation methods such as those described above are now mandatory for the certification of wind turbines, particularly at the larger sizes. A few illustrative examples of results obtained with *Bladed* are described below.

Figure 5.42 shows a *Bladed* simulation of the in- and out-of-plane bending moments at the root of one of the blades, during operation in steady, sheared wind. The in-plane moment is almost a sinusoidal function of azimuth, being dominated by the gravity loading due to the self-weight of the blade that, relative to the blade, changes direction once per revolution. The mean is offset from zero because of the mean positive aerodynamic torque developed by the blade. There is a slight distortion of the sinusoid, partly because of the variation of aerodynamic torque due to wind shear and the effect of tower shadow, and partly because of the effect of structural vibrations.

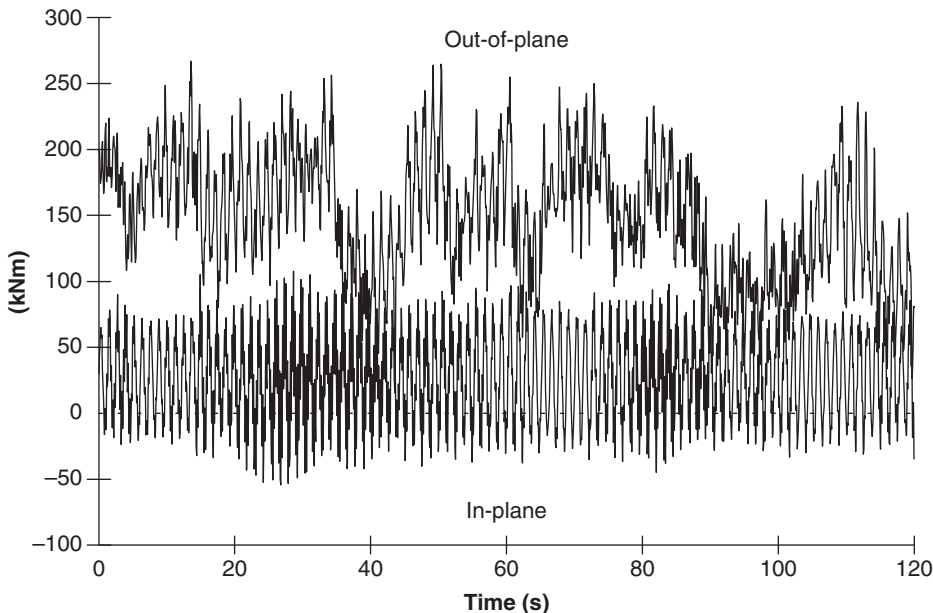


Figure 5.43 Blade root bending moment in turbulent wind for a fixed rotational-speed machine.

The out-of-plane moment is always positive, the mean value being dominated by the aerodynamic thrust on the blade. There is a systematic variation with azimuth resulting from the wind shear, giving a lower load at 180° azimuth (bottom dead centre) than at 0° . A sharp dip at 180° is also visible, and this is the effect of the tower shadow (the reduction in wind speed in the vicinity of the tower). The blade out-of-plane vibrational dynamics contribute a significant higher frequency variation.

In turbulent wind, the loads take on a much more random appearance, as shown in Figure 5.43. The out-of-plane load in particular is varying with wind speed and, as this is a pitch-controlled machine, with pitch angle. The in-plane load is more regular, because it is always dominated by the reversing gravity load.

Spectral analysis provides a useful means of understanding these variations. Figure 5.44 shows auto-spectra of the blade root out-of-plane bending moment and the hub thrust force. The out-of-plane bending moment is dominated by peaks at all multiples of the rotational frequency of 0.8 Hz. These are caused mainly by the rotational sampling of turbulence by the blade as it sweeps around, repeatedly passing through turbulent eddies. Wind shear and tower shadow also contribute to these peaks. A small peak due to the first out-of-plane mode of vibration at about 3.7 Hz is just visible. There is also a significant effect of the first tower fore-aft mode of vibration at about 0.4 Hz.

This tower effect is also visible in the spectrum of the hub thrust force. However, this force is the sum of the shear forces at the roots of the three blades. These forces are 120° out of phase with each other, with the result that the peak at the rotational frequency (1P) is eliminated, as are the peaks at multiples of this frequency such as 2P, 4P, etc. Only the peaks at multiples of 3P remain, because the loads on the three blades all have the same phase with respect to the 3P cycles.

This effect is even more significant in the in-plane load spectra (Figure 5.45). Of the blade load peaks at multiples of 1P, only the relatively small peaks at 3P and 6P come

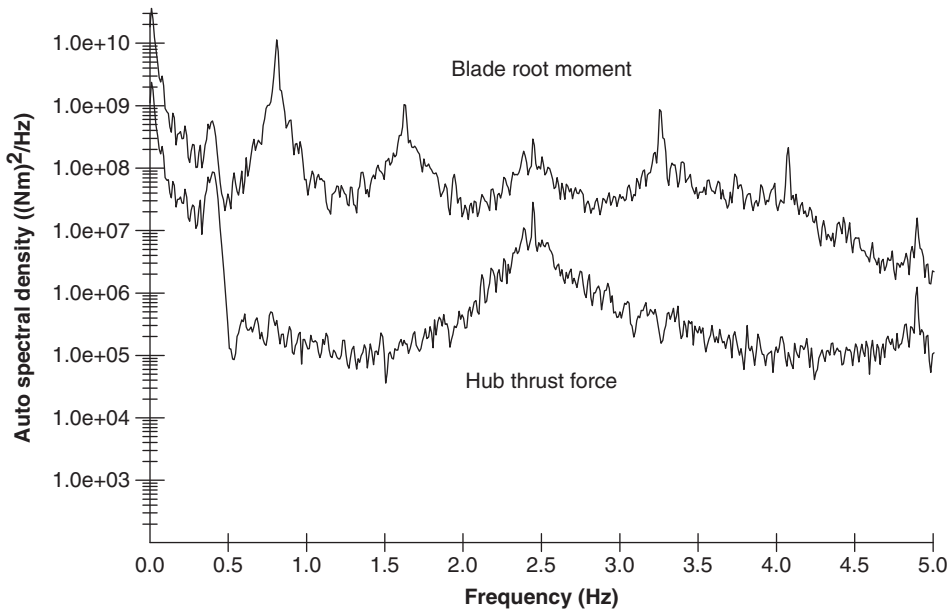


Figure 5.44 Spectra of out-of-plane loads in turbulent wind.

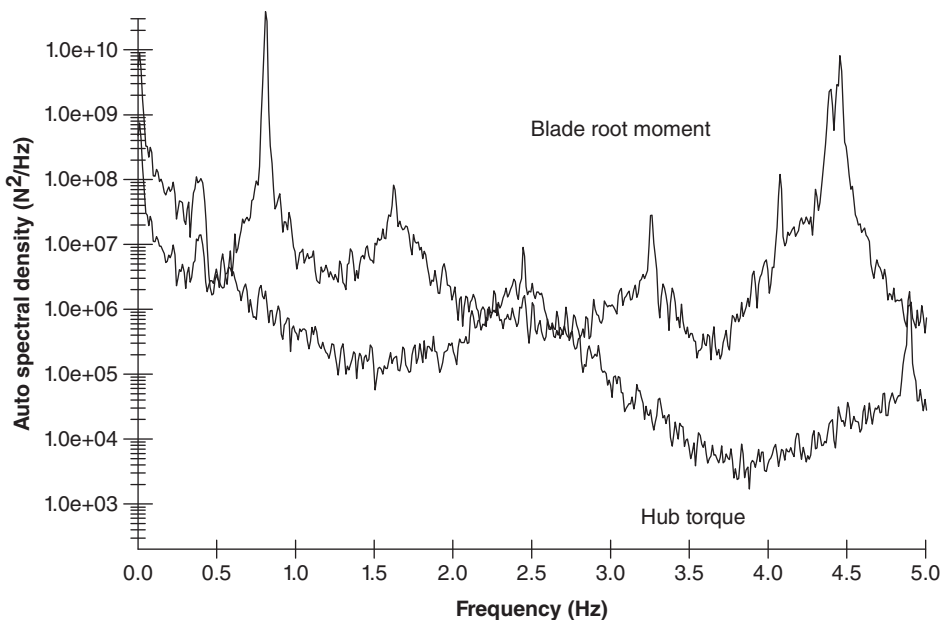


Figure 5.45 Spectra of in-plane loads in turbulent wind.

through to the hub torque. The 1P peak in the blade load, which is dominated by gravity, is particularly large, but it is completely eliminated from the hub torque. The tower peak at 0.4 Hz is visible in both loads. A large blade load peak at the first in-plane blade vibrational mode at 4.4 Hz is also seen, but this is a mode that does not include any rotation at the hub and consequently is not seen in the hub torque. Some higher frequency blade modes (not shown) will be coupled with hub rotation.

5.14 Extrapolation of extreme loads from simulations

In the case of load case 1.1 (normal operation in a turbulent wind), IEC 61400-1 edition 4 requires the characteristic blade root out-of-plane and in-plane bending moments and the characteristic tip deflection to be determined by statistical extrapolation of the extreme values of the load time series output from the simulations. For simulations of 10 minutes' duration, the characteristic value is defined as that with a 3.8×10^{-7} probability of exceedance – i.e. the load with a return period of 50 years. This section considers ways in which the load exceedance probability distribution can be derived from the simulations and extrapolated to the 3.8×10^{-7} value. As it is more convenient to work with load *non-exceedance* probability distributions – otherwise known as *cumulative distribution functions* – the following discussion is in these terms, using the notation $P(X \leq x) = F(x)$.

There are two sequences that can be followed to assemble a single load probability distribution from simulation data from different wind speed bins:

- Derivation of load non-exceedance probability distributions for each wind speed bin followed by combination of these distributions in proportion to the operating time in each bin ('fitting before aggregation').
- Aggregation of results from all wind speed bins, with the number of simulations per bin proportional to the hours of operation in each bin, followed by the derivation of a single load non-exceedance probability distribution ('aggregation before fitting').

It is also necessary to decide how many extreme values from each simulation are to be utilised. In the 'global extremes' method, only the largest extreme value in each 10 minute simulation – i.e. the global extreme – is used in the construction of the load non-exceedance probability distribution, but in the 'local extremes' method, all extreme values that can be considered independent are utilised. The local extremes method would appear to be more attractive, because it uses much more of the available data, but it throws up the problem of establishing a criterion for independence.

The various stages of the 'fitting before aggregation' sequence using the global extremes method are considered first.

5.14.1 Derivation of empirical cumulative distribution function of global extremes

Each 10 minute time series will yield a maximum value of the load under investigation, and, for n 10 minute simulations at a particular wind speed, there will be n such global extremes, which can be ranked $1, 2, \dots, i, \dots, n_k$ from smallest to largest. An empirical non-exceedance probability distribution for the 10 minute extreme load, x_k , at wind

speed U_k can then be constructed as

$$F(x_{ki}|U_k) = \frac{i}{n_k + 1}, i = 1, 2, \dots n_k \quad (5.137)$$

Harris (1996) has shown that, if $F(x)$ is a known function of x , the mean of the L non-exceedance probabilities $F(x_i)$ for the i th extremes from L sets of n 10 minute simulations, derived from the x_i simulation results, tends to the value $\frac{i}{n+1}$ for L large.

5.14.2 Fitting an extreme value distribution to the empirical distribution

There are several extreme value distributions that can be fitted to the empirical probability distributions obtained from the simulations. These include the Gumbel distribution (also known as the *Fisher-Tippett I distribution*), which was introduced in the context of extreme wind speeds in Section 2.8, the log-normal distribution, the three parameter Weibull distribution, and the generalised extreme value (GEV) distribution, which are described in turn below.

a) **Gumbel distribution:**

The probability that the variable X will not exceed the value x is given by

$$P(X \leq x) = F(x) = \exp \left[-\exp \left(-\frac{x - x_o}{c} \right) \right] \quad (5.138)$$

where x_o is the most likely extreme value or the mode of distribution, c is the dispersion, and $y = (x - x_o)/c$ is termed the *reduced variate*.

This relationship is a straight line if $y = -\ln[-\ln(F(x))]$ is plotted against x , so a Gumbel distribution can be fitted to the empirical distribution by the method of least squares and the parameters x_o and c thereby determined. However, Harris (1996) has pointed out two defects of the classical least squares method.

First of all, the mean of the function that is plotted, $-\ln[-\ln(F(x_i))]$, is not the same as the double natural logarithm of the mean of $F(x_i)$ itself, given by Eq. (5.137). Harris provides a formula by which the mean of $-\ln[-\ln(F(x_i))]$, i.e. \bar{y}_v , may be evaluated when the data should conform to a Gumbel distribution – as follows:

$$\bar{y}_v = \frac{N!}{(\nu - 1)!(N - \nu)!} \int_0^1 -\ln[-\ln(z)] z^{N-\nu} (1-z)^{\nu-1} dz \quad (5.139)$$

In this formula, N is the number of data points ($= n_k$), and ν is the rank of data points with the *largest* first, so that $\nu = (N+1) - i$ and $z = F(x_\nu)$.

Secondly, the classical least squares method assumes that the variability of each plotted ordinate is of similar magnitude, whereas, for extreme value data, the variability of the reduced variate, y , is much greater for the largest values than for the others. Accordingly, Harris proposes weighting the data points in inverse proportion to the variance of the y values, before the least squares fitting is carried out.

Values of \bar{y}_v and its standard deviation are given in Table 5.10 for the case of $N=15$, consistent with the IEC 61400-1 edition 3 requirement for at least 15 10 minute simulations for wind speeds above rated. Values of y calculated by the standard Gumbel method are also included for comparison, and it is seen that the differences are

significant for the largest of the extremes. The Harris weighting factor is included in Table 5.10 in the last column. It is seen that, in general, the Harris method will result in a steeper straight line that is less influenced by the largest extremes.

An alternative method of fitting a straight line to the $-\ln[-\ln(F(x))]$ plot is the *method of statistical moments* (Moriarty et al. 2004), in which the first two statistical moments of the data – defined as the mean and the variance, respectively – are equated to analytical expressions for these moments. Thus, for the standard Gumbel distribution, $F(y) = \exp[-\exp(-y)]$, the PDF is $f(y) = \frac{dF(y)}{dy} = \exp[-y - \exp(-y)]$ and the mean is

$$\mu_y = \int_{-\infty}^{\infty} y f(y) dy = \int_{-\infty}^{\infty} y \cdot \exp[-y - \exp(-y)] dy = \gamma = 0.5772 \quad (5.140)$$

Similarly, the variance is

$$\sigma_y^2 = \int_{-\infty}^{\infty} (y - \mu_y)^2 f(y) dy = \int_{-\infty}^{\infty} (y - \mu_y)^2 \cdot \exp[-y - \exp(-y)] dy = \frac{\pi^2}{6} \quad (5.141)$$

Denoting the mean and the standard deviation of the dataset of extreme values as μ_x and σ_x , respectively, and noting that $y = (x - x_o)/c$, we obtain $\mu_y = (\mu_x - x_o)/c = 0.5772$ and $\sigma_y = \sigma_x/c = 1.2825$.

$$\text{Hence } c = \sigma_x/1.2825 \text{ and } x_o = \mu_x - c\mu_y = \mu_x - 0.5772 \frac{\sigma_x}{1.2825} = \mu_x - 0.450\sigma_x.$$

Figure 5.46 compares the three methods described above for fitting a straight line to empirical data on a Gumbel plot, for a dataset consisting of 15 global extremes of out-of-plane blade root bending moment, taken from 15 10 minute simulations of operation in a 12 m/s wind speed. Note that the straight lines derived using the Harris method and the method of moments appear less influenced by the largest values than those based on the least squares method.

b) **Log-normal distribution:**

In the log-normal distribution, the *logarithm* of the variable is normally distributed, so the probability distribution function of the variable x is

$$f(x) = \frac{1}{\sqrt{2\pi}\sigma_z x} \exp\left[-\frac{1}{2}\left(\frac{\ln(x) - \mu_z}{\sigma_z}\right)^2\right] \quad (5.142)$$

where μ_z and σ_z are the mean and standard deviation, respectively, of $z = \ln(x)$. The mean and standard deviation of the variable x itself, μ_x and σ_x , are given in terms of μ_z and σ_z as follows:

$$\mu_x = \exp[\mu_z + \sigma_z^2/2] \quad \sigma_x = \exp[\mu_z + \sigma_z^2/2] \sqrt{\exp(\sigma_z^2) - 1} = \mu_x \sqrt{\exp(\sigma_z^2) - 1} \quad (5.143)$$

The log-normal distribution parameters, μ_z and σ_z , can again be fitted to the extreme value data by the method of statistical moments, using

$$\sigma_z = \sqrt{\ln(1 + (\sigma_x/\mu_x)^2)} \text{ and } \mu_z = \ln(\mu_x) - \sigma_z^2/2 \quad (5.144)$$

derived from (5.143).

Table 5.10 Table of mean values of the reduced variate, $y_v = -\ln[-\ln(F(x_v))]$, its standard deviation, and the Harris weighting factor, w_v .

Rank, v (largest first)	Rank, i (smallest first)	$y_v = -\ln[-\ln((N+1-v)/(N+1))]$ $= -\ln[-\ln(i/(N+1))]$ (Gumbel method)	\bar{y}_v – Eq. (5.139) (Harris method)	σ_y – standard deviation of \bar{y}_v	Harris weighting factor, w_v
1	15	2.7405	3.2853	1.2825	0.0064
2	14	2.0134	2.2504	0.8031	0.0164
3	13	1.572	1.7133	0.6291	0.0266
4	12	1.2459	1.3404	0.5341	0.037
5	11	0.9816	1.0478	0.4726	0.0472
6	10	0.755	0.8019	0.4291	0.0573
7	9	0.5528	0.5852	0.3965	0.0671
8	8	0.3665	0.3873	0.3714	0.0765
9	7	0.1903	0.201	0.3518	0.0852
10	6	0.0194	0.0206	0.3366	0.0931
11	5	-0.1511	-0.1595	0.3254	0.0996
12	4	-0.3266	-0.3458	0.3184	0.104
13	3	-0.5152	-0.5485	0.317	0.1049
14	2	-0.7321	-0.7884	0.3257	0.0994
15	1	-1.0198	-1.1326	0.3648	0.0793

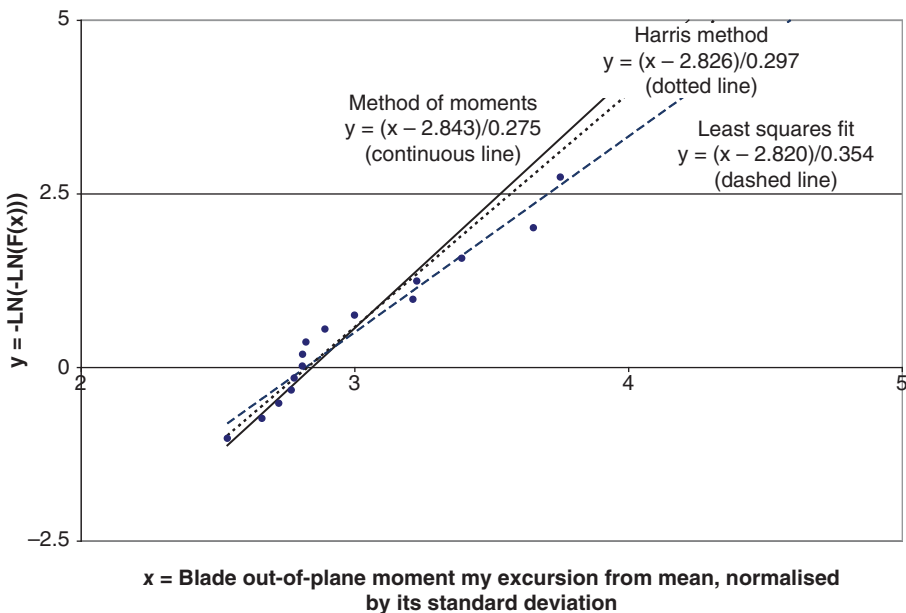


Figure 5.46 Comparison of techniques for fitting a straight line to empirical data on a Gumbel plot.

c) **Three parameter Weibull distribution:**

The three parameter Weibull distribution is defined as $P(Y \leq y) = F(y) = 1 - \exp[-y^\alpha]$, where $y = (x - x_o)/c$ as before, and $F(y)$ only applies to positive values of y . Hence the PDF, $f(y)$, is given by $\alpha y^{\alpha-1} \exp[-y^\alpha]$. The three parameters, x_o , c , and α , can be fitted to the data by the method of statistical moments described above, but in this case using the first three moments instead of the first two.

Using the shorthand $G_m(\alpha) = \frac{m}{\alpha} \Gamma\left(\frac{m}{\alpha}\right)$, where Γ is the gamma function, the first three statistical moments are as follows:

$$\begin{aligned}\mu_y &= G_1(\alpha) \\ \sigma_y^2 &= G_2(\alpha) - G_1^2(\alpha) \\ \eta_y \sigma_y^3 &= \int_{-\infty}^{\infty} (y - \mu_y)^3 f(y) dy = G_3(\alpha) - 3G_2(\alpha)G_1(\alpha) + 2G_1^3(\alpha)\end{aligned}\quad (5.145)$$

Note that η_y , the skewness parameter, is the third statistical moment normalised by the cube of the standard deviation.

d) **Generalised extreme value (GEV) distribution:**

The GEV distribution was introduced by Jenkinson in 1955 and is more versatile than the Gumbel distribution, because it allows the skewness of extreme value distributions to be modelled as well as their spread. It is defined as $P(Y \leq y) = F(y) = \exp[-\{1 - ky\}^{1/k}]$, where $y = (x - x_o)/c$ as before, and k is

the shape parameter, which determines the curvature of the distribution when it is plotted as $-\ln[-\ln(F(x))]$ against x . If k is positive, the curve is concave upwards and has an upper bound of $x_o + c/k$, whereas if k is negative, the curve is concave downwards and has a lower bound of $x_o + c/k$.

Hosking, Wallis, and Wood (1985) advocate the use of the method of probability weighted moments (PWMs) for fitting a GEV distribution to empirical data. For a probability distribution $F = F(x)$, with an inverse distribution function $x(F)$, PWMs β_0 , β_1 , and β_2 are defined by $\beta_r = \int_0^1 x(F)F^r dF$, and the parameters x_o , c , and k of the GEV are determined by equating the PWMs of the empirical data to the PWMs of the GEV.

The PWMs of the GEV are given by the formula $\beta_r = \frac{1}{r+1} \left[x_0 + \frac{c}{k} \left\{ 1 - \frac{\Gamma(1+k)}{(r+1)^k} \right\} \right]$ for $k > -1$, where Γ is the gamma function. This gives

$$\beta_0 = x_0 + \frac{c}{k} \{ 1 - \Gamma(1+k) \}, \quad 2\beta_0 - \beta_1 = \frac{c}{k} \Gamma(1+k)(1 - 2^{-k}) \text{ and } \frac{3\beta_2 - \beta_0}{2\beta_1 - \beta_0} = \frac{1 - 3^{-k}}{1 - 2^{-k}} \quad (5.146)$$

Solution of the last equation requires iterative methods, but Hosking et al. (1985) have shown that a good approximation for k is $7.8590C + 2.9554C^2$, where $C = \frac{2\beta_1 - \beta_0}{3\beta_2 - \beta_0} - \frac{\log 2}{\log 3}$. This value of k can then be substituted in the first two Eqs. (5.146) to obtain x_0 and c .

The PWMs of the empirical data can be estimated from the formula

$$\beta_r[p_{i,n}] = \frac{1}{n} \sum_{i=1}^n p_{i,n}^r x_i \quad (5.147)$$

where $p_{i,n}$ is the probability assigned to the i th global extreme, with ranking from smallest to largest. Hosking et al. propose two alternative expressions for use in estimating $p_{i,n}$ as follows:

$$\begin{aligned} p_{i,n} &= (i-a)/n, & 0 < a < 0.5 \\ p_{i,n} &= (i-a)/(n+1-2a), & -0.5 < a < 0.5 \end{aligned}$$

Another approach is to estimate the PWMs directly from the unbiased estimators b_r , given by

$$b_r = \frac{1}{n} \sum_{i=1}^n \frac{(i-1)(i-2)\dots(i-r)}{(n-1)(n-2)\dots(n-r)} x_i \quad (5.148)$$

Figure 5.47 compares two GEV distributions fitted to the dataset of 15 global extremes described above and extrapolated to a 50 year return period. In one case unbiased estimators of the PWMs are used for the fitting, and, in the other, the formula $p_{i,n} = (i-a)/n$ with $a = 0.35$ was employed for the probabilities, as this was found to give the best overall results in a computer simulation by Hosking et al. Also shown for comparison is the Gumbel distribution fitted to the dataset using the method of statistical moments.

It is seen that there is poor agreement between the two GEV distributions. This is likely to be due – at least in part – to the small size of the dataset, which results in coarse estimates of the PWMs. It should also be noted that the use of different datasets

for the same load case results in considerable variation in the shape parameter, suggesting that a dataset of 15 extreme values is not large enough to yield a meaningful result.

5.14.3 Comparison of extreme value distributions

Gumbel, three parameter Weibull, and log-normal distributions have been fitted to the dataset of 15 global extremes of out-of-plane blade root bending moment introduced above, using the method of statistical moments in each case, and compared on a Gumbel plot of $-\ln[-\ln(F(x))]$ against the normalised bending moment excursion, x , in Figure 5.48.

Figure 5.48 shows the three extreme value distribution extrapolated to the 50 year return period exceedance probability of 3.8×10^{-7} (for which $-\ln[-\ln(F(x))]$ is 14.78) to illustrate their behaviour. It is seen that there is a wide variation in the predicted value of the 50 year return load.

Although the loadings on wind turbine components are generally not narrow banded, it is instructive to investigate how well the above three extreme value distributions and the GEV distribution can be fitted to the distribution of global extremes arising from a narrow banded process. Consider a blade rotating at 15 rpm, which experiences 150 loading cycles in 10 minutes. Assuming that the extreme loads in adjacent three cycle blocks are independent of one another, there are 50 independent maxima in the 10 minute time interval, and the cumulative probability distribution of the global maximum is

$$F(x) = \left\{ 1 - \exp \left[-\frac{x^2}{2} \right] \right\}^{50} \quad (5.149)$$

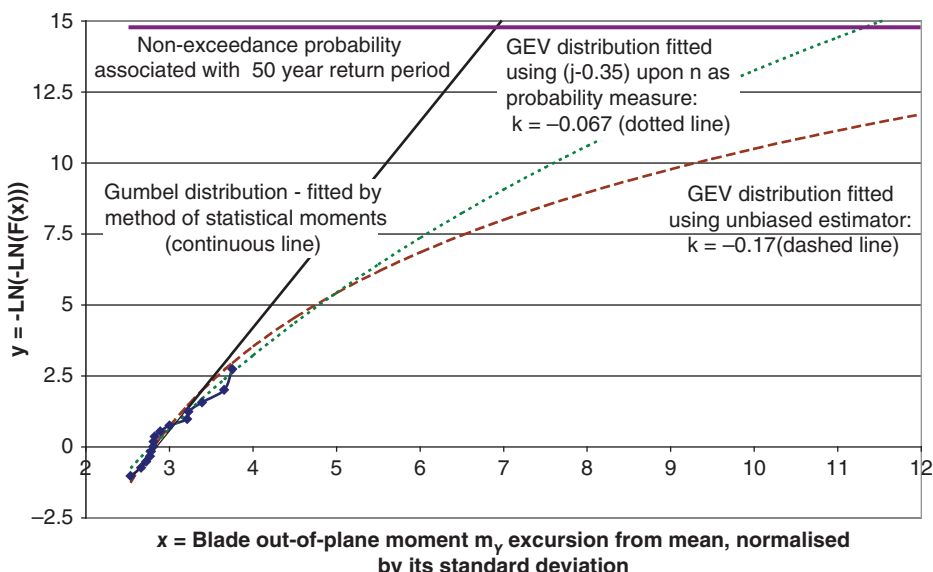


Figure 5.47 Comparison of GEV distributions fitted to empirical data on a Gumbel plot.

Gumbel, three parameter Weibull, log-normal, and GEV distributions have been fitted to this distribution using the method of statistical moments, and Gumbel plots of the fitted distributions are presented in Figure 5.49, together with their defining parameters.

It is seen that the log-normal and the three parameter Weibull distributions fit the distribution of global maxima of a narrow banded process better than the other two.

Freudenreich and Argyriadis (2008) compared extrapolations made using the above four extreme value distributions by reference to five 1 year simulations for a 5 MW pitch-regulated turbine. Using the extreme values from 30 10 minute time histories per wind speed bin as input, they concluded that the extrapolations of blade flapwise root bending moment made with the three parameter Weibull and log-normal distributions were the most accurate, whereas the Gumbel extrapolation was significantly conservative.

5.14.4 Combination of probability distributions

The procedure outlined above yields a family of load non-exceedance probability distributions conditional upon wind speed for the extreme load in the simulation period, $F(x|U_k)$ – one for each wind speed bin. These are combined to yield a single distribution for all operating wind speeds by weighting each one according to the number of hours of operation applicable to the wind speed bin and summing the results. Mathematically, the summation is expressed as follows:

$$F_{Long-term}(x) \approx \sum_{k=1}^M F(x|U_k)p_k \quad (5.150)$$

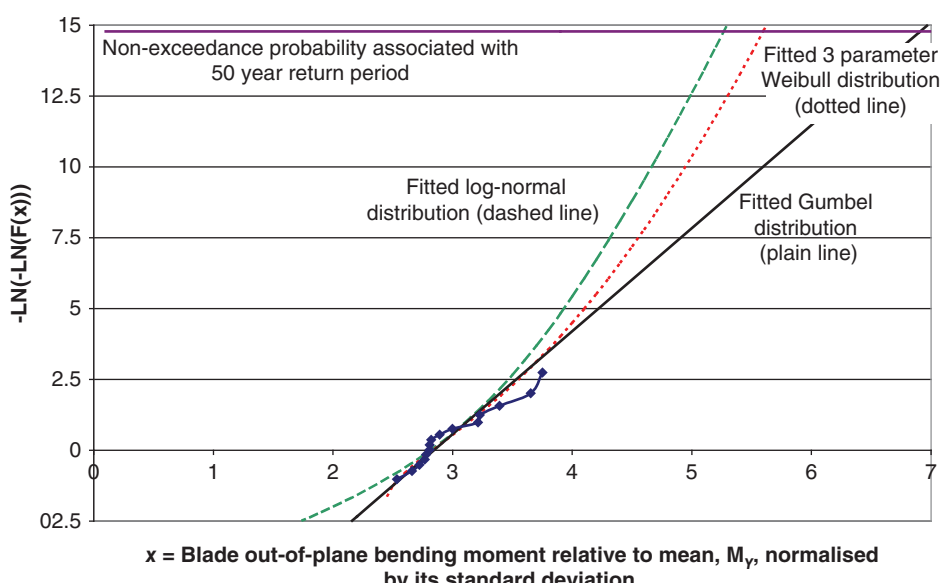


Figure 5.48 Gumbel plot comparison of three extreme value distributions fitted to empirical data.

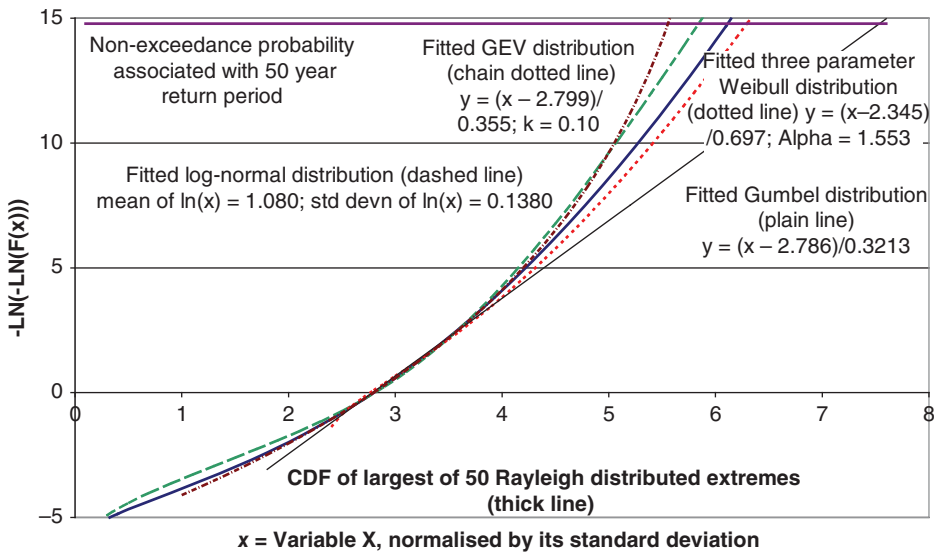


Figure 5.49 Gumbel plot comparison of four extreme value distributions fitted to the distribution of the largest of 50 Rayleigh distributed extremes.

where p_k is the proportion of operating hours in the wind speed bin with mean wind speed U_k and the operating range of wind speeds is divided into M bins.

5.14.5 Extrapolation

The load with a 50 year return period is found by extrapolating $F_{Long-term}(x)$ to the requisite non-exceedance probability – i.e. $(1-3.8 \times 10^{-7})$ for a 10 minute simulation period. As $F_{Long-term}(x)$ is the summation of several mathematically defined distributions, this is straightforward. Figure 5.48 illustrates how the extrapolation might look if a *single* wind speed bin dominated the extreme loads for the three extreme value distributions considered.

5.14.6 Fitting probability distribution after aggregation

With this sequence, the first step is to aggregate the data points from the simulations from all the wind speed bins. If the number of simulations from each wind speed bin is proportional to the number of hours of operation in that bin and there are m 10 minute simulations in all, then the m global extremes can be ranked $1, 2, \dots, i, \dots, m$ from smallest to largest, and the long-term empirical load non-exceedance probability distribution for the 10 minute extreme load, x , can be constructed according to the formula

$$F_{Long-term}(x_i) = \frac{i}{m+1} \quad i = 1, 2, \dots, m$$

In cases where the number of simulations in each wind speed bin is not proportional to the actual likelihood of that bin, then different weights need to be assigned to the global

extremes in different bins, and the probability distribution becomes

$$F_{Long-term}(x) = \sum_{k=1}^b \left(\sum_{i=1}^{n_k} \frac{I[x_{i,k} \leq x]}{m+1} \right) w_k = \sum_{k=1}^b \left(\sum_{i=1}^{n_k} \frac{I[x_{i,k} \leq x]}{m+1} \right) \frac{mp_k}{n_k} \quad (5.151)$$

where

$x_{i,k}$ is the i th extreme in the k th wind speed bin

$I[x_{i,k} \leq x] = 1$ if $x_{i,k} \leq x$ and 0 otherwise

n_k is the number of simulations in the k th wind speed bin

b is the number of wind speed bins

w_k is the weighting factor for k th wind speed bin

p_k is the proportion of operating hours in the k th wind speed bin

The second step is the fitting of an extreme value distribution to the long-term empirical load distribution to permit extrapolation to the 50 year return load. Clearly, the ‘aggregation before fitting’ approach is simpler than the ‘fitting before aggregation’ approach in that only one fitting operation is required, although the inherent complexity of the long-term empirical distribution may make a close fit more difficult to achieve.

5.14.7 Local extremes method

The local extremes method is the same as the global extremes method, except that several independent extreme values in each 10 minute simulation are utilised in constructing the empirical load non-exceedance probability distribution(s) instead of just the single largest value – i.e. the ‘global extreme’ – from each simulation.

If there are n independent extreme values in each 10 minute simulation, then the empirical non-exceedance probability distribution for the 10 minute extreme load, x_k , at wind speed U_k can be constructed from the non-exceedance probability distribution of the local extremes using

$$F(x_k | U_k) = [F_{local}(x_k | U_k)]^n$$

To ensure independence of the local extremes, annex G of IEC 61400-1 edition 4 suggests that individual extremes should be separated by at least three response cycles. A less rigorous but computationally simpler approach is to divide the 10 minute simulation period into n segments or ‘blocks’ of equal duration and use the maximum value from each. This method of extracting the local extremes is illustrated in Figure 5.50 for a turbine rotating at 15 rpm with a block size of 12 seconds, corresponding to three cycles of rotation.

Fogle et al. (2008) have applied statistical tests for independence to block maxima obtained from 200 simulated load time histories for a 5 MW turbine model developed by the National Renewable Energy Laboratory (NREL) and concluded that a block duration of 30 seconds is required to ensure independence. However, they also found that the use of block durations as short as 5 seconds made negligible difference to the tail of the empirical probability distribution.

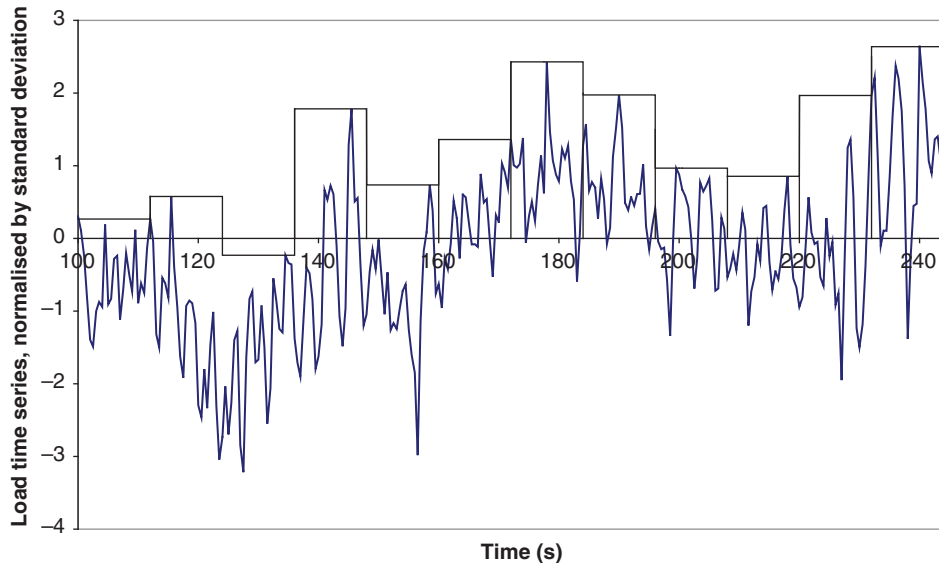


Figure 5.50 Local extremes derived from blocks of 12 seconds' duration.

5.14.8 Convergence requirements

IEC 61400-1 edition 4 imposes a limit on the uncertainty of extrapolated loads by requiring that sufficient simulations are carried out so that the 90% confidence interval on the 84% quantile load (that is, the extreme load in a 10 minute simulation likely to be exceeded 16% of the time) is less than 15% of that load. This requirement is expressed as

$$\frac{\hat{S}_{0.84,0.05} - \hat{S}_{0.84,0.95}}{\hat{S}_{0.84}} < 0.15 \quad (5.152)$$

where the confidence bounds $\hat{S}_{0.84,0.05}$ and $\hat{S}_{0.84,0.95}$ are the empirical estimates of the 84% quantile load with a 5% and 95% probability of not being exceeded, respectively.

One approach to estimating the confidence bounds utilises the binomial expansion to obtain the probability, $C(j; m, 0.84)$, of j or fewer occurrences of the non-exceedance of the 84% quantile load in m simulations. This is given by

$$C(j; m, 0.84) = \sum_{i=0}^j \frac{m!}{i!(m-i)!} 0.84^i 0.16^{m-i} \quad (5.153)$$

As an example, this probability is plotted against j for the case of $m = 15$ simulations in Figure 5.51. It is seen that the 5% and 95% confidence bounds on the number of trials in which the 84% quantile load is not exceeded are 9.5 and 14.3, respectively. The confidence bounds on the 84% quantile load, $\hat{S}_{0.84,0.05}$ and $\hat{S}_{0.84,0.95}$, required for the inequality (5.152) can then be derived by interpolating between the 9th and 10th and 14th and 15th ranked extremes, respectively. The ranking is from smallest to largest as usual.

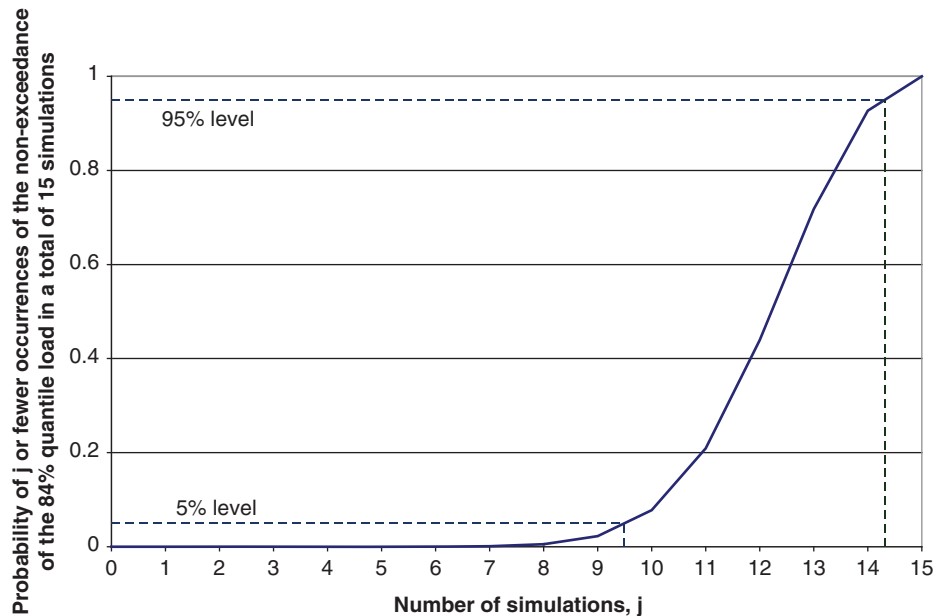


Figure 5.51 Probability of j or fewer occurrences of the non-exceedance of the 84% quantile load in a total of 15 simulations.

Table 5.11 Table of confidence bounds on the number of simulations in which the 84% load is not exceeded for different numbers of simulations in total.

Total number of simulations, m	Number of occurrences of the non-exceedance of the 84% quantile load with 5% probability of not being exceeded	Number of occurrences of the non-exceedance of the 84% quantile load with 95% probability of not being exceeded
15	9.5	14.32
20	13.35	18.83
25	17.23	23.39
30	21.18	27.83
35	25.13	32.32

Annex G of IEC 61400-1 edition 4 provides a table of 5% and 95% confidence bounds on the number of simulations in which the 84% quantile load is not exceeded for each value of m , the total number of simulations, from 15 to 35. Selected values are given in Table 5.11.

References

- Abramowitz, M. and Stegun, I.A. (1965). *Handbook of Mathematical Functions*. New York: Dover.
 Armstrong JRC and Hancock M (1991). Feasibility study of teetered, stall-regulated rotors. *ETSU Report No. WN 6022*.

- Barltrop, N.D.P. and Adams, A.J. (1991). *Dynamics of Fixed Marine Structures*, 3e. Butterworth-Heinemann.
- Batchelor, G.K. (1953). *The Theory of Homogeneous Turbulence*. Cambridge University Press.
- Bierbooms, W.A.A.M. (2005). Constrained stochastic simulation – generation of time series around some specific event in a normal process. *Extremes* 8 (3).
- Bishop NWM, Zhihua H, and Sheratt F (1991). The analysis of non-Gaussian loadings from wind turbine blades using frequency domain techniques. Proceedings of the BWEA Conference, pp. 317–323.
- Bishop NWM, Wang R, and Lack L (1995). A frequency domain fatigue predictor for wind turbine blades including deterministic components. Proceedings of the BWEA Conference, pp. 53–58.
- British Standards Institution. (1980). *BS 5400: Part 10: 1980 Steel, concrete and composite bridges – Code of practice for fatigue*.
- British Standards Institution. (1986). *BS 8100: Part 1: 1986 Lattice towers and masts – Code of practice for loading*.
- Clough, R.W. and Penzien, J. (1993). *Dynamics of Structures*. McGraw-Hill.
- Craig, R.R. Jr. and Bampton, M.C.C. (1968). Coupling of substructures for dynamic analysis. *AIAA J.* 6 (7): 1313–1319.
- Creed, R.F. (1993) High cycle tensile fatigue of unidirectional fibreglass composite tested at high frequency. PhD thesis, Montana State University.
- Davenport, A.G. (1964). Note on the distribution of the largest value of a random function with application to gust loading. *Proc. Inst. Civil Eng.* 28: 187–196.
- Dirlik, T. (1985). *Application of Computers in Fatigue Analysis*. University of Warwick thesis.
- DNVGL (2020). Bladed. <https://www.dnvg.com/services/wind-turbine-design-software-bladed-3775>.
- DNVGL – Energy (2016). Bladed theory manual version 4.8.
- DNVGL-ST-0376 (2015). *Rotor blades for wind turbines*. Akershus, Norway: DNVGL.
- DNVGL-ST-0437 (2016). *Loads and site conditions for wind turbines*. Akershus, Norway: DNVGL.
- DS 410 (1983). *Loads for the design of structures*. Copenhagen: Danish Standards Foundation.
- DS 472 (1992). *Loads and safety of wind turbine construction*. Copenhagen: Danish Standards Foundation.
- EN 1991-1-4:2005 (2005). *Eurocode 1: Actions on structures – Part 1-4: General actions – Wind actions*. Brussels: European Committee for Standardization.
- Fogle, J., Agarwal, P., and Manuel, L. (2008). Towards an improved understanding of statistical extrapolation for wind turbine extreme loads. *Wind Energy* 11: 613–635. (Expanded version published by American Institute of Aeronautics and Astronautics).
- Freudenreich, K. and Argyriadis, K. (2008). Wind turbine load level based on extrapolation and simplified methods. *Wind Energy* 11: 589–600.
- Garrad AD (1987). The use of finite element methods for wind turbine dynamics. Proceedings of the BWEA Conference, pp. 79–83.
- Garrad AD and Hassan U (1986). The dynamic response of wind turbines for fatigue life and extreme load prediction. Proceedings of the EWEA Conference, pp. 401–406.
- Germanischer Lloyd. (2010). *Rules and guidelines: IV – Industrial services: Part 1 – Guideline for the certification of wind turbines*.
- Gibson, R.F. et al. (1982). Vibration characteristics of automotive composite materials. In: *Short Fibre Reinforced Composite Materials*, 133–150. West Conshohocken, Pennsylvania, USA: ASTM.
- Hansen A C 1998. User's guide to the wind turbine dynamics computer programs YawDyn and AeroDyn for Adams, version 11.0. University of Utah.
- Harris, R.I. (1996). Gumbel re-visited – a new look at extreme value statistics applied to wind speeds. *J. Wind Eng. Ind. Aerodyn.* 59: 1–22.
- Harris, R.I., Deaves, D.M., 1980. The structure of strong winds. Proceedings of the CIRIA conference 'Wind Engineering in the Eighties', London (12–13 November 1980).

- Hoskin RE, Warren JG, and Draper J (1989). Prediction of fatigue damage in wind turbine rotors. *Proceedings of the EWEC*, pp. 389–394.
- Hosking, J.R.M., Wallis, J.R., and Wood, E.F. (1985). Estimation of the generalized extreme value distribution by the method of probability-weighted moments. *Technometrics* 27 (3): 251–261.
- IEC 1400-1 (1994). *Wind turbine generator systems – Part 1: Safety requirements*. Geneva, Switzerland: International Electrotechnical Commission.
- IEC 61400-1 (1999). *Wind turbine generator systems – Part 1: Safety requirements* (2nd edition). Geneva, Switzerland: International Electrotechnical Commission.
- IEC 61400-1 (2005). *Wind turbines – Part 1: Design requirements* (3rd edition). Geneva, Switzerland: International Electrotechnical Commission.
- IEC 61400-1 (2019). *Wind energy generation systems – Part 1: Design requirements* (4th edition). Geneva, Switzerland: International Electrotechnical Commission.
- International Energy Agency Wind Technology Collaboration Programme (1990). Recommended practice 3: Fatigue loads, 2nd edition (Task 11). <https://community.ieawind.org/publications/rp>.
- Jamieson P and Hunter C (1985). Analysis of data from Howden 300 kW wind turbine on Burgar Hill Orkney. *Proceedings of the BWEA Conference*, pp. 253–258.
- Jamieson P, Camp TR, and Quarton DC (2000). Wind turbine design for offshore. *Proceedings of the Offshore Wind Energy in Mediterranean and European Seas*, CEC/EWEA/IEA, Sicily, pp. 405–414.
- Jenkinson, A.F. (1955). The frequency distribution of the annual maximum (or minimum) of meteorological elements. *Q. J. R. Meteorol. Soc.* 81: 158–171.
- Kaimal, J.C. et al. (1972). Spectral characteristics of surface-layer turbulence. *Quarterly Journal of the Meteorological Society*, 98: 563–589.
- von Karman, T. (1948). Progress in the statistical theory of turbulence. In *Proceedings of the National Academy of Sciences*. vol. 34, pp. 530–539.
- Larsen, G.C., Ronold, K., Jorgensen, H.E., Argyriadis, K. and 2de Boer, J. (1999). Ultimate loading of wind turbines. *Riso National Laboratory No. R-1111*.
- Lobitz DWA (1984). NASTRAN based computer program for structural dynamic analysis of HAWTs. *Proceedings of the EWEA conference*.
- Madsen PH, Frandsen S, Holley WE, and Hansen JC (1984). Dynamics and fatigue damage of wind turbine rotors during steady operation. *Riso National Laboratory No. R-512*.
- Mann (1998, 1998). Wind field simulation. *J. Mann, Prob. Engng. Mech.* 13 (4): 269–282.
- Matsuishi M and Endo T (1968). ‘Fatigue of metals subject to varying stress. *Proceedings of the Japan Society of Mechanical Engineers*.
- Molenaar, D.P. and Dijkstra, S. (1999). State-of-the-art of wind turbine design codes: main features overview for cost-effective generation. *Wind Eng.* 23 (5): 295–311.
- Morgan CA and Tindal AJ (1990). Further analysis of the Orkney MS-1 data. *Proceedings of the BWEA Conference*, pp. 325–330.
- Moriarty PJ, Holley WE and Butterfield SP (2004). Extrapolation of extreme and fatigue loads using probabilistic methods. *NREL Report TP-500-34421*.
- Petersen JT, Madsen HA, Björck A, Enevoldsen P, Øye S, Ganander H, and Winkelhaar D (1998). Prediction of dynamic loads and induced vibrations in stall. *Riso National Laboratory No. R-1045*.
- Putter, S. and Manor, H. (1978). Natural frequencies of radial rotating beams. *J. Sound Vib.* 56 (2): 175–185.
- Ragan, P. and Manuel, L. (2007). Comparing estimates of wind turbine fatigue loads using time-domain and spectral methods. *Wind Eng.* 31 (2): 83–99.
- Rasmussen F. (1984). Aerodynamic performance of a new LM 17.2 m rotor. *Riso National Laboratory No. 2432*.
- Shabana, A.A. (1998). *Dynamics of Multibody Systems*, 2e. Cambridge: Cambridge University Press.

- Thomsen K (1998). The statistical variation of wind turbine fatigue loads. *Risø National Laboratory No. R-1063*.
- Thomsen K and Madsen PH (1997). Application of statistical methods to extreme loads for wind turbines. Proceedings of the EWEC, pp. 595–598.
- Veers PS (1988). Three-dimensional wind simulation. *Sandia Report SAND88-0152*.
- Warren JG, Quarton DC, Lack L, Draper J (1988). Prediction of fatigue damage in wind turbine rotors. Proceedings of the BWEA Conference.

Appendix A5 Dynamic response of stationary blade in turbulent wind

A5.1 Introduction

As described in Chapter 2, the turbulent wind contains wind speed fluctuations over a wide range of frequencies, as described by the power spectrum. Although the bulk of the turbulent energy is normally at frequencies much lower than the blade first mode out-of-plane frequency, which is typically over 1 Hz, the fraction close to the first mode frequency will excite resonant blade oscillations. This appendix describes the method by which the resonant response may be determined. Working in the frequency domain, expressions for the standard deviations of both the tip displacement and root bending moment responses are derived, and then the method of deriving the peak value in a given period is described. Initially the wind is assumed to be perfectly correlated along the blade, but subsequently the treatment is extended to include the effect of spatial variation.

A5.2 Frequency response function

A5.2.1 Equation of motion

The dynamic response of a cantilever blade to the fluctuating aerodynamic loads upon it is most conveniently investigated by means of modal analysis, in which the excitations of the various different natural modes of vibration are computed separately and the results superposed. Thus the deflection $x(r, t)$ at radius r is given by

$$x(r, t) = \sum_{i=1}^{\infty} f_i(t) \mu_i(t)$$

Normally, in the case of a stationary blade, the first mode dominates and higher modes do not need to be considered. The equation of motion for the i th mode, which is derived in Section 5.8.1, is as follows:

$$m_i \ddot{f}_i(t) + c_i \dot{f}_i(t) + m_i \omega_i^2 f_i(t) = \int_0^R \mu_i(r) q(r, t) dr \quad (\text{A5.1})$$

where

$q(r,t)$ is the applied loading

$f_i(t)$ is the tip displacement

$\mu_i(r)$ is the non-dimensional mode shape of the i th mode, normalised to give a tip displacement of unity

ω_i is the natural frequency in radians per second

m_i is the generalised mass, $\int_0^R m(r)\mu_i^2(r)dr$

and c_i is the generalised damping, $\int_0^R \hat{c}(r)\mu_i^2(r)dr$

A5.2.2 Frequency response function

If $q(r,t)$ varies harmonically, with frequency ω and amplitude $q_0(r)$, then it can be shown that

$$\begin{aligned} f_i(t) &= \frac{1}{m_i} \frac{\int_0^R \mu_i(r)q_0(r)dr}{\sqrt{(\omega_i^2 - \omega^2)^2 + (c_i/m_i)^2\omega^2}} \cos(\omega t + \phi_i) \\ &= \frac{1}{m_i\omega_i^2} \frac{\int_0^R \mu_i(r)q_0(r)dr}{\sqrt{(1 - \omega^2/\omega_i^2)^2 + (c_i/m_i\omega_i^2)^2\omega^2}} \cos(\omega t + \phi_i) \end{aligned} \quad (\text{A5.2})$$

Defining $k_i = m_i\omega_i^2$, and noting that the damping ratio $\xi_i = c_i/2m_i\omega_i$, this becomes

$$f_i(t) = \frac{1}{k_i} \frac{\int_0^R \mu_i(r)q_0(r)dr}{\sqrt{(1 - \omega^2/\omega_i^2)^2 + 4\xi_i^2\omega^2/\omega_i^2}} \cos(\omega t + \phi_i) = A_i \cos(\omega t + \phi_i) \quad (\text{A5.3})$$

The numerator $\int_0^R \mu_i(r)q_0(r)dr$ is the amplitude of the equivalent harmonic loading at the tip of the cantilever that would result in the same tip displacement as the loading $q(r,t)$, and is known as the *generalised load* with respect to the i th mode, $Q_i(t)$. Thus, the ratio between the tip displacement amplitude and the amplitude of the generalised load is

$$\begin{aligned} \frac{A_i}{\int_0^R \mu_i(r)q_0(r)dr} &= \frac{1}{k_i \sqrt{(1 - \omega^2/\omega_i^2)^2 + 4\xi_i^2\omega^2/\omega_i^2}} \\ &= \frac{1}{k_i \sqrt{(1 - n^2/n_i^2)^2 + 4\xi_i^2n^2/n_i^2}} = |H_i(n)| \end{aligned} \quad (\text{A5.4})$$

The ratio $|H_i(n)|$ is the modulus of the complex frequency response function, $H_i(n)$, and its square can be used to transform the power spectrum of the wind incident on the blade into the power spectrum of the i th mode tip displacement. Thus, in the case of the dominant first mode, the tip displacement in response to a harmonic generalised loading, $Q_1(t)$, of frequency n is given by

$$x_1(R, t) = f_1(t) = Q_1(t).|H_1(n)|$$

and the power spectrum of the first mode tip deflection is $S_{1x}(n) = S_{Q1}(n).|H_1(n)|^2$.

In what follows, the simplifying assumption is made initially that the wind is perfectly correlated along the blade.

A5.3 Resonant displacement response ignoring wind variations along the blade

A5.3.1 Linearisation of wind loading

For a fluctuating wind speed $U(t) = \bar{U} + u(t)$, the wind load per unit length on the blade is $\frac{1}{2}C_f\rho U^2(t)c(r) = \frac{1}{2}C_f\rho [\bar{U}^2 + 2\bar{U}u(t) + u^2(t)]c(r)$, where C_f is the lift or drag coefficient, as appropriate, and $c(r)$ is the local blade chord dimension. In order to permit a linear treatment, the third term in the square brackets, which will normally be small compared to the first two, is ignored, so that the fluctuating load $q(r, t)$ becomes $C_f\rho\bar{U}u(t)c(r)$.

A5.3.2 First mode displacement response

Setting $q(r, t) = C_f\rho\bar{U}u(t)c(r)$, the first mode tip displacement response to a sinusoidal wind fluctuation of frequency n ($=\omega/2\pi$) and amplitude $u_o(n)$ given by Eq. (A5.3) becomes

$$\begin{aligned} f_1(t) &= \int_0^R \mu_1(r)C_f\rho\bar{U}c(r)dr.u_o(n).|H_1(n)|.\cos(2\pi nt + \phi_1) \\ &= C_f\rho\bar{U} \int_0^R \mu_1(r)c(r)dr.u_o(n).|H_1(n)|.\cos(2\pi nt + \phi_1) \end{aligned} \quad (\text{A5.5})$$

Hence the power spectrum of first mode tip displacement is

$$S_{1x}(n) = \left[C_f\rho\bar{U} \int_0^R \mu_1(r)c(r)dr \right]^2 . S_u(n).|H_1(n)|^2 \quad (\text{A5.6})$$

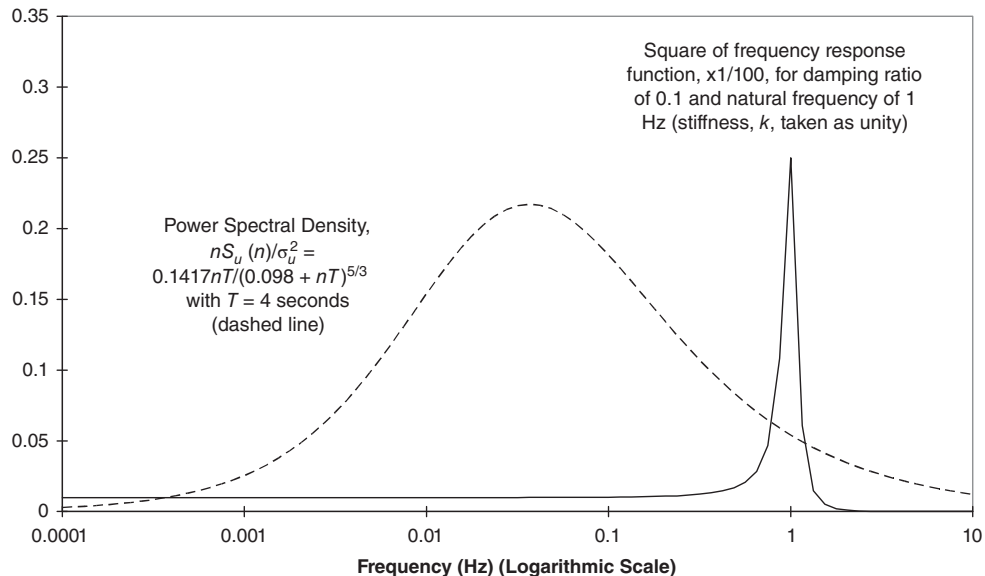


Figure A5.1 Power spectrum of wind turbulence and frequency response function.

where $S_u(n)$ is the power spectrum for the along wind turbulence. Thus, the standard deviation of the first mode tip displacement is given by

$$\sigma_{1x}^2 = \left[C_f \rho \bar{U} \int_0^R \mu_1(r) c(r) dr \right]^2 \int_0^\infty S_u(n) |H_1(n)|^2 dn \quad (\text{A5.7})$$

A5.3.3 Background and resonant response

Normally the bulk of the turbulent energy in the wind is at frequencies well below the frequency of the first out-of-plane blade mode. This is illustrated in Figure A5.1, where a typical power spectrum for wind turbulence is compared with the square, $|H_1(n)|^2$, of an example frequency response function for a 1 Hz resonant frequency.

The power spectrum is that due to Kaimal (and adopted in Eurocode 1 [EN 1991-1-4:2005]):

$$n.S_u(n) = \sigma_u^2 \frac{6.8nL_u^x/\bar{U}}{(1 + 10.2n.L_u^x/\bar{U})^{5/3}} \quad (\text{A5.8})$$

and is plotted as the non-dimensional power spectral density function, $R_u(n) = n.S_u(n)/\sigma_u^2$, against a logarithmic frequency scale. The timescale, L_u^x/\bar{U} , chosen is 4 seconds, based on a mean wind speed, \bar{U} , of 50 m/s and an integral length scale, L_u^x , of 200 m.

In view of the fact that the resonant response usually occurs over a narrow band of frequencies on the tail of the power spectrum, it is normal to treat it separately from the quasi-static response at lower frequencies and to ignore the variation in $n.S_u(n)$ on either

side of the resonant frequency, n_1 . (See, for example, Wyatt 1980). The variance of total tip displacement then becomes

$$\sigma_x^2 = \sigma_B^2 + \sigma_{x1}^2$$

in which the variance of the first mode resonant response, σ_{x1} , is given by

$$\sigma_{x1}^2 = \left[C_f \rho \bar{U} \int_0^R \mu_1(r) c(r) dr \right]^2 \cdot S_u(n_1) \int_0^\infty |H_1(n)|^2 dn \quad (\text{A5.9})$$

and the resonant response of higher modes, σ_{x2}^2 , σ_{x3}^2 etc. is ignored. The non-resonant response, σ_B , is termed the *background response* and can be derived from simple static beam theory.

It has been shown by Newland (1984) that $\int_0^\infty |H_1(n)|^2 dn$ reduces to $\frac{\pi^2}{2\delta} \cdot \frac{n_1}{k_1^2}$, where δ is the logarithmic decrement of damping. The logarithmic decrement, δ , is 2π times the damping ratio, ξ_1 , defined as $\xi_1 = c_1/2m_1\omega_1$. Hence Eq. (A5.9) becomes

$$\sigma_{x1}^2 = \left[C_f \rho \bar{U} \int_0^R \mu_1(r) c(r) dr \right]^2 \cdot S_u(n_1) \frac{\pi^2}{2\delta} \frac{n_1}{k_1^2} \quad (\text{A5.10})$$

For comparison, the first mode component, \bar{x}_1 , of the steady response is obtained by setting $\omega = 0$ and $q_0(r) = \frac{1}{2}\rho \bar{U}^2 C_f c(r)$ in Eq. (A5.3), yielding

$$\bar{x}_1 = \frac{1}{2} \rho \bar{U}^2 C_f \cdot \frac{1}{k_1} \cdot \int_0^R \mu_1(r) c(r) dr \quad (\text{A5.11})$$

Hence, the ratio of the standard deviation of the first mode resonant response to the first mode component of the steady response is

$$\frac{\sigma_{x1}}{\bar{x}_1} = 2 \cdot \frac{\sigma_u}{\bar{U}} \cdot \frac{\pi}{\sqrt{2\delta}} \cdot \sqrt{\frac{n_1 S_u(n_1)}{\sigma_u^2}} = 2 \cdot \frac{\sigma_u}{\bar{U}} \cdot \frac{\pi}{\sqrt{2\delta}} \cdot \sqrt{R_u(n_1)} \quad (\text{A5.12})$$

Note that towards the upper tail of the power spectrum of along wind turbulence, where n_1 is likely to be located, $\sqrt{R_u(n_1)}$ tends to $\sqrt{0.1417/(n L_u^x / \bar{U})^{2/3}}$.

A5.4 Effect of across wind turbulence distribution on resonant displacement response

In the foregoing treatment, the wind was assumed to be perfectly correlated along the blade. The implications of removing this simplifying assumption will now be examined.

The fluctuating load on the blade, $q(r, t)$, becomes $C_f \rho \bar{U} u(r, t) c(r)$ per unit length, and the generalised fluctuating load with respect to the first mode becomes

$$Q_1(t) = \int_0^R \mu_1(r) q(r, t) dr = C_f \rho \bar{U} \int_0^R u(r, t) c(r) \mu_1(r) dr \quad (\text{A5.13})$$

The standard deviation, σ_{Q1} , of $Q_1(t)$ is given by

$$\begin{aligned} \sigma_{Q1}^2 &= \frac{1}{T} \int_0^T Q_1^2(t) dt = (\rho \bar{U} C_f)^2 \frac{1}{T} \int_0^T \left[\int_0^R u(r, t) c(r) \mu_1(r) dr \right] \left[\int_0^R u(r', t) c(r') \mu_1(r') dr' \right] dt \\ &= (\rho \bar{U} C_f)^2 \int_0^R \int_0^R \left[\frac{1}{T} \int_0^T u(r, t) u(r', t) dt \right] c(r) c(r') \mu_1(r) \mu_1(r') dr dr' \quad (\text{A5.14}) \end{aligned}$$

Now the expression within the square brackets is the cross-correlation function, $\kappa_u(r, r', \tau) = E\{u(r, t)u(r', t + \tau)\}$, with τ set equal to zero. The cross-correlation function is related to the cross-spectrum, $S_{uu}(r, r', n)$, as follows:

$$\kappa_u(r, r', 0) = \frac{1}{2} \int_{-\infty}^{\infty} S_{uu}(r, r', n) \exp(i.2\pi n \tau) dn,$$

giving

$$\kappa_u(r, r', 0) = \left[\frac{1}{T} \int_0^T u(r, t) u(r', t) dt \right] = \int_0^{\infty} S_{uu}(r, r', n) dn \quad \text{for } \tau = 0 \quad (\text{A5.15})$$

Hence,

$$\sigma_{Q1}^2 = (\rho \bar{U} C_f)^2 \int_0^R \int_0^R \left[\int_0^{\infty} S_{uu}(r, r', n) dn \right] c(r) c(r') \mu_1(r) \mu_1(r') dr dr' \quad (\text{A5.16})$$

The normalised cross-spectrum is defined as $S_{uu}^N(r, r', n) = \frac{S_{uu}(r, r', n)}{S_u(n)}$, and like $S_{uu}(r, r', n)$, is in general a complex quantity, because of phase differences between the wind speed fluctuations at different heights. As only in-phase wind speed fluctuations will affect the response, we consider only the real part of the normalised cross-spectrum, known as the *normalised co-spectrum* and denoted by $\psi_{uu}^N(r, r', n)$. Substituting in Eq. (A5.16), we obtain

$$\sigma_{Q1}^2 = (\rho \bar{U} C_f)^2 \int_0^R \int_0^R \left[\int_0^{\infty} S_u(n) \psi_{uu}^N(r, r', n) dn \right] c(r) c(r') \mu_1(r) \mu_1(r') dr dr' \quad (\text{A5.17})$$

From this, it can be deduced that the power spectrum of the generalised load with respect to the first mode is

$$S_{Q1}(n) = (\rho \bar{U} C_f)^2 \int_0^R \int_0^R S_u(n) \psi_{uu}^N(r, r', n) c(r) c(r') \mu_1(r) \mu_1(r') dr dr' \quad (\text{A5.18})$$

Note that the power spectrum for the along wind turbulence shows some variation with height, and so should strictly be written $S_u(n, z)$ instead of $S_u(n)$. However, the variation along the length of a vertical blade is small and is ignored here.

As for the initial case when wind loadings along the blade were assumed to be perfectly correlated, the power spectrum for first mode tip displacement is equal to the product of the power spectrum of the generalised load (with respect to the first mode) and the square of the frequency response function, i.e.

$$S_{1x}(n) = S_{Q1}(n).|H_1(n)|^2 \quad (\text{A5.19})$$

As before, $S_{Q1}(n)$ is assumed constant over the narrow band of frequencies straddling the resonant frequency, and the standard deviation of resonant tip response becomes

$$\sigma_{x1}^2 = S_{Q1}(n_1). \int_0^\infty |H_1(n)|^2 dn = S_{Q1}(n_1). \frac{\pi^2}{2\delta} \cdot \frac{n_1}{k_1^2}. \quad (\text{A5.20})$$

A5.4.1 Formula for normalised co-spectrum

It remains to evaluate $S_{Q1}(n_1) = (\rho \bar{U} C_f)^2 \cdot S_u(n_1) \int_0^R \int_0^R \psi_{uu}^N(r, r', n) \cdot c(r) \cdot c(r') \cdot \mu_1(r) \cdot \mu_1(r') \cdot dr \cdot dr'$. The normalised co-spectrum, $\psi_{uu}^N(r, r', n)$, must decrease as the spacing $|r - r'|$ between the two points considered increases, and intuitively it is to be expected that the decrease would be more rapid for the higher frequency components of wind fluctuation. On an empirical basis, Davenport (1962) has proposed an exponential expression for the normalised co-spectrum as follows:

$$\psi_{uu}^N(r, r', n) = \exp[-C|r - r'|n/\bar{U}] \quad (\text{A5.21})$$

where C is a non-dimensional decay constant. Davenport noted that measurements by Cramer (1958) indicated values of C ranging from 7 in unstable conditions to 50 in stable conditions but recommended the use of the lower figure as being the more conservative despite the likelihood of stable conditions in high winds. Dyrbye and Hansen (1997) quote Risø measurements reported by Mann (1994) that indicate a value of C of 9.4, and they recommend a value of 10 for use in design. A value of 11.5 is implicitly assumed in Eurocode 1.

There is an obvious inconsistency in the exponential expression for the normalised co-spectrum – when it is integrated up over the plane perpendicular to the wind direction, the result is positive instead of zero, as it should be. This has led to the development of more complex expressions by Harris (1971) and Krenk (1995). However, the Davenport formulation will be used here, giving

$$\begin{aligned} \sigma_{x1}^2 &= S_{Q1}(n_1) \cdot \frac{\pi^2}{2\delta} \cdot \frac{n_1}{k_1^2} \\ &= (\rho \bar{U} C_f)^2 \cdot S_u(n_1) \int_0^R \int_0^R \exp[-C|r - r'|n_1/\bar{U}] \cdot c(r) \cdot c(r') \cdot \mu_1(r) \cdot \mu_1(r') \cdot dr \cdot dr' \left[\frac{\pi^2}{2\delta} \frac{n_1}{k_1^2} \right] \end{aligned} \quad (\text{A5.22})$$

The resonant response can be expressed in terms of the first mode component, \bar{x}_1 , of the steady response, $\frac{1}{2}\rho \overline{U}^2 C_f \frac{1}{k_1} \int_0^R \mu_1(r) c(r) dr$, from Eq. (A5.11), giving

$$\frac{\sigma_{x1}^2}{\bar{x}_1^2} = 4 \cdot \frac{\sigma_u^2}{\overline{U}^2} \cdot \frac{\pi^2}{2\delta} \cdot R_u(n_1) \frac{\int_0^R \int_0^R \exp[-C|r - r'|n_1/\overline{U}] \cdot c(r) \cdot c(r') \cdot \mu_1(r) \cdot \mu_1(r') \cdot dr \cdot dr'}{\left(\int_0^R c(r) \cdot \mu_1(r) \cdot dr \right)^2} \quad (\text{A5.23})$$

Hence,

$$\frac{\sigma_{x1}}{\bar{x}_1} = 2 \cdot \frac{\sigma_u}{\overline{U}} \cdot \frac{\pi}{\sqrt{2\delta}} \cdot \sqrt{R_u(n_1)} \cdot \sqrt{K_{Sx}(n_1)} \quad (\text{A5.24})$$

where

$$K_{Sx}(n_1) = \frac{\int_0^R \int_0^R \exp[-C|r - r'|n_1/\overline{U}] \cdot c(r) \cdot c(r') \cdot \mu_1(r) \cdot \mu_1(r') \cdot dr \cdot dr'}{\left(\int_0^R c(r) \cdot \mu_1(r) \cdot dr \right)^2} \quad (\text{A5.25})$$

is denoted the size reduction factor, which results from the lack of correlation of the wind along the blade. As an example, the size reduction factor, $K_{Sx}(n_1)$, is plotted out against frequency in Figure A5.2 for the case of a 40 m blade with chord $c(r) = 0.0961R - 0.06467r$ (Blade SC40), assuming a decay constant C of 10 and a mean wind speed \overline{U} of 50 m/s. The mode shape taken is the same as for the example in Section 5.6.3 in edition 2 (see Figure 5.4). Also shown for comparison is the corresponding parameter for a uniform cantilever.

A5.5 Resonant root bending moment

For design purposes, it is the augmentation of blade bending moments due to dynamic effects that is of principal significance. The ratio of the standard deviation of the first mode resonant root bending moment to the steady root bending moment (allowing for the lack of correlation of wind fluctuations along the blade) is derived below.

Defining $M_1(t)$ as the fluctuating root bending moment due to wind excitation of the first mode, we have

$$M_1(t) = \int_0^R m(r) \ddot{x}_1(t, r) r dr = \int_0^R m(r) \omega_1^2 x_1(t, r) r dr = \omega_1^2 f_1(t) \int_0^R m(r) \mu_1(r) r dr \quad (\text{A5.26})$$

Hence, the standard deviation of $M_1(t)$,

$$\sigma_{M1} = \omega_1^2 \sigma_{x1} \int_0^R m(r) \mu_1(r) r dr \quad (\text{A5.27})$$

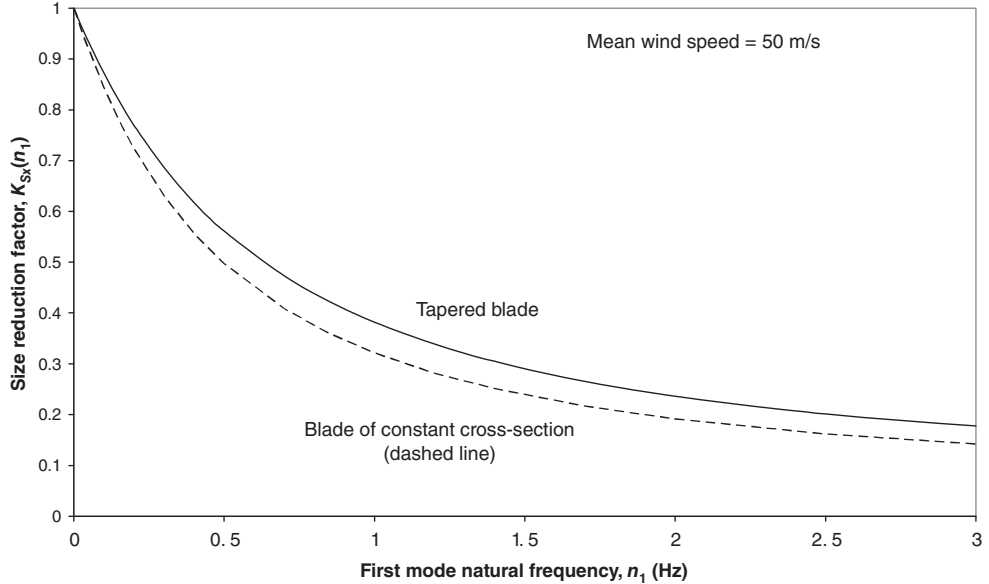


Figure A5.2 Size reduction factors for the first mode resonant response due to lack of correlation of wind loading along the blade: variation with frequency for 40 m blade.

The steady root bending moment,

$$\bar{M} = \int_0^R \frac{1}{2} \rho \bar{U}^2 C_f c(r) r dr = \frac{1}{2} \rho \bar{U}^2 C_f \int_0^R c(r) r dr \quad (\text{A5.28})$$

Hence, the ratio

$$\frac{\sigma_{M1}}{M} = \frac{\omega_1^2 \sigma_{x1} \int_0^R m(r) \mu_1(r) r dr}{\frac{1}{2} \rho \bar{U}^2 C_f \int_0^R c(r) r dr} \quad (\text{A5.29})$$

Substituting the expression for σ_{x1} from Eq. (A5.22), we obtain

$$\frac{\sigma_{M1}}{M} = \frac{\omega_1^2 \cdot \rho \bar{U} C_f \cdot \frac{\pi}{\sqrt{2\delta}} \frac{\sqrt{n_1 S_u(n_1)}}{k_1} \int_0^R m(r) \mu_1(r) r dr}{\frac{1}{2} \rho \bar{U}^2 C_f \int_0^R c(r) r dr} \sqrt{\int_0^R \int_0^R \exp[-C|r - r'|n_1/\bar{U}].c(r).c(r').\mu_1(r).\mu_1(r').dr.dr'} \quad (\text{A5.30})$$

Noting that $R_u(n) = n.S_u(n)/\sigma_u^2$, and that $k_1 = m_1 \omega_1^2$, this simplifies to

$$\frac{\sigma_{M1}}{M} = 2 \frac{\sigma_u}{\bar{U}} \frac{\pi}{\sqrt{2\delta}} \sqrt{R_u(n)} \frac{\int_0^R m(r) \mu_1(r) r dr}{m_1 \cdot \int_0^R c(r) r dr} \sqrt{\int_0^R \int_0^R \exp[-C|r - r'|n_1/\bar{U}].c(r).c(r').\mu_1(r).\mu_1(r').dr.dr'} \quad (\text{A5.31})$$

where $m_1 = \int_0^R m(r) \mu_1^2(r) dr$ is the generalised mass with respect to the first mode, and the exponential expression within the double integral allows for the lack of correlation

of wind fluctuations along the blade. Substituting $\left(\int_0^R c(r).\mu_1(r).dr\right) \cdot \sqrt{K_{Sx}(n_1)}$ for the square root of the double integral, using Eq. (A5.25), leads to

$$\frac{\sigma_{M1}}{M} = 2 \frac{\sigma_u}{U} \frac{\pi}{\sqrt{2\delta}} \sqrt{R_u(n)} \frac{\int_0^R m(r)\mu_1(r)rdr}{m_1 \cdot \int_0^R c(r)rdr} \left(\int_0^R c(r).\mu_1(r).dr \right) \cdot \sqrt{K_{Sx}(n_1)} \quad (\text{A5.32})$$

Defining the ratio of the integrals,

$$\frac{\int_0^R m(r)\mu_1(r)rdr}{m_1 \cdot \int_0^R c(r)rdr} \left(\int_0^R c(r).\mu_1(r).dr \right) = \frac{\sigma_{M1}}{M} / \frac{\sigma_{x1}}{\bar{x}_1}, \text{ as } \lambda_{M1} \quad (\text{A5.33})$$

we obtain

$$\frac{\sigma_{M1}}{M} = 2 \frac{\sigma_u}{U} \frac{\pi}{\sqrt{2\delta}} \cdot \sqrt{R_u(n_1)} \cdot \sqrt{K_{Sx}(n_1)} \cdot \lambda_{M1} \quad (\text{A5.34})$$

A5.6 Root bending moment background response

The root bending moment background response can be expressed in terms of the standard deviation of the root bending moment excluding resonant effects. If the wind is perfectly correlated along the blade, this is given by

$$\sigma_{MB} = C_f \rho \bar{U} \cdot \sigma_u \int_0^R c(r)rdr \quad (\text{A5.35})$$

However, if the lack of correlation of wind fluctuations along the blade is taken into account,

$$\sigma_{MB} = C_f \rho \bar{U} \cdot \sigma_u \sqrt{\int_0^R \int_0^R \rho_u(r - r').c(r).c(r').r.r'.dr.dr'} \quad (\text{A5.36})$$

where $\rho_u(r - r')$ is the normalised cross-correlation function between simultaneous wind speed fluctuations at two different blade radii and is defined as

$$\rho_u(r - r') = \frac{1}{\sigma_u^2} E\{u(r, t).u(r', t + \tau)\} \quad (\text{A5.37})$$

with τ set equal to zero.

Measurements indicate that the normalised cross-correlation function decays exponentially, so it can be expressed as

$$\rho_u(r - r') = \exp[-|r - r'|/L_u^r] \quad (\text{A5.38})$$

where L_u^r is the integral length scale for the longitudinal turbulence component measured in the across wind direction along the blade and is thus defined as $\int_0^\infty \rho_u(r - r').d(r - r')$. As the integral length scale for longitudinal turbulence measured vertically in the across wind direction (L_u^z), is, if anything, less than that measured horizontally (L_u^y), it is conservative to treat it as being equal to that measured horizontally, with the result that L_u^r can be taken as equal to L_u^y also. Typically, L_u^y is approximately equal to 30% of L_u^x , the integral length scale for longitudinal turbulence measured in the along wind direction. Observing that

$$\overline{M} = \frac{1}{2}\rho\overline{U}^2 C_f \int_0^R c(r).r.dr$$

we can therefore write

$$\frac{\sigma_{MB}}{\overline{M}} = 2\frac{\sigma_u}{\overline{U}} \cdot \sqrt{K_{SMB}} \quad (\text{A5.39})$$

where K_{SMB} , the size reduction factor for the root bending moment background response, is defined as

$$K_{SMB} = \frac{\int_0^R \int_0^R \exp[-|r - r'|/0.3L_u^x].c(r).c(r').r.r'.dr.dr'}{\left(\int_0^R c(r).rdr\right)^2} \quad (\text{A5.40})$$

For a blade with a uniform chord, the integral is straightforward, giving

$$K_{SMB} = 4 \left[\frac{2}{3\phi} - \frac{1}{\phi^2} + \frac{2}{\phi^4} - \exp(-\phi) \left\{ \frac{2}{\phi^3} + \frac{2}{\phi^4} \right\} \right] \quad \text{where } \phi = \frac{R}{0.3L_u^x} \quad (\text{A5.41})$$

As an example, K_{SMB} comes to 0.837 for the case of $R = 40$ m and $L_u^x = 189$ m, indicating that the lack of correlation of the wind fluctuations reduces the root bending moment appreciably.

For blades with a normal tapering chord, K_{SMB} can be evaluated numerically. In the case of a blade with a tip chord equal to 33% of the maximum chord, K_{SMB} is 0.829 for the same value of ϕ as before. It is seen that the taper has an almost negligible effect on the end result.

A5.7 Peak response

One of the key parameters required in blade design is the extreme value of the out-of-plane bending moment. The 50 year return moment is defined as the expected maximum moment occurring during the mean wind averaging period when the mean takes the 50 year return value. Treating the moment as a Gaussian process, Davenport

(1964) has shown that the expected value of the maximum departure from the mean is the standard deviation multiplied by the peak factor, g , where

$$g = \sqrt{2 \ln(\nu T)} + \frac{0.5772}{\sqrt{2 \ln(\nu T)}} \quad (\text{A5.42})$$

In this formula, ν is the mean zero up-crossing frequency of the root moment fluctuations, and T is the mean wind speed averaging period. The variance of the root bending moment is, in the same way as for the tip displacement, equal to the sum of the variances of the background and resonant root bending moment responses, i.e.

$$\sigma_M^2 = \sigma_{MB}^2 + \sigma_{M1}^2 \quad (\text{A5.43})$$

Hence, from Eqs. (A5.39) and (A5.34), we obtain

$$\sigma_M^2 = \sigma_{MB}^2 + \sigma_{M1}^2 = 4 \overline{M}^2 \frac{\sigma_u^2}{\overline{U}^2} \left[K_{SMB} + \frac{\pi^2}{2\delta} R_u(n_1) \cdot K_{Sx}(n_1) \cdot \lambda_{M1}^2 \right] \quad (\text{A5.44})$$

Thus,

$$M_{\max} = \overline{M} + g \cdot \sigma_M = \overline{M} \left(1 + 2g \frac{\sigma_u}{\overline{U}} \sqrt{K_{SMB} + \frac{\pi^2}{2\delta} R_u(n_1) \cdot K_{Sx}(n_1) \cdot \lambda_{M1}^2} \right) \quad (\text{A5.45})$$

The mean zero up-crossing frequency of the root moment fluctuations, ν , is defined as

$$\nu = \sqrt{\frac{\int_0^\infty n^2 S_M(n) dn}{\int_0^\infty S_M(n) dn}} \quad (\text{A5.46})$$

where $S_M(n)$ is the power spectrum of the root moment fluctuations. If we separate the power spectrum of the background response from the first mode resonant response at frequency n_1 , then the above expression can be written

$$\nu = \sqrt{\frac{(\int_0^\infty n^2 S_{MB}(n) dn) + n_1^2 \sigma_{M1}^2}{\sigma_{MB}^2 + \sigma_{M1}^2}} \quad (\text{A5.47})$$

Now

$$S_{MB}(n) = (C_f \rho \overline{U})^2 \cdot S_u(n) \cdot \int_0^R \int_0^R \psi_{uu}^N(r, r', n) \cdot c(r) \cdot c(r') \cdot r \cdot r' \cdot dr \cdot dr' \quad (\text{A5.48})$$

and

$$\overline{M} = C_f \cdot \frac{1}{2} \rho \overline{U}^2 \cdot \int_0^R c(r) \cdot r \cdot dr \quad (\text{A5.49})$$

giving

$$C_f \rho \overline{U} = 2 \frac{\overline{M}}{\overline{U}} \frac{1}{\int_0^R c(r) r dr}$$

so

$$S_{MB}(n) = 4 \frac{\overline{M}^2}{\overline{U}^2} \cdot S_u(n) \cdot \frac{\int_0^R \int_0^R \psi_{uu}^N(r, r', n) \cdot c(r) \cdot c(r') \cdot r \cdot r' \cdot dr \cdot dr'}{\left(\int_0^R c(r) \cdot r \cdot dr \right)^2} \quad (\text{A5.50})$$

Defining

$$K_{SMB}(n) = \frac{\int_0^R \int_0^R \psi_{uu}^N(r, r', n) \cdot c(r) \cdot c(r') \cdot r \cdot r' \cdot dr \cdot dr'}{\left(\int_0^R c(r) \cdot r \cdot dr \right)^2} \quad (\text{A5.51})$$

we obtain

$$S_{MB}(n) = 4 \frac{\overline{M}^2}{\overline{U}^2} \cdot S_u(n) \cdot K_{SMB}(n) \quad (\text{A5.52})$$

Substituting into Eq. (A5.47) gives

$$\nu = \sqrt{\frac{4 \frac{\overline{M}^2}{\overline{U}^2} \left(\int_0^\infty n^2 S_u(n) K_{SMB}(n) dn \right) + n_1^2 \sigma_{M1}^2}{\sigma_{MB}^2 + \sigma_{M1}^2}} \quad (\text{A5.53})$$

Noting from Eq. (A5.52) that $\sigma_{MB}^2 = 4 \frac{\overline{M}^2}{\overline{U}^2} \int_0^\infty S_u(n) K_{SMB}(n) dn$, the expression for ν becomes

$$\nu = \sqrt{\frac{n_0^2 \sigma_{MB}^2 + n_1^2 \sigma_{M1}^2}{\sigma_{MB}^2 + \sigma_{M1}^2}} \quad (\text{A5.54})$$

where

$$n_0^2 = \frac{\int_0^\infty n^2 S_u(n) K_{SMB}(n) dn}{\int_0^\infty S_u(n) K_{SMB}(n) dn} \quad (\text{A5.55})$$

Substituting $\psi_{uu}^N(r, r', n) = \exp[-C(r - r')n/\overline{U}]$ into the expression for $K_{SMB}(n)$ in the numerator of Eq. (A5.55) gives

$$\int_0^\infty n^2 S_u(n) K_{SMB}(n) dn = \int_0^\infty n^2 S_u(n) \cdot \frac{\int_0^R \int_0^R \exp[-C(r - r')n/\overline{U}] \cdot c(r) \cdot c(r') \cdot r \cdot r' \cdot dr \cdot dr'}{\left(\int_0^R c(r) \cdot r \cdot dr \right)^2} \cdot dn \quad (\text{A5.56})$$

For high frequencies, the double integral is, in the limit, inversely proportional to frequency, so the integrand $n^2 S_u(n) K_{SMB}(n)$ is proportional to $n^2 n^{-\frac{5}{3}} n^{-1} = n^{-\frac{2}{3}}$ and the integral does not converge. Consequently, it is necessary to take account of the chordwise lack of correlation of wind fluctuation at high frequencies, and if this is done, it is found that, in the limit, the integrand is proportional to $n^{-\frac{5}{3}}$ for which the integral is finite. The evaluation of the integral $\int_0^\infty n^2 S_u(n) K_{SMB}(n) dn$ taking chordwise lack of correlation into account is a formidable task, so the use of an approximate formula for the frequency, n_0 , is preferable, especially as the influence of n_0 on the peak factor, g , is

slight. Dyrbye and Hansen (1997) give an approximate formula for a uniform cantilever as follows:

$$n_0 = 0.3 \frac{\bar{U}}{\sqrt{L_u^x} \sqrt{Rc}} \quad (\text{A5.57})$$

Here R is the blade tip radius and c is the blade chord, assumed constant. For a tapering chord, the mean chord, \bar{c} , can be substituted.

A5.8 Bending moments at intermediate blade positions

A5.8.1 Background response

Denoting the standard deviation of the quasi-static or background bending moment fluctuations at radius r^* as $\sigma_{MB}(r^*)$, it is apparent that

$$\frac{\sigma_{MB}(r^*)}{\sigma_{MB}(0)} = \sqrt{\frac{K_{SMB}(r^*)}{K_{SMB}(0)} \frac{\int_{r^*}^R c(r)[r - r^*]dr}{\int_0^R c(r)rdr}} \quad (\text{A5.58})$$

The ratio of the steady moment at radius r^* to that at the root is $\frac{\int_{r^*}^R c(r)[r - r^*]dr}{\int_0^R c(r)rdr}$, so the ratio of the standard deviation of the quasi-static fluctuations at radius r^* to the steady value there is

$$\frac{\sigma_{MB}(r^*)}{\bar{M}(r^*)} = \frac{\sigma_{MB}(r^*)}{\sigma_{MB}(0)} \frac{\sigma_{MB}(0)}{\bar{M}(0)} \frac{\bar{M}(0)}{\bar{M}(r^*)} = \frac{\sigma_{MB}(0)}{\bar{M}(0)} \sqrt{\frac{K_{SMB}(r^*)}{K_{SMB}(0)}} \quad (\text{A5.59})$$

Generally, the square root will be close to unity, so $\frac{\sigma_{MB}(r^*)}{\bar{M}(r^*)}$ will be nearly constant.

A5.8.2 Resonant response

In Section A5.5, it was shown that the standard deviation of the first mode resonant root bending moment is equal to $\omega_1^2 \sigma_{x1} \int_0^R m(r)\mu_1(r)r dr$ (Eq. A5.27). The corresponding quantity at other radii can be derived similarly, giving

$$\sigma_{M1}(r^*) = \omega_1^2 \sigma_{x1} \int_{r^*}^R m(r)\mu_1(r)[r - r^*]dr \quad (\text{A5.60})$$

Hence, the ratio of the standard deviation of the first mode resonant root bending moment at radius r^* to the steady value there is

$$\frac{\sigma_{M1}(r^*)}{\bar{M}(r^*)} = \frac{\sigma_{M1}(r^*)}{\sigma_{M1}(0)} \frac{\sigma_{M1}(0)}{\bar{M}(0)} \frac{\bar{M}(0)}{\bar{M}(r^*)} = \frac{\int_{r^*}^R m(r)\mu_1(r)[r - r^*]dr}{\int_0^R m(r)\mu_1(r)r dr} \frac{\int_0^R c(r)r dr}{\int_{r^*}^R c(r)[r - r^*]dr} \frac{\sigma_{M1}(0)}{\bar{M}(0)} \quad (\text{A5.61})$$

References

- Cramer, H.E. (1958). Use of power spectra and scales of turbulence in estimating wind loads. Proceedings of the Second National Conference on Applied Meteorology, Ann Arbor, Michigan, USA.
- Davenport, A.G. (1962). The response of slender, line-like structures to a gusty wind. *Proc. Inst. Civ. Eng.* 23: 389–408.
- Davenport, A.G. (1964). Note on the distribution of the largest value of a random function with application to gust loading. *Proc. Inst. Civil Eng.* 28: 187–196.
- Dyrbye, C. and Hansen, S.O. (1997). *Wind Loads on Structures*. Wiley.
- EN 1991-1-4:2005 (2005). *Eurocode 1: Actions on structures – Part 1-4: General actions – Wind actions*. Brussels: European Committee for Standardization.
- Harris, R.I. (1971). The nature of the wind. Proceedings of the CIRIA Conference, pp 29–55.
- Krenk, S. (1995). Wind field coherence and dynamic wind forces. Proceedings of the Symposium on the Advances in Non-linear Stochastic Mechanics.
- Mann, J. (1994). The spatial structure of neutral atmospheric surface-layer turbulence. *J. Ind. Aerodyn.* 1: 167–175.
- Newland, D.E. (1984). *Random Vibration and Spectral Analysis*. UK: Longman.
- Wyatt, T.A. (1980). The dynamic behaviour of structures subject to gust loading. Proceedings of the CIRIA Conference Wind Engineering in the Eighties, pp. 6-1–6-22.

6

Conceptual design of horizontal axis wind turbines

6.1 Introduction

Within the general category of horizontal axis wind turbines for grid applications, there exists a great variety of possible machine configurations, power control strategies, and braking systems. This chapter looks at the different areas where design choices have to be made and considers the advantages and disadvantages of the more conventional options in each case. Inevitably, there are situations in which decisions in one area can impact those in another, and some of these are noted.

Alongside these discrete design choices, there are several fundamental design parameters, such as rotor diameter, machine rating, and rotational speed, which also have to be established at the start of the design process. Continuous variables such as these lend themselves to mathematical optimisation, as described in the opening sections of the chapter.

An illuminating overview of the evolution of turbine design, including the power control strategies and drive train configurations adopted by particular manufacturers, is provided in *Wind Energy – The Facts* (EWEA 2009) published by the European Wind Energy Association (EWEA).

6.2 Rotor diameter

The issue of what size of turbine produces energy at minimum cost has been fiercely debated for a long time. Protagonists of large machines cite economies of scale and the increase in wind speed with height in their favour. On the other hand, the economics of large machines suffer as a result of the ‘square-cube law’, whereby energy capture increases as the square of the diameter, whereas rotor mass (and therefore cost) increases as the cube.

In reality, both arguments are correct, and there is a trade-off between economies of scale and a variant of the ‘square-cube law’ that takes into account the wind shear effect. This trade-off can be examined with the help of simple cost modelling, which is considered next. However, it should be recognised that, in the case of blades at least, the ‘square-cube’ law has, to a significant extent, been circumvented up till the time of writing by the introduction of improved materials and increased structural efficiency as diameters have increased.

6.2.1 Cost modelling

The sensitivity of the cost of energy to changes in the values of parameters governing turbine design can be examined with the aid of a model of the way component costs vary in response. The normal procedure is to start with a baseline design, for which the costs of the various components are known. In a rigorous analysis, the chosen parameter is then assigned a different value and a fresh design developed, leading to revised component weights, based on which new component costs can be assigned.

In general, the cost of a component will not simply increase pro rata with its mass but will contain elements that increase more slowly. Examples are the tower surface protective coating and tower longitudinal welds (assuming the number required is constant), the costs of which increase approximately as the *square* of the tower height, if all dimensions are proportional to this height. If the design parameter variation considered is only about $\pm 50\%$, it is usually sufficiently accurate to represent the relationship between component cost and mass as a linear one with a fixed component, as follows:

$$C(x) = C_B \left(\mu \frac{m(x)}{m_B} + (1 - \mu) \right) \quad (6.1)$$

where $C(x)$ and $m(x)$ are the cost and mass of the component, respectively, when the design parameter takes the value x , and C_B and m_B are the baseline values. μ is the proportion of the cost that varies with mass, which will obviously differ for different baseline machine sizes and for different components.

The choice of the value of μ inevitably requires considerable expertise as regards the way manufacturing costs vary with scale, which may be limited in the case of products at the early stage of development. In view of this, the effort of developing fresh designs for different design parameter values may well not be justified, so resort is often made to scaling ratios based on similarity relationships. This approach is adopted in the investigation of optimum machine size that follows.

6.2.2 Simplified cost model for machine size optimisation: an illustration

The baseline machine design is taken as a 60 m diameter, 1.5 MW turbine, with the costs of the various components taken from the Risø publication ‘Cost Optimisation of Wind Turbines for Large-Scale Offshore Wind Farms’, by Fuglsang and Thomsen (1998). These are given in Table 6.1 as a percentage of the total.

Table 6.1 Component costs expressed as a percentage of total machine cost for a 1.5 MW, 60 m diameter, fixed-speed, stall-regulated wind turbine on land

Component	Cost as a percentage of total	Component	Cost as a percentage of total
Blades	18.3%	Controller	4.2%
Hub	2.5%	Tower	17.5%
Main shaft	4.2%	Brake system	1.7%
Gearbox	12.5%	Foundation	4.2%
Generator	7.5%	Assembly	2.1%
Nacelle	10.8%	Transport	2.0%
Yaw system	4.2%	Grid connection	8.3%
		Total	100%

Source: From Risø-R-1000, Fuglsang and Thomsen (1998).

Machine designs for other diameters are obtained by scaling *all* dimensions of all components in the same proportion, except in the case of the gearbox, generator, grid connection, and controller. Rotational speed is kept inversely proportional to rotor diameter to maintain constant tip speed and hence constant tip speed ratio at a given wind speed. As a result, the maximum rotor aerodynamic thrust increases with the square of rotor diameter, and the peak aerodynamic bending moment in each structural element, which is assumed to govern its design, increases with rotor diameter cubed. Given the assumption that all cross-sectional dimensions increase in proportion to rotor diameter, the bending section moduli increase as diameter cubed, so each critical stress remains invariant with diameter.

Maintenance of constant tip speed also means that all machine designs reach rated power at the same wind speed, so that rated power is proportional to diameter squared. However, the low-speed shaft torque increases as diameter cubed, which is the basis for assuming the gearbox mass increases as the cube of rotor diameter, even though the gearbox ratio changes.

In the following illustration a blanket value of μ of 0.9 for all components is adopted for simplicity. Accordingly, the cost of all components apart from generator, controller, and the grid connection, for a machine of diameter D , is given by

$$C_1(D) = 0.8 C_T(60) \left(0.9 \left(\frac{D}{60} \right)^3 + 0.1 \right) \quad (6.2)$$

where $C_T(60)$ is the total cost of the 60 m diameter baseline machine.

The rating of the generator and the grid connection is proportional only to the diameter squared. It is assumed that Eq. (6.1) applies to the cost of these components, but with mass replaced by rating. Thus the cost of the generator and grid connection are given by

$$C_2(D) = 0.158 C_T(60) \left(0.9 \left(\frac{D}{60} \right)^2 + 0.1 \right) \quad (6.3)$$

The controller cost is assumed to be fixed, regardless of turbine size. Hence the resulting turbine cost as a function of diameter is

$$\begin{aligned} C_T(D) &= C_T(60) \left(0.8 \left\{ 0.9 \left(\frac{D}{60} \right)^3 + 0.1 \right\} + 0.158 \left\{ 0.9 \left(\frac{D}{60} \right)^2 + 0.1 \right\} + 0.042 \right) \\ &= C_T(60) \left(0.72 \left(\frac{D}{60} \right)^3 + 0.1422 \left(\frac{D}{60} \right)^2 + 0.1378 \right) \end{aligned} \quad (6.4)$$

As the tower height, along with all other dimensions, is assumed to increase in proportion to rotor diameter, the annual mean wind speed (*amws*) at hub height will increase with rotor diameter because of wind shear. This has a significant effect on energy yield, as the energy yield per unit of swept area is found to vary as the *amws* raised to the power of 1.9 for perturbations about the *amws* central value of 8 m s^{-1} taken in this example. The cost of energy (excluding operation and maintenance costs) can then be calculated in €/kWh/annum by dividing the turbine cost by the annual energy yield. The variation of energy cost with diameter, calculated according to the assumptions described above, is plotted in Figure 6.1 for two levels of wind shear corresponding to roughness lengths, z_0 , of 0.001 m and 0.05 m, the hub-height wind speed being scaled according to the relation $\bar{U}(z) \propto \ln(z/z_0)$ (see Section 2.6.2). Also included is a plot for the case of zero wind shear.

It is apparent that the level of wind shear has a noticeable effect on the optimum machine diameter, which varies from 44 m for zero wind shear to 52 m for the wind shear corresponding to a surface roughness length of 0.05 m, which is applicable to farmland with boundary hedges and occasional buildings. Strictly, the impact of the increased annual mean wind speed with hub height on the fatigue design of the rotor and other components should also be taken into account, which would reduce the optimum machine size slightly.

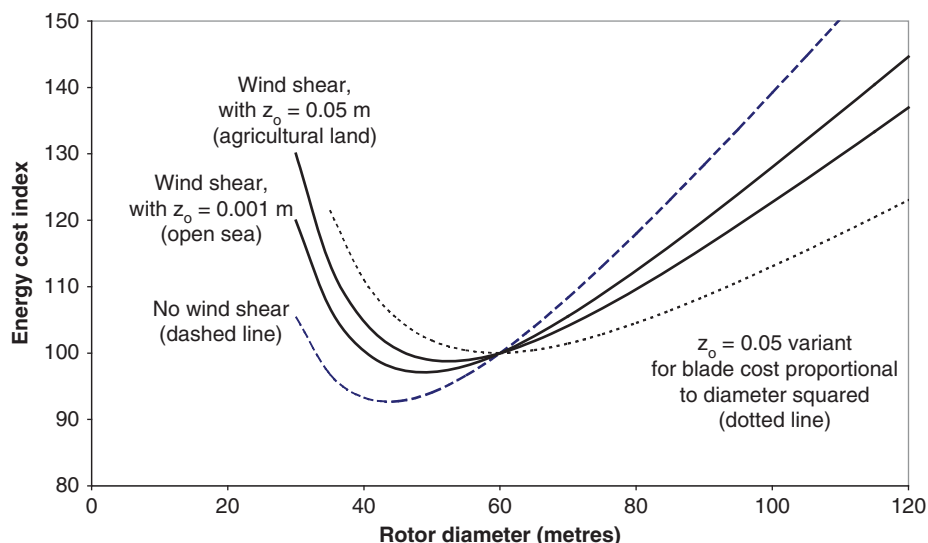


Figure 6.1 Variation of optimum turbine size with wind shear based on simplified cost model (assuming hub height equal to diameter)

It should be emphasised that the optimum sizes derived above depend critically on the value of μ adopted. For example, if μ were taken as 0.8 instead of 0.9, the optimum diameter would increase to 64 m for the wind shear corresponding to a surface roughness length of 0.05 m, although the minimum cost of energy would alter by only 0.9%. The correct approach would be to allocate different values of μ to different components, as is done in Fuglsang and Thomsen (1998). Ideally, these would be based on cost data on components of the same design but different sizes.

The cost model outlined and illustrated above provides a straightforward means of investigating scale effects on machine economics for a chosen machine design. In practice, the use of different materials or different machine configurations may prove more economic at different machine sizes and will yield a series of alternative cost versus diameter curves.

An example of the impact technological developments can have on simple scaling rules is provided by the trajectory of specific blade mass – defined as blade mass divided by turbine diameter cubed – as longer blade designs have evolved over time. Figure 6.2a shows a plot of specific blade mass against diameter for blades manufactured by LM Glasfiber that were available in 2004.

It is seen that the specific blade mass is approximately inversely proportional to diameter – i.e. the blade mass has increased with diameter squared rather than with diameter cubed. The decline in specific blade mass is partly due to a lower practical limit on skin thicknesses, which made the smaller blades heavier than they would otherwise need to be, and partly due to technological improvements in the manufacture of glass fibre reinforced plastic (GFRP) blades, which have permitted increased fibre volume fractions and hence higher strengths.

The blade cost scaling rule adopted in the cost model obviously has a decisive effect on the optimum rotor diameter, which (for the case of wind shear corresponding to a surface roughness of 0.05 m) increases from 52 to 59 m when the blade cost is scaled as the square of diameter, as indicated by the dotted line in Figure 6.1. This does not take into account the knock-on savings in the costs of other components due to the reduction in rotor mass.

In recent years, data on the weights of blades in production has become increasingly scarce, but the few figures available suggest that the trend in Figure 6.2a may be continuing as turbine diameters increase. See Figure 6.2b, which also includes the specific blade masses of the National Renewable Energy Laboratory (NREL) 5 MW and DTU 10 MW reference blade designs (Jonkman et al. [2009] and Bak et al. [2013]).

6.2.3 The NREL cost model

Research at NREL, reported in ‘Wind Turbine Design Cost and Scaling Model’ (Fingersh et al. [2006]), has resulted in a useful set of mass and cost scaling rules for several wind turbine configurations, which serve as benchmarks against which innovations in the design of individual components can be judged. It is intended that the scaling rules are updated over time as additional data becomes available.

The baseline turbine design is a 70 m diameter, 1.5 MW variable-speed pitch-regulated machine, fitted with a three stage planetary gearbox. Many of the scaling rules are similar to those set out in the preceding section, with the main differences being as follows:

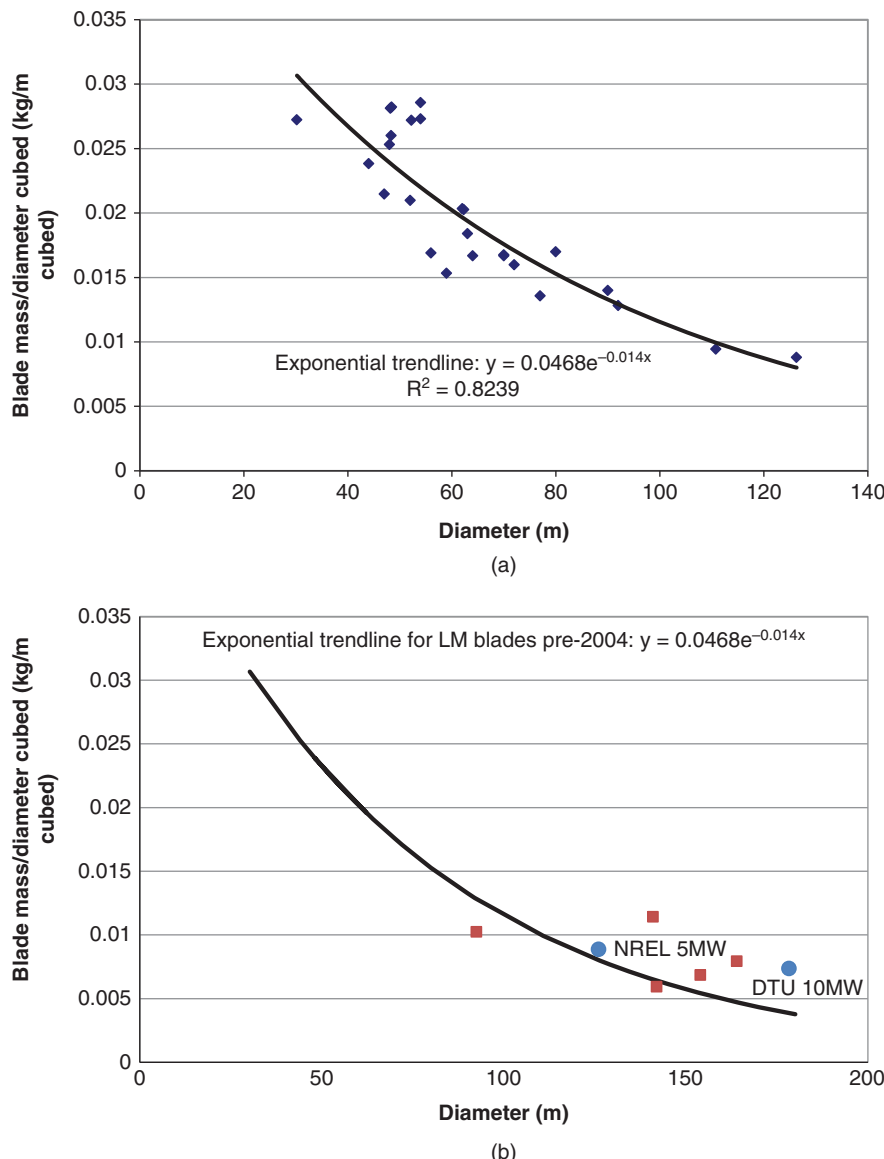


Figure 6.2 (a) Variation of specific blade mass with diameter for LM blades available in 2004. (b) Variation of specific blade mass with diameter for large turbines, based on limited published data available in 2019

- Blade cost split into material and labour costs of similar magnitudes, with the former scaling as diameter cubed (D^3) and the latter scaling as $D^{2.5}$.
- Gearbox and main bearings costs scaled as $D^{2.5}$ rather than D^3 .
- Nacelle cost scaled as $D^{1.95}$ rather than D^3 .

- Foundation cost scaled as $D^{1.2}$ rather than D^3 .
- An element of transport cost increasing as the fourth power of diameter.

Some of the cost formulae include a fixed element, which can be negative.

The cost of the pitch mechanism and bearings is assumed to be proportional to $D^{2.66}$, and the cost of the variable-speed electronics is taken to be proportional to machine rating.

Table 6.2 presents the component costs of the baseline turbine in 2005 dollars and the respective percentages of the total. Also shown are the corresponding percentages for the 60 m diameter 1.5 MW machine of the preceding section, where applicable. Caution should be exercised in making comparisons, however, as component definitions may vary.

Figure 6.3 presents the variation of the cost of energy capital component with turbine diameter, based on the NREL cost model for the machine described previously. The annual mean wind speed at 50 m height is taken as 7.25 m/s, and wind speed is assumed to vary with hub height according to the power law $\bar{U}(z) = \bar{U}(50).(z/50)^{0.14}$. Hub height is taken as equal to turbine diameter as before, and the rated wind speed in all cases is 11.55 m/s. Turbine life is taken as 20 years, and a discount rate of 10% is used.

It is seen that the model indicates that the optimum turbine diameter is just over 70 m – rather greater than that given by the cost model in the preceding section. This is to be expected in view of the reduced diameter exponents of the scaling rules for some components.

6.2.4 The INNWIND.EU cost model

A comprehensive cost model in the form of a spreadsheet was developed as part of the INNWIND project - Innovative Wind Conversion Systems (10–20 MW) for Offshore Applications – (INNWIND [2016]). This updated and expanded the NREL cost model, adding alternative options for the costing of blades, drive trains, towers, and offshore foundations.

6.2.5 Machine size growth

During the 1980s and 1990s, the size of the largest turbines in commercial production doubled about every 7 years. More recently, the driver to increased diameters has undoubtedly been the extension of wind farm development offshore, where substantial fixed elements of support structure and undersea cable installation costs favour the deployment of much larger machines than on land. Nevertheless, *Wind Energy – The Facts* (EWEA 2009) pointed out that the diameter of the largest commercially available wind turbine plateaued at about 125 m between 2004 and 2008 – a striking pause in the rapid growth in machine size hitherto. Turbine size growth has subsequently resumed, however, with the result that in 2019 about 40 different turbines were being marketed with diameters in excess of 130 m, although some differed only in power rating. Offshore, Siemens has been deploying 154 m diameter turbines since 2015, and Vestas has been deploying 164 m diameter turbines since 2017. Moreover, General Electric built a 220 m diameter prototype in 2019 – the 12 MW Haliade-X.

The increasing popularity of turbines over 100 m in diameter for sites on land begs the question of why sizes larger than the apparent optimum are being chosen. Part of

Table 6.2 Component costs and percentages for NREL 1.5 MW 70 m diameter baseline machine

Component	Component costs for 1.5 MW, 70 m diameter NREL baseline turbine (with 70 m hub height) \$1000 (2005)	Percentage component costs for NREL baseline turbine	Percentage component costs for Risø-R-1000 1.5 MW, 60 m diameter turbine
Blades	151	11.4%	18.3%
Hub and nose cone	47	3.6%	2.9%
Pitch bearings and mechanism, including hydraulics	56	4.3%	N/A
Low-speed shaft and main bearings	33	2.5%	4.2%
Gearbox	152	11.6%	12.9%
Generator	98	7.4%	7.5%
Variable-speed electronics	119	9.0%	N/A
Nacelle main frame and cover	117	8.9%	10.8%
Yaw drive and bearing	20	1.5%	4.2%
Control system	35	2.7%	4.2%
Tower	158	12.0%	17.5%
Brake and high-speed coupling	3	0.2%	1.7%
Foundation	47	3.6%	4.2%
Assembly and installation	42	3.2%	2.1%
Transportation	51	3.9%	2.0%
Internal electrical connections	60	4.6%	8.3%
Electrical connection to substation	127	9.6%	
	1317	100%	100%

the answer may lie in imperfections of the cost models. However, a significant factor encouraging the selection of larger turbines is undoubtedly that their use enables better exploitation of sites of limited area. For example, the total rated capacity that can be installed on a narrow ridge increases roughly linearly with turbine diameter, assuming (as is normally the case) that the minimum spacing permitted by the manufacturer is

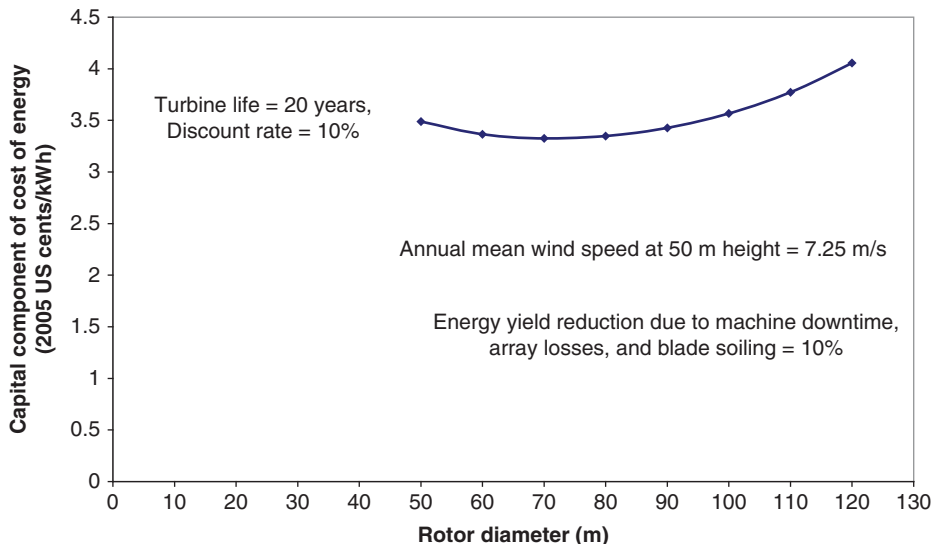


Figure 6.3 Variation of cost of energy with turbine diameter for NREL baseline machine – capital cost component only

specified in terms of a fixed number of turbine diameters. Given that some site development costs, such as permitting and grid connection, do not vary significantly with wind farm rated capacity, there is always an incentive to maximise the installed capacity.

6.2.6 Gravity limitations

The simplified cost model described above was based on the assumption that blade design is governed solely by aerodynamic loads. However, as diameters increase, it is inevitable that edgewise moments due to blade self-weight will become increasingly important. For a family of blade designs derived from a baseline design by simply scaling the diameter and all other dimensions by the same amount, the blade root gravity moment will increase as the fourth power of diameter while the section modulus only increases by the third power. Although there will initially be some scope for catering for the increased gravity moment by redeployment of material closer to the leading and trailing edges, a limit on the practicable diameter for any particular blade material must eventually be reached.

6.2.7 Variable diameter rotors

The reduction of turbine diameter as wind speed increases offers the possibility of increased energy capture at low winds without the penalty of increased loads at high winds. The diameter reduction can be achieved either by reducing the cone angle if the blades are hinged at the root or by retracting a sliding blade tip section, which would necessarily have to be of uniform cross-section, on a rigid hub rotor. Jamieson (2018) describes these concepts in more detail and work carried out to evaluate them.

6.3 Machine rating

The machine rating determines the wind speed (known as *rated wind speed*) at which rated power is reached. If the rating is too high for a given rotor diameter, the rated power will only be reached rarely, so the cost of the drive train and generator will not be justified by the energy yield. However, if the rating is reduced below the optimum, then the cost of the rotor and its supporting structure will be excessive in relation to energy yield.

The investigation of the optimum relationship between rotor diameter and rated power can be carried out with the help of the cost modelling technique described in the previous section.

6.3.1 Simplified cost model for optimising machine rating in relation to diameter

The way in which the design of the various wind turbine components is influenced by changes in the rated speed is critically dependent on the nature of any accompanying changes in rotational speed. However, in view of the fact that the maximum rotational speed of land based machines is generally restricted to limit noise emission (see Section 6.4), it is assumed here that the maximum tip speed is limited to 80 m/s, regardless of the rated wind speed.

The simplified cost model is applied to a pitch-regulated, variable-speed machine, as these are now the turbine of choice. It is assumed that the machine is designed for optimum performance at a tip speed ratio of 8 and that it operates at this tip speed ratio up to a wind speed of 10 m/s, with the nominal tip speed remaining at 80 m/s at higher wind speeds.

Assuming that the blade plan-form and twist distribution are fixed, the annual energy yield can be calculated for a number of rated wind speeds, for a given annual mean wind speed and Weibull shape factor. The aim of the optimisation is to obtain the minimum cost of energy, which requires knowledge of how the costs of the various turbine components would be affected by the rating change. Although in theory this could only be rigorously derived by carrying out a series of detailed turbine designs, in practice it is possible to obtain a useful indication of cost trends by identifying the parameters driving the design of each component category and investigating their dependence on the rated wind speed. If the cost split between various components is known for a baseline machine, these cost trends can then be applied to it to determine the optimum rating. In this case the cost shares given in Table 6.2 for the 70 m diameter, 1.5 MW NREL machine are used.

The manner in which the design of each of the major components is influenced by rated wind speed is set out as follows:

1. *Blade weight*: The following assumptions are made:
 - The blade plan-form is constant.
 - The blade design is governed by out-of-plane bending moments in fatigue.
 - The out-of-plane bending moment fluctuations are proportional to the product of the wind speed fluctuation and the rotational speed [see Eq. (5.25) in Section 5.7.5].

- The rotational speed is a function of prevailing wind speed but is independent of rated wind speed assuming the latter is 10 m/s or above.
 - The blade skin thickness is independent of rated wind speed.
Hence, the blade skin thickness and therefore the blade weight are unaffected by changes in the rated wind speed.
2. *Hub and pitch system weights*: It is assumed that each is proportional to the blade out-of-plane bending moments in fatigue – i.e. independent of rated wind speed.
 3. *Low-speed shaft weight*: This is assumed to be governed by the shaft bending moment due to the cantilevered rotor and hub weights, which are unaffected by changes in rated wind speed.
 4. *Gearbox and brake*: Gearbox and brake design are governed by the rated torque, P/Ω . The maximum rotational speed is fixed, so the rated torque varies as the power rating. The weights of the gearbox and brake are therefore taken to be proportional to the rated power.
 5. *Generator and variable-speed electronics*: The design of the generator and the variable-speed electronics are governed by rated power, and the weight is assumed to be proportional to rated power in each case.
 6. *Nacelle structure, yaw system, tower, and foundation*: The design of these is governed principally by either extreme or fluctuating loads on the rotor, both of which are assumed to be independent of rated wind speed. The weights are therefore taken to be unaffected by rated wind speed.
 7. *Grid connection*: The weight of cables, switchgear, and transformers are assumed to be proportional to rated power.
 8. *Controller, assembly, and transport*: The costs of these items are taken as independent of rated speed.

The various components just listed are classified into two categories in Table 6.3, according to whether their weights are fixed or vary with the rated power. Also tabulated are the component costs as a percentage of the total for the baseline machine, together with the sum for each category.

Accordingly, the following expression is obtained for machine cost as a function of the ratio of the rated power to that of the baseline machine, P_R/P_{RB} :

$$C_T = C_{TB}(0.576 + 0.424(P_R/P_{RB})) \quad (6.5)$$

The capital component of the cost of energy is obtained by dividing the machine cost from Eq. (6.5) by the discounted lifetime annual energy yield, which is calculated for each rated wind speed by combining the corresponding power curve with the Weibull distribution of wind speeds. This exercise has been carried out using the 70 m diameter, 1.5 MW pitch-regulated, variable-speed NREL machine as baseline, assuming an annual mean wind speed of 7.5 m/s and taking the rated wind speed of the baseline machine as 11.55 m/s. The results are presented in Figure 6.4, which indicates that the optimum machine rating is very close to the 1.5 MW baseline. The variation in cost of energy with

Table 6.3 Percentage contribution of different components to machine cost for the 70 m diameter, 1.5 MW NREL baseline machine, classified according to whether their cost varies with rated power or not

Components for which the weight/cost is independent of rated wind speed		Components for which the weight varies as rated power	
Component	Cost	Component	Cost
Blades	11.4%	Gearbox	11.6%
Hub and spinner	3.6%	Generator	7.4%
Pitch bearings and mechanism	4.3%	Variable-speed electronics	9%
Low-speed shaft and bearings	2.5%	Brake and high-speed coupling	0.2%
Nacelle	8.9%	Internal cables and grid connection	14.2%
Yaw drive and bearing	1.5%		
Control system	2.7%		
Tower	12%		
Foundation	3.6%		
Assembly	3.2%		
Transport	3.9%		
Total	57.6%	Total	42.4%

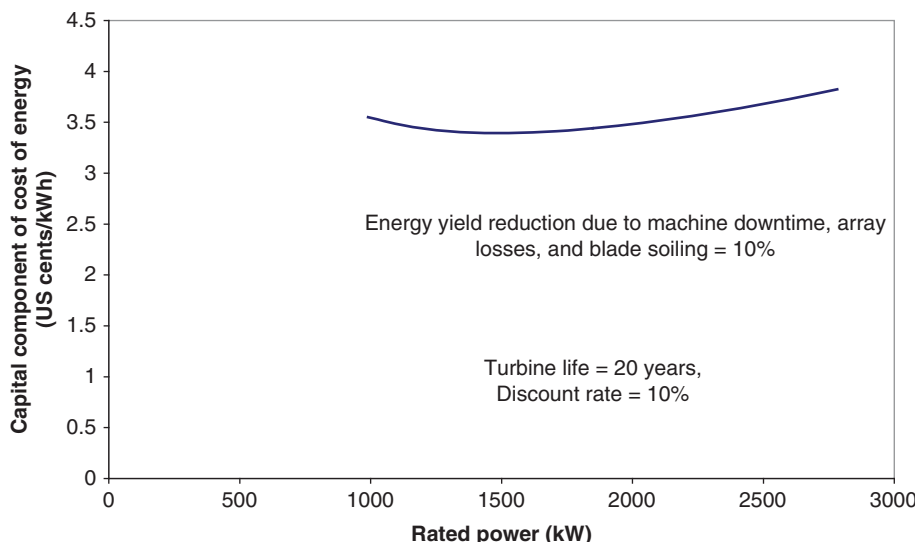


Figure 6.4 Variation in cost of energy with rated power for a 70 m diameter, pitch-regulated variable-speed machine for an annual mean wind speed of 7.5 m s^{-1} , based on simplified cost model

rated power on either side of the optimum is very small, with the maximum increase in the cost of energy over the range 1100–2000 kW being only 3%.

6.3.2 Relationship between optimum rated wind speed and annual mean

The optimum power rating is, of course, heavily dependent on the annual mean wind speed, U_{ave} . The optimum rated wind speed, U_{Ro} for the above 70 m diameter pitch-regulated machine is given for a range of annual mean wind speeds in Table 6.4. The ratio $U_{\text{Ro}}/U_{\text{ave}}$ is in the range 1.6–1.4, decreasing with increasing wind speed.

A similar exercise can be carried out to determine the optimum rated power of a stall-regulated machine and would yield similar results. However, because stall-regulated machines reach rated power at a substantially higher wind speed than pitch-regulated machines of the same rating, the $U_{\text{Ro}}/U_{\text{ave}}$ ratio for stall-regulated machines is typically about 2.

6.3.3 Specific power of production machines

It is instructive to investigate the relationship between rated power and swept area for production machines, and these quantities are plotted against each other in Figure 6.5 for 79 machines in production in 2008. Although different machines will have been designed for different annual mean wind speeds, the degree of scatter is not large, and a clear trend is apparent, with the line of best fit being close to a straight line passing through the origin. The mean specific power, defined as rated power divided by swept area, is 380 W per square metre for the 79 machines - close to the optimum value in Table 6.4 for an annual wind speed of 7.5 m/s.

When a similar exercise is carried out for turbines in production in 2019, the picture is rather different – see Figure 6.6. This covers 100 turbines produced by six of the largest wind turbine manufacturers and includes a few large turbine designs that have been announced but not yet manufactured. It is seen that the mean value of the power to swept area ratio has much reduced – from 380 to 297 W/sqm, indicating that more designs are being tailored to low wind sites. As a result, there is an increased spread of

Table 6.4 Variation of optimum rated wind speed with annual mean for 70 m diameter pitch-regulated machines

Annual mean wind speed, U_{ave} (m/s)	Optimum rated wind speed, U_{Ro} (m/s)	Ratio $U_{\text{Ro}}/U_{\text{ave}}$	Optimum rated power (kW)	Specific power, defined as rated power per unit swept area (W/sqm)	Cost index, with cost of energy for amws of 7.5 m/s taken as 100
7	11.1	1.59	1340	349	113
7.5	11.5	1.54	1495	388	100
8	11.9	1.49	1635	425	90
8.5	12.3	1.445	1770	460	81
9	12.65	1.405	1905	495	75

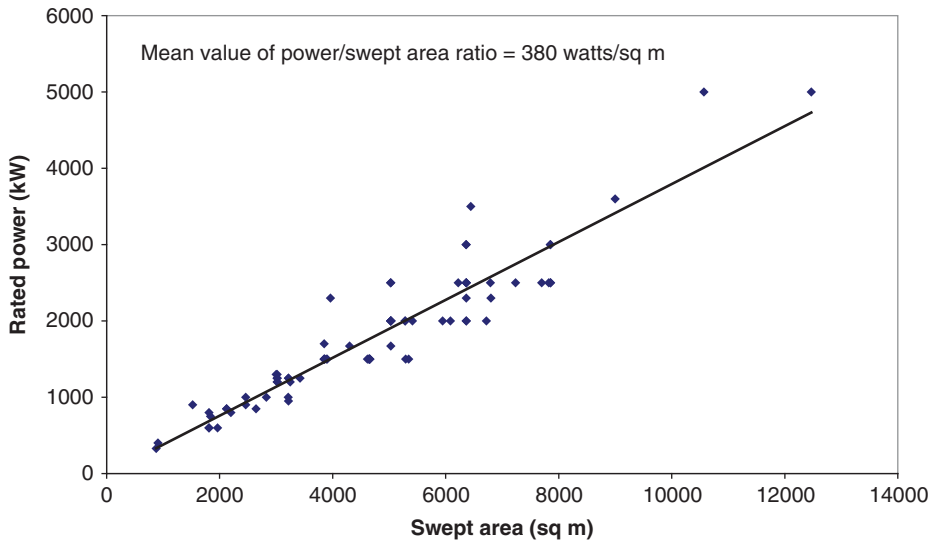


Figure 6.5 Rated power vs swept area for turbines in production in 2008

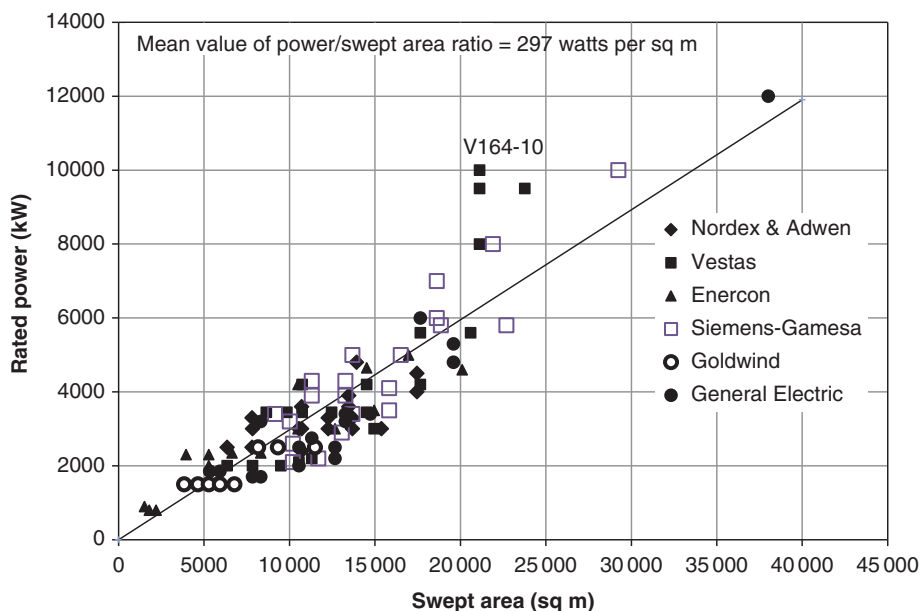


Figure 6.6 Rated power vs swept area for turbines in or close to production in 2019

power ratings for a given turbine diameter, reflecting the availability of turbines to suit a wide range of wind speeds. However, the largest turbines, which are deployed at higher wind speed sites offshore, generally exhibit significantly higher power to swept area ratios, with the Vestas V164 10 MW machine having the highest ratio of 473 W/sqm.

6.4 Rotational speed

The aim of the wind turbine designer is the production of energy at minimum cost, subject to constraints imposed by environmental impact considerations. However, blade designs optimised for a number of different rotational speeds but the same rated power produce substantially the same energy yield, so the choice of rotational speed is based on machine cost rather than energy yield.

One of the key cost drivers is the rotor torque at rated power, as this is the main determinant of the drive train cost. For a given tip radius and machine rating, the rotor torque is inversely proportional to rotational speed, which argues for the adoption of a high rotational speed. However, increasing the rotational speed has adverse effects on the rotor design, which are explored in the following sections.

6.4.1 Ideal relationship between rotational speed and solidity

Equation (3.72) in Section 3.8.2 gives the chord distribution of a blade optimised to give maximum power at a particular tip speed ratio in terms of the lift coefficient, ignoring drag and tip-loss:

$$\sigma_r \lambda \mu C_l = \frac{8/9}{\sqrt{\left(1 - \frac{1}{3}\right)^2 + \lambda^2 \mu^2 \left[1 + \frac{2}{9\lambda^2 \mu^2}\right]^2}}$$

where λ is the tip speed ratio, σ_r is the solidity, and $\mu = r/R$. Over the outboard half of the blade, which produces the bulk of the power, the local speed ratio, $\lambda\mu$, will normally be large enough to enable the denominator to be approximated as $\lambda\mu$, giving

$$\sigma_r \lambda \mu C_l = \frac{B c(\mu)}{2\pi R} \lambda C_l = \frac{8}{9\lambda\mu} \quad (6.6)$$

where B is the number of blades. After rearrangement, this gives

$$c(\mu) \left(\frac{\Omega R}{U_\infty} \right)^2 = \frac{16\pi R}{9C_l B} \cdot \frac{1}{\mu} \quad (6.7)$$

Hence it can be seen that, for a family of designs optimised for different rotational speeds at the same wind speed, the blade chord at a particular radius is inversely proportional to the square of the rotational speed, assuming that B and R are fixed and the lift coefficient is maintained at a constant value by altering the local blade pitch to maintain a constant angle of attack.

Note that Eq. (6.7) does not apply if energy yield is optimised over the full range of operating wind speeds for a fixed-speed pitch-regulated machine. In this case, it has been demonstrated that the blade chord at a particular radius is approximately inversely proportional to rotational speed rather than to the square of it (Jamieson and Brown (1992)).

6.4.2 Influence of rotational speed on blade weight

The effect of rotational speed on blade weight can be explored with reference to the family of blade designs just described. As in Section 6.3.1, it is assumed that the blade design is governed by out-of-plane bending moments in fatigue and that the moment fluctuations are proportional to the product of the wind speed fluctuation, the rotational speed, and the chord scaling factor, based on Eq. (5.26):

$$\sigma_M = \int_0^R \sigma_L r dr = \frac{1}{2} \rho \Omega \frac{dC_L}{d\alpha} \sigma_u \int_0^R c(r) r^2 dr$$

By Eq. (6.7) the chord scaling factor is inversely proportional to the square of the rotational speed, so the moment fluctuations simply vary inversely as the rotational speed.

If the thickness to chord ratios at each radius are assumed to be unaffected by the chord scaling, the blade section modulus for out-of-plane bending at a given radius is proportional to the product of the blade shell skin thickness, $w(r)$, and the square of the local chord. Thus,

$$Z(r) \propto w(r).c(r)^2 \propto w(r)/\Omega^4 \quad (6.8)$$

To maintain the fatigue stress ranges at the same level, we require the blade section modulus, $Z(r)$, to vary as the moment fluctuations, which, as shown above, vary inversely as rotational speed. Thus,

$$Z(r) \propto 1/\Omega \quad \text{so} \quad w(r)/\Omega^4 \propto 1/\Omega \quad \text{and} \quad w(r) \propto \Omega^3 \quad (6.9)$$

Blade weight is proportional to the skin thickness times chord and thus varies as rotational speed:

$$m(r) \propto w(r).c(r) \propto \Omega^3/\Omega^2 \propto \Omega$$

6.4.3 High-speed rotors

On the basis of the assumptions of Section 6.4.2 (which will by no means always apply), blade weight increases in proportion to rotational speed. However, as shown in Section 6.4.2, the blade out-of-plane fatigue loads, which may govern the design of the nacelle structure and tower, vary *inversely* as the rotational speed. It is therefore likely that, as rotational speed is increased, there will be a trade-off between reducing costs of the drive train, nacelle structure, and tower on the one hand and increasing rotor cost on the other, which will determine the optimum value.

As explained in Section 6.4.5, the scope for increasing the tip speeds of onshore machines is severely limited. However, there has been considerable interest in the development of high-speed designs for use offshore, because of the potential drive train cost savings. Jamieson (2009) investigated a substantial increase in tip speed to 120 m/s and proposed a downwind configuration to avoid the risk of tower strike by the resulting flexible, low solidity blades.

More recently, NREL investigated the benefits of increasing the maximum tip speed of its 126 m diameter 5 MW variable-speed reference wind turbine from 80 m/s to 100 m/s (Dykes et al. [2014]), considering both upwind and downwind designs. They found that a 9% increase in blade weight was required for the upwind 100 m/s tip speed design to

satisfy the limitations on tip deflection. The increased blade costs largely cancelled out the significant drive train savings, so the overall reduction in the cost of energy was relatively small at 1.5%. However, in the case of the downwind design, without the same constraints on tip deflection, the blade weight reduces by 9%, resulting in a 5.5% reduction in the cost of energy, before allowance for the energy loss due to the reduced swept area associated with the large tip deflection.

Task 2.1 of the INNWIND project was devoted to aerodynamic concepts for high-speed, low solidity offshore rotors. This included investigation of the performance of the thicker aerofoils required to maintain structural strength in the face of reduced chords (INNWIND [2015a]) and consideration of the adverse effects of air compressibility at higher tip speeds (INNWIND [2013]).

6.4.4 Low induction rotors

Low induction rotors are a subset of the high-speed rotors considered above that are designed to operate at a reduced axial induction factor. Typically, the assumption is made that designing a rotor to operate at the maximum coefficient of performance, corresponding to an induction factor of $a = 1/3$, will result in the most economic overall design. However, when an increase in tip speed is permissible, there is scope to increase power output at a given wind speed by operating at a lower induction factor and increasing the diameter, without changing the steady state out-of-plane bending moment at the root. It is then found that, although the percentage increase in energy yield is less than the percentage increase in blade cost, it exceeds the percentage increase in the cost of the wind turbine as a whole.

Consider a baseline turbine of radius R_0 , operating at an induction factor of $1/3$ and a low induction turbine of radius R operating at an induction factor a . If drag and tip-loss are ignored, the coefficient of performance is given by $C_p = 4a(1-a)^2$ [Eq. (3.12)], and it can be shown that the out-of-plane bending moment at the root is

$$M_0 = \frac{1}{2} \rho V^2 \pi R^3 \frac{8}{9} a(1-a) \quad (6.10)$$

which can be written $M_0 = \frac{1}{2} \rho V^2 \pi R^3 C_{M0}$. The variation of these quantities with the induction factor is plotted in Figure 6.7, and it can be shown that C_{M0} reduces more rapidly than C_p as the induction factor is reduced below $1/3$, so that increasing the diameter can yield increased power without increasing the root bending moment. The turbine radius that maintains the same root bending moment is also plotted in Figure 6.7 as R/R_0 , together with the normalised power output, which reaches a maximum at an induction factor of 0.2.

When drag and tip-loss are included, it is found that a maximum increase in power output of 8.7% is obtained at an induction ratio of 0.187 with an increase in radius of 13.6% (INNWIND [2013]). The baseline machine has a tip speed ratio of 8.85, which yields the maximum coefficient of performance for the chosen lift/drag ratio of 100, so the tip speed ratio of the low induction variant is 10. Given that the steady state out-of-plane bending moments in the extended blade remain the same as a function of normalised radius, μ ($= r/R$), as for the baseline blade, it is assumed that the blade strength will remain adequate if the original chord and section moduli distribution are retained as a function of μ . The cost of the blade can then be treated as proportional to its length.

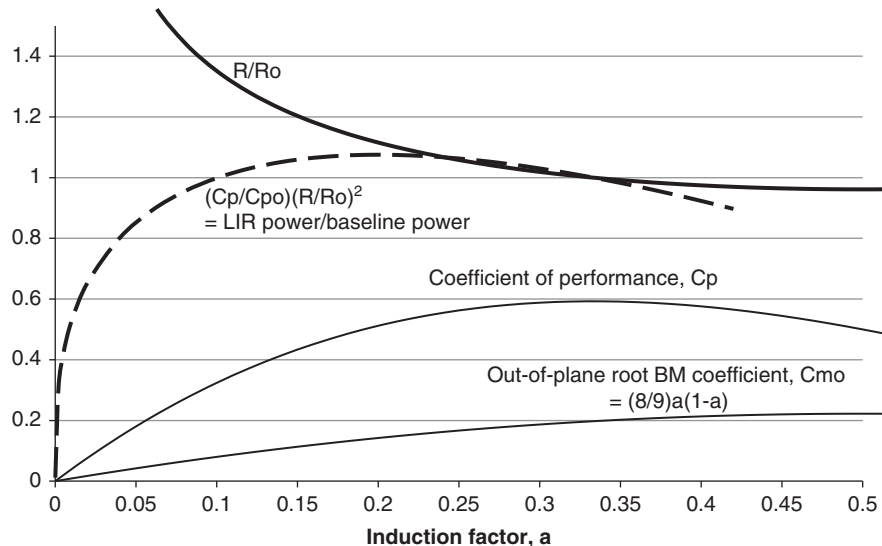


Figure 6.7 Variation of coefficient of performance, root bending moment coefficient, turbine radius to maintain constant out-of-plane root bending moment, and low induction rotor power ratio with axial induction factor

The INNWIND cost model (see Section 6.2.4) indicates that the blade cost amounts to about 6% of the total installed cost of a 10 MW offshore turbine, so a 13.6% increase in blade cost would result in a 0.8% increase in total installed cost. Assuming the turbine rating remains 10 MW, the 8.7% increase in power below rated would increase the capacity factor by 4%, so the overall reduction in the cost of energy would be 3.2%.

To achieve the required reduced induction factor, the lift coefficient, C_l , has to be significantly reduced by increasing the blade twist.

6.4.5 Noise constraint on rotational speed

The aerodynamic noise generated by a wind turbine is approximately proportional to the fifth power of the tip speed. It is therefore highly desirable to restrict the rotational speed of onshore turbines, especially when the wind speed – and therefore ambient noise levels – are low. Consequently, manufacturers of turbines to be deployed at normal sites on land generally limit the tip speed of fixed-speed machines to about 65 m/s.

In the case of variable-speed machines, the maximum tip speed is usually significantly higher – typically in the range of 70–85 m/s, but of course these tip speeds are only reached at higher wind speeds, when ambient noise levels are higher also.

Offshore machines are not subject to the noise constraints on maximum tip speeds that apply on land, so machines designed primarily for offshore siting typically have somewhat higher tip speeds.

6.4.6 Visual considerations

There is a consensus that turbines are more disturbing to look at the faster they rotate.

6.5 Number of blades

6.5.1 Overview

European windmills traditionally had four sails, perhaps because pre-industrial techniques for attaching the sail stocks to the shaft lent themselves to a cruciform arrangement in which the stocks for opposite sails formed a continuous wooden beam. By contrast, the vast majority of horizontal axis wind turbines manufactured today have either two or three blades, although at least one manufacturer used to specialise in one bladed machines. As the latter are now only of theoretical or historical interest, consideration of them will be restricted to Section 6.5.8, and the rest of Section 6.5 will concentrate on two and three bladed machines.

In comparing the relative merits of machines with differing numbers of blades, the following factors need to be considered:

- Performance.
- Loads.
- Cost of rotor.
- Impact on drive train cost.
- Noise emission,
- Visual appearance.

Some of these factors are strongly influenced by rotational speed and rotor solidity, and the ideal relationship between these parameters and the number of blades is considered in the next section. Tip loss and drag both diminish performance and these effects are compared for different numbers of blades in Section 6.5.3. Section 6.5.4 investigates alternative two bladed derivatives of a realistic three bladed variable-speed baseline design and compares their relative energy yields and notional costs. Section 6.5.5 reviews the differences in loading imposed by two and three bladed rotors on the supporting structure, and Section 6.5.6 considers the constraint on rotational speed imposed by noise emission. Visual appearance is considered briefly in Section 6.5.7.

6.5.2 Ideal relationship between number of blades, rotational speed, and solidity

In the absence of drag and tip-loss, the relationship between the chord distribution optimised for a particular wind speed, the rotational speed, and the number of blades can be deduced from Eq. (6.6) rearranged as follows:

$$Bc(\mu) \left(\frac{\Omega R}{U_\infty} \right)^2 = \frac{16\pi R}{9C_l} \cdot \frac{1}{\mu}$$

Thus, if the number of blades is reduced from three to two, optimised operation at the selected wind speed can be maintained by either increasing the chord by 50% or increasing the rotational speed by 22.5% (assuming that the lift coefficient is maintained at a constant value by altering the local blade pitch to maintain a constant angle of attack). In either case, the coefficient of performance would remain at the Betz limit because of the assumed absence of tip-loss and drag.

6.5.3 Effect of number of blades on optimum C_P in the presence of tip-loss and drag

The reduction in performance due to tip-loss increases as the number of blades is reduced and cannot be fully compensated by increasing rotational speed because of the increased drag that results. Except at very low tip speeds, the coefficient of performance is given reasonably accurately by Eq. (6.11),

$$C_P = \int_0^1 \frac{8a(1-a)}{1 + \frac{a'}{f}} \left(1 - \frac{a}{f} - \frac{\lambda\mu \left(1 + \frac{a'}{f} \right)}{k} \right) \mu d\mu \quad (6.11)$$

which can be derived by substituting the chord, $c(r)$, obtained from the solidity, σ_r , given by Eq. (3.54c) into the expression for elemental torque in Eq. (3.49) and writing $r/R = \mu$. k is the lift to drag ratio at the operating point and is assumed constant with radius for simplicity. The optimised induction factor, a , and the tip-loss factor, f , are 1/3 and unity, respectively, in the inboard region but vary with radius towards the tip, as described in Section 3.9.3. The rotational induction factor, a' , is taken as $a' = \frac{a \left(1 - \frac{a}{f} \right)}{\lambda^2 \mu^2}$ (Eq. [3.89]). Both a and a' are azimuthally averaged values.

Equation (6.11) can be used to compute the C_P value at a range of tip speed ratios, enabling the maximum C_P value to be determined together with the tip speed ratio at which it occurs. Plots of these parameters against lift/drag ratio, k , are presented for different numbers of blades in Figure 6.8. The benefit of increasing the Lift/Drag ratio is clearly shown, as is the diminishing benefit of adding each extra blade.

The dotted line in Figure 6.8 shows the variation of maximum C_P and corresponding tip speed ratio with lift/drag ratio for the case of a three bladed rotor, under the assumption that the tip-loss factor is applied to the rates of change of linear and angular momentum rather than to the induction factors in the expressions for these quantities (see Section 3.9.5). This results in the altered expression for C_P given by Eq. (6.12):

$$C_P = \int_0^1 \frac{8a \left(1 - \frac{a}{f} \right)}{1 + \frac{a'}{f}} \left(1 - \frac{a}{f} - \frac{\lambda\mu \left(1 + \frac{a'}{f} \right)}{k} \right) \mu d\mu \quad (6.12)$$

It is apparent that this alternative application of the tip-loss factor results in predicted optimum C_P values that are approximately 2% smaller.

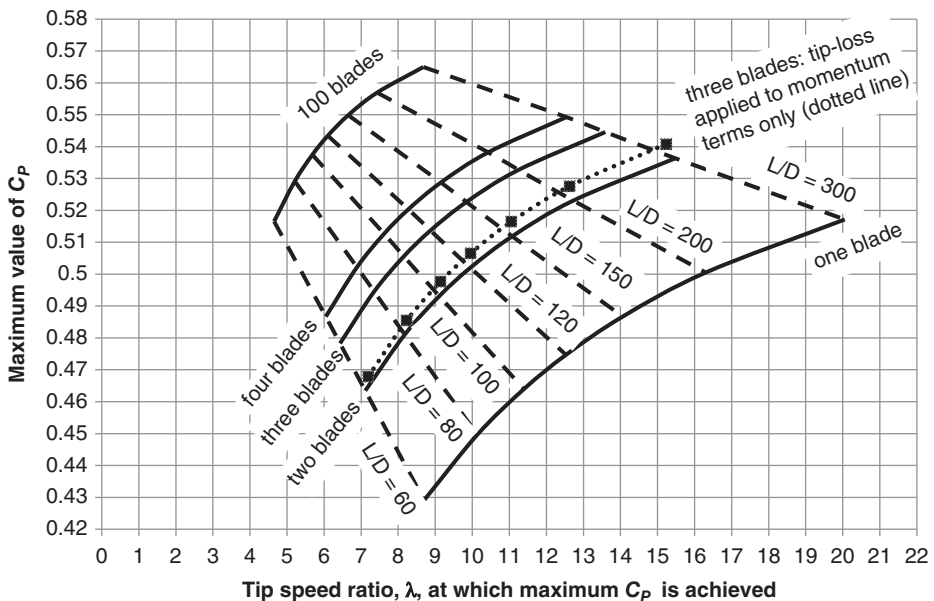


Figure 6.8 Variation of maximum C_p and corresponding tip speed ratio with lift/drag ratio k for different numbers of blades

6.5.4 Some performance and cost comparisons

Clear-cut cost comparisons between two and three bladed machines are notoriously difficult because of the impossibility of establishing equivalent designs. Conceptually, the simplest option is to increase the chord by 50% at all radii and leave everything else – including rotational speed – unchanged. In the absence of tip-loss, the induction factors, and hence the annual energy yield, remain the same, but when tip-loss is included, the annual energy yield of a stall-regulated machine drops by about 2.5%. However, retention of the same rotor solidity largely negates one of the main benefits of reducing the number of blades, namely reduction in rotor cost, and so this option will not be pursued further. Instead it is proposed to take a realistic blade design for a three bladed machine and look at the performance and cost implications of using the same blade on a two bladed machine rotating at different speeds.

Performance comparisons are affected both by the power rating in relation to swept area (Section 6.3) and by the aerofoil data used. In this case a 70 m diameter, 1.5 MW, pitch-regulated variable-speed three bladed turbine operating at a tip speed ratio of 8 for wind speeds below 10 m/s and constant tip speed above is adopted as the baseline machine. The maximum rotational speed is thus $80/35 = 2.29$ rad/sec or 21.8 rpm. The blade plan-form and thickness distribution are scaled down from those for the SC40 blade given in Figure 5.4a. Empirical three-dimensional aerofoil data for an LM 19.0 blade is used (see Figure 5.9), with maximum lift coefficient increasing from blade tip

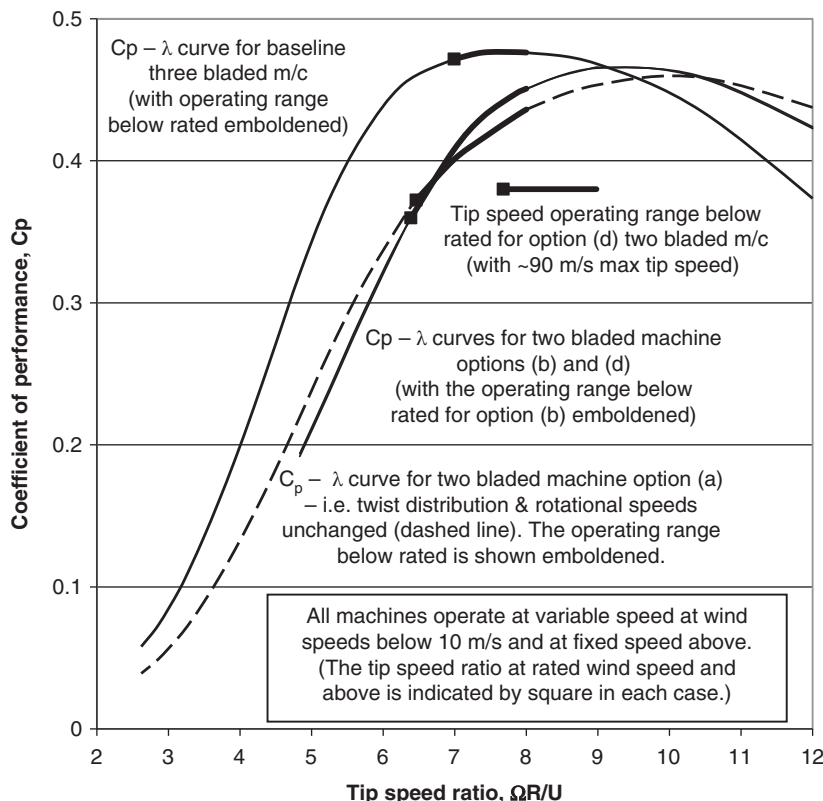


Figure 6.9 Comparison of $C_p - \lambda$ curves for three bladed baseline machine and two bladed options (a), (b), and (d)

to blade root, as this results in more accurate power curve predictions. The data is taken from the Risø publication ‘Prediction of Dynamic Loads and Induced Vibrations in Stall’ by Petersen et al. (1998). The blade twist distribution is set to give maximum energy yield at a site where the annual mean wind speed is 7.5 m/s, resulting in an annual energy yield at 100% availability of 4937 MWh. The performance curve for the baseline turbine is shown in Figure 6.9.

Four options for a corresponding 70 m diameter pitch-regulated, variable-speed, two bladed design at a site with the same annual mean wind speed are examined and the notional energy costs compared with that for the baseline three bladed machine. The costs of the two bladed design options in relation to the baseline three bladed machine are considered with reference to changes in the weights of the components, using the cost shares for the NREL baseline machine given in Table 6.2.

Blade design is assumed to be governed by out-of-plane fatigue bending moments, with the moment fluctuations increasing in proportion to rotational speed [see Eq. (5.25) in Section 5.7.5]. Accordingly, the blade weight is assumed to increase linearly with rotational speed, but the total blade weight for the two bladed machine at the baseline rotational speed is, of course, reduced by 1/3. The weights of the hub, pitch system, shaft, and

yaw system are also assumed to increase with rotational speed, but no account is taken of the increased loads on these components for a fixed hub, two bladed machine.

It is assumed initially that the design of the nacelle structure is fatigue driven and governed by the fluctuating moment on the nacelle due to differential blade out-of-plane root bending moment, which increases with rotational speed. Tower design is also assumed to be governed by fatigue in the first instance, so tower weight is similarly taken as proportional to rotational speed. The cyclic thrust loads on the rotor due to turbulence are virtually the same for two and three bladed machines rotating at the same speed if the blade plan-forms are the same, so the tower cost element at the baseline rotational speed is left unchanged.

The costs of the gearbox and brake are taken to be proportional to the rated torque, P_R/Ω , while those of the generator, the variable-speed electronics, and the cables and equipment forming the grid connection are taken as proportional to rated power, P_R .

The various components are classified into different categories according to the way in which their costs vary with rotational speed and rated power in Table 6.5. Also tabulated are the two bladed baseline machine component costs as a percentage of the total for the baseline three bladed machine, together with the sum for each category. The total cost of the baseline two bladed machine is 3.8% less than the cost of the baseline three bladed machine due to the reduction in the number of blades.

The following expression is obtained for machine cost as a function of rotational speed and rated power:

$$C_T = C_{TB}(0.134 + 0.4047\{\Omega/\Omega_B\} + 0.118\{\Omega_B/\Omega\}(P_R/P_{RB}) + 0.305(P_R/P_{RB})) \quad (6.13)$$

Here, P_{RB} and Ω_B are the baseline values of rated power and maximum nominal rotational speed, 1500 kW and 21.8 rpm, respectively, and C_{TB} is the cost of the baseline three bladed machine. The four design options can now be examined:

(a) *Plan-form, twist, and rotational speed unchanged from baseline:* The reduction in the number of blades necessitates an increase in the rated wind speed from 11.4 to 12.4 m/s to maintain the same power rating. At the tip speed ratio of 8, which applies at wind speeds less than 10 m/s, the coefficient of performance is reduced by 8.4%, but the overall energy yield reduction is less at 6.3%. The corresponding $C_p - \lambda$ curve is shown over the full range of tip speed ratios by the dashed line on Figure 6.9, with the much more limited operating range below rated shown emboldened, and it is evident that the optimum tip speed ratio has increased from about 7.7 for the baseline three bladed machine to about 10. Clearly the limit on the upper tip speed of 80 m/s imposes a significant penalty on performance.

Combination of the reduced energy yield with the machine capital cost saving of 3.8% due to the elimination of one blade results in an increased cost of energy of 2.6%.

(b) *As option (a), but twist distribution re-optimised:* Re-optimisation of the twist distribution reduces the energy yield penalty compared with the baseline three bladed machine from 6.3% to 4.6%. As a result, the increase in the cost of energy is reduced to 0.8%. The corresponding $C_p - \lambda$ curve is shown over the full range of tip speed ratios in Figure 6.9, with the much more limited operating range below rated shown emboldened. The rated wind speed is increased slightly to 12.5 m/s.

(c) *Tip speed ratio schedule scaled in conjunction with twist distribution optimisation to obtain minimum cost of energy based on machine cost function of Eq. (6.13) (with tower and nacelle cost increasing with maximum rotational speed)*: The tip speed at each wind speed can be scaled up by the same ratio so as to produce maximum energy yield, with simultaneous re-optimisation of the twist distribution. This enables the energy yield penalty compared with the baseline three bladed machine to be reduced to only 1.3%, for a tip speed scaling factor of 1.21. However, application of Eq. (6.13) results in a capital cost increase of 2.5% relative to the baseline machine, resulting in a cost of energy increase – again relative to the baseline machine – of 3.8%.

Minimisation of the cost of energy, on the other hand, leads to a much lower tip speed scaling factor of 1.035 and a rated wind speed of 12.15 m/s. The energy yield penalty and capital cost reduction relative to the baseline machine are now 3.3% and 2.8%, respectively, resulting in an increase in the cost of energy of only 0.5%.

(d) *Tip speed ratio schedule scaled in conjunction with twist distribution optimisation to obtain minimum cost of energy based on machine cost function of Eq. (6.13) modified so that tower and nacelle cost are fixed*: It is apparent that, with the weight of nacelle and tower assumed to increase in proportion to rotational speed, the two bladed variant (c) considered above results in a small increase in the cost of energy

Table 6.5 Contribution of different components to the cost of a two bladed machine (expressed as percentages of three bladed baseline machine cost) and classified according to the relationship assumed between the component cost and rotational speed/rated torque/rated power

Components for which the weight/cost is independent of rated power or rotational speed		Components for which the weight/cost varies as rotational speed, Ω		Components for which the weight/cost varies as rated torque, P_R/Ω		Components for which the weight/cost varies as rated power, P_R	
Component	Cost	Component	Cost	Component	Cost	Component	Cost
Foundation	3.6%	Blades	7.7%	Gearbox	11.6%	Generator	7.4%
Controller	2.7%	Hub	3.6%	Brake system	0.2%	Variable-speed electronics	9.0%
Assembly	3.2%	Pitch system	4.3%			Grid connection	14.1%
Transport	3.9%	Low-speed shaft and bearings	2.5%				
		Nacelle	8.9%				
		Yaw system	1.5%				
		Tower	12.0%				
Total	13.4%	Total	40.5%	Total	11.8%	Total	30.5%

relative to the three bladed machine. However, if the weight of the nacelle structure is driven by the size of the enclosure required to accommodate the gearbox, generator, and other equipment, rather than by fatigue loading, it will be constant for machines of fixed rating. If it is also assumed that the tower design is governed by extreme loads rather than fatigue loads, the expression for machine cost as a function of rotational speed and rated power becomes

$$C_T = C_{TB}(0.343 + 0.1957\{\Omega/\Omega_B\} + 0.118\{\Omega_B/\Omega\}(P_R/P_{RB}) + 0.305(P_R/P_{RB})) \quad (6.14)$$

The tip speed scaling factor resulting in the minimum cost of energy then increases to 1.12, the rated wind speed reduces to 11.7 m/s, and the cost of energy reduces to 1.1% below that of the baseline machine. As shown in Figure 6.9, the corresponding $C_P - \lambda$ curve over the full range of tip speed ratios is almost identical to that for option (b), but the tip speed ratio operating range differs.

The above results are summarised in Table 6.6. The results shown in Table 6.6 indicate that two bladed, rigid hub machines have the potential to yield marginal cost benefits vis-à-vis three bladed machines, if nacelle and tower design are not impacted by increases in rotational speed. However, the results should be treated with caution, because no account has been taken of increased component costs due to the increased loadings on the hub, low-speed shaft, yaw drive, and nacelle inherent in a rigid hub two bladed turbine. (Loads on rigid hub two bladed machines are compared with those on three bladed machines in more detail in the next section.)

The loadings on the nacelle of a two bladed machine can be reduced significantly by the introduction of a teeter hinge between the rotor and the low-speed shaft, with consequent potential cost benefits. The hinge eliminates the transfer of out-of-plane aerodynamic moments from the rotor to the low-speed shaft, resulting in large reductions in the operational loadings on the shaft, nacelle, and yaw drive. The dependence of these loads on rotational speed is also largely removed, with the result that the optimum rotational speed for a two bladed machine in energy cost terms is increased, approaching the value giving maximum energy yield.

Although teetering provides scope for significant cost savings on the shaft, nacelle, and yaw drive (which account for nearly 20% of the baseline machine cost), these savings are offset by the additional costs associated with the teeter hinge and teeter restraint system.

6.5.5 Effect of number of blades on loads

Moment loadings on the low-speed shaft and nacelle structure from three bladed and rigid hub two bladed machines were examined in Sections 5.10 and 5.11, and are compared in Table 6.7 for machines of the same diameter and rotational speed. The stochastic loading comparison is based on a turbulence length scale to rotor diameter ratio of 1.84.

It is seen that loadings from a rigid hub two bladed rotor are significantly larger than from a three bladed rotor. However, in most two bladed machine designs, the rotor is allowed to teeter instead of being rigidly mounted, with the result that aerodynamic moments on the shaft and nacelle structure quoted in Table 6.7 are eliminated and the

Table 6.6 Comparison of two bladed design variants on a 70 m diameter, 1.5 MW three bladed variable-speed, pitch-regulated baseline machine, using blades of same plan-form and thickness/chord ratio distribution

Two bladed 70 m diameter, 1.5 MW, machine design options	Maximum nominal speed and tip speed	Annual energy yield (MWh)	Reduction in annual energy yield cf. baseline m/c	Reduction in overall machine cost cf. three bladed baseline	Increase/ reduction in cost of energy
a) Same blade and tip speed schedule	21.8 rpm 80 m/s	4625	6.3%	3.8%	+2.6%
b) As above, but with optimisation of blade twist distribution	21.8 rpm 80 m/s	4709	4.6%	3.8%	+0.8%
c) Tip speeds and twist distribution varied to give minimum C of E as per Eq. (6.13)	22.6 rpm 83 m/s	4775	3.3%	2.8%	+0.5%
d) Tip speeds and twist distribution varied to give minimum C of E assuming nacelle and tower costs fixed – i.e. using Eq. (6.14)	24.5 rpm 90 m/s	4857	1.6%	2.7%	-1.1%

blade out-of-plane root bending moments reduced. The benefits and drawbacks of teetering the rotor are examined in Section 6.6.

The rotor thrust variations at blade passing frequency due to stochastic loading, which are a dominant factor in tower fatigue design, are very similar for two and three bladed machines rotating at the same speed. However, two bladed machines usually rotate faster than three bladed machines of the same diameter, so the cyclic rotor thrust variations are higher.

6.5.6 Noise constraint on rotational speed

As noted in Section 6.5.4, there may be significant cost benefits to be gained from a two bladed design with increased rotational speeds, because, in addition to the blade saving, the cost of the whole of the drive train is reduced because of the reduced torque. However,

Table 6.7 Comparison of loads on shaft and nacelle for three bladed and rigid hub two bladed machines (ψ is blade azimuth)

Location of moment loading	Deterministic loading arising from wind shear and/or yaw misalignment, in terms of blade root out-of-plane bending moment amplitude, M_o		Stochastic loading % increase for rigid hub two bladed machine compared with three bladed m/c
	Three bladed machine	Rigid hub two bladed machine	
Shaft bending moment amplitude	$1.5 M_o$	$2 M_o$	22%
Nacelle nodding moment	$1.5 M_o$	$M_o(1 + \cos 2\psi)$	22%
Nacelle yaw moment	Zero	$M_o \sin 2\psi$	22%

as noted in Section 6.4.5, it is normal to restrict the tip speeds of fixed-speed and variable-speed machines to about 65 or 85 m/s respectively, to limit aerodynamic noise emission. At 80 m/s, the tip speed of the baseline machine discussed in Section 6.5.4 is within this limit, but the tip speed of option (d) of 90 m/s would be less likely to be acceptable, except at remote sites or offshore. This subject is considered further in Section 6.9.

6.5.7 Visual appearance

Although the assessment of visual appearance is essentially subjective, there is an emerging consensus that three bladed machines are more restful to look at than two bladed ones. One possible reason for this is that the apparent ‘bulk’ of a three bladed machine changes only slightly over time, whereas a two bladed machine appears to contract down to a one-dimensional line element, when the rotor is vertical, twice per revolution. A secondary factor is that two bladed machines generally rotate faster, which an observer can also find more disturbing.

6.5.8 Single bladed turbines

Apart from the saving in rotor cost itself, the single bladed turbine concept is an attractive one because of the reduction in drive train cost realisable through increased rotational speed (Section 6.5.2). An obvious disadvantage is the increased noise emission resulting from the faster rotation, but this would not be an issue offshore. Another consideration is the reduced yield due to increased tip-loss. For example, a single bladed version of the 70 m diameter, 1.5 MW pitch-regulated, variable-speed three bladed baseline design considered in Section 6.5.4, with the rotational speed at each wind speed scaled up by $\sqrt{3}$ in accordance with Eq. (6.7) and with the twist distribution re-optimised to give maximum energy yield, will produce an annual energy output 5.5% less than the baseline machine.

The single blade must be counterweighted to eliminate torque fluctuations and any whirling tendency due to centrifugal loads. Furthermore, as a rigid hub would expose the nacelle to very large nodding and yawing moments in comparison with two or three bladed machines, it is customary to mount the rotor on a teeter hinge, so that the unbalanced aerodynamic out-of-plane moment can be resisted by a centrifugal couple, thereby reducing the hub moment. However, the teeter motion of the blade is significantly greater than that of a two bladed machine, so it is normal to mount the rotor downwind. Morgan (1994) reports that particular difficulties have been encountered in predicting teeter excursions after grid loss and emergency stops, leading to excessive risk of teeter stop impacts.

6.6 Teetering

6.6.1 Load relief benefits

Two bladed rotors are often mounted on a teeter hinge – with hinge axis perpendicular to the shaft axis but not necessarily perpendicular to the longitudinal axis of the blades – to prevent differential blade root out-of-plane bending moments arising during operation. Instead, differential aerodynamic loads on the two blades result in rotor angular acceleration about the teeter axis, with large teeter excursions being prevented by the restoring moment generated by centrifugal forces, as described in Section 5.8.8. However, when the machine is shut down, the centrifugal restoring moment is absent, so differential blade loading will cause the rotor to teeter until it reaches the teeter end stops, which need to be suitably buffered. Consequently, the teeter hinge is unlikely to provide any amelioration of extreme blade root out-of-plane moments when the machine is shut down.

The load relief afforded by the teeter hinge benefits the main structural elements in the load path to the ground in varying degrees, as outlined below:

- 1) *Blade*: The main benefit is the elimination of the cyclic variations in out-of-plane bending moment due to yaw (Figure 5.10), shaft tilt, wind shear (Figure 5.11), and tower shadow (Figure 5.14). By contrast, there is only a small reduction in blade root out-of-plane bending moment due to stochastic loadings – see the example in Section 5.8.8, where an 11% reduction is quoted. Thus, teetering results in a large overall reduction in out-of-plane fatigue loading, although the significance of this will be tempered by the influence of the unaltered edgewise gravity moment.
- 2) *Low-speed shaft*: Low-speed shaft design is governed by fatigue loading, which is normally dominated by the cyclic gravity moment due to the cantilevered rotor mass. On a rigid hub machine, the shaft moment damage equivalent load or DEL (defined in Section 5.12.6) due to deterministic and stochastic rotor out-of-plane loadings combined can be of similar magnitude, so the insertion of a teeter hinge can produce a substantial reduction in overall shaft moment DEL. It should be noted, however, that the cyclic shaft moment due to wind shear *relieves* that due to gravity on a rigid hub machine, so teetering is not beneficial in respect of this load component.

A rough estimate of the overall shaft moment DEL on a rigid hub machine, excluding yaw error and tower shadow effects, can be obtained by taking the square root of the sum of the squares of the shaft moment DEL due to stochastic

loads and that due to the combined cyclic loads due to gravity, wind shear, and shaft tilt.

- 3) *Nacelle structure*: The provision of a teeter hinge should eliminate nodding and yawing moments on the nacelle completely during operation, leaving only rotor torque, thrust, and in-plane loadings. This will benefit the fatigue design of the nacelle structure considerably, but not the extreme load design, for the reasons already explained.
- 4) *Yaw bearing and yaw drive*: Rigid hub machines experience severe yaw moments due to both deterministic and stochastic loads, which were underestimated on many early designs. The introduction of a teeter hinge dramatically reduces yaw moments during operation by eliminating rotor out-of-plane moments on the hub, but yaw moments due to in-plane loads on the rotor still remain.

The relative magnitude of the yaw moments due to in-plane as opposed to out-of-plane loads on a rigid hub rotor can be appreciated by comparing the effect of wind speed fluctuation, u , on the in-plane and out-of-plane loads on a blade element. Assuming that the blade is not stalled and that ϕ is small, the in-plane load per unit length is, from Eq. (5.131a), given approximately by

$$-F_Y = \left(\frac{1}{2} \rho \Omega \frac{dC_l}{da} \right) c(r).r.u \left[\frac{C_l}{dC_l/d\alpha} + \sin \phi \right] \quad (6.15)$$

whereas the out-of-plane load per unit length is, from Eq. (5.25), approximately

$$F_X = \left(\frac{1}{2} \rho \Omega \frac{dC_l}{da} \right) c(r).r.u \quad (6.16)$$

Defining the distance between the hub centre and the tower centreline as e , it is seen that the yaw moment due to the in-plane rotor load per unit length at radius r is $\frac{e}{r} \left[\frac{C_l}{dC_l/d\alpha} + \sin \phi \right]$ times the maximum yaw moment due to out-of-plane load. As e is typically about 1/10 of the tip radius, it is seen that the yaw moments due to in-plane loads are at least an order of magnitude smaller than those due to out-of-plane moments, so that the introduction of the teeter hinge results in a very significant reduction.

- 5) *Tower*: The fatigue loadings due to the M_Y moment and M_Z torque will clearly be significantly reduced at the top of the tower if the rotor is teetered, but the effect will be negligible towards the base where thrust loads dominate the moments.

6.6.2 Limitation of large excursions

Some limitation on teeter excursions has to be provided, if only to prevent collision between the blade and the tower. If the teeter hinge is located close to the axis of the blades, with the low-speed shaft passing through an aperture in the wall of the hub shell (see Figure 6.10), then the maximum teeter excursion is governed by the size of the aperture.

The teeter response to deterministic and stochastic loads is considered in Section 5.8.8. Although it is evident that a permitted teeter angle range of the order of $\pm 5^\circ$

will accommodate the vast majority of teeter excursions during normal operation, it is usually impracticable to accommodate the largest that can occur. Hence, to minimise the occurrence of metal-to-metal impacts on the teeter end stops, buffers incorporating spring and/or damping elements normally have to be fitted. These also perform an important role in limiting the much larger teeter excursions that would otherwise arise during start-up and shut-down, when the centrifugal restoring moment is reduced.

6.6.3 Pitch-teeter coupling

As described in Section 5.8.8, the magnitude of teeter excursions can be reduced by coupling blade pitch to teeter angle to generate an aerodynamic restoring moment proportional to the teeter angle. This can be done simply by setting the teeter hinge at an angle, known as the *Delta 3 angle*, perpendicular to the rotor axis. Alternatively, on pitch-controlled machines, pitch-teeter coupling can be introduced by actuating the blade pitch by the fore-aft motion of a rod passing through a hollow low-speed shaft. See Figure 6.10.

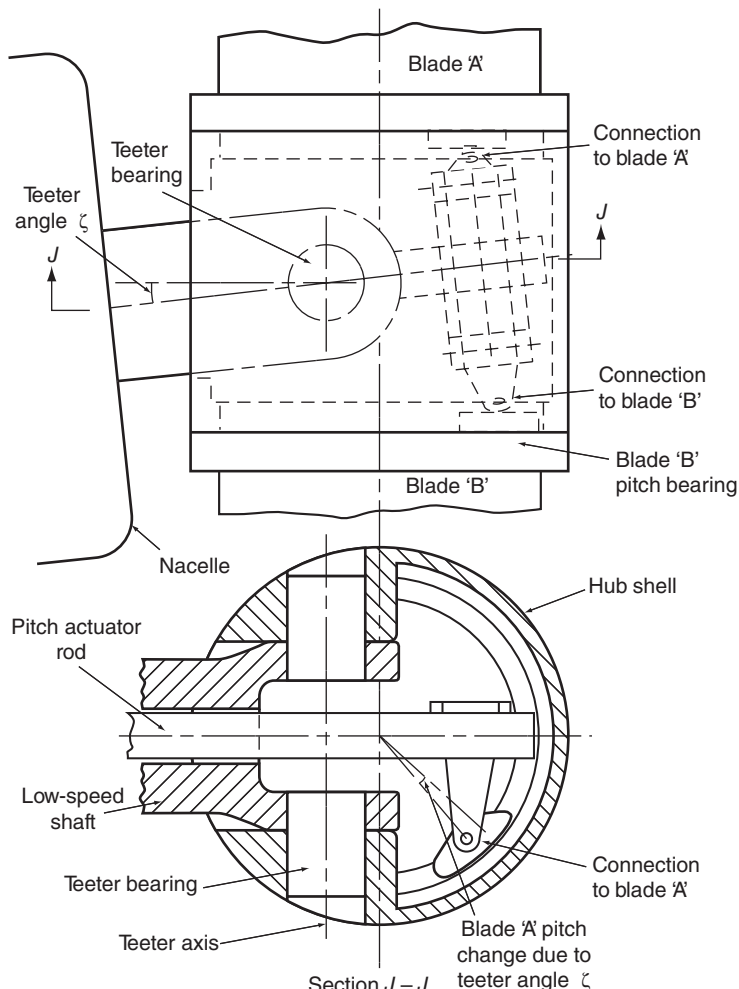


Figure 6.10 Pitch-teeter coupling

6.6.4 Teeter stability on stall-regulated machines

At first sight, it might be thought that the teeter motion of a stalled rotor would be unstable because of negative damping resulting from the negative slope of the $C_l - \alpha$ curve post-stall. However, two-dimensional aerodynamic theory is a poor predictor of post-stall behaviour, and it has proved possible to design teetered rotors that are stable in practice, such as the Gamma 60 (Falchetta et al. [1996]) and Nordic 1000 (Engstrom et al. [1997]). The concept is explored in detail in investigations by Armstrong and Hancock (1991) and Rawlinson-Smith (1994).

6.7 Power control

6.7.1 Passive stall control

The simplest form of power control is passive stall control, which makes use of the post-stall reduction in lift coefficient and associated increase in drag coefficient to place a ceiling on output power as wind speed increases, without the need for any changes in blade geometry. The fixed blade pitch is chosen so that the turbine reaches its maximum or rated power at the desired wind speed.

Stall-regulated machines suffer from the disadvantage of uncertainties in aerodynamic behaviour post-stall that can result in inaccurate prediction of power levels and blade loadings at rated wind speed and above. These aspects are considered in greater detail in Sections 3.13.3 and 3.15. See also Section 8.2.2.

6.7.2 Active pitch control

Active pitch control achieves power limitation above rated wind speed by rotating all or part of each blade about its axis in the direction that reduces the angle of attack and hence the lift coefficient – a process known as *blade feathering*. The main benefits of active pitch control are increased energy capture, the aerodynamic braking facility it provides, and the reduced extreme loads on the turbine when shut down. See also Sections 3.14 and 8.2.1.

The pitch change system has to act rapidly – i.e. to give pitch change rates of 5° per second or better – to limit power excursions due to gusts enveloping the whole rotor to an acceptable value. However, it is not normally found practicable to smooth the cyclic power fluctuations at blade passing frequency due to blades successively slicing through a localised gust (Section 5.7.5), with the result that large power swings of up to about 100% can sometimes occur in the case of fixed-speed machines.

The extra energy obtainable with pitch control is not all that large. A pitch-regulated machine with the same power rating as a stall-regulated machine, utilising the same blades and rotating at the same speed, will operate at a larger pitch angle below rated wind speed than the stall-regulated machine to reduce the angle of attack and hence increase the power output at wind speeds approaching rated. For example, if the 1500 kW, 70 m diameter, three bladed variable-speed baseline machine described in Section 6.5.4 were operated at a fixed speed of 17.1 rpm (corresponding to a tip speed of 62.8 m/s), a pitch-regulated version would produce about 2.7% more energy than a stall-regulated version for a 7.5 m/s annual mean wind speed, assuming optimisation of the blade twist distribution in each case. The power curves of the two fixed-speed machines are compared in Figure 6.11. Also shown is the power curve for the variable-speed pitch-regulated machine described in Section 6.5.4. This would produce 5% more energy than the fixed-speed, pitch-regulated machine. Note that

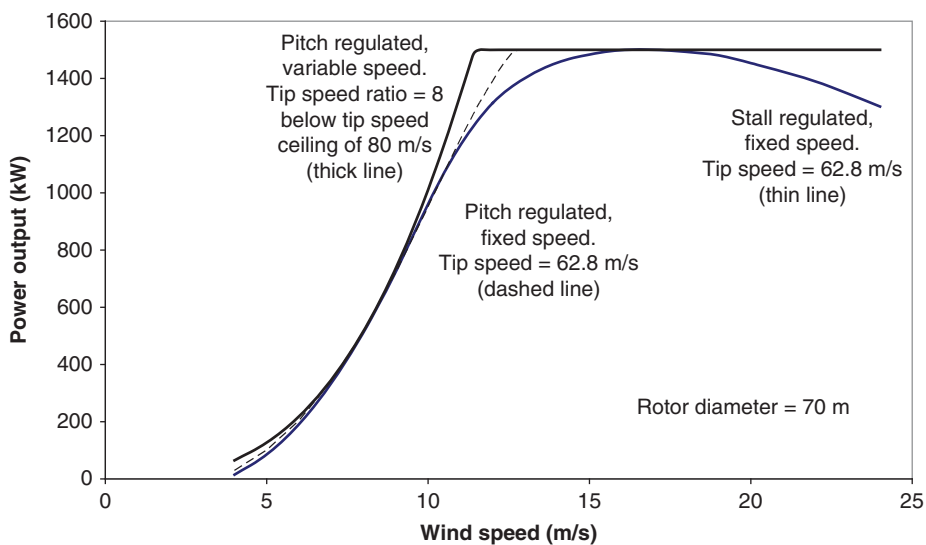


Figure 6.11 Comparison of power curves for (i) stall-regulated, fixed-speed; (ii) pitch-regulated, fixed-speed; and (iii) pitch-regulated, variable-speed 1.5 MW rated machines

the knees in the power curves of the pitch-regulated machines at rated speed will be more rounded in practice because the pitch control will not keep pace with the higher frequency components of turbulence.

Figure 6.12 shows a family of power curves for a range of positive pitch angles for the 1500 kW, 70 m diameter pitch-controlled machine rotating at 17.1 rpm. The intersections of these curves with the 1500 kW ordinate define the relationship between steady wind speed and pitch angle required for power control (Figure 6.13). It is readily apparent from the power curve gradients at the intersection points that rapid changes of wind speed will result in large power swings when the mean wind speed is high.

The range of blade pitch angles required for power control is typically from 0° (often referred to as *fine pitch*), at which the tip chord is in the plane of rotation or very close to it, and about 35°. However, for effective aerodynamic braking, the blades have to be pitched to 90° or full feather, when the tip chord is parallel to the rotor shaft with the leading edge into the wind.

A variety of pitch actuation systems have been adopted (see also Section 8.5). They are divided between those in which each blade has its own actuator and those in which a single actuator pitches all the blades. The former arrangement has the advantage that it provides two or three independent aerodynamic braking systems to control overspeed, and the disadvantage that it requires very precise control of pitch on each blade to avoid unacceptable pitch angle differences during normal operation. An advantage of the latter arrangement is that the pitch actuator – e.g. a hydraulic cylinder – can be located in the nacelle, producing fore-aft motion of the pitch linkages in the hub by means of a rod passing down the middle of a hollow low-speed shaft (see Figure 6.14). Alternatively, the axial position of the rod can be controlled by means of a ball-screw and ball-nut

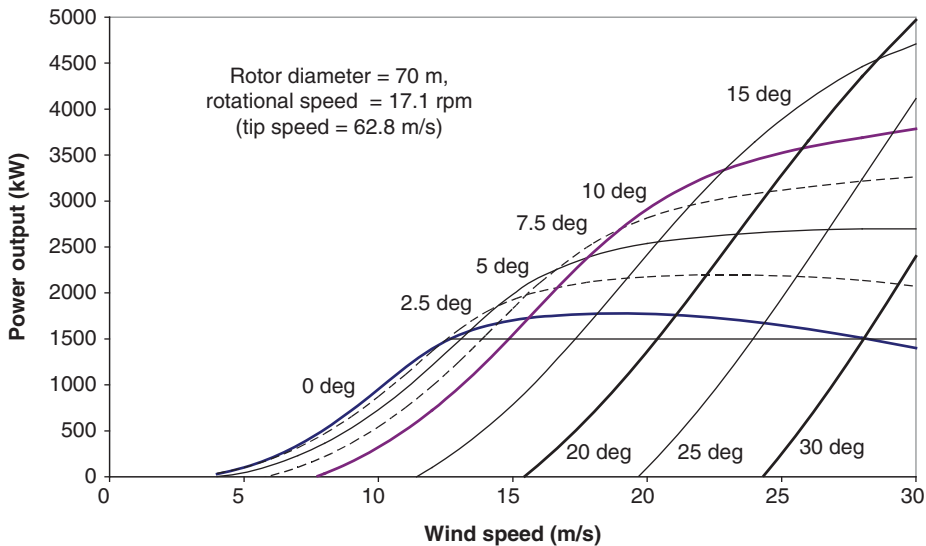


Figure 6.12 Power curves for different positive pitch angles: 70 m diameter three bladed rotor rotating at 17.1 rpm

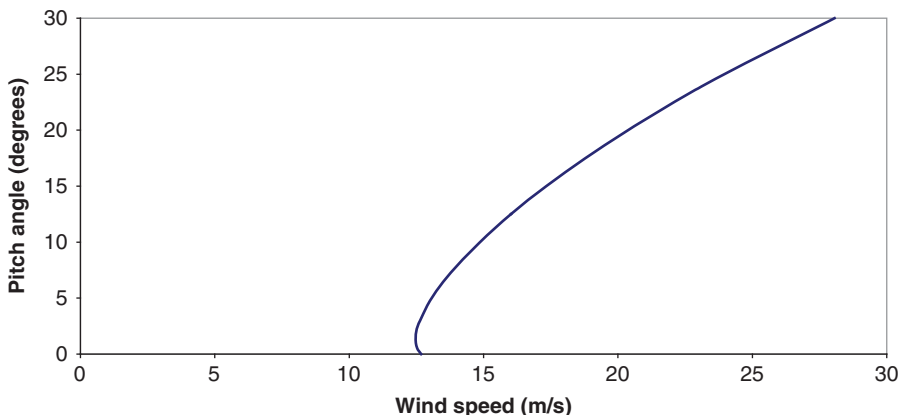


Figure 6.13 Schedule of pitch angles vs wind speed for limiting the power output of the machine featured in Figure 6.12 to 1.5 MW

arrangement, in which the ball-nut is driven by a servomotor. Normally the ball-nut is driven at the same speed as the rotor, but when a change of pitch is required, the ball-nut rotational speed is altered temporarily. This system is arranged to be fail-safe, so that should the servomotor or its control system fail, the servomotor is braked automatically, and the ball-nut drives the blade pitch to feather.

Where hydraulic cylinders are used to pitch blades individually, they are mounted within the hub, and each piston rod is usually connected directly to an attachment on the



Figure 6.14 Pitch linkage system used in conjunction with a single hydraulic actuator located in the nacelle. (The central triangular ‘spider’ is connected to the actuator by a rod passing through the hollow low-speed shaft. Links from the spider drive the blade pitch via braced arms cantilevering into the hub from each blade. Each arm is parallel to its blade axis but eccentric to it.)

blade bearing (see Figure 6.15). The attachment point follows a circular path as the blade pitches, so the cylinder has to be allowed to pivot. The alternative solution of employing an electric motor to drive a pinion engaging with teeth on the inside of the blade bearing consequently appears rather neater (see Figure 6.16). Both systems require a hollow shaft to accommodate either hydraulic hoses or power cables for pitch actuation together with signal cables for pitch angle sensing. In addition, appropriate slip rings are required at the rear end of the shaft.

Methods of providing back-up power supplies to ensure blade feathering in the event of grid loss are considered in Section 8.5.

Although full-span pitch control is the option favoured by the overwhelming majority of manufacturers, power control can still be fully effective even if only the outer 15% of the blade is pitched. The principal benefits are that the duty of the pitch actuators is significantly reduced and that the inboard portion of the blade remains in stall, significantly reducing the blade load fluctuations. However, there are several disadvantages as follows:

- The introduction of extra weight near the tip.
- The difficulty of physically accommodating the actuator within the blade profile.
- The high bending moments to be carried by the tip blade shaft.
- The need to design the equipment for the high centrifugal loadings found at large radii.
- The difficulty of access for maintenance.



Figure 6.15 Blade pitching system using separate hydraulic actuators for each blade. (Each actuator cylinder is supported on a gimbal-type mounting bolted to the hub, and its piston applies a pitching torque to the blade via a cantilevered conical tube eccentric to the blade axis. The blade is attached to the outer ring of the pitch bearings.)

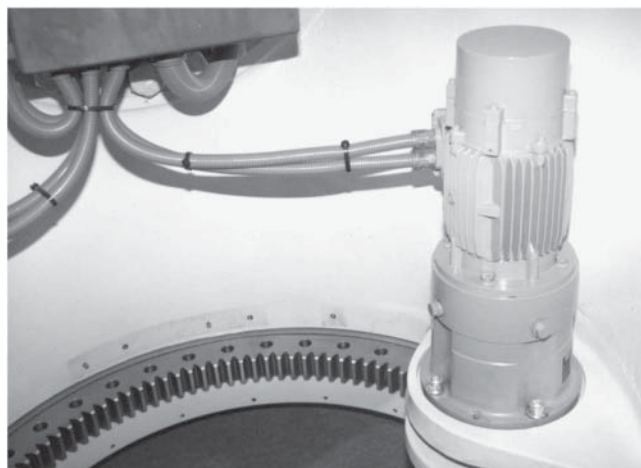


Figure 6.16 Blade pitching system using a separate electric motor for each blade. (A pinion, driven by the motor via a planetary gearbox, engages with gear teeth on the inside of the inner ring of the pitch bearing, to which the blade is bolted. The blade is not attached to the bearing in this photograph, so the fixing holes are visible.)

It should be apparent from the above brief survey of pitch actuation systems that the design of the hardware required for pitch regulation is a significant task. Moreover, as regards the controller, pitch regulation introduces the need for fast response closed-loop control, which is not required for the supervisory functions on a stall-regulated machine. Thus, the benefits of pitch control have to be weighed carefully against all the additional costs involved, including the cost of maintenance.

Another factor that needs to be considered is fatigue loading. This increases significantly on full-span pitch-regulated machines, because the rate of change of lift coefficient with angle of attack remains at about 2π (see Section A3.7 in Appendix A3) instead of reducing to zero as the blade goes into stall, with the result that rapid changes in wind speed above rated will cause bigger thrust load changes.

Pitch system controller design is considered in detail in Chapter 8.

6.7.3 Passive pitch control

An attractive alternative to active control of blade pitch to limit power is to design the blade and/or its hub mounting to twist under the action of loads on the blades, to achieve the desired pitch changes at higher wind speeds. Unfortunately, although the principle is easy to state, it is difficult to achieve it in practice, because the required variation in blade twist with wind speed generally does not match the corresponding variation of blade twist with blade load. However, passive blade pitching can play a useful role in load alleviation. One means of achieving limited passive blade pitching for this purpose is by orientating the fibres of the composite blade shell at angle to the blade axis, resulting in ‘bend-twist coupling’, as described in Section 7.1.20.

Corbet & Morgan (1991) give a survey of how different types of blade loads might be utilised for passive pitch control purposes. Harnessing the centrifugal load is obviously promising in the case of variable-speed machines, and this has been demonstrated using a screw cylinder and pre-loaded spring to passively control each tip blade, within the Dutch FLEXHAT programme. When the centrifugal load on the tip exceeds the pre-load, the tip blade is driven outwards against the spring and pitches (see Figure 6.17 for illustration of the concept).

Joose & Kraan (1997) have proposed replacing this mechanism by a maintenance-free ‘Tentortube’, which would twist under tension loading. This tube would be carbon-fibre reinforced with all of the fibres set at an angle to the axis, so that centrifugal loading induced twist. It would be placed inside a hollow steel tip shaft, which would carry the aerodynamic loading on the tip blade.

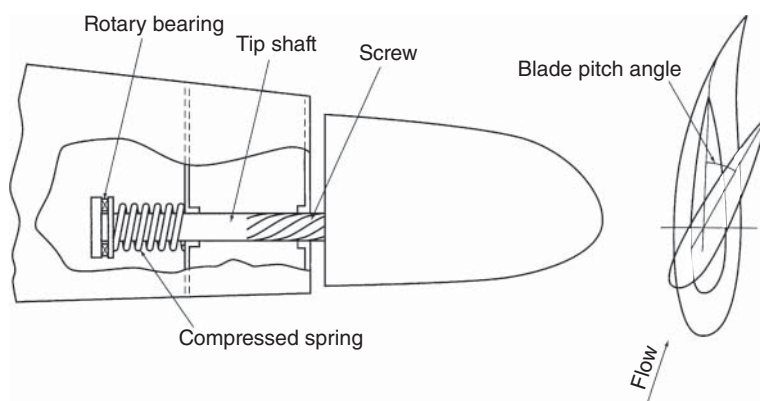


Figure 6.17 Passive control of tip blade, using screw on tip shaft and spring

6.7.4 Active stall control

Active stall control achieves power limitation above rated wind speed by pitching the blades initially *into* stall – i.e. in the opposite direction to that employed for active pitch control – and is thus sometimes known as *negative pitch control*. At higher wind speeds, however, it is usually necessary to pitch the blades back towards feather to maintain power output at rated.

A significant advantage of active stall control is that the blade remains essentially stalled above the rated wind speed, so that gust slicing (see Section 5.7.5) results in much smaller cyclic fluctuations in blade loads and power output. It is found that only small changes of pitch angle are required to maintain the power output at rated, so pitch rates do not need to be as large as for positive pitch control. Moreover, full aerodynamic braking requires pitch angles of only about -20° , so the travel of the pitch mechanism is very much reduced compared with positive pitch control.

Figure 6.18 shows a schedule of pitch angle against wind speed for active stall control. The active stall control schedule is derived from the intersection of the family of power curves for different negative pitch angles for the 70 m diameter machine considered above with the 1500 kW ordinate in Figure 6.19. Note that the rotational speed has been increased by 10% so that the machine operates further away from stall below rated wind speed – otherwise the range of negative pitch angles utilised would be very small.

The principal disadvantage of active stall control is the difficulty in predicting aerodynamic behaviour accurately in stalled flow conditions. Active stall control is considered further in Section 8.2.1.

6.7.5 Yaw control

As most horizontal axis wind turbines employ a yaw drive mechanism to keep the turbine headed into the wind, the use of the same mechanism to yaw the turbine out of wind to limit power output is obviously an attractive one. However, there are two factors that militate against the rapid response of such a system to limit power – firstly, the large

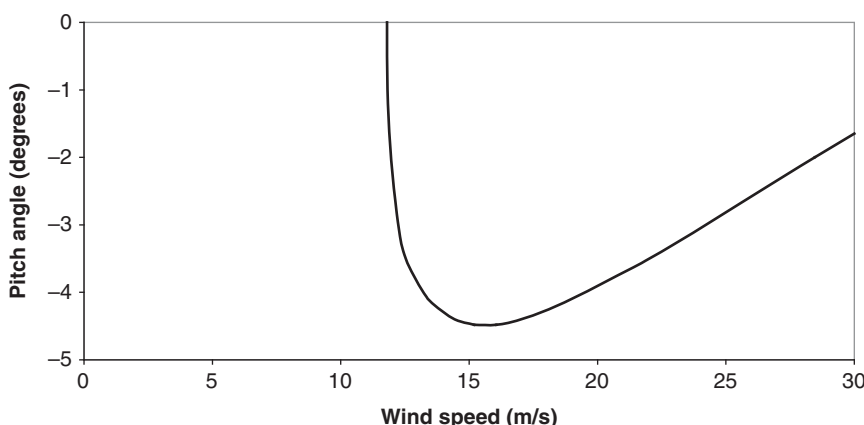


Figure 6.18 Schedule of pitch angles required to limit 70 m diameter turbine output to 1.5 MW at different wind speeds using active stall control

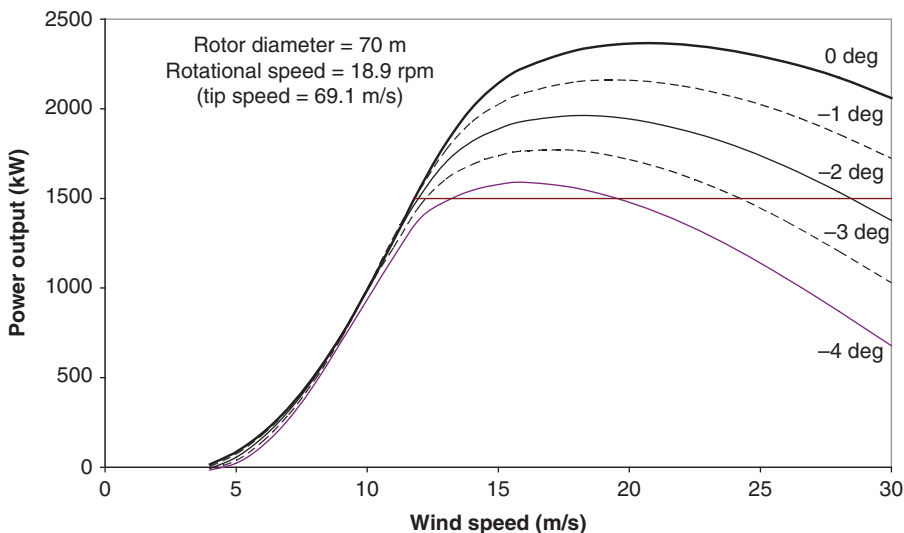


Figure 6.19 Power curves for different negative pitch angles: 70 m diameter three bladed rotor rotating at 18.9 rpm

moment of inertia of the nacelle and rotor about the yaw axis, and secondly, the cosine relationship between the component of wind speed perpendicular to the rotor disc and the yaw angle. The latter factor means that, at small initial yaw angles, yaw changes of, say, 10° only bring about reductions in power of a few percent, whereas blade pitch changes of this magnitude can easily halve the power output. Thus, active yaw control is only practicable for variable-speed machines where the extra energy of a wind gust can be stored as rotor kinetic energy until the yaw drive has made the necessary yaw correction. This design philosophy has been exploited successfully in Italy on the 60 m diameter Gamma 60 prototype, which had an impressive maximum yaw rate of 8° per second (Coiante et al. [1989]).

6.8 Braking systems

6.8.1 Independent braking systems: requirements of standards

The Germanischer Lloyd (GL) rules require that a wind turbine shall have two independent braking systems. However, IEC 61400-1 does not explicitly require the provision of two braking systems, but it does require the protection system to remain effective even after the failure of any non-safe-life protection system component.

IEC 61400-1 and the GL rules require that at least one of the braking systems should act on the rotor or low-speed shaft.

Normal practice is to provide both aerodynamic and mechanical braking. However, if independent aerodynamic braking systems are provided on each blade, and each has the capacity to decelerate the rotor after the worst-case grid loss, then the mechanical brake will not normally be designed to do this as well. The function of the mechanical

brake in this case is solely to bring the rotor to rest – i.e. to park it – as aerodynamic braking is unable do this.

6.8.2 Aerodynamic brake options

Active pitch control: Blade pitching to feather (i.e. to align the blade chord with the wind direction) provides a highly effective means of aerodynamic braking. Blade pitch rates of 10° per second are generally found adequate, and this is of the same order as the pitch rate required for power control. The utilisation of the blade pitch system for start-up and power control means that it is regularly exercised with the result that the existence of a dormant fault is highly unlikely.

In machines relying solely on blade pitching for emergency braking, independent actuation of each blade is required, together with fail-safe operation should power or hydraulic supplies passing through a hollow low-speed shaft from the nacelle be interrupted. In the case of hydraulic actuators, oil at pressure is commonly stored in accumulators in the hub for this purpose.

Pitching blade tips: Blade tips that pitch to feather have become the standard form of aerodynamic braking for stall-regulated turbines. Typically, the tip blade is mounted on a tip shaft, as illustrated in Figure 6.17, and held in against centrifugal force during normal operation by a hydraulic cylinder. On release of the hydraulic pressure (which is triggered by the control system or directly by an overspeed sensor), the tip blade flies outwards under the action of centrifugal force, pitching to feather simultaneously on the shaft screw. The length of the tip blade is commonly some 15% of the tip radius.

The ability of the control system to trigger blade tip activation is of crucial importance. On a number of early machine designs, the blade tips were centrifugally activated only, so there could be long periods without overspeed events when they did not operate. As a result, there was a risk of seizure when operation was eventually required. With the now commonplace arrangement enabling the control system to activate the tip as well, the system can be routinely tested automatically. The penalty is that the low-speed shaft needs to be hollow to accommodate the feed to the hydraulic cylinder.

Spoilers: Spoilers are hinged flaps that conform to the aerofoil profile when retracted and stick out at right angles to it when deployed. However, although such devices have been used in the past, they have to be of considerable length to decelerate the rotor adequately (Jamieson and Agius 1990). Moreover, unless the design allows for their operation to be regularly tested, there is a risk that they will fail to deploy when actually needed.

Other devices: Various other devices have been suggested, such as

- Ailerons.
- The sliding leading edge device or SLEDGE, in which a length of leading edge at the tip slides radially outwards.
- The flying leading edge device or FLEDGE, in which the whole leading edge together with an adjacent section of the camber face is pitched towards feather.

Jamieson and Agius (1990) and Armstrong and Hancock (1991) give useful surveys of these and other aerodynamic braking devices and note that the SLEDGE device, which

utilises only 2% or 3% of the blade area, is highly effective aerodynamically. Derrick (1992) examines the capabilities of the SLEDGE and FLEDGE devices for both braking and power control in more detail. Despite their promise, these devices have not yet found commercial application.

6.8.3 Mechanical brake options

As noted in Section 6.8.1, the duty of the mechanical brake need only be that of a parking brake on machines where the aerodynamic brakes can be actuated independently. However, on pitch-regulated machines where blade position is controlled by a single actuator, full independent braking capability has to be provided by the mechanical brake. It is worth noting that several manufacturers of stall-regulated machines fitted with independent tip brakes ensure that the mechanical brake can stop the rotor unassisted. This may be to satisfy requirements in certain countries that two independent braking systems of a different type are provided.

A wind turbine brake typically consists of a steel brake disc acted on by one or more brake callipers. The disc can be mounted on either the rotor shaft (known as the *low-speed shaft*) or on the shaft between the gearbox and the generator (known as the *high-speed shaft*). The latter option is much the more common because the braking torque is reduced in inverse proportion to the shaft speeds, but it carries with it the significant disadvantage that the braking torques are experienced by the gear train. This can increase the gearbox torque rating required by as much as ~50%, depending on the frequency of brake application – see Section 7.4.5. Another consideration is that the material quality of brake discs mounted on the high-speed shaft is more critical, because of the magnitude of the centrifugal stresses developed.

The brake callipers are almost always arranged so that the brakes are spring applied and hydraulically retracted – i.e. fail-safe.

Aerodynamic braking is much more benign than mechanical braking as far as loading of the blade structure and drive train is concerned, so it is always used in preference for normal shut-downs.

6.8.4 Parking versus idling

Although a mechanical parking brake is essential for bringing the rotor to rest for maintenance purposes, many manufacturers allow their machines to idle in low winds, and some do so during high wind shut-downs. The idling strategy has two clear advantages – it reduces the frequency of imposition of braking loads on the gear train and gives the impression to members of the public that the turbine is operating even when it is not generating. On the other hand, gearbox and bearing lubrication must be maintained throughout.

6.9 Fixed-speed, two-speed, variable-slip, and variable-speed operation

Wind turbine rotors work at their maximum power coefficient (C_p) at only one particular tip speed ratio (see Figure 3.15), and turbines that use a single-speed induction

generator rotate at an almost fixed speed. Hence, below rated wind speed, fixed-speed turbines operate at less than their maximum potential output power except at the wind speed corresponding to this tip speed ratio. Continually varying the rotational speed so that the turbine runs at optimum tip speed ratio over a range of wind speeds below rated increases energy capture.

A slightly reduced improvement can be obtained by running the turbine at two fixed speeds so that the tip speed ratio is closer to the optimum more often than with a single fixed speed. The aerodynamic noise generated by a wind turbine blade is proportional to the fifth or sixth power of the tip speed. Both variable-speed and two-speed operation reduce the rotational speed of the rotor in low winds, thus limiting aerodynamic noise when it might otherwise be objectionable because of low levels of background noise.

Continuous variable-speed operation leads to a reduction in turbine mechanical loads as the control system can be arranged to allow small variations in the rotor speed in response to wind gusts and cyclic torque variations (e.g. those caused by tower shadow). Large wind farms are required by the electricity Transmission System Operators to comply within the Grid Code regulations (see Section 11.5) that specify the electrical performance required to ensure that wind farms support the electrical power system. These requirements are difficult to meet with fixed- or two-speed induction generators.

For all these reasons, all modern large wind turbines operate at variable speed, using power electronic converters to connect the varying frequency output of the generator to the constant frequency of the power network (Hau 2013; EWEA 2009; Blaabjerg and Ma 2013). In the past, fixed-speed and two-speed turbines of ratings up to 1.5 MW were common commercially, but these types of generator are now confined to smaller turbines.

6.9.1 Fixed-speed operation

The design of wind turbines that was common up to around the mid-1990s (known as the *Danish concept*) had a stall-regulated rotor, a three stage gearbox, and a simple squirrel cage induction machine operating at 750, 1000, or 1500 rpm, on a 50 Hz electricity system. The generator had a slip at full output of up to 2–3%, and this provided damping in the drive train. Braking against loss of connection to the grid was either by mechanical brakes on both the high- and low-speed shafts or by a single shaft brake and rotating blade tips.

6.9.2 Two-speed operation

Two-speed operation can be implemented using two simple induction generators that are designed for different rotational speeds. In low wind speeds, a lower power and slower electrical generator is operated over a range of low wind speeds. When the wind speed rises and the power limit of this generator is reached, the smaller generator is disconnected and a full power, higher-speed generator is connected. Similarly, when the wind speed drops, the full power generator is disconnected and the smaller generator used. A hysteresis control system, measuring power, is used to restrict the number of switching operations (Figure 6.20).

Either generators with different numbers of magnetic poles (giving different speeds of rotation) are connected to a single output shaft of the gearbox or generators with

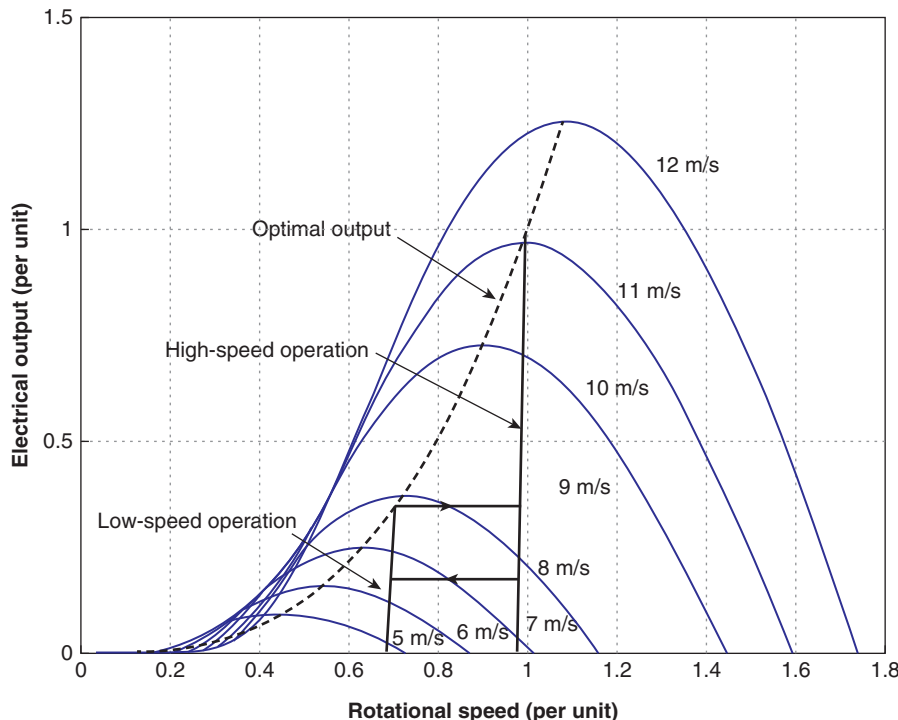


Figure 6.20 Locus of operation of a two-speed wind turbine

the same number of poles are connected to separate output shafts rotating at differing speeds. The power rating of the smaller generator for low-speed operation is typically 1/3 of the turbine rotor rating. The development of induction generators with two sets of stator windings in the same frame allows the number of poles to be varied within a single generator by connecting the windings together in different configurations. Generators of this type are available that can be switched between four and six pole operation, giving a speed ratio of 1.5 (1500 and 1000 rpm). With correct selection of the gearbox, this ratio produces an increase in energy capture of around 2–3% over a turbine operating at a single fixed speed. Two-speed operation can also be worthwhile because of the lower aerodynamic noise at low wind speeds.

Some disadvantages of two-speed compared to single-speed operation are because of the

- Additional generator cost.
- Extra switchgear required, which is subjected to frequent operation.
- Turbine speed, which must be controlled during each speed change.
- Energy that is lost while the generator is disconnected during each speed change.

6.9.3 Variable-slip operation (see also Section 8.3.8)

Variable slip represents a compromise between fixed- and variable-speed operation. The generator is a wound rotor induction machine with a variable resistor that is controlled in series with the rotor circuit by a high frequency semiconductor switch. Below rated power or torque, the external resistor is short-circuited and the generator acts as a conventional fixed-speed induction machine. Above rated power, control of the resistance allows the generator torque to be varied and the generator speed to increase so the behaviour of the turbine is then similar to a variable-speed system. A maximum speed increase of about 10% above nominal rotational speed is typical.

This arrangement is simpler and cheaper than a full variable-speed system and gives some of the advantages, in particular the control of torque in the drive train and the smoothing of aerodynamic torque variations at above rated power. Below rated wind speed, it does not offer increased aerodynamic efficiency although it does not then suffer from switching losses in the power electronics. It does not provide control of the power factor of the electrical output. Electrical flicker in the network is reduced above rated wind speed as the output power is smoothed.

The entire power circuit can be mounted on the generator shaft including the additional resistor(s) and power electronic switch or connected via slip rings. Mounting the resistor on the generator shaft avoids the use of slip rings carrying the rotor current. The signal controlling the power electronic switch is transmitted to the rotating shaft using a non-contact optical device. However, an advantage of mounting the resistors outside the generator and connected via slip rings is that it is then easier to dissipate the heat that is generated above rated wind speed. This heat may be a limiting factor with large generators that have the rotor resistors mounted on the rotor shaft.

6.9.4 Variable-speed operation

Variable-speed operation of the aerodynamic rotor can be achieved by interposing a frequency converter carrying all of the output power of the turbine between the generator and network. All of the power is converted to direct current, and so the fixed relationship that would otherwise exist between the speed of rotation of the generator and the network frequency is broken. The generator may be synchronous or induction type. As well as allowing the rotor speed to vary and so maximise energy capture, the generator air-gap torque may be controlled and so transient mechanical loads reduced. An alternative way to vary the rotor speed is to use a wound rotor induction generator as with variable slip but replace the external resistors in the rotor circuit with a power electronic frequency converter. Only a fraction of the wind turbine output power passes through the rotor circuit.

Variable-speed operation has a number of advantages:

- Below rated wind speed, the rotor torque and hence speed can be made to vary to maintain peak aerodynamic efficiency.
- The reduced rotor speed in low winds results in a significant reduction in aerodynamically generated acoustic noise. Noise is especially important in low winds, where ambient wind noise is less effective at masking the turbine noise.

- The rotor can act as a flywheel, smoothing out aerodynamic torque fluctuations before they enter the drive train. This is particularly important for torque fluctuations at the blade passing frequency.
- Direct control of the air-gap torque allows gearbox torque variations above the mean rated level to be kept small.
- Both active and reactive power exported to the network can be controlled, so that either any particular power factor can be maintained or the terminal voltage controlled. For large wind farms, it is much easier to meet the Grid Code requirements with variable-speed wind turbines than with fixed-speed, induction generator turbines.
- Variable-speed turbines will also give better power (network voltage) quality due to the smoother output power they develop. The use of power electronic converters to connect the generator gradually to the network on start-up minimises electrical transients on connection.

In practice, losses in the frequency converters may amount to several percent of their rated power, counteracting the increased aerodynamic efficiency below rated wind speed. However, the possible load reductions and the requirements of the Grid Codes mean that all MW-scale turbines now operate at variable speed. Variations in aerodynamic torque at blade passing frequency are particularly significant for larger turbines because of the size of the rotor compared to the lateral and vertical length scales of turbulence. The turbine control system is tuned to allow the aerodynamic power variations to be absorbed as slight changes in rotational speed, i.e. as variations in kinetic energy stored in the rotor.

There is a significant cost associated with the variable-speed equipment, which must be weighed against the advantages. Other drawbacks include increased complexity and the generation of electrical noise and harmonics by the inverters. Modern pulse width modulated (PWM) inverters operate at high switching frequency (up to 10 kHz) using silicon insulated gate bipolar transistors (IGBTs). A high switching frequency reduces the lower order harmonics (e.g. fifth, seventh, 11th, 13th, etc.) compared to the earlier, naturally commutated converters that used thyristors, but with silicon power electronic switches there is a trade-off between reduced harmonics and increased electrical losses. The emerging semiconductor materials of silicon carbide and gallium nitride allow switching frequencies of up to 100 kHz with limited losses, but these switches are expensive at present; their use may increase in the future. At high switching frequencies, electrical noise can be a problem for control signals within the turbine if insufficient care is taken with grounding and shielding of instrumentation and control cables. Fibre optic transmission is increasingly being used for monitoring and communications links, and currents in adjacent cables do not affect these circuits.

There are two principal methods of achieving variable-speed operation. In broad range or full power conversion (FPC) variable-speed operation, the generator stator is connected to the network via a fully rated ac–dc–ac frequency converter. Narrow range variable-speed operation uses a doubly fed induction generator (DFIG) with both the generator stator and rotor connected to the network. The stator is connected directly and the rotor through slip rings, and a smaller frequency converter is used (Anaya-Lara et al. 2009).

Broad range variable speed allows the generator and rotor speed to vary from close to zero to the full rated speed, but all the power output passes through the frequency converter. Either a synchronous or induction generator can be used. Narrow range variable speed uses a smaller, and hence cheaper, frequency converter. Only a fraction of the power passes through it, but the speed can only vary by, typically, $\pm 30\text{--}40\%$ either side of synchronous speed.¹ In practice, this is enough to achieve almost all of the advantages of variable-speed operation. A disadvantage is the need to use a wound rotor induction machine with a small air-gap, and the maintenance requirements of the slip rings.

In both broad and narrow speed range wind turbines, the frequency conversion is made by two back-to-back voltage source converters that are connected through a direct current link. These converters rectify the power into the dc link and then invert it to network frequency or supply the generator. This rectification into direct current and inversion isolates the network frequency from either the generator speed in the case of broad range or the rotor frequency in the case of a DFIG wind turbine. In both systems, control is by measuring the generator rotational speed and applying the torque required to keep the aerodynamic rotor at optimum tip speed ratio over a wide a range of wind speeds.

Figure 6.21 shows the control of a variable-speed wind turbine. The rotor speed is measured and, once cut-in speed is reached, a controlled torque is applied to the generator by the variable-speed converter. The rotor speed is controlled by the restraining torque of the generator to stay close to the optimum curve (O-A). At maximum rotational speed, this speed is maintained by increasing the restraining torque applied to the

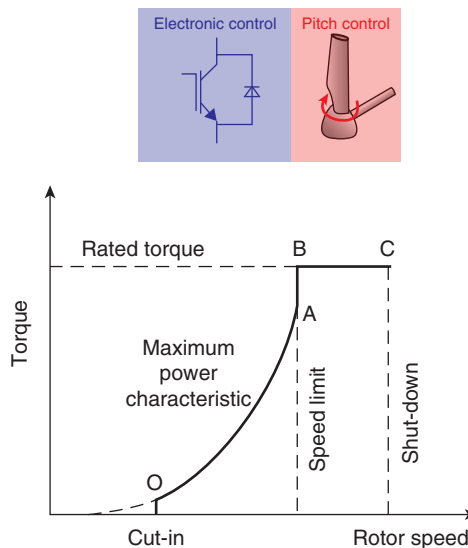


Figure 6.21 Control objective of a variable-speed wind turbine (see also Chapter 8, Figure 8.3)

¹ Synchronous speed is fixed by the frequency of the network (50 or 60 Hz) and the number of magnetic poles of the generator construction.

generator by the converter (A-B) until the blades are pitched to control incoming wind power and torque (B-C).

6.9.5 Generator system architectures

Figures 6.22a–e show the architectures of the commonly used wind turbine generator systems.

- Figure 6.22a shows a fixed-speed (squirrel cage) induction generator with shunt capacitors to improve the output power factor. These capacitors may be switched to provide more reactive power as the generated power increases.
- In Figure 6.22b, the rotor circuit has controllable resistors to give variable-speed operation. Power factor correction capacitors are connected to the stator of the wound rotor induction machine.
- In Figure 6.22c, the controllable rotor resistors are replaced by back-to-back voltage source converters (using IGBTs) to connect the rotor to the network. This gives variable-speed operation over a restricted speed range above and below synchronous speed depending on the direction of power flow in the rotor circuit. Although there are switching losses in the converters, this arrangement avoids energy being dissipated in an external rotor resistance. Control of the generator speed and power factor is by the rotor side converter while the grid side converter maintains the dc link voltage. The crowbar circuit is to protect the generator side converter when faults occur on the ac network and to assist in ensuring continuous operation of the wind turbine during these faults.
- All of the power from the generator (that may be synchronous or induction type) is rectified to dc in the arrangement of Figure 6.22d. Again, control of the generator torque (and hence speed) and excitation is by the machine side converter while the grid side converter maintains the dc link voltage. The network side converter can be used to control the network voltage or reactive power flow into the network.
- An alternative arrangement is shown in Figure 6.22e with the network side converter controlling the output power of the generator (and hence the wind turbine speed) while the machine side converter is a simple diode rectifier followed by a dc to dc voltage converter. With this arrangement, the generator must be of the synchronous type, either wound rotor or permanent magnet, but the diode rectifier has lower losses than a controllable IGBT converter.

The relative popularity of the different architectures is described by Serrano-González and Lacal-Arántegui (2016).

6.9.6 Low-speed direct drive generators

Over the last 15 years, there has been considerable development of low-speed generators that are designed to be driven directly by wind turbine rotors without a speed-increasing gearbox. A number of manufacturers offer wind turbines with direct drive generators. The obvious advantages are the elimination of the gearbox with its associated energy losses, weight, noise, and maintenance requirements.

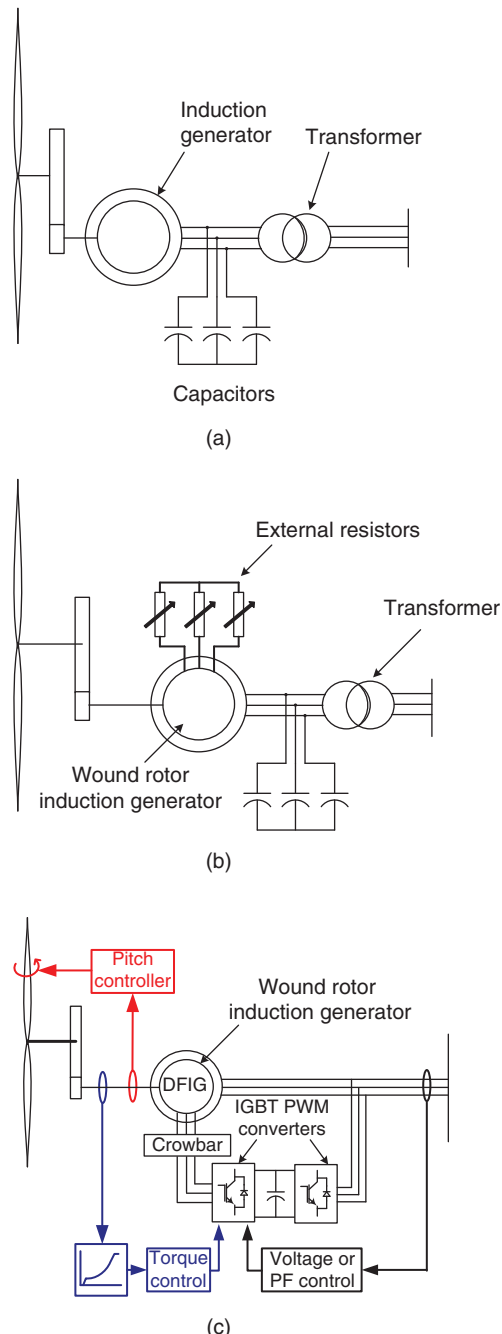


Figure 6.22 Wind turbine architectures. (a) Fixed-speed induction generator, Type 1 (IEC 61400-27-1 [2015]). (b) Variable-speed generator, Type 2. (c) Doubly fed induction generator, Type 3. (d) Full power converter wind turbine, Type 4. (e) Full power converter wind turbine (diode rectifier) (Anaya-Lara et al. 2009)

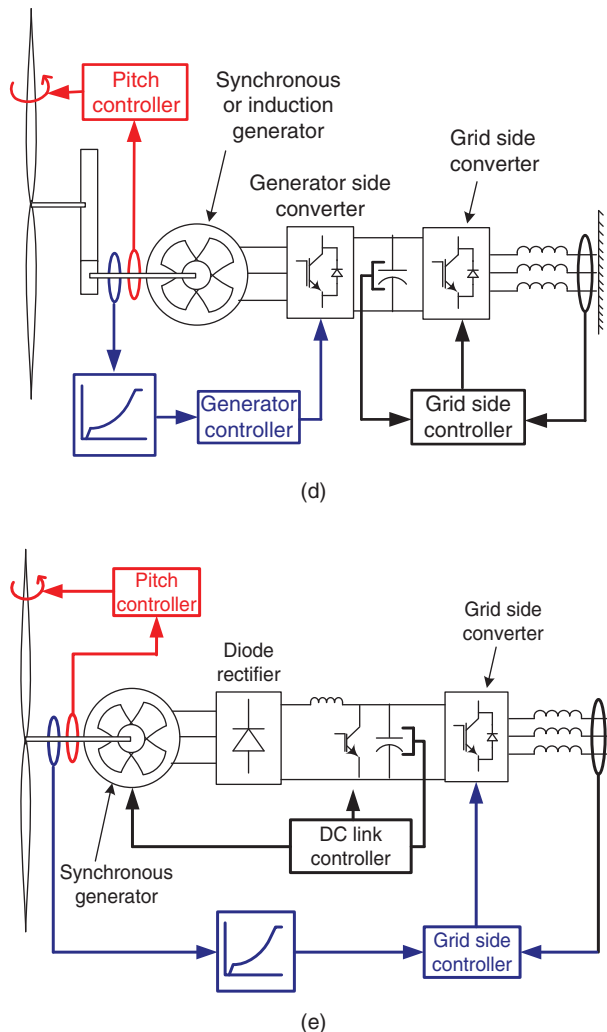


Figure 6.22 (Continued)

The power output of a cylindrical electrical machine may be generally described by (Mueller and Polinder 2013)

$$P = \omega 2\pi R^2 L F_d$$

where

ω is the rotational speed of the rotor (rad/s)

R is the air-gap radius (m)

L is the axial length (m)

F_d is the air-gap shear strength (kNm/m^2)

F_d is determined by the electromagnetic design and typically has a maximum of 30–60 kNm/m^2

It may be seen that if the rotational speed is reduced, then it is necessary either to lengthen the generator in proportion or to increase the diameter. It is cheaper and lighter to increase the diameter because this raises the power by the square rather than linearly. Thus, direct drive generators for wind turbines have large diameters, and hence weights, but with limited length.

Induction generators require a small radial distance between the surface of the rotor and the stator (known as the *air-gap*). This is necessary to ensure that an adequate magnetic flux links the rotor because all of the excitation is provided from the stator. It is difficult to manufacture large diameter electrical machines with small air-gaps for mechanical and thermal reasons. In contrast, synchronous generators have excitation systems on the rotor and so can operate with larger air-gaps. Hence direct drive wind turbines all use synchronous generators (either with permanent magnet excitation or are electrically excited with a wound rotor and electromagnets providing the magnetic field). The use of a synchronous generator leads to the requirement for fully rated frequency conversion equipment to de-couple the generator speed from the network frequency through two fully rated power converters.

The stator of a synchronous generator has a distributed winding located in slots in a laminated iron core. This creates a rotating field from the three phase supply onto which the rotor field locks. An electrically excited synchronous machine uses a direct current circuit on its rotor to create the magnetic field that is fixed to the rotor and rotates with it. The direct current may be supplied either through slip rings and brushes or by a small rotating transformer and rectifier in a brushless excitation system, but this arrangement is less common in wind turbines. The power dissipated in the field circuit creates some electrical losses, but the advantage is that the field current can be varied as the rotational speed changes, and hence the output voltage and power factor of the generator can be controlled. Electrically excited synchronous generators are well established for direct drive wind turbines and are used up to the highest ratings.

As an alternative to electrical excitation, rare-earth permanent magnets, typically neodymium iron boron (NdFeB), are used to create the rotor field. This eliminates the electrical losses in the field circuit and the consequent generation of heat. Several manufacturers offer wind turbines up to the highest ratings using such permanent magnet generators. If permanent magnets are used, then there is no control over the excitation of the synchronous machine, and the generator output voltage will vary with rotational speed. Then it may be necessary to use an additional power electronic converter to control the voltage of the dc link voltage of the frequency converter (see Figure 6.22e). The manufacture of very large, permanent magnet generators can be difficult because the forces developed by the magnets during assembly can be very great.

There are two basic architectures of permanent magnet generators, radial and axial flux. A figure discussed later (Figure 6.34) shows a radial flux generator with the rotor located inside the stator. A similar layout can be used for permanent magnet or electrically excited generators. Inverting the design and locating a rotating permanent magnet rotor outside the stator can reduce the overall diameter of the generator, as the magnets themselves can be made quite thin.

Table 6.8 Main parameters of a 3 MW, 15 rpm radial flux generator design

Stator radius	2.5 m
Stator length	1.2 m
Air-gap	5 mm
No. of pole pairs	82
Weight of active material (copper, iron, and permanent magnet)	24 t
Losses at full output	130 kW

An example design of the active elements of a radial flux permanent magnet generator suitable for a 3 MW wind turbine is given in Polinder et al. (2006) and is detailed in Table 6.8.

An alternative, if less common, architecture is to arrange the air-gap flux to be parallel to the axis of the rotor. A single air-gap creates very large axial forces, and so it is common to use two air-gaps to balance these forces. In addition to these two basic approaches, a number of innovative designs of permanent magnet generators for wind turbines have been proposed but have yet to achieve commercial breakthrough.

6.9.7 Hybrid gearboxes, medium-speed generators

Several manufacturers have developed designs of hybrid drive trains based on a two stage gearbox and a medium-speed electrical generator with a nominal rotational speed of around 500 rpm. The generator and gearbox are then of similar size, and so this hybrid arrangement leads to a more balanced and compact nacelle. The medium-speed synchronous generators use permanent magnet excitation with full power frequency converters.

In some designs, a gearbox with multiple output shafts splits the power equally, and several identical smaller generators and power converters are used. The smaller individual generators and power converters are then easier to handle and can be cheaper.

6.9.8 Evolution of generator systems

Figure 6.23 shows the evolution of wind turbine generator systems. Early wind turbines used fixed-speed induction generators (FSIGs). These operated at almost constant speed (with slip less than 2–3%) using either stall regulation of the aerodynamic rotor or pitch regulation of the blades. The arrangement was applied to wind turbines as large as 1.5 MW, but above this rating there are increasing difficulties in controlling drive train oscillations and limiting mechanical loads. In addition, FSIG wind turbines have difficulties meeting the requirements of the Transmission Grid Codes that are applied to large wind farms.

From around the year 2000, DFIGs became increasingly common in large wind turbines with the benefits of limited variable-speed operation but at the reduced cost of controlling only a fraction of the output power. However, slip rings are required on the generator rotor, and the air-gap of a wound rotor induction generator must be kept small.

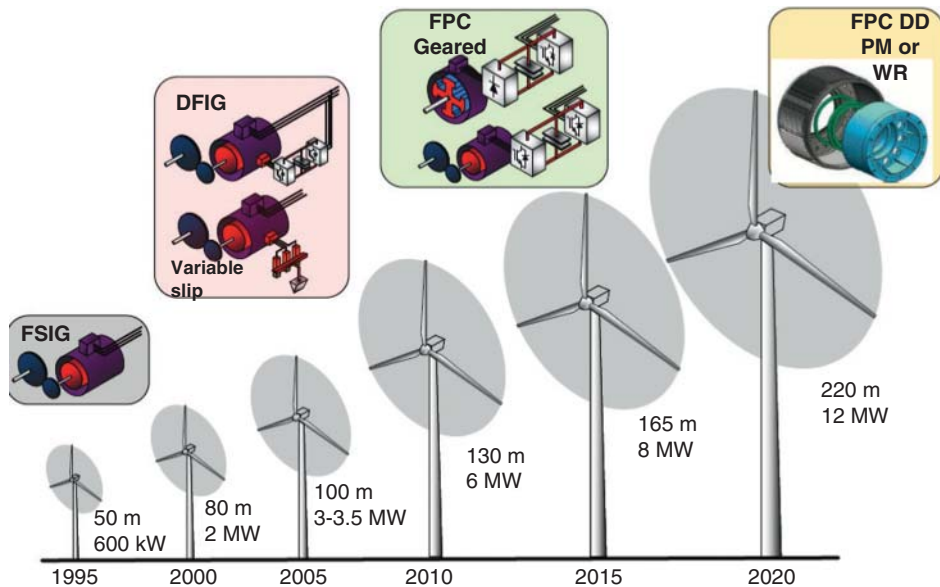


Figure 6.23 Evolution of commercially available wind turbine generator systems.
FSIG: Fixed-speed induction generator; DFIG: doubly fed induction generator; FPC: full power conversion; DD: direct drive; PM: permanent magnet; WR: wound rotor

At the same time as the DFIG architecture was being implemented widely, FPC was being used with generators either driven through a gearbox or driven directly by the aerodynamic rotor. Both electrically excited wound rotor and permanent magnet low-speed, large diameter synchronous generators have been used for direct drive applications. At present, there remains limited consensus on the architecture of future electrical generator systems for very large wind turbines.

6.10 Other drive trains and generators

Section 6.9 described the generation systems that are, or have been, widely used commercially. However, a very large number of other concepts and approaches to drive trains and power conversion have been investigated and prototypes constructed, but they are not commercially significant at present.

6.10.1 Directly connected, fixed-speed generators

Large hydro, fossil fired, or nuclear power stations use synchronous generators connected directly to the power system, and the design and operation of all large power systems is based on the performance of synchronous generators. Induction generators are much less useful than synchronous generators for large-scale power generation and are rarely used at sizes greater than 10 MW. Hence, in the early development of wind turbines,

considerable efforts were made by engineers to use the familiar synchronous generators in wind turbines.

The disadvantages of directly connected induction generators are the following:

- The damping action in the rotor results in higher energy losses than with a synchronous generator. It is then necessary to arrange for the removal of the heat dissipated in the rotor.
- All the reactive power necessary to energise the magnetic circuits must be supplied from the network (or by local capacitors). If local capacitors are used, there is the danger of self-excitation.
- There is no direct control over the terminal voltage or reactive power flow.
- Induction generators do not produce sustained fault current for three phase faults on the network.
- They suffer from problems of voltage instability. This was not an important issue with a limited capacity of wind generation, but with large wind farms on weak networks, it can limit the size of the wind farm that can be connected.

Synchronous and induction generators have similar windings on their stators that, when connected to the three phase mains voltage, produce a fixed-speed, rotating magnetic field. However, the rotors of the two machines are quite different (Hindmarsh 1984; McPherson 1990). A synchronous machine has magnets (either permanent or electromagnets) mounted on its rotor, and the rotor magnetic field locks into the constant-speed, rotating field produced by the stator. The rotor turns at the same speed as the stator magnetic field, and the drive train is stiffly coupled to the constant frequency of the electrical network, although it leads the stator field by an angle depending on the torque. This is in contrast to the rotor of a simple induction generator that has a squirrel cage winding into which currents are induced when the rotor rotates slightly faster than the stator field. An induction generator can only develop torque at a rotational speed slightly greater than that of the stator field, and the drive train is more loosely coupled to the frequency of the electrical network.

Considering a reference frame rotating at grid frequency and to a first approximation, the behaviour of a synchronous machine connected directly to an electricity network may be considered to be analogous to a torsional spring. The torque is proportional to the angle between the rotor and the stator field. This angle is known as the *load or power angle*. In contrast, an induction generator can be thought of as a torsional damper where the torque is proportional to the difference in speed between the rotor and the stator field (the slip speed). This is illustrated in simple schematic form in Figure 6.24.

It may be seen that if the simple model of a fixed-speed wind turbine equipped with a synchronous generator is excited by the cyclic torque from the wind turbine rotor, there is no damping in the drive train to control the torsional oscillations. It is a simple two spring, two mass system. The main cyclic torque of the wind turbine rotor will be at blade passing frequency, and it is an unfortunate coincidence that this often matches quite closely the natural frequency of oscillation of a synchronous generator connected to an electrical network. Early attempts to operate wind turbines with directly connected synchronous generators failed due to unacceptable drive train oscillations. Synchronous

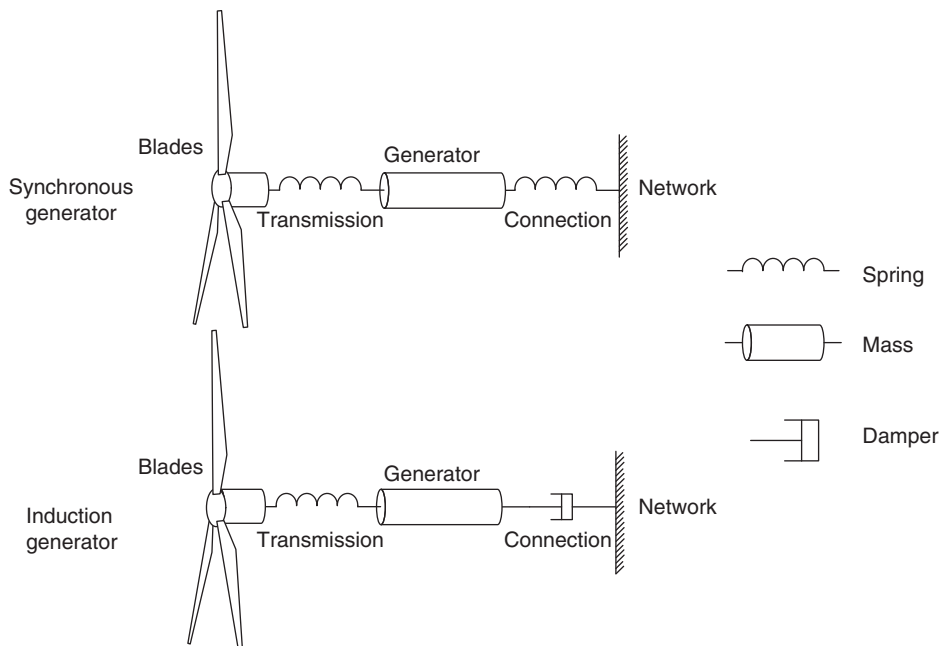


Figure 6.24 Mechanical analogues of directly connected generators

generators can be fitted with additional cage damper windings, but due to space limitations, it is not practical to provide the degree of damping required for the large cyclic torque oscillations of wind turbine rotors.

An induction generator connected to the network can be represented by a torsional damper, and this performance was exploited in the simple architecture of a stall-regulated rotor, gearbox, and directly connected induction generator (the Danish concept) that was used for some years. FSIGs of up to 1.5 MW were widely used in these turbines until the 1990s (Anderson 2020). The generators typically had slips of 1–2%, exceptionally up to 3%. At higher power ratings, second order electromagnetic effects reduce the damping energy that can be extracted, and the wind turbine architecture becomes ineffective (Saad-Saoud and Jenkins 1999).

Attempts have also been made to use variable pitch wind turbine rotors to drive FSIGs directly. However, it was found to be difficult to control the drive train torque effectively, and transient overpowers of up to twice the continuous rating were common. This was due to a combination of the resonant behaviour of the drive train, the speed of response of the blade pitch control, and the absence of the drive damping of stall regulation.

From the mid-1990s, directly connected generators were gradually superseded by power electronic variable-speed systems that remove the direct link between the generator and network. In a variable-speed operation, the generator is not connected directly to the network but is de-coupled by the frequency converter. The generator side voltage source inverter presents an actively controlled voltage to the electrical machine, and the simple analogues of Figure 6.24 do not apply.

6.10.2 Innovations to allow the use of directly connected generators

There have been a number of attempts to provide additional torque limiting, torsional damping, torsional compliance, and wide range variable-speed operation through innovations in mechanical drive trains to allow wind turbines with either synchronous or low slip induction generators to be connected directly to the network. These approaches have now largely been superseded by the use of power electronic frequency conversion, but similar arrangements continue to be proposed from time to time.

A fluid coupling has an impeller and a turbine runner in a constant volume of fluid. The impeller drives the turbine through the speed difference (slip) between them. The slip (and energy lost as heat) is typically 2–6% at full power output. The coupling provides torsional damping and has similar performance to that of a high slip induction generator. Historically, the Smith–Putnam and Mod-0A turbines both used a fluid coupling to drive a synchronous generator, whereas Westinghouse and Howden used fluid couplings in their early commercial medium sized turbines (Spera 1994; Hau 2013).

A flexible (quill) low-speed shaft was used to drive a fixed-speed synchronous generator in the Mod-2 turbines. Such shafts provide torsional compliance, but the only damping is from the shaft material itself. It is interesting to note that the next turbine to be developed in this series (the Mod-5) used variable speed using power electronics (Spera 1994).

Several early prototypes fixed the gearbox to the nacelle frame using springs and dampers. This arrangement allows controlled angular rotation of the gearbox and provides torsional compliance and damping. It enabled the use of synchronous generator on the 250 kW MS-1 (Law et al. 1984) and the 4 MW WTS-4 prototypes (Hau 2013).

The LS-1 prototype had a 3 MW directly connected synchronous generator and a variable-speed differential mechanical gearbox to give a $\pm 5\%$ speed variation. The sun wheel of the planetary gearbox was controlled by a four quadrant 300 kW power electronic electrical drive to vary the speed of rotation of the aerodynamic rotor and limit torque transients (Law et al. 1984). Some years later, this concept was developed further by replacing the electrical variable-speed drive by a hydraulic system controlling the gearbox sun wheel. Depending on the control of the hydraulic system, variable-speed operation as well as torsional damping and compliance can be provided without power electronics. Turbines using these types of controlled differential gearbox and a synchronous generator were offered commercially by several manufacturers (Pengfei and Wang 2011). A differential gearbox with four quadrant control of the sun wheel can be thought of as the mechanical analogue of a power electronic DFIG.

High-pressure fluid systems have a very high energy density, both with respect to volume and weight, and can conveniently store energy. They can be used to provide drive train compliance and damping and also longer-term energy storage in pressurised energy accumulators. This concept is described in the comprehensive review of future emerging technologies in the wind power sector by Watson et al. (2019). The early Schacle–Bendix prototype used a hydraulic transmission to drive a synchronous generator, and several studies examined the use of high-pressure hydraulics for wind turbine transmission. The studies concluded that at that time, this approach suffered from limited availability of components at the ratings needed, relatively poor efficiency, low reliability, and limited life (Jamieson 2018).

6.10.3 Generator and drive train innovations

A large number of other innovations have been investigated or demonstrated to various levels of technology readiness but have yet to achieve commercial breakthrough. Examples include those discussed in the following sections.

Superconducting generators

Many large offshore wind turbines use direct drive, permanent magnet synchronous generators to eliminate the gearbox and so that the generator rotor can be a simple robust construction suitable for the demanding offshore environment. However, the flux density that can be developed in the air-gap of a permanent magnet synchronous generator is limited, and so a large diameter, heavy, and expensive generator is needed to develop the torque required. In the past, there has also been concern over the availability and price of the rare-earth permanent magnetics; up to 800–1000 kg of permanent magnet material is required for each MW of installed wind power capacity. Superconducting generators offer the possibility of a more compact and lower weight high torque drive train, but questions of their cost and reliability has impeded their use in commercial turbines (Moore 2018).

Superconductors allow very high magnetic fields to be created by thin wires or tapes with little electrical loss and are typically used in the dc rotor circuit of generators to increase the flux density in the air-gap and increase the peak torque by a factor of two or three over a permanent magnet generator. Figure 6.25 is a cross-section of a generator with a superconducting rotor. Design studies of such machines have suggested that the superconductors could have a current density of 300 A/mm^2 in an applied field of 4 tesla and develop an air-gap flux density of 2.5 tesla (Abrahamsen et al. 2012). In the arrangement shown, the rotor is superconducting and the stator is conventional, although some designs have proposed superconducting windings on both stator and rotor.

Table 6.9 shows the two types of superconductor that are likely to be suitable for use in wind turbine generators. Both can sustain an applied flux density of 3 tesla and

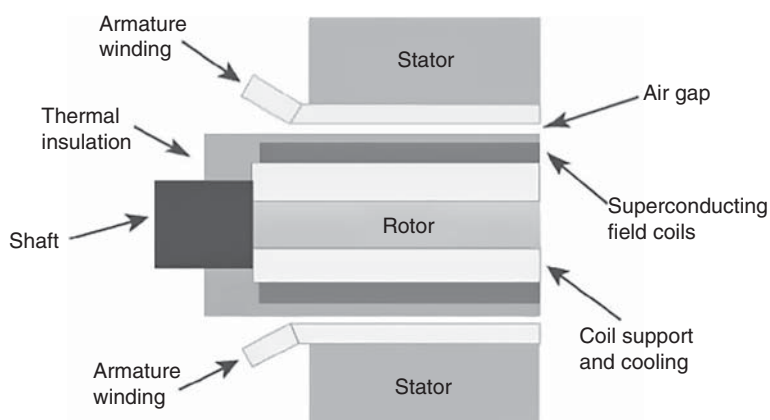


Figure 6.25 Superconducting rotor synchronous generator

Table 6.9 Superconducting materials suitable for wind turbine generators

Type of superconductor	Material	Critical temperature K	Practical operating temperature K	Comparative price of material
Medium temperature	MgB ₂ , magnesium diboride	39	20	1–4
High temperature	RBCO, rare-earth barium copper oxide tape	90–110	20–50	20–30

maximum current density of around 100 A/mm² while maintaining their superconducting properties. These materials have been the subject of a number of studies (INNWIND 2018; Jensen et al. 2012). The medium temperature MgB₂ is generally considered to be cheaper than a high temperature superconductor but is more difficult to manufacture and use in a generator.

The EcoSwing Project (Winkler 2019) has demonstrated a 4 m diameter, direct drive superconducting generator in a 128 m diameter, 15 rpm wind turbine. The modified turbine and generator ran successfully for 630 hours and reached a maximum output of 3 MW. The rotor magnets were made from a composite tape with a ceramic superconducting layer of gadolinium–barium–copper oxide (GdBaCuO) on a steel ribbon. Cryogenic coolers were used to cool the superconductor to 33 K.

Magnetic gearboxes

The availability of high strength NdFeB permanent magnets has allowed the development of magnetic gearboxes (Attallah and Howe 2001; Wang and Gerber 2014; Jamieson 2018). These convert the low-speed, high torque rotation of the aerodynamic rotor of a large wind turbine to a higher-speed, lower torque rotation more suitable for electricity generation without any direct physical contact as occurs in a conventional gearbox. The torque is transmitted by the magnetic fields of the permanent magnets, which are modified by an intermediate ferromagnetic element (Figure 6.26). Radial flux designs appear to be promising and a competitive technology to superconducting generators (INNWIND 2018).

If two concentric sets of permanent magnets with different numbers of pole pairs are separated by an intermediate rotor of pole pieces of soft ferromagnetic material, then torque can be transferred provided the number of pole pairs of the permanent magnets and the number of pole pieces of the soft magnetic material are related by

$$p_i + p_o = n_m$$

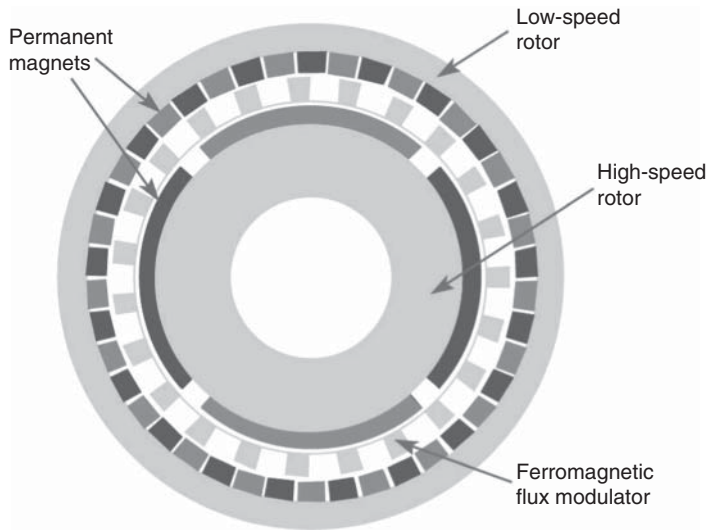


Figure 6.26 Radial flux magnetic gearbox

where

p_i is the number of pole pairs of permanent magnetic material on the inner shaft

p_o is the number of pole pairs of permanent magnetic material on the outer shaft

n_m is the number of pole pieces of ferromagnetic material, and the speed of rotation of the rotors is given by

$$\omega_i p_i + \omega_o p_o = \omega_m n_m$$

where

ω_i is the rotational speed of the inner shaft

ω_o is the rotational speed of the outer shaft

ω_m is the rotational speed of the ferromagnetic rotor.

If the intermediate ferromagnetic rotor is held fixed, then the gear ratio (high speed/low speed) is

$$G = -\frac{p_o}{p_i}$$

If the outer set of permanent magnets is held fixed, then the gear ratio becomes

$$G = \frac{n_m}{p_i} = 1 + \frac{p_o}{p_i}$$

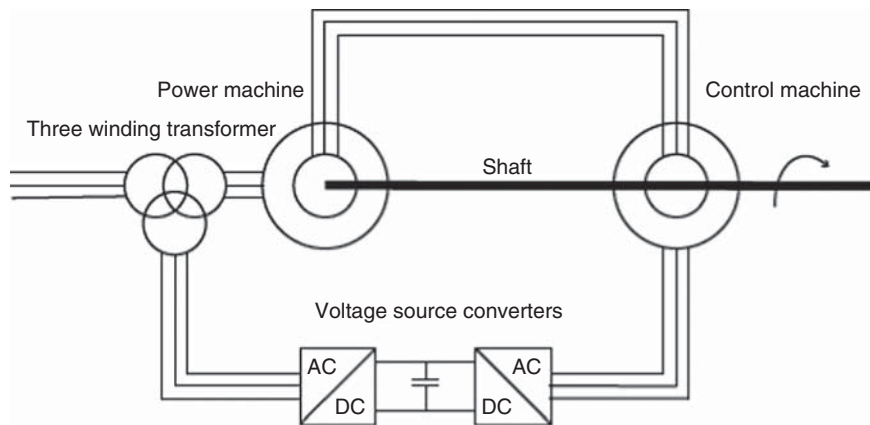


Figure 6.27 Principle of a cascaded brushless doubly fed induction generator

This concept has been developed into the ‘pseudo direct drive’ permanent magnet generator by integrating the magnetic gearbox with a permanent electrical generator. This leads to a reduction in the use of permanent magnetic material (Attallah et al. 2008).

Brushless doubly fed induction generators

A DFIG uses a wound rotor induction machine that has slip rings to transfer power from a voltage source converter onto the rotor. If two wound rotor induction machines are connected in cascade, there is no need for slip rings. The generators are mounted on the same shaft so that power can be transferred between the rotors by a direct connection that rotates with the shaft. The stator of the lower rated control machine is supplied through a back-to-back voltage source converter while the stator of the power machine is connected to the network. This principle is shown in Figure 6.27 and formed the basis of the development of the modern brushless doubly fed induction machine.

Rather than two separate machines, the modern brushless doubly fed induction machine has two separate stator windings on the same core and a nested rotor. This magnetically coupled concept has received considerable academic attention, but its construction is complex, the machine is expected to be larger and more expensive than a DFIG with slip rings, and the control is expected to be more difficult. In spite of a number of claimed advantages over a DFIG, such as elimination of the slip rings and improved fault ride through, this technology has not yet been used commercially in wind turbines (EWEA 2009; Strous et al. 2017).

Direct current power collection

The established architectures of variable-speed turbines (Figure 6.22c–e) all use a back-to-back frequency converters, and each wind turbine produces alternating current at a constant frequency of 50 or 60 Hz. This constant output frequency allows the use of conventional electrical plant for the wind farm power collection circuits, including transformers and switchgear, but a large number of power electronic converters are required.

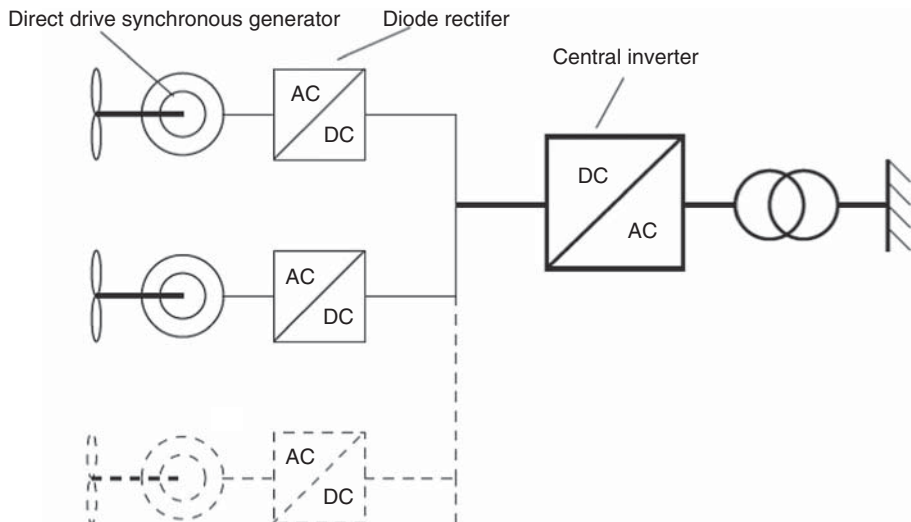


Figure 6.28 Parallel connection of direct current wind turbine generators

The use of direct current in the wind farm power collection and a smaller number of larger dc/ac inverters was demonstrated in Holland in the 1980s. ABB took the concept further with its Windformer design (Dahlgren et al. 2000). This proposed the use of a direct drive synchronous generator with a radial flux permanent magnet rotor and novel high voltage cable windings on the stator. The variable frequency alternating current output of each generator (at a voltage of more than 20 kV) would be rectified to direct current by a simple diode rectifier within the turbine. The direct current output of several wind turbines would be connected in parallel and their output inverted by a central inverter (see Figure 6.28). It was intended that this innovative design would be demonstrated on a 3 MW prototype, but the project was discontinued before the wind turbine was constructed. Gjerde et al. (2014) used simulation and a laboratory-scale prototype to investigate a modular direct drive generator and series connected power converter arrangement to allow connection to the wind farm power collector circuits without a transformer.

A number of studies have investigated the connection of the dc output of wind turbines in series. Series connection can potentially reduce the length of array cabling needed but requires an additional dc/dc converter at each turbine to control the rotor torque (Veilleux and Lehn 2014). This converter must withstand the voltage of the string of turbines. To date, no modern wind farm has used a direct current power collection circuit.

6.11 Drive train mounting arrangement options

6.11.1 Low-speed shaft mounting

The functions of the low-speed shaft are the transmission of drive torque from the rotor hub to the gearbox and the transfer of all other rotor loadings to the nacelle structure.

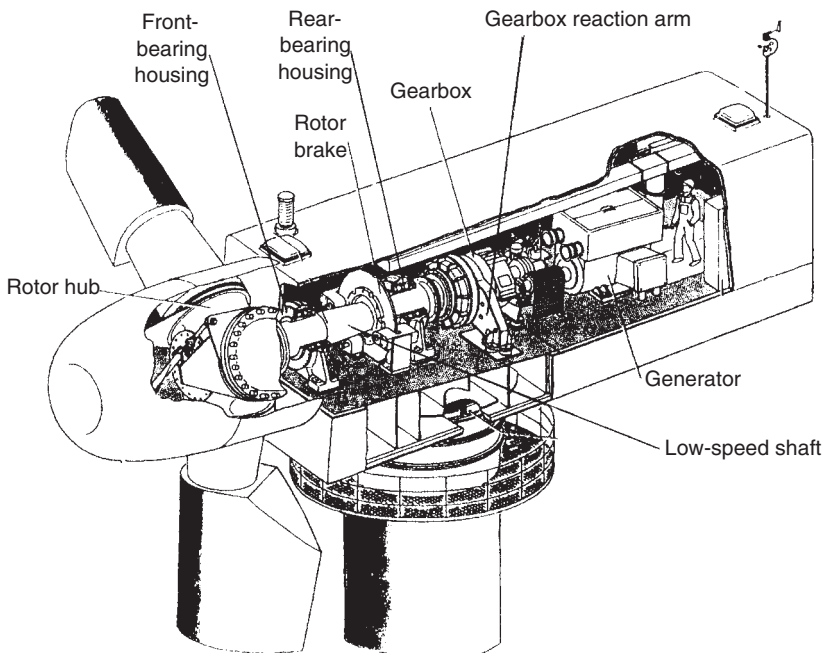


Figure 6.29 View of nacelle showing traditional drive shaft arrangement

Traditionally, the mounting of the low-speed shaft on fore and aft bearings has allowed these two functions to be catered for separately: the gearbox is hung on the rear end of the shaft projecting beyond the rear bearing, and the drive torque is resisted by a torque arm. The front bearing is positioned as close as possible to the shaft/hub flange connection to minimise the gravity moment due to the cantilevered rotor mass, which usually governs shaft fatigue design. The spacing between the two bearings will normally be greater than that between front bearing and rotor hub to moderate the bearing loads due to shaft moment. See Figure 6.29 for an illustration of a typical arrangement.

The opposite approach is to make the gearbox an integral part of the load path between the low-speed shaft and tower top, i.e. an ‘integrated gearbox’. The fore and aft low-speed shaft bearings are absorbed within the gearbox, which moves to the front of the nacelle to minimise the rotor cantilever distance, and the gearbox casing then transmits the loads to the nacelle bedplate (Figure 6.35). Clearly, this approach requires a much more robust gearbox casing, which must not merely resist the rotor loads but do so without deflecting sufficiently to impair its functioning. Moreover, its fore–aft length has to be increased to moderate the bearing loads due to shaft moment. The benefits lie in the reduced extent of the bedplate and the elimination of separate bearings requiring separate provision for lubrication, but a significant disadvantage is that gearbox replacement requires the removal of the rotor.

A configuration that is becoming increasingly popular is one intermediate between the two extremes just described, in which only the rear low-speed shaft bearing is absorbed into the gearbox. The gearbox is usually set well back from the front bearing to reduce the rear bearing loads and is rigidly fixed to supporting pedestals positioned on

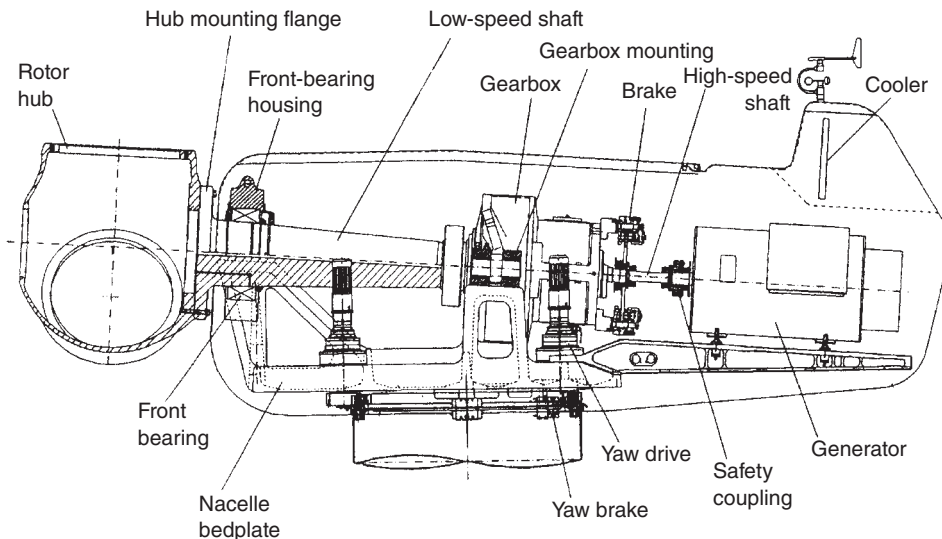


Figure 6.30 Nacelle arrangement for the Nordex N60 turbine. Source: Reproduced by permission of Nordex

either side of the nacelle. Typical arrangements are shown in Figure 6.30, which shows a cross-section through the nacelle of the Nordex N-60 turbine, and in Figure 6.31. Note that the shaft tapers down in diameter towards the rear reflecting the reducing bending moment. The advantage of this arrangement is that the gearbox casing is not called upon to carry any moments due to cantilevered rotor mass or rotor out-of-plane loadings.

Figures 6.32 and 6.33 are aerial views of the nacelle of a NEG Micon 1.5 MW machine with a similar drive train arrangement, after installation of the low-speed shaft.

In the case of wind turbines with direct drive generators, the low-speed shaft arrangement is dramatically different. The low-speed shaft, which now connects the rotor hub to the rotor of the generator, is hollow, so that it can be mounted on a concentric fixed shaft cantilevered out from the nacelle bedplate. See Figure 6.34.

6.11.2 High-speed shaft and generator mounting

The generator is normally mounted to the rear of the gearbox on an extension of the nacelle bedplate, and the connecting drive shaft – the ‘high-speed shaft’ – is fitted with flexible couplings at each end, to cater for small misalignments between the generator and gearbox.

The generator axis is normally offset from the low-speed shaft axis. This is because, except in the case of machines fitted with a mechanical brake acting on the rotor, access is required to the rear end of the low-speed shaft for hydraulic pipes, electrical cables, or an actuator rod passing through the shaft, which is made hollow for blade pitch control or the activation of tip brakes. Usually the generator is either offset to one side of the nacelle, which introduces asymmetry into the nacelle bedplate, or it is offset vertically upwards, which requires a vertical step in the bedplate.

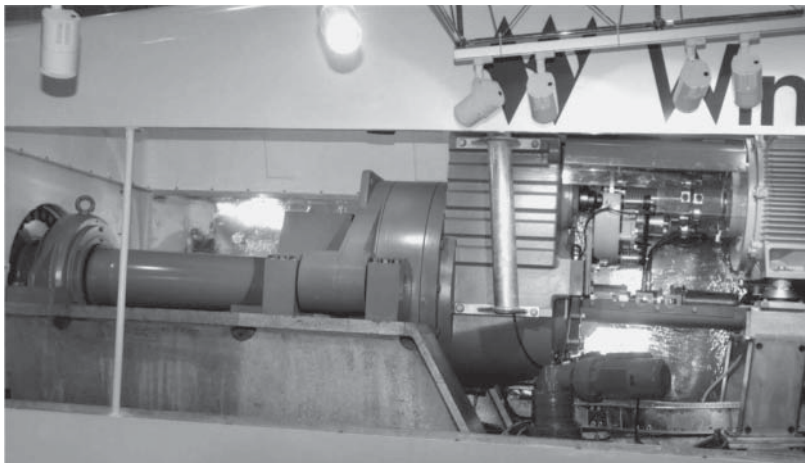


Figure 6.31 Drive train side view. From left to right the components visible through the cut-out in the nacelle wall are (1) low-speed shaft front bearing, (2) low-speed shaft, (3) gearbox mountings, (4) gearbox, (5) high-speed shaft with brake, (6) generator. The fabricated bedplate is also visible



Figure 6.32 Turbine assembly in the air (1): View of nacelle of 1.5 MW NEG Micon turbine after installation of low-speed shaft (front) and gearbox. The ring of bolt holes in the low-speed shaft for hub mounting is clearly visible. Source: Reproduced by permission of NEG Micon



Figure 6.33 Turbine assembly in the air (2): View of low-speed shaft and front bearing after installation on 1.5 MW NEG Micon turbine. Source: Reproduced by permission of NEG Micon

A much more compact arrangement can be obtained by bolting the generator rigidly onto the rear of the gearbox via an adaptor tube (see Figure 6.35). The surfaces of the mating interfaces have to be carefully machined to ensure shaft alignment, and suitable access has to be provided to the coupling between the generator and gearbox output shafts. Despite the neatness of this layout, it has only been adopted by one or two manufacturers.

One consequence of locating the generator in the nacelle is that power cables running down the tower are required to twist as the nacelle yaws. On some large machines, the problems associated with the twisting of heavy cables have been avoided by mounting the generator vertically in the top of the tower and driving the high-speed shaft via a bevel gear. An alternative solution to the problem of heavy twisting cables, however, is to leave the generator in the nacelle and to transform to a higher voltage there as well.

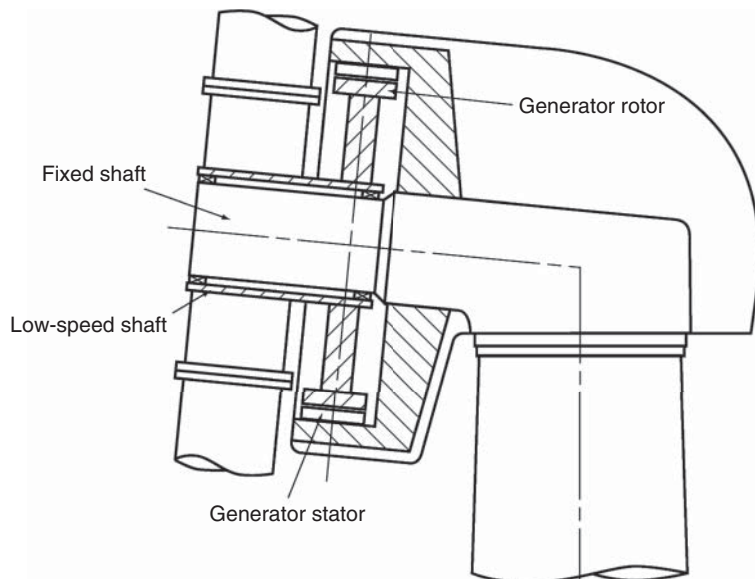


Figure 6.34 Direct drive generator arrangement

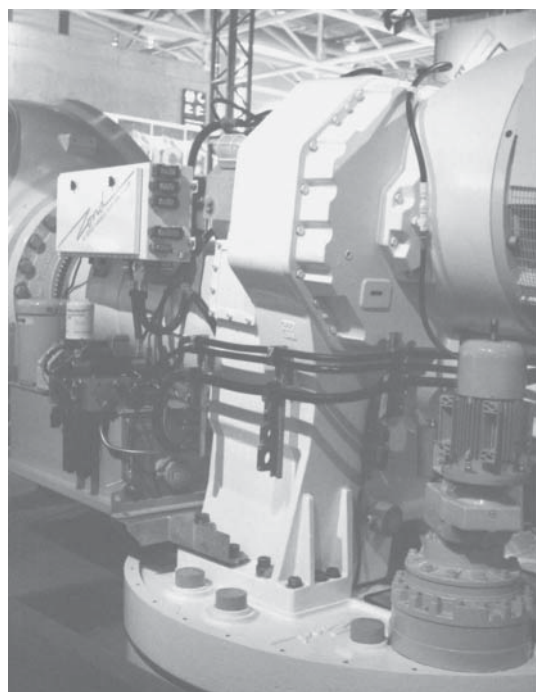


Figure 6.35 Integrated gearbox on the Zond Z-750 turbine. (The gearbox is mounted on a circular nacelle bedplate, with the hub to the left and generator at rear. An electrically driven yaw drive can be seen beneath the generator.)

6.12 Drive train compliance

The rotational dynamics of the drive train can have a major effect on loading. The effect is very different in fixed- and variable-speed turbines, but in each case the consequence of ignoring drive train dynamics at the design stage can be very severe.

In the variable-speed case, the dynamics may be quite simple: the drive train may be modelled as a rotor and a generator inertia, separated by a torsional spring. Typically, the natural frequency of this resonant system is quite high, of the order of 3–4 Hz. However, this mode is subject to very little damping, especially above rated where the generator torque is held constant. (Below rated the torque will be varied as a function of rotational speed, thus providing a small amount of damping.) There is very little aerodynamic damping from the rotor, and this mode of vibration can potentially generate very large gearbox torque oscillations. Chapter 8 explains how the control system can be used to damp this mode by appropriate control of the generator torque, but it is important to ensure that the resonant frequency does not coincide with a significant forcing frequency such as 6P, which can make it very difficult to achieve sufficient damping through the control system.

In the fixed-speed case, the directly coupled induction generator provides a lot of damping because the air-gap torque increases steeply with generator speed. The smaller the slip, the greater this damping. This might be expected to be beneficial, but in practice the reverse is likely to be true. Consider the drive train as a two degree of freedom system, with four elements in series: the rotor inertia, the shaft torsional spring, the generator inertia, and finally the damper representing the slip curve, connected to ground (the constant frequency grid). If the damping is very large, the generator can almost be considered to be locked (i.e. rotating at nearly constant speed), and the dynamics are dominated by the degree of freedom represented by the rotor inertia and the torsional spring, which has very little damping, as in the variable-speed case. With higher generator slip, the lower generator damping allows more movement of the generator inertia, causing more coupling between the two degrees of freedom. This gives a system in which there are two coupled torsional modes, each involving some movement of both rotor and generator inertias and involving both the spring and the damper. Effectively, the generator damping now affects both modes significantly: instead of a very lightly damped spring mode and a very heavily damped damper mode, we now have two modes with intermediate damping, so the peak dynamic magnification is much lower. Thus 0.5% rated generator slip can give a peak dynamic magnification of perhaps 2 to 5 at the resonant frequency, whereas with 2% slip the peak magnification may be no more than 1 to 1.5. The position of the peak with respect to blade passing frequency is critical – if the blade passing frequency is close to the peak, very large gearbox torque and electrical power oscillations will occur at this frequency, and it is very difficult to reduce these significantly using pitch control. Ideally the blade passing frequency should be well above the resonant frequency so that the dynamic amplification will be less than one, but it is not uncommon for power and torque oscillations at the blade passing frequency to be as large as $\pm 50\text{--}100\%$ of rated in high winds.

The use of a high slip generator greatly improves the situation, but there are two main drawbacks: Firstly, each 1% of slip corresponds to 1% of extra losses, which significantly reduces the energy yield below rated wind speed. Secondly, these extra losses equate with heat dissipation in the generator, making it more difficult to keep the generator cool, especially in large machines.

An alternative to high generator slip that has occasionally been used is a fluid coupling between the gearbox and the generator. This is also a device that generates a torque proportional to slip speed, and it suffers from the same drawbacks as a high slip generator.

Another technique that has sometimes been used is to reduce the resonant frequency by introducing additional torsional flexibility into the drive train. This can be done by means of a quill shaft, a flexible low-speed coupling, or flexible mounts for the gearbox or even for the whole bedplate. The frequency reduction is, however, accompanied by a further loss of damping, and it may therefore be necessary to incorporate additional mechanical damping with the torsional flexibility, which is not always easy to engineer. Torsional flexibility in the high-speed shaft is not usually practical because of the large angular movement required to achieve the necessary flexibility – half a revolution may be necessary, compared to just one or two degrees at the low-speed shaft. An interesting variant (Leithead and Rogers 1995) is to mount the generator on flexible mounts. This system can be tuned to absorb energy at the blade passing frequency through an additional mode of vibration of the generator casing against its mountings. This mode also affects the generator slip speed (the difference between rotor and casing speeds) and is therefore damped by the slip curve. Nevertheless, generator casing displacements would still need to be of the order of 10–15°, which is still not easy to engineer.

6.13 Rotor position with respect to tower

6.13.1 Upwind configuration

The upwind configuration is the one most commonly chosen. The principal advantage is that the tower shadow effect is much less for the same blade–tower spacing, reducing both dynamic loads on the blade and rhythmic noise effects. Set against this is the need to take great care to avoid the risk of blade–tower strikes with upwind machines, requiring accurate prediction of blade deflections under turbulent wind loading.

There are several ways of increasing the clearance between the undeflected blade and the tower. These include increasing the shaft tilt, inclining the blades forward ('rotor coning'), applying pre-bend to the outer portion of the blades, and increasing rotor overhang. However, it is desirable to keep the rotor overhang small to minimise low-speed shaft and nacelle bedplate bending moments, so the low-speed shaft is normally tilted upwards by 5° or 6° to provide the necessary blade–tower clearance, with rotor coning and/or pre-bend sometimes applied as well.

Inevitably the tilting of the rotor plane results in a small reduction in power output. According to the axial momentum theory for a yawed turbine (Section 4.2.1), the coefficient of performance is reduced by the factor $\cos^3\theta$, leading to a 1.1% reduction in power output for a 5° shaft tilt if the air flow is horizontal. However, the vortex cylinder theory (Section 4.2.3) predicts a smaller reduction of 0.6% for this case.

6.13.2 Downwind configuration

The wake velocity deficit behind a wind turbine tower is much greater than that in front of it, to the extent that Powles (1983) has reported a turbulent region with essentially

no forward velocity extending up to four tower diameters downstream of an octagonal tower. Beyond this distance, recovery is relatively rapid, with the deficit reduced to about 25% at seven tower diameters downstream.

In addition to the mean wind speed velocity deficit behind the tower, vortex shedding results in additional wind speed fluctuations over and above those already present due to turbulence. The two effects combine to present a harsh environment to the blades immediately behind the tower. The blades are subjected to a large negative impulsive load each time they pass the tower, which contributes significantly to blade fatigue damage, and the audible tower ‘thump’ that results is liable to be unwelcome. Designers usually mitigate both effects by positioning the rotor plane well clear of the tower, but this inevitably increases nacelle costs somewhat.

An important benefit of the downwind configuration is that it allows the use of very flexible blades without the risk of tower strike during normal operation. Such blades benefit by being less severely unloaded by the tower shadow, because wind loading deflects them farther from the tower in the first place. However, care must be taken to avoid the risk of tower strike during emergency braking, when the blades pitch rapidly to feather.

6.14 Tower stiffness

A key consideration in wind turbine design is the avoidance of resonant tower oscillations excited by rotor thrust fluctuations at rotational or blade passing frequency. The damping ratio may be only 2–3% for tower fore–aft oscillations and an order of magnitude less for side-to-side motion, so unacceptably large stresses and deflections could develop if the blade passing frequency or rotational frequency coincided with tower natural frequency. This section begins by looking at the relative magnitudes of some of the excitations.

6.14.1 Stochastic thrust loading at blade passing frequency

Whereas the deterministic variations in blade loading due to wind shear, yaw, etc. largely cancel out when the loadings on three blades are added together, the stochastic loadings due to turbulence do not, resulting in a significant rotor thrust load component at blade passing frequency. The magnitude of this quantity can be estimated fairly easily by assuming a linear relationship between fluctuations in the incident wind speed and the resultant load fluctuations according to Eq. (5.25).

For the example three bladed machine considered in Section 5.12.4, the total variance of rotor thrust is only about 20% less than it would be if the wind speed variations across the rotor were fully correlated. Thus, from Eq. (5.129):

$$\sigma_T = \left(\frac{1}{2} \rho \Omega \frac{dC_l}{d\alpha} \right) \sigma_u \oint cr dr (0.8) \quad (6.17)$$

where the integral sign \oint signifies that the integration is carried out over the whole rotor. Using the expression for the power spectrum of rotor thrust in Eq. (5.130), it can be shown that the variance of the thrust fluctuations within $\pm 10\%$ of blade passing frequency is about 1.4% of the total for the case considered. Although this is a small proportion (as can be seen from inspection of Figure 5.40), the standard deviation of thrust fluctuations in this frequency range is a much higher proportion of σ_T , i.e. $\sqrt{0.014} \cong 12\%$.

Denoting the standard deviation of thrust fluctuations within $\pm 10\%$ of blade passing frequency as $\sigma_{T,3p}$, we have

$$\sigma_{T,3p} \cong 0.1 \left(\frac{1}{2} \rho \Omega \frac{dC_l}{d\alpha} \right) \sigma_u \oint cr dr \quad (6.18)$$

How does this compare with the maximum steady operational thrust load? Considering a pitch-regulated machine operating at rated wind speed, the rotor thrust is approximately

$$T = \frac{1}{2} \rho \Omega^2 \oint C_l(r) cr^2 dr$$

and its maximum steady value can be estimated by setting $C_l(r)$ equal to 1.5, giving

$$T_{Max} = \frac{1}{2} \rho \Omega^2 1.5 \oint cr^2 dr \quad (6.19)$$

Hence the ratio of thrust fluctuations within $\pm 10\%$ of blade passing frequency to the maximum steady thrust is

$$\frac{\sigma_{T,3p}}{T_{Max}} \cong \frac{0.1 \left(\frac{1}{2} \rho \Omega \frac{dC_l}{d\alpha} \right) \sigma_u \oint cr dr}{\frac{1}{2} \rho \Omega^2 1.5 \oint cr^2 dr} = \frac{0.1 \left(\frac{dC_l}{d\alpha} \right) \sigma_u \oint cr dr}{1.5 \Omega \oint cr^2 dr} \quad (6.20)$$

Setting $\frac{dC_l}{d\alpha}$ equal to 2π , and noting that $\frac{\oint cr^2 dr}{\oint cr dr}$ is approximately equal to $0.6R$, one obtains

$$\frac{\sigma_{T,3p}}{T_{Max}} \cong \frac{0.1(2\pi)\sigma_u}{1.5\Omega(0.6R)} \cong 0.7 \frac{\sigma_u}{\Omega R} \quad (6.21)$$

If the standard deviation of turbulence, σ_u , is 1.8 m/s and the tip speed is 65 m/s, the moment ratio approximates to 0.02.

Noting that the damage equivalent fatigue stress range for a material with an $S-N$ curve log-log plot inverse slope of $m = 4$ is 3.36 times the standard deviation of stress for a narrow banded process [see Eq. (12.71) in Chapter 12], it is seen that, in relation to the design of the tower against fatigue, the DEL range of the thrust fluctuations close to blade passing frequency is about 6.5% of the maximum thrust in the case considered.

6.14.2 Tower top moment fluctuations due to blade pitch errors

Unintended differences between the pitches of the three blades will cause a permanent difference in the blade root moments M_{Y1} , M_{Y2} , and M_{Y3} (see Figure 5.36), which will translate into a rotating moment applied to the nacelle. This in turn will impose a sinusoidal M_Y moment on the tower top at the rotational frequency.

Consider a turbine with blade pitch errors of $\Delta\theta$, $-\Delta\theta$ and zero on blades 1, 2, and 3. The angle of attack is reduced by $\Delta\theta$ on blade 1, changing the blade root moment by

$$\Delta M_{Y1} = \frac{1}{2} \rho \Omega^2 \frac{dC_l}{d\alpha} \{-\Delta\theta\} \int_0^R cr^3 dr \quad (6.22)$$

The fluctuating tower top moment reaches its maximum and minimum when blades 1 and 2 are at 30° to the vertical and its amplitude is

$$\Delta M_Y = \frac{1}{2} \rho \Omega^2 \cdot 2\pi \{\Delta\theta\} \int_0^R cr^3 dr (2 \cos 30^\circ) \quad (6.23)$$

It is instructive to compare this moment with the average value in the tower due to the maximum steady thrust. At a depth of R below the hub, the moment ratio is

$$\frac{\Delta M_Y}{T_{Max} R} = \frac{\frac{1}{2} \rho \Omega^2 \cdot 2\pi \{\Delta\theta\} \int_0^R cr^3 dr (\sqrt{3})}{\frac{1}{2} \rho \Omega^2 1.5 \oint cr^2 dr R} \cong \frac{2\pi \{\Delta\theta\} 0.7 (\sqrt{3})}{1.5(3)} \cong 1.7 \{\Delta\theta\} \quad (6.24)$$

as $\frac{\int_0^R cr^3 dr}{\oint cr^2 dr}$ is approximately equal to $0.7R/3$.

The moment ratio equates to 0.9% if the default blade pitch error of 0.3° specified in the 2003 edition of the GL ‘Guideline for the Certification of Wind Turbines’ (Germanischer Lloyd 2003) is used. Thus the moment *range* at rotational frequency due to this blade pitch error is about 1.8% of that due to rated thrust at a depth R below the hub – i.e. significantly less than the damage equivalent moment range at this location due to stochastic thrust loading at blade passing frequency of about 6.5%.

6.14.3 Tower top moment fluctuations due to rotor mass imbalance

Unintended differences between the masses of the three blades will result in a sinusoidal gravitational moment about the low-speed shaft axis, which will be transmitted to the tower. While IEC 61400-1 edition 3 and the 2003 edition of the GL ‘Guideline for the Certification of Wind Turbines’ stipulate that the rotor mass imbalance taken into account should be based on the manufacturer’s specification, the 1999 edition of the latter specified a rotor mass eccentricity of 0.005R in the case of a ‘balanced’ rotor, which will be considered here.

In the case of an 80 m diameter turbine, the blade mass is typically about 7.5 t, so, taking the hub mass equal to that of three blades, the total rotor mass comes to 45 t. With an eccentricity of $0.005 \times 40 = 0.2$ m, the tower top side-to-side moment *range* comes to about 180 kNm.

As before, it is instructive to compare this moment with the average value in the tower due to the maximum steady thrust. Taking the latter as 250 kN (Figure 5.39), the moment in the tower at a depth of R below the hub is 10 000 kNm. Hence the tower moment *range* at rotational frequency due to rotor mass imbalance is about 1.8% of that due to rated thrust at a depth R below the hub.

Based on the above, it would appear that the impact of mass imbalance is much the same as that of blade pitch error for the mass eccentricity and pitch error considered. However, when dynamic magnification is taken into account, the effects of mass imbalance are potentially much more damaging, because the damping ratio for side-to-side tower oscillations may be an order of magnitude less than for fore-aft oscillations. This is because aerodynamic damping makes a negligible contribution to the damping of side-to-side motion.

6.14.4 Tower stiffness categories

Wind turbine towers are customarily categorised according to the relationship between the tower natural frequency and the exciting frequencies. Towers with a natural frequency greater than the blade passing frequency are said to be stiff, while those with a natural frequency lying between rotational frequency and blade passing frequency are said to be soft. If the natural frequency is less than rotational frequency, the tower is described as soft-soft.

If the tower is designed to meet strength requirements and no more, its frequency category is primarily determined by the ratio of tower height to turbine diameter, with the higher ratios producing the softer towers. The principal benefits of stiff towers are modest – they allow the turbine to run up to speed without passing through resonance and tend to radiate less sound. However, because stiff towers usually require the provision of extra material not otherwise required for strength, soft towers are generally preferred.

6.15 Multiple rotor structures

As noted in Section 6.2.2, technological improvements in blade manufacture and design have allowed the adverse effects of the square-cube law (whereby energy capture increases with the square of diameter and component weights increase as the cube) to be largely circumvented as diameters have increased. Given that large diameter machines permit the more effective exploitation of onshore sites of limited area (Section 6.2.5), significant cost savings ought to be realisable without loss of energy capture if a large diameter turbine is replaced by a closely spaced array of much smaller diameter turbines that provide the same swept area in total and are all mounted on the same structure. This proposition will be examined in this section.

The key to the multiple rotor concept is the design of an efficient structure to support the rotor array. This is assumed to consist of a planar structure that yaws to face the wind, mounted on a yaw bearing at the top of a conventional tower.

Consider 19 rotors, each 28.9 m in diameter and rated at 263 kW, arranged in a hexagonal array at 30 m spacing. These would have the same swept area as the NREL 5 MW reference turbine (Jonkman et al. [2009]), so the hexagonal array could be supported on the same yaw bearing and tower. It is assumed that the maximum combined steady thrust for the 19 rotors is the same as for the NREL reference turbine – i.e. about 800 kN (although in practice the thrust would be higher, as would be the energy capture, because of the close rotor spacing – see Section 6.15.6).

6.15.1 Space frame support structure

A lattice space frame would be an obvious candidate structure to support the array, which could be centrally mounted on a yaw bearing at the top of a tubular tower. It could take the form of two vertical planar parallel lattices about 26 m apart and connected by ‘web’ members, with 19 nodes in the front lattice each supporting a rotor. Chord members would be aligned at 0, +60, and – 60° to the horizontal. See Figure 6.36.

However, buckling considerations would seriously limit permissible stresses with a 30 m node spacing, so it would be desirable to reduce both the chord member spacing

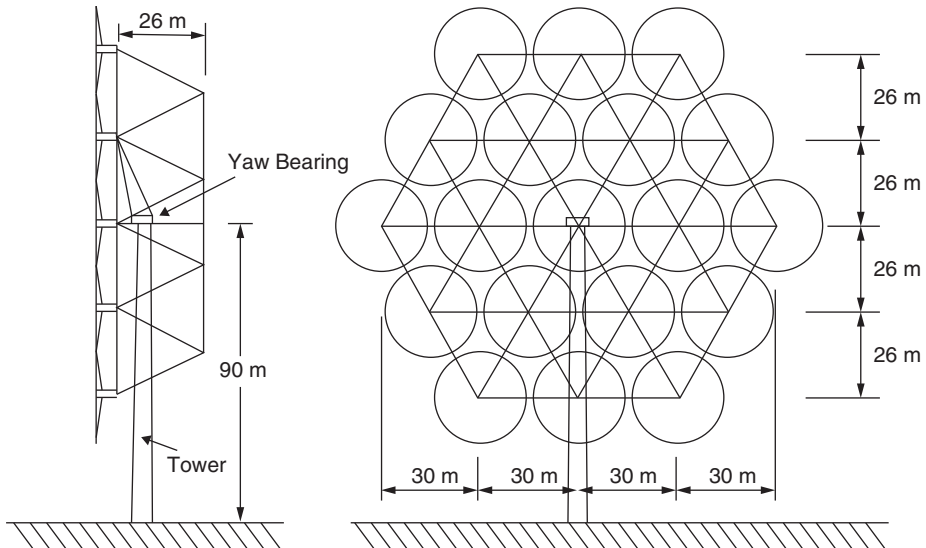


Figure 6.36 Nineteen rotors spaced at 30 m mounted on a space frame structure

and the separation distance between the two planar lattices. If the lattice node spacings and web member lengths are both reduced to 10 m, then nearly all members can be 168 mm dia \times 5 mm \times 20.14 kg/m thick circular hollow sections, although stresses still have to be limited to about 45 MPa under the maximum thrust loading to provide adequate resistance to buckling. This compares with a tower base stress of about 74 MPa at the base of the NREL 5 MW turbine due to the maximum steady thrust loading. Unfortunately, lighter members cannot be used for the more lightly loaded peripheral members, as 5 mm is the minimum wall thickness for 168 mm dia circular hollow sections.

The weight of a 120 m diameter \times 8.66 m thick space frame consisting of 168 mm dia \times 5 mm thick circular hollow sections at a 10 m pitch in each direction is approximately $3600(\pi/10)(3 \times 4)20.14$ kg or 273 t. This does not seem excessive, as it is less than the weight of the tower that would support it – i.e. 347 t, based on the weight of the tower required to support the 126 m diameter NREL 5 MW turbine (Jonkman et al. [2009]). However, there are several serious objections to the concept:

- The complexity of the structure would result in a significantly higher fabrication cost per tonne.
- The space frame would be far too large to be transported to site in one piece, so extensive site welding would be required.
- The space frame would be awkward to erect.
- The space frame would not provide personnel access to the individual turbines, and any access provided would be exposed to the weather.

6.15.2 Tubular cantilever arm support structure

Given the disadvantages of the space frame listed previously, it is worth exploring a simpler support structure for the rotor array, even at the cost of reduced structural efficiency. One candidate is a series of horizontal tubular arms mounted on a central tubular stem, the lower half of which would necessarily surround the top portion of the fixed tower, with the yaw bearing forming the interface between them. The cantilever arms would act in flexure to resist both gravity and aerodynamic thrust loadings and could taper down in both diameter and thickness towards the free ends.

An outline design of such a structure to support 19 28.9 m diameter rotors has been carried out on the assumption that the stress due to the maximum steady thrust loading should nowhere exceed 74 MPa, the corresponding value obtaining at the base of the NREL 5 MW turbine – see Figure 6.37. This should ensure that the fatigue stresses are satisfactory. Based on the mass formulae in the NREL cost model, the weight of a 28.9 m turbine is similar in magnitude to the maximum thrust loading, but the fatigue element of the latter means that it drives the design. Assuming that the tubulars have a D/t ratio of 100 to avoid a significant strength reduction due to buckling, it is found that the longest arm is required to have a diameter of 1.95 m at its inner end and that the combined weight of all 10 arms and the integral stem is 292 t.

6.15.3 Vestas four-rotor array

Vestas have constructed a multi-rotor concept demonstrator utilising four reconditioned 29 m diameter 225 kW machines built prior to 1997. These are mounted at two levels on arms extending either side of a central tower. The arms are tilted up at an angle of about 17° and are effectively inclined struts with the free ends restrained by horizontal

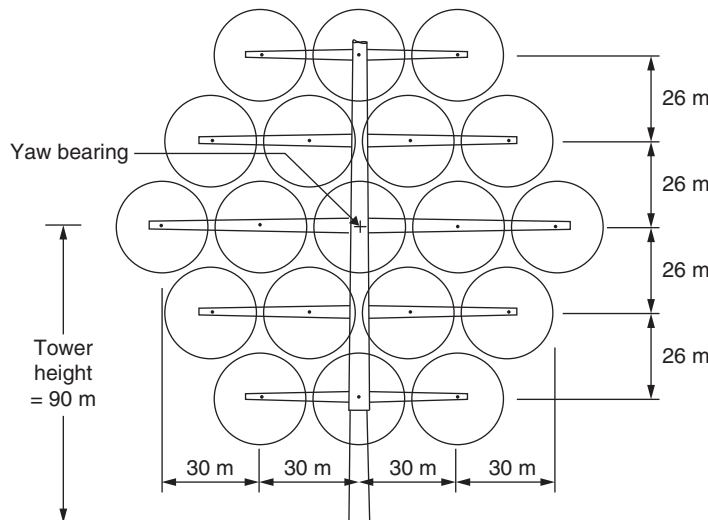


Figure 6.37 Nineteen rotors spaced at 30 m mounted on a tubular ‘tree’ structure

ties attached to a central, yawing chassis. This is a structurally more efficient arrangement than the cantilever arms acting in flexure considered in Section 6.15.2.

The four-rotor demonstrator, which was completed in 2016, is heavily instrumented to permit the dynamics of the structure to be investigated, including in the event of one of the rotors tripping out.

6.15.4 Cost comparison based on fundamental scaling rules

The costs of a 126 m diameter turbine and a 19 rotor installation providing the same swept area can be compared according to various cost models. In the first instance, it is assumed that the masses of all components apart from the generator, variable-speed electronics, electrical connections, and control system scale as the cube of diameter and that component costs are proportional to mass. The control system cost is assumed invariant with diameter, and the costs of the other three components are assumed to scale as machine rating – i.e. as the square of diameter. The base costs are those for the 70 m diameter NREL turbine given in Table 6.2, resulting in the scaled costs shown in Table 6.10. Note that the costs of the yaw drive and tower for the 19 rotor installation are assumed to be the same as for the 126 m diameter turbine, and foundation, assembly and installation, transportation, and grid connection costs are excluded from consideration. It is seen that there is a cost saving of 29%.

6.15.5 Cost comparison based on NREL scaling indices

According to the NREL cost model (Section 6.2.3), some key cost elements, such as the blade manufacture labour cost, main bearing costs, and gearbox cost, vary as the diameter raised to the power of 2.5 instead of the cube, while others, such as the nacelle, brake, and hydraulics cost only vary as the square. The base costs of the 70 m diameter

Table 6.10 Cost comparison between a 126 m diameter turbine and an array of 19 turbines having the same total swept area, using fundamental mass scaling rules and assuming component cost to be proportional to mass

Diameter, D (m)	70	126	28.906	28.906	% saving
Number of rotors	1	1	1	19	
Component costs varying as D cubed (\$k)	561	3269	39.5	750	
Component costs varying as D squared (\$k)	276	894	47.1	894	
Control system cost (\$k)	35	35	35	665	
Yaw drive cost (\$k)	20	116		116	
Tower cost (\$k)	113	656		656	
Array support structure cost (\$k)	0	0		439	
Sum (\$k)	1004	4971		3521	29.2

Table 6.11 Cost comparison between a 126 m diameter turbine and an array of 19 turbines having the same total swept area, using the cost scaling indices in the NREL cost model

Diameter (m)	70			126	28.906	28.906
No. of rotors	1	Costs \$k	%	Power law scaling indices	1	19
Blades - materials	68	6.8	3	396	5	91
Blades - labour	84	8.3	2.5	363	9	174
Hub and nose cone	47	4.7	2.92	262	4	68
Pitch mechanism	38	3.8	2.66	184	4	70
Low-speed shaft	21	2.1	2.89	116	2	31
Main bearings	12	1.2	2.5	52	1	25
Gearbox	153	15.2	2.5	663	17	318
Generator	98	9.7	2	316	17	316
Variable-speed electronics	119	11.8	2	384	20	384
Nacelle frame and cover	117	11.6	1.95	367	21	396
Electrical connections	60	6	2	194	10	194
Hydraulics	18	1.8	2	58	3	58
Control system	35	3.5	0	35	35	665
Brake and high-speed coupling	3	0.3	2	10	1	10
Tower	113	11.2	3	656	0	656
Yaw drive	20	2	2.96	114	0	114
Array support structure						438
Totals	1004	100		4171	0	4007

NREL turbine given in Table 6.2 have been scaled using the NREL cost model power law indices in Table 6.11. (This omits the effect of any fixed cost elements because these are considered liable to cause misleading results at the small diameter of 28.9 m.)

It is seen that the effect of using the lower scaling power law indices is to reduce the cost saving predicted for the multiple rotor array to only 4%.

6.15.6 Discussion

It is clear from the range of results from the two capital cost comparisons above that the benefit of multiple rotor arrays is uncertain. To provide greater certainty, the way forward would necessarily involve the design and construction of a small diameter turbine that takes advantage of all technological advances in blade manufacture and drive systems since turbines of this size were deployed in large numbers.

The cost of maintenance also needs to be considered. Set against the potential benefit of being able to swap out a whole turbine if required is the likely increase in the time required for the routine maintenance of many small machines as opposed to one large one. Provision of safe access routes to all of the nacelles will also carry an extra cost.

The feasibility of the multi-rotor concept was investigated in greater detail as part of the INNWIND project (INNWIND [2015b]). This extended to loading, energy capture, yaw bearing configuration and operation and maintenance as well as the supporting structure. A key finding was that closely spaced rotors (at $1.025D$ or $1.05D$) would achieve 8% greater energy capture at the cost of an 8% increase in thrust. It was also concluded that individual small rotors would be better at tracking short-term wind speed changes due to turbulence, yielding a further gain in energy capture of a few percent.

Jamieson (2018) provides a useful overview of multi-rotor concepts and their benefits.

6.16 Augmented flow

The performance of a wind turbine can be enhanced by placing it inside a duct (or ‘diffuser’) shaped in such a way as to augment the air velocity within it. Although it is sometimes claimed that rotor coefficient of performance can be increased by the cube of the speed-up factor, the pressure drop across the rotor is unchanged when it operates at optimum C_P , so the increase in C_P is simply proportional to the speed-up factor.

Jamieson (2018) has developed the theory of augmented flow and diffuser loading and describes some of the designs that have been developed – e.g. the 5 kW wind lens ducted turbine (Ohya and Karasudani [2010]), which has been upscaled to 100 kW. Inevitably the success of the concept in the future depends on whether the cost of the diffuser and its support structure can be reduced below the value of the extra energy captured.

6.17 Personnel safety and access issues

An integral part of wind turbine design is the inclusion of the necessary safety equipment for operation and maintenance staff. Minimum requirements include the following:

- Provision of ‘emergency stop’ push buttons located at key locations in the tower, nacelle, and hub to enable personnel to stop the turbine and its systems operating in the event of an emergency.
- Provision of a ‘remote/local’ switch placed at the bottom of each tower. This enables a technician to take full control of the turbine when entering to carry out maintenance by changing the switch to the ‘local’ position. This eliminates the risk of a third party trying to command the turbine to restart remotely.
- Provision of a fall-arrest system on the tower ladder(s). This consists of a fall arrester that slides on either a steel cable running the full length of the ladder in the middle or on a rigid rail bolted to the ladder in sections. In normal use the fall arrester is pulled up or lowered down by the anchor line attached to the climber. The tension in this anchor line releases a clamp, which locks onto the cable or rail again in the event of a fall.

- Provision of intermediate landings or smaller rest platforms in the tower to allow personnel to rest while climbing.
- An alternative means of egress from the nacelle, for use in case of fire in the tower. This can take the form of an inertia reel device, enabling personnel to lower themselves through a hatch in the nacelle floor.
- Locking devices for immobilising the rotor and the yawing mechanism. Rotor brakes and yaw brakes are not considered sufficient, because of the risk of accidental release and the occasional need to deactivate them for maintenance purposes. Ideally, the rotor locking device should act on the low-speed shaft, so that its effectiveness is not dependent on the integrity of the gearbox. However, it is usually physically easier to engage a rotor lock acting on the high-speed shaft. Typically, the device consists of a pin mounted in a fixed housing, which can be engaged in a hole in a shaft-mounted disc.
- Guards to shield any rotating parts within the nacelle.
- Suitable fixtures for the attachment of safety harnesses for personnel working outside the nacelle.

Careful attention needs to be paid to the route between the tower top and nacelle to avoid hazards arising from sudden yawing movements. Some modern turbines have safety systems in place that only allow access to the nacelle in the event that the turbine has been shut down.

The designer needs to assess the requirement for all-weather access to the nacelle at an early stage. Lattice towers afford no protection from the weather when climbing, so the number of days on which access for maintenance is possible will be restricted. Similar restrictions will arise if the nacelle cover has to be opened to the elements to provide space for personnel to enter. Consideration also needs to be given to the means of raising and lowering tools and spares. If the interior of the tower is interrupted by intermediate platforms, these operations have to be performed outside, with consequent weather limitations. Many wind turbines are equipped with lifting hoists and/or cranes for this purpose.

With the increase of turbine diameters and, consequently, of tower heights, unassisted climbing of towers is becoming a physically demanding activity. Accordingly, EN 50308:2004, *Wind Turbines – Protective Measures – Requirements for Design, Operation, and Maintenance*, stipulates lifts as the preferred method of turbine access as opposed to ladders. However, the reduced diameter at the top of tapering towers usually means it is impracticable for a lift to extend right to the top of the tower, and, in any case, a significant number of ladder climbs are still required during lift installation and maintenance. In larger turbines, generally over 60 m hub height, the provision of lifts is a legislative requirement in some countries with a ladder only used in the event of an emergency.

An alternative approach to reducing the physical demands on maintenance personnel is the use of a climb assist device, whereby a cable attached to a powered hoist bears a significant proportion of the climber's bodyweight during ascent.

A TUV/NEL report (2007) provides a useful review of turbine access options.

Standard rules for electrical safety apply to all electrical equipment. However, particular care must be taken with the routing of electrical cables between tower and nacelle

to avoid potential damage due to chafing when they twist. If the power transformer is located in the tower base or nacelle instead of in a separate enclosure at ground level, it should be partitioned off to minimise the fire risk to personnel.

References

- Abrahamsen, A.B., Magnusson, N., Jensen, B.B., and Rund, M. (2012). Large superconducting wind turbine generators. *Energy Procedia*. 24: 60–67.
- Anaya-Lara, O., Jenkins, N., Ekanayake, J. et al. (2009). *Wind Energy Generation, Modelling and Control*. Chichester: Wiley.
- Anderson, C. (2020). *Wind Turbines: Theory and Practice*. Cambridge University Press.
- Armstrong, J.R.C. and Hancock, M. (1991). Feasibility study of teetered, stall-regulated rotors. *ETSU Report No. WN 6022*.
- Attallah, K. and Howe, D. (2001). A novel high performance magnetic gear. *IEEE Trans. Magn.* 37 (4): 2844–2847;
- Attallah, K., Rens, J., Mezani, S., and Howe, D. (2008). A novel pseudo direct-drive brushless permanent magnet machine. *IEEE Trans. Magn.* 44 (11): 2195–2198.
- Bak, C., Zahle F., Bitsche R., et al (2013). Description of the DTU 10 MW reference wind turbine. *DTU Wind Energy Report I-0092*.
- Blaabjerg, F. and Ma, K. (2013). Future of power electronics for wind turbine systems. *IEEE J. Emerg. Sel. Top. P. 1* (3): 139–152.
- Coiate, D. et al. (1989). Gamma 60 1.5 MW wind turbine generator. In: *Proceedings of the European Wind Energy Conference, Glasgow*, 1027–1032.
- Corbet, D.C. and Morgan, C.A. (1991). Passive control of horizontal axis wind turbines. In: *Proc. 13th BWEA Annual Conference*, 131–136. Swansea: Mechanical Engineering Publications.
- Dahlgren, M., Frank, H., Leujon, M. et al. (2000). Windformer: Wind power goes large scale. *ABB Review* 3: 31–37.
- Derrick, A. (1992). Aerodynamic characteristics of novel tip brakes and control devices for HAWTs. In: *Proc. 14th BWEA Annual Conference*, 73–78. Nottingham: Mechanical Engineering Publications.
- Dykes, K et al (2014). Effect of tip-speed constraints on the optimized design of a wind turbine. *NREL Technical Report NREL/TP-5000-61726*.
- EN 50308:2004 (2004). *Wind turbines – Protective measures – Requirements for design, operation, and maintenance*. Brussels: CENELEC.
- Engstrom et al (1997). Evaluation of the Nordic 1000 prototype. Proceedings of the European Wind Energy Conference, Dublin, pp. 213–216.
- European Wind Energy Association (2009). *Wind Energy – The Facts*. London: Earthscan.
- Falchetta et al (1996). Structural behaviour of the Gamma 60 prototype. Proceedings of the European Union Wind Energy Conference, Göteborg, pp. 269–271.
- Fingersh, L., Hand, M., and Laxson, A. (2006). Wind turbine design cost and scaling model. *NREL Technical Report NREL/TP-500-40566*.
- Fuglsang P and Thomsen K (1998). Cost optimisation of wind turbines for large-scale offshore wind farms. *Risø National Laboratory Report No. R-1000*.
- Germanischer Lloyd. (2003). *Rules and guidelines: IV – Industrial services: Part 1 – Guideline for the certification of wind turbines*.
- Gjerde, S., Ljøkelsøy, K., Nilsen, R., and Undeland, T. (2014). A modular series connected converter structure suitable for a high-voltage direct current transformerless offshore wind turbine. *Wind Eng.* 17: 1855–1874.
- Hau, E. (2013). *Wind Turbines: Fundamentals, Technologies, Application, Economics*, 3e. Heidelberg: Springer.

- Hindmarsh, J. (1984). *Electrical Machines and Their Applications*. London: Butterworth Heinemann.
- IEC EN 61400-27-1 (2015). *Wind turbines: Part 27-1: Electrical simulation models*. Geneva, Switzerland: International Electrotechnical Commission.
- INNWIND (2013). New aerodynamics rotor concepts specifically for very large offshore wind turbines. *Deliverable 2.11* by Chavariopoulos, T. et al. www.innwind.eu.
- INNWIND (2015a). New airfoils for high rotational speed wind turbines. *Deliverable 2.12* by Boorsma, K. et al.
- INNWIND (2015b). Innovative turbine concepts –Multi-rotor system. *Deliverable 2.33* by Jamieson, P. et al. www.innwind.eu.
- INNWIND (2016). Costs-models-v1-02-1 Mar 2016-10MW-RWT.xls. www.innwind.eu.
- INNWIND (2018). Innwind EU Project. *Deliverable 3.44*. <http://www.innwind.eu/publications> (accessed 26 March 2020).
- Jamieson, P. (2009). Light-weight, high-speed rotors for offshore. Proceedings of the European Offshore Wind Conference, Stockholm, pp. 1026 – 1036.
- Jamieson, P. (2018). *Innovation in Wind Turbine Design 2nd Edition*. Chichester: Wiley.
- Jamieson, P. and Agius (1990). A comparison of aerodynamic devices for control and overspeed protection of HAWTs. In: *Proc. 12th BWEA Annual Conference*, 205–213. Norwich: Mechanical Engineering Publications.
- Jamieson, P. and Brown, C.J. (1992). The optimisation of stall regulated rotor design. In: *Proc. 14th BWEA Annual Conference*, 79–84. Nottingham: Mechanical Engineering Publications.
- Jensen, B.B., Mijatovic, N., and Abrahamsen, A.B. (2012). Development of superconducting wind turbine generators. Proceedings of the EWEA 2012. https://backend.orbit.dtu.dk/ws/portalfiles/portal/7894274/Development_of_Superconducting_Wind_Turbine_Generators.pdf (accessed 10 April 2020).
- Jonkman, J., Butterfield, S., Musial, W., and Scott, G. (2009). Definition of a 5-MW reference wind turbine for offshore system development. *NREL Technical Report NREL/TP-500-38060*.
- Joose, P.A. and Kraan, I. (1997). Development of a tentortube for blade tip mechanisms. European Wind Energy Conference, Dublin, pp. 638–641.
- Law, H., Doubt, H.A., and Cooper, B.J. (1984). Power control systems for the Orkney wind turbine generators. *GEC Engineering, No 2*.
- Leithead, W.E. and Rogers, M.C. (1995). Improving damping by a simple modification to the drive train. In: *Proc. 17th BWEA Annual Conference*. Warwick: Mechanical Engineering Publications.
- McPherson, G. (1990). *An Introduction to Electrical Machines and Transformers*, 2e. New York: Wiley.
- Moore, S.K. (2018). The troubled quest for the superconducting wind turbine. *IEEE Spectrum*, 26 July 2018. <https://spectrum.ieee.org/green-tech/wind/the-troubled-quest-for-the-superconducting-wind-turbine> (accessed 27 March 2020).
- Morgan, C. (1994). The prospects for single-bladed horizontal axis wind turbines. *ETSU Report No. W/45/00232/REP*.
- Mueller, M. and Polinder, H. (eds.) (2013). *Electrical Drives for Direct Drive Renewable Energy Generators*. Cambridge: Woodhead Publishing Ltd.
- Ohya, Y. and Karasudani, T. (2010). A shrouded wind turbine generating high output power with wind-lens technology. *Energies* 2010 (3): 634–649. <https://doi.org/10.3390/en3040634>.
- Pengfei, L. and Wang, W. (2011). Principle, structure and application of advanced hydrodynamic converted variable speed planetary gear (Vorecon and Winddrive) for industrial drive and wind power transmission. Proceedings of 2011 International Conference on Fluid Power and Mechatronics, Beijing, pp. 839–843.
- Petersen, J.T., Madsen, H.A., Bkörk, A., Enevoldsen, P., Øye, S., Ganander, H., and Winkelaar, D. (1998). Prediction of dynamic loads and induced vibrations in stall. *Riso National Laboratory Report No. R-1045*.

- Polinder, H., van der Piji, F.F.A., de Vilder, G.J., and Tavner, P. (2006). Comparison of direct drive and geared generator concepts for wind turbines. *IEEE Trans. Energy Convers.* 21: 725–733.
- Powles, S.J.R. (1983). The effects of tower shadow on the dynamics of horizontal axis wind turbines. *Wind Eng.* 7 (1): 26–42.
- Rawlinson-Smith RI (1994). Investigation of the teeter stability of stalled rotors. *ETSU Report No. W.43/00256/REP*.
- Saad-Saoud, Z. and Jenkins, N. (1999). Models for predicting flicker induced by large wind turbines. *IEEE Trans. Energy Convers.* 14 (3): 743–748.
- Serrano-González, J. and Lacal-Arántegui, R. (2016). Technological evolution of onshore wind turbines - a market-based analysis. *Wind Eng.* 19: 2171–2187.
- Spera, D.A. (1994). *Wind Turbine Technology*. New York: ASME Press.
- Strous, T.D., Polinder, H., and Ferreira, J.A. (2017). Brushless doubly-fed induction machines for wind turbines: Developments and research challenges. *IET Electr. Power Appl.* 11 (6): 991–1000.
- TUV NEL Ltd (East Kilbride) and Risktec (2007). Safe wind turbine access: A decision making framework. *Report No. 2007/219*.
- Veilleux, E. and Lehn, P.W. (2014). Interconnection of direct-drive wind turbines using a series-connected DC grid. *IEEE Trans. Sustain. Energy* (5, 1): 139–147.
- Wang, R. and Gerber, S. (2014). Magnetically geared wind generator technologies: opportunities and challenges. *Appl. Eng.* 136: 817–826.
- Watson, S., Moro, A., Reis, V. et al. (2019). Future emerging technologies in the wind power sector: a European perspective. *Renew. Sust. Eng. Rev.* 113: 109270.
- Winkler, T. (2019). The EcoSwing Project. <https://iopscience.iop.org/article/10.1088/1757-899X/502/1/012004> (accessed 26 March 2020).

7

Component design

7.1 Blades

7.1.1 Introduction

A successful blade design must satisfy a wide range of objectives, some of which are in conflict. These objectives can be summarised as follows:

1. Maximise annual energy yield for the specified wind speed distribution.
2. Limit maximum power output (in the case of stall-regulated machines).
3. Resist extreme and fatigue loads.
4. Restrict tip deflections to avoid blade/tower collisions (in the case of upwind machines).
5. Avoid resonances.
6. Minimise weight and cost.

The design process can be divided into two stages: the aerodynamic design, in which objectives 1 and 2 are satisfied, and the structural design. The aerodynamic design addresses the selection of the optimum geometry of the blade *external* surface – normally simply referred to as the *blade geometry* – which is defined by the aerofoil family and the chord, twist, and thickness distributions. The structural design consists of blade material selection and the determination of a structural cross-section or *spar* within the external envelope that meets objectives 4–6. Inevitably, there is interaction between the two stages, as the blade thickness needs to be large enough to accommodate a spar that is structurally efficient in resisting flapwise bending.

The focus of Section 7.1 is on blade structural design. After a brief consideration of the aerodynamic design in Section 7.1.2, practical constraints on the optimum design are noted in Section 7.1.3 and the key structural design criteria summarised in Section 7.1.4. Section 7.1.5 surveys different blade structure options, and an overview of the properties

of some potential blade materials is given in Section 7.1.6. The static and fatigue properties of glass fibre reinforced plastic (GFRP), which is now used in the overwhelming majority of blades, are described in more detail in Sections 7.1.7 and 7.1.8, while the properties of carbon fibre and laminated wood are surveyed in Sections 7.1.9 and 7.1.10. Section 7.1.11 provides an introduction to the different categories of material safety factors that are applied in blade design.

Blade shell assembly is inevitably a complex procedure, so manufacturing methods are discussed in Section 7.1.12.

Governing load cases are considered in Sections 7.1.13 with reference to both stall- and pitch-regulated machines, and the steps involved in the design of a large blade against fatigue loading are illustrated by means of an example in Section 7.1.14. Section 7.1.15 explores blade susceptibility to vibrations in stall.

Rotor thrust loading puts the suction side of the blade spar into compression, resulting in potential buckling, so design against buckling is considered in Section 7.1.16.

Sections 7.1.17–7.1.19 describe blade root fixings, blade testing, and the phenomenon of leading edge erosion, respectively, while the final section (7.1.20) investigates the potential of blade twist coupling to alleviate blade loadings.

7.1.2 Aerodynamic design

The aerodynamic design encompasses the selection of aerofoil family and optimisation of the chord and twist distributions. The variation of thickness to chord ratio along the blade also has to be considered, but this ratio is usually set at the minimum value permitted by structural design considerations, as this minimises drag losses.

An indication of the complexity of blade geometry is provided by Figure 7.1, which shows the blade outline at a series of cross-sections along the blade length for a particular design. The progressive reduction in twist from a maximum at the cross-section with maximum chord to close to zero at the tip is clearly visible.

A survey of aerofoil families designed for wind turbine use is given in Section 3.17.

The process for optimising the blade design of machines operating at a fixed tip speed ratio is described in Section 3.7.2, where analytical expressions for the blade geometry parameter,

$$\sigma_r \lambda \mu C_l = \frac{Bc(\mu)}{2\pi R} \lambda C_l$$

and the local inflow angle, ϕ , are derived as a function of the local tip speed ratio, $\lambda \mu = \lambda r/R$ [Eqs. (3.72) and (3.74)]. If $\lambda \mu > > 1$, the expressions can be approximated by

$$\sigma_r \lambda \mu C_l = \frac{Bc(\mu)}{2\pi R} \lambda C_l = \frac{8}{9\lambda\mu} \text{ and } \phi = \frac{2}{3\lambda\mu} \quad (7.1)$$

If it is decided to maintain the angle of attack, α , and hence the lift coefficient, C_l , constant along the blade, then these relations translate to

$$c(\mu) = \frac{16\pi R}{9C_l B\lambda^2} \cdot \frac{1}{\mu} \text{ and } \beta = \frac{2}{3\lambda\mu} - \alpha \quad (7.2)$$

so that both the chord and twist, β , are inversely proportional to radius.

In the case of machines operating at constant rotational speed, and hence at varying tip speed ratio, no parallel analytical solution for the optimum blade geometry exists.

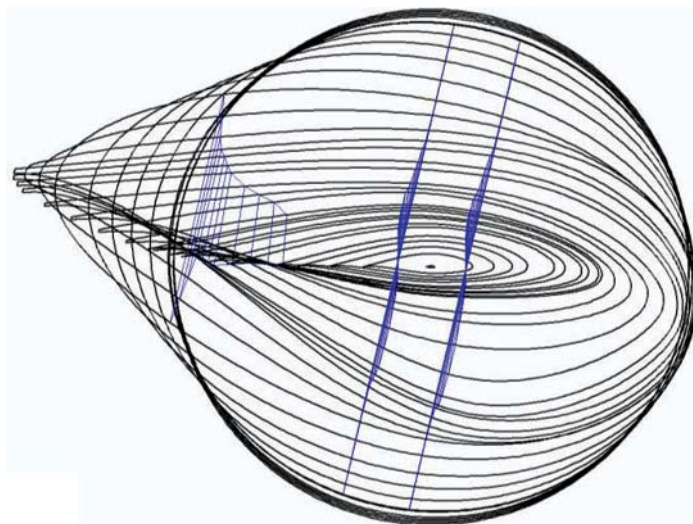


Figure 7.1 Blade cross-sectional outlines at stations along the length of a 100 m blade. Also shown are the positions of the two main shear webs and the additional trailing edge shear web at each station. Source: Reproduced from Sandia report ‘The SNL 100-01 Blade: Carbon Design Studies for the Sandia 100-Metre Blade’ (Griffith 2013)

Instead, resort must be made to numerical methods based on blade-element/momentum theory – for example, using Eqs. (3.54c) and (3.55a) in Section 3.9.6.

For pitch-regulated machines, the annual energy capture attributed to the annular ring swept out by each blade element is determined for the chosen wind speed distribution and the variation of energy capture with blade chord and twist at each ‘blade station’ computed. In this way, the values of blade chord and twist at each ‘blade station’ yielding maximum energy capture are identified.

For stall-regulated machines, the method is similar, but the total annual energy capture has to be maximised within the constraint of limiting the maximum total power output to the machine rating. The results of such an investigation are reported in ‘A Design Study of a 1 MW Stall-Regulated Rotor’ by Fuglsang and Madsen (1995).

7.1.3 Practical modifications to optimum aerodynamic design

The result of the optimisation described in the previous section is typically a blade geometry in which both blade chord and blade twist vary approximately inversely with radius, as illustrated in Figure 3.19. However, because the inboard section of the blade makes only a small contribution to total power output (Figure 3.30), the aerofoil section is generally not continued inboard of about 15% radius in practice, and the chord at this radius is substantially reduced, to perhaps half the theoretical optimum. It is then often found expedient to taper the chord uniformly over the active length of the blade, with the tip chord and chord taper set so that the chord distribution approximates closely to the optimum over the outboard half of the blade (Figure 3.20).

The blade root area is normally circular in cross-section to match up with the pitch bearing in the case of pitchable blades or to allow pitch angle adjustment at the bolted flange (to compensate for non-standard air density) in the case of stall-regulated blades. The transition from the root section to the aerofoil section outboard of 15% radius should be a smooth one for structural reasons, with the result that the latter section will have a high thickness to chord ratio of up to about 50%.

Contrary to the general rule, one manufacturer, Enercon, has found it worthwhile to extend the aerofoil over the inboard section of the blade all of the way to the fairing enclosing the rotor hub on some of its designs.

7.1.4 Structural design criteria

The blade structure must be able to

- Resist extreme loads – i.e. satisfy the ultimate limit state (ULS).
- Resist fatigue loads.
- Limit deflections to maintain adequate tip clearance.
- Achieve blade natural frequencies that are not susceptible to excitation at the blade passing frequency or its harmonics.
- Avoid aeroelastic instability.

Blade structures are typically thin-walled shells, so buckling is a possibility under compression and must be allowed for in the investigation of the ULS.

In the case of unboxed, straight blades, it is sometimes necessary to add material to increase blade stiffness to meet the tip clearance requirement. However, this can be avoided by coning the rotor and/or introducing forward pre-bend of the blade to increase the clearance.

7.1.5 Form of blade structure

A hollow shell corresponding to the blade envelope defined by the aerofoil section clearly provides a simple, efficient structure to resist flexural and torsional loads, and some blade manufacturers have adopted this form of construction (see Figure 7.2).

However, there is greater benefit in concentrating skin material in the forward half of the blade, where the blade thickness is a maximum, so that it acts more efficiently in resisting out-of-plane bending moments (see Figures 7.3 and 7.4). The weakened areas of the shell towards the trailing edge are then typically stiffened by means of sandwich construction utilising a PVC foam filling.

The hollow shell structure defined by the aerofoil section is not very efficient at resisting out-of-plane shear loads, so these are catered for by the inclusion of one or more shear webs oriented perpendicular to the blade chord.

An increasingly common form of construction is the use of longitudinal flange elements known as *spar caps* in conjunction with shear webs to form one or two I-beams. A typical arrangement with two I-beams is shown in Figure 7.5. The spar caps conform to the local aerodynamic profile, and the perimeter of the aerofoil section is completed by foam or balsa sandwich panels.

The efficiency of the cross-section in resisting flapwise bending moments can be improved by replacing the separate spar caps attached to each shear web by a single spar cap spanning between them, as this increases the lever arm – see Figure 7.6. However,

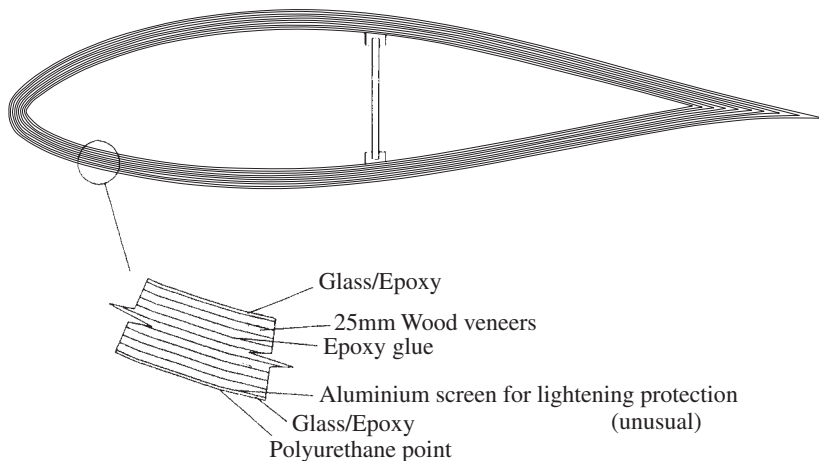


Figure 7.2 Wood-epoxy blade construction utilising full blade shell. Source: Reproduced from Corbet (1991) by permission of the RTI Renewable Energy R&D Programme

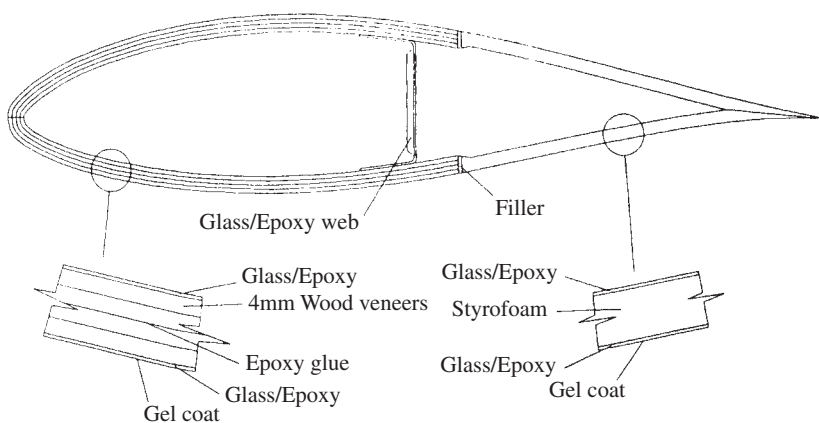


Figure 7.3 Wood-epoxy blade construction utilising forward half of blade shell. Source: Reproduced from Corbet (1991) by permission of the RTI Renewable Energy R&D Programme

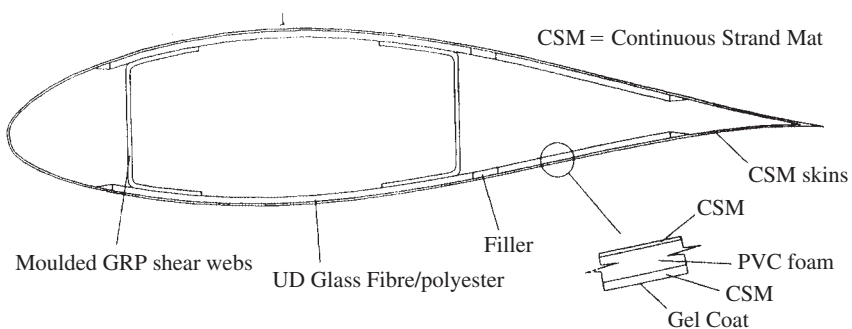


Figure 7.4 Glass fibre blade construction using blade skins in forward portion of blade cross-section and linking shear webs. Source: Reproduced from Corbet (1991) by permission of the RTI Renewable Energy R&D Programme

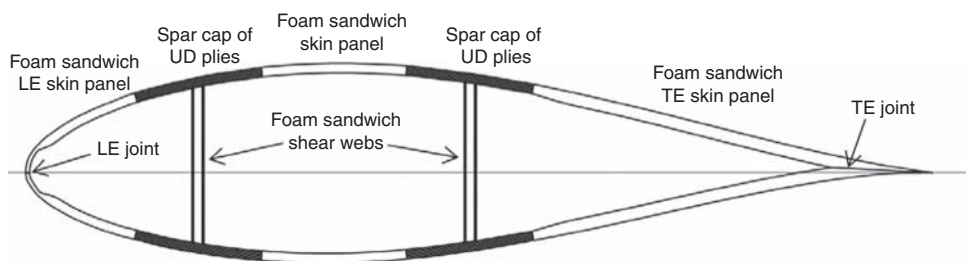


Figure 7.5 Glass fibre blade construction with twin I-beams, each formed of spar caps and a linking shear web. The remainder of the aerofoil perimeter is formed of foam sandwich panels

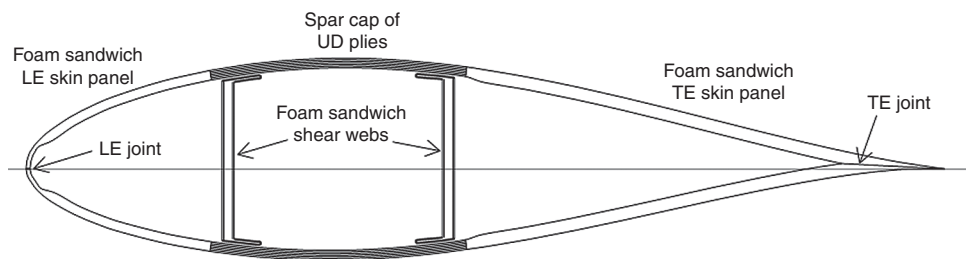


Figure 7.6 Glass fibre blade construction with box section spar consisting of spar caps and linking shear webs. Note that the shear webs are shown with integral flanges, enabling the width of the bonded joint to the spar caps to be significantly increased. The remainder of the aerofoil perimeter is formed of foam sandwich panels

this is at the expense of reducing the ability to resist edgewise moments, assuming no change in the total cross-sectional area of spar cap. The spar caps typically consist of mainly unidirectional (UD) plies of constant width, but taper down in thickness with increasing radius.

The shear webs will normally be of sandwich construction, with biaxial plies, in which the fibres are aligned at $+45/-45^\circ$ to the blade radius, forming the outer skins.

The sandwich panels between the spar caps and the leading and trailing edges contribute to both flapwise and edgewise bending resistance as well as the transmission of edgewise shear, so their outer skins comprise both UD and biaxial plies. The thickness of these panels is driven by resistance to buckling. Additional material is sometimes added at the trailing edge to increase the resistance of the cross-section to edgewise bending.

Although the outboard portion of the blade beyond the maximum chord position is characterised by progressive reductions in chord and thickness roughly corresponding to the reduction in bending moments, the *reduction* in chord between the maximum chord position and the hub does not match the rapid increase in edgewise moment there, requiring a disproportionate increase in material at the leading and trailing edges towards the root. Thus, while spar caps perform a key role in resisting flapwise bending moments outboard of the maximum chord position, they are not required at the blade root, because the best structural cross-section to resist out-of-plane and in-plane root bending moments of similar magnitude is a cylindrical shell of uniform thickness. Thus the inboard portion of the blade is characterised by a gradual transition from the uniform cylindrical shell at the root to the more complicated cross-section of spar caps, sandwich panels, and shear webs at the maximum chord position.

7.1.6 Blade materials and properties

The ideal material for blade construction will combine the necessary structural properties – namely, high strength to weight ratio, fatigue life, and stiffness – with low cost and the ability to be formed into the desired aerofoil shape.

Table 7.1 lists the structural properties of the materials in general use for blade manufacture and those of some other candidate materials. In the case of composites, there is a great variation in properties depending on the fibre volume fraction and the fibres and matrices used, so the values quoted are simply representative examples. For comparative purposes, values are also presented for

- Compressive strength to weight ratio.
- Fatigue strength as a percentage of compressive strength.
- Stiffness to weight ratio

It is evident that glass fibre composites (i.e. GFRP) have a substantial higher compressive strength to weight ratio compared with wood and metals. However, this apparent advantage is not as decisive as it appears, for two reasons. First of all, the fibres of some of the plies making up the laminated blade shell have to be aligned off-axis (typically at $\pm 45^\circ$) to resist shear loads, giving reduced strengths in the axial direction. Secondly, the relatively low Young's modulus of these composites means that blade tip deflection or resistance to buckling of the thin skins governs the design rather than simple compression yielding. Design against buckling is considered in Section 7.1.16.

Carbon fibre composites (i.e. carbon fibre reinforced polymer [CFRP]) offer significant benefits in terms of reduced tip deflections, as industrial grade carbon fibres have a Young's modulus about three times that of E-glass.

It should be noted that the low strength of wood laminate compared with other materials renders it unsuitable for blades with slender chords operating at high tip speed, where the flapwise bending moments during operation are inevitably high in relation to blade thickness. For example, Jamieson and Brown (1992) have shown that, in the case of a family of stall-regulated machines, the blade stress is highly sensitive to rotational speed, increasing as the fourth power, if the skin thickness to chord ratio is maintained constant. Although stresses can be reduced by increasing the skin thickness, this represents a less and less efficient use of the additional material beyond a skin thickness to chord ratio of 3–4%, especially in the outboard part of the blade, where the blade thickness to chord ratio is low.

Fatigue performance is conveniently measured by mean fatigue strength at 10^7 cycles, as a percentage of ultimate compressive strength (UCS). Clearly, GFRP, CFRP and khaya/epoxy perform best with a value of about 30%. The low value for welded steel (10%), combined with steel's low strength to weight ratio, renders it uncompetitive for large diameter machines where gravity fatigue loading becomes important, although it was chosen for some of the early prototype megawatt-scale machines when the fatigue properties of composite materials were less well understood.

The stiffness per unit weight ratio determines blade natural frequency. CFRP has a ratio three or four times larger than those of all of the other materials, which are in a relatively small range (18–27 GPa).

From the above brief survey, it is apparent that the material with the best all-round structural properties is CFRP. However, it has not found common use, because it is an order of magnitude more costly than other materials. Instead, the most popular materials are glass/polyester and glass/epoxy. Wood/epoxy has also been found satisfactory, but its use is limited by the shortage of wood of consistent quality.

Table 7.1 Structural properties of materials for wind turbine blades

Material (NB: UD denotes unidirectional fibres – i.e., all fibres running longitudinally)	Ultimate tensile strength (UTS) (MPa)	Ultimate compressive strength (UCS) (MPa)	Specific gravity (s.g.)	Compressive strength to weight ratio UCS/s.g. (MPa)	Mean fatigue strength at 10^7 cycles for reverse loading (amplitude) (MPa)	Mean fatigue strength as percentage of UCS	Young's modulus, E (GPa)	Stiffness ratio E/s.g. (GPa)
(mean for composites, minimum for metals)								
1. Glass/polyester UD composite [1][2]	860–900 [1][2]	360–720 [2][1]	1.85 [2]	195–390	140 [3]	19–39%	38 [2]	20.5
2. Glass/epoxy laminate from PPG-Devold L1200/G50-E07 fabric with 92% UD fibres and 59% fibre volume fraction. Vacuum infused. Values derived from data in [14] unless noted otherwise.	1025 MPa (standard deviation = ~90 MPa)	575 MPa (standard deviation = ~15 MPa)	2.00 (based on typical s.g. values of 2.55 for fibres and 1.2 for resin)	290	180	31%	44	22
3. Carbon fibre/epoxy Hexply 8552 laminate made from Hexcel AS4 carbon fibre with 60% fibre volume fraction and UD lay-up [15][4]	2205	1530	1.55	985	480 [5]	32% [5]	141	91

4. Carbon fibre/glass fibre/epoxy hybrid P2B laminates with 55% fibre volume fraction and $[\pm 45/0_4]$ lay-up; 85% (by volume) carbon fibre (Newport NCT-307-D1-34-600 pre-preg) in 0 deg direction & 15% (by volume) glass fibre in ± 45 deg directions [4][14]	1550	1050	1.57	670	560 [16]	54%	100	64
5. Khaya ivorensis/epoxy laminates	82 [6]	50 [6]	0.55	90	15 [7]	30%	10 [8]	18
6. Birch/epoxy laminates	117 [9]	81 [10]	0.67	121	16.5 [7]	20%	15 [10]	22.5
7. High yield steel (Grade S 355 – formerly Fe 510)	510	510	7.85	65	50 [11]	10%	210	27
8. Weldable aluminium alloy AA6082 (formerly) H30	295 [12]	295 [12]	2.71	109	17 [13]	6%	69 [12]	25.5

(Continued)

Table 7.1 (continued)

Sources:

- [1] Mayer (1996) Table 2.4.
- [2] Barbero (2018) Table 1.2.
- [3] Mayer (1996) Figure 14.4 – DNVR curve.
- [4] Carbon fibres exhibit a wide range of properties; figures given here are for particular example materials only.
- [5] Based on S-N curve index of $m = 14$ and an $N = 1$ amplitude equal to the UCS.
- [6] Bonfield and Ansell (1991). Moisture content = 10%.
- [7] Based on S-N curve index of $m = 13.4$ for scarf-jointed wood laminates, taken from Hancock and Bond (1995).
- [8] Bonfield *et al.* (1992).
- [9] Mayer (1996) Table 7.3.
- [10] Hancock (personal communication). Moisture content = 10%.
- [11] Mean value for butt-welded joints with weld profile ground smooth (Class C), taken from BS 5400, *Steel Concrete and Composite Bridges – Part 10: Code of Practice for Fatigue* (1980).
- [12] CP 118:1969, *The Structural Use of Aluminium*.
- [13] Mean value estimated from mean minus two standard deviations value for ground butt-welded joint with shallow thickness transition, Detail Cat 221, in IIW, *Fatigue Design of Welded Joints and Components* (Woodhead, 1996).
- [14] Montana State University, SNL/MSU/DOE Composite Materials Fatigue Database: Mechanical Properties of Composite Materials for Wind Turbine Blades, Version 25.0 (2016).
- [15] HexTow AS4 product datasheet, downloaded from www.hexcel.com 11 October 2018.
- [16] Based on $R = -1$ S-N curve reported in Montana State University paper ‘Comparison of Tensile Fatigue Resistance and Constant Life Diagrams for Several Potential Wind Turbine Blade Laminates’ (Samborsky *et al.* 2007).

Steel is the cheapest material in the raw state and can be formed into tapering, curved panels following the aerofoil profile, except in the sharply curved region near the leading edge. However, it is much harder to introduce a twist into such panels, and this consideration, together with the poor fatigue properties, means that steel is rarely used. By contrast, glass and CFRPs lend themselves to lay-up in half moulds profiled to give the correct aerofoil shape, plan-form, and twist. Laminated wood composite blades are built up in a similar way, but the veneer thickness has to be restricted to enable the veneers to flex to the required curvature during lay-up.

In the following paragraphs, the properties of the materials in most common use for blade manufacture are considered in more detail.

7.1.7 Static properties of glass/polyester and glass/epoxy composites

The tensile properties of glass/polyester and glass/epoxy plies with the same fibre volume fraction and lay-up are generally similar – i.e. the influence of the matrix is slight. However, the matrix properties are more important in compression, as fibre buckling is resisted by the matrix in shear.

The plate elements making up the GFRP blade structure are normally laminates consisting of several plies, with fibres orientated appropriately to resist the design loads. Within a ply (typically 0.5–1.0 mm in thickness), the fibres may be arranged in a variety of different ways. In the simplest case, fibres, in the form of strand, or collections of strands known as *rovings*, are all be laid in the same direction to form a uniaxial ply – also termed *UD* (short for unidirectional). Alternatively, the fibres may run in two, three, or even four different directions in a wide variety of woven or non-woven fabrics, to form a biaxial, triaxial, or quadriaxial ply, respectively. Normally the two directions of a biaxial ply are at right angles.

Glass fibre properties

Glass fibres with differing chemical compositions have been developed for a variety of purposes, and they have been given letter designations reflecting their special properties. The glass most commonly used in blade construction is E-glass, which has good structural properties in relation to its cost. The E designation reflects another property, its low electrical resistance. R-glass (R for reinforcement) and H-glass with hollow fibres both have superior strength and modulus of elasticity, and their use is increasing, despite their greater cost. Typical chemical compositions and mechanical properties of these glasses are given in Table 7.2, based on information from a number of manufacturers. As shown, the mechanical properties of a particular glass type can vary. This is the result of differing chemical compositions and manufacturing processes. Note that the strengths of resin impregnated strands are up to 50% less than the strengths of virgin filaments.

The strengths of the individual fibres of a particular E-glass are widely dispersed about the mean and are better represented by a Weibull distribution than by a normal distribution. The Weibull shape factor can vary from 3 (wide dispersion) to 7 (narrow dispersion).

Table 7.2 Compositions and properties of E-glass, R-glass, and H-glass

Glass type	Units	E-glass	R-glass	H-glass
Composition				
Silicate SiO ₂	%	53–57	55–60	As E-glass
Aluminate Al ₂ O ₃	%	12–16	23–28	
Borate B ₂ O ₃	%	5–10	< 0.5	
Calcium oxide CaO	%	16–25	8–15	
Magnesium oxide MgO	%	0–5	4–7	
Property				
Specific gravity		2.54–2.60	2.54	2.61
Young's modulus at 23 deg. C	GPa	72–80	86	87.5
Elongation at filament break	%	4.5–5	4.8	4.9
Mean tensile strength at 23 deg. C – virgin filament	MPa	3100–3850	4125–4450	4130
Tensile strength at 23 deg. C – impregnated strand as a percentage of virgin filament strength	%	50–70	70–80	60–70

Table 7.3 Typical matrix properties

Matrix	Polyester and vinyl ester	Epoxy
Specific gravity	1.1	1.15–1.3
Tensile modulus (GPa)	3.4	3–5
Poisson's ratio	0.38	0.34–0.38
Tensile strength (MPa)	50–80	60–100

Source: Taken from Barbero (2018).

Matrix properties

Typical matrix properties are given in Table 7.3. Polyester used to be the resin of choice, partly because of its low cost, but now epoxy resin is generally preferred because of its slightly better mechanical properties and significantly reduced shrinkage during curing.

Uniaxial plies

In general, the testing of multiple samples is required to determine the mechanical properties of individual laminates. However, at the design stage, it is useful to be able to estimate ply properties from the fibre and matrix properties using simple rules, although they are not always very accurate. Thus, for a ply reinforced by UD fibres, the longitudinal stiffness modulus, E_1 , can be derived accurately from the rule of mixtures formula:

$$E_1 = E_f V_f + E_m (1 - V_f) \quad (7.3)$$

where E_f is the fibre modulus, E_m is the matrix modulus, and V_f is the fibre volume fraction. However, the inverse form of this formula – e.g.

$$\frac{1}{E_2} = \frac{(1 - V_f)}{E_m} + \frac{V_f}{E_f} \quad (7.4)$$

significantly underestimates the transverse modulus, E_2 , and the in-plane shear modulus, G_{12} . More accurate formulae based on more sophisticated models are given in Barbero (2018). In particular, the Halpin–Tsai semi-empirical formula:

$$E_2 = E_m \left[\frac{1 + 2\eta V_f}{1 - \eta V_f} \right] \text{ where } \eta = \frac{(E_f/E_m) - 1}{(E_f/E_m) + 2} \quad (7.5)$$

and the cylindrical assemblage model formula:

$$G_{12} = G_m \left[\frac{(1 + V_f) + (1 - V_f)G_m/G_f}{(1 - V_f) + (1 + V_f)G_m/G_f} \right] \quad (7.6)$$

provide more accurate estimates of transverse modulus and in-plane shear modulus, respectively.

The longitudinal tensile strength of a ply reinforced by UD fibres, σ_{1t} , can be estimated from

$$\sigma_{1t} = \sigma_{fu} \left[V_f + \frac{E_m}{E_f}(1 - V_f) \right] \quad (7.7a)$$

where σ_{fu} is the ultimate tensile strength (UTS) of the fibres. However, as noted previously, the tensile strengths of pristine glass filaments cannot be realised in a composite, so σ_{fu} can only be obtained by back-calculation using Eq. (7.7a) from test results on samples of composite manufactured in a similar way. These indicate fibre strength reductions of up to 50%, so a value of σ_{fu} of 1750 MPa can be used in Eq. (7.7a) in the first instance.

It is clear from Eq. (7.7a) that the longitudinal strength of a UD ply increases linearly with fibre volume fraction. However, it is found that the failure strain exhibits much less dependence on volume fraction, so it is a useful proxy for ply strength, which is related to failure strain, ε_{1t} , by

$$\sigma_{1t} = \varepsilon_{1t}[E_f V_f + E_m(1 - V_f)] \quad (7.7b)$$

For their design of a blade for a 10 MW turbine, the Danish Technical University (DTU), took a UD ply characteristic failure strain value of 2.1% (Bak et al. 2013), which compares with the 2.44% value adopted by Sandia National Laboratories for their 100 m blade design (Griffith and Ashwill 2011). Both values are roughly in line with the mean failure strains in the range 2.7–3.0% reported for a series of static tests on four different UD composites in the US Department of Energy (DOE)/Montana State University (MSU) Composite Materials Fatigue Database published by MSU in 2010.

As noted earlier, the glass fibre strengths are widely dispersed, with the result that, as the tensile loading on a specimen is increased, more and more fibres fail. Eventually the load increment due to a small strain increase is balanced by the loss of load due to fibre failures, and the ultimate strength of the specimen is reached. This behaviour is illustrated in Figure 7.7, where the strength distribution of individual fibres and the

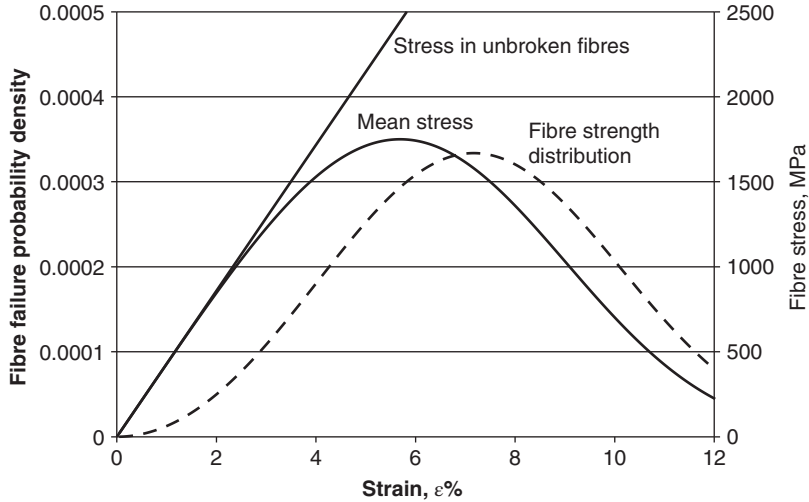


Figure 7.7 Failure strain distribution of individual fibres compared with plot of mean fibre stress against strain

mean fibre stress are plotted out against strain assuming a Weibull distribution of fibre strength of the form

$$F(\sigma) = 1 - \exp \left[-\left(\frac{\sigma}{\beta} \right)^m \right] \quad (7.8)$$

where β is the scale factor and m is the shape factor, taken as 3.

The proportion of unbroken fibres attaining the stress σ is $\exp \left[-\left(\frac{\sigma}{\beta} \right)^m \right]$, so the average stress in all fibres is given by

$$\sigma_{eff} = \sigma \exp \left[-\left(\frac{\sigma}{\beta} \right)^m \right] \quad (7.9)$$

This reaches a maximum at $\sigma = \frac{\beta}{m^{\frac{1}{m}}}$ of $\sigma_{eff,max} = \frac{\beta}{(e.m)^{\frac{1}{m}}}$ - i.e. 0.4968β for $m = 3$. In Figure 7.7, $\sigma_{eff,max}$ is taken as 1750 MPa, giving a scale factor β of 3522 MPa and a UTS of 1000 MPa (assuming a 75 GPa fibre modulus and 0.55 fibre volume fraction). The stress in the unbroken fibres at specimen failure, $\sigma = \frac{\beta}{m^{\frac{1}{m}}}$, is 2442 MPa. Note that the mean strength of individual fibres, $\beta\Gamma(1 + 1/m)$, is 3145 MPa, well above the average stress in the fibres at the failure of the composite.

The longitudinal compressive strength of a ply reinforced by UD fibres is always significantly less than the tensile strength because of microbuckling of the fibres, which is governed by the shear strength of the matrix and the degree of fibre misalignment – see Barbero (1998). Typically, the longitudinal compressive strength is between 50% and 70% of the tensile strength. DTU assumed a characteristic compressive failure strain of 1.5% for their 10 MW turbine blade design (Bak et al. 2013).

Biaxial plies

Biaxial plies are formed by impregnating fabrics with fibres in two directions normally at right angles. In wind turbine blades, biaxial plies are used with the fibres aligned at $\pm 45^\circ$ to the blade axis to resist shear loading. As the compression stress in one set of fibres is equal to the tensile stress in the other set, the shear strength is governed by the fibre compression strength.

The ply compression resistance in the $+45^\circ$ direction is made up of the longitudinal resistance of the $+45^\circ$ fibres and associate matrix, $\sigma_{fcu} \cdot (V_f + [1 - V_f]E_m/E_f)/2$, and the transverse resistance of the -45° fibres and associate matrix, $\sigma_{fcu} \cdot (E_2/E_f)/2$, assuming that they are subject to the same strain σ_{fcu}/E_f – i.e. $\sigma_{fcu} \cdot (V_f + (1 - V_f)E_m/E_f + (E_2/E_f))/2$ in total. Hence, assuming equal and opposite stresses act in the -45° direction, it is easy to show that the ply shear resistance is given by

$$\tau_u = \sigma_{fcu} \left(V_f + (1 - V_f) \frac{E_m}{E_f} + \frac{E_2}{E_f} \right) \quad (7.10)$$

Triaxial laminate

The inner and outer skins of the sandwich panels forming the blade shell are often triaxial laminates designed to resist both in-plane shear and axial loading due to blade flexure. Accordingly, they are constructed of a mixture of $+45/-45$ biaxial plies and uniaxial (0°) plies.

Clearly the biaxial plies can make a useful contribution to the axial strength, and this can be estimated by multiplying the modulus of the biaxial plies in axial direction, referred to here as E_{45} , by the axial strain in the UD plies. To derive the required modulus, we consider the two stress distributions in the biaxial plies shown in Figure 7.8, which together are equivalent to the axial stress, σ .

The first stress distribution is one of uniform tension in all directions, resulting in uniform strain in all directions. The stiffness of the laminate under this loading can be derived as follows. First consider a UD ply subject to longitudinal and transverse stresses σ_1 and σ_2 . The resulting strains are given by the equations $\epsilon_1 = \frac{\sigma_1}{E_1} - \nu_{21} \frac{\sigma_2}{E_2}$ and $\epsilon_2 = -\nu_{12} \frac{\sigma_1}{E_1} + \frac{\sigma_2}{E_2}$, which can be solved to give the stresses in terms of strains as follows:

$$\sigma_1 = \frac{E_1}{\Delta} (\epsilon_1 + \nu_{21} \epsilon_2) \text{ and } \sigma_2 = \frac{E_2}{\Delta} (\epsilon_2 + \nu_{12} \epsilon_1) \text{ where } \Delta = 1 - \nu_{12} \nu_{21} \quad (7.11)$$

Noting that $E_1 \nu_{21} = E_2 \nu_{12}$ by the reciprocal theorem, we obtain

$$\sigma_1 = \frac{1}{\Delta} (\epsilon_1 E_1 + \nu_{12} \epsilon_2 E_2) \quad (7.12)$$

Now consider a $0/90^\circ$ biaxial laminate subjected to a uniform strain, ϵ , in both directions. The stress in both the 0° and 90° directions will be the average of the expressions σ_1 and σ_2 above with ϵ substituted for ϵ_1 and ϵ_2 – i.e.

$$\sigma = \epsilon \left(\frac{E_1 + E_2}{2\Delta} + \frac{\nu_{12} E_2}{\Delta} \right) \quad (7.13)$$

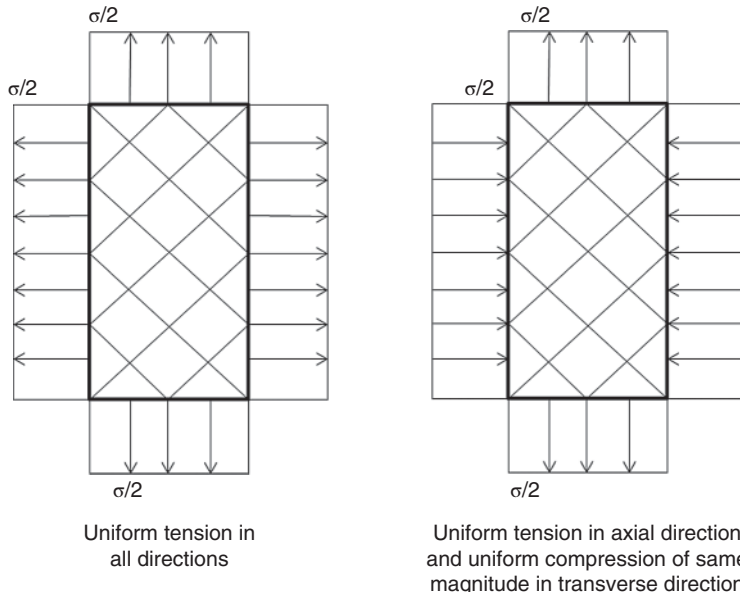


Figure 7.8 Two stress distributions on a $+45/-45^\circ$ laminate, which, when combined, result in axial tensile stress of σ

Hence the laminate stiffness under uniform loading in both directions is

$$\bar{E} = \left(\frac{E_1 + E_2}{2\Delta} + \frac{\nu_{12}E_2}{\Delta} \right) \quad (7.14)$$

The second stress distribution in the $+45/-45^\circ$ laminate consists of uniform tension, $\sigma/2$ in the axial direction and uniform compression of the same magnitude in the transverse direction, which is equivalent to a pure shear $\tau = \sigma/2$ with respect to the $+45/-45^\circ$ fibre directions. This results in a shear strain of $\sigma/(2G_{12})$, where G_{12} is the shear modulus of both the $+45$ and -45° plies. The corresponding axial strain is $\sigma/(4G_{12})$.

The total strain in the axial direction resulting from the combination of the stress distributions in Figure 7.8 is:

$$\frac{\sigma}{2E} + \frac{\sigma}{4G_{12}} = \frac{\sigma}{2} / \left(\frac{E_1 + E_2}{2\Delta} + \frac{\nu_{12}E_2}{\Delta} \right) + \frac{\sigma}{4G_{12}} = \sigma \left(\frac{\Delta}{E_1 + E_2 + 2\nu_{12}E_2} + \frac{1}{4G_{12}} \right) \quad (7.15)$$

Hence the axial stiffness of the $+45/-45^\circ$ laminate, denoted E_{45} , is $1 / \left(\frac{\Delta}{E_1 + E_2 + 2\nu_{12}E_2} + \frac{1}{4G_{12}} \right)$. It is largely governed by the ply shear modulus G_{12} . A calculation of $+45/-45$ laminate axial stiffness is set out in the example below. The result is about 1/3 the longitudinal stiffness of a UD ply, so the contribution of the biaxial plies to the axial stiffness of a triaxial laminate is clearly a useful one.

Example 7.1 Calculate the axial stiffness of a $+45/-45^\circ$ laminate. Assume $E_f = 75$ GPa, $E_m = 4$ GPa, $\nu_f = 0.38$, $\nu_m = 0.22$ with a fibre volume fraction of 0.55.

First of all, the stiffness properties of a uniaxial ply are calculated, as follows:

$E_1 = 43.05 \text{ GPa}$ from Eq. (7.3), $E_2 = 14.66 \text{ GPa}$ from Eq. (7.5), $\nu_{12} = 0.292$ from the rule of mixtures, $G_{12} = 4.353 \text{ GPa}$ from Eq. (7.6), and $\Delta = 0.97096$ from Eq. (7.11).

The biaxial laminate stiffness under uniform loading in both directions, \bar{E} , is given by Eq. (7.14) as $[(43.05 + 14.66)/2 + 0.292(14.66)]/0.97096 = 34.13 \text{ GPa}$.

The axial stiffness of the $+45/-45^\circ$ laminate, E_{45} , is given by

$$\frac{1}{E_{45}} = \frac{1}{2\bar{E}} + \frac{1}{4G_{12}} = \frac{1}{2(34.13)} + \frac{1}{4(4.353)} = 0.01465 + 0.05743 = 0.07208 \text{ GPa}^{-1}$$

resulting in $E_{45} = 13.87 \text{ GPa}$.

7.1.8 Fatigue properties of glass/polyester and glass/epoxy composites

Composites are manufactured from a wide variety of rovings and fabrics utilising different matrices and manufacturing processes. This fact, combined with the inherent variability in the raw materials, lay-up, resin application, and curing, means that the characterisation of composite fatigue properties is a challenging undertaking, requiring extensive programmes of testing. This section can only provide a brief introduction to a complicated subject. For an in-depth survey, the reader is referred to Nijssen (2007).

S-N curves

S-N curves are normally derived by fitting a curve to a lifetime vs stress plot of constant amplitude fatigue test results. When expressed in terms of stress, the fatigue properties of composite laminates extend over a wide range, depending on fibre volume fraction and the number of plies with fibres in the longitudinal direction. However, data from constant stress amplitude fatigue test results becomes much more intelligible if stress ranges are converted into initial strain ranges, allowing the fatigue properties of composites with different lay-ups to be compared. (The Young's modulus of a composite reduces over time during a fatigue test – hence the need to specify that the strain range is measured at the start of the test.)

The fatigue behaviour of composites depends on both the stress range *and* the mean stress level, which can both be described in terms of the maximum stress, σ_{\max} , and the ratio of minimum to maximum stress, R . It is convenient initially to consider fatigue behaviour under reverse loading, i.e. with $R = -1$, for which the mean stress is zero, and then relate behaviour at other R ratios to it.

It should be noted that there is no agreed convention governing which stress or strain parameter should be used for *S-N* curves for composites. The amplitude or maximum value of stress or strain are both regularly used.

The constant amplitude fatigue behaviour of glass fibre composites can best be characterised either by a power law relationship between the number of cycles and the stress or strain amplitude, viz.:

$$\varepsilon = \varepsilon_0 N^{-1/m} \text{ or } N = K\varepsilon^{-m} \text{ where } K = (\varepsilon_0)^m \text{ or } \log N = \log K - m \log \varepsilon \quad (7.16)$$

or by a linear relationship between the logarithm of the number of cycles and the stress or strain amplitude, viz.:

$$\log N = a - b \log \varepsilon \quad (7.17)$$

but the first relation is the one in most common use.

Echtermeyer et al. (1996) carried out a regression analysis on a total of 111 constant amplitude, reverse loading fatigue test results for 10 different laminates tested at DnV, assuming that they all conformed to the same ε - N curve, and obtained values for ε_0 , $\log K$, and m of 2.84%, 3.552, and 7.838, respectively, with a standard deviation of $\log N$ of 0.437. The DnV regression line is compared with another derived from 19 tests on a $0^\circ/+45^\circ,-45^\circ$ laminate at ECN, giving $\varepsilon_0 = 2.34\%$, $\log K = 3.775$, and $m = 10.204$, in Figure 7.9. The researchers did not constrain the regression lines to pass through the strain value at either UTS or UCS at $\log N = 0$ (ca 2.4% and 2.0%): had they done so, the DnV line would have had a shallower slope – i.e. a larger value of m . After comparison with regressions on other fatigue test datasets, they concluded that the DnV line provided a reasonable basis for initial design.

There is no clear consensus as to whether S - N or ε - N regression lines should be constrained to pass through the static test values at $N = 1$. Although the static test can be considered as a single fatigue cycle, the static test strain rate usually differs from that of the fatigue tests, and the maximum tensile load is significantly affected by the static test rate. Another consideration is that the constraint usually results in a slightly worse fit to the fatigue test data, with negative implications for the accuracy of the extrapolation of the S - N curve beyond 10^6 cycles, the usual upper limit of testing.

Nevertheless, there is some agreement in relation to the S - N curve slope for reverse loading that can be adopted in the absence of testing. The 2010 edition of the Germanischer Lloyd (GL) *Guideline for the Certification of Wind Turbines* suggests that, if the fibre volume fraction lies between 30% and 55%, the index m can be taken as 9 or 10 for composites with polyester and epoxy matrices, respectively, with the $N = 1$ strain, ε_0 , taken as the ultimate tensile strain divided by a partial material safety factor. Similar guidance

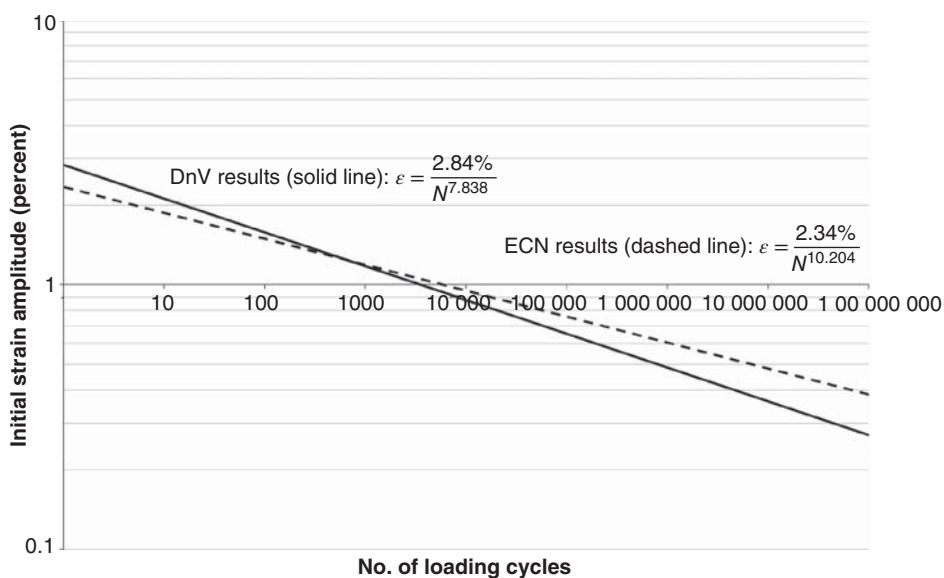


Figure 7.9 Strain-life regression lines fitted to results of constant amplitude, reverse loading fatigue tests on GFRP composites

in relation to the index m is provided in the draft IEC CD 61400-5 (2016) standard for the design of wind turbine rotor blades, and m values of 9–10 are quoted for GFRP in the DNVGL standard *Rotor Blades for Wind Turbines* (2015).

No evidence has been found for the existence of a fatigue limit in the case of GFRP (Nijssen 2007).

Influences of fibre content, matrix, and fabric

The fatigue of blade materials has been the subject of in-depth research by the Composite Material Technologies Research Group at MSU, which publishes a comprehensive database of test results and regular research reviews. Some interesting findings are reported here.

The increased fibre volume fractions made possible by improvements in manufacturing techniques has not been entirely beneficial as far as high cycle fatigue performance is concerned. A useful measure of this performance is the 10^6 cycle fatigue strain, defined as the initial maximum strain corresponding to the stress range that can be endured for one million tensile loading cycles. Table 7.4 compares values at low and high fibre volume content for three different resins reported by Samborsky et al. (2010). It is shown that the million cycle fatigue strains for the three resins at low fibre volume fraction are in a narrow range of 1.1–1.2% but drop significantly at high fibre volume fraction. The reduction is highest (−62%) for the polyester matrix and lowest (−36%) for the epoxy matrix.

The S - N curve inverse slopes of 9 and 10 for polyester and epoxy matrices, respectively, referred to above imply that the 10^6 cycle fatigue loading performance of a polyester laminate is about 15% inferior to that of an epoxy laminate under reverse loading, but the divergences in Table 7.4, albeit under tensile loading, suggest that a single inverse slope value is unlikely to be appropriate for all fibre volume fractions.

The fatigue performances of polyester and epoxy resin laminates with high fibre volume fraction (43–55%) and different fabric structures are compared in Table 7.5, based on Samborsky et al. (2012). For the UD laminate with polyester matrix, the million cycle fatigue strain is close to half that of the UD laminate with epoxy matrix, and the difference is only slightly less marked in the case of the multidirectional (MD) laminate.

The glass fibre reinforcement of UD laminates often consists of a fabric of 0° fibres stitched to a backing of transverse fibres and/or random matting, with the proportion of 0° fibres typically being in excess of 90%. It has been found that transverse strands and stitching impact negatively on the fatigue performance when compared with aligned strand laminates, with the million cycle tensile strain dropping by approaching 60%

Table 7.4 Comparison of 10^6 cycle maximum tensile strains in laminates with high and low fibre volume fraction and different resins under $R = 0.1$ fatigue loading

Fibre volume fraction	Maximum initial tensile strain for 10^6 cycles of tensile fatigue loading		
	Epoxy matrix	Vinyl ester matrix	Polyester matrix
35–37%	1.20%	1.11%	1.16%
50–60%	0.77%	0.52%	0.44%

Table 7.5 Comparison of 10^6 cycle maximum tensile strains in laminates with epoxy and polyester matrices under $R = 0.1$ fatigue loading

Laminate type	Maximum initial tensile strain for 10^6 cycles of tensile fatigue loading ($R = 0.1$)	
	Epoxy matrix	Polyester matrix
UD	0.81%	0.41%
MD containing UD	0.85%	0.48%
Biaxial (+45/-45° strands plus mat and/or strand backing)	0.56%	0.43%

Table 7.6 Comparison of 10^6 cycle maximum tensile strains in aligned strand and stitched fabric laminates for different matrices under $R = 0.1$ fatigue loading

Laminate type	Maximum initial tensile strain for 10^6 cycles of tensile fatigue loading		
	Epoxy matrix	Vinyl ester matrix	Polyester matrix
Aligned strand	1.20%	1.23%	0.93%
Stitched fabric with 92%/4%/4% split between 0° and 90° fibres and matting	0.88%	0.53%	0.39%
Percentage reduction in 10^6 cycle maximum tensile strain for stitched fabric	-27%	-57%	-58%

when the matrix is polyester or vinyl ester compared with 27% when the matrix is epoxy (Samborsky et al. 2012). Values of the million cycle fatigue strain are compared in Table 7.6. The fibre volume fractions were 64–68% for the aligned strand laminates and 54–58% for the fabric laminates.

Constant life diagrams

Constant amplitude tests at other R ratios generally show reducing fatigue lives as the mean stress increases above zero – whether in tension or in compression. It is customary to represent the results on a constant life diagram (or CLD), in which the stress (or strain) range to failure is plotted against mean stress (or strain) for different fatigue lives. Regression analyses can be carried out on families of test results at different R ratios to give a series of σ - N or ε - N relations in the form of Eq. (7.16), which can be used to plot the CLD, in which the results of each regression analysis are plotted out along a radial straight line corresponding to the appropriate R -value.

Figure 7.10 shows an example CLD constructed from a set of power law S - N curves fitted to MSU fatigue data for an MD laminate designated DD16 (Samborsky et al. 2007). The laminate was fabricated from E-glass non-woven fabric in

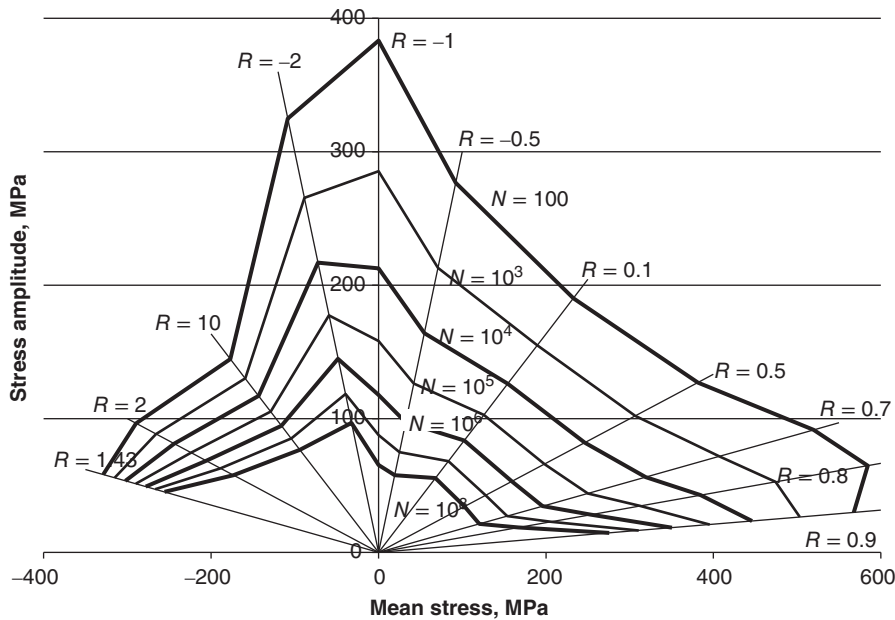


Figure 7.10 CLD in terms of stress for DD16 MD laminate with 36% fibre volume fraction, based on tests at MSU

a polyester matrix using vacuum assisted resin transfer moulding (VARTM – see Section 7.12). The lay-up was [90/0/ ± 45]_S with 53% of fibres in the axial (0°) direction, and the fibre volume fraction was relatively low at 36%. Note that the fatigue performance when the mean stress is tensile is inferior to that when the mean stress is compressive for an R ratio of $-0.5/-2$.

Clearly a significant number of fatigue tests need to be run to characterise the $S-N$ curve at each R ratio, so it is undesirable to investigate fatigue behaviour at more R ratios than necessary. Sutherland and Mandell (2004) computed the damages arising from the action of three different representative blade fatigue load spectra on the DD16 laminate, utilising the CLD reproduced in Figure 7.10, and investigated how the calculated damages changed as the number of R ratios used to produce the CLD was reduced.

One of the fatigue load spectra applied was that for a three bladed upwind turbine, and in this case more than 70% of the damage under edgewise bending occurred for $R = -0.5$, no doubt reflecting a tensile mean stress due to centrifugal loading. In the case of flapwise bending, the damage was slightly more dispersed, with more than 70% of the damage split between $R = 0.1$ and $R = 0.5$ on the tension bending side of the blade and almost 90% of the damage split between $R = -1$ and $R = -0.5$ on the compression side. As a result of this concentration of damage, it was found that a CLD constructed from tests at only five R ratios ($-2, -1, -0.5, 0.1$, and 0.7) resulted in a maximum error in lifetime prediction of only 8%, which was deemed to be acceptable. However, the draft IEC CD 61400-5 (2016) standard only requires testing at three representative R -values to satisfy its requirements for ‘full fatigue characterisation’.

The DD16 laminate was an early glass/polyester laminate, which had a fibre volume fraction much lower than is usual in wind turbine blade laminates today. More recent work at MSU (Samborsky et al. 2007) has established the CLD of glass/epoxy triaxial laminate QQ1 with a fibre volume fraction of 53%, which is more representative of current practice, and this is presented in terms of strain in Figure 7.11. The diagram has been derived from the best fit power law S - N curves by dividing the stresses by the laminate longitudinal modulus of 33 GPa. The lay-up was $[\pm 45/0_2]_S$, with 64% of fibres in the axial (0°) direction.

It is evident that the performance of laminate QQ1 is significantly worse in tension at high cycles, both when compared with laminate DD16 and with itself in compression. This was reported to be a common feature of many earlier infused laminates with a high fibre volume fraction.

The fatigue performance of a similar triaxial glass/epoxy laminate, MD2, was investigated as part of the OPTIMAT project, which was a relatively large rotor blade materials research project partially funded by the European Union and completed in 2006. The MD2 fibre volume fraction was similar to that of QQ1 at 54%, and the lay-up was $([\pm 45/0]_4; \pm 45)$, with 55% of fibres in the axial (0°) direction. Figure 7.12 shows the CLD for laminate MD2 in terms of strain derived from the best fit power law S - N curves reported in Krause and Kensche (2006) by dividing the stresses by a representative longitudinal modulus of 27.5 GPa. Also shown for comparison is the CLD for laminate QQ1 (dashed line), and it is apparent that, while a disparity between tensile and compressive fatigue performance remains for laminate MD2, it is less marked than for laminate QQ1.

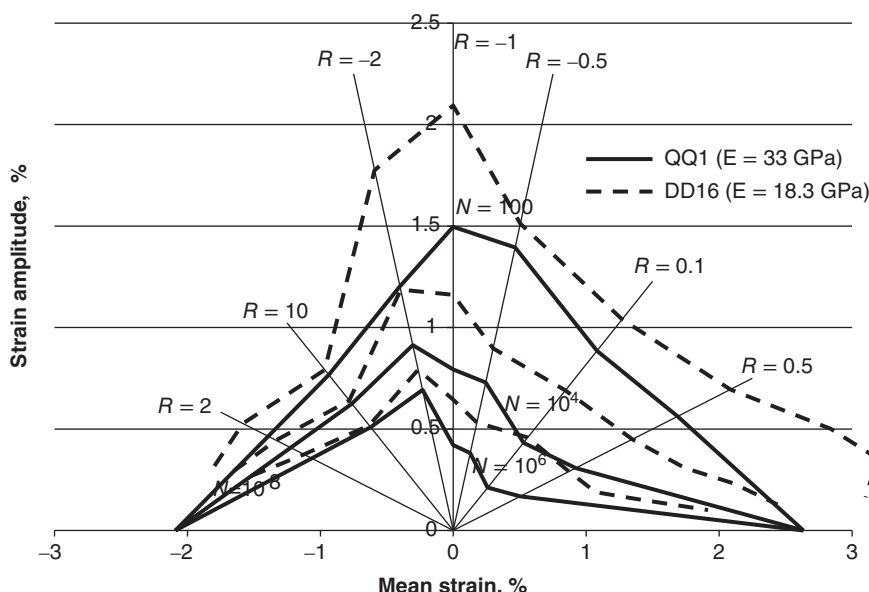


Figure 7.11 CLD in terms of strain for QQ1 triaxial laminate with 53% fibre volume fraction. The CLD for laminate DD16 is also shown (with dashed lines) for comparison, derived from Figure 7.10 using the laminate longitudinal modulus of 18.3 GPa

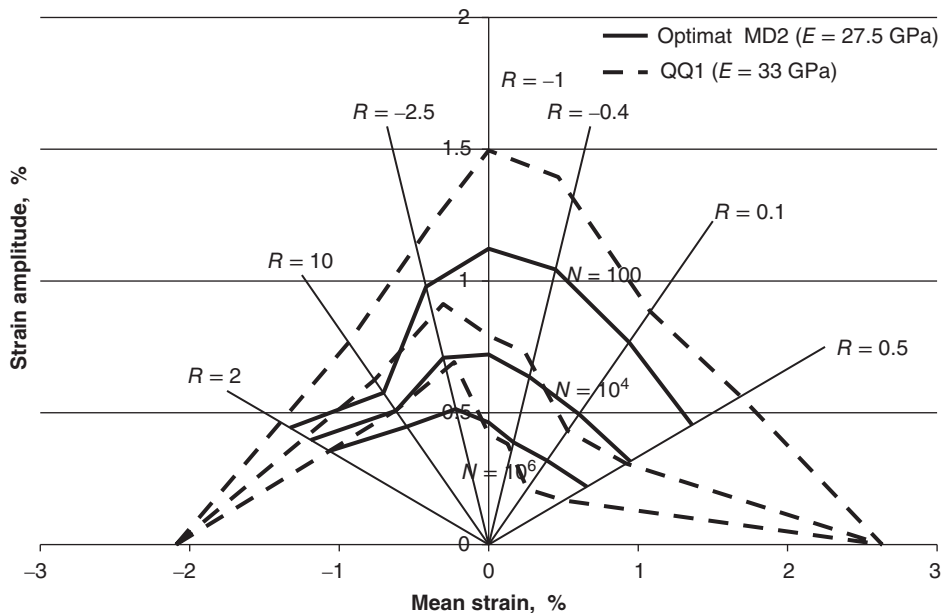


Figure 7.12 CLD in terms of strain for Optimat MD2 triaxial laminate with 64% fibre volume fraction. The CLD for laminate QQ1 is also shown (with dashed lines) for comparison

Linear Goodman diagram

In the preliminary stages of design, it is often convenient to use a much simpler, linear version of the CLD known as the *Goodman diagram*. This is based on the *S-N* curve for simple reverse fatigue loading (i.e. for $R = -1$) and assumes that the permitted strain amplitude reduces linearly with increasing mean strain for a given fatigue life, reaching zero at a mean strain corresponding to either the ultimate tensile or compressive strength. Such a linear CLD is shown in Figure 7.13 in terms of characteristic strains, based on an inverse slope of the $R = -1$ *S-N* curve of 10. The characteristic strain amplitude for $N = 1$ of 1.92% is estimated from the corresponding ECN regression line mean strain amplitude of 2.34% (Figure 7.9) by subtracting two standard deviations, assuming a coefficient of variation (COV) of 9%.

Note that an inherent feature of a linear CLD is that the *S-N* curves for R -values other than -1 do not plot as straight lines on a log-log plot.

In a linear CLD used for design, the characteristic strains ε_{0k} , ε_{tk} , and ε_{ck} in Figure 7.13 are replaced by design values. Thus the design strain amplitude when the mean stress is compressive becomes

$$\varepsilon_d(\bar{\sigma}, N) = \varepsilon_{0d} N^{-\frac{1}{m}} \left(1 - \frac{\bar{\sigma}}{\sigma_{cd}} \right) \quad (7.18)$$

where $\varepsilon_{0d} = \frac{\varepsilon_{0k}}{\gamma_{mf}}$, $\sigma_{cd} = \frac{\sigma_{ck}}{\gamma_{mu}}$, ε_0 is the value of ε given by the ε - N curve when $\log N$ is zero, $\bar{\sigma}$ is the mean stress for the loading cycles under consideration, and σ_{cd} is the design

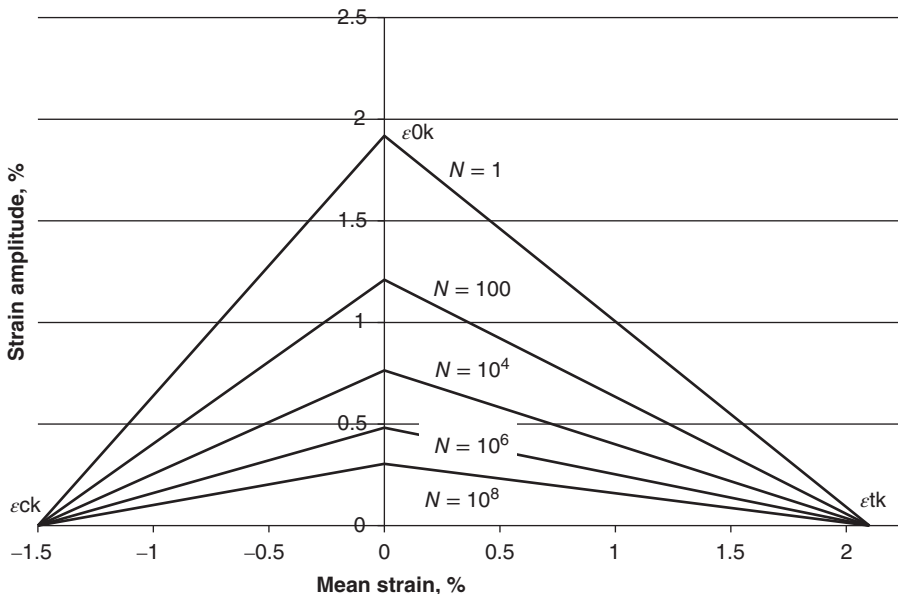


Figure 7.13 Linear CLD in terms of characteristic strains

ultimate compressive stress. γ_{mf} is the partial safety factor for fatigue strength, γ_{mu} is the partial safety factor for ultimate strength, and the suffixes d and k signify design and characteristic values, respectively.

In the simplified approach for taking account of mean stresses in the DNVGL standard *Rotor Blades for Wind Turbines* DNVGL-ST-0376 (2015), the CLD is similar to Figure 7.13 but is symmetrical about a strain level midway between the ultimate tensile and compressive strains, with ϵ_0 set equal to the mean of the absolute ultimate tensile and compressive strains. An example CLD is illustrated in Figure 7.14 for $m = 10$, but with the materials safety factors omitted.

Thus the number of cycles permitted for a strain range of $0.45/\gamma_{mf}\%$ and a mean strain of $0.3/\gamma_{mu}\%$ would be 10^6 .

Miner's damage sum

Equation (7.18), together with its equivalent for mean tensile loading, can be used to calculate the permissible number of load cycles, N_i , for each stress or strain range in the fatigue loading spectrum for the point in the blade cross-section under examination. These are then combined with the predicted number of cycles for each stress or strain range, n_i , to yield Miner's damage sum, $\sum_i \frac{n_i}{N_i}$, which is normally required to be less than unity.

Load sequence effects

There is inevitably a degree of uncertainty as regards the accuracy of Miner's rule in predicting the fatigue damage due to variable amplitude loading from constant amplitude test data, as it is unable to take into account the fatigue loading sequence. To investigate

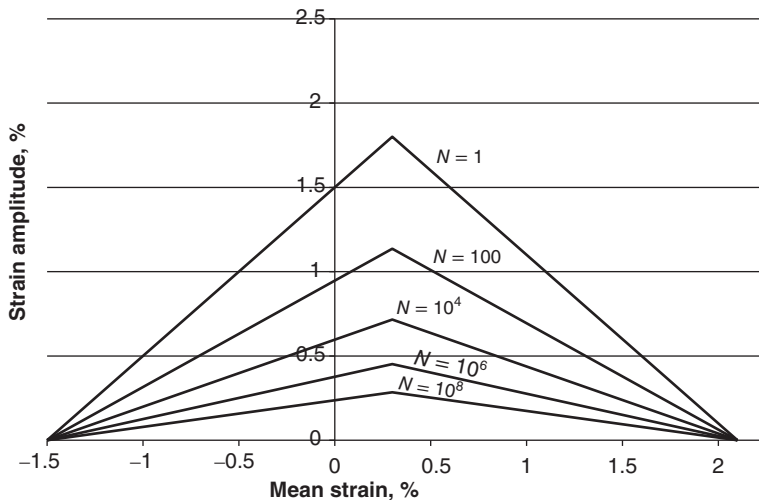


Figure 7.14 Modified linear CLD in terms of characteristic strains, based on the DNVGL simplified approach

this, fatigue test programmes have been carried out using the WISPER (Wind SPEctrum Reference) and WISPERX variable amplitude fatigue load spectra, which have been devised to be representative of those experienced by wind turbine blades. (WISPERX is a modification of WISPER in which the large number of small cycles, accounting for approximately 90% of the total, are omitted to reduce test durations.) For each test specimen, the WISPER (or WISPERX) load sequence is scaled to give a chosen maximum stress level and applied repeatedly until the specimen fails.

Van Delft et al. (1996) analysed the results of a series of tests carried out at ECN and Delft Technical University on a 0° , $+/-45^\circ$ laminate and found that, for a maximum stress of about 150 MPa, the actual fatigue lives of specimens subjected to repetitions of the WISPER or WISPERX load sequences were about 100 times less than predicted for these sequences on the basis of constant amplitude, reverse loading test data, and Miner's rule, with the effect of mean stress allowed for using the linear relation described above. The $R = -1$ test data led to an $S-N$ curve given by $N = (\sigma/\sigma_{tu})^{-10}$, where σ is the amplitude of the stress cycles and σ_{tu} is the UTS, so the number of cycles to failure for constant amplitude loading at other R -values was taken as $N = \left(\frac{\sigma}{\sigma_{tu}(1 - \bar{\sigma}/\sigma_{tu})} \right)^{-10}$ for a tensile mean and $N = \left(\frac{\sigma}{\sigma_{tu}(1 - \bar{\sigma}/\sigma_{cu})} \right)^{-10}$ for a compressive mean in calculating the Miner's damage sum. The difference in fatigue lives at the stated maximum stress level quoted above translates to an approximate ratio of 1:1.5 between actual and predicted maximum stress levels of the WISPER sequence to cause failure over the design fatigue life, which would clearly use up a substantial proportion of the safety factors used in design. However, other investigators working with different laminates have found reasonable agreement between measured and predicted fatigue lives under WISPER loading (see chapter entitled 'Influence of Spectral Loading' in Mayer 1996).

Further testing of specimens using repetitions of WISPER and WISPERX load sequences scaled to varying maximum stresses was carried out as part of the OPTIMAT

project and the results compared with predictions based on Miner's damage summations, using both linear and multiple R -value CLDs (Nijssen 2005). The life predictions based on the linear CLDs were found to be between 10 and 100 times greater than the measured lives, with the DNVGL variant being slightly less conservative than the standard one. However, the predictions based on a CLD plotted from S - N curves at six different R -values were much more accurate.

The OPTIMAT project also developed a new reference fatigue load spectrum for test purposes that was designed to be more representative of the flapwise bending loading cycles experienced by pitch-regulated blades on megawatt or multi-megawatt turbines (Bulder 2005).

Strength degradation models

In strength degradation models, the residual static strength of the composite is taken to reduce monotonically as fatigue loading is applied, with failure occurring when the maximum stress of a fatigue loading cycle exceeds it.

In one of the simpler models, the reduction in static strength under constant amplitude loading is proportional to the number of loading cycles raised a certain power:

$$S_r = S_0 - (S_0 - S_{max}) \left(\frac{n}{N} \right)^C \quad (7.19)$$

where S_r is the residual static strength, S_0 is the initial strength, S_{max} is the maximum fatigue stress, and C is the strength degradation parameter. The reduction in residual strength during constant amplitude fatigue loading is illustrated in Figure 7.15 for three different strength degradation parameters.

Static testing of specimens subjected to varying proportions of expected fatigue life was carried out to characterise strength degradation as part of the OPTIMAT project (Nijssen 2007). This work demonstrated that when a tensile loading component was present, the tensile strength degradation was approximately linear, with C close to

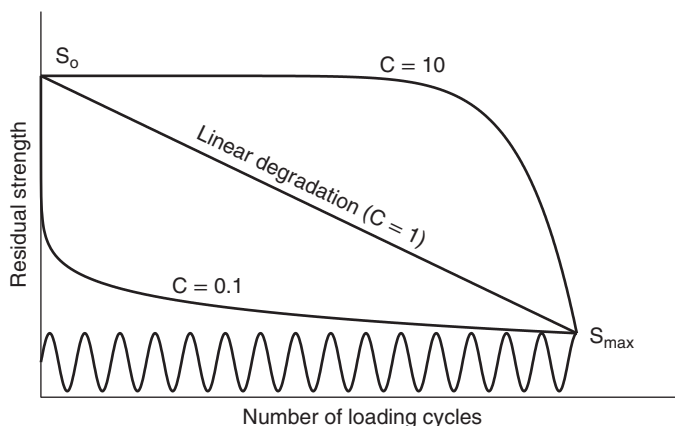


Figure 7.15 Reduction of residual strength with number of constant amplitude loading cycles for different strength degradation parameters

unity. In the case of compression loading, however, very little strength degradation was observed before failure, corresponding to a high value of C .

The OPTIMAT project went on to investigate the effect of load sequence in a series of tests in which a block of high amplitude fatigue cycles was followed by a block of low amplitude fatigue cycles (high–low loading) and vice-versa. In each case, the first block used up half of the nominal fatigue life. Figures 7.16 and 7.17 compare the theoretical residual strength profiles for high–low and low–high loading, respectively, for load levels predicted to result in failure after 10^4 and 10^6 cycles. Based on an assumed linear strength degradation, the figures demonstrate that the Miner's sum at failure is much higher for high–low loading than for the reverse. The OPTIMAT two-block tests fell into a similar pattern for $R = 0.1$ and $R = -1$ loading.

The OPTIMAT project also compared life predictions for repeated WISPER fatigue loading sequences made using the strength degradation model with those based on the Miner's damage sum, utilising the full CLD in each case, but found that there was hardly any difference between them (Nijssen 2005).

This led to the conclusion that there is no benefit from the use of the significantly more computationally intensive strength degradation model.

Fatigue at structural details

Besides the uniform thickness laminates considered previously, a wind turbine blade contains steps in laminate thickness ('ply drops') and a variety of joints (e.g. spar to web, spar to sandwich panel, and sandwich panel to sandwich panel at the trailing edge) involving adhesives, which require separate fatigue testing.

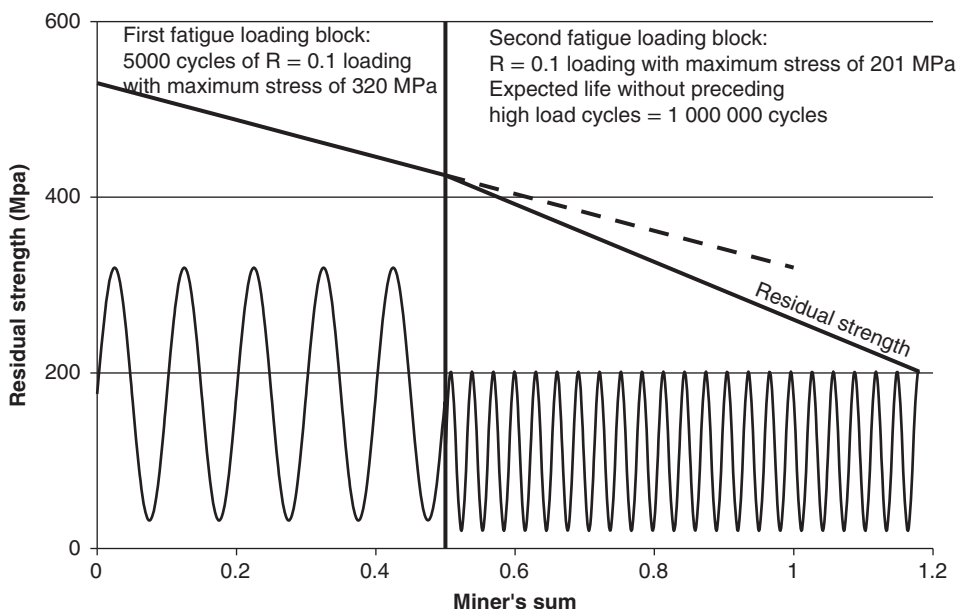


Figure 7.16 Two-block high–low $R = 0.1$ fatigue loading, with half the predicted number of cycles to failure in the first block

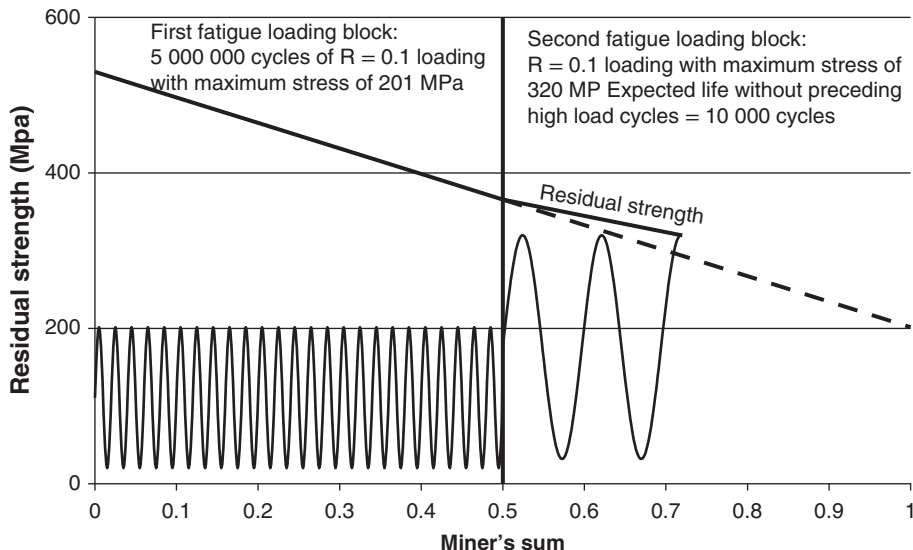


Figure 7.17 Two-block low–high $R = 0.1$ fatigue loading, with half the predicted number of cycles to failure in the first block

7.1.9 Carbon fibre composites

Carbon fibre properties

Carbon fibres can be separated into two main types, PAN and pitch, according to the raw material used for their manufacture – i.e. polyacrylonitrile and petroleum pitch, respectively. The properties of each type can vary considerably, depending on the manufacturing process, but PAN fibres, which are preferred for wind turbine blades, are generally of higher strength and lower modulus than pitch fibres.

The modulus of elasticity of PAN carbon fibres ranges from 200 to 500 GPa, but cost increases steeply with modulus, so wind turbine blades normally utilise fibres with a modulus at the lower end of this range. Example properties of two such fibres are given in Table 7.7.

Table 7.7 Properties of two PAN carbon fibres used in composites for wind turbine blades

Name of manufacturer and carbon fibre designation	Zoltek PX35	Hexcel AS4/12k
Tensile modulus (GPa)	242	231
Tensile strength (GPa)	4.137	4.413
Elongation %	1.7	1.7
Density (gm/cm ³)	1.81	1.79
Fibre diameter (microns)	7.2	7.1
No. of filaments in tow	50 000	12 000
% carbon	95	94

Carbon fibre composite properties

Static properties of two example CFRPs are given in Table 7.1.

CFRPs are subject to a significantly smaller reduction in fatigue strength with increasing number of loading cycles compared with glass fibre composites, with the draft IEC CD 61400-5 (2016) recommending the use of an *S-N* curve inverse slope of 14 for CFRP as opposed to 10 for glass/epoxy laminates in the absence of fatigue testing. In practice, *S-N* curve slopes much less than 1/14 have been obtained from test results, with a maximum slope of 1/25 being reported from tests at a variety of R-values on the P2B hybrid laminate detailed in Table 7.1. These low *S-N* curve slopes are reflected in the CLD for the P2B hybrid laminate – see Figure 7.18.

Pultrusion

Pultruded plates are increasingly being used in spar caps in place of pre-pregs, as they offer significant benefits in terms of product uniformity, fibre straightness, and low void content. After passing through a resin bath, carbon fibre tows are pulled through a heated die where the resin undergoes polymerisation. The pultruded plates are typically a few millimetres thick and are stacked together in the mould to form the spar cap. One of the key advantages of pultrusion is the fibre straightness inherent in the process, which results in increased strength in compression.

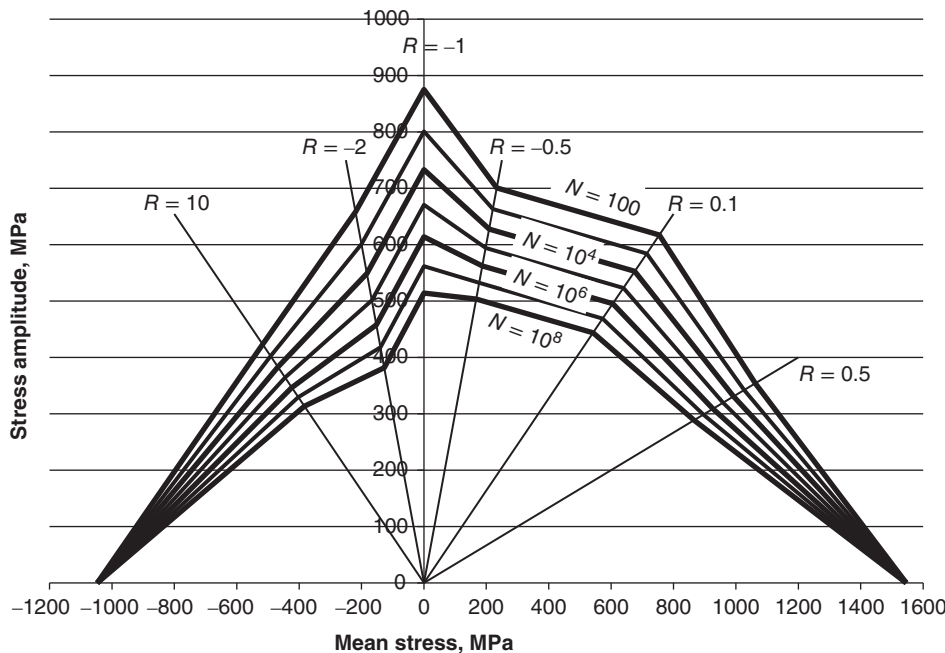


Figure 7.18 CLD for P2B hybrid laminate with 55% fibre volume fraction and $[\pm 45/0_4]$ lay-up; 85% (by volume) carbon fibre (Newport NCT-307-D1-34-600 pre-preg) in 0 deg. direction and 15% (by volume) glass fibre in ± 45 deg. directions based on tests at MSU (Samborsky et al. 2007)

Benefits versus cost

A rough like for like comparison of GFRP and CFRP UD laminate mechanical properties can be carried out by comparing those of the PPG-Devold glass-epoxy laminate (material 2 in Table 7.1) with those of the hybrid P2B carbon fibre laminate (material 4 in Table 7.1) scaled by the product of the fibre volume fraction ratio (59/55) and the UD % ratio (92/85) – see Table 7.8.

The table indicates that the benefit of increased static strength afforded by carbon fibre is less than the increase in stiffness, but that the increase in fatigue strength is significantly greater.

An indication of the potential blade weight savings achievable with carbon fibre is given in the Sandia report on the SNL100-01 blade (Griffith 2013). This investigated the replacement of the glass fibre spar caps on the SNL 100-00 all-glass 100 m long blade (Griffith and Ashwill 2011) by narrower carbon fibre ones sized to maintain approximately the same flapwise stiffness. It was concluded that the spar cap cross-sectional area could be reduced by 63%, resulting in a 36% weight reduction (from 115.7 t to 74 t).

Table 7.8 Comparison between GFRP UD laminate mechanical properties and CFRP ones scaled to the same fibre volume fraction and percentage of UD fibres

Material	Fibre volume fraction V _f	% of UD fibres	Density (gm/cm ³)	Modulus E GPa	UTS MPa	UCS MPa	10 ⁷ cycle fatigue strength (amplitude)
PPG-Devold glass/epoxy laminate (material 2 in Table 7.1)	59%	92%	2	44	1025	575	180
P2B carbon fibre/glass fibre/epoxy hybrid laminate (material 4 in Table 7.1)	55%	85%	1.57	100	1550	1050	560
Scaled P2B properties – i.e. multiplied by (59/55)(92/85)				116	1800	1220	650
Ratios of scaled P2B CFRP mechanical properties to GFRP values				2.64	1.76	2.12	3.61

Materials and manufacturing costs of the SNL 100 m blades were investigated in Griffith and Johanns (2013) using the Sandia Blade Manufacturing Cost Tool (Johanns and Griffith 2013). Based on the glass fibre and epoxy resin costs of \$2.97/kg and \$4.65/kg quoted in the Cost Tool and assuming densities of 2.55 and 1.15 g/cc, respectively, the materials cost per unit volume of a UD GFRP laminate with 55% fibre volume fraction comes to \$6570/cum. Similarly, based on a carbon fibre cost of \$26.4/kg and a density of 1.8 g/cc, the materials cost per unit volume of a UD CFRP laminate with the same fibre volume fraction comes to \$28 500/cum – about 4.3 times as much as for the GFRP. Thus, if the blade design is governed by tip deflection so that the CFRP spar cap cross-sectional area can be made 1/3 that of the GFRP spar cap, there will still be a spar cap cost increase of more than 40%. This may, however, be justified by material savings in the hub, pitch mechanism, low-speed shaft, and nacelle bedplate made possible by the reduced gravity loading from the rotor. In the case of the SNL 100 m blades, it was estimated that, while the replacement of the GFRP spar caps by CFRP increased the total materials cost of the blade by 15% (from \$459k to \$530k, based on the respective bills of materials and the Cost Tool materials costs/kg), the installed capital cost of the whole wind turbine reduced by 0.8% (Griffith and Johanns 2013).

It is estimated that, globally, about 25% of wind turbine blades are now manufactured with carbon fibre spar caps (Legault 2018).

7.1.10 Properties of wood laminates

Although laminated wood/epoxy is classed as a composite, it is markedly different in form from GFRP. Individual plies are made up of large sheets of wood veneer (plate 2) instead of a multiplicity of fibres laid up in a matrix, and the epoxy behaves as an adhesive rather than a matrix, bonding the sheets together at the longitudinal and transverse joints and bonding each ply to its neighbour. Thus the fibre volume fraction is close to 100%, and the anisotropic properties of the wood laminate derive principally from the anisotropic properties of the wood itself.

Static properties

Wood strength properties are much greater in the direction parallel to the grain, so all of the veneers are orientated with the grain parallel to the blade axis to resist blade bending loads efficiently. However, the veneers cannot be produced in lengths much greater than 2.5 m, so transverse joints have to be included, which introduces lines of weakness not normally found in GFRP blades. The effect is minimised by staggering the joints and by using scarf joints in preference to butt joints.

The epoxy adhesive has a secondary function of sealing the veneers against moisture ingress; additional moisture protection is provided by a layer of glass/epoxy on both the external and internal surfaces. It is important to maintain moisture content at a low level, because veneer strength decreases about 6% for every 1% rise in moisture content.

A comparison of some of the properties of wood laminates used, or considered for use, in wind turbine blades is given in Table 7.9. Khaya ivorensis, an African mahogany, and Douglas fir used to be the main species used for blade manufacture in the UK and US, respectively, but environmental pressures have led to the phasing out of Khaya in favour of European species such as poplar and birch.

Table 7.9 Properties of unjointed wood/epoxy laminates

Species	Specific gravity	Mean tensile strength along the grain, MPa	Mean compression strength along the grain, MPa	Young's modulus along the grain, GPa	Shear strength, MPa
Khaya ivorensis	0.55	82	50	10	9.5
Poplar	0.45	63	52	10	9
Baltic pine	0.55	105	40	16	
Birch	0.67	117	81	15	16
Beech	0.72	103	69	10	16
Douglas fir	0.58	100	61	15	12

The table gives tensile strengths of unjointed specimens. Bonfield et al. (1992) report the results of tests on jointed specimens, which showed a significant reduction in tensile strength to 50 MPa for butt jointed Khaya. Scarf jointed Khaya specimens, with a 1:6 length to thickness ratio, performed much better, achieving a tensile strength of 75 MPa. In all cases the joints in the different veneers making up the laminate were staggered.

An important consideration for design is the variability of strength properties, particularly as wood is an inherently variable material. Strength tends to increase with density, and density varies according to the growing conditions of the tree and the part of the tree from which the wood is taken. Such variability can be reduced by careful grading and the rejection of damaged veneers before laminating. Bonfield and Ansell (1991) report compression tests on 32 carefully selected Khaya samples that yielded the compression strength of 50 MPa given in the table with a standard deviation of only 3 MPa. It should be noted that the lack of annual growth rings in equatorially grown wood may reduce the degree of scatter.

Wood strengths perpendicular to the grain are typically much less than those along the grain – for example, the compressive strength of transversely loaded Khaya is only 12.6 MPa.

Fatigue properties

The fatigue properties of wood laminates have been the subject of a sustained programme of work at Bath University, starting with Khaya and then extending to other species (Bonfield et al. 1992). A useful summary of this work appears in Bond and Ansell (1998). The general conclusion is that wood performs very well in fatigue with a shallow *S-N* curve slope, and that fatigue strengths at high cycles do not vary greatly between species.

If the *S-N* curve for constant amplitude, reverse loading ($R = -1$) fatigue is normalised with respect to the UCS, σ_{cu} – i.e. $\sigma = \sigma_{cu}N^{-\frac{1}{m}}$, then the results of tests on unjointed Khaya indicate a value of the index m of about 20. However, the value of m reduces to about 16 for scarf jointed khaya, poplar, and beech and to about 13 for butt jointed specimens. Hancock and Bond (1995) have proposed the use of an index of 13.4 for design purposes for scarf jointed wood laminates in general.

7.1.11 Material safety factors

Limit state design requires that the characteristic strength of a material be divided by a partial safety factor for material strength. In the case of GFRP, this factor needs to take account of degradation of the material over time as well as the material's inherent variability.

In both the DNVGL standard *Rotor Blades for Wind Turbines* DNVGL-ST-0376 (2015) and the draft IEC CD 61400-5 (2016) standard, the partial safety factor for material strength is expressed as the product of a series of component factors designed to account for different areas of uncertainty, as follows:

$$\gamma_m = \gamma_{m0} \cdot \gamma_{mc} \cdot \gamma_{m1} \cdot \gamma_{m2} \cdot \gamma_{m3} \cdot \gamma_{m4} \cdot \gamma_{m5} \quad (7.20)$$

γ_{m0} is the ‘base material factor’ and is always 1.2. γ_{mc} is a ‘factor for the criticality of the failure mode’ that features in the DNVGL standard only and takes the value 1.08. Values of the components of the partial safety factor for material strength in the two standards are given for the ultimate strength and fatigue limit states in Table 7.10. Somewhat surprisingly, the last component, γ_{m5} , relates to the potential inaccuracy of the loads rather than material strength uncertainty. The standards also give values of $\gamma_{m1}-\gamma_{m5}$ to be used for the investigation of inter-fibre failure, sandwich core failure, sandwich skin buckling, global panel buckling, and bonded joint failure.

7.1.12 Manufacture of composite blades

The vast majority of blades are manufactured in moulds in two halves, which are afterwards glued together. As blades become longer, however, some manufacturers are exploring segmental construction involving one or more transverse joints. An alternative approach is to construct the blade spar by filament winding onto a mandrel and build out the rest of the aerofoil section subsequently. This rest of this section describes the different approaches to blade construction in more detail.

Mould lay-up

The half shells forming the pressure and suction faces of a blade are typically manufactured separately and then glued together, with the shear webs placed between them. Separate moulds conforming to the geometry of the pressure and suction faces are constructed, and the fibre reinforcement, in the form of fabric or rovings, is laid in each mould in combination with sheets of foam or balsa for the sandwich panel cores. It is normally necessary to make longitudinal incisions in the core sheets so that they can be deformed to follow the curvature of the aerofoil section. The positioning of the glass fibre fabrics in the moulds does not lend itself to automation because of complex geometries, so hand lay-up is the norm.

A blade surface coating – often utilising the same material as the blade structure matrix – is frequently applied to the inside of the moulds before fibre reinforcement lay-up. Alternatively, a different coating material can be applied to the completed blade as a paint or spray. The surface coating is often referred to as *gel-coat*, irrespective of the material used or the method of application.

Table 7.10 Partial material factors for composite blades

Structural element		Laminate ultimate strength		Laminate fatigue strength	
Code		IEC 61400-5 (draft)	DNVGL -ST-0376	IEC 61400-5 (draft)	DNVGL -ST-0376
Symbol	Type of effects covered	Design basis			
γ_{m0}	'Base' material factor	Applies always	1.2	1.2	1.2
γ_{mc}	Criticality of failure mode	DNVGL-ST-0376 only. Applies always	N/A	1.08	N/A
γ_{m1}	Environmental degradation (non-reversible)	Properties based on room temp, dry mechanical props Properties account for degradation	1.2 1.0	1.2/1.3 Epoxy/ polyester	1.1 1.1 1.0
γ_{m2}	Temperature effects (reversible)	Properties based on room temp. Properties tested over operational temp range	1.1 1.0	1.1 1.0	1.0 1.0
γ_{m3}	Manufacturing effects	Nominal design props Properties allowing for manufacturing tolerances Properties based on validated effect of manufacturing tolerances	1.3 1.1 1.0	1.3 1.1 1.0	1.3 1.1 1.0
γ_{m4} (A)	Calculation accuracy and validation	Strain calculation not verified Strain calculation correlated to full blade test	1.2 1.0	1.0 1.0	1.2 1.0

(Continued)

Table 7.10 (*continued*)

Structural element		Laminate ultimate strength	Laminate fatigue strength		
Υ_{m4} (B)	Calculation accuracy and validation: fatigue model	Static strength and assumed Wohler slope in conjunction with linear Goodman diagram	N/A	N/A	1.2
		Static strength and measured Wohler slope in conjunction with linear Goodman diagram	N/A	N/A	1.1
		Full fatigue characterisation	N/A	N/A	1.0
Υ_{m5} (A)	Resolution of load direction	Loads in two orthogonal directions	1.2	1.2	1.2
		Loads in directions spaced at 30°	1.0	1.0	1.05
		Strain spectrum evaluated from exact strain history (from time series)	N/A	N/A	1.0
Υ_{m5} (B)	Resolution of fatigue load spectrum	Use of equivalent moments	N/A	N/A	1.1
		Use of full fatigue load description – e.g. Markov matrix, time series	N/A	N/A	1.0
Minimum combined materials factor		1.2	1.711	1.2	1.426
Maximum combined materials factor		2.965	2.891	3.262	3.94
Maximum combined materials factor with accurate loads and $S-N$ curve (assuming epoxy matrix for DNVGL-ST-0376)		$1.2 \times 1.2 \times 1.1 \times 1.3 \times 1.2 = 2.471$	$1.2 \times 1.08 \times 1.2 \times 1.1 \times 1.3 = 2.224$	$1.2 \times 1.1 \times 1.3 \times 1.2 = 2.059$	$1.2 \times 1.08 \times 1.1 \times 1.3 = 1.853$

Resin application

Fabric lay-up is followed by resin application and curing. The resin can be applied by hand using brush or roller, resulting in fibre volume contents of typically 30–40%, but use of ‘vacuum bagging’, in which trapped air and excess volatile compounds, such as residual solvent, are extracted, consolidates the composite and allows a volume fraction of 50% or more to be achieved.

Vacuum resin infusion

Vacuum resin infusion, or VARTM, uses atmospheric pressure to drive the resin into fibre reinforcement and is now increasingly preferred, as it has the advantage of enabling a higher fibre volume fraction of 55–60% to be achieved, resulting in increased stiffness and strength. Other important benefits are a reduction in the wastage of resin and a better working environment, because of reduced exposure to resin fumes.

As usual, it is essential that the resin has impregnated the reinforcement in all parts of the blade before it has begun to harden. Accordingly, it is normal to insert a layer of a suitable flow medium between the glass layers to facilitate the flow of resin from the entry points. Several different flow media are available, ranging from a matting of randomly oriented entangled nylon filaments to dual-purpose sandwich core foam material, which incorporates grooves and perforations to allow the resin to flow along the laminate.

The preparations for vacuum resin infusion can be broken down into the following stages:

1. Lay-up of the fibre reinforcement fabrics and rovings within the mould, together with foam or balsa sheets for the sandwich panels and sheets of the flow medium.
2. Positioning of resin delivery tubes within the mould. These can have permeable walls to allow delivery of resin along their length.
3. Enclosure of the mould and contents inside a plastic vacuum bag.
4. Connection of the vacuum pump to the bag and proving of the vacuum. Much attention must be given to this as even the smallest leak can be very damaging.
5. Catalysis of the resin.

Pre-pregs

Pre-pregs are UD fibre reinforcements or woven fabrics that have been pre-impregnated with either a thermoset or thermoplastic resin. Their use allows the resin content to be controlled accurately and results in better mechanical properties per unit weight.

The thermoset resin partially cures on application, leaving the pre-preg pliable, but the product has to be stored in refrigerated conditions until use. After lay-up in a mould, curing is completed at temperatures in the range 70°–120° C, with close control of temperatures during heating, soaking, and cool down. Pressure also needs to be applied to remove entrapped air – this is done by vacuum bagging or in an autoclave.

If a thermoplastic resin is used, the pre-pregs do not need to be stored in a refrigerator but instead need to be heated to permit lay-up as they are rigid at room temperature. Thermoplastic pre-pregs offer benefits in terms of shorter mould cycle times

and recyclability, but despite significant R&D effort, have yet to be taken up by manufacturers, probably because of the high processing temperatures, which are in the range 160°–250° C.

Assembly of half shells

Following curing of the two half shells, one of them must be turned upside down to offer it up to the other. This can most conveniently be accomplished if the two moulds are supported side by side in a single frame and the two halves hinged along the longitudinal axis midway between them.

Before the two half shells are assembled, the shear web(s) must be glued in position on one of the halves. Depending on the size of the blade, access to the glued joint between the shear webs and the second half shell for inspection purposes after assembly may be limited or impossible, so a thick adhesive paste is applied to the exposed upper edge (or flange) of the shear web(s) to take up the inevitable variations in the expected gap and ensure a sound joint. At the leading edge, the joint between the two half shells is often made with a lap joint.

Segmental construction

The difficulties inherent in transporting long blades along sinuous roads has meant that the largest turbine size considered for onshore sites has, until recently, normally been in the range 2–3 MW. However, some manufacturers are now circumventing these difficulties by constructing blades in two or more sections and assembling them on site. For example, the blades of the Gamesa G128 4.5 MW turbine consist of a 30.5 m inboard section and a 32 m outboard section, allowing each to be transported to site on a standard 90 ft (27.4 m) flatbed trailer (Gardiner 2013) before they are bolted together. Each blade section is connected to metallic adaptors at the joint centre by rows of bolts oriented parallel to the blade axis and lying just within each face. Metallic inserts transfer the bolt loads into the blade laminate via a double-lap shear joint.

Enercon have also adopted segmented blade construction with a bolted transverse joint for their larger blades (Windblatt 2013).

Metallic blade joints inevitably add significant localised masses, reducing the blade's natural frequency. In the case of the Gamesa G128, it is reported that the estimated 10% increase in cost is more than offset by transport savings. However, Blade Dynamics have demonstrated that the need for bolted joints can be avoided in segmented blades, using bonding to join the blade sections instead.

Filament winding

If the load-bearing structure is limited to a compact closed hollow section spar, consisting of two shear webs and the skin sections between them, then it lends itself to filament winding, a semi-automated process in which a continuous reinforcement is wound onto a rotating mandrel. The reinforcement is fed through a resin bath and then through a delivery eye that moves to and fro along the mandrel, with the relative speeds of the delivery eye and of the rotation of the mandrel controlling the final fibre orientation. Unfortunately, a drawback inherent in the process is that the filament cannot be laid in the axial direction along which the bending stresses act.

Enercon have adopted filament winding for the manufacture of the inner sections of the blades for their 115, 126, and 141 m diameter turbines (Windblatt 2013, 2016). The inner sections transition from a cylindrical cross-section at the root to oval at the outer end. On the 115 m diameter turbine the inner section is about 12 m long and on the larger turbines longer, identical inner sections are used on both blades.

7.1.13 Blade loading overview

This section explores the variation of extreme and fatigue loading with wind speed and yaw angle, utilising the theory of Section 4.2 and focussing on flapwise bending close to the blade root by way of example. The turbine considered is an 80 m diameter machine, with SC40 blades, as described in Figure 5.4a.

Extreme loading during operation: stall-regulated machines

The stall-regulated machine considered operates at a single rotational speed of 15 rpm and generates 2.0 MW at a rated speed of 16 m/s.

The blade loadings on the outer half of the blade are calculated using empirical three-dimensional (3-D) aerodynamic data taken from Petersen et al. (1998), with extrapolation of the lift and drag coefficient curves beyond 30° angle of attack (the upper limit of the data). The 3-D data displays a gentler stall than typical two-dimensional data, so there is no significant reduction in blade out-of-plane bending moment as the blade goes into stall. The blade loadings on the inner half of the blade are calculated using corrected 3-D data developed for the DTU 10 MW reference wind turbine (Bak et al. 2013) for t/c ratios of 24.1, 30.1, 36, 48, and 60%, accessed from the data repository. These utilise values of lift and drag coefficients for flat plates at large angles of attack. Above about 20 m/s, the out-of-plane bending moment begins to increase progressively once again as drag begins to become significant. The predicted variation of blade 0 m radius out-of-plane bending moment (i.e. the bending moment at the hub centre) with wind speed is plotted out for a zero shear exponent, zero shaft tilt, and a range of yaw angles on Figure 7.19, with the yaw direction defined as positive when the lateral component of air flow with respect to the rotor disc is in the same direction as the blade movement at zero azimuth (i.e. at 12 o'clock). For negative yaw, the effect of the increase in relative velocity outweighs that of the reduction of angle of attack at wind speeds beyond stall, so the bending moment at 0° azimuth is increased. If wind shear were included, maximum moments would occur at negative yaw angles and 0° azimuth rather than at positive yaw angles and 180° azimuth, because wind shear augments the wind speed in the former case. The effect of wind shear on blade root out-of-plane bending moment at 0° azimuth for zero yaw is shown by the dashed line.

The plots of the extreme out-of-plane bending moment in Figure 7.19 are conservative on three counts, because no allowance is made for the following:

- Lack of correlation of the wind over the blade length.
- Limitation on maximum wind speed seen during operation by high wind cut-out.
- Limitation on maximum yaw angle by yaw control.

The alleviation of extreme loadings by high wind cut-out and yaw control depends on the averaging times applied to the wind speed and direction signals by the control system.

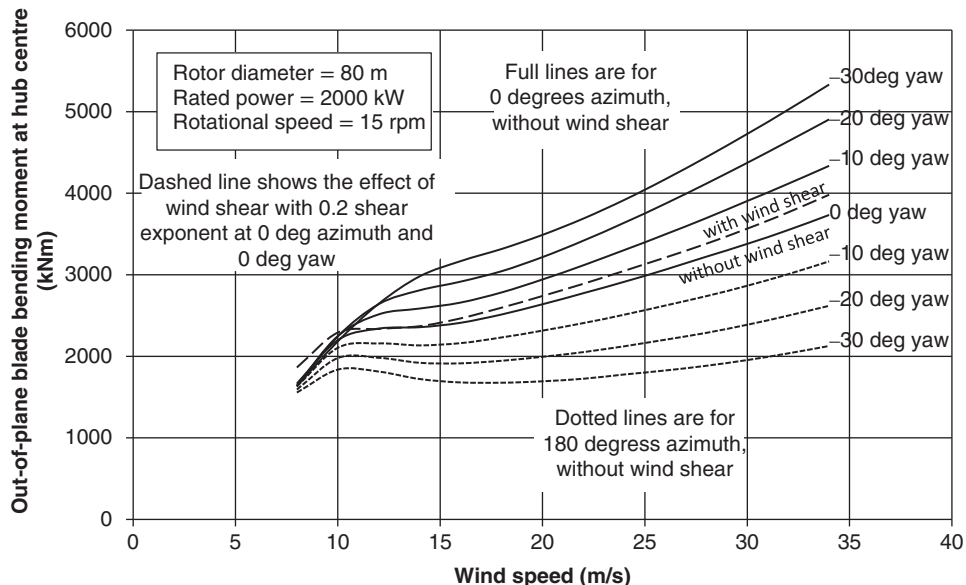


Figure 7.19 Variation of blade root out-of-plane bending moment with wind speed at various yaw angles for an example 80 m diameter stall-regulated turbine

Extreme loading during operation: pitch-regulated machines

The characterisation of extreme operational loadings on pitch-regulated machines is inevitably more complicated than for stall-regulated machines, although at the same time it should be more accurate because of the avoidance of uncertainties associated with stall. It is instructive to focus comparisons on the blade bending moment about the weak axis at the root once again. This time it is referred to as the *flapwise bending moment* rather than the out-of-plane (of rotation) moment because of blade pitching.

Figure 7.20 presents the variation of 0 m radius flapwise bending moment (i.e. the bending moment at the hub centre) with short-term mean wind speed at several yaw angles for a 1700 kW, 80 m diameter pitch-regulated machine rotating at 15 rpm. The rated speed is 11.2 m/s, and other parameters, including the zero wind shear exponent, are the same as in the stall-regulated example above. The blade loadings are calculated using the same aerodynamic data as for the stall-regulated machine but with extrapolation of the Petersen et al. (1998) lift and drag coefficient curves to negative angle of attack. The figure only shows the bending moments resulting from slow variations in wind speed – i.e. those that can be followed by the pitch control system – so moments arising from faster wind speed fluctuations must be added to obtain the total.

The curves are very different in shape from those obtained for the stall-regulated machine. The 0 m radius flapwise bending moment reaches a peak at rated wind speed, and then drops off sharply, for all yaw angles. At high wind speeds, increasingly large negative bending moments are developed at 180° azimuth for positive yaw angles and at 0° azimuth for negative yaw angles, which can be comparable in magnitude to the peak positive moment at rated speed. Note that the bending moment *reduces* with increasingly

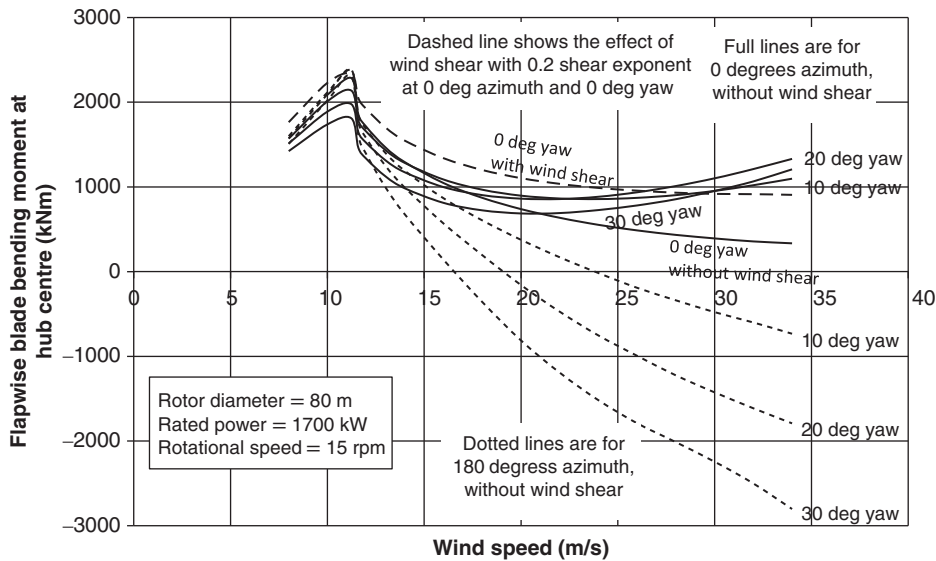


Figure 7.20 Variation of blade root flapwise bending moment with wind speed at various yaw angles for an example 80 m diameter pitch-regulated turbine

negative yaw angle at zero azimuth, instead of increasing as it does for stall-regulated operation. This is because blade pitching renders angle of attack, which starts to become negative under these conditions, more critical than relative velocity.

To the extent that the pitch control system can keep pace with the wind speed transients, the curves in Figure 7.20 can be used to provide an approximate indication of the extreme bending moments arising from some of the IEC 61400-1 deterministic load cases. It is seen that the extreme moments are only about 1/2 of the maximum value for the stall-regulated machine.

The spectrum of the longitudinal wind speed fluctuations will contain significant energy at frequencies above the level at which the pitch control system can respond, and these have to be considered in the analysis of the ‘normal turbulence model’ load case. Figure 7.21 illustrates the perturbations in the 0 m radius flapwise bending moment at 0° and 180° degrees azimuth for the above machine, as a result of such high frequency wind speed fluctuations with respect to sharp rises and falls in wind speed with respect to steady wind speeds of 14 and 20 m/s for a +20° yaw angle.

Over the machine lifetime, the maximum increase in wind speed above rated that does not produce a blade pitch response can be estimated using

$$\begin{aligned}
 u_{\max} &= \sigma_u \sqrt{\frac{\int_{\Omega/2}^{\infty} S_u(n)}{\int_0^{\infty} S_u(n)}} \left[\sqrt{2 \ln(\Omega T)} + \frac{\gamma}{\sqrt{2 \ln(\Omega T)}} \right] \\
 &= (\sigma_u)_{n>\Omega/2} \left[\sqrt{2 \ln(\Omega T)} + \frac{0.5772}{\sqrt{2 \ln(\Omega T)}} \right]
 \end{aligned} \tag{7.21}$$

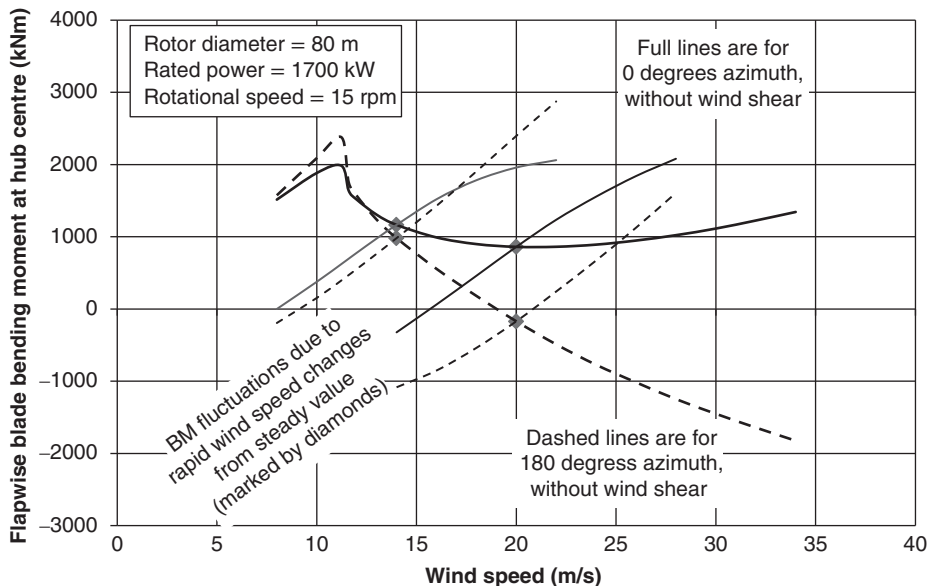


Figure 7.21 Effect of rapid wind speed fluctuations on 0 m radius flapwise bending moment for the example 80 m dia pitch-regulated machine for a +20° yaw angle

where $(\sigma_u)_{n>\Omega/2}$ is the standard deviation of wind speed fluctuations above the pitch response cut-off frequency (assumed to be half the rotational frequency) and T is the total period of operation in the wind speed band centred on the rated speed. For the IEC 61400-1 edition 4 normal turbulence model, the turbulence is given by

$$\sigma_u = I_{ref}(0.75\bar{U} + 5.6) \quad (7.22)$$

For an integral length scale of 147 m, the standard deviation of wind speed fluctuations above half rotational frequency seen by a point on a rotating blade at 28 m – i.e. at 70% of the 40 m tip radius, is 61% of the standard deviation of all wind speed fluctuations. Hence, for an 11 m/s rated wind speed, with $I_{ref} = 0.16$ for a Class A site, $\sigma_u = 2.22 \text{ m/s}$ and $(\sigma_u)_{n>\Omega/2} = 2.2 \times 0.61 = 1.35 \text{ m/s}$. Taking a wind speed band of 2 m/s, the expression in square brackets (i.e. the peak factor) comes to 5.9, so that the lifetime extreme value of the wind speed increase without pitch response is about 8 m/s. If the wind speed fluctuations over the blade are treated as perfectly correlated, this results in a maximum increment of 0 m radius flapwise bending moment of 1900 kNm, based on the BM increment applicable for a steady wind of 14 m/s (see Figure 7.21). When this is added to the maximum steady wind flapwise moment of about 2400 kNm, an extreme flapwise root bending moment ignoring wind shear of about 4300 kNm is obtained. Thus, the extreme flapwise bending moment during operation occurs at winds around rated rather than around the upper cut-out speed – a phenomenon that is a normal feature of pitch-regulated machines. Also, the extreme flapwise bending moment is slightly less than for the stall-regulated machine with the same diameter considered above.

Fatigue loading

The importance of fatigue loading relative to extreme loading is very much a function of material properties. As the vast majority of blades are manufactured from composite materials with similar fatigue properties, discussion in this sub-section will be based on these.

As set out in Sections 7.1.8–7.1.10, composite materials are characterised by a very shallow S - N curve – i.e. the reciprocal index m in the relation $\bar{\sigma} \propto \bar{N}^{-1/m}$ for constant amplitude, reversed loading ($R = -1$) is typically 10 or more. As a result, fatigue damage can be dominated by the small number of high range stress cycles associated with unusual wind conditions, rather than by the routine medium range cycles.

The other significant property of composite materials is the increase in fatigue damage with mean stress level, which is usually accounted for by scaling up the stress amplitude entered in the $R = -1$ S - N curve formulation by the factor $\frac{1}{(1 - \bar{\sigma}/\sigma_d)}$, where σ_d is the design strength in compression for a compression mean or in tension for a tension mean. This increases the relative importance of stress cycles with a high mean.

Behaviour of stall-regulated machines in fatigue

For stall-regulated machines, the highest out-of-plane bending moment ranges and means normally occur at high wind speeds and yaw angles. This is illustrated in Figure 7.19, which shows the variation in this moment with wind speed and yaw angle at 0% radius for an 80 m diameter machine, based on the 3-D data referred to above. Note that above rated wind speed, the bending moment plots level off, so that a given departure of the lateral wind component from the zero mean, sustained over half a revolution, results in a larger bending moment fluctuation than a change in the longitudinal component of twice this magnitude. For example, if the mean wind speed is 20 m/s, a lateral component of 4 m/s (corresponding to a yaw angle of 11.3°) causes a bending moment variation of 700 KNm when the blade rotates from 0° to 180° azimuth, compared to a variation of 500 KNm as a result of a $+/- 4$ m/s fluctuation in longitudinal wind speed.

Similar comments apply to vertical wind speed fluctuations, but here there is a built-in initial tilt angle between the air flow and the shaft axis because of shaft angle tilt and updraft. Thus, bending moment plots derived from 3-D wind simulations above rated are dominated by fluctuations at rotational frequency that bloom and decay as the angle between the air flow and the shaft axis rises and falls. Superimposed on these are lower frequency fluctuations caused by changes in the longitudinal wind speed.

Clearly high wind/high yaw cycles will be a major source of fatigue damage, although the contribution of cycles at wind speeds below stall may also be important, because of the more rapid variation of moment with wind speed there, and the much increased number of cycles.

Thomsen (1998) has investigated for blade root out-of-plane bending on a 1.5 MW, 64 m diameter 3 bladed machine, taking a constant turbulence intensity of 15% and a S - N curve index of 12. The results, including allowance for mean stress, are plotted in Figure 7.22 (dotted), and indicate that the damage is concentrated at wind speeds of 20 m/s and above. The figure also shows the effect of adopting a steeper S - N curve (with $m = 10$) and the IEC Class A turbulence distribution (with increasing intensities as mean

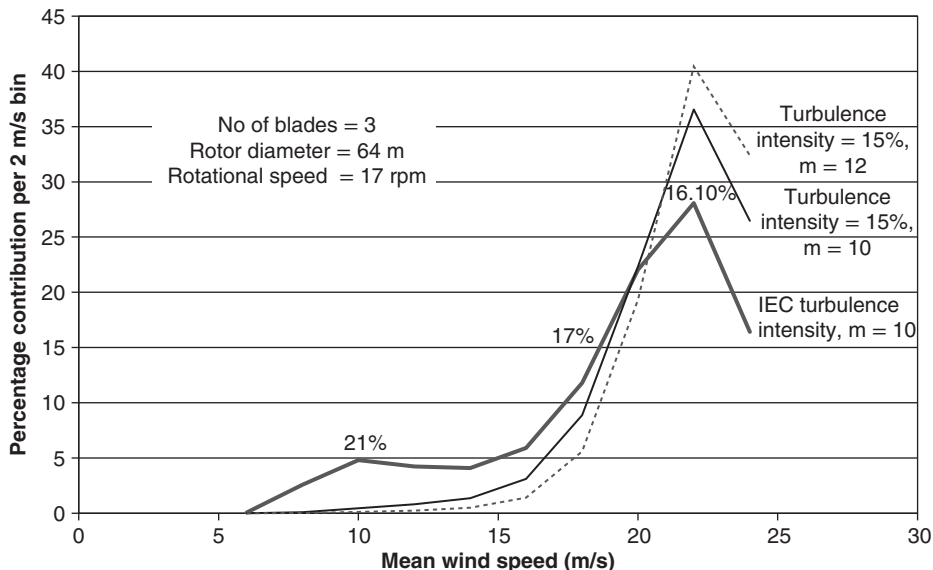


Figure 7.22 Relative contribution to lifetime fatigue damage for different wind speeds for a 1.5 MW stall-regulated machine, including effect of mean load, after Thomsen (1998)

wind speed decreases). In each case, the relative damage contribution at high wind speeds is reduced, but the switch to the IEC turbulence distribution causes the more significant change.

Behaviour of pitch-regulated machines in fatigue

For pitch-regulated machines, the highest out-of-plane bending moment ranges occur at high wind speeds and yaw angles, but the largest mean values occur around rated wind speed. Moreover, blade pitching results in a rapid fall-off in bending moment with short-term mean wind speed just above rated. This behaviour is illustrated in Figure 7.21, which shows the variation in out-of-plane moment with short-term mean wind speed for 20° yaw angle at 0 m radius for an 80 m diameter machine. It transpires that the combination of the steep bending moment/short-term wind speed characteristic, high mean bending moment and large number of loading cycles just above rated wind speed results in more fatigue damage at this wind speed than at higher wind speeds, where the increasing bending moment fluctuations due to yaw offset are mitigated by reducing mean loads and numbers of cycles.

The nature of the bending moment fluctuations at a mean wind speed just above rated is shown on Figure 7.23, which is a time history obtained from a 3-D wind speed simulation, for a 2000 kW pitch-regulated machine rotating at 21 rpm in a mean wind speed of 14 m/s. The increased rotational speed results in steeper bending moment/short-term mean wind speed characteristics than those presented in Figure 7.21. The effect of wind shear is included (based on a 60 m hub height), but the effects of yaw angle and shaft tilt

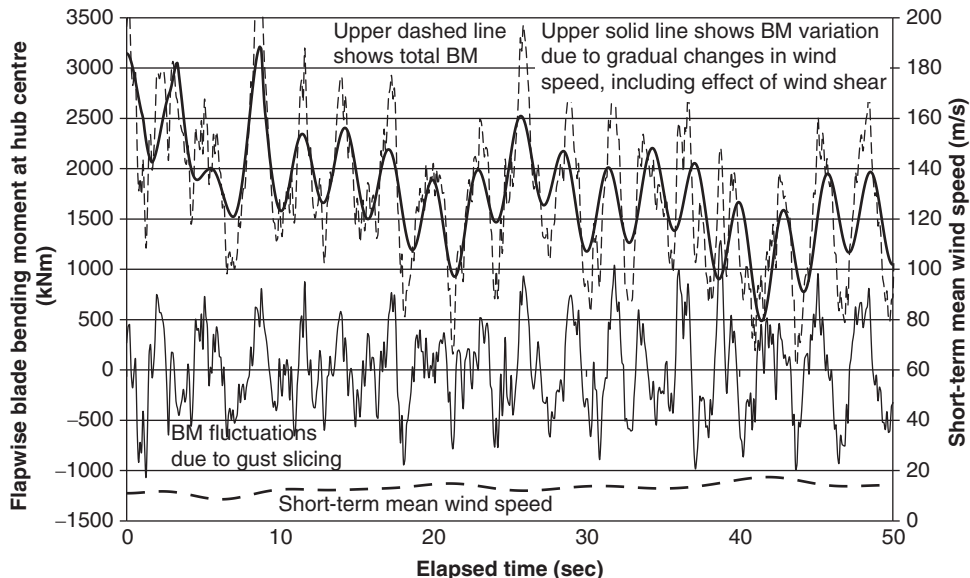


Figure 7.23 Time history of flapwise BM at 0 m radius, with breakdown between bending moments due to gradual wind speed changes (to which blade pitching responds) about a 14 m/s mean and additional fluctuations due to gust slicing – for an 80 m dia, 2000 kW pitch-regulated m/c rotating at 21 rpm, based on 3-D wind simulation

are omitted for simplicity as these are smaller. Figure 7.23 also shows the breakdown of the 0 m radius bending moment between the bending moment resulting from wind shear and gradual wind speed changes (to which blade pitching responds) and the additional bending moment fluctuations due to gust slicing. As with the case of a stall-regulated machine operating at high wind speed discussed above, there are considerable bending moment fluctuations at the rotational speed, but this time they are largely due to spatial variations in longitudinal wind speed across the disc (i.e. ‘gust slicing’) and wind shear rather than due to yaw or tilt offset. In addition, there are large low frequency bending moment fluctuations as a result of short-term mean wind speed changes – indeed, inspection of the bending moment and short-term mean wind speed plots reveals an inverse relationship between the two.

Factors affecting fatigue criticality

The relative criticality of fatigue and extreme loading is determined by the material properties and safety factors adopted, as well as by the loadings themselves. As an aid to comparison, the fatigue loading can be described in terms of the notional one cycle equivalent load, $\sigma_{eq(n=1)}$, which is defined as the stress range of the single reverse loading cycle that would cause the same total fatigue damage as the actual fatigue loading on the basis of the design *S-N* curve, including the effects of mean stress. Then fatigue is critical if

$$\frac{\sigma_{eq(n=1)}}{2\sigma_{0d}} > \gamma_L \frac{\sigma_{ext}}{\sigma_{cd}} \quad (7.23)$$

where σ_{0d} is the stress *amplitude* given by the reverse loading fatigue design curve at $N = 1$, σ_{ext} is the stress resulting from the extreme loading case, γ_L is the load factor and σ_{cd} is the design compression stress (which is assumed not to be governed by buckling considerations). The condition may be rewritten in terms of characteristic stress values as follows:

$$\frac{\sigma_{eq(n=1)}}{\sigma_{ext}} > 2\gamma_L \frac{\gamma_{mu}}{\gamma_{mf}} \frac{\sigma_{0k}}{\sigma_{ck}} \quad (7.24)$$

or as $\frac{\sigma_{eq(n=1)}}{\sigma_{ext}} > 2.7 \frac{\gamma_{mu}}{\gamma_{mf}} \frac{\sigma_{0k}}{\sigma_{ck}}$ with γ_L set to 1.35.

As is apparent from the survey of GFRP *S-N* curves in Section 7.1.8, the value of σ_{0k}/σ_{ck} can vary between about 1.0 and 1.4. As is indicated in Table 7.10, the overall partial safety factor for materials to be used in fatigue design depends on the accuracy of both the fatigue model and the fatigue loading description. Accordingly, the ratio of the materials partial safety factor for ultimate loads to that for fatigue loads varies from 0.91 (IEC 61400-5) or 0.74 (DNVGL-ST-0376) to 1.2, with the larger ratio applying when specific material *S-N* curves for a range of different *R* ratios are used in combination with a Markov matrix load description. Thus in principle the parameter $2\gamma_L \frac{\gamma_{mu}}{\gamma_{mf}} \frac{\sigma_{0k}}{\sigma_{ck}}$ governing fatigue criticality can take a wide range of values of between about 2.0 and 4.5.

The other important material property governing the criticality of fatigue loading is, of course, the slope index of the log – log *S-N* curve, *m*, which affects the value of the notional one cycle equivalent load, $\sigma_{eq(n=1)}$. With the high values applicable to wood laminates, fatigue is much less likely to govern.

Other sources of variability

There are a number of other sources of variability in fatigue damage calculations, apart from uncertainty about the material properties themselves, some of which are detailed below.

1. Three alternative stochastic turbulence models are in common use – those due to von Karman, Kaimal, and Mann. The von Karman model is isotropic, whereas in the Kaimal model, which is more realistic in this respect, the standard deviations of lateral and vertical turbulences are 80% and 50% of the longitudinal turbulence, respectively. The Mann model is closer to the Kaimal model with corresponding ratios of 0.7 and 0.5. In the case of stall-regulated machines, where wind misalignment at high wind speeds is often the main source of fatigue damage, the choice of turbulence model could clearly have a decisive effect.
2. When the fatigue assessment is based on simulations of limited duration (typically 300–600 seconds), the damage is often dominated by a few extreme cycles, which are subject to significant statistical variation from one simulation to another. Accordingly, several simulations at a given mean wind speed are necessary to obtain an accurate result. See ‘The Statistical Variation of Wind Turbine Fatigue Loads’ by Thomsen (1998).
3. In allowing for the reduction in fatigue strength due to mean stress (e.g. according to Eq. (7.18)), the mean stress can either be calculated over each stress range obtained by rainflow cycle counting or over the length of the simulation.

Fatigue due to gravity loading

In-plane fatigue loads arise from gravity loading and fluctuations in the in-plane aerodynamic loadings, but gravity loadings dominate for machines large enough to be grid connected.

Over most of the blade length, the chord dimension is much larger than the blade thickness, so the section modulus for edgewise bending will generally exceed that for flapwise bending. However, for blades attached to the hub or pitch bearing by a circular ring of bolts, which is the normal arrangement, the blade structure adjacent to the root is a cylindrical shell, which will have the same section modulus about both axes if the wall thickness is uniform. As a consequence, the blade root is the first area that should be checked for in-plane fatigue loading.

Tip deflection

Under extreme operating conditions, tip deflections of up to about 20% of blade radius can occur, so care is needed to avoid the risk of blade/tower collisions in the case of upwind machines. DNVGL-ST-0376 (2015) specifies that the maximum tip deflection under the extreme unfactored operational loading is not to exceed 70% of the clearance without blade deflection, which implies a safety factor of 1.43. IEC 61400-5, however, requires that there should be no blade/tower contact when the extreme loads are multiplied by the partial safety factor for loads and by the partial safety factor for the elastic properties of the blade material – i.e. by $1.35 \times 1.1 = 1.485$ for normal load cases. Relaxations in these requirements are permitted where supported by test measurements.

It is instructive to compare the tip deflections for similar blades designed in different materials. If the skin thickness distributions are chosen so that the design compression strength of each material is fully mobilised under the extreme load case, then the tip deflection will be proportional to the design compression strength to Young's Modulus ratio, σ_{cd}/E , of the blade material. These ratios are compared for different materials in Table 7.11.

It is clear from the table that a GFRP blade will be more flexible than blades in the other materials, provided that the spar is stocky enough for buckling not to govern the design. In the case of thin walled cross-sections, however, such as that in Figure 7.4, the GFRP compressive design stress has to be reduced significantly to guard against buckling, with the result that blade flexibility is reduced.

7.1.14 Simplified fatigue design example

Rigorous calculation of wind turbine blade fatigue damage requires numerous simulations of blade loading in the time domain for each wind speed, followed by post processing of the results to determine the fatigue stress spectra seen by different parts of the blade cross-section at each blade station. As number crunching on such a large scale does not necessarily facilitate the understanding of the main factors driving fatigue, this section presents simplified fatigue calculations for an example blade design – designated FC40 – on an 80 m diameter pitch-regulated variable-speed machine, in order to shed light on them.

After describing the blade geometry and structure, the following paragraphs outline the derivation of the stochastic and deterministic blade bending moments and the combination of the resultant stresses at critical points on the cross-section.

Table 7.11 Design strength to stiffness ratios for different wind turbine blade materials

Material	Ultimate compression strength, σ_{cu} MPa	Partial safety factor for material strength, γ_{mu}	Compression design strength, σ_{cd} MPa	Young's modulus, E GPa	Strength to stiffness ratio, $(\sigma_{cd}/E) \times 10^3$
Glass/epoxy laminate from PPG-Devold L1200/G50-E07 fabric with 92% UD fibres and 59% fibre volume fraction. Vacuum infused	575	2.47	233 (ignoring buckling)	44	5.3
Carbon fibre/epoxy Hexply 8552 laminate plymade from Hexcel AS4 carbon fibre with 60% fibre volume fraction and UD lay-up	1530	2.47	619	141	4.4
Khaya/epoxy laminate	50	1.5	33	10	3.3
Birch/epoxy laminate	81	1.5	54	15	3.6
High yield steel (grade Fe 510)	σ_y	γ_{my}			
Weldable aluminium alloy AA6082	355	1.1	323	210	1.54
	240	1.1	218	69	3.2

Blade geometry

The FC40 blade plan-form is illustrated in Figure 7.24, while the FC40 blade twist and thickness/chord ratio distributions are shown in Figure 7.25.

Blade structure description

A box spar consisting of two spar caps linked by two shear webs constitutes the main load-bearing structure. The spar caps are a constant width of 50 cm from the root to 25 m radius, but then taper down to 27.5 cm width at the tip to maintain adequate resistance to buckling. The spar is supplemented by the 0° plies in the 0°/±45° triaxial laminate that

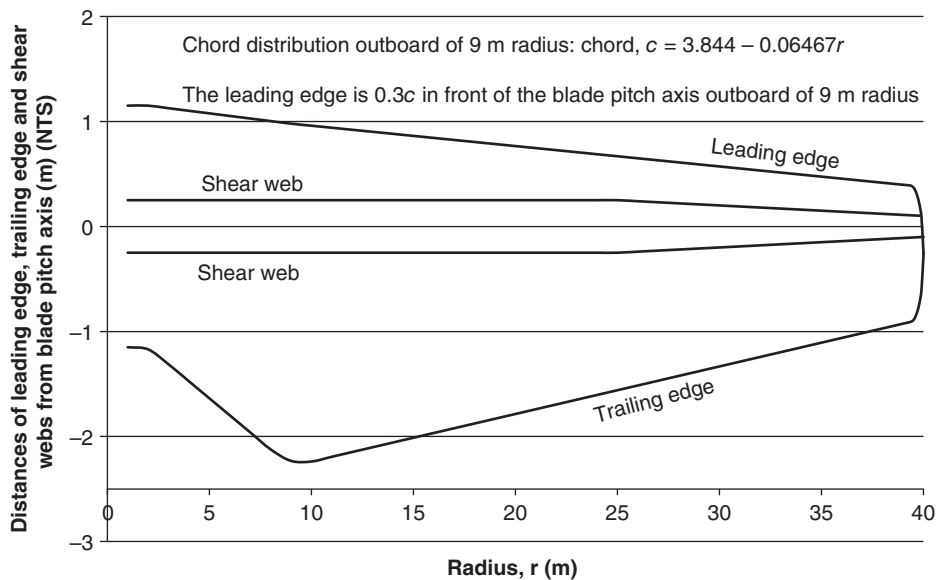


Figure 7.24 FC40 blade plan-form

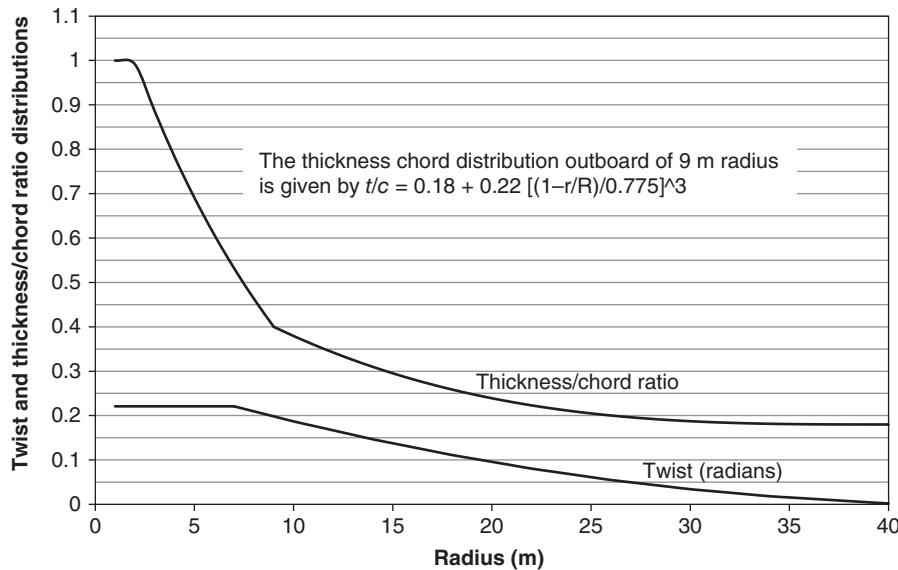


Figure 7.25 FC40 blade twist and thickness/chord ratio distributions

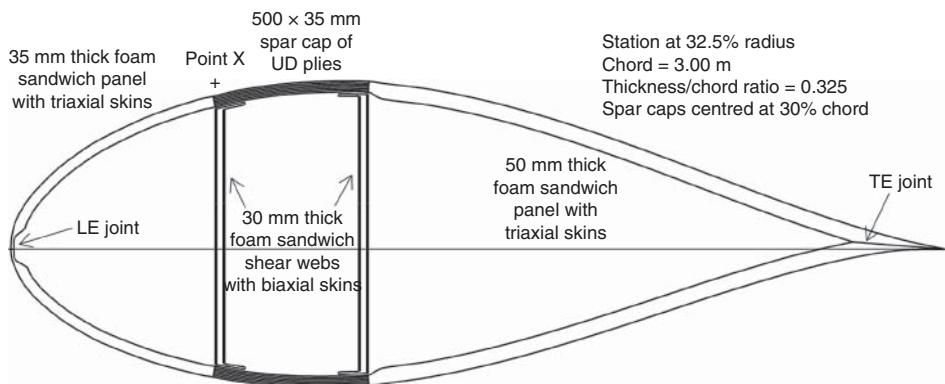


Figure 7.26 Cross-section of blade at 32.5% radius

forms the skins of the foam sandwich panels over the rest of the perimeter. The general arrangement is illustrated with respect to the cross-section at 32.5% radius in Figure 7.26.

Outboard of the maximum chord section at 9 m radius, the thicknesses of both the foam sandwich and its inner and outer skins taper down in proportion to the chord dimension, c , with the sandwich thickness set at $c/60$ to the rear of the spar and the skin thickness set at $c/1560$. The spar cap thickness profile outboard of 9 m radius is chosen so that the fatigue damage at the critical point on the cross-section at each blade station is less than unity.

Inboard of 9 m radius, the blade cross-section transitions gradually to a circular cross-section at the root. The thickness of the spar caps is assumed to taper linearly down to zero at the root, with the thickness of inner and outer skins progressively increasing to provide the requisite fatigue strength.

Operating regime

The torque vs rotational speed schedule is set so that the turbine operates at a tip speed ratio of 8 up to a wind speed of 11 m/s and a rotational speed of 21 rpm (2.2 rad/s) and at constant rotational speed thereafter. The rated power of 2000 kW is reached at 11.32 m/s, beyond which pitch control is activated to limit rotational speed excursions above 21 rpm.

Deterministic loading

Wind shear, tower shadow, yaw and shaft tilt all contribute to cyclic fatigue loading, principally in the flapwise direction. Wind shear and tower shadow bending moment ranges are additive, but those due to yaw can be in-phase or out-of-phase depending on yaw direction, so overall they make only a small net contribution to damage. Accordingly, stress ranges due to yaw are omitted from the fatigue analysis presented here in the interests of simplicity. The cyclic loading due to shaft tilt is 90° out-of-phase with that due to wind shear and tower shadow and is much smaller in magnitude, so its impact is negligible, allowing its contribution to be omitted also.

The out-of-plane and in-plane bending moment ranges due to wind shear and tower shadow are resolved about the blade principal axes and divided by the appropriate section

moduli to obtain the stress ranges at two critical locations. In view of the uncertainty regarding the position of the critical location for fatigue on the curved spar caps, stress ranges are conservatively calculated at the point X shown on Figure 7.26. This is at the same distance from the major and minor axes as the respective extreme fibres of the suction side spar cap. Stress ranges are also calculated at the trailing edge.

The gravity stress ranges at each of the critical locations are calculated in the same way, but as they are 90° out of phase with the wind shear plus tower shadow stress ranges, the combined stress range is calculated as the square root of the sum of the squares.

Stochastic loading

As described in Section 5.7.5, the gust slicing effect means that the power spectrum of the wind speed fluctuations incident on a point on the rotating blade differs significantly from the power spectrum of the wind speed fluctuations at a fixed point, with a marked concentration of energy at rotational frequency and to a lesser extent at its harmonics. However, at very low frequency the effect on the power spectrum is small – see Figure 5.19.

The trough in the rotationally sampled power spectrum between very low frequency and rotational frequency opens the way to the separate treatment of fatigue arising from stochastic loading concentrated at the two frequencies. The standard deviation of the blade bending moment fluctuations at rotational frequency and above at radius r_l , σ_{ML} , is given by

$$\sigma_{ML}^2 = \left(\frac{1}{2} \rho \Omega \frac{dC_L}{d\alpha} \right)^2 \sum_{j=l}^m \sum_{k=l}^m \left[\int_{\Omega/2}^{\infty} S_u^o(r_j, r_k, n) dn \right] c(r_j)c(r_k)r_jr_k(r_j - r_l)(r_k - r_l)(\Delta r)^2 \quad (7.25)$$

The combination of the stochastic bending moments at rotational frequency with the deterministic ones is considered in the next sub-section. The stochastic loads are considered to act at right angles to the untwisted chord for simplicity, as this is only expected to have a marginal effect on bending stresses.

The load ranges at very low frequency are additive to the stochastic and deterministic load ranges at rotational frequency and will be discussed later.

Combination of deterministic and stochastic stresses

For stationary conditions, the deterministic stress peaks occur at the same azimuth for each blade, but the stochastic stress peaks will occur at any azimuth with the same probability, so the damages resulting from the combined deterministic and stochastic stress ranges need to be calculated over the full 0–360° range of relative phase angles and summed. The stochastic stress ranges are concentrated at the rotational frequency with lesser peaks at the harmonics so, for simplicity, they are treated as narrow banded at the rotational frequency, with the stress ranges, $\Delta\sigma_S$ distributed according to the Rayleigh distribution:

$$P(\Delta\sigma_S) = 1 - \exp \left[-\frac{1}{8} \left(\frac{\Delta\sigma_S}{\sigma_{\sigma_S}} \right)^2 \right] \quad (7.26)$$

where σ_{σ_S} is the standard deviation of the stochastic stress. Each individual stochastic stress range can be combined with the deterministic stress range using the

cosine formula:

$$\Delta\sigma(\varphi_j) = \sqrt{\Delta\sigma_S^2 + \Delta\sigma_D^2 + 2\Delta\sigma_S\Delta\sigma_D\cos\varphi_j} \quad (7.27)$$

where φ_j is the phase angle between the occurrences of the deterministic and stochastic peak loadings on the blade.

Assuming the permitted number of cycles, N , at stress range, $\Delta\sigma$, is $[2\sigma_{0d}/\Delta\sigma]^m$, the damage arising over a time period, T , from rotational cycles with a phase angle of φ_j between the stochastic and deterministic stress cycles is given by

$$\frac{n}{N} = \frac{\Delta\varphi}{2\pi} \sum_{\Delta\sigma_S} \frac{\Omega T \Delta P(\Delta\sigma_S)}{[2\sigma_{0d}/\Delta\sigma]^m} = \frac{\Delta\varphi}{2\pi} \frac{\Omega T}{[2\sigma_{0d}]^m} \sum_{\Delta\sigma_S} \Delta P(\Delta\sigma_S) [\Delta\sigma_S^2 + \Delta\sigma_D^2 + 2\Delta\sigma_S\Delta\sigma_D\cos\varphi_j]^{\frac{m}{2}} \quad (7.28)$$

assuming a phase angle bin width of $\Delta\varphi$. The total damage is obtained by summing the above expression over all phase angles, and it can be shown that the same damage would be produced if all of the cycles had an equal range of

$$\Delta\sigma_{eff} = \left[\sum_j \left\{ \frac{\Delta\varphi}{2\pi} \sum_{\Delta\sigma_S} \Delta P(\Delta\sigma_S) [\Delta\sigma_S^2 + \Delta\sigma_D^2 + 2\Delta\sigma_S\Delta\sigma_D\cos\varphi_j]^{\frac{m}{2}} \right\} \right]^{\frac{1}{m}} \quad (7.29)$$

Very low frequency cycles

The mean frequency of the very low frequency blade bending moment fluctuations is a function of the power spectrum of the longitudinal component of turbulence and approximates to 0.015 Hz for a mean wind speed of 13 m/s, resulting in about nine loading cycles over a 10 minute period, the usual length specified for time domain simulations. These very low frequency cycles will cause relatively large fatigue stress cycles because the stress range at rotational frequency has to be added to each of them.

The standard deviation of the very low frequency wind speed fluctuations incident on a point on a rotating blade is smaller than the equivalent for a fixed point. In the case of a point at 28 m radius (i.e. at 70% radius for a 80 m diameter turbine), the former is about 80% of the latter, assuming that the turbulence length scales of the longitudinal wind speed fluctuations in the transverse and vertical directions are both 147 m.

The blades will pitch in response to the low frequency wind speed fluctuations, so blade bending moments will drop off rapidly as the wind speed rises above rated speed. It is convenient to estimate the ranges of the bending moment fluctuations by multiplying the standard deviation of the wind speed fluctuations by the local slope of the moment/wind speed characteristic for the radius concerned, allowing for the bending moment ceiling at rated wind speed, and applying a set of peak factors based on the Rayleigh distribution of peaks. Then the likely moment range for the j th largest cycle is given by:

$$\Delta M = 0.8\sigma_u \frac{dM}{dU} 2k_j \quad (7.30)$$

where k_j is the amplitude of the peak with a $(j - 0.5)/9$ probability of being exceeded.

Spar cap thickness profile

The spar cap thickness profile designed to resist the fatigue loading is shown in Figure 7.27. This is based on the IEC 61400-5 partial materials factor in fatigue of 2.06

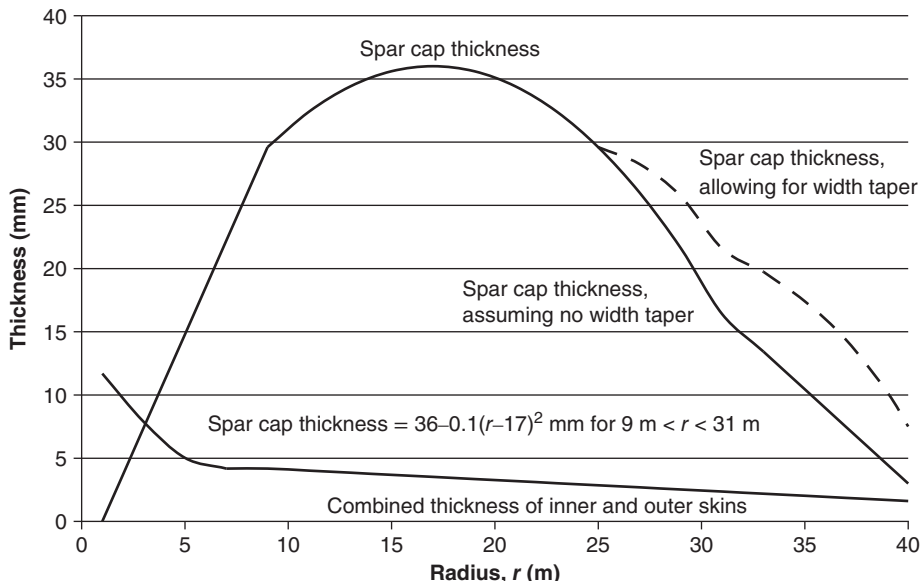


Figure 7.27 Spar cap thickness profile and combined thickness of inner and outer skins

that would apply if an accurate fatigue model and accurate loads had been employed. The utilisation ratio on this artificial basis is between 0.97 and unity between the root and 21 m radius. It is found that the design is governed by fatigue stresses calculated at the point X in Figure 7.26 rather than those at the trailing edge, indicating that there would be scope for some material saving if the proportion in the spar caps were increased.

Note that the width of the spar cap is gradually reduced beyond 25 m radius to resist buckling, resulting in increased thicknesses as shown by the dashed line. The variation with radius of the combined thickness of the inner and outer skins of the foam sandwich panels forming the aerodynamic section is also shown.

Variation of fatigue stresses and damage with wind speed

Figure 7.28 shows how the fatigue stress ranges vary with wind speed at 17 m radius, considering wind speeds at 2 m/s intervals. The gravity stress range increases above rated wind speed, because blade pitching leads to an increasing component of the gravity moment about the flapwise axis. The DEL stress range due to stochastic loading at rotational frequency and above is proportional to the product of rotational speed and the standard deviation of the turbulent wind speed fluctuations, so it increases rapidly up to rated speed but less rapidly thereafter, as the rotational speed has reached its ceiling. When the effect of the low frequency stochastic load cycles is included (with the rotational frequency DEL stress range added to each), the DEL stochastic stress range increases significantly. This is a consequence of the low slope of the S-N curve with $m = 10$, which results in a relatively small number of large loading cycles having a significant effect.

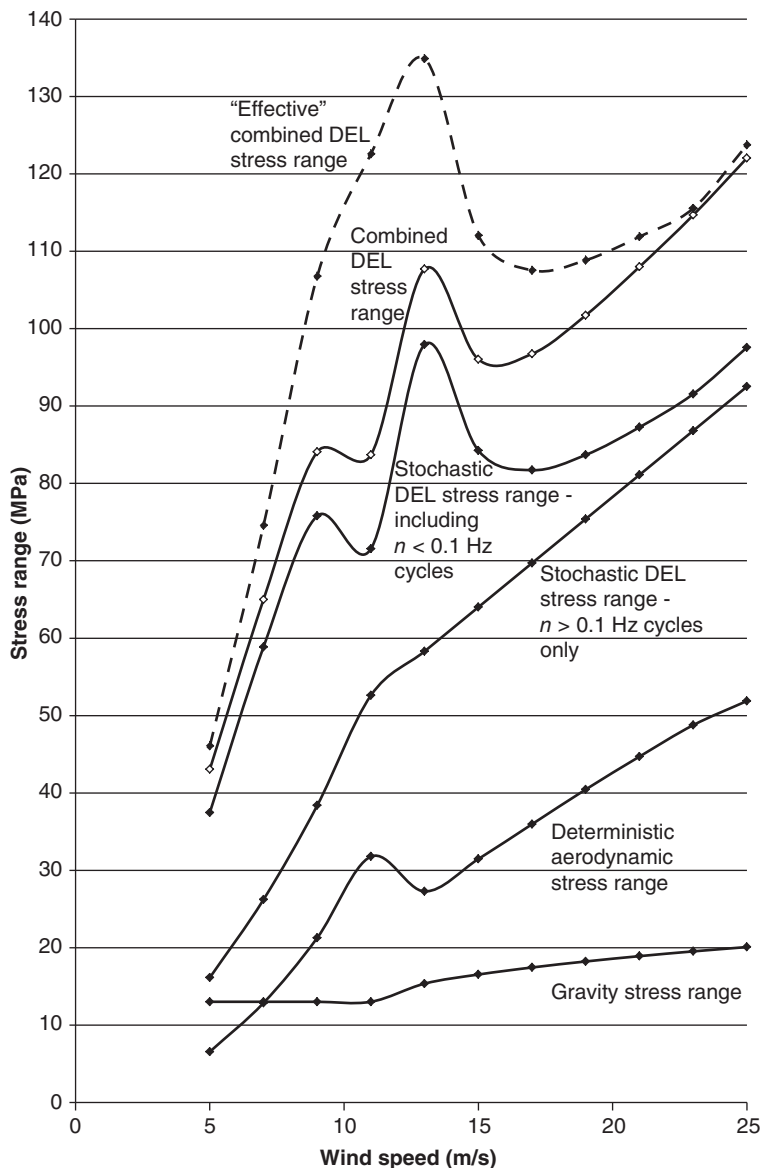


Figure 7.28 Variation of fatigue stresses at 17 m radius with wind speed for point X. (Here the DEL stress ranges are the constant amplitude ranges giving the same damage for the same number of loading cycles.)

Note that the stress range at 11 m/s is less than at either 9 or 13 m/s, because the bending moment due to slow wind speed changes reaches a ceiling at the rated wind speed of 11.32 m/s, so bending moment fluctuations are curtailed. At high wind speeds, blade bending moments are less affected by slow wind speed changes, so these have less effect on the DEL stochastic stress range.

When the stochastic stress ranges are combined with the deterministic ones, the latter have a relatively small impact at low wind speeds, but a greater impact at high wind speeds. The ‘effective’ combined DEL stress shown by the dashed line is derived from the combined DEL stress by dividing it by μ , which is a measure of the reduction of the permitted stress range due to a finite mean stress, assuming a linear Goodman Diagram – see Eq. (7.18). μ is defined as

$$\mu = 1 - \frac{\bar{\sigma}}{\sigma_{cd}} \quad (7.31)$$

and reaches a minimum at rated speed when mean stress is at a maximum. Consequently in Figure 7.28 the ‘effective’ combined DEL stress range exhibits the biggest increase relative to the combined DEL stress range at a wind speed of 11 m/s.

Figure 7.29 shows how the fatigue damage varies with wind speed at 17 m radius, again considering wind speeds at 2 m/s intervals. The ‘effective’ combined stress range and the proportion of time the turbine operates in each 2 m/s wind speed bin are shown for comparison. It is seen that nearly all of the damage is accumulated in the 11 and 13 m/s wind speed bins – i.e. around rated wind speed.

Fatigue criticality at root

It is found that fatigue is dominated by out-of-plane loading at the root as well as elsewhere for this diameter, with the critical bending axis only rotated about 5° from the plane of rotation. The ‘effective’ combined DEL stress about the critical bending axis at the root comes to 118 MPa compared with an extreme fibre stress range due to gravity loading of only 44 MPa.

The extreme factored BM results in an extreme fibre stress of 222 MPa, so the expression $\sigma_{eq(n=1)}/\sigma_{ext}$ comes to $118 \times (1.8 \times 10^8)^{0.1}/222 = 118 \times 6.69/222 = 790/222 = 3.56$. As set out in the preceding section, fatigue is critical if $\frac{\sigma_{eq(n=1)}}{\sigma_{ext}} > 2\gamma_L \frac{\gamma_{mu}}{\gamma_{mf}} \frac{\sigma_{0k}}{\sigma_{ck}}$. If the partial

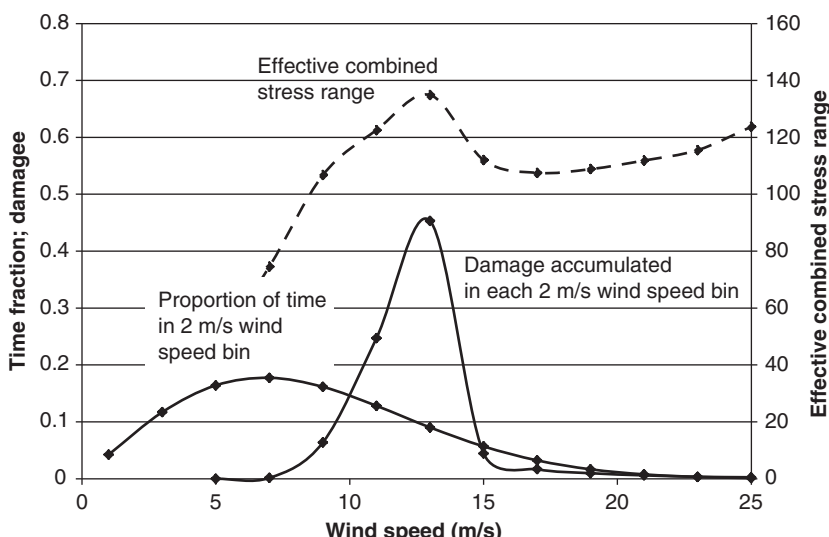


Figure 7.29 Variation of fatigue damage with wind speed at 17 m radius

materials safety factors in fatigue and at ultimate are based on the hypotheses of accurately described loads and an accurate fatigue model, the ratio $\Upsilon_{\text{mu}}/\Upsilon_{\text{mf}}$ would be 1.2. Hence, if the ratio σ_{0k}/σ_{ck} was at the upper end of the range (1.4), the threshold $2\gamma_L \frac{\Upsilon_{\text{mu}}}{\Upsilon_{\text{mf}}} \frac{\sigma_{0k}}{\sigma_{ck}}$ would be $2(1.35)1.2(1.4) = 4.54$, so the inequality would not be satisfied and fatigue would not be critical at the root.

Tip clearance

The 175–185° azimuth tip deflection under the extreme turbulence load case (IEC 61400-1 DLC 1.3), which is often the governing load case, is approximately 6.5 m, including the load factor of 1.35. Assuming a shaft tilt of 5°, a hub overhang of 3.2 m and a tower diameter of 3.4 m, the nominal clearance would be $40\sin 5^\circ + 3.2 - 1.7 = 3.5 + 1.5 = 5.0$ m, which is clearly inadequate. The potential clash could be avoided by increasing the spar cap thickness to provide increased stiffness, which would mean that the design was stiffness governed rather than fatigue governed. However, a more economical alternative would be to alter the rotor configuration to increase the nominal clearance. This could take the form of rotor coning, in which all of the blades are tilted forward by the same amount, or blade prebend, in which the blade has a permanent forward curvature, or a combination of the two.

Scaling the fatigue design to 160 m diameter

It is relatively straightforward to scale the FC40 blade design up to a larger diameter. If the blade chord and thickness distributions are scaled up by the diameter ratio and the rotational speed divided by the diameter ratio, then aerodynamic loads increase as the square of diameter and the corresponding moments increase as the cube of diameter, ignoring the changes to wind shear effects. If the spar cap width and thickness and the inner and outer skin thicknesses are all increased in proportion to diameter, then the section moduli used in the calculation of bending stresses increase as the cube of diameter, paralleling the aerodynamic moments, with the result that the aerodynamic stresses are unchanged.

By contrast, the gravity loads increase as the cube of diameter, so the gravity moments increase as the fourth power. The effect of a diameter increase on the fatigue stress ranges due to gravity and aerodynamic loads combined can be modelled by keeping the diameter and, initially, all other dimensions the same in the calculations, but at the same time multiplying the densities used to calculate the gravity stress ranges by the diameter ratio. If this approach is adopted to adapt the FC40 blade design for 160 m diameter, it is found that fatigue at the trailing edge becomes critical instead of that at the spar caps, so that the thickness of the inner and outer skins has to be increased. A 30% increase in skin thickness reduces the trailing edge damage to an acceptable value everywhere apart from in the immediate vicinity of the maximum chord position at 22.5% radius, where a 1% overstress is registered. The increase in skin thickness results in a 7.5% increase in blade mass over and above the eightfold increase if all dimensions are simply doubled.

7.1.15 Blade resonance

One of the most important objectives of blade design is the avoidance of resonant oscillations, which, in a mild form, exacerbate fatigue damage and in an extreme form can lead to rapid failure. The excitation of blade resonance can be minimised by maximising the

damping and ensuring that the blade flapwise and edgewise natural frequencies are well separated from the exciting frequencies – i.e. the rotational frequency and its harmonics, particularly the blade passing frequency – and from the frequencies of other vibration modes with which there is an identifiable risk of coupled oscillations.

Vibrations in stall

On stall-regulated machines, the lift curve slope, $dC_l/d\alpha$, goes negative when a section of the blade goes into stall, resulting in local negative aerodynamic damping of blade motion in the lift direction. If the overall aerodynamic damping for a particular mode shape is negative, and exceeds the modal structural damping in magnitude, then divergent oscillations can develop from any initial disturbance, regardless of the relationship between the mode natural frequency and exciting frequencies. The first mode in each direction is most susceptible to such behaviour because the structural damping increases with frequency while the aerodynamic damping diminishes. If conditions favouring first mode oscillations are to be avoided, the factors affecting the aerodynamic damping of both edgewise and flapwise oscillations need to be understood, so these are explored below.

Consider a turbine operating in steady conditions in a perpendicular air flow. If a blade cross-section at radius r experiences out-of-plane and in-plane perturbations with velocities \dot{x} in the downwind direction and \dot{y} in the direction opposite to that of blade rotation (assumed clockwise), then the relative velocity triangle is as in Figure 7.30a. The lift and drag forces per unit length on a blade element, L and D , can be resolved into out-of-plane and in-plane forces F_Y and F_X (see Figure 7.30b), leading to

$$F_Y = \frac{1}{2}\rho W^2(-C_l \sin \varphi + C_d \cos \varphi)c$$

$$F_X = \frac{1}{2}\rho W^2(C_l \cos \varphi + C_d \sin \varphi)c$$

Ignoring the small rotational induction factor, which is very small, these may be rewritten as

$$F_Y = W[-C_l(U_\infty(1-a) - \dot{x}) + C_d(\Omega r - \dot{y})]\frac{1}{2}\rho c \quad (7.32)$$

$$F_X = W[C_l(\Omega r - \dot{y}) + C_d(U_\infty(1-a) - \dot{x})]\frac{1}{2}\rho c \quad (7.33)$$

Here U_∞ is the free stream wind speed and $U_\infty(1-a)$ the reduced wind speed at the rotor plane as usual. The damping coefficients per unit length for vibrations in the in-plane and out-of-plane directions are then given by

$$\hat{c}_Y(r) = -\frac{\partial F_Y}{\partial \dot{y}} \quad (7.34a)$$

$$\hat{c}_X(r) = -\frac{\partial F_X}{\partial \dot{x}} \quad (7.34b)$$

Analogous ‘cross’ coefficients relating the in-plane force to the out-of-plane velocity and vice versa can also be defined as

$$\hat{c}_{YX}(r) = -\frac{\partial F_Y}{\partial \dot{x}} \quad (7.35a)$$

$$\hat{c}_{XY}(r) = -\frac{\partial F_X}{\partial \dot{y}} \quad (7.35b)$$

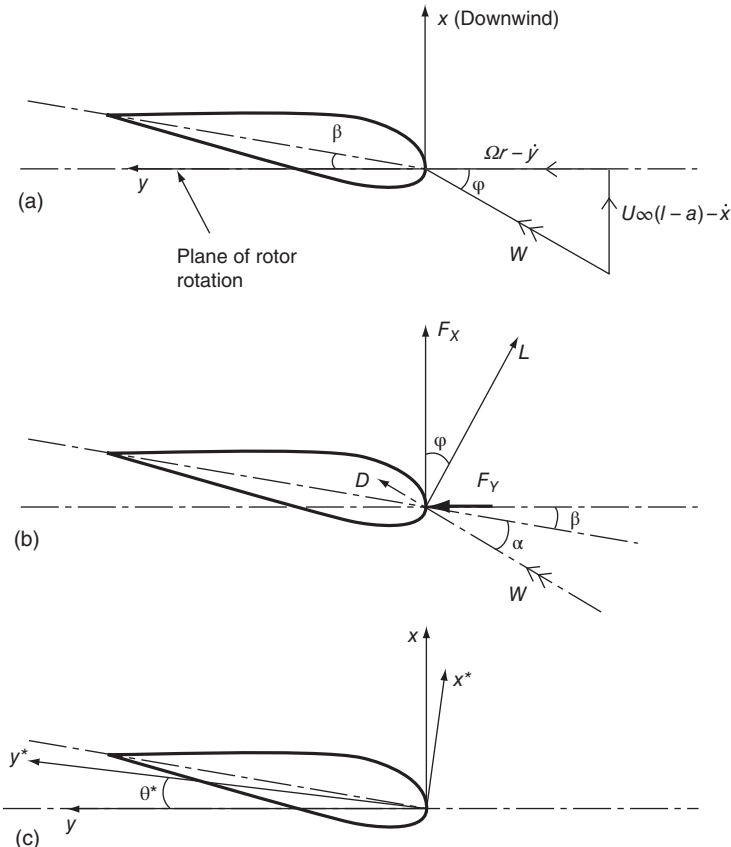


Figure 7.30 (a) Velocity diagram for vibrating blade (looking towards hub). (b) Out-of-plane and in-plane components of lift and drag forces. (c) Directions of vibrations x^* and y^*

Substituting V for $U_\infty(1-a)$ for brevity, the in-plane damping coefficient is derived as follows:

$$\hat{c}_Y(r) = -\frac{\partial F_Y}{\partial \dot{y}} = -\frac{1}{2} \rho c \left\{ \frac{\partial W}{\partial \dot{y}} [-C_l V + C_d \Omega r] + W \left[-\frac{\partial C_l}{\partial \dot{y}} V + \frac{\partial C_d}{\partial \dot{y}} \Omega r - C_d \right] \right\} \quad (7.36)$$

Noting that $\frac{\partial W}{\partial \dot{y}} = -\frac{\Omega r}{W}$ and $\frac{\partial C_l}{\partial \dot{y}} = \frac{\partial C_l}{\partial \alpha} \frac{\partial \alpha}{\partial \dot{y}} = \frac{\partial C_l}{\partial \alpha} \frac{\partial \varphi}{\partial \dot{y}} = \frac{\partial C_l}{\partial \alpha} \frac{V}{W^2}$, this equation becomes

$$\hat{c}_Y(r) = \frac{1}{2} \rho c \frac{\Omega r}{W} \left\{ -V C_l + \frac{V^2}{\Omega r} \frac{\partial C_l}{\partial \alpha} + \frac{2\Omega^2 r^2 + V^2}{\Omega r} C_d - V \frac{\partial C_d}{\partial \alpha} \right\} \quad (7.37)$$

The ‘cross’ coefficients and the out-of-plane damping coefficient are derived by a similar procedure:

$$\hat{c}_{YX}(r) = \frac{1}{2} \rho c \frac{\Omega r}{W} \left\{ -\frac{\Omega^2 r^2 + 2V^2}{\Omega r} C_l - V \frac{\partial C_l}{\partial \alpha} + V C_d + \Omega r \frac{\partial C_d}{\partial \alpha} \right\} \quad (7.38)$$

$$\hat{c}_{XY}(r) = \frac{1}{2} \rho c \frac{\Omega r}{W} \left\{ + \frac{2\Omega^2 r^2 + V^2}{\Omega r} C_l - V \frac{\partial C_l}{\partial \alpha} + V C_d - \frac{V^2}{\Omega r} \frac{\partial C_d}{\partial \alpha} \right\} \quad (7.39)$$

$$\hat{c}_X(r) = \frac{1}{2} \rho c \frac{\Omega r}{W} \left\{ + V C_l + \Omega r \frac{\partial C_l}{\partial \alpha} + \frac{\Omega^2 r^2 + 2V^2}{\Omega r} C_d + V \frac{\partial C_d}{\partial \alpha} \right\} \quad (7.40)$$

It is apparent from inspection of the expressions for the two damping coefficients, \hat{c}_Y and \hat{c}_X , that the choice of an aerofoil with a gentler stall – i.e. with a smaller lift curve slope after stall onset – will increase the damping coefficient in both cases. Note that the modal damping coefficient is dominated by the damping per unit length over the outboard part of the blade, so it is important to select an aerofoil with a gentle stall in this area only.

The choice of aerofoil also affects performance, so there is merit in expressing the damping coefficients in terms of the power output to investigate possible trade-offs between them. It transpires that the damping and ‘cross’ coefficients per unit length can be formulated quite simply in terms of the power output per unit length of blade, $P'(r, V) = \Omega r(-F_Y)$, and the blade thrust per unit length, F_X , as follows:

$$\hat{c}_Y = -\frac{2}{\Omega^2 r^2} P' + \frac{V}{\Omega^2 r^2} \frac{\partial P'}{\partial V} = \frac{1}{\Omega^2 r^2} \left(-2P' + V \frac{\partial P'}{\partial V} \right) \quad (7.41)$$

$$\hat{c}_{XY} = -\frac{\partial F_Y}{\partial \dot{x}} = \frac{\partial F_Y}{\partial V} = \frac{1}{\Omega r} \frac{\partial}{\partial V} (\Omega r F_Y) = -\frac{1}{\Omega r} \frac{\partial P'}{\partial V} \quad (7.42)$$

$$\hat{c}_{XY} = \frac{1}{\Omega r} \left(2F_X - V \frac{\partial F_X}{\partial V} \right) \quad (7.43)$$

$$\hat{c}_X = -\frac{\partial F_X}{\partial \dot{x}} = \frac{\partial F_X}{\partial V} \quad (7.44)$$

Equations (7.41) and (7.43) are derived from the equations $\Omega r \hat{c}_Y + V \hat{c}_{XY} = 2F_Y = -2P'/\Omega r$ and $\Omega r \hat{c}_{XY} + V \hat{c}_X = 2F_X$ which may be verified using Eqs. (7.37)–(7.40).

From Eq. (7.41), it is clear that the damping coefficient in the in-plane direction, \hat{c}_Y , will always be negative unless $\frac{\partial P'}{\partial V}$ exceeds $2\frac{P'}{V}$, and that a negative power curve slope should be avoided if the size of the negative damping is to be kept small.

Effect of blade twist

In the discussion so far, damping of vibrations in the out-of-plane and in-plane directions only has been considered. In practice, blade twist will result in the flapwise and edgewise vibrations taking place in directions rotated from the out-of-plane and in-plane directions in the same sense as the blade twist, but by a lesser amount (see Section 5.8.1). If we define x^* and y^* axes in the directions of the flapwise and edgewise displacements, each making an angle of θ^* to the x and y axes, respectively, as shown in Figure 7.30c, then the edgewise damping coefficient per unit length is given by

$$\hat{c}_{Y*} = \hat{c}_Y \cos^2 \theta^* - (\hat{c}_{YX} + \hat{c}_{XY}) \sin \theta^* \cos \theta^* + \hat{c}_X \sin^2 \theta^* \quad (7.45)$$

Substitution of Eqs. (7.41)–(7.44) in Eq. (7.45) yields

$$\begin{aligned} \hat{c}_{Y*} = & \cos^2 \theta^* \left[\frac{1}{\Omega^2 r^2} \left(-2P' + V \frac{\partial P'}{\partial V} \right) \right] + \cos \theta^* \sin \theta^* \left[\frac{1}{\Omega r} \left(-\frac{\partial P'}{\partial V} + 2F_X - V \frac{\partial F_X}{\partial V} \right) \right] \\ & + \sin^2 \theta^* \left(\frac{\partial F_X}{\partial V} \right) \end{aligned} \quad (7.46)$$

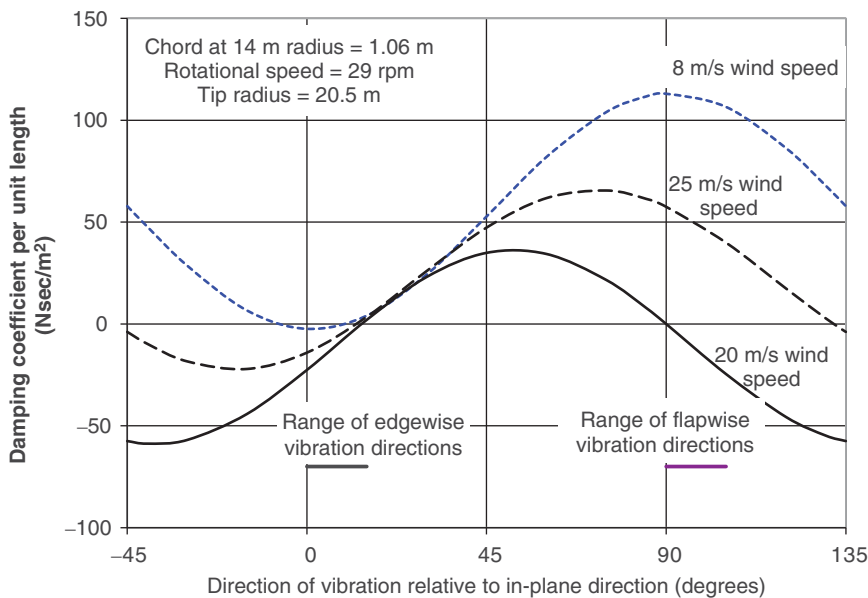


Figure 7.31 Variation in damping coefficient at 14 m radius with vibration direction for example aerofoil

This expression also gives the flapwise damping coefficient per unit length if θ^* is replaced by $\theta^* + 90^\circ$ throughout.

The variation of the damping coefficient \hat{c}_{Y*} per unit length at 14 m radius with vibration direction, θ^* , at three different wind speeds is illustrated in Figure 7.31 for a specimen aerofoil section on a 20.5 m tip radius blade rotating at 29 rpm. The data is taken from Petersen et al. (1998), and does not include allowance for the axial induction factor. It can be seen that negative damping is worst at 20 m/s, and that negative edgewise damping is ameliorated by increasing θ^* at the expense of increasing negative flapwise damping.

Although a plot of the local damping coefficient at ca 70% radius can provide a useful indication of trends, the best guide to the likelihood of divergent oscillations is provided by the modal damping coefficient for the mode under consideration. This is obtained by multiplying the right hand side of Eq. (7.46) by the square of the local modal amplitude and integrating over the length of the blade.

If comparison of the first mode edgewise and flapwise modal damping coefficients shows there is a benefit to be gained from altering the direction of vibration, small changes can be made by redistributing material within the blade cross-section. Alternatively the blade pitch could be altered in conjunction with a compensatory change in aerofoil camber so that the aerodynamic properties for any given inflow angle are unchanged.

The prediction of edgewise vibrations in stall is examined in detail by Petersen et al. (1998), whose work provides the basis of the introductory survey given here. They concluded that the fundamental cause of edgewise blade oscillations that had been observed on some stall-regulated machines of 40 m diameter and over was negative aerodynamic damping, but found that the use of dynamic stall models improved the level of agreement with measurements.

Coupling of edgewise blade mode and rotor whirl modes

A further important finding was that, on one machine subject to stall-induced vibrations that was investigated in detail, there was coupling between the blade first edgewise mode and one of the second rotor whirl modes. The rotor whirl modes arise from the combination of simultaneous nodding and yawing oscillations of the rotor shaft, which occur at the same frequency during operation due to gyroscopic effects. As a result, the rotor hub traces out a circular or elliptical path, running either in the same direction as rotor rotation or in reverse, which explains the existence of two first and second modes.

The explanation for the coupling was as follows. When a pair of blades vibrate in the edgewise direction in anti-phase, they impart a sinusoidally varying in-plane force to the rotor hub even though their edgewise root bending moments cancel out. The direction of this oscillating force rotates with the rotor, so it has horizontal and vertical components of the form $\sin(\omega_1 t + \eta) \cdot \sin \Omega t$ and $\sin(\omega_1 t + \eta) \cdot \cos \Omega t$, where ω_1 is the frequency of the blade first edgewise mod, and Ω is the speed of rotor rotation. With respect to stationary axes the in-plane loads on the hub therefore act at two frequencies – namely, $\omega_1 + \Omega$ and $\omega_1 - \Omega$. In the case of the machine investigated by Petersen et al., the upper frequency of $2.9 + 0.5 = 3.4$ Hz coincided with the backward second rotor whirl mode, allowing interaction between this mode and the blade first edgewise mode.

Simulations were carried out on an aeroelastic model of the turbine at various wind speeds and satisfactory agreement obtained between simulated and measured behaviour. In particular, the simulation at 23.2 m/s predicted the build-up of large blade root edgewise moment oscillations at the first mode frequency, as observed on the real machine at this wind speed. Significantly, when the latter simulation was repeated with the rotor shaft stiffness increased sufficiently to increase the backward second rotor whirl mode frequency to 3.6 Hz, the predicted blade root edgewise moment oscillations were negligible by comparison.

Mechanical damping

An alternative strategy for preventing damaging edgewise vibrations is the incorporation of a tuned mass damper inside the blade towards the tip. The performance of such a damper on a 22 m tip radius blade is reported by Anderson et al. (1998). It was found that the fitting of a damper tuned to the first mode edgewise frequency, and weighing only 0.4% of the total blade weight, effectively suppressed the edgewise vibrations that had previously been observed during high wind speed operation.

7.1.16 Design against buckling

Thrust loading on the wind turbine rotor during operation subjects the blade shell and spar cap on the suction face of the blade to fluctuating axial compression loading. Moreover, axial compression will be generated in either face by wind loads during standstill. Figures 7.32 and 7.33 illustrate the buckling mode shapes for the suction face trailing panel and suction side spar cap of the DTU 10 MW reference wind turbine design.

This section explores how the spar cap and sandwich panels forming the blade shell may be designed against buckling.

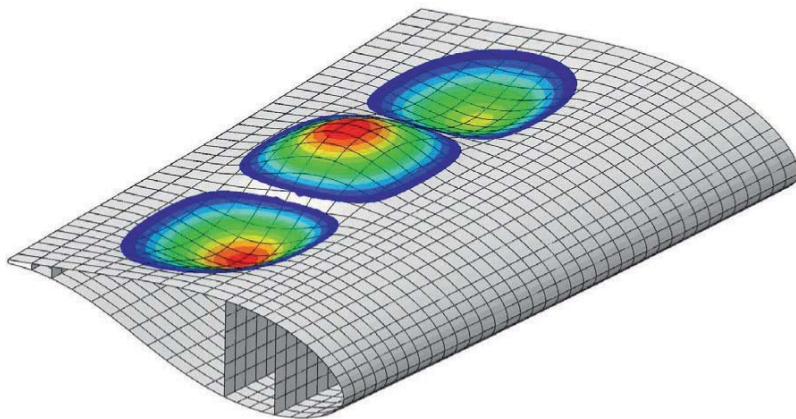


Figure 7.32 Typical buckling mode shape of DTU 10 MW reference turbine suction face trailing sandwich panel. Taken from DTU Wind Energy Report I-0092, ‘Description of the DTU 10 MW Reference Wind Turbine’ (Bak et al. 2013), and reproduced with the permission of the publisher, Danish Technical University

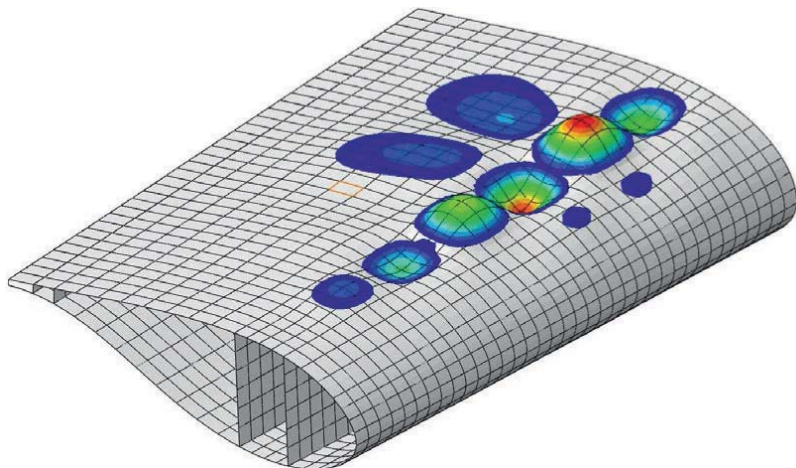


Figure 7.33 Typical buckling mode shape of DTU 10 MW reference turbine suction side spar cap. Taken from DTU Wind Energy Report I-0092, ‘Description of the DTU 10 MW Reference Wind Turbine’ (Bak et al. 2013), and reproduced with the permission of the publisher, Danish Technical University

Critical buckling stress

The stress at which a slender plate element without imperfections buckles under compression loading is known as the *critical buckling stress*. The derivation of the critical buckling stresses for thin walled curved panels bounded by stiffeners, which typically form the blade load-bearing structure, is relatively straightforward when the

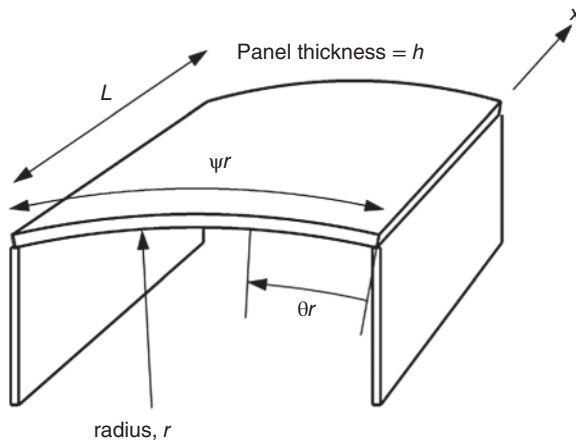


Figure 7.34 Curved panel spanning between shear webs

panel material is isotropic and solutions are provided in Timoshenko and Gere (1961). These do not apply to composite materials such as the GFRP and wood laminates commonly used in blade manufacture, however, as these are anisotropic, but solutions can be derived using the energy method, as outlined below.

Consider a long cylindrical panel of length L , radius r and thickness h , supported along two generators and subtending an angle ψ at the cylinder axis (Figure 7.34), which is axially loaded in compression. If it deflects to form n half waves around the circumference between supports and m half waves along its length, then its out-of-plane deflection can be written as

$$w = C \sin \frac{n\pi\theta}{\psi} \sin \frac{m\pi x}{L} \quad (7.47)$$

where θ and x are the coordinates of the deflected point with respect to one of the long edges and one end, respectively. In the absence of in-plane direct strains in the plate, this out-of-plane deflected profile will result in circumferential deflections:

$$v_0 = \frac{C\psi}{n\pi} \cos \frac{n\pi\theta}{\psi} \sin \frac{m\pi x}{L} \quad (7.48)$$

These deflections will result in in-plane shear stresses, which reach a maximum at the corners of each rectangular buckled panel. In practice, additional in-plane deflections occur to moderate these shear stresses, as follows:

$$\begin{aligned} u &= A \sin \frac{n\pi\theta}{\psi} \cos \frac{m\pi x}{L} \text{ in the axial direction} \\ v &= B \cos \frac{n\pi\theta}{\psi} \sin \frac{m\pi x}{L} \text{ in the circumferential direction} \end{aligned} \quad (7.49)$$

The in-plane strain energy is calculated as

$$U_2 = \frac{1}{2} h \iint (\sigma_1 \epsilon_1 + \sigma_2 \epsilon_2 + \tau \gamma) r d\theta dx \quad (7.50)$$

with the suffixes 1 and 2 denoting the axial and circumferential directions, respectively, so that

$$\varepsilon_1 = \frac{\partial u}{\partial x}, \quad \varepsilon_2 = \frac{\partial v}{r\partial\theta}, \quad \gamma = \frac{\partial u}{r\partial\theta} + \frac{\partial(v_0 + v)}{\partial x} \quad (7.51)$$

Substituting $\sigma_1 = E_x(\varepsilon_1 + v_y\varepsilon_2)/(1 - v_xv_y)$, $\sigma_2 = E_y(\varepsilon_2 + v_x\varepsilon_1)/(1 - v_xv_y)$ and $\tau = G_{xy}\gamma$, where E_x , E_y , and G_{xy} are the longitudinal, transverse, and shear moduli of the laminate, respectively (obtained by averaging the corresponding moduli of the individual plies), and v_x and v_y are the effective Poisson's ratios, the in-plane strain energy becomes

$$U_2 = \frac{h}{2(1 - v_xv_y)} \iint [E_x\varepsilon_1^2 + E_y\varepsilon_2^2 + 2E_xv_y\varepsilon_1\varepsilon_2 + (1 - v_xv_y)\gamma^2G_{xy}]rd\theta dx \quad (7.52)$$

Substituting the expressions for ε_1 , ε_2 , and γ from Eq. (7.51) and integrating over the width of the panel, ψr , and the length of one half wave, L/m , we obtain

$$U_2 = \frac{E_x h}{1 - v_x v_y} \psi r \frac{L}{m} \left(\frac{m\pi}{L} \right)^2 \frac{C^2}{8} \left[\alpha^2 + \beta^2 \frac{E_y}{E_x} \left(\frac{n}{\lambda} \right)^2 + 2v_y \alpha \beta \left(\frac{n}{\lambda} \right) + (1 - v_x v_y) \frac{G_{xy}}{E_x} \left\{ \alpha \left(\frac{n}{\lambda} \right) + \beta + \frac{\psi}{n\pi} \right\}^2 \right] \quad (7.53)$$

where $\lambda = \frac{m\psi r}{L}$ and the ratios $\alpha = A/C$ and $\beta = B/C$ are yet to be determined.

The expression for the strain energy of curvature is derived as follows. Replacing the angular coordinate θ by the linear coordinate $y (= r\theta)$, the bending energy absorbed in an area $dx dy$ is

$$dU_b = -\frac{1}{2} \left(M_x \frac{\partial^2 w}{\partial x^2} + M_y \frac{\partial^2 w}{\partial y^2} \right) dx dy$$

where $M_x = -D_x \frac{\partial^2 w}{\partial x^2} - D_{xy} \frac{\partial^2 w}{\partial y^2}$ and $M_y = -D_y \frac{\partial^2 w}{\partial y^2} - D_{xy} \frac{\partial^2 w}{\partial x^2}$ for a specially orthotropic laminate – i.e. one in which the reinforcement in each layer is either oriented at 0° or 90° , or is bidirectional with the same amount of fibres at $+θ^\circ$ and $-θ^\circ$. D_x and D_y are the flexural rigidities of the laminate when flat, for bending about the y axis and x axis, respectively, and D_{xy} is the ‘cross-flexural rigidity’ – i.e. the moment per unit width about one axis generated by unit curvature about the other. Hence

$$dU_b = \frac{1}{2} \left(D_x \left(\frac{\partial^2 w}{\partial x^2} \right)^2 + 2D_{xy} \frac{\partial^2 w}{\partial x^2} \frac{\partial^2 w}{\partial y^2} + D_y \left(\frac{\partial^2 w}{\partial y^2} \right)^2 \right) dx dy \quad (7.54)$$

The twisting energy absorbed in an area $dx dy$ is

$$dU_t = \frac{1}{2} (M_{xy} + M_{yx}) \frac{\partial^2 w}{\partial x \partial y} dx dy$$

where $M_{xy} = 2 \left[\int_{-h/2}^{h/2} G_{xy}(z) z^2 dz \right] \frac{\partial^2 w}{\partial x \partial y}$, in which z is the distance measured from the mid-plane of the laminate, $G_{xy}(z)$ is the in-plane shear modulus at that distance and h is the laminate thickness. Denoting the torsional rigidity, $\left[\int_{-h/2}^{h/2} G_{xy}(z) z^2 dz \right]$, by D_T , then

$$dU_t = \frac{1}{2} .4 D_T \left(\frac{\partial^2 w}{\partial x \partial y} \right)^2 dx dy \quad (7.55)$$

The total strain energy of curvature over the width of the panel and the length of one half wave is found by substituting the out-of-plane deflection given by Eq. (7.47) in Eqs. (7.54) and (7.55) and integrating over this area, which gives

$$U_1 = U_b + U_t = \frac{C^2}{8} \frac{\psi r L}{m} D_x \left(\frac{m\pi}{L} \right)^4 \left[1 + \left(\frac{n}{\lambda} \right)^4 \frac{D_y}{D_x} + \left(\frac{n}{\lambda} \right)^2 \left\{ 2 \frac{D_{xy}}{D_x} + 4 \frac{D_T}{D_x} \right\} \right] \quad (7.56)$$

The energy absorbed by the panel during buckling as a result of in-plane strains and out-of-plane curvature is equal to the work done by the critical axial load as the panel shortens. The shortening of the panel over one half wave length is given by

$$\int_o^{L/m} \frac{1}{2} \left(\frac{\partial w}{\partial x} \right)^2 dx = \frac{\pi^2}{4} C^2 \frac{m}{L} \sin^2 \frac{n\pi\theta}{\psi} \quad (7.57)$$

so the work done by the axial force of N_x per unit width over the panel width is

$$T_1 = \frac{\pi^2}{8} C^2 \frac{m}{L} \psi r N_x \quad (7.58)$$

The equality $T_1 = U_1 + U_2$ yields the critical value of the axial force as follows:

$$(N_x)_{cr} = D_x \left(\frac{m\pi}{L} \right)^2 \left[1 + \left(\frac{n}{\lambda} \right)^4 \frac{D_y}{D_x} + \left(\frac{n}{\lambda} \right)^2 \left\{ 2 \frac{D_{xy}}{D_x} + 4 \frac{D_T}{D_x} \right\} \right] + \frac{E_x h}{1 - v_x v_y} \left[\alpha^2 + \beta^2 \frac{E_y}{E_x} \left(\frac{n}{\lambda} \right)^2 + 2\alpha\beta v_y \frac{n}{\lambda} + (1 - v_x v_y) \frac{G_{xy}}{E_x} \left\{ \alpha \frac{n}{\lambda} + \beta + \frac{\psi}{n\pi} \right\}^2 \right] \quad (7.59)$$

Noting that $\frac{m\pi}{L} = \frac{m\psi r n\pi}{nL \psi r} = \frac{\lambda n\pi}{n \psi r}$, this equation becomes

$$(\sigma_x)_{cr} = \frac{D_x}{h} \left(\frac{\lambda n\pi}{n \psi r} \right)^2 \left[1 + \left(\frac{n}{\lambda} \right)^4 \frac{D_y}{D_x} + \left(\frac{n}{\lambda} \right)^2 \left\{ 2 \frac{D_{xy}}{D_x} + 4 \frac{D_T}{D_x} \right\} \right] + \frac{E_x}{1 - v_x v_y} \left[\alpha^2 + \beta^2 \frac{E_y}{E_x} \left(\frac{n}{\lambda} \right)^2 + 2\alpha\beta v_y \frac{n}{\lambda} + (1 - v_x v_y) \frac{G_{xy}}{E_x} \left\{ \alpha \frac{n}{\lambda} + \beta + \frac{\psi}{n\pi} \right\}^2 \right] \quad (7.60)$$

The right hand side of Eq. (7.60) contains four unknowns, the number of transverse half waves, n , the ratio of longitudinal to transverse half wave length, n/λ , and the factors α and β . Assuming that there is only one transverse half wave, as is normally the case, the expression is minimised with respect to α and β for each value of n/λ , and then with respect to n/λ to obtain the critical stress.

The results of this exercise are illustrated for curved UD laminate panels of varying widths in Figure 7.35. The radius of curvature, r , of 2000 mm and thickness, h , of 30 mm are kept constant and chosen to be representative of the values likely to obtain on the suction face near mid-span on a blade with 40 m tip radius. The fibres of all of the laminate plies are orientated axially, and the longitudinal and transverse moduli are taken as 43.0 GPa and 14.7 GPa, respectively, based on a fibre modulus of 75 GPa and a fibre volume fraction of 0.55. The other laminate properties required for evaluation of the critical stress are detailed on the figure.

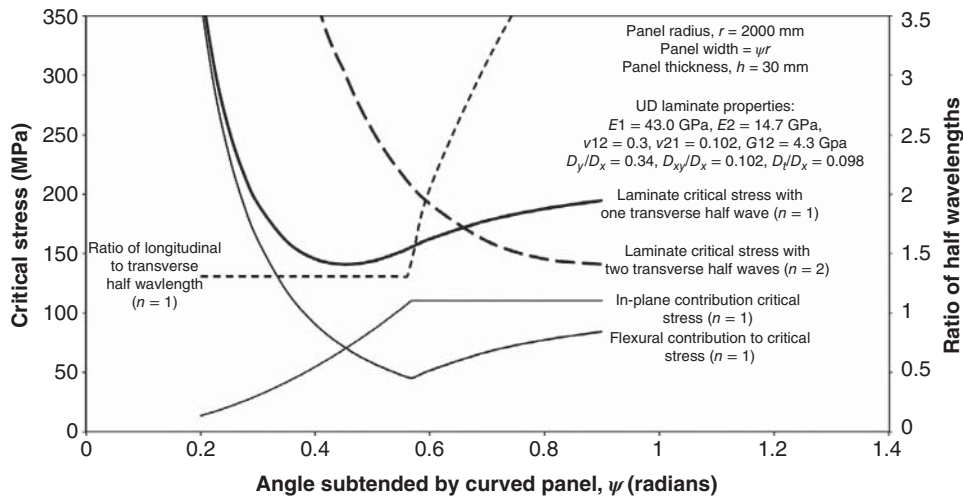


Figure 7.35 Variation of axial critical buckling stress with panel width for a 2000 mm radius \times 30 mm thick curved anisotropic panel of UD laminate

The heavy curve in Figure 7.35 shows the variation in axial critical stress with panel width (in terms of subtended angle) when the buckled shape has only a single half wave in the transverse direction and the fine lines below show the separate in-plane and flexural contributions. The minimum stress of 141 MPa occurs when the angle subtended by the panel is about 25°, but there is only a gradual increase in critical stress as the angle increases above this. When the subtended angle exceeds about 37°, buckling with two half waves in the transverse direction takes over as the critical mode – see dashed line.

The ratio of the longitudinal half wave length to the transverse half wave length is constant and equal to the quartic root of the ratio D_x/D_y – i.e. 1.309 for an angle subtended by the panel of less than 32° or 0.56 rad. The maximum additional in-plane deflections are a relatively small constant proportion of the maximum circumferential deflection due to the out of plane deflection, $C\psi/\pi$, with $\alpha/(\psi/\pi) = -0.085$ and $\beta/(\psi/\pi) = -0.111$ for $\psi < 0.56$ rad.

Figure 7.36 shows how the critical buckling stress increases with panel curvature for a panel of fixed width. As noted above, a radius of curvature of 2000 mm is representative of the values likely to obtain on the suction face near mid-span on a blade with 40 m tip radius. Thus, for a 500 mm wide curved spar cap subtending an angle of 0.25 rad (about 14°), the effect of the curvature is to increase the critical buckling stress from 232 to 253 MPa in this example, which corresponds to an increase of about 9% in comparison with an equivalent flat plate.

Allowance for imperfections

In practice, there will be small out-of-plane deviations from the theoretical panel shape due to manufacturing tolerances, with the result that compression loading will generate additional bending stresses. In the worst case, the profile of the deviation will correspond to the buckling mode shape, and the compression load will magnify the deviation by

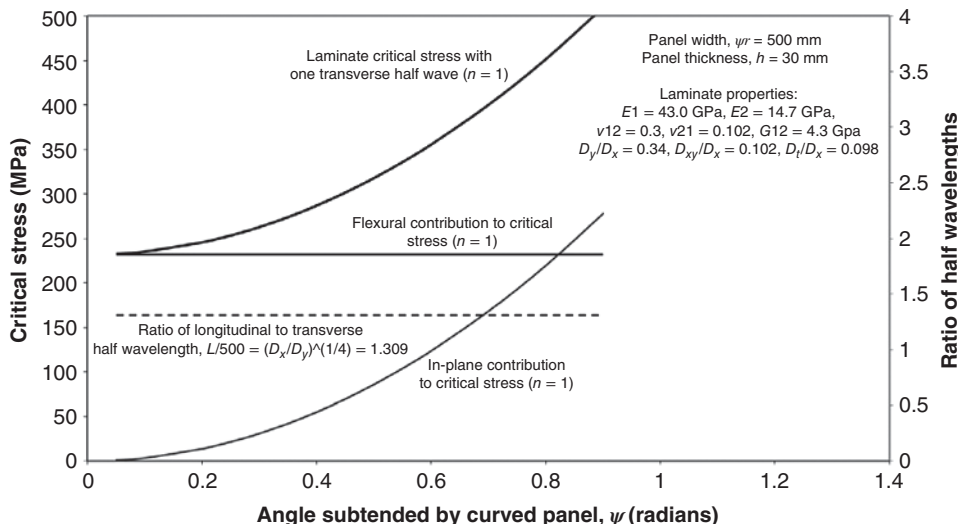


Figure 7.36 Variation of axial critical buckling stress with curvature for 500 mm wide \times 30 mm thick curved anisotropic panel

the factor $1/(1 - P/P_{crit})$, where P is the load applied to the panel and P_{crit} is its critical buckling load. The Germanischer Lloyd *Guideline for the Certification of Wind Turbines* (2010) specifies that a maximum out-of-plane deviation of 1/400 of the buckling wavelength – i.e. the distance between adjacent nodes of the buckling mode shape – should be allowed for unless a smaller value can be justified by measurements. The design is deemed to be satisfactory if the total compression stress (axial plus bending) is less than the permitted value. Alternatively, the effect of imperfections may be allowed for by the application of an appropriate additional partial safety factor.

7.1.17 Blade root fixings

The fixing of the blade root to the hub is one of the most critical areas of blade design, because the order of magnitude difference between the relative stiffnesses of the steel hub and the blade material – usually GFRP or wood – militates against a smooth load transfer. The connection is usually made by steel bolts, which can either be embedded in the blade material in the axial direction or aligned radially to pass through the blade skin, but in either case stress concentrations are inevitable.

Figure 7.37 illustrates four different types of blade root fixings in section. The blade structure is usually a cylindrical shell at the root, in which case the stud or bolt fixings are arranged in a circle.

Figure 7.37a shows the carrot connector, which is the standard fixing for laminated wood blades. The connector consists of a tapered portion carbon-epoxy grouted into a stepped hole drilled into the end of the blade, together with a projecting threaded stud for attachment to the hub or pitch bearing. Connectors are either machined from high strength steel or cast from spheroidal graphite iron (SGI). They are normally pre-loaded

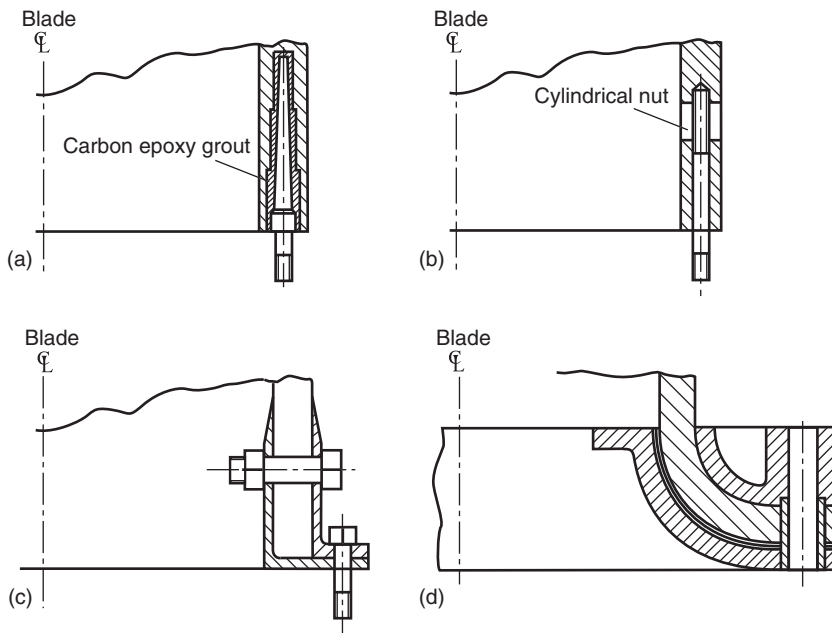


Figure 7.37 (a) Carrot connector, (b) T-bolt connector, (c) pin-hole flange, and (d) trumpet flange

to reduce fatigue loading. A similar connector, in which the embedded portion is cylindrical rather than tapered, is in common use on GFRP blades. The surface of the cylinder is often ribbed externally to improve anchorage within the surrounding GFRP.

Figures 7.37b–d show three further fixing arrangements used on GFRP blades. The T-bolt connector, shown in Figure 7.37b, consists of a steel stud inserted into a longitudinal hole in the blade skin, which engages with a cylindrical nut held in a transverse hole. The stud is pre-loaded to reduce fatigue loading.

The ‘pin-hole flange’ arrangement in Figure 7.37c uses the same method of load transfer between the GFRP and the steel – i.e. bearing on a transverse bolt – but the interface does not lend itself to pre-loading. Moreover, the bolts attaching the flange to the hub are eccentric to the blade shell, so the flange has to resist the resultant bending moment as well.

In the trumpet flange detailed in Figure 7.37d, the blade root is splayed out in the form of a trumpet mouth and clamped between inner and outer flanges by the ring of bolts that attach the flange to the hub. These bolts also pass through the GFRP skin to provide positive anchorage. Again, the flange has to resist bending moments arising from the eccentricity of the fixing bolts to the blade shell where it emerges from the flange. The pin-hole and trumpet flange arrangements are rarely used for larger blades.

The stress distributions calculated for blade root fixings are subject to significant levels of uncertainty, so it is normal to conduct both static and fatigue tests on them to verify the suitability of the design. Static pull-out failures of carrot connectors occur as a result of shearing of the GFRP or wood surrounding the grout, but fatigue failures can

also occur in the connector itself or the grout. However, SGI studs subjected to $R = 0.1$ fatigue loading at over 60% of the UTS have survived for approximately 10^6 cycles.

Mayer (1996) records the results of fatigue tests on the other blade root fixings featured in Figure 7.37, but in no case did failure occur as a result of fatigue of the GFRP in the region of the root fixing. In the case of the T-bolt fixing arrangement, failure occurred in the studs rather than in the GRP. The pin-hole flange specimens developed fatigue cracks in the GFRP in areas remote from the root fixings and the trumpet flange specimens developed cracks in the flanges themselves.

7.1.18 Blade testing

Although sophisticated analytical tools are available to underpin the development of a blade design, certain blade features are difficult to model accurately. These include:

- Adhesive joints between webs and spar caps, some of which are assembled ‘blind’.
- Adhesive joints at leading edge and trailing edge, also assembled ‘blind’.
- Ply drops.
- Manufacturing defects.
- Manufacturing tolerances.

In view of this, recourse is usually made to full-scale blade testing, in order to determine blade strength more accurately, together with the testing of individual structural details such as joints. This in turn facilitates more economical design, as it enables a reduced partial safety factor for material strength to be used (γ_{m4} (A) in Table 7.10). Technical requirements for blade testing are set out in IEC 61400-23: 2014 and DNVGL-ST-0376 (2015).

There are three types of full-scale blade tests – modal, static and fatigue. In each case, the blade is attached to a rigid structure at its root, with its axis horizontal for loadings sideways or tilted upwards for loading vertically downwards. In modal testing, a number of modes – e.g. the first and second flapwise, first and second edgewise and torsional – are separately manually excited and the frequencies measured and compared with predicted values.

Static testing

Four separate static tests are normally carried out, with the loads applied in the two flapwise and edgewise directions in turn. Loading in one flapwise and one edgewise direction is generally not considered sufficient, because of the differing buckling behaviour in each case. Loads are introduced at several radii to approximate reasonably closely to the design load profile and increased in stages until a loading 10% above the design loading is reached. The maximum deflection will be very large – up to around 30% of blade length for a GFRP blade. The blade will have been strain gauged at regular intervals along its length on both the suction and pressure sides and the leading and trailing edges, enabling strain readings to be recorded at each loading stage, together with deflection measurements. Following completion of the load test, the blade is thoroughly inspected for any signs of damage.

Fatigue testing

Fatigue tests have to be designed so that the fatigue critical areas of the blade are subjected to load cycles that will cause at least the target fatigue damage, defined as the calculated lifetime fatigue damage due to the lifetime fatigue loads multiplied by a specified factor. Although it is simpler to run separate, sequential tests for fatigue loading in the flapwise and edgewise directions, it is difficult to apply the target fatigue damage to points remote from both principal axes without overloading points close to these axes. This drawback can be ameliorated by applying loading cycles about both axes simultaneously in a single test ('biaxial' or 'multi-axial' testing) – see IEC 61400-23 Annex D.

Fatigue loads are normally applied by exciting the blade at its resonant frequency, either by means of a ground-mounted hydraulic actuator or an oscillating mass device fixed to the blade. It may be necessary to add weights to the blade to reduce the natural frequency so that the hydraulic pump can supply fluid fast enough. Given the low natural frequencies of large blades (ca 0.6 Hz flapwise for an 80 m blade), it is normal to increase the magnitude of the loading cycles to reduce the number required and hence the duration of the test. A target cycle count of a million cycles is often adopted. Fatigue loading may be either constant amplitude or variable amplitude, but in the latter case it may not be practicable to scale up the magnitude of the larger cycles because of non-linear behaviour at higher loading. The mean loading should be close to that occurring under the operating conditions resulting in maximum fatigue damage.

DNVGL-ST-0376 (2015) specifies that the target fatigue loading should be obtained by multiplying the lifetime design equivalent load for the requisite number of test cycles by three factors, Y_{nf} , Y_{sf} , and Y_{ef} , where $Y_{nf} = 1.15$, $Y_{sf} = 1.1$ and takes account of blade to blade variation and Y_{ef} takes account of the possible error in adopting a reduced number of cycles and is taken as 1.05 when the number of test cycles is about a million. Thus the overall factor is about 1.33. Individual factors with the same values are specified in IEC 61400-23, the first one being termed the partial factor for consequences of failure.

Biaxial testing can be carried out in two different ways. In one, the blade is forced to oscillate at the same frequency in the flapwise and edgewise directions – e.g. by hydraulic actuators. The relative phase angle between the oscillations can be set at 90°, mirroring the phase difference between flapwise and edgewise deterministic loads in operation. Alternatively the blade can be excited in the flapwise and edgewise directions at the respective resonant frequencies, with the result that the phase angle between the flapwise and edgewise load peaks is constantly changing. This test method requires a complex control system to continuously maintain the desired load amplitudes, as there is a degree of interaction between the flapwise and edgewise oscillations (Snowberg et al. 2014).

The blade should be inspected for signs of damage at frequent intervals during fatigue testing, as well as at the end. Acoustic emissions may be recorded during the test to provide warning of any incipient laminate failure.

7.1.19 Leading edge erosion

The principal causes of leading edge erosion are impact by raindrops, hailstones and air-borne solids, such as sand, with the severity of the problem varying considerably from place to place because of climatic variation. A valuable overview of the incidence of leading edge erosion is provided by Keegan et al. (2013). The rate of erosion is critically dependent on tip speed.

The roughening of the smooth aerofoil arising from leading edge erosion results in reduced lift and increased drag, leading to reduced energy generation. In extreme cases, erosion may cause loss of structural strength. Much effort has therefore been directed at identifying suitable leading edge protection to reduce energy loss and the need for in-situ blade repairs.

Energy loss

Measured data on power curve degradation due to roughening of the blade surface is scarce. A Sandia Laboratories Report analysed data from four years of operation of a pitch-regulated, megawatt-scale turbine (Ehrmann et al. 2017). In this case the source of roughness was general soiling of the blade during the dry months when the rain was not cleaning the blades, so the data was averaged separately over the wet and dry months, with mean rainfall of 1.7 in and 0.1 in, respectively. It was found that the power output in the dry months was reduced by an average of 4% for wind speeds between 50% and 90% of rated.

Ehrmann et al. went on to investigate the effect of artificial surface roughening on aerofoil properties measured in a wind tunnel. Vinyl decals were affixed to the leading edge, with roughness simulated by large numbers of randomly positioned raised discs approximately 3 mm in diameter. In a series of six experiments carried out with 0.14 mm tall discs and areal densities of 0%, 3%, 6%, 9%, 12%, and 15%, there was a clear trend of reducing lift curve slope and reducing maximum lift as disc density increased, reaching 7.3% reduction for 15% density. Drag also increased, leading to a maximum drop of the lift to drag ratio of 40%. The predicted loss in annual energy production for the NREL 5 MW turbine at a site with an 8.5 m/s mean wind speed was 2.3% for the higher disc densities. The NREL 5 MW turbine is pitch regulated, so losses due to blade roughness only occur below the rated speed of 11.4 m/s.

The gain in turbine annual energy production resulting from the repair of moderately eroded blades has been measured at an offshore site under the auspices of the UK Offshore Renewable Energy (ORE) Catapult, taking advantage of light detection and ranging (LiDAR) technology to measure incident wind speeds over the rotor swept area. This established that a gain in energy production of 1.5–2% was possible as a result of the repairs (ORE Catapult 2016).

Rain drop impact

A coarse estimate of the maximum pressure exerted on a rigid plate during initial raindrop impact is provided by the water hammer equation, $p = \rho WV_s$, where W is the velocity of the raindrop relative to the blade and V_s is the speed of sound in water (about 1500 m/s). Raindrop terminal velocities can reach 9 m/s for large droplets, so, for a 90 m/s tip speed, the relative velocity can reach around 100 m/s at 270° azimuth, giving a pressure estimate of 150 MPa. This reduces by about one third if allowance is made for the elasticity of the wind turbine blade matrix. Keegan et al. (2012) carried out numerical modelling of a 3 mm diameter rain drop impact on a wind turbine blade, treating it as an epoxy resin plate. For a 100 m/s impact velocity, the maximum von Mises stress was calculated at about 90 MPa, which exceeds the tensile strength of many epoxies.

Although the use of advanced computer software enables impact stresses to be estimated, the prediction of damage development is far more challenging, so experimental

testing is required for the evaluation of different surface finishes. Typically, the test specimen is mounted at the end of an arm that is rotated at a speed of about 150 m/s in a chamber with water drops falling at a rate of about 30 mm/hr. Testing is usually in accordance with ASTM G73-10 (2017). Erosion, which begins at the outer tip of the specimen, can then be tracked through the duration of the test, as it advances towards the root.

Eisenberg et al. (2016) developed a model of leading edge erosion due to rainfall based on the work of Springer (1976). This identified an incubation period in which fatigue damage takes place with no visible effect, followed by a period of steady weight loss as erosion proceeds. The duration of the incubation period is determined by the rainfall intensity and the number of raindrop impacts per unit area needed to initiate erosion, the latter being inversely proportional to the raindrop impact velocity raised to a power of 5.7. The model was found to be able to predict with reasonable accuracy the incubation periods for blades in the field on the basis of whirling arm rain erosion tests for the same material. The subsequent rate of erosion was predicted to be inversely proportional to the raindrop impact velocity raised to a power of 6.7.

Protection against erosion

Leading edge protection has normally been provided by polyurethane adhesive tape or polyurethane paint. The former is typically made of transparent, abrasion-resistant and UV-resistant polyurethane elastomer and should last for 20 years at blade tip speeds of 70 m/s (Offshore Wind Industry 2015), but might last only a year or two at the tip speeds of 90 m/s, which are the norm offshore. Polyurethane paint can provide three times the life of tape, potentially enabling the leading edge of an offshore blade to outlast the blade's five year guarantee period but little more.

Other types of leading edge protection that have been developed or are in the process of development include the following:

- The affixing of tough, semi-flexible thermoplastic shields pre-formed to the leading edge profile (www.armouredge.com).
- The affixing of a metallic shield of nickel cobalt alloy. This is pre-formed to the leading edge profile by means of electrodeposition onto a mandrel in a chemical bath (Windtech International 2019).

7.1.20 Bend-twist coupling

The main function of blade pitching is to limit the power output to rated, but an important secondary benefit is the reduction of the magnitude of blade flapwise bending moment fluctuations due to fluctuations caused by low frequency turbulent variations. In principle, pitching can be used to reduce bending moment fluctuations due to rapid wind speed changes through blade independent pitch control, but the scope for this is limited by the blade pitching rates that are practically possible.

Off-axis fibres

An alternative approach to reducing loads at rotational frequency is passive pitching, in which increased loading on the blade in the downwind direction causes it to twist to

feather to reduce the angle of attack. This can be achieved by orientating the fibres in the spar caps at an angle to the axis of the blade, so that blade bending induces blade twisting at the same time – a behaviour known as *bend-twist coupling*. Note that the fibres in each spar cap are aligned parallel to one another and run from the leading edge outboard to the trailing edge inboard to reduce the angle of attack under increased thrust loading. See illustration in Figure 7.38. (It can be noted in passing that off-axis fibre orientation in the opposite direction has been considered on stall-regulated machines. For example, Lobitz et al. [1996] investigated the extent to which bend-twist coupling could increase the power output at moderate wind speeds relative to the rated power.)

The bending and torsional rotations per unit length, $\dot{\theta}$ and $\dot{\phi}$, respectively, are described by the following equations:

$$\dot{\theta} = \frac{M}{\langle E_x I \rangle} + \lambda T; \dot{\phi} = \frac{T}{\langle GJ \rangle} + \lambda M \quad (7.61)$$

where the $\langle \rangle$ brackets indicate that the bending and torsional stiffnesses within the brackets apply when the blade is free to twist or flex, respectively. The moment M is defined

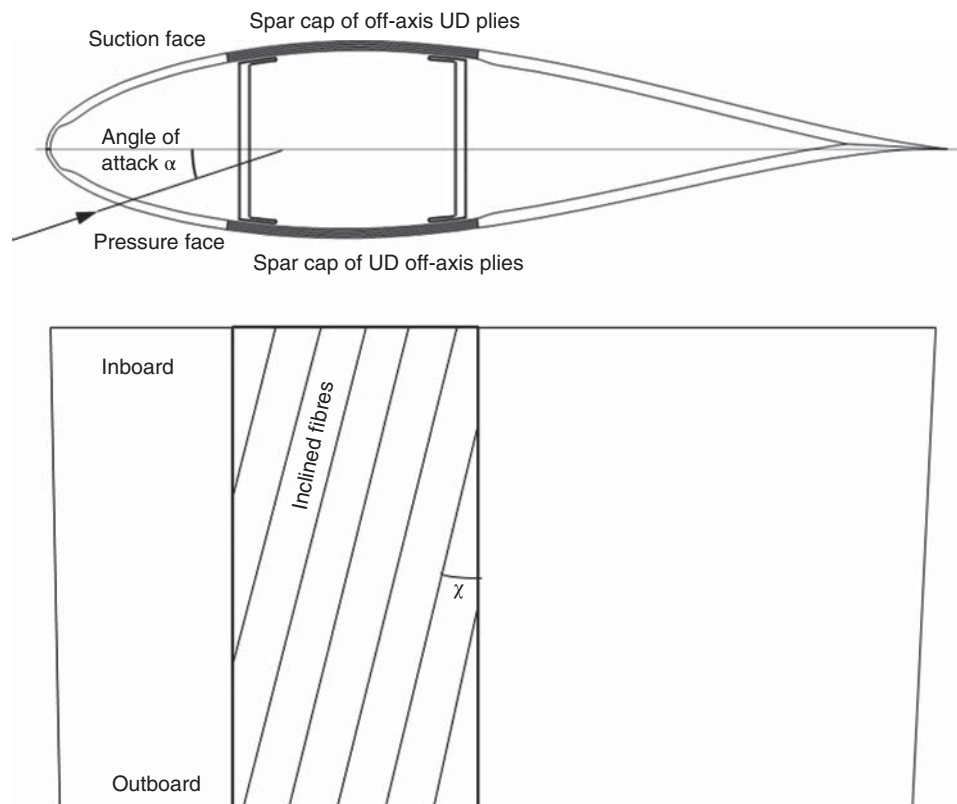


Figure 7.38 Blade cross-section (looking towards hub) and plan view on blade element suction face showing inclination of spar cap UD fibres designed to reduce angle of attack when flapwise blade loading increases

as positive when it causes the blade to deflect downwind and the torque T is defined as positive when it acts in the anti-clockwise direction. The quantity λ is a measure of the bend-twist coupling and equates to the torsional rotation per unit length due to a unit moment and to the flexural rotation per unit length due to a unit torque.

Ratio of twisting and bending rotations under the action of applied moment

It is relatively straightforward to estimate the degree of coupling if some simplifying assumptions are made. A blade spar consisting of two spar caps linked together by two shear webs, as illustrated in Figure 7.38, can be treated as a rectangular tube and initially considered on its own. The in-plane shortening and accompanying shear distortion of a length of suction face spar cap when the blade is subject to thrust loading are shown in Figure 7.39.

It can be shown (Barbero (2018)) that the longitudinal strain, ε_x , due to the longitudinal stress, σ_x , is given by

$$\varepsilon_x = \bar{S}_{11}\sigma_x = \left(\frac{\cos^4\chi}{E_1} + \left(\frac{1}{G_{12}} - 2\frac{\nu_{12}}{E_1} \right) \cos^2\chi \sin^2\chi + \frac{\sin^4\chi}{E_2} \right) \sigma_x \quad (7.62)$$

and that the shear strain, γ_{xy} , is

$$\begin{aligned} \gamma_{xy} = \bar{S}_{16}\sigma_x &= \left[\left(\frac{2}{E_1}(1 + \nu_{12}) - \frac{1}{G_{12}} \right) \cos^3\chi \sin\chi \right. \\ &\quad \left. - \left(\frac{2}{E_2} \left(1 + \nu_{12} \frac{E_2}{E_1} \right) - \frac{1}{G_{12}} \right) \sin^3\chi \cos\chi \right] \sigma_x \end{aligned} \quad (7.63)$$

where χ is the inclination of the fibres to the blade axis, E_1 and E_2 are the elastic moduli of the laminate parallel and perpendicular to the fibres, respectively, G_{12} is the shear

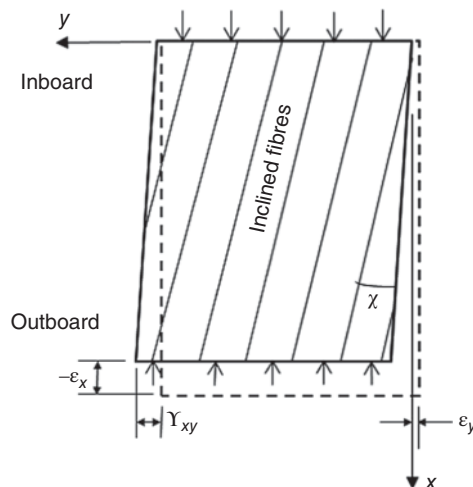


Figure 7.39 In-plane contraction and shear distortion of section of suction face spar cap resulting from application of a longitudinal compression stress

modulus with respect to these directions, and $-v_{12}$ is the ratio of the transverse strain to longitudinal strain when the laminate is loaded parallel to the fibres.

It is assumed that the shear strain occurring in each spar cap is accommodated by twisting of the rectangular tube accompanied by warping of the cross-section, so that no shear stresses are generated. In these circumstances it can be shown that the twist per unit length of the tube is

$$\dot{\phi} = \frac{\gamma_{xy}}{d} = \frac{\bar{S}_{16}\sigma_x}{d} = -\frac{\bar{S}_{16}M}{2I} = \lambda M \quad (7.64)$$

where positive twist is taken to be in the anti-clockwise direction looking towards the hub, and d and I are the depth of the rectangular tube and its second moment of area, respectively. \bar{S}_{16} and σ_x are both negative, so the twist per unit length is positive – i.e. it reduces the angle of attack. It is seen that the torsional rotation per unit length accompanying a unit moment, λ , is $-\bar{S}_{16}/2I$. Also the bending rotation per unit length is

$$\dot{\theta} = \frac{1}{R} = \frac{M}{E_x^* I} = -\frac{\sigma_x}{E_x^* d/2} = -\frac{\sigma_x \bar{S}_{11}}{d/2} = -\frac{\epsilon_x}{d/2} \quad (7.65)$$

where the asterisk in E_x^* signifies that it applies when the tube is not restrained against twisting – i.e. $E_x^* = 1/\bar{S}_{11}$. Thus when the rectangular tube is subject to loading in flexure, the ratio between the twisting and bending rotations per unit length is $\frac{\dot{\phi}}{\dot{\theta}} = -\frac{1}{2} \frac{\bar{S}_{16}}{\bar{S}_{11}}$.

In the case of a blade consisting of a box spar and a structural aerodynamic shell, the twisting is moderated by the torsional stiffness of the aerodynamic shell, so that

$$\frac{\dot{\phi}}{\dot{\theta}} = -\frac{1}{2} \frac{\bar{S}_{16}}{\bar{S}_{11}} \frac{G_B^* J_B}{G_B^* J_B + G_S J_S} = -\frac{1}{2} \frac{\bar{S}_{16}}{\bar{S}_{11}} \beta \quad (7.66)$$

where $G_B^* J_B$ and $G_S J_S$ are the torsional stiffnesses of the box spar and the aerodynamic shell, respectively. The asterisk in $G_B^* J_B$ signifies that the stiffness applies when the tube is not restrained against bending. The ratio of negative shear strain to bending stress, $-\gamma_{xy}/\sigma_x = -\bar{S}_{16}$ is plotted out against fibre inclination, χ , in Figure 7.40 for a 55% fibre volume fraction laminate with fibre and matrix moduli of 75 and 4 GPa, respectively. Also shown are the spar cap longitudinal modulus, $E_x^* = 1/\bar{S}_{11}$, and the ratio of twist angle to flexural rotation for a case in which the spar torsional stiffness is 50% of the total torsional stiffness – i.e. for $\beta = 0.5$. This applies at about 60% radius for the FC40 blade design described in Section 7.1.14. It is seen that the ratio of shear strain to bending stress reaches a maximum at a fibre inclination of about 25°, but that the ratio of twist angle to flexural rotation reaches a maximum at a rather lower fibre inclination of about 15°, because of the pronounced reduction in the spar cap longitudinal modulus as fibre inclination increases.

Coupling coefficient

Lobitz et al. (2001) introduce a coupling coefficient, α , as a measure of the degree of bend-twist coupling. This is defined as $\alpha = \frac{K}{\sqrt{[E_x I][GJ]}}$, where K is the bending moment

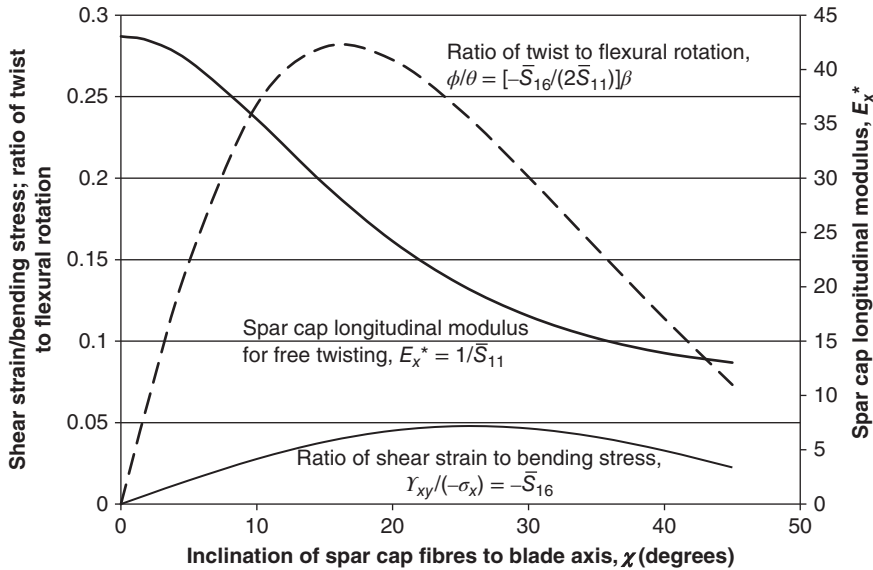


Figure 7.40 Variation with fibre inclination of $Y_{xy}/\sigma_x = \bar{S}_{16}$, spar cap longitudinal modulus and ratio of twist to flexural rotation with $\beta = 0.5$

divided by twist per unit length in the absence of bending deflection (or the torque divided by bending rotation per unit length in the absence of torsional rotation), and the stiffnesses $[E_x I]$ and $[GJ]$ are those that apply when the length of blade is restrained against torsion and flexure, respectively. If, as before, $\langle E_x I \rangle$ and $\langle GJ \rangle$ denote the stiffnesses that apply when the length of blade is *not* restrained against torsion and flexure, respectively, then it can be shown that

$$K = \frac{\lambda \langle GJ \rangle \langle E_x I \rangle}{1 - \lambda^2 \langle GJ \rangle \langle E_x I \rangle}, [E_x I] = \frac{\langle E_x I \rangle}{(1 - \lambda^2 \langle GJ \rangle \langle E_x I \rangle)} \text{ and } [GJ] = \frac{\langle GJ \rangle}{(1 - \lambda^2 \langle GJ \rangle \langle E_x I \rangle)} \quad (7.67)$$

and it follows that $\alpha = \lambda \sqrt{\langle GJ \rangle \langle E_x I \rangle}$. The coupling coefficient, α , is plotted against spar cap fibre inclination for the FC40 blade design at 62.5% and 32.5% radii in Figure 7.41. In each case the coupling coefficient reaches a maximum for a fibre inclination of about 25°, but its magnitude at 32.5% radius (0.11) is about half that at 62.5% radius (0.22), largely because the adoption of a constant spar cap width inboard of 62.5% radius results in a reduced spar torsional stiffness at 32.5% radius as a proportion of the total.

Fedorov (2012) investigated the bend-twist coupling resulting from the inclination of spar cap fibres on a representative GFRP commercial wind turbine blade design using FE analysis and reported a maximum coupling coefficient of about 0.2 at 25° fibre inclination. However, when the glass fibres in the spar cap were replaced by carbon fibres, the maximum coupling coefficient rose to 0.4.

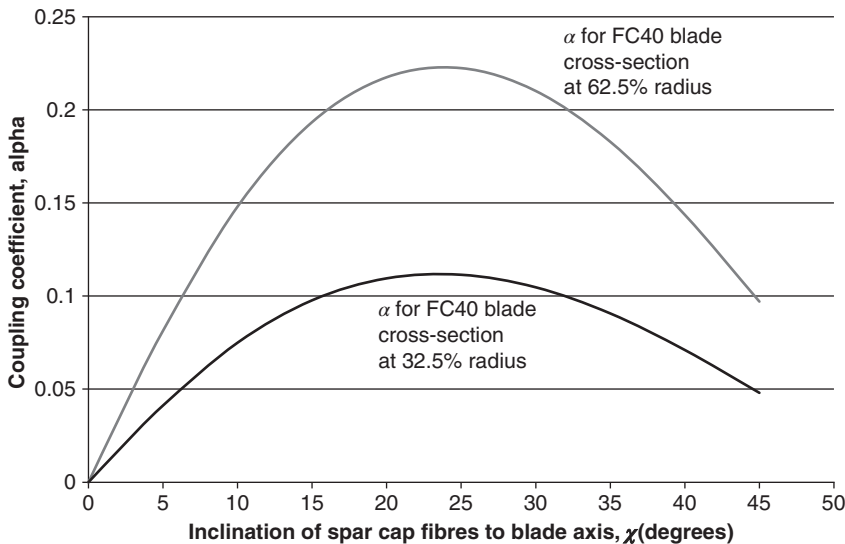


Figure 7.41 Variation of coupling coefficients at 62.5% and 32.5% radius for blade FC40 (see Section 7.1.14) with spar cap fibre inclination

Bending moment reduction

The reduction in fluctuating moment resulting from bend twist coupling can be estimated using the following procedure:

1. Choose the fibre inclination, χ , to be investigated.
2. Select a trial value for the bending moment reduction factor, η .
3. Calculate the flexural rotation per unit length at each blade station due to the reduced moment distribution.
4. Calculate the ratio between the twisting and bending rotations per unit length, $\dot{\phi}/\dot{\theta}$, at each blade station.
5. Calculate the imposed twist per unit length at each blade station by multiplying the flexural rotation per unit length by $\dot{\phi}/\dot{\theta}$.
6. Integrate over the length of the blade to obtain the imposed twist, $\Delta\phi$, at each station.
7. Calculate the resulting reduction in load on each blade element according to the formula:

$$\Delta L = \frac{1}{2} \rho W^2 \Delta C_L c \Delta r = \frac{1}{2} \rho (\Omega r)^2 2\pi (-\Delta\phi) c \Delta r$$
8. Derive distributions of shear and bending moment reductions.
9. Subtract the bending moment reduction from the original applied moment at each blade station to obtain improved estimate of reduced bending moments.
10. Repeat steps 3–9 using improved estimate of reduced bending moments as input. A further iteration may be needed if the initial estimate of η was poor.

The bending moment reduction factor has been estimated for the spar cap fibre inclinations of 5, 10, and 15° for the case of the FC40 blade, using the method above. Reduction factors of 0.87, 0.81, and 0.78 were obtained, indicating diminishing returns with increasing fibre inclination.

Blade pitch correction

Given that a steady blade twist of about 1–2° will be induced at rated wind speed by the bend twist coupling resulting from a 5° spar cap fibre inclination, a correction to the initial blade twist distribution is desirable so that the optimum twist distribution is attained at or close to rated wind speed. Small pitch adjustments are then required at lower wind speeds to maximise energy yield below rated power.

Tower clearance

As blade design is often governed by the need to maintain adequate tower clearance, the effect of the reduced blade stiffness due to spar cap fibre inclination needs to be considered alongside that of the reduced loading. At 180° azimuth the bending moment fluctuation due to wind shear subtracts from that due to gust loading, so the extreme bending moment at 180° azimuth is likely to be only about 50% greater than the average moment over a full revolution. On this assumption, the above reduction factors become 0.957, 0.937, and 0.927 respectively in relation to the total bending moment for the three fibre inclinations. Figure 7.42 shows how the bending moment fluctuation at blade passing frequency, the extreme bending moment at 180° azimuth, the spar cap stiffness and the tip deflection at 180° azimuth vary with spar cap fibre inclination, each parameter being normalised by its value when the fibre inclination is zero. It can be seen that the penalty of increased tip deflection starts to become significant at fibre inclination angles above 5°.

Several investigations of the benefits of bend-twist coupling were carried out as part of the EU INNWIND project (INNWIND 2015). For example, researchers at Polimi (Polytechnico Milano) investigated the use of off-axis fibres in the spar caps of the DTU 10 MW turbine and concluded that this would result in a reduction in the cost of energy of close to 1% for fibre inclinations of 3, 4, and 5°, reducing to 0.9% and 0.75% for fibre inclinations of 6 and 7° respectively. The flapwise fatigue damage equivalent load at the blade root was found to reduce by about 3.5% for a fibre inclination of 5°. Researchers at DTU carried out a similar exercise with the spar cap fibres inclined at 8° and concluded that the flapwise blade root fatigue damage equivalent load would reduce by 7.5%.

Swept-back blades

An alternative method of introducing bend-twist coupling is to change the geometry of the blade towards the tip, so that the blade centre-line is curved backwards in relation to the direction of blade rotation. This results in a lift loading on the outboard part of the blade that is offset with respect to the inboard part and generates a torque that twists the blade towards feather. The swept-back blade has the advantage that there is no loss of blade bending stiffness to erode tower clearance, but it comes at the cost of increased blade torsional loadings.

Scott et al. (2017) investigate using a combination of material bend-twist coupling (using fibre alignment) and geometric bend-twist coupling. An aeroelastically tailored

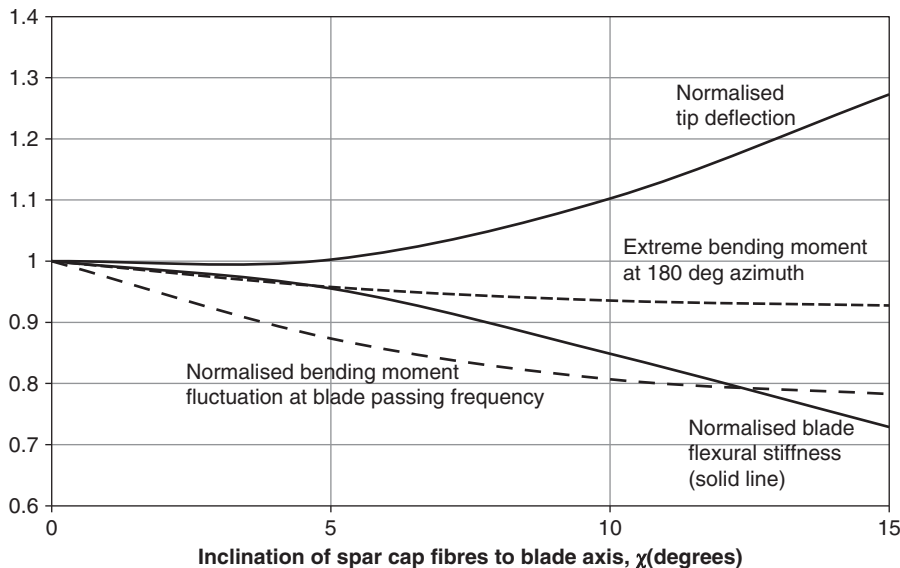


Figure 7.42 Variation of bending moment fluctuations at blade passing frequency, extreme bending moment at 180° azimuth, blade flexural stiffness and tip deflection at 180° azimuth with spar cap fibre inclination. In each case the values are normalised by the value at zero fibre inclination

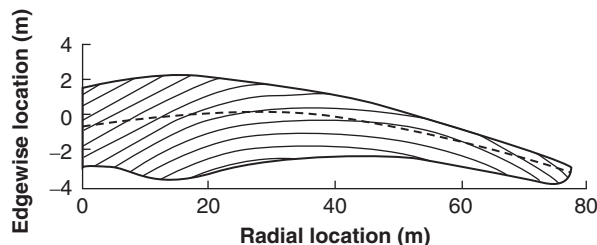


Figure 7.43 Proposed use of fore and aft blade sweep in combination with off-axis fibres to provide bend-twist coupling. Source: Reproduced with permission from Scott et al. (2017), ‘Effects of Aeroelastic Tailoring on Performance Characteristics of Wind Turbine Systems’, *Renewable Energy*, 114(B), 887–903

blade design is proposed in which both of these features are varied along the blade, to try to achieve reduced flapwise fatigue and extreme operational gust loading, reduced pitch rate, and some increase in energy capture, although blade root torsional moments might increase. However, these increases can be partially offset by employing a second order sweep curve that passes ahead of the pitch axis at around mid-span and then rearwards of the pitch axis at the tip. See Figure 7.43.

The effect of sweeping back the DTU 10 MW blade tip by 2 m starting at 80% radius was investigated as part of the INNWIND project and found to yield a 3% reduction in flapwise fatigue damage equivalent load at the blade root.

Commercial application

Bend-twist coupling has been commercially applied in the case of the Siemens 53 m blade.

7.2 Pitch bearings

On pitch-regulated machines a bearing similar to a crane slewing ring is interposed between each blade and the hub to allow the blade to be rotated or ‘pitched’ about its axis. A typical arrangement is as shown in Figure 7.44, in which the inner and outer rings of the bearing are bolted to the blade and hub, respectively.

The different types of bearings available can be classified according to the rolling elements used and their arrangement, in order of increasing moment capacity, as follows:

1. Single-row roller bearings, with alternate rollers inclined at $+45^\circ$ and -45° to the plane of the bearing.
2. Single-row ball bearings.
3. Double-row ball bearings.
4. Three-row roller bearings.

These are shown in cross-section in Figure 7.45. The single-row ball bearing slewing rings are normally designed to transmit axial loads in both directions and are therefore known as *four-point contact bearings*. Low contact stresses are achieved by making the radii on each side of the grooves only slightly larger than that of the balls.

At low wind speeds, the cyclic in-plane bending moment at the blade root due to gravity is of similar magnitude to the out-of-plane moment due to blade thrust, so bearing loads will alternate in direction over portions of the bearing circumference. Accordingly,

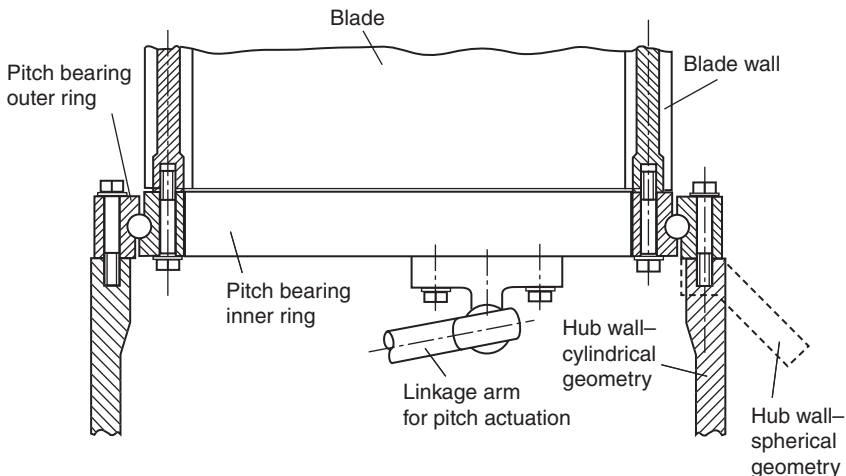


Figure 7.44 Typical pitch bearing arrangement

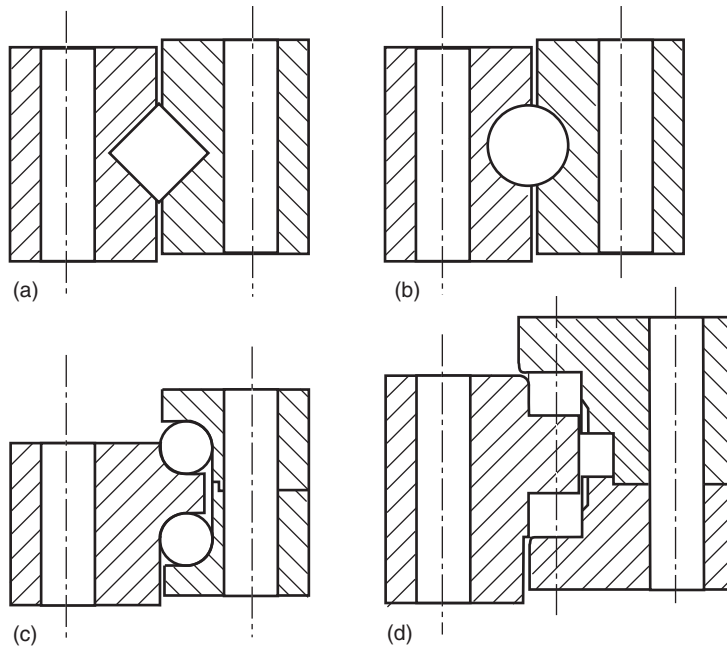


Figure 7.45 (a) Single-row crossed roller bearings, (b) single-row ball bearings, (c) double-row ball bearings, and (d) three-row roller bearings

it is desirable to avoid the risk of play by pre-loading the bearing. This can be achieved relatively easily on bearings in which one of the rings is split on a plane normal to the axis, such as types 3 and 4, but is more difficult when both rings are solid. In this case it is necessary to force the rolling elements into the races one by one during manufacture.

The bearing selected for a particular application needs to have sufficient moment capacity to both resist the extreme blade root bending moments and provide adequate fatigue life. Manufacturers catalogues typically specify both the extreme moment capacity and the steady moment loading that will give a life of, say, 30 000 bearing revolutions, so the wind turbine designer's chief task is to convert the anticipated pitch bearing duty into the equivalent constant loading at the appropriate number of revolutions. If the rolling elements are ball bearings, the bearing life is inversely proportional to the cube of the bearing loading, so the equivalent loading at N revolutions of the pitch bearing can be calculated according to the formula:

$$M_{eqt} = \left[\frac{\sum_i n_i M_i^3}{N} \right]^{1/3} \quad (7.68)$$

where n_i is the total pitch bearing movement anticipated over the design life at moment loading M_i , expressed as a number of revolutions. In the case of roller bearings, the index of the S-N curve is 10/3 instead of 3, so the above formula should be modified accordingly. As the blade root out-of-plane moment drops as the wind speed increases above rated, the fatigue damage will be concentrated at wind speeds near rated.

The total pitch bearing movement over a period of operation at a particular wind speed is a function of the turbulence intensity and the pitch control algorithm, and is best predicted by means of a wind simulation. The mean blade pitching rate during operation above rated wind speed is found to be of the order of $1^\circ/\text{s}$, assuming the pitch system only responds to wind speed fluctuations at a frequency less than the speed of rotation. On turbines with individual pitch control, however, additional pitching takes place at rotational frequency to reduce the cyclic variation in blade out-of-plane moment (Section 8.3.9), and it is estimated that lifetime pitch travel may increase by a factor of 3 as a result (Section 8.3.13). This has led some manufacturers to switch from four-point contact bearings to three-row roller bearings to meet the extended duty.

The uncertainties inherent in predicting pitch bearing life can be reduced by testing, e.g. with a steady lateral load applied at the end of a root spar. Normal pitch behaviour is simulated by cycling the pitch over a range of about 5° about a mean that is slowly varied over the full range of normal pitch activity. A test to simulate 20 years of turbine operation can last 6 months.

The performance of slewing ring bearings such as those employed as pitch bearings is critically dependent on the extent of bearing distortion under load, so manufacturers normally specify a maximum axial deflection and tilt of the bolted contact surfaces. For example, the limiting values given by Rothe-Erde for a single-row ball bearing slewing ring with a 1000 mm track diameter were 0.6 mm and 0.17° respectively. Local tilting of the bearing rings could clearly be minimised if the blade wall, bearing track and hub wall were all positioned in the same plane. However, this would necessitate the provision of flanges, so the simpler arrangement shown in Figure 7.44, in which the fixing bolts are inserted centrally into the blade and hub walls, is generally preferred. The designer must then ensure that the blade and hub structures are of sufficient stiffness to limit the bearing distortion due to the eccentric loading to acceptable values.

It is standard practice to pre-load the bearing fixing bolts to minimise bolt fatigue loading. Grade 10.9 bolts are commonly used so that the pre-load can be maximised.

7.3 Rotor hub

The relatively complex three dimensional geometry of rotor hubs favours the use of casting in their manufacture, with spheroidal graphite iron (SGI) being the material generally chosen.

Two distinct shapes of hub for three bladed machines can be identified: tri-cylindrical or spherical. The former consists of three cylindrical shells concentric with the blade axes, which flare into each other where they meet, while the latter consists simply of a spherical shell with cut-outs at the three blade mounting positions. Diagrams of both types are shown in Figure 7.46, while an actual spherical hub is illustrated in Figure 7.47. The structural action of the hub in resisting three loadings is discussed in the following paragraphs:

1. *Symmetric rotor thrust loading:* The blade root bending moments due to symmetric rotor thrust loading put the front of the hub in bi-axial tension near the rotor axis and the rear in bi-axial compression, while the thrust itself generates out-of-plane bending stresses in the hub shell adjacent to the low-speed shaft flange connection. The load paths are easy to visualise in this case.

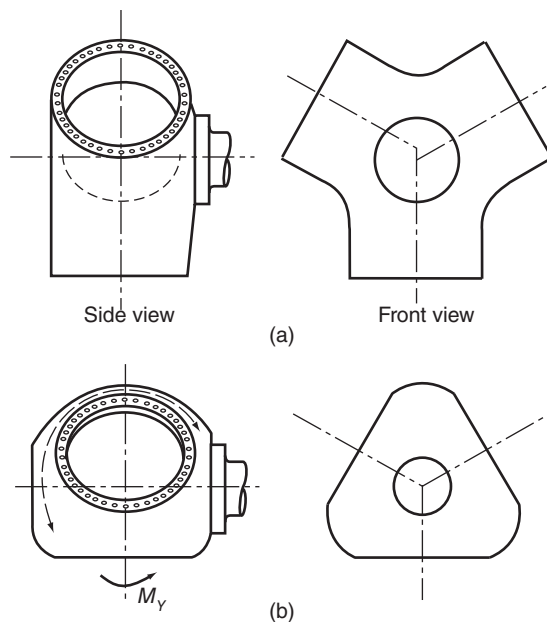


Figure 7.46 (a) Tri-cylindrical hub, and (b) spherical hub



Figure 7.47 Rotor hub. View of spherical-shaped rotor hub for the 1.5 MW NEG Micon turbine awaiting installation. The hub and spinner are temporarily oriented with the rotor shaft axis vertical. The hub and spinner are temporarily oriented with the rotor shaft axis vertical. The turbine is stall-regulated, so slotted blade fixing holes are provided to allow for the fine adjustment of blade pitch to suit the site. Reproduced with permission of NEG Micon

2. *Thrust loading on a single blade:* This generates out-of-plane bending stresses in the hub shell at the rear, and in-plane tensile stresses around a curved load path between the upwind side of the blade bearing and the portion of the low-speed

shaft flange connection remote from the blade (see dashed line in Figure 7.46b). The resultant lateral loads will result in out-of-plane bending.

3. *Blade gravity moments:* On the tri-cylindrical hub, equal and opposite blade gravity moments are communicated via the cylindrical shells to areas near the rotor axis at front and rear where they cancel each other out. It is less straightforward to visualise the corresponding load paths on the spherical hub, as out-of-plane bending is likely to be mobilised.

The complexity of the stress states arising from the latter two types of loading renders finite element (FE) analysis of rotor hubs more or less mandatory. At the most, six load cases need to be analysed, corresponding to the separate application of moments about the three axes and forces along the three axes at a single hub/blade interface. Then the distribution of hub stresses due to combinations of loadings on different blades can be obtained by superposition. Similarly the fluctuation of hub stresses over time can be derived by inputting the time histories of the blade loads obtained from a wind simulation.

The critical stresses for hub design are the in-plane stresses at the inner or outer surface, where they reach a maximum because of shell bending. For any one location on the hub, these are defined by three quantities at each surface – the in-plane direct stresses in two directions at right angles and the in-plane shear stress. In general, these stresses will not vary in-phase with each other over time, so the principal stress directions will change, complicating the fatigue assessment.

There is, as yet, no generally recognised procedure for calculating the fatigue damage accumulation due to multi-axial stress fluctuations, although the following methods have been used, despite their acknowledged imperfections. They all cater for one or more series of repeated stress cycles rather than the random stress fluctuations resulting from turbulent loading.

1. *Maximum shear method:* Here the fatigue evaluation is based on the maximum shear stress ranges, calculated from either the $(\sigma_1 - \sigma_2)/2$, $\sigma_1/2$ or $\sigma_2/2$ time histories. The effect of mean stress is allowed for using the Goodman relationship:

$$\frac{\tau_a}{S_{SN}} + \frac{\tau_m}{S_{Su}} = \frac{1}{\gamma} \quad (7.69)$$

where

τ_a is the alternating shear stress

τ_m is the mean shear stress

S_{SN} is the alternating shear stress for N loading cycles from the material $S-N$ curve

S_{Su} is the ultimate shear strength

γ is the safety factor

Having used Eq. (7.69) to determine S_{SN} , the permitted number of cycles for this loading range can be derived from the $S-N$ curve, enabling the corresponding fatigue damage to be calculated.

2. *ASME boiler and pressure vessel code method:* This is similar to the maximum shear method, but the shear stress ranges are based on notional principal stresses calculated from the changes in the values of σ_x , σ_y , σ_z , τ_{xy} , τ_{yz} and τ_{zx} from datum values occurring at one of the extremes of the stress cycle. Mean stress effects are not included.
3. *Distortion energy method:* In this method, the fatigue evaluation is based on the fluctuations of the effective or von Mises stress. In the case of the hub shell, the stress perpendicular to the hub surface (and hence the third principal stress) is zero, so the effective stress is given by

$$\sigma_t = \sqrt{\frac{(\sigma_1 - \sigma_2)^2 + \sigma_1^2 + \sigma_2^2}{2}} \quad (7.70)$$

As the effective stress is based on the distortion energy, it is a scalar quantity, so it needs to be assigned a sign corresponding to that of the dominant principal stress. The effect of mean stress is allowed for in the same way as for the maximum shear method, except that the stresses in Eq. (7.69) are now direct stresses instead of shear stresses.

S-N curves for SGI are given in Hück (1983).

7.4 Gearbox

7.4.1 Introduction

The function of the gearbox is to step up the speed of rotor rotation to a value suitable for the generator, which, in the case of induction generators for fixed-speed machines or two-speed machines operating at the higher speed, is usually 1500 rpm plus the requisite slip. For machines of this type rated between 300 kW and 5 MW, with upper rotational speeds between 48 and 12 rpm, overall gear ratios of between about 1:31 and 1:125 are therefore required, with similar ratios usually applying in the case of variable speed machines. Normally these large step-ups are achieved by three separate stages with ratios of between 1:3 and 1:5 each.

The design of industrial fixed ratio gearboxes is a large subject in itself and well beyond the scope of the present work. However, it is important to recognise that the use of such gearboxes in wind turbines is a special application, because of the unusual environment and load characteristics, and the sections that follow focus on these aspects. Sections 7.4.2–7.4.6 consider variable loading, including drive train dynamics and the impact of emergency braking loads, and examine how gear fatigue design is adapted to take account of it. The relative benefits of parallel and epicyclic shaft arrangements are discussed in Section 7.4.7, while subsequent sections deal with noise reduction measures and lubrication and cooling.

A useful reference is the American Gear Manufacturers Association (AGMA) information sheet entitled *Recommended Practices for Design and Specification of Gearboxes for Wind Turbine Generator Systems* published in 1996 in conjunction with the American Wind Energy Association, which covers the special requirements of wind turbine gearboxes in some detail. This has since been expanded into the standard *Design and*

Specification of Gearboxes for Wind Turbines (ANSI/AGMA/AWEA 6006-A03 2003). More recently, the IEC has published its own standard, IEC 61400-4:2012, *Wind Turbines – Part 4: Design Requirements for Wind Turbine Gearboxes*. This references ISO 6336, *Calculation of Load Capacity of Spur and Helical Gears*, which is in six parts and was re-issued in 2019.

7.4.2 Variable loads during operation

The torque level in a wind turbine gearbox will vary between zero and rated torque according to the wind speed, with excursions above rated on fixed-speed pitch-regulated machines due to slow pitch response. The short-term torque fluctuations will be subject to dynamic magnification to the extent that they excite drive train resonances (see Section 7.4.3). In addition, there will be occasional much larger torques of short duration due to braking events, unless the brake is fitted to the low-speed shaft. Figure 7.48 shows example load-duration curves (excluding dynamic effects and braking) for two 500 kW, two bladed fixed-speed machines – one stall and the other pitch regulated. The curve for the former is calculated by simply combining the power curve with the distribution of instantaneous wind speeds, which is obtained by superposing the turbulent variations about each mean wind speed on the Weibull distribution of hourly means. Excursions above rated power are not included.

In the case of a pitch-regulated machine, the pitch control system is not normally designed to respond to wind speed fluctuations at blade passing frequency or above, as this would impose excessive loads on the control mechanism. Thus there is no attenuation of the significant power fluctuations that occur at blade passing frequency due to

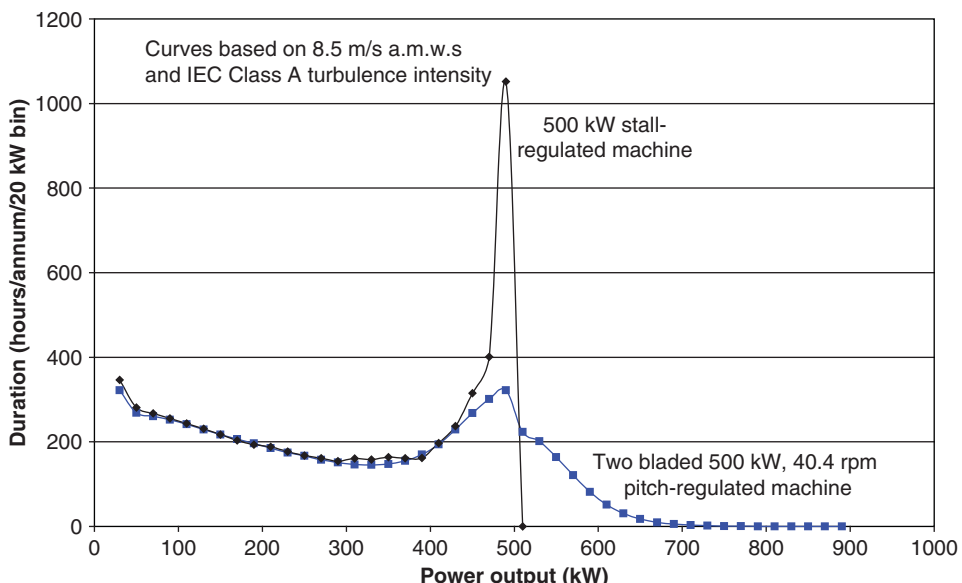


Figure 7.48 Load duration curves for 500 kW, two bladed pitch-regulated and 500 kW, stall-regulated fixed-speed machines

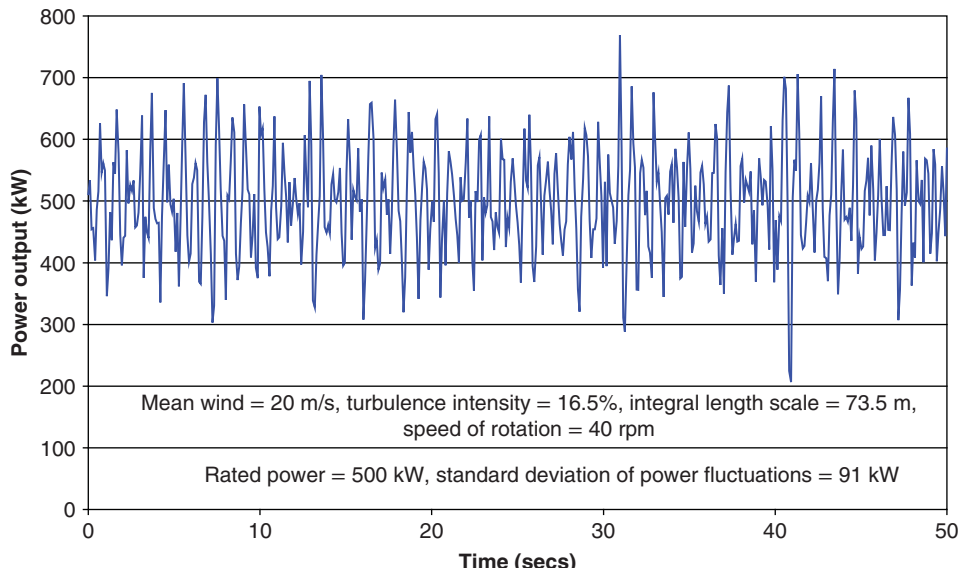


Figure 7.49 Simulated power output for two bladed, 40 m dia pitch-regulated m/c operating in above rated wind speed

turbulence, which are illustrated for the example two bladed, 500 kW machine operating in a 20 m/s mean wind with 16.5% turbulence intensity in Figure 7.49.

The load duration curve for a fixed-speed pitch-regulated machine can be derived approximately from the distribution of instantaneous wind speeds below rated wind speed, and the distribution of short-term mean wind speeds (i.e. those to which the pitch system can respond) above. The former can be combined with the power curve to give the power distribution due to instantaneous winds below rated directly, while the winds above rated are assumed to produce Gaussian spreads of power outputs about the rated value, with the standard deviation depending on the short-term mean wind. The standard deviation of power fluctuations when the pitch control system is operational can be related to that portion of the wind fluctuations above the pitch control system cut-off frequency as follows:

$$\sigma_P^2 = \frac{1}{B^2} \sum_j \sum_k \left[\int_{\Omega}^{\infty} S_u^o(r_j, r_k, n) dn \right] \left(\frac{dp}{du} \right)_j \left(\frac{dp}{du} \right)_k \quad (7.71)$$

where $S_u^o(r_i, r_k, n)$ is the rotationally sampled cross-spectrum of the wind speed fluctuations at a pair of points, j and k , on the rotor (see Section 5.7.5), and $\left(\frac{dp}{du} \right)_j$ is the rate of change with wind speed of the power generated by the blade elements at r_j on all B blades if the pitch does not change. The summations are carried out over the whole rotor, and give $\sigma_P = 0.213 \left(\frac{dp}{du} \right) \sigma_u = 91 \text{ kW}$ for the example two bladed machine operating at 40.4 rpm in a 20 m/s mean wind with 16.5% turbulence intensity. Here $\frac{dp}{du}$ is the rate of change of turbine power with wind if the pitch does not change. The standard deviation

of the power fluctuations for a three bladed machine of similar size would be about one third less.

7.4.3 Drive train dynamics

All wind turbines experience aerodynamic torque fluctuations at blade passing frequency and multiples thereof because of the ‘gust slicing’ phenomenon, and these fluctuations will inevitably interact with the dynamics of the drive train, modifying the torques transmitted. In the case of a fixed-speed wind turbine with an induction generator, the resulting drive train torque fluctuations can be assessed by dynamic analysis of a drive train model consisting of the following elements connected in series:

- A body with rotational inertia and damping (representing the turbine rotor).
- A torsional spring (representing the gearbox).
- A body with rotational inertia (representing the generator rotor).
- A torsional damper (modelling the resistance produced by slip on an induction generator).
- A body of infinite rotational inertia rotating at constant speed (the mechanical equivalent of the electrical grid).

The inertias, spring stiffness, and damping must all be referred to the same shaft.

7.4.4 Braking loads

Most turbines have the mechanical brake located on the high-speed shaft, with the result that braking loads are transmitted through the gearbox. If, as is sometimes the case, the mechanical brake is one of the two independent braking systems required, then it must be capable of decelerating the rotor to a standstill from an overspeed – e.g. after a grid loss. This typically requires a torque of about three times rated torque.

The mechanical brake is only required to act alone during emergency shut-downs, which are comparatively rare. During normal shut-downs, the rotor is decelerated to a much lower speed by aerodynamic braking, so the duration of mechanical braking is much less, but the braking torque is the same, unless there is provision for two different braking torque levels.

Figure 7.50 is a typical record of low-speed shaft torque during a normal shut-down, in which the mechanical brake is applied as soon as the generator has been taken off-line. It is apparent that the braking torque is far from constant, taking a couple of seconds to reach its first maximum and then falling off slightly before reaching a higher maximum just before the high-speed shaft stops. Following this, there are significant torque oscillations due to the release of wind-up in the drive train. These result in torque reversals accompanied by tooth impacts and take some time to decay.

Although braking loads are infrequent and of short duration, their magnitude means that they can have a decisive effect on fatigue damage. The AGMA/AWEA document recommends that the time histories of braking and other transient events are simulated with the aid of a dynamic model of the drive train for input into both the gear extreme load design calculations and the fatigue load spectrum.

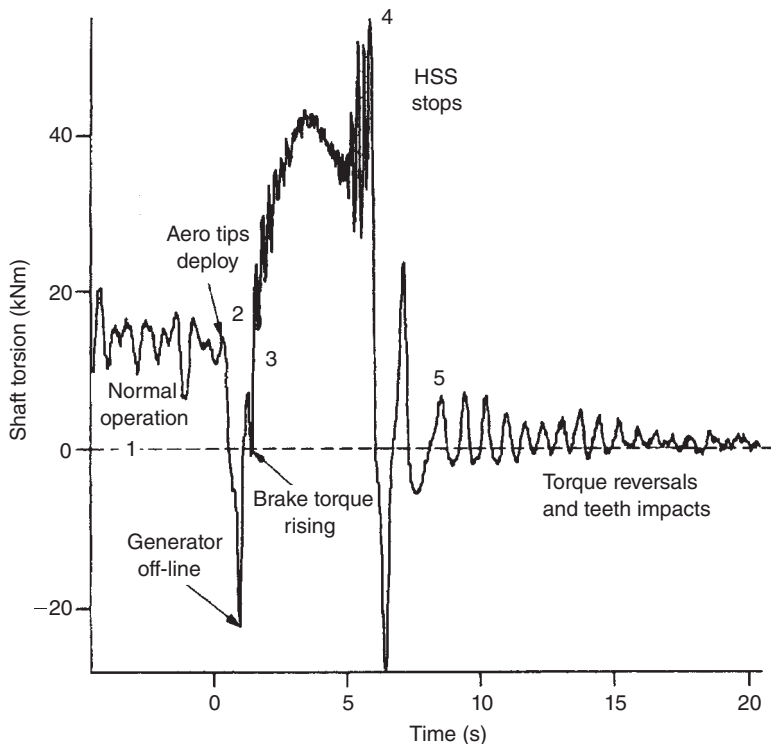


Figure 7.50 Low-speed shaft torque during braking at normal shut-down. Extracted from AGMA/AWEA 921-A97, *Recommended Practices for Design and Specification of Gearboxes for Wind-Turbine Generator Systems*, with permission of the publisher, the American Gear Manufacturers Association, 1500 King Street, Suite 201, Alexandria, Virginia 22314, USA (AGMA/AWEA 921-A97 1996)

7.4.5 Effect of variable loading on fatigue design of gear teeth

Gear teeth must be designed in fatigue to achieve both acceptable contact stresses on the flanks and acceptable bending stresses at the roots. In non-wind-turbine applications, gearboxes typically operate at rated torque throughout their lives, so the gear strengths are traditionally modified by 'life factors' that are derived from the material S-N curves on the basis of the predicted number of tooth load cycles for the gear in question. The British code for determining permissible gear contact stresses, BS 436: Part 3: 1986 (since replaced by BS ISO 6336, *Calculation of Load Capacity of Spur and Helical Gears*) (2006), recognises an endurance limit for both contact stress and bending stress, so that the life factors are unity when the number of tooth load cycles exceeds 10^9 and 3×10^6 respectively, but increase for lesser numbers of cycles.

The Hertzian compression stress between a pair of spur gear teeth in contact at the pitch point (i.e. at the point on the line joining the gear centres) is given by

$$\sigma_c = \sqrt{\frac{F_t}{bd_1} \frac{E}{\pi(1-v^2)} \frac{u+1}{u} \frac{1}{\sin \alpha \cos \alpha}} \quad (7.72)$$

where

F_t is the force between the gear teeth at right angles to the line joining the gear centres

b is the gear face width

d_1 is the pinion pitch diameter

u is the gear ratio (greater than unity)

α is the pressure angle – i.e. the angle at which the force acts between the gears – usually 20° – 25°

Note that the contact stress increases only as the square root of the force between the teeth because the area in contact increases with the force as well.

The maximum bending stress at the tooth root is given by

$$\sigma_B = \frac{F_t h}{\frac{1}{6} b t^2} K_S \quad (7.73)$$

where

h is the maximum height of single tooth contact above the critical root section

t is the tooth thickness at the critical root section

K_S is a factor to allow for stress concentration at the root

For gearing operating at rated torque only, the designer needs to show that the resultant bending stress multiplied by an appropriate safety factor is less than the endurance limit multiplied by the life factor, Y_N , and a number of stress modifying factors, as follows:

$$\sigma_B \cdot \gamma \leq \sigma_{B \text{ lim.}} \cdot Y_N \cdot Y_R \cdot Y_X \dots \dots \quad (7.74)$$

A similar calculation is required in relation to the contact stress.

Given the predicted turbine load spectrum (Section 7.4.2), which should include dynamic effects (see Section 7.4.3), it is then necessary to establish the required design torque at the endurance limit. Normally this is done by invoking Miner's rule and determining the infinite life torque for which the design torque spectrum yields unity fatigue damage in conjunction with the prescribed S - N curve. Y_N in Eq. (7.74) can then be set to unity, as the life factor has been accounted for in the derivation of the required infinite life torque.

Figure 7.51 shows specimen torque–endurance curves laid down by BS 436 (British Standards Institution 1986) for case hardened gears for tooth bending and tooth contact stress (with no pitting allowed) plotted in terms of the torque at the endurance limit. Hence in each case the design infinite life torque, T_∞ , is calculated according to

$$T_\infty = \left[\sum_i \left(\frac{N_i}{N_\infty} T_i^m \right) \right]^{1/m} \quad (7.75)$$

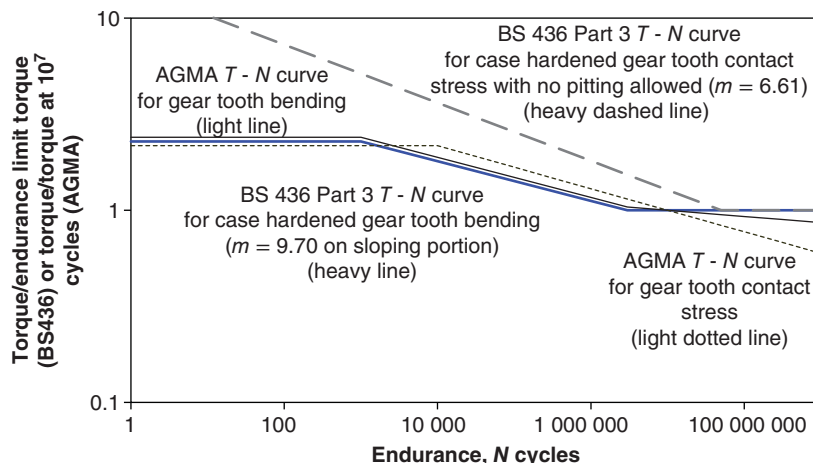


Figure 7.51 Specimen torque–endurance curves for gear tooth design

where N_i is the number of cycles at torque level T_i , and torques less than T_∞ are omitted from the summation. The number of cycles at the lower knee of the torque–endurance curve, N_∞ , is always 3×10^6 cycles for tooth bending but is generally higher for contact stress, varying according to the material. Note that the slope index, m , of the torque–endurance curve for contact stress is half that of the contact stress – endurance curve because contact stress only increases as the square root of torque [Eq. (7.72)].

Leaving braking loads out of consideration to begin with, the design infinite life torque will be equal to the rated torque if there are no power fluctuations above rated, because the number of gear tooth loading cycles at rated torque will be well above N_∞ . For example, in the case of the 500 kW stall-regulated machine featured in Figure 7.48, the teeth on the critical pinion driven by the 30 rpm low-speed shaft will experience $3 \times 30 \times 60 \times 1050 \times 20 = 1.13 \times 10^8$ load cycles at rated torque over 20 years, assuming a first stage gear ratio of 3. However, for the 500 kW, two bladed pitch-regulated machine, the power fluctuations above rated detailed in the Figure 7.48 load duration curve result in a design infinite life torque for the first stage pinion tooth bending stress of 1.36 times the rated torque, with most of the damage coming from torques just above this value. (The first stage gear ratio is assumed to be three as before and the turbine rotational speed is taken as 40.4 rpm.) The design infinite life torque for tooth contact stress is only $1.17 \times$ rated torque – significantly less than for bending, as expected from comparison of the BS 436 Part 3 torque–endurance curves in Figure 7.51.

Figure 7.51 also shows specimen torque–endurance curves derived from S-N curves in the ANSI/AGMA standard 2001-C95, *Fundamental Rating Factors and Calculation Methods for Involute Spur and Helical Gear Teeth* (ANSI/AGMA 2001-C95 1995), plotted in terms of the torque at 10^7 cycles. The torque–endurance curve for tooth bending stress, which is based on a middle of the range Brinell Hardness value of 250 HB, closely parallels the selected BS 436 Part 3 curve, except that the curve continues with a very shallow slope beyond 3×10^6 cycles instead of displaying an endurance limit. The design torques at 10^7 cycles for tooth bending for the example 500 kW machines featured in

Figure 7.48 are similar to the design infinite life torques obtained using the BS 436 Part 3 torque-endurance curves.

The ANSI/AGMA 2001-C95 (1995) torque-endurance curves for tooth contact stress are significantly more conservative than the selected BS 436 Part 3 curve. This is particularly so in the case of the ANSI/AGMA curve selected, which is the one recommended for wind turbine applications, in view of the elimination of the lower knee. The absence of the lower knee increases the design torque at 10^7 cycles for tooth contact to 1.4 times the rated torque for the stall-regulated machine, but the figure for the pitch-regulated machine is only about 10% higher.

From the above discussion, the general conclusion can be drawn that tooth bending fatigue usually governs the increased gearbox rating required to take care of load excursions above rated.

The effect of braking loads on the design infinite life torque according to BS 436 Part 3 can be illustrated with respect to the example machines discussed in Section 7.4.2. Although the mechanical brake must be capable of decelerating an overspeeding rotor unassisted, a shut-down under these conditions will be a very rare event. Accordingly, the typical emergency shut-down considered for fatigue design purposes is deceleration from normal rotational speed under the action of mechanical and aerodynamic braking combined, with an assumed stopping time of 3 seconds. An emergency shut-down frequency of 20 per annum is assumed. Normal shut-downs are assumed to occur on average twice a day, with a stopping time of 1.5 seconds, because of the reduced rotational speed at which mechanical braking is initiated for parking. In each case the braking torque is assumed to remain constant at three times rated torque throughout the brake application for simplicity. Based on these assumptions, the percentage increases in design infinite life torque for gear tooth bending in fatigue, due to the inclusion of braking loads in the load spectrum, are shown in Table 7.12 for emergency braking alone on the one hand and normal plus emergency shut-downs on the other.

Also shown in the table are the percentage increases in the ANSI/AGMA design torque for gear tooth bending at 10^7 cycles due to the inclusion of braking loads. It is seen that the inclusion of emergency braking loads alone makes very little difference to design torques in the case of the pitch-regulated machine, but is significant in the case of the stall-regulated machine. The addition of braking loads at normal shut-downs incurs a much greater penalty in both cases because of the large number of stops involved, indicating that provision for brake application at reduced torque on these occasions would probably be worthwhile. Note that the larger percentage increases in design torques due to braking indicated by BS 436 Part 3 are a consequence of the assumption that there is an endurance limit.

7.4.6 Effect of variable loading on fatigue design of bearings and shafts

Bearing lives are approximately inversely proportional to the cube of the bearing loading. Applying Miner's rule, the equivalent steady bearing loading over the gearbox design life can thus be calculated from the load duration spectrum according to the formula

$$F_{eqt} = \left[\frac{\sum_i N_i F_i^3}{\sum_i N_i} \right]^{1/3} \quad (7.76)$$

Table 7.12 Illustrative increases in design torques for gear tooth bending due to inclusion of braking loads in fatigue load spectrum, according to BS 436 and AGMA rules

	500 kW stall-regulated machine		500 kW two bladed pitch-regulated machine	
	Percentage increase in BS 436 design infinite life torque for tooth bending	Percentage increase in ANSI/AGMA 250 HB design torque at 10 ⁷ cycles for tooth bending	Percentage increase in BS 436 design infinite life torque for tooth bending	Percentage increase in ANSI/AGMA 250 HB design torque at 10 ⁷ cycles for tooth bending
Emergency braking at 3 × FLT	30%	16%	4%	3%
Emergency plus normal braking, each at 3 × FLT	65%	47%	25%	21%

where N_i is the number of revolutions at bearing load level F_i . Gravity often dominates the loading on the low-speed shaft bearings, but on the other shafts the bearing loads result from drive torque only, so the bearing load duration spectrum can be scaled directly from the torque duration spectrum. Note that the *S-N* curve for bearings is much steeper than those for gear tooth design, so that occasional large braking loads will be of less significance.

The nature of the fatigue loading of intermediate shafts is essentially different from that of gear teeth, as the former is governed by the torque *fluctuations* as opposed to the absolute torque magnitude. Consequently the fatigue load spectrum for shaft design should be derived from rainflow cycle counts on simulated torque time histories rather than on the load duration curve used for gear tooth design.

7.4.7 Gear arrangements

Parallel axis gears may be arranged in one of two ways in each gear stage. The simplest arrangement within a stage consists of two external gears meshing with each other and is commonly referred to as ‘parallel shaft’. The alternative ‘epicyclic’ arrangement consists of a ring of planet gears mounted on a planet carrier and meshing with a sun gear on the inside and an annulus gear on the outside. The sun and planets are external gears and the annulus is an internal gear as its teeth are on the inside. Usually either the annulus or planet carrier are held fixed, but the gear ratio is larger if the annulus is fixed.

The epicyclic arrangement allows the load to be shared out between the planets, reducing the load at any one gear interface. Consequently the gears and gearbox can be made smaller and lighter, at the cost of increased complexity. The scope for material savings are greatest in the input stages of the gear train, so it is common to use the

epicyclic arrangement for the first two stages and the parallel shaft arrangement for the output stage. A further advantage of epicyclic gearboxes is greater efficiency as a result of the reduced sliding that takes place between the annulus and planet teeth.

The derivation of the optimum gear ratio in a series of parallel shaft stages is fairly straightforward and is described below. Eq. (7.73) for tooth bending stress can be modified as follows:

$$\sigma_B = \frac{F_t h}{\frac{1}{6} b t^2} K_S = F_t \frac{6(h/m)}{bm(t/m)^2} \cdot K_S = F_t \frac{6z_1(h/m)}{bd_1(t/m)^2} \cdot K_S \quad (7.73a)$$

where m is the module, defined as d_1/z_1 for spur gears and z_1 is the number of pinion teeth. If the ratios h/m and t/m are treated as constants, then the bending stress is proportional to the number of teeth for a given size of gear. Hence the design of the gears is governed by contact stress because, in principle, the bending stress can always be reduced by reducing the number of pinion teeth. Thus, based on Eq. (7.72), the permitted tangential force, F_t , is proportional to $bd_1 u/(u+1)$ so that the permitted low-speed shaft torque, $T_{LSS} = F_t d_2/2$ is given by

$$T_{LSS} \propto d_2 bd_1 u/(u+1) = bd_2^2/(u+1) \quad (7.77)$$

Hence the volumes of the low-speed shaft gear wheel and the meshing pinion can be expressed as $V_2 = kT_{LSS}(u+1)$, where k is a constant, and, $V_1 = V_2/u^2$ respectively. These can be used to derive an expression for the volume of gears in a drive train with an infinite number of stages each with the same ratio. It is found that the total gear volume is a minimum for a gear stage ratio of 2.9, but increases by only 10% when the ratio drops to 2.1 or rises to 4.3.

The gear teeth of parallel shaft gear stages are only loaded in one direction, so the permitted alternating bending stress amplitude in fatigue, σ_{alt} , is modified to account for the non-zero mean value in accordance with the Goodman relation:

$$\frac{\sigma_{alt}}{\sigma_{lim}} = 1 - \frac{\bar{\sigma}}{\sigma_{ult}} \quad (7.78)$$

where σ_{lim} is the permitted alternating bending stress amplitude with zero mean, $\bar{\sigma}$ is the mean bending stress and σ_{ult} is the UTS. Setting $\bar{\sigma} = \sigma_{alt}$ results in:

$$\sigma_{alt} = \frac{\sigma_{lim}\sigma_{ult}}{(\sigma_{ult} + \sigma_{lim})} \quad (7.79)$$

If the $\sigma_{lim}/\sigma_{ult}$ ratio is 0.2, then $\sigma_{alt} = 0.833\sigma_{lim}$ and the permitted peak bending stress at the endurance limit is $1.667\sigma_{lim}$. In epicyclic gearboxes, by contrast, the gear teeth on the planets wheels are loaded in both directions, so the permitted peak bending stress at the endurance limit is only σ_{lim} . As the number of teeth on the smallest gear cannot be reduced indefinitely, this means that tooth bending is more likely to govern in the case of epicyclic gearing.

The minimum total gear volume for an infinite series of epicyclic gear stages with fixed annuli is obtained for a gear stage ratio of two, which implies that the radius of the sun gear is the same as that of the annulus gear and that there are an infinite number of planets! This is not realistic, and the annulus radius is in practice typically double the sun radius, giving a gear ratio of three. It is instructive to compare the volume of gears

for epicyclic and parallel gear stages with this ratio, assuming that tooth bending stress governs in each case.

For the parallel stage, it can be shown using Eq. (7.73a) that the volume of the pinion is

$$\frac{\pi}{4}bd_1^2 = k_B F_t d_1 z_1 / \sigma_B = k_B \frac{F_t d_2 z_1}{2\sigma_{alt} u} = k_B \frac{2T_{LSS} z_1}{1.667\sigma_{lim} u} \quad (7.80)$$

where k_B is a constant. This gives a volume for gear wheel and pinion of $1.2k_B T_{LSS} z_1 (1 + 1/u^2) u / \sigma_{lim} = 4k_B T_{LSS} z_1 / \sigma_{lim}$ for $u = 3$.

For the epicyclic stage, the volume of the planet, which is assumed to have the same number of teeth as the pinion of the parallel stage – i.e. the minimum permissible – is

$$\frac{\pi}{4}bd_{Pl}^2 = k_B F_t d_{PL} z_1 / \sigma_{lim} \quad (7.81)$$

If the low-speed shaft drives the planet carrier and the N planets are spaced at 1.15 diameters, then the low-speed shaft torque is

$$T_{LSS} = F_t N(r_A + r_S) \text{ where } N = \frac{\pi(r_A + r_S)}{1.15(r_A - r_S)}, \text{ } r_A \text{ is the annulus radius and } r_S \text{ is the sun radius.}$$

Hence, putting $a = r_A/r_S$, the volume of a planet is $k_B T_{LSS} \frac{1.15(a-1)}{\pi(a+1)^2 r_S} \frac{d_{PL} z_1}{\sigma_{lim}}$ and the volume of the sun is $4/(a-1)^2$ times as big. The total volume of planets and sun becomes

$$V = k_B T_{LSS} \frac{1}{a+1} \frac{d_{PL} z_1}{r_S \sigma_{lim}} \left(1 + \frac{4}{(a-1)^2 N} \right) \quad (7.82)$$

Substituting $a = 2$, we obtain

$$N = \frac{3\pi}{1.15} = 8.195$$

which is rounded down to 8, giving

$$V = k_B T_{LSS} \frac{z_1}{3\sigma_{lim}} \left(1 + \frac{4}{8} \right) = 0.5k_B T_{LSS} z_1 / \sigma_{lim}$$

Hence the volume of the sun and planets of the epicyclic stage is only one eighth of the volume of the gearwheel and pinion of the equivalent parallel stage, assuming the designs are governed by gear tooth bending stress. If contact stress were to govern, the relative volume of the epicyclic stage would be even less.

The dramatic materials savings obtainable with epicyclic gearboxes depend on equal sharing of loads between the planets. Although this is theoretically achievable through accuracy of manufacture, it is in practice desirable to introduce some flexibility in the planet mountings to take up any planet position errors – for example by supporting the planets on slender pins cantilevered out from the planet carrier. Note that the fatigue design of such pins is, like the design of intermediate shafts, governed by torque fluctuations rather than by torque absolute magnitude.

7.4.8 Gearbox noise

The main source of gearbox noise arises from the meshing of individual teeth. Loaded teeth deflect slightly, so that if no tooth profile correction is made, unloaded teeth are misaligned when they come into contact, resulting in a series of impacts at the meshing

frequency. It is therefore standard practice to adjust the tooth profile – usually by removing material from the tip area of both gears, referred to as ‘tip relief’ – to bring the unloaded teeth back into alignment at the rated gear loading. In the case of wind turbines, the gear loading is variable, so it is necessary to select the load level at which the tip relief provides the correct compensation. If the tip relief load level is too high, there will be excessive loss of tooth contact near the tips at low powers, while if it is set too low the noise level at rated power will be too high. However, if gearbox noise is expected to be more intrusive at low wind speeds, when it is less likely to be masked by aerodynamic noise, then a low compensation load level should be selected.

Helical gears are usually quieter than spur gears (with teeth parallel to the gear axis) because the width of the tooth comes into mesh over a finite time interval rather than all at once. Moreover, the peak tooth deflections of helical gears are less than those of spur gears because there are always at least two teeth in contact rather than one, and because the varying bending moment across the tooth width means that the less heavily loaded portions of the tooth can provide restraint to the part that is most heavily loaded. As a result, the tooth misalignments due to insufficient/excessive tip relief at a particular load level will be reduced.

Epicyclic gears are normally quieter than parallel shaft gears because the reduced gear size results in lower pitch line velocities. However, this benefit is lost if spur gears are used rather than helical gears, in order to avoid problems with planet alignment. One way of maintaining the alignment of helical planet gears is to provide thrust collars on the sun and annulus.

As the annulus of an epicyclic gear stage is often fixed, it would be convenient to integrate it with the gearbox casing. However, this would enable annulus gear meshing noise to be radiated directly from the casing, so it is preferable to make the annulus a separate element, supported on resilient mountings. Similarly, resilient gearbox mountings should be used to attenuate the transmission of gearbox noise to the nacelle structure and tower.

The noise produced by gear tooth meshing can reach the environment outside the wind turbine by a variety of routes, as follows:

- Through the shaft directly to the blades, which may radiate efficiently.
- Through the resilient mounts of the gearbox to the support structure and thereby to the tower, which can radiate efficiently under some circumstances.
- Through the resilient mounts of the gearbox to the support structure and thereby to the nacelle structure, which can also radiate.
- Through the casing wall to the nacelle air and then via air intake and exhaust ducts.
- Through the casing wall to the nacelle air and then via the nacelle structure.

All of these paths are modally dense, and it is virtually impossible to design out a selected frequency. If noise is a problem then the options are to reduce the source sound level, perhaps by improving the tip relief as described above, or to modify the major path to reduce transmission. Identification of the major path is not straightforward, but one way of doing so is to use Statistical Energy Analysis (SEA), which combines a theoretical model with extensive field measurements. The path may not be simple, as non-linearity in the system can make one path the predominant one at low wind speeds and another

path critical at higher wind speeds. Treatment of a radiating path can involve damping treatment such as shear layer damping or even just sand or bitumen layers added to the tower wall, for instance. In some cases the treatment can have more than one effect. When blades are the major source of radiation and damping material is added inside the blades then this material can act as a stiffening material as well as a damping mechanism. Sometimes it is useful to add tuned absorbers to parts of the structure to damp out one particular frequency. An alternative use of such tuned absorbers is to design them to raise the impedance at the tuned frequency so that the offending vibration does not pass that point on the structure.

7.4.9 Integrated gearboxes

As noted in Section 6.11.1, the cases of integrated gearboxes must be very robust to transmit the rotor loads to the nacelle structure without experiencing deflections that would impair the proper functioning of the gears. In view of the complex shape of the casing, stress distributions due to each load vector usually have to be determined using FE analysis – these can then be superposed in line with the different extreme load combinations. The fatigue analysis will require the superposition of stress histories resulting from simultaneous time histories of rotor thrust, yaw moment and tilt moment derived from simulations at different wind speeds.

7.4.10 Lubrication and cooling

The function of the lubrication system is to maintain an oil film on gear teeth and the rolling elements of bearings, in order to minimise surface pitting and wear (abrasion, adhesion, and scuffing). Varying levels of the elastohydrodynamic lubrication provided by the oil film can be identified, depending on oil film thickness. These range from full hydrodynamic lubrication, which exists when the metal surfaces are separated by a relatively thick oil film, to boundary lubrication when the asperities of the metal surfaces may be separated by lubricant films only a few molecular dimensions in thickness. Scuffing, which is a severe form of adhesive wear involving localised welding and particle transfer from one gear to the other, can occur under boundary lubrication conditions, which are promoted by high loading and low pitch line velocity and oil viscosity.

Two alternative methods of lubrication are available – splash lubrication and pressure fed. In the former, the low-speed gear dips into an oil bath and the oil thrown up against the inside of the casing is channelled down to the bearings. In the latter, oil is circulated by a shaft driven pump, filtered and delivered under pressure to the gears and bearings. The advantage of splash lubrication is its simplicity and hence reliability, but pressure fed lubrication is usually preferred for the following reasons:

- Oil can be positively directed to the locations where it is required by jets.
- Wear particles are removed by filtration.
- The churning of oil in the bath, which can result in a net efficiency loss, is avoided.
- The oil circulation system enables heat to be removed much more effectively from the gearbox by passing the oil through a cooler mounted outside the nacelle.
- It allows for intermittent lubrication when the machine is shut down if a standby electric pump is incorporated.

With a pressure fed system, it is normal practice to fit temperature and pressure switches downstream of the filter to trip the machine for excessive temperature or insufficient pressure.

Guidance on the selection of lubricant, which has to take into account the ambient temperatures at the site in question, is given in the AGMA/AWEA document. Sump heaters may be needed to enable oil to be circulated when the turbine starts up at low temperatures.

7.4.11 Gearbox efficiency

Gearbox efficiency can vary between about 95% and 98%, depending on the relative number of epicyclic and parallel shaft stages and on the type of lubrication.

7.5 Generator

7.5.1 Fixed-speed induction generators

The induction generators commonly used in fixed-speed wind turbines are very similar to conventional industrial induction motors. In principle the only differences between an induction machine operating as a generator and as a motor are the direction of power flow in the connecting wires, whether torque is applied to or taken from the shaft and if the rotor speed is slightly above or below synchronous speed. The size of the market for induction motors is very large, and so, in many cases, an induction generator design will be based on the same stator and rotor laminations as a range of induction motors to take advantage of high manufacturing volumes. Some detailed design modifications, e.g., changes in rotor bar material, may be made by the machine manufacturers to reflect the different operating regime of wind turbine generator, particularly the need for high efficiency at part load, but the principles of operation are those of conventional induction machines. The synchronous speed, which is determined by the number of magnetic poles chosen in the design and the network frequency, will be 1500 rpm (four pole), 1000 rpm (six pole), or 750 rpm (eight pole) for connection to a 50 Hz network. The physical protection of the generator windings is arranged to avoid the ingress of moisture, i.e. a totally enclosed design, and in some wind turbines liquid cooling is used to reduce air-borne noise. A high slip (in some cases up to 2–3% at rated output power) is often requested by the wind turbine designer as this increases torsional compliance and damping in the wind turbine drive train and helps limit torsional oscillations in the drive train induced by the periodic torque variations of the aerodynamic rotor. However, this is at the expense of electrical losses in the rotor and the consequent generation of heat; a 2% slip generator creates electrical losses of 2% of its rating at full output.

Figure 7.52 shows the conventional equivalent circuit of an induction machine that may be used to analyse its steady state behaviour (Anaya-Lara et al. 2009; Hindmarsh 1984; McPherson 1990). The slip (s) is the difference between the angular speed of the stator field and rotor:

$$s = \frac{\omega_s - \omega_r}{\omega_s}$$

For motor operation, the rotor runs slightly slower than the stator field and the slip is positive. For generator operation the rotor runs slightly faster than the stator field and the slip is negative.

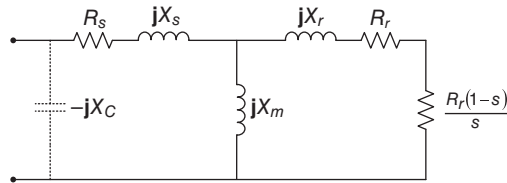


Figure 7.52 Steady state equivalent circuit of an induction machine with power factor correction capacitors. R_s , stator resistance; X_s , stator reactance; R_r , rotor resistance; X_r , rotor reactance; X_m , magnetising reactance; X_C , power factor correction reactance. j is the imaginary operator

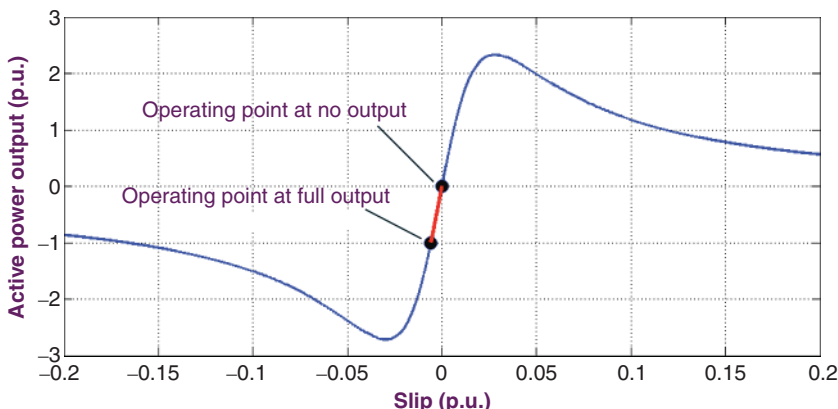


Figure 7.53 Variation of active power with slip for an induction machine showing operation as a generator

Figure 7.53 shows how the active power varies with slip for a 1 MW induction machine. A convention has been chosen with the current flowing into the induction machine as positive and so the normal operating region for a generator is between 0 and -1 MW (marked as -1 p.u. in the figure). In this example, at 1 MW generation the slip is around -1% (-0.01 per unit) with the rotor rotating faster than the synchronous speed of the stator field. It may be seen that the maximum power that can be generated before the peak of the curve is reached is around 2.6 MW. If the generator is connected to a distribution network with a low short-circuit level (and hence a high source impedance) the maximum power that may be exported before the peak of the curve is reached, is reduced

By combining Figure 7.53 and the variation of the reactive power drawn by the generator with slip, the conventional circle diagram representation of an induction machine shown in Figure 7.54 may be derived. Again, the normal generating region is shown. At 1 MW output the generator draws some 500 kVar. It may be shown that the reactive power requirement increases very rapidly if the output power rises above its rated value of 1 p.u.

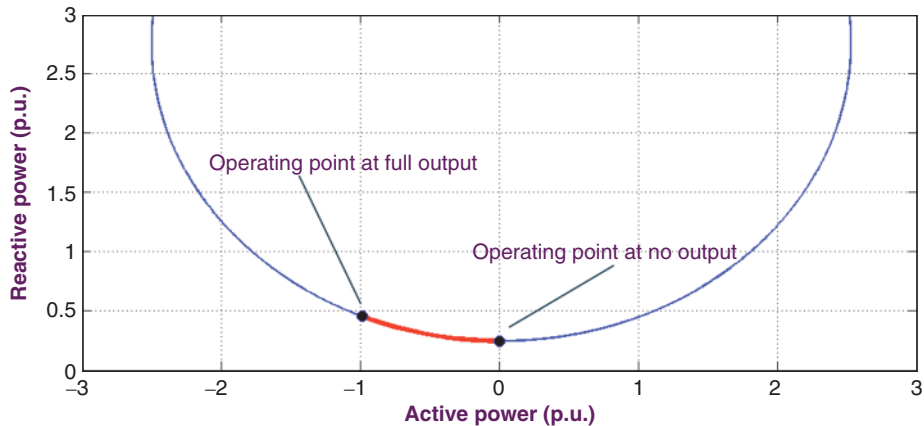


Figure 7.54 Circle diagram of 1 MW induction machine

Fixed power factor correction capacitors (X_C) are used to reduce the requirement for reactive power from the network and so translate the circle diagram along the y axis towards the origin (but not all of the way, otherwise there is a danger of self-excitation). The equations used to describe the steady state performance of induction generators are given in any standard textbook (e.g. Hindmarsh 1984; McPherson 1990). Dynamic analysis is more complex but is dealt with by Krause (1986).

When they are first connected to the network, induction generators draw a large current transient due partly to the need to flux the magnetic circuits and partly because the slip tends to be high and so the term $\frac{R_r(1-s)}{s}$ in the equivalent circuit shown in Figure 7.52 becomes small. Thyristor soft-starts shown in Figure 7.55 are commonly used to limit the connection current. Their mode of operation is initially for the thyristors to be fired late in the voltage cycle and then the firing angle advanced (over several seconds) until the entire voltage wave is applied to the generator (Anaya-Lara et al. 2009). Thus the network voltage is applied gradually to the generator. Generally the soft-start units are only used for a few seconds before the by-pass contactor is closed and the induction generator connected directly to the network.

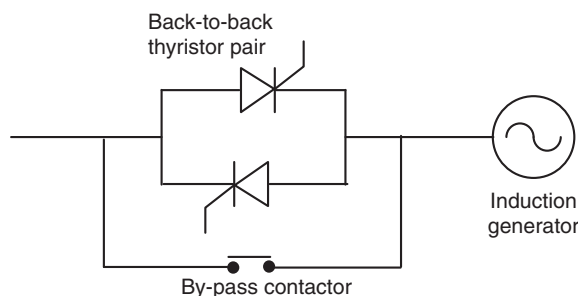


Figure 7.55 Soft-start unit for an induction generator (one phase only shown)

7.5.2 Variable-slip induction generators

Variable-slip operation is achieved by introducing an external resistance into the rotor circuit, as shown in Figure 7.56. Note that in this figure the resistors R_r and $R_r \frac{(1-s)}{s}$ in Figure 7.52 are combined into $\frac{R_r}{s}$.

The external resistance (R_{ext}) is controlled by a power electronic switch. Below rated torque the switch short-circuits the external resistor to give no effect on the generator. Above rated torque, pulse width modulation (PWM) control is used to introduce the external resistance progressively into the rotor circuit. The alteration of the torque-slip curve is shown in Figure 7.57. As more external resistance is added, the slope of the torque slip curve is reduced, for example, to O-B. Below rated power, operation along O-A is just like that of a fixed-speed generator, but above rated the external resistor is varied continuously to maintain constant reaction torque, resulting in variable-speed operation along A-B. Operation at point B, -2.8% slip (1542 rpm for a four pole, 50 Hz generator) would result in losses of approximately 28 kW in a 1 MW generator. Increasing the rotor resistance R_r still further makes the machine lose its stability as the pull-out peak torque reduces with the external resistance.

As with a fixed-speed induction generator, power factor correction capacitors are used to reduce the reactive power drawn from the network.

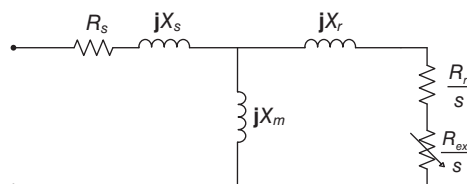


Figure 7.56 Steady state equivalent circuit of variable-slip induction generator showing addition of external resistor R_{ext}

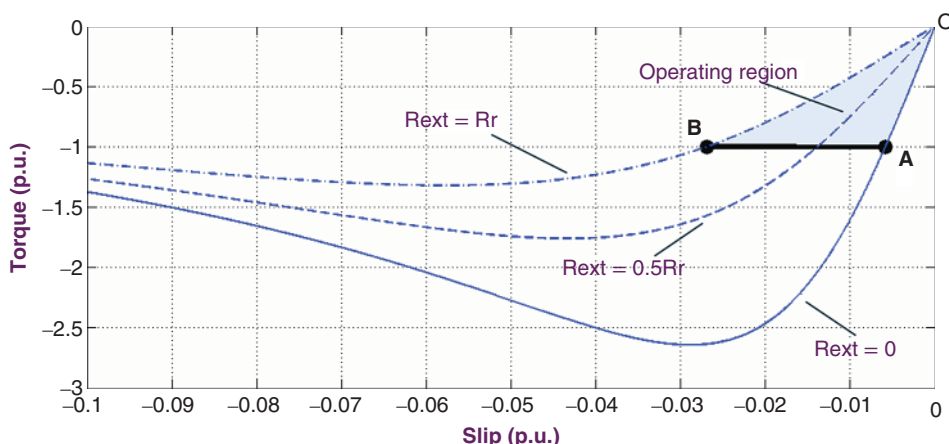


Figure 7.57 Effect of external resistance on the torque-slip curve of an induction generator

7.5.3 Variable-speed operation

There are two main approaches to electrical variable-speed operation. Either all of the output power of the wind turbine is passed through two back-to-back frequency converters to give a wide range of variable-speed operation (full power conversion [FPC]), or a restricted speed range is achieved by converting only that fraction of the output power flowing in the rotor of a wound rotor induction machine (doubly fed induction generator [DFIG]).

In both cases, a Graetz bridge voltage source converter as shown in Figure 7.58 is used to create an *ac* voltage of any frequency and magnitude from a *dc* source. Insulated gate bipolar transistors (IGBTs) are used as the switching devices; they operate typically at between 2 and 8 kHz with PWM, to produce a close approximation to a sine wave voltage. Common techniques used to synthesise the sine wave voltage include carrier modulated (sine-triangular) PWM, hysteresis control and space vector modulation. All of these modulation techniques produce quite similar results but space vector control is easier to implement in a digital control system. With more rapid switching the voltage waveform approximates closely to a sine wave but at the expense of increased switching losses. The generator side converter rectifies all of the power to *dc*, which is then inverted by the network side converter. Operation of this type of voltage source converter is described in Mohan et al. (1995) and Anaya-Lara et al. (2009).

Figure 7.59 shows how the IGBTs are switched to produce an approximation to a sine wave. Comparing the triangular carrier wave with the modulation signal produces variable width pulses from a *dc* source that have a fundamental component equal to the modulation signal. Figure 7.59a shows the control of the network side converter with a modulation signal of 50 Hz that is locked to the mains. The generator side converter produces a varying frequency to control the speed of the generator. The output of a pulse width modulated voltage source converter before and after filtering is as shown in Figure 7.59b. Within their operating limits, the voltage source converters can create a voltage of any frequency, phase or magnitude. They can be used to interface to the 50 or 60 Hz power system or to the variable-speed generator. In the DFIG they are used to apply a voltage to the wound rotor induction machine at its slip frequency. The operation of a voltage source converter at fundamental frequency can be represented as shown in Figure 7.60.

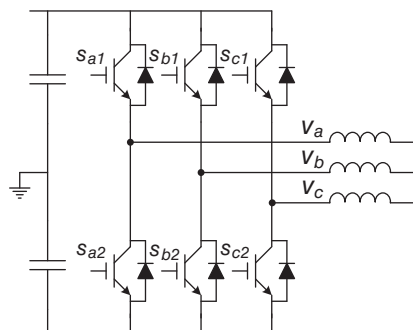


Figure 7.58 Voltage source converter

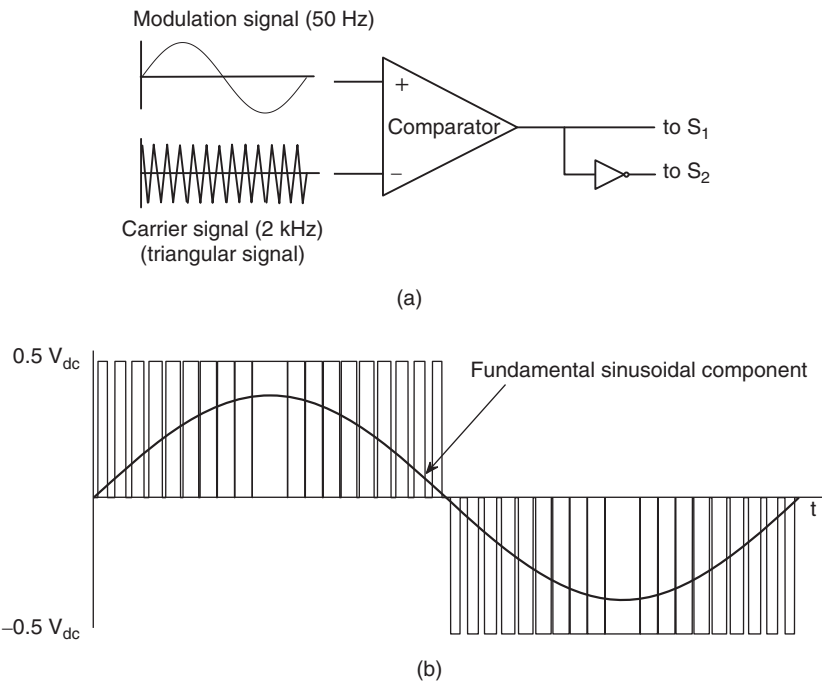


Figure 7.59 (a) Sine-triangular modulation circuit, and (b) PWM output of sine-triangular modulation

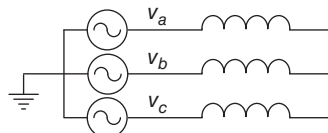


Figure 7.60 Ideal voltage sources representation of a voltage source converter

Even though the representation shown in Figure 7.60 is correct for the fundamental voltage (50 or 60 Hz), the voltage source converter operating under PWM switching pattern shown in Figure 7.59b produces harmonics. Figure 7.61 shows the harmonic voltages of a PWM converter. The rapid switching of PWM gives a large reduction in low order harmonics but the voltage will have significant harmonic components around the switching frequency and multiples of the switching frequency.

7.5.4 Variable-speed operation using a DFIG

In a variable-slip generator, a speed increase of the wound rotor induction generator, is achieved by adding resistance into the rotor circuit using an external resistor. The power consumed in the external resistor is directly proportional to slip speed. Thus a 10% speed increase leads to losses in the external resistor of approximately 10% of the generator stator output power.

These additional losses do not compromise energy production because they occur only above rated, where surplus wind energy is being discarded anyway. However this

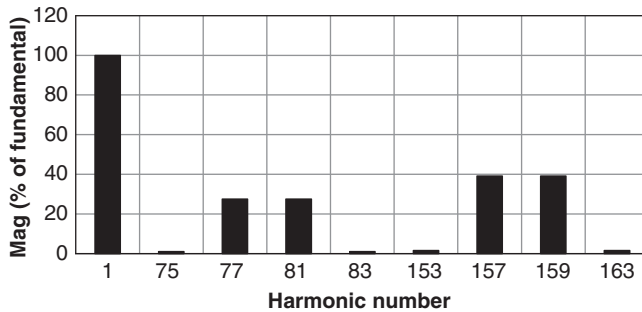


Figure 7.61 Typical harmonic spectrum of three phase voltage of a PWM inverter. Carrier frequency 3950 Hz (79th harmonic) and amplitude modulation 0.8 (after Mohan et al. 1995)

high level of losses is undesirable in large wind turbines because of the cooling required to dispose of the resulting heat. Hence a development of the variable-slip system has been to replace the external controlled resistance with a pair of back-to-back voltage source converters; see Figure 6.22c. These apply a variable voltage (and hence inject current) at the rotor slip frequency and so allow operation above and below the synchronous speed of the stator field. The synchronous speed of the stator field is determined by the network frequency and number of poles of the stator winding (e.g. 1500 rpm for a four pole winding on a 50 Hz system) and with $\pm 30\%$ speed variation around this will require the power rating of rotor circuit converters to be approximately 30% of rated power.

The steady state equivalent circuit of the DFIG is shown in Figure 7.62. The external resistor of the variable-slip generator is replaced by a voltage source. This applies a voltage to the slip rings of the wound rotor at slip frequency. The equivalent circuit has the rotor circuit referred to the stator and so the injected rotor voltage is divided by slip in the equivalent circuit.

The effect of injecting a voltage into the rotor is shown in Figure 7.63. The applied rotor voltages are quite small because, as shown in the equivalent circuit, the rotor voltage is divided by the slip. The extent of the speed range that is possible depends on the equivalent circuit parameters of the induction machine as well as the power rating of the converters.

Thus with rated applied torque (-1 per unit), the speed may be varied between point A and B by adjusting the voltage injected into the rotor circuit. Point B gives super-synchronous operation with power flowing out of the generator rotor. Point

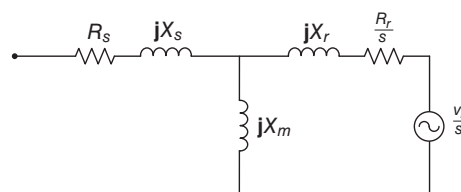


Figure 7.62 Steady state equivalent circuit of the DFIG. V_r is the injected rotor voltage

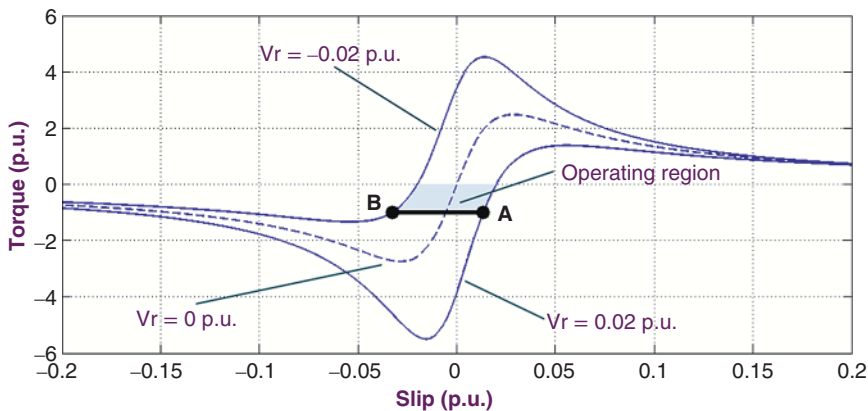


Figure 7.63 Steady state torque slip curves of a DFIG

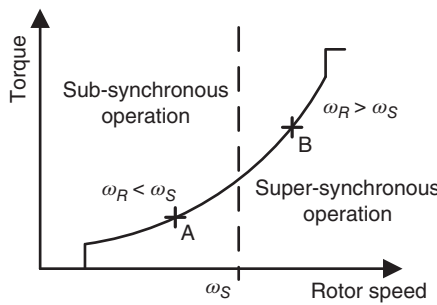


Figure 7.64 Torque speed curve of a DFIG

A gives sub-synchronous operation with power flowing into the generator rotor. The operating characteristic of the generator is shown in Figure 7.64.

The direction of real power flows in the rotor circuit of a DFIG may be understood from a simple analysis of the speed and torque of the generator. If the stator and rotor generator losses are neglected, the power transferred across the air gap of the generator (P_{airgap}) is the same as the power in the stator. This is the mechanical input power (P_{mech}) minus the power flowing in the rotor circuit (P_{rotor}), and so:

$$\begin{aligned}
 P_{airgap} &= P_{stator} = P_{mech} - P_{rotor} \\
 T\omega_s &= T\omega_r - P_{rotor} \\
 P_{rotor} &= -T(\omega_s - \omega_r) \\
 &= -Ts\omega_s = -sP_{airgap} \\
 &= -sP_{stator}
 \end{aligned}$$

where

T : torque on generator shaft,

ω_s : synchronous speed,

ω_r : rotor speed,

s : slip

Thus, the direction of power flows into or out of the rotor changes with the sign of the slip. For a negative slip (super-synchronous operation) power flows out of the generator rotor while for positive slip (sub-synchronous operation) power flows into the generator rotor.

Figure 7.65 shows the direction of the power flows in the rotor circuit of a DFIG.

The doubly fed concept was used in some early large prototype wind turbines, e.g. the 3 MW Growian constructed in Germany in the early 1980s and the Boeing Mod 5b in the USA at around the same time. At that time, cyclo-converters were used to change the frequency of the rotor circuit but modern practice is to use two back-to-back voltage source converters in the rotor circuit.

Control techniques to operate a DFIG vary but one approach is to use vector control (Pena et al. 1996; Muller et al. 2002). In this technique, the three phase voltages and

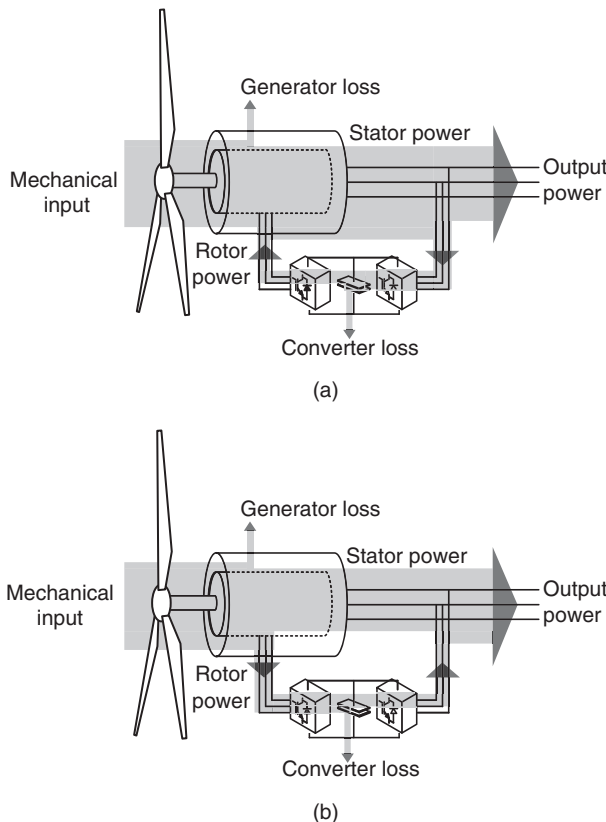


Figure 7.65 Power flows in a DFIG. (a) Sub-synchronous operation. (b) Super-synchronous operation

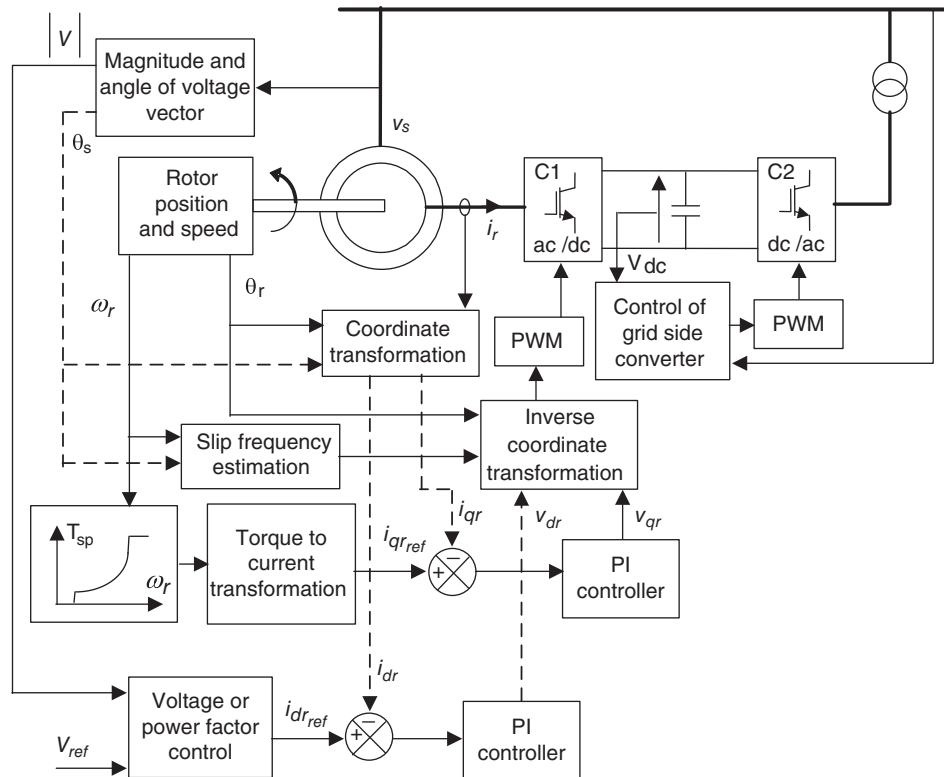


Figure 7.66 Schematic of a DFIG wind turbine typical control system

currents are transformed into two orthogonal vectors called *direct (d)* and *quadrature (q) components*. The PWM of each converter is driven by *d* and *q* components of the two controllers. The machine side converter is controlled to adjust torque of the generator and power factor/voltage independently. The network side converter maintains the voltage of the dc link. A simplified diagram of the control scheme used for the DFIG wind turbine is shown in Figure 7.66 (Ekanayake et al. 2003).

7.5.5 Variable-speed operation using a full power converter

Figure 7.67 shows the power flows in an FPC, variable-speed generation system. All of the power from the generator is rectified to dc and then inverted to the network voltage. This arrangement can be used with a range of generators. Induction generators with a gearbox mechanical transmission may be used in a configuration that is the inverse of the variable-speed drives used for large mechanical loads, e.g. pumps and fans. Electrically excited or permanent magnet synchronous generators may be used, either with a high- or medium-speed generator coupled to the aerodynamic rotor through a gearbox, or with a slow-speed multi-pole direct drive generator, which avoids the need for a gearbox.

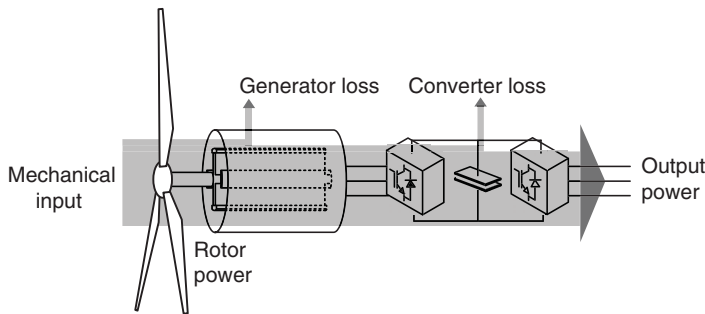


Figure 7.67 Power flows in a full power converter

Early broad range variable-speed wind turbines used a diode rectifier bridge in the generator converter and a naturally commutated thyristor current source converter on the network side (Freris 1990). However, naturally commutated thyristor converters always consume reactive power and generate considerable levels of characteristic low order harmonic currents. On weak distribution systems it is difficult to provide suitable filtering and power factor correction for this type of equipment.

Hence modern practice is to use two voltage source converters (Heier 2014) in a manner similar to the arrangement of the rotor circuit of the DFIG, although all of the equipment must be rated at the full power of the wind turbine. The generator converter rectifies all of the power to *dc*, which is then inverted back to *ac* by the network converter.

Control strategies vary but one approach is to use the two degrees of freedom of the generator converter output (magnitude and angle of the output voltage, or direct and quadrature axis voltages) to control the torque and excitation of the generator. Vector control as shown in Figure 7.66 is used to control the torque to a set-point obtained from the optimal wind turbine speed characteristic (Figure 6.21) while the reactive power flow is used to supply excitation to the generator. The network converter then maintains the *dc* link voltage and exchanges reactive power with the network. This arrangement is shown in Figure 6.22d.

An alternative approach is to control the generator converter to maintain the *dc* link voltage at a constant value and then use the network converter to control the active power flowing out of the system and hence the torque on the generator (Anaya-Lara et al. 2009). The network side converter is arranged to operate at any power factor within the rating of the equipment.

The voltage source converters employed in both DFIG and FPC systems need a method to obtain the angle of the network voltages (θ_s , shown in Figure 7.66) and it is usual to use a phase-locked loop (PLL). Different filtering techniques may be employed to filter out distorted grid voltages before they enter the PLL. Although it is quite straightforward to implement, a simple PLL can have a poor performance with rapidly changing harmonics and/or unbalanced voltage conditions on the grid. A number of network operators have expressed concern over the transient stability of variable-speed wind turbines with control systems based on PLLs.

7.6 Mechanical brake

7.6.1 Brake duty

As indicated in Section 6.8.3, a mechanical brake can be called on to fulfil a variety of roles, according to the braking philosophy adopted for the machine in question. The minimum requirement is for the mechanical brake to act as a parking brake, so that the machine can be stopped for maintenance purposes. The brake may also be used to bring the rotor to a standstill during high wind shut-downs, and during low-speed shut-downs as well in some cases. Aerodynamic braking is used to decelerate the rotor initially, so the mechanical brake torque can be quite low. However, IEC 61400-1:2019 requires that the mechanical brake be capable of bringing the rotor to a complete stop in a wind speed 5 m/s greater than the manufacturer's maximum wind speed for maintenance or repair.

If the mechanical brake is required to arrest the rotor in the event of a complete failure of the aerodynamic braking system, then there are two deployment options to consider. Either the mechanical brake can be actuated when an overspeed resulting from the failure of the aerodynamic system is detected, or actuated simultaneously with the aerodynamic brake as part of the standard emergency shut-down procedure. The advantage of the former strategy is that the mechanical brake will rarely, if ever, have to be deployed in this way, so that some pad or even disc damage can be tolerated when deployment actually occurs. In addition, fatigue loading of the gearbox will be reduced if the brake is mounted on the high-speed shaft. However, if the mechanical brake is actuated before significant overspeed has developed, then the aerodynamic torque to be overcome by the mechanical brake in the event of aerodynamic braking failure will be less.

The most severe emergency braking case will arise following a grid loss during generation in winds above rated. In the case of pitch-regulated machines, the maximum overspeed will occur after grid loss at rated wind speed because the rate of change of aerodynamic torque with rotational speed decreases and soon becomes negative at higher wind speeds. Conversely, if the pitch mechanism should jam, the braking duty becomes more severe at wind speeds at or above cut-out, because much higher aerodynamic torques are developed as the rotor slows down and the angle of attack increases. For stall-regulated machines the critical wind speed is generally at an intermediate value between rated and cut-out.

7.6.2 Factors governing brake design

The braking torque provided by callipers gripping a disc brake (Figure 7.68) is simply the product of twice the calliper force, the coefficient of friction (typically 0.4), the number of callipers and the effective pad radius. Callipers providing clamping forces of up to 500 KN are available. However the brake design is also limited by

- Centrifugal stresses in the disc.
- Pad rubbing speed.
- Power dissipation per unit area of pad.
- Disc temperature rise.



Figure 7.68 High-speed shaft brake disc and calliper (reproduced by permission of NEG Micon)

The nature of these constraints is described below.

The critical stress generated by centrifugal stresses is in the tangential direction at the inner radius of the brake disc, but it is governed principally by the disc rim speed according to the following formula:

$$\sigma_\theta(a) = \frac{3 + \nu}{4} \rho \omega^2 b^2 \left(1 + \frac{1 - \nu}{3 + \nu} \frac{a^2}{b^2} \right) \quad (7.83)$$

where a and b are the inner and outer disc radii, respectively, and ω is the disc rotational speed. One brake manufacturer, Twiflex, quotes a maximum safe disc rim speeds of around 90 m/s for their discs manufactured in spheroidal graphite cast iron.

Brake pads are generally made from sintered metal or a cheaper, resin based material. The former can accept rubbing speeds of up to 100 m/s, but some manufacturers quote permitted rubbing speeds for the latter of only about 30 m/s. However, Wilson (1990) reports satisfactory performance of resin based pads at a rubbing speed of up to 105 m/s if the power dissipation rate per unit area, Q , is kept low enough. The criterion, ascribed to Ferodo, is that $Q = \mu PV \leq 11.6 \text{ MW/m}^2$, where μ is the coefficient of friction, P is the brake pad pressure in KN/m², and V is the rubbing speed in m/s. This requires the pad pressure to be reduced to 275 KN/m², assuming a friction coefficient of 0.4.

During braking the kinetic energy of the rotor and drive train together with the additional energy fed in by the aerodynamic torque are dissipated in the brake disc and pads as heat, resulting in rapid initial temperature rise near the surface of the brake disc. The rate of energy dissipation is equal to the product of the braking torque and the disc rotational speed, so in the latter stages of braking the rate of energy dissipation cannot sustain the high surface temperatures and they begin to fall again.

The coefficient of friction for pads of resin based materials is sensibly constant at a level of about 0.4 at temperatures up to 250° C, but begins to drop thereafter, reaching 0.25 at 400° C. Although in theory the brake can be designed to reach the latter temperature, in practice the varying torque complicates the calculations and leaves little margin

of error against a runaway loss of brake torque. Accordingly, 300° C is often taken as the upper temperature limit for resin based pads.

Sintered metal pads have a constant coefficient of friction of about 0.4 up to a temperature of at least 400° C, but manufacturers indicate that the material can perform satisfactorily at temperatures up to 600° C on a routine basis, or up to 850° intermittently. Wilson (1990) reports a reduced friction coefficient of 0.33 at 750° C. Such temperatures cannot be realised in practice because the temperature of the disc itself is limited to 600° C in the case of spheroidal graphite cast iron or to a much smaller value in the case of steel (Wilson 1990).

Clearly the use of the more expensive sintered brake pads allows the brake disc to absorb much more energy. However, the sintered metal is a much more effective conductor of heat than resin based material, so it is often necessary to incorporate heat insulation into the calliper design to prevent overheating of the oil in the hydraulic cylinder.

A method of calculating brake disc temperature rise is given in the next section.

7.6.3 Calculation of brake disc temperature rise

The build-up in temperature across the width of a brake disc over the duration of the stop can be calculated quite easily if a number of assumptions are made. Firstly the heat generated is assumed to be fed into the disc at a uniform intensity over the areas swept out by the brake pads as the disc rotates. This is a reasonable approximation for a high-speed shaft-mounted brake and for a low-speed shaft-mounted brake with several callipers until rotation has almost ceased, but the energy input by this stage is much lower. Within the disc heat flow is assumed to be perpendicular to the disc faces only – i.e. radial flows are ignored.

Consider a brake disc slice at a distance x from the nearest braking surface, of thickness Δx and cross-sectional area A . The rate of heat flow away from the nearest braking surface entering the slice is $\dot{Q} = -kA \frac{d\theta}{dx}$ (where θ is the temperature and k the thermal conductivity) and the rate of heat flow leaving it on the far side is $\dot{Q} + \frac{d\dot{Q}}{dx} \Delta x$. The temperature rise of an element of thickness Δx over a time interval Δt is given by

$$\Delta\theta \cdot A \cdot \Delta x \rho C_p = \Delta Q = -\frac{d\dot{Q}}{dx} \Delta x \Delta t = kA \frac{d^2\theta}{dx^2} \Delta x \Delta t$$

where ρ is the density and C_p is the specific heat, so that

$$\frac{d\theta}{dt} = \frac{k}{\rho C_p} \frac{d^2\theta}{dx^2} \quad (7.84)$$

Adopting an FE approach, Eq. (7.84) can be written as

$$\theta(x, t + \Delta t) = \theta(x, t) + \frac{k}{\rho C_p (\Delta x)^2} \frac{\Delta t}{(\Delta x)^2} [\theta(x + \Delta x, t) + \theta(x - \Delta x, t) - 2\theta(x, t)] \quad (7.85)$$

Substituting values of $k = 36 \text{ W/m per } ^\circ\text{K}$, $C_p = 502 \text{ J/kg per } ^\circ\text{K}$ and $\rho = 7085 \text{ kg/m}^3$ for Grade 450 spheroidal graphite cast iron yields a value for the thermal diffusivity $\alpha = k/(\rho C_p)$ of $1.01 \times 10^{-5} \text{ m}^2/\text{s}$. If the time increment, Δt , is selected at 0.025 seconds and the element thickness is taken as 1.005 mm, then Eq. (7.85) simplifies to

$$\theta(x, t + \Delta t) = \theta(x, t) + 0.25[\theta(x + \Delta x, t) + \theta(x - \Delta x, t) - 2\theta(x, t)] \quad (7.86)$$

This equation can be used to calculate the temperature distribution across the brake disc, starting with a uniform distribution and imposing suitable increments at the braking surfaces at the boundaries. The behaviour at the boundaries is simpler to follow through if they are treated as planes of symmetry like the disc mid-plane, with imagined discs flanking the real one. The temperature increment at the boundary at each timestep, which is added to that calculated from Eq. (7.86), is given by

$$\Delta\theta_0 = \frac{2T\omega(t)\Delta t}{\rho C_p S \Delta x} \quad (7.87)$$

where T is the braking torque per disc face (assumed constant), $\omega(t)$ is the disc rotational speed at time t , and S is the area swept out by the brake pad (or pads) on one side of the disc. For a disc diameter D and pad width w , S is $\pi(D-w)w$. The factor 2 is required because heat is assumed to flow into the imagined disc as well as into the real one. Hence the initial temperature build-up can be calculated as illustrated in Table 7.13, taking an arbitrary value of $\Delta\theta_0$ of 40° C. (The gradual reduction in $\Delta\theta_0$ over time due to deceleration is ignored here for simplicity.)

The brake disc surface temperature rise is found to be a minimum when the ratio of the braking torque to the maximum aerodynamic torque is about 1.6. As the ratio is reduced below this value, the extended stopping time results in more energy being abstracted from the wind, so temperatures begin to rise rapidly. However, the maximum brake temperature is relatively insensitive to increases in the ratio above 1.6. The variation in maximum brake disc surface temperature with braking torque is illustrated for the emergency braking of a stall-regulated machine following an overspeed in Figure 7.69, where the continuous line gives the surface temperature rise calculated by the FE method outlined above. It transpires that the maximum temperature rise can be estimated quite

Table 7.13 Illustrative example of calculation of brake disc temperature rise using an FE model

Timestep	Time (sec)	Element Distance from braking surface (mm)	0	1	2	3	4	5
			0	1.0	2.0	3.0	4.0	5.0
1	0.025	Initial temperature	0	0	0	0	0	0
		Boundary temperature increment	40					
2	0.05	Temperature at end of timestep	20	10	0	0	0	0
		Boundary temperature increment	40					
3	0.075	Sum	60	10	0	0	0	0
		Temperature at end of timestep	35	20	2.5	0	0	0
4	0.1	Boundary temperature increment	40					
		Sum	75	20	2.5	0	0	0
		Temperature at end of timestep	47.5	29.4	6.3	0.6	0	0
		Boundary temperature increment	40					
		Sum	87.5	29.4	6.3	0.6	0	0
		Temperature at end of timestep	58.5	38.2	10.6	1.9	0.1	0

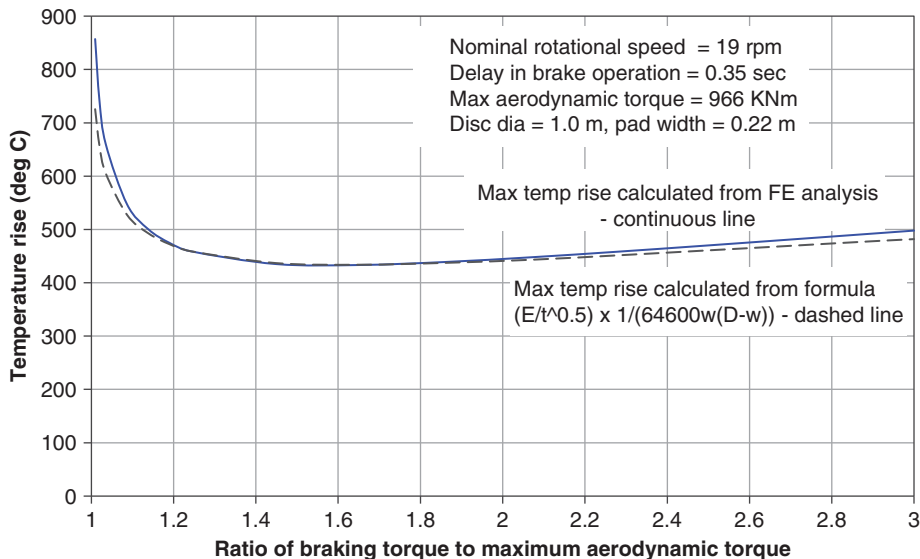


Figure 7.69 Brake disc surface maximum temperature rise for emergency braking of 60 m dia, 1.3 MW stall-regulated turbine from 10% overspeed in 20 m/s wind with high-speed shaft brake acting alone

accurately by the following empirical formula:

$$\theta_{\max} - \theta_0 = \frac{E}{\sqrt{t}} \frac{1}{64600w(D-w)} = \frac{E}{\sqrt{t}} \frac{\pi}{64600S} \quad (7.88)$$

where E is the total energy dissipated in Joules, t is the duration of the stop in seconds, and S is the area of the disc surfaces swept by the brake pads. The temperature derived using this formula is plotted as a dotted line in Figure 7.69 for comparison.

7.6.4 High-speed shaft brake design

A key parameter to be chosen in brake design is the design braking torque. The coefficient of friction can vary substantially above and below the design value due to such factors as bedding in of the brake pads and contamination, so the design braking torque calculated on the nominal friction value must be increased by a suitable materials factor. The 1993 edition of the GL guidelines (Germanischer Lloyd 1993) specified a materials factor of 1.2 for the coefficient of friction, and added in another factor of 1.1 for possible loss of calliper spring force. If these factors are adopted, the minimum design braking moment is 1.78 times the maximum aerodynamic torque, after including the aerodynamic load factor of 1.35. A small additional margin of, say, 5% should be added to ensure that the rotor is still brought to rest without a very large temperature rise should the 1.78 safety factor be completely eroded.

The procedure to be followed for the design of a brake on the high-speed shaft can conveniently be illustrated by the following example.

Example 7.2 Design a high-speed shaft brake for a 60 m diameter, 1.3 MW stall-regulated machine capable of shutting the machine down in a 20 m/s wind from a 10% overspeed occurring after a grid loss, with or without assistance from the aerodynamic braking system. The nominal low-speed shaft and high-speed shaft rotational speeds are 19 rpm and 1500 rpm, respectively, ignoring generator slip. Assume that the brake application delay time is 0.35 sec, and that the inertia of the turbine rotor, drive train, brake disc and generator rotor – all referred to the low-speed shaft – totals 2873 Tm².

1. *Derivation of the brake design torque:* The peak aerodynamic torque occurs when the maximum rotational speed is reached just prior to brake application. The first step is to determine the relationship between rotational speed and aerodynamic torque for the stated wind speed of 20 m/s. From this the acceleration of the rotor and build-up of aerodynamic torque during the 0.35 seconds of delay before the brake comes on can be determined. The speed increase in this case is 1 rpm, giving a maximum rotor speed of $19 \times 1.1 + 1 = 21.9$ rpm and peak aerodynamic torque of 966 KNm. Hence the brake design torque is $966 \times 1.78 \times 1.05 = 1800$ KNm referred to the low-speed shaft, or $1800 \times 19/1500 = 22.8$ KNm at the brake.
2. *Brake disc diameter selection:* The maximum rotor speed corresponds to a high-speed shaft speed of $21.9 \times (1500/19) = 1729$ rpm = 181 rad/sec, so the maximum permissible brake disc radius as regards centrifugal stresses is about $90/181 = 0.497$ m. It is advisable to choose the largest permitted size to minimise temperature rise, so 1.0 m diameter is selected in this case. The pad rubbing speed will be quite acceptable if sintered pads are used.
3. *Selection of number and size of brake pads:* The total brake pad area is governed by the need to keep the maximum power dissipation per unit pad area below 11.6 MW/m². The power dissipation is equal to the product of the braking torque and the rotational speed, so it is at a maximum at the onset of braking – i.e. $22.8 \times 181 = 4128$ kW, giving a required total area of the brake pads of $4128/11600 = 0.356$ m². This area can be provided by four callipers fitted with 0.22×0.22 m pads, giving 0.387 m² in all.
4. *Maximum brake disc temperature check:* The variation in disc surface temperature over the duration of the stop can be calculated using the FE method outlined in the preceding section. The resulting variation in this case is plotted in Figure 7.70. The surface temperature reaches a maximum of 440°C, just after halfway through the stop, which lasts 4.7 seconds from the time the brake comes on. This temperature is well below the limit for sintered pads.
5. *Calliper force:* The braking friction force required is 58.5 KN, calculated from the torque divided by the effective pad radius of 0.39 m. Hence the required calliper force is $58.5/(8 \times 0.4) = 17.3$ KN, which is rather low for a calliper sized for a 0.22×0.22 m brake pad.

The design process outlined above results in an excessive number of lightly loaded callipers, because of the limitation on power dissipation per unit area. If the relative infrequency of emergency braking events allowed this limitation to be relaxed, then a more economic solution would result.

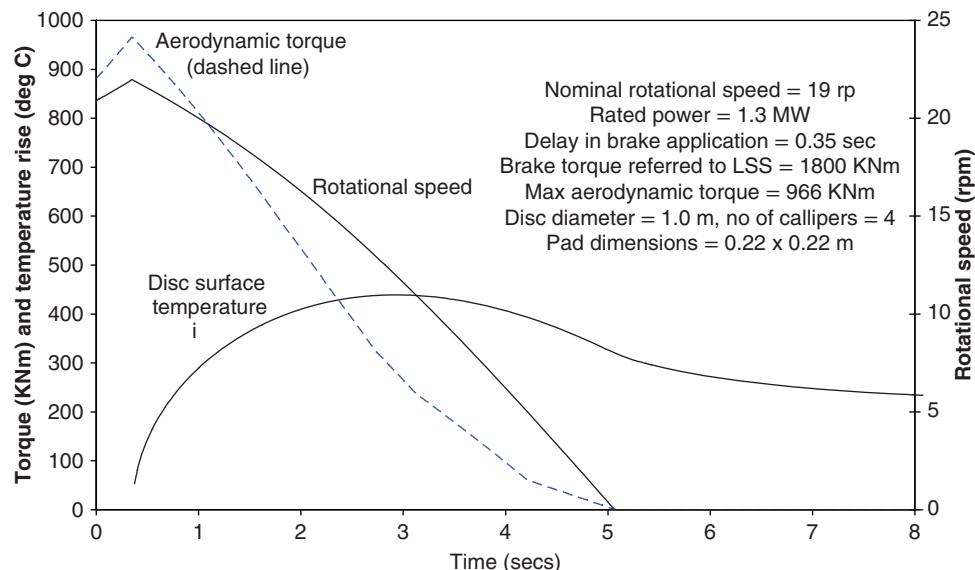


Figure 7.70 Emergency braking of stall-regulated 60 m dia turbine from 10% overspeed in 20 m/s wind with high-speed shaft mechanical brake acting alone

7.6.5 Two-level braking

During normal as opposed to emergency shut-downs, the rotor is decelerated to a much lower speed by aerodynamic braking before the brake is applied, so the brake torque required is much reduced. In view of the benefit of reduced loads on the braking system, and on the gearbox in particular, some manufacturers arrange for a reduced braking torque for normal shut-downs. This is achieved on the usual ‘spring applied, hydraulically released’ brake callipers by allowing oil to discharge from the hydraulic cylinder via a pressure relief valve when the brake is applied, so that the hydraulic pressure drops to a reduced level. After the rotor has come to rest, the remaining hydraulic pressure can be released, so that the brake torque rises to the full level.

7.6.6 Low-speed shaft brake design

The procedure for designing a low-speed shaft disc brake is much simpler than that for the high-speed shaft brake, because the limits on disc rim speed, pad rubbing speed, power dissipation per unit area and temperature rise do not influence the design, which is solely torque driven. The large braking torque required means that a brake placed on the low-speed shaft will be much bulkier than one with the same duty placed on the high-speed shaft. For example, the design low-speed shaft braking torque of 1800 KNm from the example above would require a 1.8 m diameter disc fitted with seven callipers.

A study by Corbet et al. (1993), which investigated a range of machine diameters, concluded that the brake cost would double or treble if the brake were placed on the low-speed shaft rather than on the high-speed shaft. However, when the extra gearbox

costs associated with a high-speed brake were taken into account, the cost advantage of the high-speed shaft brake disappeared.

In the case of direct drive turbines, the mechanical brake has to act on the low speed shaft, as no high-speed shaft is available.

7.7 Nacelle bedplate

The functions of the nacelle bedplate are to transfer the rotor loadings to the yaw bearing and to provide mountings for the gearbox and generator. Normally it is a separate entity, although in machines with an integrated gearbox, the gearbox casing and the nacelle bedplate can be a single unit. The bedplate can either be a welded fabrication consisting of longitudinal and transverse beam members or a casting sculpted to fit the desired load paths more precisely. One fairly common arrangement is a casting in the form of an inverted frustum that supports the low-speed shaft main bearing at the front and the port and starboard gearbox supports towards the rear, with the generator mounted on a fabricated platform projecting to the rear and attached to the main casting by bolts.

Although conventional methods of analysis can be used to design the bed plate for extreme loads, the complicated shape renders an FE analysis essential for calculating the stress concentration effects needed for fatigue design. Fatigue analysis is complicated by the need to take into account up to six rotor load components. However, given stress distributions for each load component obtained by separate FE analyses, the stress time history at any point can be obtained by combining appropriately scaled load component time histories previously obtained from a load case simulation.

7.8 Yaw drive

The yaw drive is the name given to the mechanism used to rotate the nacelle with respect to the tower on its slewing bearing, in order to keep the turbine facing into the wind and to unwind the power and other cables when they become excessively twisted. It usually consists of a number of electric or hydraulic motors mounted on the nacelle, each of which drives a pinion mounted on a vertical shaft via a reducing gearbox. The pinion engages with gear teeth on the fixed slewing ring bolted to the tower, as shown in Figure 7.71. These gear teeth can either be on the inside or the outside of the tower, depending on the bearing arrangement, but they are generally located on the outside on smaller machines so that the gear does not present a safety hazard in the restricted space available for personnel access.

On large wind turbines it is often expedient to fit numerous small yaw motors rather than a few large ones and, in the case of the Siemens-Gamesa SWT-7.0-154 turbine, there are 16. These are each rated at 40 Nm and drive through a 960:1 gearbox (IECRE 2019), producing a total nominal torque of 615 kNm.

The yaw moments on rigid hub machines arise from differential loading on the blades, which may be broken down into deterministic and stochastic components. On a three bladed machine, the dominant deterministic yaw loading is at 3P, but it is generated by 2P blade loading, as is demonstrated below. The blade out-of-plane root bending moments

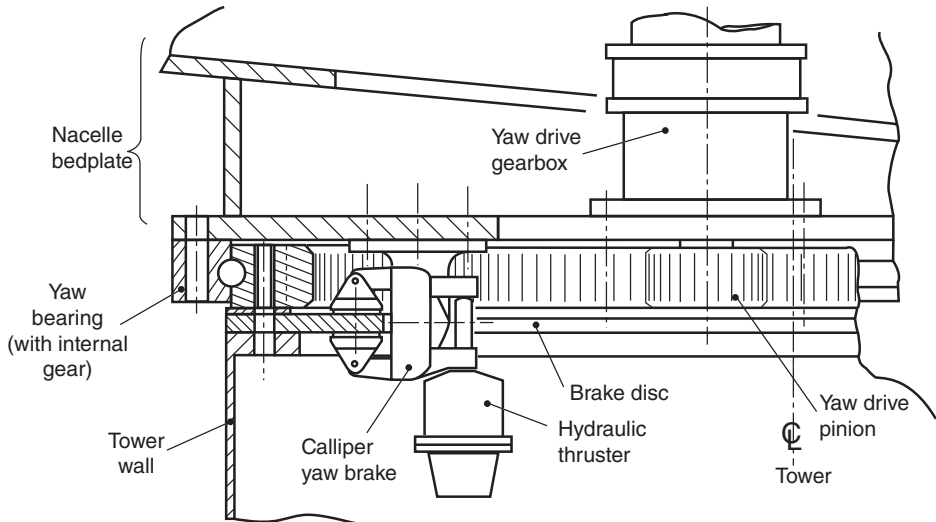


Figure 7.71 Typical arrangement of yaw bearing, yaw drive, and yaw brake

can be described in terms of harmonics of the rotational frequency, Ω , as follows:

$$M_{Yj} = \sum_n a_n \sin \left(n \left\{ \omega t + \frac{2\pi(j-1)}{3} \right\} + \phi_n \right) \quad (7.89)$$

Hence the yaw moment from all three blades is given by

$$\begin{aligned} M_{ZT} = & \sin \omega t \sum_n a_n \sin(n\omega t + \phi_n) + \sin \left(\omega t + \frac{2\pi}{3} \right) \sum_n a_n \sin \left(n \left\{ \omega t + \frac{2\pi}{3} \right\} + \phi_n \right) \\ & + \sin \left(\omega t - \frac{2\pi}{3} \right) \sum_n a_n \sin \left(n \left\{ \omega t - \frac{2\pi}{3} \right\} + \phi_n \right) \end{aligned} \quad (7.90)$$

i.e.

$$M_{ZT} = \sum_n a_n \left[\sin \omega t \sin(n\omega t + \phi_n) \left\{ 1 - \cos \frac{2\pi n}{3} \right\} + \sqrt{3} \cos \omega t \cos(n\omega t + \phi_n) \sin \frac{2\pi n}{3} \right] \quad (7.91)$$

For the first four harmonics, this gives

$$M_{ZT} = 1.5 \{ a_1 \cos \phi_1 - a_2 \cos(3\omega t + \phi_2) + a_4 \cos(3\omega t + \phi_4) \} \quad (7.92)$$

Thus it is seen that the blade out-of-plane bending harmonics at 2P and 4P produce yaw moment at 3P, while those at 1P and 3P produce steady and zero yaw moments, respectively.

As turbine size increases, the turbine diameter becomes larger in relation to gust dimensions, and the scope for differential loading on the blades due to turbulence increases. The expression for the standard deviation of the stochastic yawing moment on a three bladed machine is the same as that for the shaft moment standard deviation – see Eq. (5.119a).

Anderson et al. (1993) investigated yaw moments on two sizes of Howden three bladed turbines (33 m dia 330 kW and 55 m dia 1 MW) and concluded that the major source of cyclic yaw loading is stochastic at 3P. Yaw error, however, was not found to make a significant contribution. Given that yaw error results in a blade out-of-plane load fluctuation at rotational frequency, this result is in accordance with Eq. (7.92).

Several different strategies have been evolved for dealing with the large cyclic yaw moments that arise on rigid hub machines due to turbulence, as follows.

1. *Fixed yaw:* A yaw brake is provided in the form of one or more callipers acting on an annular brake disc and is designed to prevent unwanted yaw motion under all circumstances. See Figure 7.71. This can require 6 callipers on a 60 m diameter machine. During yawing, the yaw motors drive against the brake callipers, which are partly released, so that the motion is smooth.
2. *Friction damped yaw:* Yaw motion is damped by friction in one of three different ways. In the first, the nacelle is supported on friction pads resting on a horizontal annular surface on the top of the tower. The yaw drive has to work against the friction pads, which also allow slippage under extreme yaw loads. This system was employed on the 500 kW Vestas V39 and the 3 MW WEG LS1.

In the second, the nacelle is mounted on a conventional rolling element slewing bearing, and the friction is provided by a permanently applied brake, using the same configuration as for fixed yaw. Optionally, the pressure on the brake pads can be increased when the machine is shut down for high winds.

In the third, the nacelle is supported on a three-row roller type slewing bearing (see Figure 7.45d), but with the rollers replaced by pads of elastomer composite to generate friction.

3. *Soft yaw:* This is hydraulically damped fixed yaw. The oil lines to each side of the hydraulic yaw motor are each connected to an accumulator via a choke valve, allowing limited damped motion to and fro to alleviate sudden yaw loads. This system is used on the 300 kW WEG MS3, which has a two bladed, teetered rotor, but experiences significant yaw loads when teeter impacts occur.
4. *Damped free yaw:* A hydraulic yaw motor is used as before, but the oil lines to each side of the motor are connected together in a loop via a check valve, rather than being connected to a hydraulic power pack. This arrangement prevents sudden yaw movements in response to gusts, but depends on yaw stability over the full range of wind speeds. Unfortunately, yaw stability in high winds is rare.
5. *Controlled free yaw:* This is the same as damped free yaw, except that provision is made for yaw corrections when necessary. This strategy was adopted successfully on several Windmaster machines, including the two bladed, fixed hub 750 kW machine.

Friction damped yaw is the strategy most commonly adopted.

7.9 Tower

7.9.1 Introduction

Wind turbine towers are normally of tubular or lattice steel construction, but steel is sometimes replaced by pre-cast concrete in the lower part of higher towers. There have been instances of in-situ construction of concrete towers for prototype wind turbines, but this is not generally viable because of the higher costs associated with work on site.

Sections 7.9.3 and 7.9.4 consider the design of tubular and lattice towers, respectively, while Section 7.9.5 describes Enercon's hybrid tower. Minimisation of turbine excitation of tower natural frequency is a key design objective, so this is discussed first.

7.9.2 Constraints on first mode natural frequency

As noted in Section 6.14, it is important to avoid the excitation of resonant tower oscillations by rotor thrust fluctuations at blade passing frequency or, to a lesser extent, at rotational frequency. Dynamic magnification impacts directly on fatigue loads, so the further the first mode tower natural frequency is from the exciting frequencies, the better.

In the case of machines operating at one of two fixed speeds, the latitude available for the selection of the tower natural frequency is more restricted. Figure 7.72 shows the variation of dynamic magnification factor with tower natural frequency for excitation at upper and lower blade passing and rotational frequencies for a three bladed machine with a 3:2 ratio between the upper and lower speeds. The curves are plotted for a damping ratio of zero, but the difference if the curves were plotted for a realistic damping ratio of about 5% would be small. The figure also shows the tower natural frequency bands available if the dynamic magnification ratio were to be limited to 4 for all four sources of

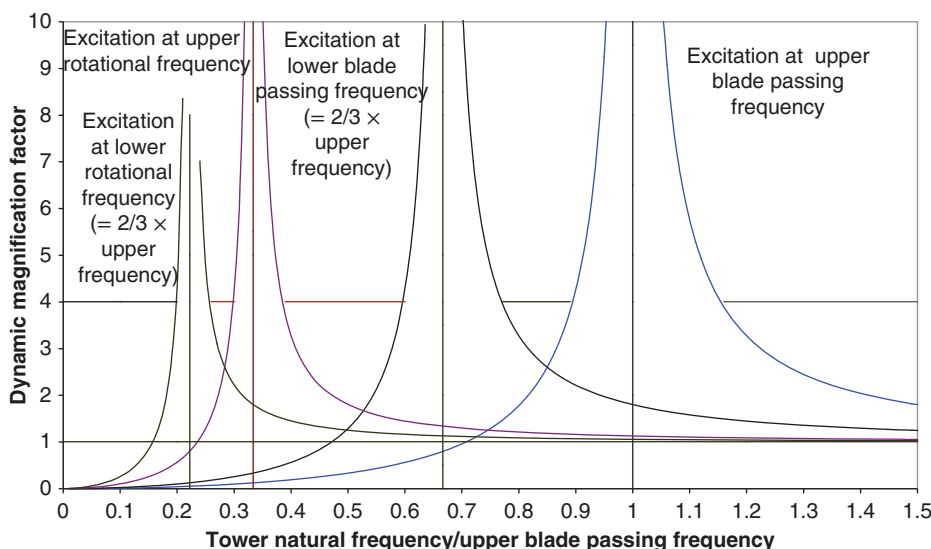


Figure 7.72 Variation of dynamic magnification factors with tower natural frequency for a two-speed, three bladed m/c

excitation. It is apparent that the minimum dynamic magnification ratio obtainable with a tower natural frequency between the upper rotational frequency and lower blade passing frequency is 1.65, for a tower natural frequency of 0.79 times the lower blade passing frequency.

Although the same minimum dynamic magnification ratio would also apply to a variable-speed machine with a 3:2 ratio between the upper and lower rotational speeds, this ratio is above 2:1 for most variable-speed machines, resulting in a much higher minimum dynamic magnification. In these circumstances, the controller may have to impose an exclusion zone preventing operation in a critical rotational speed band – see Section 8.3.4.

Once a satisfactory tower design – in terms of strength and natural frequency – has been evolved for a given turbine, it is a straightforward matter to scale up the machine to larger rotor sizes, provided all of the tower dimensions are scaled similarly, the hub height wind speed is unchanged, and the tip speed is maintained constant. It can be shown that in these circumstances the tower natural frequency varies inversely with rotor diameter, as does the rotational speed of the rotor, so that the dynamic magnification factors are unchanged. Similarly, tower stresses due to extreme wind loading are the same as before.

The situation is less straightforward if the tower height is to be varied for a particular turbine. Assuming, as before, that the extreme hub height wind speed remains the same, and that the wind loading on the tower is negligible compared with the wind loading on the rotor, then the tower base overturning moment is simply proportional to hub height, H . Constant stresses can be maintained at the tower base by scaling all cross-section dimensions up in proportion to the cube root of the hub height. If the same scaling is maintained all of the way up the tower, then the tower natural frequency will vary as $\sqrt{I_B/H^3} = \sqrt{H^{4/3}/H^3} = 1/H^{5/6}$, neglecting tower mass, where I_B is the second moment of area of the tower base cross-section. Thus, doubling the tower height would result in a 44% reduction in natural frequency. Alternatively, if the tower base overturning moment were assumed to vary as $H^{1.5}$ to allow for the effect of wind shear on hub height wind speed and the contribution of wind loading on the tower, then constant tower base stresses could be maintained by scaling the cross-section dimensions up by \sqrt{H} . On this basis, tower natural frequency would vary as $1/\sqrt{H}$.

The practical consequences of ‘tuning’ the tower natural frequency are discussed with respect to tubular towers in the next section.

7.9.3 Steel tubular towers

In the absence of buckling, a waisted conical shell, with a semi angle of 45° below the critical zone for tip clearance, would be the most efficient structure for transferring a horizontal rotor thrust acting in any direction to ground level. However, apart from the practicalities of transport and erection, instability of thin walled shells in compression precludes such a design solution, and the steel tubular towers in common use have a very modest taper. It can be noted in passing that the manufacture of gently tapering towers has only been made possible by the development of increasingly sophisticated rolling techniques, and that early tubular towers were constructed from a series of cylindrical tubes of decreasing diameter with short ‘adaptor’ sections welded between them.

A tapered tower is generally fabricated from a series of pairs of plates rolled into half frusta and joined by two vertical welds. The height of each frustum so formed is limited to two or three metres by the capacity of the rolling equipment. Care has to be taken in the execution of the horizontal welds to minimise local distortion, which weakens the tower under compression loading.

Assuming that a tower design with a uniform taper is to be adopted, the key design parameters to establish are the diameter and wall thickness at the tower base. The tower top diameter, however, is governed by the size of the yaw bearing.

The main considerations determining the tower dimensions at the base are buckling of the shell wall in compression, strength under fatigue loading and stiffness requirements for ‘tuning’ the natural frequency. These are dealt with in separate sub-sections below.

As machines get larger, another important consideration is the maximum tower base diameter that can be accommodated on the highway when tower sections are transported overland. In the flat terrain of North Germany and Denmark, this limit is generally 4.0–4.2 m, but elsewhere it will often be less.

Design against buckling

Given perfect geometry, the strength of a cylindrical steel tube in axial compression is the lesser of the yield strength and the elastic critical buckling stress, given by

$$\sigma_{cr} = 0.605Et/r \quad (7.93)$$

where r is the cylinder radius and t is the wall thickness. Yield strength governs for r/t less than $0.605Ef_y$, which equates to 506 for mild steel, with $f_y = 245$ MPa. However, the presence of imperfections, particularly those introduced by welding, means that the tower wall compression resistance is significantly reduced, even at the relatively low tower wall radius to thickness ratios normally adopted. There is quite a wide disparity between the provisions of different national codes, with some making an explicit link between compression resistance and tolerances on imperfections and others not.

The provisions of EN 1993-1-6:2007, *Eurocode 3: Design of Steel Structures – Part 1.6: Strength and Stability of Shell Structures*, will be described here.

The first step is to decide the fabrication tolerance quality class, based on the imperfection tolerances that can be realistically achieved in the production facility.

The limits on the out-of-plane deviations, w , of the cylinder, or ‘dimples’, measured with either

- (i) a rod of length $L = 4\sqrt{rt}$ placed vertically, away from welds; or
- (ii) a circular template of the same length placed horizontally, away from welds; or
- (iii) a rod of length $L = 25t$ placed vertically across horizontal welds

as a percentage of the requisite gauge lengths are given for different fabrication tolerance quality classes in Table 7.14, which also gives corresponding values of the fabrication quality parameter, Q .

Having determined the appropriate fabrication quality parameter, the meridional elastic imperfection reduction factor, α_x , and the plastic limit relative slenderness, λ_p , can be determined according to

$$\alpha_x = \frac{0.62}{1 + 1.91\left(\frac{1}{Q}\sqrt{\frac{r}{t}}\right)^{1.44}} \quad (7.94)$$

Table 7.14 Recommended dimple tolerance and corresponding value of the fabrication quality parameter for different fabrication tolerance quality classes

Fabrication tolerance quality class	Description	Recommended limit on percentage deviation	Fabrication quality parameter, Q
Class A	Excellent	0.6%	40
Class B	High	1.0%	25
Class C	Normal	1.6%	16

and

$$\lambda_p = \sqrt{\frac{\alpha_x}{0.4}} \quad (7.95)$$

The buckling strength reduction factor, χ , is then given by

$$\chi = 1 - 0.6 \left(\frac{\lambda - \lambda_0}{\lambda_p - \lambda_0} \right) \quad (7.96)$$

where λ is the relative shell slenderness, $\sqrt{f_y/\sigma_{cr}}$, σ_{cr} is the elastic critical meridional buckling stress and λ_0 is the squash limit relative slenderness. Both the latter parameters depend on the proportion, ε , the axial stress forms of the total, as follows:

$$\sigma_{cr} = 0.605E \frac{t}{r} (1 - 0.4\varepsilon) \quad (7.97)$$

and

$$\lambda_0 = 0.3 - 0.1\varepsilon \quad (7.98)$$

As wind turbine tower stresses are dominated by bending stress, ε is small and can be ignored for preliminary design. Figure 7.73 shows how the buckling strength reduction factor varies with the shell radius to thickness ratio for the different fabrication tolerance quality classes under the assumption that axial stress is negligible. Note that the plot shows the buckling strength reduction factor divided by the partial safety factor for materials strength of 1.1 specified in IEC 61400-1:2019 for global buckling of curved shells assessed according to EN 1993-1-6:2007 (reduced from the 1.2 value specified in previous editions). Also plotted (as a dashed line) is the corresponding curve specified in the GL rules (2005) for a 1% limit on dimple depth. In this case the buckling strength reduction factor is divided by partial safety factor for materials strength given by the GL rules/DIN (which varies with relative shell slenderness, λ), allowing the comparison of the design strengths obtained by the two methods.

The effect of the choice of tower base diameter on total tower weight is best illustrated by reference to a concrete example. Consider the design of a 50 m hub height tower in mild steel for a 60 m diameter, 3 bladed, stall-regulated turbine at a site with a 60 m/s extreme wind speed. The tower base wall thickness required to resist the overturning moment produced by this wind speed has been calculated for a range of tower base diameters with the aid of Eq. (7.96) and plotted on Figure 7.74. Corresponding tower weights have also been plotted, based on a tower top diameter and wall thickness of 2.25 m and 11 mm, respectively, and assuming an idealised linear wall thickness variation between tower top and tower base. It can be seen that the tower weight reaches a minimum value at about

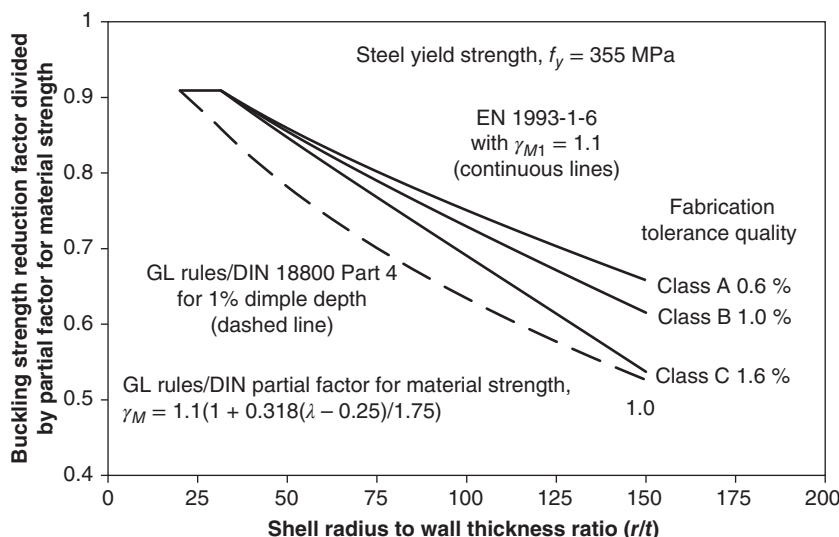


Figure 7.73 Variation of buckling strength reduction factor, divided by partial safety factor for material strength, with shell radius to thickness ratio, for zero axial stress

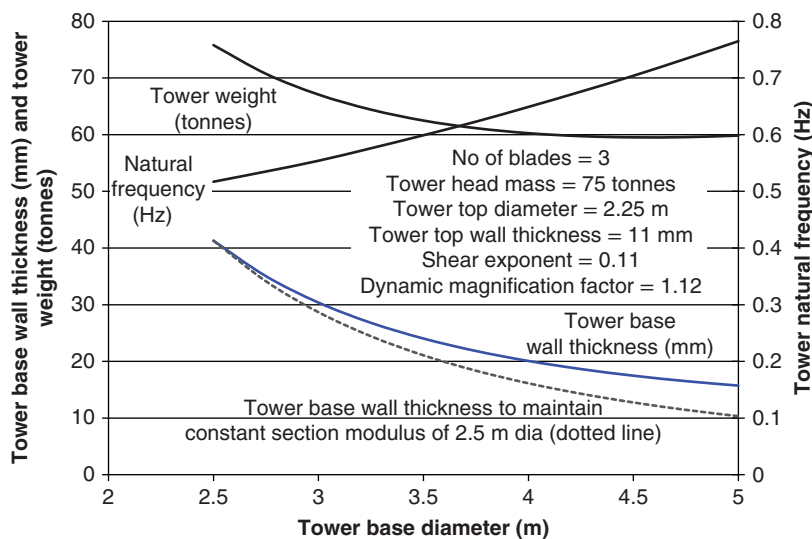


Figure 7.74 Variation in tower base wall thickness with diameter required for support of 60 m dia stall-regulated wind turbine at 50 m hub height in 60 m/s extreme wind speed

4.5 m diameter, indicating that beyond this point the reduction in cross-sectional area for constant section modulus is offset by the effects of the reducing buckling strength and the increasing wind loading on the tower itself. The weight penalty resulting from restricting the tower base diameter to 4.0 m for transport purposes would, in this case, be negligible.

Fatigue design

Clear rules for the fatigue design of steel welded structures are given in EN 1993-1-9:2005, *Eurocode 3: Design of Steel Structures – Part 1.9: Fatigue*, where a family of S-N curves is defined for different weld details. On a log–log plot these curves in fact consist of two straight lines, with slopes of 1/5 and 1/3 for numbers of cycles above and below 5×10^6 respectively. In addition, there is a cut-off limit at $N = 10^8$ cycles, so that stress cycles with a stress range smaller than that defined at 10^8 cycles are deemed not to cause any fatigue damage at all.

Excluding the tower doorway (which is considered later) the critical weld details on a steel tubular tower are likely to be at welded attachments for intermediate platform and cable support members and the horizontal welds to the tower base flange and intermediate bolted flanges. Assuming a full penetration butt weld is provided (see upper joint in Figure 7.76), the detail category number for the horizontal welds is 71 (where the number 71 indicates the stress range applicable at 2×10^6 cycles in MPa). The detail category number for longitudinal welded attachments reduces as the length of the attachment increases, but if the attachment length can be restricted to 80 mm, the detail category number of 71 applies here as well. The S-N curve for this detail category is shown in Figure 7.75.

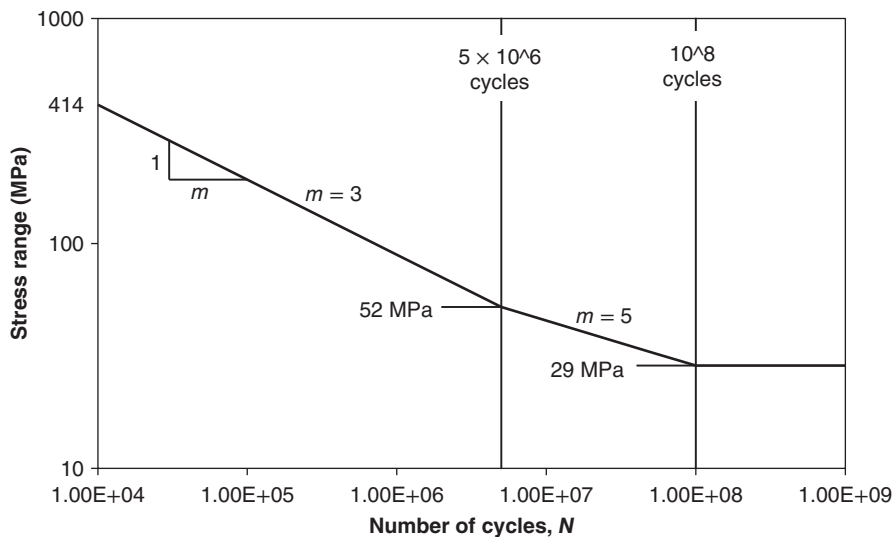


Figure 7.75 EN 1993-1-9:2005 fatigue strength curve for detail category 71 (butt-welded T joint)

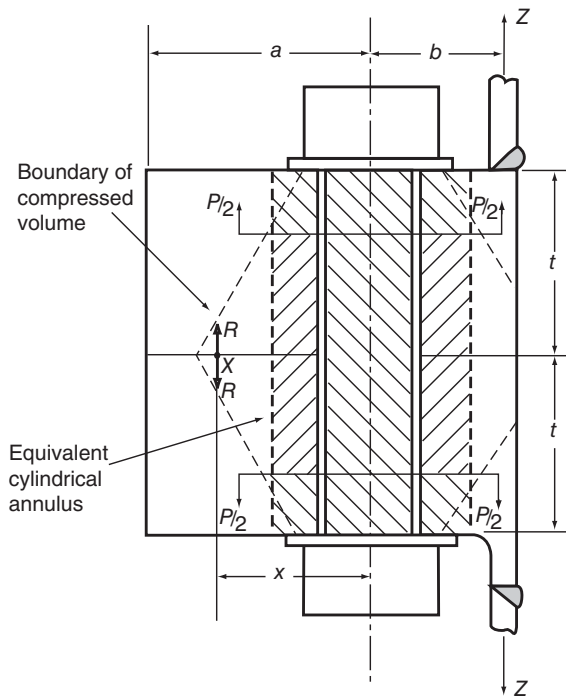


Figure 7.76 Bolted flange joint

Where tower design is governed by fatigue, tower weight can be reduced by selecting weld details corresponding to higher detail categories. This has led to the introduction of ‘weld-neck’ flanges, where the ‘neck’ constitutes a short section of the tower wall (see lower joint in Figure 7.76), so that the weld is a standard transverse butt weld (detail category 90) rather than a tee-but weld (detail category 71). Similarly, the length of welded attachments can be reduced to 50 mm, to raise the detail category to 80.

EN 1993-1-9:2005 recommends different partial safety factors for fatigue strength, γ_{Mf} , according to the consequences of failure and the assessment method. If load redistribution can occur in the event of fatigue damage, then the component concerned can be assessed by the ‘damage tolerant method’, with γ_{Mf} taken as 1.0 and 1.15, for low and high consequence of failure, respectively. However, if local formation of cracks in a structural element could rapidly lead to its failure, assessment should be by the ‘safe-life method’, with increased values of γ_{Mf} of 1.15 and 1.35. In a welded tubular structure, there is no barrier to the propagation of a fatigue crack that has reached a critical length, so the designer must decide whether an inspection regime can be designed to detect incipient cracks before they become critical. Otherwise the tower needs to be assessed by the ‘safe-life’ method.

IEC 61400-1 adopts a similar approach, but some of the partial safety factors for fatigue strength are less conservative. The derivation of fatigue load spectra and the combination of stress ranges due to M_x and M_y load spectra are discussed in Section 5.12.6.

Relative criticality of extreme and fatigue loads

The relative criticality of buckling failure (under extreme loads) and fatigue loads depends on a variety of factors. However, fatigue is more likely to be critical on pitch-regulated machines than on stall-regulated ones, because of the increased rotor thrust fluctuations above rated and the reduced extreme loading at standstill. Fatigue is also more likely to be critical at low wind speed sites, because the percentage reduction in extreme loads is less than the percentage reduction in fatigue equivalent load.

Tuning of tower natural frequency

Considerable scope exists, at least in theory, for adjusting the tower natural frequency to a suitable value by varying the base diameter, while maintaining the necessary strength against extreme and fatigue loading. The effect on natural frequency of varying tower base diameter by a factor of 2, for a case where extreme loading governs, is illustrated for a 60 m dia stall-regulated machine at 50 m hub height in Figure 7.74. The frequency increases from 0.517 Hz for a 2.5 m base diameter to 0.765 Hz for a 5.0 m diameter. Now the rotational speed of a 60 m dia turbine to yield a 60 m/s tip speed is about 19 rpm. If we assume that the machine is two speed, with a lower rotational speed of $19 \times 2/3 = 12.67$ rpm, then the lower blade passing frequency will be 0.633 Hz – right in the middle of the available tower natural frequency range. Adopting a +15% / -15% frequency exclusion zone, the tower natural frequency is required to be less than 0.538 Hz or more than 0.728 Hz. However, a frequency of 0.728 Hz would require a diameter of about 4.7 m (without making the tower wall thicker than necessary for the strength requirement), which is likely to be ruled out by transport considerations. Thus the only strength limited design option is one with a base diameter of 2.75 m, with a weight penalty of about 10 t compared with the 60 t optimum design, giving a natural frequency of about 0.535 Hz. Alternatively, a 4 m base diameter could be chosen and the wall thickness increased by 37% to 27.5 mm to give a frequency of about 0.728 Hz. However, the weight penalty in this case is over 15 t.

The above case study illustrates the fact that it is not always economic to satisfy the natural frequency requirements for a particular combination of turbine and hub height. In these circumstances it may well be preferable to change the hub height. For example, a hub height of 55 m would work much better for the case described, with a tower base diameter of 3.5 m yielding a natural frequency of 0.535 Hz and a tower weight of 74 Tonnes.

Joints between tower sections

Towers are normally fabricated in several sections for transport reasons, so joints are required. Welding on site is an expensive operation, so bolted joints are almost always used, although sleeved joints, in which each tapered tower section is threaded over the one beneath and forced into place by jacking, have been used successfully.

Bolted flange joints

The most widely used bolted arrangement is the internal flanged joint as illustrated in Figure 7.76. The flanges are butt welded to the ends of the mating sections, with the

flange outer edge flush with the tower wall. Alternatively, the flange may be formed with a stub section of tower wall already attached. Such flanges, which are termed *weld neck flanges*, provide a smoother transition from wall to flange (as illustrated in the lower half of Figure 7.76) and result in a higher butt weld detail category.

After assembly, each bolt is torqued or tensioned to induce a pre-load between the flanges to minimise in-service bolt fatigue stresses. The bolt should be initially sized to resist the prying force induced by the extreme tower wall tensile stresses – taking the fulcrum adjacent to the flange inner edge – and then checked for fatigue.

The fatigue calculation for the bolts in a flanged joint depends on the relationship between the bolt load and tower wall stress, which only remains linear while contact is maintained over the full flange width. The Verein Deutscher Ingenieure (VDI) guideline for *The Systematic Calculation of High Duty Bolted Joints*, VDI 2230 (1986), gives a method for calculating the bolt load increment as a proportion of the load increment in the ‘tributary’ width of tower wall under these conditions. The axial loading on the flanged joint and the effect of the moment due to the eccentricity of loading are considered separately. The axial load is assumed to be shared between the bolt and the pre-loaded flanges in proportion to the stiffnesses of the load paths, which, in the case of the flanges, is based on a reduced cross-sectional area related to the volume compressed by the pre-load according to

$$A_{ers} = \frac{\pi}{4}(d_w^2 - d_h^2) + \frac{\pi}{8}d_w(D_A - d_w)[(k + 1)^2 - 1] \text{ where } k = \sqrt[3]{\frac{l_k d_w}{D_A^2}} \quad (7.99)$$

and

d_w is the washer face diameter on the bolt head and nut

d_h is the bolt hole diameter

l_k is the clamping length between bolt head and nut

D_A is twice the distance from the bolt centreline to the nearest flange edge, or the bolt spacing, whichever is the less

The guideline recognises that the effective plane of introduction of the external load will not necessarily be immediately under the bolt head or nut, but may lie nearer the flange mid-plane, giving the load paths distinguished by different cross-hatching in Figure 7.76. Stresses due to the eccentricity of the tower wall load to the flange contact area are dealt with by ordinary bending theory applied to the whole contact area.

The VDI 2230 method outlined above no longer applies once a gap has opened up between the flanges at the outer edge. For larger fluctuations in the externally applied load, Z , the fulcrum model can be used, although it is inevitably conservative at low loads. The axial load, P , applied to the bolt/flange combination is calculated on the basis that a fulcrum exists at X , a distance x from the bolt, so that $P = Z(1 + b/x)$, and the load share between the bolt and the compressed volume of flange is calculated according to the relative stiffnesses as before.

In Figure 7.77, the two linear relationships between bolt load increment and externally applied load are compared with experimental results for a particular test specimen with a single flange bolt. The bolt pre-load is F_0 . It is assumed that the planes of introduction of the load on the bolt/flange combination are immediately under the bolt head

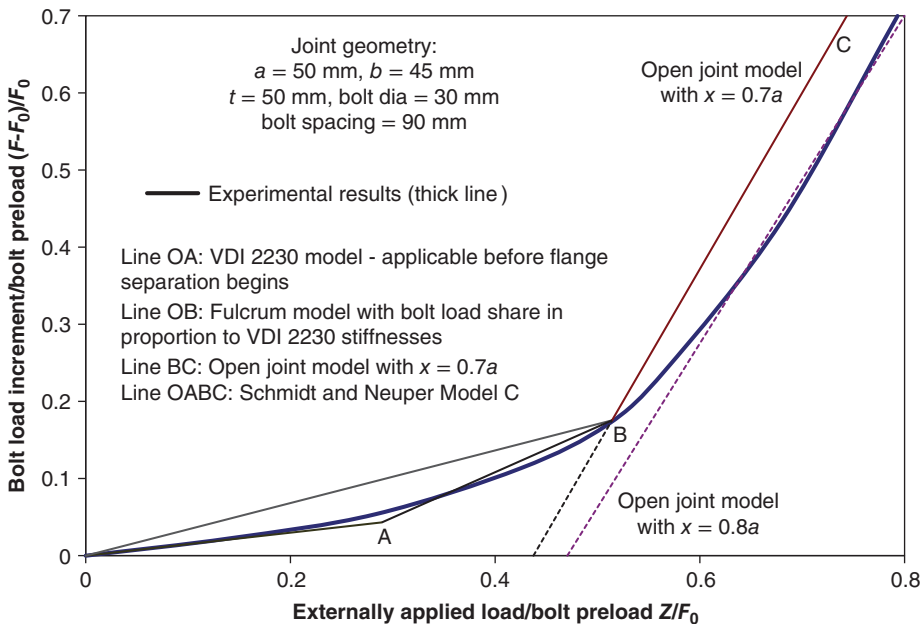


Figure 7.77 Flange joint bolt load variation with externally applied load, Z , and bolt pre-load, F_0 – experimental results and engineering models compared

and nut in each case. Line OA shows the VDI 2230 model, with the point A representing the limit of its validity. Line OB shows the fulcrum model, with B representing the point at which the pre-load between the flanges at the position of the bolts disappears. Thereafter, the bolt load varies as $Z(1 + b/x)$ – i.e. along line BC for $x/a = 0.7$. It may be noted from Figure 7.77 that a value of x/a of 0.8 results in better agreement with the test results at high loads, but these are not of interest for design purposes.

Schmidt and Neuper (1997) have proposed a more sophisticated model identified as *Model C*, which combines aspects of the two models already described and gives a bolt load characteristic consisting of the three straight lines OA, AB, and BC (see Figure 7.77). Clearly this agrees much better with the experimental results, but it adds to the complexity of the fatigue load calculation.

Uniformity of bolt loading around the tower clearly depends on the accuracy of the mating flange surfaces. Schmidt et al. (1999) have investigated the effects of various imperfections using an FE model and made tentative suggestions regarding permitted tolerance levels.

Bolted lap joints

The structurally most effective joint is made with friction grip bolted splice plates oriented vertically and sandwiching the walls of the abutting tower sections between them. Provided the grip force is adequate, the joint will not slip even under the extreme load, with the result that the bolts are not subject to fatigue loads. Apart from the effect of splice plates on the external appearance, the main drawback is the practical difficulty

of joint assembly, because this form of bolting requires the provision of some form of personnel access to the outside of the tower.

As hub heights have increased, manufacturers have sought to avoid the constraint on tower diameter imposed by transport requirements by introducing vertical joints, so that the lower sections of tower can be split into narrower segments. In view of the low stresses in the horizontal direction, this can usually be accomplished by a simple lap joint.

Lagerwey is one among several manufacturers utilising modular towers. Their 166 m high tower for the 4.0–4.5 MW L136 turbine utilises 12 m long pre-bent steel sheets with pre-drilled bolt holes along the four edges. At site the sheets are bolted together into full-circle assemblies using tension controlled high strength friction grip bolts (TCB 2020). Each assembly is then craned into position and secured to the one below by a horizontal bolted joint with six rows of bolts.

Tower tie-down

The tower is normally fitted with a base flange, which can either be attached to the foundation by screwed rods cast into the concrete or bolted to an embedded tower stub.

If screwed rods are employed, they are normally anchored by a steel annular plate at their base, and their capacity to resist overturning moment is determined by the pull-out resistance of the semi-circle of rods on the upwind side. As this is governed by the concrete shear strength, the rods have to be anchored quite deep into the concrete, so that their length is typically similar to the tower base radius.

The gap between the tower base flange and the concrete foundation is grouted and the tie-down rods are then stressed to induce a pre-load between the base flange and the concrete. This considerably reduces the stress ranges in the tie-down rods themselves due to turbine loading that would otherwise result in unacceptable fatigue damage. The share of tower wall uplift loads taken by the rods can be based on an estimate of the relative stiffnesses of the rod and the loaded volume of the concrete, assuming a dispersion angle of about 30° in the radial direction. The screwed rods should be sheathed, so that the pre-tension is applied over the full length.

Tower doorways

A doorway is required for access at or near the tower base, and additional doorways are sometimes required for a transformer in the tower base or for maintenance access to the blade tip mechanism. Often they have vertical sides with semi-circular ends at top and bottom. Vertical stiffeners have to be provided as standard down each side to compensate for the missing section of wall and to resist compression buckling, but attention has to be paid to the weld detail at the stiffener ends, where stress concentration due to the opening is likely to be an additional factor.

The weld detail at the stiffener end can be eliminated by reinforcing the inside edge of the doorway with a continuous flange all of the way round. The detail category of the flange to tower wall butt weld under transverse loading is then 71, but there is no stress concentration factor to contend with at the top and bottom of the doorway. The stress concentration factor at the side of the doorway can be reduced further by making it elliptical.

7.9.4 Steel lattice towers

Steel lattice towers are usually assembled from angle sections, with bolting used for attaching the bracing members to the legs and splicing the leg sections together. Typically, the towers are square in plan with four legs, facilitating the attachment of the bracing members.

One of the advantages of lattice towers is that material savings can be obtained by splaying the legs widely apart at the base, without jeopardising stability or posing transport problems. The latitude for doing this higher up is limited by tip clearance considerations, so waisted tower designs are common. A more elegant tower design results if the legs are rolled to a gentle concave curve, however.

The load capacity of compression members reduces as the slenderness ratio, defined as ‘effective length’ divided by radius of gyration, increases. The effective length equates to the spacing of intersections, unless reduced by moment restraint provided by other members at intersections, so it is desirable to restrict leg intersection spacing. On truss towers, this can result in an excessive number of web members near the tower base, where the legs are widely spaced.

The loads in the legs (or ‘chords’) result from the tower bending moments, while the loads in the bracing (or ‘web’) members result from a combination of tower shear and torsional loads. In each case member buckling under extreme loads has to be considered, and fatigue loading at the joints. Two devices are sometimes employed to improve member stability – the web members are arranged as pairs of intersecting diagonals rather than adopting a single triangulated system, so that the tension diagonal can stabilise the compression diagonal at each intersection, and the web/chord intersection points on either side of each chord member are staggered vertically to reduce the spacing of chord supports restraining flexure about the minor axis. Note that care with detailing is needed at the waist, if present, to ensure adequate lateral restraint for the chords at the change of direction.

To avoid the inefficient use of web members near the base of truss towers, some designers have adopted bracing systems akin to those used on electricity pylons, where multiple sub-bracings are introduced to reduce the effective lengths of both leg and web members.

The development of very high lattice towers has been limited to some extent by the size of angle available for the legs, which are the most heavily loaded members. Although it is possible to construct a leg member from multiple smaller angles battened together, the increased complexity is unwelcome. However, the largest angle sections available have grown over time, from $250 \times 250 \times 28$ in 2006 to $300 \times 300 \times 35$ in 2014, according to ArcelorMittal (2014). They compare the three $250 \times 250 \times 28$ angles required to make up each leg of a 160 m tall wind turbine tower constructed in 2006 that could be replaced by two $300 \times 300 \times 35$ angles today. The tower is at Laasow, Brandenburg, Germany, and supports a 2.5 MW 90 m diameter Fuhrländer turbine.

Fatigue loading of bolts is avoided by the use of friction grip bolts. Accordingly, galvanising is normally used for corrosion protection rather than painting, in order to achieve an adequate coefficient of friction.

The main advantage of lattice towers is the reduction in material costs through both the larger footprint and the use of ‘off-the-shelf’ rolled sections, instead of the more costly fabrications required for tubular towers. Set against this is the cost of the considerable extra activity needed on site for assembly. ArcelorMittal (2014) cite a cost comparison

by P E Concepts, Germany that indicated that lattice towers are cheaper than tubular towers at hub heights above 100 m when site assembly and erection costs and the cost of the foundation and lift are all included. For a hub height of 120 m, the cost of the lattice tower was estimated at EUR 6000 per metre height, compared with EUR 8000 per metre height for the tubular tower.

A significant disadvantage of lattice towers is that the normal access route to the nacelle has traditionally been by a ladder fully exposed to the elements, requiring exceptional levels of fitness of the maintenance personnel. However, in 2014, GE launched a five legged 139 m lattice tower enclosed in a fabric to protect it from the elements (Green Tech Media 2014) and equipped with a lift.

7.9.5 Hybrid towers

Hybrid towers consisting of steel upper sections supported on pre-cast concrete lower sections are often preferred when large hub heights are involved. Enercon offer a range of such towers, extending to hub heights of up to 159 m. They utilise different combinations of standard conical and cylindrical pre-cast concrete sections, with the lower sections split into two vertically to facilitate transport. Once the individual concrete segments have been installed, they are tensioned together using vertical pre-stressing tendons. Pre-casting means that manufacture can be carried out to high standards in factory conditions and enable site work to be minimised.

7.10 Foundations

The design of wind turbine foundations is largely driven by the tower base overturning moment under extreme wind conditions. A variety of slab, multi-pile, and monopile solutions have been adopted for tubular towers, and these are discussed in turn below.

7.10.1 Slab foundations

Slab foundations are chosen when competent material exists within a few metres of the surface. The overturning moment is resisted by an eccentric reaction to the weight of the turbine, tower, foundation and overburden (allowing for buoyancy, if the water table can rise above the base of the slab). The eccentricity of the reaction, and hence the magnitude of the restoring moment, is limited by the load carrying capacity of the sub-strata, which determines the width of the area at the edge of the slab required to carry the gravity loads. Brinch Hansen (1970) provides straightforward rules for calculating the slab bearing capacity under these conditions, based on the simplifying assumption of uniform loading over the loaded area.

The reduction in foundation bearing under the action of extreme overturning moments inevitably results in the opening of a small gap at the windward side of the foundation, which sucks in any water that is present. If this process is repeated too many times, there is a risk of erosion of soil under the foundation, so it is normal to place limits on the amount of gapping that can occur. For example, DNVGL-ST-0126 (2016) requires that positive bearing stress is maintained over the whole width of the foundation for 99% of turbine lifetime. This corresponds to an overturning moment of $WB/6$ for a square slab, where W is the gravity load and B is the slab width.

Care is needed in the determination of the water table level, as a significantly larger slab is needed if it can be submerged. On gently sloping ground it is often advantageous to instal a French drain around the base of the foundation to ensure the water table cannot rise.

Four alternative slab foundation arrangements are shown in Figure 7.78. Figure 7.78a shows a slab of uniform thickness, with its upper surface just above ground level, which is chosen when bedrock is near the ground surface. The main reinforcement consists of top and bottom mats to resist slab bending and the slab is made thick enough for shear reinforcement not to be required. The second variant shown in Figure 7.78b is a slab surmounted by a pedestal. This is used when the bedrock is at a greater depth than the slab thickness required to resist the slab bending moments and shear loads. The gravity load on the substrata is increased by virtue of the overburden, so the overall slab plan dimensions can be reduced somewhat.

The third variant, shown in Figure 7.78c is similar to the second but embodies two possible modifications that can be applied independently – replacement of the pedestal by a stub tower embedded in the slab and introduction of a tapering slab depth. The stub tower has to be perforated near the top of the slab to allow radial top face reinforcement to pass through it, and reinforcement to resist punching shear loads from the tower stub bottom flange must be incorporated. Tapering the slab depth has the merit of saving material, but is slightly more difficult to execute.

Poor detailing has led to cracks opening up between the embedded tower stub and the surrounding concrete on some foundations and Elforsk (2012) provides a survey of these and other construction defects in ‘Cracks in Onshore Wind Power Foundations – Causes and Consequences’.

Rock anchors eliminate the need to add weight to a gravity foundation for counterbalance purposes, and thus enable the foundation size to be significantly reduced,

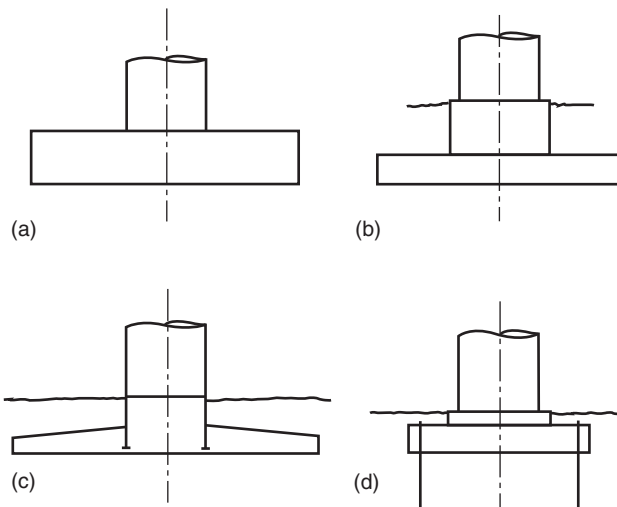


Figure 7.78 (a) Plain slab, (b) slab and pedestal, (c) stub tower embedded in tapered slab, and (d) slab held down by rock anchors

provided bearing capacities are sufficiently high. See Figure 7.78d. Specialist contractors are needed for rock anchor installation, so they only find occasional use.

The ideal shape of gravity foundation in plan is a circle, but in view of the complications of providing circular formwork, an octagonal shape is often chosen instead. Sometimes slabs are square in plan to simplify the shuddering and reinforcement further.

7.10.2 Multi-pile foundations

In weaker ground, a piled foundation often makes more efficient use of materials than a slab. Figure 7.79a illustrates a foundation consisting of a pile cap resting on eight cylindrical piles arranged in a circle. Overturning is resisted by both pile vertical and lateral loads, the latter being generated by moments applied to the head of each pile. Consequently the reinforcement must be arranged to provide full moment continuity between the piles and the pile cap. Holes for the piles can be auger drilled and the piles cast in situ after the positioning of the reinforcement cage.

7.10.3 Concrete monopile foundations

A concrete monopile foundation consists of a single large diameter concrete cylinder, which resists overturning by mobilising soil lateral loads alone. See Figure 7.79b. These lateral loads can be calculated conservatively for sand by using either simple Rankine theory for passive pressures on retaining walls, which ignores soil/wall friction, or Coulomb theory, which includes it. However, in the case of a monopile, friction on the sides of the soil wedge notionally displaced when the pile begins to tilt provides further resistance, and this is accounted for in the solution due to Brinch Hansen (1961).

This type of foundation is an attractive option when the water table is low and the soil properties enable a deep hole to be excavated from above without the sides caving in. However, while simple, the concept is relatively expensive in terms of materials.

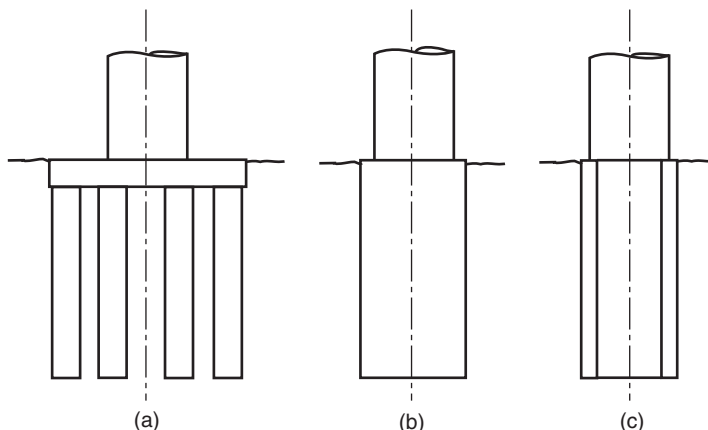


Figure 7.79 (a) Pile group and cap, (b) solid monopile, and (c) hollow monopile

The hollow cylinder variant illustrated in Figure 7.79c uses materials much less extravagantly by replacing the concrete in the body of the cylinder, which has no structural role to play, with fill. Durability is improved by vertical prestressing, which can be integrated with tower hold-down by the use of the same rods for each.

7.10.4 Foundations for steel lattice towers

The legs of steel lattice towers are relatively widely spaced, and lend themselves to separate foundations. Bored cast in-situ piles are commonly used – see Figure 7.80. The mechanism for resisting overturning is simply uplift and downthrust on the piles, but the piles must also be designed for the bending moments induced by the horizontal shear load. Pile uplift is resisted by friction on the surface of the piles, which depends on both the soil/pile friction angle and the lateral soil pressure. Considerable uncertainty surrounds the magnitude of these quantities, so Eurocode 7 recommends the use of pile testing to establish pile capacity.

The angle sections forming the base of the tower legs are cast in place when the concrete for the piles is poured. A framework is assembled in advance, incorporating the leg base sections, so that the legs can be set at the correct spacing and inclination before concreting.

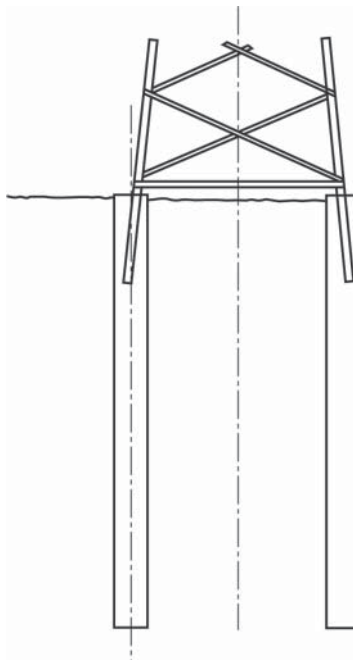


Figure 7.80 Piled foundation for steel lattice tower

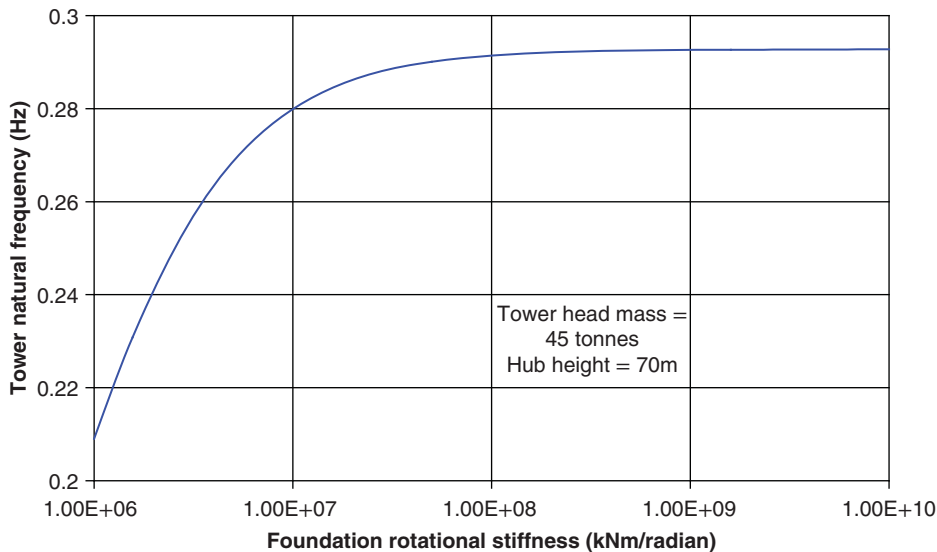


Figure 7.81 Example of variation of tower natural frequency with foundation rotational stiffness

7.10.5 Foundation rotational stiffness

The assessment of foundation rotational stiffness is an important part of the design process because of the effect it has on tower natural frequency, and hence on fatigue loading. Figure 7.81 illustrates the effect of varying the foundation rotational stiffness for a tower supporting a 45 t turbine at 70 m hub height. Manufacturers normally specify a minimum foundation rotational stiffness to ensure that the tower natural frequency is high enough for the fatigue loadings on which the tower design is based to be valid. It is then the task of the foundation designer to ensure that the foundation footprint (or depth, in the case of a monopile foundation) is sufficiently large to achieve this rotational stiffness.

A closed form solution exists for the rotational stiffness, K_θ of a rigid disc resting on an elastic half space, as follows:

$$K_\theta = \frac{8GR^3}{3(1-\nu)} \quad (7.100)$$

where G is the shear modulus of the soil, R is the disc radius and ν is Poisson's ratio. The Det Norske Veritas/Risø *Guidelines for Design of Wind Turbines* (2002) give modified versions of this formula that account for foundation embedment and soil layers with different shear moduli.

Tower base rotation will be increased by flexibility of the foundation itself and this may need to be accounted for as well.

References

- AGMA/AWEA 921-A97 (1996). *Recommended practices for design and specification of gearboxes for wind turbine generator systems*. American Gear Manufacturers Association/American Wind Energy Association.

- Anaya-Lara, O. et al. (2009). *Wind Energy Generation, Modelling and Control*. Chichester, UK: Wiley.
- Anderson CG et al (1993). Yaw system loads of HAWTS. *ETSU Report No W/42/00195/REP*.
- Anderson, C.G., Heerkes, H., and Yemm, R. (1998). Prevention of edgewise vibration on large stall regulated blades. *Proc. BWEA Conf.* 1998: 95–102.
- ANSI/AGMA 2001-C95 (1995). *Fundamental rating factors and calculation methods for involute spur and helical gear teeth*. American National Standards Institute/American Gear Manufacturers Association.
- ANSI/AGMA/AWEA 6006-A03 (2003). *Design and specification of gearboxes for wind turbines*. American National Standards Institute/American Gear Manufacturers Association/American Wind Energy Association.
- ArcelorMittal (2014). Lattice towers for wind energy and power line pylons. <http://www.iposteelnetwork.org/images/meetings/GeneralManager/2014-zuerich/GA-lgc-lattice-tower-for-windmills-pylons.pdf> (accessed 6 February 2020).
- Bak, C., Zahle, F., and Bitsche, R. et al (2013). Description of the DTU 10 MW reference wind turbine. *DTU Wind Energy Report I-0092*.
- Barbero, E.J. (1998). Prediction of compression strength of unidirectional polymer matrix composites. *J. Compos. Mater.* 32 (5): 483–502.
- Barbero, E.J. (2018). *Introduction to Composite Materials Design*, 3e. CRC Press.
- Bonfield, P.W. and Ansell, M.,P. (1991). Fatigue properties of wood in tension, compression and shear. *J. Mat. Sci.* 26: 4765–4773.
- Bond, I.P. and Ansell, M.P. (1998). Fatigue properties of jointed wood composites', Part I: 'Statistical analysis, fatigue master curves and constant life diagrams', Part II: 'Life prediction analysis for variable amplitude loading. *J. Mater. Sci.* 33: 2751, 4121–2762, 4129.
- Bonfield PW, Bond IP, Hacker CL, and Ansell MP (1992). Fatigue testing of wood composites for aerogenerator blades. Part VII. Alternative wood species and joints. Proceedings of the BWEA Conference, 243–249.
- Brinch Hansen J (1961). The ultimate resistance of rigid piles against transverse forces. *Danish Geotechnical Institute Report No. 12*.
- Brinch Hansen J (1970). A revised and extended formula for bearing capacity. *Danish Geotechnical Institute Bulletin No 28*.
- British Standards Institution (1986). *BS 436: Spur and helical gears – Part 3: Method for calculation of contact and root bending stress limitations for metallic involute gears*.
- British Standards Institution (2006). *BS ISO 6336: Calculation of load capacity of spar and helical gears*.
- Bulder, B. (2005) NEW WISPER – creating a new standard load sequence from modern wind turbine data. *Optimat Blades OB_TG1_R020*.
- Corbet, D.C. (1991). *Investigation of materials and manufacturing methods for wind turbine blades*. ETSU W/44/00261. Harwell, UK: Energy Technology Support Unit.
- Corbet DC, Brown C, and Jamieson P (1993). The selection and cost of brakes for horizontal axis stall regulated wind turbines. *ETSU WN 6065*.
- Det Norske Veritas/Risø National Laboratory (2002). *Guidelines for Design of Wind Turbines*. DNV/Risø.
- DNVGL-ST-0126 (2016). *Standard for support structures for wind turbines*.
- DNVGL-ST-0376 (2015). *Rotor blades for wind turbines*.
- DOE/MSU 2010. DOE/MSU composite materials fatigue database. Montana State University.
- Echtermeyer, A.T., Hayman, E., and Ronold, K.O. (1996). Comparison of fatigue curves for glass composite laminates. In: *Design of Composite Structures Against Fatigue* (ed. R.M. Mayer). Mechanical Engineering Publications.
- Ehrmann, R.S., Wilcox, B., and White, E.B. (2017). Effect of surface roughness on wind turbine performance. *Sandia Report SAND2017-10669*.

- Eisenberg, D., Laustsen, S. and Stege, J. (2016). Leading edge protection lifetime prediction model creation and validation. <https://windeurope.org/summit2016/conference/allposters/PO078g.pdf> (accessed 31 January 2019).
- Ekanayake, J.B., Holdsworth, L., and Jenkins, N. (2003). Control of DFIG wind turbines. *Power Eng. J.* 17 (1): 28–32.
- Elforsk (2012). Cracks in onshore wind power foundations – causes and consequences. *Elforsk rapport* 11: 56.
- EN 1993-1-9:2005 (2005), *Eurocode 3: Design of steel structures – Part 1.9: Fatigue*. Brussels: European Committee for Standardization.
- EN 1993-1-6:2007 (2007). *Eurocode 3: Design of steel structures – Part 1.6: Strength and stability of shell structures*. Brussels: European Committee for Standardization.
- Fedorov, V. (2012). Bend-twist coupling effects in wind turbine blades. PhD thesis. DTU Wind Energy.
- Freris, L. (ed.) (1990). *Wind Energy Conversion Systems*. Prentice Hall.
- Fuglsang PL and Madsen HA (1995). A design study of a 1 MW stall regulated rotor. *Riso R-799*.
- Gardiner (2013). Modular design eases big wind blade build. *Composites World*, July 2013. <https://www.compositesworld.com/articles>.
- Germanischer Lloyd (1993). *Rules and regulations IV – Non-marine technology: Part 1 – Wind energy: Regulation for the certification of wind energy conversion systems*.
- Germanischer Lloyd (2010). *Rules and guidelines IV – Industrial services: Part 1 – Guideline for the certification of wind turbines*.
- Green Tech Media (2014). Is GE's space frame tower the future of wind power? <https://www.greentechmedia.com/articles/read>.
- Griffith, D.T. (2013). The SNL 100–01 blade: carbon design studies for the Sandia 100-metre blade. *Sandia Report SAND2013-1178*.
- Griffith, D.T. and Ashwill, T.D. (2011). The Sandia 100-metre all-glass baseline wind turbine blade: SNL 100–00. *Sandia Report SAND2011-3779*.
- Griffith, D.T. and Johanns, W. (2013). Large blade manufacturing costs studies using the Sandia blade manufacturing cost tool and Sandia 100 m blades. *Sandia Report SAND2013-2734*.
- Hancock M and Bond IP (1995). The new generation of wood composite wind turbine rotor blades – design and verification. Proceedings of the BWEA Conference, pp. 47–52.
- Heier, S. (2014). *Grid Integration of Wind Energy Conversion Systems*, 3e. Chichester, UK: Wiley.
- Hindmarsh, J. (1984). *Electrical Machines and Their Applications*. UK: Butterworth Heinemann.
- Hück (1983). Calculation of S/N curves for steel, cast steel and cast iron – synthetic S/N curves. *Verein Deutsher Eisenhüttenleute Report No. ABF 11*.
- IEC 61400-1 (2019). *Wind energy generation systems – Part 1: Design requirements* (edition 4). Geneva, Switzerland: International Electrotechnical Commission.
- IEC 61400-4 (2012). *Wind turbines – Part 4: Design requirements for wind turbine gearboxes*. Geneva, Switzerland: International Electrotechnical Commission.
- IEC 61400-23 (2014). *Wind turbines – Part 23: Full-scale structural testing of rotor blades*. Geneva, Switzerland: International Electrotechnical Commission.
- IEC CD 61400-5 (2016). *Wind energy generation systems – Part 5: Wind turbine rotor blades*, draft. Geneva, Switzerland: International Electrotechnical Commission.
- IECRE (2019). Wind turbine type certificate, IECRE.WE.TC.19.0025-R0. <https://www.iecre.org/certificates/windenergy>.
- INNWIND (2015). New lightweight structural blade designs and blade designs with build-in structural couplings. *Deliverable 1.22*.
- ISO 6336 (2019). *Calculation of load capacity of spur and helical gears: Parts 1–6*.
- Jamieson P and Brown CJ (1992). The optimisation of stall regulated rotor design. Proceedings of the BWEA Conference, pp. 79–84.

- Johanns, W. and Griffith, D.T. (2013). User manual for Sandia blade manufacturing cost tool: Version 1.0. *Sandia Report SAND2013-2733*.
- Keegan, M.H., Nash, D.H., and Stack, M.M. (2012). Modelling rain drop impact of offshore wind turbine blades. Proceedings of the ASME TURBO EXPO, Copenhagen.
- Keegan, M.H., Nash, D.H., and Stack, M.M. (2013). *On Erosion Issues Associated with the Leading Edge of Wind Turbine Blades*. Glasgow, UK: University of Strathclyde.
- Krause, O. and Kensche, C. (2006). Summary fatigue test report. *Optimat Blades OB_TG_R026*.
- Krause, P.C. (1986). *Analysis of Electric Machinery*. New York, USA: McGraw Hill.
- Legault, M. (2018). Wind blade spar caps: pultruded to perfection? *Composites World*, 27 March 2018.
- Lobitz, D.W., Veers, P.S., Eisler, G.R., et al (2001). The use of twist-coupled blades to enhance the performance of horizontal axis wind turbines. *Sandia Report SAND2001-1303*.
- Lobitz, D.W., Veers, P.S., and Migliore, P.G. (1996). Enhanced performance of HAWTs using adaptive blades. *Wind Energy* 96: 41–45.
- Mayer, R.M. (1996). *Design of Composite Structures Against Fatigue*. Mechanical Engineering Publications.
- McPherson, G. (1990). *An Introduction to Electrical Machines and Transformers*, 2e. New York, USA: Wiley.
- Mohan, N., Undeland, T.M., and Robbins, W.P. (1995). *Power Electronics: Converters, Applications, and Design*, 3e. New York, USA: Wiley.
- Muller, S., Deicke, M., and De Doncker, R. (2002). Doubly fed induction generator systems for wind turbines. *IEEE Ind. Appl. Mag.* 8 (3): 26–33.
- Nijssen, R.P.L. (2005). (NEW) WISPER(X) load spectra test results and analysis. *Optimat Blades OB_TG_R024*.
- Nijssen, R.P.L. (2007). Fatigue life prediction and strength degradation of wind turbine rotor blade composites. *Sandia Report SAND2006-7810P*.
- Offshore Wind Industry (2015) Protection for the leading edge. <http://www.offshorewindindustry.com/news/protection-leading-edge> (accessed 31 January 2019).
- ORE Catapult (2016) Catapult delivers first blade leading edge erosion measurement campaign. <https://ore.catapult.org.uk/press-releases/catapult-delivers-first-blade-leading-edge-erosion-measurement-campaign> (accessed 31 January 2019).
- Pena, R., Clare, J.C., and Asher, G.M. (1996). Doubly fed induction generator using back-back PWM converters and its application to variable speed wind energy generators. *IEE Proc. Elec. Power Appli.* 143: 231–241.
- Petersen JT, Madsen HA, Björck A, Enevoldsen P, Øye S, Ganander H, and Winkelaar D (1998), Prediction of dynamic loads and induced vibrations in stall. *Riso R-1045*.
- Samborsky, D.D., Agastra, P., and Mandell, J.F. (2010). Fatigue trends for wind blade infusion resins and fabrics. *AIAA-2010-2820*.
- Samborsky, D.D., Mandell, J.F., and Miller, D. (2012). The SNL/MSU/DOE fatigue of composite materials database: recent trends. *AIAA-2012-1573*.
- Samborsky, D.D., Wilson, T.J., and Mandell, J.F. (2007). Comparison of tensile fatigue resistance and constant life diagrams for several potential wind turbine blade laminates. *AIAA: 2007-67056*.
- Schmidt, H. and Neuper, M. (1997). ‘Zum elastostatischen Tragverhalten exzentrisch gezogener L-Stöße mit vorgespannten Schrauben’ (‘on the elastostatic behaviour of an eccentrically tensioned L-joint with prestressed bolts’). *Stahlbau* 66: 163–168.
- Schmidt H, Winterstetter TA, and Kramer M (1999). Non-linear elastic behaviour of imperfect, eccentrically tensioned L-flange ring joints with prestressed bolts as basis for fatigue design. Proceedings of the European Conference on Computational Mechanics.
- Scott et al. (2017). Effects of aeroelastic tailoring on performance characteristics of wind turbine systems. *Renew. Energy* 114 (B): 887–903.

- Snowberg, S., Dana, S., and Hughes, S. et al (2014). Implementation of a biaxial resonant fatigue test method on a large wind turbine blade. *NREL/TP-5000-61127*, National Renewable Energy Laboratory.
- Springer, G.S. (1976). *Erosion by Liquid Impact*. Washington D.C: Scripta Publishing Co.
- Sutherland, H. and J. Mandell (2004). Updated Goodman diagrams for fiberglass composite materials using the DOE/MSU fatigue database Proceedings of AWEA Global Windpower.
- TCB (2020). Lagerwey modular steel tower. <https://www tcbolts.com/en/projects/wind-energy/108-lagerwey-modular-steel-tower>.
- Thomsen K (1998). The statistical variation of wind turbine fatigue loads. *Riso R-1063*.
- Timoshenko, S.P. and Gere, J.M. (1961). *Theory of Elastic Stability*, 2e. Mc Graw-Hill.
- Van Delft DRV, de Winkel GD, and Joose PA (1996). Fatigue behaviour of fibreglass wind turbine blade material under variable amplitude loading. Proceedings of the EUWEC, Göteborg.
- Verein Deutscher Ingenieure (1986/1988). *VDI 2230 Part 1: Systematic Calculation of High Duty Bolted Joints – Joints with One Cylindrical Bolt*.
- Wilson R A (1990). Implementation and optimisation of mechanical brakes and safety systems. Proceedings of a DEn/BWEA Workshop on ‘Mechanical Systems for Wind Turbines’.
- Windblatt (2013). Wrapped instead of glued. March 2013.
- Windblatt (2016) Series production of EP4 components launched. April 2016.
- Windtech International (2019). Research project brings aerospace blade protection to wind turbine industry. <https://www.windtech-international.com/product-news/research-project-brings-aerospace-blade-protection-to-wind-turbine-industry> (accessed 31 January 2019).

8

The controller

In the most general sense, the wind turbine control system consists of a number of sensors, a number of actuators, and a system consisting of hardware and software that processes the input signals from the sensors and generates output signals for the actuators.

The sensors might include, for example,

- An anemometer.
- A wind vane.
- At least one rotor speed sensor.
- An electrical power sensor.
- Accelerometers.
- Load sensors.
- A pitch position sensor.
- Various limit switches.
- Vibration sensors.
- Temperature and oil level indicators.
- Hydraulic pressure sensors.
- Operator switches, push buttons, etc.

The actuators might include hydraulic or electric pitch actuators, the electrical generator, which can be considered to be a torque actuator, generator contactors, switches for activating shaft brakes, yaw motors, etc.

The system that processes the inputs to generate outputs usually consists of a computer or microprocessor based controller that carries out the normal control functions needed to operate the turbine, supplemented by a highly reliable hard-wired safety system. The safety system must be capable of overriding the normal controller to bring the turbine to a safe state if a serious problem occurs.

8.1 Functions of the wind turbine controller

8.1.1 Supervisory control

Supervisory control can be considered as the means whereby the turbine is brought from one operational state to another. The operational states might, for example, include the following:

- Standby, when the turbine is available to run if external conditions permit.
- Start-up.
- Power production.
- Shut-down.
- Stopped with fault.

It is possible to envisage other states, or it may be useful to further subdivide some of these states. As well as deciding when to initiate a switch from one state to another, the supervisory controller will carry out the sequence control required. As an example, the start-up control for a pitch-regulated wind turbine might consist of a sequence of steps such as the following:

- Power up the pitch actuators and other subsystems.
- Release the shaft brake.
- Ramp the pitch position demand at a fixed rate to some starting pitch.
- Wait until the rotor speed exceeds a certain small value.
- Engage the closed-loop pitch control of speed.
- Ramp the speed demand up to the generator minimum speed.
- Wait until the speed has been close to the target speed for a specified time.
- Close the generator contactors.
- Engage power or torque controller.
- Ramp the power/torque/speed set-points up to the rated level.

The supervisory controller must check that each stage is successfully completed before moving on to the next. If any stage is not completed within a certain time, or if any faults are detected, the supervisory controller should change to shut-down mode.

8.1.2 Closed-loop control

The closed-loop controller is usually a software based system that automatically adjusts the operational state of the turbine to keep it on some pre-defined operating curve or characteristic. Some examples of such control loops are

- Control of blade pitch to regulate the power output or rotational speed of the turbine to a fixed or slowly varying set-point (for example, the rated level in above rated wind speeds, or a predetermined speed ramp during start-up or shut-down of the turbine).
- Control of generator torque to regulate the rotational speed of a variable-speed turbine.
- Control of yaw motors to minimise the yaw tracking error.

Some of these control loops may require very fast response to prevent the turbine wandering far from its correct operating curve. Such controllers may need to be designed very carefully if good performance is to be achieved without detrimental effects on other aspects of the turbine's operation. Others, such as yaw control, are typically rather slow acting, and careful design is then much less critical.

This chapter examines the main issues behind closed-loop controller design and presents some of the techniques that can be used to effect a successful design.

8.1.3 The safety system

It is helpful to consider the safety system as quite distinct from the main or 'normal' control system of the turbine. Its function is to bring the turbine to a safe condition in the event of a serious or potentially serious problem. This usually means bringing the turbine to rest or to a slow idling speed with the blades feathered and the generator switched off.

The normal wind turbine supervisory controller should be capable of starting and stopping the turbine safely in all foreseeable 'normal' conditions, including extreme winds, loss of the electrical network, and most fault conditions that are detected by the controller. The safety system acts as a backup to the main control system, and takes over if the main system appears to be failing to do this. It may also be activated by an operator-controlled emergency stop button.

Thus, the safety system must be independent from the main control system as far as possible, and must be designed to be fail-safe and highly reliable. Rather than utilising any form of computer or microprocessor based logic, the safety system would normally

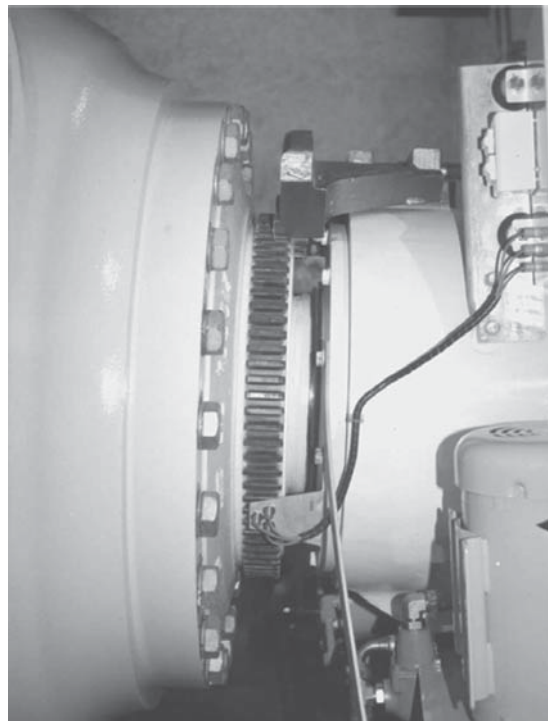


Figure 8.1 Low-speed shaft sensing system. Three proximity sensors mounted on a bracket attached to the front of the (integrated) gearbox register the passage of the teeth on the shaft circumference and provide an independent speed signal for the control and safety systems. The flange onto which the hub is bolted is immediately to the left of the teeth

consist of a hard-wired fail-safe circuit linking a number of normally open relay contacts that are held closed when all is healthy. Then if any one of those contacts is lost, the safety system trips, causing the appropriate fail-safe actions to operate. This might include disconnecting all electrical systems from the supply and allowing fail-safe pitching to the feather position, for example.

The safety system might, for example, be tripped by any one of the following:

- Rotor overspeed, that is, reaching the hardware overspeed limit. This is set higher than the software overspeed limit, which would cause the normal supervisory controller to initiate a shut-down. Figure 8.1 shows a typical arrangement of rotor speed sensing equipment on the low-speed shaft.
- Vibration sensor trip, which might indicate that a major structural failure has occurred.
- Controller watchdog timer expired: the controller should have a watchdog timer that it resets every controller timestep. If it is not reset within this time, this indicates that the controller is faulty and the safety system should shut down the turbine.

- Emergency stop button pressed by an operator.
- Other faults indicating that the main controller might not be able to control the turbine.

In some cases, the safety system may involve more than one circuit. For example, any safety system trip would normally cause the blades to pitch, but it may be feasible for the relay that disconnects the generator system to be on a different circuit that omits certain sensors, so that in the event of certain faults unrelated to the electrical system the braking action of the generator can be maintained to assist the shut-down.

8.2 Closed-loop control: issues and objectives

8.2.1 Pitch control

Pitch control (see also Sections 3.14 and 6.7.2) is the most common means of controlling the aerodynamic power generated by the turbine rotor. Pitch control also has a major effect on all of the aerodynamic loads generated by the rotor.

Below rated wind speed, the turbine should simply be trying to produce as much power as possible, so there is generally no need to vary the pitch angle because the optimum pitch angle does not change much with wind speed. The aerodynamic loads below rated wind speed are generally lower than above rated, so again there is no need to modulate these using pitch control, although some pitch action to reduce fatigue loads is possible as explained below. However, for turbines operating below rated at constant speed, the optimum pitch angle for aerodynamic efficiency varies slightly with tip speed ratio, and therefore with wind speed. In this case the pitch angle can be varied slowly (by no more than a few degrees) to maintain optimum power production as the mean wind speed changes. This applies also to variable-speed turbines when operating on a constant-speed portion of the operating curve. However, if minimisation of thrust-related loads is important, small gains in energy capture may be traded off and the pitch increased slightly instead to reduce thrust in the region of rated wind speed where the mean thrust is at its highest – so-called ‘thrust clipping’.

Above rated wind speed, pitch control provides a very effective means of regulating the aerodynamic power and loads produced by the rotor so that design limits are not exceeded. To achieve good regulation, however, the pitch control needs to respond very rapidly to changing conditions. This highly active control action needs very careful design as it interacts strongly with the turbine dynamics.

One of the strongest interactions is with the tower dynamics. As the blades pitch to regulate the aerodynamic torque, the aerodynamic thrust on the rotor also changes substantially, and this feeds into the tower vibration. As the wind increases above rated, the pitch angle increases to maintain constant torque, but the rotor thrust decreases. This allows the downwind tower deflection to decrease, and as the tower top moves upwind the relative wind speed seen by the rotor increases. The aerodynamic torque increases further, causing more pitch action. Clearly if the pitch controller gain is too high this positive feedback can result in instability. It is therefore vital to take the tower dynamics into account when designing a pitch controller.

Below rated wind speed, the pitch setting should be at its optimum value to give maximum power. It follows that when the wind speed rises above rated, either an increase or a decrease in pitch angle will result in a reduction in torque. An increase in pitch angle, defined as turning the leading edge into wind, reduces the torque by decreasing the angle of attack and hence the lift. This is known as *pitching towards feather*. A decrease in pitch, that is, turning the leading edge downwind, reduces the torque by increasing the angle of attack towards stall, where the lift starts to decrease and the drag increases. This is known as *pitching towards stall*.

Although pitching towards feather is the more common strategy, some turbines pitch towards stall. This is commonly known as *active stall* or *assisted stall* (see Section 6.7.4). Pitching to feather requires much more dynamic pitch activity than pitching to stall: once a large part of the blade is in stall, very small pitch movements suffice to control the torque. Pitching to stall results in significantly greater thrust loads because of the increased drag. However, the thrust is much more constant once the blade is stalled, so thrust-driven fatigue loads may well be smaller.

A further problem with pitching to stall is that the lift curve slope at the start of the stalled region is negative, i.e. the lift coefficient decreases with increasing angle of attack. This results in negative aerodynamic damping, which can result in instability of the blade bending modes, both in-plane and out-of-plane. This can be a problem also with fixed pitch stall-regulated turbines.

Most pitch-controlled turbines use full-span pitch control, in which the pitch bearing is close to the hub. It is also possible, though not common, to achieve aerodynamic control by pitching only the blade tips, or by using ailerons, flaps, air-jets or other devices to modify the aerodynamic properties. These strategies will result in most of the blade being stalled in high winds. If only the blade tips are pitched, it may be difficult to fit a suitable actuator into the outboard portion of the blade, and accessibility for maintenance is problematic.

8.2.2 Stall control

Many smaller and older turbines are stall-regulated, which means that the blades are designed to stall in high winds without any pitch action being required. This means that pitch actuators are not required, although some means of aerodynamic braking is likely to be required, if only for emergencies (see Section 6.8.2).

To achieve stall regulation at reasonable wind speeds, the turbine must operate closer to stall than its pitch-regulated counterpart, resulting in lower aerodynamic efficiency below rated. This disadvantage may be mitigated in a variable-speed turbine, when the rotor speed can be varied below rated to maintain peak power coefficient.

In order for the turbine to stall rather than accelerate in high winds, the rotor speed must be restrained. In a fixed-speed turbine the rotor speed is restrained by the generator, which is governed by the network frequency, as long as the torque remains below the pull-out torque. In a variable-speed turbine, the speed is maintained by ensuring that the generator torque is varied to match the aerodynamic torque. A variable-speed turbine offers the possibility to slow the rotor down in high winds to bring it into stall. This means that the turbine can operate further from the stall point in low winds, resulting in higher aerodynamic efficiency. However, this strategy means that when a gust hits the turbine, the load torque not only has to rise to match the wind torque but also has to increase

further to slow the rotor down into stall. This removes one of the main advantages of variable-speed operation, namely that it allows very smooth control of torque and power above rated.

The benefits of pitch control as a means of braking mean that stall control is now rarely used for large commercial turbines.

8.2.3 Generator torque control

The torque developed by a fixed-speed (i.e. directly connected) induction generator is determined purely by the slip speed (see also Sections 6.9 and 7.5). As the aerodynamic torque varies, the rotor speed varies by a very small amount such that the generator torque changes to match the aerodynamic torque. The generator torque cannot therefore be actively controlled.

However, if a frequency converter is interposed between the generator and the network, the generator speed will be able to vary. The frequency converter can be actively controlled to maintain constant generator torque or power output above rated wind speed. Below rated, the torque can be controlled to any desired value – for example, with the aim of varying the rotor speed to maintain maximum aerodynamic efficiency.

There are two principal means of achieving variable-speed operation. One is to connect the generator stator to the network through a frequency converter, which must then be rated for the full power output of the turbine. An alternative arrangement is the doubly fed induction generator, a wound-rotor machine in which the stator is connected directly to the network and the rotor is connected to the network through slip rings and a frequency converter. This means that the frequency converter need only be rated to handle a fraction of the total power, although the larger this fraction, the larger the achievable speed range will be. This arrangement has been very widely used in recent years, but the fully rated converter is more advantageous from the network point of view, and is becoming the favoured option as wind penetration increases.

A special case is the variable-slip induction generator, where active control of a resistance in series with the rotor windings allows the torque/speed relationship to be modified. By means of closed-loop control based on measured currents, it is possible to maintain constant torque above rated, effectively allowing variable-speed operation in this region. Below rated it behaves just like a normal induction generator (Bossanyi and Gamble 1991; Pedersen 1995).

8.2.4 Yaw control

Turbines, whether upwind or downwind, can be designed to be stable in yaw (Section 3.10), in the sense that if the nacelle is free to yaw, the turbine will naturally remain pointing into the wind. However, it may not point exactly into wind, in which case some active control of the nacelle angle may be needed to maximise the energy capture. Because a yaw drive is usually required anyway – for example, for start-up and for unwinding the pendant cable – it may as well be used for active yaw tracking. Free yaw has the advantage that it does not generate any yaw moments at the yaw bearing. However, it is usually necessary to have at least some yaw damping, in which case there will be a yaw moment at the bearing.

In practice, almost all turbines now use active yaw control. A yaw error signal from the nacelle-mounted wind vane is then used to calculate a demand signal for the yaw actuator. Frequently the demand signal will simply be a command to yaw at a slow fixed rate in one or the other direction. The yaw vane signal must be heavily averaged, especially for upwind turbines where the vane is behind the rotor. Because of the slow response of the yaw control system, a simple dead-band controller is often sufficient. The yaw motor is switched on when the averaged yaw error exceeds a certain value, and switched off again after a certain time or when the nacelle has moved through a certain angle. A yaw brake is usually applied when the turbine is not yawing, and often even while yawing to prevent frequent load reversals at the yaw pinion due to the highly variable nature of the yawing moments.

More complex control algorithms are sometimes used, but the control is always slow-acting, and does not demand any special closed-loop design analysis; in fact rapid yawing is unnecessary, and can generate large gyroscopic loads. Because of this, yaw control is often classed as part of the supervisory controller; also because it remains active in standby mode to keep the turbine pointing into wind (except in very low winds when the wind direction becomes too variable).

Active yaw control can be used to regulate aerodynamic power in high winds, as on the experimental variable-speed Gamma 60 turbine referred to in Section 6.7.5. This clearly requires very rapid yaw rates, and results in large yaw loads and gyroscopic and asymmetric aerodynamic loads on the rotor. This method of power regulation would be too slow for a fixed-speed turbine, and even on the Gamma 60 the speed excursions during above rated operation were quite large. This approach has not found commercial application.

Instead of a yaw actuator, it is possible to use individual pitch control to generate a yawing moment – see Section 8.3.14.

A typical yaw control algorithm might be configured as follows: when a heavily low-pass-filtered yaw error signal from the nacelle wind vane becomes greater than a given threshold, the turbine yaws at a fixed rated (typically below $1^\circ/\text{s}$) to bring the averaged yaw error back to 0° . Yaw algorithm parameters, such as filter time constants and yaw error thresholds, are often fixed by experience based on trial and error, so that yaw misalignments are kept small and yawing manoeuvres do not occur more frequently than, say, every few minutes. Optimum settings – for example, to achieve a suitable trade-off between the frequency of yawing operations and loss of energy production due to yaw misalignment – are difficult to define theoretically as they depend on the low-frequency variability of wind direction, which can be very site-specific. Long-term simulation modelling based on site wind data can be used for this (Bossanyi et al. 2013). In a wind farm, sharing of information about wind direction between adjacent turbines can also be helpful (Bossanyi 2019).

8.2.5 Influence of the controller on loads

As well as regulating the turbine power in high winds and optimising it in low winds, it is clear that the action of the control system can have a major impact on the loads experienced by the turbine. The design of the controller must take into account the effect on loads, and at least ensure that excessive loads will not result from the control action. It is possible to go further than this, and explicitly design the controller with the reduction of certain loads as an additional objective.

The reduction of certain loads is clearly compatible with the primary objective of limiting power in high winds. For example, the limitation of power output is clearly compatible with limitation of gearbox torque. In other cases however, there may be a conflict, in which case the controller design is bound to be a compromise involving a trade-off between competing goals. For example, there is a clear trade-off between good control of power output and pitch actuator loads. The more actuator activity can be tolerated, the better the power control can be. Of course it is always possible to reduce loads by reducing energy capture (after all of the loads are minimised with the turbine switched off), but economic optimisation generally implies that reduced capital cost due to reduced loading is often only justified if it causes very little or no loss of energy production.

The interaction between pitch control and tower vibration referred to in Section 8.2.1 is another important example, because the amount of tower vibration has a major effect on tower base loads. The tighter the control of rotor speed by means of pitch control, the greater the tower vibration is likely to be. Blade, hub, and other structural loads will also be influenced by pitch control activity. Generator torque control can have a major impact on gearbox loads, as described below.

8.2.6 Defining controller objectives

The primary objective of the closed-loop controller can usually be stated fairly simply. For example, the primary objective of the pitch controller may be to limit power or rotor speed in high winds. There may be more than one ‘primary’ objective, as in the case where the pitch controller is also used to optimise energy capture in low winds.

However, because the controller can also have a major effect on structural loads and vibrations, it is vital to consider these when designing the control algorithm. Thus a fuller description of the pitch controller objectives might be

- To optimise power production in below rated wind speeds.
- To regulate or limit aerodynamic torque in above rated wind speeds.
- To minimise peaks in gearbox torque.
- To avoid excessive pitch activity.
- To minimise tower base loads as far as possible by controlling tower vibration.
- To avoid exacerbating hub and blade root loads.

Especially with individual pitch control (Section 8.3.12), the last of these should be replaced by a much more positive objective:

- To actively reduce the loading on the rotor and the rest of the system.

Clearly some of these objectives may conflict with others, so the control design process will inevitably involve some degree of trade-off or optimisation. To do this, it is necessary to be able to quantify the different objectives. It is usually almost impossible to do this with any precision, because the various loads may affect not only the costs of different components (sometimes in complex ways) but also their reliability. Even the trade-off between energy capture and component cost is not straightforward, as it will depend

on the wind regime, the discount rate, and knowledge of future prices for the sale of electricity. Therefore, some degree of judgement will always be required in arriving at an acceptable controller design.

8.2.7 PI and PID controllers

A brief general description is given here of proportional and integral (PI) and proportional–integral–derivative (PID) controllers, because they will be referred to a number of times in the subsequent sections.

The PI controller is an algorithm that is very widely used for controlling all kinds of equipment and processes. The control action is calculated as the sum of two terms, one proportional to the control error, which is the difference between the desired and actual values of the quantity to be controlled, and one proportional to the integral of the control error. The integral term ensures that in the steady state the control error tends to zero, because if it did not, the control action would continue to increase indefinitely. The proportional term makes the algorithm more responsive to rapid changes in the quantity being controlled.

A differential term is often added, which gives a contribution to the control action proportional to the rate of change of the control error. This is then known as a *PID controller*. In terms of the Laplace operator s , which can usefully be thought of as a differentiation operator, the PID controller from measured signal x to control signal y can be written as follows:

$$y = \left(K_p + \frac{K_i}{s} + \frac{K_d s}{1 + sT_d} \right) x \quad (8.1)$$

where K_p , K_i , and K_d are the proportional, integral, and derivative gains, respectively. The denominator of the differential term is essentially a low-pass filter, and is needed to ensure that the gain of the algorithm does not increase indefinitely with frequency, which would make the algorithm very sensitive to signal noise. Setting $K_d = 0$ results in a PI controller.

It is often the case that the control action is subject to limits. For example, if the control action represents the blade pitch used to control power above rated, then when the power drops below rated the pitch will be limited to the fine pitch setting and will not be allowed to drop further. In this situation the integral term of the PI or PID controller will grow more and more negative as the power remains below rated. Then when the wind speed rises again and the power rises above rated, the integral term will start to grow again towards zero, but until it gets close to zero it can dominate over the proportional and derivative terms. Therefore the pitch may remain ‘stuck’ at fine pitch for a considerable time, depending on how long the power has been below rated, until the integral term has come back close to zero. This is known as *integrator wind-up*, and clearly it must be prevented. This is done in effect by disabling the integrator when the pitch is on the limit. This is known as *integrator desaturation*, which is described more fully in Section 8.6.

The design of PI and PID controllers, including the choice of gains, is described in more detail in Section 8.4.

8.3 Closed-loop control: general techniques

This section outlines the principles behind many of the types of closed-loop controllers to be found in wind turbines. Mathematical methods for designing the closed-loop algorithms are covered in Section 8.4.

8.3.1 Control of fixed-speed, pitch-regulated turbines

A fixed-speed pitch-regulated turbine usually means a turbine that has an induction generator connected directly to the ac network and that therefore rotates at a nearly constant speed. As the wind speed varies, the power produced will vary roughly as the cube of the wind speed. At rated wind speed, the electrical power generated becomes equal to the rating of the turbine, and the blades are then pitched to reduce the aerodynamic efficiency of the rotor and limit the power to the rated value. The usual strategy is to pitch the blades in response to the power error, defined as the difference between the rated power and the actual power being generated, as measured by a power transducer. The primary objective is then to devise a dynamic pitch control algorithm that minimises the power error, although as explained above, this may not be the only objective.

The main elements of the control loop are shown in Figure 8.2. A PI or PID algorithm is often used for the controller.

When the power falls below rated, the pitch demand saturates at the fine pitch limit, maximising the aerodynamic efficiency of the rotor. Because the optimum pitch angle depends on the tip speed ratio, it is possible to increase energy capture below rated by a small percentage if the fine pitch limit is varied in response to the wind speed. The measured power itself is the best available measure of wind speed over the whole turbine (effectively using the whole turbine as an anemometer). However, the fine pitch limit should be varied relatively slowly compared to the control loop dynamics. Good performance can be obtained by changing the fine pitch limit in response to a moving average of the measured power, using the calculated steady-state relationship between power output and optimum pitch angle at each wind speed. The moving average time constant can be quite long because the underlying wind speed (averaged over the rotor swept area) varies relatively slowly. Of course, it should be significantly slower than the blade passing frequency and the lowest structural frequency (generally the first tower mode) to avoid unnecessary pitch activity below rated.

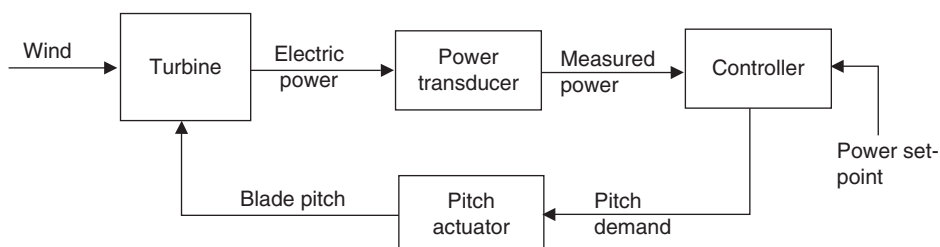


Figure 8.2 Main control loop for a fixed-speed pitch-regulated turbine

8.3.2 Control of variable-speed, pitch-regulated turbines

A variable-speed generator is decoupled from the grid frequency by a power converter, which can control the load torque at the generator directly, so that the speed of the turbine rotor can be allowed to vary between certain limits. An often-quoted advantage of variable-speed operation is that below rated wind speed, the rotor speed can be adjusted in proportion to the wind speed so that the optimum tip speed ratio is maintained. At this tip speed ratio the power coefficient, C_p , is a maximum, which means that the aerodynamic power captured by the rotor is maximised. This is often used to suggest that a variable-speed turbine can capture much more energy than a fixed-speed turbine of the same diameter. In practice it may not be possible to realise all of this gain, partly because of losses in the power converter and partly because it is not possible to track optimum C_p perfectly.

Maximum aerodynamic efficiency is achieved at the optimum tip speed ratio $\lambda = \lambda_{\text{opt}}$, at which the power coefficient C_p has its maximum value $C_{p(\max)}$. Because the rotor speed Ω is then proportional to wind speed U , the power increases with U^3 and Ω^3 , and the torque with U^2 and Ω^2 . The aerodynamic torque is given by

$$Q_a = \frac{1}{2} \rho A C_q U^2 R = \frac{1}{2} \rho \pi R^3 \frac{C_p}{\lambda} U^2 \quad (8.2)$$

Since $U = \Omega R / \lambda$ we have

$$Q_a = \frac{1}{2} \rho \pi R^5 \frac{C_p}{\lambda^3} \Omega^2 \quad (8.3)$$

In the steady state therefore, the optimum tip speed ratio can be maintained by setting the load torque at the generator, Q_g , to balance the aerodynamic torque, that is,

$$Q_g = \frac{1}{2} \frac{\pi \rho R^5 C_p}{\lambda^3 G^3} \omega_g^2 - Q_L \quad (8.4)$$

Here Q_L represents the mechanical torque loss in the drive train (which may itself be a function of rotational speed and torque), referred to the high-speed shaft. The generator speed is $\omega_g = G\Omega$, where G is the gearbox ratio.

This torque-speed relationship is shown schematically in Figure 8.3 as the curve B1–C1. Although it represents the steady-state solution for optimum C_p , it can also be used dynamically to control generator torque demand as a function of measured generator speed. In many cases, this is a very benign and satisfactory way of controlling generator torque below rated wind speed.

For tracking peak C_p below rated in a variable-speed turbine, the quadratic algorithm of Eq. (8.4) works well and gives smooth, stable control. However, in turbulent winds, the large rotor inertia prevents it from changing speed fast enough to follow the wind, so rather than staying on the peak of the C_p curve it will constantly fall off either side, resulting in a lower mean C_p . This problem is clearly worse for heavy rotors, and also if the $C_p - \lambda$ curve has a sharp peak. Thus, in optimising a blade design for variable-speed operation, it is not only important to try to maximise the peak C_p , but also to ensure that the $C_p - \lambda$ curve is reasonably flat-topped.

It is possible to manipulate the generator torque to cause the rotor speed to change faster when required, so staying closer to the peak of the C_p curve. One way to do this

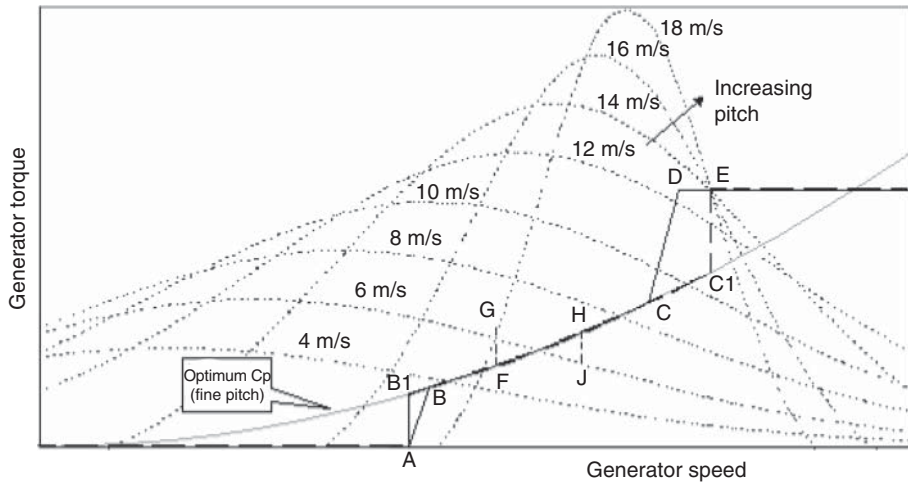


Figure 8.3 Schematic torque-speed curve for a variable-speed pitch-regulated turbine

is to modify the torque demand by a term proportional to rotor acceleration (Bossanyi 1994):

$$Q_g = \frac{1}{2} \frac{\pi \rho R^5 C_p}{\lambda^3 G^3} \omega_g^2 - Q_L - B \dot{\omega}_g \quad (8.5)$$

where B is a gain that determines the amount of inertia compensation. For a stiff drive train, and ignoring frequency converter dynamics, the torque balance gives

$$I \dot{\Omega} = Q_a - G Q_g \quad (8.6)$$

where I is the total inertia (of rotor, drive train and generator, referred to the low-speed shaft) and Ω is the rotational speed of the rotor. Hence

$$(I - G^2 B) \dot{\Omega} = Q_a - \frac{1}{2} \frac{\pi \rho R^5 C_p}{\lambda^3 G^2} \omega_g^2 + G Q_L \quad (8.7)$$

Thus, the effective inertia is reduced from I to $I - G^2 B$, allowing the rotor speed to respond more rapidly to changes in wind speed. The gain B should remain significantly smaller than I/G^2 otherwise the effective inertia will approach zero, requiring huge power swings to force the rotor speed to track closely the changes in wind speed.

Another possible method is to use available measurements to make an estimate of the wind speed, calculate the rotor speed required for optimum C_p , and then use the generator torque to achieve that speed as rapidly as possible. The aerodynamic torque can be expressed as

$$Q_a = \frac{1}{2} \rho A C_q R U^2 = \frac{1}{2} \rho \pi R^5 \Omega^2 C_q / \lambda^2 \quad (8.8)$$

where R is the turbine radius, Ω the rotational speed, and C_q the torque coefficient. If drive train torsional flexibility is ignored, a simple estimator for the aerodynamic torque is

$$Q_a^* = G Q_g + I \dot{\Omega} = G Q_g + I \dot{\omega}_g / G \quad (8.9)$$

where I is the total inertia. A more sophisticated estimator could take into account drive train torsion, etc. From this it is possible to estimate the value of the function $F(\lambda) = C_q(\lambda)/\lambda^2$ as

$$F^*(\lambda) = \frac{Q_a^*}{\frac{1}{2}\rho\pi R^5(\omega_g/G)^2} \quad (8.10)$$

Knowing the function $F(\lambda)$ from steady state aerodynamic analysis, one can then deduce the current estimated tip speed ratio λ^* (see also Section 8.3.16 for a better estimation method). The desired generator speed for optimum tip speed ratio can then be calculated as

$$\omega_d = \omega_g \hat{\lambda}/\lambda^* \quad (8.11)$$

where $\hat{\lambda}$ is the optimum tip speed ratio to be tracked. A simple PI controller can then be used, acting on the speed error $\omega_g - \omega_d$, to calculate a generator torque demand that will track ω_d . The higher the gain of PI controller, the better will be the C_p tracking, but at the expense of larger power variations. Simulations for a particular turbine showed that a below rated energy gain of almost 1% could be achieved, with large but not unacceptable power variations.

Holley et al. (1999) demonstrated similar results with a more sophisticated scheme, and also showed that a perfect C_p tracker could capture 3% more energy below rated, but only by demanding huge power swings of plus and minus three to four times rated power, which is totally unacceptable.

Because such large torque variations are required to achieve only a modest increase in power output, it is usual to use the simple quadratic law, possibly augmented by some inertia compensation as in Eq. (8.5) if the rotor inertia is large enough to justify it.

As turbine diameters increase in relation to the lateral and vertical length scales of turbulence, it becomes more difficult to achieve peak C_p anyway because of the non-uniformity of the wind speed over the rotor swept area. Thus if one part of a blade is at its optimum angle of attack at some instant, other parts will not be.

In most cases, it is actually not practical to maintain peak C_p from cut-in all of the way to rated wind speed. Although some variable-speed systems can operate all of the way down to zero rotational speed, this is not the case with limited range variable-speed systems based on the widely used doubly fed induction generators. These systems only need a power converter rated to handle a fraction of the turbine power, which is a major cost saving. This means that in low wind speeds, just above cut-in, it may be necessary to operate at an essentially constant rotational speed, with the tip speed ratio above the optimum value.

At the other end of the range, it is usual to limit the rotational speed to some level, usually determined by aerodynamic noise constraints or blade leading-edge erosion, which is reached at a wind speed that is still some way below rated. It is then cost-effective to increase to torque demand further, at essentially constant rotational speed, until rated power is reached. Figure 8.3 illustrates some typical torque-speed trajectories, which are explained in more detail below. Turbines designed for noise-insensitive sites may be designed to operate along the optimum C_p trajectory all of the way until rated power is reached. The higher rotational speed implies lower torque and in-plane loads, but higher out-of-plane loads, for the same rated power. This strategy might be of interest for offshore wind turbines.

8.3.3 Pitch control for variable-speed turbines

Once the rated torque has been reached, no further increase in load torque can occur, so the turbine will start to speed up. Pitch control is then used to regulate the rotor speed, with the load torque held constant. A PI or PID controller is often satisfactory for this application. In some situations, it may be useful to include notch filters on the speed error to prevent excessive pitch action at, for example, the blade passing frequency or significant structural resonant frequencies, such as the drive train torsional frequency.

Rather than maintain a constant torque demand while the pitch control is regulating the rotational speed, it is possible to vary the torque demand in inverse proportion to the measured speed to keep the power output, rather than the torque, at a constant level. Provided the pitch controller is able to maintain the speed close to the set-point, there will be little difference between these two approaches. The reduction of load torque with increasing speed has a slight destabilising effect on the pitch controller, but this is often not serious, and provided the gearbox torque and rotor speed variations are not greatly affected, the constant power approach is attractive from the perspective of power quality.

8.3.4 Switching between torque and pitch control

In practice, acoustic noise, loads or other design constraints usually mean that the maximum allowable rotor speed is reached at a relatively low wind speed. As the wind speed increases further, it is desirable to increase the torque and power without any further speed increase, to capture more energy from the wind. The simplest strategy is to implement a torque-speed ramp: line CD in Figure 8.3. Once rated power or torque is reached, pitch control is used to maintain the rotor speed at its rated value. To prevent the torque and pitch controllers from interfering with one another, the speed set-point for the pitch controller is set a little higher, at point E in Figure 8.3. If the speed set-point were at D then there would constantly be power dips in above rated winds, whenever the speed fell transiently below D. Furthermore the pitch controller would act below rated, as the pitch and torque controllers would both be trying to control the speed.

It would be an improvement if the torque-speed trajectory A-B-C-D-E in Figure 8.3 could be changed to A-B1-C1-E. The turbine would then stay close to optimum C_p over a wider range of wind speeds, giving slightly higher energy capture for the same maximum operating speed (Bossanyi 1994). The vertical sections A-B1 and C1-E can be achieved by using a PI controller for the torque demand, in response to the generator speed error with the set-point at A or C1. Transitions between constant speed and optimum C_p operation are conveniently handled by using the optimum C_p curve as the upper torque limit of the PI controller when operating at A, or the lower limit when at C1. The set-point flips between A and C1 when the measured speed crosses the mid-point between A and C1. Despite this step change in set-point the transition is completely smooth because the controller will be saturated on the optimum C_p limit curve both before and after the transition.

This logic can easily be extended to implement ‘speed exclusion zones’ to avoid speeds at which blade passing frequency would excite, for example, the tower resonance, by introducing additional speed set-points and some logic for switching between them – see lines FG, HJ in Figure 8.3. When the torque demand exceeds G for a certain time, the set-point ramps smoothly from F to H. Then if it falls below J, the set-point ramps back again.

Another advantage of PI control of the torque is that the ‘compliance’ of the system can be controlled. Controlling to a steep ramp (CD in Figure 8.3) can be quite harsh in that the torque demand will be varying rapidly up and down the slope. A PI controller, however, can be tuned to achieve a desired level of ‘softness’. With high gain, the speed will be tightly controlled to the set-point, requiring large torque variations. Lower gains will result in more benign torque variations, while the speed is allowed to vary more around the set-point.

To use point C1 as the speed set-point for both the torque and the pitch controllers, it is necessary to decouple the two. One technique is to arrange some switching logic that ensures that only one of the control loops is active at any one time. Thus below rated the torque controller is active and the pitch demand is fixed at fine pitch, while above rated the pitch controller is active and the torque demand is fixed at the rated value. This can be done with fairly simple logic, although there will always be occasions when the controller is caught briefly in the ‘wrong’ mode. For example, if the wind is just below rated but rising rapidly, it might be useful to start pitching the blades a little before the torque demand reaches rated. If the pitch does not start moving until the torque reaches rated, it then has to move some way before it starts to control the acceleration, and a small overspeed may result.

A more satisfactory approach is to run both control loops together but to couple them together with terms that drive one or the other loop into saturation when far above or below the rated wind speed. Thus most of the time only one of the controllers is active, but they can be made to interact constructively when close to the rated point.

A useful method is to include a torque error term in the pitch PID in addition to the speed error. Above rated, because the torque demand saturates at rated, the torque error will be zero, but below rated it will be negative. An integral term will bias the pitch demand towards fine pitch, preventing the pitch controller from acting in low winds, while a proportional term may help to start the pitch moving a little before the torque reaches rated if the wind speed is rising rapidly.

It is also necessary to prevent the torque demand from dropping when operating well above rated wind speed. Here a useful strategy is a ‘ratchet’ which prevents the torque demand from falling while the pitch is not at fine. This can also smooth over brief lulls in the wind around rated, using the rotor kinetic energy to avoid transient power drops.

An alternative approach is to introduce separate bias terms to the speed errors for the two control loops, effectively modifying the set-points of both loops, which remain active throughout. When the torque is below rated, the pitch controller sees a higher speed set-point, forcing the pitch towards fine. As the torque approaches rated, the set-point is reduced to the nominal value so that the pitch control gradually takes over. As the pitch rises above fine, the torque controller set-point is pushed down, forcing the torque up to the rated power limit. As the pitch comes down again the torque controller set-point rises back to the nominal value, allowing the torque controller to resume its duties by the time fine pitch is reached, and as the torque falls further the pitch controller set-point rises again to keep the pitch at the fine limit. The movement of the set-points is decoupled from the control loop dynamics by introducing first order lags with appropriate time constants. Shorter time constants are appropriate for rising set-points than for falling

set-points. This helps prevent overspeeds and also prevents the pitch angle from falling too sharply during a temporary wind lull that could cause unnecessary tower vibration.

A further development of this approach is to use a wind speed estimator, as in Section 8.3.16. A transition zone is defined around the rated wind speed, and the estimated wind speed then defines the fractional position through this transition zone. The torque bias is ramped from zero at the lower end of the transition zone to maximum at the upper end, and vice-versa for the pitch bias. This is likely to give a cleaner response, and there are no time constants to tune.

8.3.5 Control of tower vibration

For both fixed and variable-speed machines the influence of the pitch controller on tower vibration and loading, described in Section 8.2.1, is one of the major constraints on the design of the control algorithm. The first tower fore-aft vibrational mode is essentially very lightly damped, exhibiting a strong resonant response that can be maintained at quite a high level even by a small amount of excitation, which is naturally present in the wind. The strength of the response depends critically on the small amount of damping that is present, mostly aerodynamic damping from the rotor. The pitch control action modifies the effective damping of that mode. In designing the pitch controller, it is therefore important to avoid further reducing the already small level of damping, and if possible to increase it.

The design of control algorithms is covered in Section 8.4. This includes the choice of PID gains, as well as the addition of further terms to the controller that modify the overall dynamics in such a way as to help increase the tower damping. The use of modern control methods such as optimal state feedback is also discussed. This technique can help to achieve a suitable compromise between the competing objectives of speed or power control (achieved by regulating the in-plane loading) and tower vibration control (which depends on modifying the out-of-plane loading).

There is, however, only a certain amount of information in the measured speed or power signal. State estimators such as Kalman filters (Section 8.4.5) can be used to try to distinguish between the effects of wind speed changes and tower motion on the measured signal. However, it is also possible to enhance the information available to the controller by using an accelerometer mounted in the nacelle, which provides a very direct measure of tower fore-aft motion. By using this extra signal, it is in fact possible to reduce tower loads significantly without adversely affecting the quality of speed or power regulation.

The tower dynamics can be modelled approximately as a second order system exhibiting damped simple harmonic motion, that is,

$$M\ddot{x} + D\dot{x} + Kx = F + \Delta F \quad (8.12)$$

where x is tower displacement and F is the applied force, which in this case is predominantly the rotor thrust. ΔF is the additional thrust caused by pitch action. We can equate M with the tower modal mass and K with the modal stiffness, such that the tower frequency is $\sqrt{K/M}$ rad/s. The damping term D is small. The effective damping can clearly be increased if ΔF is proportional to $-\dot{x}$. Clearly it is easier to measure acceleration than

velocity, so the tower acceleration would have to be integrated to provide a measure of \dot{x} . A suitable gain for ΔF can be estimated from the partial derivative from pitch to thrust, $\partial F/\partial\beta$ where β is the pitch angle, to achieve any particular additional damping D_p :

$$\delta F = \frac{\partial F}{\partial \beta} \delta \beta = -D_p \dot{x}$$

$$\delta \beta = \frac{-D_p}{\partial F / \partial \beta} \dot{x} \quad (8.13)$$

It may sometimes be necessary to place a notch filter in series with this feedback term to prevent unwanted feedback from other components of tower acceleration, for example, at blade passing frequency. Lead-lag or other loop-shaping filters may also help to adjust the phase of the feedback to ensure maximum damping, taking into account the full dynamics of the system that are actually more complex than Eq. (8.13). For example, the dynamic response of the pitch actuator should be taken into account, as well as other modes of vibration that couple to the tower dynamics. Figure 8.4 shows the results of a simulation with and without such an acceleration feedback term, in combination with a PID controller to control rotational speed. The simulations were driven with a realistic three-dimensional turbulent wind input. The speed control was hardly affected, and although there is a significant increase in pitch actuator activity, the additional pitch rates required are modest. Clearly this technique is capable of increasing the tower damping substantially, almost eliminating the resonant response and significantly reducing tower

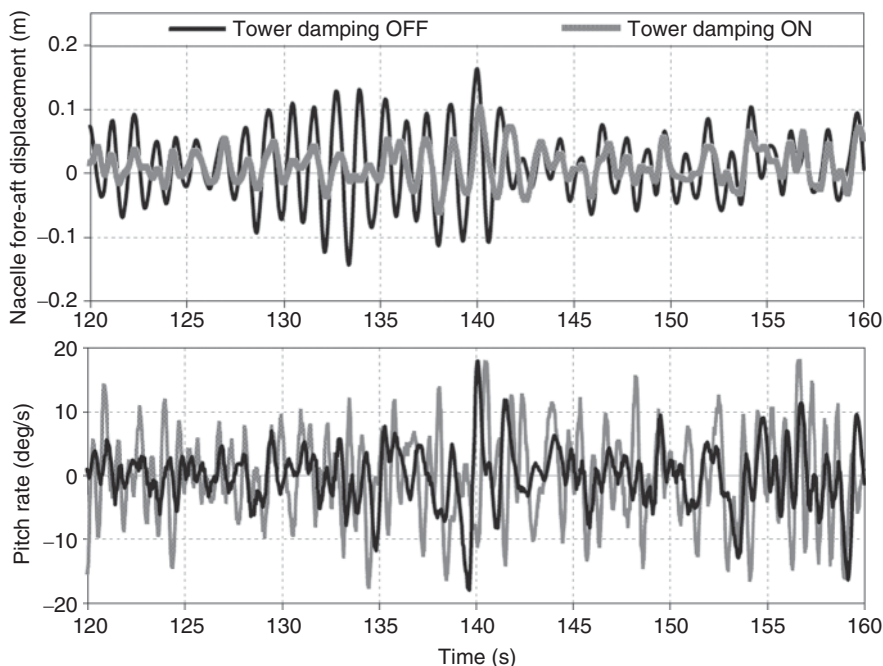


Figure 8.4 Use of a tower accelerometer to help control tower vibration

base loads. Although it requires an accelerometer, this is usually present anyway to trigger a shut-down in the event of excessive vibration. Accelerometers are also relatively cheap, robust, and reliable devices.

Field test results demonstrating the effectiveness of this tower damping action have been published by Rossetti and Bossanyi (2004) and Bossanyi et al. (2010).

Because rotor thrust varies rapidly with pitch angle close to fine pitch, a common cause of fore-aft tower excitation is the case of a short-lived lull in wind speed starting a little above rated wind speed. The pitch responds by falling rapidly towards fine pitch, causing a rapid thrust reduction and large consequent tower vibration. This can be avoided by preventing the rapid decrease in pitch: if the wind picks up again quickly, as is often the case, little energy is lost. Various algorithms can be used for this. Simply limiting the negative pitch rate when close to fine pitch is a possibility, although this will generally reduce the effectiveness of speed regulation in this region, and the asymmetrical rate limits will result in loss of energy (restoring symmetry by similarly decreasing the positive rate limit is not advisable, as transient overspeeds will result). These disadvantages can be mitigated to some extent by limiting the downward pitch rate only after a large negative rate has already been sustained for a short time. However, a particularly effective technique is to use a dynamically varying fine pitch angle: whenever the pitch angle is above fine pitch, the fine pitch limit is increased, but always staying below the actual pitch by at least a certain margin, so that it is always well below the actual pitch in high winds. The dynamic fine pitch is allowed to decrease only slowly, so during a wind lull the pitch may decrease to the level of the dynamic fine pitch, which then continues to fall slowly to ensure that the true fine pitch is reached if the lull is prolonged. The generator torque control can act while the pitch is on the dynamic fine pitch limit, preventing any significant reduction in rotor speed during a short wind lull.

Tower loading is generally dominated by the fore-aft vibration, but side-side vibration can be significant in some situations – for example, in offshore turbines operating during periods of wind-wave misalignment. The side-side vibration is even more lightly damped than fore-aft, because there is even less aerodynamic damping from the rotor in this direction. When the principal wave direction is coming from the side therefore, the excitation of the side-side vibrations can be considerable, and may even become more significant than the fore-aft vibration at such times. In principle, the damping of the side-side vibration can be increased by appropriate control of the generator torque, adding a component of torque demand derived from the measured side-side acceleration, in addition to the torsional damping described in the next section (Markou and Larsen 2009; Fischer et al. 2010).

In the special case of floating wind turbines, particular attention must be paid to the interaction of pitch control and tower motion. Depending somewhat on the type of moorings, there is likely to be a very low-frequency rigid-body oscillatory mode where the entire structure rocks backwards and forwards with a period that can be tens of seconds or even more, and can be significantly excited by wave frequencies. More seriously however, an instability can arise: as the nacelle moves forward, the relative wind speed increases, causing the rotor speed to increase. The pitch increase needed to counteract this results in significantly reduced rotor thrust, which can allow the motion to accelerate, resulting in an increasing amplitude of oscillation that could ultimately be catastrophic. Fortunately, the motion can be stabilised by suitable design of the controller. This can be addressed by multivariable controller design, but Vanni et al. (2015) compare two

different stabilisation methods that use an additional single input, single output feedback loop based on measured nacelle acceleration, generating a modification either to the pitch demand or to the generator torque demand. The former results in somewhat higher rotor speed deviations, while the latter increases electrical power variations. A compromise might be found by tuning both loops to run in parallel.

8.3.6 Control of drive train torsional vibration

A typical drive train can be considered to consist of a large rotor inertia and a (smaller) high-speed shaft inertia (mainly the generator and brake disc), separated by a torsional spring that represents twisting of shafts and couplings, bending of gear teeth and deflection of any soft mountings. It is important to consider also the coupling of the torsional mode of vibration with the first rotor in-plane collective mode, in which case the drive train can be approximated by three inertias and two torsional springs (Ramtharan et al. 2007). In some cases the coupling to the second tower side-to-side mode, which has a lot of rotation at the tower top, is also important.

In a fixed-speed turbine, the induction generator slip curve (Section 7.5) essentially acts like a strong damper, with the torque increasing rapidly with speed – see Figure 7.53. Therefore, the torsional mode of the drive train is well damped and generally does not cause a problem. In a variable-speed turbine operating at constant generator torque however, there is very little damping for this mode, because the torque no longer varies with generator speed. The aerodynamic damping due to the rotor is small because the blades are vibrating in the in-plane direction. There is a small amount of structural damping in shafts and couplings, and some damping from the gearbox, but these effects contribute typically only a small fraction of 1% of critical damping. The very low damping can lead to large torque oscillations at the gearbox, effectively negating one of the principal advantages of variable-speed operation, the ability to control the torque.

Although it may be possible to provide some further damping mechanically – for example, by means of appropriately designed rubber mounts or couplings – it is difficult to provide enough damping and there is a cost associated with this. A widely used solution, which has been successfully adopted on many variable-speed turbines, is to modify the generator torque control to provide some damping. Instead of demanding a constant generator torque above rated (or a torque varying slightly in inverse proportion to speed in the case of the constant power algorithm described in Section 8.3.3), a small ripple at the drive train frequency is added on to this basic torque demand, with the phase adjusted to counteract the effect of the resonance and effectively increase the damping. A band-pass filter of the form

$$G \frac{2\zeta\omega s(1+s\tau)}{s^2 + 2\zeta\omega s + \omega^2} \quad (8.14)$$

(where G is a gain) acting on the measured generator speed can be used to generate this additional ripple. The frequency ω must be close to the resonant frequency that is to be damped. The time constant τ modifies the phase and contributes more of a high-pass filter characteristic, and can sometimes be used to compensate for time lags or other dynamics in the system. A root locus plot (Section 8.4) is very useful for tuning the filter parameters.

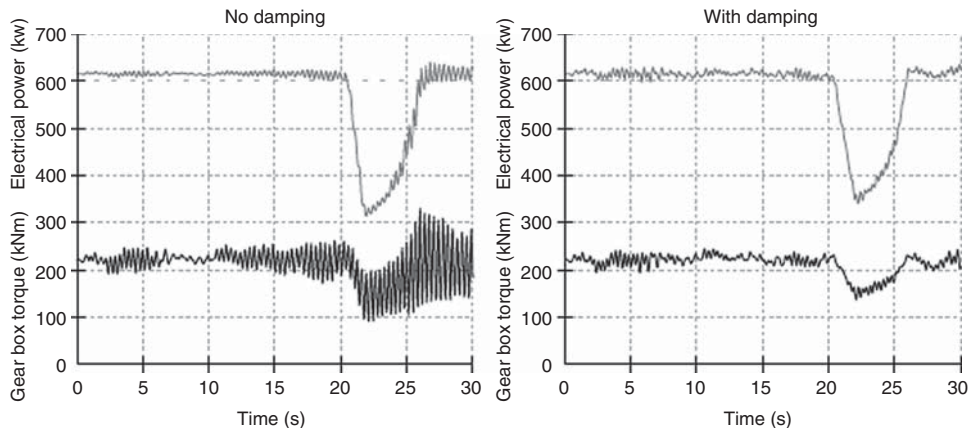


Figure 8.5 Effect of a drive train damping filter

Although a very effective filter can be made by tuning it to give a frequency response with a very broad peak (large ζ), this may be detrimental to the overall performance in that more low frequency variations in torque and power are then introduced. Even with a narrow peak, there can be sufficient response at multiples of blade passing frequency such as 3P or 6P to disturb the system, in which case a notch filter (Section 8.4) can be cascaded with the filter of Eq. (8.14). Of course if the resonant frequency nearly coincides with an excitation frequency such as 6P then the resonance will be very difficult to control because it will be strongly excited.

Figure 8.5 shows some simulation results for a variable-speed turbine operating in simulated three-dimensional turbulence. A large drive train resonance can be seen to be building up. Although the power and generator torque are smooth, the gearbox would be very badly affected. The effect of introducing a damping filter as described above is also shown. It almost completely damps out the resonance without increasing the electrical power variations. This is because the torque ripple needed to damp the resonance is actually very small, because the amount of excitation is small.

In many cases the drive train damping can be further improved by using an input signal representative of the ‘twisting speed’ rather than just the generator speed: the twisting speed is just the difference between the generator speed and the rotor speed (scaled by gearbox ratio). However, this requires two speed measurements, and the low-speed shaft sensor in particular sometimes has insufficient resolution and may need to be upgraded. Care is needed to ensure that the required difference between the two signals is not too susceptible to noise on the signals.

These torsional vibrations are typically much less of a problem on direct drive systems, where in some cases a damping filter of this sort may not even be required at all.

8.3.7 Variable-speed stall regulation

Figure 8.6 shows two power curves for the same rotor, one running as a 600 kW fixed-speed pitch-regulated turbine and one adjusted to run as a fixed-speed stall-regulated turbine with the same rating. The rotational speed of the stall-regulated turbine has been

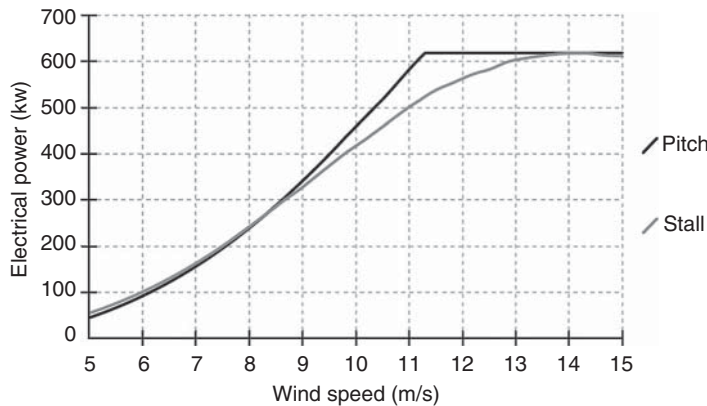


Figure 8.6 Comparison of pitch and stall control

reduced to limit the power to the same rated level. Therefore, although the stall-regulated turbine generates slightly more energy at very low wind speeds, as the blades approach stall above 8 m/s there is a large loss of output compared to the pitch-regulated machine. (In practice of course, if the turbine was designed to operate in stall, the blade design, solidity, and rotor speed could be re-optimised, reducing this difference.)

By making use of variable speed, it is quite possible to correct this loss of energy by operating either turbine at the optimum tip speed ratio up to rated, or until the maximum rpm is reached. At rated power, it is then possible to reduce the speed of the rotor to bring it into stall, although this has rarely been done to date on commercial machines. This can be done by closed-loop control of the generator torque in response to power error, allowing the turbine to follow exactly the same power curve as the pitch-regulated turbine. Thus, the variable-speed stall-regulated turbine can achieve the same energy output as the variable-speed pitch-regulated turbine, but without the need for an active pitch mechanism. As explained in Section 8.2.2 however, significant torque and power transients will result from this strategy. The smooth torque and power, which are one of the main advantages of variable-speed systems, will therefore not be realised.

One simple and effective control algorithm for this case is illustrated in Figure 8.7. It consists of two nested loops, an outer power loop that demands a generator speed and an inner speed loop that demands a generator torque. As in Section 8.3.4, a PI controller can

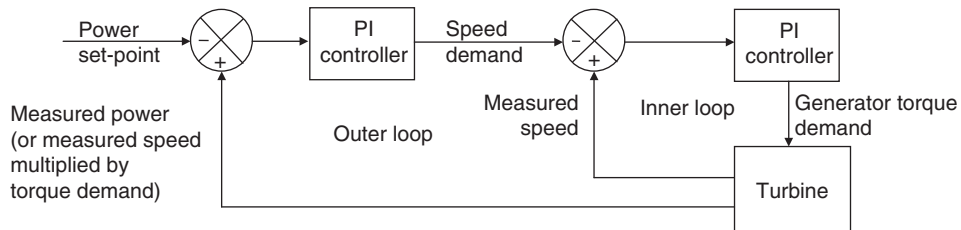


Figure 8.7 A simple control algorithm for variable-speed stall regulation

be used for the inner loop. This is the same controller as for sections A-B1 and C1-E of Figure 8.3, making it particularly easy to arrange the transition between control modes at the rated point because the inner loop is always active.

8.3.8 Control of variable-slip turbines

The operating envelope for a variable-slip generator is shown in Figure 8.8. Note that the slip speed represents the increase in speed above synchronous (conventionally for motors this would be a negative slip). Below rated, the generator acts just like a conventional induction machine, with the torque related to the slip speed according to the slip curve AB. Once point B is reached, a resistor in series with the rotor circuit, previously short-circuited by a semiconductor switch, is progressively brought into play by switching the semiconductor switch on and off at several kilohertz, and varying the mark-space ratio to change the average resistance. As the average resistance increases, the generator slip curve changes so that its slope varies inversely with the total resistance of the rotor circuit. Figure 8.8 shows a typical example in which the rotor resistance can increase by a factor 10, changing the slip curve from AB to AD. By controlling the resistance therefore, the generator can operate anywhere within the shaded region. The resistance is usually varied by a closed-loop algorithm that seeks to regulate the torque to any desired value. For example, this might be PI algorithm with torque error input and the mark-space ratio of the switch as output.

In practice, it is usual to keep the torque demand at the rated value. Then the generator will simply act as a conventional induction generator following the slip curve AB until rated torque is reached, at which point it will accelerate along the constant torque line BCD just like a variable-speed system. If the speed increases beyond D the torque is forced to increase again. Pitch control is used to regulate the speed to a chosen set-point such as point C. The higher the speed C, the higher the mechanical power input for the same output power. Thus, the power dissipated in the rotor circuit corresponds exactly to the slip. Therefore, C should be chosen as low as possible to minimise the cooling requirements (as well as turbine loads that increase with speed). However, if C is too close to B then the torque will occasionally dip down the slope AB as the speed varies around the set-point, causing power dips even when operating well above rated wind

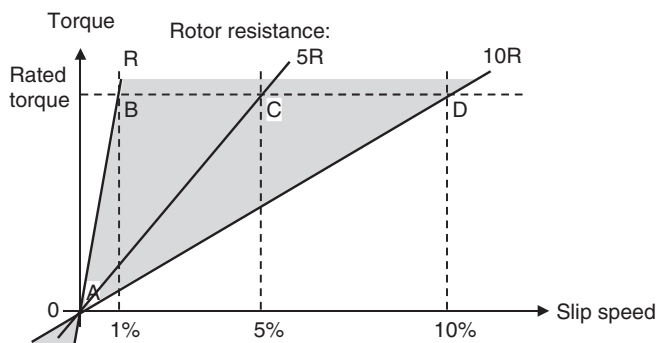


Figure 8.8 Operating envelope for a variable-slip generator

speed. How small the interval between B and C can be made depends on the rotor inertia and the responsiveness of the pitch control algorithm. As for a variable-speed system, the latter can be a PI or PID algorithm. It is possible to change the rate limits of the PID to force the pitch towards fine at maximum rate if the speed gets too close to B, or to feather at maximum rate if it gets too close to D.

As with a variable-speed system, it may be desirable to modify the torque demand as in Section 8.3.6 to control drive train torsional vibrations. However, to do this, it is necessary to be able to update the torque demand at relatively high frequency, at least five and preferably 10 times the drive train frequency, which is typically of the order of 3–5 Hz.

8.3.9 Individual pitch control

Large pitch-regulated turbines invariably have a separate pitch actuator for each blade, because these can be used to provide effectively independent aerodynamic braking systems on the rotor. This means that no shaft brake is required, other than a small parking brake, because if one pitch actuator fails, the remaining actuator(s) should still be capable of stopping the rotor. Given that each blade has its own independent actuator, it is possible to send different pitch demands to each blade, and this can be used to reduce the asymmetrical aerodynamic loadings across the rotor, which are responsible for a significant contribution to fatigue loads (Donham and Heimbold 1979; Caselitz et al. 1997; Bossanyi 2004).

The simplest concept is cyclic pitch control based on the rotor azimuth. There are a number of effects that cause a systematic azimuthal variation of loading on each blade, in particular the wind speed variations caused by wind shear and tower shadow, and changes in angle of attack due to yaw misalignment, shaft tilt, and upflow. In principle it should be possible to impose an azimuth-dependent change to the demanded pitch for each blade to compensate for these effects.

The tower shadow is very systematic and predictable, but to have any effect would require a very rapid and short-lived ‘blip’ in pitch demand as each blade passed the tower, which could have other adverse consequences. The effect of shaft tilt is also very predictable, and possibly upflow too in some situations, but these will affect only the angle of attack and not the local wind speed. Yaw misalignment also affects just the angle of attack, and to compensate for it would require an additional sensor to measure it, because the magnitude and direction of the misalignment will vary continuously. Wind shear does cause a significant difference in wind speed across the rotor, and therefore causes large blade load variations at the rotational frequency (1P), but again it is not a constant effect and would require one or more additional sensors to detect it. Furthermore, the wind shear can only be regarded as a mean effect, and because of turbulence the instantaneous variation in wind speed across the rotor may be very different: in fact the highest wind speed could occur instantaneously anywhere on the rotor disc, not always at the top.

Indeed, it is the turbulent variations in wind speed across a large wind turbine rotor that usually dominate the asymmetrical loading, because the size of a large rotor is comparable to the scale of turbulent eddies. Therefore azimuth-dependent cyclic pitch control tends not to be very successful: while on average some reduction in loading ought to be achievable by compensating for the mean wind shear, this is insignificant compared to the

stochastic effects of turbulence. An exception might be for a turbine operating in highly stratified flow with low turbulence.

Normally though, to achieve any significant reduction in these asymmetrical loads requires some additional measurement of the instantaneous turbulence, so that the individual pitch angles can be adjusted to compensate for these effects.

One possibility is actually to measure the incident wind flow just in front of each blade – for example, using a set of pitot tubes along the blades – or to use pressure taps at appropriate locations, and then to adjust the pitch of each blade in response to the measurements on that blade. Such sensors have also been proposed to control ‘smart’ blades, which have actuators distributed along the span of the blade to alter its aerodynamic properties locally, such as flaps or ailerons, deformable trailing edges, or possibly air jets to modify the boundary layer flow. Such ideas are the subject of ongoing research and are currently a long way from any commercial deployment.

A more realistic possibility is to use load sensors to measure the blade bending moments at the root, or possibly at various points along the blade. It makes some sense to measure the very loads that we wish to reduce. With full-span pitch control, it would seem to make sense to measure the blade root loads on each blade and use the measurements to adjust the pitch of each blade in a feedback loop. Such a scheme could be called *independent pitch control*, although there is no definite consensus on nomenclature.

The possibility then arises to use the load measurement on each blade root as a predictor of the load that will be seen by the next blade when it sweeps past that position. This provides a degree of anticipation that should allow a further improvement in the control of each blade, and it works because turbulent eddies tend to be large enough so that as they pass through the rotor, each blade will slice through the same turbulence structure, perhaps even several times, before it has passed. Because the pitch of each blade is now calculated from the load measurements on all of the blades, this can no longer be called ‘independent’ pitch control, and the term *individual pitch control* may be more appropriate.

Individual pitch control is described in more detail in Section 8.3.11.

8.3.10 Multivariable control – decoupling the wind turbine control loops

The wind turbine controller is now a multivariable controller, with a number of inputs and outputs:

Inputs (measured signals):

- Generator speed (for speed regulation and drive train damping).
- Two tower accelerations (for tower damping).
- Three blade root loads (for a three bladed turbine).

Outputs (demanded signals):

- Generator torque.
- Three pitch angles or rates (for a three bladed turbine).

There are modern control methods that are appropriate to the design of controllers for such MIMO (multiple input, multiple output) systems – see Section 8.4.5. However, a MIMO system can sometimes be ‘diagonalised’ or transformed into a set of independent SISO (single input, single output) systems, in which case the controller for each SISO system can be optimised in isolation from the others. In fact, this is possible to some extent for a wind turbine controller, and so all of the control loops previously mentioned can be designed using classical SISO design methods (Section 8.4.1). Actually the SISO loops are not quite independent, but the dynamic coupling between them can be small enough to make this a very successful approach in many cases.

It is relatively straightforward to decouple the pitch control from the torque control, as implied in the discussions above. In fact it is also possible to decouple the individual pitch control from the collective pitch control – the latter provides a collective pitch demand for speed regulation and tower damping, while the individual pitch control generates a separate pitch demand increment for each blade for minimising asymmetrical rotor loads. The pitch demand increments are all zero-mean, in such a way that the collective pitch control is not affected.

The main independent turbine control loops can now be summarised as follows:

1. Speed regulation loop using torque (using generator speed error to calculate the torque demand).
2. Drive train damping loop (using generator speed to calculate a modification to the torque demand).
3. Side–side tower damping loop (using side–side nacelle acceleration to calculate a further modification to the torque demand).
4. Speed regulation loop (using generator speed error to calculate the collective pitch demand).
5. Fore–aft tower damping loop (using fore–aft nacelle acceleration to calculate a modification to the collective pitch demand).
6. Individual pitch loop (using blade root loads to calculate individual pitch demand increments).

Loop 3 is not generally used but may become more interesting for offshore turbines that can be excited by wave action when this is misaligned with the wind direction.

There is actually some interaction between some of these loops; for example, loops 1 and 4 sometimes require notch filters tuned to the drive train resonant frequency to suppress coupling that would otherwise arise through the control action itself. Also loops 4 and 5 must be coupled in principle, because any change in pitch angle affects both the torque and the thrust; but because loop 5 acts only in a restricted frequency range close to the first tower frequency, it is usually possible to tune the loops independently. However, a better result can be obtained with one or two iterations: one of the loops is tuned first using the open-loop plant model, then the plant is redefined by closing this loop while the other loop is tuned, and so on.

Loop 6 is still a MIMO loop, with as many inputs and outputs as there are blades. However, this can also be decoupled as explained in the next section, by exploiting the symmetry that exists between the blades.

8.3.11 Two axis decoupling for individual pitch control

To first order, the asymmetrical wind field across the rotor swept area can be linearised and described by two orthogonal components, for example, as wind speed shear gradients in the horizontal vertical directions. Blade loading is closely related to wind speed, so this representation can also be used for a ‘blade load field’ (the ‘blade load field’ can be considered to include the effects of all three components of the local wind speed on the blade load). This description is independent of the number of blades or their speed of rotation, and the actual load seen by a blade at any instant can be thought of as the value of that field as sampled by the blade at its instantaneous position.

Furthermore, the pitch action needed to compensate for this variation in loading can also be described by a ‘field’ covering the swept area, and at any instant the pitch required by each blade is obtained by sampling that field at the instantaneous position of the blade.

Because each field is described by just two orthogonal components, a two-input, two-output controller is required to generate the pitch action ‘field’ from the load ‘field’. Again this is independent of the number of blades.

Thus for a three bladed rotor, the three measured blade root loads can be used to calculate the two components of the ‘load field’ at that instant. These are used to calculate the two components of the ‘pitch field’, from which the three individual pitch increments are calculated. The transformation between the three rotating blades and the two (non-rotating) field components is identical to Park’s transformation for three-phase electrical machines (Park 1929), which relates the currents or voltages in each phase winding to two notional orthogonal currents or voltages in the ‘direct’ and ‘quadrature’ axes. For this reason it is known as the *d-q axis transformation*. The same concept has also been used for helicopter rotors, where it is known as the *Coleman transformation* (Coleman and Feingold 1957). The transformation from three rotating blade root loads L_1 , L_2 , L_3 to the non-rotating d and q axes can be written as follows:

$$\begin{bmatrix} L_d \\ L_q \end{bmatrix} = \frac{2}{3} \begin{bmatrix} \cos(\varphi) & \cos(\varphi + 2\pi/3) & \cos(\varphi + 4\pi/3) \\ \sin(\varphi) & \sin(\varphi + 2\pi/3) & \sin(\varphi + 4\pi/3) \end{bmatrix} \begin{bmatrix} L_1 \\ L_2 \\ L_3 \end{bmatrix} \quad (8.15)$$

where φ is the azimuth angle. The reverse transformation is

$$\begin{bmatrix} \theta_1 \\ \theta_2 \\ \theta_3 \end{bmatrix} = \begin{bmatrix} \cos(\varphi) & \sin(\varphi) \\ \cos(\varphi + 2\pi/3) & \sin(\varphi + 2\pi/3) \\ \cos(\varphi + 4\pi/3) & \sin(\varphi + 4\pi/3) \end{bmatrix} \begin{bmatrix} \theta_d \\ \theta_q \end{bmatrix} \quad (8.16)$$

where θ would represent pitch angle in this case. This can be extended to any number of blades B , as follows:

$$\begin{bmatrix} L_d \\ L_q \end{bmatrix} = \frac{2}{B} \begin{bmatrix} \cos(\varphi) & \cos(\varphi + 2\pi/B) & \cos(\varphi + 4\pi/B) & \dots \\ \sin(\varphi) & \sin(\varphi + 2\pi/B) & \sin(\varphi + 4\pi/B) & \dots \end{bmatrix} \begin{bmatrix} L_1 \\ L_2 \\ L_3 \\ \dots \end{bmatrix} \quad (8.17)$$

$$\begin{bmatrix} \theta_1 \\ \theta_2 \\ \theta_3 \\ \dots \end{bmatrix} = \begin{bmatrix} \cos(\varphi) & \sin(\varphi) \\ \cos(\varphi + 2\pi/B) & \sin(\varphi + 2\pi/B) \\ \cos(\varphi + 4\pi/B) & \sin(\varphi + 4\pi/B) \\ \dots & \dots \end{bmatrix} \begin{bmatrix} \theta_d \\ \theta_q \end{bmatrix} \quad (8.18)$$

For a two bladed machine this reduces simply to

$$\begin{aligned} L_d &= (L_1 - L_2) \cos(\varphi) \\ L_q &= (L_1 - L_2) \sin(\varphi) \end{aligned} \quad (8.19)$$

and

$$\theta_1 = -\theta_2 = \theta_d \cos(\varphi) + \theta_q \sin(\varphi) \quad (8.20)$$

In practice it is important to introduce an azimuthal phase shift into the reverse d-q axis transformation, by adding an offset to the rotor azimuth angle to account for the fact that a pure d axis pitch action generates both d and q axis loading, as a consequence of the aerodynamic properties of the rotating rotor; for example, an increase in pitch angle when a blade is at the top of its sweep will reduce the rotor tilt moment, but will also generate some yaw moment. The azimuthal phase shift can also compensate for the controller timestep and any other time delays in the control loop – in other words, the pitch angle is calculated for the azimuth angle, which will be reached by the time the pitch demand has been fully realised.

All that remains is to design a two-input, two-output controller $[C]$ to calculate the d-q axis pitch demands from the d-q axis loads:

$$\begin{bmatrix} \theta_d \\ \theta_q \end{bmatrix} = [C] \begin{bmatrix} L_d \\ L_q \end{bmatrix} \quad (8.21)$$

In the steady state there is clearly a one-to-one correspondence between the load and the pitch angle needed to compensate for it, once the azimuthal phase shift described above has been taken into account. It seems logical therefore to suppose that $[C]$ can be diagonal matrix, and furthermore because the rotor is rotationally symmetrical, the two diagonal terms should be identical. The design of the controller therefore boils down to designing a single SISO controller, and using two independent instances of it for the d and q axes. Because the wind field in the non-rotating frame varies relatively slowly, a straightforward, fairly low-bandwidth PI controller can be used for this.

Taking into account the dynamics, rotational sampling at the blade passing frequency means that there will be a certain speed variation at that frequency, resulting in corresponding variations in L_d and L_q . A notch filter at the blade passing frequency is therefore added in series with each PI controller. As for other PI loops, further notch or loop-shaping filters can be added if required.

Once the dynamics are taken into account, the rotor is no longer symmetrical because of its interaction with the tower dynamics. In principle this could lead to some asymmetry between the d and q axes, and possibly also a small amount of dynamic coupling. Therefore, in principle there might be some advantage in designing in a coupled 2-input, 2-output controller (Bossanyi 2003). In practice however, any advantage is likely to be small, and two independent and identical SISO controllers have been found to work extremely well. Furthermore, these simple controllers have been found to be very robust: they tend to be rather insensitive to the turbine dynamics, and also to load sensor calibration errors or drift.

The inverse d-q transformation converts the relatively slowly varying d-q pitch demands into near-sinusoidal individual pitch demand increments for each blade. The near-sinusoids are of frequency 1P and phase-shifted between the blades, for example,

by 120° for a three bladed turbine. This form of control is therefore sometimes referred to as cyclic pitch control, but this is not strictly correct: the controller is responding dynamically to the changing loads, so the pitch action is not actually sinusoidal, although it could be interpreted as sinusoidal with constantly changing amplitudes and phases. With PI controllers it is easy to limit the controller output to a maximum level, which corresponds to an upper limit on the amplitude of the sinusoids, and given the frequency (1P), this also determines the maximum additional pitch rate that would be demanded. This upper limit can be ramped down to zero in low winds, preventing any individual pitch action when the loads are small enough to contribute little to lifetime fatigue damage, so that the additional pitch action would not be worthwhile. It can also be used to ensure that the pitch demand does not fall below any physical pitch limit if this is close to the collective pitch demand in low winds. Another use is to prevent individual pitch action when it is more important to use the available pitch rates for collective pitch control – for example, if the rotor is accelerating rapidly towards an overspeed trip (Savini and Bossanyi 2010).

8.3.12 Load reduction with individual pitch control

The main effect of the once-per-revolution (1P) individual pitch control is to reduce the 1P out-of-plane loading on the blades, and hence also the rotating hub or shaft moments. Figure 8.9 shows spectra of the blade root out-of-plane and shaft bending moments in simulations with and without individual pitch control. In fact the spectral peak in these loads at the 1P frequency is virtually eliminated, an effect that has been confirmed also in field tests on an actual turbine (Bossanyi et al. 2012a). Since the 1P load component dominates the fatigue, significant fatigue load reductions are obtained: typically of the order of 20% for blade root out-of-plane bending moment, and more for shaft bending moments (30–40%) because the low frequency variations cancel out between the blades so the 1P peak is even more significant.

On a two bladed turbine therefore, the use of individual pitch control represents a good alternative to the use of a teetered hub (Bossanyi and Wright 2009). Although it

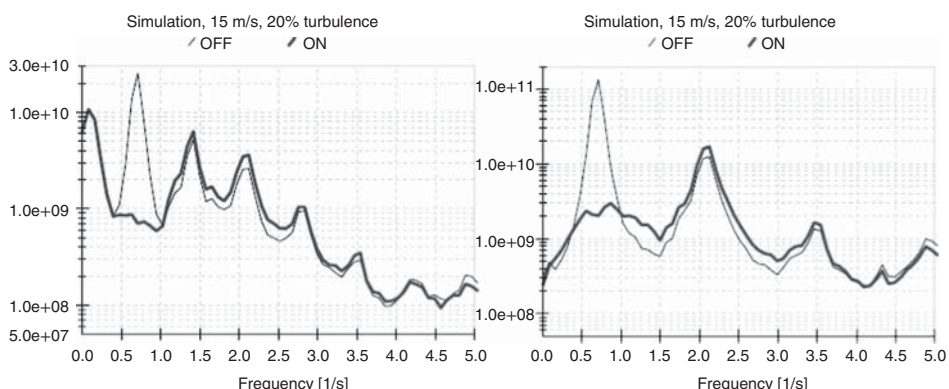


Figure 8.9 Effect of individual pitch control on rotating out-of-plane loads: blade root out-of-plane moment (left) and shaft bending moment (right)

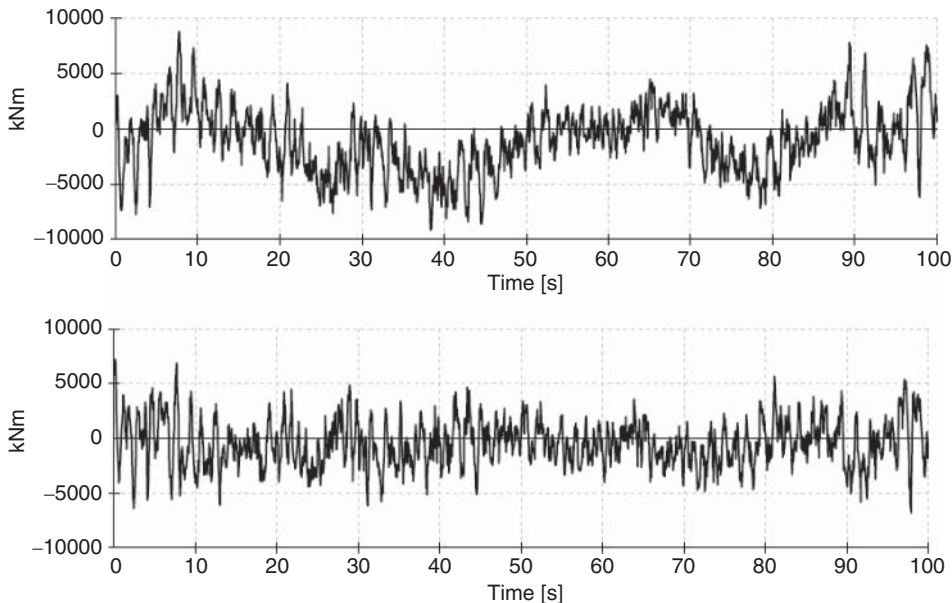


Figure 8.10 Effect of individual pitch control on yaw moment. Top: without individual pitch control; bottom: with individual pitch control

does not eliminate the teetering moment completely, a teetered hub often needs some kind of teeter restraint, which re-introduces a moment, and it is almost certainly necessary to consider the possibility of a teeter end-stop impact that can generate huge loads.

The 1P loading component on the rotor, when transformed to the non-rotating reference frame, results in loading contributions at 0P and 2P, so it is these load components that are reduced by individual pitch control. Hence the low frequency variation of nacelle nodding and yawing moments is removed, resulting in a reduction in peak loading – Figure 8.10 shows the effect on yaw moment, which may be of significant benefit in reducing the required yaw motor rating and duty. The nodding moment is reduced in a very similar way.

On a three bladed turbine, there is no significant 2P component in the non-rotating loads, so only the low frequency load reduction is important here – the dominant source of fatigue loading on the non-rotating components is at 3P, and so is largely unaffected by the individual pitch control. However, for a two bladed turbine, where this fatigue loading is dominated by 2P, the individual pitch control does significantly reduce the non-rotating fatigue loading. Again this has been confirmed in field tests (Bossanyi et al. 2012a) – by ‘toggling’ the individual pitch control on and off every few minutes, the improvement in loading is clearly demonstrated.

However, even for a three bladed turbine it is possible to reduce these non-rotating fatigue loads by making use of second-harmonic individual pitch control. Taking 1P as the first harmonic, second-harmonic individual pitch control is achieved in exactly the same way but with the arguments to the sine and cosine functions in the rotational transformations multiplied by two, or by n for the n th harmonic (although it may not

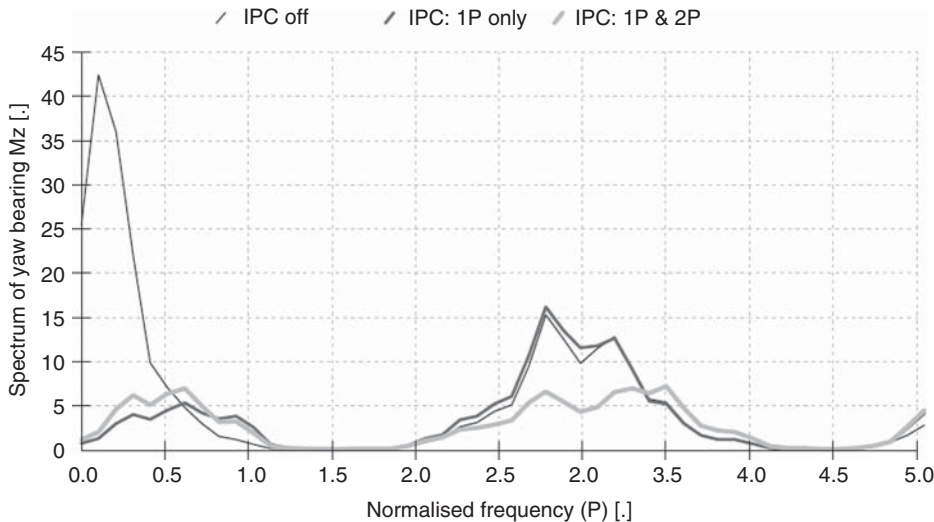


Figure 8.11 Effect of 1P and 2P individual pitch control on non-rotating loads

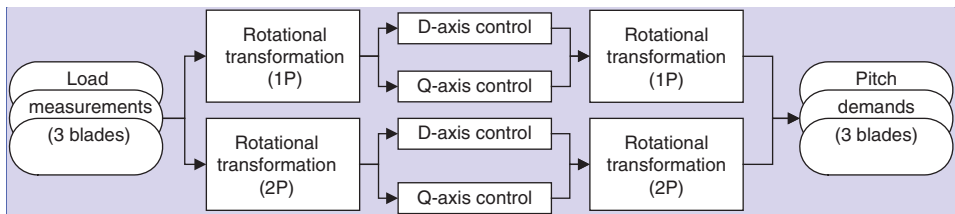


Figure 8.12 Adding higher harmonic individual pitch control loops

be worthwhile to use more than the second harmonic in practice). Second-harmonic control results in 2P pitch action, hence any 2P loading in the rotating components is reduced, but also the 1P and 3P loading in the non-rotating components (van Engelen and van der Hooft 2005; Bossanyi and Wright 2009). On a three bladed turbine therefore, the dominant 3P non-rotating fatigue loads are reduced by this means, as shown in Figure 8.11.

Any number of harmonics may be used together as shown in Figure 8.12, simply by using parallel control loops.

8.3.13 Individual pitch control implementation

Individual pitch control requires additional sensors, so it is important to ensure that these are very reliable, otherwise the overall reliability of the turbine would be compromised. Conventional strain gauges are notoriously unreliable, although they certainly can last well if very carefully installed. However, strain sensors based on fibre Bragg gratings are now available that have the potential to be sufficiently reliable for this application.

Pulses of laser light are directed along an optical fibre, and a fine grating ‘burnt’ into the fibre at a certain location reflects light of the same wavelength as the grating. The frequency of the reflected light is detected, and gives a direct measure of the strain at the position of the grating. Many gratings can be burnt into the same fibre, so strains at multiple locations can be measured at little extra cost: the time delay between sending the pulse and detecting the reflected signal determines the position of each grating. The components required are based on communications technology and therefore becoming readily available. Furthermore, the special optical fibres can easily be included as part of the glass reinforced plastic (GRP) layup during construction of a wind turbine blade.

Individual pitch control could equally be implemented using shaft bending sensors or even other sensors in the nacelle or tower top (Bossanyi 2003), but it may be difficult to find suitable sensor locations. However, if blade root sensors are used, they can also provide a measure of hub torque and rotor thrust. Although not currently used in this way, they might be useful as additional or alternative inputs to the other control loops described above; for example, for damping tower fore-aft or drive train torsional vibrations.

If there is any failure of the strain sensors, there is the potential for individual pitch control to increase rather than reduce loading, which could be serious. Some failures are readily detected in a well-designed sensor system, but it is always possible that some types of failure may be hard to detect without some analysis of the signals by the controller – for example, by comparing the sensor signals between different blades. If any failure is detected or suspected, the individual pitch control (being completely decoupled from the other control loops) can simply be switched off without the necessity to shut down the turbine, at least for a limited period or at a reduced power level until the fault can be rectified.

Below rated, the individual pitch control would normally be phased out because the loads are already smaller and so the additional pitch activity may not be justified. Also in principle there should be a small loss of energy output because the pitch angles are constantly moving either side of the optimum, although in practice this loss of output is usually very small. Above rated there is no loss of output, as the pitch angles are already well away from the optimum, and the collective pitch control loop ensures that rated output is maintained.

Clearly individual pitch control results in additional pitch actuator duty. The additional pitch action is concentrated around the 1P frequency. As turbines grow larger, the pitch rates required will diminish, because the rotational frequency will decrease as rotor diameter increases. If higher harmonic individual pitch control is used – for example, at 2P – then there will also be additional pitch action at that frequency. Because the pitch action is near-sinusoidal, the maximum pitch rate required can be estimated as the product of the maximum amplitude limit and the frequency; this should be multiplied by $\sqrt{2}$ in case the d and q axis demands are simultaneously at the limit. The required actuator torque is no greater than normal (and may even be slightly reduced because the lower blade root bending moment implies lower bearing friction), but the actuators will be working harder because of the increased pitch rates. This will have implications for the thermal rating of the actuators.

The total lifetime pitch travel will increase, typically by a factor of around 3 (Bossanyi 2003), which must be taken into account in the design of the pitch bearings.

Although fatigue loads can be significantly reduced by individual pitch control, there remains the possibility of increased extreme loads in the event of a forced shut-down by the safety system: if the pitch angles are all different by several degrees and that difference is maintained as the pitch angles are ramped to feather, large asymmetrical loads, sometimes design-driving, can be generated. Where possible the individual pitch control is ramped out during the shut-down, but the safety system is unlikely to be allowed the sophistication required to do this. However, by reducing the individual pitch control amplitude as a function of rotor acceleration, this situation can effectively be avoided because the pitch angles are then likely to be much closer together when a safety system trip occurs (Savini and Bossanyi 2010). The fatigue load reduction is hardly affected because these situations occur only rarely.

8.3.14 Further extensions to individual pitch control

Another theoretical possibility for individual pitch control is for actually generating yawing loads in response to measured yaw misalignment, to keep the turbine pointing into the wind without the use of a yaw motor. A yaw moment can easily be generated, simply by setting a non-zero set-point for one of the PI controllers. However, it is unlikely that the yaw motor can be dispensed with completely, as it will probably be needed to yaw the nacelle while the rotor is not turning, and also for cable unwinds, etc., so it may be better simply to use the individual pitch control with zero set-point to minimise the yaw moment that the yaw actuator has to overcome.

It is also possible that the d-q axis loads could help to infer rotor averaged yaw misalignment, conceivably leading to better yaw control than just using the wind vane.

Nodding moments can be generated in the same way as yaw moments by setting a non-zero set-point: this could possibly be used for damping of higher fore-aft tower modes, or to help stabilise floating turbines (Namik and Stol 2010). Some damping of side-side tower vibration is also possible by means of azimuth-dependent individual pitch control responding to side-side acceleration (Fischer et al. 2010). Any of these applications would of course compromise the reduction of blade fatigue loads.

8.3.15 Commercial use of individual pitch control

Although the benefits of individual pitch control have been clear for some time, the small but repetitive motion required of the pitch bearings is unusual; although it can help to prevent some types of bearing wear such as brinelling, uncertainty about its long-term effect on bearing life was a factor in the slow initial uptake of individual pitch control by some wind turbine manufacturers. While it makes little sense as an add-on to an existing design, new commercial designs benefit from the reduced loads in two main ways:

- Some existing designs have been uprated or the rotor diameter increased, with individual pitch control being added at the same time to keep the loads within the existing design envelope, resulting in higher energy capture with minimal redesign of components and hence minimal change in capital cost.
- Some completely new turbines are now designed with individual pitch control from the start, leading to lower component costs. The significant change in the loading regime gives scope to re-optimise the whole design.

Also, now that older wind farms are approaching the end of their design lives, there may be a case for retrofitting individual pitch control to the turbines as a way to extend their lifetime.

Individual pitch control may also find a place in wind farm control, to mitigate any additional loading caused by yawing turbines for wake steering control (see Chapter 9).

8.3.16 Estimation of rotor average wind speed

Wind turbines usually have a nacelle-mounted anemometer, but while knowledge of the wind speed might seem useful for the controller, the control schemes described above do not make use of the anemometer, because it provides a point measurement rather than a rotor average, and because it is located in highly disturbed flow behind the rotor. It is used for supervisory control actions, especially when the turbine is not operating, such as for deciding whether the wind speed is within range for initiating a turbine start-up, or too low for yaw control to be useful (because the wind direction becomes extremely variable in very low winds). When the turbine is operating, the rotor itself makes a better anemometer. The pitch and torque control schemes described above use the rotor speed as input, and high wind shut-down, for example, can be triggered on the basis of the pitch angle, which makes a useful proxy for the wind speed in that situation. Nevertheless, a direct estimate of rotor average wind speed can be useful in some situations: one of these is for the bias terms described in Section 8.3.4. Another is for delta control, where the power production of the turbine is reduced to suit grid system requirements (Section 9.4.1); an estimate of the wind speed is useful for knowing how much power the turbine would have been producing if operating normally.

A simple way to estimate wind speed using the known function $F(\lambda) = C_q(\lambda)/\lambda^2$ is outlined in Section 8.3.2 for below rated conditions. This can be extended to work at any pitch angle β using $F(\lambda, \beta) = C_q(\lambda, \beta)/\lambda^2$. However, a given value of F may yield more than one possible value for the tip speed ratio λ , making the method less straightforward to implement. A useful estimator can be constructed instead using a Luenberger observer of the form

$$U_k^* = U_{k-1}^* + K(\dot{\Omega}_k - \dot{\Omega}_k^*) \quad (8.22)$$

at timestep k , where U denotes wind speed, $\dot{\Omega}$ is the rotor acceleration (obtained by differentiating the measured rotor speed with some filtering to prevent noise), and $*$ denotes an estimate. Using the same notation as in Section 8.3.2, and omitting subscript k , we can combine Eqs. (8.2) and (8.6) to give

$$\dot{\Omega} = (\frac{1}{2}\rho\pi R^3 C_q U^2 - GQ_g)/I \quad (8.23)$$

Differentiating with respect to U gives $\Delta\dot{\Omega} = C\Delta U$ where the factor C is given by

$$C = \rho\pi R^3(2C_q U + U^2 dC_q/dU)/2I \quad (8.24)$$

C can be calculated at each step from the latest estimated values, i.e. U^* , $\lambda^* = \Omega R/U^*$ and $C_q(\lambda^*, \beta)$, and the derivative can be approximated numerically. Then the prediction error $e = U - U^*$ will obey

$$\Delta e_k = (1 - KC)\Delta e_{k-1} \quad (8.25)$$

If we aim for a response with time constant τ (of the order of a second, say, depending on the application), then integrating over one time step of length T gives $1 - KC = e^{-T/\tau}$. From this we obtain the Kalman gain $K = (1 - e^{-T/\tau})/C$. This is evaluated at each time step, and used together with \dot{Q}^* (using Eq. (8.23) with latest estimated values) to update the estimate of U using Eq. (8.22). However, C may become positive or negative, and if it gets close to zero, the estimator becomes unstable. A pragmatic solution is to multiply K by a function like $(C/C_0)^2$ whenever $C < C_0$, to ensure that it crosses zero smoothly, where C_0 is a small value chosen such that $|C|$ is almost always greater than C_0 .

8.3.17 LiDAR-assisted control

In recent years, the development of LiDAR (light detection and ranging) systems for laser Doppler anemometry has reached the point where these devices can be used effectively for wind speed measurements at a distance. A laser beam is emitted by the unit, and reflections returned from small particles or aerosol droplets carried in the air are detected. The Doppler shift in frequency between the outgoing beam and the reflected signal allows the speed of the reflecting particle, and hence the wind speed, to be determined quite accurately. By means of a scanning laser beam, a significant volume of space can be sampled, and the changing beam angle can help in estimating the wind vector rather than just its component in the beam direction. Alternatively, multiple beams can be used.

Ground based LiDARs are now being used as an alternative to meteorological masts for site wind speed assessment, and floating LiDARs are especially useful offshore where met mast installation is very expensive. A forward-pointing LiDAR on the turbine nacelle has a number of advantages for power curve measurements compared to a fixed mast. The possibility to use a nacelle-mounted LiDAR to scan the approaching wind field in front of the turbine for the purposes of improving the control has been suggested many times over the years, and is now a possibility. The cost of these devices is still substantial, but LiDAR-assisted control may be worthwhile if sufficient gains can be demonstrated, especially for large turbines where the cost of the LiDAR is a smaller proportion of the total. This section considers the possibilities of LiDAR-assisted wind turbine control.

A continuous-wave LiDAR focusses its beam on a sampling volume a certain distance away, with the length of the sampling volume determined by the lens area. Simley et al. (2011) consider how this may be used for wind turbine control. In contrast, a pulsed LiDAR sends out short pulses, allowing it to measure the time before the reflected signal is received, from which the distance to the reflecting particle is calculated; by analysing the Doppler shift for different ‘range gates’, the wind speed can be measured simultaneously at a number of distances along the beam. With either type, to sample the approaching wind over the rotor swept area requires either scanning or multiple beams. A wind turbine simulation model that includes turbulence and a detailed representation of any particular LiDAR characteristics can be used to investigate the effectiveness of different LiDAR configurations for various possible control applications (Bossanyi et al. 2012b). Good coverage of the rotor swept area is clearly important, whether this is achieved by one scanning beam or by multiple fixed beams. Multiple sampling distances along the angled beam(s) also help improve coverage. However, there is inevitably some trade-off between the number of points sampled and the time taken to sample them all. A sharply focussed measurement is not necessarily advantageous, perhaps because a more distributed sample

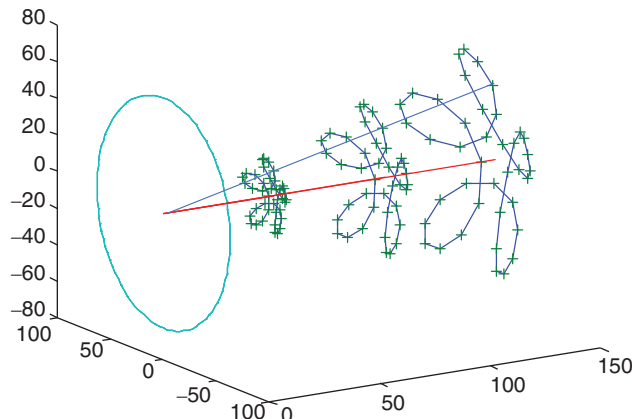


Figure 8.13 Possible LiDAR scanning pattern: a five-lobed cycloidal scan is shown, with 40 sampling points per scan at three measurement distances

along an angled beam is representative of more of the swept area, even though the resolution in terms of look-ahead time will be less precise. An accelerometer can be used to correct the measurement for the effect of tower motion. Different mounting options are possible, with generally similar performance. A spinner-mounted LiDAR has the advantage of avoiding beam blockage by the rotating blades, and correcting the measurements for shaft tilt and rotor azimuth is not difficult. Even fixed blade-mounted beams at about two-thirds span, with a slow circular scan from the rotor rotation, can be effective despite the changing blade pitch angle.

Figure 8.13 illustrates a possible scanning pattern for a nacelle- or spinner-mount LiDAR. Note that the coverage of rotor area decreases for measurement points closer to the rotor. Current commercially available configurations currently include a circular scan with 50 points per scan or four fixed beams, although much more complex scan patterns are sometimes used for research purposes.

LiDAR measurements can be much more representative of the wind that the rotor experiences than the conventional nacelle-mounted anemometer and wind vane, because they can sample much more of the rotor swept area, and because they measure the ‘clean’ incoming wind field. In contrast, the conventional instruments measure at a single point that is behind the rotor, and thus highly disturbed by the passage of the rotating blades and by the hub and nacelle. In addition, the LiDAR measurement provides a preview of the approaching wind speed before it reaches the turbine, potentially allowing the controller to anticipate gusts rather than reacting once the effect of the gust has already been felt; but the further ahead the measurement is, the more the wind will have changed by the time it reaches the turbine. Measurements closer to the turbine will need greater beam angles to cover the rotor area, leading to poorer estimation of the longitudinal wind component, but better estimation of transverse components and hence wind direction.

Four main ways in which these LiDAR characteristics could potentially improve wind turbine control have been investigated, as described in the following paragraphs.

Collective pitch control: Above rated, LiDAR preview of approaching wind speed changes can improve collective pitch control, by avoiding the delays caused by first having to measure the change in rotor speed and by the response time of the pitch system. This has clear potential to reduce particularly the thrust-related loads. A very simple feed-forward scheme can be used in which a pitch rate demand, calculated to move the pitch to the steady-state angle corresponding to the preview wind speed by the time this reaches the turbine, is simply added on to the normal pitch rate demand from the closed-loop feedback controller (Section 8.3.3). This can significantly improve the speed regulation, with rotor speed variations reduced by a factor of 2 or more. This may be of some benefit in itself, but more importantly, the gain of the feedback controller can then be reduced, so as to leave the tightness of the speed control unchanged, but allowing the amount of pitch activity to reduced, with a consequent reduction in fore-aft tower vibration. This has the potential to reduce tower base fatigue loading by around 20%, and out-of-plane blade root fatigue by about 5%. For a fatigue-driven design, this could significantly reduce capital cost, particularly of the tower.

Individual pitch control: LiDAR measurement of wind shear gradients can be used as a feed-forward input to an individual pitch controller instead of using strain gauges. Good coverage of the rotor swept area is important. In this case, the preview shows no clear benefit, however, and the control action may be no better than using conventional feedback control with blade root strain gauges, for example, which have the advantage of directly measuring the loads that are to be controlled. Using LiDAR and strain gauges in combination can give slightly better load alleviation, but the improvement may be too small to justify the additional expense and complexity of the LiDAR, unless it is already there for other reasons.

Optimum C_p tracking: Below rated, the torque control, which is attempting to maintain the optimum tip speed ratio, can anticipate changes by planning a rotor speed trajectory that maximises energy capture, taking into account the effect of the large rotor inertia on the rate of acceleration and deceleration. As with other methods of tighter C_p tracking, a very slight increase in energy capture is probably achievable, but only at the expense of prohibitive increases in the variation of power and drive-train torque needed to accelerate and decelerate the rotor.

Yaw control: For the reasons described above, the LiDAR provides a cleaner and more representative measurement of the wind direction relative to the nacelle, and may avoid the calibration errors and drift and the need for heavy averaging when a wind vane is used. However, yaw control has to be slow to prevent excessive yaw system duty, so if the wind vane is well calibrated, the advantage of using LiDAR may not be great, and the preview of a few seconds is of little value. Nevertheless, it is not easy to calibrate a wind vane to the required accuracy, especially as the calibration should depend on rotor speed and pitch angle (Krugh et al. 2013), so the use of LiDAR might be worthwhile, especially if it is installed anyway for other reasons, such as pitch control. A spinner anemometer (Friis Pedersen and Arranz 2018), consisting of a triple sonic anemometer mounted on the spinner, might provide a better compromise between cost and effectiveness. Of course, a LiDAR could be used temporarily for initial wind vane calibration, but a suitable mounting would be needed, and the wind vane calibration can easily drift afterwards, or change due to unintentional movement.

Depending on site conditions, the LiDAR signal may not always be available or reliable enough. This can happen if the air is so clean that there are not enough particles

to give a sufficient reflected signal, or if thick fog or heavy precipitation disrupts the signal. In this situation, the control must switch back to standard or ‘safe’ mode, not using the LiDAR. The implications for fatigue load reduction are straightforward to assess: the fatigue load reduction can simply be factored by the proportion of time for which the LiDAR signal is expected to be available, in each wind condition. If used for yaw control, the controller would switch back to using the wind vane.

LiDAR-assisted control can reduce fatigue loads and hence the cost of components whose design is fatigue load driven, but for a component whose design is driven by extreme operational gust loads, the cost can only be reduced by LiDAR-assisted control if it can be relied upon to respond appropriately to the specific extreme gust. However, it is not possible to know the exact characteristics of the extreme gust that a turbine will see. Some extreme coherent gusts are defined in the International Electrotechnical Commission (IEC) standards, but these are not physically realistic, and do not specify how the gust might advect and evolve between being measured by the LiDAR and arriving at the rotor. It is even possible that the LiDAR-assisted controller, with its reduced feedback gains, might exacerbate the extreme load if it fails to detect the gust properly – for example, if the gust is not advecting with the mean flow.

If extreme loads are calculated by statistical extrapolation, the probable effect of the LiDAR on the extreme load can be assessed by comparing extrapolations from simulations with and without LiDAR (Bossanyi et al. 2012b).

It is also necessary to take into account the possibility that the LiDAR signal is not available at the moment of the extreme gust. If this is due to a LiDAR fault, a gust with a lower return period can be used, but if it is due to atmospheric conditions, either thick fog or clean air providing very little reflected signal, the controller would have switched to its standard or ‘safe’ mode where no load reduction is possible.

8.3.18 LiDAR signal processing

A LiDAR beam only measures the component of wind speed along the beam direction. With a scanning beam or a LiDAR with multiple fixed beams, the beam angle at each measurement point is different. Therefore, if an assumption is made that the flow field over the whole rotor can be characterised by a given set of parameters – for example, mean wind speed, direction, and a vertical wind shear profile – then these parameters can be estimated by combining the measurements from each point, as long as there are at least as many points as parameters to estimate. If the number of points equals the number of parameters, a set of simultaneous equations can be solved to give the parameters. If there are more measurement points, a least squares fit can be used. Five parameters are often considered to characterise the flow: speed (for collective pitch control), direction (for yaw control), vertical and horizontal shear gradients (for individual pitch control), and possibly the upflow angle. Assuming these parameters are the same over all of the measurement points, the component of wind speed along the beam can be calculated for each measurement point, as a function of these parameters. The parameters values that minimise the root-mean-square differences between the calculated and measured velocities can then be calculated.

However, with a single LiDAR source, it is not possible to directly distinguish between direction and horizontal shear, or between vertical shear and upflow (the so-called ‘cyclops dilemma’), unless further assumptions are made (for example, that

the direction changes more slowly than the horizontal shear, or that the upflow angle is known from the terrain). More complex approaches take account of time variation or measurements at multiple distances, and may make further assumptions about mass conservation or compliance with simplified Navier–Stokes equations.

By using three LiDAR beams emanating from different points and controlled to converge at a single measurement point, all three components of velocity at that point can be calculated. This measurement point can be caused to scan around by scanning the three beams in a coordinated fashion, as, for example, with the DTU Windscanner (Vasiljević et al. 2017).

8.4 Closed-loop control: analytical design methods

Clearly the choice of controller gains is crucial to the performance of the controller. With too little overall gain, the turbine will wander around the set-point, while too much gain can make the system completely unstable. Inappropriate combinations of gains can cause structural responses to become excited. This section outlines some of the techniques that have been found useful in designing closed-loop control algorithms for wind turbines, such as the gains of a PI or PID controller, for example. Clearly it is only appropriate here to give some useful hints and pointers. There are many standard texts on control theory and controller design methods to which the reader should refer for more detailed information, for example, D’Azzo and Houpis (1981), Anderson and Moore (1979), and Astrom and Wittenmark (1990).

8.4.1 Classical design methods

A linearised model of the turbine dynamics is an essential starting point for controller design. This allows various techniques to be used for rapidly evaluating the performance and stability of the control algorithm. Detailed non-linear simulations using a three-dimensional turbulent wind input should then be used to verify the design before it is implemented on the real turbine.

For a variable-speed turbine below rated wind speed, a PI speed controller using demanded torque can be quite slow and gentle, and the linearised model can be very simple. It must include the rotational dynamics of the drive train, but other dynamics are not usually important. For pitch control however, the aerodynamics of the rotor and some of the structural dynamics can be critical. The linearised model for pitch controller design should contain at least the following dynamics:

- Rotor and generator rotation.
- Tower fore–aft vibration.
- Power or speed transducer response.
- Pitch actuator response.

The generator characteristics are also necessary for fixed-speed systems, and drive train torsion is particularly important for variable-speed turbines. In all cases a linearised description of the aerodynamics of the rotor is required – for example, as a set of partial

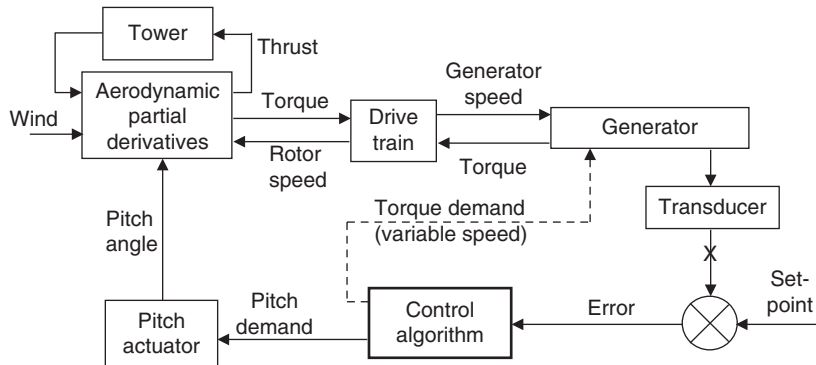


Figure 8.14 Typical linearised turbine model

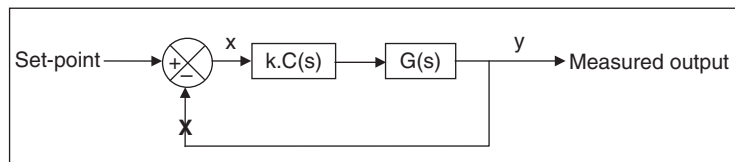


Figure 8.15 Simplified general model of plant and controller

derivatives of torque and thrust with respect to pitch angle, wind speed, and rotor speed. The thrust is important because it affects the tower dynamics, which couple strongly with pitch control.

A typical linear model is shown in Figure 8.14. With such a linear model, it is then possible to vary the gains and other parameters, and then rapidly carry out a number of tests that help to evaluate the performance of the controller with those gain settings. Some of these tests are open-loop tests, which means they are applied to the open-loop system obtained by breaking the feedback loop; for example, at the symbol X in Figure 8.14. Other tests are carried out on the closed-loop system. Before describing some of these tests, some basic theory on open and closed-loop dynamics is outlined.

Figure 8.15 shows a simplified general model in which the turbine (i.e. from pitch actuator to transducer in Figure 8.14) is represented by the ‘plant model’ with transfer function $G(s)$, and the control algorithm is represented by the controller transfer function $k.C(s)$, where s is the Laplace variable and k an overall controller gain.

Now the open-loop system can be represented by the transfer function $k.C(s).G(s) = H(s)$. If the input to the transfer function is denoted x and the output is y , then $Y(s) = H(s).X(s)$, where $X(s)$ and $Y(s)$ are the Laplace transforms of x and y . When the loop is closed at X the closed-loop dynamics can be derived as

$$Y'(s) = H(s)(X(s) - Y(s)) \quad (8.26)$$

where $Y'(s)$ is the Laplace transform of the closed-loop output y' . This can be rewritten as

$$Y'(s) = \frac{H(s)}{1 + H(s)}X(s) \quad (8.27)$$

In other words, if the open-loop system is $H(s)$, the closed-loop system will have dynamics represented by $H'(s) = H(s) / (1 + H(s))$.

Now a linear transfer function can be expressed as the ratio of two polynomials in s . Thus, for the open-loop system, $A(s)Y(s) = B(s)X(s)$, and so $H(s) = B(s)/A(s)$, where $A(s)$ and $B(s)$ are polynomials in s . The roots of the polynomial $A(s)$ give important information about the system response. Consider, for example, a first order system

$$\tau \dot{y}_1 = x - y_1 \quad (8.28)$$

representing a first order lagged response of y_1 with respect to x . This system can be represented by the transfer function

$$H(s) = \frac{B(s)}{A(s)}, \text{ where } B(s) = 1 \text{ and } A(s) = 1 + \tau s \quad (8.29)$$

The single root of $A(s)$ is given by $\sigma = -1/\tau$, while Eq. (8.28) has solutions of the form $y = a + be^{\sigma t}$, with $\sigma = -1/\tau$ again. These solutions are stable if τ is positive – in other words, if the root of $A(s)$ is negative. A second order system will have solutions of the form $y = a + be^{\sigma_1 t} + ce^{\sigma_2 t}$, where once again σ_1 and σ_2 are the roots of the second order polynomial that forms the denominator of the transfer function. Now σ_1 and σ_2 may be real numbers or they may form a complex conjugate pair $\sigma \pm j\omega$. The solutions are stable if σ_1 and σ_2 are both negative, or if σ is negative. In general, it can be stated that a linear system is stable if all of the roots of the denominator polynomial have negative real parts. These roots are known as the *poles* of the system, and they represent values of the Laplace variable that make the transfer function infinite. The roots of the numerator polynomial are known as the *zeros* of the system, because the transfer function is zero at these points.

Now let us rewrite Eq. (8.27) in terms of the polynomials A and B :

$$Y(s) = \frac{B(s)}{A(s) + B(s)} X(s) = \frac{k \cdot B'(s)}{A(s) + k \cdot B'(s)} X(s) \quad (8.30)$$

where we have reintroduced the overall controller gain k such that $B(s) = k \cdot B'(s)$. Clearly when the gain k is small, the closed-loop transfer function tends towards the open-loop transfer function $k \cdot B'/A$. However, when the gain is large, A can be neglected and so the poles will tend towards the roots of B' . In other words, as the gain increases from zero to infinity, the poles of the closed-loop system move from the open-loop poles and end up at the open-loop zeros. They move along complicated trajectories in the complex plane. A plot of these trajectories is known as a *root locus plot*, and is very useful for helping to select the feedback gain k . The gain is selected such that all of the closed-loop poles are in the left half-plane, making the system stable, and preferably as well damped as possible. The damping factor for a pole pair at $\sigma \pm j\omega = re^{j\theta}$ is given by $-\cos(\theta) = -\sigma/r$, as shown in Figure 8.16.

Figure 8.17 shows an example of a root locus plot for a variable-speed pitch controller. As the gain increases, the closed-loop poles (+) move from the open-loop poles (x), corresponding to zero feedback gain, to the open-loop zeros (O). (Actually there are usually more poles than zeros; the ‘missing’ zeros can be considered to be equally spaced around a circle of infinite radius.) In this example, the gain has been chosen to maximise the damping of the lightly damped tower poles (B). Any further increase in gain would

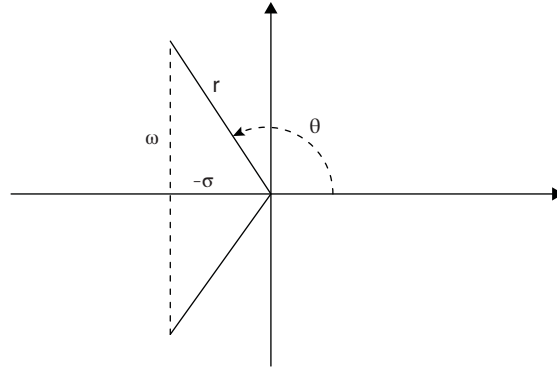


Figure 8.16 Damping ratio for a complex pole pair

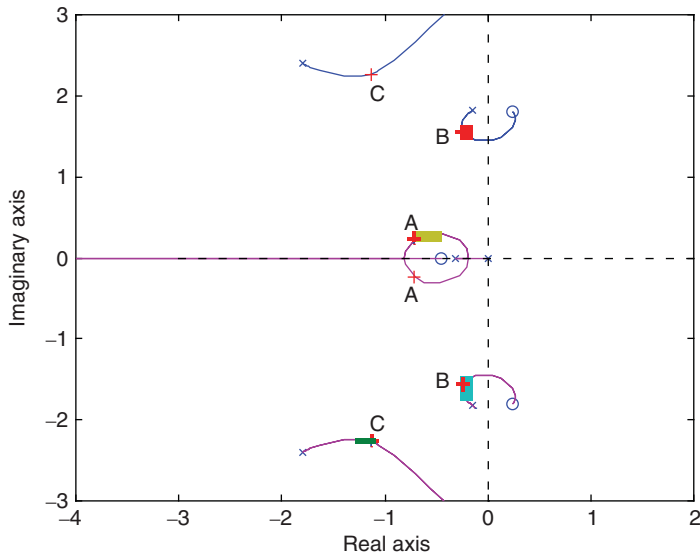


Figure 8.17 Example root locus plot for a variable-speed pitch controller

exacerbate tower vibration, eventually leading to instability as the poles cross the imaginary axis. At the chosen gain, the controller poles (A) are well damped. The poles at (C) result from the pitch actuator dynamics. They remain sufficiently well damped, although again, excessive gain would drive them to instability.

Although a root locus plot is useful for helping to select the overall controller gain, this can only be done once the other parameters defining the controller have been fixed. A PI controller (Eq. 8.1 with $k_d = 0$) is characterised by only two parameters, K_p and K_i . It can be re-written as

$$y = K_p \left(1 + \frac{1}{sT_i} \right) x \quad (8.31)$$

where $T_i = K_p/K_i$ is known as the *integral time constant*. The root locus plot can be used to select K_p once T_i has been defined, but the shape of the loci will change with different T_i . However, it is relatively straightforward to iterate on the value of T_i , using the root locus plot each time to select K_p , until a suitable overall performance is achieved, using criteria such as those listed below. In the case of PID and more complex controllers, where more than two parameters must be selected, other ways must be found to select the parameters, although it is always possible to use a root locus plot for the final choice of the overall gain.

The choice of parameters will usually be an iterative process, often using a certain amount of trial and error, and on each iteration the performance of the resulting controller must be assessed. Useful measures of performance include:

- Gain and phase margins: These are calculated from the open-loop frequency response, and give an indication of how close the system is to instability. If the margins are too narrow, the system may tend to become unstable. The system will be unstable if the open-loop system displays a 180° phase lag with unity gain. The phase margin represents the difference between the actual phase lag and 180° at the point where the open-loop gain crosses unity. A phase margin of at least 45° is usually recommended, although there is no firm rule. Similarly, the gain margin represents the amount by which the open-loop gain is less than unity where the open-loop phase lag crosses 180° . A gain margin of at least a few decibels is recommended.
- The cross-over frequency, which is the frequency at which the open-loop gain crosses unity, gives a useful measure of the responsiveness of the controller.
- The positions of the closed-loop poles of the system indicate how well various resonances will be damped.
- Closed-loop step responses – for example, the response of the system to a step change in wind speed – give a useful indication of the effectiveness of the controller. For example, in tuning a pitch controller, the rotor speed and power excursions should return rapidly and smoothly to zero, the tower vibration should damp out reasonably fast, and the pitch angle should change smoothly to its new value, without too much overshoot and without too much oscillation.
- Frequency responses of the closed-loop system also give some very useful indications. For example, in the case of pitch controller: (i) The frequency response from wind speed to rotor speed or electrical power should die away at low frequencies, as the low frequency wind variations are controlled away. (ii) The frequency response from wind speed to pitch angle must die away at high frequencies and must not be too great at critical disturbance frequencies such as the blade passing frequency, or the drive train resonant frequency in variable-speed systems. (iii) The frequency response from wind speed to tower velocity should not have too large a peak at the tower resonant frequency, and so forth.

With experience, it is possible, by examining measures such as these, to converge rapidly on a controller tuning that will work well in practice.

8.4.2 Gain scheduling for pitch controllers

Close to rated wind speed, because the fine pitch angle is selected to maximise power, it follows that the sensitivity of aerodynamic torque to pitch angle is very small. Thus, a much larger controller gain is required here than at higher wind speeds, where small change in pitch can have a large effect on torque. Frequently the torque sensitivity changes almost linearly with pitch angle, and so can be compensated for by varying the overall gain of the controller linearly in inverse proportion to the pitch angle. Such a modification of gain with operating point is termed a *gain schedule*. However, the sensitivity of thrust to pitch angle varies in a different way, and because of its effect on tower dynamics, which couples strongly with the pitch controller, it may be necessary to modify the gain schedule further to ensure good performance in all winds. In some cases just varying the overall gain may not be sufficient to achieve satisfactory response at all operating points, in which case it may be necessary to change the proportional and integral gains separately, each as a different function of pitch angle.

It is therefore important to generate linearised models of the system corresponding to several different operating points between rated and cut-out wind speed, and to choose a gain schedule that ensures that the above performance measures are satisfactory over the whole range.

For an active stall controller, the pitch angle may not change much with operating point; a gain schedule may not be required, but if it is, it may have to be a direct function of wind speed rather than pitch angle. This is one of the few occasions when the nacelle anemometer signal may have to be used as an input to the controller.

8.4.3 Adding more terms to the controller

It is often possible to improve the performance of a basic PI or PID controller by adding extra terms to modify the behaviour in a particular frequency range.

For example, a pitch control algorithm may be found to cause a large amount of pitch actuator activity at a relatively high frequency, which is of little benefit in controlling the turbine and may be quite counter-productive. This may occur if some dynamic mode was not taken into account in the linearised model that was used to design the turbine. An example of this is the drive train torsional resonance in a variable-speed turbine, which can feed through to the measured generator speed and hence to the pitch control, causing high frequency pitch activity that is of no benefit. Another likely cause is the pitch response to a major external forcing frequency, such as the blade passing frequency. While a low pass filter in series with the controller will certainly reduce high frequency response, the resulting phase shift at lower frequencies may significantly impair the overall performance of the controller. A better ‘cure’ for excessive activity at some well-defined frequency is to include a notch filter in series with the controller. A simple second order notch filter tuned to filter out a particular frequency of ω rad/s has a transfer function

$$\frac{1 + s^2/\omega^2}{1 + 2\zeta s/\omega + s^2/\omega^2} \quad (8.32)$$

where the ‘damping’ parameter ζ represents the width or ‘strength’ of the notch filter. This should be increased until the filtering effect is sufficient at the target frequency, without too much detriment to the control performance at lower frequencies.

Another useful filter is the phase advance or phase lag filter,

$$\frac{(1 + s/\omega_1)}{(1 + s/\omega_2)} \quad (8.33)$$

which increases the open-loop phase lag between frequencies ω_1 and ω_2 ($\omega_1 < \omega_2$), or decreases it if $\omega_1 > \omega_2$. Phase advance can sometimes be useful for improving the stability margins. Open-loop gain and phase plots can, therefore, be useful for helping to select ω_1 and ω_2 . A PID controller can be rewritten as a PI controller in series with a phase advance (or phase lag) filter.

A general second order filter of the form

$$\frac{1 + 2\zeta_1 s/\omega_1 + s^2/\omega_1^2}{1 + 2\zeta_2 s/\omega_2 + s^2/\omega_2^2} \quad (8.34)$$

can sometimes be useful for modifying the frequency response in a particular area. With $\omega_1 = \omega_2$ and $\zeta_1 = 0$ this is just a notch filter, as described above. With $\zeta_1 > \zeta_2$ the filter has a bandpass effect, which can be used to increase control action at a particular frequency. With different ω_1 and ω_2 there is also a high-pass or low-pass effect, because the high-frequency gain tends towards $(\omega_2/\omega_1)^2$.

A root locus plot is often useful for investigating the effect of such filters. With experience, the effect on the loci of placing the filter poles and zeros in particular ways can be anticipated. Such techniques can help to see how, for example, a pair of lightly damped poles due to a structural resonance can be dragged further away from the imaginary axis, so as to increase the damping.

8.4.4 Other extensions to classical controllers

Other extensions to classical controllers have sometimes been used to further improve the performance in particular ways; for example, the use of non-linear gains and variable or asymmetrical limits.

Non-linear gains are sometimes used to penalise large peaks or excursions in controlled variables. For example, the gain of a PI pitch controller can be increased as the power or speed error increases; or, rather than changing the gain, an additional term can be added to the demanded pitch rate that may be a function of the error, its rate of change, or both. Often the additional term would be normally zero, increasing only in case of large deviations from the desired operating condition. The extra term can conveniently be added before the PI integrator (see Section 8.6.2). Such techniques should be used with caution, however, as too much non-linearity will drive the system towards instability, in much the same way as if the linear gain is too high. This technique requires a trial-and-error approach because it is very difficult to analyse the closed-loop behaviour of non-linear systems using standard methods. Any asymmetry in the additional term, e.g. if used only when the power or speed is above the set-point to help reduce peaks, will cause a reduction in the mean power or speed relative to the set-point.

Asymmetrical pitch rate limits can also be used to reduce peaks. By allowing the blades to pitch faster towards feather than towards fine, power, or speed peaks will be reduced. Once again the mean level will also be reduced by introducing this asymmetry.

However, this technique is somewhat more ‘comfortable’ than the use of non-linear gains because it is less likely to lead to instability.

There is often a desire to reduce the set-point in high winds, to reduce the infrequent but highly damaging loads experienced in those conditions at the expense of a small loss of output. It is straightforward to reduce the set-point as a function of wind speed (the pitch angle is usually used as a measure of the rotor averaged wind speed, as for gain scheduling). However, the most damaging loads occur during high turbulence, and so it would be better to reduce the set-point in high winds only when the turbulence is also high. Rather than actually reducing the set-point, asymmetrical rate limits provide a simple but effective means of achieving this effect, because the rate limits will only be reached when the turbulence is high.

A further extension of this technique is to modify the rate limits dynamically, even to the extent of changing the sign of a rate limit to force the pitch in one direction during certain conditions such as large power or speed excursions. A useful application of this is in the control of variable-slip systems, where it is important to keep the speed above the minimum slip point (point B in Figure 8.8). If the speed falls below this point, it then ceases to vary much as it is constrained by the minimum slip curve, and so the proportional term in the PI controller ceases to respond. Modifying the rate limits as a function of speed error as in Figure 8.18 is a useful technique to prevent this happening. Another useful application is to force some temporary pitch action such as a pitch ramp in response to a severe gust: by ramping the pitch rate limits, perhaps in response to an unusually large rate of generator acceleration, the PI controller can continue to act, albeit constrained by the rate limits, so that it resumes normal duty seamlessly when the rate limits are relaxed again.

Another case for set-point modification in high winds is to prevent a sudden loss of power arising from high wind cut-out (Bossanyi and King 2012). If an increase in wind speed can cause all of the turbines in a large wind farm to shut down suddenly within a few minutes, the network will have to cope with this by maintaining spinning reserve. Instead of shutting down suddenly at 25 m/s, ramping the power output down smoothly from full power to zero between, say, 24 and 35 m/s will result in a much lower probability of a sudden shortfall, and the wind farm output can be considered more

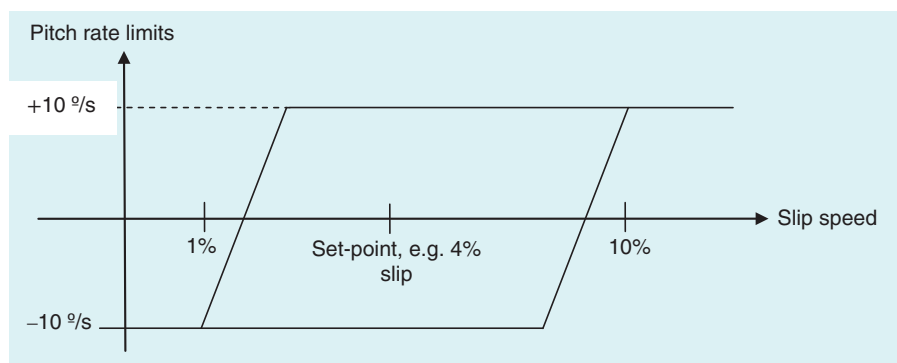


Figure 8.18 Pitch rate limit modification for a variable-slip wind turbine

predictable (Bossanyi 1982), both effects leading to lower spinning reserve requirements and hence a higher value for the generated power. This will have little effect on fatigue loading and energy yield because of the small number of hours involved, but the effect on extreme loads will need to be considered. For offshore turbines, where wave-induced tower vibration is better damped if the turbine is operating, extending the operating range to higher wind speeds may help to reduce tower loading (Markou and Larsen 2009).

8.4.5 Optimal feedback methods

The controller design methods described above are based on classical design techniques, and often result in relatively simple PI or PID algorithms together with various filters in series or in parallel, such as phase shift, notch, or bandpass filters, and sometimes using additional sensor inputs. These methods can be used to design fairly complex high order controllers, but only with a considerable amount of experience on the part of the designer.

There is, however, a huge body of theory (and practice, although to a lesser degree) relating to more advanced controller design methods, some of which have been investigated to some extent in the context of wind turbine control, for example:

- Self-tuning controllers.
- Model based controllers such as LQG/optimal feedback, H_∞ , or model predictive control.
- Fuzzy logic controllers.
- Neural network methods.

Self-tuning controllers (Clarke and Gawthrop 1975) are generally fixed order controllers defined by a set of coefficients, which are based on an empirical linear model of the system. The model is used to make predictions of the sensor measurements, and the prediction errors are used to update the coefficients of the model and the feedback law.

If the system dynamics are known, then some very similar mathematical theory can be used, but applied in a different way. Rather than fitting an empirical model, a linearised physical model is used to predict sensor outputs, and the prediction errors are used to update estimates of the system state variables. These variables may include rotational speeds, torques, deflections, etc. as well as the actual wind speed, and so their values can be used to calculate appropriate control actions even though those particular variables are not actually measured.

Observers: A subset of the known dynamics may be used to make estimates of a particular variable – for example, some controllers use a wind speed observer to estimate the wind speed seen by the rotor from the measured power and/or rotational speed and the pitch angle. The estimated wind speed can then be used to define the appropriate desired pitch angle.

State estimators: Alternatively, using a full model of the dynamics, a Kalman filter can be used to estimate all of the system states from the prediction errors (Bossanyi 1987). This technique can explicitly use knowledge of the variance of any stochastic contributions to the dynamics, as well as noise on the measured signals, in a mathematically optimum way to generate the best estimates of the states. This relies on an assumption of Gaussian characteristics for the stochastic inputs. Thus it is possible explicitly to take

account of the stochastic nature of the wind input by formulating a wind model driven by a Gaussian input. This can even be extended to include blade passing effects.

The Kalman filter can readily take account of more than one sensor input in generating its ‘optimal’ state estimates. Thus it is ideal for making use of, for example, an accelerometer measuring tower fore-aft motion as well as the normal power or speed transducer. It would be straightforward to add other sensors, if available, to improve the state estimates further.

Optimal feedback: Knowing the state estimates, it is then possible to define a cost function, which is a function of the system states and control actions. The controller objective can then be defined mathematically: the objective is to minimise the selected cost function. If the cost function is defined as a quadratic function of the states and control actions (which is actually a rather convenient formulation), then it is relatively straightforward to calculate the ‘optimal’ feedback law. This is defined as the feedback law that generates control signals as a linear combination of the states such that the cost function will be minimised. Because a linear model is required, with a quadratic cost function and Gaussian disturbances, this is known as an *LQG controller*.

This cost function approach means that the trade-off between a number of partially competing objectives is explicitly defined, by selecting suitable weights for the terms of the cost function. This makes such a method ideal for a controller that attempts to reduce loads as well as achieving its primary function of regulating power or speed. Although it is not practical to calculate the weightings in the cost function rigorously, they can be adjusted in a very intuitive way. This approach is also readily configured for multiple inputs and outputs, so, for example, as well as using generator speed and tower acceleration inputs, it can in principle simultaneously produce the pitch demand and torque demand outputs that will minimise the cost function.

Figure 8.19 illustrates the structure of the LQG controller, showing the state estimator and the optimal state feedback. For implementation, the entire controller can be reduced to a set of difference equations connecting the measured outputs (y) to the new control signals (u). This means that once the design is completed, the algorithm is easy to implement and does not require massive processing power.

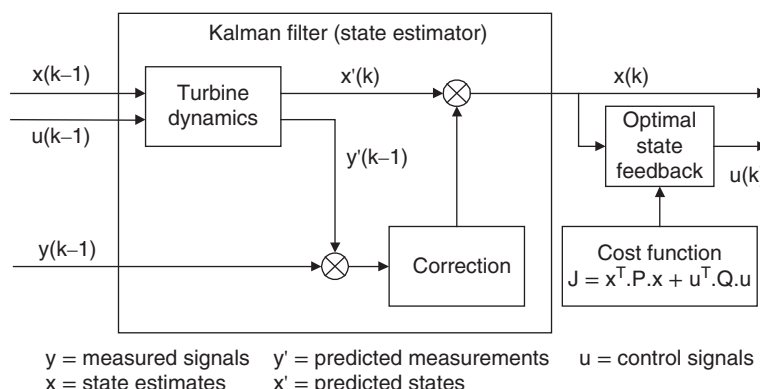


Figure 8.19 Structure of the LQG controller

The linearised dynamics of the system are expressed in discrete state-space form:

$$\mathbf{x}'(k) = \mathbf{A}\mathbf{x}(k-1) + \mathbf{B}\mathbf{u}(k-1) \quad (8.35)$$

The Kalman gain \mathbf{L} is calculated taking into account the stochastic disturbances affecting the system, and allows the state estimates to be improved by comparing the predicted sensor outputs \mathbf{y}' to the actual outputs \mathbf{y} :

$$\mathbf{x}(k) = \mathbf{x}'(k) + \mathbf{L}(\mathbf{y}(k-1) - \mathbf{y}'(k-1)) \quad (8.36)$$

where

$$\mathbf{y}'(k-1) = \mathbf{C}\mathbf{x}(k-1) + \mathbf{D}\mathbf{u}(k-1) \quad (8.37)$$

The optimal state feedback gain \mathbf{K} generates the control actions

$$\mathbf{u}(k) = -\mathbf{K}\mathbf{x}(k) \quad (8.38)$$

where \mathbf{K} is calculated such that the quadratic cost function J is minimised. The cost function is

$$J = \mathbf{x}^T \mathbf{P} \mathbf{x} + \mathbf{u}^T \mathbf{Q} \mathbf{u} \quad (8.39)$$

(actually the integral, or the mean value over time, or the expected value of this quantity). \mathbf{P} and \mathbf{Q} are the state and control weighting matrices. It is usually more useful to define the cost function in terms of other quantities, \mathbf{v} , which can be considered as extra (often unmeasured) outputs of the system:

$$\mathbf{v} = \mathbf{C}_v \mathbf{x} + \mathbf{D}_v \mathbf{u} \quad (8.40)$$

Hence the cost function is

$$J = \mathbf{v}^T \mathbf{R} \mathbf{v} + \mathbf{u}^T \mathbf{S} \mathbf{u} = \mathbf{x}^T \mathbf{C}_v^T \mathbf{R} \mathbf{C}_v \mathbf{x} + \mathbf{u}^T \mathbf{D}_v^T \mathbf{R} \mathbf{D}_v \mathbf{u} + \mathbf{u}^T \mathbf{S} \mathbf{u} \quad (8.41)$$

so that $\mathbf{P} = \mathbf{C}_v^T \mathbf{R} \mathbf{C}_v$ and $\mathbf{Q} = \mathbf{D}_v^T \mathbf{R} \mathbf{D}_v + \mathbf{S}$.

Another possibility is to generate optimal control signals directly as a function of the sensor outputs. This is known as *optimal output feedback* (Steinbuch 1989). However, the mathematical solution of this problem is based on *necessary* conditions for optimality that are not always *sufficient* for optimality. Therefore, the solutions generated can be, and in practice often are, non-optimal and potentially very far from optimal. This variation is therefore rather problematic.

As turbines become larger and the requirements placed on the controller become more demanding, advanced control methods such as LQG are likely to become increasingly used, although as yet there are few published examples of the practical application of these techniques in commercial wind turbines. However, this approach was used to design a controller for a 300 kW fixed-speed two bladed teetered turbine in the UK in 1992. After testing on a prototype turbine in the field, this controller was shown to give significant reductions in pitch activity and power excursions compared to the original PI controller, and it was subsequently adopted for the production machine and successfully used on over 70 turbines (Bossanyi 2000). Stol and Fingersh (2004) reported tests with a similar control scheme on a 600 kW research turbine.

LQG controllers are not necessarily robust, which means that they can be sensitive to errors in the turbine model. A similar approach is the H_∞ controller, in which uncertainties in the turbine and wind models can explicitly be taken into account. Such a controller was evaluated in the field on a 400 kW fixed-speed pitch-regulated turbine by (Knudsen et al. 1997), who reported a reduction in pitch activity and some potential for reduced fatigue loads compared to a PI controller.

8.4.6 Pros and cons of model based control methods

The methods of Section 8.4.5 are appealing as they use mathematical rigour to calculate an ‘optimal’ controller in the sense that it minimises a pre-defined and reasonably intuitive cost function, suggesting that the tuning could be an automatic process, whereas the classical approach relies on the skill and experience of the designer for each new tuning. They are also ideal for designing MIMO controllers, which could require a cumbersome iterative approach using classical design methods.

There are also some disadvantages, however, which may explain the continuing prevalence of classically designed controllers in commercial wind turbines.

In practice, ‘tuning’ the cost function may end up being just as difficult as tuning a classical controller, and the tuning may need to be repeated for each new turbine even though in principle this ought to be unnecessary. The cost function needs to include terms for any states or outputs that should be minimised, but the choice of such variables is not as straightforward as it might appear. For example, for a variable-speed controller it would be logical to include a term to minimise the speed error; but in practice a term is also required to minimise the integral of the speed error, and adjusting the relative weights for these two terms is very similar to adjusting the proportional and integral gains in a classical design.

Also the cost function is defined as a quadratic function of the states and other variables, and this may not be appropriate for minimisation of fatigue loads for example, as fatigue is a highly non-linear process. Even for speed regulation, one could argue that minimising the speed error is not important (this may even contradict the need to minimise loads), but minimising extreme speed excursions to avoid any overspeed trips is all that matters. A quadratic cost function is not ideal for this, as the true ‘cost’ increases dramatically at the overspeed trip limit.

Classical controllers are simpler to implement; they can easily deal with nonlinearities through techniques such as gain scheduling, and simple adjustments such as the addition of notch filters is straightforward, as is the imposition of fixed or variable rate limits. Model based controllers require further sophistication such as extended Kalman filters or fuzzy transitions to deal with non-linearities, and any adjustment requires a complete recalculation of the controller. Integration with the supervisory control is also much less straightforward; for example, it might be desirable to modify the tower acceleration feedback and/or the individual pitch control during a shut-down to reduce extreme loads. With a classical controller it is easy to impose variable schedules or limits to achieve this, but it is much more difficult to do this with model based controllers.

As explained in Section 8.3.10, most of the wind turbine control problem can be decomposed into separate, almost uncoupled SISO loops. This makes it perfectly feasible to use straightforward classical tuning techniques. The only significant coupling between

these loops is between speed regulation and tower damping, but this is easily dealt with by means of just one or two iterations, tuning each loop on its own with the other loop implemented as part of the plant.

Nevertheless, as turbines become larger, lighter, and more flexible, it is possible that model based multivariable methods, perhaps in conjunction with additional sensors, will increasingly find a role.

8.4.7 Other methods

Rule based or ‘fuzzy logic’ controllers are useful when the system dynamics are not well known or when they contain important non-linearities. Control actions are calculated by weighting the outcomes of a set of rules applied to the measured signals. Although there has been some work on fuzzy controllers for wind turbines, there is no clear evidence of benefits. In practice, quite a good knowledge of the system dynamics is usually available, and the dynamics can reasonably be linearised at each operating point, so there is no clear motivation for such an approach.

The same could be said of controllers based on neural networks. These are learning algorithms, which are ‘trained’ to generate suitable control actions using a particular set of conditions, and then allowed to use their learnt behaviour as a general control algorithm. While this is potentially a powerful technique, it is difficult to be sure that such a controller will generate acceptable control actions in all circumstances.

Nevertheless, there may be some potential for such methods where significant non-linearities or non-stationary dynamics are involved. These might be in the turbine itself (stall hysteresis might be one example), in the driving disturbances (the wind characteristics are not stationary), or in the controller objectives. For example, the controller objectives might change around rated wind speed, or non-linear effects such as fatigue damage might be included in the cost function.

8.5 Pitch actuators

An important part of the control system of a pitch-controlled turbine is the pitch actuation system (see also Section 6.7.2). Both hydraulic and electric actuators are commonly used, each type having its own particular advantages and disadvantages that should be considered at the design stage.

Smaller machines might have a single pitch actuator to control all of the blades simultaneously, but the current commercial turbines usually have individual pitch actuators for each blade. This has the advantage that it is then possible to dispense with the large and expensive shaft brake that would otherwise be needed. This is because of the requirement for a turbine to have at least two independent braking systems capable of bringing the turbine from full load to a safe state in the event of a failure. Provided the individual pitch actuators can be made independently fail-safe, and as long as the aerodynamic braking torque is always sufficient to slow the rotor down to a safe speed even if one pitch actuator has failed at the working pitch angle, then multiple actuators may be considered to be independent braking systems for this purpose. There may still be a need for a parking brake, at least for the use of maintenance crews, but this may then be fairly small. It must at least be capable of bringing the rotor to a complete stop from a low speed, not

necessarily in high or extreme wind speeds, for long enough to allow a rotor lock to be inserted.

Smaller, older turbines used a collective pitch actuation system that commonly consisted of an electric or hydraulic actuator in the nacelle, driving a push-rod that passes through the centre of the gearbox and hollow main shaft. The push-rod is attached to the pitchable blade roots through mechanical linkages in the hub. The actuator in the nacelle is often a simple hydraulic cylinder and piston. A charged hydraulic accumulator ensures that the blades can always be feathered even if the hydraulic pump loses power. An alternative arrangement is to use an electric servo motor to drive a ball-nut that engages with a ball-screw on the push-rod. Because the push-rod turns with the rotor, loss of power to the motor causes the ball-screw to wind the pitch to feather, giving failsafe pitch action. This requires a failsafe brake on the servo motor to ensure that the ball-nut stops turning if power is lost.

Individual pitch control requires separate actuators in the hub for each blade. Therefore, there must be some means of transmitting power to the rotating hub to drive the actuators. This can be achieved by means of slip rings in the case of electric actuators, or a rotary hydraulic joint for hydraulic actuators if the hydraulic power pack is located in the nacelle. A rotary transformer could be used to transmit electrical power to the hub without the inconvenience of slip rings, which require maintenance.

The need to ensure a backup power supply on the hub to enable the blades to pitch even in the event of power loss can be a source of problems. A hydraulic system needs an accumulator for each blade, while electric actuators usually have battery packs in the hub for this purpose. Such battery packs are large, heavy, and expensive, and alternative methods such as the use of hub-mounted generators, which can always generate power as long as the hub is turning, have been proposed. If a battery is used, the actuator motors must either be dc motors or (more commonly) ac motors with a frequency converter, with the batteries on the dc link. Because this will form part of the safety system, the reliability of the inverter between the dc link and the pitch motor is important. A hub-mounted generator would produce either dc or variable frequency ac, and once again the reliability of the connection to the pitch motor is important. Because the pitch actuators have to be independently failsafe, separate battery packs or generators and frequency converters, etc. must be provided for each blade.

The friction in the pitch bearing is often a significant factor in the design of the pitch actuation system. The bearing friction depends on the loading applied to the bearing, and the large overturning moment acting on the bearing can lead to very high levels of friction: often most of the actuator torque is required to overcome the bearing friction.

A hydraulic actuator would usually be controlled by means of a proportional valve controlling the flow of oil to the actuator cylinder. The valve opening, and hence the oil flow rate, would be set in proportion to the required pitch rate. The demanded pitch rate may come directly from the turbine controller, or it might come from a pitch position feedback loop. In this case the turbine controller generates a pitch position demand. This is compared to the measured pitch position, and the pitch position error is turned into a pitch rate demand through a fast PI or PID control loop, implemented either digitally or by means of a simple analogue circuit.

In the case of an electric actuator, the motor controller usually requires a torque demand signal. This may be derived from a speed controller, which uses a fast PI or

PID controller acting on speed error to generate a torque demand. Once again the speed demand may come directly from the turbine controller or from a position feedback loop.

Simpler actuators could be used if a fast pitch response is not important – for example, in a turbine that is controlled by pitching to stall rather than to feather. In this case an actuator that merely pitches at a fixed rate in either direction may be adequate.

8.6 Control system implementation

Previous sections have explained some of the techniques whereby control algorithms can be designed. The system and controller dynamics have been described in continuous time in terms of the Laplace operator, s . While it is possible to implement a continuous-time controller – for example, using analogue circuitry – the use of digital controllers is now almost universal. The greater flexibility of digital systems is a factor here: simply by making software changes, the control logic can be changed completely.

A consequence of using digital control is that the control actions are calculated and updated on a discrete time step, rather than in continuous time. Control algorithms designed in continuous time must therefore be converted to discrete time for implementation in a digital controller. It is also possible to design controllers in discrete time, if the linearised model of the turbine is first discretised.

The following sections briefly describe some of the practical issues involved in implementing a control algorithm in a real digital controller. Once again, the reader is referred to standard control theory texts for more detailed treatments.

8.6.1 Discretisation

Supposing a control algorithm has been designed in continuous time as a transfer function (such as Eq. (8.1) for a PID controller, for example), it must be discretised before it can be implemented in a digital controller. Discretised transfer functions are usually represented in terms of the delay operator, z , where $z^{-k}x$ represents the value of x sampled k timesteps ago. As a simple example, a moving average or first order lag filter from x to y is often implemented as

$$y_k = Fy_{k-1} + (1 - F)x_k \quad (8.42)$$

This is a difference equation that can readily be implemented in code in a discrete controller. In terms of the delay operator, it can be written as

$$(1 - Fz^{-1})y = (1 - F)x \quad (8.43)$$

or alternatively as a transfer function consisting of a ratio of polynomials in z^{-1} :

$$y = \frac{(1 - F)}{(1 - Fz^{-1})}x \quad (8.44)$$

Now the Laplace operator can be considered as a differentiation operator, and so as a simple approximation, it might be possible to convert a continuous transfer function into discrete form by replacing s by $(1 - z^{-1})/T$, where T is the timestep.

In fact by simple algebraic manipulation, it is straightforward to show that with this substitution, the above discrete transfer function is in fact equivalent to the continuous transfer function representation of a first order lag with time constant τ , namely

$$y = \frac{1}{1 + s\tau} x \quad (8.45)$$

with the factor F being given by $\tau/(T + \tau)$.

Clearly any discretised equation can only be an approximation to the continuous-time behaviour. There are other discretisation methods, and the so-called ‘bilinear’ or ‘Tustin’ approximation often works better in practice. In this case the Laplace operator is replaced by

$$\frac{2(1 - z^{-1})}{T(1 + z^{-1})} \quad (8.46)$$

Discretisation results in a phase shift compared to the continuous time process. This phase shift increases with frequency. If the algorithm performance is particularly sensitive to the phase shift at a certain frequency, then the discretisation can be ‘pre-warped’ to this frequency. Pre-warping modifies the phase shift so that the phase of the discrete transfer function is correct at the chosen frequency, but deviates at lower and higher frequencies. An example of a situation where pre-warping may be important is in the case of a drive train resonance damper in a variable-speed turbine (Section 8.3.5). The resonant frequency that is being targeted is usually fairly high, typically around 3 or 4 Hz, and unless the controller timestep is very short the phase lag caused by discretisation may significantly affect the performance of the damping algorithm.

The approximation for s used for discretisation with pre-warping about a frequency ω is

$$\frac{\omega}{\tan(\omega T/2)} \frac{(1 - z^{-1})}{(1 + z^{-1})} \quad (8.47)$$

8.6.2 Integrator desaturation

Controllers containing integral terms, such as PI or PID controllers, experience a particular problem known as integrator wind-up when the control action saturates at a limiting value. A common example is in pitch control, where the pitch angle is limited to the fine pitch position when the wind is below rated. For example, a PI pitch controller for a variable-speed turbine can be represented as in Figure 8.20.

Above rated wind speed, the speed error will be zero on average because of the integral term. Below rated, the pitch saturates at the fine pitch position, and the speed error will remain negative. The integral of the error will therefore grow more and more negative, and only the application of the limits prevents the actual pitch demand from doing the same.

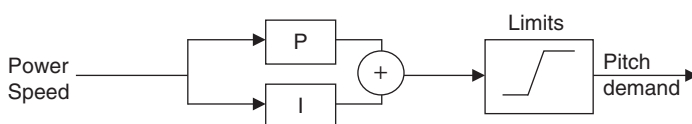


Figure 8.20 Limits applied to a PI controller

However, when the wind speed reaches rated again and the speed error becomes positive, it will take a long time before the integrated power error climbs back up to zero and starts to demand a positive pitch angle. To prevent this problem of integrator wind-up, the integral term must be prevented from integrating when the pitch is at the limit. This is easily implemented by separating out the integrator, $I(z)$, from the rest of the controller, $R(z)$. $R(z)$ generates a change in demanded pitch angle, and $I(z)$ then integrates this by adding it to the previous pitch demand *after* the limits have been applied.

As an example, a PI controller [Eq. (8.31)] discretised using the bilinear approximation would be

$$y = K_p[(T/2T_i + 1) + (T/2T_i - 1)z^{-1}] \cdot \frac{1}{[1 - z^{-1}]} \cdot x = R(z) \cdot I(z) \cdot x \quad (8.48)$$

To avoid integrator wind-up, this can be implemented as follows:

$$\Delta y_k = K_p[(T/2T_i + 1)x_k + (T/2T_i - 1)x_{k-1}] \text{ (implementation of } R(z))$$

$$y^*_k = y_{k-1} + \Delta y_k \text{ (integrator } I(z) \text{ using previous limited output } y_{k-1})$$

$$y_k = \lim(y^*_k) \text{ (application of limits)}$$

References

- Anderson, B.D.O. and Moore, J.B. (1979). *Optimal Filtering*. Prentice-Hall.
- Astrom, K.J. and Wittenmark, B. (1990). *Computer-Controlled Systems*. Prentice-Hall.
- Bossanyi, E.A. (1982). Probabilities of sudden drop in power from a wind turbine cluster. Proceedings of the 4th International Symposium on Wind Energy Systems, Cranfield, England (21–24 September 1982).
- Bossanyi, E.A. (1987). Adaptive pitch control for a 250 kW wind turbine. In: *Proc. 9th BWEA Conference, Edinburgh*, 85–92. Mechanical Engineering Publications.
- Bossanyi, E.A. (1994). Electrical aspects of variable speed operation of horizontal axis wind turbine generators. *ETSU W/33/00221/REP*, Energy Technology Support Unit, Harwell, UK.
- Bossanyi, E.A. (2000). Developments in closed loop controller design for wind turbines. Proceedings of the 2000 ASME Wind Energy Symposium, Reno, Nevada.
- Bossanyi, E.A. (2003). Individual blade pitch control for load reduction. *Wind Energy* 6 (2): 119–128.
- Bossanyi, E.A. (2004). Developments in individual blade pitch control. Proceedings of the EWEA conference ‘The Science of Making Torque from Wind’, Delft University of Technology (19–21 April 2004).
- Bossanyi, E. (2019). Optimising yaw control at wind farm level. *J. Phys.: Conf. Ser.* 1222: 1, 12023.
- Bossanyi, E., Delouvré, T., and Lindahl, S. (2013). Long-term simulations for optimising yaw control and start-stop strategies. Proceedings of the European Wind Energy Conference, Vienna.
- Bossanyi, E., Fleming, P., and Wright, A. (2012a). Validation of individual pitch control by field tests on two- and three-bladed wind turbines. Special issue on control in wind energy. *IEEE Trans. Control Syst. Technol.* 21 (4): 1067–1078.
- Bossanyi, E.A. and Gamble, C.R. (1991). Investigation of torque control using a variable slip induction generator, *ETSU WN-6018*, Energy Technology Support Unit, Harwell, UK.
- Bossanyi, E.A. and King, J. (2012). Improving wind farm output predictability by means of a soft cut-out strategy. Proceedings European Wind Energy Conference, Copenhagen, EWEA 2012.
- Bossanyi, E.A., Kumar, A., and Hugues-Salas, O. (2012b). Wind turbine control applications of turbine-mounted LIDAR. *J. Phys.: Conf. Ser.* 555 (1): 12011.

- Bossanyi, E. and Wright, A. (2009). Field testing of individual pitch control. Proceedings of the European Wind Energy Conference, Marseille.
- Bossanyi, E., Wright, A., and Fleming, P. (2010). Progress with field testing of individual pitch control. Proceedings of the EWEA conference 'The Science of Making Torque from Wind', Heraklion (28–30 June 2010).
- Caselitz, P., Kleinkauf, W., Krüger, T. et al. (1997). Reduction of fatigue loads on wind energy converters by advanced control methods. In: *Proc. European Wind Energy Conference, Dublin*, October 1997, 555–558. European Wind Energy Association.
- Clarke, D. and Gawthrop, P. (1975). Self-tuning controller. In: *Proc. IEE 122, No. 9*, 929–934.
- Coleman, R.P. and Feingold, A.M., (1957). Theory of self-excited mechanical oscillations of helicopter rotors with hinged blades. *National Advisory Committee for Aeronautics Report 1351*.
- D'Azzo, J.J. and Houpis, C.H. (1981). *Linear Control System Analysis and Design*. McGraw-Hill.
- Donham, R.E. and Heimbolt R.L. (1979). Wind turbine. US Patent 4,297,076, filed 8 June 1979 and issued 1981.
- Fischer, T., Rainey, P., Bossanyi, E. and Kühn, M. (2010). Control strategies for an offshore wind turbine on a monopile under misaligned wind and wave loading. Proceedings of the EWEA conference 'The Science of making Torque from Wind', Heraklion (28–30 June 2010).
- Holley, W., Rock, S., and Chaney, K., (1999). Control of variable speed wind turbines below-rated wind speed. Proceedings of the 3rd ASME/JSME Conference, California.
- Knudsen, T., Andersen, P., and Töffner-Clausen, S. (1997). Comparing PI and robust pitch controllers on a 400 kW wind turbine by full-scale tests. In: *Proc. European Wind Energy Conference, Dublin*, October 1997, 546–550. European Wind Energy Association.
- Kragh, K.A., Fleming, P.A., and Scholbrock, A.K. (2013). Increased power capture by rotor speed-dependent yaw control of wind turbines. *J. Sol. Energy Eng.* 135 (3): 031018. <https://doi.org/10.1115/1.4023971>.
- Helen Markou and Torben J. Larsen (2009). Control strategies for operation of pitch regulated turbines above cut-out wind speeds. Proceedings of the European Wind Energy Conference, Marseille.
- Namik, H. and Stol, K. (2010). Individual blade pitch control of floating offshore wind turbines. *Wind Energy* 13: 74–85.
- Park, R.H. (1929). Two-reaction theory of synchronous machines. *Trans. AIEE* 48.
- Pedersen, T.K. (1995). Semi-variable speed – a compromise? In: *Proc. Wind Energy Conversion 1995, 17th British Wind Energy Association Conference, Warwick*, 249–260. Mechanical Engineering Publications.
- Pedersen, T.F. and Gómez Arranz, P. (2018). Spinner anemometer – best practice. *DTU Wind Energy E*, No. 165, https://backend.orbit.dtu.dk/ws/portalfiles/portal/149827433/DTU_E_0165_Spinner_Anemometry_Best_Practice.pdf.
- Ramtharan, G., Jenkins, N., Anaya-Lara, O., and Bossanyi, E. (2007). Influence of rotor structural dynamics representations on the electrical transient performance of FSIG and DFIG wind turbines. *Wind Energy* 10 (4): 293–301.
- Rossetti, M. and Bossanyi, E. (2004). Damping of tower motions via pitch control – theory and practice. Proceedings of the European Wind Energy Conference.
- Savini, B. and Bossanyi, E.A. (2010). Supervisory control logic design for individual pitch control. Proceedings of the European Wind Energy Conference.
- Eric Simley, Lucy Pao, Rod Frehlich, Bonnie Jonkman, and Neil Kelley (2011). Analysis of wind speed measurements using continuous wave LIDAR for wind turbine control. Proceedings of the 49th AIAA Aerospace Sciences Meeting, <https://arc.aiaa.org/doi/abs/10.2514/6.2011-263>.
- Steinbuch, M., (1989). Dynamic modelling and robust control of a wind energy conversion system. PhD Thesis, University of Delft.

- Stol, K. and Fingersh, L. (2004). Wind turbine field testing of state-space controller designs. *NREL/SR-500-35061*, National Renewable Energy Laboratory.
- van Engelen, T. and van der Hooft, E. (2005). Individual pitch control inventory. *ECN-C-03-138*.
- Vanni, F., Rainey, P.J., and Bossanyi, E. (2015). A comparison of control-based platform stabilisation strategies for floating wind turbines. Proceedings of the European Wind Energy Association Conference, Paris.
- Vasiljević, N., Lea, G., Courtney, M. et al. (2017). Long-range WindScanner system. *Remote Sens.* 8 (11): 896. <https://doi.org/10.3390/rs8110896>.

9

Wake effects and wind farm control

9.1 Introduction

As it extracts energy from the wind, a turbine leaves behind it a wake characterised by reduced wind speeds and increased levels of turbulence. Another turbine operating in this wake, or deep inside a wind farm where the effects of a number of wakes may be felt simultaneously, will therefore produce less energy and suffer greater structural loading than a turbine operating in the free stream. In a large wind farm, depending on the layout and the wind regime, 10–20% of energy production can easily be lost due to wake effects, and fatigue loads can increase substantially (see Chapter 12). These wake effects have to be taken into account when planning wind farm layouts, along with many other factors, for example,

- Topography (onshore), and its effect on wind speeds across the site.
- Variations in ground or seabed conditions for positioning the foundations.
- Cost of roadways (or turbine access offshore), grid connection, and other infrastructure.
- Cost of electrical interconnections, and energy losses in cables, etc.
- Site boundaries, and constraints due to land use, human activity, wildlife, etc.

The wake losses depend very much on inter-turbine spacings, and they vary with wind speed (through its effect on turbine thrust), wind direction (which determines which wakes affect which turbines), and turbulence intensity (which affects the rate of wake dissipation) as well as atmospheric stability. When the wind is blowing along a closely spaced row of turbines, the energy losses from the row could be very high, so the layout design should try to ensure, taking account of the long-term wind speed and direction distribution for the site, that any large losses will occur infrequently.

The International Electrotechnical Commission (IEC) 61400 standard (IEC 61400-1 2019) includes guidelines for assessing the increased turbulence inside wind farms and

ensuring that design load limits will not be breached. This may result in the need for stronger, more expensive turbines or support structures to achieve a given lifetime. Maintenance costs may also be increased because of higher turbulence within the wind farm.

Because of the importance of wake effects in reducing energy production and increasing loads, there has been much interest in recent years in the concept of minimising wake effects through a form of wind farm control also known as *active wake control* or *wind farm flow control*. Instead of allowing each turbine to behave as designed, to achieve the best combination of energy production and loading for itself (sometimes known as *selfish* or *greedy control*), the concept is that the wind farm controller commands changes to the operation of individual turbines to achieve the optimum performance for the wind farm as a whole. This will mean that in any particular wind condition, the performance of some turbines will be sacrificed to improve the performance of others, such that the overall performance of the wind farm is optimised. This kind of wind farm control has been discussed for at least 25 years (Spruce 1993), but the recent focus on optimisation of wind farm management has started to arouse serious commercial interest in such techniques.

This chapter describes wake characteristics and how they can be modelled, and Section 9.3 goes on to explain different possible approaches to active wake control that are now beginning to be evaluated in commercial wind farms.

Finally, Section 9.4 briefly covers some other aspects of wind farm control, particularly in relation to the grid.

9.2 Wake characteristics

An operating wind turbine extracts energy from the wind flow, and also has a blocking effect on the flow. The wind exerts a thrust force on the turbine rotor, which can be equated to a reduction in the momentum flux. This means that the wind speed behind the rotor is reduced compared to the free-stream velocity (e.g. Vermeulen 1980) in a way that depends on the turbine thrust coefficient: the momentum extracted from the flow must equate to the total thrust force on the turbine. The physical mechanism by which the wake forms is very complex. Immediately around the blades, the aerofoil lift that is responsible for the rotor torque results in vorticity being shed into the flow. Tip vortices leave each rotating blade tip, forming vortex spirals that advect downstream. These vortices disturb one another, eventually breaking down into smaller eddies that result in a general increase in the turbulence of the flow. By the end of the near-wake region, about two diameters downstream, the effect of individual blades can no longer be clearly distinguished, and the wake has become approximately axisymmetric, with a velocity deficit that is largest at the centre, decaying towards the edges with a Gaussian-like profile, while the turbulence intensity is significantly higher than ambient.

From this point, the wake advects further downstream in a self-similar way: the shape of the velocity deficit profile is preserved, but it becomes wider and shallower: the velocity gradients at the sides of the wake result in entrainment of momentum from the surrounding flow, causing the wake to widen while maintaining the same overall momentum deficit. The entrainment increases with turbulence intensity, so in higher ambient turbulence the wake spreads faster.

The wake velocity deficit means that a downstream turbine operating in the wake will effectively experience a lower wind speed, causing a reduction of power output, and a higher level of turbulence, causing higher mechanical loads. There may also be an increase in asymmetrical loads and fluctuating blade loads due to velocity gradients across a downstream turbine rotor when it is partially immersed in a wake whose centreline passes some distance from the rotor centre.

The wake behind a turbine cannot simply be represented by a static velocity deficit field extending downstream in the prevailing wind direction. Firstly, the wake centreline may be displaced laterally by any yaw misalignment of the turbine, and vertically because of rotor tilt and wind shear. Secondly, there is the phenomenon of wake meandering: low-frequency variations in lateral and vertical components of turbulence can be considered to push the wake centreline around, so that the wake immersion of a downstream turbine varies, along with the effect on power production and loads.

9.2.1 Modelling wake effects

A wind farm is a highly complex physical system. Detailed modelling of the system is required to understand the complex atmospheric and wake flows and the resulting behaviour of turbines in sufficient detail to allow accurate estimation of wake losses and realistic practical design of active wake controllers for wind farms. High-fidelity flow models based on computational fluid dynamics (CFD) can capture most of the relevant detail by solving the Navier–Stokes equation with suitable turbulence modelling, but they may require large computational resources. At the other end of the scale, semi-empirical engineering models requiring minimal computational power are essential tools for designing and testing wind farm controllers, although some of them may require tuning for different conditions.

9.2.2 Wake turbulence in the IEC standard

Deep inside a wind farm, the reduction in wind speed and the increase in turbulence intensity are the result of the superposition of wakes from many upwind turbines. Frandsen and Thøgersen (1999) and Frandsen (2007) propose a model based on the geostrophic drag law that takes into account the additional ‘surface roughness’ caused by the turbines themselves. This leads to a formula for added turbulence above hub height:

$$I_{++} = \frac{0.36}{1 + 0.2\sqrt{s_1 s / C_T}} \quad (9.1)$$

where s_1 and s are the inter-turbine spacings, normalised by rotor diameter, within a row and between rows, and C_T is the turbine thrust coefficient. Because this does not apply below hub height, the average added turbulence intensity I_+ is then calculated as

$$I_+ = \frac{1}{2}(I_0 + \sqrt{I_0^2 + I_{++}^2}) \quad (9.2)$$

This general model appears to give conservative results, which may be appropriate in a design standard, but it does not account for the detailed effect of individual wakes on individual turbines, and is therefore unsuitable for evaluating detailed wind farm wake effects, including the effects of wind farm control. As from edition 4 of the standard, a

more detailed Gaussian wake meandering model is provided as an option. Section 9.2.4 provides details of this and other similar models.

9.2.3 CFD models

To model a system as complex as a wind farm, where multiple rotating turbines interact with an already highly complex atmospheric boundary layer, direct numerical solution of the Navier–Stokes equations is quite impractical, and simplifications are required. It is simply not practical to model the entire range of physical phenomena from large-scale atmospheric flows through the aerodynamics of turbine blades and down to the final decay of turbulent eddies into heat at the microscopic scale. The most sophisticated CFD models currently used in this area are large eddy simulations (LES), which solve the flow dynamics of the larger eddies while using simplifying approximations at the smaller scales. An example is the SOWFA code (Churchfield et al. 2012), which couples a LES flow model with embedded turbine models, allowing very detailed time-domain simulations of a complete wind farm to be carried out. However, a short simulation of a sizeable wind farm could require weeks of simulation time on a very powerful supercomputer. Rather than modelling the detailed flow around the turbine's aerofoils, a faster ‘actuator line’ approach is used where the lift and drag curves of the aerofoils are used to calculate ‘body forces’ which act mutually between the air flow and the turbine blade in the vicinity of a line representing the position of the blade as it rotates. Further simplifying the turbine to an actuator disk model, where the individual blades are not resolved, reduces the computational requirement even more, while still allowing many useful effects to be examined. It is possible to use an actuator disk with a non-uniform force distribution, for example if the rotor is yawed or the flow through it is non-uniform, and the ‘body forces’ can include both in-plane and out of plane forces, so the in-plane forces corresponding to rotor torque will impart a swirl to the flow.

Such an actuator disk model can also be used for the next level of approximation, the Reynolds-averaged Navier–Stokes (RANS) models, which do not track the evolution of individual eddies in the flow, but model only their averaged effect. Such models are fast enough to be used quite widely for steady-state calculations of wind farm performance, for example. Although much faster than LES, RANS models of sufficient accuracy still need to be run on a large cluster.

Detailed consideration of CFD models is beyond the scope of this book, but a general description and some further comments on the application of CFD models to wind turbine and wind farm flows are given in Section 4.7. The following sections describe some of the simplified engineering models that are essential for many practical applications – for example, if many repeat simulations are needed for tuning and evaluation of wind farm controllers.

9.2.4 Simplified or ‘engineering’ wake models

Owing to the huge computational resources required for CFD modelling, and especially for high-fidelity LES, the use of simplified wake models, sometimes referred to as ‘engineering’ models, remains widespread. Some of these originally date back to the 1980s or earlier, but continual improvements are still being made. There is a spectrum of models

from the purely empirical through to more physical models, including various simplifications of the Navier–Stokes equations.

Engineering wake models generally represent a single wake as a region of reduced wind speed and increased turbulence that is assumed to be embedded within the ambient flow, which is assumed to be otherwise unchanged by the presence of the turbines. They also require rules defining how to combine the wakes from more than one turbine, to give an effect representative of the multiple-wake situations occurring within a wind farm.

The wakes are typically defined as a static region behind the turbine, to which dynamic effects can be added when required, for example to represent wake meandering, where the wake is pushed around by low-frequency variations in the wind field, and the advection downstream of any changes in wake properties.

The following paragraphs explain how some of the common engineering models deal with each of these specific aspects.

Velocity deficit

The simplest model for the wake velocity deficit is the PARK or Jensen model (Katic et al. 1986). An area of uniform velocity deficit is defined immediately behind the rotor, with the same diameter as the rotor, such that the loss of momentum equals the turbine thrust; the radius of this deficit region then increases linearly with distance downstream, at a rate determined by an empirical ‘wake expansion factor’ k_w . The wake diameter at downstream distance x is $D_w = D + 2k_w x$ (where D is the turbine diameter) while the fractional velocity deficit δ decreases so as to conserve the momentum in the flow, according to

$$\delta = 1 - U_c/U_0 = (1 - \sqrt{1 - C_T})(D/D_w)^2 \quad (9.3)$$

where C_T is the turbine thrust coefficient (see Figure 9.1). The velocity immediately behind the rotor is $U_c(0)$, and U_0 is the free-stream velocity.

The Jensen model has been used quite widely for overall wake losses when the detailed nature of the wakes is not considered important, and works quite well as long as the wake expansion factor is selected by fitting to appropriate data.

For applications such as active wake control or understanding the loads of waked turbines, a model is required that provides a more realistic and detailed description of

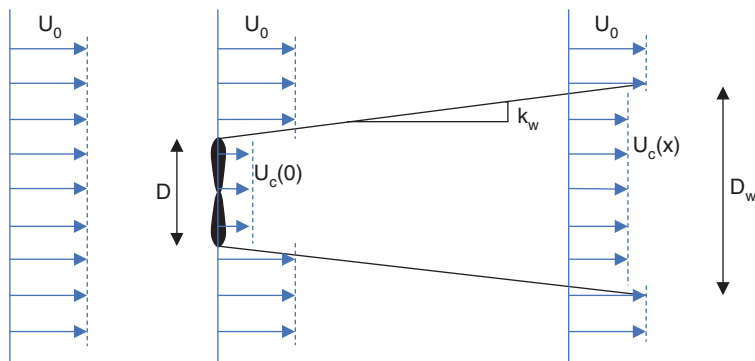


Figure 9.1 Diagram of the Jensen velocity deficit model.

the wake geometry. It is important to distinguish between the near-wake region where the tip vortices are interacting and breaking down and the flow is developing, and the far wake where the rotor detail can no longer be distinguished. Various modifications to the Jensen model have been proposed. For example, Gebraad (2014) uses a wake with three concentric regions, each with its own uniform velocity deficit, all of which change in diameter linearly with downstream distance: a near-wake core region that decreases in diameter until it disappears, a far-wake region that grows linearly from zero, and an intermediate mixing region. The expansion factors are empirically fitted, and the deficits change to conserve the total momentum. Such a model is implemented in the open-source FLORIS code (NREL 2019). This code also includes a more sophisticated model (Bastankah and Porté-Agel 2016) in which, like the earlier Ainslie (1988) model, the wake deficit profile in the far wake is assumed to reach a Gaussian profile that develops further downstream in self-similar fashion, growing weaker and broader as it decays. Figure 9.2 illustrates a typical velocity profile calculated using the Ainslie model.

The Ainslie model is based on a thin shear layer approximation of the RANS equation with the assumption of an axisymmetric wake:

$$U \frac{\partial U}{\partial x} + V \frac{\partial U}{\partial r} = -\frac{1}{r} \frac{\partial(r\bar{u}v)}{\partial r} \quad (9.4)$$

It uses an eddy viscosity model to relate the shear stress $\bar{u}v$ to the velocity gradient in the wake:

$$\bar{u}v = -\varepsilon \frac{\partial U}{\partial r} \quad (9.5)$$

where ε is known as the *eddy viscosity*, giving

$$U \frac{\partial U}{\partial x} + V \frac{\partial U}{\partial r} = \frac{\varepsilon}{r} \left(\frac{\partial U}{\partial r} + r \frac{\partial^2 U}{\partial r^2} \right) \quad (9.6)$$

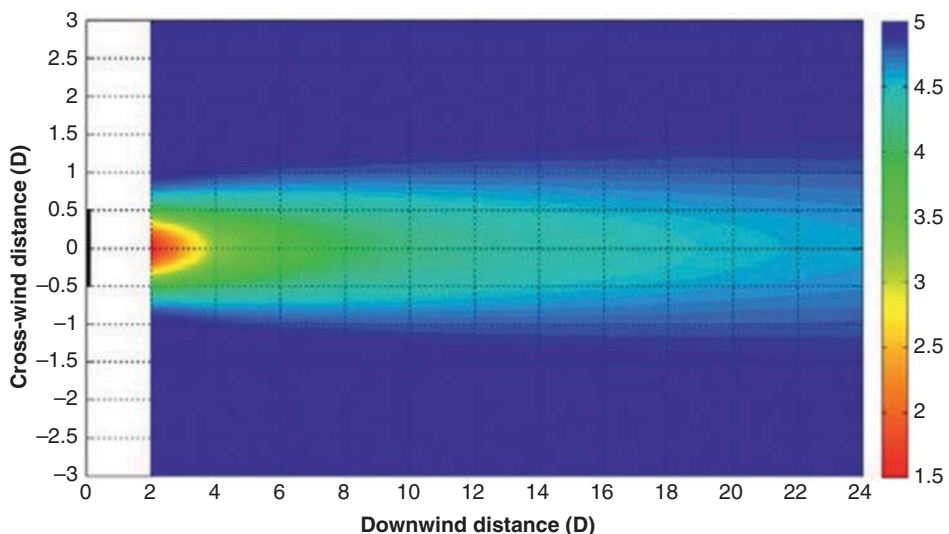


Figure 9.2 Typical Gaussian wake velocity profile from the Ainslie model.

The eddy viscosity is considered to have two contributions: one that is the product of a characteristic length scale and velocity scale, and one attributable to the ambient momentum diffusivity. Ainslie uses the wake width b as the length scale and the difference between the ambient and the wake centreline wind speeds as the velocity scale, and an ambient diffusivity term K_M :

$$\varepsilon = F[k_1 b(U_0 - U_c) + K_M] \quad (9.7)$$

where k_1 is a dimensionless constant. A value of 0.015 was originally suggested by Ainslie based on wind tunnel data, but other values have also been suggested. The factor F is 1 in the far wake but is assumed to be smaller in the near wake before the wake turbulence has built up. The ambient term depends on the friction velocity u_* and the height above ground, z :

$$K_M = \kappa u_* z / \varphi \quad (9.8)$$

where κ is the von Karman constant (0.4) and $\varphi = 1$ for neutral atmospheric stability. In these conditions, a logarithmic shear profile $U_0 = (u_*/\kappa) \ln(H/z_0)$ applies, giving

$$\varepsilon = F[k_1 b(U_0 - U_c) + \kappa^2 H U_0 / \ln(H/z_0)] \quad (9.9)$$

where H is the hub height. Using $\sigma_u \approx 2.5u_*$ from Section 2.6.3, and noting that $\kappa \approx 1/2.5$, we get a turbulence intensity of $I_0 = \sigma_u/U_0 \approx 1/\ln(z/z_0)$, which makes K_M proportional to the turbulence intensity:

$$\varepsilon = F[k_1 b(U_0 - U_c) + \kappa^2 H U_0 I_0] \quad (9.10)$$

Note that a dimensionless form of the eddy viscosity is often used, in which ε is normalised by dividing by the rotor diameter D and the wind speed U_0 :

$$\bar{\varepsilon} = F[k_1(b/D)\delta + \kappa^2(H/D)I_0] \quad (9.11)$$

where δ is the fractional centreline velocity deficit.

Such a definition of eddy viscosity has been used for many years in the WindFarmer code (DNVGL 2014) and other implementations of the Ainslie model, sometimes with the further approximation of $H \approx D$, although this can lead to inconsistencies (Gunn 2019).

In recent years, the importance of considering atmospheric stability has been increasingly recognised. Ruisi and Bossanyi (2019) proposed a stability-dependent model that has been found to fit experimental data well. The term φ in Eq. (9.8) above, which is 1 for neutral atmospheric stability, is replaced by the following expressions dependent on the Obukhov length L , from Högström (1988):

$$\begin{aligned} \varphi &= 1 \text{ (neutral case)} \\ \varphi &= 1 + 5H/L \text{ (stable case, } L > 0\text{)} \\ \varphi &= (1 - 19.3H/L)^{-0.25} \text{ (unstable case, } L < 0\text{)} \end{aligned} \quad (9.12)$$

Furthermore, the shear profile becomes $U_0 = (u_*/\kappa) \ln(H/z_0 + \psi)$ where the additional stability correction term ψ is also a function of L . According to Dyer (1974) and Högström (1988),

$$\psi = 0 \text{ (neutral case)}$$

$$\psi = -5H/L \text{ (stable case, } L > 0\text{)}$$

$$\psi = \ln \left[\frac{(1+x^2)(1+x)^2}{8} \right] - 2\arctan(x) + \pi/2 \text{ (unstable case, } L < 0\text{)} \quad (9.13)$$

where $x = \left(1 - \frac{19.3H}{L}\right)^{1/4}$. The normalised eddy viscosity can then be written as

$$\bar{\varepsilon} = F \left[k_1 \left(\frac{b}{D} \right) \delta + \frac{\kappa^2 H U_0}{\varphi \ln(H/z_0 + \psi)} \right] \quad (9.14)$$

although the effect of ψ is typically small.

Once the wake core and tip vortices have decayed, i.e. in the far wake region, the velocity profile in the wake can be assumed to have a Gaussian shape, according to

$$U = U_0 - \Delta U = U_0 \left(1 - \delta e^{-3.56 \left(\frac{r}{b} \right)^2} \right) \quad (9.15)$$

where U_0 is the ambient wind speed and δ the fractional centreline velocity deficit. This equation serves as a definition of the wake width b which has been used above in defining the eddy viscosity. The velocity profile then decays in self-similar fashion, i.e. maintaining its Gaussian shape but with the centreline deficit δ decreasing as the width b increases, so as to conserve momentum in the flow. Integrating the change in momentum flux per unit area $\rho U \Delta U$ over the area from $r = 0$ to infinity and azimuth angles from 0° to 360° , where ρ is the air density, we get the total change in momentum of the flow. Equating this to the rotor thrust $\frac{1}{2} \rho A U_0^2 C_T$ allows the Gaussian width parameter b to be calculated as a function of δ :

$$b = D \sqrt{\frac{3.56 C_T}{8\delta(1 - 0.5\delta)}} \quad (9.16)$$

where D is the rotor diameter, and C_T is constant because it represents the rotor thrust coefficient at the time this part of the wake was generated. Because momentum must be conserved, this equation must hold for all distances further downstream. All that remains is to calculate how δ changes with downstream distance.

As a starting point, a widely used empirical expression proposed by Ainslie (1988) gives the centreline velocity deficit two diameters downstream:

$$\delta_{(x=2D)} = C_T - 0.05 - (16C_T - 0.5)I_0/10 \quad (9.17)$$

The wake expansion further downstream is found by solving Eq. (9.4) using the eddy viscosity as defined above. Anderson (2009) derives a useful method for this. Given Eqs. (9.15, 9.16), only the development of the centreline velocity deficit is needed. The continuity equation

$$\frac{\partial U}{\partial x} = -\frac{1}{r} \left(r \frac{\partial V}{\partial r} + V \right) = -\frac{\partial V}{\partial r} - \frac{V}{r} \quad (9.18)$$

is valid for incompressible flow, and approaching the centreline, $\frac{\partial V}{\partial r} \rightarrow 0$ by symmetry, so $V = -r \frac{\partial U}{\partial x}$. Putting this into Eq. (9.4), then on the centreline where r and $\frac{\partial U}{\partial r}$ are both zero, we obtain for the centreline velocity U_c :

$$\frac{\partial U_c}{\partial x} = \frac{\varepsilon}{U_c} \left(\frac{1}{r} \frac{\partial U_c}{\partial r} + \frac{\partial^2 U_c}{\partial r^2} \right) \quad (9.19)$$

The derivatives on the right hand side are obtained from the Gaussian shape in Eq. (9.15). In non-dimensional form (normalising by U_0 and D), substituting these into the equation and looking only at the centreline, where $r=0$ and the exponential is 1, we see that the normalised centreline velocity $u_c = U_c/U_0 = 1 - \delta$ is defined by the following differential equation:

$$\frac{du_c}{dx'} = 16\varepsilon \frac{(u_c^3 - u_c^2 - u_c + 1)}{u_c C_T} \quad (9.20)$$

which can easily be solved numerically to give u_c and hence δ for any downstream distance $x = Dx'$. Equation (9.16) can then be used to obtain the Gaussian width parameter b at that point, and the wake velocity deficit is then fully defined.

Other Gaussian wake models have also been proposed, in which Eqs. (9.15, 9.16) remain true, but the downwind development of the centreline deficit is defined differently. The model of Bastankah and Porté-Agel (2016) for example uses a linear growth in the wake width with downstream position, beyond a near wake length x_0 (see below). Ishihara and Qian (2018) develops this further by parameterising the wake growth rate as a function of thrust coefficient and turbulence. These models are flexible in that they have empirical parameters that can be adjusted to fit measured data. The more parameters can be adjusted, the better the model can be made to fit the data, but it is not clear that there is a universally applicable parameter set.

Wake turbulence

In addition to the ambient turbulence and the shear-generated turbulence caused by the velocity gradient between the wake centreline and the ambient flow, the turbine itself generates additional turbulence directly, as a result of the tip vortices shed by the blades and the general disturbance to the flow caused by the blades, nacelle and tower. This ‘mechanical’ component of turbulence is of relatively high frequency, and decays relatively quickly: large eddies give rise to smaller ones, and so the turbulent energy moves to higher and higher frequencies until it is eventually dissipated as heat. A model from Bossanyi (1983) predicts a faster rate of decay in low winds and in high ambient turbulence intensities.

While the velocity deficit in a single wake can be reasonably well predicted as above, theoretical models for the turbulence level in the wake are less well developed. Wake turbulence is important, as it affects both the loads experienced by wake-affected turbines and the development of their own wakes, which is important in multiple-wake situations within wind farms.

Quarton and Ainslie (1989) examined a number of different sets of wake turbulence measurements, both in wind tunnels using small wind turbine models or gauze simulators, and behind full-size turbines in the free stream. An empirical formula for added

turbulence I_+ at a downstream distance x from the turbine was found to give a good fit to the various measurements:

$$I_+ = 0.048 C_T^{0.7} (100 I_0)^{0.68} (x/x_n)^{-0.57} \quad (9.21)$$

where C_T is the turbine thrust coefficient, I_0 the ambient turbulence intensity, and x_n the length of the near wake region. On the basis of further work, an improved expression was subsequently proposed by Hassan (1992):

$$I_+ = 0.057 C_T^{0.7} (100 I_0)^{0.68} (x/x_n)^{-0.96} \quad (9.22)$$

The added turbulence is defined as the square root of the additional wind speed variance normalised by the mean wind speed, i.e. $I_+ = \sqrt{I_{\text{wake}}^2 - I_0^2}$, where I_{wake} is the total wake turbulence intensity at any given downstream distance.

The length of the near wake region, x_n , is calculated according to Vermeulen (1980) in terms of the rotor radius R and the thrust coefficient C_T as

$$x_n = \frac{nR\sqrt{(m+1)/2}}{dr/dx} \quad (9.23)$$

where

$$m = 1/\sqrt{1 - C_T} \quad (9.24)$$

with C_T limited to a maximum of 0.96,

$$n = \frac{\sqrt{0.214 + 0.144m} (1 - \sqrt{0.134 + 0.124m})}{(1 - \sqrt{0.214 + 0.144m}) \sqrt{0.134 + 0.124m}} \quad (9.25)$$

and dr/dx is the wake growth rate, with three components:

$$dr/dx = \sqrt{\left(\frac{dr}{dx}\right)_a^2 + \left(\frac{dr}{dx}\right)_m^2 + \left(\frac{dr}{dx}\right)_\lambda^2} \quad (9.26)$$

where

$\left(\frac{dr}{dx}\right)_a = 2.5I_0 + 0.005$ is the growth rate contribution due to ambient turbulence,

$\left(\frac{dr}{dx}\right)_m = \frac{(1-m)\sqrt{1.49+m}}{9.76(1+m)}$ is the contribution due to shear-generated turbulence, and

$\left(\frac{dr}{dx}\right)_\lambda = 0.012B\lambda$ is the contribution due to mechanical turbulence, where B is the number of blades and λ is the tip speed ratio.

An alternative model, which generally gives similar results, is proposed by Crespo and Hernandez (1996):

$$I_+ = 0.73a^{0.8325} I_0^{0.0325} (x/D)^{-0.32} \quad (9.27)$$

for $x/D \geq 3$, or $0.724a$ for $x/D < 3$, where a is the induction factor, which is related to the thrust coefficient by

$$a = 0.5 (1 - \sqrt{1 - C_T}) \quad (9.28)$$

These empirical models for added turbulence are not useful in the near wake region. Equations (9.21, 9.22) are assumed to apply for $x/x_n > 1.5$, and Eq. (9.28) for $x/D \geq 3$, and the value is assumed to stay constant for smaller downstream distances.

Although these models provide a way to define a turbulence intensity in the wake region, this gives a rather simplistic view of what is actually a complex and inhomogeneous flow phenomenon. It assumes that the added turbulence can be modelled simply as an increase in the ambient turbulence intensity, which implicitly assumes that the length scales in the ambient turbulence are maintained, whereas in practice the added turbulence is likely to be generated with much shorter length scales. Also it does not say anything about the spatial distribution of the added turbulence. Usually a ‘top hat’ distribution is assumed, i.e. the added turbulence is found only in a cylindrical region behind the turbine, although this is clearly artificial. In WindFarmer, the radius of the cylinder is taken as b , whereas Bastankah effectively assumes $0.75b$. For a partially wake-immersed turbine, the turbulence distribution is averaged over the rotor area of the downstream turbine. For greater physical realism, Ishihara proposes a double-Gaussian function for the added turbulence distribution in the wake cross-section, with a peak value at the radius of each rotor tip, with the Gaussian half-width the same as for the velocity deficit.

The wake turbulence is important because it affects the loading of downstream turbines. Usually, the loading is simply characterised as a function of the total turbulence intensity, assuming the same loading as if the ambient turbulence intensity were increased to that value. However, this ignores various effects: the length scales may be shorter than for ambient turbulence, its characteristics may vary over the rotor, and the passage of blades through the non-uniform velocity field also contributes to the loading.

The wake turbulence is also important because it may affect the wake growth and dissipation. In the Ainslie model, the eddy viscosity is a function of turbulence, and the WindFarmer implementation, for example, assumes that the wake turbulence contributes to this, changing the wake development for waked turbines. In contrast, the Floris implementation of the Bastankah model assumes a linear growth rate that depends only on the ambient turbulence and is therefore no different for the wakes of turbines that are themselves wake affected.

Wake deflection due to yaw

It has been well established that when a turbine is not aligned with the wind direction, its wake is deflected to one side. The deflected wake follows a curved trajectory, with the deflection angle decreasing with downstream distance. This effect can be exploited for wake steering applications (see Section 9.3). The reason is that the thrust force remains approximately normal to the rotor, and therefore has a component perpendicular to the wind direction. Therefore, the wake motion must have a component perpendicular to the flow to conserve momentum. Jimenez (2010), by applying mass and momentum conservation to a suitable control volume, develops an expression for the angle α between the flow direction in the wake and the ambient flow direction, as a function of the lateral component of the thrust force f_z and the cross-sectional area A_w of the wake, assuming a uniform (Jensen) velocity deficit:

$$\alpha = -f_z / (\rho A_w U_0^2) \quad (9.29)$$

where ρ is the air density. Jimenez refers to α as the *skew angle*, but here we call it the *deflection angle*, to distinguish it from the skew angle χ in Chapter 4, which is the angle between the wake centerline and the rotor axis. Equation (9.29) assumes that the velocity deficit is small, and also that α is small, and it shows that the deflection angle decreases as the wake expands downstream. The lateral force, of course, depends on the thrust coefficient C_T and the yaw misalignment of the rotor, γ , but when the turbine is yawed, it is important to be clear about the definition of C_T . In general, $F = \frac{1}{2}\rho A C_T V^2$ but for yawed rotors, F might be the actual thrust force F_{\perp} , usually assumed exactly perpendicular to the rotor, or the force component in the wind direction, $F_{\perp} \cos \gamma$; likewise V might be the actual wind speed U_0 , or the component perpendicular to the rotor, $U_0 \cos \gamma$. This gives four possible definitions for C_T , and different authors use different definitions, sometimes implicitly. In Jimenez, F and V are both taken perpendicular to the rotor, so $C_T^{(J)} = 2F_{\perp}/\rho A(U_0 \cos \gamma)^2$ and the lateral force component is

$$f_z = -\frac{1}{2}\rho A C_T^{(J)}(U_0 \cos \gamma)^2 \sin \gamma \quad (9.30)$$

The wake deflection angle can then be expressed as

$$\alpha = \frac{C_T^{(J)} A}{2A_w} \cos^2 \gamma \sin \gamma \quad (9.31)$$

Using the linear wake growth rate k_w as in Figure 9.1, Gebraad derives the lateral centreline displacement by integrating the tangent of the deflection angle. Using a second order Taylor approximation, the resulting wake centreline displacement y_{γ} is given by

$$\frac{y_{\gamma}}{D} = \frac{\alpha_0}{30k_w} \left(\frac{[15\zeta^4 + \alpha_0^2]}{\zeta^5} - [15 + \alpha_0^2] \right) \quad (9.32)$$

where $\alpha_0 = \frac{C_T^{(J)}}{2} \cos^2 \gamma \sin \gamma$ and $\zeta = 1 + 2k_w x/D$ for downwind distance x . This expression is sometimes used for other (e.g. Gaussian) wake deficit models, by interpreting k_w simply as a tuning parameter that can be fitted to measured data.

Note that if this is done, it is especially important to consider which definition of C_T should be used for the wake deficit model when used in the yawed condition. When using the Ainslie model, for instance, it is reasonable to assume that the wake deficit is calculated using the momentum balance in the along-wind direction, meaning that in the definition of thrust coefficient, $F = \frac{1}{2}\rho A C_T V^2$, the force F and velocity V should both be measured in the along-wind direction – the use of the model for yawed rotors was not considered – so $C_T^{(A)} = \frac{2F_{\perp} \cos \gamma}{\rho A U_0^2} = C_T^{(J)} \cos^3 \gamma$ should be used for calculating the velocity deficit with the Ainslie model.

The thrust coefficient definition adopted by Bastankah is different again, using the actual thrust force and the actual wind speed: $C_T^{(B)} = \frac{2F_{\perp}}{\rho A U_0^2}$. Based on results from CFD calculations and wind tunnel tests, their paper deals explicitly with the wake of a yawed rotor, by assuming that a pair of counter-rotating vortices is created one above the other. The Gaussian wake deficit profile is modelled as elliptical, with the width parameter b [see Eq. (9.16)] in the vertical direction given by

$$b_v = D \sqrt{7.12} \sigma_v = D \sqrt{\frac{7.12(1 + \sqrt{1 - C_T^{(B)} \cos \gamma})}{8(1 + \sqrt{1 - C_T^{(B)}})}} \quad (9.33)$$

while in the horizontal direction it is reduced to $b_h = b_v \cos \gamma$, or $b_h = D\sqrt{7.12}\sigma_h$ where $\sigma_h = \sigma_v \cos \gamma$. The initial wake deflection angle is given by

$$\alpha_0 = \frac{0.3\gamma}{\cos \gamma} (1 - \sqrt{1 - C_T^{(B)} \cos \gamma}) \quad (9.34)$$

and this is assumed to be constant over the near wake length x_0 , so the lateral wake deflection a distance x downstream is $y_\gamma = \alpha_0 x$ for $x \leq x_0$, where

$$x_0 = \frac{D \cos \gamma (1 + \sqrt{1 - C_T^{(B)}})}{\sqrt{2} (2.32 I_0 + 0.154(1 - \sqrt{1 - C_T^{(B)}}))} \quad (9.35)$$

Further downstream ($x > x_0$), the lateral deflection is

$$y_\gamma = \alpha_0 x_0 + L_y \ln \left(\frac{\left(1.6 + \sqrt{C_T^{(B)}} \right) \left(1.6 S_y - \sqrt{C_T^{(B)}} \right)}{\left(1.6 - \sqrt{C_T^{(B)}} \right) \left(1.6 S_y + \sqrt{C_T^{(B)}} \right)} \right) \quad (9.36)$$

where $S_y = \sqrt{8\sigma_h \sigma_v / \cos \gamma}$ and $L_y = \alpha_0 D \sqrt{\cos \gamma / C_T^{(B)}} \left(2.9 + 1.3 \sqrt{1 - C_T^{(B)}} - C_T^{(B)} \right) / (14.7 k_w)$, where k_w is the linear wake growth rate.

A further effect of the vortex pair is to further increase the wake centreline deflection at hub height, making the wake deficit kidney-shaped rather than elliptical, an effect that has been observed in full-scale measurements by Fleming et al. (2018) using a rear-facing nacelle-mounted light detection and ranging (LiDAR). Fleming shows that on reaching a downstream turbine, the vortices cause the wake of that second turbine to deflect even if it does not have a yaw misalignment of its own. This effect, called *secondary wake steering*, could result in additional benefits from wake steering control. Altun (2019) and King et al. (2020) propose different ways to model this effect.

Wake superposition

Within a wind farm, a turbine may be subject to the wakes of several upstream turbines at the same time. If an engineering approach to wake modelling is used, a wake superposition model is needed to calculate the combined effect of several wakes on a downstream turbine. Several possible models are available in the literature:

Dominant wake model If a downstream wind turbine is subject to several wakes, only the wake with the greatest effect at the downstream turbine is considered (usually the nearest upstream turbine), and other wakes are ignored. The ‘greatest effect’ can be interpreted in different ways: usually the fractional velocity deficit integrated over the rotor area is used to choose the dominant wake, but the model can also be applied at each point in the rotor area, and the resulting deficit then integrated over the rotor area. The difference between these two approaches is likely to be small. Wake turbulence can be treated in the same way, with the highest wake turbulence (either rotor-integrated or point-by-point) being used. Usually the same wake will be dominant in terms of both deficit and added turbulence, but it is possible that the dominant wake for velocity deficit is not the same wake as the dominant wake for added turbulence. Wind farm measurements indicate that

dominant wake superposition works well for directly aligned turbine rows, but empirical ‘large wind farm’ corrections may be needed to achieve more general applicability.

Sum of deficits/momentum conservation Early models simply added together the fractional velocity deficits from all of the wakes at the downstream turbine position (again, either rotor-integrated or point-by-point approaches are possible). Some adjustment had to be made to prevent the sum of fractional deficits exceeding 1. Later authors, e.g. Bastankah, prefer to add together the absolute velocity deficits, i.e. the reduction in wind speed compared to the unwaked case: this is more consistent with the principle of momentum conservation. Even this can be applied in different ways: the absolute deficit for each wake can be measured relative to the free-stream wind speed, or relative to the incident wind speed at the turbine generating that wake (this is different because that turbine might itself be waked). The latter approach can be considered more consistent with the principle of momentum conservation, as well as being more physical in the sense that a waked turbine only experiences its own incident wind speed and does not ‘know’ what the free-stream wind speed is.

Product of deficits To get around the problem of the sum of deficits exceeding 1, some authors proposed multiplying together the fractional deficits. While this makes some intuitive sense, it does not have an obvious physical meaning.

Root-sum-square/energy conservation Based on the principle of conservation of kinetic energy, some authors propose summing the kinetic energy deficits expressed in terms of velocity squared. Katic et al propose summing the squares of velocity deficits: $(U_0 - U)^2 = \sum (U_0 - U_i)^2$ where the summation is over all wakes i . Gunn points out that for conservation of kinetic energy, we actually need to use $U_0^2 - U^2 = \sum(U_0^2 - U_i^2)$. As for momentum conservation, it may be more correct to use the turbine incident wind speed for U_0 rather than the free-stream wind speed. It can also be argued that it is more correct to conserve momentum rather than kinetic energy, because the latter model does not account for the change in turbulent kinetic energy that also occurs.

Other models Based on CFD simulations, Gunn et al. (2016) concluded that the dominant wake model for velocity deficit works well when the turbines are directly aligned, when a linear combination method greatly overestimates the deficit, but when the wake is off-centre, the linear combination model works better. Subsequently, Gunn (2019) proposes to use a root-sum-square model (though it could also be a linear combination model), coupled with a streamtube expansion model that modifies the wake when the turbines are closely aligned. The idea is that the diverging streamlines of the flow around the downstream turbine also cause the impinging wake to expand in a similar way. The combined model has a strong physical rationale and gives good results whether or not the turbines are aligned, possibly avoiding the need for the more empirical ‘large wind farm’ corrections. The wake expansion e for a directly aligned turbine can be calculated by momentum conservation from the downwind turbine’s induction factor (Eq. (9.28) above) as

$$e = D\sqrt{1-a} \left(\frac{1}{\sqrt{1-2a}} - 1 \right) \quad (9.37)$$

The width of the impinging wake is increased by this amount, and the velocity deficit is reduced correspondingly by momentum conservation according to Eq. (9.16). For misaligned turbines, Gunn proposes an approximation where the wake expansion e decreases as a Gaussian function (with empirically fitted parameters) of the distance from the rotor centre to the wake centreline.

Turbulence superposition A similar range of superposition models for added turbulence could be envisaged, and the choice can in principle be made independently of the velocity deficit superposition model, but this is an aspect that requires further development and experimental validation.

Wake meandering and advection

The engineering wake models described above generate a steady-state waked wind field behind one or a number of turbines. In reality, the wind flow is constantly varying, and the waked wind field will therefore also change with time. For example, low-frequency variations in the lateral and vertical components of wind speed can be considered to push the wakes around as if they are embedded in the underlying flowfield, a process known as *wake meandering*. Larsen et al. (2008) modelled this using a cascade of ‘instantaneous’ wake deficits being transported downstream at the longitudinal mean wind speed and pushed laterally and vertically according to low-pass filtered turbulent velocity components, where the low-pass filtering removes turbulent variations of wavelength shorter than two turbine diameters. Comparison to wind farm measurements in Larsen et al. (2013) indicate that this is a realistic approach. Such a model is also proposed in the recent editions of the IEC 61400 standard (IEC 61400-1 2019).

Ainslie (1988) proposes a meandering correction whereby the time-averaged wake width is increased by an amount depending on the standard deviation of the wind direction. In the LongSim model (Bossanyi 2018), this correction is applied in reverse, so that wake parameters tuned to 10 minute measurement data that includes the effect of meandering are adjusted to give a narrower, deeper instantaneous wake deficit suitable for dynamic time-domain simulations.

To use these wake models for time-domain simulations where the turbine thrust, yaw angle, etc. may be varying, the properties of the wake generated by the turbine will also change with time. Any change in the wake properties will advect downstream from the turbine. It is unlikely that the advection will occur at the mean wind speed, because the wind speed behind the turbine is reduced by the wake deficit itself. There is little information available in the literature to quantify this effect; de Mare (2015) reviews some results, suggesting that the advection speed may be around 80% of the free wind speed, but that it also depends on turbulence and downstream distance. Also, by analogy with wake meandering, low frequency longitudinal turbulent variations can be expected to play a part.

9.2.5 Wind farm models

As mentioned above, CFD (both LES and RANS) models can be used to simulate the behaviour of an entire wind farm including atmospheric and wake flows. Some, by coupling to multiple instances of an aeroelastic turbine model, can simultaneously model the

flows and the detailed structural and control dynamics of the turbines. Such ‘high-fidelity’ models are computationally very expensive to run, so faster models incorporating the engineering wake models described above have been developed, which are much more practical to use for designing and testing wind farm controllers. Generally, the wakes are simply embedded in the underlying ambient flow field, which is assumed to be otherwise unchanged by the presence of the turbines. While the representation of the flow may be greatly simplified, it is adequate for many applications, and in some cases the turbine may still be modelled to a high level of fidelity. It is clearly important to choose an appropriate model based on the accuracy to which different features need to be represented, which is very dependent on the specific application.

An early engineering wind farm model, SimWindFarm (Grunnet et al. 2010) was developed as part of the Aeolus research project. The wind field consists of time series generated at each turbine location according to the spectra and spatial correlations of the IEC standard, with constant mean wind speed and direction, into which Jensen wake effects (Figure 9.1) are embedded. The turbine is represented by a simplified aeroelastic model with aerodynamic lookup tables, and some drive train and tower structural degrees of freedom so that fatigue loads can be represented to some extent. The LongSim model (Bossanyi 2018) is similar in its basic concept, but with a number of extensions. The mean wind speed and direction may vary according to measured site conditions, so the model can test the ability of a controller to track realistically changing conditions, and a range of different wake models and features is available, such as those described above. The turbine controller, including supervisory control, is modelled in detail, and the model has also been linked to a grid simulator (Bossanyi et al. 2020) to allow tuning and evaluation of controller features to provide grid ancillary services such as fast frequency regulation. Turbine loads are estimated from a database of pre-calculated results from the Bladed aeroelastic code.

Other models attempt an intermediate level of fidelity on the flow field using different levels of simplification of the Navier–Stokes equations. As an example, the eddy viscosity formulation as used in the Ainslie wake model can be extended to cover the whole wind farm. Some examples of intermediate-fidelity models include FarmFlow, Fast.Farm, and WFSim, all of which, as well as SimWindFarm and LongSim mentioned above, are described in Bossanyi et al. (2018).

This report also includes the high-fidelity model SOWFA, mentioned above, which uses LES for the flow simulation and can include full structural and controller dynamics and resolve the motion of individual turbine blades, which allows turbine loads to be computed. Other high-fidelity models include PALM and Ellipsis3D – see Andersen (2015).

9.3 Active wake control methods

Active wake control means optimising the control set-points of each turbine to achieve optimum overall performance of the wind farm. The optimum may involve energy, loading, and other considerations, as explained in Section 9.3.2.

9.3.1 Wake control options

The principal types of active wake control are described in the following sections.

Conventional sector management

A simple approach, which has been used for many years on some wind farms where wake effects are sometimes problematic, is to switch off some turbines when they are heavily wake affected (for example, every other turbine along a closely spaced row) to prevent excessive fatigue loading or vibration. Clearly this results in a significant loss of energy production, and is unlikely to be an optimal solution.

An understanding of the wake interactions can be used to pre-determine the best combination of turbines to switch off in any given wind condition. However, reducing power on some turbines is likely to be a better solution than shutting them down.

Axial induction control

By changing the operation of an upstream turbine to reduce its thrust force, the wake effect is reduced. A turbine downstream will see increased power production, but this must be balanced against the reduced power production at the upstream turbine. Whether the total power is increased or reduced depends on the details of the situation. The downstream turbine will see reduced turbulence, so most fatigue loads are likely to decrease, although some may increase due to the increased wind speed. With many turbines interacting in this way, the determination of the optimal thrust for each turbine is far from trivial.

There are different ways in which the turbine controller can be made to reduce rotor thrust. The most straightforward way is to increase the pitch angle, while maintaining the same rotor speed. Some change in rotor speed may be desirable though, to minimise the power loss for any given thrust reduction – see Section 9.4.1.

Wake steering control

Any yaw misalignment of the turbine results in a lateral force on the turbine, which by conservation of momentum implies that the wake must move sideways – see Section 9.2.4. This gives rise to the concept of wake steering control, whereby the yaw misalignment of each turbine is adjusted to move its wake away from downstream turbines, as shown schematically in Figure 9.3. The upstream turbine experiences lower power and some higher fatigue loads due to asymmetrical flow across the rotor (unless mitigated by individual pitch control; see Section 8.3.9), as well as some reduced loads due to lower thrust, while the downstream turbine may see an increase in power and possibly reduced loads. As for induction control, optimisation of yaw offsets across a wind farm is clearly not trivial. Whether a particular turbine is yawed or is wake-affected changes with wind direction, so the lifetime effect on loads depends on the long-term frequency distribution of wind conditions.

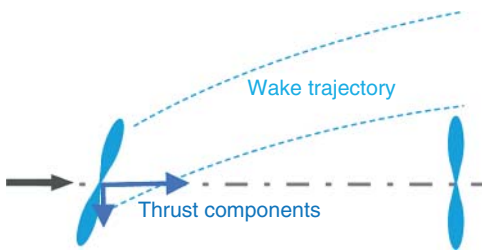


Figure 9.3 Wake steering control by yawing (schematic).

Combining axial induction and wake steering control

In general, it would be desirable to combine induction control and wake steering, by optimising the thrust and yaw set-points simultaneously to achieve an overall optimum (Bossanyi 2018). The optimisation process automatically determines which set-points to change on each turbine.

Other possibilities

Apart from axial induction control and wake steering, some other control concepts have been suggested, but these are very speculative at this stage. An interesting contender is to dynamically vary the turbine thrust to cause enhanced wake dissipation. While this must add to fatigue loading, the frequency at which the thrust should be varied is actually rather low (Munters and Meyers 2018), so an overall benefit may be possible. Another possibility is to use individual pitch control to disturb the wake and increase wake dissipation (Frederik et al. 2020), causing increased variations in asymmetric loads but not in overall thrust.

9.3.2 Control objectives

The ultimate aim of wind farm wake control is to improve the economics of a wind power plant. This is conventionally measured in terms of the levelised cost of energy (LCoE), essentially the sum of all capital, operating, and end-of-life costs (discounted to a fixed point in time) divided by the lifetime energy production – see Appendix A12. Wind farm control may affect the LCoE in several ways:

- Higher energy capture.
- Management of fatigue loading.
- Better management of grid ancillary services provision.

This section expands on these three objectives. In principle, the objectives can be combined by including appropriate variables (power, fatigue loads, etc.) with suitable weightings (e.g. reflecting the economic importance of each term) into a merit function, and the control design is then carried out with the aim of optimising this merit function. Control design methods are outlined in Section 9.3.3.

Higher energy capture

This is often seen as the primary objective of wind farm control, as it is easily quantified, given the electricity price, and feeds through directly to cost-effectiveness: in principle, each 1% increase in energy production reduces the LCoE by 1%. However, it may be hard to achieve, because the control action on any one turbine reduces its power output, so the overall power output can only increase if the power losses on some turbines are outweighed by gains on others. This is a subtle trade-off, depending on inter-turbine spacing and detailed wake behaviour, which can change with meteorological conditions: not just wind speed and direction but also atmospheric stability through its influence on turbulence, wind shear, veer, and boundary layer height. Confidence in the predicted changes in energy capture therefore depends critically on the accuracy of the models used.

Management of fatigue loading

Significant additional fatigue loading is caused by high levels of wake turbulence and the wind gradients resulting from partial wake immersion. The extra loading may affect many components, including blades, hub, bearings, transmission system, yaw system, and tower. Induction control potentially leads to lower loads on all turbines, even though the reduction in turbulence and the increased wind speed may have opposing effects on wake-affected turbines. With wake steering control, load reductions on wake-affected turbines must be traded against increased asymmetrical loads on the yawed turbines, although there is the possibility to mitigate this using individual pitch control. Overall loading reductions may be quite significant, although a full understanding of loading on waked turbines within a wind farm requires detailed modelling.

However, the economic value of load reductions is harder to assess than changes in energy production. Some benefits may be realised in the pre-construction phase through changes in plant design, while others accrue post-construction.

Pre-construction benefits: Once there is sufficient confidence in the load reductions achievable with wind farm control, changes to the plant at the design stage could lead to a reduction in LCoE. If the load reduction is significant, then it may be possible to choose cheaper turbines, towers, or foundations, perhaps designed for a lower turbulence class, at least for some locations in the wind farm. Alternatively, the benefit could be taken by reducing the turbine spacing, allowing more turbines in a given area or reducing cabling/roadway costs.

Post-construction benefits: If the additional loading can be mitigated, this may lead to an improvement in reliability, resulting in reduced energy losses from downtime and/or a reduction in operation and maintenance costs. Reduced fatigue loading may also allow lifetime extension, so energy can be generated over a longer period.

Better management of grid ancillary services provision

Where the provision of certain grid ancillary services involves any modification to the active power output from the wind farm, the ability to control wake interactions may lead to improvements in the way these services are provided. For example, if a certain reduction in total power output is demanded, simply reducing power levels at all of the turbines by the required percentage will not have the desired effect, because wake effects will decrease and wind speeds will increase, leading to less power reduction than

requested. This can be corrected by feedback control, so that turbine power levels continue to be reduced until the desired total output is achieved. However, this may not be the optimal strategy in terms of turbine loads – it may be better to reduce power more at some turbines than at others, in such a way as to minimise fatigue loads generally, or at the most highly loaded turbines.

9.3.3 Control design methods for active wake control

Some different concepts for designing active wake controllers are outlined here, although only the first of these has so far been implemented at full scale on a wind farm. Such implementations are still at an experimental stage, and some examples are given in Section 9.3.4. These methods apply equally to induction control and wake steering.

Quasi-static open-loop or feedforward control

This is a relatively straightforward concept in which a database of optimal set-points for all of the turbines (for induction control, wake steering, or both together) is pre-calculated for a matrix of different wind conditions by optimising for each wind condition against a chosen merit function. Then during operation, given the wind condition at any time, the set-points for each turbine are obtained by interpolation from this set-point database. As a minimum, the wind condition should be defined in terms of wind speed, wind direction and turbulence intensity, although atmospheric stability may also be included. These wind conditions may be derived from measurements at a met mast if there is one on site. Generally, low-pass filtering should be applied so that the wind condition can be considered representative of the wind farm as a whole. Alternatively, it may be better to use SCADA data from the turbines (or at least those that are currently unwaked) to define or estimate the current wind condition. Many wind turbine controllers already include an estimation of rotor-average wind speed (without relying on nacelle-mounted anemometry), and direction can be obtained using the nacelle position measurement, as long as it is suitably accurate and well calibrated, and adjusted for any yaw misalignment using a filtered wind vane signal. A wind condition for the whole farm can then be estimated by combining measurement from all of the turbines.

This sort of control scheme is also referred to as an ‘advanced sector management’ strategy. If the optimisation of set-points can be carried out in real time, i.e. sufficiently rapidly compared to the rate at which wind conditions change (probably a few minutes or less), then it may not be necessary to pre-calculate optimal set-points for a wide range of conditions.

Because the set-points are calculated for a set of steady wind conditions, this form of control is called *quasi-static*, although any practical implementation is dynamic in the sense that it has to follow changing wind conditions. For wake steering, it is also important to consider that the optimal yaw set-point changes sign as the wind direction moves from one side to the other of the line joining adjacent turbines. This may require some form of hysteresis to decide when to flip to the other side. Sometimes yaw misalignments are restricted to one direction only, that in which some of the asymmetric loads are reduced rather than increased, but this must sacrifice some of the possible energy benefit.

Because wind conditions can never be known precisely and are never actually uniform across the whole farm, it is useful to account for the uncertainty in wind conditions

when designing the set-point schedule to use. An assumed uncertainty can be built into the optimisation process: for each wind condition, the optimum is calculated assuming a distribution of wind conditions around that central point, for example a multivariate Gaussian distribution with appropriate standard deviations for wind speed, direction, etc., although this makes the optimisation process much more time-consuming. As a pragmatic alternative, the set-point tables calculated for individual wind conditions can be ‘smeared’ by applying the Gaussian distributions post-hoc; although the theoretical justification is less rigorous, the result is very similar, and the smearing can then be adjusted dynamically according to the measurement uncertainties. Kern et al. (2019) describes how both approaches were used in the design of controllers used for field tests on a full-scale wind farm.

Such quasi-static control schemes might be expected to work reasonably well as long as the wind conditions vary relatively slowly in time, and are fairly homogenous over the wind farm area. Indeed, this may be the case for most of the time. However, to work satisfactorily, they are very reliant on the accuracy of the wake models on which they are based. For this reason, there is much ongoing research on more advanced dynamic closed-loop feedback control schemes.

Dynamic closed-loop feedback control

A dynamic closed-loop feedback controller attempts to use detailed measurements across the wind farm to keep track of the wakes and wind flows in real time, and use this information to make rapid adjustments to individual turbine set-points. If adequate measurement feedback is available, such a control scheme can compensate for inaccurate models, and have the potential to be much more reactive to rapid changes in conditions. Model based predictive control schemes have been proposed to continually re-calculate the control actions that will maximise the merit function over a short future time horizon, e.g. Vali (2019), although one problem here is the long wake propagation delay between a control action at one turbine and detection of its effect at the next downstream turbine. Measurements for feedback could include anything from turbine power and load measurements to LiDAR scans of the wind field to detect wake positions directly. High-definition measurement feedback gives the potential for much more dynamic response that should be less sensitive to inaccuracies in the underlying models.

Such control schemes are still at the research stage, and for a realistic practical application it is not yet clear how suitable different types of measurements might be for informing the required state estimation algorithms. Doekemeijer et al. (2018) present simulation results in which the states of a medium-fidelity wake flow model are estimated using the measured power at the turbines. Bertelé et al. (2019) use measurements of asymmetric rotor loads to detect the presence of a wake impinging on the turbine, and this information could be used to update modelled wake states. Raach (2019) simulates wake steering control where the wake trajectories are measured using scanning LiDAR.

Machine learning

Machine learning is a very generic term, and there may be scope for using it in a variety of ways as part of wind farm control. At one extreme, a pure ‘black box’ approach would dispense with any attempt to model the complex underlying physics and attempt to ‘learn’ by experimenting with set-point changes to converge on a control scheme that provides

a measurable benefit. At the other extreme, it could be used to enhance or adjust some of the more uncertain parameters in an underlying physics based model. This may be a more realistic target, possibly requiring much less training data before it starts to become useful.

9.3.4 Field testing for active wake control

The accuracy of models used to design and test active wake control is critically important; the results are often very sensitive to the details of the wake characteristics, which themselves vary significantly with different atmospheric conditions. To some extent, wind tunnel tests and high-fidelity LES models help to build more confidence in some aspects, but the remaining uncertainties are significant and can only be resolved by extensive and carefully designed field tests on full-scale wind farms. Only a small number of experimental tests have been conducted to date. In Kern et al. (2019), model validations against LES models, wind tunnel tests and full-scale field tests are described.

These tests must be carefully designed so that rather small increases in energy production can be identified in the presence of much noise, particularly in the sense of wind conditions varying significantly in both space and time, in ways that it is impractical to measure precisely. As for single turbine control, toggle tests are vital for this: the control action is switched on and off at regular intervals, long enough for wake changes to propagate through the farm, but short enough that the wind conditions are likely to be comparable during adjacent on and off periods. This toggling should then be maintained for long enough to get a statistically meaningful number of points in a suitably large range of wind condition bins (wind speed, direction, turbulence, stability, etc.). For some wind farms offshore or in simple homogeneous terrain, it may be possible to identify two very similar groups of turbines that can be assumed to see similar conditions, e.g. two adjacent straight parallel rows, in which case alternate toggling for each group can be used: one group is ‘off’ when the other is ‘on’, and the groups are switched at regular intervals. To gain enough data for a statistically meaningful result, such tests will probably have to continue for at least a few months. The data will inevitably be polluted by a host of real-world effects, which must be dealt with very carefully to guard against introducing any unintended biases.

Results from some of the more recent full-scale tests are starting to provide some convincing evidence for the viability of active wake control. Positive results with wake steering using three turbines on an onshore wind farm are presented by Fleming et al. (2020), while van der Hoek et al. (2019) report on a successful test of axial induction control on three rows of five to six turbines in an onshore wind farm. Kern et al. (2019) describe full-scale field tests on an onshore wind farm of 1.5 MW turbines: a wake steering controller was implemented on groups of three turbines, with results reported by Doekemeijer et al. (2020), and an axial induction control on a staggered row of nine turbines, with results reported by Bossanyi and Ruisi (2020).

9.4 Wind farm control and the grid system

At a simplistic level, wind power might be thought of as an uncontrollable resource because wind turbines can only produce as much power as is available to them from

the wind at any given time. In reality, however, there is much scope to optimise the use of wind plant by means of appropriate control. For example, appropriate control can reduce wake losses and increase energy capture, as well as mitigating the additional turbine loads caused by wake effects.

Now or in the future, a wind farm controller might be required to perform some or all of the following tasks:

1. Curtailment: reducing the output of the wind farm at times when the grid cannot accept all of the power, or of individual turbines to meet local environmental constraints such as noise.
2. Delta control: reducing the output by a given amount, to provide a reserve margin of power in case the grid suddenly requires it.
3. Fast frequency response (FFR): transiently adjusting the power output in response to variations in the grid frequency, to help stabilise the frequency.
4. Regulation of voltage and reactive power flow at the point of connection to the grid.
5. Grid forming and black start capabilities, to ensure that a grid with a large proportion of wind power would be capable of restarting after a system collapse.
6. Active wake control: modifying individual turbine control actions to manipulate wake interactions to optimise the performance of the wind farm as a whole.

Voltage and reactive power regulation involves controlling the turbine power converters and any STATCOMs (static var compensators), typically on millisecond timescales. This is largely independent of the other control actions, which are only concerned with the active power flow, as long as total current limits are not reached, as these depend on both active and reactive power. FFR has to act in timescales of around 0.1–10 seconds, while the other tasks act on timescales of seconds to minutes. The exception is the black start/grid forming capability, where the wind farm itself has to define the frequency, voltage and power flow as it starts up in isolation from the external grid – this is a new control mode, which is likely to become a requirement on systems with very high wind penetration.

The remainder of this section deals briefly with active power control features 1, 2, and 3 above. Active wake control (6) has already been covered in Section 9.3.

9.4.1 Curtailment and delta control

The output of wind farms may be curtailed for different reasons:

- The grid is unable to accept more than a certain level of power at a particular time, so any power exceeding a certain level has to be discarded.
- The grid cannot accept more than a certain rate of increase of power from a wind farm, so any power exceeding a certain ramp rate has to be discarded.
- The grid requires the wind farm to maintain a margin of power that can be called upon at short notice if required by the grid. ‘Delta control’ maintains power at a

variable level that remains below the potential amount of power available in the current wind conditions by a given margin.

- Environmental constraints: the output of one or more turbines has to be curtailed in certain wind conditions to limit noise or prevent shadow flicker at certain locations.
- Wake effects: for some wind directions, wake turbulence in rows of closely spaced turbines may lead to high fatigue loading at some wind speeds unless some of the turbines are stopped or their output curtailed.
- Other operational reasons: turbines may sometimes run at reduced output as a result of faults that may cause excess loading and that are awaiting maintenance action.

In most of these cases, the simplest way to curtail a turbine is to shut it down. This is often done, but often a better strategy is to reduce its power enough to achieve the desired effect. This avoids delays associated with restarting and fatigue associated with stop/start cycles, and can maintain higher wind farm output when the curtailment is not needed simply to reduce the power.

To reduce output without shutting down the turbine, the pitch angle has to be increased. Above rated, this is easily achieved by reducing the maximum power set-point; the pitch controller continues to regulate to the speed set-point and will automatically increase the pitch angle as needed. This can also happen below rated, although the speed set-point may reduce as the controller follows its torque-speed curve.

For delta control, the controller needs to have a wind speed estimate, so that it can calculate how much power it would have been producing, and subtract the delta to give a new power set-point. As an alternative to simply reducing the maximum power set-point, the current power demand can be set either directly or by changing the torque-speed curve that the controller is following in the variable-speed region. At the same time, the fine pitch limit is increased to maintain the desired rotor speed, which may be the same or different from the speed that would have been followed at that wind speed.

What to do with the rotor speed depends on the reason for the curtailment. For axial induction control of wake interactions (see Section 9.3), the aim is to reduce the rotor thrust while maintaining as much power as possible. This can be done by increasing the fine pitch and changing the torque-speed curve to maintain the optimum power coefficient for that pitch angle. This can be done as follows, using the C_P and C_T surfaces (as a function of tip speed ratio and pitch): for each fine pitch increment, calculate the tip speed ratio that maximises the power coefficient, and use Eq. (8.4) in Chapter 8 to calculate the optimal torque-speed curve, and at the same time calculate the reduction in C_P and the corresponding thrust coefficient C_T . This can be used to construct a look-up table, from which the desired fine pitch and torque-speed characteristic can be found for the desired C_T or the desired reduction in C_P (for delta control, this is calculated from the power delta and the estimated wind speed). If the aim is to reduce environmental noise, a similar strategy is likely to be suitable, as tip speed probably needs to be reduced as far as possible; similarly for reducing power export to the grid, as this strategy is likely to reduce loads.

However, if FFR is used in combination with delta control, it may be beneficial to allow the rotor speed to increase, to maximise the available rotor kinetic energy – see the next section.

There is increasing interest in hybrid power plants, where a wind farm may be combined with some form of energy storage, either electrical or by converting to gas. In this case, of course, curtailment would if possible be achieved by diverting the power into the storage medium while maintaining maximum available output from the wind turbines.

9.4.2 Fast frequency response

With a high penetration of renewables including variable-speed wind turbines, the increasing proportion of non-synchronous generation feeding into the grid through inverters, as opposed to conventional directly connected synchronous generators, causes grid system operators to worry about reduced system inertia and its effect on grid frequency stability. However, wind turbine controllers can easily be modified to provide FFR, so that the turbine can reduce as well as transiently increase its power production in response to measured grid frequency. This has the potential to mitigate this problem, and allow significantly greater penetration of wind energy on the system.

Changing the turbine power output by an amount proportional to the measured rate of change of frequency gives synthetic or emulated inertia, which is similar to true inertia except for the control loop delays, including the time required to measure the frequency (including filtering), and the actuation time for changing the power converter output. This is typically a fraction of a second, so this sort of response can help mitigate the sudden drop in frequency caused by, for example, the sudden tripping out of a major generator station or transmission line: the frequency nadir is typically reached in a few seconds, which is long enough for the synthetic inertia to have its effect. Alternatively, or in addition, the controller can demand a fixed power boost for a few seconds, which will also help to minimise the frequency dip. Below rated, the rotor will have slowed down to provide the extra power, so at some point it will have to recover, when the turbine will produce less power than it would have done. It is helpful if the controller can delay this recovery until the frequency has recovered a little (Bossanyi 2015), otherwise a second frequency dip might occur.

Synthetic inertia will also result in a continuous reduction in the normal frequency variations over time. Because the response is determined by the controller, other options are also possible, such as a droop response where the additional power is proportional to the frequency deviation, perhaps with a dead-band. Combining synthetic inertia and droop results in something like a PI controller. However, the integral term resulting from droop must not be allowed to persist indefinitely or the turbine will slow down too much.

Of course, if the turbine is running with delta control, then a more sustained power increase from FFR is possible, because the turbine has more power available in reserve.

A transient increase above rated power may be possible, depending on the current limit of the power converter, as long as it is not allowed to overheat.

References

- Ainslie, J.F. (1988). Calculating the flowfield in the wake of wind turbines. *J. Wind Eng. Ind. Aerodyn.* 27: 213–224.
- S B Altun (2019). Improving wake steering engineering models with wake deflection coupling effects. Wind Energy Science Conference, Cork.
- Andersen, S.J., Witha, B., Breton, S.-P. et al. (2015). Quantifying variability of large eddy simulations of very large wind farms. *J. Phys.: Conf. Ser.* 625: 012027.

- M Anderson (2009). Simplified solution to the eddy-viscosity wake model. *RES technical report 01327 000202*.
- Bastankah, M. and Porté-Agel, F. (2016). Experimental and theoretical study of wind turbine wakes in yawed conditions. *J. Fluid Mech.* 806: 506–541.
- Bertelè, M., Bottasso, C.L., and Cacciola, S. (2019). Brief communication: wind inflow observation from load harmonics – wind tunnel validation of the rotationally symmetric formulation. *Wind Energy Sci.* 4: 89–97. <https://doi.org/10.5194/wes-4-89-2019>.
- E A Bossanyi (1983). Windmill wake turbulence decay – a preliminary theoretical model. *SERI/TR-635-1280*, Solar Energy Research Institute, Golden, Colorado.
- E A Bossanyi (2015). Generic grid frequency response capability for wind power plant. Proceedings of the European Wind Energy Association Conference, Paris.
- Bossanyi, E. (2018). Combining induction control and wake steering for wind farm energy and fatigue loads optimisation. *J. Phys.: Conf. Ser.* 1037: 032011.
- Bossanyi, E.A. and Ruisi, R. (2020). Axial induction controller field test at Sedini wind farm. *Wind Energ. Sci. Discuss.* <https://doi.org/10.5194/wes-2020-88>.
- Bossanyi, E., Potenza, G., Calabretta, F., Bot, E., Kanev, S., Elorza, I., Campagnolo, F., Fortes-Plaza, A., Schreiber, J., Doekemeijer, B., Eguinoza-Erdozain, I., Gomez-Iradi, S., Astrain-Juangarcia, D., Cantero-Nouqueret, E., Irigoyen-Martinez, U., Fernandes-Correia, P., Benito, P., Kern, S., Kim, Y., Raach, S., Knudsen, T., and Schito, P. (2018). Description of the reference and the control-oriented wind farm models. *CL-Windcon Deliverable D1.2*, <https://ec.europa.eu/research/participants/documents/downloadPublic?documentIds=080166e5ba664d11&appId=PPGMS>.
- Bossanyi, E., D'Arco, S., Lu, L., Madariaga, A., de Boer, W., and Schoot, W. (2020). Control algorithms for primary frequency and voltage support. *TotalControl Deliverable no. D4.1*, <https://cordis.europa.eu/project/id/727680/results>.
- M J Churchfield, S Lee, and PJ Moriarty *et al.* (2012). A large-eddy simulation of wind-plant aerodynamics. Proceedings of the 50th AIAA Aerospace Sciences Meeting.
- Crespo, A. and Hernandez, J. (1996). Turbulence characteristics in wind-turbine wakes. *J. Wind Eng. Ind. Aerodyn.* 61 (1): 71–85.
- DNVGL (2014). WindFarmer theory manual version 5.3.
- Doekemeijer, B.M., Boersma, S., Pao, L.Y. *et al.* (2018). Online model calibration for a simplified LES model in pursuit of real-time closed-loop wind farm control. *Wind Energy Sci.* 3: 749–765. <https://www.wind-energ-sci.net/3/749/2018>.
- Doekemeijer, B.M., Kern, S., Maturu, S. *et al.* (2020). Field experiment for open-loop yaw-based wake steering at a commercial onshore wind farm in Italy. *Wind Energ. Sci. Discuss.* <https://doi.org/10.5194/wes-2020-80>.
- Dyer, A.J. (1974). A review of flux-profile relationships. *Boundary Layer Meteorol.* 7 (3): 363.
- Fleming, P., Annoni, J., Martínez-Tossas, L.A. *et al.* (2018). Investigation into the shape of a wake of a yawed full-scale turbine. *J. Phys.: Conf. Ser.* 1037: 032010. <http://stacks.iop.org/1742-6596/1037/i=3/a=032010>.
- Fleming, P., King, J., Simley, E. *et al.* (2020). Continued results from a field campaign of wake steering applied at a commercial wind farm: part 2. *Wind Energy Sci.* <https://doi.org/10.5194/wes-2019-104>.
- S Frandsen (2007). Turbulence and turbulence-generated structural loading in wind turbine clusters. *Risø R-1188*.
- Frandsen, S. and Thøgersen, M. (1999). Integrated fatigue loading for wind turbines in wind farms by combining ambient turbulence and wakes. *Wind Eng.* 23 (6): 327–339.
- Frederik, J., Doekemeijer, B., Mulders, S., and van Wingerden, J.-W. (2020). On wind farm wake mixing strategies using dynamic individual pitch control. *J. Phys.: Conf. Ser.* 1618: 022050. <https://iopscience.iop.org/article/10.1088/1742-6596/1618/2/022050/pdf>.
- P M O Gebraad (2014). Data-driven wind plant control. PhD thesis, Delft University of Technology.

- J Grunnet, M Soltani, T Knudsen, M Kragelund, and T Bak (2010). Aeolus toolbox for dynamic wind farm model, simulation and control. Proceedings of the European Wind Energy Conference, Warsaw.
- Gunn, K. (2019). Improvements to the eddy viscosity wind turbine wake model. *J. Phys.: Conf. Ser.* 1222: 012003.
- Gunn, K., Stock-Williams, C., Burke, M. et al. (2016). Limitations to the validity of single wake superposition in wind farm yield assessment. *J. Phys.: Conf. Ser.* 749: 012003.
- U Hassan (1992). A wind tunnel investigation of the wake structure within small wind turbine farms. *E/5A/CON/5113/1890*, UK Department of Energy, ETSU.
- van der Hoek, D., Kanev, S., Allin, J. et al. (2019). Effects of axial induction control on wind farm energy production – a field test. *Renewable Energy* 140: 994–1003.
- Högström, U. (1988). Non-dimensional wind and temperature profiles in the atmospheric surface layer: a re-evaluation. *Boundary Layer Meteorol.* 42 (1–2): 55–78.
- IEC 61400-1 (2019). *Wind energy systems – Part 1: Design requirements*. Geneva, Switzerland: International Electrotechnical Commission.
- Ishihara, T. and Qian, G.W. (2018). A new Gaussian-based analytical wake model for wind turbines considering ambient turbulence intensities and thrust coefficient effects. *J. Wind Eng. Ind. Aerodyn.* 177: 275–292.
- Jimenez, A., Crespo, A., and Migoya, E. (2010). Application of a LES technique to characterize the wake deflection of a wind turbine in yaw. *Wind Energy* 13: 559–572.
- I Katic, J Højstrup, and N O Jensen (1986). A simple model for cluster efficiency. Proceedings of the European Wind Energy Association Conference and Exhibition, Rome, pp. 407–410.
- Kern, S., Doekemeijer, B., van Wingerden, J.-W., Gomez-Iradi, S., Neumann, T., Wilts, F., Astrain, D., Aparicio, M., Fernandez, L., Campagnolo, F., Wang, C., Schreiber, J., Andueza, I., Bot, E., Kanev, S., Bossanyi, E., and Ruisi, R. (2019). Final validation report. *CL-Windcon Deliverable D3.7*, <https://ec.europa.eu/research/participants/documents/downloadPublic?documentIds=080166e5c8dba6cd&appId=PPGMS>, 2019.
- King, J., Fleming, P., King, R. et al. (2020). Controls-oriented model to capture secondary effects of wake steering. *Wind Energy Sci.* <https://doi.org/10.5194/wes-2020-3>.
- Larsen, G.C., Madsen, H.A., Thomsen, K., and Larsen, T.J. (2008). Wake meandering: a pragmatic approach. *Wind Energy* 11 (4): 377–395.
- Larsen, T.J., Madsen, H.A., Larsen, G.C., and Hansen, K.S. (2013). Validation of the dynamic wake meander model for loads and power production in the Egmond aan Zee wind farm. *Wind Energy* 16 (4): 605–624. <https://doi.org/10.1002/we.1563>.
- M de Mare (2015). Wake dynamics in offshore wind farms. PhD thesis, DTU Wind Energy PhD-0048 (EN).
- Munters, M. and Meyers, J. (2018). Towards practical dynamic induction control of windfarms: analysis of optimally controlled wind farm boundary layers and sinusoidal induction control of first-row turbines. *Wind Energy Sci.* 3 (1): 409–425.
- NREL (2019). FLORIS, v. 1.1.4, <https://github.com/NREL/floris>.
- D C Quarton and J F Ainslie (1989). Turbulence in wind turbine wakes. Proceedings of the European Wind Energy Conference '89, BWEA/EWEA.
- S Raach (2019). Lidar-assisted wake redirection control. PhD thesis, University of Stuttgart.
- Ruisi, R. and Bossanyi, E. (2019). Engineering models for turbine wake velocity deficit and wake deflection: a new proposed approach for onshore and offshore applications. *J. Phys.: Conf. Ser.* 1222: 012004.
- C J Spruce (1993). Simulation and control of windfarms. PhD thesis, University of Oxford.
- M Vali (2019). Model predictive control framework for power maximisation and active power control with load equalisation of wind farms. PhD thesis, Oldenburg University.
- P E J Vermeulen (1980). An experimental analysis of wind turbine wakes. Proceedings of the 3rd International Symposium on Wind Energy Systems, Copenhagen.

10

Onshore wind turbine installations and wind farms

There are certain additional activities that must be undertaken for any wind farm, including construction of the foundations and access roads, electrical connection, crane pads and lay-down areas for turbine erection, and project development and management. These are sometimes referred to as the *balance of plant* or *balance of system*. A typical breakdown is shown in Table 10.1.

Wind farm costs vary with the details of the project, and prices change with market conditions. Civil engineering costs are increased by poor ground conditions such as rock or very boggy soil and difficult access. High wind speed sites will give greater energy output but require more expensive foundations to withstand the increased extreme loads. Costs of the electrical grid connection are determined by the distance to the point of connection and the voltage level at which connection is made. The ex-works price of the turbines depends on the state of the market for wind turbines at the time the order is placed. Stehly and Beiter (2020) in a comprehensive study of the cost of wind energy estimate the breakdown of wind farm capital costs as wind turbines 68.8%, balance of system 22.6%, and financial 8.6%. An open-source, balance of system cost model tool (LandBOSSE) is available and is described in Eberle et al. (2019).

Commercial developers of wind farms often prefer larger projects because the costs that are largely fixed, such as grid connection, project development, and management, may then be spread over a bigger investment. A further encouragement for large projects is that the costs of arranging project finance can be high. However, there are individuals, community groups, and commercial organisations that develop smaller wind farms or projects with individual turbines, often with considerable local involvement. The advantage of community involvement in the project is that then there is increased public acceptance of the scheme, and planning permission is obtained more easily if it is seen that

Table 10.1 Typical breakdown of cost of an onshore wind farm (IRENA 2012).

Element of wind farm	% of total wind farm cost
Wind turbines	65–84
Construction and civil works	4–16
Grid connection	9–14
Project development and management	4–10

there is involvement of local people and there is benefit to the surrounding community (Warren and MacFadyen 2010).

10.1 Project development

The development of a wind farm follows a broadly similar process to that of any other power generation project, but with the particular requirements that the wind turbines must be located in high wind speed sites to maximise energy production and their size makes visual effects a particularly important aspect of the environmental assessment. Comprehensive guidance on the development of wind farms and many aspects of environmental assessment is given in (EWEA 2009; DCLG 2015).

Three main elements of the development of a wind farm project may be identified as (i) technical and commercial issues, (ii) environmental considerations, and (iii) public dialogue and consultation. Perhaps surprisingly to many engineers and technologists, the technical and commercial considerations are often the more straightforward and the success of a wind farm project hinges critically on environmental considerations and the dialogue and consultation process with local residents and planning authorities (Jones and Eiser 2010).

Wind farm development may be divided into a number of phases:

- Initial site selection.
- Project feasibility assessment.
- Preparation and submission of the planning (permitting) application.
- Construction.
- Operation.
- De-commissioning and land reinstatement.

Consideration needs to be given as to how the wind farm will be connected to the electrical network and also how the electrical energy will be sold. In many areas of good wind resource the population density is low and so the public electrical distribution system is weak and may need expensive and time-consuming reinforcement before generation can be connected to it. This situation is made worse if other wind farms are already connected to the circuits.

The sale of the electrical energy is straightforward in countries with a Feed-in Tariff but with other support mechanisms, such as a Renewable Portfolio Standard, it is necessary to identify a purchaser of the electrical energy as well as any Green Certificates if these are traded separately. Depending on the national support regime, it may be necessary to bid for government support perhaps through an auction for a Contract for Difference.

10.1.1 Initial site selection

Initially a desk study is carried out to locate a suitable site and to confirm it as a potential candidate for the location of a wind farm. It may be recalled that the electrical energy produced by a wind turbine, assuming 100% availability, is given by (see Section 3.16)

$$E = T \int P(U)f(U)dU \quad (10.1)$$

where E is the electrical energy generated, $P(U)$ is the power curve of the wind turbine, $f(U)$ is the probability density function (PDF) of the wind speed, and T is the time period.

The power curve is available from potential turbine supplier(s) while an initial estimate of the PDF of the wind speed may be obtained from a wind atlas (e.g. Troen and Petersen 1989; Rodrigo et al. 2020) or a database such as MERRA-2 (Bosilovich, Cullather, and National Centre for Atmospheric Research Staff 2019).

The PDF is often described by a Weibull distribution and takes account of regional climatology, roughness of the surrounding terrain, local obstacles, and topology. PDFs are calculated for 12 30° sectors and integrated with the power curve. Only an approximate indication of the wind farm output is required at this stage of the project development to confirm the potential of the site. However, it may be useful to supplement data from the wind atlas with initial computer modelling.

If measured site wind speed data is available then the energy yield of a wind turbine can be estimated as shown in Figure 10.1. The binned wind speeds (Figure 10.1a) are multiplied by the power curve (Figure 10.1b) to give the energy generated (Figure 10.1c). This simple process is shown in Eq. (10.2):

$$\text{Energy} = \sum_{i=1}^{i=n} H(U_i)W(U_i) \quad (10.2)$$

where $H(U_i)$ is the number of hours in wind speed bin U_i , $W(U_i)$ is the power output at that wind speed and there are n wind speed bins

In addition to estimating the wind resource it is necessary to confirm that road access for transporting the turbines and other equipment is suitable, or can be developed at reasonable cost. Blades of large onshore wind turbines can be more than 50 m long and so pose difficulties for transport on minor roads. For a large wind farm with a substation located at the site, the heaviest single piece of equipment is likely to be the main transformer.

The local electricity utility should be able to provide information on the amount of generation that the distribution network can accept although for a first approximation it may be useful to consider rules-of-thumb as shown in Table 11.5. Such rules-of-thumb give approximate guidance only and ignore the effect of any other wind farms or other

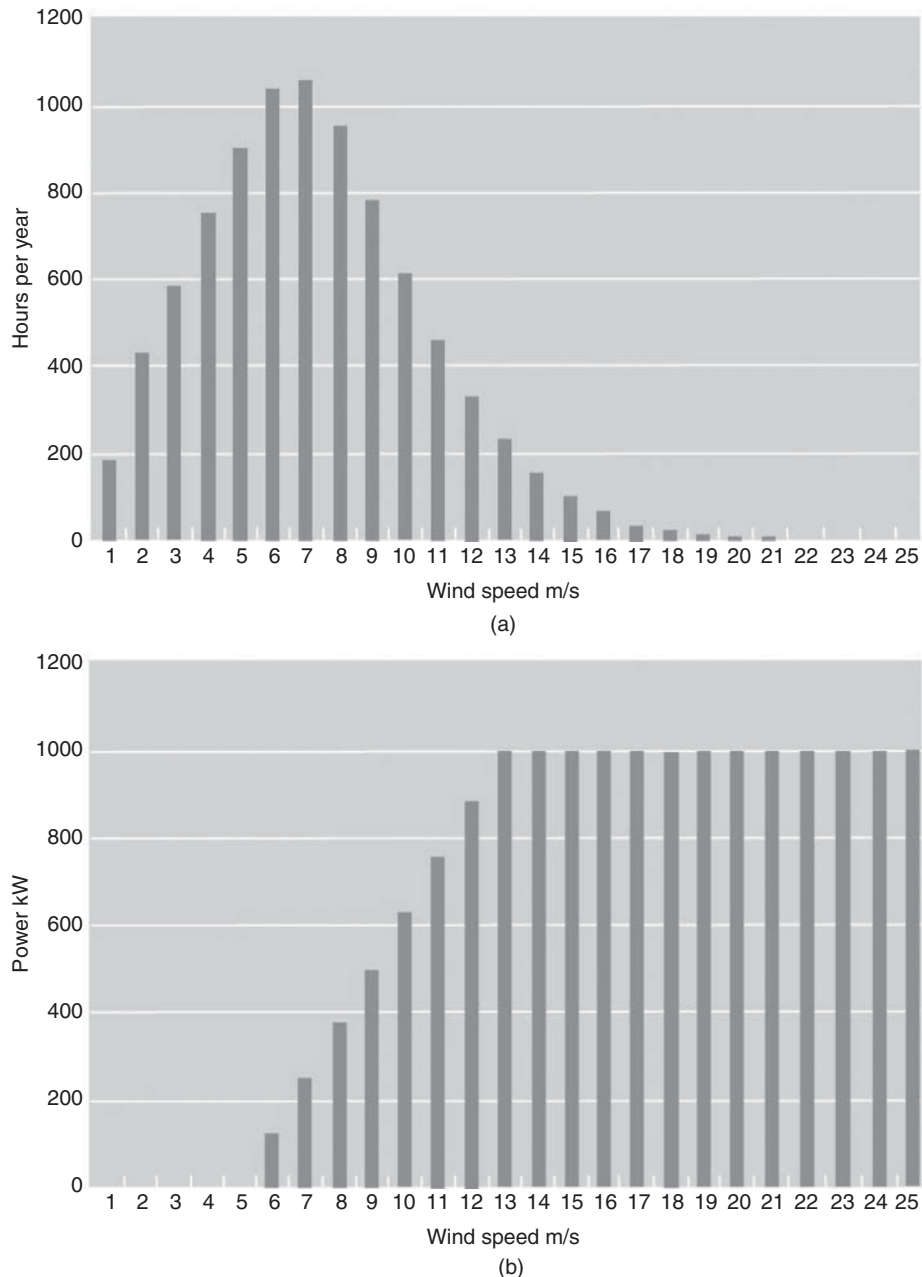


Figure 10.1 (a) Binned PDF of wind speed. (b) Power curve at each wind speed bin. (c) Energy generated at each wind speed bin. Annual energy calculation of a wind turbine.

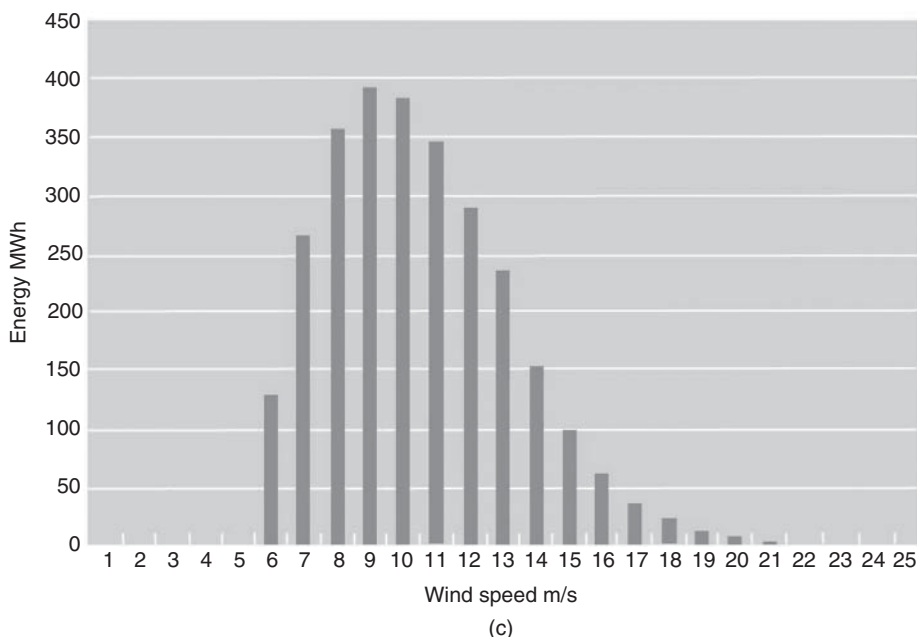


Figure 10.1 (Continued)

generators in the area. However, they do serve to highlight those sites where the electrical connection will require significant extensions of the power network with the associated high cost, environmental impact, and delay.

The initial technical assessment will be accompanied by a review of the main environmental considerations. The most important constraints include avoidance of national parks or other areas designated as being of particular environmental or amenity value and ensuring that no turbine is located so close to a dwelling that a nuisance will be caused (e.g. by noise, visual domination, or light shadow flicker). Table 10.2 shows some typical separation distances commonly used for medium sized wind turbines. Electricity Networks Association (2012) recommends a clearance of three rotor diameters to avoid wake effects on overhead line conductors.

A preliminary assessment of visual effects is also required to consider the visibility of the wind farm from important public viewpoints and if multiple wind farms can be seen. If, within the wind farm perimeter, there are areas of particular ecological value, such as rare or protected flora or fauna, these need to be avoided as well as any locations of particular archaeological or historical interest. Wind turbines may adversely affect communication systems (e.g. radio, TV, microwave links, or radar) and the effect of wind turbines on these systems needs to be considered at an early stage.

In parallel with the technical and environmental assessments it is usual to open discussion with the local civic and planning/permitting authorities to identify and agree the major issues that will need to be addressed in more detail if the project development is to continue. These issues are recorded in the scoping report of the Environmental Impact Assessment. The scoping report is an important document that defines the extent of the investigations required and is agreed with the planning authorities at an early stage.

Table 10.2 Typical separation distances for medium sized wind turbines.

Feature	Typical separation distances
Residential property	350–500 m
Motorway, trunk road, railway	Tip height of turbine +10%
Public right-of-way (e.g. footpath)	50 m or tip height of turbine, depending on use of right-of-way
Electric overhead line	Tip height of turbine +10% 3 rotor diameters
Other turbines	5–6 rotor diameters in prevailing wind direction 3–4 rotor diameters across prevailing wind direction

10.1.2 Project feasibility assessment

Once a potential site has been identified, more detailed and expensive investigations are undertaken to confirm the feasibility of the project. The wind farm energy output, and hence the financial viability of the scheme, will be very sensitive to the wind speeds seen by the turbines. It is not generally considered acceptable, especially in complex (undulating) terrain, to rely on the coarse estimates of wind speed made during the initial site selection. If adequate long-term wind measurements are not available for the actual site, the measure–correlate–predict (MCP) technique may be used to establish a prediction of the long-term wind resource.

10.1.3 Measure–correlate–predict

It is rare that a long-term record of the wind speed at a prospective wind farm site is available. MCP addresses this by taking measurements of wind speed and direction at the wind farm site and correlating them with simultaneous measurements made at a nearby meteorological station or airport with a data set that has been made over many years (Derrick 1993; EWEA 2009; Carta et al. 2013). In the simplest implementation of MCP, the averaging period of the measured site data is chosen to be the same as that of the meteorological station data. Simple linear regression is used to establish a relationship between the measured (target) site wind speed and the long-term (reference) meteorological station wind speed data using an equation of the form

$$U_{\text{target}} = a + b U_{\text{reference}} \quad (10.3)$$

Coefficients (known as *speed-up factors*) are calculated for the twelve 30° directional sectors and estimates of the site wind speed made by applying them to the long-term data record of the meteorological station. In this way, the long-term wind speed record held by the meteorological station is used to estimate what the wind speed at the wind farm site would have been over the last, say, 20 years. It is then assumed that the future long-term wind speed at the site is represented by this estimate, which is used as a prediction of the wind speed during the life of the project. Some attempt may also be made to predict the effect of climate change on the wind resource over the project life.

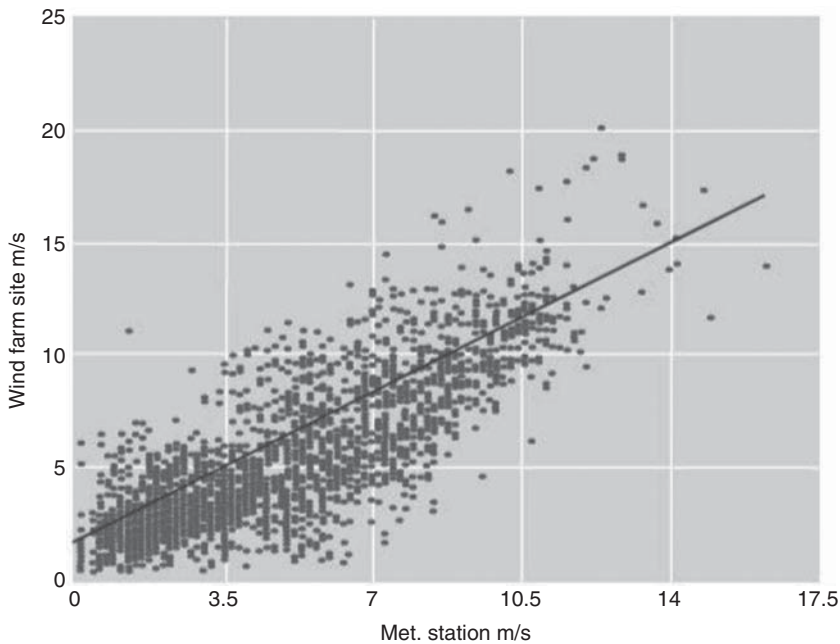


Figure 10.2 Scatter plot for MCP.

A typical scatter plot for MCP is shown in Figure 10.2.

Traditionally MCP has used a meteorological mast at the wind farm site on which a number of anemometers and wind vanes are mounted. If possible, one anemometer is mounted at the hub height of the proposed wind turbines with others lower to allow wind shear to be measured. Recently, remote sensing techniques such as LiDAR (light detection and ranging)¹ have begun to be used for site wind speed and direction measurements so avoiding the need to erect a high meteorological mast at the wind farm site. Measurements are made over at least a six-month period, including (winter) periods of high wind speed although the more data obtained the greater confidence there will be in the result.

The use of MCP can have a number of difficulties (Landberg and Mortensen 1993), including:

- If high site meteorological masts are used, these may themselves require planning permission.
- There may not be a suitable meteorological station nearby (within, say, 50–100 km) or with a similar exposure and wind climate.
- The data obtained from the meteorological station may not always be of good quality and may include gaps. Therefore, it may be time consuming to ensure that it can be properly correlated with the site data.
- It is based on the assumption that the long-term record provides a good estimate of the wind resource over the lifetime of the wind farm.

¹ LiDAR is described in Sections 8.3.17 and 8.3.18.

There are a number of variations in the detail of how the MCP method can be applied (EWEA 2009; Carta et al. 2013). If the site and long-term wind speeds are well correlated these different approaches to their correlation are of limited significance. Difficulties due to the location of the site meteorological mast and the quality of the data of the long-term record from the meteorological stations(s) are likely to be more important. The MCP technique is now well established and specially designed site data-loggers, temporary meteorological masts and software programs for data processing and analysis, are commercially available.

10.1.4 Micrositing

Once an estimate of the long-term wind speed at the site met-mast has been obtained, a wind farm design software package is used to investigate how the maximum energy can be generated from the site. Sophisticated programs such as WindFarm take the wind speed data and combine it with local topographic wind speed variations and the effect of the wakes of the other wind turbines to generate the energy yield of any particular layout of turbines.

Two models commonly used to calculate the effect of topology and surface roughness of the site and surrounding area are the Wind Atlas Analysis and Application Program (WA^sP 2020) and MS-Micro/3 that is a development of the MS3DJH/3R model (Walsley et al. 1982, 1986). With increasing computer power, the use of computational fluid dynamic techniques to calculate the wind flows over a site is becoming more common. Figure 10.3 shows an energy map of a prospective wind farm site created with wind farm design software. The figure shows the energy yield of a single wind turbine that might be used on the site. The absolute energy yield would change with different turbines and wake losses but it is clear that the area along the ridge has the highest energy density.

Constraints such as turbine separation, terrain slope, wind turbine noise, radar and land ownership boundaries may be applied using the wind farm design software. Optimisation techniques are then used to optimise the layout of the turbines across the site for maximum energy yield. Wind farm design packages also have visualisation facilities to generate zones of visual impact, views of the wind farm as wire frames and photomontages, and some use three-dimensional (3-D) virtual reality techniques.

10.1.5 Site investigations

At the same time as wind speed data is being collected, more detailed investigations of the site are undertaken. These include a careful assessment of existing land use and how best the wind farm may be integrated with, for example, agricultural operations. Although remote upland areas may appear initially not to be heavily used, it will be found that, almost always, there are existing users with interests in any piece of land.

The ground conditions at the site need to be investigated to ensure that the turbine foundations, access roads and construction areas can be provided at reasonable cost. Geotechnical investigations of the strength of the ground at the turbine sites are undertaken for foundation design. Local ground conditions may influence the position of turbines to reduce foundation costs. More detailed investigations of the access to the site will include assessment of bend radii, width, gradient, and any weight restrictions on approach roads. It may also be important to undertake a hydrological study to determine

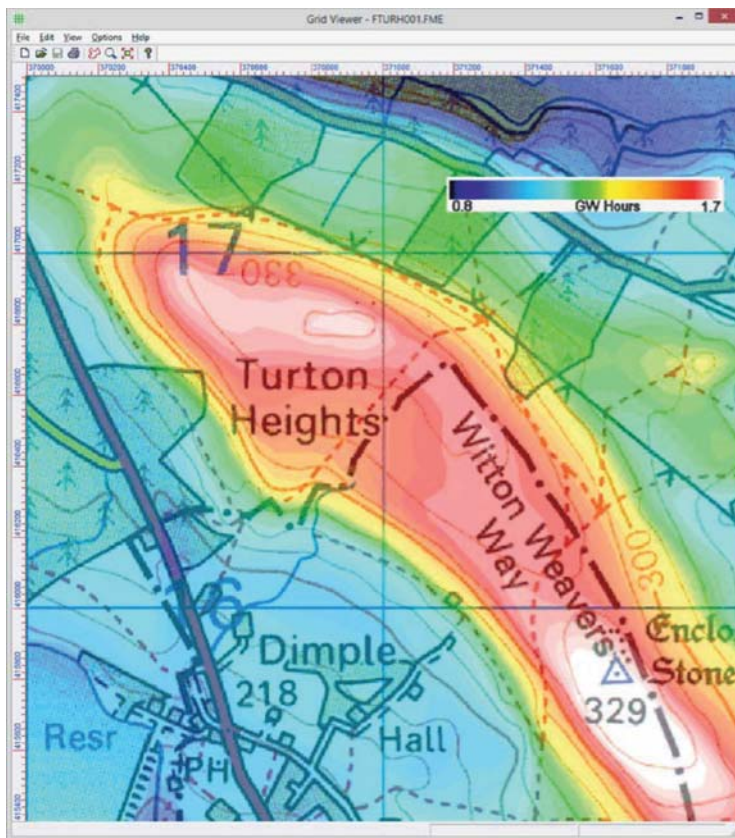


Figure 10.3 Example of an energy map (GWh/year) of a prospective wind farm site created with WindFarm software. See Plate 3 for clearer version in colour. Source: Reproduced by permission of ReSoft, © Crown copyright (2019) OS 100061895.

whether water supplies are taken from the wind farm site and if the proposed foundations or trenches will cause disruption of the ground water flow. Discussions are also likely to continue with the local electricity company concerning the connection to the distribution network and with potential purchaser(s) of the power that will be exported from the wind farm.

10.1.6 Public consultation

Prior to the erection of the site anemometer masts or other visible signs of preparation, the wind farm developer may wish to initiate some form of informal public consultation. This is likely to involve local community organisations, environmental societies, and wildlife trusts. It may also be appropriate to keep local politicians informed. Of course, the erection of a meteorological mast does not necessarily imply that the wind farm will be constructed but, as they are highly visible structures, careful consultation is required to ensure that unnecessary public concern is avoided.

10.1.7 Preparation of the planning application and environmental statement

Wind farms are recognised as having significant impact on the environment and it is usual for an Environmental Impact Assessment to be required. The Environmental Impact Assessment forms the basis of the Environmental Statement that is a major part of the application for planning/permitting permission. The Environmental Impact Assessment and preparation of the Environmental Statement is an expensive and time-consuming undertaking and usually requires the assistance of several specialists.

The purpose of a wind farm Environmental Statement may be summarised as to

- Establish the environmental character of the proposed site and the surrounding area.
- Describe the physical characteristics of the wind turbines and their land-use requirements.
- Predict the environmental impact of the wind farm.
- Describe measures that will be taken to minimise and mitigate any adverse impacts.
- Explain the need for the wind farm and provide details to allow the planning authority and general public to make a decision on the application.

Topics covered in the Environmental Statement will typically include (Glasson et al. 2012; Morris and Therivel 2009) the following:

- *Policy framework:* The application is placed in the context of national and regional policy.
- *Site selection:* The choice of the particular site that has been selected is justified.
- *Designated areas:* The potential impact of the wind farm on any designated areas (e.g. national parks) is evaluated.
- *Landscape character and visual impact assessment:* This is generally the most important consideration and is certainly the most open to subjective judgement. Hence it is usual to employ a professional consultancy to prepare the assessments. The main techniques that will be used for visual impact assessment include zones of theoretical visibility (ZTVs) (known formerly as zones of visual influence, ZVIs) to indicate where the wind farm will be visible from, wireframe analyses that show the location of the turbines from particular views, and photomontage production, which is computer-generated images overlaid on a photograph of the site.
- *Noise assessment:* After landscape and visual impact, noise is likely to be the next most important topic. Hence predictions of the sound produced by the proposed development are required, with special attention being paid to the nearest dwellings in each direction. It may be necessary to establish the background noise at the dwellings by a series of measurements so that realistic assessments can be made after the wind farm is in operation.

- *Ecological assessment:* The impact of the wind farm, including its construction, on the local flora and fauna needs to be considered. This may well require site surveys at particular seasons of the year. Particular studies may need to be carried out of the potential impact on birds and bats.
- *Archaeological and historical assessment:* This is an extension of the investigation undertaken during the site selection.
- *Hydrological assessment:* Depending on the site, it may be necessary to evaluate the impact of the project on watercourses and water supplies.
- *Interference with telecommunication systems:* Although wind turbines do cause some interference with television transmission, this is normally only a local effect and can usually be remedied at modest cost. Any interference with major point-to-point communication facilities (e.g. microwave systems) is likely to be a much more significant issue.
- *Aircraft safety and interference with radar:* The proximity to airfields or military training areas needs to be considered carefully. The effects of wind farms on aircraft radar, both civil and military, has become a most important issue in several countries and requires early attention.
- *Safety:* An assessment is required of the safety of the site including the structural integrity of the turbines. Particular local issues may include highway safety and shadow flicker.
- *Traffic management and access construction:* The Environmental Statement addresses all phases of the project, and so both the access tracks and the increase in vehicle movements on the public roads during construction and operation need to be considered.
- *Electrical connection:* There may be significant environmental impact associated with the electrical connection (e.g. the construction of a substation and new circuits). Any requirement made by the planning authorities to place long high voltage circuits underground will be expensive.
- *Economic effects on the local economy, global environmental benefits:* It is common to emphasise the benefit that the wind farm will bring both to the local economy and to reduction in gaseous emissions.
- *De-commissioning:* The assessment should also include proposals for the de-commissioning of the wind farm and the removal of the turbines at the end of the project. De-commissioning measures are likely to involve the removal of all equipment that is above ground and restoration of the surface of all areas.
- *Mitigating measures:* It is obvious that the wind farm will have some impact on the local environment, and so this section details the steps that are proposed to mitigate any adverse effects. This is likely to emphasise the attempts that have been made to minimise visual intrusion and control noise.
- *Non-technical summary:* Finally, a non-technical summary is required, and this may be widely distributed to local residents.

10.1.8 Planning requirements in the UK

In heavily populated countries as the number of onshore wind farms increases, it is becoming increasingly difficult to find suitable sites that are likely to receive planning permission. DCLG (2015)² lists the main issues that are considered in any planning application and gives useful links to more detailed guidance on

- Acoustic noise.
- Safety, including wind turbine overturning distances.
- Air traffic, including collisions with low-flying aircrew and interference with Air Traffic and Defence radar.
- Electromagnetic transmissions.
- Ecology, including birds and bats.
- Heritage.
- Shadow flicker.
- Cumulative landscape and visual impacts of multiple wind farms.

10.1.9 Procurement of wind farms

A wind farm may be procured either as a single turnkey project or by letting a number of contracts to specialist suppliers. A turnkey arrangement, whereby a single main contract for the engineering, procurement and construction of the entire wind farm is made with one supplier, transfers risk from the developer on to the main contractor. This approach is known as Engineer, Procure, and Construct (EPC). The main contractor undertakes detailed design, places contracts and assumes responsibility for the equipment needed as well as for overall project management. After commissioning, a fully working plant is handed over to the developer who may appoint a specialist operator. The project developer will probably still have to accept the risks of the wind resource differing from that anticipated and the sale price of the electricity not being fixed over the life of the project.

Alternatively, separate contracts can be placed for the supply and erection of the wind turbines, and the balance-of-plant civil and electrical works. The construction is split into a number of work packages e.g. supply and erection of wind turbines, civil works, electrical equipment and contracts are let for each. This may result in a lower price of the project but leaves the responsibility for the overall design and coordination of the work with the project developer or an engineer that is appointed for this purpose.

10.1.10 Financing of wind farms

Even if the project developer is an organisation with large financial resources, many wind farms are financed using loans from a bank or other financial institution. The wind farm is financed mainly through debt that is repaid from the revenue generated from electricity

² Construction of onshore wind farms in England and Wales is effectively paused at the time of writing but is expected to recommence. There are likely to be similar environmental issues in any heavily populated country.

sales over the life of the project. The debt is repaid at an agreed rate of interest and so the lender does not benefit if the project performs better than expected but is exposed to risk if the project underperforms. This form of finance is known as *project or non-recourse funding*.

The project developer will invest some equity in the project but most of the funds will be borrowed as debt. The debt is secured only on the assets of the wind farm project and so the bank (or the engineer and lawyer they appoint) will examine all aspects of the project very carefully during the feasibility phase. This process of establishing due diligence is to ensure that all risks are adequately identified and controlled. Legal due diligence ensures that there is always one party responsible for each part of the project while technical due diligence ensures the physical requirements of the project are completed. There are likely to be a very large number of agreements and contracts that need to be scrutinised in the due diligence process before funds are released and construction can start.

It is common that a separate company is created to construct each wind farm. This company is known as a *Special Purpose Vehicle (SPV)*. The advantage of establishing a SPV for each project is that the parent company is protected if the project performs poorly and the project is not affected by the performance of the parent organisation or its other projects. Table 10.3 lists the agreements that are typically made between the SPV and other parties.

Some lenders may agree to finance a project on the basis of the ratio of debt to the equity provided by the developer. This ratio might typically be 85/15% depending on the perceived risks in the project. Other lenders will require the projected financial performance of the wind farm to be modelled and the debt service cover ratio calculated. The debt service cover ratio is the ratio of the anticipated income to the debt repayments and typically might be 1.4:1.

The financial performance of a wind farm is very sensitive to the wind speed and hence energy generated. The anticipated energy generated may be calculated as the P50

Table 10.3 Agreements for the development of a wind farm using project finance.

Agreement	Party
Planning permission	Planning authority
Land rights	Landowner
Grid connection	Network operator
Turbine supply	Manufacturer
Energy yield assessment	Consultant
Civil works	Civil contractor
Electrical works	Electrical contractor
Power purchase agreement	Energy supplier
Operation and maintenance	Operation and maintenance contractor
Insurance	Insurance company
Bank security	Bank
Corporate governance	Multiple parties
Warranties and step-in agreements	Multiple parties

estimate, that assumes there is a 50% chance of the energy generated being lower or higher than the estimate, or P90 estimate where there is a 90% probability of the energy generated being higher than the estimate. A bank or other lender of project finance that is at risk if the project underperforms, but does not benefit from any over-performance, may require the energy prediction to be for a probability of P90.

10.2 Landscape and visual impact assessment

Modern onshore wind turbines are large structures, sometimes more than 100 m in height to the blade tip, and must be sited in exposed locations of high wind speed if they are to operate effectively. Within a wind farm, the individual turbines are spaced at up to 6 rotor diameters and so large wind farms extend over a wide area. A compromise often has to be made between energy yield and visibility of the wind turbines. The appearance of a wind power development and the reaction of the public to it are critical in determining if permission to construct the project will be granted by the civic authorities.

Landscape and visual impact assessment is a key aspect of the Environmental Impact Assessment and is required for any significant wind farm development. The assessment forms an important, often self-contained, section of the Environmental Statement that is submitted with the planning application. The two aspects of landscape and visual effects are distinct, if inter-related (University of Newcastle 2002). The landscape character assessment assesses the landscape in terms of its characteristics, quality and condition, and the likely impact of the wind farm (Tudor 2014). In some countries, strategic environmental assessments have been completed for many areas of good wind resource and general guidance may be available whether permission for a wind farm in an area is likely to be refused on the grounds of changes to the landscape. The visual assessment study of the project assesses the visibility of the turbines and buildings and any overhead power lines as well as the importance of the locations from which they are visible, known as the *receptors* (Scottish National Heritage 2017).

The assessment of landscape and visual effects of a wind farm is usually undertaken by a consultant specialising in such work. They will attempt to quantify the visual impacts but it is recognised that a degree of subjective interpretation is required (Swanick 2013). The assessment process is iterative and will influence the design and layout of the wind farm. However, it may be divided into

- Landscape character assessment (including landscape policy and designation).
- Design of the wind farm and measures to mitigate landscape and visual impact.
- Assessment of visual impacts (including visibility and viewpoint analysis).
- Assessment of shadow flicker.

The landscapes in which wind farms are constructed vary widely, and the turbine layout is chosen to take account of the landscape character as well as the wind resource. In Figure 10.4 the turbines are located along a field boundary in flat terrain while a linear arrangement on a ridge in complex terrain is shown in Figure 10.5 and along the coast in Figure 10.6. Figure 10.7 shows a large wind farm on flat upland terrain.



Figure 10.4 Wind farm of six 660 kW turbines in flat terrain. Source: Reproduced by permission of Cumbria Wind Farms Ltd. Paul Carter.

It is also essential to consider the wider context of the development. An individual's perception of a wind farm development will be determined not only by the physical parameters (e.g. wind turbine size, number, colour, etc.) but also by his/her opinion of wind energy as a means of supplying electricity (Devine-Wright 2005).

10.2.1 Landscape character assessment

A fundamental step when planning a wind farm is to identify an appropriate site and ensure that the proposed development is in harmony with the location. Many exposed upland areas are valued by the population and have been designated as areas of significant landscape value or even as national parks. Obtaining permission to develop a wind farm within a national park, or even one clearly visible from within it, is likely to be extremely difficult.



Figure 10.5 Wind farm of 600 kW turbines at Tarifa, Spain. Source: Reproduced by permission of NEG Micon.



Figure 10.6 Wind farm of 700 kW turbines along a coast. Source: Reproduced by permission of PowerGen Renewables/Wind Prospect Ltd.



Figure 10.7 Large wind farm on flat upland terrain. Source: *Photo: Tony Mills/Shutterstock.com.*

Stanton (1994) suggests some characteristics of the wind farm image that are considered to be desirable. The development should be simple, logical, and avoiding visual confusion. Although one landscape type is no more appropriate for a wind farm development than another this author considers that their suitability for different types of development varies greatly. Five different landscape zones are identified and discussed for the most appropriate type of development. Flat agricultural land is considered suitable for either a small number of wind turbines or large wind farms of similar, regularly spaced machines. Coastal areas are considered appropriate for large numbers of wind turbines but the development should relate to the linear quality of the coastal space. There is some opportunity to install a small number of wind turbines in industrial areas. In areas of high aesthetic value, such as mountains and moorland the turbines should be arranged either along ridgelines or as a grid layout within flat land. Finally in areas of variable and rolling relief it is proposed that only small wind turbines or single wind turbines are appropriate. Such views are, of course, open to debate but they do illustrate that it is essential to consider the character of the landscape before a wind farm development is proposed.

The cumulative effect of multiple wind farms within an area is becoming increasingly important, as wind energy makes a greater contribution to electricity generation. If more than one wind farm is visible from a viewpoint then this can be an important consideration. Local features such as buildings and hedges, which restrict views, may mean that a landscape is able to accommodate additional wind turbines, but detailed investigation is required to establish this.

10.2.2 Turbine and wind farm design for minimum visual impact

Wind turbine designers have recognised for some years that the appearance of a large wind turbine has to be pleasing and this aspect of industrial design is considered early in the development of any new machine. It is now generally recognised that for aesthetic reasons three bladed turbines are preferred (see Section 6.5.7). Two bladed rotors sometimes give the illusion of varying speed of rotation; the blades appear to flick as they pass in front of the tower and this can be disconcerting. In addition, for a similar swept area, a two bladed rotor will operate faster than one with three blades and there is some

evidence that a slower speed of rotation is more pleasing (Gipe 1995). This effect works to the advantage of the large diameter modern wind turbines, which operate typically at less than 30 rpm.

Lattice steel towers are now rarely used for wind turbines. Lattice towers can reduce the costs of the foundations (see Section 7.10.4), but the upper section of the tower must be tapered to provide adequate clearance for the blades. From a distance and in certain light conditions lattice towers can disappear leaving only the rotors visible and this effect is thought to be undesirable. In Europe, only solid tubular towers are generally considered to be acceptable. Tower heights can vary greatly in response to both wind conditions and planning constraints. In parts of Germany, very high towers are used to increase the rotor wind speed or raise the rotor above the trees in forests. Conversely, in western parts of the UK that have high mean wind speeds, tower heights have been reduced to minimise the surrounding area from which the wind turbines are visible.

The appearance of the turbines can be influenced to some extent by their colour. In the upland sites of the UK, the turbines will generally be seen against the sky and so an off-white or mid-grey tone is generally considered to be appropriate. Where the wind farm is seen against other backgrounds a colour to blend in with the ground conditions may be more suitable. There is general agreement that the outer gel-coat of the blades should be a matt or semi-matt finish to minimise reflections. During the early development of wind energy in the USA some wind farms used a variety of wind turbines sometimes of quite different design (i.e. with differing numbers of blades, direction of rotation, tower types). It is unlikely that such developments made up of different designs of wind turbines on a site would now be acceptable.

The layout and design of the wind farm is important in determining if planning consent is to be received. The preliminary wind farm layout may be determined by engineering considerations (e.g. local wind speeds, turbine separation, noise, ground conditions) but will then be modified to take account of visual and landscape effects. Usually the developer will wish to maximise the number of turbines on a site within all of the environmental and grid constraints and hence the revenue. On open, flat land, the turbines are often arranged in a regular layout to provide a simple and logical visual image and maximum power output. Alternatively, on sites where there are hedges or field boundaries the turbine layout is arranged around these features. When viewed from up to 1–2 km, wind turbines are considered to dominate the field of vision and so it is desirable that the number of views within this distance are minimised (e.g. by moving turbines to make use of local screening features or by tree planting). When turbines are seen one behind another there is an increase in visual confusion and this ‘stacking’ effect is considered to be undesirable. Some viewpoints are likely to be particularly important (e.g. from local viewing points or market places) and it may be appropriate to arrange the turbines so that these views of the wind farm are as clear and uncluttered as possible.

In addition to the wind turbines, there are a number of other structures required, including the wind farm meteorological mast(s) and the electrical equipment. With smaller wind turbines, the local transformers may be located adjacent to the towers, often in a fibreglass enclosure to provide protection against the weather and vandalism. However, the towers of large turbines are wide enough to accommodate the transformers inside the tower base and this obviously reduces visual clutter. There is often a requirement for a main wind farm electrical substation, transformer, and a local control building. Engineering considerations would indicate that the substation should be located at the centre or edge of the wind farm but, to reduce visual impact,

it is often placed some distance away, where it can be screened. Within European wind farms all power collection circuits are underground and it may also be appropriate, if rather expensive, to use underground cable rather than overhead lines to make the final connection to the local utility system. Roads are required within the wind farm for construction and it is a common requirement of the planning consent that their hard surface is removed after commissioning. This of course can lead to very considerable expense if the road has to be reinstated to allow a large crane to be used later for maintenance or repair.

10.2.3 Assessment of visual impact

Visual impact assessment of wind farms is now an important specialist subject with its own specialist practitioners and literature, e.g. Scottish National Heritage (2017). Two main techniques are used: (i) visibility analysis using ZTV, and (ii) viewpoint analysis usually using wireframes and photomontages.

ZTV show those areas of the surrounding country, often up to 30 km radius, from which a wind turbine, or any part of a wind turbine, is visible. The ZTV is generated using computer methods based on a digital terrain model and shows how the local topology will influence the visibility of the wind farm. Usually ZTVs ignore local features such as screening from trees and buildings. Also, weather conditions are not considered and clear visibility is assumed. ZTVs may consider the visibility of the tips of the wind turbine blades or the nacelles. Figure 10.8 shows an example of a ZTV of a single wind farm generated using wind farm design software. The wind farm is the dot at Turton Heights and the colour shading shows the number of turbines visible from a location.

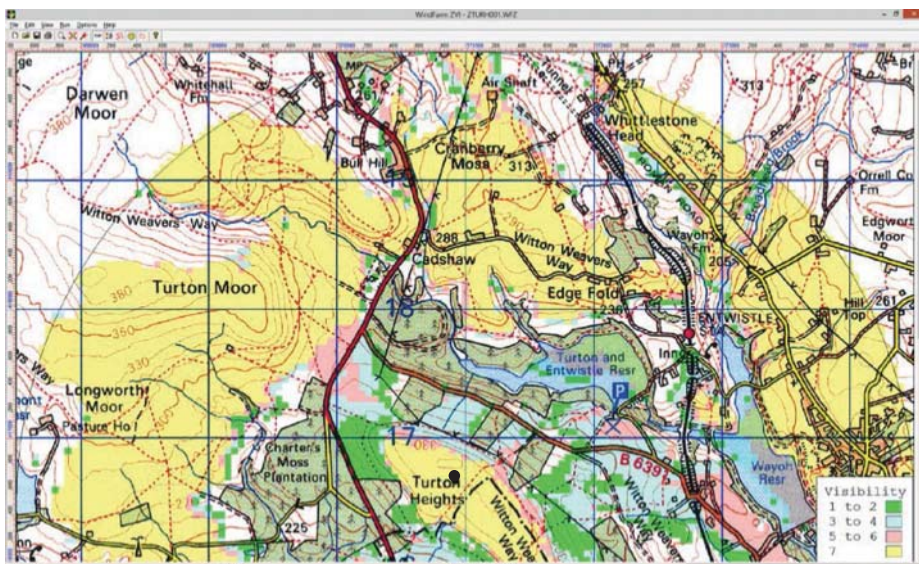


Figure 10.8 Example of ZTV (visual impact) of a wind farm. See Plate 4 for clearer version in colour. Source: Reproduced by permission of ReSoft, © Crown copyright (2019) OS 100061895.

Viewpoint analysis starts by selecting a number of important locations from which the wind farm is visible and applying professional judgement of the change in the view likely to be caused by the development. The viewpoints are selected in consultation with the civic planning authorities and for a large wind farm more than 20 locations may be chosen.

Some years ago it was common to use quantitative criteria to assess visual impact. Although approaches varied, the assessment often involved consideration of two aspects: (i) the sensitivity of the viewpoint, and (ii) the magnitude of the change in the view. For example, a viewpoint in a residential area or one that has high recreational value (e.g. a scenic viewpoint inside a national park) might have been described to be of high sensitivity. Conversely, a view from a location used only for employment (e.g. a local industrial estate) might be considered to have a low sensitivity. The magnitude of the impact was described in a similar manner depending, for example, on the number of turbines visible, the distance to the wind farm, and the prominence of the development. Combining these factors then assessed the overall significance of the impact. In recent years, this quantitative approach has been largely superseded (Landscape Institute and Institute of Environmental Management & Assessment 2013) although it is still a useful intellectual framework.

Tools for viewpoint assessment include wireframes and photomontages. Both the photomontage and wireframe figure can be generated using wind farm design software. Wireframes are line drawings of the proposed wind farm superimposed on a representation of the view made using digital terrain data. They are often used in the early stages of the design of a wind farm and provide a precise impression of turbine position and scale. Figure 10.9 shows a wireframe image generated from a viewpoint from which three wind farms are visible. This illustrates why, as wind energy develops, the planning authorities are becoming increasingly concerned about cumulative environmental impacts.

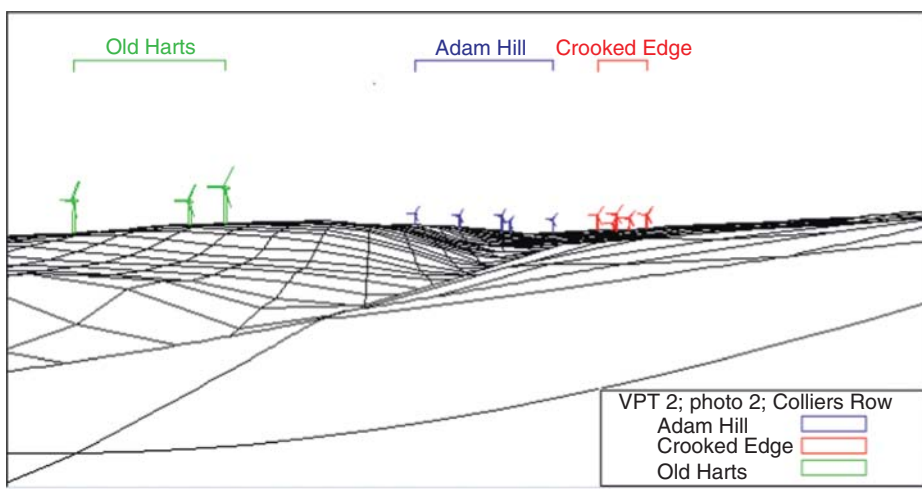


Figure 10.9 Example of wireframe showing visibility of three wind farms. Source: Reproduced by permission of ReSoft.

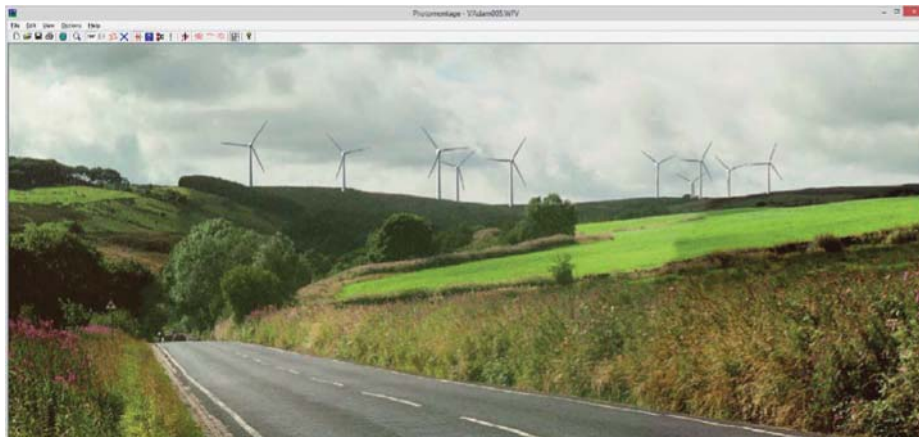


Figure 10.10 Example of photomontage. Source: Reproduced by permission of ReSoft.

Photomontage is a technique to superimpose images of wind turbines on a series of photographs. Photomontages are the normal tool used to give an overall impression of the visual effect of a wind farm. Considerable care is necessary with both the background photograph and turbine image if a useful representation is to be obtained. Figure 10.10 shows an example of a photomontage.

Video montages are sometimes used to give an impression of the movement of turbine blades. Figure 10.11 illustrates how 3-D virtual reality allows the user to navigate around the wind farm for different views

10.2.4 Shadow flicker

Shadow flicker is the term used to describe the stroboscopic effect of the shadows cast by rotating blades of wind turbines when the sun is behind them. The shadow can create a disturbance to people inside buildings exposed to such light passing through a narrow window (EWEA 2009). The frequencies that can cause disturbance are between 2.5–30 Hz. The effect on the human eye–brain is the same as that caused by variations in voltage varying the intensity of light from the now obsolete incandescent electric light bulbs (see Section 11.7.1).

The main concern is variations in light at frequencies of 2.5–3 Hz, which have been shown to cause anomalous EEG (electroencephalogram) reactions in some sufferers from epilepsy. In the UK, approximately 0.5% of the population suffers from epilepsy, but only 5% of these from photosensitive epilepsy. Large modern three bladed wind turbines rotate at less than 20 rpm, giving blade-passing frequencies of less than 1 Hz, which is below the critical frequency of 2.5 Hz. In the latitude of the UK, only properties within 130° either side of North of a turbine are affected by shadow flicker. It has been found that a spacing of 10 rotor diameters between a turbine and dwelling eliminates the problem (DECC 2011).

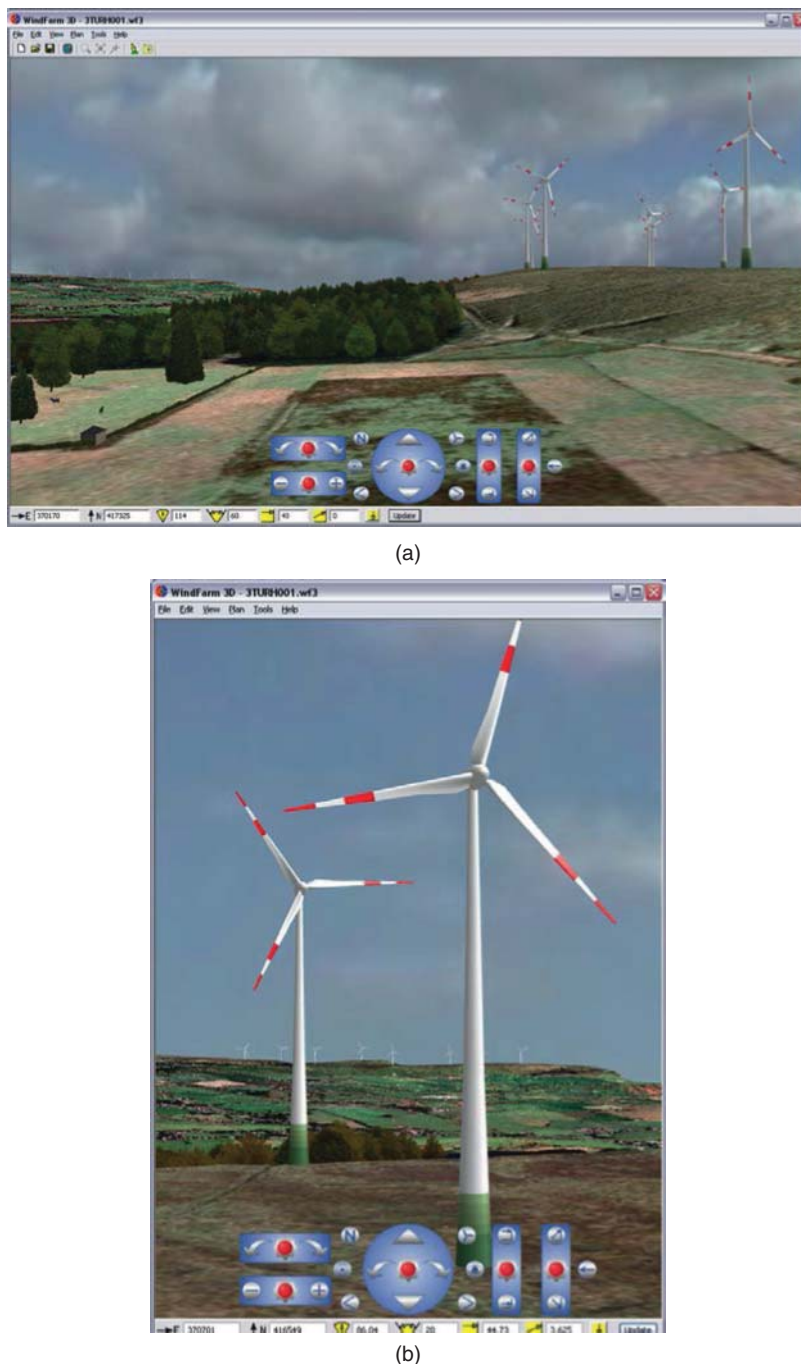


Figure 10.11 (a) 3-D view of a wind farm. (b) 3-D view within a wind farm. (a) and (b) show 3-D views of the same wind farm from different viewpoints. The controls to navigate around the wind farm are shown. Source: Reproduced by permission of ReSoft.

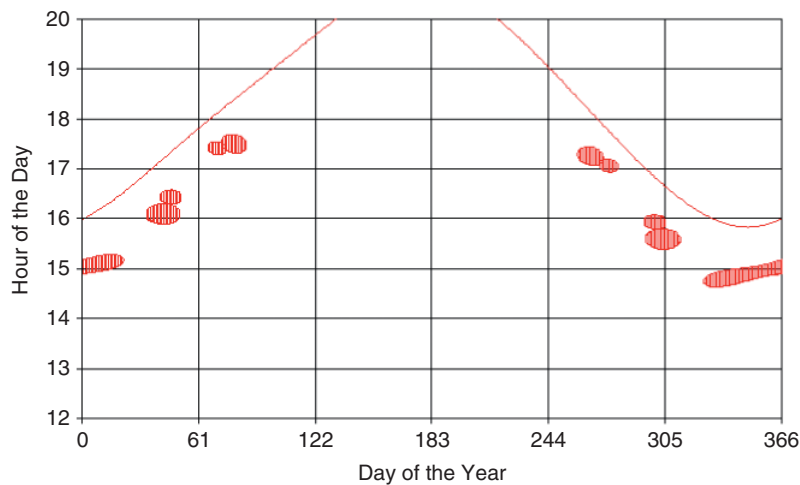


Figure 10.12 Example of shadow flicker prediction. The continuous line shows the time of sunset. Source: Reproduced by permission of ReSoft.

The wind farm SCADA system can be arranged to stop those wind turbines that might create a shadow flicker nuisance temporarily at the critical times. This control may be either through a timer or by measurement of light intensity and leads to only a limited loss of wind energy generated. Figure 10.12 shows an example of when shadow flicker might cause disturbance in a dwelling close to a wind turbine. It may be seen that this occurs during late afternoon (from around 15:00 to 17:30) in the spring and autumn. Shadow flicker, noise constraints and avoidance of visual domination all need to be addressed when considering how close a turbine should be located to a dwelling.

10.3 Noise

Noise from wind turbines is one of the more significant environmental impacts (Wagner et al. 1996). During the early development of wind energy in the 1980s, some turbines were noisy and this led to justified complaints from those living close to them. The acoustic performance of several of the early large turbines of the US national programme (the Mod-0 and Mod-1) was studied intensively at that time. These prototypes had two bladed, downwind rotors and lattice steel towers (Spera 1994; Hau 2013), and this architecture, which is now obsolete, generated considerable impulsive aerodynamic noise. Since then, the architecture of modern turbines has converged on three bladed upwind designs with tubular towers, and there has been very considerable development both in techniques for reducing noise from wind turbines and in predicting the noise that a wind farm will create.

It is common for the Environmental Statement of any wind farm proposal to provide a prediction of noise levels. This will include

- Results of independent measurements of the noise emitted from the proposed wind turbines, including sound power level as a total value and across the frequency spectrum.

- Predicted sound pressure levels at specific locations (often dwellings) close to the wind farm over a range of wind speeds.
- Measured background noise levels at these locations over a range of wind speeds.
- A scale map showing the proposed wind turbines and anticipated noise at nearby existing developments.

Figure 10.13 shows an example of predicted sound pressure levels from a small wind farm. Five turbines and four houses are shown, as well as noise contours of 40 and 50 dB(A).

Bullmore and Peplow in Bowdler and Leventhal (2011) list the main factors influencing the propagation of sound outdoors as geometric attenuation and atmospheric absorption. These effects are represented in the results of Figure 10.13. A number of additional effects including: some details of the ground surface, inhomogeneity in the atmosphere through wind and temperature variations, and the effect of wind turbulence are often not included in the simpler noise propagation models.

10.3.1 Terminology and basic concepts

Two distinctly different measures are used to describe wind turbine noise (Bowdler and Leventhal 2011; Rogers et al. 2002; Wagner et al. 1996). These are the sound power level L_W of the source (i.e. the wind turbine) and the sound pressure level L_P at a location. Because of the response of the human ear, a logarithmic scale is used, based on reference levels that correspond to the limit of hearing. The units of both L_P and L_W are the decibel (dB).

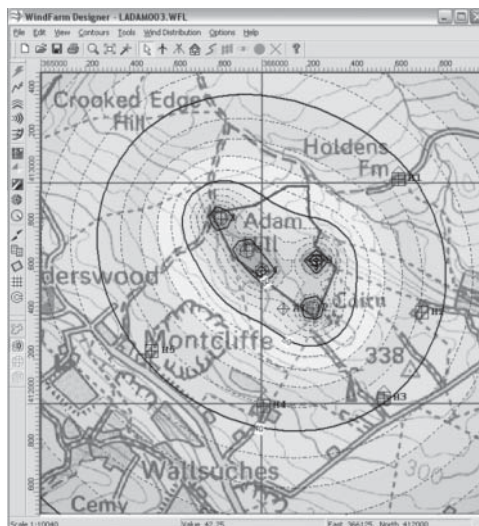


Figure 10.13 Noise contours around a small wind farm. Source: Reproduced by permission of ReSoft © Crown copyright (2019) OS 100061895.

The sound pressure level at a location (immission) is related to the sound power level of a source (emission) by

$$L_P = L_W + K - A$$

where A is absorption between source and receiver and K is a penalty for tonal or impulsive noise. A includes absorption due to geometrical divergence, atmospheric absorption and may also include the ground effect (Nieuwenhuizen and Kohl 2015).

A noise source is described in terms of its sound power level, L_W :

$$L_W = 10 \log_{10} \left(\frac{W}{W_0} \right) \quad (10.4)$$

where W is the total sound power level emitted from the source (in watts) and W_0 is the reference value of 10^{-12} W.

The sound pressure level, L_P is defined as

$$L_P = 10 \log_{10} \left(\frac{P^2}{P_0^2} \right) \quad (10.5)$$

where P is the root mean square (rms) value of the sound pressure and P_0 is the reference value of 2×10^{-5} Pa.

By simple manipulation it may be seen that the addition of n sound pressure levels (expressed in dB) is carried out as

$$L_{Pn} = 10 \log_{10} \sum_{j=1}^{j=n} 10^{\frac{L_P(j)}{10}} \quad (10.6)$$

Thus, adding two sound pressure levels of the same magnitude results in an increase of 3 dB. Sound power levels may be added in a similar manner.

Table 10.4 gives an indication of the typical range of sound pressure levels.

The human ear is capable of detecting sounds between 20 Hz and 20 kHz and analysis is usually undertaken over this frequency range. A narrow-band spectrum, with a defined bandwidth of measurement, gives the fullest information of the signal and may be used to detect particular tones. It is conventional to use octave and 1/3-octave bands for wind farm noise analysis. The upper frequency of an octave band is twice that of the

Table 10.4 Examples of sound pressure levels.

Example	Sound pressure level dB(A)
Threshold of hearing	0
Rural nighttime background	20–40
In a busy general office	60
Inside a factory	80–100
Jet aircraft at 100 m	120
Wind farm at 400 m	35–45

Table 10.5 Centre frequency of octave bands and A-weighting.

Octave band centre frequency (Hz)	A-weighting (dB)
16	-56.7
31.5	-39.4
63	-26.2
125	-16.1
250	-8.6
500	-3.2
1000	0.0
2000	1.2
4000	1.0
8000	-1.1
16 000	-6.6

lower frequency while for the 1/3-octave band the upper frequency is $\sqrt[3]{2}$ times the lower frequency.

It is common to weight the measurements to reflect the response of the human ear with frequency. This is done by applying the so-called ‘A-weighted filter’. Measurements made with this filter are referred to as dBA or dB(A). Table 10.5 shows the centre frequencies of the octave bands together with the A-weighting in dB. It may be seen that frequencies below 250 Hz and above 16 kHz are heavily attenuated.

An equivalent sound pressure level $L_{eq,T}$ is the value of a continuous steady sound that, within the specified time interval (T), has the same mean square sound pressure level as the sound under consideration, which varies with time:

$$L_{eq,T} = 10 \log_{10} \left(\frac{1}{T} \int_0^T \frac{P^2}{P_0^2} dt \right) \quad (10.7)$$

A similar calculation may be undertaken using A-weighting values to give $L_{Aeq,T}$:

$$L_{Aeq,T} = 10 \log 10 \left(\frac{1}{T} \int_0^T \frac{P_A^2}{P_0^2} dt \right) \quad (10.8)$$

where $L_{Aeq,T}$ is the equivalent continuous A-weighted sound pressure level determined over time T and P_A is the instantaneous A-weighted sound pressure.

The exceedance level, L_{A90} , is defined as the A-weighted sound pressure level that is exceeded for 90% of the time. Some civic planning authorities prefer the use of the L_{A90} sound pressure level, particularly for measurements of background noise, as the L_{Aeq} measurement may be heavily influenced by short-term effects such as passing aircraft or traffic. A wind farm is a fairly constant source of noise and its contribution to the L_{A90} sound pressure level (measured over a 10 minute period) is likely to be some 1.5–2.5 dB(A) less than to the 10 minute L_{Aeq} value (ETSU-R-97 1997).

The sound intensity I is the power transmitted through a unit area, A ,

$$I = \frac{W}{A} \quad (10.9)$$

and far from the source of sound with a uniform flux

$$I = \frac{P^2}{Z_0} \quad (10.10)$$

where P is the rms value of the sound pressure level, and Z_0 is the specific acoustic impedance.

$Z_0 = \rho_0 c_0$, the product of the density of air and the speed of sound, with units $\text{kg/m}^2\text{s}$. It can be thought of simply as the opposition that the air presents to the flow of sound power. An analogy with electrical impedance can be seen by considering sound pressure as analogous to voltage with sound intensity as electrical power and the acoustic impedance as electrical impedance both per unit of area.

Choosing a suitable value for I_{ref} (10^{-12} W/m^2), the sound pressure level may be expressed in terms of sound intensity as

$$L_P = 10 \log_{10} \left(\frac{I}{I_{ref}} \right) \quad (10.11)$$

For spherical spreading

$$I = \frac{W}{4\pi r^2} \quad (10.12)$$

where r is the distance from the source.

Hence, under conditions of ideal spherical spreading the sound pressure level at a location can be related to the sound power level of a point source by

$$L_P = 10 \log_{10} \left(\frac{W}{4\pi r^2 10^{-12}} \right) = L_W - 10 \log_{10}(4\pi r^2)$$

that may be written as

$$L_P = L_W - 20 \log_{10} r - 11 \quad (10.13)$$

and similarly, if hemi-spherical spreading is assumed,

$$L_P = 10 \log_{10} \left(\frac{W}{2\pi r^2 10^{-12}} \right) = L_W - 10 \log_{10}(2\pi r^2)$$

that may be written as

$$L_P = L_W - 20 \log_{10} r - 8 \quad (10.14)$$

Sound pressure level from a point source decays with distance according to the inverse square law under both spherical and hemi-spherical spreading assumptions. Hence for each doubling of distance the sound pressure level is reduced by 6 dB.

For a line source of noise the sound pressure level is given by

$$L_P = 10 \log_{10} \left(\frac{L_{wl}}{2\pi r 10^{-12}} \right) = L_{wl} - 10 \log_{10}(2\pi r) \quad (10.15)$$

L_{wl} is the sound power level per unit length of the source.

For this cylindrical spreading the decay is only proportional to distance, resulting in a 3 dB reduction of sound pressure level for each doubling of distance perpendicular to the line source.

10.3.2 Wind turbine noise

Noise from wind turbines may be divided into mechanical and aerodynamic.

Mechanical noise is generated mainly from the rotating machinery in the nacelle particularly the gearbox and generator although there may also be contributions from cooling fans, auxiliary equipment (such as pumps and compressors) and the yaw system. Mechanical noise is often at an identifiable frequency or tone (e.g. caused by the meshing frequency of a stage of the gearbox). Noise containing discrete tones is more likely to lead to complaints and so attracts a 5 dB penalty in many noise standards for wind turbines. Mechanical noise may be air-borne (e.g. the cooling fan of an air-cooled generator) or transmitted through the structure (e.g. gearbox meshing, which is transmitted through the gearbox casing, the nacelle bedplate, the blades, and the tower).

Pinder (1992) gives the values of sound power level compiled into Table 10.6 for a 2 MW experimental wind turbine. It may be seen that in this example of an early upwind turbine, the gearbox is the dominant noise source through structure borne transmission.

Techniques to reduce the mechanical noise generated from wind turbines include careful design and machining of the gearbox, use of anti-vibration mountings and couplings to limit structure-borne noise, acoustic damping of the nacelle and liquid cooling of the generator. Small changes in the design of gearboxes (e.g. ratio and tooth shape) can have a significant effect on noise generation (IEC 61400-14 2005).

The source of noise from modern wind turbines is mainly aerodynamic, and aerodynamic noise is addressed in Section 3.19 of this book. Aerodynamic noise is due to a number of causes, including

- Trailing edge noise.
- Inflow turbulence noise.
- Tip noise.

Trailing edge noise is thought to be the main source of aerodynamic noise (Bowdler and Leventhall 2011) and is perceived as a broadband swishing sound with frequencies in the range 400–1000 Hz. Because of its directional property it appears to an observer to vary with the azimuthal position of the blade. It is due to interaction of the turbulent boundary layer with the trailing edge of the blade; a blunt trailing edge can give rise to

Table 10.6 Sound power levels of mechanical noise of a 2 MW experimental wind turbine.

Element	Sound power level dB(A)	Air-borne or structure-borne
Gearbox	97.2	Structure-borne
Gearbox	84.2	Air-borne
Generator	84.2	Air-borne
Hub	89.2	Structure-borne
Blades	91.2	Air-borne
Tower	71.2	Structure-borne
Auxiliaries	76.2	Air-borne

vortex shedding and tonal noise. Sharpening the trailing edge can reduce trailing edge noise but this has implications for manufacturing and erection of turbines.

Inflow turbulence creates broadband noise as the blades interact with the eddies in atmospheric turbulence. It generates frequencies up to 1000 Hz and is influenced by the blade velocity, aerofoil section, and turbulence intensity. Wagner et al. (1996) describe this phenomenon in some detail, remarking that it is not fully understood, and quote the results of one field experiment where the sound pressure level actually decreased with increasing turbulence intensity. The literature is not clear as to whether three-dimensional tip effects are a major contributor to wind turbine noise. However, the majority of the blade noise, as well as the turbine power, emanates from the outer 25% of the blade, and so there has been very considerable investigation of novel blade tips to reduce noise, although these are not used in current commercial designs. Imperfections in the blade shape due to tip-brakes or other control surfaces are another potential source of noise.

Blade stall causes unsteady flow around the airfoil, which can give rise to broadband sound radiation, while surface imperfections such as those caused by damage during erection or due to lightning strikes can be a significant source of tonal noise.

The noise from a wind turbine blade is proportional to the 5th or 6th power of the incident wind speed. Hence an obvious approach to reducing aerodynamic noise is to lower the rotational speed of the rotor, although this may result in some loss of energy. The ability to reduce noise in low wind speed conditions is a major benefit of variable-speed wind turbines and it is common practice to keep the tip speed of an onshore wind turbine to less than 75 m/s. An informative annex of IEC 61400-14 (2005) gives a relationship between tip speed of a turbine and sound power level as

$$L_W \approx (50 \text{ to } 60) \log V_{\text{tip}} \quad (10.16)$$

An alternative technique to decrease aerodynamic noise is to reduce the angle of attack of the blade although again with a potential loss of energy. Several wind turbine manufacturers include facilities in their control systems to reduce noise at night or when background noise is low. Wind farm control schemes can be designed to implement these noise reduction modes on selected turbines in particular wind directions to reduce noise at sensitive locations.

10.3.3 Measurement of wind turbine noise

The sound power level of a wind turbine is determined by measuring sound pressure levels in field experiments. Outdoor experiments are necessary because of the large size of modern wind turbines and the need to determine their noise performance during operation. The sound power level cannot be measured directly but is found from a series of measurements of sound pressure levels made around the turbine at various wind speeds from which the background sound pressure levels have been deducted. The method provides the apparent A-weighted sound power levels, octave and 1/3 octave spectra and tonality of a single wind turbine at wind speeds between 6 and 10 m/s, and, optionally, the directivity of the noise source.

The measurements are taken at a distance, R_0 , from the base of the tower:

$$R_0 = H + \frac{D}{2} \quad (10.17)$$

where H is the hub height and D is the diameter of the rotor. This distance is a compromise to allow an adequate distance from the source but with minimum influence of the terrain, atmospheric conditions or wind-induced noise. The microphones are located on boards at ground level so that the effect of ground interference on tones may be evaluated.

Simultaneous A-weighted sound pressure level measurements (more than 30 measurements each of not less than 1 minute duration) are taken with measurements of wind speed. All wind speeds are corrected to a reference height of 10 m. The preferred method of determining wind speed, when the turbine is operating, is from the electrical power output of the turbine and the power curve. The main sound pressure level measurement is that of the downwind position while the other microphones located around the turbine are used for determining directivity. Measurements are taken with and without the turbine operating over wind speeds between 6 and 10 m/s. A correction for background noise is applied as shown in Eq. (10.18):

$$L_P = 10 \log_{10} \left(10^{\frac{L_{P+N}}{10}} - 10^{\frac{L_N}{10}} \right) \quad (10.18)$$

where

L_P is the sound pressure level of the wind turbine

L_{P+N} is the sound pressure level of the wind turbine and the background sound

L_N is the sound pressure level of the background sound

At each of the wind speeds, the apparent A-weighted sound power level of the turbine is then calculated from

$$L_W = L_{PAeq} + 10 \log_{10}(4\pi R_i^2) - 6 \quad (10.19)$$

R_i is the slant distance from the microphone to the wind turbine hub.

It may be seen that the calculation of sound power level assumes spherical radiation of the noise from the hub of the turbine. The subtraction of 6 dB is to determine the free field sound pressure level from the measurements and to correct for the approximate pressure doubling that occurs with the microphone located on a reflecting board at ground level.

IEC 61400-11 (2006) describes how tests to determine the noise emissions from a wind turbine should be conducted and IEC 61400-14 (2005) details how the results of these tests should be declared so that they are likely to be representative of a number of turbines of the same design.

An illustrative example of sound power levels of a wind turbine is shown in Table 10.7.

The wind turbine supplier provides such test results to the wind farm noise consultant to assess the noise around the wind farm.

Table 10.7 Octave band sound power levels of a large wind turbine (Bowdler and Leventhal 2011).

Centre frequency (Hz)	63	125	250	500	1000	2000	4000	8000	dB(A)
Sound power level (dB)	118	113	109	106	103	99	92	82	108

10.3.4 Prediction and assessment of wind farm noise

The noise from wind turbines at dwellings or other sensitive locations can be predicted using propagation models of various complexity. It has been found that in flat terrain simple models can give good results (Jakobsen 2012).

An early IEA document (now superseded) assumed hemi-spherical spreading to give an approximate method to estimate the sound pressure level of a single turbine or group of turbines at a distance R provided that they are located in flat and open terrain as

$$L_P(R) = L_W - 10 \log_{10}(2\pi R^2) - \Delta L_a \quad (10.20)$$

The correction ΔL_a was for atmospheric absorption and calculated from $\Delta L_a = R\alpha$, where α was a coefficient for sound absorption in each octave band and R the distance to the turbine hub. A simpler alternative approach was to use Eq. (10.20) but with L_W specified as a single, broadband sound power level and α as 5 dB/m.

The simple model used in the Danish Statutory Order (2011) is given by

$$L_P = L_W - 10 \log_{10}(l^2 + d^2) - 11 + \Delta L_g - \Delta L_a$$

where

l is the distance to turbine base

d is the height of the turbine

11 dB is the correction for spherical spreading

ΔL_g is the correction for ground effect (1.5 dB for onshore turbines, 3 dB for offshore turbines)

ΔL_a is the air absorption coefficient (see Table 10.8)

If there are several wind turbines that influence the sound pressure level, the individual contributions are calculated separately and summed using

$$L_{1+2+\dots} = 10 \log_{10} \left(10^{\frac{L_1}{10}} + 10^{\frac{L_2}{10}} + \dots \right) \quad (10.21)$$

These simple methods for determining sound pressure levels at a point are based on spreading following an inverse square law with a correction for atmospheric absorption. Under some conditions, particularly downwind, this may be an optimistic assumption and a reduction of 3 dB per doubling of distance is more realistic. The simple models usually ignore any effects of meteorological gradients (Wagner et al. 1996; Bowdler and Leventhal 2011). Under normal atmospheric conditions, air temperature decreases with height and so the sound speed will decrease with increasing height and cause the path of the sound to curve upwards. However, under conditions of temperature inversion,

Table 10.8 Air absorption coefficient in octave bands (Danish Statutory Order 2011).

Centre frequency (Hz)	63	125	250	500	1000	2000	4000	8000
Absorption coefficient (dB/km)	0.1	0.4	1.0	2.0	3.6	8.8	29.0	104.5

e.g. as might prevail on cold winter nights, the temperature increases with height causing the sound to curve downwards. Wind direction will also affect sound propagation. Downwind the sound is bent downwards and so may experience reduced attenuation over the ground and vegetation while a shadow zone is formed upwind and can result in lower sound levels. Over distances greater than e.g. 300 m, the upwind sound reduction is greater than the downwind sound level increase.

A more comprehensive method for calculating the attenuation of sound outdoors is given in (ISO 9613-2 1996). This standard applies generally to outdoor noise propagation, not specifically from wind turbines, and calculates the sound pressure level at a point due to a source taking into account: geometrical divergence, atmospheric absorption, ground effect, reflection from surfaces and screening by obstacles. The calculation is undertaken using octave frequency bands. The Nord2000 (2006) model was developed to estimate sound levels from railway and road traffic and includes a more sophisticated noise propagation model that takes account of atmospheric refraction of the sound.

Permitted noise levels vary widely from country to country and even within countries according to local planning conditions. Calculation methods also differ (Nieuwenhuizen and Kohl 2015). In many countries, the limits are expressed in terms of a maximum permitted (often calculated) value of the sound pressure level in the open air close to dwellings (Table 10.9).

In contrast to the use of fixed limits, the approach that has been adopted in the UK (ETSU-R-97 1997) is to base the permitted noise level of a wind farm on an increase of 5 dB(A) of the $L_{A90,10\text{min}}$ sound pressure level above background noise. The 5 dB(A) limit was selected as being a reasonable compromise between protecting the internal and external environment while not unduly restricting the development of wind energy. In addition, it is suggested that a limit of less than 5 dB(A) would be difficult to monitor. BS 4142 (British Standards Institution 2014), which is a general standard for industrial noise and may not be directly applicable to wind farms, states that a difference of +10 dB or more indicates that complaints are likely, while a difference of around +5 dB is of

Table 10.9 Noise limits for sound pressure levels L_{Aeq} in different European countries (after Hansen et al. 2017).

Country	Residential dB(A)	Rural dB(A)
Germany		
Day	55	50
Night	35	35
Netherlands		
Day	47	47
Night	41	41
Denmark (wind speed 6–8 m/s)		
Outdoor	37–39	42–44
Indoor	20–25	20–25
France		
Day	35	35
Night	35	35

Note the definition of locations varies from country to country.

marginal significance. If the predicted sound pressure level is below 35 dB(A) then measurements of background noise are not required.

A lower fixed limit of 35–40 dB(A) during daytime and 43 dB(A) during nighttime is also applied. The selection of the daytime limit of either 35 or 40 dB(A) is made by considering

- The number of dwellings in the neighbourhood of the wind farm.
- The effect of noise limits on the number of kWh generated.
- The duration and level of exposure.

The nighttime lower limit of 43 dB(A) is derived from a 35 dB(A) sleep disturbance criterion, an allowance of 10 dB(A) for attenuation through an open window and with 2 dB subtracted for the use of $L_{A90,10\text{min}}$ rather than $L_{Aeq,10\text{min}}$. Examples of the noise criteria are shown in Figures 10.14 and 10.15. There is also a penalty for audible tones, which rises to a maximum of 5 dB. This early recommendation is still used to assess noise from wind farms in the UK and has been supplemented by a Code of Practice providing guidance on its use (IOA 2013).

10.3.5 Low frequency noise

Wind farm noise limits in most countries are based on A-weighted sound pressure levels across the full audible spectrum. However, over recent years, and particularly in some countries, e.g. Australia and Canada, there has been concern over wind farm low frequency noise. *Low frequency wind farm noise* is a general term used to classify three categories of sound emissions:

- Low frequency noise is in the audible range between 20 and 160 (or 200) Hz.
- Infrasound is in the inaudible range below 20 Hz.
- Aerodynamic modulation (AM) is sound associated with rotating wind turbine blades.

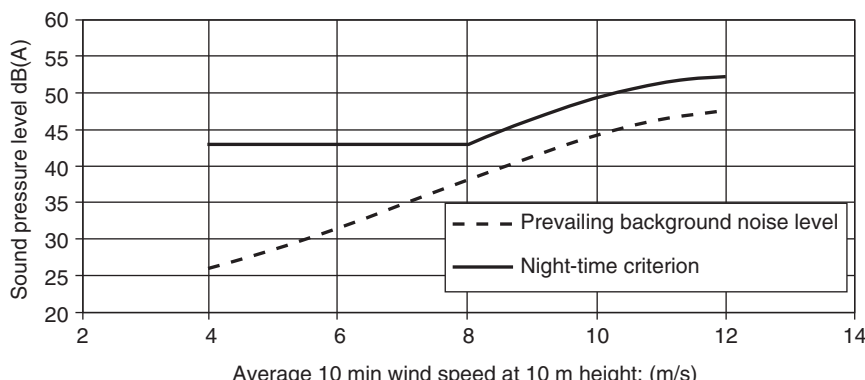


Figure 10.14 Example of noise criterion proposed by the UK Working Group on Noise from Wind Turbines. Night-time criterion (ETSU 1997). Source: Reproduced by permission of ETSU on behalf of the DTI.

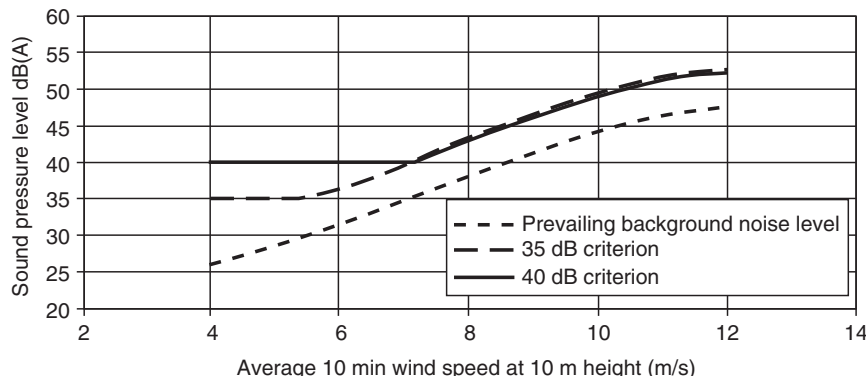


Figure 10.15 Example of noise criterion proposed by the UK Working Group on Noise from Wind Turbines. Daytime criterion (ETSU 1997). Source: Reproduced by permission of ETSU on behalf of the DTI.

The Danish standard has been extended to define a maximum sound pressure level of 20 dB(A) of low frequency noise (20–160 Hz) permitted within a building (Jakobsen 2012). This value is calculated using an A-weighted sound power level in a similar manner to Eq. (10.18) but over a restricted frequency range and includes a term to represent the attenuation of sound through the building fabric. In the UK, the Institute of Acoustics (IOA 2016) formed a Working Group on Amplitude Modulation and proposed a method to characterise amplitude modulation but reported experience of its use is limited.

Low frequency and infrasound from wind turbines and their effect on human health remain controversial (Colby et al. 2009; Hansen et al. 2017; Chapman and Crichton 2017). The literature is contested, but it appears that low frequency noise can in some circumstances cause annoyance. This type of sound remains of concern because it is less attenuated by the atmosphere and can in some circumstances propagate over large distances. The levels of infrasound from wind turbines are so low that they are generally considered to be inaudible. There is no clear evidence that either low frequency noise or infrasound from wind turbines has a direct effect on human health.

10.4 Electromagnetic interference

Wind turbines have the potential to interfere with the electromagnetic signals that form the basis of a wide range of modern communication systems and their siting requires careful assessment in respect of electromagnetic interference (EMI). Wind energy developments often compete with radio and other communication systems for hilltops and other open sites where high wind speeds provide attractive energy output from wind farms and good propagation paths for electromagnetic signals. There is a large and increasing number of types of radio systems with quite different requirements for their effective operation and that react to the presence of wind turbines in different ways. In

many countries it is likely that communication links will cross a wind farm site requiring careful micro-siting of the turbines. Historically, wind turbines interfered with the reception of the now obsolete analogue TV signals. Modern digital TV transmission systems are less susceptible to wind turbines although the strength of the signal may be reduced. Concern over the interaction of wind turbines with defence and civilian radar continues to lead to restrictions on siting and delays in construction of a number of wind farms.

The electrical generator, control gear and electronics of a wind turbine can produce emissions at radio frequencies but these may be minimised by appropriate screening and suppression. Rather than behave as an aerial, a steel tubular tower has a substantial screening effect on internal emissions. The nacelle forms a Faraday cage against lightning and this will screen emissions from within the nacelle itself. Additional precautions are necessary with the power electronic converters of variable-speed wind turbines that operate at increasingly high switching frequencies but measures to deal with conducted or radiated EMI from any power electronic equipment are standard. Electromagnetic emission from wind turbines is not a common problem.

Scattering of external signals is, however, an important EMI mechanism associated with wind turbines. An object exposed to an electromagnetic wave disperses incident energy in all directions and it is this spatial distribution that is referred to as scattering. There are two fundamental interference mechanisms for EMI from wind turbines, back scattering and forward scattering. These are shown in Figure 10.16. Forward scattering occurs when the wind turbine is located between the transmitter and receiver. The interference mechanism is one of scatter or refraction of the signal by the wind turbine. Back scattering occurs when the turbine is located behind the receiver and causes the signal to be reflected. Both mechanisms result in a time delay between the desired signal and the interference.

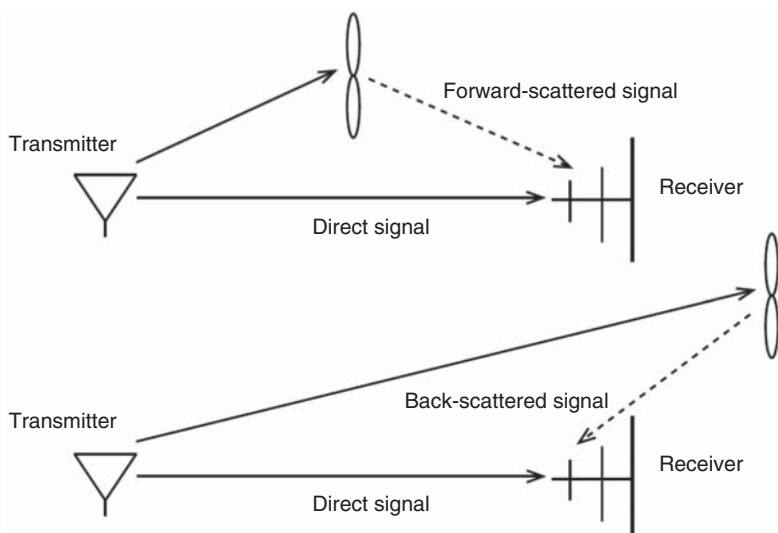


Figure 10.16 Interference mechanisms of wind turbines with radio systems.

The problem of the interaction of wind turbines and radio communication systems is complex as the scattering mechanisms are not readily characterised and the signal is modulated by the rotation of the blades (Angulo et al. 2014). The electromagnetic properties of wind turbine rotors, and hence scattering, will be influenced by

- Rotor diameter and rotational speed.
- Rotor surface area, plan-form, and blade orientation, including yaw angle.
- Hub height.
- Structural blade materials and surface finish.
- Hub construction.
- Surface contamination (including rain and ice).
- Internal metallic components, including lightning protection.

The practices of various authorities differ in determining if a wind farm is likely to give rise to EMI problems. It is emphasised by the radio and radar authorities that each wind farm proposal needs to be considered individually for its potential impact on a range of systems. Contact with the relevant authorities should be made early when considering a wind farm site (Ofcom 2009).

10.4.1 Impact of wind turbines on communication systems

A simple, general analysis of the electro-magnetic interference caused by a wind turbine using the carrier to interference ratio (C/I) was proposed by Moglia et al. (1996) (using the earlier work by van Kats and van Rees 1989). The C/I defines the quality of a radio link. For example, a fixed microwave link may have a C/I requirement of 50–70 dB while for a mobile radio service the requirement may be only 15–30 dB.

The useful carrier signal received, C , is given by

$$C = P_T - A_{TR} + G_{TR} \quad (10.22)$$

where

P_T is the transmitter power (dB)

A_{TR} is the attenuation between the transmitter and receiver (dB)

G_{TR} is the receiver antenna gain in the direction of the required signal (dB)

The interfering signal, I , is given by

$$I = P_T - A_{TW} + 10 \log_{10} \left(\frac{4\pi\sigma}{\lambda^2} \right) - A_{WR} + G_{WR} \quad (10.23)$$

where A_{TW} is the attenuation between the transmitter and wind turbine (dB), A_{WR} is the attenuation between the wind turbine and receiver (dB), G_{WR} is the receiver antenna gain in the direction of the reflected signal (dB), and $10 \log_{10} \left(\frac{4\pi\sigma}{\lambda^2} \right)$ is the contribution of the

wind turbine to scattering. σ is the radar cross-section and, if more reliable information is not available, may be taken as the optical silhouette of the complete blade set as viewed parallel to the axis of rotation (Bacon 2002). λ is the wavelength of the signal.

It may be seen that the ratio of useful signal to interference is

$$C - I = A_{TW} - 10 \log_{10} \left(\frac{4\pi\sigma}{\lambda^2} \right) + A_{WR} - A_{TR} + G_{TR} - G_{WR} \quad (10.24)$$

Assuming the distance between the transmitter and receiver is much greater than the distance of the wind turbine to the receiver, then $A_{TW} = A_{TR}$. Assume the free space loss is $A_{WR} = 20 \log_{10} \frac{4\pi r}{\lambda}$, and define the antenna discrimination factor as $\Delta G = G_{TR} - G_{WR}$.

Then the C/I ratio reduces to

$$C - I = 10 \log_{10} 4\pi + 20 \log_{10} r - 10 \log_{10} \sigma + \Delta G \quad (10.25)$$

Equation (10.25) shows that the ratio of the useful carrier signal to interference may be improved by

- Increasing the distance from the turbine to the receiver, r .
- Reducing the radar cross-section, σ .
- Improving the discrimination factor of the antenna, ΔG .

Equation (10.25) may be rearranged to define a ‘forbidden zone’ within which a wind turbine may not be located if an adequate C/I is to be maintained:

$$20 \log_{10} r = C/I_{\text{required}} + 10 \log_{10} \sigma - \Delta G - 11 \quad (10.26)$$

It may be seen that the ‘forbidden zone’ depends critically on the radar cross-section, σ . This interference region or forbidden zone is shown in Figure 10.17.

The back-scattering region (for a given required C/I value) has a smaller radius than the forward-scattering region. This is because the back-scatter wind turbine radar

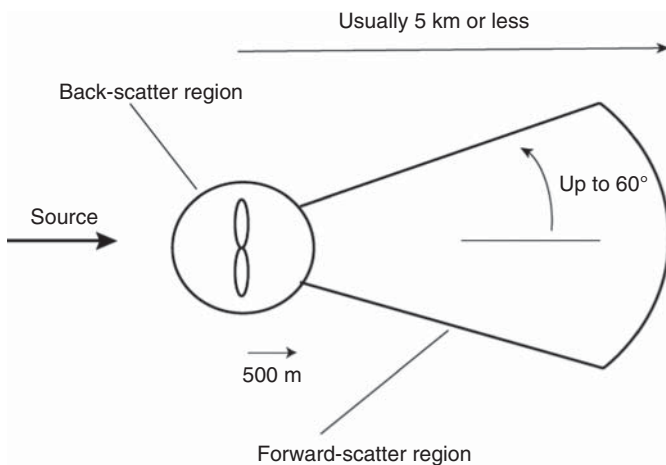


Figure 10.17 Interference regions of a wind turbine.

cross-section is much smaller than for forward scatter and also it is possible to take advantage of the directivity of the receiving antenna (ΔG). Equation (10.26) defines only the radii of the two regions, and it is also necessary to determine the angle over which the two regions extend.

Determination of the radar cross-section of a wind turbine is not straightforward although it can be obtained from sophisticated calculation (Jenn and Cuong 2012; Poupart 2003) or field tests (Randhawa and Rudd 2009). For initial estimates of the effect of wind turbines on radio signals, the interference zone around a turbine is often assumed as a key-hole shape of defined size. Typically, the forward-scatter region is of radius up to 5 km and arc up to 120° and the back-scatter region is of radius of 500 m (Ofcom 2009).

Randhawa and Rudd (2009) measured the radar cross-section of an individual wind turbine and wind farm (Table 10.10).

Van Kats and Van Rees (1989) reported a comprehensive series of site measurements on a 45-m diameter wind turbine. They estimated a radar cross-section in the back-scatter region of 24 dBm² and a worst-case value in the forward-scatter region of 46.5 dBm². For this turbine, back-scatter region radii of 100 m (C/I contour of 27 dB) and 200 m (C/I contour of 33 dB) were determined. The forward-scattering region was much larger with radii of 1.3 km (C/I contour of 27 dB) and 2.7 km (C/I contour of 33 dB). They suggested that a C/I value of 33 dB should result in no visible interference of an analogue TV. Moglia et al. applied their method to medium sized wind turbines (33 and 34 m diameter) to give a back-scatter radius of approximately 80 m and a forward-scatter radius of 450 m for a 46 dB C/I contour. Their calculations were supported by measured site results that gave reasonable agreement with the predictions. In these two examples back scattering was unlikely to be a significant problem as other constraints (e.g. acoustic noise and visual effects) would ensure that the any dwelling is outside the ‘forbidden zone’.

Fixed links carry large amounts of data and are of great economic importance, and both theoretical and experimental investigations of the impact of wind turbines on them have been undertaken (Bacon 2002; Randhawa and Rudd 2009). It is important that there is a clear line-of-sight between the transmitter and receiver of a microwave link and that a proportion of the Fresnel zone must be free from obstructions. The Fresnel zone is an ellipsoid region of space that makes the major contribution to the signal received and

Table 10.10 Example of radar cross-section of a wind turbine and wind farm.

Frequency (MHz)	Radar cross-section (dBm ²)	
	Back scatter	Forward scatter
Individual turbine		
436	47	53
1477	32	50
Wind farm		
436	38	60
1477	42	54
3430	—	41

within which component parts of the signal will be in phase (Figure 10.18). To ensure free space propagation conditions, at least 60% of the first Fresnel zone must be free from obstruction. The radius of the Fresnel zone (R_F) is given by

$$R_F = \sqrt{\frac{n\lambda d_1 d_2}{d_1 + d_2}} \quad (10.27)$$

where

d_1 and d_2 are the distance from the two microwave terminals to the point of reference

λ is the wavelength

n is the Fresnel zone number

In practice, it is usually considered necessary to be completely outside the first Fresnel zone of the link with an additional exclusion zone of around 100–200 m to avoid unwanted reflections. These additional allowances for reflections are rather conservative rules-of-thumb and may be reduced following detailed studies.

In summary, the accurate analytical determination of the way wind turbines may interfere with radio communication systems remains difficult. In particular, techniques to determine the effects of irregular terrain and the details of the blade shape and materials to allow a radar cross-section to be determined reliably have yet to be developed and validated. Approaches that rely on simplified assumptions to estimate the radar cross-section can only be considered approximate. However, they do provide a useful qualitative understanding of the problem. In practice, a dialogue with the local telecommunications authorities is required to determine if a wind turbine or wind farm development is likely to cause EMI.

10.4.2 Impact of wind turbines on aviation radar

The potential impact of wind turbines on aviation radar, both civil and military, is of major concern and has resulted in a number of proposed wind farm projects not proceeding. Primary radar uses passive echoes to determine the location and movement of the target while secondary radar uses an active device in the target to generate a response signal.

A radar system works by emitting a pulse of electromagnetic energy at radio frequency, receiving and amplifying the reflected signal and then processing it. The distance to the target object is calculated from the time difference between the pulse being emitted

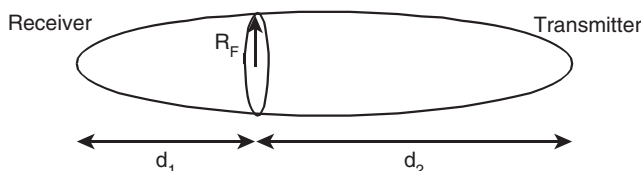


Figure 10.18 Illustration of first Fresnel zone (Fresnel ellipsoid).

and the signal received. A large reflected signal, such as may be caused by the large radar cross-section of a wind turbine, can result in amplitude limiting and distortion within the receiving or signal processing circuits. In addition, primary radars use the Doppler effect to distinguish between fixed and moving objects and can have difficulty in distinguishing between moving wind turbine blades in a wind farm and a moving aircraft.

The main impacts of a wind farm on radar are (ETSU 2002)

- *Masking*: Radars operate at high frequency and so require a clear ‘line-of-sight’. Wind turbines can cause shadowing effects and the creation of areas where targets cannot be detected. Masking of military radars is an obvious problem but is also of concern for meteorological radars that look at a very narrow angle just above the ground
- *Radar clutter*: Unwanted radar returns are known as *clutter* and rotating wind turbines can lead to a large number of, sometimes intermittent, returns that may be interpreted by the radar as a moving object.

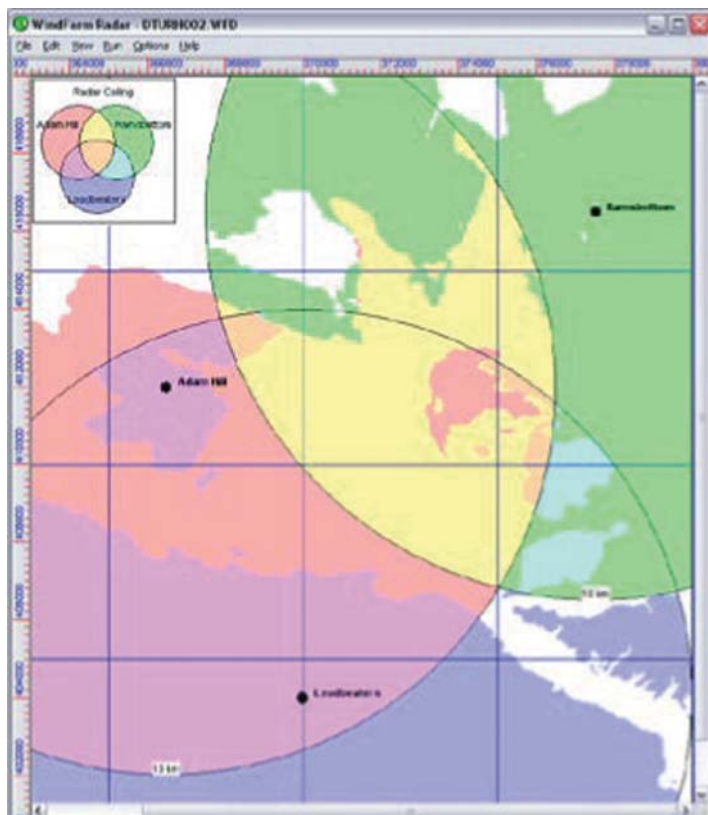


Figure 10.19 Example of areas where a wind turbine would mask radar. Source: Reproduced by permission of ReSoft.

- *Scattering:* Scattering occurs when the radar signal is reflected or refracted by rotating wind turbine blades and detected by the emitting radar system. This can lead to multiple false radar returns being displayed or even returns from genuine aircraft being assigned a wrong location.

NTIA (2008) provides guidance on how to assess whether or not wind turbines are likely to impact civil Air Traffic Control surveillance radars. A digital terrain model of the area surrounding the potential wind farm is used to determine where wind turbines would be visible to radar taking into account the curvature of the earth and local topography. The assessment is based on the radar line-of-sight, which is analogous to the optical line-of-sight but modified for atmospheric refraction of the radar signal. Figure 10.19 is an example of the calculation of the areas where masking of each of the three radars can occur.

Figure 10.20 summarises a simple process for the evaluation of the likely impact of wind turbines on radar.

EUROCONTROL (2014) defines four zones for the assessment of the impact of wind turbines on radar. In the ‘safeguarding’ zone, the closest area to the sensor, wind turbines

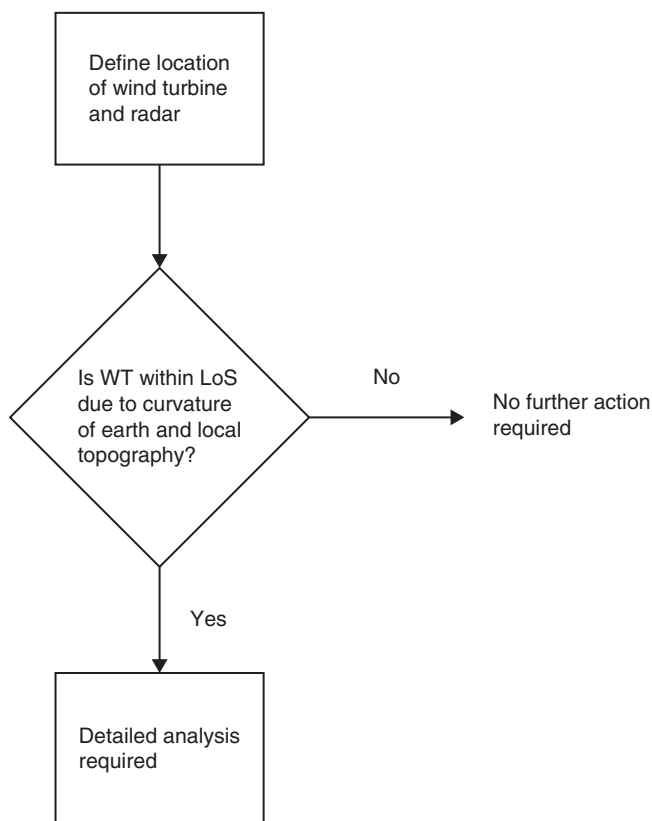


Figure 10.20 Evaluation of the impact of wind turbines on radar.

Table 10.11 Recommended ranges for assessment of primary surveillance radar.

Zone	1	2	3	4
Description	0–500 m	500 m–15 km and in radar line-of-sight	Greater than 15 km and within maximum range and in radar line-of-sight	Anywhere within range but not in radar line-of-sight
Assessment requirement	Safeguarding	Detailed assessment	Simple assessment	No assessment

may not to be built. In the second zone, wind turbines can be built provided that an impact assessment analysis demonstrates that the impact can be tolerated. In the third zone, wind turbine can be built on the basis of the results of a simple and generic impact assessment. Table 10.11 summarises these zones for primary surveillance radar.

Options for reducing the impact of wind farms on aviation radar include modifying the operation of the radar system, changing the layout or location of the wind farm as well as reducing the radar cross-section of the wind turbines, particularly the blades. A number of research projects have been undertaken to investigate the use of aircraft stealth technology to reduce the radar cross-section of wind turbine blades by changing the shape of the blades or using radar-absorbing materials. To date such approaches have not entered widespread commercial production due to their cost, reduction in wind turbine performance and the increased precision that would be required in the blade manufacturing process.

The assessment of the EMI of wind farms on communication and radar systems is now a very specialist area and consultants are likely to be involved in this aspect of the preparation of the Environmental Statement for wind farms of any significant size.

10.5 Ecological assessment

Wind farms are often constructed in areas of ecological importance and the Environmental Statement will include a comprehensive assessment of the local ecology, its conservation importance, the impact of the wind farm (during construction and operation) and mitigation measures. A study of the site hydrology is also likely to be included, not least because of its importance for the ecology. When considering the ecological impact of renewable energy schemes, the following categories of effects are considered:

- Immediate damage to wildlife habitats during construction.
- Direct effects on individual species during operation.
- Longer-term changes to wildlife habitats as a consequence of construction or because of changed land-use management practices.

The scope of the ecological assessment is likely to include

- A full botanical survey, including identification and mapping of plant species on the site.
- A desk and field survey of existing bird and non-avian fauna.
- An assessment of how the site hydrological conditions relate to the ecology.
- Evaluation of the conservation importance of the ecology of the site.
- Assessment of the potential impact of the wind farm.
- Proposed mitigation measures, including which part(s) of the site should be avoided.

Gipe (1995) suggested that the main impact on plants and wildlife (excluding birds) is from road building and the disturbance of habitat. Direct loss of habitat due to a wind farm is small (approximately 3%) and this can be reduced further by reinstating roads and construction areas once the wind farm is built. However, during construction there is likely to be considerable disturbance including from the frequent traffic of heavy vehicles and it may be necessary to timetable major work to avoid sensitive periods (e.g. breeding seasons). In many countries, the early wind farms of relatively small turbines that were built last century are being re-powered with larger turbines and/or extended. These developments of established wind farm sites need to be assessed in the same manner as a new wind farm.

Perrow (2017) provides a comprehensive overview of the impact of wind farms on wildlife based on a review of literature. Most studies identified were from Europe and North America addressing issues of birds and bats. There was a lack of peer-reviewed studies found from China and India that are rapidly increasing their wind farm capacity.

10.5.1 Impact on birds

The impact of wind energy developments on birds was particularly controversial in the 1990s because of concern over migrating birds and raptors colliding with wind turbines in the USA and in the south of Spain at Tarifa. Raptors are rare and long-lived birds and so collisions are of particular concern. Elsewhere in Europe, the main concern was not collisions of birds with turbines but issues associated with disturbance and habitat loss. Since then, there has been very considerable research into the impact of wind farms on birds and it would appear that by careful assessment and monitoring, before construction and during operation of the wind farm, the environmental impact on birds may be managed effectively. Pearce-Higgins et al. (2012) identified that the main impact on the populations of some bird species occurred during construction of the wind farm. Comprehensive guidance on how the effect of wind turbines on birds should be managed and surveys conducted to assess the impact of proposed wind farms on birds is given in Scottish National Heritage (2019a) and Royal Society for the Protection of Birds (2019).

The presence of a wind farm may affect bird life in one or more of the following ways:

- Collision or interaction with wind turbine blades.
- Displacement due to disturbance.

- Barrier effect, in which birds are deterred from using their normal routes to feeding or roosting grounds.
- Habitat change and loss, particularly during construction.

These risks should be evaluated for every species of bird that uses the wind farm site.

A useful early review of the effects of wind farms on birds and guidance on environmental assessment criteria and site selection issues is given in Langston and Pullan (2003). Drewitt and Langston (2006) conducted an extensive literature survey to assess the impact of wind farms on birds. They found annual collision rates reported varying between 0.01–23 birds/turbine. The higher numbers are corrected for scavenger removal and are from a coastal site and relate to gulls, terns and ducks. They also found that none of the barrier effects identified had resulted in significant impact on bird populations while the studies of displacement due to disturbance were largely inconclusive. Typical habitat loss due to a wind farm was approximately 2–5% of the total development area. Lloyd (ETSU 1996) stated that, because the removal of habitat is comparatively small in a wind farm development, the main issues are the effect on bird behaviour either from construction or operation and direct mortality from birds colliding with wind turbines.

A number of important studies reported collisions of raptors with wind turbines in California (Committee on Environmental Impacts of Wind Energy Projects 2007). It was found that the wind farms of the Altamont pass in the early 1990s were not typical of European projects or more recent developments in the USA. The turbines were very numerous, some 7000 turbines in 200 km², rather small in size (typically 100 kW), often on lattice steel towers and with close spacing along the rows facing the prevailing winds. Lloyd (ETSU 1996) suggested that a number of factors may have led to the high collision rate among raptors. The Altamont turbines were often located on low rises and ridges in the pass to exploit local acceleration of the wind speed. A large number of the collisions appeared to be at the end of the turbine rows where the birds may have attempted to fly around the densely packed turbines. In Altamont there are few trees and it is suggested that some species used the lattice steel towers as perches and even for nesting.

The bird strike rate for early UK wind farms is quoted by Lowther (ETSU 1996) and is shown in Table 10.12.

The three experimental turbines on Burgar Hill, including a 3 MW 60 m diameter prototype, were adjacent to the habitats of a number of bird populations of national significance, including 4% of the UK breeding population of the hen harrier. Studies were undertaken over a 9 year period, and during that time four mortalities (three

Table 10.12 Bird strikes at wind farms in the UK.

Wind farm	Number of turbines	Bird strikes/turbine year
Burgar Hill, Orkney	3	0.15
Haverigg, Cumbria	5	0
Blyth Harbour, Northumberland	9	1.34
Bryn Titli, Powys	22	0
Cold Northcott, Cornwall	22	0
Mynydd y Cemmaes, Powys	24	0.04

black-headed gulls and one peregrine) were noted as possibly being the result of turbine strike.

The Blyth Harbour wind farm consisted of nine 300 kW wind turbines positioned along the breakwater of a harbour that was designated a Site of Special Scientific Interest. As it had the highest density of birds of any UK wind farm site at that time (110 varieties identified with more than 1100 bird movements per day), it was the subject of a monitoring programme. The main species that inhabit the area were the cormorant, eider, purple sandpiper, and three types of gull. There was particular concern over the purple sandpiper, which winters in the harbour, and so special measures were taken to improve its roosting habitat by providing additional shelter. Over a 3 year period, 31 collision victims were identified. The mortality by collision was mainly in eider and among the gulls. This was calculated not to have a significant adverse impact on the local populations. In common with studies undertaken on Dutch and Danish coastal wind farms, it appeared that most species had adapted to the wind turbines. With respect to disturbance and habitat loss, the study indicated that there was no significant long-term impact. The purple sandpiper population was not affected adversely by the wind farm and, although temporary displacement of cormorant occurred during construction, the population returned to its previous haunts once construction was completed.

The Bryn Tilly wind farm is adjacent to a Site of Special Scientific Interest that holds important breeding communities of buzzard, peregrine, red grouse, snipe, curlew, and raven. The wind farm was the subject of a bird impact study that showed no statistically significant impact on breeding birds, and a bird strike study undertaken in 1994/1995 indicated that it is unlikely that there were any collision mortalities during that time.

Clausager (ETSU 1996) undertook an extensive review of both the American and European early literature of the impact of wind turbines on birds. He concluded that, of the mainly coastal locations studied, the risk of death by collision with wind turbine rotors is minor and creates no immediate concern of an impact on the population level of common species. Drawing on 16 studies, and using a multiplier of 2.2 for birds not found, he estimated the highest number of mortalities due to collisions to be six to seven birds/turbine year. With approximately 3500 wind turbines in Denmark at that time, this led to a maximum number of birds dying from collision as 20 000 to 25 000. This number was compared with at least one million birds being killed from traffic in Denmark each year. He dismissed the direct loss of habitat as being small and of minor importance but draws attention to the issues of changes in the area due to the wind farm construction, particularly draining of low-lying areas. He also noted that some species of birds temporarily staying in an area may be adversely affected and that an effect has been recorded within a zone of 250–800 m from a turbine, particularly for geese and waders.

The Committee on Environmental Impacts of Wind Energy Projects (2007) undertook a comprehensive review of the literature of the impacts of wind turbines on birds and bats. Although clearly recognising the limitations of the data, they estimated that in 2003 wind turbines accounted for 0.003% of bird deaths in the USA. They also quote the results of 14 studies on raptors to give an average fatality rate from wind turbines of 0.03 birds per turbine/year.

Measures that may be taken to protect important bird species while allowing wind energy development to continue include

- Baseline studies should be undertaken at every wind farm site to determine which species are present and how the birds use the site. This should be a mandatory part of the Environmental Statement for all wind farms.

- Known bird migration corridors and areas of high bird concentrations should be avoided unless site-specific investigation indicates otherwise. Where there are significant migration routes, the turbines should be arranged to leave suitable gaps (e.g. by leaving large spaces between groups of wind turbines).
- Microhabitats of rare/sensitive species, including nesting and roosting sites, should be avoided by turbines and auxiliary structures. (It may be noted that meteorological masts as well as wind turbines can pose a hazard for birds.)
- Particular care is necessary during construction, and it is proposed that access for contractors should be limited to avoid general disturbance over the entire site. If possible, construction should take place outside the breeding season. If this is not possible, then construction should begin before the breeding season to avoid displacing nesting birds.
- Tubular turbine towers are preferred to lattice structures. Consideration should be given to using unguyed meteorological masts.
- Fewer large turbines are preferred to larger numbers of small turbines. Larger turbines with lower rotational speeds are probably more readily visible to birds than smaller machines.
- Within the wind farm, the electrical power collection system should be underground.
- Turbines should be laid out so that adequate space is available to allow birds to fly through them without encountering severe wake interaction. A minimum spacing of 120 m between rotor tips is tentatively suggested as having led to minimum collision mortalities on UK wind farms. Turbines should be set back from ridges and avoid saddles and folds that are used by birds to traverse uplands.

Drewitt and Langston (2006) suggest wind farm development should be avoided where there is

- A high density of waterfowl and waders.
- A high level of raptor activity.
- A high level of breeding and wintering activity.

It is interesting to note that a 30 MW wind farm development in Scotland was only able to proceed after an extensive study of raptors and the conversion of 450 ha of coniferous forest to heather dominated moorland and the exclusion of sheep from a further 230 ha. It was anticipated that this extension of the moorland habitat would increase the amount of prey away from the wind farm and so reduce the risk of collisions by golden eagles and other raptors.

10.5.2 Impact on bats

Bats and their roosts are protected either by primary legislation (law) or regulations in many countries; in the UK it is an offence to intentionally disturb a bat. It is now accepted that wind turbines can pose a risk to bats (Horn et al. 2008; Mathews et al. 2016) and that this needs to be assessed in the Environmental Impact Assessment of any wind farm

development. Guidance on how this assessment should be undertaken and the impact of wind farms on bat populations managed is given in Rodrigues et al. (2008) and Scottish National Heritage (2019b).

Wind farms can affect bats through: injuries or mortality during flight through collision or barotrauma caused by the blades; disturbance of foraging habitats and commuting corridors; damage or disturbance to roosts and displacement of individuals or species particularly during wind farm construction.

When a wind farm development is being considered it is necessary to undertake a detailed assessment of its potential impact on bats. This process is similar to that required for birds. The assessment will consider

- The extent of bat activity at the site, including identification of species.
- The risk of turbine-related mortality.
- The effect on the population of the species.

The assessment is undertaken initially through a desk study and then by field surveys, often using bat detectors. Bat detectors transform the inaudible ultrasonic sounds made by the bats into audible sounds that can be used to identify the species. There are many species of bats but those common in Britain have echolocation calls with a useful range of only a few metres and so prefer to fly close to habitat features such as hedgerows, woodlands, walls, rivers, and within and just above the tree canopy as they transit the site or search for insects. Bat activity in Britain has been shown to decline more than 50 m away from the tree line. It has also been shown that bat fatalities in British wind farms occur mainly between April and October during still warm nights with a maximum temperature of 10 °C and a ground wind speed of less than 5 m/s (Mathews et al. 2016).

The impact of a wind farm on bats can be minimised by careful micro siting and positioning the turbines away from bat activity, particularly their roosts. A buffer zone should be established around woodland or wetland areas where bats are likely to be present. A distance of 200 m between the tip of the blade of the nearest turbine and nearest tree line is recommended in Rodrigues et al. (2008), but this buffer zone is reduced to 50 m in Britain, based on the species of bat likely to be present.

It has been shown that if the idling speed of a wind turbine in low wind speed is reduced to less than 2 rpm this reduces bat mortality rates by 50% and so one strategy is to adjust the turbine control systems to reduce the speed of rotation of the rotor when idling in low wind speeds. Also, increasing the cut-in wind speed on warm summer nights between April–October reduces bat mortality with only a limited loss of energy. It has been suggested that if bat activity is detected in a wind farm, the turbines should remain idling for wind speeds at ground level of less than 6.5 m/s at nighttimes of the summer months.

An appendix of Scottish National Heritage (2019b) describes how bats were identified in a large wind farm after construction. A study of the problem was undertaken and found that most bat activity took place between mid-August and mid-September when nighttime temperature exceeded 11.5 °C and the wind speed was below 5 m/s. The mitigation adopted was to curtail the turbines at night when the wind speed was below 5 m/s, with a restart at 5.5 m/s, and when temperatures were greater than 11.5 °C. After this modification to the control system was made, bat mortality was assessed using site surveys by trained dog teams and found to be eliminated by these measures.

References

- Angulo, I., de la Vega, D., Cascón, I. et al. (2014). Impact analysis of wind farms on telecommunication service. *Renewable Sustainable Energy Rev.* 32: 84–99.
- Bacon, D. F. (2002) Fixed link wind turbine exclusion zone method. Radiocommunications Agency. <http://licensing.ofcom.org.uk/binaries/spectrum/fixedterrestrial-links/wind-farms/windfarmdavidbacon.pdf> (accessed 21 August 2019).
- Bosilovich M., Cullather R. and National Centre for Atmospheric Research Staff (2019). The climate guide: NASA's MERRA2 reanalysis. <https://climatedataguide.ucar.edu/climate-data/nasas-merra2-reanalysis> (accessed 15 April 2020).
- Bowdler, D. and Leventhal, G. (eds.) (2011). *Wind Turbine Noise*. Multi Science.
- British Standards Institution (2014). *BS 4142: Method for rating industrial noise affecting mixed residential and industrial areas*.
- Carta, J.A., Velazquez, S., and Cabrera, P. (2013). A review of measure-correlate-predict (MCP) methods used to estimate long-term wind characteristics at a target site. *Renewable Sustainable Energy Rev.* 27: 362–400.
- Chapman, S. and Crichton, F. (2017). *Wind Turbine Syndrome: A Communicated Disease*. Sydney University Press.
- Colby, W., Dobie, R., Leventhal, G., Lipscomb, D., McCunney, R., Seilo, M., Søndergaard, B. (2009). Wind turbine sound and health effects: an expert panel review. Report by American Wind Energy Association (AWEA).
- Committee on Environmental Impacts of Wind Energy Projects (2007). Environmental impacts of wind-energy projects. <https://www.nap.edu/search/?term=0-309-10835-7&x=0&y=0> (accessed 26 March 2019).
- Danish Statutory Order on Noise from Wind Turbines (2011), *Statutory Order No. 1284 of 15 December 2011*. <https://eng.mst.dk/media/mst/69035/Statutory%20Order%20on%20noise%20from%20wind%20turbines.pdf> (accessed 26 February 2019).
- DCLG (2015). *Planning practice guidance for renewable and low carbon energy*. <https://www.gov.uk/guidance/renewable-and-low-carbon-energy> (accessed 17 March 2019)
- DECC (2011) Update of UK shadow flicker evidence base. Report by Parsons Brinckerhoff. <https://www.gov.uk/government/news/update-of-uk-shadow-flicker-evidence-base> (accessed 17 March 2019).
- Derrick, A. (1993). Development of the measure-correlate-predict strategy for site assessment. Proceedings of the European Wind Energy Association Conference, Travemunde, pp. 681–685.
- Devine-Wright, P. (2005). Beyond NIMBYism: towards an integrated framework for understanding public perceptions of wind energy. *Wind Energy* 8 (2): 125–139.
- Drewitt, A.L. and Langston, R.H.W. (2006). Assessing the impacts of wind farms on birds. *Ibis* 148: 29–42.
- Eberle, A., Roberts O., Key A., Bhaskar P., and Dykes K. 2019. NREL's balance of system cost model for land based wind. *NREL/TP-6A20-72201*. <https://www.nrel.gov/docs/fy19osti/72201.pdf> (accessed 15 April 2020).
- Electricity Networks Association (2012). Separation between wind turbines and overhead lines, principles of good practice. *Engineering Recommendation L44*.
- ETSU (1996). Birds and wind turbines: can they co-exist?. Proceedings of a seminar held at the Institute for Terrestrial Ecology, Huntingdon, England (26 March 1996).
- ETSU (2002). Wind energy and aviation interests – interim guidelines. Wind Energy Defense and Civil Aviation Interests Working Group. *ETSU Report W/14/00626/REP*.
- ETSU-R-97 (1997). The assessment and rating of noise from wind farms. Final Report of the Working Group on Noise from Wind Turbines, 1997. <http://webarchive.nationalarchives.gov.uk/+/www.berr.gov.uk/energy/sources/renewables/explained/wind/onshore-offshore/page21743.html> (accessed 5 February 2019).

- EUROCONTROL (2014) Guidelines; how to assess the potential impact of wind turbines on surveillance sensors. *EUROCONTROL-GUID-130*. <https://www.eurocontrol.int/sites/default/files/publication/files/20140909-impact-wind-turbines-sur-sensors-guid-v1.2.pdf> (accessed 21 March 2019).
- EWEA (2009). *Wind Energy – The Facts*. London: Earthscan.
- Gipe, P. (1995). *Wind Energy Comes of Age*. Chichester: Wiley.
- Glasson, J., Therivel, R., and Chadwick, A. (2012). *Introduction to Environmental Impact Assessment*, 4e. Routledge.
- Hansen, C.H., Doolan, C.J., and Hansen, K.L. (2017). *Wind Farm Noise*. Chichester: Wiley.
- Hau, E. (2013). *Wind Turbines: Fundamentals, Technologies, Applications, Economics*, 3e. Berlin: Springer Verlag.
- Horn, J.W., Arnett, E.B., and Kunz, T.H. (2008). Behavioral responses of bats to operating wind turbines. *J. Wildl. Manage.* 72: 123–132.
- IEC 61400-11 (2006). *Wind turbine generator systems – Part 11: Acoustic noise measurement techniques*. Geneva, Switzerland: International Electrotechnical Commission.
- IEC 61400-14 (2005). *Wind turbines – Part 14: Declaration of apparent sound power level and tonality values*. Geneva, Switzerland: International Electrotechnical Commission.
- IOA (2013). Good practice guide to the application of ETSU-R-97 for the assessment and rating of wind turbine noise.
- IOA (2016). IOA Noise Working Group (Wind Turbine Noise) Amplitude Modulation Working Group Final Report.
- IRENA (2012) Renewable energy technologies cost analysis series, volume 1: power sector, issue 5/5 – wind power. https://www.irena.org/documentdownloads/publications/re_technologies_cost_analysis-wind_power.pdf (accessed 15 April 2020).
- ISO 9613-2 (1996). *Acoustics – Attenuation of sound during propagation outdoors – Part 2: General method of calculation*. Geneva, Switzerland: International Organization for Standardization.
- Jakobsen, J. (2012). Danish regulation of low frequency noise from wind turbines. *J. Low Freq. Noise Vibr. Act. Control* 31 (4): 239–246.
- Jenn, D. and Cuong, T. (2012). Wind turbine radar cross section. *Int. J Antennas Propag.* 2012: 252689.
- Jones, C.R. and Eiser, J.R. (2010). Understanding ‘local’ opposition to wind development in the UK: how big is a backyard? *Energy Policy* 38 (6): 3106–3117.
- Landberg, L. and Mortensen, N.G. (1993). A comparison of physical and statistical methods for estimating the wind resource at a site. Proceedings of the 15th British Wind Energy Association Conference (6–8 October 1993), pp. 119–125,
- Landscape Institute and Institute of Environmental Management & Assessment (2013). *Guidelines for Landscape and Visual Impact Assessment*, 3e. Routledge.
- Langston, R. H. W. and Pullan J. D. (2003). Windfarms and birds: an analysis of the effects of windfarms on birds, and guidance on environmental assessment criteria and site selection issues. BirdLife International on behalf of the Bern Convention. *T-PVS/Inf* (2003) 12, p. 58. <https://tethys.pnnl.gov/sites/default/files/publications/Langston%20and%20Pullan%202003.pdf> (accessed April 2019).
- Mathews, F., Richardson, S., Lintott, P., and Hosken, D. (2016). Understanding the risk to European protected species (bats) at onshore wind turbine sites to inform risk management. University of Exeter. <https://tethys.pnnl.gov/publications/understanding-risk-european-protected-species-bats-onshore-wind-turbine-sites-inform> (accessed April 2019).
- Moglia, A., Trusszi, G., and Orsenigo, L (1996). Evaluation methods for the electromagnetic interferences due to wind farms. Proceedings of the Conference on Integration of Wind Power Plants in the Environment and Electric Systems, Rome (7–9 October 1996), paper 4.6.
- Morris, P. and Therivel, R. (2009). *Methods of Environmental Impact Analysis*, 3e. Routledge.

- Nieuwenhuizen, E. and Kohl, M. (2015), Differences in noise regulation for wind turbines in four European countries. Proceedings of EuroNoise 2015, Maastricht (31 May–3 June). <https://www.conforg.fr/euronoise2015/proceedings/data/articles/000575.pdf> (accessed 12 August 2019).
- Nord2000 (2006). Comprehensive sound propagation model. DELTA Danish Electronics, Light and Acoustics. <http://vejdirektoratet.dk/DA/vejsektor/vejregler-og-tilladelser/tilladelser/Documents/av185100rev%20propagation%202.pdf> (accessed February 2019).
- NTIA (2008). Assessment of the effects of wind turbines on air traffic control radar. *NTIA Technical Report TR-08-454*. file:///Users/scenj/Downloads/TR-08-454%20(3).pdf (accessed 3 March 2019).
- Ofcom (2009) Tall structures and their impact on broadcast and other wireless services. www.ofcom.org.uk/data/assets/pdf_file/0026/63494/tall_structures.pdf (accessed August 2019).
- Pearce-Higgins, J.W., Stephen, L., Douse, A., and Langston, R.H.W. (2012). Greater impacts of wind farms on bird populations during construction than subsequent operation: results of a multi-site and multi-species analysis. *J. Appl. Ecol.* 49: 386–394. <https://besjournals.onlinelibrary.wiley.com/doi/full/10.1111/j.1365-2664.2012.02110.x> (accessed April 2019).
- Perrow, M.R. (ed.) (2017). *Wildlife and Wind Farms Conflicts and Solutions, Volume 1: Onshore Potential Effects*. Exeter, UK: Pelagic Publishing.
- Pinder, J.N. (1992). Mechanical noise from wind turbines. *Wind Eng.* 16 (3): 158–168.
- Poupart G. J. (2003), Wind farms impact on radar aviation interests final report. Qinetiq for DTI. *DTI PUB URN 03/1294*. Part 1: <http://webarchive.nationalarchives.gov.uk/20060216231311/www.dti.gov.uk/energy/renewables/publications/pdfs/w1400614part1.pdf>. Part 2: <http://webarchive.nationalarchives.gov.uk/20060216231311/www.dti.gov.uk/energy/renewables/publications/pdfs/w1400614part2.pdf> (accessed August 2019).
- Randhawa, B.S. and Rudd, R. (2009), RF measurement assessment of potential wind farm interference to fixed links and scanning telemetry devices. ERA Technology for Ofcom. *Report No. 2008-0568*.
- Rodrigo, J.S., Chávez Arroyo, R.A., Witha, B. et al. (2020). The new European wind atlas model chain. *J. Phys. Conf. Ser.* 1452 (1): 012087. <https://doi.org/10.1088/1742-6596/1452/1/012087> (accessed 15 April 2020).
- Rodrigues, L., Bach, L., Dubourg-Savage, M.-J. et al. (2008). *Guidelines for Consideration of Bats in Wind Farm Projects*. UNEP/EUROBATS, EUROBATS Publication Series No 3. ISBN 978-92-95058-10-1.
- Rogers, A.L., Manwell, J.F., and Wright, S. (2002) Wind turbine acoustic noise – a white paper. https://docs.wind-watch.org/rogers-windturbinenoise_rev2006.pdf (accessed August 2019).
- Royal Society for the Protection of Birds (2019). How do wind farms affect birds? www.rspb.org.uk/our-work/our-positions-and-casework/our-positions/climate-change/action-to-tackle-climate-change/uk-energy-policy/wind-farms (accessed March 2019).
- Scottish National Heritage (2017). Visual representation of wind farms – guidance, version 2.2. <https://www.nature.scot/professional-advice/planning-and-development/renewable-energy-development/visual-representation-guidance> (accessed March 2019).
- Scottish National Heritage (2019a). Wind farm impacts on birds. <https://www.nature.scot/professional-advice/planning-and-development/renewable-energy-development/types-renewable-technologies/onshore-wind-energy/wind-farm-impacts-birds> (accessed March 2019).
- Scottish National Heritage (2019b). Bats and onshore wind turbines: survey, assessment and mitigation.
- Spera, D.A. (ed.) (1994). *Wind Turbine Technology – Fundamental Concepts of Wind Turbine Engineering*. New York: ASME Press.
- Stanton, C. (1994). The visual impact and design of wind farms in the landscape. Proceedings of the British Wind Energy Association Conference, Sterling (15–17 June 1994), pp. 249–255.
- Stehly T. and Beiter P. (2020). 2018 cost of wind energy review. *NREL/TP-5000-74598*. <https://www.nrel.gov/docs/fy20osti/74598.pdf> (accessed 15 April 2020).

- Swanick, C. (2013). *Guidelines for Landscape and Visual Impact Assessment*, 3e. Routledge.
- Troen, I. and Petersen, E.L. (1989). *European Wind Atlas* 656 pp. Roskilde: Risø National Laboratory ISBN 87-550-1482-8. http://orbit.dtu.dk/files/112135732/European_Wind_Atlas.pdf (accessed October 2018).
- Tudor, C. (2014). An approach to landscape character assessment. Natural England. https://assets.publishing.service.gov.uk/government/uploads/system/uploads/attachment_data/file/691184/landscape-character-assessment.pdf (accessed April 2019).
- University of Newcastle (2002). Visual assessment of windfarms best practice. *Scottish Natural Heritage Commissioned Report F01AA303A*. www.snh.gov.uk/docs/A305437.pdf (accessed January 2019).
- Van Kats, P.J. and Van Rees, J. (1989). Large wind turbines: a source of interference for TV broadcast reception. In: *Wind Energy and the Environment*, IEE Energy Series (ed. D.T. Swift-Hook). Institution of Electrical Engineers.
- Wagner, S., Bareis, R., and Guidati, G. (1996). *Wind Turbine Noise*. Berlin: Springer-Verlag.
- Walmsley, J.L., Salmon, J.R., and Taylor, P.A. (1982). On the application of a model of boundary-layer flow over low hills to real terrain. *Boundary Layer Meteorol.* 23: 17–46.
- Walmsley, J.L., Taylor, P.A., and Keith, T. (1986). A simple model of neutrally stratified boundary-layer flow over complex terrain with surface roughness modulations – MS3DJH/3R. *Boundary Layer Meteorol.* 36: 157–186.
- Warren, C.R. and MacFadyen, M. (2010). Does community ownership affect public attitudes to wind energy? A case study from south-west Scotland. *Land Use Policy* 27: 204–213.
- WA^sP (2020). Welcome to the world of WAsP by DTU Wind Energy. www.wasp.dk and Chapter 8 of *European Wind Atlas*, published by Risø National Laboratory, Denmark, for the Commission of the European Communities.

Software

LandBOSSE Land-Based Balance of System Systems Engineering: <https://pypi.org/project/landbosse> (accessed 15 April 2020).

MERRA-2 Modern Era Retrospective Analysis for Research and Application version 2: <https://gmao.gsfc.nasa.gov/reanalysis/MERRA-2> (accessed 15 April 2020).

New European Wind Atlas (2019): <https://map.neweuropeanwindatlas.eu> (accessed 15 April 2020).

WindFarm wind farm design software: www.resoft.co.uk (accessed 12 December 2019).

11

Wind energy and the electric power system

11.1 Introduction

The wind is a diffuse source of energy, and so wind farms and individual wind turbines are distributed over wide geographic areas. The public electricity networks, which were originally constructed to supply customer loads from central generators (fossil and hydro), are used and extended to gather the electrical energy. Transmission systems interconnect large generators and provide bulk power transfer from generating stations to load centres. Very large wind farms (typically more than 100 MW) are connected directly to the transmission system. Smaller wind farms and individual turbines are connected to the distribution system and are described as *distributed* or *embedded generation* (Jenkins et al. 2010). Distributed generation was not considered in the design of many modern power systems and alters the way they operate. If the distributed generation exceeds the local load, then the direction of power flowing in the distribution circuits is reversed, which may cause unusual operating conditions. The output of much embedded generation is neither controlled by nor even visible to Transmission System Operators.

In some countries, the output of wind farms is now large enough to have a significant impact on the technical and commercial operation of national generation and transmission systems. A limited capacity of wind generation can be considered as negative load, but larger wind farms must be able to contribute to the services that are necessary for secure operation of the power system (particularly fault ride through, voltage control, and frequency response). Wind generation has a very low operating cost and always operates if the wind is blowing and the networks are able to accept the power. In some electricity markets with a high capacity of wind generation, the wholesale price of electrical energy has become negative at times of high winds and low load. Additional commercial mechanisms, beyond the price of MWh, are then necessary to ensure that the conventional, controllable synchronous generators that are needed to maintain power system operation continue to operate.

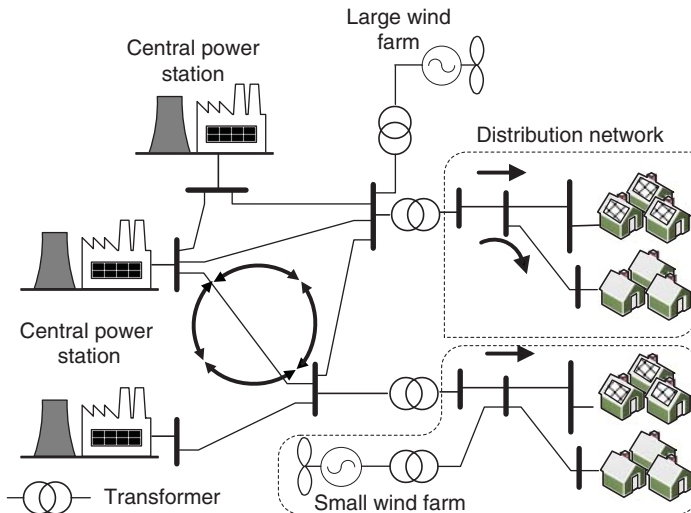


Figure 11.1 Large electric power system.

11.1.1 The electric power system

Figure 11.1 is a representation of a typical electric power system. The electrical power is generated by large central generating sets and is then fed into an interconnected high voltage (HV) transmission system. The generating units may be fossil fuel, nuclear or hydro sets and each will have a capacity of up to 1000 MW. The transmission network is interconnected, or meshed, and so there are many paths for the electrical power to flow from the generators to the transformers that supply the distribution systems. The path of the power flowing from each generating station to the transformers feeding the distribution circuits is not controlled directly but depends on the impedance of the transmission circuits and the operating conditions of the generators and loads.

Bulk supply transformers extract power from the transmission network and provide it to the distribution networks at lower voltages. Practice varies from country to country but the voltage used in the interconnected primary distribution networks can be as high as 150 kV. Lower voltage distribution networks (e.g. 10–11 kV or 30–33 kV) are normally operated radially with a single path between the bulk supply transformers and the loads. In urban or industrial areas with high load density the distribution networks use large diameter underground cables and transformers with a high capacity. However, in rural areas the customer loads are small and so the distribution circuits have been designed to have only a limited capacity to transport power while maintaining the voltage within the required limits. Small wind farms and individual turbines are often connected to rural, overhead distribution lines. The design of these networks tends to be limited by consideration of voltage drop or rise, rather than by the thermal capacity of the conductors, and this can limit severely the ability of rural overhead circuits to accept wind generation.

Table 11.1 shows the voltage levels used in different countries, although these are only approximate as practice varies, often depending on historical precedent.

Table 11.1 Voltage levels of the power system.

Network	UK	Continental Europe	USA
Supplies to households	230 V single phase	230 V single phase or 400 V three phase	120 V single phase or 208 V three phase
LV distribution	400 V	400 V	120–600 V
MV distribution	11–132 kV	11–150 kV	2.4–34.5 kV
HV and extra-HV transmission	275–400 kV	220–400 kV	46–765 kV

11.1.2 Electrical distribution networks

The traditional function of an electrical distribution network is to transport electrical energy from a transmission system to customer loads. This is to be done reliably, with minimum electrical losses and with the voltage maintained within limits. The voltage drop of a circuit is directly proportional to the current, whereas the energy lost in heating the conductors is proportional to the square of the current. Therefore, the currents must be kept low, which, as power is the product of current and voltage, implies that the network voltage level must be high. However, high voltage plant (e.g. lines, cables, and transformers) is expensive due to the cost of insulation, and so the selection of appropriate distribution network voltage levels is an economic choice.

Figure 11.2 is a schematic representation of a typical UK distribution system although most countries have similar networks. Power is extracted from the interconnected transmission grid and then transformed down to the primary distribution voltage (132 kV in this case). The electrical energy is then transported via a series of underground cable and overhead line circuits to the customers. Most domestic or small commercial customers typically receive electrical energy at 400 V (for a 3 phase connection) or 230 V (for a single phase connection). As the power that needs to be transported through a distribution network reduces, transformers lower the voltage level. In this example intermediate voltage levels of 33 and 11 kV are shown.

The majority of distribution circuits are three phase, although in some rural areas with low load density, particularly in the USA, long single phase circuits are used. Only balanced three phase networks are suitable for the connection of wind generators larger than about 10 kW. Three phase transformer windings may be connected either in star or in delta, and the winding arrangement chosen varies from region to region and generally follows historical precedent. One advantage of the star connection is that the neutral point of the transformer is directly accessible and so can easily be grounded (or earthed). When a transformer has a delta winding, an earthing transformer must be used to create a star point. UK practice is generally to earth the neutral points of each voltage level of the distribution system at one point only (usually at the transformer at the connection to the transmission network or to a higher voltage distribution circuit) although in certain continental European countries some distribution networks are operated with the neutral point isolated. In parts of the USA, the neutral conductor of distribution circuits is grounded at multiple points.

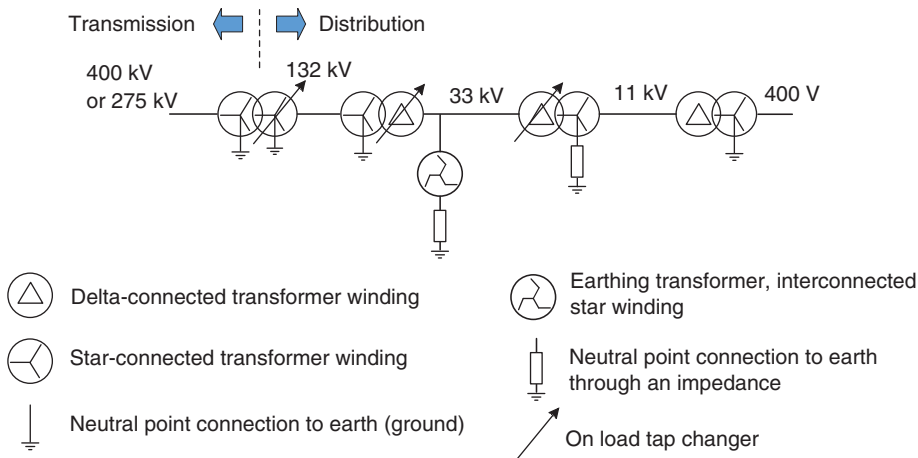


Figure 11.2 Typical UK distribution transformer and earthing arrangements.

The current passing through a circuit leads to a change in voltage, and Appendix A11 shows a simple manual calculation of the type needed to assess the electrical connection of a small wind farm. The ratio of the source transformer is altered to compensate for voltage changes by changing its taps. 11 kV/400 V transformers have fixed taps that can only be changed manually when the transformer is de-energised. Higher voltage transformers have on-load tap changers that are operated automatically when the current causes a change in network voltage.

The simplest control strategy of an on-load tap changer is to use an automatic voltage controller (AVC) to maintain the lower voltage terminals of the transformer close to a set-point (Figure 11.3). The AVC operates by measuring the voltage on the transformer lower voltage busbar, comparing it to a set-point value and then issuing an instruction to the on-load tap changer to alter the ratio of the transformer. Control systems of this type are unaffected by the presence of generators connected to the lower voltage network. Even if the power flow through the transformer is reversed and real and/or reactive power flows from the lower voltage to the higher voltage network this control system will work satisfactorily. This is because the source impedance of the higher voltage network is much less than the equivalent source impedance of the distributed generator. The voltage of the network is controlled predominantly by the voltage of the higher voltage network and the tap-changer, not by the generator. Some designs of tap changer have a reduced current rating if power flows from the low voltage side to the high voltage side of the transformer.

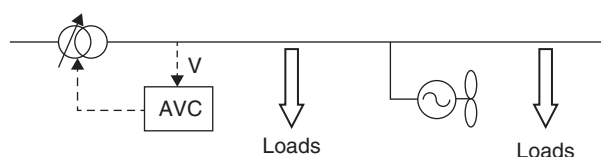


Figure 11.3 Voltage control of a distribution circuit.

However, it is rare for distributed wind generation to require the full reverse power flow capacity of a transformer on the distribution network because some of the wind power is likely to be taken by local loads.

In some distribution networks, the voltage at a remote point along the circuit is controlled using a technique known as *line drop compensation* or *current compounding* (Lakervi and Holmes 1995). This is achieved by adding a signal that is proportional to the voltage drop on the network to the local voltage measured by the AVC relay. If wind generators are connected to a network fed from a transformer controlled with line drop compensation then the current flow in the circuit will be changed, and the technique may no longer work correctly.

11.1.3 Electrical transmission systems

Electrical transmission circuits are meshed interconnected grids operating at voltage levels from 220 to 400 kV in most of Europe and up to 765 kV in large countries (e.g. USA and China). Because of their strategic importance, transmission grids are normally operated with multiple circuits in parallel so that when an electrical fault occurs that circuit is isolated and the grid continues to supply power to the loads satisfactorily. This results in quite low utilisation of the circuits during normal operation, and so the electrical energy lost as heat within a transmission grid is usually less than 2% of the energy transmitted through it, whereas in a distribution network with fewer parallel paths, the energy losses are typically 6%. The voltages within an interconnected transmission grid are determined primarily by the flows of reactive power and so the reactive power output of a large wind farm has to be able to be controlled in response to the requirements of the Transmission System Operator.

The frequency of an ac power system is the same across the network and is determined by the balance between the real power being generated and the load demanded. If the load demand exceeds the generated power then the frequency will drop while if the power being generated exceeds demand the frequency will rise. The speed with which the frequency changes for a mismatch of supply and demand power depends on the inertia of all of the spinning machines (generators and loads) connected to the power system. Some isolated electrical power systems (e.g. Great Britain with a peak demand of 50–60 GW) can be considered effectively as a single node for frequency control but larger interconnected systems such as that in mainland Europe and in the USA have considerable restrictions on the flows of power from region to region. Within each control area, generation, and load must be balanced at all times and as wind generation output varies with wind speed, other forms of generation must change their output to ensure the load is met and interconnecting circuits not overloaded.

11.2 Wind turbine electrical systems

Large wind turbines are designed to operate only when they are connected to a stable three phase ac network; they cannot operate independently (or islanded). The main power system provides a reference voltage and frequency that is used for control of the turbines and ensures stability of the wind generators. The network also provides power for the turbine auxiliaries when the wind speed is low. For fixed-speed wind turbines the network provides the reactive power that is necessary for the operation of the induction

generators while for variable-speed generator systems, the power electronic converters are synchronised to the network frequency through their control systems. The wind turbines inject power into the network that varies with wind speed and the large conventional (fossil or hydro) generators provide the frequency and voltage stability of the network. Wind turbines are not yet used for black starting a de-energised network.

The voltage level chosen for the generator and main power circuits within a wind turbine nacelle is usually less than 1000 V and is often selected to be one of the internationally standard voltages, in Europe typically 690 V between phases, in the USA 575 V. This voltage is surprisingly low for a large electrical machine and leads to rather high currents. For example, a 3 MW wind turbine generating at 1000 V has a current of over 1700 A in each phase. Even for wind turbines of rating up to around 4–5 MW it has been found to be cost-effective to restrict the voltage of the wind turbine generator to less than 1000 V. In many countries, the safety requirements become very much more onerous for voltages above 1000 V and special precautions are required including the provision of dedicated equipment to earth the circuits before work on them is permitted. Further reasons for this low voltage include higher production volumes, wider choice and lower costs of switchgear, generators and the flexible pendant cables that connect the nacelle to the tower base. Some recent designs of very large turbines, of rating greater than 4–5 MW, use an internal turbine voltage of 5–6 kV to reduce the currents in the converters and generators.

11.2.1 Wind turbine transformers

The low generator voltage leads to a requirement for a transformer and its associated switchgear to connect the wind turbine to the wind farm power collection system, which typically operates at medium voltage (MV) (11 or 33 kV in the UK). Many manufacturers supply the transformer and switchgear with the turbine. The transformer can be located either in the nacelle, at the top of the tower below the yaw bearing, in the base of the tower or in an enclosure immediately adjacent to it (see Figure 11.4). Depending on its location the transformer may be liquid insulated or use cast resin solid insulation. In some early wind farms a number of small wind turbines were connected to one transformer but as turbine ratings have increased, with consequently higher currents, it was recognised that this approach leads to excessive voltage variations and electrical losses in the low voltage cables. The connection of multiple turbines to one transformer is likely to be cost-effective only with rather small wind turbines located close together. Modern large wind turbines all have one transformer per turbine.

Historically, off-the-shelf distribution transformers were used with wind turbines. However, due to the large number of failures experienced it is now common to use transformers designed specifically for wind turbines (Jose and Chako 2014). The key factors that should be considered when designing a transformer for a wind turbine are

- *Unusual transformer loading:* In contrast to most transformers used in public electricity supply distribution networks, wind turbine transformers are subjected to frequent changes in the level of power flowing through them. This causes repeated thermal stress on the windings of the transformer. Also, wind turbine transformers operate below rated power for most of the time and have a low capacity (load) factor of less than 30–35%. At low power the copper losses, which are proportional

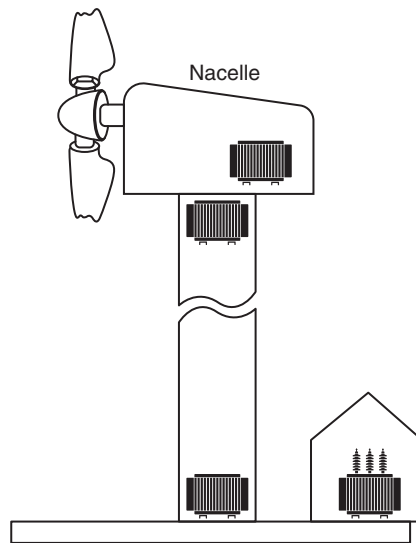


Figure 11.4 Alternative locations of a transformer in a wind turbine.

to the square of the current through the transformer, are small but core magnetic losses continue to be present whenever it is energised. Therefore, when calculating the total cost of ownership of a wind turbine transformer, the variation of its losses with wind speed is important.

- *Harmonics:* As discussed in Section 7.5.3, modern variable-speed wind turbine generator systems create harmonic currents that pass through the wind turbine transformer. These harmonic currents can cause unusual flux paths, losses, and heat in the transformer.

The particularly onerous conditions of wind turbine transformers are recognised in a special section of the IEC power transformer standard, 60076-16 (2015).

11.2.2 Protection of wind turbine electrical systems

All electrical circuits are vulnerable to short-circuit faults when their insulation fails either due to ageing and general degradation or mechanical damage, and so need automatic protection to detect the fault and isolate that part of the system. The electrical protection of wind turbines follows the same general principles that are applied to any other items of an electrical plant (Alstom Grid 2011), but there are significant differences. Distribution networks normally detect short-circuit faults by measuring an abnormally high value of the current flowing in a circuit and opening a circuit breaker after a defined time (less than 3 seconds). Neither induction generators nor voltage source converters (VSCs) can be assumed to provide sustained overcurrents into a short-circuit and so their fault current cannot be detected reliably using conventional time-delayed overcurrent protection. Rather, the overcurrent from the main network is detected, the wind generators are isolated and then islanded operation is detected by the change in frequency

and voltage of the isolated generators. This sequential tripping of first detecting an over-current from the network, isolating the turbine and then detecting abnormal generator voltage or frequency is not considered good practice in traditional distribution networks but with distributed generators that do not produce large currents into faults there is no practical alternative.

The fault current from a fixed-speed induction generator with a three phase short-circuit applied to its terminals dies away rapidly (within a few cycles) as the stored magnetic energy in the electrical machine decays. There is no sustained fault current because an induction generator draws its magnetising current from the network or local capacitors, and this is not possible when the voltage at the terminals has been collapsed by a three phase fault. Some asymmetrical faults (e.g. two phase faults) can lead to sustained fault currents of two to three times the generator full output, but again these currents are not usually relied on to operate protective relays. One simple approach to the modelling of a fixed-speed induction generator for short-circuit calculations is to represent it as a 1 per unit voltage source in series with the generator reactance, although the generator reactance varies with time after the fault (Jenkins et al. 2010; Veers 2019). This is a simple approach that may give a slightly low initial current as the internal voltage may be high if the induction machine is generating. Variable-slip wind turbines with rotor resistors can be treated in the same way and a conservative assumption is made as to whether the external rotor resistance is in the rotor circuit.

The fault current contribution of all converter connected generators (doubly fed induction generator [DFIG] and full power converter types) depends on the detailed design and control system of the converters. Hence test data from the manufacturer showing how the generator system responds to a short-circuit and network voltage depressions is used to construct models for use in fault calculators. The resulting models are usually quite simple and are of the form of a voltage in series with a reactance. For a simple assessment, the response of a DFIG to a local fault can be divided into two phases (Kanellos and Kabouris 2009; Morren and de Haan 2007). During the first phase (approximately two to three cycles), it can be considered to operate as a fixed-speed induction generator but with an increased internal voltage, particularly if it is operating super-synchronously and exporting power through both the rotor and stator circuits. In the second phase, the current through the rotor-side converter is limited by the control action of the crowbar protection that diverts current away from the sensitive power electronics of the machine-side converter to flow in a more robust circuit.

The short-circuit current that flows into the network from full power converters is determined by the network side power electronic converter and normally does not significantly exceed 110% of its full load current. The full power converter wind turbine can therefore be approximated as a constant current source of approximately rated current, although IEC 60909 (2016) recommends that three times the nominal current is assumed for the fault current contribution of variable-speed drives that are able to regenerate.

Most of the lower voltage circuits within a wind turbine are protected by fuses, as these are cheaper than circuit breakers and have the advantage of operating very rapidly (within a half cycle) although the main electrical connection to the wind turbine is protected by relays and switchgear. Wind turbine manufacturers usually provide switchgear to connect the turbine transformer to the wind farm power collection system with a relay

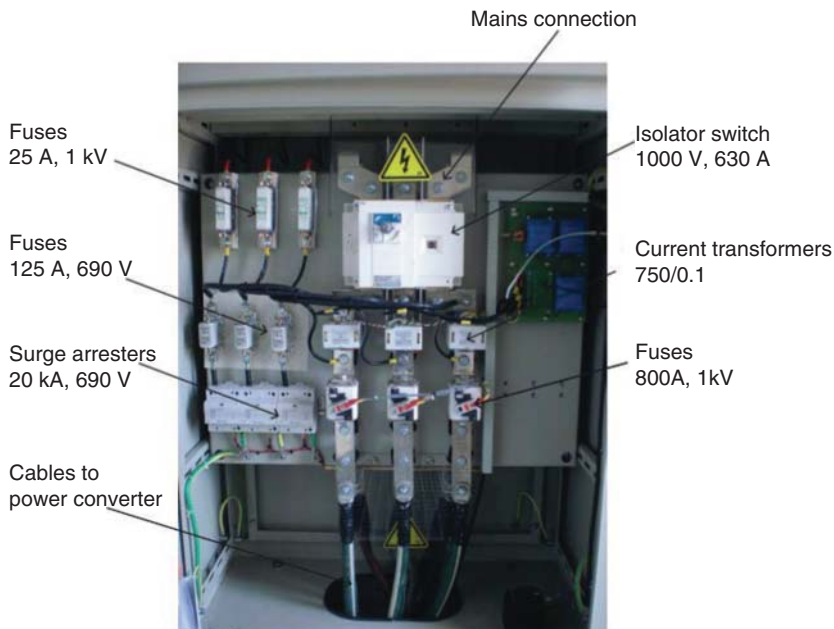


Figure 11.5 Protection circuitry of a wind turbine. Source: WindForce, Sri Lanka.

having over/under voltage and over/under frequency elements. The settings of these elements and their time delays depend on whether the operating philosophy of the wind turbine is to disconnect when network short-circuit faults occur or try to continue operating.

Figure 11.5 shows the fuse and protection arrangement of an 800 kW wind turbine. The output current of the power converter is connected to the collector network through 800 A fuses and a 630 A isolator. Just before the isolator three surge arresters are connected to ground through 125 A fuses. The auxiliary power to the control circuit is provided through 25 A fuses.

Figure 11.6 shows the switchgear of a 1.5 MW wind turbine. The MV switchgear is on the right shown being operated by a technician and the low voltage (LV) switchgear on the left. The MV switchgear is a ring main unit that isolates and earths the unit from the power collector circuits while the LV switchgear is a moulded case circuit breaker to protect the cables running into the tower. The transformer (not shown) is immediately behind the switchgear and the whole assembly is placed outside the turbine tower in a weatherproof enclosure.

11.2.3 Lightning protection of wind turbines

Lightning is a significant hazard to wind turbines and appropriate protection measures need to be taken particularly to protect the blades and structure from direct strikes and the electrical and control systems from both direct strikes and induced over voltages.



Figure 11.6 Transformer and switchgear of 1.5 MW wind turbine. Source: NEG Micon.

Figure 11.7 shows the unprotected blade of an early wind turbine that was damaged by lightning.

Guidance on lightning protection of wind turbines is given in the comprehensive standard IEC 61400-24 (2010) with further details on the application of surge protection devices in the Technical Specification DD CLC/TS 50539-22 (2010). Following the advice given in these documents can significantly reduce, if not entirely eliminate, damage and loss of generation caused by lightning.

Lightning is a complex natural phenomenon with both its frequency and intensity varying markedly across the globe. The term *lightning flash* is used to describe the sequence of discharges that use the same ionised path and may last up to a second. The individual components of a flash are called *strokes*.

Lightning flashes are usually divided into four main categories:

- Downward inception, negative and positive polarity.
- Upward inception, negative and positive polarity.

Downward inception – negative polarity flashes that start with a stepped leader from the thunder cloud and transfer negative charge to earth are the most common. Downward negative flashes typically consist of a high amplitude burst of current lasting for a few microseconds followed by continuing current of several hundred amps. Then, following the extinction of the initial current transfer between cloud and earth there may be a number of restrikes. However, offshore and in coastal areas there may be a majority of positive flashes of downward inception, which consist of a single long duration stroke



Figure 11.7 Unprotected GRP wind turbine blade damaged by a positive lightning strike ($>80\text{ kA}$). (Cotton et al. 1999).

with high charge transfer and specific energy content. Upward inception is normally associated with very high objects (e.g. communication towers as well as very large wind turbines) and the lightning has very different characteristics. Although the maximum peak current is low (some 15 kA) the charge transfer can be very high and hence there is significant potential for damage. The top of wind turbine blades can now be over 150 m above ground and so there is growing concern over the effect of upward negative lightning flashes. Upward positive flashes are rare.

Table 11.2 shows the parameters normally used to characterise lighting and some aspects of their potential for damage in wind turbines. The peak current of a single lightning stroke may be over 200 kA but the median value is only approximately 30 kA. Corresponding values for charge transfer are 400 C (peak), 5 C (median) and specific energy 20 MJ/ Ω (peak) and 55 kJ/ Ω (median) (appendix A of IEC 61400-24 [2010]). The very large range of these parameters illustrates that the initial step in any consideration of lightning protection of a wind farm or wind turbine is to undertake a risk assessment. The risk assessment will include consideration of the location of the turbines as the frequency and intensity of lightning varies considerably with geography and topology. On flat terrain a wind turbine is assumed to attract the same frequency of lightning as a circular

Table 11.2 Effects of various aspects of lighting on a wind turbine.

Parameter	Effect on wind turbine
Peak current (A)	Heating of conductors, shock effects, pressures, electromagnetic forces
Specific energy (J/Ω)	Heating of conductors, shock effects, melting of attachment components
Rate of rise of current (A/s)	Induced voltages on wiring, flashovers, shock effects
Long duration charge transfer (C)	Damage at arc attachments point or other arc sites (e.g. bearing damage)

area with a radius of three times the height of the wind turbine and the number of flashes to a turbine over a year N_d can then be estimated from:

$$N_d = N_g \cdot 9\pi \cdot H^2 \cdot 10^{-6}$$

where

H is the height of the blade tip (m)

N_g is the annual average ground flash density ($\text{km}^{-2} \text{ year}^{-1}$)

Table 11.3 shows some historical data of the frequency of lightning damage (Cotton 2000; Lorentzou et al. 2004). Although this data is now rather old and both wind turbine design and lightning protection systems have evolved greatly since it was produced, the data does indicate the potential scale of the problem and the importance of effective lightning protection. A large number of the faults shown in Table 11.3 were due to indirect strokes affecting the control systems of the wind turbines and wind farms. The data showed that the number of faults was dominated by incidents affecting the control and electrical systems, whereas blade damage gave the highest repair costs and loss of turbine availability, and hence reduction in wind farm revenue. A study of the lightning performance of the Nysted offshore wind farm and a comparison of the severity of the strikes against the standards is given in Peespati et al. (2011).

Some years ago it was thought that if the blades of wind turbines were made from non-conducting material (i.e. glass reinforced plastic [GRP] or wood-epoxy) then it was not necessary to provide explicit protection for these types of blades provided they did

Table 11.3 Wind turbine lightning damage frequency.

Country	Period	Turbine years	Lightning faults	Faults per 110 turbine years
Germany	1991–1998	9204	738	8.0
Denmark	1991–1998	22 000	851	3.9
Sweden	1992–1998	1487	86	5.8

not include metallic elements for the operation of devices such as tip brakes. However, there is now a large body of site experience to show that lightning will attach to blades even if they are made from non-conducting materials and can cause catastrophic damage if suitable protection systems have not been fitted (Cotton et al. 2001; Glushakov 2007). Lightning is a current source and if it enters a blade and is not conducted to earth by a suitably sized metallic lightning conductor then the arc may cause an increase in pressure that will damage the blade catastrophically. If carbon fibre, which is conducting but with a rather high resistance, is used to reinforce the structure of the blades then additional precautions are necessary. The very rapid rate of rise of lightning currents can lead to very high induced voltages that damage control and instrumentation circuits.

Modern wind turbine blades are very long hollow structures with large voids, and a direct strike to a wind turbine rotor typically causes damage if the lightning penetrates the outer skin of the blade and forms an arc. The pressure shock wave caused by the arc may explode the blade or, less dramatically, cause cracks in the blade structure. Thus, for effective protection it is essential that the lightning attaches directly to the protection system and then is conducted safely down the length of the blade in a metallic conductor of adequate cross-section. The region around the tip is most vulnerable. It is thought that blades up to 20–30 m long are protected effectively by receptors each side of the tip but longer blades required intermediate receptors.

Although practice varies, a typical protection system of a modern large turbine blade might consist of a 200 mm long metallic tip and additional metallic receptors (buttons) at intervals of between 1 and 5 m placed along both surfaces of the blade towards the tip. The receptors are connected to an insulated aluminium or copper down conductor within the blade that is in turn connected to the blade root pitch bearing. A typical approach is shown in Figure 11.8.

Once the lightning current has been conducted to the root of the blade, there remains the problem of ensuring its safe passage to the outside of the tower and hence to earth. This is not straightforward as it is necessary for the current to pass safely across the pitch, shaft and yaw bearings while not damaging the generator and sensitive control equipment in the nacelle. The present understanding of how wind turbine bearings may be damaged by the passage of lightning current is summarised in IEC 61400-24 (2010). Generally, large heavily loaded bearings are unlikely to be catastrophically damaged by lightning, although there may be a reduction in their service life. Blade pitch bearings, that are large and usually static, normally pass lightning current with little damage. Main shaft bearings that rotate rapidly and form a hydrodynamic layer of oil are more susceptible to damage. There is, so far, no effective means of shunting lightning current around a large bearing as the bearing itself is the lowest inductance path and so the preferred route for the high frequency lightning current.

The control and electrical systems can be damaged by lightning attaching to the wind turbine but also indirectly by the currents and subsequent voltages induced by adjacent flashes to ground. The principal damage mechanisms are direct conduction and magnetic coupling while the main protective measures are good bonding, effective shielding, and the use of appropriate surge protection devices. Turbine control and electrical systems are protected against lightning by dividing the turbine into zones depending on whether direct attachment of lightning is possible and the magnitude of the current and hence electromagnetic field expected in each zone. This is known as the lightning protection zone (LPZ) approach (IEC 61400-24 2010). The blades of a turbine are defined as being in

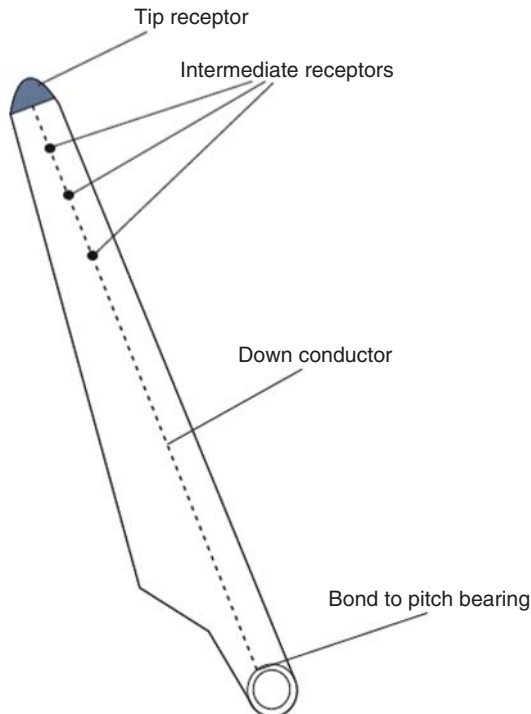


Figure 11.8 Blade lightning protection for a large wind turbine.

LPZ 0 while the nacelle that includes conducting material to create a protective Faraday cage typically creates LPZ 1. Equipment mounted in earthed cabinets within the nacelle or within a metal tower is considered to be in LPZ 2. Suitable surge protection devices are required when conductors pass from a lower to higher LPZ. Wind turbines are often connected to extensive overhead public distribution networks and surge diverters may also be required to protect the turbine transformer against transient voltages caused by lightning on the power network. If metallic communications circuits are used, rather than fibre optic cables, then similar considerations apply to them.

11.3 Wind farm electrical systems

11.3.1 Power collection system

Wind farms aggregate the power generated by a large number of wind turbines, each up to about 3 MW in rating, that are spread over a large area. The energy generated by each unit is collected through an MV power collection system. A typical wind farm power collection network is shown in Figure 11.9.

The location of the turbines within the farm is fixed by the wind resource, local topography and the requirements of the planning (permitting) authorities. The power

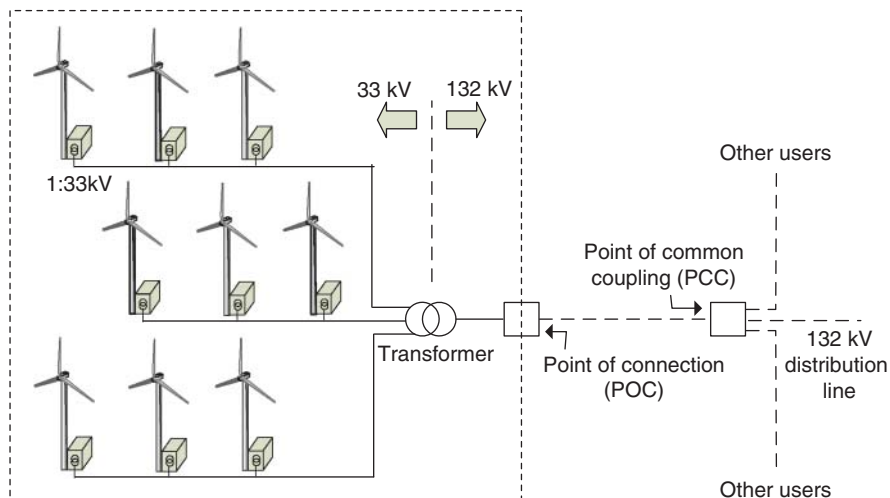


Figure 11.9 Electrical power collection system of a wind farm.

collection network is then designed to collect the power and transport it to the public electricity system.

The choice of MV level for the wind farm power collection system usually follows the practice of the local distribution utility. In this way cables and switchgear are readily available. Thus, in the UK the choice is between 11 and 33 kV (66 kV for very large offshore wind farms) while in continental Europe wind farm collection circuits are likely to be between 10 and 30 kV. In the USA 34.5 kV is commonly used. Larger wind farms include a transformer (e.g. 33/132 kV or 33/275 kV in the UK) to increase the voltage for onward transport of the national transmission network.

Local utility practice influences the choice of the neutral earthing arrangement of the wind farm MV circuits (see Figure 11.2). 11 kV circuits in the UK usually have their neutral point either solidly earthed, or connected to ground, through an impedance, typically a low value resistor or reactor (often $6.35\ \Omega$ to allow 1000 A to flow into a phase/ground fault). Solid neutral earthing is cheaper as it requires no extra equipment but can lead to high earth fault currents, which may cause damage and high step or touch voltages (ANSI/IEEE 80 2000). 33 or 66 kV circuits are often resistance earthed while those operating at 132 kV are solidly earthed. The continental European practice of leaving the neutral points of some MV circuits unearthing allows operation of the wind farm to continue with a single phase earth fault but with the voltages of the healthy phases increased by a factor of $\sqrt{3}$.

The design of the power collection is very similar to that of any public utility MV power network but with one or two particular aspects. It is generally not appropriate to provide any redundancy in the circuits to take account of failures of the MV electrical equipment. Both operating experience and reliability calculations have shown that the power collection system of a wind farm is so much more reliable than the individual wind turbines that it is not cost-effective to provide any duplicate circuits. This also applies to the single circuit or transformer linking the wind farm to the utility network where duplication cannot usually be justified. If part of the wind power collection circuit

does fail then the only consequence is the lost revenue from the energy output of that part of the wind farm. This is easily estimated and is generally modest. In contrast, if a public distribution utility circuit fails then the consequence is that the customers do not have electrical power. The social and commercial value of this loss of supply to customers is difficult to quantify but is generally considered to be two orders of magnitude higher than the retail price of electricity. Thus, MV distribution circuits for public electricity supply usually are duplicated while wind farm power collection networks usually consist of simple radial circuits with limited switchgear for isolation and switching. The wind turbine transformers are connected to the radial circuits through simple switchgear. The MV power collection cables are usually connected in and out of the wind turbine transformer switchgear to avoid cable branch joints.

In Europe almost all power collection circuits within wind farms use underground cable. This is for reasons of visual amenity and for safety, as large cranes are required for the erection or repair of the turbines. In other parts of the world, overhead MV lines have sometimes been used within wind farms to reduce costs. When underground cables are used, their low series inductive reactance leads to small variations of voltage with current and so the circuits are dimensioned primarily on considerations of current rating and electrical losses. Any wind farm project that reaches the stage of requiring a detailed design of the electrical system should also have a good estimate of the wind resource and hence energy output. Then it is straightforward to use this data to calculate the energy losses in the electrical equipment at various wind turbine output powers using a load flow program, sum these over the life of the project and, using discounted cash flow techniques, choose the optimum cable size and transformer rating. In countries where wind generated electricity attracts a high price, it is likely to be cost-effective to install cables and transformers with a thermal rating higher than that required at full wind farm output, in order to reduce electrical losses. It may also be worthwhile to consider using low-loss transformers.

The point of connection is defined as the point where the wind farm power collection system joins the utility distribution network. The point of common coupling is the nearest point to the wind farm on the utility network to which other customers are (or can be) connected. In many circumstances, these points may coincide, but the point of connection defines the ownership boundary, whereas the impact of the wind turbines on power quality is measured at the point of common coupling.

11.3.2 Earthing (grounding) of wind farms

The power system neutral points (system earthing) as well as the metallic enclosures and external conducting parts of all electrical equipment (equipment earthing) require a connection to the general mass of earth in order to

- Establish a low impedance path for earth fault currents and hence satisfactory operation of electrical (overcurrent) protection.
- Minimise shock hazards to personnel and animals, including control of step and touch potentials.
- Ensure satisfactory discharge of lightning currents and control the associated voltages.

- Prevent large potential differences occurring that are potentially hazardous to both personnel and equipment.

In the UK, this subject is referred to as *earthing*, whereas in the US it is called *grounding*. The terms are synonymous.

The neutral points of the three phase power circuit are usually connected to earth at each voltage level to provide a path for earth fault current. Also the metallic enclosures of electrical equipment are earthed to ensure they do not rise in potential if an internal insulation failure occurs. High structures, such as wind turbines are earthed to ensure there is a low impedance path for lightning current. These three rather different objectives are achieved with a common earthing and bonding system of the wind farm.

Because earthing has obvious safety implications, there is considerable guidance available in both national and international standards for conventional electrical plant. For earthing of ac substations, the US standard ANSI/IEEE 80 (2000) is widely applied, and Charlton has written an informative guide (Copper Development Association 1997) that discusses UK practice.

Wind farm earthing systems are rather unusual. They are very extensive, often extending over several kilometres, are subject to lightning strikes because of the height of modern wind turbines and are often on high resistivity ground being located on rocky terrain on the tops of hills. Thus, normal earthing practice tends not to be easily applicable and special consideration is required. A single, wind farm wide earthing system for both 50/60 Hz fault currents and lightning protection is recommended by IEC 61400-24 (2010) and is often implemented with ring electrodes in the soil around the wind turbine foundations. The electrodes are connected to the foundation reinforcement, and bare earthing conductors laid in the cable trenches above the power collection cables to connect each turbine earth to the next. These conductors provide both bonding of all parts of the wind farm as well as a long horizontal electrode to reduce the impedance to ground of the earthing system.

Although it is conventional to use the same physical earthing network for power frequency and lightning currents the response of the earthing system to the high frequency components of lighting current is quite different to that at 50/60 Hz. The performance of a wind farm earthing system may be understood qualitatively by considering Figure 11.10.

At each wind turbine a local earth is provided, typically by placing one or more rings of bare conductor around the foundation at a depth of about 1 m (sometimes known as a *counterpoise earth*) and, if possible, by driving vertical rods into the ground. It is common to bond the steel reinforcing of the wind turbine foundation as well as the steel tower into this local earthing network. The purpose of this local earth is to provide equipotential bonding against the effects of both lightning and power frequency fault currents and to provide one element of the overall wind farm earthing system. These local turbines earths are shown as $R_{turbine}$ in Figure 11.10.

The long horizontal electrodes linking one turbine to the next have a complex behaviour similar to that of a transmission line and are represented in Figure 11.10 as a π equivalent circuit. The resistance to ground is indicated by R_{shunt} while the series impedance is the combination of R_{series} and L_{series} . R_{series} comes about simply from the longitudinal resistance of the earth wire while L_{series} is the self-inductance of the earth circuit. On the long earthing networks that are found on large wind farms this series impedance cannot be ignored. It may be seen immediately that for the high

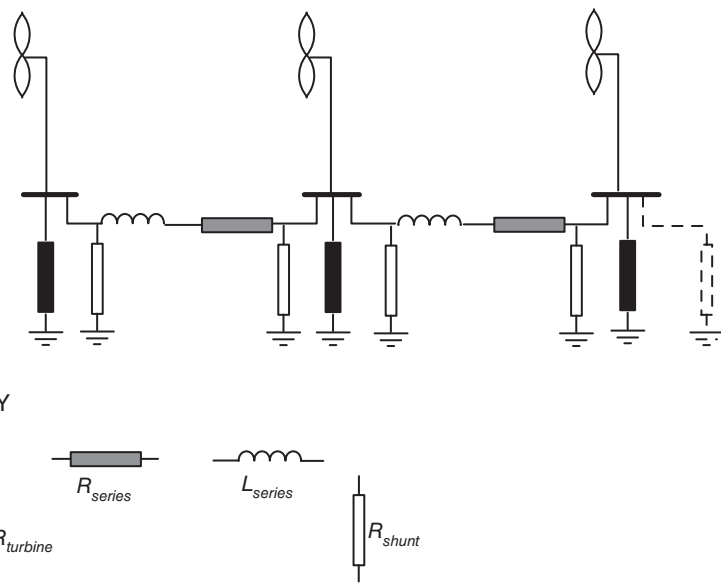


Figure 11.10 Schematic of a wind farm earthing system.

Table 11.4 Measured earth impedance at substations of two wind farms.

Capacity of wind farm (MW)	No. of turbines	Route length of horizontal earth conductor (km)	Earth impedance at main substation (ohms at 50 Hz)
7.2	24	6.7	$0.89 + j0.92$
33.6	56	17.7	$0.46 + j0.51$

frequency of a lightning strike on a wind turbine the series inductance acts to reduce the effective earthing network to only the local turbine earth. IEC 61400-24 (2010) states that horizontal conductors longer than 80 m do not reduce the effective impedance to ground of the earthing system for high frequency lightning currents. Even with 50 Hz fault current the series impedance leads to significantly higher earthing impedances than would be expected with a geographically small earthing system where series impedance may be neglected. In this discussion shunt capacitance and soil ionisation have been ignored although these may become significant at high frequencies and currents.

This complex behaviour of wind farm earthing systems has been confirmed by site measurements, and Table 11.4 shows the measured values for the earth impedance at the main substations of two UK wind farms.

It may be seen that even at 50 Hz the impedance to earth consists of almost equal resistive and inductive parts (i.e. the X/R ratio of the impedance of the earthing system to

ground is almost unity). This has the important implication that simple conventional calculation techniques that were developed for small, fully resistive, earthing networks may give optimistic results for wind farms. The impedance of the long horizontal conductors at lightning frequencies needs to be considered. Sophisticated computer programmes to do this are available and these may be used to calculate the performance of the grounding system at both 50 Hz and the frequencies of lighting surges. Similarly, simple testing methods are only intended to measure resistance to earth and will give optimistic results on large wind farms.

An effective measurement method to determine the 50 Hz earth impedance of a large wind farm is by a current injection test. In this test a current (typically 10–20 A) is injected into the earth electrodes at the wind farm and the potential rise measured with respect to a remote ‘true’ earth. However, the return path of the injected current must be remote from the wind farm (usually some 5–10 km away) to ensure that it does not affect measurements at the wind farm. Hence it is conventional to use the de-energised circuit connecting the wind farm to the main power network as the path of the test current. The rise in potential of the wind farm earthing systems is measured against a remote earth that classically is transferred to the site over a metallic telephone circuit. Ideally the route of the telephone circuit should be orthogonal to the power circuit to avoid induced effects. It may be seen that tests of this type are difficult and expensive to undertake and they involve taking the wind farm out of service and arranging a temporary earth at the remote end of the current injection circuit. Also it is becoming difficult to use a telephone circuit to provide the remote earth reference as telecommunication companies increasingly use non-metallic media. However, it is very questionable whether simpler tests give useful results on large earthing networks with significant series inductance.

11.4 Connection of wind farms to distribution networks

Distribution utilities have an obligation to operate the electrical distribution networks in such a way as to provide power to their customers at an agreed power quality and consideration of whether a wind generation scheme may be connected to a distribution circuit is based on its impact on other users of the network. Similar considerations apply to the connection of any other form of distributed generation or load. The voltage that a customer might expect to receive is detailed in British Standard EN 50160 (British Standards Institution 2010) while the standards that apply to the public distribution networks are described in Electricity Networks Association (2003, 2019a).

The main impacts of wind turbines on distribution networks are

- Slow (or steady state) voltage variations.
- Rapid voltage changes (leading to flicker).
- Waveform distortion (i.e. harmonics).

The operation of wind turbines is affected by

- Voltage unbalance (negative phase sequence voltage).
- Transient voltage variations (dips and sags).

The steady state voltage variations caused by wind turbines are usually assessed assuming conditions of minimum (or zero) network load with maximum wind generation and maximum network load with no generation. These are rather conservative assumptions, and if followed, mean that the steady state voltage limits of the network will never be violated. They ensure that the output power of the wind turbines can always be exported to the network (other than when network faults occur) but their strict application can lead to high costs of network reinforcement or permission to connect the turbines being refused.

In some cases, project specific agreements have been reached between the network and generator operators so that a wind farm of increased capacity can be connected but the output of the wind farm is limited (curtailed) at times of high wind speeds and low network load, or abnormal network conditions. This then allows a larger capacity wind farm to be connected than would otherwise be acceptable but the risk of not being able to generate at times of network constraints is transferred to the wind farm operator. The risk of not being able to generate can be estimated from the wind resource and load pattern. Accepting the risk of a loss of income from curtailed wind generation for only a few hours a year can result in significant reductions in connection costs. The control system required to implement such a scheme is usually relatively low cost when compared to network reinforcement.

The steady state voltage change permitted in 11 kV circuits is small (typically $\pm 1\%$ or 2%) as any voltage variation passes directly through the fixed tap 11/0.4 kV transformers to the circuits supplying customers. In contrast, 33 and 132 kV circuits are allowed to operate over a wider voltage range (e.g. up to $\pm 6\%$) as the automatic on-load tap changers supplying the lower voltage networks can compensate for variations in the higher voltage networks. Hence, it is common to find that only a limited capacity of wind generation can be connected at 11 kV as the high impedance of the circuits and relatively large currents flowing from the generators result in unacceptable variations in voltage. Determining the size of a wind farm that may be connected to a particular point in the distribution network requires a series of calculations for the specific project (see Appendix A11). However, Table 11.5 gives some indication of the maximum capacities of wind farms that may be connected to particular voltage levels. Table 11.5 assumes that the wind farms are made up of a number of turbines and so the connection assessment is driven by voltage rise effects and not by higher frequency power quality issues caused by individual large machines.

For large wind farms, the calculations required are involved and require computer power system studies. The expense of these calculations may be difficult to justify for

Table 11.5 Indication of possible connection of wind farms to distribution networks (WPD 2018).

Connection voltage (kV)	Wind farm rating (MW)
0.4	0–0.25
11	0.25–4
33	4–20
132	20+

Table 11.6 Ratio of site capacity to connection short-circuit level for two large (fixed-speed induction generator) wind farms.

Wind farm capacity (MW)	Number of turbines	Short-circuit level of connection (MVA)	Ratio of wind farm capacity (MW) to short-circuit level (MVA) (%)
21.6	36	121	18
30.9	113	145	21

very small wind farms and in the early days of wind energy some countries adopted an assessment approach to allow connection based on the ratio of wind farm capacity (in MW) to symmetrical short-circuit level without the wind farm connected (in MVA).¹ Typical values chosen ranged from 2% to 5% based on studies and experience (Gardner 1996). However, such simple rules can be too restrictive and lead to refusal of permission to connect or to excessive reinforcement of the distribution system. Table 11.6 gives data on two large wind farms in successful commercial operation in Great Britain with much higher ratios of wind farm capacity to short-circuit level. Both wind farms have operated successfully for some years but it should be noted that the number of turbines on each site is large and so the impact of any individual generator is small. Both sites are connected to 33 kV circuits from which other customers are supplied only through transformers fitted with automatic tap-changers.

11.4.1 Power system studies

Power system studies are required to assess the impact of large wind farms on the network and to ensure that the network conditions are such as to allow the wind generators to operate effectively. Sophisticated computer programs are now available and are always used on large projects.

Loadflow (or power flow) programs are used to ensure that the voltages on the system will be within limits, that circuits will not be overloaded and to calculate losses. They take as inputs the network topology and impedances of the lines, cables, and transformers. The customer loads and generator outputs are then used to calculate the steady state performance of the network in terms of voltages, real and reactive power flows and network losses. Generally, a balanced three phase system is assumed. For wind energy applications it is important that the load flow program includes a good model of the tap-changers on the network transformers and an effective representation of the wind turbine generators. A simple load flow gives the state of the network at a single instant, but some programs allow the use of daily load and generator profiles to repeat the calculations many times to

¹ The electrical ‘strength’ of a circuit is indicated by its short-circuit or fault level. The short-circuit level is the product of the pre-fault voltage and the current that would flow if a three phase symmetrical fault were to occur. Clearly, this combination of current and voltage cannot occur simultaneously, but the fault level (expressed in MVA) is a useful parameter that gives an immediate understanding of the capacity of the circuit to deliver fault current and resist voltage variations. In the per unit system, the fault level is the inverse of the magnitude of the source impedance (Weedy et al. 2012).

show the network performance over a period of time. This is known as *sequential steady state analysis*.

Fault calculators are used to check that the current that is supplied by wind turbines during a network short-circuit fault does not over stress switchgear or other network components. Adding generation to distribution networks can lead to the original protection no longer operating as it was intended. Thus fault calculators are also used to confirm that additional short-circuit current from wind turbines does not lead to mal-operation of relays on the distribution system by providing local support of the network voltage. Both balanced and unbalanced faults may be investigated. The calculations use the method of symmetrical components to calculate the effect of unbalanced short-circuits on the power system. Fault calculators that are used to examine the connection of wind turbines require good models of the induction generators or power electronic converters. A conservative approach is to consider the purpose of the short-circuit study and, for example, assume maximum fault current contribution for the rating of circuit breakers while calculating both minimum and maximum fault current for the operation of fuses and protection relays. Fault calculators give as output the fault current flows and network voltages at particular times after the fault occurs. Some programs use analytical methods to estimate the decay of fault currents with time but the main analysis uses a steady-state technique.

Transient stability programs allow investigation of how wind generators will respond to disturbances on the network. A balanced network is assumed as the calculation is based on an equivalent single phase representation using fundamental frequency phasors with an integration algorithm to calculate how the network conditions change over time. Traditionally, transient stability programs were used to investigate the angle stability of synchronous generators and a good model of the wind turbine generators is required for useful results.

Electromagnetic programs are among the more sophisticated tools and unlike the previous programs do not assume perfect, fundamental frequency waveforms. Detailed representation of both the induction generators and power electronic converters is possible. These programs use detailed time-domain simulations that allow reconstruction of the distorted wave forms generated by power electronic converters as well as investigation of high frequency transients such as those due to lightning. They may be used to investigate almost any condition on the power system but at the cost of considerable complexity and computation time. Electromagnetic simulations are not routinely used for basic design of small wind farms but only to investigate particular problems.

There are many more specialised calculation techniques and associated tools including probabilistic power flow, optimal power flow, harmonic load flow, and various earthing/grounding codes. However, their use requires specialist knowledge, and they are not in common use for small wind farm projects.

11.4.2 Electrical protection of a wind farm

Figure 11.11 shows a simplified protection scheme of a small wind farm connected to an MV distribution network. Detailed guidance on the protection required for the connection of wind turbines to the public electricity network is given in Electricity Networks Association (2019b) and IEEE 1547 (2018).

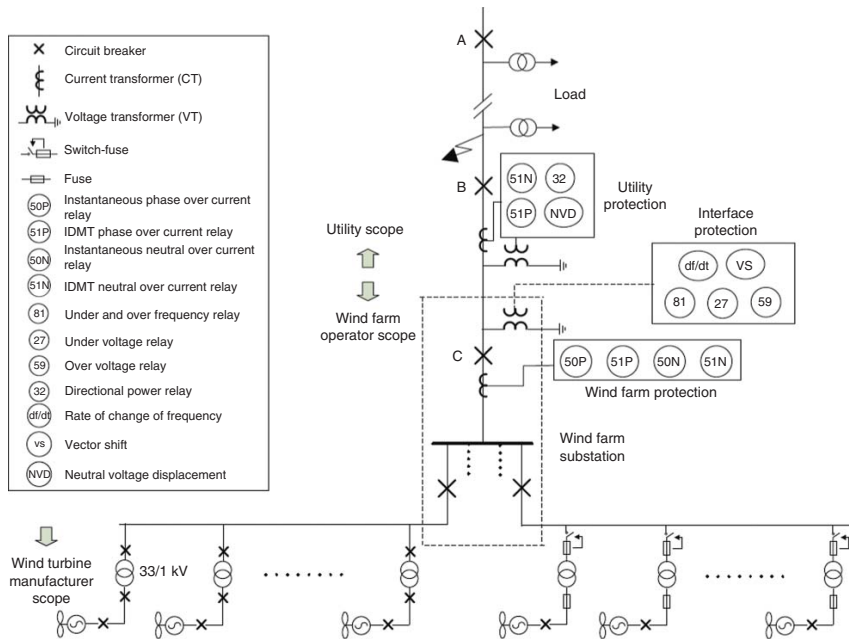


Figure 11.11 Simplified typical protection scheme for a small wind farm connected to a public utility network.

Recalling that most of the current into a short-circuit in the wind farm flows from the network, a circuit breaker (usually a moulded case type) is fitted in the base of each wind turbine tower to protect the pendant cables (see Figure 11.11). The LV cables running from the tower base cabinet to the turbine transformer are protected either by another circuit breaker (left hand side circuits) or lower cost fuses (right hand side circuits). These provide a point of isolation so that all of the electrical circuits of the turbine may be isolated from the network without switching at MV.

The region around the LV terminals of the MV/LV transformer is a particularly difficult zone to protect using MV fuses as they must be robust enough to withstand the magnetising inrush current of the transformer while sensitive enough to detect earth faults on the LV terminals when the fault current is limited by the impedances of the transformer and the resistance of the fault, as well as the delta/star winding configuration. This problem is common to the MV/LV transformers used in a public distribution network and a typical solution is to use a combination fuse-disconnect (sometimes known as a *switch-fuse*). These are shown connected to the right hand side busbar of Figure 11.11. Faults on the MV winding of the transformer will lead to high fault currents that are cleared by the MV fuse. However, faults on the LV terminals pose a problem, as a simple MV fuse may not clear these low fault currents effectively. Hence, once the fuse operates, a striker pin in the fuse cartridge causes a mechanism to open the disconnect switch to clear all of the phases. An alternative solution is to use restricted earth fault protection to detect currents to ground from faults on the LV winding and terminal area but this requires a more expensive MV circuit breaker (left hand side busbar).

The MV cable circuits of the wind farm power collection network are protected by the wind farm protection in the conventional manner by overcurrent and earth fault relays, operating circuit breaker C. In the protection of a public supply network, it is important to isolate only the faulty section or circuit and so maintain supply to as many customers as possible. Discrimination is less important in a wind farm as only some additional loss of generation will occur if some wind turbines are isolated unnecessarily. Hence a small number of MV circuit breakers and simple and low cost protection may be appropriate. The difficulty then remains, however, of ensuring that effective protection is installed to detect all credible fault conditions, even with limited fault currents, and then to be able to identify the faulted section of circuit.

The protection of the wind farm from insulation failure and subsequent short-circuit currents relies on fault current that is supplied by the distribution network. However, protection is also required to ensure that the wind farm does not feed current into faults on the distribution network. A wind turbine is not a reliable source of fault current and so conventional overcurrent protection may not be effective. When a short-circuit occurs on the network (marked in Figure 11.11), current operated protection operated by fault current from the distribution network opens circuit breaker A. This isolates the wind farm and, unless its output matches exactly the real and reactive power of the local load the voltage and frequency of the wind farm will change. The interface protection then trips circuit breaker B by the Loss-of-Mains over/under frequency or under/over voltage relays that detect that the connection to the network has been lost. It is common for the over/under frequency and voltage relays to be time delayed by 500 ms to reduce spurious operation. Muljadi et al. in Veers (2019) describe US practice.

11.4.3 Islanding and anti-islanding protection

Islanding is the condition where a generator continues to operate and supply a local load when disconnected from the network. Many distribution utilities require interface protection to avoid islanded operation for a number of reasons:

- The possibility that customers may receive supply outside the required limits of frequency and voltage.
- The possibility that part of the network may be operated without adequate neutral earths.
- The danger associated with out-of-phase reclosing.
- That it is against the regulations governing operation of the distribution network.
- The potential danger to staff operating the distribution network who do not realise that a circuit that is disconnected from the network is energised from the turbines.

From the point of view of the wind farm operator the main danger is out-of-phase reclosing. Many distribution circuits have automatic reclosing of circuit breakers to allow transient faults on overhead lines to be cleared without prolonged interruption to customers. Referring to Figure 11.11, circuit breaker A may be arranged to reclose up to a few seconds after opening on a fault. If the wind farm continues to operate and circuit breakers B and C are still closed then very high currents and torques on the generator shafts may occur as the network voltage is applied out-of-phase to the wind turbines. This is the main technical driver for fast anti-islanding protection as, particularly with wind turbines, it is very unlikely that the required matching of generator output (both real and reactive power) to the load will be sustained for any length of time.

Considerable efforts have been made to devise robust protection systems to detect islanding. However, this is very difficult as if the wind farm output matches the local load precisely there is no current flowing to or from the network and it makes no difference to the network conditions seen at the wind farm whether a circuit breaker is open or closed. The commonly used relays have been the RoCoF (rate of change of frequency or $d\text{f}/dt$) devices or vector-shift protection (VSP), which measures the jump in the voltage vector when islanding occurs. Both relays rely on some current flowing in the circuit and can be adjusted to provide varying levels of sensitivity. However, if they are set too sensitive then they are prone to spurious tripping caused by external disturbances on the power system (e.g. the tripping of a large remote load or conventional power plant). Regulations in Great Britain have recently increased the settings of RoCoF relays to reduce their sensitivity from 0.125 to 1 Hz/s with a 500 ms delay to improve the resilience of the power system. VSP has also been shown to operate unnecessarily in some cases and is no longer to be used (Electricity Networks Association 2019b).

Loss-of-mains protection techniques vary widely between different countries. Some countries favour the use of transfer tripping whereby when any upstream utility circuit breaker is opened this action is communicated to the wind farm circuit breaker, which is then immediately opened. Although this provides a guarantee against islanded operation it can be expensive to implement as communication channels from a number of

remote circuit breakers may be required. It is interesting to note that where almost all of the distribution system is underground and transient overhead line faults do not occur, auto-reclose is not used, and so there may be reduced requirement for loss-of-mains protection and simple under/over frequency protection is considered to be sufficient. Very large wind farms do not have sensitive interface protection because it is important they continue to operate during network disturbances to support the power system. The operating philosophies of the network operators and standards with respect to islanding are developing rapidly.

11.4.4 Utility protection of a wind farm

The utility protection is owned by the distribution network operator and is intended to ensure that faults on the wind farm cannot damage the network. It consists of inverse definite minimum time (IDMT) overcurrent and earth fault, directional power and neutral voltage protection. The IDMT protection duplicates that of the wind farm. The directional power relay is to ensure the wind turbines do not act to take power from the network and act as fans, and the neutral voltage relay detects unearthed operation of the network.

A complication occurs if the fault on the line between circuit breakers A and B is not between phases but is between a single phase and ground. Faults of this type are particularly common on overhead line circuits. The turbine transformers (e.g. 33/0.69 kV) have a delta winding on the MV side. This has no accessible neutral point and no connection to ground is made. Thus, when the wind farm is isolated and circuit breaker A is open, there is no path in which a ground current may flow and so, in principle, the single phase earth fault will remain indefinitely with no current flowing. In practice, some stray capacitive currents will flow, but these will not be enough to operate conventional earth fault protection, which may lead to intermittent arcing. The conventional solution is to use a neutral voltage displacement relay to detect that one phase of the circuit is connected to ground and so the neutral is displaced. The disadvantage of this scheme is the cost of the complex (five limb) electromagnetic voltage transformer that is required on the high voltage circuit. Although this cost can be accommodated for a large wind farm the expense is sometimes difficult to justify for individual wind turbines.

11.5 Grid codes and the connection of large wind farms to transmission networks

Individual turbines and small wind farms are connected to the MV distribution network while large wind farms feed into the HV distribution or transmission systems. Historically, the distribution and transmission networks have had different operating philosophies, and the size of a wind farm and the voltage level of the network to which it was connected determined the different regulations that applied to it. However, the difference between transmission and distribution networks is diminishing as distributed generation increases and the regulations for the connection of different power ratings of wind farms and their connection to networks of different voltage levels have begun to converge.

At present the regulations that apply to individual wind turbines or small wind farms connected at MV require that they must disconnect quickly if there is a disturbance in the power system or if a section of the network becomes islanded. When the network voltage or frequency moves outside the normal operating range the turbines are rapidly disconnected and not reconnected until normal network conditions have been restored. These regulations reflect the desire of the distribution network operators to avoid islanded operation and to ensure there is no possibility of out-of-phase reclosing, back-feeding isolated sections of the network with the possible safety hazards, or operating an ungrounded section of network. This requirement for rapid disconnection when network conditions are abnormal is met by loss-of-mains protection. Small wind farms and individual wind turbines make no active contribution to maintaining system frequency.

Large wind farms fall under the Grid Codes. The increasing number and capacity of large wind farms now mean they influence the network frequency by their generation of real power and the voltage of the transmission system through their exchange of reactive power with the network. The operating philosophy of large wind farms is that, rather than disconnect if the voltage and frequency of the power system are outside their normal limits, they should stay connected to support the power system. In addition, a large wind farm must be able to control its terminal voltage and regulate its output power as required by system operators.

The voltage of the transmission system is determined mainly by the effect of the reactive power flows from large central generators on the transmission circuits. Then tap-changing transformers establish the voltage levels of the distribution networks. The wind turbines connected to the lower voltage distribution network have only a local impact on voltage and operate with power factor control or by exchanging a set quantity of reactive power, and take their voltage from the network.

Many countries have their own national regulations for the connection of small distributed generators and their own Grid Codes for large wind farms. The standards are continually evolving as the importance of wind generation and other forms of distributed generation increases. The European Network Transmission System Operators (ENTSOE 2019) has developed common approaches and procedures for the connection of wind farms (described as *power park modules*) to European power networks, and these are translated into national standards (e.g. Electricity Networks Association 2019b).

The size of wind farm and voltage level at which the two different operating philosophies of small and large wind farms change reflects the relative significance of wind generation compared to the size and number of the conventional generators. Thus, the GB Grid Codes apply to wind farms above 50 MW in England, which has a strong power system, but above 10 MW in sparsely populated parts of Scotland where the networks are weak. As wind energy continues to increase, it is likely that more aspects of the Grid Codes will apply to smaller wind farms to ensure they contribute to the operation of the power system. Operating practice of distribution networks will be revised to reflect the increasing capacity of distributed generation and actively controlled loads.

In Great Britain, equipment failures and malfunctions have recently caused a large central generator and an offshore wind farm to trip almost simultaneously, leading to a low frequency event that was made worse by a significant capacity of distributed generation tripping as loss-of-mains protection operated incorrectly (National Grid: ESO 2019b). Detecting rapidly dropping system frequency, low frequency relays disconnected customers to maintain the integrity of the power system. In response to this incorrect operation, measures have been taken to ensure the protection of distributed generation

that is intended to protect against loss-of-mains is made less sensitive to transient low frequency events and spurious tripping is avoided. A similar event has been reported in the US affecting solar photovoltaic inverters (NERC 2017).

11.5.1 Continuous operation capability

The Grid Codes were originally developed for the connection of large fossil and hydro central generators but now also apply to large wind farms. They do not address individual wind turbines but only the performance of the entire farm at the point of connection to the transmission network.

Large wind farms are required to be able to operate continuously over the range of frequency and voltage that might be expected on the power system and not to trip during system disturbances. This is to ensure that they continue to provide energy into the power system when the transmission network voltage and frequencies are disturbed. Figure 11.12 shows the typical requirements for large wind farms connected to HV networks. The precise values of frequency and voltage limits (f_1-f_4 and V_1-V_4) vary country by country depending on the technical characteristics of the national power system and practice of the operators. Continuous operation over a range of frequencies and voltages ensures that large wind farms contribute to the stability of the power system.

11.5.2 Reactive power capability

The voltage of a transmission network is determined by the terminal voltage of the large generators and flows of reactive power through the transmission circuits. Large wind farms are required to operate either controlling their terminal voltage or by exchanging a defined level of reactive power with the transmission network.

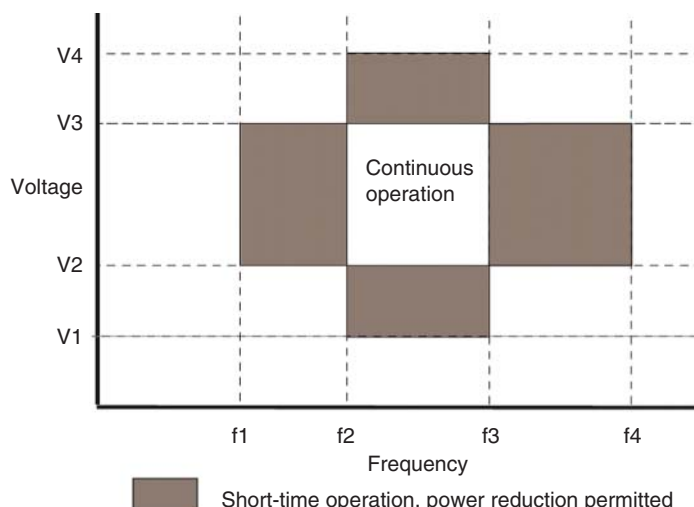


Figure 11.12 Typical shape of continuous and short-time operating regions.

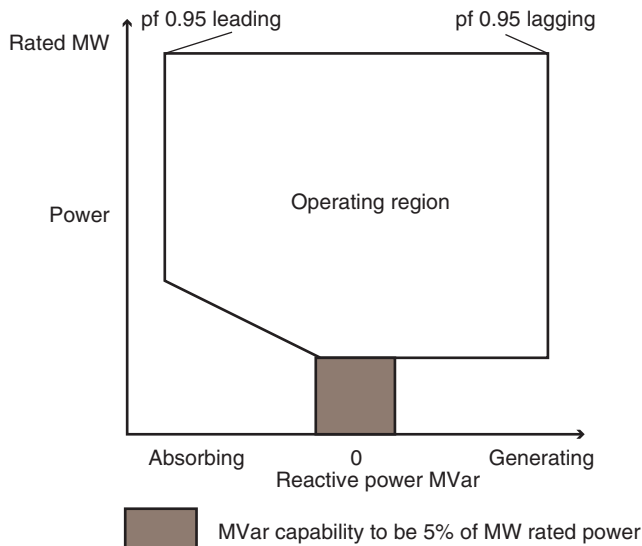


Figure 11.13 Reactive power/power characteristics required in Great Britain.

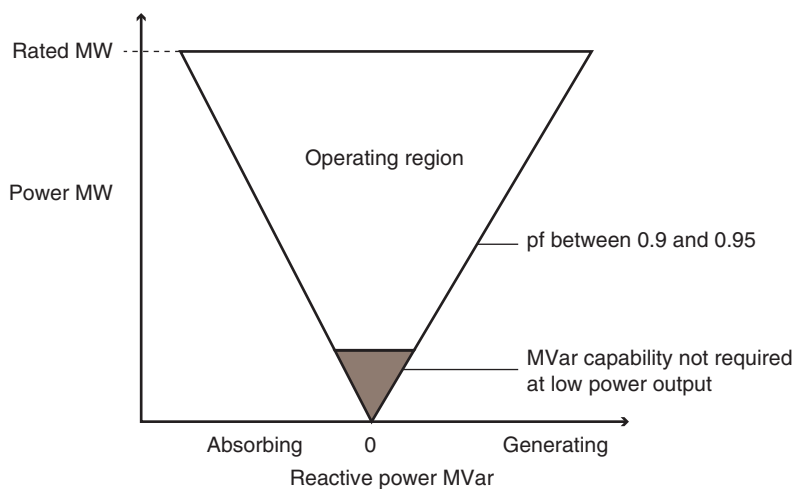


Figure 11.14 Reactive power/power characteristics required in two continental European countries.

Typical requirements of the capability of a wind farm to produce or absorb reactive power are shown in Figures 11.13 and 11.14. A wind farm is required to be able to operate anywhere within a defined area as instructed by the Transmission System Operator. The different shapes of the characteristics and the ranges of power over which this performance is required reflect the needs of the different national power systems.

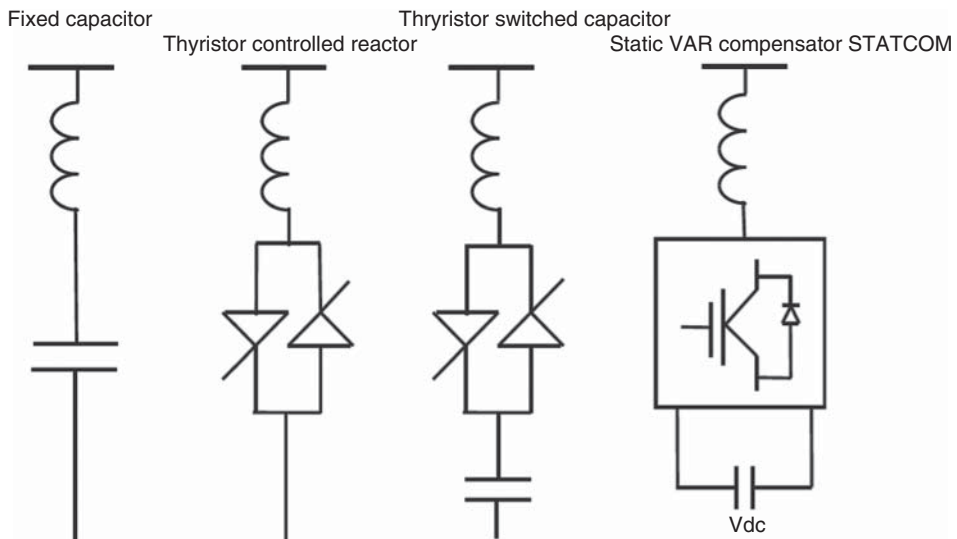


Figure 11.15 Commonly used reactive power compensators.

Variable-speed wind turbines can, in principle, operate at any power factor within the rating of their power electronic converters. In practice, it is difficult to ensure full compliance with the Grid Code requirements for the reactive power output of a large wind farm using the power electronic converters of the individual turbines alone because

- It is difficult to coordinate rapidly the reactive power generation of a large number of geographically dispersed wind turbines with different power outputs.
- The reactive power drawn by a wind farm transformer varies with both the real and reactive power exchanged with the network.
- The costs of the wind turbine converters increase if a large reactive power range is specified.

Hence, it is common for additional reactive power compensation equipment to be installed at the point of connection of the wind farm to the network to assist in meeting the Grid Code requirement. Figure 11.15 shows one phase of the different types of reactive power compensation equipment commonly found in wind farms. The connection of the phase to the neutral star point is omitted in the diagram.

Fixed capacitors provide a constant capacitive reactance and in normal operation supply a constant level of reactive power to the network. Thyristor switched capacitors provide variable reactive power in discrete steps. The inductance of a fixed capacitor or thyristor switched capacitor is usually small to limit inrush currents and provide some harmonic filtering. A thyristor controlled reactor provides a continuously varying inductive reactance as the thyristors are switched to apply the network voltage progressively. The reactive power output of all of these devices is proportional to the square of the terminal voltage and so falls rapidly during network faults. An alternative approach is to use a Static Compensator (STATCOM) based on a VSC. This has a smaller footprint and

provides a continuously variable reactive current, and its reactive power output is proportional only to the network voltage. A STATCOM works not by generating or absorbing reactive power from ac capacitors or inductors but by generating a voltage using a small dc capacitor as an energy store and passing a current across a coupling reactor.

11.5.3 Frequency response

The frequency of a power system is determined by the instantaneous balance of the real power generated and the power consumed by the load. If the load exceeds the generation the system frequency will drop and if there is an excess of generation the frequency will rise. Thus if the frequency of the power system increases, perhaps because a large load is disconnected, the wind turbines must reduce their real power output.

Figure 11.16 shows a typical frequency response required in many of the Grid Codes. Typical values for high and low frequency response are shown. To be able to provide low frequency response, the wind turbines must first be de-loaded either by adjusting the blade pitch angle or by operating at off-optimal rotational speed.

Figure 11.17 shows one strategy for de-loading wind turbines to provide reserve capacity, known as *delta control*. At the time the control is initiated, the output of the wind farm is reduced below the maximum that would be possible with the prevailing wind conditions so creating a reserve capacity that can be used to support the system in the event of a deficit of generation. Even though the requirement for de-loaded operation is specified in many of the Grid Codes, the power system operator rarely calls it as this would result in wind energy being wasted (EWEA 2009).

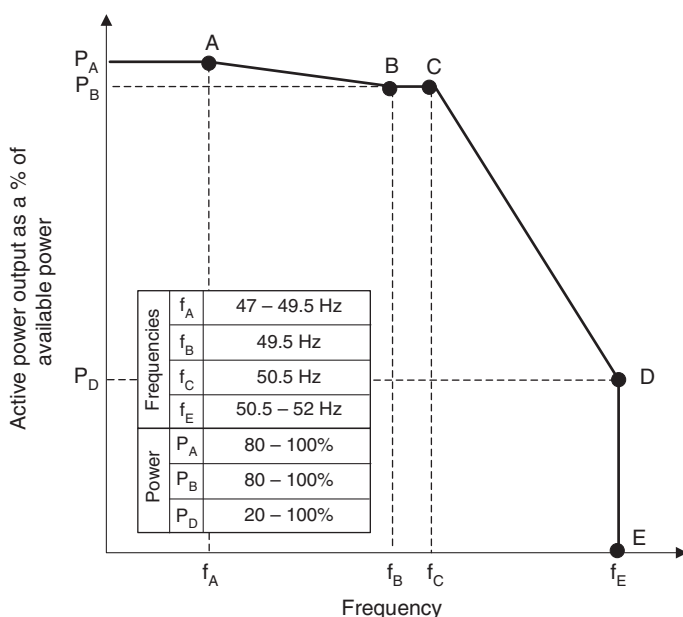


Figure 11.16 Frequency response.

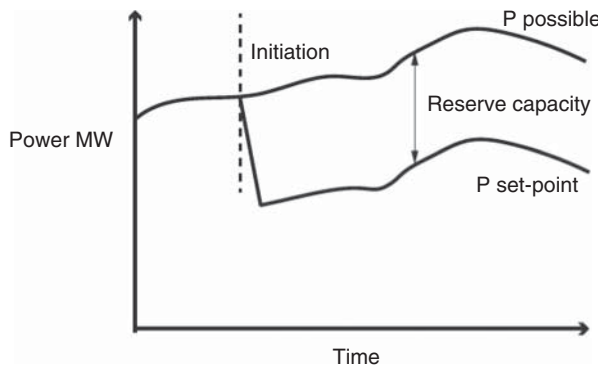


Figure 11.17 Delta control of real power.

11.5.4 Fault ride through

Short-circuit faults on the transmission network cause the voltage to be depressed over a wide area. Faults are inevitable in any power system (e.g. due to lightning) and the voltage depressions may extend for 100s of kilometres. Circuit breakers will clear faults on the transmission system in approximately 100 ms by isolating the faulted section of network, and the network voltage then recovers if suitable generators remain connected. A network fault may result in the isolation of a circuit and loss of central generation and it is just at this time that the wind farms should continue to provide energy into the power system. Thus the Grid Codes require large wind farms to remain stable and connected during any network disturbance and they must be able to demonstrate an ability to ride through voltage depressions caused by short-circuit faults on the transmission network.

The power that any generator can export is the product of voltage and current and so if its terminal voltage is depressed the generator cannot export its power to the network and the turbines will overspeed. The mechanical energy that would have been generated as electrical energy is stored as rotational kinetic energy in the generator and blades. When a fixed-speed induction generator wind turbine overspeeds due to a network fault and the voltage is subsequently restored it will draw large amounts of reactive power, which results in a further voltage depression and possible voltage instability. Thus fixed-speed wind turbines are unlikely to be able to ride through transient voltage depressions. A variable-speed wind turbine is better able to ride through a voltage depression and a transient reduction in output power by allowing the rotor speed to increase. However, a robust control system is needed to ensure that the converter remains synchronised with the network during the voltage depression.

Figure 11.18 shows a typical voltage–time envelope within which a wind farm must continue to operate.

11.5.5 Fast fault current injection

The widespread network low voltage caused by faults on the transmission network can be mitigated by injection of reactive current once the fault is cleared. Thus, some Grid Codes require large wind farms to be able to inject reactive current rapidly after transient

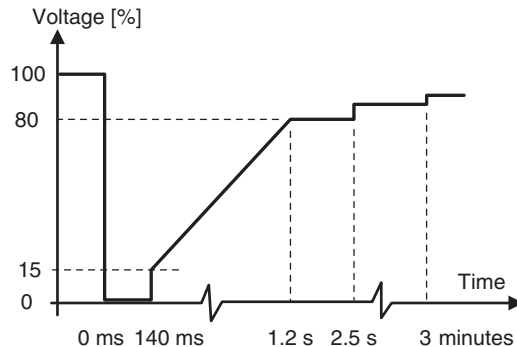


Figure 11.18 Typical fault ride through characteristic.

network low voltages. This function is known as *fast fault current injection*. As only reactive power is required there is no need to de-load the turbines to provide this service.

11.5.6 Synthetic inertia

Power system operators are becoming increasingly concerned that the inertia of the power system is reducing as conventional rotating synchronous generators are replaced by a converter connected plant (e.g. photovoltaic solar energy or variable-speed wind turbines). Power electronic converters isolate the spinning mass of the turbines from the power system. Then, when a mismatch occurs between generation and load the rate of change of system frequency increases. The inertia of the power system can only be increased by adding spinning mass (e.g. flywheels) or by manipulating the control of the converters and injecting stored energy when the system frequency drops.

The conventional control system of a variable-speed wind turbine does not use the power system frequency as a primary input variable. The phase angle and frequency of the network voltage is used to synchronise the switching of the power electronics of the network side converter, but the main control loop measures the rotational speed of the generator and applies a torque so that the wind turbine follows a pre-determined operating characteristic. In the event of a drop in power system frequency, caused, for example, by the sudden disconnection of a large central generator, a variable-speed wind turbine will not provide any additional energy automatically as the system frequency falls. This is in contrast to a conventional synchronous generator, or a fixed-speed induction generator, that will passively transfer some of its kinetic energy to the power system as the system frequency and the speed of rotation of the generator and prime mover falls. The power injected during the drop in frequency is proportional to the inertia of the generator and rate of change of the system frequency. Synthetic inertia describes an active control system of a variable-speed generator that emulates this effect and injects power into the network as the system frequency falls.

Synthetic inertia can be implemented by adding additional control loops as shown in Figure 11.19. Inertia is synthesised by measuring the rate of change of system frequency and injecting power in proportion (Loop 1). Applying an additional restraining torque to the wind turbine rotor injects energy into the power system as the wind turbine rotor

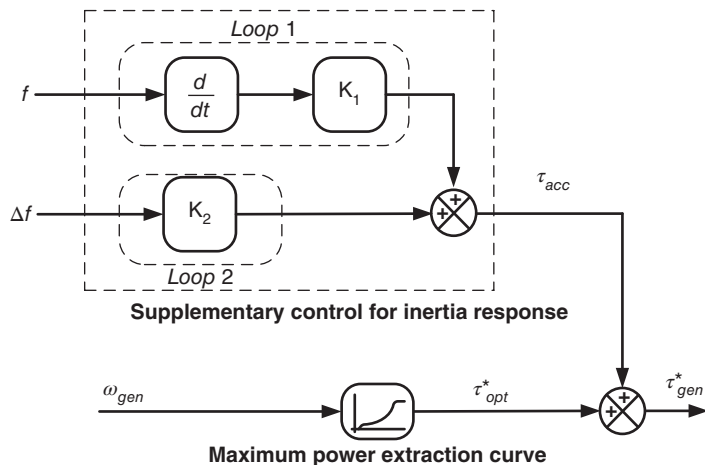


Figure 11.19 Additional control loops to provide synthetic inertia to a variable-speed wind turbine.

slows. The magnitude of the frequency drop may also be used to apply additional torque to the rotor in proportional to frequency (Loop 2). The ability to provide synthetic inertia is required by some but not all Grid Codes and some Transmission System Operators dispute its efficacy. These system operators are concerned that the effect is transitory and the rotor must be re-accelerated after the frequency has recovered

11.6 Wind energy and the generation system

Wind turbines are now an important source of electricity in many power systems and are changing the way that generating capacity is developed and operated. Because electricity cannot be stored cost-effectively in large quantities, the role of a generator in a power system is to supply electrical energy over a period of time (MWh) but also the power (MW) that is needed to meet the demand at any time. Fossil fuelled generators use energy stored in the fossil fuel and their output is easily controlled while wind turbines operate whenever the wind blows and, without de-loading them and wasting some of their potential output, there is little energy that can be called on to meet an increase in load.

The capacity factor of any generator is defined as the energy generated over a period of time divided by the energy that would have been generated if it had operated at its rated power continuously. It is an average measure, typically calculated over a year, and indicates how effectively the generating plant is utilised. The capacity factor is reduced below 100% by plant breakdowns, inability to find a use for the electricity, and, importantly for renewables, by lack of input energy, i.e. low wind speeds. Wind turbines can have typical annual capacity factors of 25–30% in a good wind resource onshore and 45–50% for very large wind turbines that are sited a long way offshore. If the performance of wind turbines is compared with that of fossil or nuclear plant, which have typical capacity factors of up to 80–90%, it can be seen that a much larger installed capacity of wind energy generation

is needed to supply a national load. Capacity factor is a good indicator to an operator of how effectively a wind turbine is working but does not describe the contribution that wind energy makes to the supply of power at a particular time.

Wind turbines have low operating costs and so, once they have been built, operate whenever the wind blows and reduce the time that the (higher operating cost) fossil fuelled generators are needed. This has the desirable effects of reducing CO₂ emissions but a high fraction of wind generation in a power system reduces the income of the conventional controllable (fossil) generators by reducing their hours of operation. The increase in the capacity of renewable generation and the consequent reduction in the opportunities for controllable generation to operate and gain revenue has led some generating companies with fleets of fossil fuelled generators to experience commercial difficulties. To address this, some countries have introduced payments for flexible generating capacity (i.e. the ability to generate power when it is needed) in addition to payments for the electrical energy supplied.

In many countries, the electricity system is liberalised and separated into companies dealing with generation, energy retail, transmission and distribution. Some parts of a liberalised electricity system operate as a market (generation and energy retail) while others are natural monopolies (the transmission and distribution networks) and are regulated by the state for the benefit of customers. Although the market influences the way generators and energy retailers behave in the short term, the underlying operation of the electric power system is the same as with a vertically integrated state monopoly, and markets and regulation can be considered merely as mechanisms to discover the most efficient way for the various actors to behave.

11.6.1 Development (planning) of a generation system including wind energy

All generators have a probability of not being available due to breakdown, but wind generation may not operate because of low wind speeds as well as equipment failure. Adding wind energy to the generation portfolio has the effect of requiring more generating capacity and widening the generation planning margin (i.e. the difference between nameplate generating capacity and peak load). A generating system is planned always to meet demand other than in exceptional circumstances and is assessed by evaluating its adequacy.

The principle of planning for a defined level of generation adequacy is illustrated in Figure 11.20. This shows the hourly probability distributions of the demand and the generation available of a power system. The risk of insufficient generation being available occurs over the intersection of these discrete probability distributions and can be quantified by a number of indices including loss of load probability (LOLP) or loss of load expectation (LOLE). LOLP is a measure of how many times the load can be expected to exceed available generation in a year, while LOLE indicates the duration of this condition.

With the rapid increase in renewables in GB, the use of LOLP and planning margin as metrics of generation adequacy has been superseded by the use of LOLE. LOLE is used to assess the adequacy of many national power systems with typical values of between 3 hours/year (France) to 8 hours/year (Ireland). It is also used by a number of the synchronous generation areas of the USA. The optimal level of LOLE of around 3

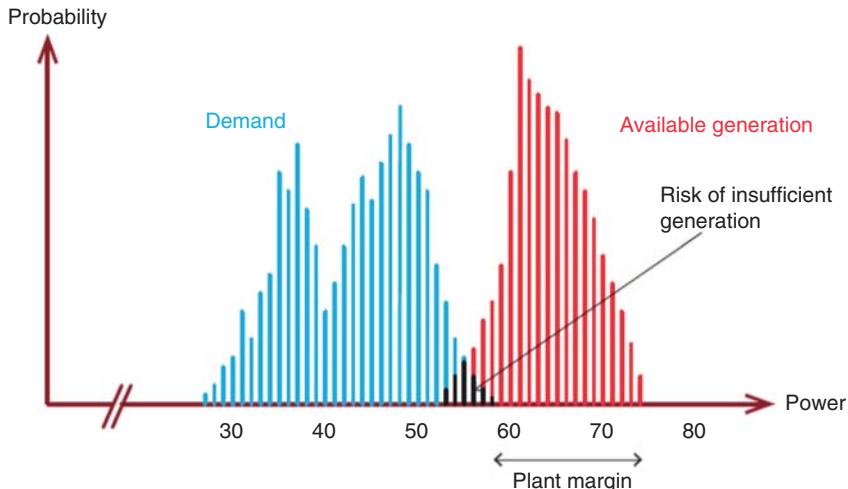


Figure 11.20 Illustration of generation adequacy.

hours/year for GB was determined by comparing the yearly cost of providing new gas turbine generating capacity (£47/kW) to the marginal cost of loss of energy due to blackouts (£17/kWh) (Department of Energy and Climate Change 2013). LOLE is an adequacy calculation, and a certain expectation of loss of load is not equivalent to the expected time of blackouts because the system operator can reduce load or increase supply through measures not represented in the adequacy calculation (e.g. by reducing the network voltage or in certain conditions by temporarily asking for the nominal rating of generators to be exceeded). The principle of the calculation of LOLP and LOLE from discrete probability distributions of the peak power consumed and the generation available in each hour is described in Weedy et al. (2012).

The calculation of the adequacy of a generation system has become increasingly sophisticated as power systems have de-carbonised. This has seen a steady increase in the numbers of: different types of low carbon generation, capacity of renewable generation with no natural stored energy, energy storage technologies such as batteries with a limited store of energy and demand side response measures. The current approach in GB is to calculate a de-rated capacity margin using de-rating factors for the various generating technologies. A de-rating factor represents the proportion of a source of electrical power that is likely to be technically available to generate at a time of peak demand (which in GB is an early evening in January). The de-rating factor of a generating technology depends on its characteristics and the fraction of each technology that is within the power system. The de-rating factor of a renewable generation technology decreases as more capacity of it is connected to the system, as a particular renewable technology (e.g. wind or solar) is likely to generate in a similar manner at approximately the same time.

Table 11.7 shows some of the de-rated capacity factors used to assess the adequacy of the GB generating system in 2019 (National Grid: ESO 2019a). The de-rating factors of wind energy appear low as this shows the proportion of an additional source of wind generated electricity that is likely to be available to generate at times of peak demand.

Table 11.7 Examples of de-rating factors used in GB.

Plant types	De-rating factor %
Nuclear	81
Combined cycle gas turbine	90
Storage (2 h duration, batteries)	41–62
Storage (4 h duration, pumped hydro)	66–95
Demand side response	86
Onshore wind	7.4–9.0
Offshore wind	10.5–14.5
Solar photovoltaic	2.3–3.2

For GB the calculation of LOLE is undertaken using the de-rating factors and a model of the generation system. A time-collapsed calculation compares the probability distributions of load and available de-rated generation to produce single-point estimates of loss of load expectation while more comprehensive results, including uncertainties, are obtained from a full sequential Monte Carlo simulation (Lane Clark and Peacock 2017).

11.6.2 Operation of a generation system including wind energy

The merit order is the classical representation of the operation of a generating system. It shows the generators ordered by their operating cost (short run marginal cost). For minimum cost of operation, the generators are called on to supply the load in order of ascending marginal cost. It is assumed that the generators have been constructed and so only fuel and operating costs are considered. The demand varies throughout the day and year and different units are called on to run following this principle. The price of electricity is the cost of operating the most expensive generating unit needed. The implementation of the merit order principle can either be by central control or through a market. Figure 11.21 shows a typical generation merit order with the operating cost of generation and the range of load that might be experienced during summer and winter.

Wind generation has a low marginal cost and so always operates if the turbines are available and the wind speed is suitable. When a wind energy plant operates, it is positioned at the extreme left and the rest of the merit order is translated towards the right. This has the effect of reducing the price of electricity and also the number of hours that fossil generators have the opportunity to generate.

Some plants with intrinsic energy storage (e.g. fossil or hydro generation or batteries) are required in order to follow the net load (the consumer load minus low carbon generation) and as reserve for plant breakdowns and network constraints. These operating requirements are incompatible with the traditional practice of rewarding generation only by the electrical energy generated (MWh), and increasingly generators are rewarded through capacity payments as well as through payments for ancillary services. Capacity payments are made to ensure generators are available when needed even if they are not called on to operate. Ancillary services are specific operating services, e.g. frequency response and provision of reactive power, that are needed to operate a power system.

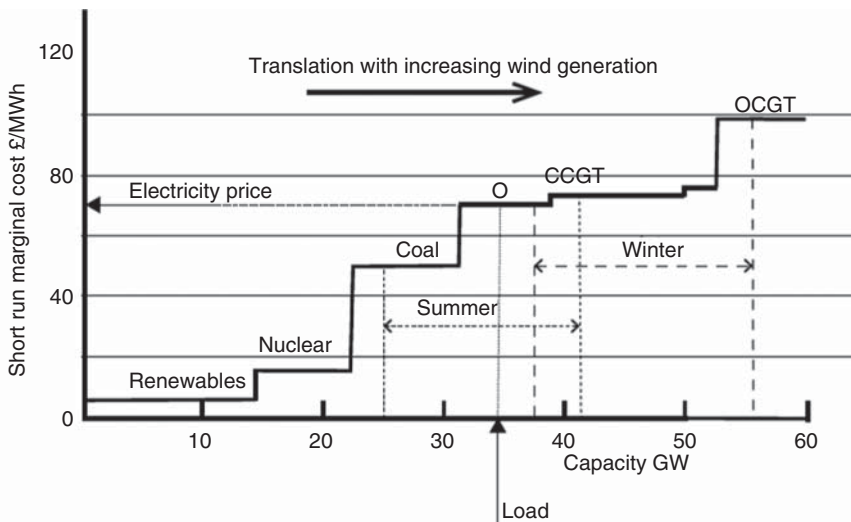


Figure 11.21 Generation merit order, showing the effect of increasing wind generation. Point 'O' is the operating point. CCGT, combined cycle gas turbine; OCGT, open cycle gas turbine.

11.6.3 Wind power forecasting

In a traditional vertically integrated electric power system, thermal generators are operated in two stages: Unit Commitment and Economic Despatch. Unit commitment is the selection of the optimum choice of generators to meet the load (e.g. for minimum cost or minimum emissions). The constraints of this optimisation include the maximum and minimum output power of each generator, ramp rates, minimum up and down times, network constraints such as loading of circuits and the requirement to maintain adequate reserves of partially loaded generators. Once the generators are connected to the network, their most economic output is determined through economic despatch. Unit commitment and economic despatch are referred to as *generation scheduling* (Wood et al. 2013).

In a market based power system each generating company optimises its own portfolio of generators with the objective of meeting the contracts they have struck with energy retailers at minimum cost. However, the principle remains of having to commit generating plant, often up to 8 hours in advance for large thermal generators, and then optimise its operation. The Transmission System Operator controls the final balancing of supply and demand and the management of frequency, reactive power and reserve.

The introduction of large quantities of wind energy into the power system significantly decreases the average net load supplied by thermal generators but increases the uncertainty of the generation that will be available. Forecasting of wind power output then becomes extremely important for power system operation (Boyle 2009).

Forecasting of wind power output is required over a range of spatial and temporal scales for a number of purposes. These include

- The scheduling of generators to balance supply and demand.
- Determining the reserve generation needed, as part-loaded generators, batteries, or fast-start gas turbine. This requires an assessment of the accuracy of the forecast.
- Operation of the transmission system and managing congestion on circuits.
- Operation of a generation portfolio to maximise return.

Wind power forecasting may be categorised as very short-term forecasts (up to 4–6 hours ahead), short term in the range of 48–72 hours ahead, and medium term up to 7 days ahead, although these definitions are applied loosely.

Methods of forecasting wind power output use include

- Time series analysis.
- Statistical or machine learning models with NWP (numerical weather prediction).
- Physical models with NWP.
- Hybrid models.

Very short-term forecasts of the output power of a wind farm (or a group of wind farms) can be based only on a past time-series of the measured data of the variable that will be predicted (e.g. wind speeds or wind farm power output). This avoids the cost and complexity of buying and integrating NWP weather forecasts. A number of techniques have been investigated (e.g. Kalman filters) and improvements of 15–20% over persistence have been reported. Persistence assumes simply that the forecast is the same as the last measured value. Very short-term forecasts are used for intraday energy trading and management of ancillary services.

Forecasts more than 4–6 hours ahead are based on NWP. Global NWP models are operated by national weather services to provide general weather forecasts, one element of which is wind speeds and direction. These use meteorological observations from weather stations and satellites together with a numerical model to predict the future state of the earth's atmosphere. They are very computationally intensive and so use a rather coarse spatial mesh. Local area NWP models take as their input the results of the global model to provide higher resolution but over only a part of the earth. It is common for the national and local NWP forecasts to use ensemble forecasting by combining the results of multiple forecasts either created with an individual forecast model and using different initial conditions, or with a number of different physical parameters. Local NWP forecasts may be purchased from national weather services. Short-term and medium-term forecasts are used for unit commitment of generators, trading in day-ahead markets and maintenance scheduling.

Two basic models are used for forecasting, statistical and physical. Statistical or machine learning wind power prediction models use a large amount of data to form relationships between variables and do not explicitly represent physical processes. A relationship between past power generation and weather is determined and then used to forecast future power outputs in a single step using an NWP wind forecast. Typical techniques include time series analysis and the use of artificial neural networks or support vector machines.

Tools based on physical modelling represent the wind flow in the wind farms and the power curve of the turbines. They take the wind speed forecasts from the local NWP model on a grid perhaps 20 km square, every 8 hours over a 48 hour time horizon. These are then translated (downscaled) to the wind farm site at the height of the turbines. In flat terrain this may be done by spatial interpolation but in more complex terrain a mesoscale model is used, sometimes in combination with a computerised fluid dynamics microscale model. Using this site wind speed, the wind farm output is then modelled taking into account the turbine power curves, local topography, and loss of energy in wind turbine wakes. Model output statistics are used to refine the model by comparing its outputs with measurements from the wind farms of power output and wind speeds. Prediction of the output of wind farms in an area is made by combining results from several well-instrumented wind farms, together with basic data from other wind farms that have less detailed monitoring, in a process known as *upscaleing*.

Figure 11.22 shows the information flows of a wind power prediction tool. The information flows of a tool using statistical model are similar to a physical model but exclude the detailed wind farm and terrain model. Hybrid models use a combination of statistical and physical models. Reviews of wind power forecasting are given in (Monteiro et al. 2009; Giebel et al. 2011; Foley et al. 2012).

11.7 Power quality

Power quality describes how closely the electrical power delivered to customers corresponds to the appropriate standards and so operates their end-use equipment correctly (Dugan et al. 1996). Thus, it is essentially a customer focused measure although greatly affected by the operation of the distribution and transmission network. Wind turbines, and other forms of distributed generation, can reduce power quality by distorting the voltage supplied to customers but also can increase power quality by raising the network short-circuit level and so stabilising the voltage. A network with a high short-circuit level has a lower source impedance, maintains a more constant voltage as the current varies and so gives higher power quality.

There are a large number of ways in which the electrical supply (i.e. voltage or frequency) can deviate from the required values. These range from transients and short-duration variations (e.g. voltage sags or swells) to long-term waveform distortions (e.g. light flicker, harmonics, or unbalance). Sustained complete interruptions of supply are generally considered an issue of network operation rather than power quality. The importance of power quality is due to the increasing use of sensitive load equipment including computer based controllers and power electronic converters as well as the awareness of customers of the commercial consequences of equipment mal-operating due to disturbances originating in the power system.

The issues of power quality are of particular importance to distributed wind turbines connected to rural distribution networks. Individual terrestrial wind turbines can be large, up to 3 MW, feeding into a distribution circuit with a high source impedance (i.e. a low short-circuit level) and with customers connected in close electrical proximity. For variable-speed wind turbines, which use power electronic converters, harmonic distortion of the network voltage may be important while the connection of fixed-speed

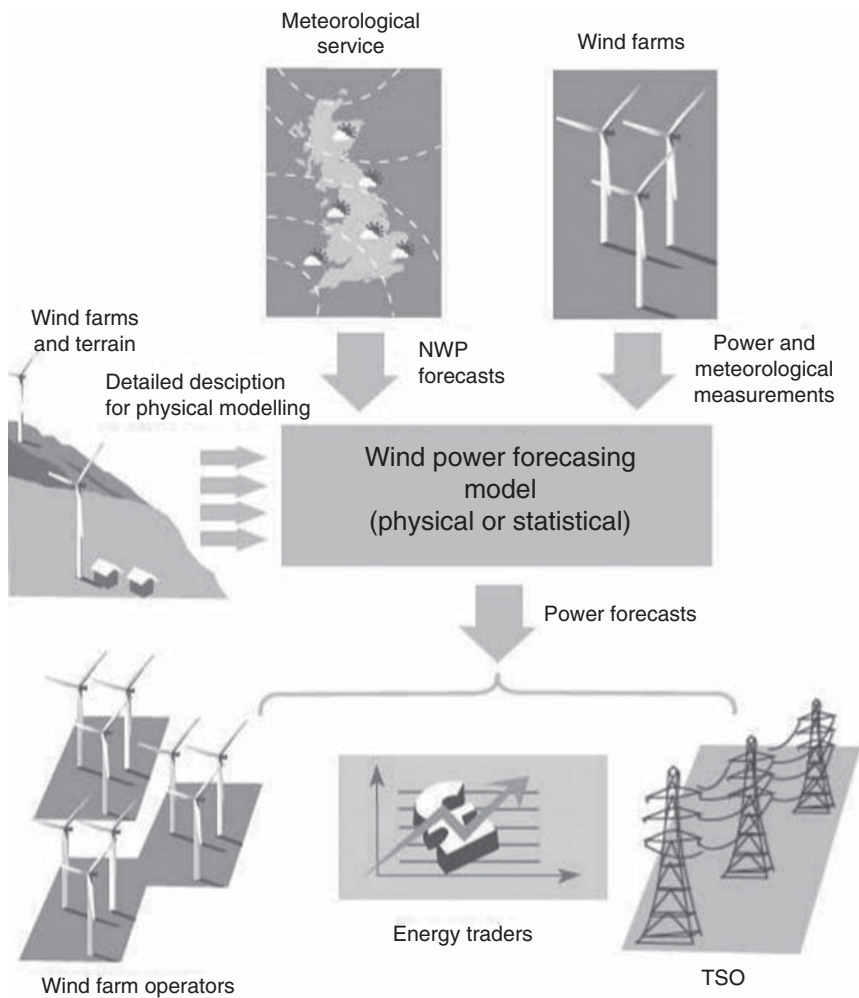


Figure 11.22 Flows of information in a wind power forecasting tool.

induction generator turbines to the network needs to be managed carefully if excessive voltage transients are to be avoided.

Wind turbines produce continuously varying output power during normal operation. The higher frequency variations in output power are caused by the effects of turbulence, the wind shear, tower shadow and the operation of the turbine control system. In fixed-speed and in some variable-speed wind turbines, depending on their control system, these effects lead to periodic power pulsations at the frequency that the blades pass the tower (typically around 1 Hz for a large turbine), which are superimposed on the slower variations in power caused by changes in wind speed. There may also be power variations (at up to a few Hz) caused by the dynamics of the turbine. Variable-speed operation of the rotor has the advantage that many of the faster variations in wind power are

not transmitted to the network but are smoothed by the flywheel action of the rotor. However, a poorly tuned control system of a variable speed turbine or fixed-speed operation using a low slip induction generator will lead to cyclic variations in output power, at blade passing frequency (3P), and to a lesser extent rotor rotational frequency (1P), and cause network voltage changes at these frequencies. The instant of connection of large generators on to weak networks may lead to transient voltage changes.

It is essential that wind turbines do not degrade the power quality of the distribution network as otherwise permission for their connection or continued operation will be refused by the distribution utility. In addition to national standards describing the limits of voltage variations that are caused by the connection of any equipment, e.g. Electricity Networks Association (2019a), the particular importance of the influence of wind turbines on power quality has been recognised in the international standard IEC 61400-21, *Measurements and Assessment of Power Quality Characteristics of Grid Connected Wind Turbines* (2008a). This standard lists the voltage quality indicators that should be provided by the turbine manufacturer to describe the voltage quality of wind turbine power output. It also details the testing procedures required to determine the wind turbine's response to a network voltage drop as well as the operation of its power control and grid protection systems.

The main aspects considered in IEC 61400-21 are

- 1) Voltage fluctuations:
 - Flicker coefficient for continuous operation as a function of network source impedance phase angle and annual average wind speed. The flicker coefficient describes the extent of the transient voltage changes that the wind turbine will create on the network.
 - Maximum number of wind turbine starts within 10 and 120 minute periods.
 - Flicker step factor and voltage change factor at start-up as a function of network source impedance phase angle.
- 2) Current harmonics and inter-harmonics:
 - Harmonic currents, up to the 50th, during continuous operation but excluding harmonics during wind turbine start-up.
- 3) Response to network voltage drops.
- 4) Active power control:
 - Maximum output power (11 minute average, 60 second average, and 200 ms average values).
 - Ramp-rate limitation after wind turbine start-up.
 - Active power set-point control for network frequency support.
- 5) Reactive power capability and set-point control.
- 6) Grid protection: settings of under/over voltage and frequency relays and reconnection time.

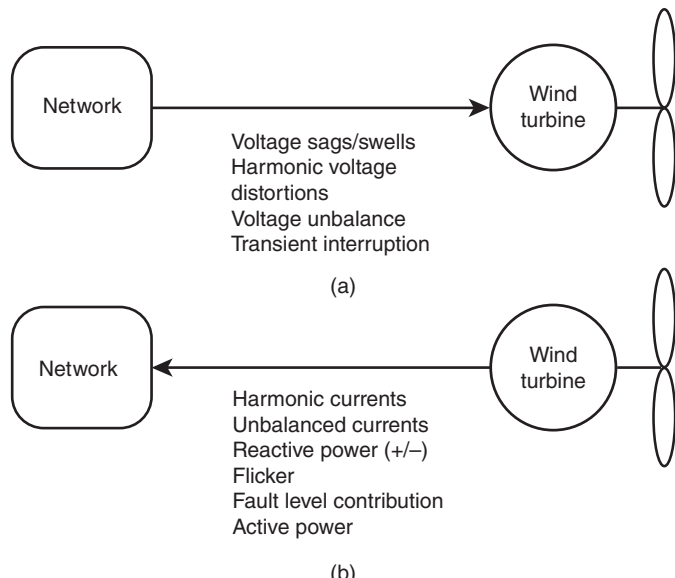


Figure 11.23 Origin of power quality issues. (a) Disturbances originating in the distribution network. (b) Disturbances originating in the wind turbines.

The main issue when connecting wind farms with a large number of generators (>10 turbines) is likely to be steady state power flow and voltage rise, while for individual large turbines on weak networks the limiting factor is often transient voltage changes. Power quality is an important consideration in the design and development of a new large wind turbine and is one factor that has led to the adoption of variable-speed operation as it reduces transient variations in output power.

Figure 11.23 shows how power quality may be viewed with respect to wind generation. 11.23a shows the various effects that may be considered to originate in the transmission and distribution networks and that can affect the voltage to which the wind turbines are connected.

Voltage sags, are a decrease to between 10% and 90% of nominal voltage for a period of up to 1 minute, usually caused by faults on the transmission or distribution network. They are of particular concern as they will cause fixed-speed induction generator wind turbines to overspeed as the load on the generator is removed. This in turn can lead to a high demand for reactive power that further depresses the network voltage. The depressed voltage may cause contactors to open and voltage sensitive control circuits to operate.

The control systems of variable-speed wind turbines may mal-operate during voltage sags as they rely on phase-locked loop(s) to synchronise the operation of the power electronic switches with the network voltage. The continued use of phase-locked loops for the control of inverters is being questioned by some Transmission System Operators that are considering requiring that simpler, more robust voltage control of power converters is used to increase the stability of the generators. The voltage of the dc links of variable-speed wind turbines will rise during network voltage sags as the wind turbines continue to generate power that cannot be injected into the grid due to its low voltage.

Solutions include the use of a crowbar resistor across the dc link of a variable-speed wind turbine or allowing the aerodynamic rotor to speed up and store kinetic energy during the voltage sag. Voltage swells (an increase in voltage over 110%) are less common and tend not to be a major problem for wind turbines in many countries.

Ambient harmonic voltage distortion is increasing in many power systems, due to a proliferation of power supplies of electronic equipment (TVs and PCs), and in the UK it is not uncommon to find levels of harmonics at some times of the day in excess of those that are considered acceptable by network planners (Electricity Networks Association 2020). Harmonic voltage distortions will lead to increased losses in the generators of wind turbines and may also disturb the operation of the control systems and the performance of power electronic converters. It is common practice to use power factor correction capacitors with fixed-speed, induction generator wind turbines, and these will have a low impedance to harmonic currents and the potential for harmonic resonances with the inductive reactance of other plant items on the network.

Network phase voltage unbalance will affect fixed-speed induction generators by increasing losses and introducing torque ripple (Electricity Networks Association 2003). Phase voltage unbalance can also cause power converters to inject unexpected harmonic currents into the network unless their design has considered an unbalanced supply voltage. Voltage unbalance is usually described in terms of negative phase sequence voltage. Using the method of symmetrical components (Weedy et al. 2012), the three phase voltage phasors are split into a set describing balanced (positive phase sequence) and unbalanced operation (negative phase sequence).

Unbalance and single phase voltage distortion can lead to difficulties with the network side converters of variable-speed generator systems that synthesise a three phase ac voltage from the dc voltage. This three phase ac voltage is used to inject current through a coupling reactance connected to the network. If the network voltage is distorted or all three voltages not balanced, unbalanced currents may be injected or the current waveform distorted. One solution is to use an independent phase-locked loop to detect the network voltages of each phase.

Figure 11.23b indicates how a distributed wind generator might introduce disturbances into the distribution network and so cause a reduction in power quality. A variable-speed turbine using a power electronic converter may inject harmonic currents into the network. Unbalanced operation will lead to negative phase sequence currents being injected into the network that, in turn, will cause network voltage unbalance. Variable-speed wind turbine generators can either produce or absorb reactive power while exporting active power and, depending on the details of the network, load and generation, this may lead to undesirable steady state voltage variations. Voltage flicker refers to the effect of dynamic changes in voltage caused by output power variations due to blade passing or other transient effects. There is considerable similarity between the power quality issues of wind turbines and large industrial loads and, in general, the same standards apply to both.

11.7.1 Voltage flicker perception

Voltage flicker describes dynamic variations in the network voltage that may be caused either by wind turbines or by varying loads (Bossanyi et al. 1998; Tande 2003; Tande 2005). The origin of the term is the fluctuations in the brightness of incandescent lights

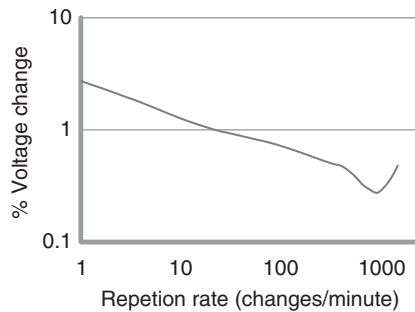


Figure 11.24 Influence of frequency on the human perception of sinusoidal voltage changes.

and the subsequent annoyance to customers caused by rapid voltage changes. The use of voltage flicker as an indicator of acceptable dynamic voltage variations on the network is rather unusual as the assessment is based on the experimentally measured effect of changes of the intensity of incandescent lamps on the human eye and brain. Human sensitivity to variations of light intensity is frequency dependent, and Figure 11.24 shows the magnitude of sinusoidal voltage changes that laboratory tests have shown are likely to be perceptible to observers. It may be seen that the eye is most sensitive to voltage variations around 15 Hz (900 changes per minute). The various national and international standards for flicker on networks are based on curves of this type. Incandescent lamps are being replaced with more efficient types fed through power electronic converters, but the flicker standards are generally used to characterise transient voltage variations and are of considerable significance for distributed wind generation.

Flicker is usually evaluated over a 10 minute period to give a ‘short-term severity value’ Pst . The Pst value is obtained from a 10 minute time series of measured network voltage using an algorithm based on the nuisance perceived by the human eye in fluctuating light. This is shown in Figure 11.25, which indicates how flicker is measured. Pst is linear with respect to the magnitudes of the voltage change but includes the frequency dependency shown in Figure 11.24. Twelve Pst values may be combined using a cube root of the sum of the cubes calculation to give a long-term severity value, Plt , over a 2 hour period (Electricity Networks Association 2019a), although IEC 614000-21 makes no distinction between Pst and Plt limits (2008a).

If a number of wind turbines are subject to uncorrelated variations in torque then their power outputs and effect on network flicker will reduce as

$$\frac{\Delta P}{P} = \frac{1}{\sqrt{n}} \frac{\Delta p}{p}$$

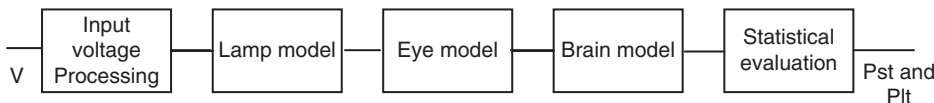


Figure 11.25 Principle of flicker measurement (IEC 61400-4-15 2008b).

where n is the number of generators, P is the rated power of the wind farm and p the rated power of each wind turbine and ΔP and Δp are the magnitudes of their power fluctuations.

A range of permissible limits for flicker on distribution networks is given in national and international standards. Engineering Recommendation P28 (Electricity Networks Association 2019a) specifies an absolute maximum values of P_{st} on a network, from all sources, to be 1.0 with a 2 hour Pl_t value of 0.6. However, extreme caution is advised if these limits are approached as the risk of complaints increases at between the 6th and 8th power of the change in voltage magnitude once the limits are reached and the approximate assessment method proposed in the same document is based on P_{st} not exceeding 0.5. BS EN 50160 (British Standards Institution 2010) is significantly less stringent, specifying that over a 1 week period Pl_t must be less than 1 for 95% of the time. Gardner (1996) describes P_{st} limits from a number of utilities in the range 0.25–0.5.

11.7.2 Measurement and assessment of power quality characteristics of grid connected wind turbines

Determination of the power quality of wind turbines and prediction of their performance in service is not straightforward, and IEC 61400-21 (2008a) provides guidance. There are a number of difficulties when assessing the power quality of wind turbines because their performance will depend on:

- The design of the entire wind turbine (including the aerodynamic rotor and control system).
- The condition of the electrical network to which it is connected.
- The wind conditions in which it operates.

Simple measurement of voltage variations at the terminals of a test turbine is not satisfactory as ambient levels of flicker in the electrical network and the X/R ratio of the network source impedance at the test site will have a significant impact on the outcome. Hence for evaluating flicker a procedure has been developed where current measurements are made of the output of a test turbine and used to synthesise the voltage variations that would be caused on distribution networks with defined short-circuit levels and X/R ratios of their source impedance. This is illustrated in Figure 11.26 and is referred to as simulation using a fictitious grid. These synthesised voltage variations are then passed through a flicker algorithm to calculate the flicker that the test turbine would cause on the defined networks. When the installation of the particular turbine is considered at a point on the real distribution network these test results are then scaled to reflect the actual short-circuit level and interpolated for the X/R ratio of the point of connection. A weighting factor, based on an assumed Rayleigh distribution of wind speed, is also applied to provide flicker coefficients that may be used on sites with various average annual mean wind speeds.

IEC 61400-21 also defines methods to evaluate the impact of wind turbine start-up at cut-in and rated wind speeds and during speed changing of two-speed generators. Again currents are measured, combined with the fictitious grid to provide a voltage time series and then passed through a flicker algorithm.

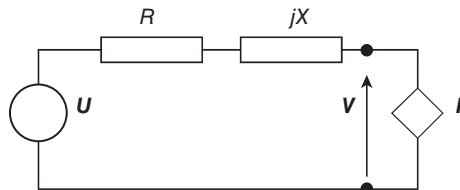


Figure 11.26 Use of a fictitious grid to establish voltage variations for various potential networks. I , measured current (complex quantity); R , resistance of fictitious grid; jX , inductive reactance of fictitious grid; U , ideal source voltage; V , synthesised voltage $|V|$ passed through flicker algorithm.

11.7.3 Harmonics

Neither the currents produced by wind turbine nor the voltages of the power system are perfect sine waves. This distortion of the sine waves can result in equipment mal-operating and is characterised by harmonics using Fourier analysis.

Harmonic currents produced by wind turbines depend on the type of wind turbine. As discussed in Section 7.5.1, fixed-speed induction generator wind turbines use anti-parallel thyristor soft starters to reduce the current when the induction machine is first connected to the network. These soft starters produce continuously varying harmonic currents as the network voltage is applied gradually to the generator. Because these harmonic currents are constantly varying and are of short duration (usually less than 5 seconds) they can normally be ignored.

Variable-speed wind turbines equipped with controlled back-to-back power electronic converters always produce some harmonic currents. As discussed in Section 7.5.3, pulse width modulation (PWM) switching introduces harmonics at the carrier frequency and multiples of it. These are usually above the 50th harmonic (i.e. above 2500 Hz on a 50 Hz system). To minimise the voltage harmonics at the output of the wind turbine converters, a passive filter formed by a line reactor and a shunt capacitor is usually used.

The impact of harmonic currents generated by wind power plants is assessed by harmonic emission and harmonic susceptibility studies. Harmonic emission studies evaluate the distortion of the current and voltage waveforms and compliance with Grid Codes or harmonic standards. They include conventional harmonic penetration studies. For harmonic penetration studies a simple method to represent the wind turbine is to use an ideal harmonic current source and assume constant network parameters. However, unlike a current source converter, where the surrounding network does not alter the harmonic distortion at the terminals of the harmonic source, harmonic currents generated by a voltage source convertor of a wind turbine generator vary according to turbine operating conditions, the converter control actions and even network conditions. In practice, a range of network short-circuit values will occur, and representing a VSC by an ideal harmonic current source may give rise to inaccuracies.

A VSC connected to the Thevenin equivalent of the grid is shown in Figure 11.27. The internal filter and generator inductances, external grid capacitors and grid inductances will all contribute to the overall grid impedance. This impedance has maxima and minima

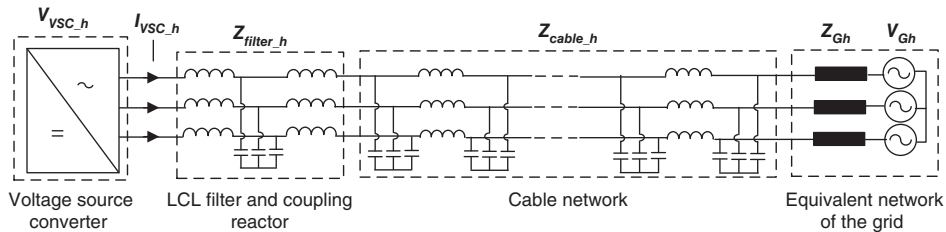


Figure 11.27 Harmonic equivalent circuit of a VSC based wind turbine generator connected to the grid.

at various frequencies and will effectively amplify or attenuate the harmonic voltages generated by the operation of the wind turbine generator.

In most guidelines and standards, the requirements for the individual and total harmonic distortion are up to the 50th harmonic. This is generally valid for line- or load-commutated current source converters. However, with VSCs higher order harmonics in excess of 10 kHz can be generated. Even though at such high frequencies current distortion generally does not penetrate far into the network, to assess these harmonics the IEC standard 61400-21 requires that harmonic currents should be stated individually up to the 50th harmonic and then grouped in spans of 200 Hz from 2 to 9 kHz.

In harmonic susceptibility studies the primary interest is potential instability of the operation of wind farm and wind turbine components or excitation of a system resonance frequency. The investigation of harmonic susceptibility requires more advanced analysis techniques such as electromagnetic transient simulation methods (Glasdan 2016; Kocewiak 2012).

References

- Alstom Grid (2011). Network protection and automation guide. <http://www.alstom.com/press-centre/2011/9/alstom-grid-offers-new-edition-of-network-protection-and-automation-guide> (accessed 11 February 2018).
- ANSI/IEEE 80 (2000). *IEEE guide for safety in AC substation grounding*.
- Bossanyi, E., Saad-Saoud, Z., and Jenkins, N. (1998). Prediction of flicker caused by wind turbines. *Wind Energy* 1 (1): 35–50.
- Boyle, G. (ed.) (2009). *Renewable Energy and the Grid*. Earthscan.
- British Standards Institution (2010). *BS EN 50160: Voltage characteristics of electricity supplied by public distribution systems*.
- Copper Development Association (1997). Earthing practice. *CDA Publication No 119*. Copper Development Association, Potters Bar. <http://copperalliance.org.uk/docs/librariesprovider5/resources/pub-119-earthing-practice-pdf.pdf?Status=Master&sfvrsn=0> (accessed 2 January 2018).
- Cotton, I. (2000). Lightning protection for wind turbines. Proceedings of the International Conference on Lightning Protection, pp. 848–853.
- Cotton, I., Jenkins, N., and Pandiaraj, K. (2001). Lightning protection for wind turbine blades and bearings. *Wind Energy* 4: 23–37.
- DD CLC/TS 50539-22 (2010). *Low-voltage surge protective devices – Surge protective devices for specific application including dc. Part 22: Selection and application principles – Wind turbine applications*.

- Department of Energy and Climate Change (2013). *Annex C: Reliability standard methodology*. https://assets.publishing.service.gov.uk/government/uploads/system/uploads/attachment_data/file/223653/emr_consultation_annex_c.pdf (accessed 4 April 2020).
- Dugan, R.C., McGranaghan, M.F., and Beaty, H.W. (1996). *Electrical Power Systems Quality*. New York: McGraw-Hill.
- Electricity Networks Association (2003). Planning limits for voltage unbalance in the UK for 132 kV and below. *Engineering Recommendation EREC P29*. [http://www.energynetworks.org/assets/files/ENA_ER_P29_Issue_1_\(1990\).pdf](http://www.energynetworks.org/assets/files/ENA_ER_P29_Issue_1_(1990).pdf) (accessed 15 December 2019).
- Electricity Networks Association (2019a). Planning limits for voltage fluctuations caused by industrial, commercial and domestic equipment in the UK. *Engineering Recommendation EREC P28*. [http://www.energynetworks.org/assets/files/ENA_EREC_P28_Issue%202_\(2019\).pdf](http://www.energynetworks.org/assets/files/ENA_EREC_P28_Issue%202_(2019).pdf) (accessed 15 December 2019).
- Electricity Networks Association (2019b). Requirements for the connection of generation equipment in parallel with public distribution networks on or after 27 April 2019. *Engineering Recommendation G99/1-4*. [http://www.energynetworks.org/assets/files/electricity/engineering/engineering%20documents/ENA_EREC_G99_Issue%201_Amendment_4_\(2019\).pdf](http://www.energynetworks.org/assets/files/electricity/engineering/engineering%20documents/ENA_EREC_G99_Issue%201_Amendment_4_(2019).pdf) (accessed 16 December 2019).
- Electricity Networks Association (2020). Limits for harmonics in the UK electricity supply system. *Engineering Recommendation G5/5*. [http://www.energynetworks.org/assets/files/ENA_EREC_G5_Issue_5_\(2020\).pdf](http://www.energynetworks.org/assets/files/ENA_EREC_G5_Issue_5_(2020).pdf) (accessed 15 December 2019).
- ENTSOE (2019). *Requirements for Types B, C and D power park modules*. www.entsoe.eu (accessed 22 December 2019).
- EWEA (2009). *Wind Energy – The Facts*. London: Earthscan.
- Foley, A.M., Leahy, P.G., Marvuglia, A., and Keogh, E.J. (2012). Current methods and advances in forecasting of wind power generation. *Renewable Energy* 37: 1–8.
- Gardner, P. (1996). Experience of wind farm electrical issues in Europe and further afield. Proceedings of the 18th British Wind Energy Association Conference, pp. 59–64.
- Giebel G., Brownsword R., Kariniotakis G., Denhard M., and Draxi C. (2011). A state-of-the-art in short term prediction of wind power: a literature overview 2nd edition. ANEMOS plus. <https://orbit.dtu.dk/en/publications/the-state-of-the-art-in-short-term-prediction-of-wind-power-a-lit> (accessed 10 April 2020).
- Glasdan G. (2016) Harmonics in offshore wind power plants – application of power electronic devices in transmission systems. PhD thesis, Aalborg University. <https://www.springer.com/gp/book/9783319264752> (accessed 26 April 2020).
- Glushakov, B. (2007). Effective lightning protection for wind turbine generators. *IEEE Trans. Energy Convers.* 22 (1): 214–222.
- IEC 61400-21 (2008a). *Measurements and assessment of power quality characteristics of grid connected wind turbines*. Geneva, Switzerland: International Electrotechnical Commission.
- IEC 61400-4-15 (2008b). *Electromagnetic compatibility (EMC) – Part 4: Testing and measurement techniques – Section 15: Flickermeter – Functional and design specifications*. Geneva, Switzerland: International Electrotechnical Commission.
- IEC 61400-24 (2010). *Lightning protection for wind turbines*. Geneva, Switzerland: International Electrotechnical Commission.
- IEC 60076-16 (2015). *Power transformers – Part 16: Transformers for wind turbine applications* (edition 2). Geneva, Switzerland: International Electrotechnical Commission.
- IEC 60909-0:2001 (2016). *Short circuit current calculations in 3-phase a.c. systems*. Geneva, Switzerland: International Electrotechnical Commission.
- IEEE 1547 (2018). *Standard for interconnection and interoperability of distributed energy resources with associated electric power systems interfaces*.
- Jenkins, N., Ekanayake, J.B., and Strbac, G. (2010). *Distributed Generation*. London: Institution of Engineering and Technology.
- Jose, G. and Chako, R. (2014). A review of wind turbine transformers. Proceedings of the International Conference on Magnetics, Machines and Drives (24–26 July 2014). Kottoyam, India.

- Kanellos, F.D. and Kabouris, J. (2009). Wind farm modelling for short circuit level calculations in large power systems. *IEEE Trans. Power Delivery* 24 (3): 1687–1695.
- Kocewiak L.H. (2012) Harmonics in large offshore wind farms. PhD thesis Department of Energy Technology, Aalborg University. https://vbn.aau.dk/ws/portalfiles/portal/316423403/lukasz_kocewiak.pdf (accessed 26 April 2020).
- Lakervi, E. and Holmes, E.J. (1995). *Electricity Distribution Network Design*, 2e. Bristol: Peter Peregrinus.
- Lane Clark and Peacock (2017) Unserved energy model. Report for BEIS and NG: ESO. <https://insight.lcp.uk.com/acton/attachment/20628/f-060f/1/-/-/-/LCP%20Unserved%20Energy%20Model.pdf> (accessed 4 April 2020).
- Lorentzou M.I., Hatziargyriou N.D., and Cotton I. (2004). Key issues in lightning protection of wind turbines. Proceedings of the WSEAS Conference on Circuits, Greece. <http://citeseerx.ist.psu.edu/viewdoc/download?Doi=10.1.1.559.1824&rep=rep1&type=pdf> (accessed 10 February 2018).
- Monteiro C., Bessa R, Miranda V., Botterud A, Wang J., and Conzelmann G. (2009). Wind power forecasting: state-of-the-art. <https://www.osti.gov>. (accessed 10 April 2020).
- Morren, J. and de Haan, S.W.H. (2007). Short-circuit current of wind turbines with doubly-fed induction generator. *IEEE Trans. Energy Convers.* 22 (1): 174–180.
- National Grid: ESO (2019a) Electricity capacity report. <https://www.emrdeliverybody.com/Capacity%20Markets%20Document%20Library/Electricity%20Capacity%20Report%202019.pdf> (accessed 4 April 2020).
- National Grid: ESO (2019b). Technical Report on the events of 9 August 2019. www.ofgem.gov.uk/system/files/docs/2019/09/eso_technical_report_-_final.pdf (accessed 16 December 2019).
- NERC (2017). 1,200 MW fault induced solar photovoltaic resource interruption disturbance report Southern California 8/16/2016 event . https://www.nerc.com/pa/rrm/ea/1200_MW_Fault_Induced_Solar_Photovoltaic_Resource_1200_MW_Fault_Induced_Solar_Photovoltaic_Resource INTERRUPTION_Final.pdf (accessed 15 December 2019).
- Peespati, V., Cotton, I., Soerensen, T.S. et al. (2011). Lightning protection of wind turbines – a comparison of measured data with protection levels. *IET Renew. Power Gener.* 5 (1): 48–57.
- Tande, J.O.G. (2003). Grid integration of wind farms. *Wind Energy* 6 (3): 281–296.
- Tande, J.O.G. (2005). *Power quality*. In: *Wind Power in Power Systems* (ed. T. Ackermann), 159–174. Chichester: Wiley.
- Veers, P. (ed.) (2019). *Wind Energy Modeling and Simulation*. IET.
- Weedy, B.M., Cory, B.J., Jenkins, N. et al. (2012). *Electric Power Systems*, 5e. Chichester: Wiley.
- Wood, A.J., Wollenberg, B.F., and Sheble, B. (2013). *Power Generation Operation and Control*. Wiley.
- WPD (2018) Long term development statement for Western Power Distribution (South Wales) Plc's electricity distribution system. November 2018. www.westernpower.co.uk/our-network/long-term-development (accessed 10 April 2020).

Appendix A11 Simple calculations for the connection of wind turbines

A11.1 The per-unit system

The per-unit system (Weedy et al. 2012) is simply a technique used by electrical power engineers to simplify calculation by expressing all values as a ratio of

$$\frac{\text{actual value (in any unit)}}{\text{base or reference value (in any unit)}}$$

Its advantages include (i) a reduction in the appearance of $\sqrt{3}$ in the calculations, (ii) that similar per-unit values apply to systems and plants of various sizes, and (iii) by appropriate choice of voltage bases, the solution of networks containing several transformers is facilitated.

For simple calculations, such as those required for assessment of a wind turbine or small wind farm on a simple distribution circuit, all that is required is to

- 1) Assume an arbitrary base VA (e.g. 10 MVA for a small wind farm connection).
- 2) Select voltage bases of each voltage level of the network (e.g. 33 and 11 kV). These voltage bases should be related by the nominal turns ratios of the transformers.
- 3) Calculate the appropriate real and reactive power flows at the generator terminals in per unit (i.e. for a power flow of 5 MW with the base VA chosen as 10 MVA, the per-unit value is $P = 5/10$ or 0.5 per unit. Similarly, for a reactive power flow of 1 MVar, the per-unit value is $Q = 1/10$ or 0.1 per unit).
- 4) If necessary, transform the impedances of the circuit from ohmic to per-unit values using a base impedance of

$$Z_{base} = V_{base}^2 / VA_{base}$$

- 5) The base current at any particular voltage level is calculated from

$$I_{base} = VA_{base} / \sqrt{3} V_{base}$$

A11.2 Power flows, slow voltage variations, and network losses

If the output from a distributed wind turbine generator is absorbed locally by an adjacent load, then the effect on the distribution network steady state voltage and losses is likely to be beneficial. However, if it is necessary to transport the power through the distribution network, then increased losses may occur, and slow voltage variations may become excessive (Jenkins et al. 2010).

If the wind generator operates at unity power factor (i.e. reactive power $Q = 0$), then the voltage rise in a lightly loaded radial circuit (Figure A11.1) is given approximately by

$$\Delta V = V_1 - V_0 = PR / V_0 \quad (\text{A11.1})$$

Operating the generator at a leading power factor (absorbing reactive power) acts to reduce the voltage rise but at the expense of increased network losses. In this case the voltage rise is given by

$$\Delta V = V_1 - V_0 = (PR - XQ) / V_0 \quad (\text{A11.2})$$

The impedance of an overhead 11 kV distribution circuit may, typically, have a ratio of inductive reactance to resistance (X/R ratio) of 2. An uncompensated induction generator at rated output, typically, has a power factor of 0.89 leading, i.e. $P = -2Q$. Thus, under these conditions, there is no apparent voltage rise in the circuit at full power. However, the real power loss (W) in the circuit is given approximately by

$$W = (P^2 + Q^2)R / V_0^2 \quad (\text{A11.3})$$

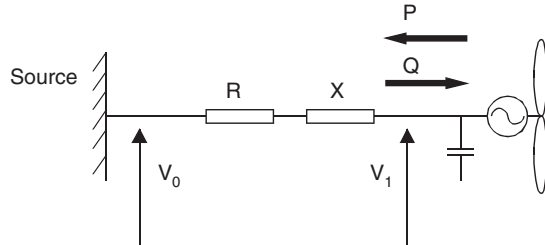


Figure A11.1 Fixed-speed wind turbine on a radial circuit.

The reactive power drawn by the generator acts to limit the voltage rise, but higher real power losses are incurred in the connecting circuit.

Equations (A11.1)–(A11.3) for voltage rise and circuit losses are approximate only and do not apply to heavily loaded circuits. A simple but precise calculation for voltage rise in any radial circuit may be carried out using an iterative technique.

Complex quantities are indicated by bold type.

At the generator terminals of Figure A11.1, the *apparent power* (sometimes known as the *complex power*) \mathbf{S}_I is given by

$$\mathbf{S}_I = P - jQ \quad (\text{A11.4})$$

(For a generator operating at lagging power factor, exporting VArS, \mathbf{S}_I would be given by $P + jQ$.)

By definition, $\mathbf{S} = \mathbf{V}\mathbf{I}^*$. * indicates the complex conjugate (i.e. the sign of the imaginary component of the complex number is reversed).

Therefore, the current flowing in the circuit is given by

$$\mathbf{I} = \mathbf{S}_I^* / \mathbf{V}_I^* = (P + jQ) / \mathbf{V}_I^* \quad (\text{A11.5})$$

The voltage rise in the circuit is given by \mathbf{IZ} , and so

$$\mathbf{V}_I = \mathbf{V}_0 + \mathbf{IZ} = \mathbf{V}_0 + (R + jX)(P + jQ) / \mathbf{V}_I^* \quad (\text{A11.6})$$

It is common for the network voltage \mathbf{V}_0 to be defined and the generator busbar voltage \mathbf{V}_I required. \mathbf{V}_I can be obtained using the following simple iterative expression:

$$\mathbf{V}_I^{(n+1)} = \mathbf{V}_0 + (R + jX)(P + jQ) / \mathbf{V}_I^{(n)} \quad (\text{A11.7})$$

where n is the iteration number.

This is a simple form of the conventional Gauss–Seidel load flow algorithm (Weedy et al. 2012). Once the calculation converges, an accurate solution is obtained. More complex load flow calculations may be carried out using commercially available power system analysis programs. These include models of transformers, with their tap changers, and they can solve large interconnected circuits in only a few iterations using more advanced algorithms.

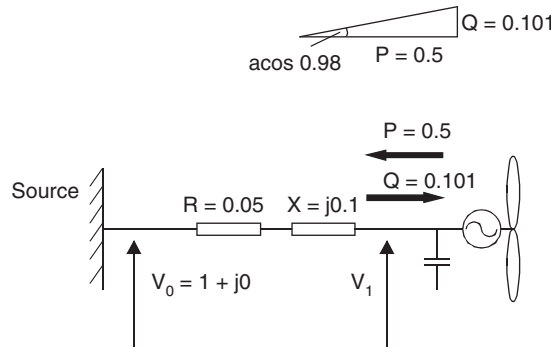


Figure A11.2 Example of calculation of voltage rise on a radial circuit (all values in per unit).

Example A11 (Calculation of Voltage Rise in a Radial Circuit) Consider a 5 MW wind farm operating at a power factor of 0.98 leading. The network voltage (V_0) is $(1 + j0)$ per unit and the circuit impedance (Z) is $(0.05 + j0.1)$ per unit on a 10 MVA base (see Figure A11.2).

A power factor of 0.98 leading implies a reactive power draw of 1.01 MVar.

Thus, following Eq. (A11.7), the calculation becomes

$$V_I^{(n+1)} = 1 + (0.05 + j0.1)(0.5 + j0.101)/V_I^{*(n)}$$

For the first iteration ($n = 0$),

assume $V_I^{*(0)} = 1 + j0$;

then $V_I^{(1)}$ may be calculated to be

$$V_I^{(1)} = 1.0149 + j0.0551$$

For the second iteration ($n = 1$),

$V_I^{*(1)} = 1.0149 - j0.0551$, then

$$V_I^{(2)} = 1.0117 + j0.0549$$

For the third iteration ($n = 2$),

$V_I^{*(2)} = 1.0117 - j0.0549$, then

$$V_I^{(3)} = 1.0117 + j0.0551, \text{ and the procedure has converged.}$$

Therefore, $V_I = 1.013$ per unit at an angle of 3° , i.e. the voltage at the generator terminals is 1.3% above that at the source. The angle between the two voltage vectors is small (3°).

The approximate calculation ($V_I = V_0 + PR - XQ$) indicates a voltage V_I of 1.015 per unit (i.e. a rise of 1.5%). This is confirmed by the results of the first iteration.

The current (I) in the circuit may be calculated from

$$\begin{aligned} I &= S^* \mathbf{1} / V^* \mathbf{1} = (0.5 + j0.101) / (1.0117 - j0.0551) \\ &= 0.4873 + j0.1264 \text{ per unit} \\ |I| &= 0.503 \text{ per unit} \end{aligned}$$

With a connection voltage of 33 kV, the base current is given by

$$I_{\text{base}} = \text{VA}_{\text{base}} / \sqrt{3} \times V_{\text{base}} = 5 \times 10^6 / 1.732 \times 33 \times 10^3 = 87.5 \text{ A}$$

and so the magnitude of the current flowing in the 33 kV circuit is 44 A.

The real power loss in the circuit (W) is²

$$W = I^2 R = 0.0127 \text{ per unit or } 127 \text{ kW.}$$

The symmetrical short-circuit level at the generator, before connection of the generators, is simply

$$\begin{aligned} S'' &= 1/|Z| = 1/(0.05^2 + 0.1^2)^{1/2} \\ S'' &= 8.94 \text{ pu or } 89.4 \text{ MVA} \end{aligned}$$

Once the generator is connected, it will make a contribution to the short-circuit current seen by a circuit breaker. This is typically some five times the rating for a directly connected, fixed-speed induction generator when it closes on to a fault, e.g. some 25 MVA in this case, giving a total short-circuit level of 115 MVA. For an inverter connected variable-speed generator, the contribution will be between one and three times the rating (5–15 MVA), giving a short-circuit level of 95–105 MVA.

However, the contribution to a three phase symmetrical fault from an induction machine decays rapidly and will make only a small contribution to the fault current that will be interrupted by an opening circuit breaker. Detailed guidance on the calculation of fault currents, including the contribution from induction generators and power converters, is given in IEC 60909 (IEC 2016).

² Note when the calculations are carried out using the per-unit system, this is the aggregated power loss of all three phases.

12

Offshore wind turbines and wind farms

12.1 Offshore wind farms

In a number of densely populated northern European countries, it is becoming increasingly difficult to obtain permission to construct large wind farms onshore due to environmental and other planning restrictions. These limitations on siting have stimulated the development of offshore wind farms in the relatively shallow waters of the North, Irish, and Baltic seas. These seas have large areas of good wind resource with water depths of less than 50 m. China is developing offshore wind farms off its eastern coast near to the load centres of large cities where there is a strong electrical grid. There are well-advanced plans to install large wind farms off the east coast of the USA.

In 2019, some 29 GW of wind farm capacity was offshore, approximately 4.8% of the worldwide total. A 2019 study estimated the annual worldwide offshore wind energy technical potential to be 36 000 TWh, more than global electricity demand (IEA 2019). These installations would use the established technologies of bottom mounted foundations and alternating current power circuits to transmit the electrical energy to shore.

The advantages of locating wind farms offshore include:

- Large areas are available for wind farm development with limited environmental and social impact.
- Very large turbines can be transported by sea directly from the factory to the wind farm site.
- Mean wind speeds are high, and this gives high capacity factors of 40–50% for new offshore wind farms a long way offshore.
- Wind turbulence is usually lower than on land.
- Landfalls of the cables and points of connection to the power network are close to cities and load centres.

The disadvantages of installing wind turbines offshore are the higher installation and operating costs offshore and the long development and construction times of these large and complex projects.

In 2019 approximately 10% of the new wind farm capacity installed that year was offshore. Figure 12.1a shows the recent historical development of worldwide capacity of offshore wind farms. Until around the year 2000, offshore wind farms were small and located in shallow water less than 5 km from shore. Then larger wind farms began to be constructed farther offshore, in particular the two large Danish wind farms at Horns Rev (160 MW, 2002) and Nysted (166 MW, 2003). Several wind farms of up to 1000 MW are now being constructed or planned off the coasts of northern Europe. The first large Chinese offshore wind farm entered service in 2008 and capacity has increased rapidly since 2010, mainly less than 10 km offshore in water depths of 5–25 m (He et al. 2016). In 2019, 2.4 GW of offshore wind energy capacity was installed in China, more than in any other country. Figure 12.1b shows the extent of offshore wind generation in the coastal waters of those countries with more than 1 GW offshore wind farm capacity in 2019.

In the past, offshore installations made up only a fraction of the total market for wind turbines and the turbines used for the early projects were marinised developments of those used onshore. Now offshore wind energy is seen as its own specialism using three bladed upwind variable-speed turbines of up to 9 MW rated output and rotor diameters up to 160 m. In 2019, 24% of the new wind farm capacity installed in Europe was offshore with an average power rating of new offshore wind turbines of 7.2 MW (Wind Europe 2020).

Wind farms that will use even larger turbines rated at 12–15 MW are under development. Monopile or gravity foundations have been used in depths of water of up to 30–35 m while jacket or tripod structures have been used in deeper waters. Efforts are continuing to use monopile foundations in deeper waters. Floating wind turbines have been demonstrated in water depths of around 100 m but this technology is not yet used widely.

For the early smaller offshore wind farms close to shore the wind farm power collection cables at 30–36 kV were extended to shore. Larger wind farms use an offshore transformer station to increase the collection voltage to around 150–200 kV for transmission to shore. A collection voltage of 66 kV and High Voltage direct current transmission are sometimes used for very large projects further offshore. Access for maintenance is generally by boat although helicopters have been used in some projects.

Table 12.1 shows the results of a study of the costs of a 1 GW offshore wind farm for commissioning in 2022 (BVG Associates 2019). The wind farm studied consisted of 100 × 10 MW turbines, located 60 km offshore in 30 m of water. The rotor diameter of the turbines was assumed to be between 170 and 200 m at a hub height of 110 m above sea level. The rotor speed varied between 5 and 15 rpm, and power conversion was through a two stage gearbox and a full power ac–dc–ac converter. The turbine considered had a maximum tip-speed of 100 m/s and the wind farm an anticipated capacity factor of 50%.

Table 12.1 shows that the turbines make up a rather lower fraction of the cost of an offshore wind farm than would be expected for an onshore project (costs shown in Table 10.1) with the foundations, cables, and electrical connection taking a greater proportion. Installation, de-commissioning, and maintenance of equipment offshore are also significant.

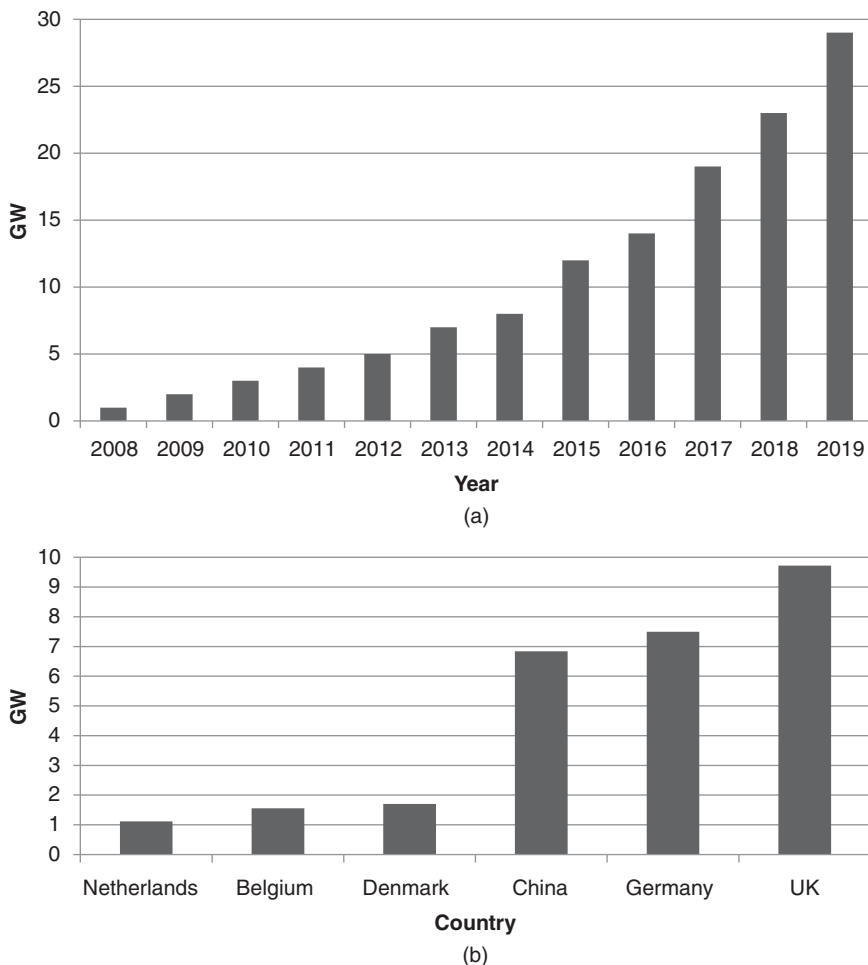


Figure 12.1 Offshore wind farm capacity. (a) Offshore wind farm capacity worldwide (Global Wind Energy Council 2020). (b) Countries with more than 1 GW of wind energy capacity in 2019 (Global Wind Energy Council 2020).

The cost of energy has varied widely over the short history of offshore wind power development. Gross et al. (2010) studied costs during the early development of UK offshore wind farms. From 2002 to 2004, capital costs for UK offshore wind farms were low at less than £1.5 m/MW. Then, as experience was gained and wind farms were located in deeper waters further offshore, capital costs doubled to £3 m/MW with the levelised cost of energy (LCOE) increasing from £85/MWh (2004) to £150/MWh (2010). This compared with a capital cost for onshore wind energy of between £1.3 – £1.8 m/MW and an LCOE of £94/MWh (DECC 2010). From 2010 to 2016 the LCOE of offshore wind energy decreased slowly to £106/MWh, at 2014 values (BEIS 2020). This compared to the cost of energy from small onshore wind farms of £63/MWh, for wind farms of less than 5 MW capacity (BEIS 2020).

Table 12.1 Indicative costs of a 1 GW offshore wind farm (BVG Associates 2019).

Element of wind farm cost	Description	Estimated cost for 1 GW wind farm £m	% of total initial cost
Development and project management	Activities up to the start of construction. These include design and engineering, securing planning consents, and EIA	£120 m	5
Wind turbines (including towers)	10 MW turbine delivered to a port near manufacturer – £10 m Installation and commissioning of each wind turbine by the manufacturer -- £1 m	£1100 m	45
Balance of plant	All of the components of the wind farm except turbines, e.g. foundations and power collection systems. Transmission circuits directly associated with the wind farm	£600 m	24
Installation and commissioning	Installation of turbines and balance of plant, offshore logistics, and project management up to handover	£650 m	26
Total initial cost		£2470 m	
Operations and maintenance	Recurring costs incurred by the wind farm operator	£75 m/yr	3
De-commissioning	Excluding any residual value	£300 m	12

Gross et al. (2010) considered that the factors that drove the escalation in cost of UK offshore wind farms from the mid-2000s to 2009 were (in descending order of importance):

1. Materials, commodities, and labour costs.
2. Currency movements.
3. Increasing prices for turbines over and above the cost of materials, due to supply chain constraints, market conditions, and engineering issues.
4. The increasing depth and distance to shore of more ambitious projects, affecting installation, foundation, and operation and maintenance (O&M) costs.

Table 12.2 Future projections of capacity factor and LCOE from wind farms.

Year of commissioning	Capacity factor %		LCOE £/MWh	
	Onshore	Offshore	Onshore	Offshore
2018 (average)	34	43	46	100
2030	30–55	36–58	23–38	38–69
2050	32–58	43–60	15–23	23–54

Source: Data from IRENA (2019a,b) converted at \$1.3/£.

5. Installation and operation supply chain constraints, notably in vessels and ports.
6. Planning and consenting delays.

Although several of these factors may no longer apply, this list does summarise the risks that apply to the costs of offshore wind farms.

Since 2010, there have been continuing reductions in costs, and IRENA (2019a, 2019b) quote an average LCOE of approximately £97.5 (\$127/MWh) for electricity from offshore wind farms commissioned in 2018. Future projections of the LCOE from wind farms anticipate a continuing increase in capacity factors and turbine rating and a decline in the cost of energy (see Table 12.2).

Auctions for public support for a guaranteed minimum price for the electricity that will be generated have revealed an even greater reduction in the costs of offshore wind energy. In the UK these costs approximately halved between 2015 and an auction in 2017 for delivery in 2022/2023. A competitive auction in 2019 resulted in a guaranteed fixed price of energy at (the strike price of a Contract for Difference [CfD]) of £39.65/MWh for the energy from two offshore wind farms with a total capacity of 2600 MW for delivery in 2023/2024 (BEIS 2019). A similar drop in the cost of energy from large offshore wind farm projects has been revealed through competitive auctions in Germany and the Netherlands. It is thought that these dramatic reductions in the public support needed for offshore wind farms are due to reductions in the cost of wind turbines and wind farm technology, economies of scale, and reduction in financing costs (Radov et al. 2017). LCOE, strike price, and CfD are described in Appendix A.12.

The costs of energy estimated through studies (LCOE) cannot be compared directly with those revealed by competitive auctions (strike prices) because the metrics are intended for different purposes and are based on different conditions and assumptions (BEIS 2020). In the UK the penalties for non-delivery of projects are limited while in some countries the initial costs of project development and the transmission of the electricity to shore are excluded from the auction bids. The full costs of integrating the wind power into the national power system, such as the need for reserve from conventional generators and wider grid development, are often not included. By convention, the strike price of these UK auctions is expressed in 2012 prices. However, the general trend is clearly towards lower costs of offshore wind energy.

Offshore wind energy is still developing and experience is being gained as wind farms are constructed further from the shore and in more demanding environments. A number of books and reports on offshore wind energy have emerged. Ackerman (2005) addresses offshore electrical systems while Hau (2006) provides an overview of the subject. Offshore

climatology and meteorology are discussed by Barthelmie et al in several papers and access by Dalen and Jakobsson in the comprehensive book on offshore wind power edited by Twiddell and Gaudiosi (2009). Installation of wind farms offshore is discussed by Thomson (2012) while Koller et al. (2006) and Perrow (2019) address the particular issues of the environmental impact of offshore wind energy. Reliability and availability are addressed by Tavner (2012) while floating offshore wind turbines are described by Cruz and Atcheson (2016). Recent developments are discussed by Ng and Ran (2016) and Anaya-Lara et al. (2018).

After a review of offshore wind meteorology, this chapter considers the design loads of offshore wind turbines, which differ significantly from those onshore. The design of fixed support structures is described including the fatigue analysis of monopile foundations, and the development of floating structures is surveyed. The main environmental considerations are reviewed and particular aspects of offshore power collection systems and the transmission of electrical energy to shore are also addressed.

12.2 The offshore wind resource

12.2.1 Winds offshore

For sites far from shore, and for sites near to the shore when the wind is blowing from open sea to land, mean wind speeds are usually higher than on land due to the absence of obstructions to the flow. Similarly, turbulence levels offshore are usually lower than on land, with limited wind shear corresponding to the low surface roughness over the sea. However, the surface roughness increases with wave height, so turbulence and wind shear may increase when there are large waves. These times are correlated with periods of strong winds, because waves are wind-driven, but there may be a significant time lag, so a wind farm may experience low wind speeds in conjunction with high waves following a storm out at sea. The lower frequency swell waves can travel long distances and may have been caused by high winds elsewhere that may never reach the wind farm. The contribution of the wind to the design loads of offshore turbines is considered in Section 12.3.2.

12.2.2 Site wind speed assessment

Quantification of the long-term wind resource at a potential wind farm site plays a central role in determining the economic feasibility of any wind energy project. For onshore wind farms, this is usually achieved through the collection of wind data from an onsite meteorological mast and/or analysis of energy production data from neighbouring operational projects (Section 10.1.3). These datasets are typically analysed in conjunction with long-term historical records from a local meteorological station together with site wind flow models to predict the long-term wind climate at the site.

A similar approach is adopted for offshore wind projects although there are significantly higher costs and delays associated with the erection of a meteorological mast at sea. Increasingly LiDAR systems, often mounted on buoys, are used to measure local wind speed profiles (IEA 2016). Preliminary wind resource estimates may be based on secondary sources such as measured wind data obtained from neighbouring sites or publicly funded measurement stations in the region. In such circumstances, the difference in wind

climate between the reference point and the target site as well as the uncertainty associated with this assessment must be determined.

Various methodologies may be applied to assess the variation of wind resource across wide areas of the offshore environment. These include conventional computational flow modelling techniques such as WA^sP (Mortensen et al. 1998) as well as more sophisticated modelling including mesoscale methods. In mesoscale modelling, a global climate model is used to find the conditions of the upper atmosphere, and these results are then either used as boundary conditions of a regional climate model (at a scale typically of 50 km × 50 km) or with empirically derived relationships with the sea surface parameters, temperature, and wind speed (Barthelmie et al. 2009). An advantage of this approach is the potential for capturing the wide scale synoptic trends as well as more localised thermal and topographic effects through application of a theoretically robust meteorological model, initiated from a large database of historical observations.

Data recorded by instruments mounted on earth observation satellites shows the offshore wind resource at a height of 10 m (Hasager 2014; Peña et al. 2013). Passive microwave measurements of ocean surface wind speeds have been made for some years at a frequency of up to six times a day and at a spatial resolution of around 25 km. More recently active microwave scatterometers have been used to derive estimates of wind speed and direction at the same spatial resolution. A scatterometer emits a beam of short microwave pulses; the intensity of the resonant backscatter is proportional to the steepness of the wind waves and hence to the surface wind speed at the time of observation (Aage et al. 1998). The relationship between the magnitude of backscatter and wind speed has been derived empirically. Whilst the absolute accuracy of the derived wind speed values is limited by the validity of the empirically derived relationship and the availability of the data is limited due to infrequent spatial and temporal sampling, methods have been developed that allow a robust estimate of the spatial variation of the wind resource to be determined over distances of several hundred kilometres. In addition, synthetic aperture radar (SAR) provides measurements at up to 1 km spatial resolution but at lower sampling frequency. SAR has been used to investigate wind farm wakes as well as to determine the wind energy resource.

In summary, a wide variety of measurement based and computer model based applications are available to determine the wind resource at any given offshore wind site. The uncertainties associated with the source data and analytical methodology adopted play a significant role in determining the level of confidence that may be ascribed to projections of long-term energy production, which in turn has a substantial influence on the economic viability of any offshore wind farm development.

12.2.3 Wakes in offshore wind farms

Wake losses in offshore wind farms can lead to a considerable loss of energy particularly at wind speeds below rated. Wake losses depend on the wind speed through a turbine, which is correlated with the thrust coefficient and so are most significant at lower operating wind speeds. Above rated wind speed, pitch-regulated turbines limit their power production by feathering the blades, which reduces the thrust coefficient and the wake losses at downstream turbines. Hence, above a certain wind speed all turbines will be producing rated power despite the wakes. Stall-regulated turbines continue to have a high thrust coefficient at high wind speeds that may cause high wake losses at all wind speeds,

but these turbines are rarely used offshore. The thrust coefficient implies an extraction of momentum from the air flow; further downstream the momentum is replenished by air mixing from the higher speed flow above the wind farm. Replenishment occurs more rapidly in the higher turbulent wind climate of onshore wind farms than in the low turbulent flow that is experienced at times offshore. Wake losses of a wind farm depend significantly on wind direction as well as turbine spacing. With a regular array of turbines, the wake losses will be high in certain wind directions, and the overall average losses will depend on the joint distribution of wind speed and direction. Wake losses of a wind farm can be in the range of 10–20% of the power generated by the front-row of turbines but as high as 70–80% for wind directions that are perfectly aligned with densely packed rows of wind turbines.

Array wake losses were exacerbated by the small separation distances of the turbines that were used in some early projects (Barthelmie et al. 2005). For example, the early Lillgrund offshore wind farm (Figure 12.2) was built with 48, 2.3 MW, 93.5 m diameter turbines (Lillgrund Pilot Project 2008, 2009a).¹ It was constructed with unusually small separation distances between turbines (3.3D along each row and 4.4D between rows).



Figure 12.2 Lillgrund wind farm layout. Lillgrund Pilot Project (2009a). Source: Reproduced by permission of Vattenfall.

¹ Lillgrund Pilot Project Reports can be found on the ETDEWEB, made available by US Dept. of Energy, <https://www.osti.gov/etdeweb>.

The small separation distances arose as the manufacturer increased the rotor diameter of the turbine part way through the project when the positions of the turbine bases had already been fixed during permitting. An extensive campaign of measurements showed that for wind blowing directly down a row, the second turbine experienced a power deficit wake loss of 80% (i.e. it produced only 20% of the power of the first turbine over a range of wind speeds below rated). Similarly at a spacing of 4.4 D the maximum power deficit between rows was up to around 70%.

Figure 12.3 shows how the wind farm array efficiency varies with wind direction for wind speeds below rated. The array efficiency is defined as the average array power generation per turbine at a given wind speed divided by the corresponding output of a turbine not suffering from wake losses – i.e. one at the windward edge of the array. Pronounced dips when the wind is blowing along the rows are seen. On the assumption of an isotropic wind direction probability distribution, the overall array efficiency of the wind farm was estimated to be 67% for wind speeds below rated and 77% for a site wind speed distribution assumed to be Rayleigh with an annual mean of 8 m/s. This implies that the power output of this rather dense offshore wind farm would be reduced by approximately 23% compared to what might be expected from a single isolated turbine (Lillgrund Pilot Project 2009a).

The Lillgrund wind farm was exceptional in its small spacing between turbines. Horns Rev 1 had a spacing of 7D along its rows and 10D between rows. Hansen et al. 2010 showed that, for a narrow range of wind directions, the maximum power deficit wake loss of the 2nd wind turbine in the array was around 40% at wind speeds of 5–9 m/s dropping to 30% at 11–13 m/s. The flow deficit sector generated by each turbine was approximately 25°–30°. The overall array losses of the wind farm were reported to be 12.4%. Wake losses at Middelgrunden wind farm (a curved single line of turbines with a lateral spacing of 2.4D) were reported to be around 10% in Barthelmie et al. (2007).



Figure 12.3 Lillgrund wind farm: variation in array efficiency with wind direction for wind speeds below rated. Lillgrund Pilot Project (2009a). Source: Reproduced by permission of Vattenfall.

Atmospheric turbulence and stability can have a significant effect on wake losses (Barthelmie and Jensen 2010). Turbulent mixing causes the wake to broaden and weaken as it moves downwind and the velocity deficit to reduce. The low levels of ambient turbulence typical of some offshore sites means the individual wakes will persist further downstream, but their effects will be felt over a narrower range of wind directions.

A number of approaches are used to predict wake losses and offshore array efficiency (Ivanell et al. 2018). These can be divided broadly into analytical wake loss models and those using Computational Fluid Dynamics. The simplest analytical model uses a simple top-hat wake profile, which is assumed to expand linearly based on a wake decay coefficient. This simple model (Katic et al. 1987) is widely used for the initial design of wind farms and was used by Cleve et al. (2009) to investigate the wakes of the Nysted offshore wind farm. Archer et al. (2018) compared six analytical wake loss models that showed that this simple model remained one of the most effective.

Barthelmie et al. (2009) compared six different wake models including simple analytical approaches and more sophisticated models derived from the Reynolds averaged Navier–Stokes equations together with empirical relationships for the wake-generated turbulence and the superposition of multiple wakes. Two of the models used full computational fluid dynamics modelling of the flow through the wind farm, treating the rotor disks as momentum sinks. The paper noted that although most of the accepted wake models gave reasonable results for single wakes or small wind farms, wake losses were under-predicted in large offshore arrays. This was thought to be due to inadequate representation of turbulence induced from the upstream turbines and the effect of atmospheric stability. On land such effects tend to be masked by the higher levels of turbulence caused by the topography. Subsequent research on the effect of wind turbine wakes on energy production and turbulence is described in (Barthelmie et al. 2010; Ivanell et al. 2018).

Relatively simple models, as long as they have been well calibrated against measurements, can give reasonable estimates of overall energy losses due to wake effects. However, there is now increasing interest in actively controlling turbines to minimise wake losses in a wind farm, and for this to work effectively, it is important to use wake models that are accurate not just on average but remain accurate across a wide range of atmospheric conditions and changes in turbine operational parameters. Chapter 9 provides a detailed account of such wake modelling and its application to wind farm control.

As more offshore wind farms are built, the effect of the wake of an entire wind farm on the energy production of another wind farm becomes of interest, as well as the impact this may have on the total wind energy resource that can be exploited from a given sea area. Figure 12.1b shows that there is already 8 GW of offshore wind farm capacity operating in UK waters and more than 6 GW off the coasts of Germany. Estimates of the capacity of European offshore wind farms by 2030 are as high as 70 GW. The wind farms are typically located in clusters in shallow seas with good access to ports and the onshore electricity networks. In most weather conditions, atmospheric turbulence causes the wakes of wind turbines to be a local effect within the offshore wind farm. Early research on the wakes of entire wind farms is summarised in Frandsen et al. (2009). Hasager (2014) showed evidence from satellite observations of the wakes of offshore wind farms persisting for tens of kilometres. Platis et al. (2018) used wind speed data recorded by an aircraft to show that under stable atmospheric conditions (when the temperature of the air is higher than the sea and vertical motion of the air is inhibited) the wakes of an

offshore wind farm can extend up to 45 km, creating wind speed deficits of up to 40% and increased turbulence.

The established models that are used to predict the energy output of a wind farm consider the reduction caused by the wakes downstream of turbines. However, there is now evidence that there might also be a small reduction in the wind speeds upstream or lateral to a turbine. This effect is known as *blockage*, and there is thought to be an individual blockage effect from every turbine and an effect of the whole wind farm. The reduction in energy generated by a wind farm due to blockage is believed to depend on a number of factors, including

- The density of turbines in an array.
- Atmospheric stability – blockage is higher in stable conditions.
- The ratio of turbine hub height to rotor diameter – higher towers will reduce blockage.

These factors are in addition to wind speed and direction (i.e. array layout) that also have a major impact on wake losses. The phenomenon of blockage has been identified and discussed widely only recently (Bleeg et al. 2018) but is a possible cause of a previously unpredicted reduction of energy from offshore farms that is significant but an order of magnitude less than the energy loss caused by the wakes of turbines. Research on improving the prediction of the power output of offshore wind farms is continuing.

12.3 Design loads

12.3.1 International standards

National design standards specifying wind and wave loadings on offshore structures were developed as North Sea oil began to be exploited, and were subsequently utilised for the design of the first offshore wind farms. However, offshore wind turbines differ from offshore oil platforms in that the wind loading on wind turbine support structures is a much more significant element of the total loading than is the case for oil platforms, so the desirability of design standards tailored to offshore wind turbines was soon recognised.

The first design standard for offshore wind turbine structures to appear was published by Det Norske Veritas in 2004. Offshore standard DNV-OS-J101, *Design of Offshore Wind Turbine Structures*, is a comprehensive document, covering marine conditions, design load cases, wave loading and structural design. The design load cases were the same as those set out in IEC 61400-1, but with appropriate wave heights or sea states specified. However, in 2007, a revised edition was published with the load cases modified to be consistent with those in the draft IEC 61400-3 (see below), with further revisions appearing at intervals until 2014.

Germanischer Lloyd (GL) published *Guideline for the Certification of Offshore Wind Turbines* in 2005. It covers the rotor and nacelle components as well as the support structure and is structured in the same way as the parallel document for onshore machines, but with individual chapters expanded to include the requirements particular to offshore siting. These guidelines were completely revised in 2012 (Germanischer Lloyd 2012).

Following the merger of Det Norske Veritas and GL in 2013, DNV-OS-J101 and the GL guidelines were replaced by DNVGL-ST-0126, *Support Structures for Wind Turbines* (2016), with the design loading requirements removed and placed in a separate standard, DNVGL-ST-0437, *Loads and Site Conditions for Wind Turbines*.

The International Electrotechnical Commission standard IEC 61400-3, *Wind Turbines – Part 3: Design Requirements for Offshore Wind Turbines* appeared in 2009, with an amended version, IEC 61400-3-1, *Part 3-1: Design Requirements for Fixed Offshore Wind Turbines* following in 2019 (IEC 61400-3-1 2019). Unlike the GL guidelines referred to above, this is not a stand-alone document but has to be read in conjunction with IEC 61400-1 (see Chapter 5). A companion technical specification for floating offshore wind turbines, IEC 61400-3-2, was published in 2019 (IEC 61400-3-2 2019).

The load cases specified in IEC 61400-3-1 closely correspond to those in IEC 61400-1, with the marine conditions to be taken into account added in each case. Stochastic sea states are specified for all load cases, requiring several 10 minute simulations to be run. A minimum of six such simulations is required for each mean hub-height wind speed and sea state for each load case, but for some load cases significantly greater numbers are required. The wind and marine conditions specified are considered in the next sections.

Some of the work in developing the IEC 61400-3 guidelines was carried out under the auspices of a European Community supported R&D project ‘Recommendation for Design of Offshore Wind Turbines’ (contract no ENK5-CT-2000-00322), or RECOFF, and was reported in some 70 papers.

12.3.2 Wind conditions

IEC 61400-3-1 requires the support structure to be designed for site-specific wind conditions, but, in the case of the rotor-nacelle assembly, the alternative approach of designing for one of the wind turbine classes defined in IEC 61400-1 may also be followed, provided it can be demonstrated that the offshore site-specific external conditions do not compromise the latter’s structural integrity.

The following hub-height wind parameters are to be determined at the site, preferably by site monitoring:

- The extreme 10 minute mean wind speed with a recurrence period of 50 years, U_{ref} , and that with a recurrence period of 1 year.
- Wind speed and direction distributions.
- Turbulence intensity for wind speeds over the operating range, and at U_{ref} .
- Standard deviation of turbulence intensity at each wind speed.
- Wind shear.
- Air density.

It is worth noting that wind shear is usually less offshore than onshore because of the reduced surface roughness – values of under 0.1 are typical.

In the absence of site monitoring, the above parameters may be estimated from local standards, or, in the case of turbulence intensity, from the surface roughness parameter, z_o . Sea roughness increases with wind speed, and z_o may be estimated from the Charnock expression:

$$z_o(\bar{U}) = \frac{A_c}{g} \left[\frac{\kappa \bar{U}}{\ln(z_{hub}/z_o(\bar{U}))} \right]^2 \quad (12.1)$$

where A_c is Charnock's constant, g is the acceleration due to gravity and κ is von Karman's constant (0.4). The standard recommends values of A_c ranging between 0.011 for open sea and 0.034 for near-coastal locations. The design value of turbulence intensity is taken as the 90% quantile given by the following equation:

$$I_u = 1/\ln(z_{hub}/z_o(\bar{U})) + 1.28(4.0I_{ref})/\bar{U} \quad (12.2)$$

The first term in this expression is an accepted formula for the *mean* turbulence intensity and the second term represents the additional 1.28 standard deviations of turbulence intensity required for the 90% quantile, where I_{ref} is the mean hub-height turbulence intensity at a reference mean wind speed, \bar{U} of 15 m/s. If I_{ref} is replaced by the mean turbulence intensity at the prevailing wind speed, \bar{U} , given by the first term, Eq. (12.2) approximates to

$$I_u = \frac{\sigma_1}{\bar{U}} = \frac{1}{\ln\left(\frac{z_{hub}}{z_o(\bar{U})}\right)} \left(1 + 1.28 \left(\frac{4.0}{\bar{U}} \right) \right)$$

Note that the numerator 4.0 m/s has been increased from 1.44 m/s in ICE 61400-3 (2009) taken from IEC 61400-1 because significantly larger standard deviations have been recorded at some offshore locations.

The resulting variations in turbulence intensity with wind speed at open sea and near-coastal locations are compared with that at an onshore site with medium turbulence (Category B) in Figure 12.4. It is seen that the turbulence intensity at an offshore coastal location is only slightly higher than over the open sea, but in both cases is significantly less than that onshore throughout the operational speed range of typically 5–25 m/s.

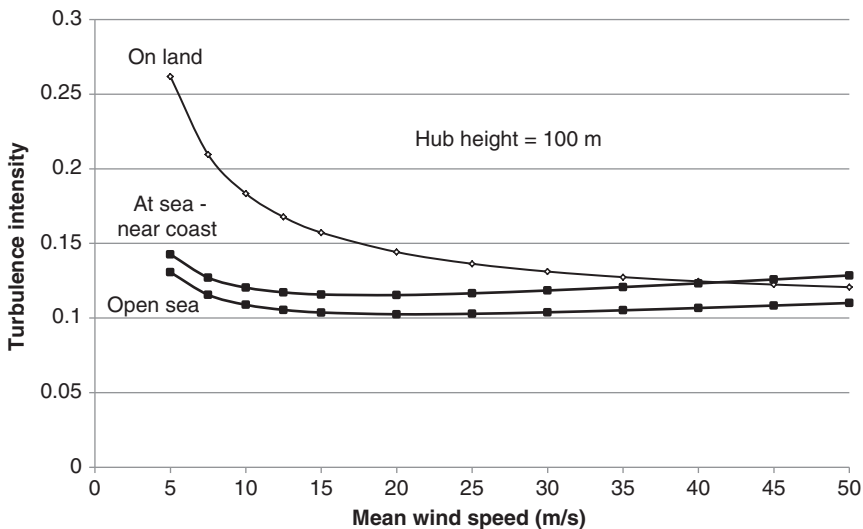


Figure 12.4 Variation of turbulence intensity with wind speed – onshore and offshore.

12.3.3 Marine conditions

The marine conditions relevant to support structure design encompass waves, currents, water level and, where appropriate, scour, seabed movement and sea ice. In the case of the IEC 61400-3-1 operational load cases that have their counterparts in IEC 61400-1 (i.e. all but load case 1.6), normal marine conditions are specified, with severe marine conditions applicable in load case 1.6 and extreme conditions applicable in a number of non-operational load cases.

The wave climate is most accurately described in terms of a stochastic sea state model but, in view of the non-linearity of wave loading models in storm conditions, it is necessary to embed a regular extreme wave in the water-level time history as well, as described in Section 12.3.10. The various sea states defined in IEC 61400-3-1, and the alternative deterministic design waves, are described in succeeding sections, together with details of the co-existent currents and water levels to be considered. Before moving to these, however, the wave spectra commonly employed in stochastic sea state models will be introduced.

12.3.4 Wave spectra

The surface profile of the sea can be considered to be the result of the superposition of a very large number of tiny advancing regular waves of different amplitudes and periods upon one another. This ensemble of waves can, in turn, be described by a frequency spectrum – that is a plot of the spectral density of the square of the deviation of the water surface elevation from mean level against frequency. This spectrum is said to define the sea state, which is usually considered to persist for a period of 3 hours.

The key parameters of the frequency spectrum are the significant wave height, H_s , and the frequency corresponding to the peak spectral density, f_p . The significant wave height is traditionally defined as the average height of the highest one third of waves in a chosen reference period – normally 3 hours – and corresponds to the height of waves that observers will typically report. The area under the spectrum is equal to the variance of the sea surface elevation, σ_η^2 .

The shape of the frequency spectrum varies according to the fetch and the way wind speeds have varied over the fetch area beforehand. The Pierson–Moscowitz (PM) spectrum is a mathematical construct that is considered to provide a good fit to the frequency spectrum of a fully developed sea. In IEC 61400-3, it was specified as

$$S_{\eta\eta}(f) = \frac{5}{16} \frac{H_s^2}{f} \left(\frac{f_p}{f} \right)^4 \exp \left(-\frac{5}{4} \left(\frac{f_p}{f} \right)^4 \right) \quad (12.3)$$

This formulation is based on the assumption that the significant wave height, H_s , is four times the standard deviation of the sea surface elevation, which is correct for a Rayleigh distribution of wave heights. However, although a Rayleigh distribution of wave heights is strictly generated only by a narrow banded frequency spectrum, it is considered to be a reasonable approximation in the case of real wave spectra. In IEC 61400-3-1 reference is made to ISO 19901-1 for wave spectra definitions.

Fully developed sea states only arise if a wind speed is maintained for long enough over a sufficient fetch. In the majority of situations, either the storm duration or the

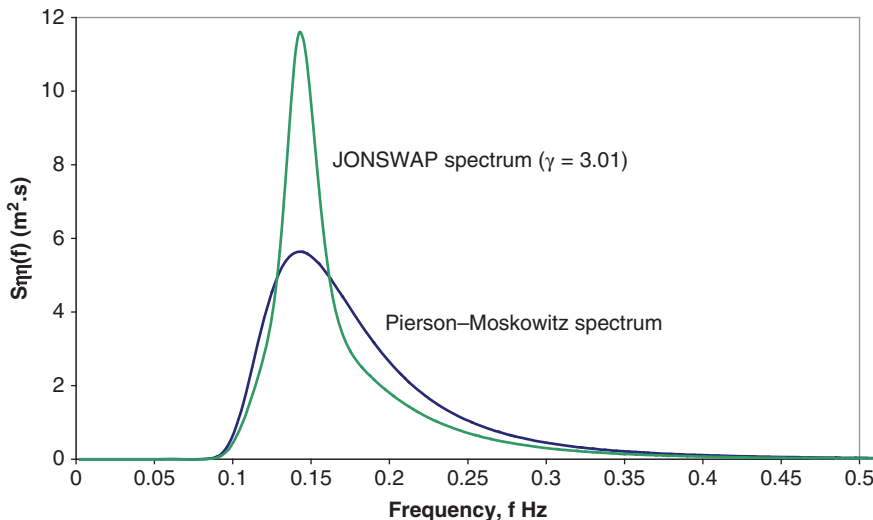


Figure 12.5 Pierson–Moskowitz (PM) and JONSWAP spectra for $H_s = 3\text{ m}$ and $T_p = 7\text{ seconds}$.

fetch or both are too small, with the result that the frequency spectra display a more exaggerated peak than the PM spectrum. The JONSWAP (Joint North Sea Wave Project) spectrum, which was developed from wave measurements near the German island of Sylt, is a variant of the PM spectrum that models this peak enhancement. Essentially the PM spectrum is multiplied by a frequency dependent peak enhancement factor (with a maximum between 1 and 5) and by a normalising factor, which ensures that the area under the JONSWAP spectrum is the same as that under the PM spectrum.

The peak enhancement factor, γ^α , is given in terms of the significant wave height, H_s , measured in metres, the peak period, $T_p = 1/f_p$ seconds, and the frequency, f . $\gamma = \exp\{5.75 - 1.15T_p/H_s^{0.5}\}$ for $T_p/H_s^{0.5}$ in the range 3.6 to 5, $\alpha = \exp\{-0.5(f/f_p - 1)^2/\sigma^2\}$, $\alpha = 0.07$ for $f < f_p$ and $\alpha = 0.09$ for $f > f_p$, and the normalising factor is $1 - 0.287\ln\gamma$. $\gamma = 5$ when $T_p/H_s^{0.5}$ is less than 3.6 and $\gamma = 1$ when $T_p/H_s^{0.5}$ exceeds 5. It is seen that the JONSWAP spectrum is identical to the PM spectrum when $T_p/H_s^{0.5}$ exceeds 5.

The JONSWAP and PM spectra are compared for a significant wave height of 3 m and peak period of 7 seconds in Figure 12.5.

Figure 12.6 shows an example time history of water surface elevation from a simulation utilising the above JONSWAP spectrum.

12.3.5 Ultimate loads: operational load cases and accompanying wave climates

An overview of the IEC 61400-3-1 ultimate load cases for operational loading is given in Table 12.3, which identifies the equivalent onshore load case in IEC 61400-1 in each case.

Normal and abnormal load cases are indicated by the letters N and A, respectively. See Table 5.2 for the applicable load factors.

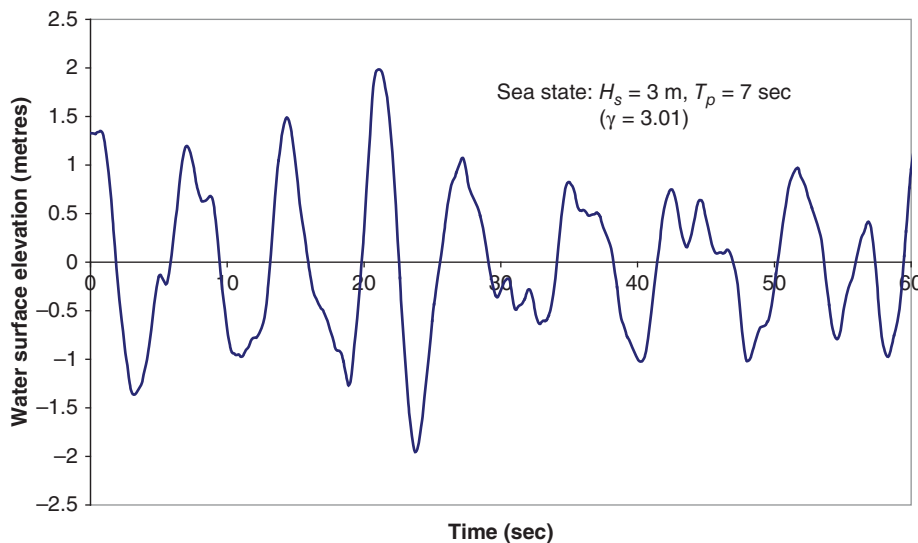


Figure 12.6 Simulated water surface elevation time history based on JONSWAP spectrum.

The wind conditions denoted by the acronyms in the table are as follows:

NTM	Normal turbulence model
NWP	Normal wind profile (following a power law with exponent of 0.14 instead of the value of 0.2 onshore), without turbulence
ETM	Extreme turbulence model
ECD	Extreme coherent gust with direction change
EWS	Extreme wind shear
EOG	Extreme operating gust
EDC	Extreme direction change

A description of each wind condition is given in Sections 5.3 and 5.4.1.

The wave conditions are specified as ‘normal sea state’ in all load cases, apart from load case 1.6, for which the ‘severe sea state’ applies. These two sea states are described below.

Normal sea state

IEC 61400-3-1 defines normal sea states in terms of a stochastic sea state model based on either the PM or JONSWAP spectrum as appropriate. For each normal sea state, the significant wave height is to be taken as the expected value at the mean wind speed under consideration, based on analysis of the site-specific metocean database. It is normal to plot the metocean data as a wind-wave scatter diagram, which can be used to derive the

Table 12.3 Ultimate load cases during operation.

M/c state	Load case no.	Equivalent load case on land	Wind conditions range	Wind speed	Wave conditions	Water level	Grid status; fault type	Load case type
Power production	1.1	1.1	NTM	Cut-in – cut-out	Normal sea state i.e. $H_s = E[H_s U]$ Extrapolations required	Mean	None	N
	1.3	1.3	ETM	Cut-in – cut-out	Normal sea state	Mean	None	N
	1.4	1.4	ECD	Rated $\pm 2 \text{ m/s}$	Normal sea state	Mean	None	N
	1.5	1.5	EWS	Cut-in – cut-out	Normal sea state	Mean	None	N
	1.6	None	NTM	Cut-in – cut-out	Severe sea state – 50 yr return H_s conditioned on chosen wind speed	Normal range	None	N
Power production with occurrence of fault	2.1	2.1	NTM	Cut-in – cut-out	Normal sea state	Mean	Control system or grid loss	N
	2.2	2.2	NTM	Cut-in – cut-out	Normal sea state	Mean	Abnormal control system fault	A
	2.3	2.3	EOG	Rated $\pm 2 \text{ m/s}$	Normal sea state	Mean	External or internal electrical fault	A
	2.5	2.5	NWP	Cut-in – Cut-out	Normal sea state	Mean	Low voltage ride through	N
Start-up	3.2	3.2	EOG	Cut-in, rated, cut-out	Normal sea state	Mean	None	N
	3.3	3.3	EDC	Cut-in, rated, cut-out	Normal sea state	Mean	None	N
Shut-down Emergency shut-down	4.2	4.2	EOG	Rated, cut-out	Normal sea state	Mean	None	N
	5.1	5.1	NTM	Rated, cut-out	Normal sea state	Mean	None	N

expected significant wave height at each wind speed. Typically, a two-dimensional (2-D) wind-wave scatter diagram is presented in the form of a table recording the percentage of time that the mean wind speed and significant wave height lie within different bins in a 2-D array. In a three-dimensional (3-D) scatter diagram, the frequency of occurrence of different peak spectral periods, T_p , or mean zero-crossing periods, T_z , is recorded also. The mean zero-crossing period can be converted to the peak spectral period by means of the relation

$$T_p = T_z \sqrt{\frac{11 + \gamma}{5 + \gamma}}$$

with gamma defined as in the preceding section.

Data from a 2-D scatter diagram for a site designated NL-1 about 15 km off Ijmuiden on the Dutch Coast is illustrated in Figure 12.7. This shows the frequency of occurrence of different mean wind speeds for each significant wave height at a 0.5 m interval, with reference to a different horizontal axis in each case.

Account should be taken of the range of peak spectral periods, T_p , encountered and care taken to investigate values of T_p close to the support structure natural frequency where appropriate. Marine conditions are essentially the same for all ultimate operational load cases except load case 1.6, and consist of the normal sea state in conjunction with ‘normal’ currents and water at mean sea level. ‘Normal’ currents comprise the current induced by the wind, estimated at 1% of the hourly mean wind speed at the surface, combined with the tidal current, taken as the mean tidal current speed.

Severe sea state

The IEC 61400-3-1 severe sea states, which, like the normal sea states, occur during machine operation (load case 1.6), differ from the normal sea states only in regard to the significant wave height. For each mean wind speed, \bar{U} , the significant wave height, $H_{s,SSS}(\bar{U})$ is to be taken at a value such that its recurrence period in combination with the mean wind speed is 50 years, based on extrapolation of the site-specific metocean database. The sub-section ‘Environmental Contours’ at the end of this section outlines how this extrapolation may be carried out. As with the normal sea state, the most adverse anticipated value of the peak spectral period should be considered.

The other marine conditions for load case 1.6, consist of ‘normal’ currents and water at any level within the ‘normal water-level range’, which may be taken as the range of astronomic tides.

Embedded extreme regular wave

The IEC 61400-3-1 load case 1.6 description requires the inclusion of an extreme regular wave, derived from the significant wave height for the severe sea state (above) at each mean wind speed, in each simulation. The height of the regular wave is the expected height of the extreme wave in the applicable severe sea state. If the wave heights are Rayleigh distributed, then the probability of an individual wave height exceeding H is

$$P(h > H) = \exp\left(-0.5\left(\frac{H/2}{\sigma_\eta}\right)^2\right) = \exp\left(-2\left(\frac{H}{H_s}\right)^2\right) \quad (12.4)$$

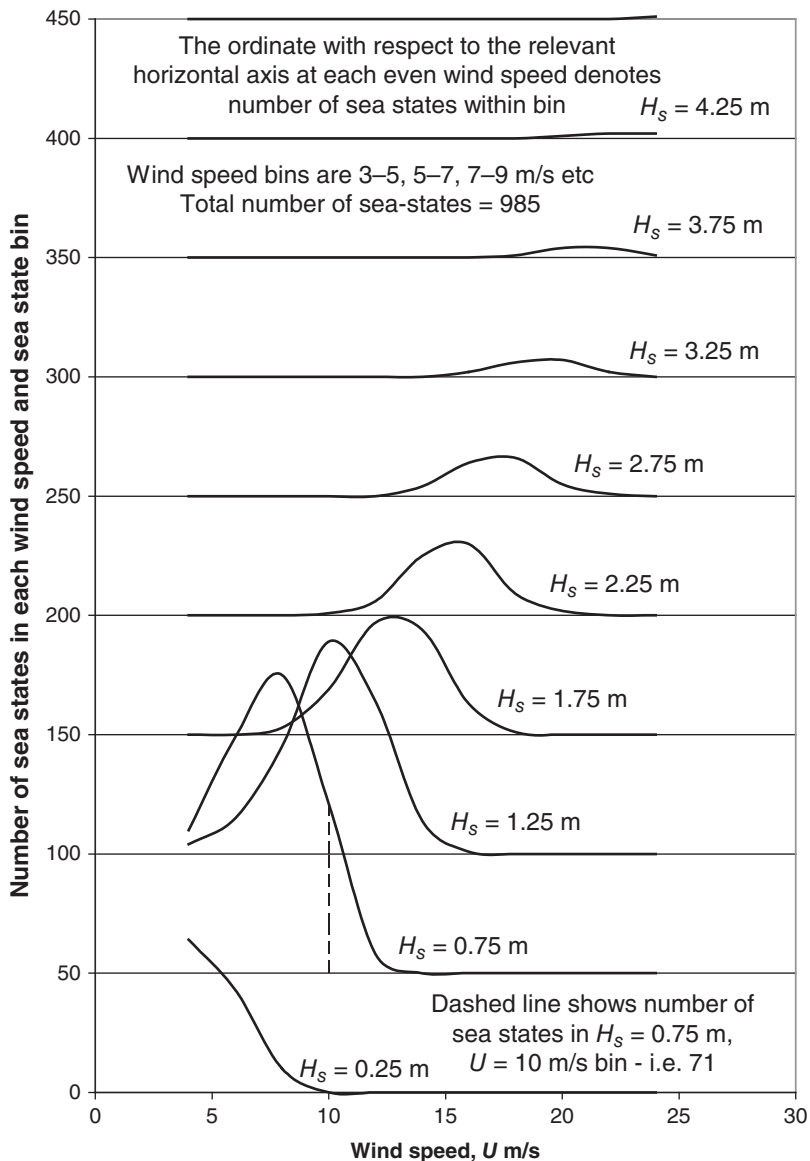


Figure 12.7 Data from wind-wave scatter diagram for site NL-1.

and the wave height likely to be exceeded by the highest of N waves is $H_s\sqrt{0.5 \ln N}$. The expected magnitude of the extreme wave is slightly higher than this at $H_s(\sqrt{0.5 \ln N} + 0.2886/\sqrt{2 \ln N})$.

For a sea state with mean wave period of 10.8 seconds, there will be 1000 waves in the 3 hour reference period, so the extreme wave is likely to exceed $1.86H_s$ and its expected magnitude is $1.94H_s$. However, Annex F of IEC 61400-3-1 permits the height of the extreme wave for each severe sea state to be calculated as $H_{SWH}(\bar{U}) = 1.86H_{s,SSS}(\bar{U})$.

The wave period to be adopted is the value within the range $11.1\sqrt{H_{s,SSS}(\bar{U})/g}$ to $14.3\sqrt{H_{s,SSS}(\bar{U})/g}$ that results in the highest wave loading. A minimum of six simulations of 1 hour duration are required.

Environmental contours

One of the load cases representing power production, load case 1.6, is concerned with 50 year return combinations of mean wind speed, \bar{U} , and significant wave height, H_s , which, taken together, can be considered as forming an environmental contour in \bar{U} , H_s space. A method for deriving such a contour using the inverse first order reliability method (IFORM) is set out in Annex F of IEC 61400-3-1 and is described in this section.

The probability that a certain combination of mean wind speed and significant wave height will not be exceeded may be written as

$$F(H_s|\bar{U}).F(\bar{U})$$

where $F(\bar{U})$ is the cumulative distribution function (CDF) of the mean wind speed, and $F(H_s|\bar{U})$ is the CDF of the significant wave height conditioned on the mean wind speed.

For the 50 year return combination, this probability must equate to $(1 - 1/N)$, where N is the number of sea states in 50 years – i.e. $50(365)24/3 = 146\,000$ for a 3 hour sea state duration.

The environmental contour may be derived by utilising a transformation from mean wind speed and significant wave height to two uncorrelated normally distributed variables, U_1 and U_2 , so that

$$F(\bar{U}) = \Phi(U_1) \text{ and } F(H_s|\bar{U}) = \Phi(U_2) \quad (12.5)$$

where

$$\Phi(U) = \frac{1}{\sqrt{2\pi}} \int_{-\infty}^U \exp[-u^2/2] du \quad (12.6)$$

The joint probability density function (PDF) of the normally distributed variables U_1 and U_2 is

$$p(U_1, U_2) = \frac{1}{\sqrt{2\pi}} \exp\left[-\frac{U_1^2}{2}\right] \cdot \frac{1}{\sqrt{2\pi}} \exp\left[-\frac{U_2^2}{2}\right] = \frac{1}{2\pi} \exp\left[-\frac{U_1^2 + U_2^2}{2}\right] \quad (12.7)$$

so the joint PDF is axisymmetric about the origin and points in U_1 , U_2 space lying at the same radius from the origin have the same probability density. The joint PDF is illustrated in Figure 12.8.

Clearly the N year return wind speed, irrespective of significant wave height, is that for which $F(\bar{U}) = \Phi(U_1) = 1 - 1/N$, i.e. for which $U_1 = \Phi^{-1}(1 - 1/N)$. In U_1 , U_2 space, the probability that the wind exceeds the N year return value is represented by the probability that the point U_1, U_2 lies to the right of the line ABC in Figure 12.9, with β set equal to $\Phi^{-1}(1 - 1/N)$.

Given that the volume under the joint probability density function surface (Figure 12.9) lying beyond any tangent to the circle radius β is the same, it follows that the probability that a point U_1, U_2 lies beyond the tangent DEF is the same as the

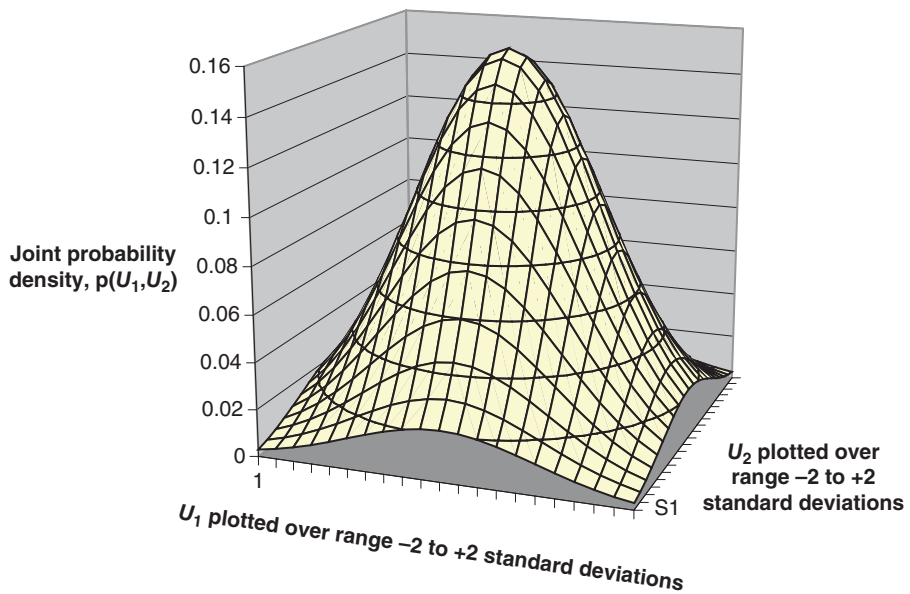


Figure 12.8 Joint probability density of two uncorrelated normally distributed variables.

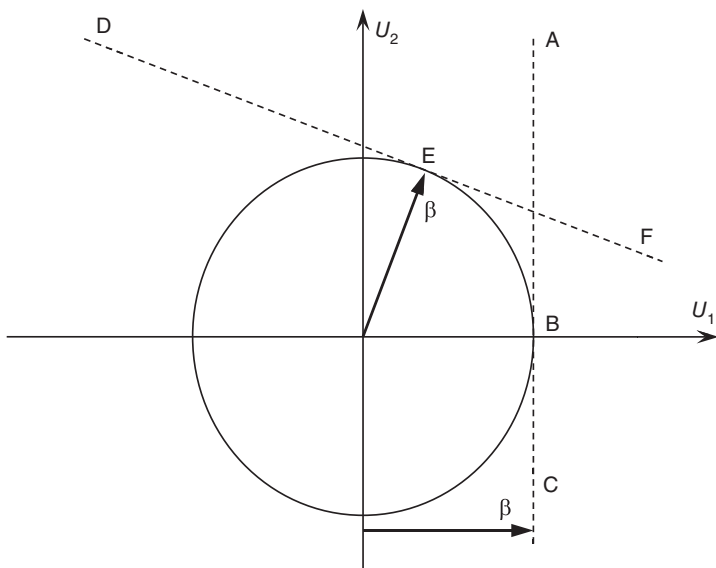


Figure 12.9 Circle of radius β in U_1, U_2 space, representing environmental contour.

probability that a point U_1, U_2 lies beyond the tangent ABC – i.e. $1/N$. Thus the circle radius β is the internal envelope of a family of tangents such that the probability of U_1, U_2 lying outside each one is $1/N$. In this sense, it represents the N year environmental contour transformed into 2-D normal space. Note that the portions of the circle for which U_1 or U_2 is negative represent N year return *minimum* values in each case.

A procedure for the practical application of the method to metocean data in the form of a mean wind speed/significant wave height scatter diagram is as follows:

1. (a) Using the scatter diagram, calculate the non-exceedance probability, $F(\bar{U})$, associated with the mean wind speed, \bar{U} , of a particular wind speed bin.
 (b) Calculate the corresponding value of the normally distributed variable $U_1 = \Phi^{-1}(F(\bar{U}))$.
 (c) Calculate $U_2 = \sqrt{\beta^2 - U_1^2}$. (The negative root corresponds to the *minimum* value of H_s .)
 (d) Calculate the 50 year return significant wave height conditional on \bar{U} as

$$H_{s,SSS}(\bar{U}) = \bar{H}_s(\bar{U}) + U_2 \sigma_{H_s}(\bar{U})$$

where $\bar{H}_s(\bar{U})$ and $\sigma_{H_s}(\bar{U})$ are the mean and standard deviation of the significant wave height conditional on \bar{U} extracted from the scatter diagram, respectively.

2. Repeat step 1 for the other wind speed bins.
3. Plot environmental contour linking the points $H_{s,SSS}(\bar{U}), \bar{U}$.

Note that in the above procedure, it is assumed that the significant wave heights conditional on \bar{U} are *normally distributed*, which may not necessarily be consistent with the data. It is more conservative to assume that the significant wave heights are log-normally distributed. Whichever model is adopted, goodness of fit tests – visual and/or statistical – should be carried out to confirm its suitability.

An example of 50 year return environmental contours derived from the scatter diagram for the NL-1 site (see Figure 12.7) is given in Figure 12.10. One contour is based on a normal distribution of significant wave heights conditional on \bar{U} and the other is based on a log-normal distribution.

12.3.6 Ultimate loads: non-operational load cases and accompanying wave climates

An overview of the IEC 61400-3-1 ultimate load cases for non-operational loading is given in Table 12.4, which identifies the equivalent onshore load case in IEC 61400-1 in each case. The design mean wind speed, U_{ref} , is the 50 year return 10 minute mean as for onshore turbines. Note that the IEC 61400-1 option of using the steady extreme wind speed model is excluded in IEC 61400-3-1, as this specifies the use of the turbulent wind model.

The wind and wave/sea state return periods are 50 years for ‘fault-free’ load cases 6.1 and 6.2 and 1 year for load cases 6.3 and 7.1, which involve extreme yaw and a machine fault, respectively. Note that the grid loss load case 6.2 can include a yaw error of up to 180° , unless six hours back-up power supply is provided for the control and yaw system.

Consideration of the effect of possible mis-alignment between wind and wave directions is required for all of the non-operational load cases.

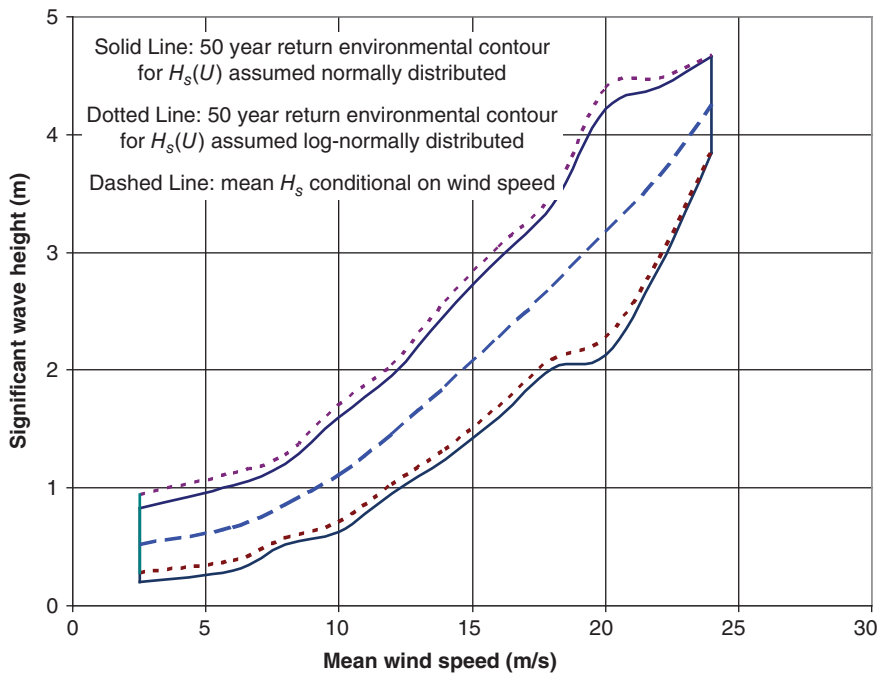


Figure 12.10 Fifty year significant wave height against mean wind speed environmental contours derived from site NL-1 scatter diagram.

Extreme sea state

IEC 61400-3-1 defines extreme sea states in terms of a stochastic sea state model based on either the PM or JONSWAP spectrum as appropriate, with the significant wave height equal to the 50 or 1 year return value, depending on the load case. These may be determined by extrapolation based on the tail of the long-term distribution of significant wave heights. As with the normal sea state, the most adverse anticipated value of the peak spectral period is to be considered.

The other marine conditions consist of extreme currents (including currents generated by tides and storm surges) and extreme water-level range, such that the global environmental loading has a return period of 50 or 1 year according to the load case. However, to avoid extensive statistical analysis, it may be preferable to use the 50 or 1 year return values for the individual parameter values. The currents generated by tides and storm surges vary with depth according to a 1/7 power law – i.e. as follows: $U_c(z) = U_c(0)((z + d)/d)^{1/7}$, where z and d are defined in Figure 12.12.

Embedded extreme regular wave

IEC 61400-3-1 requires the inclusion of an extreme regular wave in the form of a ‘constrained wave’ (see Section 12.3.10) in each 1 hour simulation. At least six 1-hour simulations are required for each extreme sea state load case. For deep water, it may be assumed that the height of the extreme wave is 1.86 times the significant wave height.

Table 12.4 Ultimate non-operational load cases.

M/c state	Load case no.	Equiv load case on land	Wind conditions	Wind speed	Wave and current conditions	Water level	Grid, yaw, and fault status	Load case type
Parked (standing still or idling)	6.1	6.1	50 yr EWM turbulent	U_{ref}	50 yr extreme sea state $H_s = H_{s50}$ and currents	Extreme range	None	N
	6.2	6.2	50 yr EWM turbulent	U_{ref}	50 yr extreme sea state $H_s = H_{s50}$ and currents	Extreme range	Grid loss, up to 180° yaw	A
	6.3	6.3	1 yr EWM turbulent	$0.8 \times U_{ref}$	1 yr extreme sea state $H_s = H_{s1}$ and currents	Normal range	Extreme yaw (20°)	N
Parked with fault condition	7.1	7.1	1 yr EWM turbulent	$0.8 \times U_{ref}$	1 yr extreme sea state $H_s = H_{s1}$ and currents	Normal range	Fault condition	A

EWM stands for extreme wind speed model.

Modification of wave climate in shallow water

Waves begin to break when the wave height reaches 78% of the mean water depth, so the upper tail of the Rayleigh distribution of wave heights becomes curtailed as deep sea waves advance into shallower water, leading to conservatism in the use of the $1.86H_s$ formula for the wave height exceeded by the largest of 1000 waves. Battjes and Groenendijk (2000) have developed a model for calculating the modified distribution of wave heights for waves propagating over a uniformly sloping seabed – see Annex B of IEC-61400-3-1. The model depends on the availability of measured site-specific wave data and is applicable provided the wave direction is within 30° of the direction of steepest seabed slope.

12.3.7 Fatigue loads

An overview of the IEC 61400-3 fatigue load cases – operational and non-operational – is given in Table 12.5, which identifies the equivalent onshore load case in IEC 61400-1 in each case.

The wind conditions and water levels denoted by the acronyms in the table are as follows:

NTM	Normal turbulence model
NWP	Normal wind profile (following a power law with exponent of 0.14), without turbulence
NSS	Normal sea state
NWLR	Normal water-level range
MSL	Mean sea level

Sea currents are ignored.

A range of significant wave heights and wave periods should be considered at each wind speed, with the duration of each combination of wind speed and sea state extracted from a site specific 3-D scatter diagram. In particular T_p values corresponding to the natural frequency of the support structure should be investigated. However, it is preferable to avoid a very large number of simulations, so it is advantageous to lump load cases together if possible. The errors due to coarsening the wave height and wave period bins can be reduced if the ‘damage equivalent mean wave height’ and ‘damage equivalent mean period’ are calculated for each bin. The former is determined as

$$H_s = \left(\frac{1}{N} \sum_{i=1}^N H_{s_i}^m \right)^{\frac{1}{m}}$$

where m is the inverse slope of the S-N curve, and the latter is taken as the reciprocal of the mean wave frequency. In a case study, Evans (2004) showed that, for a wind speed bin width of 2 m/s, the error in damage equivalent load resulting from a move from 0.5 m wave height and 0.5 second wave period bin widths to a single wave height/wave period bin with this approach was only a few per cent.

IEC 61400-3-1 specifies two fatigue load cases for machines that are parked or idling – one without and the other with a fault condition. The latter is absent from IEC

Table 12.5 Fatigue load cases.

M/c state	Load case no.	Equivalent load case on land	Wind conditions	Wind speed	Wave conditions	Water level	Grid, yaw, and fault status
Power production	1.2	1.2	NTM	Cut-in – cut-out	NSS joint prob. distribution of H_s, T_p, \bar{U} i.e. $H_s = E[H_s \bar{U}]$	NWLR or $\geq MSL$	None
Power production with fault	2.4	2.4	NTM	Cut-in – cut-out	NSS, i.e. $H_s = E[H_s \bar{U}]$	NWLR or $\geq MSL$	Fault condition
Start-up	3.1	3.1	NWP	Cut-in – cut-out	NSS, i.e. $H_s = E[H_s \bar{U}]$	NWLR or $\geq MSL$	None
Normal shut-down	4.1	4.1	NWP	Cut-in – cut-out	NSS, i.e. $H_s = E[H_s \bar{U}]$	NWLR or $\geq MSL$	None
Parked	6.4	6.4	NTM	$< 0.7 U_{ref}$	NSS joint prob. distribution of H_s, T_p, \bar{U}	NWLR or $\geq MSL$	None
Parked with fault condition	7.2	None	NTM	$<$ Cut-out	NSS joint prob. distribution of H_s, T_p, \bar{U}	NWLR or $\geq MSL$	Fault condition

61400-1 but is considered necessary offshore, because of the potentially much longer machine downtimes and the large reduction in aerodynamic damping when the turbine is shut down.

The maximum wind speed to be considered for fatigue loading on a parked turbine in the absence of a fault (DLC 6.4) is $0.7U_{\text{ref}}$ – a value likely to be exceeded for half an hour per year. However, for fatigue loading on a parked turbine with a fault condition (DLC 7.2), the upper wind speed to be considered is the cut-out speed, which is likely to be exceeded for the order of only 60 hours per year. No guidance is given on the likely total turbine downtime corresponding to DLC 7.2 and clearly this needs to be predicted with great care.

12.3.8 Wave theories

Several wave theories exist to describe the fluid motion within regular, periodic, (2-D) waves, but only three are routinely used for the calculation of loads on offshore structures – Airy, Stokes, and Dean’s stream function theories.

Airy wave theory is linear and therefore allows the water particle kinematics of a real sea state, consisting of a multitude of small waves of varying frequencies and wave lengths, to be modelled by superposition. However, as wave height increases in relation to water depth or wave-length, Airy theory becomes less accurate and non-linear theories such as Stokes and Dean’s stream function have to be employed instead. However, because of their non-linearity, these theories can only be applied to single, regular wave trains. Figure 12.11 shows which theories are applicable for different relationships between wave height, water depth, and wave period.

It is apparent from Figure 12.11 that Dean’s stream function theory can be used for all but near breaking waves. In view of this, and the relative complexity of Stokes wave theory, the latter is not discussed further and this section concentrates on the other two theories.

Airy wave theory

The fluid motion within regular, periodic two-dimensional (2-D) waves must satisfy the Laplace equation, $\nabla^2\phi(x, z, t) = 0$, where ϕ is the velocity potential, defined so that horizontal and vertical particle velocities are given by $u = -\partial\phi/\partial x$ and $w = -\partial\phi/\partial z$ respectively. x is the horizontal coordinate parallel to the direction of wave motion and z is the vertical coordinate measured upwards with respect to mean water level, as shown in Figure 12.12. [Note that the convention adopted here for the definition of velocity potential differs from that in Chapter 4, because of the inclusion of the minus signs.]

The fluid motion must also satisfy five boundary conditions as follows:

1. Zero flow vertical particle velocity, w , at the seabed, which is assumed horizontal.
2. Zero flow perpendicular to the free surface.
3. The unsteady form of the Bernoulli equation at the free surface.
4. The periodic boundary condition in time – $\phi(x, z, t) = \phi(x, z, t + T)$, where T is the wave period.

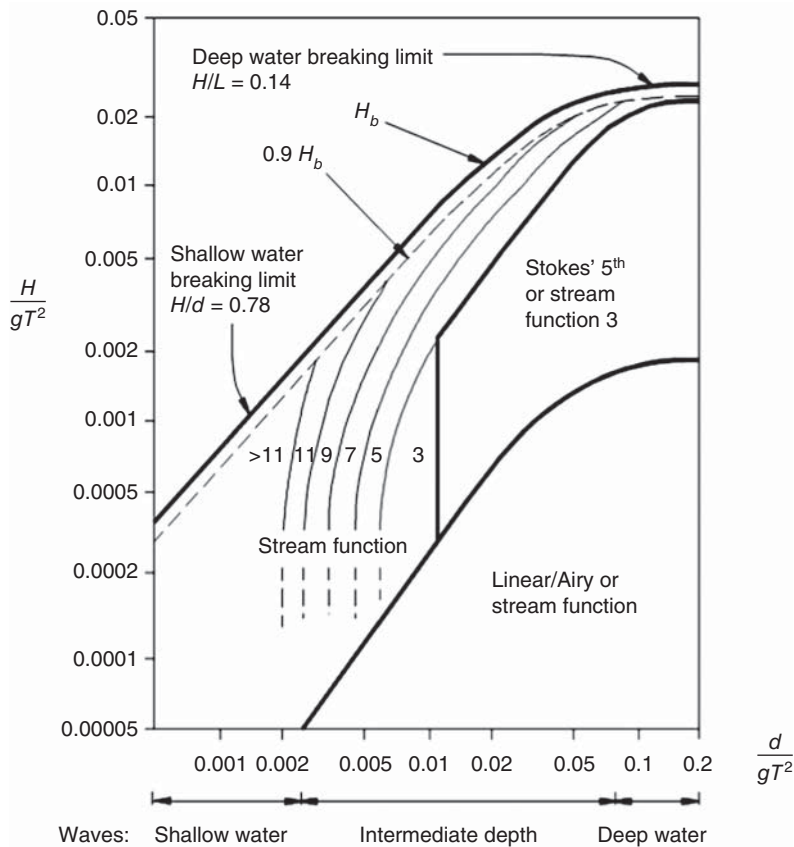


Figure 12.11 Regular wave theory selection diagram: log scales (Barltrop et al. 1990). Source: Reproduced under the Open Government License v1.0.

5. The periodic boundary condition in space – $\phi(x, z, t) = \phi(x + L, z, t)$, where L is the wave length.

Condition 2 is expressed as

$$w = \frac{\partial \eta}{\partial t} + u \frac{\partial \eta}{\partial x} \quad (12.8)$$

where η is the water surface elevation above the mean and u is the horizontal water particle velocity. The atmospheric pressure acting on the free surface of the water is treated as constant, so the unsteady form of the Bernoulli equation in condition 3 becomes

$$-\frac{\partial \phi}{\partial t} + \frac{u^2 + w^2}{2} + gz = C(t) \quad (12.9)$$

According to Airy wave theory, the velocity potential at any point in the water is

$$\phi = -\frac{Hg}{2\omega} \frac{\cosh k(z+d)}{\cosh kd} \sin(kx - \omega t) \quad (12.10)$$

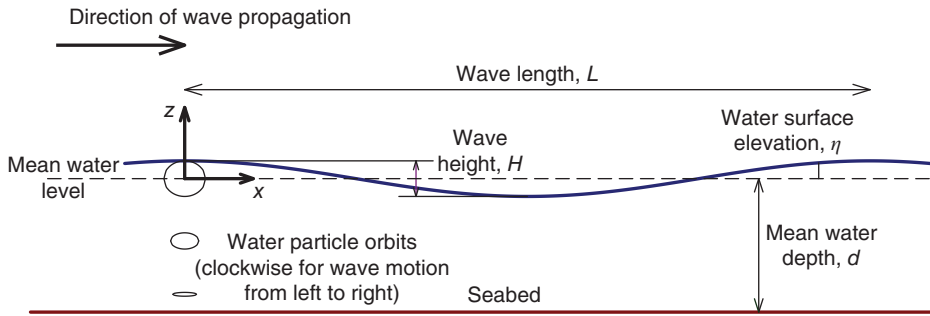


Figure 12.12 Parameter definitions and coordinates for regular, periodic, two-dimensional waves.

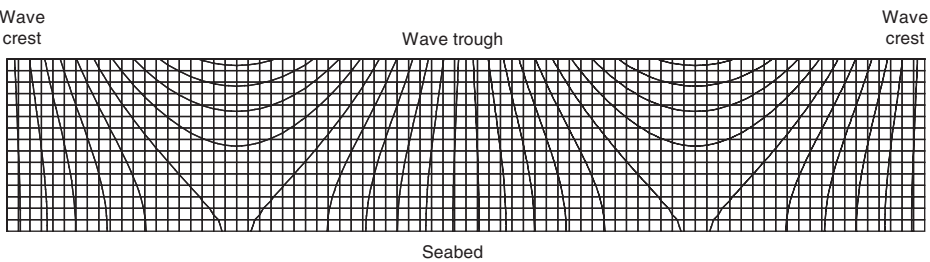


Figure 12.13 Velocity potential contours for Airy wave theory.

where H is the wave height, d is the mean water depth, $k = 2\pi/L$ and $\omega = 2\pi/T$. Figure 12.13 shows the corresponding velocity potential contours over a full wave length for the case of a 15 m water depth and 80 m wave length. Note that the contours are shown as extending only up to still water level, as Airy wave theory only approaches 100% accuracy as the wave height becomes vanishingly small. Assuming the waves are moving from left to right, the maximum velocity potential is at the water surface at the right hand quarter point.

The equation for velocity potential satisfies conditions (1), (4), and (5) above exactly but only satisfies 'linearised' versions of Eqs. (12.8, 12.9).

The 'linearised' version of Eq. (12.9) is obtained by expanding the left hand side of the equation with respect to the value at $z = 0$ using a truncated Taylor's series to give

$$\begin{aligned} \left(-\frac{\partial \phi}{\partial t} + \frac{u^2 + w^2}{2} + gz \right)_{z=\eta} &= \left(-\frac{\partial \phi}{\partial t} + \frac{u^2 + w^2}{2} + gz \right)_{z=0} \\ + \eta \left(-\frac{\partial^2 \phi}{\partial t \partial z} + \frac{\partial}{\partial z} \left(\frac{u^2 + w^2}{2} \right) + g \right)_{z=0} + \dots &= C(t) \end{aligned} \quad (12.11)$$

Then, assuming all first order terms are small, all second order terms are very small, and can be neglected, giving

$$\left(-\frac{\partial \phi}{\partial t} \right)_{z=0} + \eta g = C(t) \quad \text{or} \quad \eta = \frac{1}{g} \left(\frac{\partial \phi}{\partial t} \right)_{z=0} + \frac{1}{g} C(t) \quad (12.12)$$

Substituting Eq. (12.10) in Eq. (12.12) and noting that the spatial and temporal means of the water surface elevation are defined as zero yields $C(t) = 0$ and

$$\eta = \frac{H}{2} \cos(kx - \omega t) \quad (12.13)$$

Application of a similar procedure to Eq. (12.8) yields $w = \partial\eta/\partial t$ at $z = 0$, and substitution of

$$w = -\left(\frac{\partial\phi}{\partial z}\right)_{z=0} = \frac{Hgk}{2\omega} \frac{\sinh kd}{\cosh kd} \sin(kx - \omega t) \quad (12.14)$$

and $\left(\frac{\partial\eta}{\partial t}\right)_{z=0} = \frac{H}{2}\omega \sin(kx - \omega t)$ results in

$$L = \frac{gT^2}{2\pi} \tanh kd \quad (12.15)$$

The horizontal and vertical particle velocities and accelerations at any depth, u , \dot{u} , w , and \dot{w} are given by

$$u = -\left(\frac{\partial\phi}{\partial x}\right) = \frac{Hgk}{2\omega} \frac{\cosh k(z+d)}{\cosh kd} \cos(kx - \omega t) = \frac{H\omega}{2} \frac{\cosh k(z+d)}{\sinh kd} \cos(kx - \omega t) \quad (12.16)$$

$$\dot{u} = \left(\frac{\partial u}{\partial t}\right) = \frac{Hgk}{2} \frac{\cosh k(z+d)}{\cosh kd} \sin(kx - \omega t) = \frac{H\omega^2}{2} \frac{\cosh k(z+d)}{\sinh kd} \sin(kx - \omega t) \quad (12.16)$$

$$w = -\left(\frac{\partial\phi}{\partial z}\right) = \frac{Hgk}{2\omega} \frac{\sinh k(z+d)}{\cosh kd} \sin(kx - \omega t) = \frac{H\omega}{2} \frac{\sinh k(z+d)}{\sinh kd} \sin(kx - \omega t) \quad (12.17)$$

$$\dot{w} = \left(\frac{\partial w}{\partial t}\right) = -\frac{Hgk}{2} \frac{\sinh k(z+d)}{\cosh kd} \cos(kx - \omega t) = -\frac{H\omega^2}{2} \frac{\sinh k(z+d)}{\sinh kd} \cos(kx - \omega t) \quad (12.17)$$

The particle displacements can be obtained by integrating the above expressions. The water particles follow elliptical orbits with the major axis horizontal, as shown in Figure 12.12. This shows the wave position at time $t = 0$.

Figure 12.14 shows the accuracy of Airy wave theory in predicting the horizontal particle velocity at the wave crest by comparison with the more accurate Dean/Stokes 5th theories for different H/gT^2 and d/gT^2 ratios. This figure is taken from *Dynamics of Fixed Marine Structures* by Barltrop and Adams (1991), which contains similar figures applicable to the prediction accuracy for other parameters.

Dean's stream function theory

Dean's stream function theory (Dean and Dalrymple 1984) is effectively an extension of Airy wave theory achieved by the addition of a series of harmonic terms to the expression for velocity potential, which enable the theory to satisfy the boundary conditions at the free surface [Eqs. (12.8, 12.9)] without the need for 'linearisation'. However, rather than use the velocity potential, the theory is developed with reference to the parameter known as the *stream function*, which is now introduced.

The paths followed by water particles within the waves are termed *streamlines*, along each of which the *stream function* parameter has a constant value. The stream function

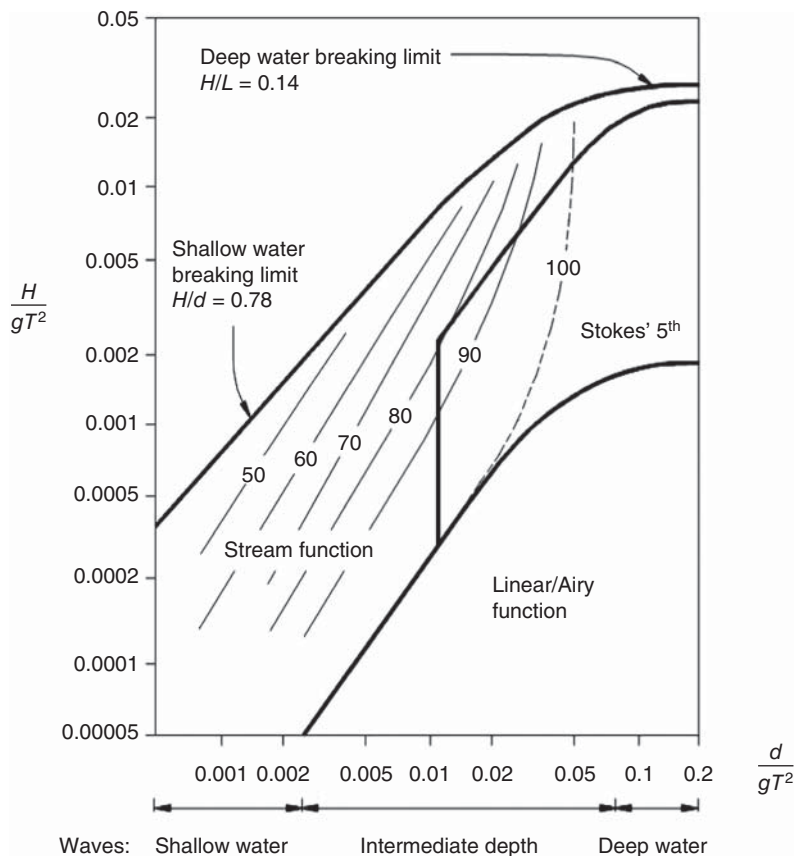


Figure 12.14 Horizontal particle velocity at the wave crest: Airy theory as % of theory shown in Figure 12.12 (Barltrop et al. 1990). Source: Reproduced under the Open Government License v1.0.

is defined such that its gradient perpendicular to the streamlines is proportional to the local particle velocity, so that

$$u = -\frac{\partial \psi}{\partial z} \text{ and } w = \frac{\partial \psi}{\partial x} \quad (12.18)$$

For Airy wave theory, the stream function is

$$\psi = -\frac{Hg}{2\omega} \frac{\sinh k(z + d)}{\cosh kd} \cos(kx - \omega t) \quad (12.19)$$

The corresponding streamlines are shown over a full wave length in Figure 12.15, for the case of a 15 m water depth and 80 m wave length.

The streamlines in Eq. (12.19) and Figure 12.15 are defined with respect to a fixed frame of reference. However, it is perfectly possible to define them with respect to a *moving* frame of reference that travels at the same speed as the wave crests and troughs – i.e. with

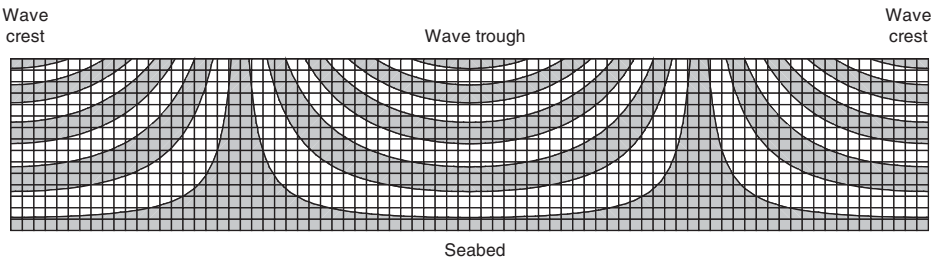


Figure 12.15 Streamlines for Airy wave theory with the frame of reference fixed. Note that, as with the figure illustrating the velocity potential contours, the streamlines are shown as only extending up to still water level, because Airy wave theory only approaches 100% accuracy as the wave height becomes vanishingly small.

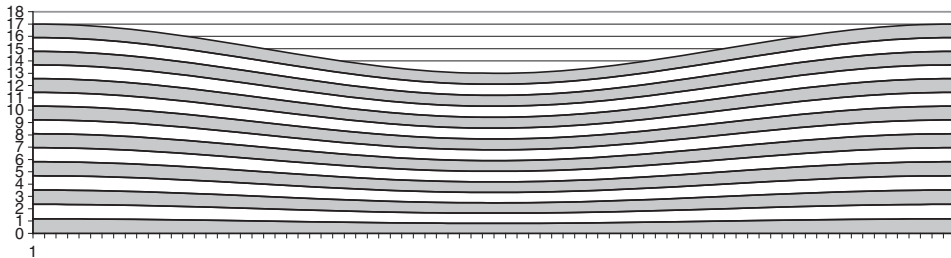


Figure 12.16 Streamlines for Airy wave theory with frame of reference moving with the wave train.

celerity $C = L/T$. Then the Airy wave theory stream function becomes

$$\bar{\psi} = Cz - \frac{Hg}{2\omega} \frac{\sinh k(z+d)}{\cosh kd} \cos(kx) \quad (12.20)$$

which has the advantage of being invariant with time. The streamlines corresponding to the moving frame of reference are shown over a full wave length in Figure 12.16, for the same case as above. However, for clarity a relatively large wave height of 4 m is chosen, for which the Airy solution is inaccurate.

Dean's stream function is defined with respect to the same moving frame of reference, and consists of a harmonic series of terms as follows:

$$\bar{\psi} = Cz + \sum_{n=1}^N X_n \sinh nk(z+d) \cos(nkx) \quad (12.21)$$

For $N = 1$, Eq. (12.21) equates to Eq. (12.20), so

$$X_1 = -\frac{Hg}{2\omega \cosh kd} \quad (12.22)$$

The corresponding water particle velocities are

$$u = -\frac{\partial \bar{\psi}}{\partial z} = -C - \sum_{n=1}^N nkX_n \cosh nk(z+d) \cos(nkx) \quad (12.23)$$

$$w = \frac{\partial \bar{\psi}}{\partial x} = - \sum_{n=1}^N nkX_n \sinh nk(z+d) \sin(nkx) \quad (12.24)$$

The number of terms, N , required increases as the height of the waves approaches the breaking limit. A solution using N terms is described as N th order. Substituting $z = \eta$ at the free surface in Eq. (12.21) gives

$$\eta = \frac{\bar{\psi}_0}{C} - \frac{1}{C} \sum_{n=1}^N X_n \sinh nk(\eta + d) \cos(nkx) \quad (12.25)$$

Given that the spatial average of the water surface elevation, η , is zero by definition, we have

$$\bar{\psi}_0 = \frac{1}{L} \int_0^L \sum_{n=1}^N X_n \sinh nk(\eta + d) \cos(nkx) dx \quad (12.26)$$

(The expression on the right hand side of this equation is non-zero by virtue of the variable weighting of $\cos(nkx)$ by the hyperbolic factor, $\sinh nk(\eta + d)$.)

The boundary conditions to be satisfied are as follows:

1. Zero flow vertical particle velocity, w , at the seabed, which is assumed horizontal.
2. Zero flow perpendicular to the free surface.
3. The steady form of the Bernoulli equation at the free surface.
4. The periodic boundary condition in space – $\bar{\psi}(x, z) = \bar{\psi}(x + L, z)$, where L is the wave length.

Equations (12.24) and (12.21) satisfy conditions 1 and 4, respectively, while condition 2 is satisfied because the free surface is a streamline.

The steady form of the Bernoulli equation at the free surface (condition 3) is

$$\left(\frac{u^2 + w^2}{2} \right) + g\eta = K \quad (12.27)$$

If the wave length, the mean water depth and the wave height, H , are the known quantities, the solution to the problem resolves itself into finding of a set of values of the X_n coefficients combined with a value of celerity, C , such that Eq. (12.27) is satisfied as closely as possible at all points along the wave profile subject to the condition $\eta_{\max} - \eta_{\min} = H$.

The following steps enable a low order solution to be obtained on a spreadsheet:

1. Set $X_2, X_3 \dots X_N$ all equal to zero.
2. Set $C = \sqrt{\frac{g}{k} \tanh kd}$, the value according to Airy wave theory.

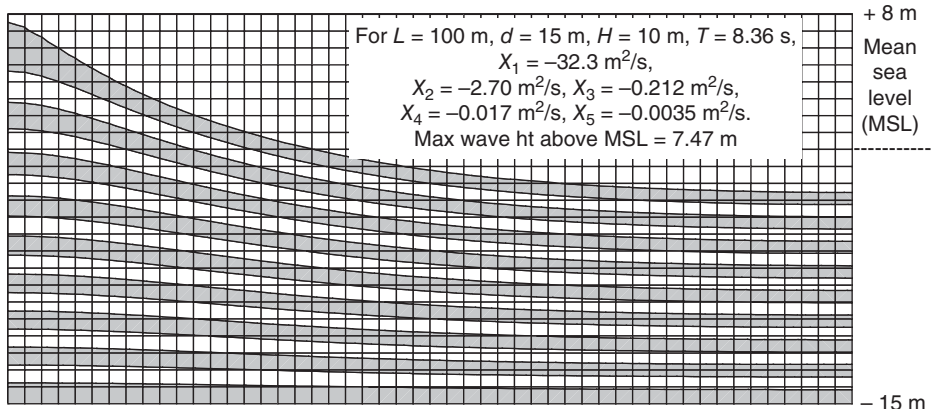


Figure 12.17 Streamlines for Dean stream function wave theory with moving frame of reference.

3. Set X_1 somewhat smaller than given by Eq. (12.22) – say $X_1 = -\frac{0.8Hg}{2\omega \cosh kd}$.
4. Calculate the water-level profile at M equally spaced points over a half wave length using repeated iterations of Eqs. (12.25, 12.26).
5. Using Eq. (12.27), calculate values of $K_1, K_2, \dots, K_m, \dots, K_M$ at these M points.
6. Calculate the summation $\sum_{m=1}^M (K_m - \bar{K})^2$, where $\bar{K} = \sum_{m=1}^M K_m / M$.
7. Minimise the above summation with respect to X_1 and C , subject to the condition $\eta_{\max} - \eta_{\min} = H$, to obtain new values of X_1 and C .
8. Repeat steps 4–7 with X_2 allowed to vary as well.
9. Repeat steps 4–7 with X_2 and X_3 allowed to vary as well.
10. Etc, etc.

Streamlines derived from a fifth order solution using this method with an M of 40 are shown over a half wave length in Figure 12.17, for the case of a 15 m water depth, 100 m wave length, and 10 m wave height. It is evident that the wave profile is far from sinusoidal, with a narrow crest and a broad trough, so that the crest is much higher above mean sea level than the trough is below it.

Horizontal particle velocities may be calculated from the stream function using Eq. (12.23). The profiles of horizontal particle velocities relative to a fixed frame of reference beneath the crest and beneath the trough are shown in Figure 12.18 for the above example.

A useful online resource providing the Dean stream function theory coefficients and the wave profile for user input wave parameters is to be found at https://homepages.cae.wisc.edu/~chinwu/Coastal_Java/streamless.html at the time of writing.

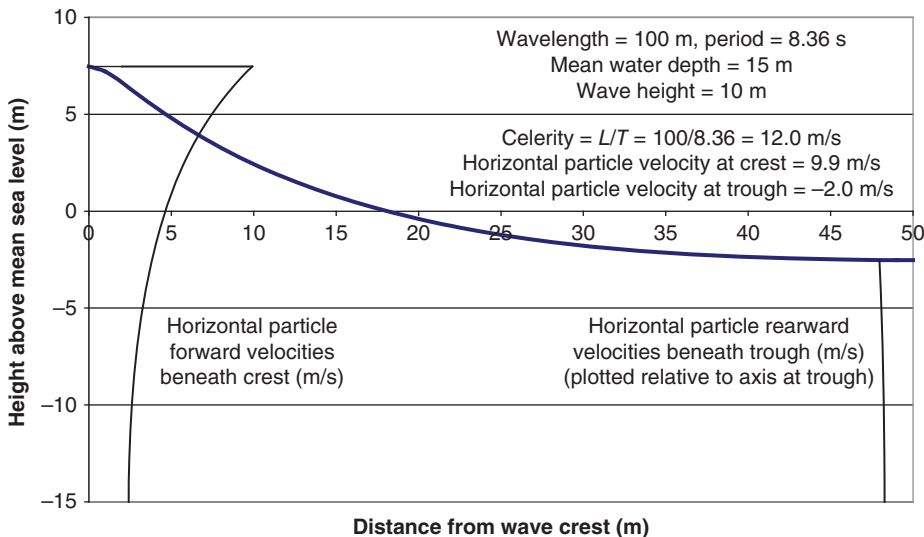


Figure 12.18 Horizontal particle velocity profiles below wave crest and trough. Note the high horizontal particle velocity at the crest, which approaches the wave celerity.

12.3.9 Wave loading on support structure

The wave loading on immersed structures depends on their size, shape and surface roughness. For elements that are small compared with the wavelength, the disturbance to wave behaviour caused by the structure can be ignored and the loading based on the undisturbed wave kinematics, using Morison's equation. However, for larger elements, it is necessary to take account of the way the wave pattern is modified. This can be done by means of a diffraction analysis, in which the varying pressures on discrete facets of the structure are calculated by numerical methods.

Morison's equation

For structural elements with a width less than about one fifth of the wave length, it is normal to describe the loading in terms of separate, additive drag and inertia components, as given by Morison's equation:

$$F = \frac{1}{2} C_D \rho D |u| u + C_M \rho A \frac{\partial u}{\partial t} \quad (12.28)$$

in which F is the force per unit length of the member, D the member width, A its cross-sectional area, C_D the drag coefficient, and C_M the inertia coefficient. The water particle velocity, u , and the acceleration are the undisturbed values that would apply at the member centreline. Note that the drag loading given by the first term is non-linear, as it depends on the square of the water particle velocity. It reaches its peak when the wave crest passes the member, whereas the inertia loading reaches its peak beforehand ($T/4$ beforehand for Airy waves). For Airy waves, the inertia loading term is

$$F_{inertia} = C_M \rho A \frac{H\omega^2}{2} \frac{\cosh k(z+d)}{\sinh kd}$$

which becomes $F_{inertia} = C_M \rho A \frac{H\omega^2}{2} e^{kz}$ in deep water.

Although Morison's equation applies to prismatic members in general, its application to cylindrical members, whether single monopiles or elements of a jacket structure, is of most interest here.

Values of drag and inertia coefficients

The empirical drag and inertia coefficients are dependent on

- The Reynolds number, uD/v , where v is the kinematic viscosity of seawater ($1.35 \times 10^{-6} \text{ m}^2/\text{s}$ at 10°C).
- The relative roughness of the cylinder, k/D , where k is the surface roughness in terms of the peak to valley height.
- The Keulegan–Carpenter number, $K_C = u_{\max} T/D$, where u_{\max} is the maximum water particle velocity (at the water surface, $u_{\max} = H\omega/(2\tanh kd)$ [Eq. (12.16)], so $K_C = \pi H/(D\tanh kd)$).
- The ratio of current to the maximum wave-induced water particle velocity.

Influence of Reynolds number In the case of wind turbine support structures, the Reynolds number will correspond to the post-critical regime in all but the calmest seas, with the result that the steady flow drag coefficient, C_{DS} , is independent of Reynolds number.

Influence of relative roughness The steady flow drag coefficient increases from about 0.65 for smooth cylinders to about 1.05 for rough cylinders, as illustrated in Figure 12.19. This shows the recommendations of ISO 19902:2007, *Petroleum and Natural Gas Industries – Fixed Steel Offshore Structures*, and DNVGL-RP-C205, *Environmental Conditions and Environmental Loads* (2017), which are fairly similar with respect to C_{DS} .

The effect of marine growth on both surface roughness and member diameter must be considered below high tide level. Terminal thicknesses of marine growth of 200 mm and 60–100 mm are quoted in HSE Offshore Technology Report 2001/010, ‘Environmental Considerations’ (HSE 2002) and DNVGL-RP-C205, respectively, but marine growth is very area specific. If it is pessimistically assumed that the surface peak to valley height approximates to the terminal thickness, then the relative roughness of a 4 m diameter wind turbine monopile may be expected to be in the range 0.015–0.05, resulting in a steady flow drag coefficient of 1.05–1.10.

Above high tide level, marine growth will be negligible, and the values of surface roughness, k , given in Table 12.6 can be used.

Influence of Keulegan–Carpenter number The oscillatory flow associated with progressive waves means that the cylinder wake transfers from one side of the cylinder to the other as the flow reverses. After flow reversal, the volume of water that was previously

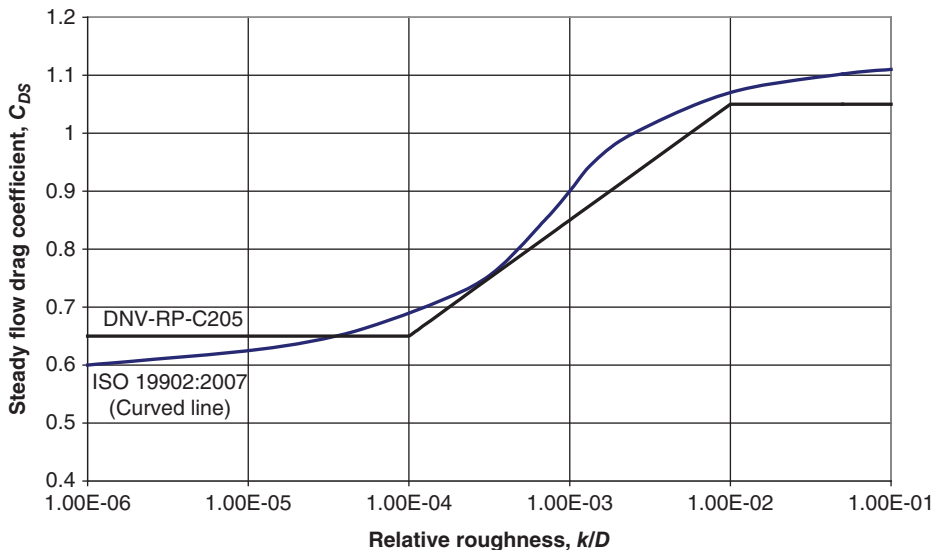


Figure 12.19 Dependence of steady flow drag coefficient on relative roughness.

Table 12.6 Surface roughnesses (from DNVGL-RP-C205 2017).

Material	Surface roughness, k (mm)
Steel, new, uncoated	0.05
Steel, painted	0.005
Steel, highly corroded	3
Concrete	3

slow moving in the wake acquires increased velocity in the reverse direction compared to that which would have obtained in the absence of the cylinder. In calculating the drag coefficient for wave loading, C_D , this effect is allowed for by multiplying the steady flow drag coefficient, C_{D_s} , by a wake amplification factor, ψ , dependent on the Keulegan–Carpenter number. Figure 12.20 shows the relationship between ψ and K_C given in DNVGL-RP-C205 for rough and smooth cylinders. Those given in ISO 19902:2007 are generally very similar.

At very low Keulegan–Carpenter numbers, the inertia coefficient may be taken as 2.0, the theoretical value from potential theory in the absence of flow separation. For $K_C > 3$ it begins to drop with the onset of flow separation, reaching asymptotic values of 1.6 and 1.2 for smooth and rough cylinders, respectively. Figure 12.21 shows the relationship between C_M and K_C given in DNVGL-RP-C205 for rough and smooth cylinders. Those given in ISO 19902:2007 are essentially the same.

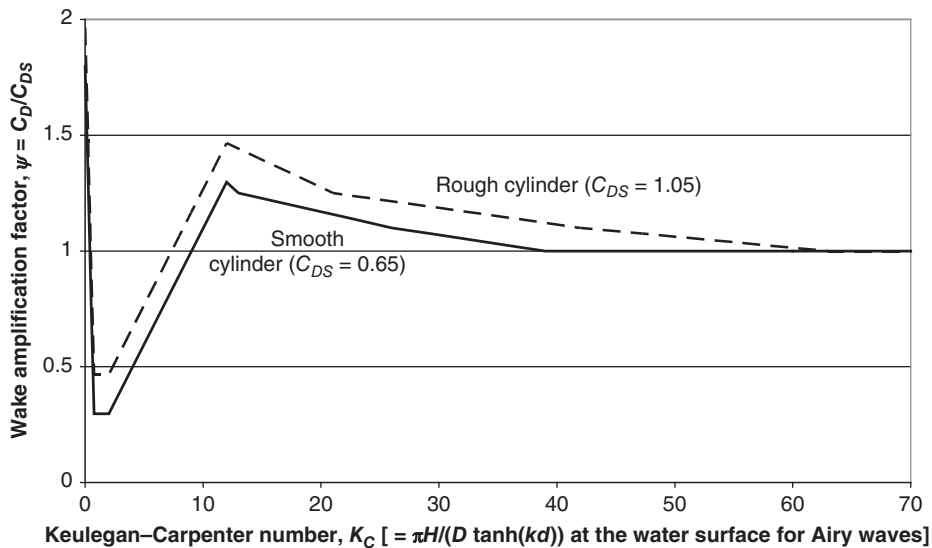


Figure 12.20 Variation of wake amplification factor, $\psi = C_D/C_{DS}$, with Keulegan–Carpenter number from DNVGL-RP-C205.

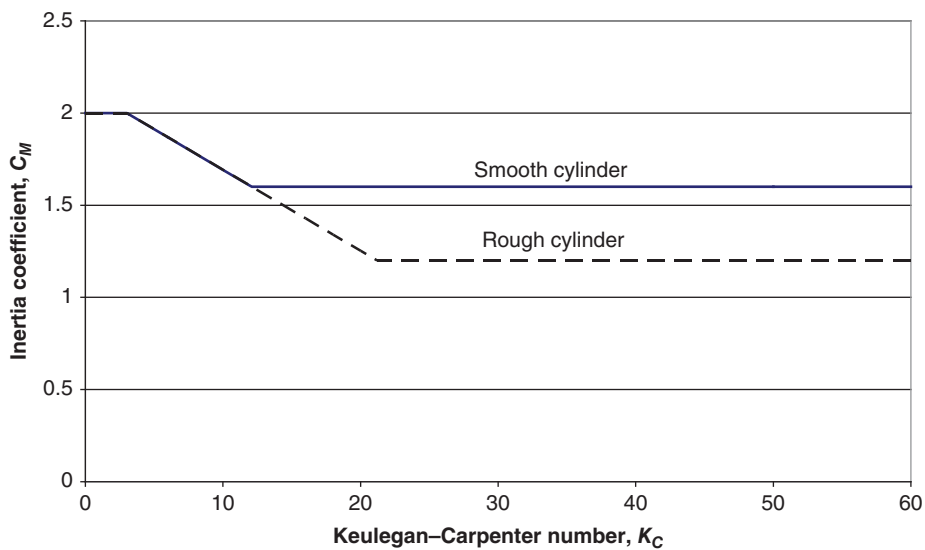


Figure 12.21 Variation of inertia coefficient, C_M , with Keulegan–Carpenter number from DNVGL-RP-C205.

Influence of current The effect of a steady current is to move the drag coefficient C_D closer to the steady flow value, C_{DS} , regardless of the direction of the current relative to the direction of wave propagation. In the case of an in-line current, C_D can be taken as equal to C_{DS} when the current is greater than 0.4 times the maximum orbital velocity due to wave motion.

Ratio of drag force to inertia force

For Airy waves, it can be shown that the ratio of the maximum drag force per unit length to the maximum inertia force per unit length at sea level is

$$\frac{F_{D,Max}}{F_{M,Max}} = \frac{C_D}{C_M} \frac{H}{\pi D} \frac{1}{\tanh(kd)} = \frac{C_D}{C_M} \frac{K_C}{\pi^2} \quad (12.29)$$

Figure 12.22 shows how C_D and C_M vary with Keulegan–Carpenter number for a rough cylinder ($C_{DS} = 1.05$), based on the recommendations of DNVGL-RP-C205. The resulting variation in the ratio of maximum drag force to maximum inertia force has been derived from Eq. (12.29), and is shown in the same figure.

Drag dominant or inertia dominant regimes can be defined according to which load component is the greater. For a rough cylinder, the transition from the inertia dominated regime to the drag dominated regime occurs when the Keulegan–Carpenter number exceeds $\pi^2 C_M / C_D$ – i.e. approximately $\pi^2(1.64/1.45) = 11.2$, so for deep water, with $\tanh kd$ approaching unity, drag force dominates when the wave height to cylinder diameter ratio exceeds $11.2/\pi$ – i.e. about 3.5. In shallow water, where $\tanh kd$ is less than unity, this threshold is reduced in proportion. It can be seen that, for normal sea states, the loading on a monopile of around 4.0 m diameter is likely to be dominated by inertia loading.

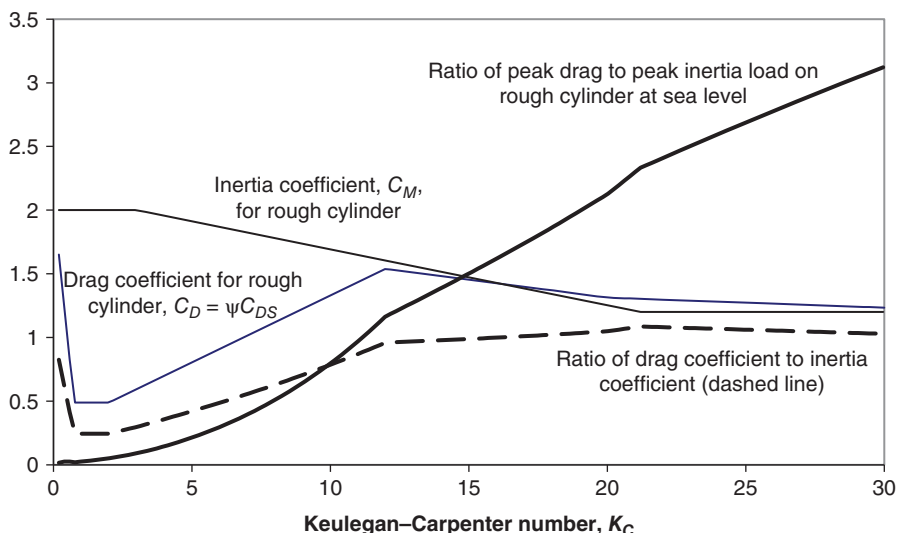


Figure 12.22 Variation of C_D , C_M , C_D/C_M , and the ratio of maximum drag force to maximum inertia force at sea level with Keulegan–Carpenter number, $K_C = \pi H/(Dtanhkd)$ for a rough cylinder.

Airy wave loading on cylinder

The cylinder loading from an Airy wave is easily found by inserting the horizontal particle velocity [Eq. (12.16)] and acceleration into Eq. (12.28). However, as Airy wave theory is based on infinitesimal waves, it does not provide velocities and accelerations above still water level. Accordingly, it is normal to make the assumption that the kinematics at the instantaneous free surface are the same as those given by Airy theory at still water level, and that at intermediate depths the kinematics are those that would be given by Airy theory after the water column had been compressed or stretched uniformly to a height corresponding to mean water depth. This procedure was proposed by Wheeler (1970) and is known as *Wheeler stretching*.

Figure 12.23 illustrates how the drag and inertia loads on a 4 m diameter vertical cylinder integrated over the full local water depth vary with time for a 3 m Airy wave. As expected, the drag component is much less than the inertia component. It can be seen that Wheeler stretching displaces the inertia load peak closer to the crest.

Clearly, in this case, the drag load does not contribute to the maximum total load at all. In the general case, the drag load only begins to affect the maximum total load when K_C exceeds $0.5\pi^2 C_M / C_D$.

Cylinder loading for non-linear waves

In the case of larger, non-linear waves, the water particle velocities and accelerations input into Morison's equation have to be based on a non-linear wave theory. Figure 12.24 shows the variation of drag and inertia loading on a 4 m diameter vertical cylinder in the case of 10 m regular waves, based on fifth order Dean stream function theory. The drag and

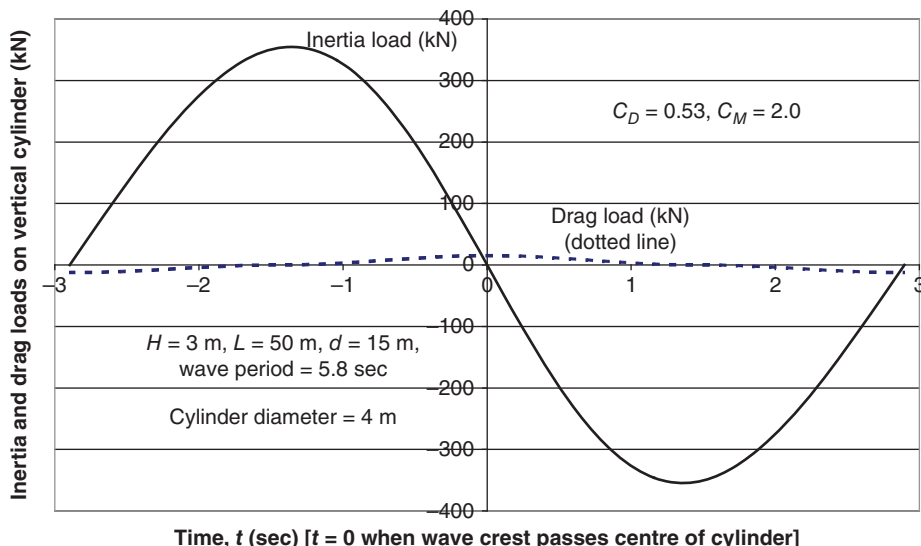


Figure 12.23 Variation of wave loading on a 4 m dia vertical cylinder over a complete wave period for a 3 m Airy wave and 15 m mean water depth.

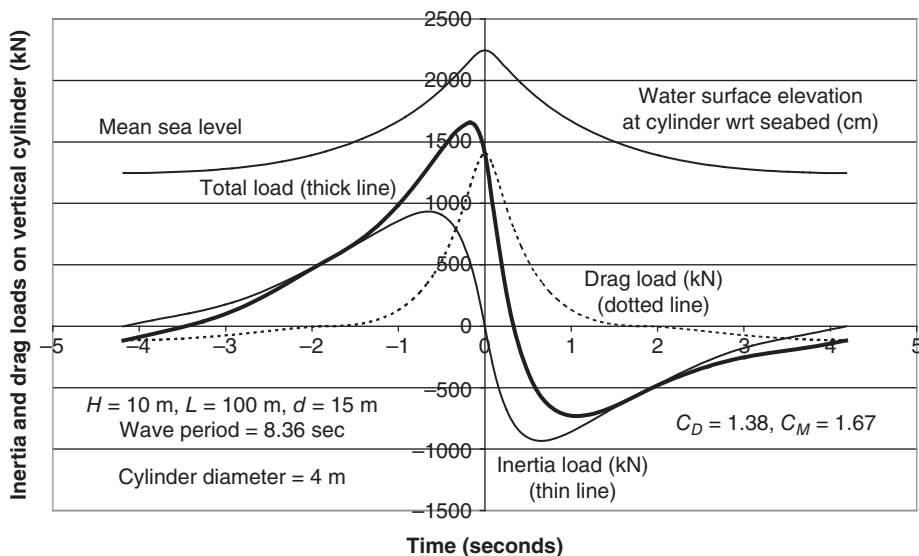


Figure 12.24 Variation of wave loading on a 4 m dia vertical cylinder over a complete wave period for a 10 m regular wave and 15 m mean water depth.

inertia coefficients used are based on the recommendations of DNVGL-RP-C205. The loads are integrated over the full local water depth as before.

It is evident that the drag loading reaches a pronounced peak as the crest passes the cylinder, due to the increased depth and high water particle velocity in the wave crest – 9.9 m/s compared with the wave celerity of 12 m/s. Also, the phase lead of the inertia loading maximum is much reduced compared with the $T/4$ applicable in the case of an Airy wave. It is striking that the ratio of the peak drag load to peak inertia load has increased by a factor of 35 compared with the Airy wave example above, although the $(C_D/C_M).(H/D)$ ratio has only increased by a factor of 10.4.

Diffraction

Structural elements that are of significant width compared with the wave length modify the wave behaviour, so the transparency assumption implicit in Morison's equation no longer applies. Instead, a diffraction analysis has to be used, in which the modified wave flow around the structure is obtained in terms of a velocity potential distribution that satisfies the extra requirement that there should be no flow perpendicular to the surface of the structure. Note that the diffraction analysis determines the inertia loading on the structure, but not the drag loading. This is normally of little concern as the drag loads on large structures are usually negligible beside the inertia loads. A more significant limitation of diffraction theory is that it is restricted to linear waves, as the velocity potential only satisfies linearised versions of the boundary conditions at the free water surface.

A closed-form analytical solution for the velocity potential in terms of Bessel functions has been developed for the case of a large vertical cylinder projecting above the

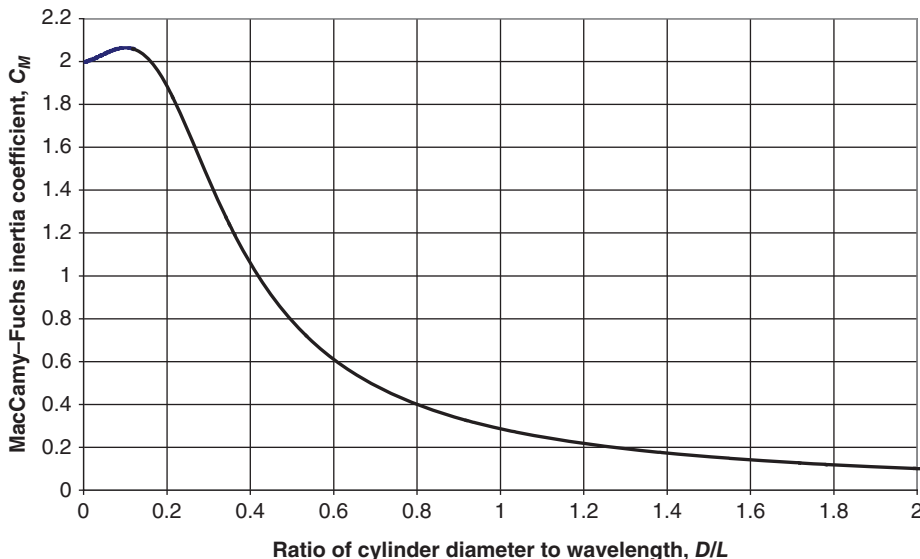


Figure 12.25 Effect of large cylinder diameter on inertia coefficient, based on MacCamay and Fuchs (1954).

water surface by MacCamay and Fuchs (1954). The method adopted is to treat the velocity potential as composed of two parts – the first the velocity potential that would exist in the absence of the cylinder and the second one that cancels out the flows across the cylinder surface postulated by the first. The result was used in conjunction with the unsteady Bernoulli equation to calculate the pressure distribution on the cylinder and hence the load per unit length. Figure 12.25 shows how the resulting inertia coefficient varies with the diameter to wave length ratio, D/L . It is seen that after an initial small increase, the inertia coefficient drops rapidly as D/L increases.

The derivation of the MacCamay and Fuchs expressions for the velocity potential and cylinder loading is described in Dean and Dalrymple (1984).

In the general case, no closed-form solution will be available and resort has to be made to numerical methods. The method again involves determination of the velocity potential that would exist in the absence of the structure and the derivation of a second velocity potential superposed upon the first that results in zero flow across the structure surface, while satisfying the Laplace equation and the other boundary conditions. The surface of the structure is divided up into N area elements or facets, each with its own oscillating flow source taken as uniformly distributed over the facet, and the second velocity potential is taken as the summation of the velocity potentials resulting from these N oscillating sources. Then application of the zero flow requirement at each facet results in N simultaneous equations for the determination of each source magnitude.

Denoting the source intensity at facet i as f_i per unit area and the velocity potential due to a unit oscillating source radiating from the centre of facet i as $\Phi_i(x, y, z, t)/4\pi$, the total potential gradient perpendicular to facet j due to all N oscillating sources becomes:

$$\begin{aligned}\left(\frac{\partial\phi_S}{\partial n}\right)_j &= \frac{1}{4\pi} \left[\left(\frac{\partial\Phi_1}{\partial n}\right)_j f_1 S_1 + \dots + \left(\frac{\partial\Phi_i}{\partial n}\right)_j f_i S_i + \dots + \left(\frac{\partial\Phi_N}{\partial n}\right)_j f_N S_N \right] \\ &= \frac{1}{4\pi} \sum_i \left(\frac{\partial\Phi_i}{\partial n}\right)_j f_i S_i\end{aligned}$$

where S_i is the surface area of facet i .

For zero flow across facet j , $\left(\frac{\partial\phi_I}{\partial n}\right)_j = -\left(\frac{\partial\phi_S}{\partial n}\right)_j$, where $\left(\frac{\partial\phi_I}{\partial n}\right)_j$ is the potential gradient perpendicular to the facet that would occur in the absence of the structure. This leads to a set of equations,

$$\left(\frac{\partial\phi_I}{\partial n}\right)_j = -\frac{1}{4\pi} \sum_i \left(\frac{\partial\Phi_i}{\partial n}\right)_j f_i S_i \quad (12.30)$$

which can be solved for the source intensities, f_i .

Wehausen and Laitone (1960) give an expression for $\Phi_i(x, y, z, t)$ on page 478 of 'Surface Waves'. In addition to the expected terms $(1/r)\cos\omega t$ associated with the point source and $(1/r_2)\cos\omega t$ associated with an imaginary 'mirror' source beneath the seabed (where r and r_2 are the radii from the point source and 'mirror' source, respectively, to the point x, y, z), there are two other terms involving Bessel functions of the first kind, one in phase and the other 90° out-of-phase with the source. These terms are required to satisfy the free surface boundary conditions and the expected decay towards infinity.

As noted above, diffraction theory can only provide an exact solution for linear waves. However, an approximate solution for non-linear waves can be obtained by increasing the load on each facet of the structure surface obtained from the diffraction analysis by the ratio of the non-linear wave particle acceleration to the linear wave particle acceleration at the facet, treating the structure as transparent.

Breaking waves

Deep water waves break when they reach shallower water such that the wave height to water depth ratio exceeds 0.78 and can result in short-term loads an order of magnitude greater than those from non-breaking waves.

Breaking waves are normally divided into three different types – spilling, plunging, or surging. Muir Wood and Fleming (1981) distinguish them as follows: 'In principle a plunging breaker occurs when the crest velocity exceeds that of the body of the wave, a spilling breaker occurs when the crest velocity remains approximately equal to that of the wave and a surging breaker occurs when the base of the wave surges up the beach before the crest can plunge forward'. Clearly plunging breakers are of greatest concern in relation to wind turbine structures, because the advancing wall of water causes impulsive loads on vertical surfaces.

The hydrodynamics of wave impact on a structure is a complex 3-D problem, depending on the form of the structure, the shape of the wavefront and the presence of entrained air, so simplifying assumptions are necessary. Figure 12.26 illustrates a plunging breaker striking a vertical cylinder. Although the surface of the front of the wave is typically concave, it is normal to treat it as vertical, with a height λ times the wave crest elevation,

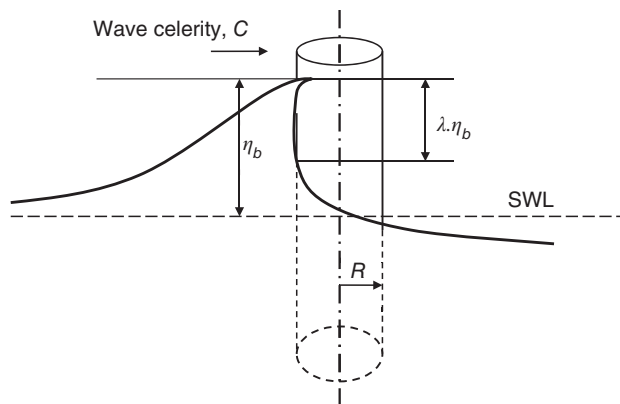


Figure 12.26 Wave breaking at vertical cylinder.

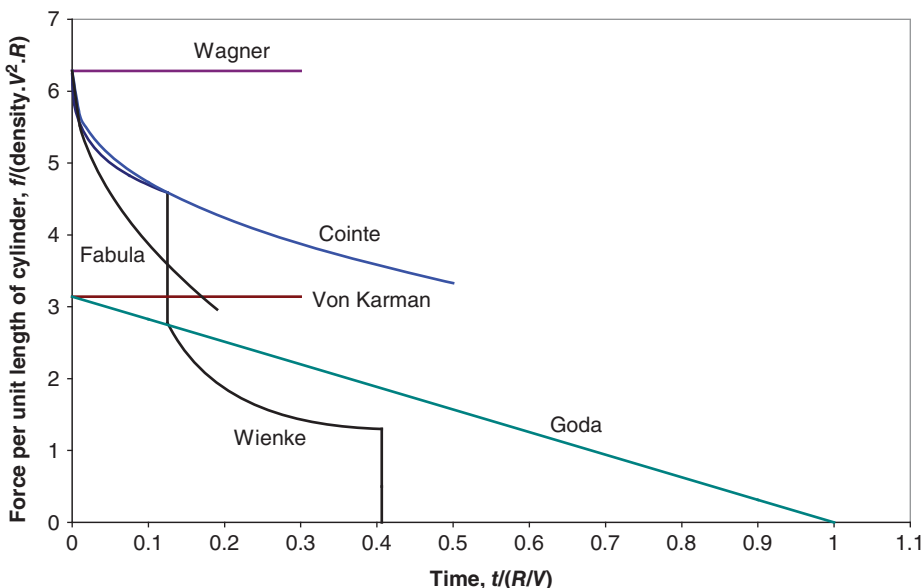


Figure 12.27 Time histories of impulsive force on cylinder according to different theories.

η_b , and consider the water flow around the cylinder as a 2-D problem. λ is known as the *curling factor*.

Various theories for the impulsive loading on the cylinder as the breaking wave envelops it have been proposed, and are summarised in Wienke and Oumeraci (2005). The time histories of the impulsive force per unit length for some of the theories are presented in Figure 12.27.

It can be seen that the magnitude of the initial impulsive force coefficient, $f/(\rho V^2 R)$, is quite uncertain, ranging from π to 2π . The higher value results from allowance being made for the pile-up of water on either side of the cylinder (see Figure 12.28).

The force on the cylinder equates to the integral of the pressure distribution over the immersed surface area, obtained from the unsteady Bernoulli equation:

$$p(x, t) = \rho \frac{\partial \phi}{\partial t} - \frac{1}{2} \rho \left[\left(\frac{\partial \phi}{\partial x} \right)^2 + \left(\frac{\partial \phi}{\partial y} \right)^2 \right] + C(t) \quad (12.31)$$

The gravity term is omitted, as the height is constant.

Velocity potential utilising flat plate idealisation The problem of determining the velocity potential, ϕ , is simplified if the instantaneous flow field is assumed to be that which would apply to flow around a *flat* plate of width equal to the immersed width of the cylinder at that instant (Figure 12.28). The complex potential for the flow around a flat plate perpendicular to the mean flow direction is given by Milne-Thomson (1967) as

$$w = iV\sqrt{z^2 - c^2} \quad (12.32)$$

where V is the flow velocity remote from the plate in the positive y direction, $z = x + iy$, and the width of the plate is $2c$. The velocity potential is given by the real part of w and equates to $\phi = V\sqrt{c^2 - x^2}$ at the upstream surface of the plate.

At a point far upstream of the plate, the fluid pressure, $\frac{\partial \phi}{\partial t}$ and $\frac{\partial \phi}{\partial x}$ are all zero, so $C(t) = 0.5\rho V^2$ and Eq. (12.31) becomes

$$p(x, t) = \rho \frac{\partial}{\partial t} (V\sqrt{c^2 - x^2}) - \frac{1}{2} \rho \left(\frac{\partial \phi}{\partial x} \right)^2 + \frac{1}{2} \rho V^2 = \frac{\rho V c}{\sqrt{c^2 - x^2}} \frac{dc}{dt} - \frac{1}{2} \rho V^2 \frac{x^2}{c^2 - x^2} + \frac{1}{2} \rho V^2 \quad (12.33)$$

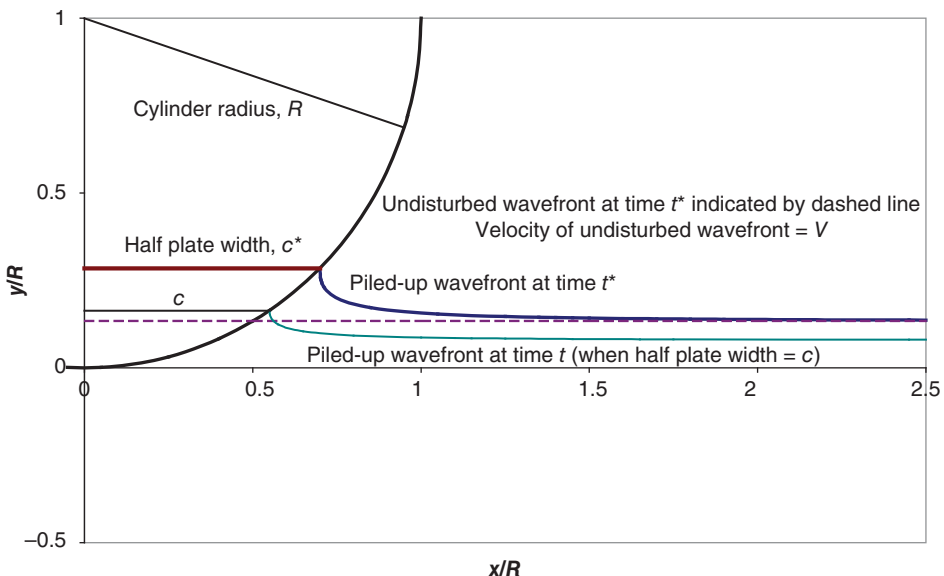


Figure 12.28 Development of water pile-up as wavefront advances around cylinder.

Wavefront pile-up Wagner (1932) set out a method for calculating the accelerated advance of the wavefront around each side of a boat hull impacting a still water surface that can be used to obtain dc/dt for a wavefront impacting on a cylinder (see Figure 12.28). From Eq. (12.32), it can be shown that the velocity of flow past the notional plate at a point in the plane of the plate is

$$-\left(\frac{\partial \phi}{\partial y}\right)_{y=0, x>c} = \frac{V}{\sqrt{1 - (c/c)^2}} \quad (12.34)$$

The integral of this expression with respect to time gives the y coordinate of the point (c^*, y) where the wavefront meets the cylinder surface at time t^* :

$$y(t^*) = \int_0^{t^*} \frac{Vdt}{\sqrt{1 - (c/c^*)^2}} \quad (12.35)$$

We now define the quantity $\mu = V/(dc/dt)$, so that $Vdt = \mu dc$ and

$$y(t^*) = \int_0^{c^*} \frac{\mu \cdot dc}{\sqrt{1 - (c/c^*)^2}} \quad (12.36)$$

If we suppose that $\mu = \alpha_1 c + \alpha_3 c^3 + \alpha_5 c^5 + \dots$, the integral can be performed and the values α_n determined from the requirement that $y(t^*)$, c^* follow the profile of the cylinder. For example, if μ is taken as $\alpha_1 c$,

$$y(t^*) = \int_0^{c^*} \frac{\alpha_1 c \cdot dc}{\sqrt{1 - (c/c^*)^2}} = \alpha_1 [-c^* \sqrt{1 - (c/c^*)^2}]_0^{c^*} = \alpha_1 c^{*2} \quad (12.37)$$

Solution for parabolic profile Equating $\alpha_1 c^{*2}$ to the parabolic approximation to a circle, $y(t^*) = 0.5c^{*2}/R$, yields $\alpha_1 = 0.5/R$. Hence $\mu = 0.5c/R$ and $dc/dt = V/\mu = V.2R/c$, which can be substituted in Eq. (12.33) to give

$$p(x, t) = \frac{2\rho V^2 R}{\sqrt{c^2 - x^2}} + \frac{1}{2}\rho V^2 - \frac{1}{2}\rho V^2 \frac{x^2}{c^2 - x^2} = \frac{2\rho V^2 R}{\sqrt{c^2 - x^2}} + \frac{1}{2}\rho V^2 \left(2 - \frac{c^2}{c^2 - x^2}\right) \quad (12.38)$$

This expression is integrated over the width of the plate to give the force per unit length on the cylinder:

$$\begin{aligned} f &= 2\rho V^2 R.2 \int_0^c \frac{dx}{\sqrt{c^2 - x^2}} + \frac{1}{2}\rho V^2.2 \int_0^c \left(2 - \frac{c^2}{c^2 - x^2}\right) dx \\ &= 4\rho V^2 R \arcsin\left(\frac{x}{c}\right) + \rho V^2 \int_0^c \left(2 - \frac{c^2}{c^2 - x^2}\right) dx \\ &= \rho V^2 R \left\{ 2\pi + \frac{2c}{R} - \frac{c}{R} \left[\tanh^{-1}\left(\frac{x}{c}\right) \right]_0^c \right\} \end{aligned} \quad (12.39)$$

The third term in Eq. (12.39) is theoretically infinitely negative because the pressure tends to minus infinity at the edge of the notional flat plate. However, if negative pressures are ignored, a conservative result may be obtained. The initial force per unit length, for $c = 0$, is $2\pi\rho V^2 R$, which is an order of magnitude greater than the drag force for this velocity.

Two stage solution Wienke (2001) approximates the circular profile by the above parabola for $c^*/R < 1/\sqrt{2}$ and by a quartic curve beyond. This results in the stepped force time history shown in Figure 12.27.

Multi-term solution for near circular profile The circular profile of the cylinder, $y(t^*)/R = 1 - \sqrt{1 - (c^*/R)^2}$, can be approximated by the binomial series

$$y(t^*) = \frac{1}{2} \left(\frac{c^*}{R} \right)^2 + \frac{1}{8} \left(\frac{c^*}{R} \right)^4 + \frac{1}{16} \left(\frac{c^*}{R} \right)^6 + \frac{5}{128} \left(\frac{c^*}{R} \right)^8 + \dots \dots \quad (12.40)$$

Substitution in Eq. (12.36) with $\mu = \alpha_1 c + \alpha_3 c^3 + \alpha_5 c^5 + \dots$ results in

$$\begin{aligned} \mu = & \frac{1}{2} \left(\frac{c}{R} \right) + \frac{3}{16} \left(\frac{c}{R} \right)^3 + \frac{15}{128} \left(\frac{c}{R} \right)^5 + \dots \\ & + \frac{(2n+1)(2n-1)(2n-3)\dots(2n-1)(2n-3)(2n-5)\dots}{2n(2n-2)(2n-4)\dots(2n+2)(2n)(2n-2)\dots} \left(\frac{c}{R} \right)^{2n+1} \end{aligned}$$

Although only a few terms of the series (12.40) are required to represent the profile for $c^*/R < 0.8$, a large number of terms are required as c^*/R approaches unity. Equation (12.33) for the pressure distribution becomes

$$p(x, t) = \frac{\rho V^2 c / \mu}{\sqrt{c^2 - x^2}} + \frac{1}{2} \rho V^2 \left(2 - \frac{c^2}{c^2 - x^2} \right) \quad (12.41)$$

The force per unit length is obtained by integrating Eq. (12.41) over the immersed width, ignoring negative pressures near the edge of the notional plate as before. Denoting the value of x at which the pressure changes sign as c' , the force per unit length on the cylinder is then

$$f = \rho V^2 R \left\{ \frac{2c}{\mu R} \arcsin \left(\frac{c'}{c} \right) + \frac{2c'}{R} - \frac{c}{R} \tanh^{-1} \left(\frac{c'}{c} \right) \right\} \quad (12.42)$$

The relationship between the time elapsed since the wave first hits the cylinder and the immersed width, $2c$, is obtained by integrating the equation $Vdt = \mu dc$. Figure 12.29 shows the resulting time history of the force per unit length obtained when 100 terms are used in the series expression for μ .

Note that the plot becomes inaccurate as c/R approaches unity, because of the inevitable inaccuracy of the series approximation to a circle there. However, this is less of a concern than the fact that the flat plate idealisation becomes unrealistic for large c/R anyway.

Experimental measurements An extensive series of measurements on vertical and inclined cylinders subjected to breaking waves in the wave tank at the Forschungszentrum Küste, Hannover, have been reported by Wienke and Oumeraci (2005). Pressure measurements around the cylinder circumference confirmed the validity of the Wagner wavefront pile-up model and measurements of the total loading indicated a maximum value of the curling factors of 0.46 for vertical cylinders. This is in line with the range of 0.4–0.5 given by Goda et al. (1966).

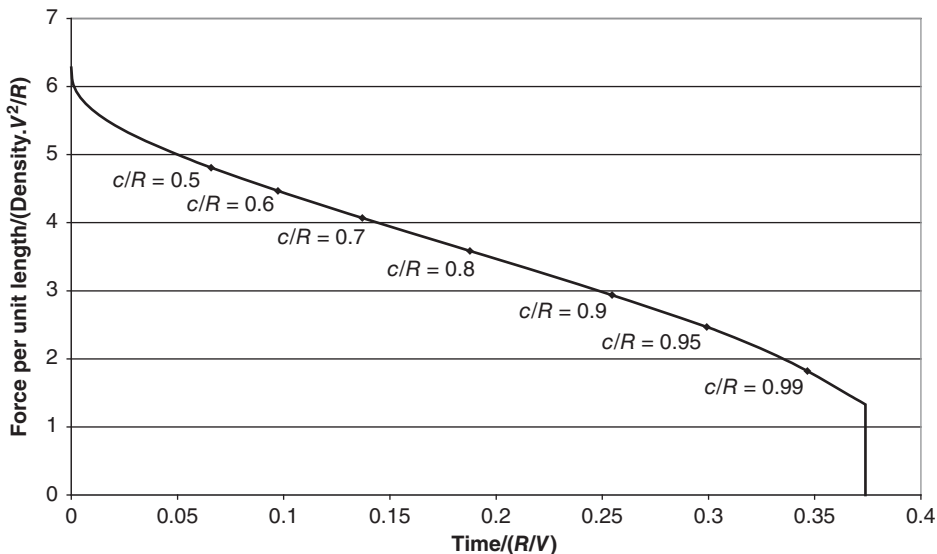


Figure 12.29 Time history of force per unit length on cylinder due to breaking wave using flat plate idealisation.

12.3.10 Constrained waves

The analysis of structural loading caused by large waves in a random sea is a complex undertaking, because the linear wave theory, which applies to the myriad individual tiny sinusoidal components of the waveform, when each is on its own, breaks down when they are combined together, because of the large resulting wave amplitude. Annex C of IEC 61400-3-1 2019 suggests the use of the constrained wave approach, which involves the embedment of a single non-linear regular wave (commencing and ending at a trough) into a series of irregular, linear waves forming a longer simulation.

Clearly, a smooth transition between the simulated waveform and the embedded wave is required to preserve a basic similarity between the wave kinematics of the two. Ideally, one would find a wave in the simulated waveform of similar magnitude to the specified regular wave and replace the former with the latter. However, many simulations are necessary to find a large enough wave, and the troughs on either side of the crest are unlikely to be of the same height. Furthermore, the crest height above still water level is normally about half the wave height for any simulated wave, instead of about three quarters for the embedded non-linear wave.

To circumvent these difficulties, Rainey and Camp (2007) have proposed constraining the elevation and slope of the simulated waveform at three points coinciding with the crest and troughs of the embedded wave. The constrained waveform can be obtained by ‘correcting’ an initial simulated waveform using new wave theory (Tromans et al. 1991) so that it satisfies the imposed conditions.

Bierbooms (2006) explains the method as applied to wind simulation, and derives an expression for the time history of a constrained gust. The analogous expression for the time history of water surface elevation constrained to have an extreme value of A at time

$t = t_0$ is as follows:

$$\eta_c(t) = \eta(t) + \kappa(t - t_0)(A - \eta(t_0)) - \frac{\dot{\kappa}(t - t_0)}{\ddot{\kappa}(0)} \dot{\eta}(t_0) \quad (12.43)$$

Here $\eta(t)$ is the water surface elevation obtained from the initial simulation, $\kappa(t - t_0)$ is the water surface elevation autocorrelation function, $\dot{\kappa}(t - t_0)$ is its time derivative and $\ddot{\kappa}(0)$ is its second time derivative at time $t = t_0$. The autocorrelation function and its time derivative (normalised by $\ddot{\kappa}(0)$) are plotted out in Figure 12.30, which illustrates how the two correction terms fluctuate at the wave frequency and attenuate as $|t - t_0|$ increases.

The method can be extended to the imposition of constraints on water surface elevation and slope at three successive points in time. Figure 12.31 shows an example water surface elevation simulated time history and desired constrained elevations of C at the crest (time t_2) and D at the preceding and succeeding troughs (times t_1 and t_3).

The equation for the simulated time history of water surface elevation with these six constraints is

$$\begin{aligned} \eta_c(t) = & \eta(t) + a\kappa(t - t_1)(D - \eta(t_1)) + b\frac{\dot{\kappa}(t - t_1)}{\ddot{\kappa}(0)}\dot{\eta}(t_1) + c\kappa(t - t_2)(C - \eta(t_2)) \\ & + d\frac{\dot{\kappa}(t - t_2)}{\ddot{\kappa}(0)}\dot{\eta}(t_2) + e\kappa(t - t_3)(D - \eta(t_3)) + f\frac{\dot{\kappa}(t - t_3)}{\ddot{\kappa}(0)}\dot{\eta}(t_3) \end{aligned} \quad (12.44)$$

where a, b, c, d, e , and f are six unknown coefficients. These can be determined by solving the six simultaneous equations obtained by substituting $t = t_1$, $t = t_2$ & $t = t_3$ in turn in Eq. (12.44) and in its time derivative, and equating $\eta_c(t_1)$ to D, $\eta_c(t_2)$ to C, $\eta_c(t_3)$ to D and $\dot{\eta}_c(t_1)$, $\dot{\eta}_c(t_2)$, and $\dot{\eta}_c(t_3)$ to zero.

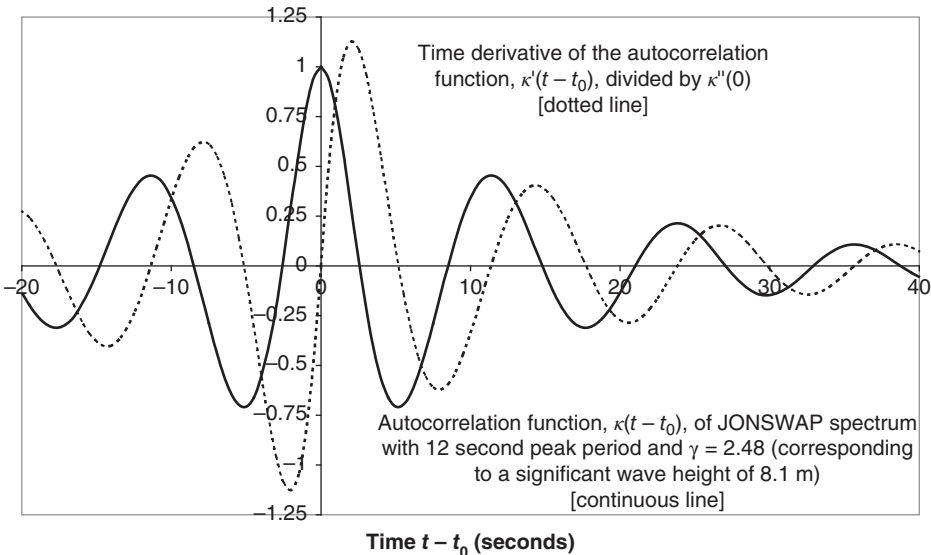


Figure 12.30 JONSWAP spectrum autocorrelation function and its time derivative.

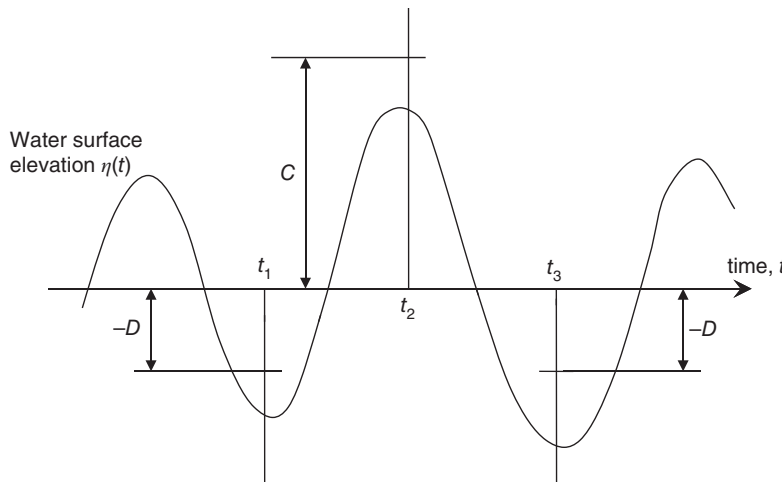


Figure 12.31 Simulated water surface time history and desired constraints at times t_1 , t_2 , and t_3 .

Figure 12.32 provides an illustration of a simulated water surface elevation time history constrained to permit the insertion of a 15 m regular wave. A JONSWAP spectrum was used for the simulation with a significant wave height of 8.1 m – i.e. that expected to yield an extreme wave exceeding 15 m in a three hour reference period. The wave period corresponding to the spectral peak frequency was 12 seconds.

The profile of the embedded wave, which replaces that of the constrained simulation over the 12 seconds commencing at 276.5 seconds, is derived from 5th order stream function theory. Rainey and Camp (2007) propose the use of cosine blending functions in the vicinity of each trough to smooth the inevitable discontinuities in the wave kinematics (and hence the wave loading) at the boundary between assumed linear and non-linear behaviour. The water particle velocities and accelerations in the transition regions are then calculated as weighted averages of those derived from the linear and non-linear solutions, with the weighting determined by the blending functions.

Although this does not provide a rigorous solution to the wave equation, it does provide a pragmatic engineering approach in which the background irregular sea state sets the initial dynamic conditions of the structure before the passage of the non-linear extreme wave.

12.3.11 Analysis of support structure loads

Loadings on oil and gas offshore structures have customarily been calculated considering deterministic, regular, non-linear waves for extreme loads and exposure to different stochastic sea states for fatigue loads. In the latter case, spectral analysis permits the dynamic behaviour of the structure to be accounted for using a frequency-dependent transfer function relating response to excitation but depends on the assumption of linear waves and relatively small drag loading, permitting ‘linearization’ of the drag term in Morison’s equation.

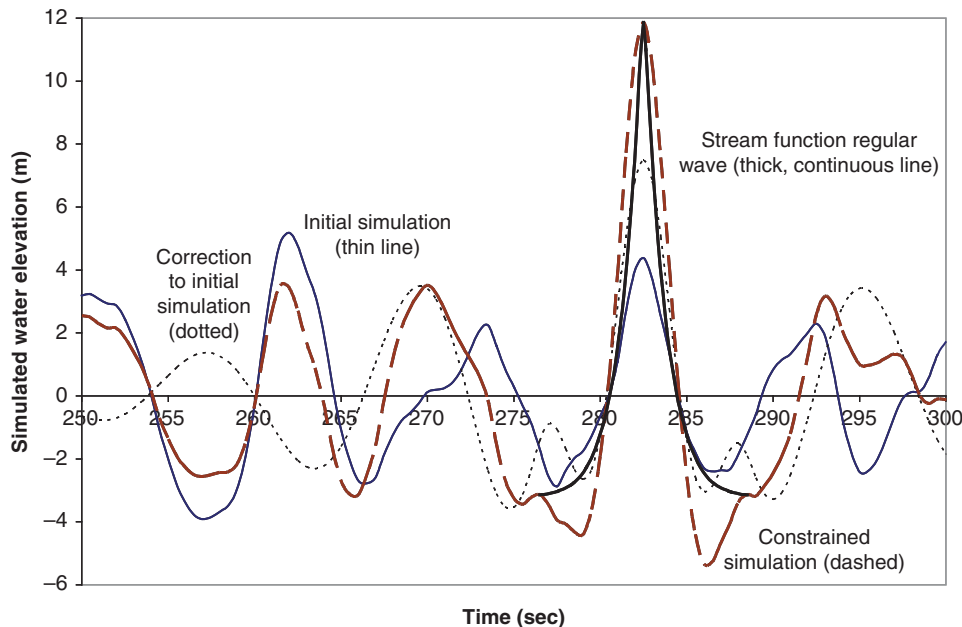


Figure 12.32 Example of a simulated water surface elevation time history constrained to enable the insertion of a 15 m regular wave.

The loading on wind turbine support structures differs from that on the typical offshore structure for oil or gas extraction in several ways:

1. Wind turbines are usually sited in shallower waters, so non-linearity of wave loading is more important.
2. Wind turbines project much higher above still water level, which, in conjunction with shallow water siting, results in wind loading being much more dominant.
3. The wind loading on the support structure of an operating wind turbine is completely different from that on an oil platform or a parked wind turbine, because of the large rotor thrust loading even in low winds, the pronounced randomly varying periodic loading resulting from gust slicing, and the active control of rotor speed and pitch angle.
4. Wind turbines are typically supported on a single column, which is less stiff than the lattice structures normally used for oil or gas platforms.

The inability to compute stress ranges arising from combined deterministic and stochastic loading in the frequency domain is one of the main factors driving the use of multiple simulations in the time domain for the analysis of wind turbine loads. In the case of offshore wind turbines, wave loads have to be input into the simulations as well.

The simulation of wave loads starts with the wave spectrum (Section 12.3.4) defining the sea state under investigation and involves the superposition of many tiny waves of different frequency and random phase, with each wave amplitude determined by the square

root of the spectral density at the frequency concerned. This enables time histories of the water surface elevation and the water particle kinematics to be generated, under the key assumption that *linear* wave theory applies. Finally, wave loads are calculated from the water particle kinematics using Morison's equation.

Although wave loads do not act on the rotor and nacelle directly, tower head accelerations due to support structure wave loading result in inertia loading on the turbine. However, these loads are normally relatively small, to the extent that onshore wind turbine designs can often be used offshore.

The treatment of wave loads in relation to extreme and fatigue load cases are considered separately below.

Extreme loads

Generally, extreme load cases are specified in terms of a turbulent wind and a stochastic sea state, which requires the assumption of linear wave theory in the calculation of the water particle kinematics and the derivation of the loads. Many of the load cases detailed in Sections 12.3.5 and 12.3.6 are principally concerned with extreme *wind* loading, so the error in the linear wave assumption is not a concern. However, in the case of load cases 1.6, 6.1, 6.2, 6.3, and 7.1, which involve extreme waves, the standard requires non-linear wave kinematics to be properly represented by the inclusion of a constrained wave in each 1 hour simulation.

Fatigue loads

As set out in Section 5.9.4, simulations in the time domain are preferred to spectral analysis for the evaluation of fatigue damage due to wind loading, because they account for both non-linear aerodynamics and the combination of deterministic and stochastic load components. In the case of offshore wind turbine structures, simulations in the time domain have the further advantage of directly modelling the aerodynamic damping of wave-induced tower motion and enabling the *combined* stress fluctuation resulting from the disparate wind and wave loadings to be obtained directly for rainflow counting of the stress cycles.

The calculation of wave loads is again based on linear wave theory, but the errors introduced by this assumption are relatively minor, because of the smaller waves.

The analysis of fatigue loading in the time domain inevitably involves a large number of simulations, particularly when several turbine sites are being investigated. Although this method is advisable for final design verification, it is demanding of computing time, so fatigue analysis in the frequency domain may be preferred for the development of an initial support structure design. This approach is discussed further in relation to monopile support structures in Section 12.7.4.

12.4 Machine size optimisation

In principle, the optimum turbine diameter for an offshore site can be estimated using a cost model and appropriate scaling rules in the same way as discussed for land

based machines in Chapter 6. One of the main challenges is to develop a realistic model for the support structure construction and installation cost, which is typically a significantly greater proportion of the total capital cost offshore. Ideally, the model should account for differing water depths and foundation types as well as for different turbine diameters and should be based on cost data from wind farms that have already been constructed, although in practice such information is rarely easy to obtain.

The INNWIND cost model (INNWIND 2016) offers the choice of a jacket or floating support structure but does not differentiate between water depths. The assumption is made that jacket costs vary as the turbine power rating raised to the power of 0.75 which, at first sight, seems rather low. However, if we consider the support structures of a family of turbines of different diameters (but the same rated wind speed) all designed for the same water depth, it can be shown that the index of 0.75 is plausible. Assuming that the turbine hub height above the interface level is proportional to turbine diameter, the tower base moment will vary as the cube of turbine diameter, so the weight of a jacket designed for wind loading alone would scale as the turbine diameter squared, if leg spacing, member diameters and wall thicknesses and bay heights all increased in proportion to turbine diameter, as the jacket height remains constant. Given that jacket leg and brace diameters are scaled with turbine diameter, the overturning moment due to wave loading increases at most as turbine diameter squared – i.e. at a lesser rate than that tower base moment, so the weight of a jacket designed for wind and wave loading combined should scale as diameter raised to a power somewhat less than two – i.e. as turbine power rating raised to a power of somewhat less than one.

Transport and installation costs are a major component of the total installed turbine cost but are very difficult to model, particularly as they are site specific. The INNWIND cost model estimates a cost of 345 Euros/MW. To this must be added the cost of the electrical power collection and transmission system, taken as 340 Euros/MW.

The variation of the capital component of the Levelised Cost of Energy (LCOE) with turbine rating has been calculated using the INNWIND cost model for jacket supported turbines under a particular set of conditions and the results are plotted in Figure 12.33 in 2012 Eurocents/kWh. A turbine life of 20 years is assumed together with a discount rate of 5%. The turbine rated wind speed and the annual mean wind speed at 119 m height are taken as 11.4 and 9.2 m/s, respectively. It is seen that a minimum cost of energy of 6.4 Eurocents/kWh is obtained at a power rating of about 4.5 MW (or 125 m diameter), but that the curve is very flat.

For comparison, Figure 12.33 shows the results of a similar calculation using a modified version of the National Renewable Energy Laboratory (NREL) offshore wind turbine cost model (NREL 2006), which was based on the use of a monopile support structure, as described in edition 2. Here the LCOE is expressed in 2002 US cents/kWh, using the same discount rate. It is seen that the minimum cost of energy occurs at the slightly lower power rating of about 3.5 MW (or 105 m diameter). The difference could be due to a more rapid rise in estimated monopile cost with turbine diameter, as this cost was assumed to vary as the square of turbine diameter rather than as diameter^{1.5} for the jacket cost.

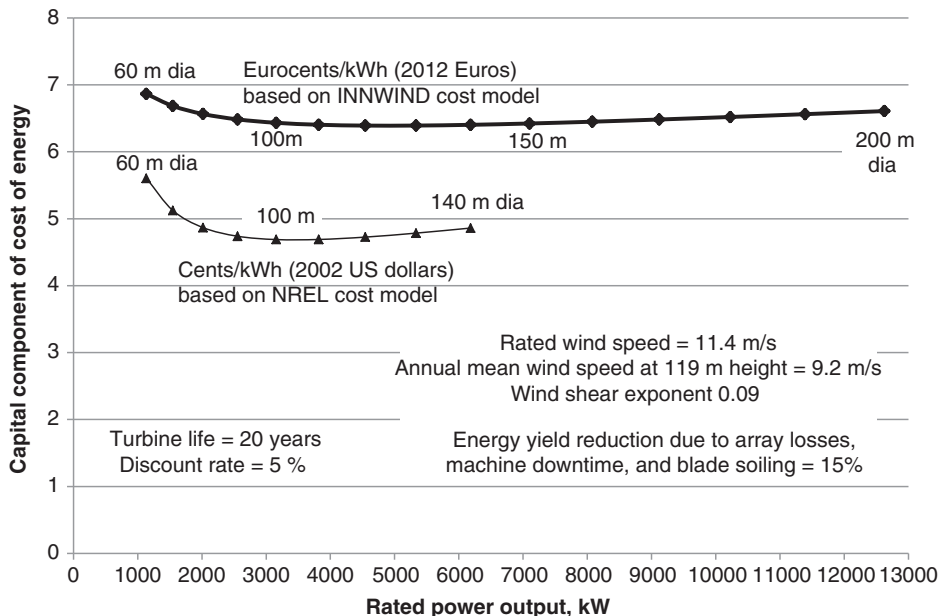


Figure 12.33 Variation of cost of energy with turbine diameter based on INNWIND cost model for turbines supported on jacket structures.

12.5 Reliability of offshore wind turbines

Wind turbines are expected to operate at high levels of reliability, whether sited on land or at sea, because any equipment failure is likely to lead to significant downtime while a repair crew is mobilised. Figure 12.34 shows the failure rates for different wind turbine sub-assemblies derived from two large European surveys, together with the downtimes per failure (WMEP = Wind Scientific Monitoring and Evaluation Programme, based at the Fraunhofer Institute of Wind Energy Systems, Kassel, and LWK = Landwirtschafts-kammer, Schleswig-Holstein).

In the case of offshore wind turbines, access is both time consuming and expensive in itself and also extremely weather sensitive, leading to much longer downtimes, so the premium on high reliability is an order of magnitude greater.

This section briefly considers measures to improve turbine reliability under the following headings – machine architecture, redundancy, protection against corrosion and condition monitoring.

12.5.1 Machine architecture

Although a wind turbine has an irreducible number of core components, the pursuit of maximum energy yield, grid compatibility and drive train compliance, particularly in the context of large machines, has led to greater complexity and the overwhelming dominance of variable-speed, pitch-regulated machines offshore. It so happens that the two additional systems required for this type of turbine – namely the frequency convertor

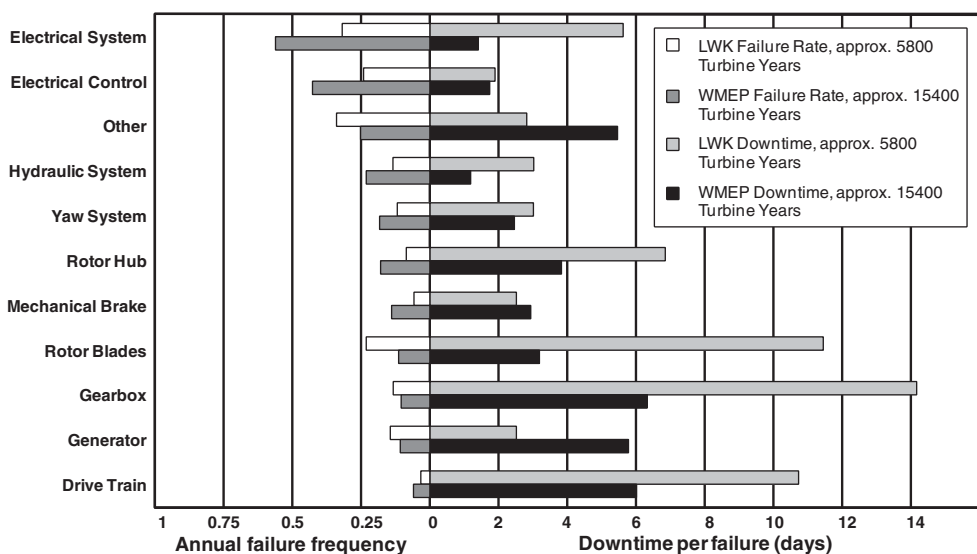
Failure Rate and Downtime from 2 Large Surveys of European Wind Turbines over 13 years

Figure 12.34 Wind turbine sub-assembly failure rates and downtime per failure based on 20 000 turbine years of data from two European surveys. Source: Reproduced with the permission of the University of Durham and the Fraunhofer Institute of Wind Energy Systems.

and the pitch control mechanism – were found to be the systems responsible for the largest percentages of downtime (20% and 13% respectively) in the Reliawind reliability field study (Wilkinson et al. 2010).

While it has to be accepted that large, fixed-speed wind turbines are impractical because power swings are insufficiently damped, the benefit of the pitch control system can be questioned offshore, it being necessary to weigh up whether the extra energy generated justifies the net additional cost, after allowing for the energy lost in extra downtime. Clearly, in the absence of pitch control, an alternative braking system has to be provided – in the form of tip-brakes, for example – and its cost accounted for.

The use of a direct drive generator enables one major component, the gearbox, and its attendant failures to be eliminated. Although gearbox failure rates are relatively low, the resultant downtime was found to be the highest of all sub-assemblies in the WMEP and LWK studies (Figure 12.34). However, research by Spinato (2009) indicates that the aggregate failure rate of generators and converters in direct drive wind turbines was greater than the aggregate failure rate of gearboxes, generators and converters in geared wind turbines, blunting the benefit of gearbox elimination. Nevertheless, the transition to direct drive may still result in improved availability as the downtimes of failed generators and converters are less than those of gearboxes.

12.5.2 Redundancy

While the provision of redundancy is mandatory for safety critical systems, the duplication of critical components to secure greater operational reliability also merits

consideration, particularly offshore. Examples already implemented by some manufacturers include the deployment of two separate systems to measure blade pitch angle and the provision of spare frequency converter modules. A similar philosophy can be extended to the design of mechanical systems such as the pitch mechanism and yaw drive, whereby a reserve of strength is built in to increase the likely service life.

12.5.3 Component quality

Reliability benefits will justify the use of higher quality components offshore in some cases. For example, double row pitch bearings will be more robust than those with only a single race.

Spinato (2009) observed that the failure rates of wind turbine generators and converters was higher than found in other industries, at least during the initial phases of operation, and recommended that they be subjected to more thorough testing. However, he found the reliability of wind turbine gearboxes to be on a par with that of comparable gearboxes in other industries.

12.5.4 Protection against corrosion

The concentration of salt particles in the marine atmosphere, which is much augmented by the wind (Gong et al. 1997), means that extra measures must be taken to protect offshore wind turbine components. Besides high-spec surface coatings, these include the use of a sealed generator with an air to air heat exchanger and similar arrangements for other items of electrical equipment, such as the transformer. Air discharged from these heat exchangers helps to maintain the air in the nacelle above the dew point and prevent condensation. In addition, the nacelle and/or hub can be pressurised, to prevent the entry of moist, salty air. In the absence of a partition between the nacelle and hub, this requires the provision of a labyrinth seal between the spinner and nacelle to minimise air leakage.

12.5.5 Condition monitoring

Clearly reliability can be much improved if incipient defects can be detected by condition monitoring before they result in a systems failure. Traditionally the health of wind turbine systems has been monitored by measures such as

- Automatic flagging of alarms when such parameters as oil pressures, bearing temperatures, and vibration exceed levels short of the trip level.
- Regular inspections – for example, of gear teeth wear and high-speed shaft alignment.
- Observation of machine running.
- Regular oil sampling.

These are all examples of condition monitoring, which has been defined as ‘the process of monitoring a parameter of condition of machinery, such that a significant change is indicative of a developing failure’.

The expense and difficulty of regular visits to offshore turbines has encouraged the expansion and development of remote or online condition monitoring techniques, particularly in relation to gear trains and bearings. They require detection of the onset of particular failure mechanisms and the establishment of measurable criteria for determining whether intervention is necessary. The CONMOW project final report titled ‘Condition Monitoring for Offshore Wind Farms’ (Wiggelinkhuizen et al. 2007) and the Offshore M&R Final Report ‘Advanced Maintenance and Repair for Offshore Wind Farms Using Fault Prediction and Condition Monitoring Techniques’ (ISET 2006) provide helpful surveys of available techniques and their usefulness, together with reports on field trials, while Crabtree (2010) lists condition monitoring systems then commercially available.

Some of the different condition monitoring techniques are considered below.

Drive train vibration monitoring

Accelerometers are mounted on the gearbox and generator casings, permitting the vibration signature at each location to be continuously monitored. For fixed-speed machines, each signal can be processed using a fast Fourier transform (FFT) to compute the vibration spectrum, which will contain spectral peaks corresponding to gear teeth meshing frequencies and shaft rotational speeds of the different gear stages. The behaviour of such vibration signatures over time can then be monitored to observe changes due to bearing wear or tooth damage, although this will be more difficult for some components, such as planet bearings, where the indirect vibration transmission path to the accelerometer on the casing makes the spectral peak difficult to detect. Also, in the case of the low-speed shaft bearing, the shaft rotational speed is too low for wear detection by accelerometer.

Vibration signatures will vary with power level, wind speed and yaw error, so they should be sorted into different bins accordingly. Irregularities will be more apparent if data is centralised, so that comparisons between different turbines of the same type can be made.

In the case of variable-speed machines, the frequencies of the various spectral peaks will be continuously changing, so order tracking techniques must be used to produce spectra in which the frequencies are normalised by the turbine rotational speed. One such method is synchronous order tracking, in which a shaft encoder is used to control the signal sampling rate at a fixed number per revolution before FFT analysis. Alternatively, a once-per-rev tachometer signal can be fed into the analyser so that its sample rate is varied in proportion to RPM. A simpler option is to restrict vibration monitoring to periods of operation above rated wind speed, when the turbine rotational speed is almost constant.

It is clear from the above that a vibration monitoring system will produce a vast amount of data, which requires dedicated signal processing software programmed to flag up suspect vibration signature changes. Ideally, a team of experts would be able to interpret the changes and rule on when action would be necessary, but the CONMOW report concluded that, in 2007, there was as yet insufficient experience to permit such predictions, so the usual response to data abnormality was to shut down the machine or increase the frequency of inspections.

Lubricant oil debris detection

Equipment to measure debris concentrations in lubricating oil can detect the onset of a wear failure, without the need for regular oil sampling and analysis. However, the equipment has to be installed in the lubrication pipework used when oil is delivered to bearings and gears under pressure so is not applicable in the case of splash lubricated gearboxes.

Nacelle vibration monitoring

Nacelle accelerometers mounted in the transverse and fore-aft directions can detect rotor mass imbalance and blade pitch errors. Rotor mass imbalance can increase due to water ingress or icing. Special accelerometers, known as *static accelerometers*, are required, capable of responding to the low blade rotation frequency (ISET 2006).

Pitch bearing resistance

In the case of electrical pitch drives, pitch bearing condition can be monitored by measuring the motor current, large peaks in the signal being indicative of jerking movements due to bearings sticking.

Added value

The benefit of a condition monitoring system is clearly reduced if there are significant numbers of false alarms, which can be due to the over cautious setting of alarm levels or faults with the system itself. Although the CONMOW study looked at the factors determining added value, including the level of false alarms, it drew no general conclusions about the overall benefits of installing a condition monitoring system.

12.6 Fixed support structures – overview

Support structures for offshore wind turbines are inevitably much more massive than those for onshore turbines, because of the greater hub height relative to the foundation and the additional loading from waves. As a result, they constitute a much higher proportion of offshore turbine installed cost than is the case on land, rendering economic design that much more important.

Minimum hub heights are governed by regulations prescribing a minimum clearance between blade tip and seawater level. In the UK the Maritime and Coastguard Agency recommends that there should be a minimum clearance between the sea level at mean high water springs (MHWS) and wind turbine rotors of 22 m (MGN 371 2008).

Most offshore wind turbine designs have evolved from onshore designs, so it has been common practice to utilise the onshore tower design offshore above wave crest level and interpose an additional structure – termed the *sub-structure* between it and the seabed. Although the term *support structure* applies to the complete structure supporting the nacelle, this section will concentrate on the sub-structure.

Sub-structure design requires considerable expertise in offshore structures and marine loading, so it is entrusted to companies experienced in this field, with the result that it is normal for different design teams to work on the sub-structure and on the

wind-turbine tower. This has led to calls for the design of the whole support structure to be integrated, to enable a more efficient allocation of materials to sub-structure and tower to be achieved. Research suggests that this could lead to significant savings – see, for example, Gentils et al. (2017).

Five different types of sub-structure have been utilised offshore to date – monopiles, gravity bases, jacket structures, tripods, and tripiles – and these are considered in turn in the following sub-sections. Monopiles have proved the most popular, accounting for about 80% of support structures, followed by jackets (~15%) and gravity bases (~5%) (BVG Associates 2019).

Fatigue analysis of monopiles in the frequency domain is explored in a separate sub-section (Section 12.7.4).

12.7 Fixed support structures

12.7.1 Monopiles – introduction

The monopile is a steel cylindrical tube driven into the seabed, with or without the assistance of excavation from within. In soft rock, a socket may be drilled out beforehand – typically at slightly reduced diameter – to receive the pile. The wave loading contribution to mudline moment increases much more rapidly with depth than the wind loading, so monopiles used to not be considered competitive for water depths much above 25 m, apart from limits imposed by manufacturing capability. Diameters are typically in the range of 4–8 m on existing wind farms, but the manufacturing capability now exists to fabricate monopiles of up to 11 m diameter (SIF 2020; EEW 2020). Monopiles have now been installed in waters of around 35 m in depth – e.g. at Greater Gabbard, Galloper, and Sandbank – and at Galloper are 7.5 m in diameter (Galloper 2020).

Most monopile foundations consist of the monopile itself and a transition piece connecting the monopile to the tower base. In view of potential difficulties in maintaining the monopile accurately vertical during the driving operation, a grouted sleeve joint is sometimes employed between the monopile and the transition piece to allow latitude for correction of monopile inclination. Figure 12.35 shows such an arrangement.

Where monopile verticality can be reasonably assured, a bolted joint can be used between the monopile and the transition piece, but the grouted sleeve joint is normally retained as well to provide mounting points for secondary steelwork (e.g. access ladder, sacrificial anode fixings) together with corrosion protection for the monopile. Alternatively, the transition piece can be eliminated and the tower bolted directly to the monopile flange. This latter solution was adopted at Scroby Sands, as driving conditions were considered sufficiently favourable. Such pile-only solutions are increasing in popularity, though they do mean long and heavy piles, with weights of 1500 tonnes or more anticipated.

Monopile design must keep steel stresses, pile top rotations and the support structure natural frequency within acceptable ranges. A simplified design procedure for achieving this in a preliminary design has been set out by Arany et al. (2016).

Inevitably the greatest area of uncertainty is the behaviour of the soil in which the pile is embedded, so this is considered in some detail in the following section, with a focus on recent research. Steel design in general is discussed in Section 12.7.3, while Section

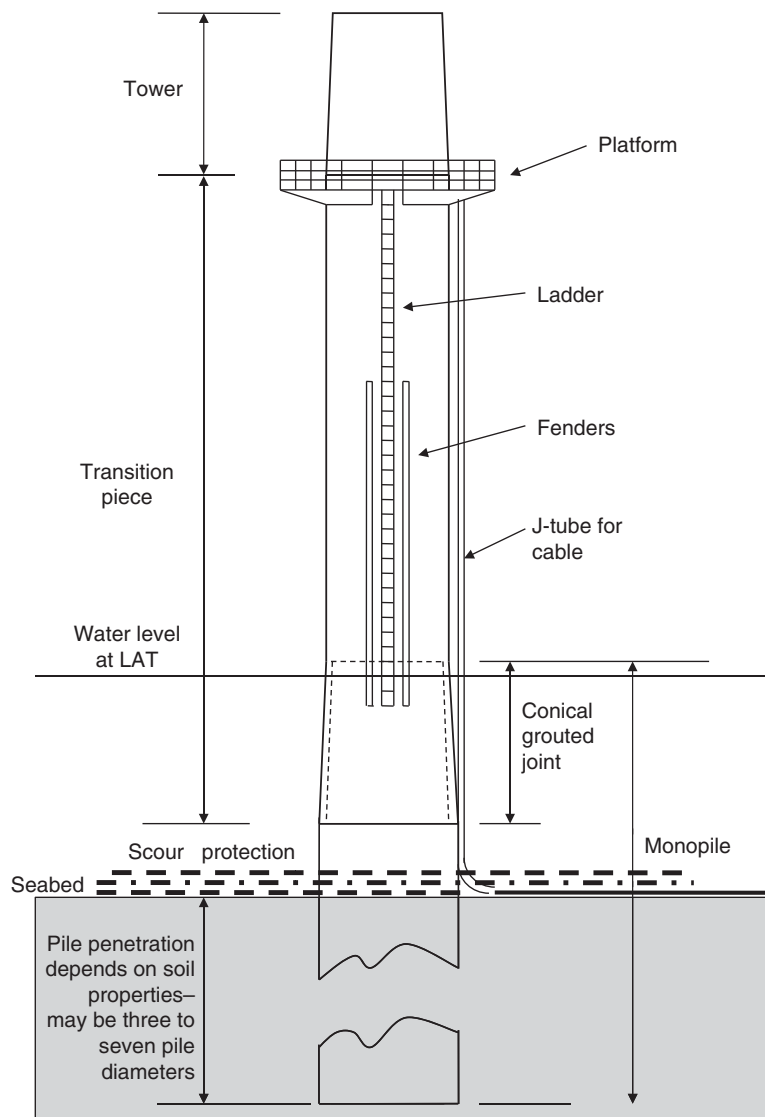


Figure 12.35 Indicative arrangement of monopile and transition piece with intermediate conical grouted joint.

12.7.4 looks at the use of spectral techniques in assessing fatigue damage due to wave loading.

12.7.2 Monopiles – geotechnical design

The geotechnical design of a monopile supporting a wind turbine has to satisfy three principal requirements – i.e. it has to

- Resist the extreme overturning moment.
- Limit the permanent rotation at the top of the monopile.
- Satisfy the constraints on support structure natural frequency.

In principle at least, any one of these can govern the diameter and embedment length required. In general, the soil in which the monopile is embedded has to be treated as a flexible medium that allows lateral movement and flexure of the pile below seabed level, with the pile rotating about some point usually in the lower half of the embedment.

The maximum permitted permanent rotation of the monopile at seabed level, including the effects of cyclic loading, is usually specified in the wind farm design basis, and the example value of 0.5° (0.0087 rad) quoted in DNVGL-ST-0126 (2016) or a higher value of 0.75° is often adopted. It is found that a rotation limit of this magnitude always governs monopile design rather than the ultimate soil resistance.

It has been normal to analyse the interaction between pile and soil by modelling the soil as a series of independent, non-linear lateral springs, known as *p-y* or *Winkler springs*, acting on the pile over the embedment depth. *P-y* curves defining the dependence of the lateral loading per unit depth on pile deflection in terms of soil properties were developed from the results of field tests on long, slender piles – i.e. 319 mm dia × 12.8 m long piles in soft clay (Matlock 1970) and 610 mm dia × 21 m long piles in sand (Reese et al. 1974) – and these formed the basis for recommendations in codes such as API RP 2A and ISO 19902.

The PISA project

The embedded length to diameter ratios (also known as the *aspect ratio*) of the monopiles supporting wind turbines are often an order of magnitude smaller than that used for the development of the *p-y* curves and, as a result, other forces acting on the pile take on much more significance. The consequent uncertainty about the validity of the *p-y* curve approach to the design of these stockier piles, combined with evidence from early offshore wind farms that support structure natural frequency measurements were higher than predicted (Kallehave et al. 2014), led to the setting up of a major research effort to establish more accurate design rules. The PISA Project, as it was known, encompassed

1. Extensive testing of piles of up to 2.0 m diameter and various aspect ratios under monotonic lateral loading at clay and sand sites.
2. 3-D finite element (FE) analyses corresponding to the geometry of the different tests utilising soil constitutive models developed for the strata at the two sites.
3. Comparison of 3-D FE analysis results with test results to validate the former.
4. Development of a one-dimensional (1-D) pile model from the 3-D FE analysis results, comprising non-dimensionalised load-displacement relationships for distributed lateral and shear loads, base shear, and base moment.

These four elements are described below in outline, but the reader is referred to Byrne et al. (2017) for a fuller overview and to the series of eight papers published in Géotechnique in 2019 and 2020 for detailed information (Byrne et al. 2019; Richards et al. 2019a

and b; Taborda et al. 2019; Zdravković et al. 2019a; Zdravković et al. 2019b; Burd 2020; Byrne et al. 2020).

Pile testing Testing was carried out in 2015 on piles in stiff clay at Cowden near Hornsea in East Yorkshire and in dense marine sand at Dunkirk in Northern France. Piles 0.76 m in diameter with embedded lengths ranging from 2.3 to 7.6 m and 2.0 m diameter piles with an embedded length of 10.5 m were all loaded horizontally at 10 m above ground level. The pile geometries selected embodied a range of embedded length to diameter (L/D) ratios extending from 3 to 10, which were deemed to be representative of monopiles deployed in wind farms.

The test piles were heavily instrumented with inclinometers, displacement transducers and high resolution fibre optic strain gauges, with the latter enabling the distribution of the soil lateral load on the pile to be computed by repeated differentiation. The results of such an analysis for a 0.76 m diameter pile embedded to a depth of 7.6 m in stiff clay are shown in Figure 12.36. The optimised model curves were obtained by solving the governing equations based on Timoshenko beam theory in such a way as to obtain the best fit to the inclinometer and strain gauge measurements shown in (b) and (c). There is excellent agreement between the model displacement, rotation, shear and moment at ground level and the actual values calculated from measurements.

3-D FE analyses 3-D FE analyses were carried out in advance for each of the pile configurations tested at the two sites so that they could be validated by the test results. In view of this objective, it was considered very important to develop soil constitutive models for the clay and the sand that reproduced the measured soil behaviour at both small and large strains as accurately as possible.

The clay till and dense sand materials were modelled using a development of the Modified Cam-Clay (MCC) model and a bounding surface plasticity type model, respectively, both formulated within the critical state framework (Zdravković et al. 2019a). The degradation of shear modulus at increasing strain levels was accounted for – e.g. as illustrated in Figure 12.37 for the clay till – and the model parameters were varied with depth to reflect the non-uniform ground conditions.

Three varieties of FE were employed to model the soil, the steel pile and the interface between them. The interface elements had zero tensile capacity in the direction perpendicular to the pile surface, so that the gap opening on one side of the loaded pile could be properly modelled.

The 3-D FE modelling of the Cowden clay and the Dunkirk sand are described in Zdravković et al. (2019b) and Taborda et al. (2019), respectively.

Validation of 3-D FE analyses The 3-D FE analyses were validated by comparing the predicted pile responses with those measured in the pile tests. Agreement was generally good, particularly at small displacements, as exemplified by the comparisons for 0.76 m diameter piles of different lengths in Figure 12.38. This gave confidence that the 3-D FE analyses would provide a sound basis for the development of the much simpler 1-D pile model.

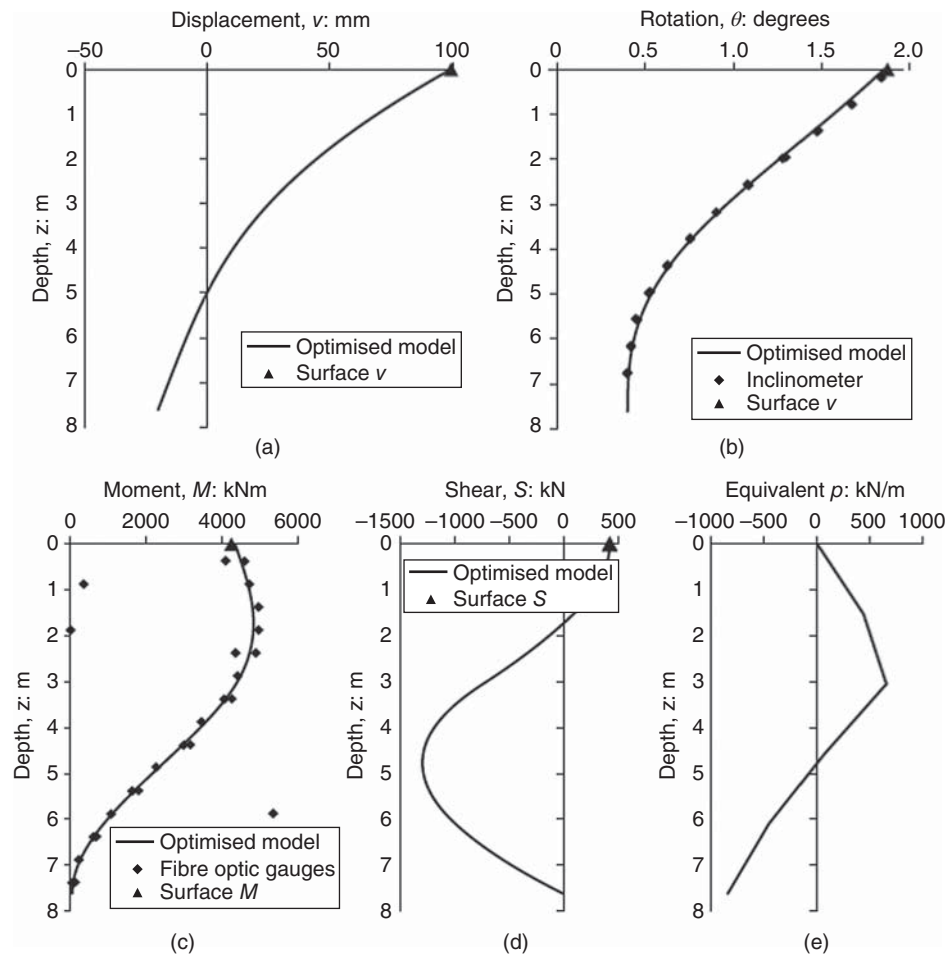


Figure 12.36 Response of 0.76 m diameter pile embedded to a depth of 7.6 m in stiff clay, computed from inclinometer and fibre optic strain gauge measurements, for a horizontal load of 425 kN applied at 10 m above ground level. Source: Reproduced from Byrne et al. (2019) licensed under CC-BY 4.0.

Development of the 1-D pile model Figure 12.39 shows the four soil reactions acting on the pile that are considered in the PISA 1-D model. These reactions are generally described by non-dimensional load-displacement curves defined by four parameters – the initial slope, the ultimate load, the displacement at which the ultimate load is reached and the curvature – see Figure 12.40.

In general, these parameters vary with depth for each load component and the forms of each depth dependency is obtained from a synthesis of the 3-D FE analysis results for each pile configuration in each case.

An illustration of the derivation of the non-dimensionalised ultimate distributed lateral load versus depth design curve for piles in clay till is shown in Figure 12.41, with

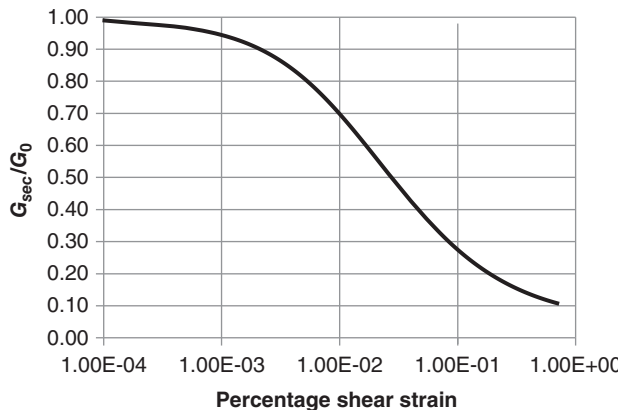


Figure 12.37 Degradation of clay secant shear modulus with increasing shear strain based on triaxial test results.

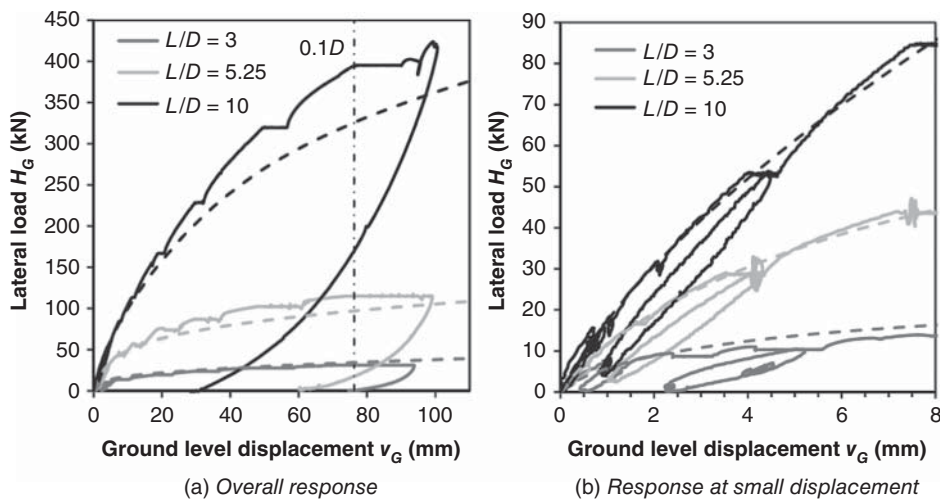


Figure 12.38 Comparison of measured and predicted ground-level load-displacement response for three L/D ratios at $D = 0.762$ m. Dashed lines represent the results of the 3-D FE calculations. Source: Reproduced with permission from Byrne et al. (2017).

the normalised variable for ultimate lateral load per unit depth taken as $\bar{p}_u = p_u/(s_u D)$. The solid lines are based on the loads and displacements computed from the various 3-D FE analyses and the best fit curve selected for design is shown by the dashed line. In this case the design curve is assumed to be of exponential form based on theoretical considerations, as follows:

$$\bar{p}_u = N_1 + N_2 \exp\left(\frac{-\xi z}{D}\right) \quad (12.45)$$

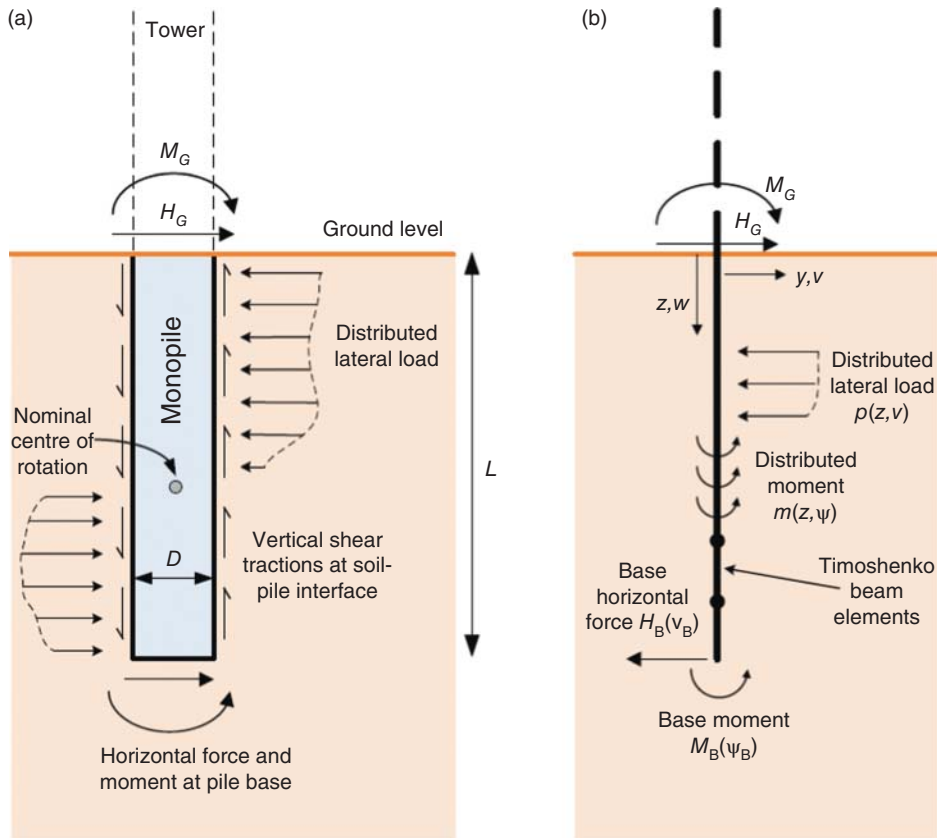


Figure 12.39 (a) PISA 1-D pile model showing the soil reaction components acting on the pile, and (b) the idealisation of the pile under these loadings in the 1-D FE model (with a consistent sign convention). Source: Reproduced from Byrne et al. (2020) licensed under CC-BY 4.0.

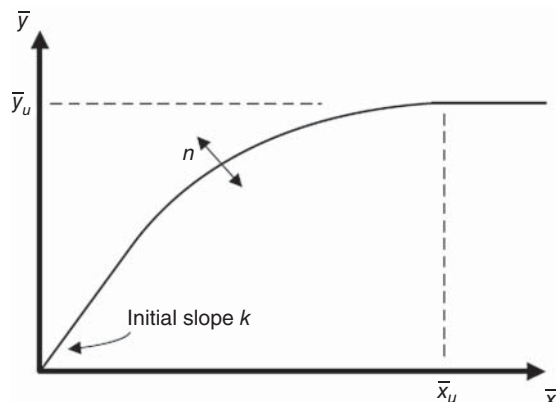


Figure 12.40 Form of non-dimensionalised load-displacement curves. Source: Reproduced from Byrne et al. (2020) licensed under CC-BY 4.0.

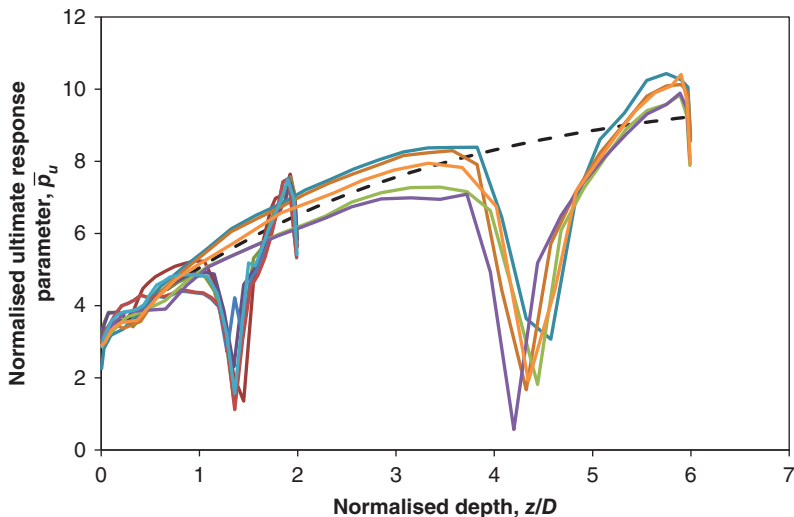


Figure 12.41 Non-dimensionalised ultimate lateral load per unit depth versus normalised depth for piles in clay till (dashed line). Source: Adapted from Byrne et al. (2020), licensed under CC-BY 4.0.

Note that the sharp dips in the ultimate lateral load plots derived from the FE analyses occur at the pile rotation points, where the ultimate load is not mobilised.

The relative contribution of the other three soil reactions was investigated and found to be over a quarter of the total for a stocky pile with $L/D = 2$ but only a 15th for a more slender pile with $L/D = 6$.

It should be emphasised that the soil reaction curve parameters derived for the clay till and dense sand are technically only valid for the soil strength profiles applicable at the respective test sites. However, in so far as the variation of soil strength with depth is similar at other sites, they can be applied with reasonable accuracy in these cases also. For detailed design calculations, it is recommended that site-specific 1-D model parameters are determined by a 3-D FE calibration process similar to that described above, utilising the actual soil strength profile obtained from the site investigation.

Layered soils

In a second phase of work, the fidelity of the PISA design model was assessed for layered soils by comparisons with data obtained from equivalent 3-D FE analyses, demonstrating a good agreement in most cases (Burd et al. 2020).

Potential benefits of PISA approach

The potential savings resulting from the adoption of the PISA design approach are best illustrated by an example (Byrne et al. 2017). The load-displacement response of an 8.75 m diameter pile embedded to 35 m depth in clay till was investigated under the action of a load applied at 87.5 m height – see Figure 12.42. It is seen that the ultimate lateral load capacity of this pile calculated according to the rules for $p-y$ models, such as in API RP 2A, is about 40% of that obtained using the 1-D PISA model.

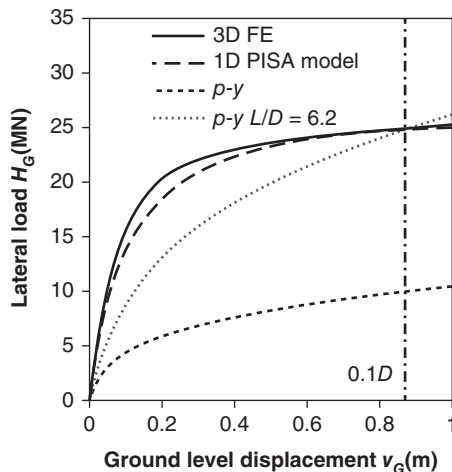


Figure 12.42 Large displacement response of an 8.75 m diameter pile embedded in clay till to a depth of 35 m ($L/D = 4$) when loaded at a height of 87.5 m. Source: Reproduced with permission from Byrne et al. (2017).

When a similar pile was designed according to the API RP 2A rules to achieve the 25 MN ultimate lateral load capacity predicted by the 1-D PISA model for 35 m embedment, it was found that an embedment of 54 m would be required ($L/D = 6.2$), indicating that use of the PISA method would have enabled a 35% material saving in the embedded portion of the pile.

Cyclic loading

Combined wind and wave loading will result in a monopile experiencing of the order of 10^8 load cycles varying in amplitude and direction during its lifetime, with significant effects on the surrounding soil. When, as is usual, there is a steady load component predominantly in one direction, a small permanent rotation in that direction will build up over time and this needs to be limited to a value acceptable to the turbine manufacturer – typically one half of one degree. Rather than analysing the soil behaviour in three dimensions, it is customary to develop models relating the monopile rotation to the moment loading over time in one or two dimensions.

The basic moment/rotation curves for a single unloading and reloading cycle can be derived from the initial loading curve, $\theta = f(M)$, using the Masing rules (Masing 1926; Beuckelaers 2017) for hysteretic behaviour. The rotation during unloading or reloading is given by $\theta = \theta_r + 2f\left(\frac{M-M_r}{2}\right)$, where θ_r and M_r are the rotation and moment at the previous stress reversal. To this must be added the permanent rotation, θ_p , which builds up over each cycle and accumulates over successive cycles – a phenomenon known as *ratchetting*. Typical initial, unloading, and reloading curves are illustrated in Figure 12.43, from which it is apparent that the secant modulus for reloading is much larger than for initial loading.

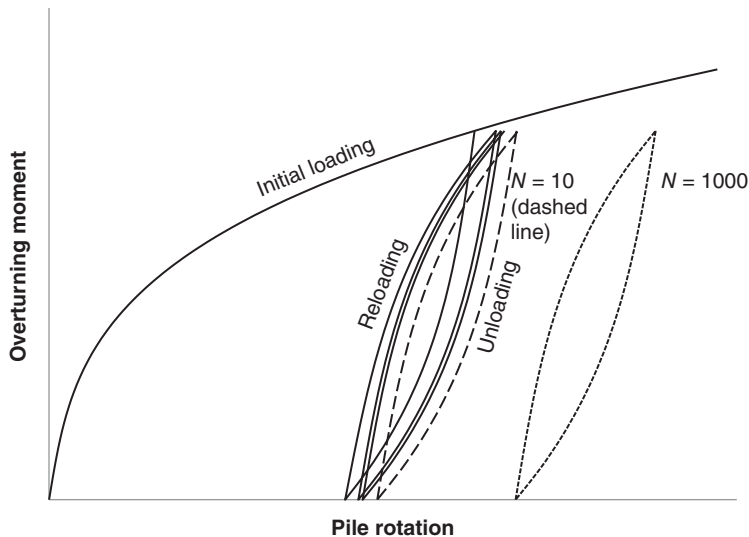


Figure 12.43 Pile rotation versus applied moment during initial loading and during unloading and reloading cycles.

Figure 12.43 shows the moment/rotation trajectories during initial loading and the first three unloading/reloading cycles. Also shown are those for the tenth and one thousandth unloading/reloading cycles.

Extensive model testing has been carried out at Oxford University (Leblanc et al. 2010; Richards et al. 2019a, b) to investigate monopile response to cyclic loading, using an 80 mm diameter rigid tube driven into sand to a depth of 360 or 320 mm. Leblanc concluded that the accumulated monopile rotation due to N constant amplitude loading cycles could be described by the equation

$$\Delta\theta(N) = \theta_s \cdot T_b \left(\frac{M_{\max}}{M_r}, R_d \right) \cdot T_c \left(\frac{M_{\min}}{M_{\max}} \right) \cdot N^{0.31} \quad (12.46)$$

where θ_s is the rotation due to initial loading, T_b and T_c are dimensionless functions depending on the load characteristics and relative density, R_d , and M_r is the monopile ultimate moment capacity. T_c defined as unity when M_{\min} is zero. The variations of T_b and T_c with M_{\max}/M_r and M_{\min}/M_{\max} , respectively, that were obtained are shown in Figure 12.44. This indicates that the accumulated rotation increases linearly with M_{\max}/M_r and grows much more rapidly when M_{\min} is negative.

LeBlanc et al. proposed that model tests and full-scale test results be compared using the following relationship between non-dimensionalised moment and rotation parameters:

$$\widetilde{M} = f(\widetilde{V}, \widetilde{e}, \eta) \widetilde{\theta} \quad (12.47)$$

where $\widetilde{M} = \frac{M}{L^3 D Y'}$, $\widetilde{V} = \frac{V}{L^2 D Y'}$, $\widetilde{e} = \frac{M}{H L}$, $\eta = \frac{L}{D}$, $\widetilde{\theta} = \theta \sqrt{\frac{p_a}{L Y'}}$, Y' is the soil effective unit weight and p_a is atmospheric pressure. The shear modulus is assumed to increase

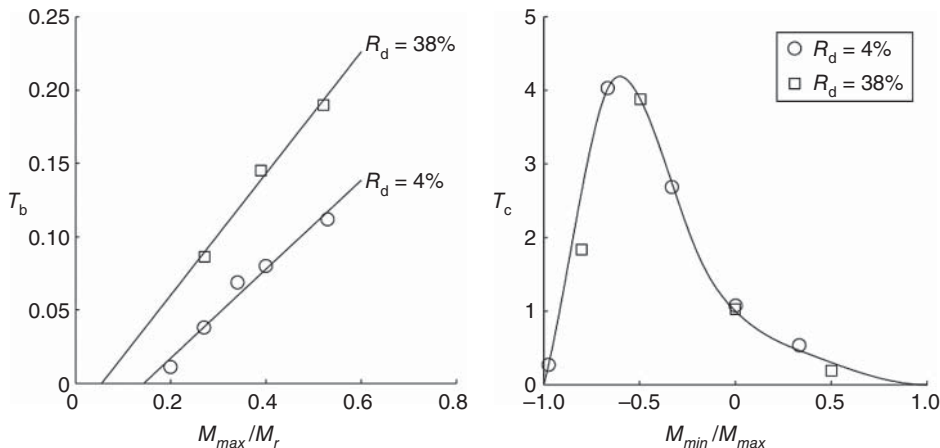


Figure 12.44 Variation of dimensionless functions T_b and T_c with M_{max}/M_r and M_{min}/M_{max} , respectively. Source: Reproduced with permission from Leblanc et al. (2010).

with depth according to the square root of the vertical effective stress. There is inevitably uncertainty in this assumption and in the translation of the full-scale relative density to an equivalent (much lower) model-scale relative density to yield the same friction angle, so caution should be exercised in applying model test results to full-scale design. However, large field-scale testing in dense sand carried out as an adjunct to the PISA project demonstrated that the accumulated pile rotation increased approximately as $N^{0.31}$ – i.e. in-line with Eq. (12.46) (Beuckelaers 2017). A similar result was obtained for parallel tests in clay.

Given the complexity of the load regime experienced by wind turbine monopiles and the large number of cycles, recourse to a suitable analytic model is a very attractive option, provided it can be suitably calibrated. One such model is the Hyperplastic Accelerated Ratcheting Model (Houlsby et al. 2017), which captures both non-linear hysteretic and ratcheting behaviour and allows the mimicking of the ratcheting taking place in a very large number of identical cycles by the use of a much smaller number in the model.

The response to cyclic loading will become a more important design consideration as the less conservative design rules for monotonic loading embodied in the PISA approach are adopted more widely.

Scour

Currents and water motion due to waves will cause significant seabed erosion around a monopile if the seabed is formed of sand or other granular material. Based on a comprehensive set of experiments, Sumer and Fredsoe (2001) concluded that the maximum scour depth occurs under the action of sea current alone, and reaches a depth of 1.3 times the pile diameter, D , on average, with a standard deviation of 0.7 D .

Scour of this magnitude clearly has implications for both foundation stability and support structure natural frequency, so it is often decided to deposit (and maintain) scour

protection in the form of rock armour to prevent it. This can be either laid on the seabed before or soon after installation of the monopile (static scour protection) or after a few weeks, when a scour pit will have developed to receive it (dynamic scour protection). The disadvantage of static scour protection laid over the seabed is that scour can occur at the edges, degrading the rock protection there, but this can be allowed for when the radial extent of protection is determined.

A design aid for scour hole depth prediction and scour protection design, known as the *Opti-Pile Design Tool* (den Boon et al. 2004), has been developed and calibrated against model test results and data from existing wind farms. This enables the size of rock that is stable under maximum current conditions to be calculated, together with the radial extent of protection required. As might be expected, the model tests reported by den Boom et al. indicated that larger rock sizes were required when the scour protection was raised proud of the seabed level, as in the static protection, than when it was recessed beneath it.

Whitehouse et al. (2011) investigated the scour depths measured at five UK offshore wind farms where the seabed material was predominantly non-cohesive but scour protection was not provided, and they found that the maximum recorded scour hole depth was $1.38D$. They also collated data from monopiles where scour protection had been provided and, perhaps surprisingly, found that greater scour depths were recorded on the periphery of the rock protection in some instances. This was ascribed to the flow disturbance caused by the rock mounds.

The susceptibility of clay to scour is less well understood, but Whitehouse et al. (2011) consider that clay with an undrained shear strength of 100 kPa or more is likely to be resistant to scour in areas of open sea.

12.7.3 Monopiles – steel design

The steel design is governed by three key factors

- Resistance to extreme loads.
- Resistance to fatigue loads.
- Tuning of support structure natural frequency to avoid excitation by cyclic loading.

Normally, extreme wave loads, being dominated by drag, increase linearly with diameter, whereas fatigue wave loads, being dominated by inertia loading, increase as the diameter squared, like the section modulus. However, the wind load component of monopile bending moment is virtually unaffected by diameter, so it would clearly be beneficial to increase monopile diameter and reduce wall thickness until the decline in buckling resistance stress precludes further reductions in cross-sectional area. Often though, practical considerations such as compatibility with the tower base diameter – assuming a parallel-sided transition piece – and manufacturing capability limit the monopile diameter to a smaller value.

Wave fatigue loads depend on the support structure mode shape [see Eq. (12.63) in Section 12.7.4], which in turn depends on the stiffness distribution, so design against fatigue loads is inevitably an iterative process. Accordingly, it is simpler to develop an initial design based on resistance to extreme loads that can then be used to obtain an

initial mode shape and set of fatigue loads. It should be noted that, when wave loading is a significant factor in the design, the extreme load bending moment distribution will exhibit a pronounced knee near wave crest level, which may well be absent from the fatigue load bending moment diagram. This is because the fatigue loads usually excite support structure resonance, for which the bending moment distribution is dominated by the tower head mass rather than the wave load itself. Consequently an onshore tower design may be unsuitable for use offshore because of wave-generated fatigue loads, even though the waves do not strike the tower itself. Example extreme and fatigue load bending moment distributions for a 5 MW turbine support structure are shown in Figure 12.45.

It is seen that extreme loads are more likely to govern the design at seabed level, whereas fatigue loads are more likely to govern at wave crest level, although, if the critical fatigue detail category is assumed to be 90, fatigue loads govern down to seabed level in this case. In the general case, a range of factors, including the relative magnitude of extreme and fatigue loads, the critical fatigue detail category and the monopile wall slenderness, will determine whether extreme or fatigue loads govern at different heights.

When the design for fatigue and extreme loads is complete, the suitability of support structure natural frequency can be verified and adjusted as necessary.

Wind turbines deployed offshore are substantially larger than most of those deployed on land, and consequently nearly always operate at variable speed, because this allows power fluctuations in the wind to be absorbed by rotor acceleration rather than by rapid fluctuations of electrical power. The ratio of maximum to minimum rotational speed is usually quite wide – from 1.5 to 2.5 – with the result that the band of frequencies available for the tower natural frequency between the maximum rotational frequency

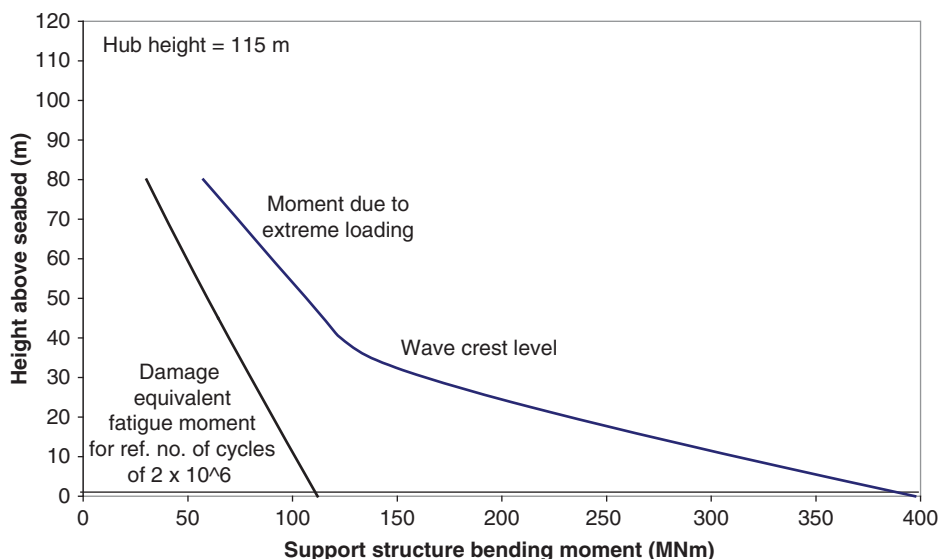


Figure 12.45 Variation of extreme and fatigue moments over height of support structure for 5 MW wind turbine.

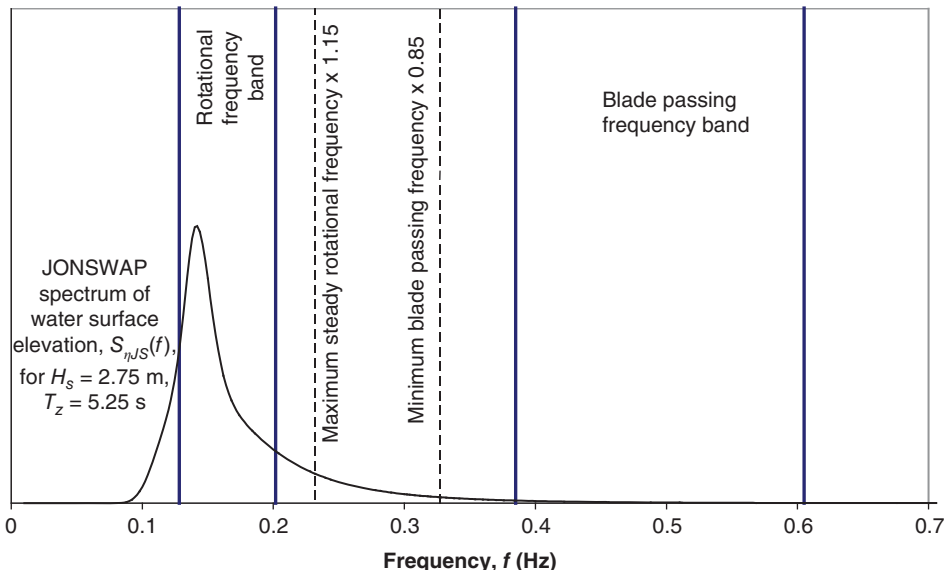


Figure 12.46 Support structure natural frequency exclusion zones for a 5 MW turbine with maximum to minimum rotational speed ratio of 1.57.

and the minimum blade passing frequency is considerably narrowed. This is illustrated for a 5 MW wind turbine in Figure 12.46.

Given that there needs to be roughly a 15% margin between a turbine exciting frequency and the support structure natural frequency, it can be seen that in this case the range of feasible frequencies is limited to 0.23–0.33 Hz.

For a 6 m diameter monopile supporting a 5 MW turbine in water of about 20 m depth it is found that a design providing adequate strength under extreme and fatigue loading has a natural frequency just above the 0.23 Hz lower limit.

Fatigue analysis is considered further in Section 12.7.4.

Transition piece

As noted in the introduction, it is normal to introduce an additional cylindrical tube – termed the *transition piece* – between the monopile and the base of the tower (see Figure 12.35). The transition piece (or TP) is usually sleeved over the monopile, with an overlap length 1.5 times the diameter being required if the sleeve joint forms the load path between the two elements. In this case, the nominal gap between the tubes is around 150 mm to allow sufficient latitude for the TP to be set vertical if the monopile is tilted. Design of the grouted joint is considered under a separate sub-heading below.

At some wind farms, there is a flanged bolted joint between the transition piece and the top of the monopile, in addition to the sleeved, grouted joint. The bolted joint is then designed for the full applied moment and the transition piece sleeve provides mountings for secondary steel work while the grout serves as corrosion protection for the monopile. This arrangement is only suitable at sites where the verticality of the driven monopiles can be assured.

It is normal to locate an external platform encircling the tower base at the top of the transition piece, to facilitate turbine access and the transfer of tools and spares. A small Davit crane is normally mounted on the platform for this purpose. Boat access is by means of a ladder fixed to the outside of the transition piece between a pair of vertical tubes that act as fenders (Plate 5).

The height of the platform, and thus of the top of the transition piece, is normally set so that there is an adequate clearance, known as the *air gap*, between the platform and the crest of the highest wave, including allowance for tidal range and storm surge. The target air gap may be 1.5 m. If, as is often the case, the top of the monopile is set at HAT, the length of the transition piece required comes to the sum of the sleeve length, the storm surge, and the crest elevation of the 50 year return wave, ηH_{50} , plus 1.5 m. In UK waters with significant tidal range, transition pieces over 25 m long may be used, leading to weights of several hundred tonnes. As an example, the 23 m × 6.5 m diameter transition pieces supporting 8 MW turbines on the Burbo Bank Extension (near Liverpool) each weigh 450 tonnes, of which 236 tonnes is primary steel (Bladt Industries 2016). In deeper waters, where monopiles 6 m in diameter and above are required, it may be beneficial to taper the transition piece diameter down above the grouted joint to reduce exposure to wave loading and match up with the smaller tower base diameter.

Cable ducts

The wind turbine power cables are routed through steel protective tubes known as *J-tubes*, which may be located either inside or outside the transition piece/monopile. The J-tubes are so-called because they incorporate a 90° bend at seabed level to enable the cable to exit horizontally. The cables can be left to hang free vertically within the pile but may need to be restrained against lateral excitation by pile motion.

Corrosion protection

The approach to corrosion protection varies over the height of the monopile and transition piece according to the type of exposure. Three zones are defined – the atmospheric zone, the splash zone, and the submerged zone, which includes the embedded portion. DNVGL-RP-0416 (2016), *Corrosion Protection for Wind Turbines*, gives recommended protection measures for these different zones as detailed in Table 12.7.

Normally the cathodic protection is in the form of sacrificial anodes, which may weigh about 5 tonnes for the external protection of a 5 m diameter pile in 20 m water depth, using zinc based anodes.

Prior to 2010, there was no requirement for corrosion protection of the monopile internal surface in the submerged zone if it was within an airtight compartment created by a sealed platform higher up. However, many instances of internal corrosion have been recorded, suggesting that air exchange through the cable seal or access hatch has been taking place. The recommendations have been strengthened as a result.

Grouted joint design

The grouted joint between the monopile and transition piece must be capable of supporting the weight above and of resisting the overturning moments and torsional loads.

Table 12.7 Support structure corrosion protection measures by zone.

Zone	Corrosion protection on external surfaces	Corrosion protection on internal surfaces
Atmospheric zone	Coating	Coating
Splash zone above mean water level (MWL) (Upper level defined as 1 yr return high water level plus half of 1 yr return significant wave height)	Coating and corrosion allowance for period when coating is life-expired (Minimum corrosion rate = 0.3 mm/yr in temperate climate)	Coating and corrosion allowance for period when coating is life-expired (Minimum temperate corrosion rate = 0.1 mm/yr)
Splash zone below MWL (Lower level defined as 1 yr return low water level minus half of 1 yr return significant wave height)	Cathodic protection and optional coating	Cathodic protection or corrosion allowance with optional coating in either case
Submerged zone	Cathodic protection and optional coating	Cathodic protection or corrosion allowance with optional coating in either case
Buried zone more than 1 m below seabed	No corrosion protection	No corrosion protection

Source: From DNVGL-RP-0416 (2016).

Axial and torsional loads produce shear at the grout/steel interfaces, whereas the overturning moment produces compression, so it is normal to treat the two types of load separately.

1. **Overturning moment:** Moment is transferred between sleeve and pile by compression stresses in the grout, which vary approximately linearly from zero at joint mid-height to maxima at the top and bottom, and by horizontal and vertical shear stresses. Assuming the transition piece is sleeved over the monopile, the compression in the upper half of the joint is on the upwind side and the compression in the lower half of the joint is on the downwind side.

The horizontal forces between sleeve and pile generate high shear stresses in the wall of each, and these approach the maximum permitted for the recommended grouted joint L/D ratio of 1.5 when the applied moment reaches the sleeve/pile moment capacity. However, although the nominal compression stresses in the grout are relatively low – of the order of 5 or 10 MPa for a fully loaded joint, there is a significant stress concentration at each end of the joint, and the design may be governed by the grout tension stress arising as a result of shear stress in the grout generated by the moment loading acting in combination with the compression stress.

2. **Axial and torsional loads:** Shear across the grout/steel interface due to axial and torsional loads can be resisted by the provision of shear keys in the form of weld beads or thin steel bars welded to the steel tube. However, each shear key introduces a fatigue stress raiser, which militates against their use.

In the absence of horizontal shear keys, the vertical load has to be transmitted by an alternative means. In many early installations, reliance was placed on friction at the cylindrical steel–grout interfaces acting in combination with the radial stresses generated by surface irregularities sliding past each other when initial slippage took place. However, it was found that slippage continued intermittently over a period of years, eventually requiring remedial measures, so the friction load path is no longer considered acceptable (Lotsberg et al. 2011). Instead, conical tapered joints with a very small cone angle are now used in place of cylindrical ones, so that the vertical load can be resisted by the vertical component of the compressive stress in the grout acting normal to the conical steel surfaces. A small amount of settlement must take place to generate the necessary hoop stresses in the steel components. The DNVGL standard *Support Structures for Wind Turbines*, DNVGL-ST-0126 (2016), specifies a maximum cone angle of 4°.

Monopiles in deeper water

Wind loads dominate monopile bending moments in shallow waters because wave loads act at a much smaller lever arm, so monopile weight would be expected to simply increase in proportion to monopile length at first. However, in deeper water, wave loading begins to dominate, monopile diameter has to increase and weight increases much more rapidly.

De Vries and Krolis (2007) prepared a family of outline support structures designs for the Vestas V90 3 MW wind turbine in various water depths between 20 and 50 m, taking a design extreme wave height of 20.3 m appropriate for a North Sea site 80 km from the Dutch coast. The designs were configured to achieve a target natural frequency of 0.32 Hz and satisfy buckling strength requirements. Figure 12.47 shows the resulting variation of the weight of the support structure (comprising monopile, transition piece, and tower) with water depth.

The weight for 20 m water depth is below the general trendline because, in this case, the extreme wave height is depth limited, so platform height and hub height are both reduced. To put the support structure weights in context, it can be noted that the turbine weight (rotor, hub and nacelle) for the Vestas V90 is only 112 tonnes.

The selected monopile diameters ranged from 4 m at 20 m water depth to 6 m at 50 m depth – well within the 10 m diameter capability of some existing production facilities.

12.7.4 Monopiles – fatigue analysis in the frequency domain

In the short term, wind and wave loading are statistically independent processes, which means that the power spectra of the loads at any cross-section of the support structure from the two sources can simply be added together to obtain the power spectrum of

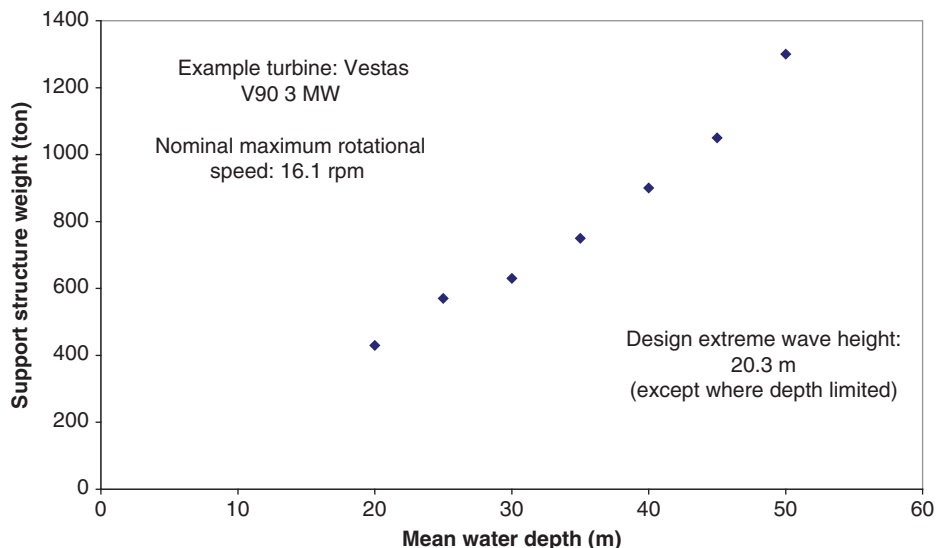


Figure 12.47 Variation of support structure weight with mean water depth. Source: From Van der Tempel (2006).

the total load. This section considers the treatment of wave and wind loading fatigue separately to begin with and then the combination of the two.

Wave loading in the frequency domain

On offshore wind turbine structures, the established method for calculating wave fatigue damage in the frequency domain on oil and gas platforms can be utilised. The attraction of the method is that it is computationally much more efficient than undertaking numerous simulations in the time domain followed by rainflow cycle counting. The procedure starts with obtaining a stress spectrum for the point under consideration from the wave spectrum for each sea state by means of a transfer function, which relates the stress amplitude to the wave height at each frequency. Each stress spectrum is then converted to a stress range probability distribution (e.g. by means of the Dirlitk formula, Section 5.9.3), which, in combination with the appropriate S-N curve, enables the fatigue damage arising from exposure to each sea state to be derived. Finally, the damages from all of the sea states are summed to obtain the total fatigue damage at the point under consideration.

The method depends on a *linear* relationship between wave loading and wave height. As set out in Section 12.3.9, Morison's equation for wave loading on a cylinder contains two terms – the inertia term, which is linear with respect to wave height, and the drag term, which is not. Fortunately, the non-linear drag term can typically be ignored when calculating fatigue loading, as inertia loading dominates for Keulegan–Carpenter numbers of less than 11 (Figure 12.22), which corresponds to a wave height to cylinder diameter ratio of less than 3.5 in deep water.

The following section considers the various stages in the fatigue damage calculation in turn.

Bending moment and stress transfer functions for a monopile

Quasi-static behaviour For a cylindrical monopile support structure with radius r , the expression for the peak quasi-static mudline moment due to wave loading, M_0 , is obtained by integrating Morison's equation over the water depth. Hence,

$$\begin{aligned} M_0 &= C_M \rho \pi r^2 \int_{-d}^0 (\dot{u})_{\max}(z+d) dz = C_M \rho \pi r^2 \frac{Hgk}{2} \int_{-d}^0 \frac{\cosh k(z+d)}{\cosh kd} (z+d) dz \\ &= C_M \rho \pi r^2 \frac{Hg}{2} \tanh kd \left\{ d + \frac{1 - \cosh kd}{k \sinh kd} \right\} \end{aligned} \quad (12.48)$$

In deep water – i.e. for conditions in which $d > 0.08gT^2$ – this approximates to

$$M_0 = C_M \rho \pi r^2 Hgd/2 \quad (12.49)$$

In general, M_0 is frequency dependent, as the wave number, k ($= 2\pi/L$), depends on the wave frequency [see Eq. (12.15)]. The transfer function giving the ratio of peak quasi-static bending moment, M_0 , to wave amplitude for different wave numbers (and hence frequencies, f) is

$$H_{M0/\eta}(f) = \frac{M_0}{H/2} = C_M \rho \pi r^2 g \tanh kd \left\{ d + \frac{1 - \cosh kd}{k \sinh kd} \right\} \quad (12.50)$$

For a monopile wall thickness of t , the bending stress is $M_0/\pi r^2 t$, so the ratio of peak bending stress to wave amplitude – the bending stress transfer function – in the absence of dynamic magnification is

$$H_{\sigma0/\eta} = C_M \rho \frac{g}{t} \tanh kd \left\{ d + \frac{1 - \cosh kd}{k \sinh kd} \right\} \quad (12.51)$$

It is worth noting that the monopile radius does not appear explicitly in this expression, although it may affect the value of the inertia coefficient, C_M .

Resonant behaviour When the wave frequency is close to the natural frequency of the support structure the latter responds dynamically and its response is amplified in an analogous manner to that of a stationary blade described in Appendix A5. If, for simplicity, the seabed is assumed to be rigid, then, by analogy with Eq. (A5.26), the mudline moment due to wave excitation of the support structure first mode is given by

$$M_1(t) = \omega_1^2 f_1(t) \int_0^{H+d} m(y) \mu_1(y) y dy \quad (12.52)$$

where ω_1 is the support structure natural frequency in rad/sec, $f_1(t)$ is the first mode hub displacement, $m(y)$ is the mass distribution per unit length, y ($= z+d$) is the height above the seabed and $\mu_1(y)$ is the first mode shape. By analogy with Eq. (A5.3), the hub displacement is given by

$$f_1(t) = \frac{1}{k_1} \frac{\int_0^{H+d} \mu_1(y) q_1(y) dy}{\sqrt{(1 - (\omega/\omega_1)^2)^2 + 4\xi_1^2(\omega/\omega_1)^2}} \cos(\omega t + \phi) \quad (12.53)$$

where $k_1 = m_1 \omega_1^2$, $q_1(y)$ is the wave loading amplitude $C_M \rho A \frac{Hgk}{2} \frac{\cosh ky}{\cosh kd}$ and ξ_1 is the first mode damping ratio. m_1 is the generalised mass, $\int_0^{H+d} m(y) \mu_1^2(y) dy$ and ω is the wave angular frequency. Hence Eq. (12.52) gives

$$M_1(t) = C_M \rho \pi r^2 \frac{Hgk}{2} \int_0^d \mu_1(y) \frac{\cosh ky}{\cosh kd} dy \frac{\int_0^{H+d} m(y) \mu_1(y) y dy}{m_1 \sqrt{(1 - (\omega/\omega_1)^2)^2 + 4\xi_1^2(\omega/\omega_1)^2}} \cos(\omega t + \phi) \quad (12.54)$$

The generalised mass, m_1 , is usually dominated by the tower head mass, so the ratio $\int_0^{H+d} m(y) \mu_1(y) y dy / m_1$ approximates to the hub height above the seabed, $H + d$. Defining an effective hub height above the seabed, $H' + d$, as equal to $\int_0^{H+d} m(y) \mu_1(y) y dy / m_1$. Equation (12.54) can be shortened to

$$M_1(t) = C_M \rho \pi r^2 \frac{Hgk}{2} \int_0^d \mu_1(y) \frac{\cosh ky}{\cosh kd} dy \frac{H' + d}{\sqrt{(1 - (\omega/\omega_1)^2)^2 + 4\xi_1^2(\omega/\omega_1)^2}} \cos(\omega t + \phi) \quad (12.55)$$

Comparing the amplitude of the resonant moment [Eq. (12.55)] with the quasi-static moment [Eq. (12.48)], it is seen that the magnification of the mudline moment due to dynamic excitation of the first mode is

$$\begin{aligned} \frac{M_1}{M_0} &= \frac{k \int_0^d \mu_1(y) \frac{\cosh ky}{\cosh kd} dy}{\tanh kd \left\{ d + \frac{1 - \cosh kd}{k \sinh kd} \right\}} \frac{H' + d}{\sqrt{(1 - (\omega/\omega_1)^2)^2 + 4\xi_1^2(\omega/\omega_1)^2}} \\ &= \frac{\lambda(d)}{\sqrt{(1 - (f/f_1)^2)^2 + 4\xi_1^2(f/f_1)^2}} \end{aligned} \quad (12.56)$$

where

$$\lambda(d) = \frac{k \int_0^d \mu_1(y) \frac{\cosh ky}{\cosh kd} dy}{\tanh kd \left\{ d + \frac{1 - \cosh kd}{k \sinh kd} \right\}} (H' + d) \quad (12.57)$$

The ratio $\lambda(d)$ is a measure of the influence of wave loading near the root of the cantilever on first mode resonance, excluding the dynamic magnification given by the dynamic magnification ratio (DMR), $1 / \sqrt{(1 - (f/f_1)^2)^2 + 4\xi_1^2(f/f_1)^2}$. For deep water waves, the wave loading is concentrated in the region around the mean water level, so the first half of the expression for $\lambda(d)$ approximates to $\mu_1(d)/d$. Moreover, as noted above, $(H' + d)$ can be approximated by $(H + d)$. Combining these two approximations leads to

$$\lambda^*(d) = \frac{\mu_1(d)(H + d)}{d} \quad (12.58)$$

where the asterisk indicates an approximate value.

Wave loading is usually applied relatively close to the base of the support structure, so $\mu_1(d)$ is much less than the ratio $d/(H + d)$ – for example, about 0.03 for a $d/(H + d)$

of 0.2 and a rigid seabed, giving a $\lambda^*(d)$ of 0.15. In practice, the seabed can rarely be considered completely rigid, and the effective pile fixity depth below the seabed, m , may be several pile diameters, leading to larger values of $\mu_1(d)$. However, in all cases, the dynamic magnification of the mudline moment due to wave loading is much less than that for the same loading applied at the tower top.

The transfer function giving the ratio of peak bending moment, M_1 , to wave amplitude for different wave frequencies, f , measured in Hz, is

$$H_{M1/\eta}(f) = \frac{M_1}{H/2} = C_M \rho \pi r^2 gk \int_0^d \mu_1(y) \frac{\cosh ky}{\cosh kd} dy \frac{(H' + d)}{\sqrt{(1 - (f/f_1)^2)^2 + 4\xi_1^2(f/f_1)^2}} \quad (12.59)$$

It is convenient to abbreviate this to

$$H_{M1/\eta}(f) = G_{M1/\eta}(f) \frac{1}{\sqrt{(1 - (f/f_1)^2)^2 + 4\xi_1^2(f/f_1)^2}} = G_{M1/\eta}(f).DMR \quad (12.60)$$

where

$$G_{M1/\eta}(f) = C_M \rho \pi r^2 gk \int_0^d \mu_1(y) \frac{\cosh ky}{\cosh kd} dy (H' + d) \quad (12.61)$$

Then

$$\lambda(d) = \frac{M_1/DMR}{M_0} = \frac{H_{M1/\eta}(f)/DMR}{H_{M0/\eta}(f)} = \frac{G_{M1/\eta}(f)}{G_{M0/\eta}(f)} \quad (12.62)$$

Example mudline bending moment transfer functions

Figure 12.48 illustrates the support structure for a 5 MW wind turbine considered in this example. The tower is mounted on a 6 m diameter monopile driven into the seabed. The soil properties are assumed to be such that the monopile is effectively fixed at a depth, m , of 20 m below the seabed. Hub height above the seabed is 115 m and the mean water depth, d , is 23 m.

The coordinate, y , defined as the distance from the cantilever root is now measured from the fixity point at a depth, m , below the seabed. This has no effect on the quasi-static mudline moment but increases the resonant mudline moment significantly. Equation (12.54) becomes

$$M_1(t) = C_M \rho \pi r^2 \frac{Hgk}{2} \int_m^{d+m} \mu_1(y) \frac{\cosh k(y-m)}{\cosh kd} dy \\ \times \frac{\int_0^{H+d+m} m(y)\mu_1(y)(y-m) dy}{m_1 \sqrt{(1 - (\omega/\omega_1)^2)^2 + 4\xi_1^2(\omega/\omega_1)^2}} \cos(\omega t + \phi) \quad (12.63)$$

in which $\int_0^{H+d+m} m(y)\mu_1(y)(y-m) dy/m_1$ can be replaced by $(H' + d)$ as before.

Determination of the mode shape leads to a normalised deflection at mean water level, $\mu_1(d+m)$, of 0.071 and $\lambda^*(d+m) = \mu_1(d+m)(H+d)/d = 0.071(115/23) = 0.355$.

The transfer functions for the quasi-static mudline moment, $H_{M0/\eta}(f)$, and for the first mode resonant mudline moment, $H_{M1/\eta}(f)$, together with an example JONSWAP

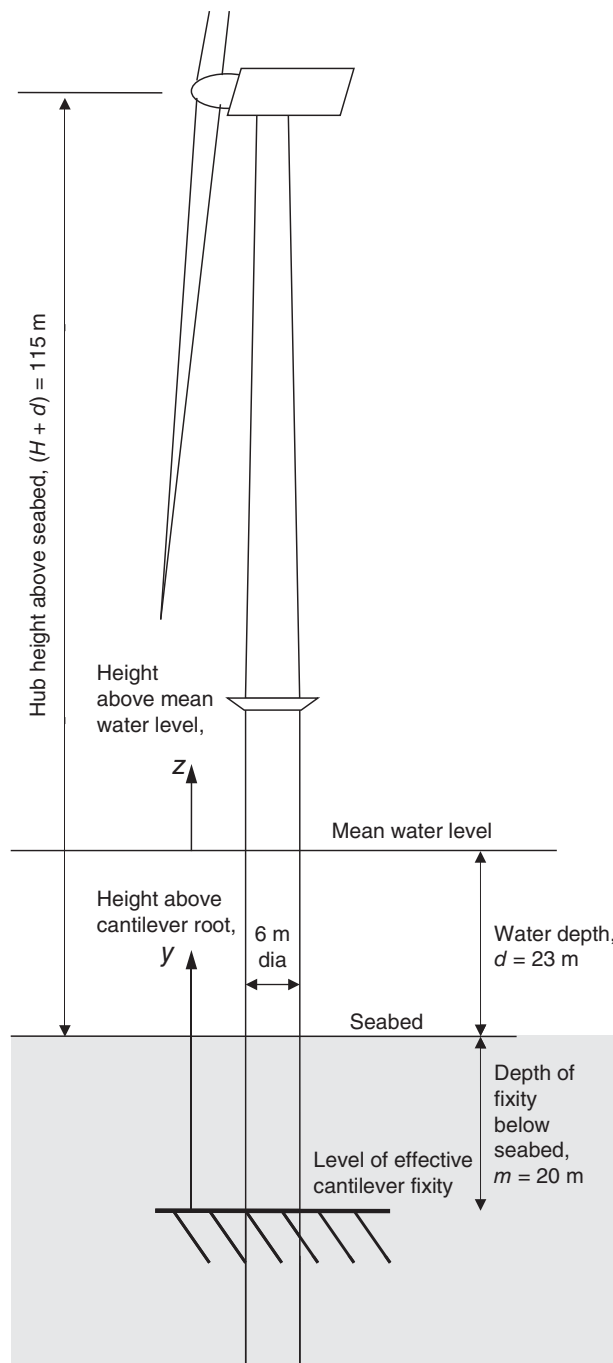


Figure 12.48 Example support structure for 5 MW turbine.

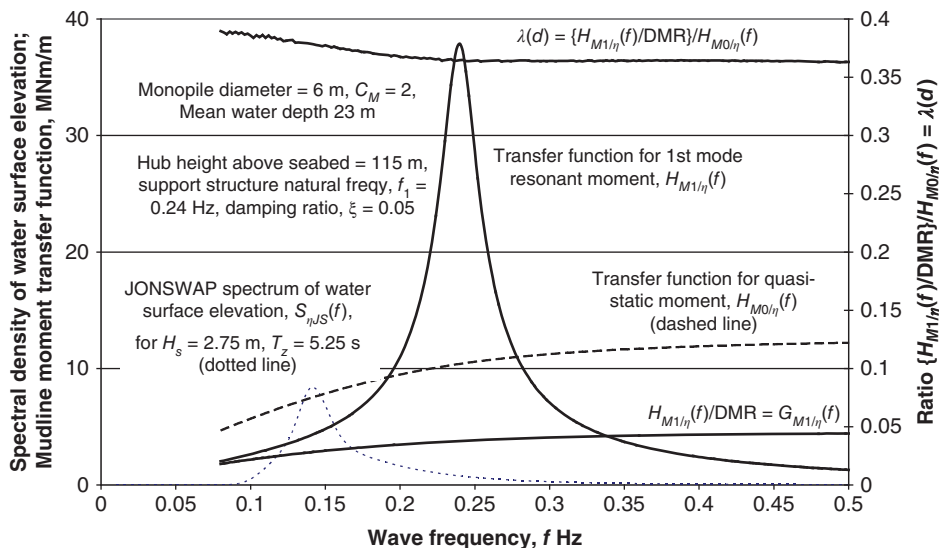


Figure 12.49 Comparison of quasi-static and resonant transfer functions for mudline moment for the example support structure of Figure 12.48.

spectrum (for $H_s = 2.75$ m and $T_z = 5.25$ seconds) are shown in Figure 12.49. The support structure natural frequency, f_1 , is 0.24 Hz and the damping ratio, ξ , is taken as 5%, giving a peak DMR of 10.

Clearly the damping ratio is of major importance in determining the resonance peak. The principal components of damping – viz. aerodynamic, structural, and that arising from soil hysteresis – are discussed in later sub-sections within this section.

It is seen that the mudline moment transfer function for quasi static loading increases with wave frequency. Thus, although water motion and hence wave loading is increasingly concentrated near the surface as the wave length reduces, increased particle accelerations overcome this effect, resulting in increasing overturning moments for waves of a given amplitude.

Figure 12.49 also shows the first mode resonant mudline moment transfer function divided by the dynamic magnification factor, $H_{M1/\eta}(f)/DMR = G_{M1/\eta}(f)$. The function, $G_{M1/\eta}(f)$, is very similar in form to the quasi-static transfer function. This is illustrated by the plot of the ratio of the two, $\lambda(d) = G_{M1/\eta}(f)/H_{M0/\eta}(f)$, which is seen to be insensitive to wave frequency and to be close to the $\lambda^*(d)$ value of 0.355.

Effect of diffraction

Section 12.3.9 set out how wave diffraction influences the inertia coefficient when the cylinder diameter is of significant size in relation to the wave length. Diffraction results in a rapid reduction of the inertia coefficient below the nominal value of 2.0 for D/L ratios above about 0.17, as shown in Figure 12.25. In Figure 12.49, the inertia coefficient was assumed to be constant at 2.0 for simplicity, but the effect of diffraction on the transfer function for the quasi-static mudline moment is illustrated in Figure 12.50. Also shown is the JONSWAP spectrum for the $H_s = 2.75$ m, $T_z = 5.25$ m sea state.

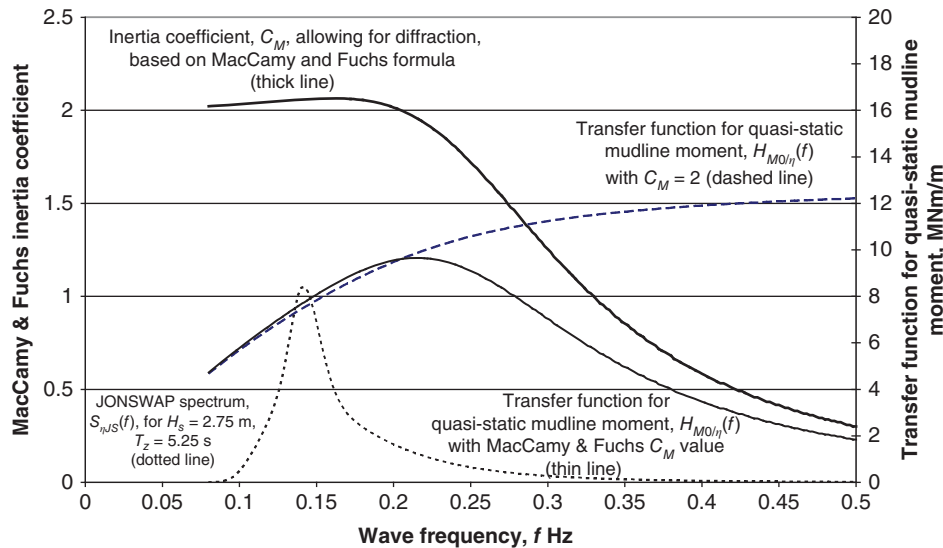


Figure 12.50 Effect of diffraction on the transfer function for quasi-static mudline moment for the example support structure of Figure 12.48.

It is apparent that, for the support structure and sea state chosen, the reduction in inertia coefficient only affects the loading due to waves in the upper tail of the wave spectrum. However, as the Mac Camy and Fuchs inertia coefficient reduces to 1.8 at the support structure resonant frequency of 0.24 Hz, the resonant moment comes down somewhat when diffraction is allowed for.

Aerodynamic damping

During turbine operation, aerodynamic damping of the rotor provides significant damping of wave-induced support structure motion in the fore-aft direction. For constant blade pitch, this is easily estimated at each wind speed using the closed-form formula in Eq. (5.135), but when the pitch system is active, the aerodynamic damping is heavily dependent on the control strategy and cannot be easily calculated.

Wind turbine simulations in the time domain automatically model support structure aerodynamic damping but do so implicitly rather than explicitly. However, values of the aerodynamic damping at different wind speeds can be deduced from time-domain simulations of transient free vibrations in response to a tower top step loading during turbine operation in a turbulent wind field, including the effects of blade pitching. In each case, it is necessary to subtract the tower top displacement time history from a parallel simulation without the tower top step loading, but with the same seeds, to determine the transient tower top displacement response to the step loading on its own. The damping ratio is then calculated from the logarithmic decrement of the first mode free vibrations.

An example plot of the variation of aerodynamic damping with mean wind speed obtained using the above method by Kuhn (2001) is shown in Figure 12.51. The reference turbine design investigated was a 3 MW, two bladed, fixed-speed, pitch-regulated

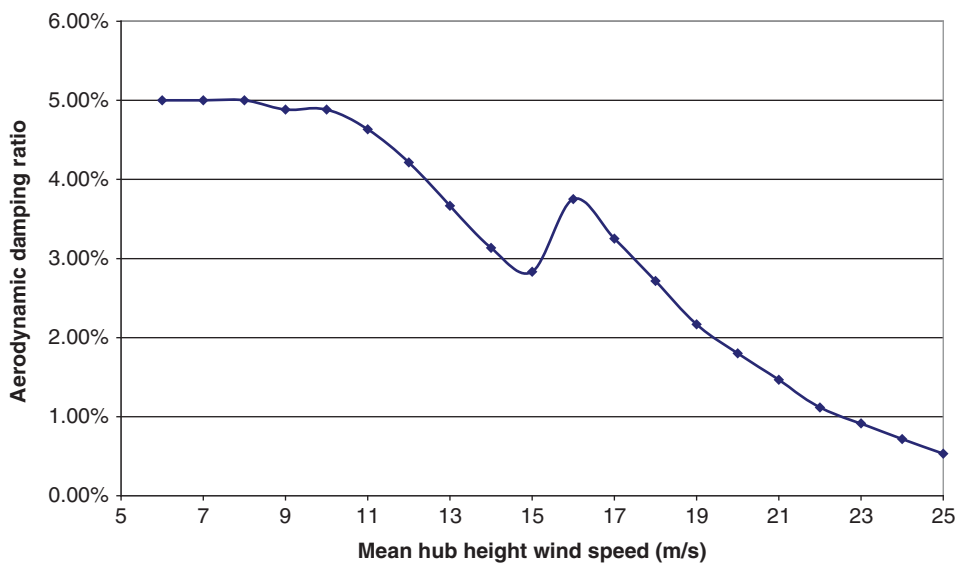


Figure 12.51 Variation of aerodynamic damping with wind speed for fixed-speed pitch-regulated machine in a turbulent wind.

machine on a soft-soft monopile support structure, with the hub 80 m above the seabed and a water depth of 21 m, which was developed during the Opti-OWECS study.

The figure shows reducing damping above 10 m/s as a result of increasing flow separation over the inner part of the blade until blade pitching above the rated wind speed of 13.7 m/s leads to flow re-attachment and damping recovery. However, above 16 m/s, increasingly rapid action of the pitch mechanism in response to tower head oscillatory motion reduces the aerodynamic damping considerably at higher wind speeds. This is because, as the tower top sways into the wind, the blades feather to curb the power increase, reducing the rotor thrust and vice versa.

It is now becoming common practice for the control system to be designed to suppress support structure oscillations at resonant frequency, which can lead to effective aerodynamic damping ratios in excess of the values for fixed pitch operation with attached flow. See Chapter 8.

Wind wave mis-alignment

When the wind and wave directions are not in alignment, the aerodynamic damping of wave-induced support structure motion will be reduced, as the aerodynamic damping of turbine side to side motion is very small, and this needs to be accounted for in the fatigue analysis.

Structural damping

The level of structural damping provided by the monopile and tower is very much less than that due to aerodynamic damping. For example, the Eurocode on wind loading, EN

1991-1-4 (2005), gives a logarithmic decrement of structural damping of 0.012, equivalent to a damping ratio of 0.19% for welded steel chimneys and DNVGL-RP-C205 *Environmental Conditions and Environmental Loads* (2017) gives a damping ratio of 0.15% for steel members in air.

Soil damping

There are two types of soil damping – radiation damping and hysteretic material damping, but the latter is negligible at frequencies of less than 1 Hz (Andersen 2008). The hysteretic damping depends on both soil properties and loading amplitudes, so the level of damping will be variable.

Tarp-Johansen (2009) investigated soil damping using a 3-D finite-element model of the seabed surrounding a monopile foundation, and concluded that the logarithmic decrement of support structure damping provided by the soil may be in the range 0.035–0.05, equivalent to a damping ratio of 0.55–0.8%. However, the pile embedment was low (4.25 diameters) resulting in larger motion in the soil and hence larger soil damping than would normally be the case.

Damgaard et al. (2012) report measurements on the decay of support structure oscillations after 10 shut-downs of an offshore turbine fitted with a tower damper and a mean damping ratio of 2.25% was calculated from the accelerometer traces. The measured contribution of the tower damper (~1.3%) and the estimated structural, aerodynamic and hydrodynamic damping contributions were then all subtracted from the total to give an estimate of the soil damping of 0.58%.

The soil damping can also be estimated analytically from the hysteresis losses over a load cycle at different depths, derived from the respective non-linear *p-y* curves. The global damping ratio is given by

$$\xi_s = \frac{\int_0^L \Delta E(z, y) dz}{\int_0^L \frac{1}{2} k(z) y^2(z) dz} 4\pi \quad (12.64)$$

where the integrals are carried out over the embedded length of the pile, $\Delta E(z, y)$ is the hysteresis loss over one load cycle, $k(z)$ is the *p-y* curve slope and $y(z)$ is the pile displacement amplitude.

Carswell et al. (2015) review experimental and analytical results from a variety of sources. Soil damping ratios between 0.17% and 1.5% are reported, but given that the soil damping ratio increases with displacement amplitude, a range of results is to be expected.

In view of the difficulties of quantifying soil damping on a site-by-site basis, some designers adopt a conservative approach and simply ignore it altogether.

Damping during turbine shut-down

When the turbine is stationary, the aerodynamic damping is negligible, and support structure damping will be limited to that provided by the welded structure and the soil foundation, with a small contribution from hydrodynamic damping. The 2005 GL *Guideline for the Certification of Offshore Wind Turbines* suggests 1% as a rough approximation to the damping ratio in these circumstances. A similar value is indicated by the measurements reported by Damgaard et al. (2012) if the contribution of the tower damper is subtracted.

The much-reduced damping level during turbine shut-down will result in considerably greater wave excitation of support structure resonance than during turbine operation, so the percentage of machine downtime assumed in the fatigue damage calculations needs to be estimated with care.

Monopile bending moment spectra

The spectrum of the first mode resonant mudline moment is obtained by multiplying the wave spectrum by the square of the first mode resonant mudline moment transfer function:

$$S_{M1}(f) = S_{\eta JS}[H_{M1/\eta}(f)]^2 \quad (12.65)$$

The transformation of a wave spectrum into support structure bending moment spectra is illustrated in Figure 12.52 for the support structure of Figure 12.48 with the sea state modelled using the JONSWAP spectrum. The sea state taken is $H_s = 2.75$ m and $T_z = 5.25$ seconds, for which the peak shape factor, γ , is 2.32 and the peak frequency, f_p , is 0.141 Hz. The figure shows the JONSWAP spectrum, the square of the transfer function for first mode resonant moment response and the resultant spectrum of first mode resonant mudline moment.

A complete analysis would investigate the dynamic response of the second and higher support structure modes, but excitation of these modes is minimal when inertia loading dominates.

It is evident that in this example the spectrum of the first mode resonant moment response is dominated by the resonance peak, with a much smaller peak occurring at the

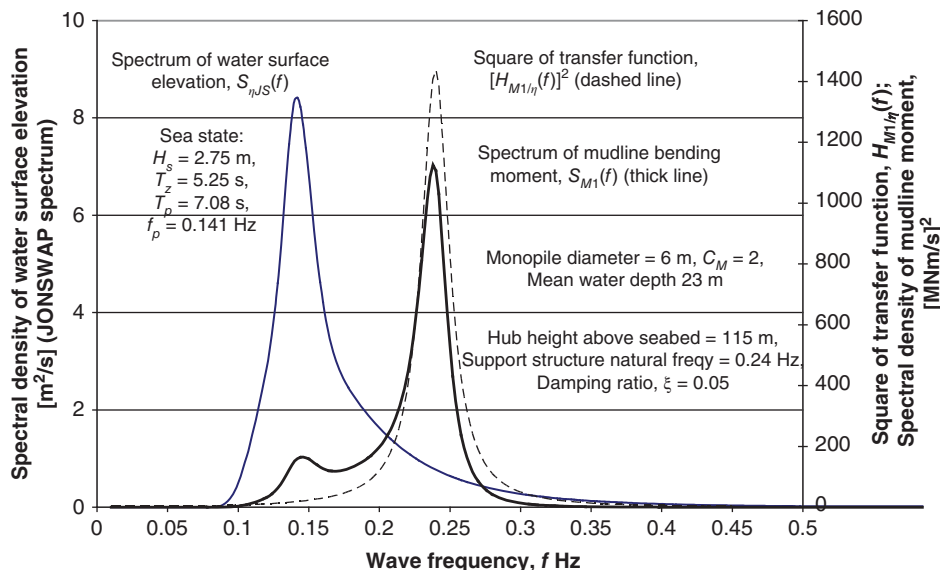


Figure 12.52 Spectra of water surface elevation and resonant mudline bending moment for the example support structure of Figure 12.48 with a natural frequency, f_1 , of 0.24 Hz for the $H_s = 2.75$ m / $T_z = 5.25$ seconds sea state.

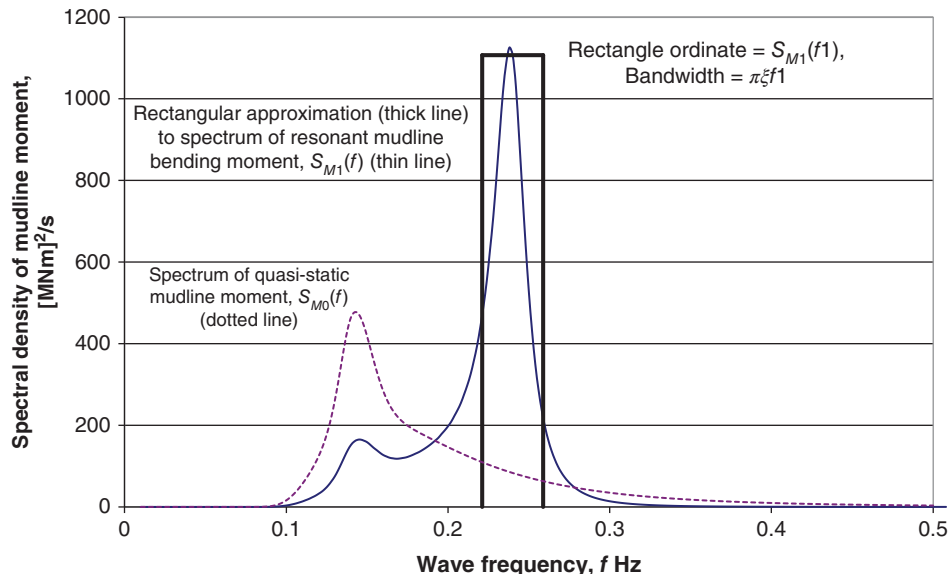


Figure 12.53 Mudline moment spectrum approximation.

peak wave frequency. The latter peak is much smaller than the peak of the quasi-static spectrum (Figure 12.53), but good agreement would be expected if the spectra of mudline moment in response to the excitation of higher support structure vibration modes were added to that shown above for the first mode.

Approximate treatment of moment response for fatigue analysis purposes

Given that the first mode resonant response is narrow banded, the resonant moment spectrum may be approximated for fatigue analysis purposes by a rectangle of height $S_{M1}(f_1)$ and width (the bandwidth) $\pi\xi f_1$, centred on the first mode resonant frequency, f_1 Hz. This is illustrated in Figure 12.53. The area within the rectangle is

$$S_{M1}(f_1)\pi\xi f_1 = S_{\eta JS}(f_1)[H_{M1/\eta}(f_1)]^2\pi\xi f_1 \quad (12.66)$$

As the transfer function is proportional to the DMR, which is equal to $1/(2\xi)$ at resonance, it follows that the area within the rectangle is inversely proportional to the damping ratio. The standard deviation of the resonant bending moment, which is equal to the square root of the area of the rectangle, is thus given by

$$\begin{aligned} \sigma_{M1} &= H_{M1/\eta}(f_1)\sqrt{S_{\eta}(f_1)\pi\xi f_1} = C_M\rho\pi r^2 gk \int_m^{d+m} \mu_1(y) \frac{\cosh k(y-m)}{\cosh kd} dy \\ &\times (H' + d)\sqrt{S_{\eta}(f_1)f_1\pi/(4\xi)} \end{aligned} \quad (12.67)$$

Given that the area of overlap between the rectangular approximation to the resonant bending spectrum and the quasi-static spectrum is small, the total moment spectrum can be conservatively approximated by the summation of the two.

A further simplification is to ignore the variation of the quasi-static transfer function with frequency, and equate the quasi-static moment spectrum to the product of the wave spectrum and the square of the quasi-static transfer function at the peak wave frequency. Then

$$S_{M0}(f) = S_{\eta JS}(f) [H_{M0/\eta}(f_p)]^2 \quad (12.68)$$

and the standard deviation of the quasi-static bending moment becomes simply

$$\sigma_{M0} = \sigma_\eta H_{M0/\eta}(f_p) = \frac{H_s}{4} C_M \rho \pi r^2 g \tanh k_p d \left\{ d + \frac{1 - \cosh k_p d}{k_p \sinh k_p d} \right\} \quad (12.69)$$

where σ_η is the standard deviation of water surface elevation and k_p is the wave number corresponding to the peak frequency, f_p . Finally, the standard deviation of the total mudline moment response is obtained as the square root of the sum of the squares of the quasi-static and resonant responses:

$$\sigma_M^2 = \sigma_{M0}^2 + \sigma_{M1}^2 \quad (12.70)$$

Derivation of fatigue damage

The method of calculating the fatigue damage from the moment spectrum depends on whether it can be treated as narrow band (i.e. occurring over a narrow range of frequencies) or not. When the resonant moment dominates, the quasi-static response centred on the peak wave frequency will have little influence, and the response can be treated as narrow banded, with all of the load cycles occurring at the resonant frequency. It is worth noting that, provided the standard deviation of the quasi-static response is included using Eq. (12.69), the narrow band assumption is conservative, because allowance for broad bandedness *reduces* the calculated fatigue damage.

It can be shown (see Barltrop and Adams 1991) that the damage equivalent stress range for a reference number of cycles, N_R , for narrow banded oscillatory loading is given by

$$\Delta\sigma_{eq} = \sigma_\sigma \sqrt{8} \sqrt{\frac{n}{N_R} \Gamma\left(\frac{2+m}{2}\right)} \quad (12.71)$$

where σ_σ is the standard deviation of the fluctuating stress ($=\sigma_M/\pi r^2 t$), m is the inverse slope of the log-log plot of the S - N curve (assumed to be a single straight line, rather than bi-linear) and n is the number of load cycles over the duration of the sea state. For $m = 4$ and $n = N_R$, $\Delta\sigma_{eq} = 3.363\sigma_\sigma$.

If, however, the total moment spectrum is broad banded, then the Dirlitk method (Section 5.9.3) can be used to derive an approximate stress range probability distribution, which is then combined with the S - N curve (see Section 12.7.9) to obtain the fatigue damage for each sea state.

Wind loading in the frequency domain

Dynamic and fatigue analysis of onshore wind turbine support structures in the frequency domain are discussed in Sections 5.12.5 and 5.12.6, respectively, and similar

considerations apply to offshore support structures under wind loading. Given the statistical independence of wind and wave loading, the moment spectrum due to wind loading is simply added to the moment spectrum due to wave loading to obtain the moment spectrum due to the combined loading.

Wind loading in the time domain

As noted at the end of the preceding section, time-domain simulations are preferred to frequency domain analysis for the evaluation of fatigue damage due to wind loading, because they account for both non-linear aerodynamics, non-linear control system behaviour and the combination of deterministic and stochastic load components. Methods of combining wind loading fatigue cycles obtained in the time domain with wave loading fatigue cycles obtained in the frequency domain are discussed below.

Combination of wind and wave loading fatigue spectra

a) Using simulations and rainflow counting for wind loading fatigue Kuhn (2001) has proposed calculating the fatigue damage due to wind and wave loading separately, using normal wind simulation and spectral fatigue analysis, respectively, and then combining the two. The procedure is shown in the schematic in Figure 12.54.

The damage equivalent stress range referred to in the schematic is defined as the stress range that, when applied over a specified number of cycles, N_R , would produce the same fatigue damage as the actual calculated fatigue stress spectrum. N_R is normally taken as 10^7 cycles.

A critical step in the procedure set out in Figure 12.54 is the combination of the wind and wave damage equivalent stress ranges, and the basis for this is set out below.

It has already been noted that the damage equivalent stress range for a reference number of cycles, N_R , for narrow banded oscillatory loading is given by

$$\Delta\sigma_{eq} = \sigma_\sigma \sqrt{8} \sqrt[m]{\frac{n}{N_R} \Gamma\left(\frac{2+m}{2}\right)} \quad (12.72)$$

Hancock and Gall (1985) have proposed an empirically based modification to the above formula for the case of broad banded loading, which multiplies it by the m -th root of β , the ratio of the mean period between crests and the zero-crossing period, T_c/T_z . Thus

$$\Delta\sigma_{eq} = \sigma_\sigma \sqrt{8} \sqrt[m]{\frac{T_c}{T_z} \frac{n}{N_R} \Gamma\left(\frac{2+m}{2}\right)} \quad (12.73)$$

The variance of the combined response, $\sigma_{\sigma,c}^2$ is equal to the sum of the variances of the responses to aerodynamic and hydrodynamic loading, $\sigma_{\sigma,a}^2 + \sigma_{\sigma,h}^2$. Hence, repeated application of Eq. (12.73) yields:

$$\Delta\sigma_{eq,c} = \sqrt{\Delta\sigma_{eq,a}^2 \left(\frac{T_{z,a}}{T_{z,c}}\right)^{\frac{2}{m}} + \Delta\sigma_{eq,h}^2 \left(\frac{T_{z,h}}{T_{z,c}}\right)^{\frac{2}{m}}} \quad (12.74)$$

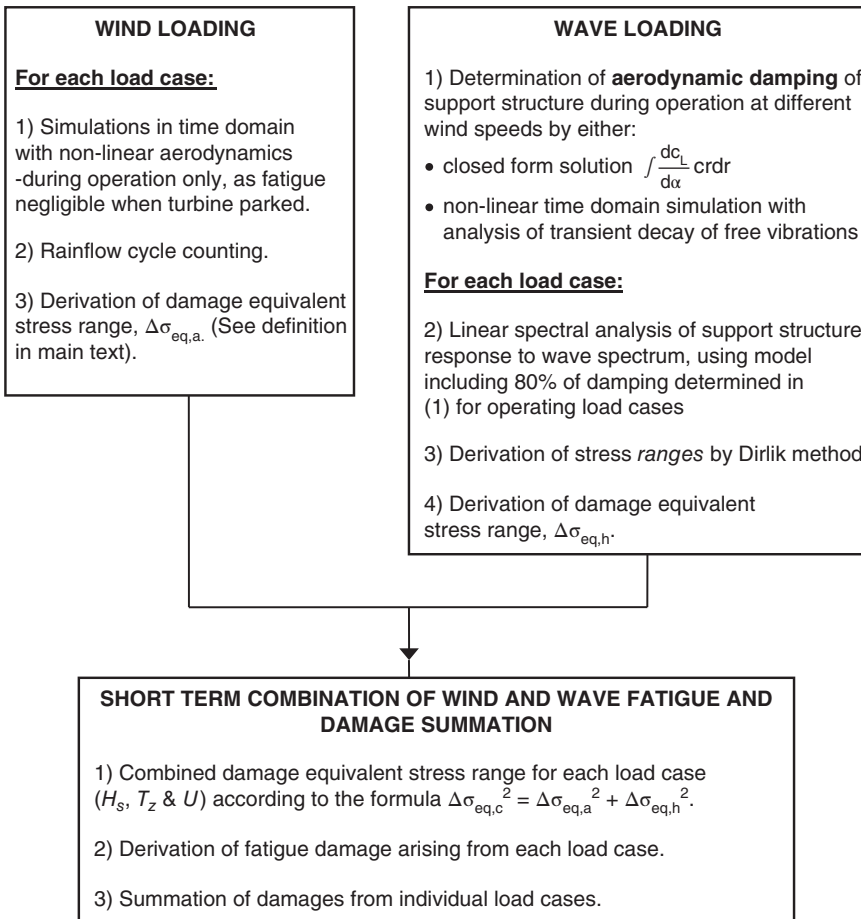


Figure 12.54 Schematic for simplified calculation of fatigue damage.

If the zero-crossing period weightings are omitted, this becomes simply

$$\Delta\sigma_{eq,c} = \sqrt{\Delta\sigma_{eq,a}^2 + \Delta\sigma_{eq,h}^2} \quad (12.75)$$

Kuhn (2001) reports an investigation of the accuracy of the above simplified method, when applied to the calculation of fatigue damage at cross-sections 5.5 m below the mud-line and 10.6 m below the tower top flange for the soft-soft monopile support structure of the reference design referred to above. Equivalent stress ranges obtained from full time-domain simulations of combined wind and wave loading were compared with those derived from the simplified method, using either weighted quadratic superposition, Eq. (12.74), or its unweighted equivalent, Eq. (12.75), to combine the equivalent stresses from aerodynamic and hydrodynamic loading. Both methods yielded accurate results, but, surprisingly, unweighted quadratic superposition was more accurate, with

a maximum error in the equivalent stress of about 3%, compared with about 5% for weighted quadratic superposition.

b) Using simulations to obtain bending stress spectra for wind loading An alternative approach has been proposed by Van Der Tempel (2006), in which time-domain simulations are used to obtain bending stress spectra due to wind loading. The key steps are as follows:

1. Carry out a time-domain simulation at each mean wind speed with the tower top *fixed*, and derive a spectrum of the resulting fluctuating load applied to the tower top from its time history.
2. Divide the latter spectrum by the turbulence spectrum of the incoming wind to obtain the transfer function between the incoming wind fluctuations and the tower top load fluctuations.
3. Obtain values of the aerodynamic damping at different wind speeds – e.g. by means of time-domain simulations of transient free vibrations in response to a tower top step loading (as described under the ‘Aerodynamic Damping’ section above).
4. Use an FE model of the support structure to derive the transfer functions between tower top loading and the required support structure bending stress for the different values of aerodynamic damping.
5. Multiply the transfer functions derived in steps 2 and 4 together to obtain the transfer function between incoming wind speed and bending stress fluctuations $H_{\sigma/U}(f, \bar{U})$ at each mean wind speed.
6. Multiply the $H_{\sigma/U}(f, \bar{U})$ transfer functions by the spectrum of the incoming wind fluctuations to obtain the spectrum of bending stress fluctuations due to wind loading at each mean wind speed.

An advantage of this approach is that the use of time-domain simulations with the tower top fixed means that the results are independent of the support structure used, so do not need to be repeated for different water depths and soil conditions.

Spectra of bending stress due to combined wind and wave loading are obtained by adding the wind loading spectrum to the wave loading spectrum for each combination of mean wind speed and sea state. These combined bending stress spectra can then be used to derive the stress range probability distribution using the Dirlik method and hence the fatigue damage.

12.7.5 Gravity bases

The structural action of a gravity base supporting an offshore wind turbine is essentially the same as that of slab foundations used on land (Section 7.10.1) – i.e. it relies on the restoring moment provided by support structure and turbine self-weight to resist overturning moments tending to tip it over. However, gravity bases deployed at sea, which are also invariably constructed in reinforced concrete (although steel or steel/concrete composite structures are feasible), are less effective in resisting overturning than those on land, because buoyancy forces reduce their effective self-weight. Consequently extra

ballast usually has to be added to compensate. It should also be noted that, in the case of bases founded on granular materials, the bearing resistance is less than for the equivalent unsubmerged material on land, because of the reduced particle effective stresses.

Gravity bases have the advantage that they avoid the need for piling operations, which can cause significant environmental disturbance and may not be feasible at all where rock forms the seabed. However, their design has to be developed in close conjunction with the transport and installation method, for which there are three principal options:

- Barge transport to site and installation by floating crane.
- Use of floating crane for both transport and installation.
- Flotation of gravity base, towage to site, and controlled sinking.

In the case of the first two options, design for minimum weight is crucial because of crane capacity limitations, whilst floating stability is a governing consideration for the third. Accordingly, cellular construction is attractive for the first two options and essential for the third. The gravity bases for three wind farms exemplifying each of the three transport and installation options are now described.

Gravity bases in the Southern Baltic

The relatively benign wave climate and negligible tidal range in the Southern Baltic render seabed preparation and gravity base transportation less challenging activities than in the more hostile conditions prevalent in the North Sea, so gravity bases have been favoured for deployment in shallow water sites close to the coasts of Denmark and Sweden.

Figure 12.55 illustrates the gravity base foundation design used to support 2.3 MW Siemens turbines, 48 in number, at the Lillgrund wind farm in Swedish waters just south of the Öresund bridge. (This information was obtained from the Lillgrund wind farm, owned and operated by Vattenfall.) The base consists of a hollow cylindrical shaft rising from a 16.45 m wide hexagonal slab (19 m across corners), which is stiffened by six radial walls bracing the shaft to an outer perimeter wall some 2.4 m high. The six-cell ballast tray thus created was backfilled with ballast rock and rock armour after foundation installation. Five variants of the design were constructed with overall heights of 10.3, 11.3, 12.3, 13.3, and 14.3 m to suit water depths ranging from 4 to 9 m. (The large inverted cone integral with the top of the cylindrical shaft is provided to reduce ice loads.) The foundations were constructed on barges moored at a quayside at Swinoujscie on the coast of Poland, with each barge accommodating four foundations (Figure 12.56), facilitating eventual transport to the site.

The site preparation work consisted of the excavation of a shallow pit in the seabed about 2.5 m in depth, the placing of a steel frame around the perimeter of the excavation, followed by the deposition of thin layer of crushed rock for the gravity base to rest on. The steel frame was set to level and used by divers to level the rock bed with the aid of a rotating beam mounted on a central support. After installation of each foundation by barge mounted crane (Figure 12.57), the excavation around the foundation was backfilled with filter rock over which rock armour was laid as scour protection. Finally, the void in the cylindrical shaft was filled with ballast material and a concrete slab cast above it. The weight of the tallest foundation was 1375 tons without ballast, increasing to 2250 tons with ballast.

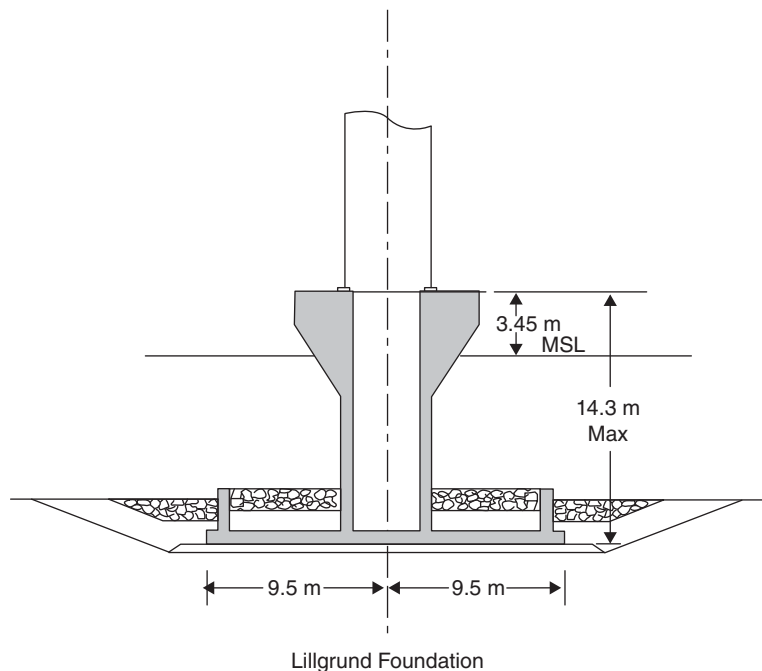


Figure 12.55 Reinforced concrete gravity base design used at Lillgrund wind farm, Sweden.

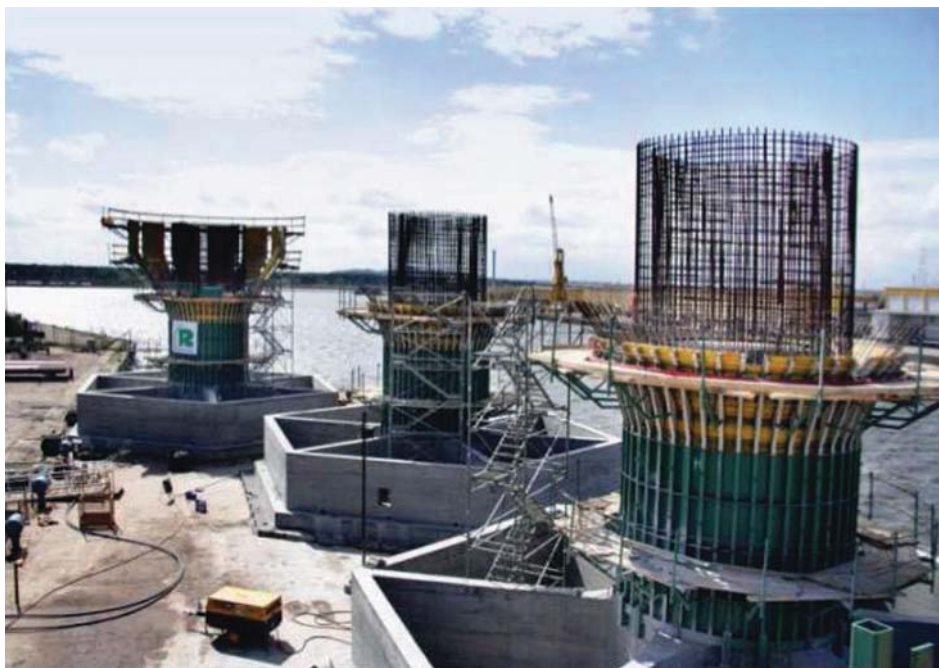


Figure 12.56 Gravity bases for Lillgrund under construction on barge at quayside at Swinoujscie (Lillgrund Pilot Project, 2008). Reproduced by permission of Vattenfall.



Figure 12.57 Lowering of gravity base by floating crane during installation at Lillgrund wind farm (Lillgrund Pilot Project, 2008). Reproduced by permission of Vattenfall.

Similar gravity base designs were used at the other large Baltic wind farms, Rodsand 1 (Nysted) and Rodsand 2, where Siemens 2.3 MW turbines were also deployed. However, in the case of Rodsand 2, the base slab is an octagon with four short sides and four long ones, and the internal walls are arranged in a cruciform. At £350k per MW installed, the cost of the Rodsand foundations, installed in 2010, is claimed to be half that of UK monopile foundations

Gravity bases in the North Sea off Belgium

Until 2008, gravity base foundations had been conspicuous by their absence in the North Sea – presumably for the reasons stated above. However, in that year, six very large gravity bases were installed in deep water on Thornton Bank, 30 km off the Belgian coast, to support REpower 5 MW turbines. See Figure 12.58.

In the planning stages of the project, both monopile and gravity base foundations were considered in detail, but the large size of monopile required in the 23 m water depth, the escalation of steel costs and driveability concerns led to the selection of a gravity base. A full description of the gravity base design and its installation is given in Peire et al. (2009).

The gravity base configuration adopted for the deep water at Thornton Bank differs considerably from the shallow water design of the Southern Baltic. In place of a shaft and cantilevered slab, the shaft is mounted on a frustum, which provides an efficient load path to the base slab perimeter, without increased exposure to wave loads near the water line. As usual the weight of the unballasted structure is critical, so the shaft and frustum are prestressed to utilise the concrete more efficiently.

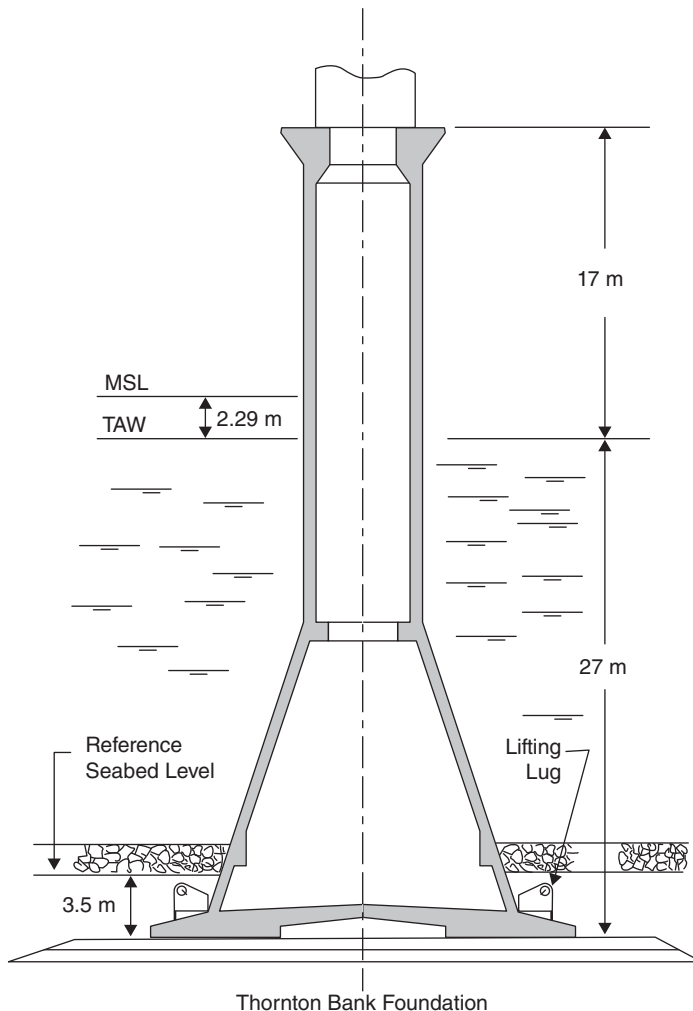


Figure 12.58 Prestressed concrete gravity base design used at Thornton Bank wind farm, Belgium.

The key dimensions are as follows:

- Height (dependent on local seabed depth): 44 m maximum.
- Shaft diameter: 6.5 m.
- Base slab diameter: 23.5 m.
- Frustum height and base diameter: 17 m.
- Wall thickness of shaft and frustum: 0.5 m.

The gravity bases are founded at a level 3.5 m below the reference seabed level, which is defined as the lowest seabed level that can be guaranteed over 30 years, after allowing for

sand wave mobility and natural erosion. The top of the gravity base, which incorporates the access platform, is 17 m above TAW, the Belgian reference level for sea levels, which is 2.29 m below mean sea level.

The bases were constructed on parallel concrete beams about 1.2 m in height, cast on a quay at Ostend. On completion of each base, self-propelled multi-axle modular trailers were positioned in the spaces between the concrete beams and their hydraulic suspensions extended to raise the base off the concrete beams. The trailers then transported the base very slowly to the edge of the quay, where the floating crane, Rambiz, was able to lift it clear, using a purpose built lifting frame and four large lifting lugs mounted on the base slab. After the voyage to Thornton Bank, the Rambiz lowered each base into position on a prepared bed and the hoisting cables were released, using a special hydraulically operated pin release mechanism.

Extensive works on the seabed were necessary at each site in advance of gravity base installation. Foundation pits 50 m wide by 80 m long were dredged to a depth of about 7 m, with the longer dimension aligned NE/SW, parallel to the prevailing current direction. The final stage of dredging over the final metre depth had to be carried out in relatively calm conditions to achieve a reasonably level surface. The 1.3 m thick foundation bed of gravel – consisting of a finer, filter layer followed by a coarser layer – was then deposited by the ‘Seahorse’, a dynamically positioned vessel with 18 000 ton capacity, working in conjunction with a remotely operated vehicle on the seabed equipped with surveying equipment. Finally, the surface was accurately levelled by dragging a purpose-built levelling tool across it. As a result, the inclination of the installed structures to the vertical was remarkably low – 0.1° on average.

Following installation, the pits surrounding each gravity base were backfilled with sand retrieved from the areas where the original dredgings had been deposited and the interior of the base was ballasted with the same material. Finally, rock armour was deposited around each base as scour protection.

The weight of the 44 m tall foundation without ballast was 3000 tons, and the volume of sand used as ballast was approximately 2000 m³.

Gravity bases in the North Sea off Blyth, United Kingdom

The first gravity bases to be floated out from construction yard to wind farm site were those for the 41.5 MW Blyth offshore wind farm off the coast of Northumberland, UK, which consists of five MHI Vestas V164-8.3 MW turbines. The gravity bases each consist of a concrete cylindrical shell, approximately 30 m in diameter and 10 m tall, surmounted by a conical shell. This in turn supports a vertical steel tube of about 7 m diameter, which extends about 60 m from the base slab to the tower interface (see Figure 12.59); 1800 m³ of concrete were required for each base (EDF Energy Renewables 2017).

The five structures were constructed in a row in a dry dock at Wallsend on the River Tyne – see Figure 12.60. Slab sectors forming the conical shell were precast separately and then craned into place once the steel tube was in place – see Plate 7. The sectors were cast with projecting loops of reinforcement along the sides, which interleave with those on the adjacent sectors after erection, providing a robust connection between them after joint concreting. At the critical joint between the top of each sector and the steel tube, the reinforcement loops interleave with 48 radial vertical steel plates welded to the tube.

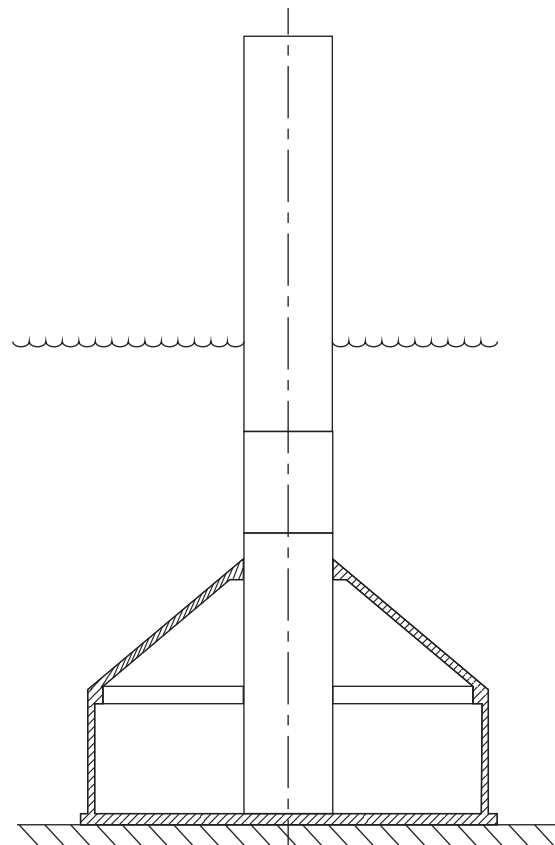


Figure 12.59 Elevation on Blyth gravity base foundation in cross-section.

The gravity bases were floated out into the River Tyne in turn and then towed to the wind farm site with the cylindrical portion almost completely submerged. Floating stability was aided by a thick concrete base slab. At the wind farm site, controlled sinking onto the prepared seabed was effected by pumping seawater into the foundation as ballast. Once located correctly on the seabed, the water ballast was replaced with sand ballast to increase resistance to overturning, increasing the weight of the gravity base to 15 000 tonnes. The float-outs took place in July and August 2017 with turbine installation completed in the following month. De-commissioning can be accomplished by a simple reversal of the installation process. The capital cost of the whole wind farm was about £145 m (Coastal Energy and Environment 2018).

12.7.6 Jacket structures

Jacket structures offer a lighter alternative to either monopiles or gravity bases in deeper waters. The basic design concept, which consists of several near-vertical tubular legs braced together by smaller tubes in each face, originates in the oil and gas industry but is undergoing a transformation in response to the more demanding economics of the wind industry.



Figure 12.60 Gravity base foundations for Blyth offshore wind farm under construction in dry dock beside the River Tyne. Source: Reproduced with permission of EDF Renewables UK.

Figure 12.61 illustrates the arrangement of the four bay, four legged structures installed in 2009 at the Alpha Ventus wind farm in the North Sea (The term ‘four bay’ indicates that each leg is divided into four sections or ‘bays’ by the brace joints.). The site is located in waters 30 m deep, 45 km North of the German island of Borkum, which is close to the Dutch border. The concept was first trialled at the Beatrice Demonstrator Project in 2006, when two taller, five bay structures were deployed in waters 45 m deep in the Moray Firth, Scotland. In 2010, 30 smaller, three bay versions, but otherwise of similar design, were installed in waters 17–21 m deep in the Irish Sea at the Ormonde project. The structures support REpower 5 MW wind turbines at all three sites.

The success of the Beatrice Demonstrator Project led to the construction of a very large wind farm in the same area. Beginning in 2017, 84 jacket structures were installed in waters up to 55 m in depth to support Siemens Gamesa 7 MW turbines, with completion of the 588 MW wind farm in 2019.

Jacket structures can yield considerable weight savings compared with monopiles because the primary loading – the overturning moment – is resisted at much higher lever arms, thanks to the wide separation of the legs. In addition, wave inertia loading on the structure, which is critical for fatigue damage, is smaller, because of the reduced total member cross-sectional area. However, the wave drag loading, which governs extreme loading, is increased, because of the increased total member width.

On the debit side, the fabrication and welding of the many geometrically complex joints between the bracing members and the legs carry a considerable cost penalty, even

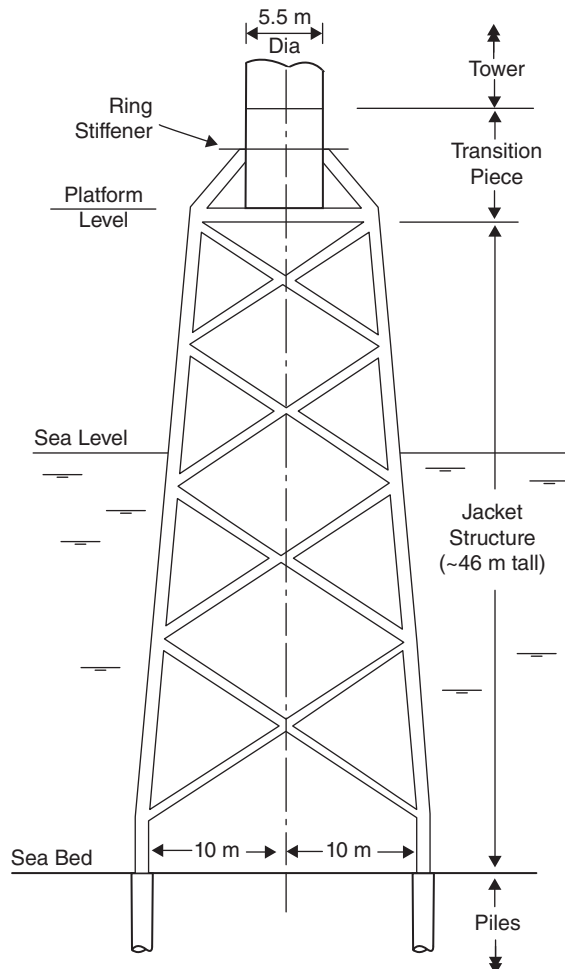


Figure 12.61 Four legged jacket structure to support REpower 5 MW turbine at Alpha Ventus wind farm (access ladder, platform handrailing, and J-tubes omitted for clarity).

before consideration of the extra material requirements arising from the higher stress concentrations and inferior performance of the weld details in fatigue. (See Section 7.9.3 for discussion of fatigue design in relation to tubular towers.) Thus the cost per ton for a jacket structure may be 2.5 times that for a monopile.

Transition section

The step down in width at the top of the jacket from the widely spaced legs to the tower diameter necessitates the provision of a substantial transition section. In early installations, this consisted of a cylindrical tower stub member supported on raking extensions to each jacket leg, together with horizontal members along the sides of a square connecting the tops of the legs and a platform at the same level integral with the base of the tower

stub section. Deformation of the wall of the tower stub section by the horizontal component of the raking jacket leg extensions is prevented by a large horizontal ring stiffener. In the case of the Beatrice Demonstrator support structures, the transition section weighed 163 t – almost half the 360 t weight of the jacket itself.

On the 2019 Beatrice wind farm, the platform is located at the top of the transition section rather than at the top of the jacket and load transfer from the tower stub to the jacket legs is by means of radial twin-webbed cantilever beams, each with a top chord tubular member sloping down to the top of its supporting jacket leg.

The considerable weight of the transition section in these designs begs the question of why the spacing of the legs at the top of the jacket cannot be reduced to equate to the tower stub radius, to achieve a much more direct load path – e.g. as illustrated in Figure 12.62.

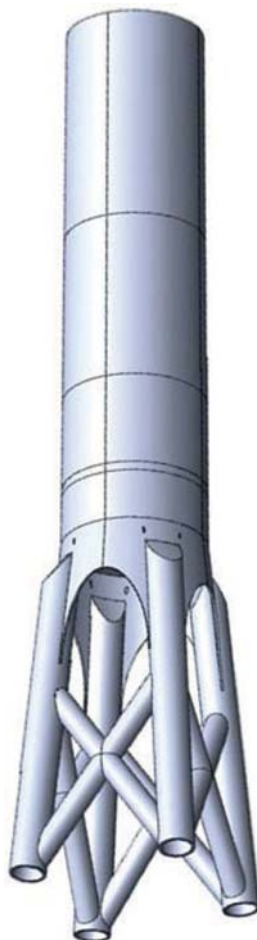


Figure 12.62 Transition section configured to provide direct load paths from tower to jacket legs. Source: Reproduced with permission of DNVGL.

In this example, the diameter of the jacket legs is one quarter of the tower diameter, which would enable the wall thickness of the jacket legs to equate to that of tower wall if the stress levels were the same in each. However, the stress concentration at the top brace to leg connection would mean that the leg wall thickness would have to be substantially increased at the top.

Three legged jackets

There is no intrinsic reason why jackets should have four legs and three legged designs have emerged in recent years, notably at East Anglia One wind farm, where they support 102 7 MW Siemens Gamesa turbines in an average water depth of 45 m, and at the European Offshore Wind Deployment Centre, off Aberdeen – a wind farm consisting of 11 Vestas 8.4 MW turbines in water depths of 20–30 m. The three leg jacket arrangement has made a more elegant transition piece design possible on both projects, with full depth cantilever box beams projecting out from the tower stub to each jacket leg (see Plate 6).

Simplified jacket models for turbine dynamic response analysis

As noted in Section 12.6, design responsibility for the wind turbine and the substructure is usually split between different entities – i.e. the turbine manufacturer and the foundation designer. In the case of jacket sub-structures, the complexity of the structure and its wave loading militate against their accurate modelling within the turbine manufacturer's own design software, so it is normal for the jacket designer to provide a simplified structural model of the jacket (known as a *superelement*) for the turbine designer to use in calculating the dynamic response to wind and wave loads.

It is generally found that a quasi-static representation of the foundation structure in terms of a superelement consisting of $[6 \times 6]$ mass, stiffness, and damping matrices for the six degrees of freedom of the jacket/tower interface is inaccurate, as it does not account for the effects of excitation of the internal vibration modes of the jacket – i.e. those for which the jacket/tower interface remains fixed. The Craig–Bampton reduction method (Craig and Bampton 1968) is commonly used to derive much larger matrices for a superelement that models the internal vibration modes as well. It is normal to include all internal modes with frequencies less than around 10 Hz. In particular, the lateral vibration modes of braces should be included, as these can be excited by harmonics of blade passing frequency. Van der Valk (2014) sets out the application of the Craig–Bampton reduction method to jacket structures in more detail.

An example sequence of tasks to be performed by the foundation designer (FD) and wind turbine designer (WTD) for load case analysis is as follows:

1. WTD provides FD with a jacket frequency constraint and estimates of interface extreme and fatigue loads at the tower/jacket interface.
2. The FD proposes a jacket design and performs analysis to calculate the wave loads on the jacket for each load case and constant gravity loads, assuming a rigid structure. The FD then carries out Craig–Bampton reduction to calculate the modal mass and stiffness matrices defining the superelement, as well as the wave load time histories on each jacket mode. Superelement damping is generally included

as Rayleigh damping based on the mass and stiffness matrices. The superelement matrices and wave loads are provided to the WTD.

3. The WTD performs analysis in an aero-elastic code, using a coupled model of the RNA, tower, and superelement (and its associated wave loads) at the tower base. The coupled response of the whole system is evaluated, and updated interface load time histories are calculated and passed back to the FD.
4. The FD analyses jacket dynamic response to the wave loading and revised interface loading time histories for each load case and verifies the adequacy of the structure to resist extreme and fatigue loads.
5. Steps 2–4 are repeated as necessary to refine the design.

This approach is compared with the integrated design approach for an example generic 7 MW turbine in Collier and Alblas (2018).

Piling

Jacket structures have to be attached to the seabed in some way at each corner, in order to resist uplift generated by overturning moments. This is normally accomplished by piling, but suction buckets were used at two wind farms installed in 2018 and are planned for another.

At the Beatrice Demonstrator Project, the jacket structures were fabricated with a pile sleeve attached to each leg. Following jacket installation, a 1.83 m diameter pile was threaded through each sleeve and driven into the seabed. Each pile and sleeve were then swaged together by expanding the pile under hydraulic pressure, deforming it into circumferential recesses in the sleeve.

A different approach was adopted at Alpha Ventus, where the piles were driven in advance. Instead of using pile sleeves, jacket leg extensions were fitted below the jacket feet and, at jacket installation, these were threaded into the piles (from which the upper part of the soil plug had previously been removed) as the jacket was lowered. With the jacket feet finally resting on the pile tops, the void between each jacket leg extension (known as the jacket *stab-in*) and its pile was grouted up to complete the anchoring of the jacket to the seabed. The arrangement is similar to that employed at the Ormonde wind farm, which is illustrated in Figure 12.63.

Elastomeric bearings are normally attached to the underside of the jacket leg base collars on four legged jackets to take up any small variation in the pile top levels. It is crucial that relative movement of the jacket stab-ins and piles is strictly limited while the grout is going off, so the grouting operation must be timed to coincide with a suitably calm weather window.

A critical element in this procedure was the accurate positioning of the piles in the first place, which was achieved by means of a two-part steel template laid on the seabed (Norwind 2010). The outer element was positioned successively at four positions around a central octagonal element, kept in place by temporary piles. The outer element incorporated a pile guide and, at each position, a fresh pile was inserted and driven home. A similar pile positioning technique was employed at the 2019 Beatrice wind farm, using a 700 tonne reusable pile installation frame.

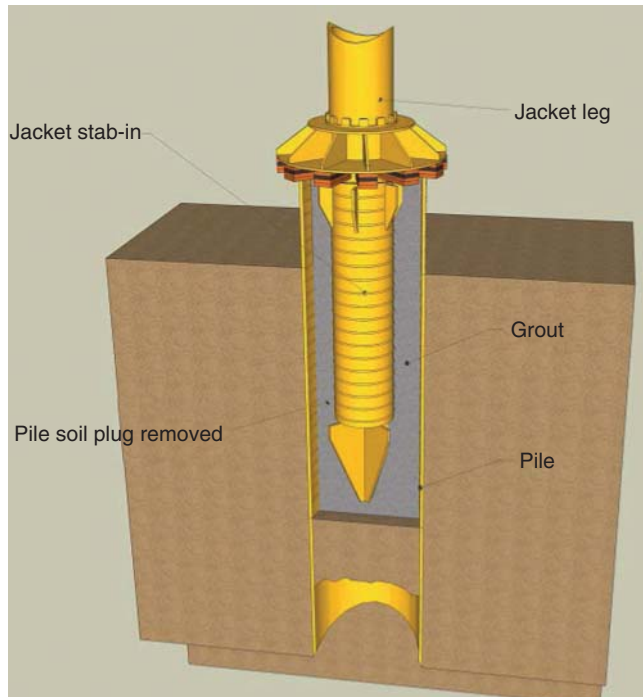


Figure 12.63 Anchorage of jacket leg to pile using concentric jacket stab-in and grouted joint – Ormonde wind farm. Source: Reproduced by permission of Offshore Design Engineering Ltd. (ode).

Suction buckets

Suction buckets are in the form of inverted buckets with parallel sides, which are attached rigidly to the base of each jacket leg. During installation the jacket is lowered into the water and, once the bucket rims are resting on the seabed, water is pumped out of each bucket chamber, so that the water pressure above drives it into the soil until the top of the bucket rests on the seabed. They can be installed in both sand and clay but may not be suitable for water depths less than 15–20 m because of the lower water pressure available. An important consideration is the possible presence of larger boulders, as these can prevent the bucket from reaching its intended depth.

The first suction bucket jacket foundation was installed at Borkum Riffgrund 1 in 2014, supporting a Siemens 3.6 MW turbine. More followed in 2018 to support MHI Vestas V-164 turbines – 20 at Borkum Riffgrund 2 and 11 at the European Offshore Wind Deployment Centre, off Aberdeen, with three legged jackets employed in all cases. At the Aberdeen site, the suction buckets were 9.5–10.5 m in diameter and 9–13 m deep (Vattenfall 2017). Oersted has published a useful description of suction bucket foundations and their limitations, complete with a list of references (Oersted 2019).



Figure 12.64 Installation of tower, nacelle, and rotor assembly by floating crane at the Beatrice Demonstrator Project.

Installation methods

Large floating cranes were used to place the jacket structures on the seabed at the Beatrice Demonstrator, the Alpha Ventus, and the 2019 Beatrice wind farms. The floating crane was also used to install the pre-assembled rotor, nacelle, and tower on each jacket structure at the Beatrice Demonstrator (Figure 12.64).

The figure shows the elaborate octagonal temporary interface frames that were attached to the jacket top and tower base to facilitate the mating process. These incorporated hydraulic rams, allowing them to compensate for the relative motion of the floating crane and the jacket structure due to swell and thus avoid hard impact. By contrast, a jack-up barge mounted crane was used for the separate installation of tower, nacelle, and rotor at the Alpha Ventus and the 2019 Beatrice wind farm.

Jacket weights

The approximate weights of the jacket structure, secondary elements, and piles at the Beatrice Demonstrator and Alpha Ventus are given in Table 12.8.

Table 12.8 Approximate weights of jacket structure, secondary elements, and piles at the Beatrice Demonstrator and Alpha Ventus (Seidel 2007a, b).

Wind farm site	Beatrice	Alpha Ventus
Water depth	45 m	30 m
<i>Component</i>		
Jacket	360 t	
Transition section, including platform	160 t	
Pile sleeves	163 t	Not applicable
Total for primary structure	683 t	425 t
Boat landings	68 t	
Anodes	52 t	
Misc. (e.g. J-tubes)	25 t	
Total for secondary elements	145 t	85 t
Piles	468 t	315 t
Overall total	1296 t	825 t

It is apparent that the pile weight accounts for over one third of the total in each case, and that at the Beatrice Demonstrator, the transition section approaches half the weight of the jacket structure.

Comparison with monopile weights

The monopile support structure weights including tower predicted by de Vries and Krolis (2007) for the Vestas V90 3 MW turbine (see ‘Monopiles in Deeper Water’ in Section 12.7.3) can be used to estimate the corresponding values for the REpower 5 MW using a scaling rule that preserves the relationship between the support structure natural frequency and the nominal rotational frequency at rated power. Treating the monopile and tower support structure as a uniform weightless cantilever of length L , supporting a tower head mass of M , it can be easily shown that the natural frequency is given by

$$\omega^2 = \frac{3EI}{ML^3} \text{ rad/s}$$

so that the second moment of area required to obtain a particular natural frequency is

$$I = \frac{ML^3\omega^2}{3E} \quad (12.76)$$

This formula will also hold true for the required mudline second moment of area of geometrically similar tapering support structures, except that the number in the denominator will be different.

If it is assumed that the wall thicknesses and radii of the monopile and tower design for the V90 3 MW turbine for a given water depth are all to be scaled up in the same proportion to achieve the larger second moments of area required for the REpower 5 MW

Table 12.9 Turbine parameter values used to derive weight scaling factors at different water depths.

Turbine	Vestas V90 3 MW	REpower 5 MW
Nominal rotational speed, ω	16.1 rpm	12.1 rpm
Tower top mass, M	112 tonnes	410 tonnes
Hub height, H	68.5 m	87 m
Monopile + tower weight scaling factor for 30 m water depth	1	2.211

turbine monopile and tower design at the same water depth, then the cross-sectional area scaling factor is equal to the square root of the second moment of area scaling factor – i.e.

$$k_A = \frac{\omega_5}{\omega_3} \sqrt{\frac{M_5}{M_3} \frac{L_5^3}{L_3^5}} = \frac{\omega_5}{\omega_3} \sqrt{\frac{M_5 (D + H_5)^3}{M_3 (D + H_3)^3}} \quad (12.77)$$

where the ratio ω_5/ω_3 is set equal to the ratio of nominal rotational speeds during operation at rated power, D is the water depth and H_5, H_3 are the respective hub heights of the 5 MW and 3 MW machines. The weight scaling factor, k_W , is obtained by multiplying the cross-sectional area scaling factor by the cantilever length ratio, $(D + H_5)/(D + H_3)$. Table 12.9 gives the parameter values adopted in the above expressions.

The estimated monopile plus tower weights required to support the Vestas V90 3 MW turbine in different water depths and the scaled up values for the REpower 5 MW turbine are plotted in Figure 12.65, together with the total weight of primary structure, piles, and tower (taken as 210 tonnes) for the jacket-type support structures at the Beatrice and Alpha Ventus wind farms. It is shown that the weight savings for the jacket structures is significant and more marked at the greater water depth.

Integrated jacket structure and tower

One means of eliminating the heavy transition section between the jacket structure and tubular tower is the combination of the former with a lattice tower. The lattice tower legs would then be simply continuations of the jacket legs. Lattice towers supporting upwind turbines are usually waisted to provide adequate tip clearance, but in the case of a downwind turbine, the legs could be straight all of the way from the seabed to the nacelle. Access from platform level to the nacelle would be by lift, which could be enclosed in a reinforced plastic tube to protect it from the elements. A support structure of this type has been proposed for a demonstration wind farm in the Firth of Forth, which would utilise a two bladed downwind turbine of up to 9 MW rating (Forthwind Ltd 2015).

12.7.7 Tripod structures

The chief advantages of tripod structures are that they are structurally more efficient than monopiles in resisting overturning moments and that wide spacing of the feet can

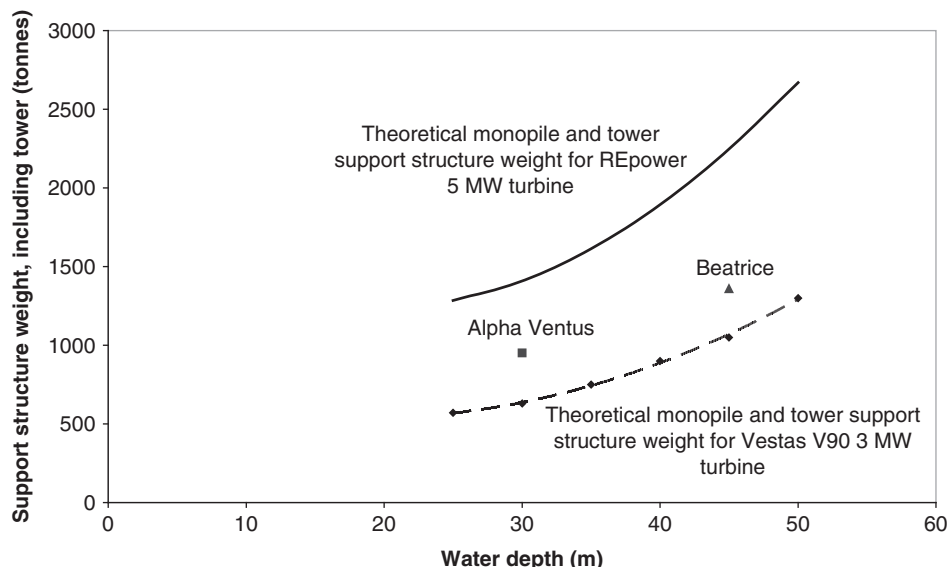


Figure 12.65 Theoretical variation of 5 MW turbine monopile support structure weight with water depth in comparison with Alpha Ventus and Beatrice Demonstrator jacket structure actual weights.

avoid the need for piling if the feet are suitably ballasted. However, unlike the jacket structure, they cannot eliminate rotor thrust-induced bending moments from the main members, although these moments are obviously reduced, as they are shared between several members and reduce linearly between the tripod apex and the seabed.

A number of different forms of tripod structure are possible. The plain tripod design consists of three inclined legs meeting at a short column at the apex, with their feet connected by tie beams forming the sides of an equilateral triangle. The tower is then attached to the top of the short column.

In a variant of this, dubbed the centre column tripod (CCT), the short column is replaced by a long column extending to the seabed, where it is connected to the feet of the inclined legs by radial tie beams, in place of the tie beams between feet.

The number of members in the tripod can be reduced by adopting the flat faced tripod configuration (FFT), in which the column moves to the 90° vertex of a right-angled isosceles triangle forming the tripod base. In this case there are only two inclined legs and two tie members tying each foot back to the base of the column.

The structural benefit of the tripod in reducing column bending moments clearly increases with tripod height, but it is advisable to avoid placing the tripod apex at wave crest level to minimise wave loading. However, boat access is potentially more awkward if the apex is placed above wave crest level.

Alpha Ventus tripod structures

Six tripod structures have been installed in water 30 m deep in the North Sea to support Multibrid M5000 turbines at the Alpha Ventus site (see previous section). These are of

Table 12.10 Comparison of tripod and jacket structure weights at Alpha Ventus.

Structure type	Tripod Estimated weights	Jacket Weights
<i>Component</i>		
Primary structure, including pile sleeves, platform, and transition section (jacket only)	840 t	425 t
Secondary elements (boat landings, J-tubes, and anodes)	85 t	85 t
Piles	370 t	315 t
Overall total	1295 t	825 t

the CCT configuration, with the tripod apex located below water level. As a consequence, the tripod base is relatively small and the tripod feet have to be secured against uplift by piling.

Table 12.10 compares an estimated tripod structure weight with that of the jacket structures at the same wind farm, based on Seidel (2007a).

It is seen that the estimated weight of the complete tripod structure including piles is over 50% greater than the corresponding figure for the jacket structure.

It is an open question as to whether larger FFT tripods would prove more economic.

Borkum West 2 tripod structures

The Borkum West 2 wind farm, commissioned in 2015, consists of 40 AREVA M5000 5 MW wind turbines supported on tripods weighing 900 tonnes each, in water depths of around 30 m.

12.7.8 Tripile structures

BARD has developed a tripile structure to support their own 5 MW turbines in water 25–40 m in depth. The design consists of three equispaced 3.35 m dia vertical piles approximately 20 m apart, which are linked together by a three-arm transition structure onto which the tower is mounted. A vertical cylindrical tube projects downwards from the end of each arm and the three tubes are inserted into the tops of the three piles and grouted in the same way as monopile transition pieces. The transition structure arms are of rectangular cross-section, enabling them to be fabricated easily from flat plate.

Figure 12.66 illustrates a tripile structure after installation.

The weight of the transition structure is 470 t and the piles weigh up to 420 t, so the total weight is comparable with that of the Alpha Ventus jacket structure (825 t).

12.7.9 S-N curves for fatigue design

Derivation of S-N curve

The derivation of the S-N curve to be used for the damage calculation must take account of the fatigue detail, corrosion, the plate thickness and the partial safety factor for materials strength.



Figure 12.66 Tripile structure after installation. The pile tops, which sport circumferential stripe markings, extend up to platform level with the cylinders above forming part of the three-arm transition structure. Source: Copyright: 'BARD Group/Scheer'.

Influence of fatigue detail Unless there are J-tube penetrations through the monopile wall or welded attachments, the critical fatigue details are likely to be the transverse butt welds. According to EN 1993-1-9 (2005), *Design of Steel Structures – Part 1-9: Fatigue*, transverse butt welds are detail category 90, provided the weld convexity is less than 10%, or 112 if the welds are ground flush. For weld convexity between 10% and 20%, detail category 80 applies.

ISO 19902:2007, *Petroleum and Natural Gas Industries – Fixed Steel Offshore Structures*, uses a different set of S-N curves, which are identified by different letters of the alphabet and have their origins in the British standard for steel bridges, BS 153. In the case of transverse butt welds, the applicable S-N curves are curve C, D, and E for ground flush welds, welds with low convexity, and welds with high convexity, respectively. The curves for low weld convexity, ISO 19902 curve D, and the EN 1993-1-9 curve for detail category 90 parallel each other fairly closely before the cut-off limit, as shown in Figure 12.45.

The S-N curves specified by DNVGL-RP-C203 (2016), *Fatigue Design of Offshore Structures*, are similar to those specified in ISO 19902 with virtually identical D and E curves but a somewhat different C curve.

Influence of corrosion Fatigue testing of specimens with cathodic protection in seawater indicates reduced fatigue strength for stress range magnitudes corresponding to fatigue

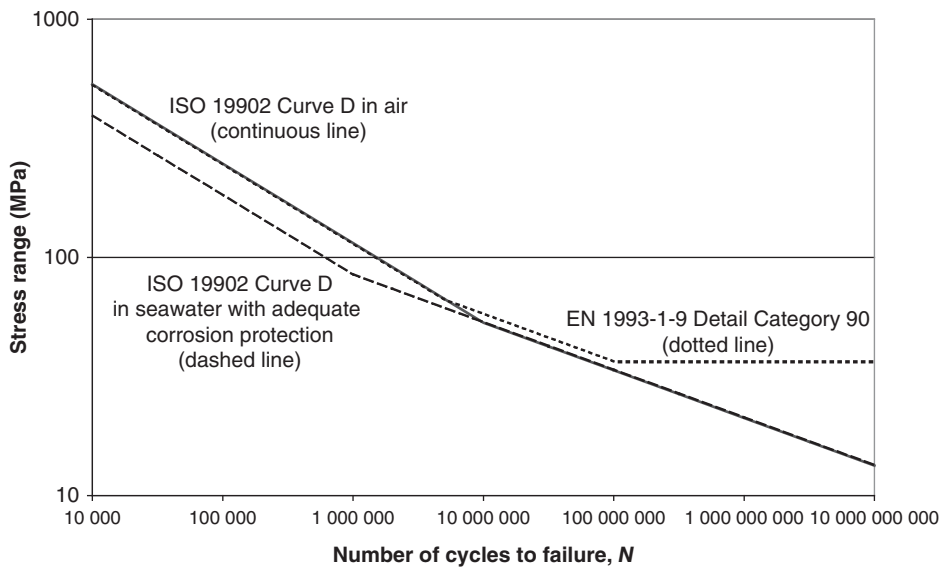


Figure 12.67 Comparison of design S-N curves for transverse butt welds without excessive reinforcement.

lives of less than 10^6 cycles, and this is reflected in separate S-N curves for structures in seawater ‘with adequate corrosion protection’ specified in ISO 19902. The curve D variant for seawater is shown in Figure 12.67.

Influence of plate thickness Recognition that increased plate thickness led to a reduction in weld fatigue strength first emerged in the 1980s in relation to cruciform joints. The reduction is thought to result from the increase with plate thickness of the geometric stress at the depth below the weld toe from which an initial crack could propagate, on the assumption that all weldment dimensions scale uniformly with the main plate thickness.

The thickness effect (or, more properly, the size effect) has been allowed for in standards by applying a fatigue strength reduction factor of $(t_{ref}/t)^k$ for thicknesses greater than the reference thickness, where k is termed the *thickness exponent*. In EN 1993-1-9, k is 0.2 and t_{ref} is 25 mm. Monopile wall thicknesses often reach 80 mm, giving a reduction factor of 0.792, so this has a significant impact on design. The ISO 19902 reduction is more severe, with a thickness exponent of 0.25 and a reference thickness of 16 mm.

Although the reduction factor of $(t_{ref}/t)^k$ is straightforward, there is evidence to suggest that the strength reduction is more closely related to the length of the weld attachment, L_t , in the direction of the applied stress than to plate thickness. Lotsberg (2014) used fracture mechanics techniques to analyse crack growth to failure for weld geometries with different attachment lengths. The results were input into a modified S-N curve formula

$$\log N = \log a - m \log \left(S \left(\frac{t_{eff}}{t_{ref}} \right)^k \right) \quad (12.78)$$

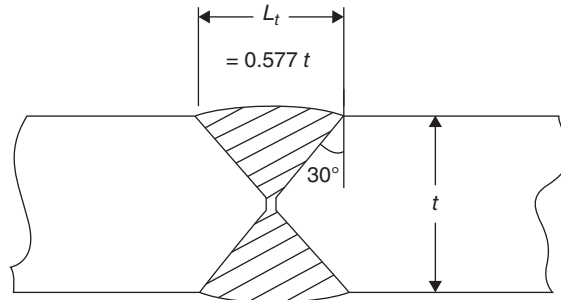


Figure 12.68 Double-sided butt weld with 30° bevel angles.

in which the plate thickness, t , was replaced by an effective thickness, t_{eff} , enabling the latter to be correlated to attachment length. Based on these results it was concluded that the relationship between effective thickness and attachment length could be expressed by the formula

$$t_{eff} = \min((14 + 0.66L_t), t) \quad (12.79)$$

where L_t , and the thicknesses are expressed in millimetres.

Equations (12.78, 12.79) have been adopted in the DNVGL recommended practice DNVGL-RP-C203 (2016), resulting in a significantly less onerous fatigue strength reduction factor, $(t_{ref}/t_{eff})^k$, to account for the size effect. For a double-sided butt weld prepped with 30° bevel angles (see Figure 12.68), the butt weld width and hence L_t , is approximately $t/\sqrt{3}$, giving the relationship between the effective thickness and actual thickness shown in Figure 12.69.

The reference thickness, t_{ref} , remains 25 mm for welded connections other than tubular joints and k takes the value 0.2 for Class D and E welds, as in DNV-RP-203, which preceded DNVGL-RP-C203 (2016). The resulting fatigue strength reduction factor for butt welds is compared with those of the other two standards in Figure 12.69.

Stress concentration factors Load transfer between the braces and legs of jacket structures of necessity results in large local stress concentrations at the welds and a suite of necessarily complex formulae has been developed for calculating the hot spot stress concentration factors (SCFs) (Efthymiou 1988). Stress concentrations also occur at girth welds on monopiles and jacket members – e.g. due to thickness change, transitions between conical and cylindrical sections or plate mis-alignments.

Historically there has been some divergence between standards over whether a modest SCF due to plate mis-alignment is already accounted for in the butt weld $S-N$ curves (Lotsberg 2016), with allowable SCF values of 1.05 and 1.1 being quoted. DNVGL-RP-C203 gives the SCF for a girth weld between cans of equal thickness as

$$SCF = 1 + \frac{3(\delta_m - \delta_0)}{t} \exp\left(-\frac{1.817L}{2\sqrt{tD}}\right) \quad (12.80)$$

where δ_m is the actual plate mis-alignment, $\delta_0 = 0.05t$ is the mis-alignment inherent in the $S-N$ data and analysis procedure and L is the butt weld width. The exponential expression

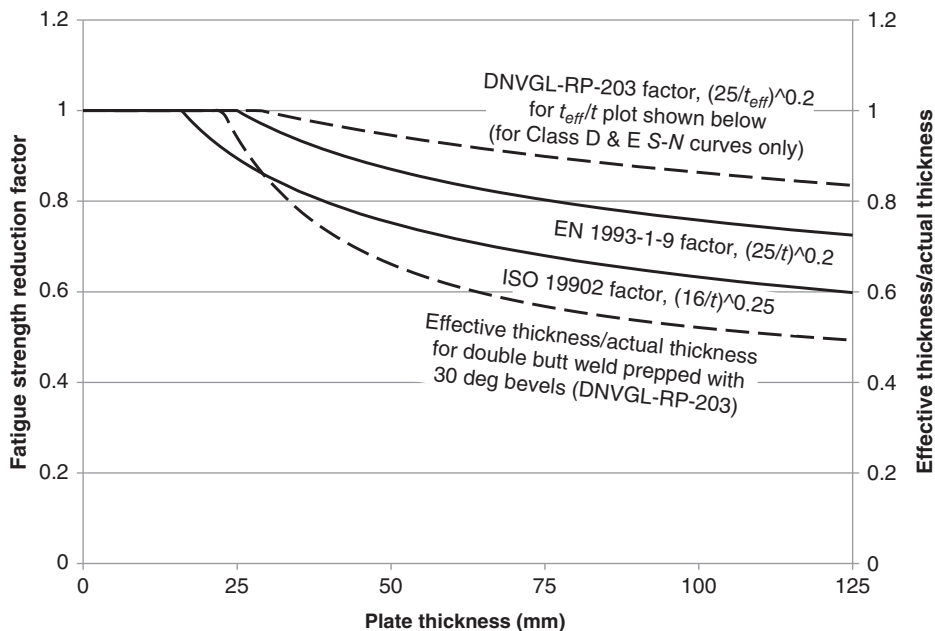


Figure 12.69 Comparison of butt weld fatigue strength reduction factors due to plate thickness given in ISO 19902 (2007), EN 1993-1-9 (2005), and DNVGL-RP-C203 (2016).

allows for the moment attenuation with distance from the joint centreline due to circumferential stresses.

Partial safety factor for material strength It is generally impracticable to inspect the monopile for fatigue damage, because of marine growth and the hazardous environment, so it must be designed for ‘safe-life’. On the basis that the consequence of monopile failure would be high, the partial factor for material strength, γ_m , recommended by EN 1993-1-9 is 1.35. This is higher than the corresponding value of 1.265 in IEC 61400-1, which is the product of a materials factor of 1.1 in the absence of periodic inspections and a consequence of failure factor of 1.15 for high consequence.

In ISO 19902, the partial safety factor for material strength is taken as unity and allowance made for the absence of periodic inspections and high consequence of failure by inflating the calculated fatigue damage sum (which is required to be less than unity as usual) by a design fatigue factor (DFF) of 10. This is equivalent to a rather high partial safety factor of material strength of 1.58 for a *S-N* curve inverse slope of $m = 5$, which reflects the higher safety criticality of oil and gas structures.

DNVGL-ST-0126, *Support Structures for Wind Turbines* (2016), adopts a lower value of DFF of 3 for uninspectable parts of the structure, as it is considered to have low consequence of failure. This corresponds to a γ_m of about 1.25 for $m = 5$.

System effect The *S-N* curves used for design are normally obtained from the mean line of test results by subtracting two standard deviations and should therefore result in

a 2.3% probability of failure for a length of weld equal to test specimen width that is designed with a DFF of unity. Welds on offshore wind turbine support structures are often many metres long, however, which can significantly increase the probability of failure if the loading is uniformly distributed rather than concentrated at a hot spot. This is an example of the system effect, which is particularly an issue for pipelines (Lotsberg 2010).

As an illustration, the increased failure probability for a girth weld in a monopile designed for constant amplitude loading in one direction with a DFF of 3 is investigated.

The DFF reduces the allowable stress range by a factor of $\left(\frac{1}{DFF}\right)^{\frac{1}{m}}$, where m , the inverse slope of the $S-N$ curve is taken as 5 for high cycle fatigue, giving a factor of $1/3^{0.2}$ or 0.8027. The length of weld in fatigue test specimens is assumed to be 100 mm and the monopile diameter is 6 m, giving a circumference of 18.85 m.

The reduction in the probability of failure due to the increased DFF depends on the standard deviation found in the test results – here the standard deviation of $\log(N)$ is assumed to be 0.2, following appendix F5 in DNVGL-RP-C203 (2016). This equates to a standard deviation of $\log(S)$ of $0.2/3 = 0.06667$ for the $S-N$ curve inverse slope of 3, which is applicable to the low cycle test results. As the girth weld is designed for a damage sum of 1/3 – i.e. for a DFF of 3, it can be shown that the probability of failure of the critical 100 mm length of weld comes to 0.03%.

In view of the unidirectional wind and wave loading, the stress ranges in the weld will vary sinusoidally around the circumference, so the failure probability will reduce away from the diameter aligned with the loading direction. The survival probabilities of each 100 mm length of weld around the circumference can then be multiplied together to obtain the overall weld survival probability. This exercise yields a weld failure probability of 0.89%, some 30 times bigger than that for the heaviest loaded 100 mm length, indicating an un-conservative design. A wall thickness increase of about 12% would be required to reduce the overall failure probability to 0.03%.

Life extension The design criterion inherent in fatigue design is the maintenance of the probability of failure below a predetermined level determined by the DFF. As noted above, this probability is 0.03% for high cycle fatigue for a DFF of 3, assuming uncertainties in the design load and Miner's sum are ignored. Figure 12.70 shows the cumulative probability of failure for a weld designed for a 20 year life on this basis. It is seen that, if the weld continues in service after the 20 years has expired, the probability of failure over the next 3 years is no more than the original target of 0.03%, leading to the conclusion that the weld's survival over the first 20 years renders it safe for service over a further 3 years.

If uncertainties in loading and Miner's sum were taken into account, the cumulative probability of failure curve would be flatter, so that the safe life extension after the original 20 year design life would be increased (although the threshold probability of failure would, of necessity, be higher).

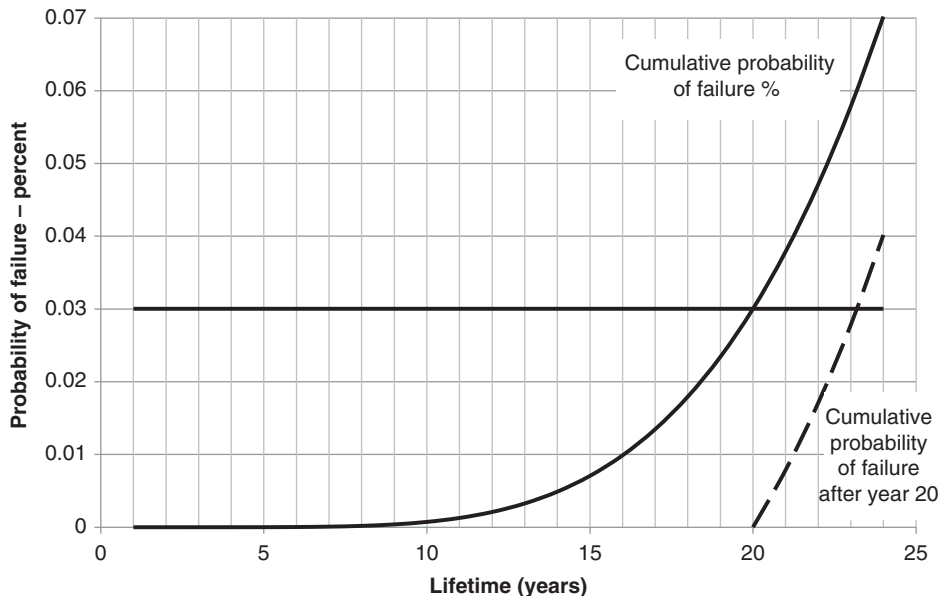


Figure 12.70 Cumulative failure probability for a weld designed using a DFF of 3, assuming high cycle loading.

12.8 Floating support structures

12.8.1 Introduction

The cost of fixed support structures inevitably increases rapidly with water depth and starts to become prohibitive at depths of over 50 m. There are many stretches of coastline with a steeply shelving seabed, where there is little or no room for bottom mounted structures, so attention has turned to the development of floating support structures that can be used to exploit these locations instead. The first megawatt scale floating wind turbine was the 2.3 MW Hywind prototype installed near the island of Karmøy in SW Norway in 2009.

Since then, more floating wind turbine prototypes of a variety of types have been commissioned and tested, with the first wind farm of five 6 MW turbines being installed off Peterhead in 2017 by Hywind Scotland.

Apart from the ability to exploit deep water sites, floating wind turbines have other advantages. Firstly, the support structure no longer needs to be tailored to the water depth and soil conditions obtaining at each turbine location, so a single design can be deployed both within a particular wind farm and across all wind farms with comparable wave climates. Secondly, floating support structures enable the erection of the wind

turbine to take place at the quayside or in sheltered waters, rendering the operation less weather dependent and eliminating the need to deploy jack-up barges in the open sea. Set against this is the need to install anchors in the seabed for moorings and connect the latter to the floating structure. A useful introduction to the engineering challenges of floating offshore wind turbines in general is provided in Butterfield et al. (2007).

The motion of a floating support structure has six degrees of freedom, which are defined in similar terms as for ships, but with reference to the wind direction rather than a ship's heading:

1. Surge: horizontal translation along the axis aligned with the wind direction (the x axis, pointing downwind).
2. Sway: horizontal translation along the axis perpendicular to the wind direction (the y axis, pointing to the right for an observer facing into the wind).
3. Heave: vertical translation (the z axis, pointing upwards).
4. Roll: rotation about the axis aligned with the wind direction.
5. Pitch: rotation about the axis perpendicular to the wind direction.
6. Yaw: rotation about the vertical axis.

The axis directions are thus the same as those in Figure C2 at the front of the book, and similarly, the direction of positive rotation is clockwise when looking along the relevant axis. Conventionally, the six motions are numbered as indicated, and the origin of the axis system is taken on the tower axis at the water level.

These six degrees of freedom mean that the analysis of the floating structure's response to wind, wave, and current loads is an order of magnitude more complex than for a bottom mounted structure. It is beyond the scope of this book to go into this in detail, but an introduction to design requirements is given in Sections 12.8.3 and 12.8.4. Station keeping is considered in Section 12.8.5, followed by case studies of a few existing installations. For a more in-depth treatment, the reader is referred to Cruz and Atcheson (2016).

12.8.2 Floater concepts

Floating support structures are best categorised by the primary stabilisation principle utilised, as follows:

- Deep draft vertical cylinder, known as a *spar buoy*. This is hollow and ballasted at its base, so that the centroid of the complete structure (comprising the turbine, tower and, spar buoy) is below the centre of buoyancy.
- Floating barge or semi-submersible. This is stabilised by the net restoring moment produced by vessel tilt in combination with the waterplane area.
- Tension leg platform (TLP), where tilt is limited by the pre-tensioned vertical moorings.

The three different types are illustrated in Figure 12.71.

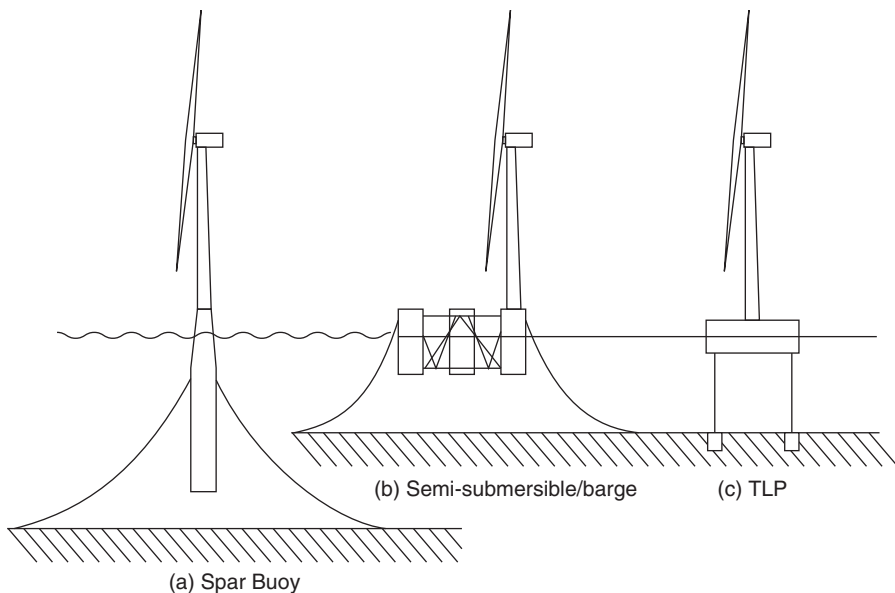


Figure 12.71 Types of floating offshore wind structures: (a) spar buoy, (b) semi-submersible/barge, and (c) TLP.

Spar buoys

The draft of a spar buoy has to be large – i.e. of the same order of magnitude as the turbine hub height with respect to sea level – in order to position the centre of gravity of the complete structure, including turbine, below the centre of buoyancy. As a result, spar buoys require deeper water than other types of floater. By the same token, deep water is also required for the installation of the wind-turbine on the spar buoy.

Besides limiting motion in surge and sway, the moorings must also provide yaw restraint. This is achieved by a yoke arrangement, in which each mooring is split into two identical short link cables attached to either side of the spar buoy.

Barges

Floating barges have minimal draft and so can be deployed from a wide range of ports. The ITI energy barge concept, consisting of a vessel 40 m square in plan by 10 m deep, was developed at the University of Strathclyde in 2006 and investigated at NREL but has not been taken further. Barges suffer from the disadvantage that their inherent stability comes at the cost of high exposure to wave loading.

Semi-submersibles

Semi-submersibles, consisting of three or four widely separated vertical cylindrical hulls braced together, offer excellent stability with reduced exposure to wave loading. They also experience less pitch and roll motion, as water particle velocities are reduced at the base of the cylinders compared with at the wave surface. The wind turbine tower can

be mounted on top of one of the cylindrical columns, with extra ballast added to the other columns to balance the turbine and tower weight. If desired, water ballast can be transferred between the columns to oppose the moment on the platform due to the rotor thrust loading, in order to minimise the inclination of the platform.

Tension leg platforms

TLPs have the obvious advantage of virtually eliminating pitch and roll motion, thereby minimising nacelle accelerations. However, the tension leg cable anchorages have to resist large uplifts, especially as they have to be stressed to a level that prevents cables going slack during the passage of a large wave trough, so they are considerably more expensive (and more critical) than the anchors for the moorings of the other platforms. The latter frequently rest on the seabed in the vicinity of the anchor, so the anchor only has to resist a horizontal force.

Additional loads on turbine

The dynamic response of floating platforms inevitably adds to the loadings on the different elements of the wind turbine. Jonkman and Matha (2010) investigated the additional loads experienced by the NREL 5 MW reference design turbine when mounted on three types of floating platform – a TLP, a spar buoy, and a barge – and compared them. In the case of extreme loads, the largest load resulting from IEC 61400-3 load cases 1.1, 1.3, 1.4, and 1.5 was computed for each floating wind turbine and compared with the corresponding maximum for the onshore turbine. The comparison was made at each of four locations – the blade root, low-speed shaft, yaw bearing, and tower base – see Figure 12.72.

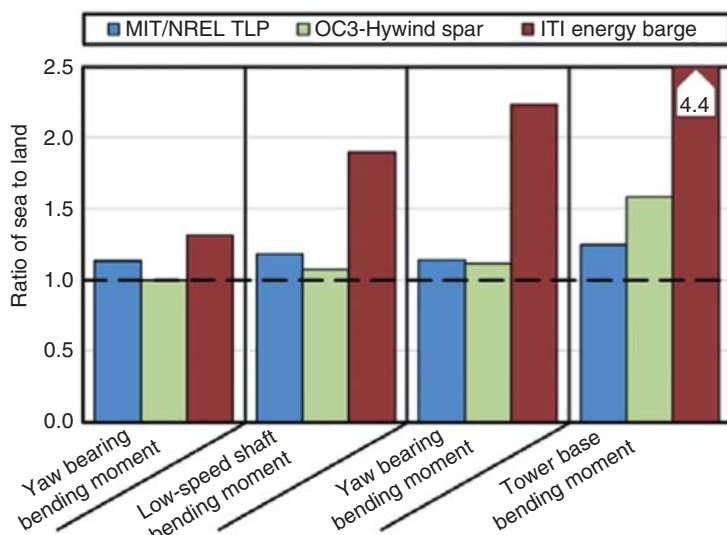


Figure 12.72 Ratios of extreme turbine loads on different floating platforms to those on land for the NREL 5 MW reference turbine. Source: Reproduced from Jonkman and Matha (2010) with permission.

It is seen that the loading increases are relatively modest for the TLP and spar above the tower but rise to 25% and 60%, respectively, at the tower base. However, the loading increases are much higher for the ITI energy barge, which experiences large pitch excitation by waves with periods close to its natural period in pitch motion of 11.6 seconds (Jonkman 2007).

12.8.3 Design standards

The first design standard for the design of floating offshore wind turbines, DNV-OS-J103, was published in 2013. It was amended in 2018 and renumbered DNVGL-ST-0119. The IEC technical specification IEC-61400-3-2, *Design Requirements for Floating Offshore Wind Turbines*, was published in 2019. Both the DNVGL and IEC documents require consideration of the load cases specified in the corresponding standards for fixed offshore structures and supplement these with a few load cases specific to floating wind turbines. Both emphasise that it is important to assume the most unfavourable directions of the wind, waves, and current for the ULS (ultimate limit state) load cases.

12.8.4 Design considerations

An overview of the various stages in the design process for a floating wind turbine platform is provided by the following list, which has been adapted from that in Sandner et al. (2014a), *INNWIND Deliverable D4.3.3, ‘Innovative Concepts for Floating Structures’*.

1. Selection of platform type (ballast, buoyancy, or mooring stabilised).
2. Hydrostatic analyses giving the design space with appropriate hydrostatic properties. The relevant structural quantities like mass, centre of mass, and moment of inertia can be formulated.
3. Material and manufacturing cost estimates for all possible designs gives an approximate capital expenditure (CAPEX) and assesses the design feasibility.
4. Dynamic analyses in the frequency domain using potential flow solvers to determine wave loadings and hydrodynamic loadings due to platform motion. These assume a rigid floating body restrained by a preliminary conceptual mooring system, allowing the dynamic behaviour to be optimised for steady state conditions.
5. Refinement of mooring system design for steady state conditions.
6. Coupled dynamic analysis with an aero-servo-hydro-elastic software tool to model the dynamics in realistic conditions for outline critical cases chosen from the load cases specified in IEC 61400-3.
7. Experimental wave tank tests to verify numerical simulations for the outline critical cases.
8. Critical load case review with advanced software tools, considering nonlinear waves, drift forces, wave overtopping, etc.
9. Detailed LCOE estimation, including CAPEX and operating expense (OPEX).

10. Detailed component design including structural dimensioning based on coupled simulations in the time domain according to offshore standards.
11. Determination of the manufacturing and installation process, maintenance, logistics, health and safety, environmental, and legislation aspects.

Some of these stages are considered in more detail below.

Initial design objectives

The over-riding design objective for any floating structure is to minimise its excitation by wave loads, which is achieved by ensuring that the natural frequencies for the six degrees of freedom lie below the range of wave frequencies with significant energy content for the full range of sea states. Sea states with a zero-crossing period of up to 17 or 18 seconds can be encountered in the North Atlantic, which would correspond to a peak period of 25 seconds for a fully developed sea state. In practice this means that the natural periods should exceed 25–30 seconds, depending on the site location.

In the case of floating wind turbines, the most critical motions are pitch and roll, as the displacements are magnified at hub height, potentially leading to high nacelle accelerations. The natural period of pitch motion is given by

$$T_{55} = 2\pi \sqrt{\frac{I_{55,S} + I_{55,A}}{C_{55}}} \quad (12.81)$$

where the 55 suffix denotes pitch motion, $I_{55,S}$ is the moment of inertia of the floating structure about the pitching axis, $I_{55,A}$ is the moment of inertia of the added mass of water associated with pitching of the structure and C_{55} is the stiffness of the restoring moment.

The second key design objective is the limitation of platform pitch due to rotor thrust, as this reduces Annual Energy Production. The maximum mean pitch angle is given by

$$\bar{\beta} = [(H + d_m)T - M_{RNA}e]/C_{55} \quad (12.82)$$

where H is the hub height with respect to the water level, d_m is the mooring attachment depth, T is the mean thrust at rated wind speed, M_{RNA} is the combined weight of the rotor and nacelle and e is the distance of its centroid forward of the tower axis. It is clearly beneficial to reduce the rated thrust for a given power output and this can be achieved with a low induction rotor (Section 6.4.4).

The INNWIND study referenced above set a target mean platform pitch angle of 3.5° during operation at rated wind speed while a subsequent concrete spar design study was based on a value of 5° (Matha et al. 2015), which corresponds to a rotor plane inclination at rated wind speed of about 10° for an upwind floating turbine, based on the typical shaft tilt of fixed-base wind turbines. Clearly a downwind turbine would be at less of a disadvantage in this respect.

Design space

For each platform topology, considerable scope exists to vary platform leading dimensions while meeting the two design requirements described above. Generally it is worth

investigating a range of values – constituting the ‘design space’ – to determine the least cost solution and this process will be illustrated in relation to varying the diameter of a spar buoy in Section 12.8.5 and of the columns of a semi-submersible in Section 12.8.6.

Response to regular waves

Procedures for determining the response of floating structures to excitation by regular, linear waves are long established and based on the solution of six equations of motion with coupled terms for the six degrees of freedom, as follows:

$$\left[\sum_{k=1}^6 (M_{jk} + A_{jk}(\omega))\ddot{\eta}_k + B_{jk}(\omega)\dot{\eta}_k + C_{jk}\eta_k \right] = F_{wj} \sin(\omega t + \phi) \quad (j = 1, \dots, 6) \quad (12.83)$$

where $B_{jk}(\omega)$ are radiative damping terms, C_{jk} are the restoring stiffnesses and $F_{wj} \sin(\omega t + \phi)$ is the wave loading on the structure considered fixed. The $A_{jk}(\omega)$ terms are known as the *added mass terms*, although they can also have units of mass \times distance or mass \times distance squared. The quantity $A_{jk}(\omega)\dot{\eta}_k$ gives the inertia force contribution to the equation of motion for the j th degree of freedom due to the acceleration of the added mass or inertia associated with the k th degree of freedom. Note that there is no coupling between the surge, heave and pitch motions and the sway, roll and yaw motions for a body symmetric about the x, z plane, as will be the case for a floating offshore wind turbine when the wind direction is aligned with a plane of symmetry.

Equation (12.83) can be extended to random sea states containing a range of frequencies using the principle of superposition and can be solved in both the time and frequency domains. In the case of floating wind turbines additional terms have to be added to the right hand side of each equation to account for the contribution of the aerodynamic loading on the rotor due to the incident turbulent wind, together with an additional term on the left hand side to account for the variation of mooring forces with horizontal displacement. The suitability of the frequency domain for the modelling of floating wind turbines has been explored by Lupton and Langley (2013).

In the general case, the wave loadings F_{wj} have to be determined from a diffraction analysis in which the potential flow equations are solved numerically (see the ‘Diffraction’ section), while similar analyses have to be carried out to determine the radiative damping and added mass terms, $B_{jk}(\omega)$ and $A_{jk}(\omega)$, but using different boundary conditions. These analyses can be carried out using potential flow solver programmes (sometimes termed *hydrodynamic panel codes*), such as WAMIT, WADAM, and ANSYS AQWA.

In the case of spar buoys or the vertical cylindrical hulls of semi-submersibles, the use of a potential flow solver programme can be avoided if the diameter is less than one fifth of the wavelength, as the hydrodynamic loads can then be adequately represented using Morison’s equation. This has the benefit of accounting for the non-linear (i.e. quadratic) viscous drag loading as well as for the linear inertia loading. The equations of motion for surge and pitch of a spar buoy then become:

$$(M_{11} + A_{11})\ddot{\eta}_1 + (M_{15} + A_{15})\ddot{\eta}_5 + K_1(\eta_1 - \eta_5 d_m) = \frac{1}{2} \rho \frac{\pi D^2}{4} C_m \int_{-d_S}^0 i u dz + \frac{1}{2} \rho D C_D \int_{-d_S}^0 |u - \dot{\eta}_1 + \dot{\eta}_5 z| (u - \dot{\eta}_1 + \dot{\eta}_5 z) dz + T(t) \quad (12.84)$$

$$(M_{51} + A_{51})\ddot{\eta}_1 + (M_{55} + A_{55})\ddot{\eta}_5 + K_1(\eta_1 - \eta_5 d_m) d_m + C_{55}\eta_5 = \frac{1}{2} \rho \frac{\pi D^2}{4} C_m \\ \int_{-d_S}^0 i u z dz + \frac{1}{2} \rho D C_D \int_{-d_S}^0 |u - \dot{\eta}_1 + \dot{\eta}_5 z| (u - \dot{\eta}_1 + \dot{\eta}_5 z) z dz + T(t) H \quad (12.85)$$

where η_1 and η_5 are the surge and pitch displacements, respectively, K_1 and d_m are the mooring stiffness in the horizontal direction and depth of attachment, respectively, d_S is the draft, and $T(t)$ is the time-varying rotor thrust. Strictly, there should be an additional term in Eq. (12.85) for the rotor pitching moment due to thrust eccentricity, but this is omitted for simplicity.

Aero-servo-hydro-elastic software tools

Computer codes for the dynamic analysis of floating wind turbines need to account for elastic deflections and the behaviour of the pitch control system, as well as for the aerodynamic and hydrodynamic loads, so they can be described as aero-servo-hydro-elastic software tools. Often they are the result of integrating a programme for the analysis of onshore wind turbines with one for the analysis of floating platforms.

A selection of dynamic analysis codes available is listed in Table 12.11, which indicates the aerodynamic, hydrodynamic, structural, and mooring models used for each. Nearly all models employ Morison's equation for the calculation of wave drag loads, but some use potential flow solvers instead for the calculation of inertia loads. Given that potential flow solvers cannot in general handle non-linear waves, the dynamic analysis of barge type structures in extreme waves remains problematic.

The performance of these dynamic analysis codes has been compared by using each to run simulations of a limited number of design load cases for a single semi-submersible wind turbine design with encouraging results (Azcona et al. 2013).

Pitch control adaptation

As wind speed increases above rated, the blades have to be pitched back to limit power output and prevent overspeed, resulting in reduced aerodynamic thrust. This can pose problems on floating wind turbines, because a platform pitching motion into the wind will be sensed as an increase in wind speed, resulting in blade pitching and thrust reduction. Over time this would result in steadily increasing platform oscillations at the platform natural frequency. Suitable modifications of the pitch control system to avoid this behaviour are discussed in Section 8.3.5.

Critical load case selection

As noted above, the analysis of the dynamic behaviour of floating offshore wind turbines is an order of magnitude more complex than that for fixed-base offshore wind turbines and the long natural periods of oscillation demand longer simulation times. When different combinations of wind speed, sea state, wind-wave mis-alignment and current are taken into account, thousands of design load cases may need to be analysed for the final design.

In view of this, there is a need for simpler models allowing rapid analysis of a large number of load cases to select the critical ones for accurate analysis. One such model is

Table 12.11 Selected dynamic analysis codes for floating offshore wind turbines.

Acronym	Institution	Code	Structural model	Platform model	Hydrodynamic model	Mooring model	Aerodynamic model	Dynamic stall
CENER	CENER	OPASS + FAST	Modal + MBS	Rigid	PF + ME	Dynamic	BEM	Yes
DTU GH	DTU GH	HAWC2 Bladed 4.4	FEM + MBS Modal + MBS	Flexible Flexible	ME (IW) ME (IW)	Dynamic Quasi-static	BEM BEM	Yes Yes
GH Adv	GH	Bladed Adv Hydro Beta	Modal + MBS	Flexible	PF + ME (IW)	Quasi-static	BEM	Yes
NTUAm NTUAp SWE	NTUA NTUA SWE	Hydro-GAST Hydro-GAST SIMPAK + HydroDyn	FEM + MBS FEM + MBS Modal + MBS	Flexible Rigid	ME (IP) PF + ME (IP) PF + QD	Dynamic Dynamic Quasi-static	BEM BEM BEM	Yes Yes Yes
CENER: National Renewable Energy Energy Centre of Spain			FEM: finite element method MBS: multi-body system		ME: Morison's equation PF: potential flow QD: quadratic drag IP: calculation of ME at instantaneous position IW: integration of ME to wave elevation		BEM: blade-element/momentum theory	
DTU: Danish Technical University		GH: Garrad Hassan NTUA: National Technical University, Athens SWE: Stuttgart Wind Energy						

Source: Reproduced from Azcona et al. (2013), *INNWIND Deliverable D4.21*, 'State-of-the-Art and Implementation of Design Tools for Floating Structures'.

the ‘Simplified Low Order Wind turbine’ or SLOW model (Matha et al. 2014), which operates in the time domain. This achieves a high level of computational efficiency by avoiding iterative solution of the blade-element/momentum equations, the use of Morrison’s equations for hydrodynamic loads instead of potential flow solvers, restriction of the number of turbine degrees of freedom and quasi-static treatment of mooring loads. Instead of the use of BEM theory, rotor thrust and torque are calculated as functions of the blade pitch angle, the rotational speed and the relative wind speed, with the fluctuating input wind speed being an effective value that produces the same instantaneous rotor thrust as a simulated turbulent wind field. The turbine degrees of freedom are limited to rotor rotation and tower fore-aft and side to side bending but all six platform degrees of freedom are retained.

The authors have also developed a simpler version omitting sway, heave, roll and yaw motions for the optimisation of floating wind turbine designs, including the blade pitch control parameters (Sandner et al. 2014b).

12.8.5 Spar buoy design space

For any given wind turbine, there are a range of spar buoy drafts and diameters that can satisfy the limitations on platform pitch angle and on the natural frequency in pitch and roll.

Consider the steel spar buoy illustrated in Figure 12.73 supporting a 180 m diameter, 9 MW turbine. If the turbine operates with a low induction factor of 0.19, the mean rated thrust at rated wind speed will be about 1100 kN. Assuming a hub height of 115 m and a 20 m mooring attachment depth, the restoring stiffness, C_{55} , is required to be $1100(135)/0.08727 = 1.70 \times 10^6$ kNm/rad to limit the mean pitch at rated to 5°, neglecting the moment due to eccentricity of the tower top mass centroid. The restoring stiffness is given by

$$C_{55} = mgh + \rho_w g \pi D^4 / 64 \quad (12.86)$$

where m is the total mass of the floating wind turbine, h is the height of the centre of buoyancy above the centre of gravity and ρ_w is the density of seawater, but the latter term due to the waterplane area is usually much smaller than the first. It is found that a considerable quantity of ballast has to be added at the base of the cylinder to bring the centre of gravity low enough. Note that, for simplicity, the spar buoy is assumed to be a uniform cylinder, although in practice the diameter would taper down at the top to reduce wave loading. It is convenient to take the freeboard, f , as fixed and here it is assumed to be 15 m.

For each spar buoy diameter, a length L can be found that, together with the corresponding weight of ballast, gives the required value of restoring stiffness. This length is approximately inversely proportional to the diameter, as shown in Figure 12.74. This figure also shows the variation of spar steel weight and ballast weight with diameter. The spar steel weight (based on an assumed 70 mm wall thickness) hardly changes with diameter and, at c. 3000 tonnes, exceeds the combined weight of the wind turbine and tower, taken as 650 and 1200 tonnes, respectively. These compare with a ballast weight of c. 12 000 tonnes for a 108 m × 15 m dia spar buoy, giving a total displacement of about 17 000 tonnes with its 93 m draft.

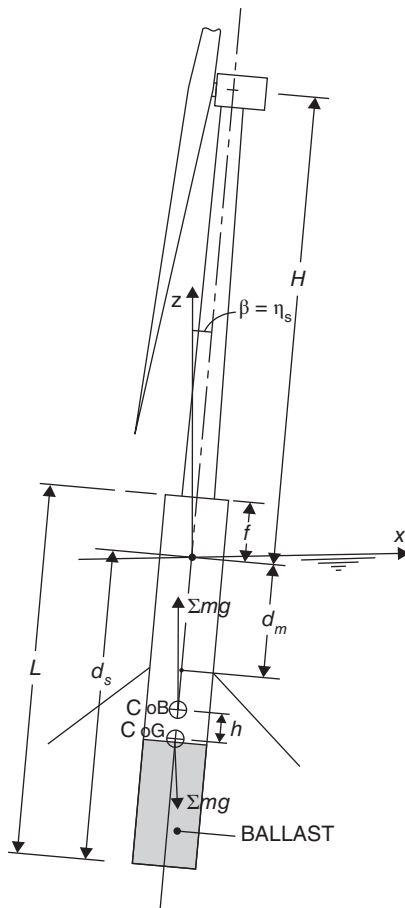


Figure 12.73 Spar buoy nomenclature.

Although spar steel weight is hardly affected, the ballast weight rises steeply with diameter and reducing water depth, suggesting that it is advantageous for a spar buoy to fully exploit the water depth available.

Figure 12.74 also shows the variation of the natural period of pitch motion with spar buoy diameter, calculated according to Eq. (12.81). The added mass of water, which needs to be counted as part of the moment of inertia of the floating structure about its horizontal axis, is taken as equal to its displacement, as the spar is cylindrical. It is found that the period exceeds 30 seconds over the range of diameters investigated.

12.8.6 Semi-submersible design space

Although a wide variety of semi-submersible configurations are possible, only designs consisting of 3 or 4 vertical cylindrical chambers (or ‘columns’) braced together will be investigated here, as illustrated in Figure 12.75. The turbine to be supported is again the notional 9 MW turbine described in the preceding section.

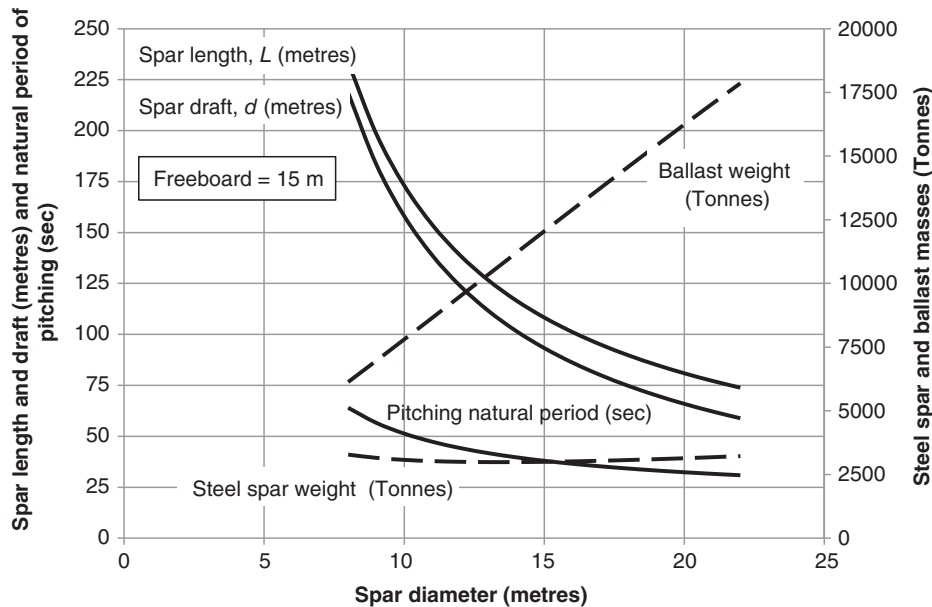


Figure 12.74 Variation of spar length, steel spar weight, ballast weight, and pitching natural period with spar diameter for 9 MW turbine on spar buoy designed to achieve a mean pitch at rated wind speed of 5 degrees.

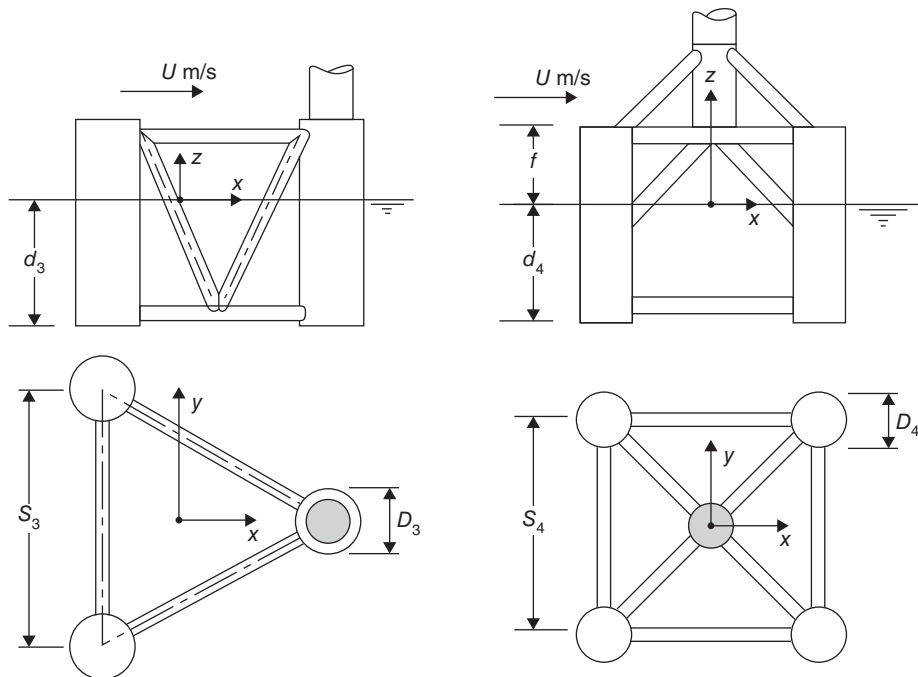


Figure 12.75 Possible arrangements of three and four column semi-submersibles.

Four column semi-submersible with central wind turbine generator tower

The restoring stiffness in pitch and roll is given by

$$C_{55} = \rho_w g \frac{\pi D^2}{4} s_4^2 + 4\rho_w g \pi D_4^4 / 64 \quad (12.87)$$

ignoring the small destabilising effect of the centre of mass being above the centre of buoyancy. If the second term, which is relatively small, is ignored, it can be seen that the column spacing needs to be inversely proportional to the column diameter if a constant restoring stiffness is to be maintained. As with the spar buoy considered above, the target restoring stiffness is 1.70×10^6 kNm/rad, in order to limit the mean pitch at rated wind speed to 5°.

The moment of inertia of the floating structure and its water added mass in pitch controls the natural pitching period according to Eq. (12.81). The wind turbine and tower masses are taken as 650 and 1200 tonnes, respectively, as before, and the freeboard, f , is again taken as fixed at 15 m. Given that the hub height of 115 m is two or three times the column spacing, the contribution of the mx^2 terms to the moment of inertia is relatively small, so increasing the draft is the most effective means of extending the natural period.

Figure 12.76 shows the column spacing required for a C_{55} of 1.70×10^6 kNm/rad for a range of column diameters, together with the draft necessary to achieve a 25 second natural period of pitching motion. Also shown are the notional weights of the steel shells forming the four columns, assuming a uniform wall thickness of 70 mm, and of the necessary ballast. These figures are notional because the steel shells have not been designed and the contributions of the inter-column bracings to displacement, moment of inertia including added mass have all been neglected. It can be seen that the ballast weight increases rapidly with column diameter and that, even at a column diameter of 12 m, the draft is quite large at 26 m.

Benefit of heave plates

Heave plates are horizontal plates projecting from a hull, which reduce heave motion by increasing both the added mass in heave and heave viscous damping, and by reducing the wave excitation loads at low frequencies. In the case of a semi-submersible consisting of vertical columns braced together, the added mass can significantly increase the natural period of pitch and roll motions, reducing the platform's susceptibility to wave excitation. In addition, the wave inertia loading on the added mass associated with the heave plate subtracts from the wave hydrodynamic loading acting on the base of the column.

It can be shown that, for linear waves in deep water, the fluctuating water pressure at a depth d is $\rho_w g \frac{H}{2} e^{-kd} \sin(\omega t)$, so, for the case of a cylindrical column of diameter D and draft d , for example, the vertical wave loading is $\rho_w \frac{\pi}{4} D^2 g \frac{H}{2} e^{-kd} \sin(\omega t)$.

The coexistent inertia loading on a heave plate at the base of the column is given by

$$A_{hp} \frac{\partial w(d)}{\partial t} = -A_{hp} \omega^2 \frac{H}{2} e^{-kd} \sin(\omega t) \quad (12.88)$$

where A_{hp} is the added mass of the heave plate at the base of the cylinder and $w(d)$ is the water particle vertical velocity at depth d . Hence the total vertical loading is

$$\left\{ \rho_w \frac{\pi}{4} D^2 g - A_{hp} \omega^2 \right\} e^{-kd} \frac{H}{2} \sin(\omega t) \quad (12.89)$$

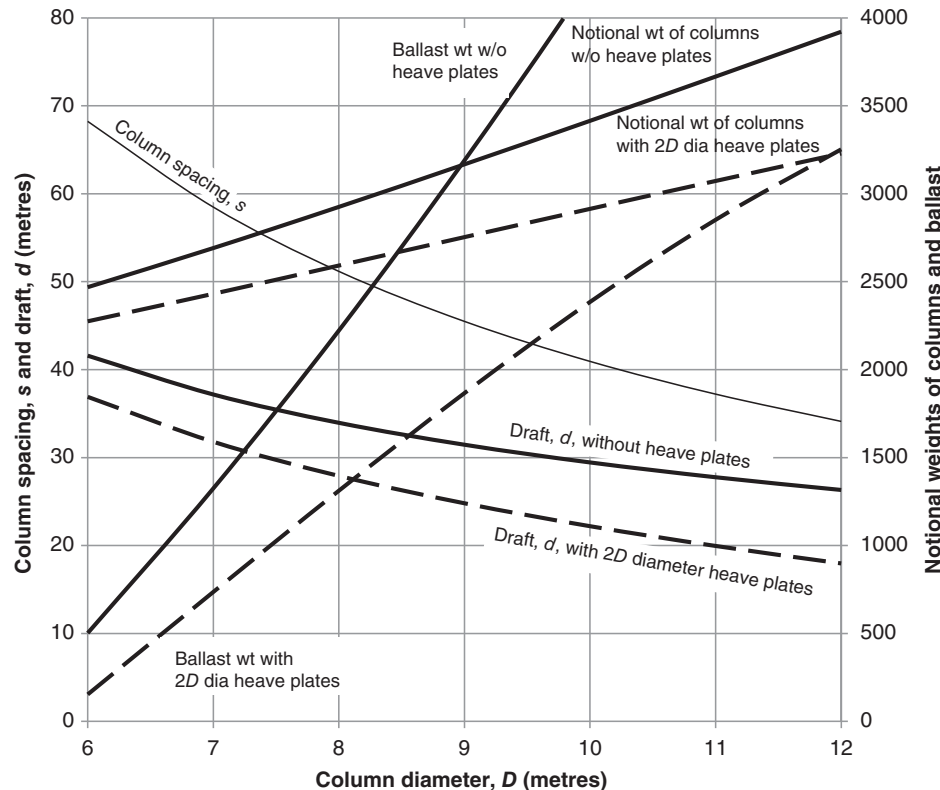


Figure 12.76 Variation of column spacing, draft, notional column steel weight, and ballast weight with column diameter for a four column semi-submersible supporting a centrally placed 9 MW turbine, to achieve a mean pitch at rated wind speed of 5 degrees and a 25 second pitching natural period.

The heave plate therefore has the effect of eliminating vertical wave loading at a wave frequency of $\sqrt{\rho_w \frac{\pi}{4} D^2 g / A_{hp}}$.

The theoretical added mass of a thin circular horizontal disc of diameter D_D oscillating vertically on its own is $\frac{1}{3} \rho_w D_D^3$. This can be considered as occupying an ellipsoid of horizontal diameter D_D and height $\frac{2}{\pi} D_D$. In the case of a heave plate of diameter D_D attached to the base of a cylinder of diameter D , the cylinder occupies part of the upper half of the ellipsoid, reducing the mass of water in the ellipsoid to

$$\frac{1}{12} \rho_w (2D_D^3 + 3\pi D_D^2 h - \pi^3 h^3 - 3\pi D_D^3 h) \quad (12.90)$$

where $h = \frac{1}{\pi} \sqrt{D_D^2 - D^2}$ (Tao et al. 2007). If it is assumed that the water within the ellipsoid moves as if attached to the heave plate, as proposed by Tao et al. (2007), Eq. (12.90) gives the heave plate theoretical added mass.

Tian et al. (2016) reported model tests on oscillating circular discs by themselves and others that found that the ratio of the measured added mass to the theoretical value increased from around unity at zero Keulegan–Carpenter number (= amplitude $x2\pi/D$) to about 1.5 at a K_C number of 1.0. Moreno et al. (2016) obtained similar results for a heave plate at the base of cylinder, with $D_D/D = 2.84$, oscillating in still water.

The impact of adding heave plates of twice the column diameter to the four column semi-submersible has been investigated, assuming resultant added masses in heave of $0.275\rho_w D_D^3$ or $2.20\rho_w D^3$ according to Eq. (12.90), and the results plotted on Figure 12.76 (dashed lines). This shows that the draft can be reduced by 25% for a column diameter of 10 m while maintaining the natural period for pitch oscillations at 25 seconds, and that there is a substantial reduction in ballast weight for all column diameters.

Three column semi-submersible with wind turbine generator tower coaxial with one of the columns

It is easy to show that the restoring stiffness in pitch and roll is given by

$$C_{55} = \frac{1}{2}\rho_w g \frac{\pi D_3^2}{4} s_3^2 + 3\rho_w g \pi D_3^4 / 64 \quad (12.91)$$

ignoring the small destabilising effect of the centre of mass being above the centre of buoyancy. Given that the wind turbine is entirely supported on one of the three columns, it is assumed that this column is unballasted and that a weight of ballast equal to that of the wind turbine has to be added to each of the other two columns to maintain platform trim. Taking the same wind turbine weights and height as before, the column spacing required for a C_{55} of 1.70×10^6 kNm/rad can be calculated for a range of column diameters, together with the draft necessary to support the combined column and wind turbine weight. The resulting natural period can then be calculated for each geometry – see Figure 12.77. As noted above, the addition of heave plates to the column bases significantly increases the natural period in pitch and roll and this is evident in the figure, which compares the natural periods of the semi-submersible with and without column heave plates of twice the column diameter.

It is instructive to compare the notional column steel weights and natural frequencies for instances of the three and four column semi-submersibles described above having the same waterplane area and same draft. It is found that the notional column steel weight of a three column semi-submersible with 11.547 m column diameter and 25.9 m draft is, at 2790 tonnes, significantly less than the corresponding 3170 tonnes weight of a four column semi-submersible with 10 m diameter columns and the same draft, while the natural period is somewhat greater (26.8 seconds cf. 25.9 seconds). Heave plates of twice the column diameter are assumed to be fitted in each case.

Natural frequency considerations

In theory, the dimensions of the above three column semi-submersibles could be scaled down to accommodate, say, a turbine of half the diameter (and half the hub height), reducing the natural periods to $1/\sqrt{2}$ of their previous values. However, such a platform would be excessively susceptible to wave excitation, suggesting that large turbines are more suitable for deployment on floating platforms than small ones.

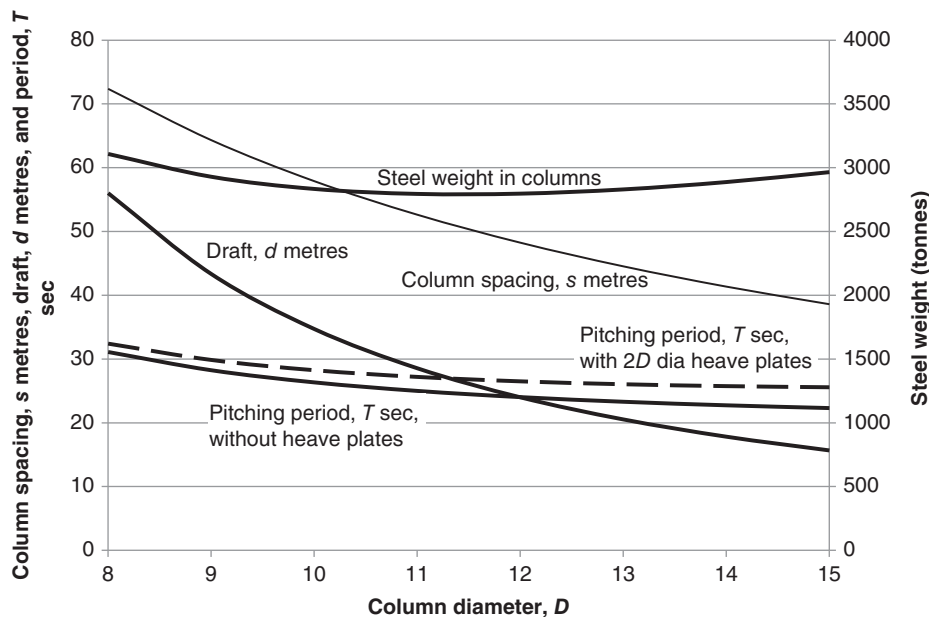


Figure 12.77 Variation of column spacing, draft, natural pitching period and notional column steel weight with column diameter for a three column semi-submersible with a 9 MW turbine supported on one of the columns, to achieve a mean pitch at rated wind speed of 5 degrees.

12.8.7 Station keeping

The mooring system for a floating platform consists of at least three radial mooring lines anchored to the seabed. Oil and gas platforms have always used at least two lines per corner to provide redundancy (Ahilan 2018), but this has not usually been considered necessary for wind turbines, as they are normally unmanned and do not store hazardous hydrocarbons.

Moorings can be categorised as slack and partially resting on the seabed, slack but not resting on the seabed and taut. The former type is preferable, as the anchors do not have to be designed for vertical uplift. The materials used are typically steel chain, steel wire rope, nylon, or polyester.

The orientation of each mooring line inevitably varies with respect to the floating platform as the latter moves, so a guide known as a *fairlead* is provided at each point of attachment. Accordingly, the term *fairlead* will be used as a shorthand for the point of mooring line attachment to the platform.

Mooring stiffness governs the platform surge and sway natural frequencies of both spar buoys and semi-submersibles, so their mooring systems should be sufficiently compliant to ensure these frequencies are below the wave frequency range. Steel chains are appropriate for systems with the moorings partially resting on the seabed but would be too stiff for use as taut moorings. In very deep water, steel chain moorings can impose excessive vertical loads on the platform, but this can be alleviated by the use of nylon or polyester over the upper portion of the mooring length.

Table 12.12 Indicative mooring system loads for a 15 m diameter spar buoy with 93 m draft, supporting a 180 m diameter 9 MW wind turbine.

Loading source	Loading conditions	Load formula	Load magnitude
Rotor thrust	Operation in steady wind at rated power		1100 kN
Sea current	$u_c = 1.5 \text{ m/s}$ at surface, 1/7 power law variation with depth. Seabed depth, $d_B = 120 \text{ m}$	$C_D \frac{1}{2} \rho u_c^2 D^{\frac{7}{9}}$ $\times \left(d_B - (d_B - d) \left[\frac{d_B - d}{d_B} \right]^{\frac{2}{7}} \right)$	1450 kN
Extreme wave	$H_s = 14.5 \text{ m}$, $T = 19 \text{ s}$, $T_I = 110 \text{ s}$, $k_{II} = 110 \text{ kN/m}$, $k = \omega^2/g$	$k_{II} \frac{1}{1 - \left(\frac{T}{T_I} \right)^2}$ $\times \frac{1.86 H_s}{2} \frac{1 - e^{-kd}}{kd}$	950 kN
Total			3500 kN

The main sources of loading on the floating platform are rotor thrust, current drag and wave loading. Table 12.12 gives formulae for the marine loadings on a spar buoy of diameter D and draft d together with indicative magnitudes for the 15 m diameter, 93 m draft spar buoy example from Section 12.8.5. The mooring line force due to wave loading is dependent on the mooring system stiffness, which is assumed to be constant at $k_{II} = 110 \text{ kN/m}$, giving a natural surge period of 110 seconds.

Although mooring lines experience dynamic loading, its effect on behaviour is small because of the low platform natural frequencies, so a quasi-static analysis is adequate for most purposes. The relationship between fairlead displacement, $X(H)$, relative to the position at which the mooring would descend vertically to the seabed (see Figure 12.78), and the mooring horizontal load, H , is as follows, assuming part of the mooring is resting on the seabed and neglecting elastic extension:

$$X(H) = Z + \frac{H}{w} \left[\operatorname{acosh} \left(1 + \frac{wZ}{H} \right) - \sqrt{2 \frac{HZ}{w} + Z^2} \right] \quad (12.92)$$

Here w is the buoyant weight per unit length of the mooring and Z is the height of the platform mooring attachment above the seabed, which is assumed to be level. Differentiation with respect to H gives the inverse of the horizontal mooring stiffness as follows:

$$\frac{dX}{dH} = \frac{1}{w} \left[\operatorname{acosh} \left(1 + \frac{wZ}{H} \right) - \frac{2}{\sqrt{1 + \frac{2H}{wZ}}} \right] \quad (12.93)$$

The horizontal stiffness of a complete mooring system can be determined by the vectorial addition of the changes in mooring line horizontal loads resulting from displacement of the floating platform from the equilibrium position. Consider a spar-buoy

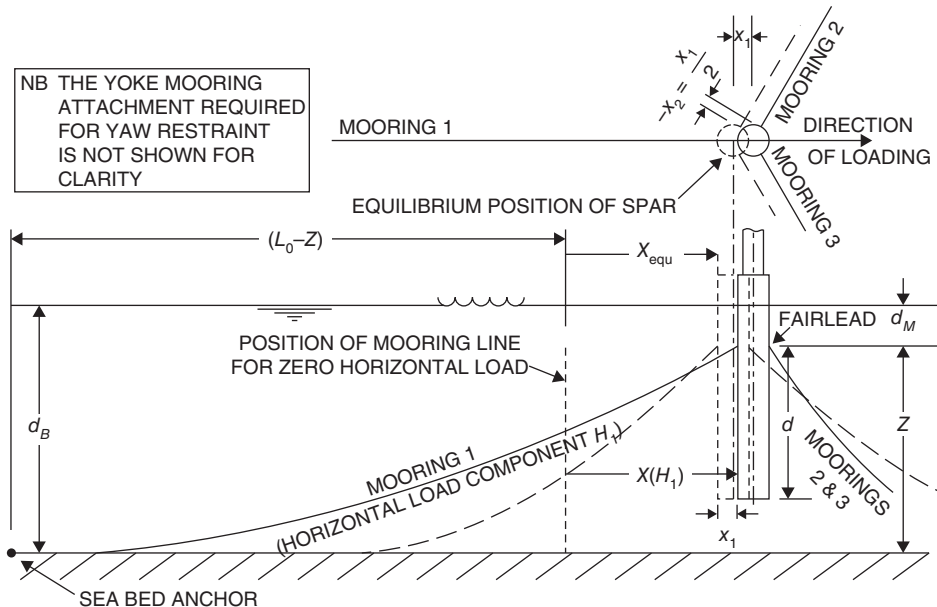


Figure 12.78 Spar buoy mooring system layout.

mooring system with 3 mooring lines of length L_o arranged at 120° spacing in plan, as illustrated in Figure 12.78. The anchors in the seabed are positioned at a horizontal distance $(L_o - Z + X_{equ})$ from the spar buoy fairlead equilibrium positions, introducing a horizontal preload, H_0 , into the system given by

$$X_{equ} = Z + \frac{H_0}{w} \left[\operatorname{acosh} \left(1 + \frac{wZ}{H_0} \right) - \sqrt{2 \frac{H_0 Z}{w} + Z^2} \right] \quad (12.94)$$

When an external horizontal load is applied to the spar buoy, it will move from its initial position, altering the mooring line forces until their resultant balances the applied load. If the horizontal load is aligned with mooring line 1 and acts away from its anchor, the total mooring system force on the platform in the direction of mooring line 1 is $H_{S1} = (H_1 - H_0) - 0.5(H_2 - H_0) - 0.5(H_3 - H_0) = H_1 - H_2$. where H_1 , H_2 and H_3 are the horizontal components of the loads in the 3 mooring lines. Given that $x_2 = -\frac{x_1}{2}$, we can write $H_{S1} = H(x_1) - H\left(-\frac{x_1}{2}\right)$, where $H(x_1)$ can be obtained in the form of a look-up table based on Eq. (12.92) with $x_1 + X_{equ}$ substituted for $X(H)$ and $H_1(x_1)$ substituted for H to give

$$x_1 + X_{equ} = Z + \frac{H_1}{w} \left[\operatorname{acosh} \left(1 + \frac{wZ}{H_1} \right) - \sqrt{2 \frac{H_1 Z}{w} + Z^2} \right] \quad (12.95)$$

Figure 12.79 shows the results of such an analysis for a mooring chain weight of 0.5 tonnes per m, a fairlead height above the seabed of 100 m and a preload H_0 of 1000 kN. The horizontal component of both the mooring 1 load and the mooring system load

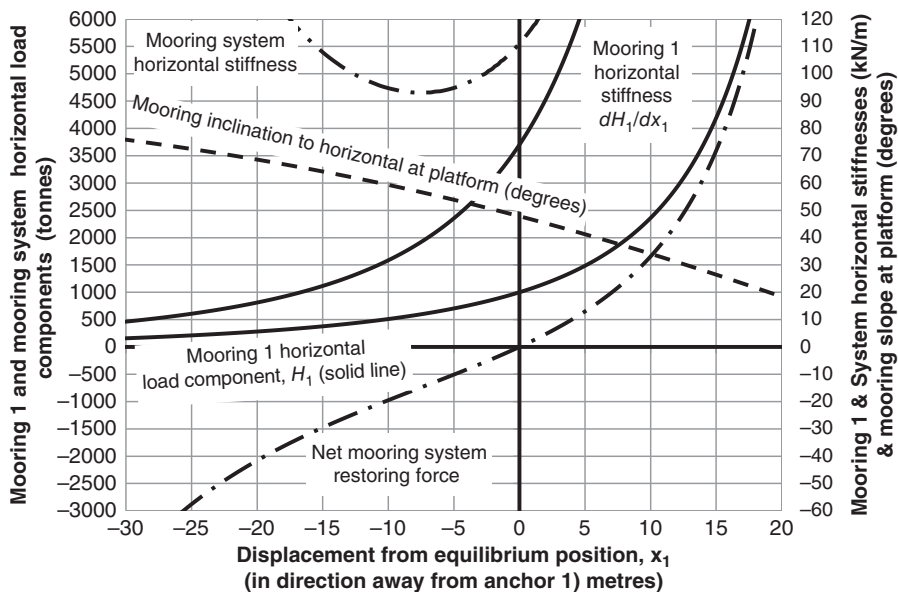


Figure 12.79 Variation of mooring loads, stiffnesses, and inclination with spar buoy displacement for a chain weight of 0.5 T/m, a fairlead height above seabed of 100 m, and a horizontal preload of 1000 kN.

are plotted as a function of spar buoy displacement, together with the corresponding stiffnesses and the mooring inclination at the fairlead. It can be seen that the relationships are far from linear, with the result that a rotor thrust loading of 1100 kN directed away from a mooring anchor will cause a displacement of about 7.5 m, whereas the displacement due to this loading in the opposite direction is significantly higher at about 11 m.

12.8.8 Spar buoy case study – Hywind Scotland

The Hywind Scotland floating wind farm (Figure 12.80) was commissioned in 2017 and consists of five 6 MW Siemens turbines mounted on spar buoys spaced about 1.4 km apart at a site located about 25 km East of Peterhead. The design is a development of a 2.3 MW spar buoy prototype installed in 2009 off Karmøy, South of Bergen, Norway. Leading weights and dimensions of the spar buoy and the wind turbine are given in Table 12.13.

Figure 12.81 shows two of the spar buoys loaded onto a vessel in preparation for flotation. Following floatation, each spar buoy was towed to the assembly site near Stord, South of Bergen, and ballasted with 8000 tonnes of seawater to rotate its axis to the vertical (Equinor 2020). After this, 5000 tonnes of the ballast water were pumped out and replaced by 5500 tonnes of rock ballast. Then the wind turbine tower, nacelle and rotor were installed (see Plate 8) and the complete assembly towed across the North Sea to the site off Peterhead for attachment to its moorings.

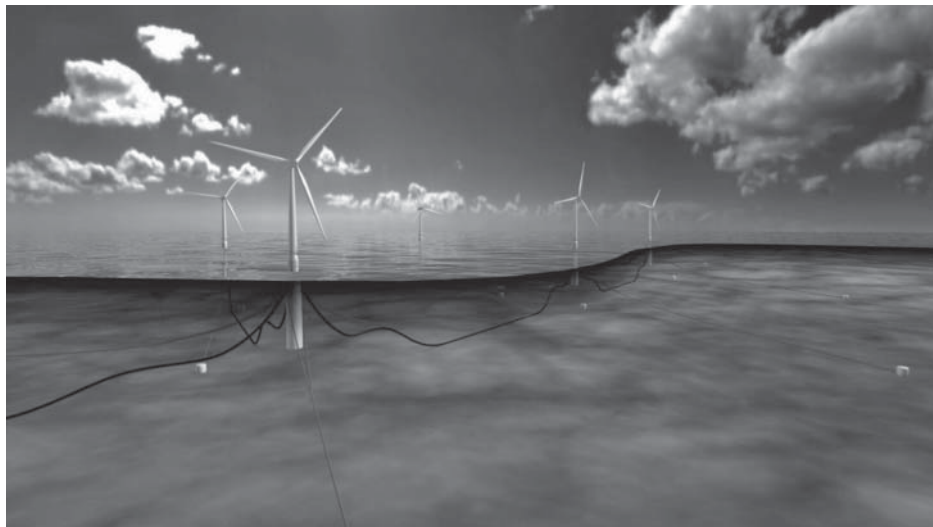


Figure 12.80 Artist's impression of Hywind Scotland wind farm. Source: Reproduced with permission of Equinor.

Table 12.13 Hywind Scotland spar buoy and wind turbine leading dimensions and weights (Hywind 2017, 2020; Siemens Gamesa 2020).

Spar buoy		Wind turbine	
Diameter	14.4 m	Rating	6 MW
Reduced diameter at water line	9.45 m	Diameter	154 m
Overall length	90.6 m	Hub height above sea level	98 m
Draft	77.6 m	Wind turbine weight	360 tonnes
Approximate water depth	100 m	Tower weight	670 tonnes
Freeboard	13.0 m	Wind turbine and tower weight	1030 tonnes
Draft of mooring attachments	20.6 m		
Depth of centroid below centre of buoyancy	~8 m		
Steel weight	2300 tonnes		
Ballast weight	~8500 tonnes		
Total spar buoy weight	~11 200 tonnes		
Wind turbine and tower weight	1030 tonnes		
Displacement	~12 000 tonnes		

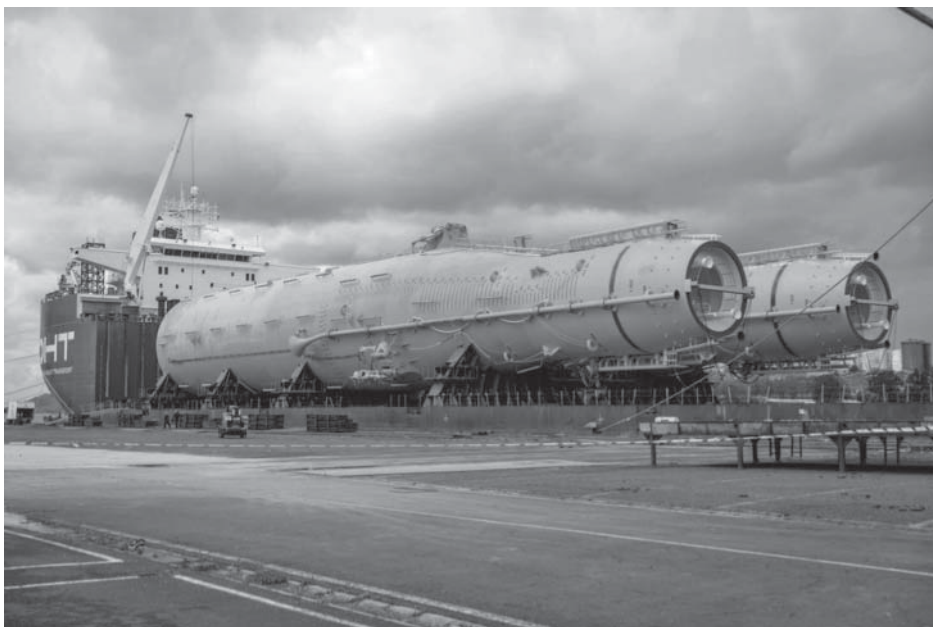


Figure 12.81 Two Hywind spar buoys loaded onto a vessel prior to flotation. Source: Reproduced with permission of Equinor.

Table 12.14 Natural periods of Hywind spar buoy floating wind turbine (Hywind 2020).

Motion	Natural period (s)	Motion	Natural period (s)
Surge	96	Roll	34
Sway	96	Pitch	34
Heave	26	Yaw	13

Each spar buoy is maintained on station by three moorings spaced at 120° in plan, which are attached to suction anchors on the seabed at about 640 m radius and 100 m depth. The 16 m deep suction anchors are 5 m in diameter and weigh about 300 T. The mooring chains weigh about 0.5 T/m and have links about 0.5 m wide. They are attached to the spar buoy using a yoke arrangement to provide yaw restraint. The natural periods of the spar buoy in each of its six degrees of freedom are given in Table 12.14 (Hywind 2020).

The very low natural frequencies in surge and sway mean that the amplitude of the spar buoy horizontal motion will approximate to that of the water particles in large waves, averaged over spar buoy depth.

The floating turbines are extensively monitored, using motion reference units in nacelle and tower, strain gauges in spar and tower and load cells on the moorings.

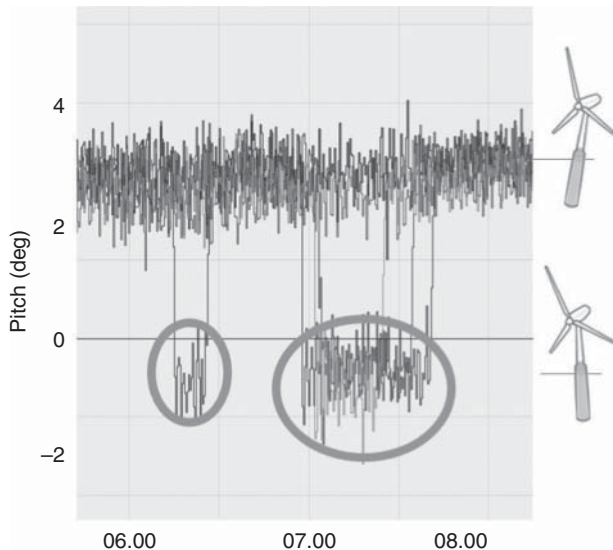


Figure 12.82 Pitch motion of all five turbines during operation in a mean wind speed of 22 m/s during Hurricane Ophelia 17 October 2017 (Hywind 2020). Source: Reproduced with permission of Equinor.

Figure 12.82 displays traces of pitch angle for all five turbines during operation during a storm. It can be seen that the mean pitch angle is about 3° during operation in a mean wind speed of about 22 m/s, when the thrust is reduced below the value at rated wind speed. The amplitude of pitch rotation rarely exceeds 1° , which corresponds to a peak nacelle acceleration of only 0.1 m/s^2 . The ringed areas indicate periods during which one or more of the turbines was shut down due to high wind. At these times the turbines lean into the wind, because of the eccentricity of the tower top mass centre of gravity.

Based on the project capital cost of about £200 m, it is possible to make an estimate of the LCOE from the wind farm if a number of assumptions are made, as follows:

- The wind farm operates at a capacity factor of 50%.
- Its design life is 20 years.
- The discount rate is 5%.

On this basis, the cost of energy comes to about £140/MWh, including O&M costs taken as £17/MWh.

12.8.9 Three column semi-submersible case study – WindFloat Atlantic

The WindFloat Atlantic floating wind farm was commissioned in 2020 and consists of three MHI Vestas 8.4 MW turbines each mounted on a semi-submersible platform about 20 km West of Viana do Castello in Northern Portugal. The platforms consist of three vertical steel columns located at the corners of an equilateral triangle and braced together



Figure 12.83 WindFloat Atlantic platform during load-out from quayside to semi-submersible vessel at Fene, prior to transfer to Ferrol for turbine erection. Source: (*credits: Navantia*) Reproduced with permission of Principle Power, Inc.

by trusses, as illustrated in Figure 12.83, with the wind turbine tower mounted on one of the columns.

The design reflects the next iteration of a 2.0 MW prototype, WindFloat 1, installed in 2011 about 5 km from Aguçadoura, also in Northern Portugal (see below). Approximate dimensions of the semi-submersibles and wind turbines deployed in 2020 as part of the WindFloat Atlantic project are given in Table 12.15. Platforms are typically outfitted with a low pretension catenary mooring system consisting of HMPE (high-modulus polyethylene) rope, chain, drag embedment anchors with no vertical load on anchor, and other components as dictated by the local conditions.

The weight of the wind turbine borne by one of the three columns is balanced by water ballast in the other two. In addition, the platform is fitted with an active-ballast system, which compensates for the rotor thrust overturning moment and changes in wind direction by pumping water between compartments in each column to maintain trim as the wind direction or thrust loading changes.

Pitch and roll motion of the platforms due to wave action is substantially reduced by the fitting of water-entrainment or heave plates to the base of each column. These entrain a large added mass of water, increasing the platform pitch and roll natural period above

Table 12.15 WindFloat Atlantic semi-submersible and wind turbine leading dimensions.

Semi-submersible		Wind turbine	
Number of vertical columns	3	Rating	8.4 MW
Approximate spacing of column centres	50 m	Diameter	164 m
Approximate column diameter	12 m	Hub height above sea level	100 m
Column height	29 m		
Approximate operational draft	18 m		
Approximate water depth	100 m		

that of even the largest the waves, while at the same time providing significant viscous damping.

The platform draft is small enough to enable the wind turbine tower, nacelle and rotor to be lifted into position on the platform sequentially at the quayside. After towing out to site, the platform is kept in place using mooring lines attached to drag embedment anchors.

The WindFloat Atlantic project is led by the Windplus consortium, comprising EDP Renewables (54.4%), Engie (25%), Repsol (19.4%), and Principle Power Inc. (1.2%). The external investment in the wind farm was approximately EUR 96 m.

WindFloat 1

The WindFloat prototype was extensively monitored with motion sensors and strain gauges on the truss members linking the columns and on the tower (Cermelli et al. 2018), and the measured data was found to be generally in good agreement with the results of numerical analyses. The influence of the following sources of loading was found to be easily discernible on spectral plots of bending moments and axial loads:

- Swells; wind sea.
- Wind gusts.
- Pitch resonance; tower resonance.
- Turbine rotational and blade passing frequencies.

The WindFloat 1 prototype was de-commissioned in 2016. A description of the whole project is given in Roddier et al. (2017).

12.8.10 Ring shaped floating platform – Floatgen, France

The Floatgen platform is of concrete cellular construction and is essentially a square barge with a large opening in the middle, so that the hull surrounds a body of water that serves to damp the platform motion. The platform supports a Vestas V80 2 MW turbine, with its tower mounted on a transition piece located at the middle of one of the four sides of the platform. See Figure 12.84. Leading dimensions are given in Table 12.16.

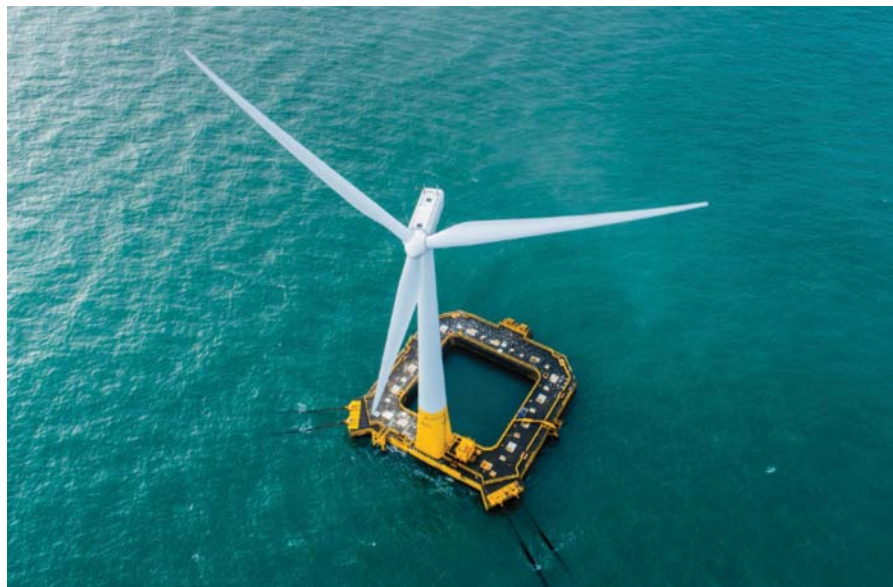


Figure 12.84 Floatgen in situ. Source: Copyright Ideol & V.Joncheray and reproduced with permission.

Table 12.16 Floatgen platform and wind turbine leading dimensions (Choisnet et al. 2018; 2020).

Floating platform		Wind turbine	
Barge external dimensions	36 m × 36 m × 9.5 m deep	Rating	2 MW
Dimensions of central opening	21 m × 21 m	Diameter	8 m
Draft	7 m	Hub height above sea level	66.6 m
Width of heave plate around perimeter	2.1 m		
Water depth	35 m approx.		
Natural period in pitch and roll	11 s		

The platform was designed by Ideol, constructed in St Nazaire by Bouygues Travaux Publics and towed to its site 20 km off Le Croisic in 2018. The platform is held in place by three pairs of nylon moorings, spaced at 120° in plan, which are clearly visible in Figure 12.84. Over one thousand sensors have been installed on turbine and platform to enable performance and sea-keeping to be monitored and compared with predictions.

The natural period in pitch and roll of 11 seconds is within the range of wave periods encountered, so the damping pool and heave plates play a vital part in limiting platform excitation. Choisnet et al. (2020) report that nacelle accelerations due to platform motions only increase blade root bending moments in operation by a small amount. However, the effect of platform motion on tower base moments was found to be much more significant.

12.9 Environmental assessment of offshore wind farms

12.9.1 Environmental impact assessment

Offshore wind farms extend over wide areas of often environmentally important waters and have the potential to make a considerable impact on the marine environment. As with any large onshore wind farm project, an Environmental Impact Assessment (EIA) is necessary before an application for consent to construct and operate an offshore wind farm is submitted. In Europe the Environmental Impact Assessment Directive (2009/31/EC 2009) requires an EIA to be undertaken and more detailed guidance on how this requirement is translated into practice for an offshore wind farm is given in (CEFAS 2004; OSPAR Commission 2008). The work of an EIA results in an Environmental Statement that is submitted to the planning/permitting authorities with the proposal to develop an offshore wind farm (DECC 2011).

In contrast to the EIA required for an individual wind farm project, Strategic Environmental Assessments (SEAs) are undertaken by national or regional governments. These identify the broad parameters of future wind energy development, the areas where offshore wind farm development is appropriate and identify where particular emphasis is required in the EIAs of individual projects. A recent SEA (OESEA3 2016) considered the potential for offshore energy developments in English waters using bottom mounted wind turbines of up to 15 MW capacity in water depths up to 60 m and floating turbines in waters up to 200 m depth. This assessment was based on a comprehensive literature survey and contains a comprehensive list of references.

The EIA of a project assesses its environmental impacts at all stages of construction, operation and de-commissioning. It considers measures that can be adopted for avoiding any undesirable impacts or, if this is not possible, mitigating them. Coastal areas are used for a range of purposes, e.g. for fishing, commerce or recreation, and there are likely to be many groups with a keen interest in any proposed offshore wind farm development. Before detailed work is undertaken, including data collection and surveys, it is usual to agree a scoping report that defines the extent of the investigations of the EIA with the permitting authority (Hornsea 4 2018).

The development of an offshore wind farm can take 10 years from the initial concept to the start of construction. Offshore wind turbine and balance of plant technology is developing rapidly and so the initially anticipated wind turbines, farm layout and construction and maintenance techniques are likely to be obsolete by the time of construction. If the wind farm is defined rigidly at the start of the consenting process then it will not be possible to take advantage of advances in technology and consequent cost reductions that occur during the wind farm development period. Planning law in several countries (including England and Wales) has evolved to allow a degree of flexibility in

the design of the wind farm while still ensuring rigorous evaluation of the environmental impacts. This is known as the *project envelope approach* (named the *Rochdale envelope* in England after a particular legal case) and is a way of dealing with a planning application and its EIA where details of a project are not completely fixed at the time when the application is submitted (Infrastructure Planning Commission 2011).

Details that may not be fully determined at the time of scoping the EIA might include:

- Type and number of turbines.
- Foundation type (this may depend upon the height and type of turbine and the seabed conditions).
- The route of the export cable route (whether this is buried or laid on the seabed).
- Location of the landfall point.
- Location of any onshore substation.

The project envelope approach defines realistic worst-case conditions and clear ranges of the critical parameters of the wind farm. For example, the minimum and maximum number of turbines, possible rotor diameters and a range of blade tip heights might be defined rather than a particular number and type of turbine. The Environmental Statement then identifies those aspects that are likely to give rise to significant adverse environmental impacts and the decision makers assess the project based on the envelope of parameters.

12.9.2 Contents of the environmental statement of an offshore wind farm

The contents of any EIA are defined in (2009/31/EC 2009) as including a description of the project and the measures proposed to avoid and mitigate significant adverse effects. It will include the data necessary to identify and assess the main effects that the project is likely to have on the environment, the mitigation measures and an outline of the alternatives studied by the project developer. The choices made in the development of the project must be justified taking into account the environmental effects. Both a comprehensive technical document and a shorter non-technical summary are required.

Environmental Statements for offshore wind farms start with a description of the complete proposed development, which will include the wind turbines, their layout and foundations, the array cabling, the offshore substation, the submarine transmission cable to shore, the land cable, and any additional works for the land substation. Considerable work is undertaken to gather baseline data of the project area including surveys of the seabed, marine biology, birds and mammals, fish resources, marine traffic, the intertidal area where the power cables come ashore, and archaeology. A landscape and seascape visual assessment is also undertaken. The potential impact of the wind farm is then considered together with mitigation measures. It is common for a period of environmental monitoring to be required after construction and commissioning.

The primary readership of the Environmental Statement is the authorities that must decide if the project is to proceed. A second readership is the various stakeholders that use or have other interests in the area and its marine environment.

Particular environmental impacts that need to be considered include:

- Seascapes and visual impact.
- Marine mammals – distribution, disturbance, displacement impacts of noise and vibration.
- Fish resources – migration patterns, nursery areas, commercial fisheries.
- Birds – distribution, disturbance, displacement, mortality.
- Benthos – the flora and fauna of the seabed.
- Wave and tidal environment.
- Water quality – turbidity.
- Coastal and sedimentary processes – sediment transport, scouring.
- Marine navigation and radar.
- Archaeology.
- Designated areas.

As with onshore wind farms, visual impact and changes to the view are likely to be of concern and a possible cause of objections to the development of the wind farm. Scottish Natural Heritage (2012) provides detailed guidance on how Seascapes and Visual Impact Assessment (SVIA) of offshore wind energy developments may be undertaken. The SVIA identifies the features of the existing seascape and the changes that the wind farm development would make to its visual character. The judgement is based on an assessment of receptor sensitivity and the capacity of the seascape to accommodate change. From the land, local residents are considered to be the most sensitive receptors with industrial activities, e.g. ports, the least sensitive. Out to sea, recreational boating has high sensitivity receptors while oil and gas rigs are less sensitive. The capacity of the seascape to accommodate change is evaluated considering the overall quality and sensitivity of the seascape to the wind farm as well as the value attached to the seascape.

The extent of the potential visibility of the development is described using zones of theoretical visibility (ZTVs). This technique defines the areas from which one or more wind turbines, or parts of a wind turbine, are visible, taking into account topography and curvature of the earth but not making any allowance for atmospheric conditions. Thus a ZTV indicates the furthest possible extent of visibility. For wind farms greater than 24 km from shore, visual impacts are likely to be minor. To take account of differing atmospheric and lighting conditions, the visual impact of the development is illustrated using wireframes and photomontages from viewpoints that have been agreed with the permitting authority during the scoping phase. For large wind farms 3-D modelling and video montages are used increasingly.

Sound travels more easily in water than air and sound impacts during both construction and operation of offshore wind farms potentially affect marine mammals and fish, and also residents if the wind farm is close to shore. The installation of monopile foundations by impact pile driving is particularly noisy. If this technique is used to install piles, visual observation and passive acoustic detectors may be required to ensure marine mammals are not present in the area during piling (JNCC 2009). Acoustic deterrent devices may be used to encourage marine mammals to vacate the area. In addition, restrictions

may be placed on hours of work if the sound is audible onshore. The noise under water during piling operations can be very loud (up to 200 dB at 1 m) and it is common practice to take steps to control this using a soft-start to piling operations so that fish and marine mammals leave the area (Huddleston 2010; Sparling et al. 2015; Herschel et al. 2015; Boyle and New 2018). Air bubble curtains are sometimes used to limit the propagation of noise (Tsouvalas and Metrikine 2016; Dahne et al. 2017)

Local scour around the turbine and substation foundations and cable routes is a common concern and scour protection (e.g. using rock dumping) may be required. This alters the surface of the seabed and can lead to changes in the benthic flora and fauns (Whitehouse et al. 2011).

Ships and boats often use simple, low cost pulsed radar rather than the more sophisticated equipment commonly found in aviation radars that use the Doppler effect to distinguish between fixed and moving targets. There is less scope to use advanced digital signal processing techniques to reduce the effect of wind farms on marine radars and trials have indicated that wind farms produce blind areas in which other turbines and vessels could not be detected unless the observing vessel was moving (Howard and Brown 2004). It was found that the high wind turbine structures produced large echoes and the radar response was strong enough to produce extraneous multiple and reflected echoes.

The effect of offshore wind farms on birds was considered in four main categories by Drewitt and Langston (2006): collisions, displacement due to disturbance, barrier effects, and habitat loss. Although the evidence was not complete, and a number of the wind farms studied were built away from large concentrations of birds, there was limited evidence of collision mortality. Similarly there was limited evidence of displacement due to disturbance but some barrier effect was reported from Horns Rev and Nysted wind farms. Loss of habitat from onshore installations (substations) and in shallow waters were highlighted as being of particular concern.

12.9.3 Environmental monitoring of wind farms in operation

A number of studies of the environmental impact of the early offshore wind farms have been funded from public sources. Although these describe the use of rather smaller turbines than are now being installed, these studies provide a useful record of early experience through reports that are publicly available.

A comprehensive environmental monitoring programme was undertaken at the two Danish offshore wind farms at Horns Rev (160 MW, 14–20 km offshore) and Nysted (166 MW, 10 km offshore) between 2000 and 2006 (Dong Energy et al. 2006). Comprehensive environmental monitoring programmes investigated the impact of the wind farms' construction and operation on

- Benthic flora and fauna, and in particular the impact of the foundations and scour protection.
- Distribution of fish around the wind farm and impact of electromagnetic fields on fish.
- Behaviour of marine mammals and their reaction to the wind farm, including construction.
- The numbers and distribution of feeding and resting birds and the impact on migrating birds, including risks of collisions.

The wind farms used hard scour protection on the sandy sediment seabed, and this resulted in a more diverse surface and an increase in the biomass of the benthic communities by 50–150 times. There was little evidence of any effect of the wind farm on the local fish population or of electromagnetic fields on fish. The main impact on marine mammals (seals and porpoises) was from pile driving during the installation of the monopile foundations when porpoises left the area. There was evidence that birds avoid the wind farms and that migration distances were extended slightly. The modelled collisions rates of eiders at Nysted were low at 0.02% (45 birds). In summary, the monitored effect of these two large wind farms on the environment was limited.

Similar studies were undertaken for the Lillgrund offshore wind farm. These included assessment of the use of photomontages for visual impact studies (Lillgrund Pilot Project 2009b) as well as a review of the environmental impact monitoring that had been undertaken (Lillgrund Pilot Project 2009c). This project also sponsored a Handbook for Marine Archeology (Lillgrund Pilot Project 2009d).

An environmental monitoring programme was undertaken at two early UK offshore wind farms, North Hoyle and Scroby Sands. Each were of 30 2 MW turbines directly connected to the 33 kV land based power system directly with no offshore substation. North Hoyle wind farm is 4–5 mi off the coast of North Wales and Scroby Sands 2 mi off the east coast of England. The environmental monitoring at North Hoyle, 2 years after commissioning, indicated small changes to the composition of marine sediment, benthic ecology and bird distribution (DTI 2006a). The trends could not be attributed to the wind farm and the overall conclusion was that there were no significant environmental effects due to the wind farm construction and 2 years of operation.

The monitoring programme at Scroby Sands (DTI 2006b) included bathymetric surveys and analysis around the turbines and the route of the export cables. There were also surveys of seal and little tern populations. The bathymetric surveys identified scour pits of up to 5 m depth and 60 m diameter around some wind turbines and these were back-filled with rocks. There was also evidence that the submarine cable depth of laying (initially 3 m) was changing with seabed conditions, and rock mattresses were placed to protect the export cables from becoming exposed or damaged. The dynamics of scour around monopile foundations and scour protection was reviewed in DECC (2008).

A series of studies has been undertaken by the Offshore Renewables Joint Industry Programme (ORJIP 2018). These include a bird collision avoidance study, a study of the efficacy of acoustic deterrent devices and of the impacts on fish of piling at offshore sites. The bird collision avoidance study (Skov et al. 2018) analysed 600 000 videos from offshore wind farms that showed evidence of bird activity in 12 000 videos with six collisions. The analysis showed that the collision risk to seabirds was much less than expected. The study showed that seabirds exhibited avoidance behaviour and changed their flight path to avoid the turbines. The efficacy of acoustic deterrent devices to establish an exclusion zone for marine mammals around wind farm construction, particularly pile driving, was also investigated. The study concluded that the measures tested could effectively deter marine mammals from offshore wind farm construction sites and so reduce the need for human observers. The impacts of piling on fish and the necessary consenting regulations remain the subject of study.

12.10 Offshore power collection and transmission systems

The first offshore wind farms, installed in the 1990s, were small demonstration projects using marinised versions of simple, well-established designs of wind turbines that had been proved onshore. These were typically 500–600 kW rating, stall-regulated with fixed-speed induction generators, i.e. the ‘Danish’ wind turbine design. The power collection voltage was 10 or 11 kV with the submarine power collection cables a few kilometres in length directly connected to the onshore electrical distribution network.

From around the year 2000, the voltage of the power collection was increased to 30–36 kV to connect larger (around 2 MW) variable-speed turbines, but the connection to shore was still at the array power collection voltage. As larger wind farms were constructed, offshore substations were used to increase the voltage to 132–150 kV for transmitting the power to shore. The higher voltage limited electrical losses and provided the transmission capacity necessary in fewer cables. The planning/permitting authorities are often concerned to reduce the number and hence environmental impact of the submarine cables crossing the beach at their landfall.

The size of offshore wind farms has now increased to more than 1000 MW using offshore wind turbines rated at up to 9 MW with a power collection voltage of 66–72 kV. Most large offshore wind farms have continued to use alternating current (ac) for transmitting the power to shore but several projects have used a direct current (dc) connection.

After the very early demonstration offshore wind farms, the electrical systems of offshore wind farms developed in three phases, corresponding to the three rounds of UK offshore wind farm development. The division into three rounds reflects an administrative and licensing process that was adopted by the UK but does mirror the technical development of offshore power collection and transmission systems in most countries (Figure 12.85).

- In Round 1, the offshore wind farms, each with 30 turbines, were of 60–90 MW rated output and located less than 30 km from shore. It was then cost-effective to use the wind farm power collection voltage of 30–36 kV to take the power ashore using two or three cables.
- The Round 2 offshore wind farms were larger (up to 500 MW) but less than 90 km from shore. Offshore substations increased the transmission voltage up to 132 or 150 kV.
- Round 3 projects are now being constructed in phases and can be up to 1000 MW in total and up to 150 km from shore. These use ac, usually at 66–72 kV, to collect the power from the turbines, and then either ac circuits at 220 kV or HVdc to transmit it to shore.

In all cases a transformer, often dry cast-resin type, is located within each turbine tower to increase the generator voltage. In larger turbines the turbine transformer may be located at the top of the tower to reduce the size, weight and losses of the pendant cable. For wind turbines up to several MW, the generator voltage is less than 1000 V. For larger turbines, the voltage of the generator and variable-speed electronic equipment is up to 6 kV. The array power collection cables enter and leave each offshore wind turbine through J-tubes attached to the transition piece connecting the foundation to the tower.

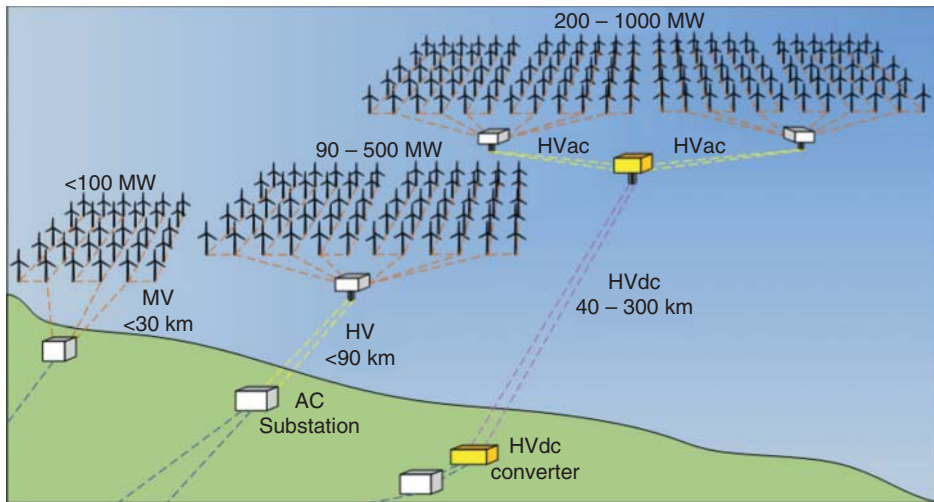


Figure 12.85 Options for transmission from offshore wind farms.

The temperature rise of the short lengths of cable in the J-tubes limits the power rating of the collection circuit.

12.10.1 Offshore wind farm transmission systems

The majority of Round 1 UK offshore wind farms used several 33 kV cable circuits each taking up to around 30–40 MW (600–800 A). The wind turbines were connected in array strings and the 3-phase submarine power collection cables of the strings were extended to the shore where they were each joined to an underground cable at a transition joint before entering a 33/132 kV transformer substation on shore.

Figure 12.86 shows a typical electrical system of Round 2 offshore wind farm. Radial 33 kV three-core XLPE (cross-linked polyethylene insulated cables) array power collection cables, each with a capacity of 30–40 MW, were used to connect up to eight turbines to a busbar at an offshore substation. The conductor diameter of these cables was often tapered away from the substation. The substation was mounted on an offshore platform and used to connect the array cables and transform the collection voltage up from 33 to 132 kV for transmission to shore. Offshore substations of up to 90 MVA capacity typically used one 33/132 kV transformer. Larger offshore substations had multiple transformers to reduce the weight of individual items of equipment and allow the wind farm to continue to operate (at less than rated output) with one transformer out of service. There was normally an auxiliary diesel generator on the offshore substation platform to maintain the auxiliary supplies and provide heat to the turbines if the transmission circuit was unavailable.

The transmission circuits to shore used three-core XLPE cables, at 132, 150, or 220 kV. Submarine ac cables ($800 \text{ mm}^2 \text{ Cu}$) have capacities of approximately 200 MVA at 132 kV and 330 MVA at 220 kV. Once on land, a transition joint connected the three-core submarine cables to three single-core underground cables. In some cases,

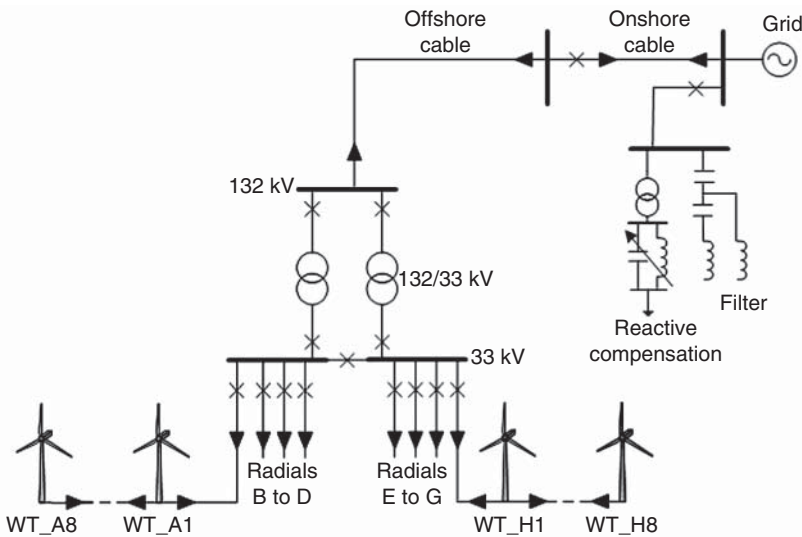


Figure 12.86 Typical UK Round 2 offshore wind farm power collection and transmission.

there was also an overhead line section before the cables connected to an onshore substation. The onshore substation was often located tens of kilometres inland from the shore and included reactive compensation and harmonic filters.

Round 3 projects are being developed and commissioned in phases. These have used turbines up to 9 MW in capacity but are expected to use turbines up to 12 MW rating in farms of more than 1000 MW. Most are expected to use ac transmission to shore at 220 kV but some will use an offshore ac hub to collect the power with HVdc transmission to shore.

Comprehensive electrical system studies are required for the design of wind farm electrical offshore systems. For the Lillgrund project, the following studies were undertaken (Lillgrund Pilot Project 2008): cable sizing, load (power) flow, short-circuits, harmonics, grounding, voltage fluctuations, reliability, arc faults, dynamic simulation, protection coordination, insulation coordination, electromagnetic interference, lightning protection.

On land, electrical networks deliver electrical energy to customers who expect a reliable supply of power. Redundant circuits are installed to ensure that a single electrical fault, or sometimes two independent faults, does not result in any loss of supply. In contrast the function of a wind farm offshore transmission system is to deliver wind generated electricity. The high costs of power electrical equipment offshore, particularly of submarine cables, and relatively modest value of the electrical energy mean that, as with onshore wind farms, total redundancy of transmission circuits cannot be justified. Partial redundancy may be provided for components with a high chance and/or a high impact of failure. An example is where two transmission transformers, each of 50% or 70% of the wind farm capacity are installed. In this case, if one transformer fails only a small fraction of the energy is curtailed, as the wind farm will only operate at its full

output a fraction of the year. Depending on the layout of the power collection network it may be cost-effective to install short lengths of cable between the strings to provide some redundancy (Anaya-Lara et al. 2018). The level of redundancy that should be installed can be evaluated through a cost-benefit analysis.

A cost-benefit analysis was undertaken to determine the most cost-effective architecture for the transmission circuits of UK Round 2 offshore wind farms. This study balanced the costs of the offshore transmission system including those of; the submarine transmission cable(s), the offshore substation platform (including transformers, reactive compensation and switchgear), onshore circuits and capitalised costs of corrective maintenance against the capitalised costs of expected constrained energy due to failures and maintenance of the transmission equipment as well as the cost of losses over the project life. The results showed that, similarly to land based wind farms, circuits for the transmission of offshore wind energy should be designed without explicit redundancy. Equipment failures in transmission circuits offshore require much longer repair times than those on shore (e.g. the mean time to repair of an offshore transformer was assumed to be six months) but the cost of offshore equipment is so high that no redundancy in either transformers or submarine transmission cable circuits was justified. Large offshore wind farms require multiple ac cable circuits due to the limited rating of submarine cables. Also the wind farm will be operating at its full output for only part of the year. Thus, even if the transmission link is designed with no redundant capacity its security is quite high. A calculation of a 600 MW offshore wind farm with 3×132 kV, three-core submarine cables indicated that failure of one cable would only result in 8% of the annual wind farm energy being curtailed. It concluded that it may even be cost-effective to choose the capacity of a transmission link capacity to be slightly lower than the simple summation of the full power ratings of all of the wind turbines if they are dispersed over a wide area.

If a large wind farm operating at full capacity were to suddenly disconnect from the terrestrial network, perhaps because of a fault on the transmission circuit, the frequency of the power system would drop rapidly. The magnitude and speed of this frequency drop would depend on the capacity and inertia of the terrestrial power system. As wind farms become larger, it is increasingly necessary to consider the effect of a sudden loss of power from an offshore wind farm on the terrestrial power system. The loss of a single power infeed in Great Britain has traditionally been restricted to 1320 MW (two 660 MW fossil fuel generating sets) and the offshore wind farm transmission circuits, and indeed the entire wind farms, are designed to ensure no single fault results in a greater loss of power.

12.10.2 Submarine AC cable systems

Large offshore wind farms have very extensive networks of submarine ac cable for power collection within the wind farm and transmission to shore. The 30–36 kV power collection circuits as well as the 132, 150, or 220 kV transmission cables to shore are unusual in being very long and without any significant load connected to them. Such extensive cable systems without loads connected to them are rarely found in land based public electricity supply systems. The electrical systems of very large, onshore wind farms, such as those found in parts of China and the USA, share some of their characteristics but often change from underground cable to overhead line as soon as is practicable in order to

reduce cost. The high voltage submarine cables use XLPE insulation with a high dielectric value and so have much higher shunt (parallel) capacitance than overhead lines that use air for their insulation. Thus the reactive power, harmonic and transient performance of offshore wind farm cable circuits is unusual and requires particular consideration.

At 50 or 60 Hz, the high shunt capacitance with the high system voltage results in generation of reactive power (Vars). This reduces the capacity of the circuit to transmit real power and also increases the network voltage. The no-load reactive power generation of a cable is given by

$$Q = 2\pi fLCV^2$$

where f is the system frequency, V is the rated voltage, and l is the length of cable. C is the capacitance of the cable per unit length.

Figure 12.87 shows the per-phase approximate equivalent circuit of a 1 km length of 132 kV cable. It will generate approximately 1 MVar when no power is transmitted through it. This reactive power increases the voltage at the wind farm and network, and also uses part of the thermal rating of the cable. The voltage rise is controlled by reactive power compensation equipment, often a fixed shunt reactor on the offshore platform and a STATCOM or SVC at the onshore substation.

In addition to reactive power generation at fundamental frequency (50 or 60 Hz), the shunt capacitance of the large cable networks can lead to resonances at harmonic frequencies. Figure 12.88 show the schematic diagram of an offshore wind farm electrical system, while Figure 12.89 shows the calculated impedance, seen from the 132 kV busbar. There are a number of series and parallel resonances caused by the interaction of the cable capacitance and inductive reactance of the cables and transformers. The resonances appear as low impedances (series resonance) and high impedances (parallel resonance). The harmonic resonant frequencies vary in frequency and magnitude depending on the number of cables and turbines in service (King and Ekanayake 2010).

The voltage of all land based power systems contains harmonics, caused by the currents drawn by non-linear loads. Hence harmonic filters are often required at the onshore substation to ensure that harmonic resonances within the wind farm network are not excited by this pre-existing distortion. In addition variable-speed wind turbines using power electronic converters and power electronic reactive compensation equipment, such as STATCOMs, inject harmonic currents into the cable networks. If these harmonics are amplified they may cause significant voltage stresses in the offshore network and may also create complex interactions with the power electronic control systems of the wind turbines causing unpredicted equipment malfunction.

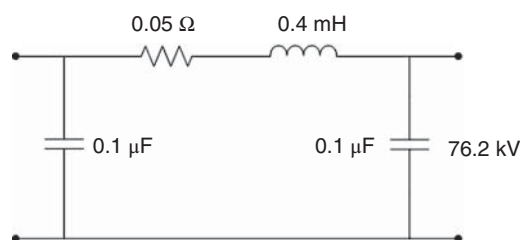


Figure 12.87 Per-phase approximate equivalent circuit of 1 km of 132 kV cable.

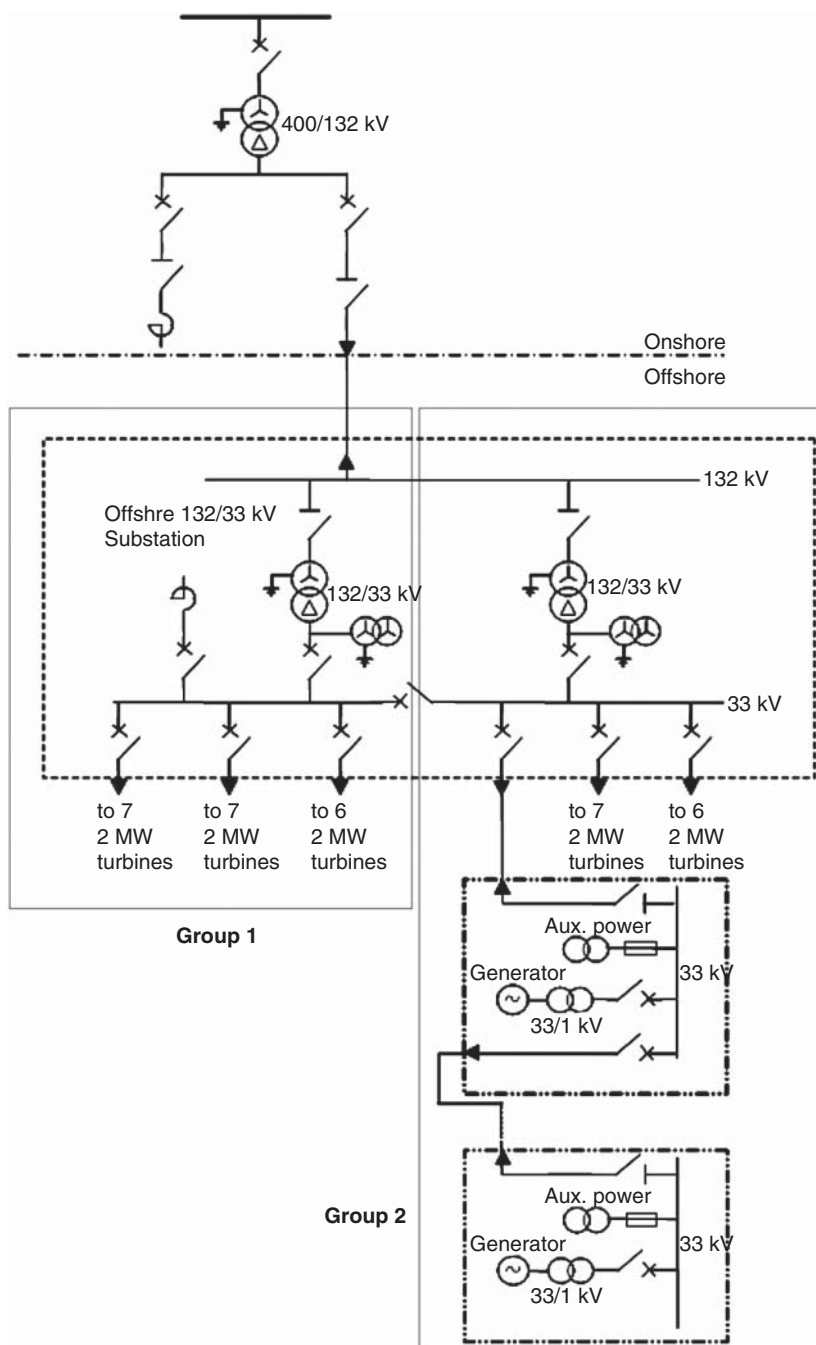


Figure 12.88 Typical offshore wind farm ac connection.

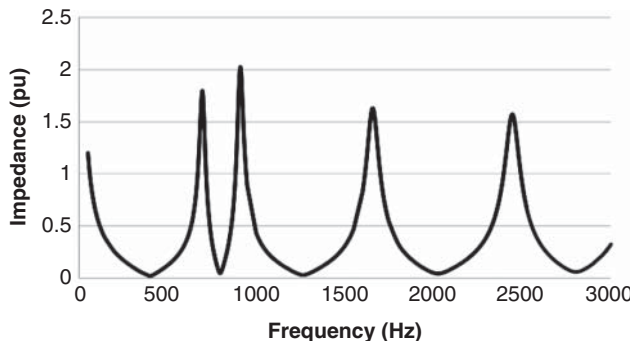


Figure 12.89 Impedance of the network of Figure 12.88 seen from 132 kV busbar.

Transient over-voltages in offshore wind farm networks can be caused by circuit breaker operation unlike in land based, overhead line systems where lightning is the main cause (Lars Liljestrand 2007). Vacuum circuit breakers are often used to control the power collection networks in offshore wind farms, due to their high reliability and low maintenance requirements. In some cases vacuum circuit breakers can cause multiple pre-strokes and re-ignitions and hence high-frequency transient currents. The extensive cable systems in offshore wind farms combined with a large number of step-up transformers results in many voltage reflections. The surge impedance of cables is less than 40Ω , whereas for overhead lines it is typically $300\text{--}400\Omega$ and a lower surge impedance results in a higher rate of rise of the transient over-voltage. Thus the extensive cable systems of offshore wind farms can lead to high transient over-voltages and demanding requirements for the circuit breakers. It may also be necessary to fit surge arrestors to protect the wind turbine transformers from switching over-voltages

Figure 12.90 shows a simulation of the voltage of the 33 kV collection cable of an offshore wind farm after it is energised by a vacuum circuit breaker.

Longer lasting temporary over-voltages may occur if the main circuit breaker at the onshore connection point disconnects the wind farm from the rest of the transmission network, so that the operating wind farm and HV cable become isolated (Akhmatov 2006; Wiechowski and Eriksen 2008). Depending on the protection system of the wind turbines, they may continue to inject active current into the isolated network, charging its capacitance. Once the turbines disconnect, the energy stored in the long ac cable capacitance and the shunt reactor inductance can oscillate with a low frequency, leading to high overvoltages lasting for several seconds. If this case is considered likely, overvoltage protection that is able to absorb the energy from the cable/reactor system may be required.

Some early offshore wind farms reported a rather high rate of transformer failures. In two offshore wind farms the turbine transformers were replaced after a large number of failures and in another offshore wind farm, a failure of the main offshore transformer led to a $4\frac{1}{2}$ month outage of the entire wind farm. The reasons for these failures were complex but it is possible that high frequency, high voltage switching transients made a significant contribution to these insulation failures. Hence proper coordination of surge-protective devices with the insulation strength of electrical power equipment is essential for protecting the offshore electrical system from over-voltages (IEEE PES Wind Plant Collector System Design Working Group 2009).

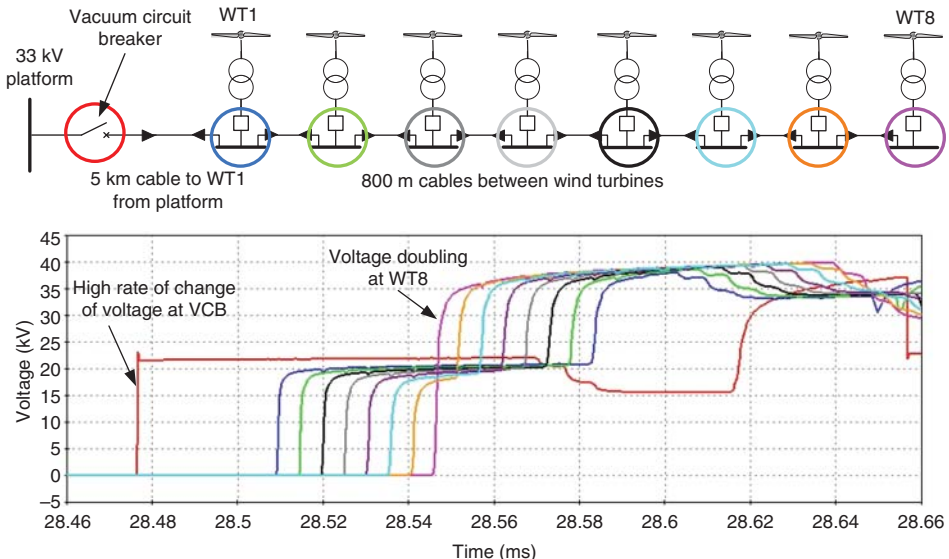


Figure 12.90 Voltage propagating through a wind turbine power collection radial circuit during energisation. Reproduced by permission of Rose King.

12.10.3 HVdc transmission

Figure 12.91 shows an HVdc transmission circuit of an offshore wind farm. The power from the wind farm is rectified to dc by the offshore converter, transmitted at dc through the cable and inverted to ac by the onshore converter. The offshore converter creates a local ac voltage and frequency for the wind farm, which operates in the conventional manner.

The useful length of high voltage ac cables is limited due to their capacitance and hence the reactive power they generate, and so very large wind farms far offshore may be connected to shore more cost-effectively using an HVdc transmission circuit. The precise length at which submarine transmission at dc becomes more cost-effective than at ac depends on the wind farm power rating, transmission voltage, ground conditions and the price of cables and substation or converter equipment, as well as the value ascribed to electrical losses. It has been suggested that, depending on the voltage, HVdc transmission from offshore wind farms would become a viable option for wind farms of more

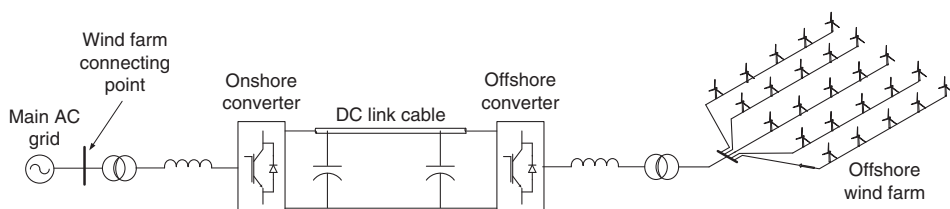


Figure 12.91 VSC HVdc transmission from an offshore wind farm.

than 300 MW and cable route lengths between 50 and 70 km (Koch and Retzmann 2010; Glasdam et al. 2012). However, a review of wind farms that are in service shows that ac transmission connection has been chosen for many surprisingly large and remote offshore wind farms.

There are two distinct HVdc technologies, current source converter (CSC) and voltage source converter (VSC). CSC technology is based on line-commutated devices such as thyristors that are switched on by a pulse and switch off when the current flowing through them reduces to zero. The converters need to be connected to a strong ac system, because the ac system voltage forces the current to commute from one phase of the converter to another. The current must always flow in the same direction through the dc circuit, and so in order to change the direction of the power flow, the voltage polarity of the converters must be reversed. CSC HVdc is not used to connect offshore wind farms.

HVdc VSC uses semiconductor switches that can be turned on and off in a controlled manner. Usually the power electronic devices are insulated gate bipolar transistors (IGBTs) switched using pulse width modulation (PWM) with either two or three voltage levels. Figures 7.58 and 7.59 show the principle of PWM that is used for the lower power levels of individual variable-speed wind turbines. An HVdc VSC is able to create the ac voltage and frequency of the offshore wind farm. Early HVdc VSC converters used PWM but for the very high levels of power needed for dc offshore transmission circuits the sinusoidal voltage is now created using modular multi-level converters (MMCs) (Glasdam et al. 2012).

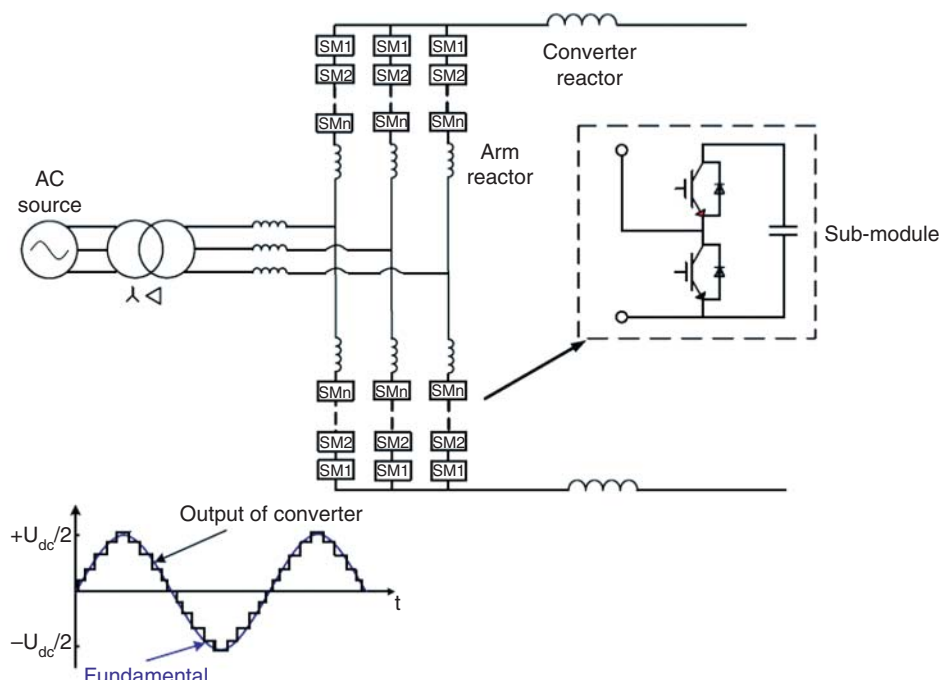


Figure 12.92 MMC using half bridges.

MMCs switch their power electronic devices more slowly than when using PWM and so create lower switching losses and rates of change of voltage. MMCs reduce the need to connect IGBTs in series and offer increased redundancy against failure of an individual semiconductor switch. They are used increasingly for higher power levels (Akagi 2011; Peralta et al. 2012), and Figure 12.92 shows a simplified schematic of a modular VSC. Each arm of the MMC consists of a number of sub-modules of a DC capacitor, IGBTs, and diodes. The IGBTs may be arranged in either a full or half bridge topology. The sub-modules are switched in sequence to form a voltage staircase approximation of a sine wave, often with some additional limited PWM of the individual sub-module voltage. The arm and converter reactors smooth the current and the very large number of sub-modules (often several hundred in each arm) limit fault current and reduce the harmonics to very low levels.

References

- 2009/31/EC (2009) *The Environmental Impact Assessment Directive*. <http://ec.europa.eu/environment/eia/eia-legalcontext.htm> (accessed 27 June 2019).
- Aage, C., Allan, T.D., Carter, D.J.T. et al. (1998). *Oceans from Space: A Textbook for Offshore Engineers and Naval Architects*. France: Ifremer Repères Océans.
- Ackerman, T. (ed.) (2005). *Wind Power in Power Systems*. Chichester: Wiley.
- Ahilan, R.V. (2018) On mooring systems for oil & gas vs floating wind, Offshore Engineering Society Presentation 10.1, <https://www.ice.org.uk/eventarchive/on-mooring-systems-for-oil-gas-vs-floating-wind>.
- Akagi, H. (2011). Classification, terminology, and application of the modular multilevel cascade converter (MMCC). *IEEE Trans. Power Electron.* 26 (11): 3119–3130.
- Akhmatov, V. (2006). Excessive overvoltage in long cables of large offshore wind farms. *Wind Engineering* 30 (5): 375–383.
- Anaya-Lara, O., Tande, J.O., Uhlen, K. et al. (2018). *Offshore Wind Energy Technology*. Chichester: Wiley.
- Andersen, L. (2008). Assessment of lumped-parameter models for rigid footings. *Comput. Struct.* 88: 1333–1347.
- Arany, L., Bhattacharya, S., Macdonald, J., and Hogan, S.J. (2016). Design of monopiles for offshore wind turbines in 10 steps. *J. Soil Dyn. Earthquake Eng.* <https://doi.org/10.1016/j.soildyn.2016.09.024>.
- Archer, C.L., Vasel-Be-Hagh, A., Yan, C. et al. (2018). Review and evaluation of wake loss models for wind energy applications. *Appl. Energy* 226: 1187–1207.
- Azcona, J., Bekirooulos, D., Bredmose, H., et al (2013) State-of-the-art and implementation of design tools for floating structures. *INNWIND Deliverable D4.21*.
- Barltrop, N.D.P. and Adams, A.J. (1991). *Dynamics of Fixed Marine Structures*. Butterworth-Heinemann. ISBN: 0 7506 1046 8.
- Barltrop, N.D.P., Mitchell, G.M., and Atkins, J.B. (1990). Fluid loading on offshore fixed structures. *Offshore Technology Report OTH90322, HMSO*.
- Barthelmie, R. and Jensen, L.E. (2010). Evaluation of power losses due to wind turbine wakes at the Nysted offshore wind farm. *Wind Energy* <https://doi.org/10.1002/we.408>.
- Barthelmie, R., Hansen, O., Enevoldsen, K. et al. (2005). Ten years of meteorological measurements for offshore wind farms. *J. Solar Energy Eng.* 127 (2): 170–176.
- Barthelmie, R., Frandsen, S.T., Nielsen, N.M. et al. (2007). Modelling and measurements of power losses and turbulence intensity in wind turbine wakes at Middelgrunden offshore wind farm. *Wind Energy* 10: 217–228.

- Barthelmie, R., Hansen, K.S., Frandsen, S.T., and Rathmann, O. (2009). Modelling and measuring flow and wind turbine wakes in large wind farms offshore. *Wind Energy* 12: 431–444.
- Barthelmie, R., Pryor, S.C., Frandsen, S.T. et al. (2010). Quantifying the impact of wind turbine wakes on power output at offshore wind farms. *J. Atmos. Oceanic Technol.* 27 (8): 1302–1317.
- Battjes, J.A. and Groenendijk, H.W. (2000). Wave height distributions on shallow foreshores. *J. Coastal Eng.* 40: 161–182.
- BEIS (2019). Contracts for Differences allocation round 3 results. <https://www.gov.uk/government/publications/contracts-for-difference-cfd-allocation-round-3-results>.
- BEIS (2020) Electricity generation costs. UK Department of Business, Energy and Industrial Strategy. <https://www.gov.uk/government/publications/beis-electricity-generation> (accessed September 2020).
- Beuckelaers, W. J. A. P. (2017). Numerical modelling of laterally loaded piles for offshore wind turbines. DPhil thesis, University of Oxford.
- Bierbooms, W.A.A.M. (2006). Constrained stochastic simulation – generation of time series around some specific event in a normal process. *Extremes* 8: 207–224.
- Bladt Industries (2016). Burbo Bank Extension - 32 offshore foundations. https://www.bladt.dk/UserFiles/05_Downloads/Foundations/Burbo_Bank_Extension_Blaa_bjaelke_Low.pdf.
- Bleeg, J., Purcell, M., Ruisi, R., and Traiger, E. (2018). Wind farm blockage and the consequences of neglecting its impact on energy production. *Energies* 11: 1609.
- den Boon J.H., Sutherland J., Whitehouse R., et al (2004). Scour behaviour and scour protection for monopile foundations of offshore wind turbines. Proceedings of the European Wind Energy Conference & Exhibition.
- Boyle, G., New P., 2018. ORJIP impacts from piling on fish at offshore wind sites: collating population information, gap analysis and appraisal of mitigation options. *Final report for the Carbon Trust*. <https://www.carbontrust.com/media/676435/orjip-piling-study-final-report-aug-2018.pdf> (accessed 9 September 2019).
- Burd, H.J., Abadie, C.N., Byrne, B.W., Houlsby, G.T., Martin, C.M., McAdam, R.A., Jardine, R.J., Pedro, A.M.G., Potts, D.M., Taborda, D.M.G., Zdravkovic, L. and Pacheco Andrade, M. (2020). Application of the PISA design model to monopiles embedded in layered soils. *Géotechnique* 70 (11): 1067–1082. <https://doi.org/10.1680/jgeot.20.PISA.009>.
- Butterfield, S., et al (2007). Engineering challenges for floating offshore wind turbines. *NREL/CP-500-38776*.
- BVG Associates (2019) Guide to an offshore wind farm – updated and extended. Crown Estate and Offshore Renewable Energy Catapult www.thecrownestate.co.uk/en-gb/media-and-insights/news/2019-guide-to-an-offshore-wind-farm-updated-to-help-businesses-access-uk-offshore-wind-market (accessed June 2019).
- Byrne, B. W., McAdam, R. A., Burd, H. J., Houlsby, G. T., Martin, C. M., Beuckelaers, W. J. A. P., Zdravković, L., Taborda, D. M. G., Potts, D. M., Jardine, R. J., Ushev, E., Liu, T., Abadias, D., Gavin, K., Igoe, D., Doherty, P., Skov Gretlund, J., Pacheco Andrade, M., Muir Wood, A., Schroeder, F. C., Turner, S. & Plummer, M. A. L., (2017). PISA: New design method for offshore wind turbine monopiles. Proceedings of the Society for Underwater Technology 8th International Conference on Offshore Site Investigation and Geotechnics, London, UK (September).
- Byrne, B.W., McAdam, R.A., Burd, H.J. et al. (2019). Monotonic laterally loaded pile testing in a stiff glacial clay till at Cowden. *Géotechnique*. <https://doi.org/10.1680/jgeot.18.PISA.003>.
- Byrne, B.W., Houlsby, G.T., Burd, H.J. et al. (2020). PISA design model for monopiles for offshore wind turbines: application to a stiff glacial clay till. *Géotechnique*. <https://doi.org/10.1680/jgeot.18.P.255>.
- Carswell, W., Johansson, J., Løvholt, F. et al. (2015). Foundation damping and the dynamics of offshore wind turbine monopiles. *Renewable Energy* 80 (2015): 724–736.
- CEFAS (2004) *Offshore wind farms: Guidance note for environmental impact assessment in respect of FEPA and CPA requirements*. www.cefas.co.uk/publications/files/windfarm-guidance.pdf (accessed 27 June 2019).

- Cermelli, C., Leroux, C., Dominguez, S. D. and Peiffer, A. (2018) Experimental measurements of WindFloat 1 prototype responses and comparison with numerical model Proceedings of the ASME 2018 37th International Conference on Ocean, Offshore and Arctic Engineering.
- Choisnet, T., Percher, Y., Adam, R. et al. (2020). On the correlation between floating wind turbine accelerations, rotor and tower loads. Proceedings of the ASME 2020 39th International Conference on Ocean, Offshore and Arctic Engineering (OMAE2020).
- Choisnet, T., Rogier, E., Percher, Y. et al (2018). Performance and mooring qualification in Floatgen: the first French offshore wind turbine project. Proceedings of the 16ièmes Journées de l'Hydrodynamique, Marseille.
- Cleve, J., Grenier, M., Enevoldsen, P. et al. (2009). Model-based analysis of wake-flow data in the Nysted offshore wind farm. *Wind Energy* 12: 2. <https://doi.org/10.1002/we.314>.
- Coastal Energy and Environment (2018) Blyth Offshore Demonstrator Array 2: a case study. <http://coastalenergyandenvironment.web.unc.edu/2018/07/16/blyth-offshore-demonstrator-array-2-a-case-study/>.
- Collier W. and Alblas L.M. (2018) Reducing cost in jacket design: comparing the integrated and superelement approach. Proceedings of the 3rd International Conference on Offshore Renewable Energy (CORE 2018), Glasgow, UK.
- Crabtree, C.J. (2010). Survey of commercially available condition monitoring systems for wind turbines. Supergen Wind Energy Technologies Consortium/Durham University.
- Craig, R.R. and Bampton, M.C.C. (1968). Coupling of substructures for dynamic analysis. *AIAA Journal* 6 (7): 1313–1319.
- Cruz, J. and Atcheson, M. (eds.) (2016). *Floating Offshore Wind Energy: The Next Generation of Wind Energy*. Switzerland: Springer.
- Dahne, M., Tougaard, J., Carstensen, J. et al. (2017). Bubble curtains attenuate noise from offshore wind farm construction and reduce temporary habitat loss for harbour porpoises. *Mar. Ecol. Prog. Ser.* 580: 221–237. <https://tethys.pnnl.gov/sites/default/files/publications/Dahne-et-al-2017.pdf> (accessed 5 March 2020).
- Damgaard, M., Andersen, J., Ibsen, L.B., and Andersen, L. (2012). Natural frequency and damping estimation of an offshore wind turbine structure. In: *Proceedings of the 22nd International Offshore and Polar Engineering Conference*, vol. 4, 300–307. International Society of Offshore & Polar Engineers.
- Dean, R.G. and Dalrymple, R.A. (1984). *Water Wave Mechanics for Engineers and Scientists*. World Scientific.
- DECC (2008). Dynamics of scour pits and scour protection – synthesis report and recommendations. randd.defra.gov.uk/Document.aspx?Document=me1110_9372_FRP.pdf (accessed 14 November 2019).
- DECC (2010). UK electricity generation costs update. www.decc.gov.uk/assets/decc/Statistics/Projections/71-uk-electricity-generation-costs-update-.pdf (accessed 30 April 2020).
- DECC (2011). National policy statement for renewable energy infrastructure. *EN-3 Department of Energy and Climate Change*. <https://www.gov.uk/government/publications/national-policy-statements-for-energy-infrastructure> (accessed 15 November 2019).
- Det Norske Veritas DNV-OS-J101 (2004). *Design of offshore wind turbine structures*.
- DNVGL-RP-0416 (2016). *Corrosion protection for wind turbines*. Akershus, Norway: DNVGL.
- DNVGL-RP-C203 (2016). *Fatigue design of offshore steel structures*. Akershus, Norway: DNVGL.
- DNVGL-RP-C205 (2017). *Environmental conditions and environmental loads*. Akershus, Norway: DNVGL.
- DNVGL-ST-0126 (2016). *Support structures for wind turbines*. Akershus, Norway: DNVGL.
- DNVGL-ST-0437 (2016). *Loads and site conditions for wind turbines*. Akershus, Norway: DNVGL.
- Dong Energy, Vattenfall, Danish Energy Authority, and Danish Forest and Nature Agency (2006). Danish offshore wind – key environmental issues. https://tethys.pnnl.gov/sites/default/files/publications/Danish_Offshore_Wind_Key_Environmental_Issues.pdf (accessed 13 November 2019).

- Drewitt, A.L. and Langston, R.H.W. (2006). Assessing the impact of wind farms on birds. *Ibis* 148: 29–42.
- DTI (2006a). Capital grants scheme for North Hoyle offshore wind farm. <https://webarchive.nationalarchives.gov.uk/+/http://www.berr.gov.uk/files/file41542.pdf> (accessed 13 November 2019).
- DTI (2006b). Capital grants scheme for Scroby Sands offshore wind farm. file:///Users/scenj/Downloads/Capital_grant_scheme_for_offshore_wind.pdf (accessed 13 November 2019).
- EDF Energy Renewables (2017) Blyth Offshore Demonstrator Wind Farm https://www.bam.com/sites/default/files/domain-606/documents/edf_er_blyth_brochure-606-14997770021779687906.pdf.
- EEW (2020). Offshore wind. <https://eew-group.com/industries/offshore-wind>.
- Efthymiou, M. (1988) Development of SCF formulae and generalised influence functions for use in fatigue analysis. Proceedings of OTJ'88, Recent Developments in Tubular Joint Technology. London.
- EN 1991-1-4 (2005) *Eurocode 1: Actions on structures – Part 1–4: General actions – Wind actions*. Brussels: European Committee for Standardization.
- EN 1993-1-9 (2005) *Eurocode 3: Design of steel structures – Part 1–9: Fatigue*. Brussels: European Committee for Standardization.
- Equinor (2020). How Hywind works. <https://www.equinor.com/en/what-we-do/floating-wind/how-hywind-works.html> (accessed 22 April 2020).
- Evans, B (2004). Lumping of fatigue load cases. *RECOFF Document No. 16a*.
- Forthwind Ltd (2015). ForthWind Offshore Wind Demonstration Project, Methil, Fife. marine.gov.scot/datafiles/lot/forthwind_methil/Forthwind_ES_Non_Technical_Summary.pdf (accessed 26 May 2020).
- Frandsen, S., Barthelmie, R.J., Jorgensen, H.E. et al. (2009). The making of a second-generation wind farm efficiency model-complex. *Wind Energy* 12 (5): 431–444.
- Galloper (2020). Galloper foundations installation completed ahead of time. <http://www.galloperwindfarm.com/galloper-foundations-installation-completed-ahead-of-time>.
- Gentils, T., Wang, L., and Kolios, A. (2017). Integrated structural optimisation of offshore wind turbine support structures based on finite element analysis and genetic algorithm. *Appl. Energy* 199: 187–204.
- Germanischer Lloyd (2012). *Rules and guidelines IV – Industrial services, 2 – Guideline for the certification of offshore wind turbines*.
- Glasdam G., Hjerrild J., Kocewiak L.H., and Bak C.L. (2012). Review on multi-level voltage source converter based HVDC technologies of large offshore wind farms. *Proceedings of the IEEE International Conference on Power System Technology (POWERCON), Auckland*.
- Global Wind Energy Council (2020). Global wind report 2019. <https://gwec.net/global-wind-report-2019/> (accessed 31 July 2020).
- Goda, Y., Haranaka, S., and Kitahata, M. (1966). Study on impulsive breaking wave forces on piles. *Port Harbour Tech. Res. Inst.* 6 (5): 1–30. (in Japanese).
- Gong, S.L., Barrie, L.A., and Blanchet, J.-P. (1997). Modelling sea-salt aerosols in the atmosphere. *J. Geophys. Res.* 102 (D3): 3805–3818.
- Gross, R., Greenacre, P., and Heptonstall, P. (2010). *Great Expectations: The Cost of Offshore Wind in UK Waters – Understanding the Past and Projecting the Future*. London: UK Energy Research Centre.
- Hancock, J.W. and Gall, D.S. (1985). Fatigue under narrow and broad band stationary loading. *Final Report of the Cohesive Programme of R&D into Fatigue of Offshore Structures*, Marine Technology Directorate Ltd, UK.
- Hansen K. S. et al. (2010). Power deficits due to wind turbine wakes at Horns Rev wind farm. Proceedings of TORQUE 2010: The Science of Making Torque from Wind (28–30 June). Crete, Greece.

- Hasager, C.B. (2014). Offshore winds mapped from satellite remote sensing. *WIREs Energy Environ.* 3: 594–693. <https://doi.org/10.1002/wene.123>.
- Hau, E. (2006). *Wind Turbine Fundamentals Technologies, Applications Economics*. Berlin: Springer.
- He, Z.-X., Xu, S.C., Shen, W.X. et al. (2016). Review of factors affecting China's offshore wind power industry. *Renewable Sustainable Energy Rev.* 56: 1372–1386.
- Herschel A., Stephenson S., Sparling C., Sams C., and Monnington J. (2015). The use of acoustic deterrents for the mitigation of injury to marine mammals during pile driving for offshore wind farm construction. ORJIP PROJECT 4. Stage one of phase two. *Report submitted to the Carbon Trust*.
- Hornsea 4 (2018). Environmental impact scoping report. <https://hornseaprojects.co.uk/-/media/WWW/Docs/Corp/UK/Hornsea-Project-Four/Scoping-Report/Hornsea-Four-Scoping-Report-LOW-RES> (accessed 15 November 2019).
- Houlsby, G.T., Abadie, C.N., Beuckelaers, W.J.A.P., and Byrne, B.W. (2017). A model for nonlinear hysteretic and ratcheting behaviour. *Int. J. Solids Struct.* 120: 67–80.
- Howard M and Brown C 2004. Results of the electromagnetic investigations and assessment of marine radar, communications and positioning systems undertaken at the North Hoyle wind farms by Qinetiq and Maritime and Coastguard Agency. http://users.ece.utexas.edu/~ling/EU1%20QuinetiQ%20effects_of_offshore_wind_farms_on_marine_systems-2.pdf (accessed 13 November 2019).
- HSE (2002). Environmental considerations – offshore technology report. 2001/010.
- Huddleston, J. (ed.) (2010). *Understanding the environmental Impacts of Offshore Wind Farms*, 238. Collaborative Offshore Wind Research into the Environment; COWRIE.
- Hywind (2017). Hywind Scotland – The world's first commercial floating wind farm. brochure-hywind-A4.pdf (accessed 10 February 2020).
- Hywind (2020). Hywind Scotland input to Wind Energy Handbook_v1.ppt.
- IEA (2016). *Recommended practices for floating LiDAR systems*. Wind Annex 32 Work Package 1.5. State-of-the-art report. https://www.ieawindtask32.org/wp-content/uploads/2016/04/IEA-StateOfArtFloatingLIDAR-2Feb2016_v1.0.pdf (accessed June 2019).
- IEA (2019) Offshore wind outlook 2019: world energy outlook special report. <https://www.iea.org/offshorewind2019> (accessed 1 November 2019).
- IEC 61400-3-1 (2019). *Wind energy generation systems – Part 3-1: Design requirements for fixed offshore wind turbines*.
- IEC 61400-3-2 (2019) *Wind energy generation systems – Part 3-2: Design requirements for floating offshore wind turbines*.
- IEEE PES Wind Plant Collector System Design Working Group (2009). Wind power plant grounding, overvoltage protection, and insulation coordination. Proceedings of the IEEE Power & Energy Society General Meeting. Calgary.
- Infrastructure Planning Commission (2011). Using the Rochdale envelope. Advice Note 9. <https://infrastructure.planninginspectorate.gov.uk/wp-content/uploads/2011/02/Advice-note-9-Rochdale-envelope-web.pdf> (accessed 23 June 2019).
- INNWIND (2016) Costs-Models-v1-02-1-Mar-2016-10MW-RWT.xls at www.innwind.eu.
- IRENA (2019a). *Renewable Power Generation Costs in 2018*. Abu Dhabi: International Renewable Energy Agency.
- IRENA (2019b). *Future of Wind: Deployment, Investment, Technology, Grid Integration and Socio-economic Aspects*. Abu Dhabi: International Renewable Energy Agency.
- ISET (2006). Advanced maintenance and repair for offshore wind farms using fault prediction and condition monitoring techniques. *Offshore M&R Final Report, NNE5/2001/710*.
- ISO 19902 (2007). *Petroleum and natural gas industries – Fixed steel offshore structures*.
- Ivanell S., Nilsson K., Eriksson O., Soderberg S., and Och I. E. (2018). Wind turbine wakes and wind farm wakes. *Energiforsk Report 2018:541*. <https://www.energiforsk.se/en/programme/>

- wind-research-industry-network/reports/wind-turbine-wakes-and-wind-farm-wakes (accessed 29 February 2020).
- JNCC (2009). *Statutory nature conservation agency protocol for minimising the risk of disturbance and injury to marine mammals from piling noise – Annex e*. Joint Nature Conservation Committee. <http://archive.jncc.gov.uk/PDF/Piling%20Protocol%20June%202009.pdf> (accessed 22 September 2019).
- Jonkman, J. M. (2007). Dynamics modeling and loads analysis of an offshore floating wind turbine. *NREL/TP-500-41958*.
- Jonkman, J. M. and Matha, D. (2010). A quantitative comparison of the responses of three floating platforms. *NREL/CP-500-46726*.
- Kallehave, D., Byrne, B.W., LeBlanc Thilsted, C., and Kousgaard Mikkelsen, K. (2014). Optimization of monopiles for offshore wind turbines. *Philos. Trans. R. Soc. Ser. A* 373: 0100.
- Katic I., Hojstrup J., Jensen N.O. (1987). A simple model for cluster efficiency. EWEC '86 Conference Proceedings. Rome. https://backend.orbit.dtu.dk/ws/portalfiles/portal/106427419/A_Simple_Model_for_Cluster_Efficiency_EWEC_86_.pdf (accessed 29 February 2020).
- King R. and Ekanayake J.B (2010). Harmonic modelling of offshore wind farms. Proceedings of the IEEE PES Meeting July 2010.
- Koch, H. and Retzmann, D. (2010) Connecting large offshore wind farms to the transmission network. Proceedings of the Transmission and Distribution Conference and Exposition, 2010 IEEE PES.
- Koller, J., Koppel, J., and Peters, W. (2006). *Offshore Wind Energy: Research on Environmental Impacts*. Springer.
- Kuhn, M.J. (2001). *Dynamics and Design Optimisation of Offshore Wind Energy Conversion Systems*. DUWIND. ISBN: 90-76468-07-9.
- Lars Liljestrand, A.S. (2007). Transients in collection grids of large offshore wind parks. *Wind Energy* 11 (1): 45–61.
- Leblanc, C., Byrne, B.W., and Houlsby, G.T. (2010). Response of stiff piles to random two-way lateral loading. *Géotechnique* 60 (9): 715–721. <https://doi.org/10.1680/geot.09.T.011>.
- Lillgrund Pilot Project (2008). Technical description Lillgrund Wind Power Plant. <https://www.osti.gov/etdeweb/servlets/purl/979747> (accessed 1 December 2019).
- Lillgrund Pilot Project (2009a). Assessment of the Lillgrund Windfarm, power performance and wake effects. <https://www.osti.gov/etdeweb/biblio/979752> (accessed 8 September 2019).
- Lillgrund Pilot Project (2009b). Lillgrund Wind Farm – visual effects. <https://www.osti.gov/etdeweb/biblio/979744> (accessed 14 November 2019).
- Lillgrund Pilot Project (2009c). Lillgrund Offshore Wind Farm – environmental monitoring. <https://www.osti.gov/etdeweb/biblio/979748> (accessed 14 November 2019).
- Lillgrund Pilot Project (2009d). Archaeological handbook for establishing offshore wind farms in Sweden. <https://www.osti.gov/etdeweb/servlets/purl/979742> (accessed 14 November 2019).
- Lotsberg, I. (2010). System effects in a fatigue design of long pipes and pipelines. Proceedings of the 29th International Conference on Offshore Mechanics and Arctic Engineering, Shanghai.
- Lotsberg, I. (2014). Assessment of the size effect for use in design standards for fatigue analysis. *Int. J. Fatigue* 66: 86–100.
- Lotsberg, I. (2016). *Fatigue Design of Marine Structures*. Cambirdge University Press.
- Lotsberg, I., Serednicki, A., Cramer, E., Bertnes, H., and Haahr, P.E. (2011). On the structural capacity of grouted connections in offshore structures. Proceedings of the 30th International Conference on Offshore Mechanics and Arctic Engineering, Rotterdam.
- Lupton, R. and Langley, R. (2013). Efficient modelling of floating wind turbines Proceedings of the 9th PhF Seminar on Wind Energy in Europe, Upsala University.
- MacCamy, R.C. and Fuchs, R.A. (1954). Wave forces in piles: A diffraction theory. *Technical Memorandum No. 69*, Beach Erosion Board, US Navy Corps of Engineers.

- Masing, G. (1926). Eigenspannungen und Verfestigung beim Messing. In: *Proceedings of the 2nd International Congress of Applied Mechanics*, 332–335. Orell Füssli Verlag.
- Matha, D., Sandner, F., and Schlipf, D. (2014). Efficient critical design load case identification for floating offshore wind turbines with a reduced nonlinear model. *J. Phys. Conf. Ser.* 555: 012069.
- Matha, D., Sandner, F., Molins, C. et al. (2015). Efficient preliminary floating offshore wind turbine design and testing methodologies and application to a concrete spar design. *Trans. R. Soc. A* 373: 0350. <https://doi.org/10.1098/rsta.2014.0350>.
- Matlock, H. (1970). Correlations for design of laterally loaded piles in soft clay. In: *Second Annual Offshore Technology Conference*, Houston, Texas, vol. 1, OTC 1204, 577–594. Offshore Technology Conference.
- MGN 371 (2008). Offshore renewable energy installations (OREIs) - Guidance on UK navigational practice, safety and emergency response issues. Maritime and Coastguard Agency.
- Milne-Thomson, L.M. (1967). *Theoretical Hydrodynamics*, 5e. Macmillan.
- Moreno, J., Thiagarajan, K.P., Cameron, M., and Urbina, R. (2016). Added mass and damping of a column with heave plate oscillating in waves. Proceedings of IWWWFB31, Plymouth, MI, USA (3–6 April 2016).
- Mortensen N.G., Landberg L., Troen I., and Petersen E.L. (1998). Wind Atlas Analysis and Applications Program WA^sP. https://orbit.dtu.dk/files/106061302/ris_i_666_EN_v.1_ed.2_.pdf (accessed 10 September 2019).
- Muir Wood, A.M. and Fleming, C.A. (1981). *Coastal Hydraulics*, 2e. Macmillan.
- Ng, C. and Ran, L. (eds.) (2016). *Offshore Wind Farms: Technologies, Design and Operation*. Woodhead, Elsevier.
- Norwind (2010). Lessons learned from the first German Offshore wind farm – Alpha Ventus. Proceedings of the SPE Conference Bergen (14 April 2010). bergen.spe.no/publish_files/ODS2010_PG_Oestvik.pdf.
- NREL (2006). Wind turbine design cost and scaling model. *NREL/TP-500-40566*.
- Oersted (2019). Our experience with suction bucket jacket foundations. <https://orsted.com/en/our-business/offshore-wind/wind-technology/suction-bucket-jacket-foundations> (accessed May 2020).
- OESEA3 (2016). UK offshore energy strategic environmental assessment. Department of Energy and Climate Change. https://assets.publishing.service.gov.uk/government/uploads/system/uploads/attachment_data/file/504827/OESEA3_Environmental_Report_Final.pdf (accessed 1 July 2019).
- ORJIP (2018). Offshore Renewables Joint Industry Programme. <https://www.carbontrust.com/offshore-wind/orjip> (accessed 14 November 2019).
- OSPAR Commission (2008). Assessment of the environmental impact of offshore wind-farms. <https://www.ospar.org/documents?d=7114> (accessed 27 June 2019).
- Peire, K., Nonneman, H., and Bosschen, E. (2009). Gravity base foundations for the Thornton Bank offshore windfarm. *Terra et Aqua* 115: 19–29.
- Peña, A., Hasager, C. B., Lange, J., Anger, J., Badger, M., Bingöl, F., ... Würth, I. (2013). Remote sensing for wind energy. DTU Wind Energy. *DTU Wind Energy E, No. 0029*. https://backend.orbit.dtu.dk/ws/portalfiles/portal/55501125/Remote_Sensing_for_Wind_Energy.pdf (accessed 6 March 2020).
- Peralta, J., Saad, H., Den netiere, S. et al. (2012). Detailed and averaged models for a 401-level MMC–HVDC system. *IEEE Trans. Power Delivery* 27 (3): 1501–1508.
- Perrow, M.R. (ed.) (2019). *Wildlife and Wind Farms, Conflicts and Solutions. Offshore: Potential Effects*, vol. 3. Pelagic Publ.
- Platis, A., Simon, K., Siedersleben, S.K. et al. (2018). First in situ evidence of wakes in the far field behind offshore wind farms. *Sci. Rep.* 8: 2163.
- Radov D., Koenig C., et al. (2017) Offshore revolution? Decoding the UK offshore wind auctions and what the results mean for a "zero-subsidy" future. NERA Economic Consulting. <https://>

- www.nera.com/publications/archive/2017/offshore-revolution--decoding-the-uk-offshore-wind-auctions-and-.html (accessed 4 January 2020).
- Rainey and Camp (2007). Constrained non-linear waves for offshore wind turbine design. *J. Phys.: Conf. Ser.* 75: 012067.
- Reese, L., Cox, W. R., and Koop, F. D. (1974). Analysis of laterally loaded piles in sand. Proceedings of the 6th Offshore Technology Conference, Houston, paper no. 2079.
- Richards, I.A., Houlsby, G. T., and Byrne, B.W. (2019a). Exploring the response of a monopile to storm loading. Proceedings of the Coastal Structures Conference 2019.
- Richards, I.A., Byrne, B.W., and Houlsby, G.T. (2019b). Monopile rotation under complex cyclic lateral loading in sand. *Géotechnique* <https://doi.org/10.1680/jgeot.18.P.302>.
- Roddier, D., Cermelli, C., Aubault, A., and Peiffer, A (2017). Summary and conclusions of the full life-cycle of the WindFloat FOWT prototype project. Proceedings of the ASME 2017 36th International Conference on Ocean, Offshore and Arctic Engineering.
- Sandner, F., Wie, Y. Matha, D. et al (2014a). Innovative concepts for floating structures. *INNWIND Deliverable D4.3.3*.
- Sandner, F., Schlipf, D., Matha, D., and Cheng, P.W. (2014b). Integrated optimization of floating wind turbine systems. Proceedings of the ASME 2014 33rd International Conference on Ocean, Offshore and Arctic Engineering.
- Scottish Natural Heritage (2012). *Guidance on assessing the impact on coastal landscape and seascapes – Guidance for scoping an environmental statement*. <https://www.nature.scot/guidance-offshore-renewables-assessing-impact-coastal-landscape-and-seascape-guidance-scoping> (accessed 22 September 2019).
- Seidel, M (2007a). Jacket substructures for the REpower 5M wind turbine. Conference Proceedings of European Offshore Wind 2007, Berlin.
- Seidel, M. (2007b, 2007). Tragstruktur und Installation der REpower 5M in 45 m Wassertiefe. *Stahlbau 76* (Heft 9).
- Siemens Gamesa (2020) SWT-6.0-154 offshore wind turbine. <https://www.siemensgamesa.com/en-int/products-and-services/offshore/wind-turbine-swt-6-0-154> (accessed 2 October 2020).
- SIF (2020). Wind foundations. <https://sif-group.com/en/wind>.
- Skov, H., Heinänen, S., Norman, T., Ward, R.M., Méndez-Roldán, S. and Ellis, I. 2018. ORJIP bird collision and avoidance study. *Final report for the Carbon Trust*.
- Sparling, C., Sams C., Stephenson S., Joy R., Wood J., Gordon J., Thompson D., Plunkett R., Miller B., and Götz T. (2015). The use of acoustic deterrents for the mitigation of injury to marine mammals during pile driving for offshore wind farm construction. ORJIP Project 4. Stage one of phase two. Submitted to the Carbon Trust (unpublished). <https://www.carbontrust.com/media/675291/orjip-add-study-final-report-stage-1-phase-2.pdf> (accessed 22 September 2019).
- Spinato, F. (2009). Reliability of wind turbine subassemblies. *IET Renew. Power Gener.* 3 (4): 387–401.
- Sumer, B.M. and Fredsoe, J. (2001). Scour around pile in combined waves and current. *J. Hydraul. Eng.* 127 (5): 403–411.
- Taborda, D.M.G., Zdravković, L., Potts, D.M. et al. (2019). Finite element modelling of laterally loaded piles in a dense marine sand at Dunkirk. *Géotechnique* <https://doi.org/10.1680/jgeot.18.PISA.006>.
- Tao, L., Molin, B., Scolan, Y.-M., and Thiagarajan, K. (2007, 2007). Spacing effects on hydrodynamics of heave plates on offshore structures. *J. Fluids Struct.* 23 (8): 1119–1136.
- Tarp-Johansen, N.J. (2009). Comparing sources of damping of cross-wind motion. Proceedings of EWEC 2009.
- Tavner, P. (2012). *Offshore Wind Turbines – Reliability, Availability and Maintenance*. London: IET.
- Thomson, K.E. (2012). *Offshore Wind: A Comprehensive Guide to Successful Wind Farm Installation*. London: Academic Press.

- Tian, X., Tao, L., Li, X., and Yang, J. (2016). Hydrodynamic coefficients of oscillating flat plates at $0:15 < KC < 3.15$. *J. Mar. Sci. Technol.* <https://doi.org/10.1007/s00773-016-0401-2>.
- Tromans, P., Anaturk, A., and Hagermeijer, P. (1991). A new model for the kinematics of large ocean waves – application as a design wave. Proceedings of the First International Offshore and Polar Engineering Conference, Edinburgh.
- Tsouvalas, A. and Metrikine, A.V. (2016). Noise reduction by the application of an air-bubble curtain in offshore pile driving. *J. Sound Vib.* 371: 150–1170. <https://www.sciencedirect.com/science/article/abs/pii/S0022460X16001681> (accessed 5 March 2020).
- Twiddell, J. and Gaudiosi, G. (eds.) (2009). *Offshore Wind Power*. Earthscan.
- Van der Tempel, J (2006) Design of support structures for offshore wind turbines. PhD Thesis, Delft University of Technology.
- Van der Valk, P.L.C. (2014) Coupled simulations of wind turbines and offshore support structures – strategies based on the dynamic substructuring paradigm. PhD thesis, Delft University of Technology.
- Vattenfall (2017). Offshore wind: suction buckets reduce cost and underwater noise. <https://group.vattenfall.com/press-and-media/news--press-releases/newsroom/2017/offshore-wind-suction-buckets-reduce-cost-and-underwater-noise>.
- de Vries, W.E and Krolis, V.D (2007). Effects of deep water on monopile support structures for offshore wind turbines. Proceedings of EWEC 2007.
- Wagner, H. (1932). Über Stoß- und Gleitvorgänge an der Oberfläche von Flüssigkeiten. *Zeitschrift für angewandte Mathematik und Mechanic* 12 (4): 193–215. (in German).
- Wehausen, J.V. and Laitone, E.V. (1960). *Surface Waves*, Encyclopedia of Physics, vol. IX. Springer-Verlag. Available online at the University of California website, www.coe.berkeley.edu.
- Wheeler, J.D. (1970). Method of calculating forces produced by irregular waves. *J. Pet. Technol.* 22: 359–367.
- Whitehouse, R.J.S., Harris, J.M., Sutherland, J., and Rees, J. (2011). The nature of scour development and scour protection at offshore wind farm foundations. *Mar. Pollut. Bull.* 62 (1): 73–88. <https://doi.org/10.1016/j.marpolbul.2010.09.007>.
- Wiechowski, W. and Eriksen, P.B. (2008). Selected studies on offshore wind farm cable connections – challenges and experience of the Danish TSO. In: *Power and Energy Society General Meeting – Conversion and Delivery of Electrical Energy in the 21st Century*, 1–8. Pittsburgh, PA: IEEE.
- Wienke, J (2001). Druckschlagbelastung auf schlanke zylindrische bauwerke durch brechende Wellen – theoretische und großmaßstäbliche Laboruntersuchungen. PhD Thesis, TU Braunschweig, www.biblio.tu-bs.de (in German).
- Wienke, J. and Oumeraci, H. (2005). Breaking wave impact force on a vertical and inclined slender pile – theoretical and large-scale model investigations. *J Coastal Eng.* 52: 435–462.
- Wiggelinkhuizen, E.J., Verbruggen T.W., Braam, H. et al (2007). Condition monitoring for offshore wind farms. *CONMOW final report ECN-E-07-044*.
- Wilkinson, M., Hendriks, B., Spinato, F., et al (2010). Methodology and results of the Reliawind reliability field study. Proceedings of EWEC 2010.
- Wind Europe (2020). Wind energy in Europe in 2019. <https://windeurope.org/wp-content/uploads/files/about-wind/statistics/WindEurope-Annual-Statistics-2019.pdf> (accessed 31 July 2020).
- Zdravković, L., Jardine, R.J., Taborda, D.M.G. et al. (2019a). Ground characterisation for PISA pile testing and analysis. *Géotechnique* <https://doi.org/10.1680/jgeot.18.PISA.001>.
- Zdravković, L., Taborda, D.M.G., Potts, D.M. et al. (2019b). Finite element modelling of laterally loaded piles in a stiff glacial clay till at Cowden. *Géotechnique*. <https://doi.org/10.1680/jgeot.18.PISA.005>.

Appendix A12 Costs of electricity

Two rather different measures are used to indicate the cost of energy from offshore wind farms and hence reflect their capital costs. The levelised cost of energy (LCOE) is an economic indicator that is used strategically by policy makers to help select which generation technology a country or organisation should invest in. In contrast, the strike price is the guaranteed price of energy that a renewable energy generating company will receive under a contract for difference (CfD). A CfD is a form of guarantee that pays a wind farm operator if the market price of electrical energy falls below the strike price but requires payment if the market price rises above the strike price. Both indicators have units of £/MWh but are used for different purposes and are based on different assumptions, e.g. year of price/cost, discount rates and what is assumed of the costs of offshore and onshore electricity transmission and integration into the operation of the power system.

A12.1 Levelised cost of electricity

The LCOE (£/MWh) of any electricity generating project (BEIS 2020) is defined as

$$\frac{\text{NPV of total cost of the project over its lifetime}}{\text{NPV of energy generated over the project lifetime}}$$

NPV is net present value.

For a wind power project, the LCOE depends largely on

- Total installed cost of the wind farm. This includes turbine, balance of plant, and installation costs.
- Capacity factor. This depends on the wind resources, the availability of the turbines, and any constraints on exporting the electricity.
- Operations and maintenance costs, both fixed and variable costs. This can represent up to 20–25% of the LCOE for an offshore wind farm.
- Cost of financing, including discount rates chosen and debt to equity ratio.

Levelised costs usually include only those costs of the wind farm and immediate electrical connection. They do not usually include wider costs, such as electricity system balancing, wider network costs, or air quality impacts.

A12.2 Strike price and contract for difference

A CfD is a financial instrument used in Great Britain to procure electrical energy from offshore wind farms. The budget available for new offshore wind farm capacity is determined by the government, and an auction is held to establish the strike price at which a government agency agrees to buy electricity for a fixed period of years starting at some

future date. A generator that obtains a CfD by submitting a low bid is then paid the difference between the strike price and an average price of electricity in the GB energy market for each MWh of electricity generated. If the average GB market price falls below the strike price, the generator is paid the difference, whereas if the price is above the market price, it reimburses the government agency.

A CfD reflects the cost of building the wind farm and allows electrical energy from wind farms to be procured at lowest cost against a fixed budget. It gives developers a guaranteed fixed price for the duration of the contract. It reduces the exposure of generators to low energy market prices while protecting consumers at times of high electricity prices.

Contracts for difference and their auctions have been credited with reducing the cost of electrical energy from offshore wind farms dramatically. The most recent strike prices identified, of £40/MWh, are comparable to the average GB wholesale market price of electricity (indicating no government subsidy is required) and are less than half the electricity retail price.

Index

- 160 m diameter turbine, blade design upscaling for 495
50 year return gust 34, 228, 237, 243, 316
50 year return significant wave height 790, 792, 794
acceleration potential 188, 191
accelerometer 579, 595–7, 614, 626, 827–8
access 431, 435–6
across-wind turbulence 242, 349–351, 355
active pitch control 391–6
active power 539, 655, 659, 768
active stall 397, 584, 622
active wake control 638–652, 653, 656, 658–9
actuator discs 41–59, 78–80, 154, 160–5, 181
actuators
 electric 394–5, 579, 629, 630
 hydraulic 392–5, 399, 579, 629, 630
 pitch 392–5, 579, 580, 584, 587, 596, 602, 610, 617, 618, 620, 622, 629–631
 for ‘smart’ blades 603
 torque 579
 yaw 586, 611
added mass 190–200, 888–9, 893, 895–7, 905
added turbulence 639, 646, 647, 649, 651
aerodynamic
 braking system 392, 398–9, 584, 602, 629
 damping 241–2, 283–5, 292, 301, 302, 317, 322–3, 429, 496, 499, 584, 595, 597, 598, 797, 822, 852–4, 859, 860
 design 441–3
 efficiency 583–5, 589
 noise 126–9, 378–9, 387, 401–3, 592, 692–3
aeroelastic feedback 325
aeroelastic instability 302
aerofoil 39, 49, 58–75, 92–6, 108
 boundary layer 122, 128, 135–9
 cambered 149–151
 circulation 49 *et seq* 124, 141–3
 data 109, 115–121
 empirical 93, 250, 381, 478
 designs 113–120
 flat back 121
 lift and drag 113–136
 low noise 128–9, 693
 stall 141–5, 201–7
 turbulence 138–9
Ainslie model 642–8, 651, 652
air density 40–1, 107, 110, 133, 644, 648
air jets 124
Airy wave theory 797–802, 805, 809, 810
all-weather access 436
Alpha-Ventus offshore wind farm 867–8, 871, 873–7
anemometer 579, 589, 612, 614, 615, 622, 670–1
angle of attack 584, 592, 602
 acceleration potential 188
 blade geometry 72, 375
 dynamic stall 201–7
 lift and drag 143–151, 240, 241, 249, 252, 261, 283, 396
 pitch regulation 106–7, 391
 rotor blade theory 59–61
 stall delay 92–4, 250
 steady yaw 153–189
 unsteady and quasi-steady flow 189–200

- angular momentum
 blade geometry and number 72–4, 88
 quasi-steady flow 194
 rotor blade theory 59
 rotor disc theory 45
 steady yaw 170 *et seq.*
 vortex cylinder model 49–58
- annual energy capture 113, 667–669, 672
 annual energy yield 364, 667–669, 672
 annual mean wind speed 14, 34, 370–1, 381–2,
 386
 annulus gear 532–5
 ANSI/AGMA curves 530–2
 ARMAX model 35
 array efficiency 672, 777–781
 array losses 777–781
 ASME boiler and pressure vessel code method
 524
 assessment of environmental impacts 674–711
 landscape 678–681
 seascape 910
 of wind-farm noise 687–698, 910
 assisted stall 106
 atmospheric boundary layer (ABL) 13, 18–20, 25,
 199, 221, 640, 655
 atmospheric stability 18, 19, 637, 643, 655, 656
 auto correlation function 239, 262–7, 270
 automatic voltage controller (AVC) 720
 average wind speed 109, 228, 233, 612, 656, 671,
 776
 A-weighted filter 690
 axial flow induction factor 249, 377–8
 actuator discs 41
 blade geometry and number 72–80, 86
 momentum theory 66
 performance 97, 380–1
 rotor blade theory 59–63
 steady yaw 165, 177
 axial induction control 653, 654, 658, 660
 axial induced velocity 46, 51, 54, 75, 154, 161, 177
 azimuth 147, 252–7, 297, 301, 313, 318, 328,
 478–482, 490, 510, 517–8, 602, 605, 606, 611,
 614, 644
 azimuthal binning 277
 background response 242, 246, 318, 349, 354–6,
 358
 back-scattering 699
 balance-of-plant 665–6, 774
 ball-screw 392, 630
 Baltic 861, 863
 band-pass filter 598
 BARD offshore wind farm 877–8
 Batchelor 263–4
 bats 710
 beam element 326–7
 bearing 309, 372, 390, 394–6, 420–3, 430,
 519–521, 531–2, 536, 555–7, 584, 585, 655,
 826–8
 distortion 521
 friction 325, 585, 630
 life 520–1, 611
 Beatrice offshore wind farm 867, 869, 871–6
 bend-twist coupling 511–9
 benthos 911
 Bernoulli's equation 42, 48, 162, 797–8, 803, 812,
 815
 Bessel functions 28, 58, 199, 263, 811, 813
 Betz limit 43, 89, 90
 biaxial plies 446, 451, 455–7
 bilinear or Tutsin approximation 632, 633
 Biot-Savart 39, 51, 52, 161, 165–6, 170
 birch 449, 471–2, 487
 birds, impact on 707–710, 909–912
 black start 659
 blade
 adhesive joints 467, 471, 477, 508
 aerodynamic design 441–3
 chord 375–7, 380–1
 chord distribution 73, 244, 375, 379, 443, 488
 DTU 10 MW reference design 453, 454, 478,
 500–1, 517, 518
 element theory 59, 161, 171, 187–8, 192, 200
 extreme operational loading 274–7, 331–8,
 478–481, 486, 495, 517–8
 extreme stationary loading 240–8
 fatigue criticality 484–5, 494
 fatigue design 302–7, 486–494
 fatigue loading 229, 231, 258, 302–5, 482–495
 FC40 blade (*see* FC40 blade)
 feathering 391, 394
see also feather
 geometry 68–74, 174, 200, 441
 inboard section 443
 optimum 68–74
 parameter 71, 75, 76, 88
 loads due to yaw 478–481
 manufacture 473, 476–8
 cost 470–1
 filament winding 477
 half shells – assembly 473, 477
 mould lay-up 451, 473, 476
 pre-pregs 476
 vacuum resin infusion 476
 mass 244, 365–6, 495
 mass imbalance 429

- materials
 safety factors 473–5
 strength/stiffness 487
- moulds 451, 473, 477
- natural frequency 241–4, 279, 281–5, 287, 289, 346, 447, 496
- noise 126–8, 370, 378–9, 386–7, 692–3
- number of (*see* number of blades)
- passing
 effects 647
 frequency 301, 318, 320, 322–3, 386, 391, 404, 412, 425–430, 444, 496, 517–8, 525, 527, 558, 565, 589, 593, 596, 599, 606, 621, 622, 626, 842, 870
- pitch error loads 428–9
- pitch set angle 105
- pitching rate 511, 521
see also pitch rate
- resonance/resonant response 241, 246, 287, 347
et seq., 495
- root 444, 446, 486, 494
 bending moment 478–482, 500
 fixings 506–8
 transition 444, 446, 478, 489
- Sandia 100 m designs 443, 453, 470–1
- segmental construction 477
- skin thickness 365, 371, 376, 447, 486, 489, 495
- structural design criteria 444
- structure 444–6, 451, 486–9, 501, 506
- swept back 517
- thickness/chord ratio 245, 252, 487–8
- tip (*see* tip)
 tip deflection 238, 279–280, 290–1, 301, 331, 347, 377, 447, 471, 486, 495, 517
- twist 73, 279, 378, 396, 442–3, 451, 498, 511–9
 distribution 73, 249–250, 252, 279, 382–7, 391, 442–3, 487–8
- wake formation and modelling 638–640
- weight 370–1, 376–7, 382, 470
- Bladed* code 301, 326–8, 652, 891
- blade design – scaling up 495
- blade testing 508–9
 biaxial 509
 fatigue 509
 modal 508
 static 508
- Blade Element Momentum (BEM) theory 59, 161, 171, 178, 187–8, 192, 200, 249, 251, 256, 274
- blade-tower clearance 238, 256, 426, 486, 495, 517, 875
- blade-wave clearance 828
- Blyth offshore wind farm – gravity bases 865–7
- bolted flange joint 564–7, 842
- bolt fatigue stresses 521, 566–7
- bolt load increment 566–7
- boundary layer
 aerofoil 135–9, 603
 atmospheric (ABL) 13, 18–20, 25, 199, 221, 640, 655
 dynamic stall 201–7
 lift and drag 141–9
 rotor blade theory 59–63
 stall delay 92–4
 turbulent 114, 127–8, 138–141, 212–3, 692
 vortex cylinder model 49–54
- bound vorticity 51–3, 91
- Bragg grating 609
- brake
 design 548–555
 high speed shaft brake 552–3
 low speed shaft brake 554
- disc 598
 centrifugal stress 549
 temperature rise 550–2
- duty 548
- fail-safe 399, 400, 630
- independent braking systems 398, 400, 527
- mechanical 398, 400–1, 421, 527, 531, 548–555
- pads 548–554
- parking 400, 531, 548, 602, 629
- shaft 579, 580, 602, 629
- torque 528, 548, 550, 554
- two level braking 554
- yaw 556–7, 586
see also aerodynamic braking system
- braking loads 259, 400, 527, 531–2
- breaking waves 797, 813–8
- broad range variable speed 405–7, 547
- buckling
 blade 446, 447, 473, 486–7, 500–6, 508
- imperfections 505–6, 560
- tower 560–5, 568, 569
- mode shape 500–1, 505–6
- cable circuit resonance 919
- cables 423, 637, 843, 886, 916–20
- calipers 548, 550, 553–5, 557
- cambered aerofoils 149–151
- Campbell diagram 287, 289
- capacitor power factor correction 539
- capacity (wind power)
 onshore 3
 offshore 773
- capacity factor 750, 904

- capital cost of offshore wind farm 369, 383–4, 434, 774, 823, 866, 904
- Carbon Fibre Reinforced Plastic (CFRP) 468–471
 benefit *vs* cost 470
 fatigue properties 469
 pultrusion 469
 static properties 468–9
- carrier to interference ratio (C/I) 701
- cathodic protection 843–4, 878
- centrifugal
 force 259, 280–3, 313, 326, 388, 390, 399
 loads 259, 281–3, 292–3, 388, 394, 396, 461
 relief 259
 stiffening 281–2, 285, 287, 326
 stresses 400, 548–9, 553
- certification 227, 327–8, 781
- Charnock's constant 783
- chord distribution, optimised 73, 375, 379
- circle diagram of induction generator 539
- circulation
 aerofoil 141–3
 atmospheric 13, 16
 blade geometry and number 70, 77–82, 84–5
 rotor blade theory 59, 63
 steady yaw 154, 160, 164, 170–180
 unsteady and quasi-steady flow 194–200
 vortex cylinder model 49–54
- classical control 623, 628
- climate models 777
- closed loop
 algorithm 589, 601
 control 580, 581, 583, 585–7, 589, 600, 615, 657
 design 617
 dynamics 618
 poles 619, 621
 step response 621
 system 618, 619, 621
 transfer function 619
- cluster efficiency *see* array efficiency
- coefficient of performance 377–8, 380, 382–3, 426, 435 *see also* power coefficient
- coherence functions 18, 27–9, 233, 271, 273
- combined periodic and random components 275
- complex terrain 27, 29, 37, 670, 680
- compliance 414, 425–6, 594, 824
- component cost 362–3, 367–8, 371–2, 383–5, 433
- composites *see* Glass Fibre Reinforced Plastic (GFRP) and Carbon Fibre Reinforced Plastic (CFRP)
- Computational Fluid Dynamics (CFD) 207–222, 327, 639
- condition monitoring 826–8
- coning 259, 426, 444, 495
- Constant Life Diagram (CLD) 460–7, 469
- constant speed 375, 378, 382, 391–2, 425, 583, 589, 594
 operation 77, 102–3, 401, 406, 537–9
- constrained
 gust 239
 stochastic simulation 238–240
 wave 793, 818–822
- contact stress 539–531, 535
- controller
 closed-loop 581, 587, 589, 657
 gain 583, 617–620, 622
 objective 587, 626, 629
- control of
 drive train torsional vibration 413, 598
 tower vibration 587, 595, 611, 615, 853
 variable-slip turbines 403, 540, 601
- control, supervisory 580–2, 586, 612, 628, 652
- control system 228, 231, 325, 327, 372, 399, 425, 433, 478–480, 525–6, 581, 582, 586, 787, 853, 890
 fault 235, 393
 implementation 631
 yaw 586
- Coriolis
 effect 18, 20
 force 13, 16, 20
 parameter 18
- corrosion protection
 monopile 842–4
 turbine 826
- cost function
 in controller 626–9
- cost model
 Riso 362–3
 NREL 365–8, 370–2, 432–4, 823–4
 INNWIND 367, 378, 823–4
- cost modelling
 offshore turbines 822–4
 onshore turbines 362–7, 370
 of wind farms 666, 774
- cost of energy 362–373, 377–8, 517, 823–4, 904
 2 *vs* 3 blades 381–6
- coupling coefficient 514–6
- C_p tracking 592, 615
- C_p – λ performance curve 64, 95, 98–100, 101, 103, 108, 110, 382
- C_Q – λ performance curve 77, 102–3
- Craig-Bampton reduction 327, 870
- critical buckling stress 501–6, 560
- critical load case for tower base 315

- cross-correlation function
 blade loads 262–7, 269–270, 296, 312, 350,
 354–5
 rotor thrust 319
 teeter response 296
 turbulence 23, 28
 cross-over frequency 621
 cross-spectrum 28, 269–271, 290, 295, 320, 350
 normalised 350
 $C_T\lambda$ performance curve 101
 cumulative distribution function 32, 331
 currents 788, 794, 806, 809, 839, 840, 884, 899
 curtailment 659–661
 cut-in wind speed 104, 111, 199, 234
 cut-out wind speed 26, 111–2, 199, 234–5, 237,
 270, 302, 478, 481, 548, 622
 cycle counting, fatigue 308
 cyclic pitch control 602, 607
- Damage Equivalent Load (DEL)** 306, 324, 388,
 428, 492–4, 517, 795, 841, 857–9
 for narrow band spectrum 428, 857
damage tolerant method 564
damping 241–2, 277–8, 299, 317, 346, 425, 490.
 536, 585, 595–9, 604, 610, 611, 619, 620, 622,
 623, 629, 632, 870, 889, 895
 aerodynamic 241–2, 283, 287, 292, 301, 322,
 496, 584, 595, 597, 797, 822, 852–3, 859, 860
 coefficients 496–9
 induction generator 412–3, 537–9
 negative 302
 non-operational turbine 854
 ratio 241, 283–5, 294–6, 301, 322, 427, 558,
 620, 848, 851, 854
 soil 854
 structural 241–2, 246, 284–5, 323, 496, 853
 tuned mass 500
- Danish wind turbine concept 2, 401, 413
Dean's stream function theory 797, 800–804, 810
deep water sites *see* sites, deep water
deep water waves *see* waves, deep water
degrees of freedom 300–1, 326, 652, 870, 884,
 888–9, 892, 903
delay, operator 631
Delft aerofoils 120–1
delta control 612, 659–660, 747–8
Delta 3 angle 293, 390
Delta 3 coupling 292–4, 390
delta winding 720
design fatigue factor (DFF) 881–3
design loads 227–240, 781–797
design tip speed ratio 68, 74–5, 87–8, 90, 110
design wave
 extreme 788–9, 793
 severe 788
deterministic
 gust 34, 35, 233, 274
 load cases 233, 480
 loads 248–9, 274, 300, 313–5, 509, 555
 aerodynamic 248–258
 blade fatigue stresses 303, 305, 486, 489–491,
 494
 inertia loading 259
 rotor loads 310, 318
 teeter response 294, 387–9
Det Norske Veritas (DNV) Standards
 offshore wind turbines 781–2, 887
DFT *see* discrete Fourier transform
diameter, optimum machine 361–9, 822–4
diffraction 811–3, 851–2
 analysis 805, 811–3, 889
diffuser 435
digital controller 631
direct current
 HVdc (high voltage direct current) 914, 920–1
 multi-modular converter (MMC) 921
 power collection 419
direct-drive generators 406–410, 424
directivity 693, 694, 702
Dirlik 305–7, 323–4
disc loading distribution 182, 184–5
discrete
 controller 631
 gust 233
 state-space form 627
 time 631
 transfer function 632
discrete Fourier transform (DFT) 266, 273
discretisation 218, 631, 632
distortion energy method 524
distributed generation 718–720
diurnal variations 12, 16, 36
**DNVGL (Det Norske Veritas Germanischer
 Lloyd)** 301, 327, 570
 DNVGL-ST-0376 227, 459, 464, 466, 473–5,
 485–6, 508–9
 DNVGL-ST-0437 227
doubly-fed induction generator (DFIG) 406–7,
 543–6
downwind configuration 376, 388, 426–7
downwind turbines 254, 257, 376–7, 388, 426–7,
 875, 888
downslope winds 13
downtime per failure 825
drag coefficient 59–63, 123–4, 134–5, 140, 145–9,
 172, 240–1, 249, 252, 274, 391, 478–9, 805–7,
 809

- drag factor 315–6
 drive train 361, 370, 375–7, 419–424, 533, 553, 825, 827
 compliance 414, 425, 824
 damping 412–3, 425, 599, 603, 604, 632
 dynamics 301, 325, 425, 527, 617
 frequency 425, 604, 621
 model 425, 527
 resonance 425, 525, 599, 622, 632
 torsional flexibility 413, 426, 581
 torsional vibration 527, 593, 598, 602, 610
 DS472 22, 227, 240, 241, 284
 DTU 10 MW reference turbine design 453, 454, 478, 500–1, 517, 518
 dynamic analysis
 codes 324–331, 890–1
 finite-element method 301–2, 326, 891
 step-by-step 284–7, 292, 294, 297, 300, 302, 307
 dynamic factor 243–4, 246–7, 316, 318
 dynamic magnification 247–8, 287, 290–1, 295–6, 322, 425, 429, 525, 558–9, 848–9, 851
 dynamic response 241–8, 277–302, 325, 855, 870–1, 886
 aerodynamic and structural damping 283–4
 aeroelastic instability 302
 centrifugal stiffening 281–3
 extreme loads 241–8, 316–8
 frequency domain 289–291, 319–322
 modal analysis 277–280, 297–301, 326, 345
 mode shape 280–1, 298
 operational loads 286–9, 322–3
 simulated loads 292
 stochastic loads 289–291, 295–7
 teeter 292–7, 607, 608, 628
 tower coupling 297–302
 dynamic stall 201–7, 324, 499, 891

 earthing 734
 ecological assessment 706–711, 909–912
 economies of scale 361, 775
 eddy viscosity 212, 642–4, 647, 652
 edgewise bending 258, 259, 281, 369, 388, 446, 508–9
 edgewise blade mode 279, 301
 edgewise blade resonance 302, 496–500
 efficiency 444, 533, 536, 537, 583–5, 589, 590
 E-glass 447, 451–2, 460
 electric actuator 629, 630
 electric distribution networks 719–721
 electrical protection 723–5
 electrical systems 717–770
 electromagnetic interference (EMI) 698–703

 ellipsoidal co-ordinates 180–1, 192
 embedded extreme regular wave 788, 793
 emergency shut-down 237, 527, 531, 548, 554
 emergency stop 388, 435, 581, 583
 EMI *see* electromagnetic interference
 empirical aerofoil data 94, 250, 381, 478
 empirical thrust coefficient 67
 endurance limit 528–531, 533
 energy
 capture 77, 100, 109, 111–4, 361, 369, 391, 430, 435, 441, 518, 583, 585, 587, 589, 593, 611, 614, 654, 655, 659, 669
 gain 391, 592
 kinetic 398, 549, 594, 650, 660
 loss 284, 377, 500, 637, 655
 yield 249, 364, 370, 371, 375, 377, 379, 381–7, 441, 517, 625, 669
 engineering wake models 640, 641, 651, 652, 777–781
 environmental contours 790–2
 Environmental Statement (Impact Assessment) 674–5, 678–687, 909–911
 see also assessment of environmental impacts
 epicyclic arrangement 532–5, 537
 epoxy 445, 447–9, 451–2, 457–460, 462, 469–472, 506, 510
 equilibrium wake 274, 295
 equivalent circuit 538–9
 equivalent load 484 *see also* damage equivalent load
 Eurocode 1 (EN 1991–1–4) 23, 24, 26, 27, 237, 240, 244, 316, 348, 351, 853
 Eurocode 3 (EN 1993–1–3 & EN 1993–1–9) 560, 563, 878–9, 881
 exceedance level, L_{A90} 690
 extreme gust 34, 231, 237, 244, 316
 extreme loads 35, 237–8, 274–7, 486
 blade design 241–8, 275–7
 closed loop control 611, 616, 625, 628
 dynamic response 241–8, 316–8
 extrapolation 331–342
 offshore 822, 840–1, 886
 operational loading 233–7
 tower 315–8, 565, 569
 Extreme Turbulence Model (ETM) 232, 234, 495, 786
 extreme values 274–5, 277, 331–342
 distributions 32, 33, 332–9
 generalised extreme value 335–7
 Gumbel 32, 33, 332–3, 336–9
 log-normal 333, 337–9
 three-parameter Weibull 335, 337–9
 local extremes method 331, 340–1

- extreme wind 13, 16, 31–3, 228, 237–8, 302, 332, 561, 570, 581, 630, 794, 822
 conditions 19, 34, 229, 237
- fail-safe component 230
- fail-safe pitching 582
- failure rate 825
- fairlead 898–901
- fall-arrest 435
- fast frequency response 659, 661, 747
- fatigue
- analysis
 - in frequency domain 303, 305–7, 822, 829, 845–857
 - corrosion influence 878–9
 - criticality 484–5, 494, 565
 - cycle counting 308
 - damage 607, 629
 - detail influence 563–4, 566, 568, 878
 - design
 - of blades (*see* blade fatigue design)
 - of gear teeth 528–531
 - of shafts 532
 - tower 563–7
 - evaluation
 - by distortion energy method 524
 - life extension 882
 - by maximum shear method 523
 - loading 229, 231, 240, 258, 302–8, 324, 388–9, 459–460, 463, 464, 466–8, 482, 484–5, 489, 507, 509, 574, 584, 602, 608, 609, 625, 637, 652–6, 660
 - combination of deterministic and stochastic components 305, 490–1, 822, 858
 - offshore 795–7, 820, 822, 840–2, 845 *et seq.*, 870–1
 - in-plane 303, 486, 489
 - reduction 583, 607–9, 611, 615, 616, 628
 - spectrum 229, 240, 303, 309, 324, 464, 858–860
 - wind and wave combination 858–860
 - from wind simulation 307–8
 - partial safety factor, material 458, 464, 473–5, 484–5, 495, 564, 877, 881
 - properties
 - of composites 457–469
 - of wood laminates 472
 - spectra combination 323–324, 858–860
 - strength 447–9, 469, 470, 472, 563–4, 878–881
 - Stress Concentration Factor (SCF) 568, 880
 - stresses 302–4, 432, 466, 486, 492–3, 566
 - ranges 307, 324, 376, 428, 491–3
 - system effect 881–2
 - thickness effect 879
 - fault 229, 231, 233, 580–3, 610, 616, 660
 - conditions 230, 794–7
 - current 412, 737
 - level 737–8
 - load cases 235–6, 238, 787, 792, 794–7
 - FC40 blade
 - fatigue design
 - deterministic loads 489
 - stochastic loads 490
 - spar cap thickness profile 491–2
 - geometry 486, 488
 - scaling to 160 m diameter 495
 - structure 489
 - tip 495
 - feather/feathering 106–7, 241, 315, 391–4, 397, 399, 427, 512, 517, 581, 582, 584, 602, 611, 623, 630, 631
 - feed-in tariffs 5
 - fibre volume fraction 447–9, 451, 453–4, 456–463, 469–471, 476, 487, 514
 - fictitious grid 763
 - field testing 658
 - filament winding 477
 - fine pitch 392, 588, 594, 597, 622, 632, 660
 - changing or varying 589, 597
 - Finite Difference Method (FDM) 218
 - finite-element analysis 301, 515, 523, 536, 550, 555, 831, 854, 891
 - Finite Element Method (FEM) 219, 302, 326, 551
 - Finite Volume Method (FVM) 218
 - fixed pitch 99, 103, 106, 584
 - fixed speed induction generator 400–1, 537–9
 - flaps/slats 123–5, 584, 603
 - flapwise bending 279, 281, 302, 441, 444, 446, 461, 466, 478–81, 484, 511
 - flexural rigidity 503, 518
 - flicker 760–1
 - shadow 685–7
 - Floatgen ring shaped platform 906–8
 - floating wind turbine support structures, moorings 883–908
 - critical load cases 887, 890
 - degrees of freedom 884, 888, 889, 892, 903
 - design space 887, 888, 892, 893
 - dynamic analysis codes 890–2
 - equations of motion 889–890
 - moorings 885, 887, 898–901
 - categories 898
 - loads 892, 899, 901
 - nylon 898, 905, 907

- floating wind turbine support structures,
 moorings (*Continued*)
 steel chain 898, 903
 suction anchors 903
 system stiffness 890, 898, 899–901
 pitch control adaptation 597, 890
 pitch motion 888–890, 893–4, 895, 897–8,
 904
 platform types 884–6
 SLOW model 892
 target mean pitch angle 888
 flow medium 476
 flow separation 92, 137
 foam sandwich 446, 489
 forecasting 13, 35–7, 754–7
 forward-scattering 699
 foundation, onshore 637, 655
 monopile 572
 piled 572
 rotational stiffness 574
 slab 570–2
 Fourier transform 30, 262, 266, 269, 305
 Frandsen method 639
 free yaw 557, 585
 frequency converter 407, 541–2, 585, 591, 630
 frequency domain
 blade dynamic response 289, 295, 345 *et seq*
 blade fatigue stress 303, 305–7
 dynamic analysis codes 325
 dynamic response 319–323, 345 *et seq*
 limitations of analysis 270
 offshore 822, 829, 845 *et seq*, 857 *et seq*, 887,
 889
 operational loading 260 *et seq*, 274, 322
 frequency response 599, 621–3, 659, 661
 function 346
 Fresnel zone 703
 friction coefficient 549
 friction velocity 19, 20, 643
 frozen turbulence hypothesis 28, 263, 264
 frozen wake 261, 274, 294–5
 full power conversion 406, 411, 547
 full-span pitch control 394, 396, 584, 603
 fuzzy logic 625, 629
- gain margin 621
 gain schedule 622
 gamma function 14, 263, 335
 Gaussian wake 640, 642, 645, 648
 gear
 meshing 532–5
 ratio 524, 530, 590, 599
 optimum 533
- stage 524, 530, 532–4
 tooth bending stress 529–534
 tooth contact stress 528–531
 tooth tip relief 535
 volume 533–4
 gearboxes 524–537
 bearing and shaft design 531–2
 braking loads 527–8, 531–2
 cost (*see* cost modelling)
 efficiency 533–7
 epicyclic 532–4
 flexible planet mounting 534
 gear arrangements 532
 gear ratios 524, 530, 533
 integrated 536
 load spectrum 527, 529, 532
 lubrication and cooling 536
 noise 534–6, 692
 torque 525, 527–8
 variable loading 525–6
 gearbox magnetic 416–7
 gel-coat 445, 473
 generalised extreme value distribution (GEV)
 335–7
 generalised load 278, 290, 346, 350
 generalised mass 242, 278, 298, 301, 317, 346,
 848
 generation 750–4
 adequacy 751–2
 de-rating factors 753
 merit order 754
 generator
 brushless doubly fed induction 418
 contactors 579, 580
 direct-drive 406–410, 424
 directly connected 411
 doubly-fed induction 544–5
 evolution of types 411–2
 fixed speed 400–1, 537–9
 full power conversion 406, 408, 547
 induction 401, 538, 585, 589, 591, 592, 598, 601
 low speed direct drive 406–410, 424
 medium speed 410
 mounting 420, 424
 superconducting 415
 supervisory control 580
 synchronous 414, 661
 system architectures 407–8, 411
 torque 544, 581, 585, 591, 592, 598–600, 603
 torque control 405, 581, 585, 587, 590, 597
 types of 410–411
 two-speed 402
 variable-slip 403, 540, 601

- variable-speed 403, 541–7, 590
wound rotor induction 540–1
- geographical variation 13
geostrophic drag law 20, 36, 639
geostrophic wind 18, 20
GFRP *see* Glass Fibre Reinforced Plastic
GEV *see* generalised extreme value distribution
GL (Germanischer Lloyd) rules 19, 21, 22, 227, 237
offshore 781
glass/epoxy composites 445, 447–9, 451–2, 457–460, 462, 469–471, 487
Glass Fibre Reinforced Plastic (GFRP) 447, 451–9, 470–1
fatigue properties 457–468
load sequence effects 464–8
Montana State University database 453
OPTIMAT project 462–3
strength degradation models 466–8
fibre properties 451–4
fibre volume fraction 447–9, 451, 453–4, 456–463, 469–471, 476, 487, 514
matrix properties 452
static properties 451–7
glass fibre strength dispersion 451, 453–4
glass/polyester composites 447–8, 451, 457, 462
Glauert's momentum theory 156–160
Goodman diagram 463, 475, 494
Goodman relation 523, 533
Graetz Bridge 541
gravity bases 829, 860–6
float-out 865–6
gravity loading 258, 312, 328, 486, 494–5, 570
grid ancillary services 652, 654, 655
Grid Codes 742–750
continuous operation 744–5
fault ride through 749
frequency response 747
voltage and power factor 745
grid loss 235, 238, 315, 326, 388, 394, 398, 548, 553, 741–2, 792
grid/mesh (computational) 219
grounding 732
grouted joint(s) *see* monopiles
Gumbel distribution 32, 33, 332 *et seq*
Gurney flaps 123–4
gust 391, 398, 556, 585, 614, 624, 786
constrained 238–240
deterministic 34, 35, 233, 274
discrete 233
extreme 34, 231, 233–7, 244, 316, 616
factor 17, 31
loading 233–7, 517, 616
slicing 262, 277, 289, 292, 305, 320, 397, 484, 527, 821
effect 231, 490
speed 30, 228, 243, 315
gyroscopic loads 259, 586
- harmonics 609, 763–4
harmonic series method 272–3
harmonic voltages 543
 H_∞ controller 625, 628
heave 884
heave plates *see* semi-submersible
helical gears 535
helical vortex 50–1, 78, 81
helicoidal vortex sheet 78, 81
hexagonal turbine array 430
H-glass 451–2
high-speed shaft 400, 421–3, 436, 527, 549, 552–5, 590, 598
historical development 3
hollow shaft 390, 392, 394, 399, 421
hub
fatigue damage 523
finite element analysis 523
stress distribution 523
hub ‘dishing’ moment 310–2
due to stochastic loading 312
hub loading 309–312, 512–4, 655
HVDC 714, 920–1
hydraulic actuator 394, 395, 399, 509, 579, 629, 630
hydraulic cylinder 392, 393, 399, 550, 554
hydrological study 673, 675, 707
hydrostatic restoring stiffness 895, 897
hyperplastic accelerated ratcheting model 839
Hywind Scotland spar buoys 883, 901–4
monitoring 903
- IEC *see* International Electro-technical Commission
impact on birds 707–710, 909–912
impact on the generation system 750–4
imperfections, tower wall 560
individual pitch control 586, 587, 602–612, 615, 616, 628–630, 653–5
induced velocity, axial 48, 51, 54, 75, 154, 159, 172, 183, 252, 261, 274
tangential 45–9, 176, 274
induction factor *see* axial flow; tangential flow
induction generators 401–2, 537–540, 585, 589, 592, 598, 601
inertia loads 259–260, 280–2, 810, 890
inertia (synthetic) 661, 750

- infinite life torque 529–532
 inflow angle or flow angle 60, 65, 72, 76
 ingress of moisture 471
 in-plane fatigue loads 486
 integral length scale
 blade dynamic response 291, 297
 operational loading 261–9
 stationary blade loading 242, 246, 355
 tower loading 320
 turbulence 22, 23
 integrated gearbox 420
 integrator desaturation 588, 632
 integrator wind-up 588, 632, 633
 interface protection 738–740
 International Electro-technical Commission (IEC)
 IEC 61400–1 19, 21–27, 29, 34, 227–234,
 236–8, 244, 254, 266, 271, 274, 315, 316,
 331–2, 341–2, 342, 398, 429, 480–1, 495, 548,
 561, 616, 637, 639, 781–5, 792, 795, 797, 881
 IEC 61400–3 781–4, 886, 887
 IEC 61400–3–1 782, 784–790, 792–5, 818
 IEC 61400–3–2 782, 887
 inverse first order reliability method (IFORM)
 790
 islanding 741–2
 isotropic turbulence 21, 24, 25, 28, 30, 37, 262–7,
 276
 jacket structures 829, 866–75, 880
 installation 871, 873
 pile installation frames 871
 piling 871
 simplified models for dynamic analysis 870–1
 suction buckets 872
 three legged 870
 vibration modes 870
 weights 823, 873–5, 877
 jack-up barge 873, 884
 Jensen model 641, 642, 647, 652
 jet flaps 124–5
 JONSWAP spectrum 785, 819, 855
 J-tube 843, 878
 Kaimal spectrum 22–7, 29, 233, 246, 271
 Kalman filter 595, 613, 625–8, 755
 Keulegan-Carpenter number 806–9, 846, 897
Khaya ivorensis 449, 471–2
 Kinner's pressure distribution theory 181–5
 $K_p-\lambda$ performance curve 102–3, 109
 Kutta condition 143
 Kutta-Joukowski theorem 39, 53, 56, 80, 145
 laminate
 DD16 multidirectional 460–2
 MD2 triaxial 462–3
 P2B hybrid 469
 PPG-Devold 448, 470, 487
 QQ1 triaxial 462–3
 specially orthotropic 503
 triaxial 455–6
 Lanchester-Betz limit 43, 89, 380
 land and sea breezes 13, 16
 landscape assessment 679
 Laplace
 equation 180–1, 190, 797, 812
 operator 588, 631, 632
 transforms 618
 variable 618, 619
 Large Eddy Simulation (LES) method 213,
 221–2, 640
 large eddy simulations 640
 lattice steel towers 436, 569–570, 875
 Legendre polynomial 181–2, 190, 199
 leading edge erosion 509–511
 energy loss 510
 rain drop impact 510
 leading edge protection 511
 Leishman-Beddoes model 201–7
 length scales 18, 22–5, 27–9, 37, 235–7, 276, 312,
 592, 643, 647
 integral 22–4, 239, 242, 246, 261–9, 273, 291,
 297, 320, 355
 levelised cost of energy (LCOE) 654, 775, 823,
 887, 904, 931
 LiDAR 613–7, 649, 657, 776
 LiDAR-assisted control 613–7
 life factor, gears 528–9
 lift coefficient 59–62, 69–73, 92–4, 114–5, 145–7,
 202, 240–1, 250, 261, 277, 302, 375, 378, 380,
 381, 391, 442, 584
 lift curve slope 283, 396, 584
 lift/drag ratio 69–70, 75, 90, 148, 377, 380–1
 lifting line theory 156
 lightning 725–730
 connection of wind farms 734
 damage frequency 728
 protection 730, 733–4
 Lillgrund offshore wind farm 778
 limit-state design 229, 473
 linear acceleration method 285–7
 linearised model 617, 622, 631
 linearity assumption for aerodynamic loading
 261, 274–6, 304
 linear wave theory 797–800, 818, 822
 line-drop compensation (LDC) 720

- load cases 229–238, 274, 315, 327, 331, 480, 486, 495
 offshore (IEC) 781–797, 822, 859, 887, 890
 fatigue 795–7
 stochastic 782
 ultimate non-operational 792–5
 ultimate operational 785–790, 886
 load-duration curves 525–6, 530, 532
 load path 388, 420, 521–3, 555, 566, 842, 845, 863, 869
 load sensor 579, 603, 606
 load sequence effects 464–7
 local extremes method 331, 340–1
 local speed ratio 375
 locking devices 436
 Loewy wake-spacing function 200
 logarithmic decrement of damping 241–2, 246, 284–5, 317, 349, 852, 854
 log-normal distribution 333, 337–8, 792
 longitudinal stiffness modulus 452
 low-speed shaft 292, 371, 388, 419–424, 426, 583, 591, 599, 886
 deterministic loading 310–1, 388
 gravity loading 229, 309, 312
 mounting arrangements 419–424, 426
 stochastic loading 311–2, 388
 torque 363, 528, 533
 LQG controller 625–8
 machine learning 657
 machine rating 370–5, 823
 machine size
 gravity limitation 369
 optimisation 362–9, 822–4
 marine growth 806, 881
 marine mammals 909–911
 Masing rules 837
 mass flow rate 40–1, 46, 154, 156–8
 mass imbalance – rotor 429
 massless/synthetic jets 122
 material safety factors 458, 464, 473–5, 484–7, 495, 508, 561–2, 564, 877, 881
 maximum shear method 523
 matrix 451–5, 459–461, 471, 510
 McCamy and Fuchs diffraction theory 812, 852
 mean strain 463–4
 mean stress 454, 457, 460–1, 463–5, 482, 484–5, 494, 523–4
 measure-correlate-predict (MCP) 671
 mechanical
 brake 400, 527–8, 548–555
 damping 500
 noise 534–6, 692
 meteorological forecast 36, 37
 microbuckling 454
 micrositing 672
 Miner's rule 303, 464–5, 529, 531
 modal analysis 277–280, 297–301, 326, 345
 modal damping coefficient 498–9
 model based control 625, 628
 mode shape
 blade dynamic response 242, 244–5, 278, 280–7, 298, 327, 346
 offshore 840, 847–9
 purification 280
 stationary blade loading 242, 244–5, 346
 tower loading 297–8, 317, 327
 moisture
 ingress 471
 wood 471
 momentum theory
 acceleration potential 180, 188, 190–2
 horizontal axis wind turbines 42, 44–53, 59, 61–7, 77, 80–1, 90–2
 quasi-steady flow 194
 steady yaw 154–160, 170–180
 monopile foundations (onshore) 572
 monopiles (offshore) 829 *et seq*
 cable ducts 843
 corrosion protection 842–4
 cyclic loading 837–9
 in deeper water 843–5
 design 830–845
 diameters 829
 embedment 831, 837, 854
 fatigue analysis 845 *et seq*
 fatigue damage 846, 857–860
 fatigue details 878
 fatigue loading 846 *et seq*
 3D FE analysis 832–3
 grouted joints 843–5
 1D model 833–6
 model testing under cyclic loading 838–9
 natural frequency 831, 839, 840–2, 847, 851, 855, 874
 permanent rotation 831, 837
 S-N curves 877–882
 surface irregularities 645
 transition piece 829–830, 842–3
 verticality 829, 842
 weights 829, 843, 845–6
 moorings *see* floating structures
 Morison's equation 805, 811, 847, 889–892
 drag coefficient 805–7, 809
 linearisation 820, 846
 drag term
 inertia coefficient 806–809

- mudline moment 829, 847–9, 851–2, 857
 spectra 855–6
- multi-body dynamics 327
- multiple rotor structures 430–5
 cost comparison 433–4
 space frame 430–1
 tubular 432
- multivariable control 603
- nacelle bedplate 420–2, 424, 426, 555
- nacelle loading 312–5
- narrow range variable speed 403, 407, 542, 544
- natural frequency
 blade 241–4, 279, 281–5, 287, 289, 346, 447, 496
 drive train 425
 generator 413
 monopile 831, 839, 840–2, 847, 851, 855, 874
 support structure 788, 795
 teeter 292, 294
 tower 317, 322–3, 427, 430, 558–560, 565, 574
- Navier Stokes 207–8, 211–2, 215, 218, 639–641, 652
- near wake region 638, 642, 646, 647
- negative damping 302, 391, 496–9
- negative pitch control 397–8
- network loss 770
- neural networks 36, 307, 625
- neutral stratification 643, 644
- Newmark 285, 286
- noise 534–6, 687–698
 aerodynamic 126–9, 378, 392, 592
 gearboxes 534–6, 692
 infrasound 697
 limits 696–8
 low frequency 696
 measurement of wind turbine 693
 mechanical 534–6, 692
 propagation 696
 signal 588, 612, 625
 terminology and basic concepts 688
 of wind-farm 659, 660, 695
- non-dimensional time 197, 203, 205
- non-linear gains 623, 624
- non-linearities 259, 276, 307, 325–7, 509, 535, 628, 629, 784, 797, 805, 810, 813, 818, 820–2, 831, 846, 858, 889
- non-operational load cases
 offshore 792–5
 onshore 237–8, 315
- normal induced velocity 159, 160, 169
- normalised co-spectrum 246, 317, 350–1
- normalised cross spectrum 350
- normal load cases 230
- normal shut-down 400, 527–8, 531, 554
- Normal Turbulence Model (NTM) 232, 234–5, 480–1, 786–7, 795–6
- Normal Wind Profile Model (NWP) 233–4, 236, 786–7, 795–6
- notch filter 593, 596, 599, 604, 606, 622, 623, 628
- NREL aerofoils 115–6
- NREL 5 MW reference turbine design 365, 430–2, 510, 886
- NREL cost model
 for turbines offshore 376, 823–4
 for turbines on land 365–372, 382, 432–4
- number of blades 379–388, 605, 646
 cost of energy comparisons 381–6
 effect on coefficient of performance 380–1
- Numerical Weather Prediction (NWP) 755, 757
- observers 625
- Obukhov length 643
- off-axis fibres 447, 511–8
- offshore
 blockage 781
 cables 916–20
 costs 774, 824
 environmental impact assessment 908–913
 transmission 913–6
 wakes and array losses 777–781
 wind conditions 19, 776, 782–3
 wind farms 771–3
 wind resource assessment 776
 wind turbines 592, 597, 604, 625
- oil sampling 826, 828
- on-load tap changer 720
- open-loop 614, 618, 619, 621, 623, 656
- operational load cases
 offshore 784–788, 795–6
 onshore 233–7
- optical fibre 610
- optimal
 blade design 65, 72–7
 blade geometry 68–77, 375, 379–380, 441, 442–3, 517
 blade structure 441, 444
- coefficient of performance 98–100
 effect of L/D ratio 380–1
 effect of No of blades 380–1
- chord distribution 73, 375
- feedback 625, 626
 state 595, 626, 627
- gear ratio 533
- machine rating 370–2
- machine size 361–9
 offshore 822–4

- rated wind speed 373
 rotational speed 376–7, 380, 385
 set-points 652, 654, 656–7
 tip speed ratio 382–5, 590, 592, 600, 615
Ormonde offshore wind farm 867, 871, 872
 orthogonality condition 278, 280, 283
 orthogonal mode shapes 278, 280, 282, 297
 out-of-plane
 bending moment 250–7, 259–260, 287–8, 291,
 307, 310, 313–4, 328–330, 370–1, 376–8, 382,
 387–9, 478–9, 482–3, 556, 607
 load 229, 240, 249–250, 277, 281, 292, 309–311,
 592, 595, 607, 615
 overspeed 231, 235, 392, 399, 527, 531, 548,
 551–4, 582, 594, 595, 597, 607, 628
- pad rubbing speed 548, 553–4
PAN carbon fibres 468
 panel method 65, 147, 209–210, 327
 parallel shaft arrangement 532
 parking brake 400, 531, 548, 602, 609
 partial safety factor
 consequences of failure 230–1, 509, 564
 load 229–230, 234–8, 315, 485–6, 495,
 552
 material 458, 464, 473–5, 484–7, 495, 508,
 561–2, 564, 877, 881
 partial-span pitch control 394
 passive pitch control 396, 511
 passive stall control 391
 peak aerodynamic torque 553
 peak factor 239, 243, 247, 275, 276, 318, 356, 357,
 481, 491
 peak period 785, 888
 peak spectral period 788, 793
 periodic coefficients 300
 periodic loading 248, 274–7, 285–6, 289, 303–7,
 537, 821
 permitted noise levels 696
 persistence forecast 35, 36, 755
 per-unit system 767
 phase advance 623
 phase margin 621
 photomontage 685
 PI and PID control 588
 PI controller 588, 592–5, 600, 606–7, 611, 620,
 623–4, 627–8, 632–3, 661
 PID controller 588, 593, 596, 617, 622, 623, 631,
 632
Pierson-Moskowitz spectrum 784–5
 piled foundation 572–3
 pile testing
 Matlock & Reese 831
 PISA, dense marine sand 832
 PISA, stiff clay 832
 piles for jacket structures *see* jacket structures
PISA project
 3D FE analyses 831–4, 836
 non-dimensionalised load-displacement curves
 831, 833–6
 soil reaction components 833, 835, 836
 pitch
 actuators 392–5, 399, 579, 580, 584, 587, 596,
 602, 610, 617, 618, 620, 622, 629, 630
 angle 59, 65, 70, 75, 77, 103, 105–7, 172, 193,
 653, 660
 optimum 583, 589
 schedules 393, 397
 bearing 506, 519–521, 584, 610, 611, 630
 bearing life 520
 distortion 521
 carbon fibres 468
 error, effect on loads 428–9
 rate 397, 399
 limits 623, 624
 regulation 106, 315, 395
 response 622, 631
 pitch control
 active 391–6
 closed loop control 590
 collective 604, 607, 610, 615, 616
 cyclic 602, 607
 full-span 394, 396, 584, 603
 horizontal axis wind turbines 106–7, 113, 116
 independent 603
 individual 586, 587, 602–612, 615, 616,
 628–630, 653–5
 negative 397
 partial-span 394
 passive 397
 system 392–6, 615
 pitching to feather 106–7, 584, 602, 611, 630,
 631
 pitching to stall 106, 584
 pitch-teeter coupling 292, 390
 Pitt and Peters 187–9
 planet carrier 532, 534
 planet gears 532–5
 planning applications 674–6
 ply
 compressive strength 454
 drops 467, 508
 tensile strength 453–4
 poles 619–621, 623
 poplar 472
 potential flow solvers 887, 889–892

- power
 coefficient 43–4, 47–8, 53, 64, 80, 102, 107–110, 155, 159, 163, 584, 590, 660 (*see also*
 coefficient of performance)
 collection 730–2
 circuit redundancy 731
 offshore 914–5
 curve 371, 382, 391–3, 397, 510, 525–6, 599, 600, 613
 factor control 746
 factor correction capacitor 538–9
 flows (load flow) 757, 766–770
 fluctuations 391, 397, 525–7, 530, 761, 841
 losses 655, 770
 output 639, 655, 659, 661
 quality 593, 756–764
 spectra containing periodic components 306
 spectrum (*see* spectrum)
 swings 391–2, 591–2
 system studies 737–8
 transducer 589
 versus wind speed curve 102–5, 107–8, 111
 Prandtl tip-loss factor 82–5, 88, 91
 prediction
 electromagnetic interference 702–6
 noise 674, 695–6
 shadow flicker 687
 weather 755, 757
 wind speed 35
 pre-loaded flanges 566–7
 pre-loading 396, 506–7, 520–1, 566–7, 568
 pre-pregs 476
 pressure correction method 216–7
 pressure drag 63, 134, 138, 158, 201
 pressure drop 44, 48–50, 59, 62, 69, 163, 182
 pressure-fed lubrication 536
 pre-tensioning 568, 884
 pre-warping 632
 probability density function (PDF) 305–6, 333, 335, 790
 probability distribution 331–3, 336–340, 846, 857, 862
 of wind speeds 14, 31–3, 260, 668
 protection, interface 739
 prying 566
 public consultation 669
 Pulse Width Modulation (PWM) 542
 pultrusion 469
 quasi-static bending moments 242–3, 246–7, 316, 318, 358
 quasi-static control 656–7
 quasi-static response 246–7, 318, 348, 358
 quasi-steady aerodynamics 194–5
 radar 703–6
 aviation 704
 cross section 701–2
 radial velocity 57–8, 82, 91
 radiative damping 889
 rainflow method 308
 raptors 707–8
 rated power 106, 114, 234, 363, 370–5, 383–5, 391, 489, 517, 525, 589, 592–4, 600, 661
 rated wind speed 589, 595, 622, 629
 component design 479, 482, 483, 494, 517, 526, 548
 conceptual design 370–1, 373, 383–5, 391, 397
 control above 581, 583, 585, 587, 594, 597, 632, 660–1
 control below 583–4, 587, 590, 592, 594, 617, 660–1
 extreme loads 234, 275–6
 optimum 373
 rate of change of frequency 661, 741
 Rayleigh distribution 14, 305, 339, 490
 of waves 784, 788, 795
 reactive power 659, 744–6, 768–770
 real power 768–770
 reduced frequency 199–200, 747
 redundancy cable network 718, 731
 equipment 825
 reference wind speed 34, 228, 237
 reliability 587, 609, 630, 656, 824–8
 condition monitoring 826
 corrosion protection 826
 lubricant debris detection 828
 machine architecture 824
 redundancy 825
 vibration monitoring 827
 reservoir method 308
 resilient mountings 535
 resin
 thermoset 476
 thermoplastic 476, 511
 resonance 621, 623
 blade 241, 287, 289, 302, 441, 495–500
 cable circuit 919
 drive train 413, 425–6, 525, 598, 599, 622, 632
 monopile 841, 847–857
 tower 316–8, 322, 430, 558, 593
 resonant
 blade root bending moment 242, 247, 291, 352–4
 frequency 593, 598, 599, 604, 621, 632
 response 347 *et seq.*, 595, 596
 size reduction factor 241–2, 246, 317, 352
 tip displacement 241, 246

- return period 34, 228–9, 235–8, 331, 336–9, 792, 793
 reverse loading 457–9, 465, 472, 484–5
 Reynolds Averaged Navier-Stokes (RANS) equations 211, 640
 Reynolds number 72, 114, 118–120, 133–6, 138–140, 145–150, 213–4, 806
 Reynolds stress 29, 30, 211–2
 R-glass 451–2
 Richardson number 25
 Riso aerofoils 116–9
 rock anchors 571
 Rodsand offshore wind farm 863
 roll, floating support structure 884
 root
 bending moment 242–7, 251–7, 269–270, 274–6, 287–8, 291–7, 310–4, 328–9, 377, 610
 locus plot 598, 619–621, 623
 loss 85–6
 vortex 52, 54
 rotary transformer 630
 rotationally sampled
 cross spectrum 267–271, 290, 295, 320
 spectrum 262–9
 rotational sampling 325, 329, 606
 rotational speed 289, 363, 370, 375–380, 382–7
 effect on blade weight 376
 high speed rotors 376
 low induction rotors 377
 noise constraint 378, 386, 693
 rotor
 blade theory 59–64
 disc 39–67, 81–2, 85, 91–2, 154–192, 602
 hub 309, 388–390, 521–4
 locking 436
 low induction 377–8
 mass imbalance 429
 thrust 259, 313, 318–323, 383, 396, 429, 430–2, 644, 653, 660
 loading at blade passing frequency 320, 386, 427–8
 power spectrum 320
 torque
 fluctuations 320, 323
 standard deviation 320
 variable diameter 369
 whirl modes 500
 rotor average wind speed
 estimation of 612, 656
 roughness length 18, 19, 21, 24, 26, 27, 37, 244, 364–5, 782
R-ratio, *R*-value 457, 460–1, 463, 465–6, 469, 485
 Runge-Kutta method 192
 safety 435–7
 safety factors
 partial
 load 229–230, 234–8, 315, 485–6, 495, 552
 material 458, 464, 473–5, 484–7, 495, 508, 561–2, 564, 877, 881
 safety system 231, 326, 580–3, 611, 630
 sandwich panels 444, 446, 455, 467, 473, 476, 489, 500–1
 scarf joints 471–2
 scatter diagram 786, 788–9, 792, 795
 scatterometer 777
 scour 839–840
 protection 840, 861, 865, 911
 scuffing 536
 seasonal variations 12, 14
 sea state 782, 784, 786–9, 793–5, 797, 809, 820–2, 846, 888–890
 extreme 793–4
 normal 786–8
 severe 788–9
 section modulus 303, 369, 376, 486, 563, 840
 sector management 653, 656
 segmental blade construction 477
 self-excitation 539
 self-tuning controllers 625
 semi-submersible 884, 885, 889, 893–8, 904–6
 column diameter 895–7
 design space 893–8
 heave plates 895–8, 905
 natural period 895, 897
 sensors 579, 582, 583, 602, 603, 609, 610, 626, 629
 separation distance 670
 shadow flicker 660, 687
 shaft
 brake 398, 400–1, 421, 527, 531, 548–555, 579, 580, 602, 629
 gravity moment 312
 moments 309–312, 607
 tilt 254, 313–4, 426, 489, 602, 614
 shallow water
 costs 821, 845
 loads 845
 see also sites, shallow water; waves, shallow water
 shear webs 443–6, 473, 477, 487, 502, 513
 shell structure 444–7, 455, 473, 477, 486, 500, 514, 521, 560–1
 short-circuit or fault level 737
 shut-down 237, 240, 315, 400, 527–8, 531, 548, 554, 787, 796, 854
 signal noise 588
 significant wave height 784–5, 788, 790, 792–3

- simulations
 wave 782, 795, 818, 821–2, 846, 888
 wind 233, 238, 270–4, 307–8, 326–8, 331 *et seq.*,
 852, 858–860
- single-bladed turbines 2, 387–8
- sites
 deep water 845, 863, 866, 883
 selection 666
 shallow water 771, 821, 861
- size reduction factor, wind loading 241–2, 246,
 317–8, 352, 355
- skew angle 160–6, 184, 188, 648
- skin thickness, blade 365, 371, 376, 447, 489
- slab foundation 570–2
- SLEDGE 399
- sleeved joints, tower 565
- slip
 rings 403, 585, 630
 speed 537–8, 545, 585, 601, 624
 variable, generator 403, 540
- S-N* curve 457–463, 465–6, 469, 472, 482–5, 492,
 520, 523–4, 528–530, 563, 877–882
- sociological aspects 665, 669
- soft-start unit 539
- soft towers 430
- soil damping 854
- solidity 375–7, 379–381, 600
- sound power level, L_W 689
- sound pressure level, L_P 689
- spanwise variation of bending moment 247–8,
 251, 258
- spar buoy 884, 885, 889, 892–4, 899–904
 ballasting 892–3
 design space 892–4
 natural period 893–4, 903
- spar cap(s) 444, 446, 469–471, 487, 489–492, 495,
 500–1, 505, 511–8
 carbon fibre 469–471
 fibre inclination 512–518
- spatial variation 27, 28
- specially orthotropic laminate 503
- specific blade mass 365–6
- specific power 373–5
- spectral analysis 329
- spectral gap 12, 17
- spectrum
 of blade root bending moment 269–270, 291
 generalized load 290
 Kaimal 22, 23, 25, 26, 233, 246, 271
 rotationally sampled (*see* rotationally sampled
 spectrum)
 of rotor thrust 320–2, 329
 of teeter angle 295
- of tip deflection 290
- van der Hoven 12
- von Karman 19, 22–30, 233, 262, 271, 273
- speed exclusion zones 593
- speed-up factor 37, 670
- spheroidal graphite iron 506, 508, 521, 524
- splash lubrication 536, 838
- splash zone 843–4
- splice plates, tower 567
- spoilers 399
- spur gears 528, 533, 535
- square-cube law 361–2, 430
- stable stratification 18, 643–4
- stall 39, 63, 73, 92–6, 101–7, 109, 113–6, 120, 122,
 145–9, 201–7
- control 584, 585
 active 397, 584, 622
 passive 391
- delay 92–6, 216, 250
- regulation 103–9, 114–6, 584, 599, 600
- stall-regulated machines 249, 251–7, 270, 315–7,
 319, 363, 373, 391–2, 399, 444, 478–9, 482,
 496, 530–1
- star connection 720
- start-up 236, 240, 580, 581, 586, 612
- state estimator 505, 625, 626
- stationary blade loading 240–8
- Statistical Energy Analysis (SEA) 535
- statistical prediction 35
- step response 621
- step-by-step dynamic analysis 284–7, 292, 294,
 297, 300, 302, 307
- step-by-step solution 302
- stick-slip friction 326
- stiff towers 430
- stochastic
 blade fatigue stresses 303–4
 combination with deterministic 305–6, 490
- loads 233, 238, 248–9, 260–270, 274–7, 295–6,
 307, 311–2, 387, 388, 490–3, 556
- rotor thrust fluctuations 319–320, 427
- sea states 784, 786, 793, 820
 tower bending moments 322
- Stodola method 280, 282
- Stokes wave theory 797, 800
- strain gauges 508, 609, 615, 832, 903
- strain-life regression lines 438
- strategic environmental assessments SEA 908
- stream function wave theory 797, 800–4, 810, 820
- stream-tube 40–4, 50, 57, 63, 67, 174, 650
- strength degradation models 466–7
- strength-to-stiffness ratio 486–7
- strength-to-weight ratio 447–8

- Stress Concentration Factor (SCF) *see* fatigue structural damping 242, 246, 283–5, 598, 853–4 loads 587, 637 properties 447–8, 451 suction buckets *see* jacket structures sun gear 532 superelement 870–1 supervisory control 580–2, 586, 612, 628, 652 support mechanisms 2, 4, 5, 667 support structure offshore, fixed 823, 828–908 analysis 820–2, 845–860, 870–1 cf oil & gas platforms 781, 820–1, 846, 866, 881 natural frequency 788, 795, 831, 839, 840–2, 847, 851, 855, 874, 892 wave loads 805–818 offshore, floating (*see* floating wind turbine support structures) space frame 430 surface roughness 18–20, 24, 27, 36, 37, 364–5, 639 cylinder 805–7 sea 776, 782 surge, floating support structure 884, 889 surge, storm 793, 843 sway, floating support structure 884 swept area 373–5, 430, 433, 589, 592, 605, 613, 614 switch-fuse 739 synchronous generators 414, 661 synchronous speed 537, 544–5 synoptic variations 16 synthetic inertia 661, 750
- tangential flow induction factor 45, 54–6, 74, 80, 82, 97, 175 tangential induced velocity 47–8, 57 Taylor's hypothesis 28, 263 teeter angle extreme value 296 power spectrum 295 end stops 302, 388, 390, 608 excursions 292, 295, 388–390 hinge 292–4, 385, 388–390 loads 292–4, 608 load relief benefits 388–9 motion 292–4 natural frequency 292, 294 response to deterministic loads 294 to stochastic loads 295 stability 302, 391 teetered hub 390, 607, 608 tension leg platform 884, 886 Theodorsen's function 198–200, 206 Thornton Bank offshore wind farm 863–5 three-bladed machine, comparison with two-bladed 381–7 thrust (or axial force) coefficient 44, 56, 66–8, 97, 154, 158, 183, 187, 192, 638–649, 660 empirical 67–8 thyristor soft-start unit 539 tilting moment coefficient 186 time domain 270, 274, 322, 325–6, 822, 852, 858, 860 methods 325, 640, 651 time histories/(& time series) 239, 271, 273–4, 303, 305, 307–9, 331, 378, 483–4, 785–6, 818–821 time-step 216–8, 283–7, 300, 326 fixed 326 variable 326 tip blade 399, 584 clearance 238, 444, 486, 495, 517, 569 deflection 238, 279–280, 290–1, 301, 331, 347, 377, 447, 471, 486 deflection power loss 377 loss 77–91, 173, 249, 380–1 relief (gear teeth) 535 speed 315, 363, 370, 376–7, 378, 382–5, 387, 509–511 speed constraints 376, 378, 387, 693 speed ratio 47, 62–6, 69–90, 95–103, 107, 109, 249, 375, 380–1, 382–5, 583, 589, 590–2, 600, 612, 615, 646, 660 vortex 78, 160 tip-loss factor 71, 80–3, 86–92 tooth bending stress 529–534 torque coefficient 61, 101, 591 control 405, 585, 587, 593–4, 597–8, 604, 612, 615 demand 590–4, 597, 598, 600–2, 604, 618, 626, 630, 631 oscillations 425, 527, 598 torque-endurance curves 529, 531 torsional oscillations 413 torsional vibration 598, 599, 602, 610 tower 558–570 bolted flange joint design 565–7 coupling 297–302 design against buckling 560–2 doorways 568

- tower (*Continued*)
 fatigue design 563–5
 height 559, 565, 570
 hybrid 570
 lap joints 567–8
 lattice 569–570, 573
 lift 436, 570
 loading 315–324, 597, 625
 deterministic 319–322
 dynamic response 316–8, 322–3
 extreme 315–6
 fatigue 323–4
 stochastic 319–322, 323
 thrust loading 320–1, 323, 427–8
 natural frequency 317, 322–3, 427, 430,
 558–560, 565, 574
 resonant excitation 316–8, 321–3
 shadow 254–8, 287–8, 301, 328–9, 426–7, 602
 soft 430
 stiff 430
 stiffness 427
 tie-down 568
 tubular 559–568
 vibration 583, 587, 595–7, 611, 615, 620, 621,
 625
 wall imperfections 560
 weight 561–5
- tower base
 critical load case for 315
 fore-aft bending moment 318–323
 load 587, 615
- tracking
 C_p 590, 592, 615
 yaw 581, 585
- trade winds 13
- transfer function 618, 619, 622, 631, 632, 820,
 846, 860
 quasi-static 847, 851, 852, 857
 resonant 849, 851, 855, 856
- transformer 720, 722–3, 726, 731
- transients, electrical 920
- transition piece (monopile) 829–830, 842–3
 bolted joint 829, 842
 sleeved joint 842, 843–5
- transition section (jacket structure) 868–870, 874
- Transmission System Operator 743
- tripile structures 877
- tripod structures 875–7
- tubular towers 559–568
- tuned absorbers 536
- tuned mass damper 500
- tuning 565, 598, 599, 621, 625, 628, 629, 639, 640,
 648, 652
- turbine wake *see* wake
- turbulence 231–9, 241 *et seq.*, 262–6, 271, 276,
 316, 319–320, 325, 328, 480–3, 485, 525–6,
 592, 599, 602, 603, 613, 624
- Extreme Turbulence Model (ETM) 232, 234,
 495, 786
- frozen 28, 263–4
- intensity 12, 17, 20–2, 27, 30, 31, 37, 231–2,
 244, 637–9, 643, 656
- offshore 782–3
- length scale (*see* length scale)
- Mann model 25, 26, 29, 30, 233, 328
- Normal Turbulence Model (NTM) 232, 234,
 235, 480–1, 786, 795
- offshore 776, 780, 782–3, 786, 795
- shear-generated 646
- spectra (*see* spectrum)
- wake 639, 643, 645–7, 649, 651, 655, 660
- TV reception 699
- two-bladed machine 260, 267, 292 *et seq.*, 297,
 299, 309–315, 320–1, 323, 388–391, 525–6,
 557, 875
 comparison with three-bladed 381–7
- two level braking 554
- two-speed operation 402
- ultimate loads 229, 785, 792
- uniaxial (UD) ply 446, 451–7, 459, 460, 470, 471
- unstable stratification 18, 643, 644
- unsteady flow 189–200
- upscaling of FC40 blade design 495
- upwind configuration 254, 376, 426, 441, 888
- vacuum bagging 476
- vacuum resin infusion 476
- variable slip induction generator 403, 540, 585,
 601, 624
- variable speed 406–8
- broad range 405
 operation 585, 590, 598
 narrow range 542–5
- stall regulation 599, 600
- wind turbines 392, 581, 583–6, 590–1, 593, 595,
 598–9, 617, 622, 632, 661
- vector-shift relays 741
- Veers 272–3
- velocity deficit 638–651
- velocity potential 797–800, 802, 811–2, 815
- Vestas four-rotor array 432
- vibration
 monitoring 827–8
 sensor 579, 582
 in stall 496–9

- visual impact 681–5, 910
 visual appearance 379, 387, 678, 910
 voltage
 control 659, 746
 flicker 760–1
 source converter 541
 von Karman
 constant 19, 643
 spectrum 22–30, 233, 262, 271, 273
 vortex generators 122
 vortex cylinder 51, 160
- Wagner function 198, 202, 205
 wake
 advection 641, 651
 control 638–641, 652–4, 656, 658–9
 deflection 647–9
 effects 637–8, 652–3, 655, 659–660
 or flow, expansion 40, 50–1, 57, 641, 644, 650–1
 losses 637, 639, 641, 659, 777–781
 meandering 639–640, 651
 mixing 66, 91
 rotation 45, 54, 84, 170–5, 188
 steering 612, 647, 649, 653–8
 superposition 649, 650
 turbulence intensity 639, 643, 645–7, 649, 651, 655, 660
 velocity deficit 639, 641, 645
 Ainslie model 642–8, 651–2
 width 643–5, 651
 watchdog timer 582
 wave
 climate 784, 785 *et seq.*, 792 *et seq.*, 861, 883
 constrained 793, 818–821
 deep water 793, 798, 801, 806, 809, 813, 848, 895
 design (*see* design wave)
 peak spectral period 785, 788, 793, 820, 888
 period 789, 790, 795, 797, 810, 811, 820, 887
 pile-up 814–7
 Rayleigh distribution 784, 788, 795
 shallow water 795
 spectra 784–7, 855
 wavefront pile-up 814–7
 wave loading
 Airy wave loading 810
 breaking waves 797, 813–8
 diffraction theory 811–3, 851–2
 drag coefficient 805–7, 809
 extreme 793, 822, 840, 899
 fatigue 822, 840–1, 846 *et seq.*
 inertia coefficient 806–9
- Morison's equation 805, 811, 847, 889–892
 non-linear wave loading 784, 805, 810–1, 813, 820–2, 846, 889, 890
 superposition 821
 wake amplification factor 807–8
 Wheeler stretching 810
- wave theories
 Airy 797–802, 805, 809, 810
 Dean's stream function 797, 800–804, 810
 diffraction (*see* diffraction)
 linear 797–803, 818, 820, 822
 Stokes 797, 800
- Weibull distribution 14–16, 31, 32, 240, 277, 371, 451, 525, 667
 three parameter 332 *et seq.*
- Weibull scale factor 16, 454
- Weibull shape factor 15, 16, 370, 451, 454
- Wheeler stretching 810
- wind and wave fatigue combination 858–860
- wind atlas 667
- wind direction change 233, 234, 238, 315
- wind farms
 costs offshore 774
 costs onshore 666
 feasibility assessment 670
 financing, project or non-recourse 677
 planning requirements 676
 procurement 672
 project development 666
 site selection 667
- Wind Float Atlantic semi-submersible 904–6
 monitoring 906
- windmill brake state 68
- wind power capacity worldwide 3–4, 773
- wind shear 18–21, 34, 232–5, 237, 254, 258, 287, 294–5, 311–4, 316, 318, 328–9, 364–5, 387, 478–480, 483–4, 489, 559, 602, 615, 616, 639, 655, 776, 782
 exponent 19, 237, 255, 288, 294, 312, 316, 318, 786, 795, 824
- wind simulation *see* simulations
- wind speed estimation 612–3
- wind speed measurement 613, 671, 777
- wind-wave misalignment 597, 604, 792, 853, 890
- Winkler springs 831
- wire frames 684
- WISPER 465
- wood laminates 445, 447, 471–2
 fatigue properties 472
 properties 471–2
- wood veneer 445, 451
- wound rotor 407, 540, 543, 585

- yaw
angle 153–5, 158–163, 169–171, 173–5, 180–1,
186–9, 302, 308, 651
brake 556, 557, 586
control 586, 611, 612, 615–7
drive 397–8, 424, 555–7, 585
error 233, 586, 792
effect on blade loads 251–3, 478–480
fixed 557
free 557, 585
friction damped 557
misalignment 238, 639, 648–9, 653, 656
moment 177–180, 184–7, 189, 191, 313–5,
387–9, 555–6
offset 653
soft 557
yawed flow 251–3, 327
yawing moment coefficient 185–7
zeros 619, 623
zero-upcrossing frequency 243
zones of theoretical visibility (ZTV) 683
zones of visual impact (ZVI) 683

WILEY END USER LICENSE AGREEMENT

Go to www.wiley.com/go/eula to access Wiley's ebook EULA.